molecules

Special Issue Reprint

Advances of Ionic Liquids in Organic, Polymer and Material Chemistry

Key Trends in Green Chemistry

Edited by
Pradip K. Bhowmik and Biplab Banerjee

mdpi.com/journal/molecules

MDPI

Advances of Ionic Liquids in Organic, Polymer and Material Chemistry: Key Trends in Green Chemistry

Advances of Ionic Liquids in Organic, Polymer and Material Chemistry: Key Trends in Green Chemistry

Guest Editors

Pradip K. Bhowmik
Biplab Banerjee

MDPI

Basel • Beijing • Wuhan • Barcelona • Belgrade • Novi Sad • Cluj • Manchester

Guest Editors
Pradip K. Bhowmik
Department of Chemistry and Biochemistry
University of Nevada Las Vegas
Las Vegas
USA

Biplab Banerjee
Department of Chemistry
Central University of Punjab
Punjab
India

Editorial Office
MDPI AG
Grosspeteranlage 5
4052 Basel, Switzerland

This is a reprint of the Special Issue, published open access by the journal *Molecules* (ISSN 1420-3049), freely accessible at: https://www.mdpi.com/journal/molecules/special_issues/Ionic_Liquids_Chemistry.

For citation purposes, cite each article independently as indicated on the article page online and as indicated below:

Lastname, A.A.; Lastname, B.B. Article Title. *Journal Name* **Year**, *Volume Number*, Page Range.

ISBN 978-3-7258-9203-7 (Hbk)
ISBN 978-3-7258-9204-4 (PDF)
https://doi.org/10.3390/books978-3-7258-9204-4

© 2026 by the authors. Articles in this reprint are Open Access and distributed under the Creative Commons Attribution (CC BY) license. The reprint as a whole is distributed by MDPI under the terms and conditions of the Creative Commons Attribution-NonCommercial-NoDerivs (CC BY-NC-ND) license (https://creativecommons.org/licenses/by-nc-nd/4.0/).

Contents

About the Editors . . . . . **ix**

Pradip K. Bhowmik and Biplab Banerjee
Special Issue: Advances of Ionic Liquids in Organic, Polymer and Material Chemistry: Key Trends in Green Chemistry
Reprinted from: *Molecules* **2026**, *31*, 2852, https://doi.org/10.3390/molecules31162852 . . . . . **1**

Jean C. Carelo, Bluma G. Soares, Debora P. Schmitz, Ruan R. Henriques, Adriana A. Silva, Guilherme M. O. Barra, et al.
Magnetic Ionic Liquid: A Multifunctional Platform for the Design of Hybrid Graphene/Carbon Nanotube Networks as Electromagnetic Wave-Absorbing Materials
Reprinted from: *Molecules* **2025**, *30*, 985, https://doi.org/10.3390/molecules30050985 . . . . . **6**

Maria Atanassova, Nina Todorova and Svetlana Simova
Synergistic Solvent Extraction of Lanthanoids with Traditional Ligands (4-Acylpyrazolone and Bidentate Nitrogen Bases) in a Nontraditional Diluent Confirmed by Slope Analysis and NMR
Reprinted from: *Molecules* **2025**, *30*, 786, https://doi.org/10.3390/molecules30040786 . . . . . **27**

Mark J. Wong, Viral Sagar and Joan G. Lynam
Reconcentrating the Ionic Liquid EMIM-HSO_4 Using Direct Contact Membrane Distillation
Reprinted from: *Molecules* **2025**, *30*, 211, https://doi.org/10.3390/molecules30020211 . . . . . **44**

Shadi Keihankhadiv and Dorota Neugebauer
Polymerizable Cholinium-Based Antibiotics for Polymer Carriers: Systems with Combined Load of Cloxacillin and Ampicillin
Reprinted from: *Molecules* **2024**, *29*, 5973, https://doi.org/10.3390/molecules29245973 . . . . . **53**

Simone Di Muzio, Fabio Ramondo, Oriele Palumbo, Francesco Trequattrini, Pascale Roy, Jean-Blaise Brubach and Annalisa Paolone
Conformational Geometry Matters: The Case of the Low-Melting-Point Systems of Tetrabutylammonium Triflate with Fumaric or Maleic Acid
Reprinted from: *Molecules* **2024**, *29*, 5093, https://doi.org/10.3390/molecules29215093 . . . . . **69**

Piotr Cysewski, Tomasz Jeliński and Maciej Przybyłek
Exploration of the Solubility Hyperspace of Selected Active Pharmaceutical Ingredients in Choline- and Betaine-Based Deep Eutectic Solvents: Machine Learning Modeling and Experimental Validation
Reprinted from: *Molecules* **2024**, *29*, 4894, https://doi.org/10.3390/molecules29204894 . . . . . **88**

Nadir Henni, Amr Henni and Hussameldin Ibrahim
Selectivities of Carbon Dioxide over Ethane in Three Methylimidazolium-Based Ionic Liquids: Experimental Data and Modeling
Reprinted from: *Molecules* **2024**, *29*, 4152, https://doi.org/10.3390/molecules29174152 . . . . . **108**

Tomasz Jeliński, Maciej Przybyłek, Rafał Różalski, Karolina Romanek, Daniel Wielewski and Piotr Cysewski
Tuning Ferulic Acid Solubility in Choline-Chloride- and Betaine-Based Deep Eutectic Solvents: Experimental Determination and Machine Learning Modeling
Reprinted from: *Molecules* **2024**, *29*, 3841, https://doi.org/10.3390/molecules29163841 . . . . . **127**

Urszula Domańska, Anna Wiśniewska, Zbigniew Dabrowski, Dorota Kolasa, Kamil Wróbel and Jakub Lach
Recovery of Metals from the "Black Mass" of Waste Portable Li-Ion Batteries with Choline Chloride-Based Deep Eutectic Solvents and Bi-Functional Ionic Liquids by Solvent Extraction
Reprinted from: *Molecules* **2024**, *29*, 3142, https://doi.org/10.3390/molecules29133142 . . . . . **147**

Eric Quaye, Amr Henni and Ezeddin Shirif
Carbon Dioxide Solubility in Three Bis Tri (Fluromethylsulfonyl) Imide-Based Ionic Liquids
Reprinted from: *Molecules* **2024**, *29*, 2784, https://doi.org/10.3390/molecules29122784 . . . . . **171**

Qiang Zhou, Yunchang Fan and Sheli Zhang
Highly Efficient and Selective Extraction of Gold from Thiosulfate Leaching Solution Using Functionalized Dicationic Ionic Liquids
Reprinted from: *Molecules* **2024**, *29*, 2659, https://doi.org/10.3390/molecules29112659 . . . . . **184**

Fatima Al-Zohbi, Fouad Ghamouss, Johan Jacquemin, Bruno Schmaltz, Mohamad Fadel Tabcheh, Mohamed Abarbri, et al.
Non-Substituted Imidazolium-Based Electrolytes as Potential Alternatives to the Conventional Acidic Electrolytes of Polyaniline-Based Electrode Materials for Supercapacitors
Reprinted from: *Molecules* **2024**, *29*, 2569, https://doi.org/10.3390/molecules29112569 . . . . . **197**

Maria Atanassova, Zhanina Petkova and Vanya Kurteva
Aliquat 336 in Solvent Extraction Chemistry of Metallic ReO_4^- Anions
Reprinted from: *Molecules* **2024**, *29*, 2257, https://doi.org/10.3390/molecules29102257 . . . . . **214**

Asmita Goswami, Navneet Kaur, Manvinder Kaur, Kishanpal Singh, Harvinder Singh Sohal, Haesook Han and Pradip K. Bhowmik
Facile One-Pot Synthesis and Anti-Microbial Activity of Novel 1,4-Dihydropyridine Derivatives in Aqueous Micellar Solution under Microwave Irradiation
Reprinted from: *Molecules* **2024**, *29*, 1115, https://doi.org/10.3390/molecules29051115 . . . . . **228**

Sergey P. Verevkin, Dzmitry H. Zaitsau and Ralf Ludwig
Molecular Liquids versus Ionic Liquids: The Interplay between Inter-Molecular and Intra-Molecular Hydrogen Bonding as Seen by Vaporisation Thermodynamics
Reprinted from: *Molecules* **2023**, *28*, 539, https://doi.org/10.3390/molecules28020539 . . . . . **240**

Nor Azrini Nadiha Azmi, Amal A. M. Elgharbawy, Hamzah Mohd Salleh and Muhammad Moniruzzaman
Preparation, Characterization and Biological Activities of an Oil-in-Water Nanoemulsion from Fish By-Products and Lemon Oil by Ultrasonication Method
Reprinted from: *Molecules* **2022**, *27*, 6725, https://doi.org/10.3390/molecules27196725 . . . . . **255**

Susanna Romano, Serena De Santis, Chiara Frezza, Monica Orsini, Giovanni Sotgiu, Marta Feroci and Daniele Rocco
Ionic Liquids as Starch Plasticizers: The State of the Art
Reprinted from: *Molecules* **2025**, *30*, 1035, https://doi.org/10.3390/molecules30051035 . . . . . **273**

Hao Zhang, Yixuan Liu, Xuehan Wang, Keying Feng, Qilin Wang, Zheng Chen and Zhenhua Jiang
Research Progress in Ionic Liquid-Based Electrolytes for Electrochromic Devices
Reprinted from: *Molecules* **2025**, *30*, 973, https://doi.org/10.3390/molecules30040973 . . . . . **291**

Anastasia Anceschi, Claudia Riccardi and Alessia Patrucco
The Role of Ionic Liquids in Textile Processes: A Comprehensive Review
Reprinted from: *Molecules* **2025**, *30*, 353, https://doi.org/10.3390/molecules30020353 . . . . . **342**

Brian R. Taylor, Nikhil Kumar, Dhirendra Kumar Mishra, Blake A. Simmons, Hemant Choudhary and Kenneth L. Sale
Computational Advances in Ionic Liquid Applications for Green Chemistry: A Critical Review of Lignin Processing and Machine Learning Approaches
Reprinted from: *Molecules* **2024**, *29*, 5073, https://doi.org/10.3390/molecules29215073 . . . . . **365**

Witold Krumplewski and Iwona Rykowska
New Materials for Thin-Film Solid-Phase Microextraction (TF-SPME) and Their Use for Isolation and Preconcentration of Selected Compounds from Aqueous, Biological and Food Matrices
Reprinted from: *Molecules* **2024**, *29*, 5025, https://doi.org/10.3390/molecules29215025 . . . . . **381**

Peng Wang and Rui Wang
Ionic Liquid-Catalyzed CO_2 Conversion for Valuable Chemicals
Reprinted from: *Molecules* **2024**, *29*, 3805, https://doi.org/10.3390/molecules29163805 . . . . . **423**

About the Editors

Pradip K. Bhowmik

Pradip K. Bhowmik received his Ph.D. from the University of Massachusetts Amherst in 1990 and is currently a Professor in the Department of Chemistry and Biochemistry at the University of Nevada Las Vegas. His research focuses on the design, synthesis, and characterization of novel functional polymers, including thermotropic liquid-crystalline polyesters; thermotropic and lyotropic liquid-crystalline poly(pyridinium salt)s; light-emitting poly(pyridinium salt)s and viologen polymers; viologen and viologen polymers as catalysts for carbohydrate fuel cells; and fire-retardant polymers. His research interests also include ionic liquids, ionic liquid crystals, organic ionic plastic crystals for battery applications, fluorescent ionic liquids, and magnetic ionic liquids. In addition, he is developing pyrylium salts that exhibit intense fluorescence in solution and in the solid state, as well as laser and nonlinear optical properties.

Biplab Banerjee

Biplab Banerjee received his Ph.D. from the Indian Association for the Cultivation of Science, Kolkata, India in 2006. Prior to joining as an Assistant Professor in the Department of Chemistry, Central University of Punjab, India, he was a Research Fellow at Nanyang Technological University, Singapore, working on peptide and protein chemistry for biopharmaceutical development. He was also a Senior Research Scientist for Albany Molecular Research at both Singapore and Hyderabad, working on anticancer drug development targeting epigenetic enzymes. His research mainly focuses on synthesis of natural products and synthetic methodology development, medicinal chemistry of anticancer and antibiotic drug development, peptide and protein chemistry, C-H activation, and photocatalysts and nanocatalysts for green chemistry.

molecules

MDPI

Editorial

Special Issue: Advances of Ionic Liquids in Organic, Polymer and Material Chemistry: Key Trends in Green Chemistry

Pradip K. Bhowmik [1,*] and Biplab Banerjee [2]

[1] Department of Chemistry and Biochemistry, University of Nevada Las Vegas, 4505 S. Maryland Parkway Box 454003, Las Vegas, NV 89154-4003, USA
[2] Department of Chemistry, Central University of Punjab, Bathinda 151001, Punjab, India; biplab.banerjee@cup.edu.in
* Correspondence: pradip.bhowmik@unlv.edu

Ionic liquids (ILs) are a class of solvents that have been extensively explored for several decades as promising materials for various applications and continue to be explored due to their tunable physicochemical properties. The physicochemical properties include low melting transitions, a wide liquid range, wide electrochemical windows, viscosity, high density, low surface tension, low vapor pressure, low flammability, wide-range solubility, highly polar yet noncoordinating solvents, and nonvolatility. They can interact with diverse materials through a multitude of interactions, including electrostatic, dispersive, hydrogen bonding, π–π, and dipolar interactions afforded by their readily tunable chemical structures of cations and anions. They are often referred to as designer solvents because most of their physicochemical properties can be tuned by the sheer combination of different cations and anions. They find increasing use across various disciplines, including organic chemistry, polymer chemistry, materials chemistry, inorganic chemistry, analytical chemistry, biotechnology, and medicine. By incorporating certain functional groups into their chemical structures, relatively new subclasses of ILs have emerged in recent years, including polymeric ionic liquids (PILs), magnetic ionic liquids (MILs), zwitterionic ionic liquids (ZILs), dicationic or dianionic liquids (DILs), chiral ionic liquids (CILs), redox-active ionic liquids (RAILs), and fluorescent ionic liquids (FILs). Although there are numerous reviews and books that appeared in the literature on the synthesis, properties, and applications over several decades, it is worthwhile to mention several recent reviews [1–11] on the topic so that trends in the field can be judged. In short, these reviews have detailed applications in drug delivery, biomedical fields [2,8,9], nanoparticle synthesis and organic synthesis [1,7], lubricants [1], biomolecule purifications [4], separations [4], and energy-related applications, including batteries and supercapacitors, fuel cells, dye-sensitized solar cells, and perovskite solar cells [1,3,5,6,10]. Deep eutectic solvents (DESs) are also an emerging class of mixtures of components that are characterized by significant depression in melting points when compared to those of constituent components. They are promising for application as inexpensive designer solvents exhibiting a unique suite of tunable physicochemical properties. They typically can be prepared from the combination of quaternary ammonium salts and metal chlorides or metal chloride hydrates or hydrogen bond donors (HBDs) such as amides, carboxylic acids, and polyols. They can also be synthesized from the combination of metal chloride hydrates and HBDs as well as nonionic versions made of hydrogen bond acceptors (HBAs) and HBDs. In brief, DESs promise superior performances over traditional ILs. They are easy to prepare in high purity without any purification steps and with a 100% atom economy. Noteworthy is the extremely low cost and the large availability of many precursors as bulk chemicals, which make DESs prepared at much lower costs than ILs and

potentially useful for large-scale applications. They have gained a lot of attractions, since they share many of the advantageous properties of ILs, namely negligible vapor pressure, good thermal and chemical stability, non-flammability, and potential as tunable solvents. They are multi-component systems as opposed to ILs [11].

This Special Issue, titled "Advances of Ionic Liquids in Organic, Polymer and Material Chemistry: Key Trends in Green Chemistry", aims to collect 16 research articles of outstanding research groups working with ionic liquids and DESs to shed light on the recent activities in this important field. Interestingly enough, we have also collected six review articles in this Special Issue that certainly demonstrated the ongoing vigorous activities of the ILs and associated ever-increasing new classes of ILs. The articles include many aspects of ILs and DESs ranging from physicochemical properties, separations (solid–liquid and liquid–liquid extractions), and drug delivery systems, among others, thus reflecting the disparate interests of the scientific community active in this field.

The articles described in this Special Issue are as follows: Reconcentrating the ionic liquid EMIM-HSO_4 using direct contact membrane distillation (Contribution 1); determination of enthalpies of vaporization for molecular and ionic liquids using vapor pressure measurements, including quartz crystals, thermogravimetric analysis, and gas chromatographic methods (Contribution 2); conformational geometry matters: the case of the low-melting-point systems of tetrabutylammonium triflate with fumaric or maleic acid (Contribution 3); selectivities of carbon dioxide over ethane in three methylimidazolium-based ionic liquids: experimental data and modeling (Contribution 4); exploration of the solubility hyperspace of selected active pharmaceutical ingredients (APIs) in choline- and betaine-based deep eutectic solvents: machine learning modeling and experimental validation (Contribution 5); and carbon dioxide solubility in three bis(trifluromethylsulfonyl) imide-based ionic liquids to mitigate carbon dioxide emission in Earth's atmosphere (Contribution 6). These articles examine the physicochemical properties of disparate ILs and DESs, including enthalpies of vaporization, solubility and selectivities of CO_2 and ethane, and solubility of APIs. Some of them also include machine learning modeling to explain experimental data. Another group of articles describes tuning ferulic acid solubility in choline–chloride- and betaine-based deep eutectic solvents: experimental determination and machine learning modeling (Contribution 7); synergistic solvent extraction of lanthanoids with traditional ligands (4-acylpyrazolone and bidentate nitrogen bases) in a nontraditional diluent confirmed by slope analysis and NMR (Contribution 8); recovery of metals such as cobalt, nickel, copper, lithium, and manganese from the "black mass" of waste portable Li-ion batteries with choline–chloride-based deep eutectic solvents and bi-functional ionic liquids by solid–liquid extraction (Contribution 9); highly efficient and selective extraction of gold from thiosulfate leaching solution using functionalized dicationic ionic liquids (Contribution 10); and study of Aliquat 336 in liquid–liquid extraction chemistry of ReO_4^- anions, including diluents such as carbon tetrachloride, chloroform, and cyclohexane (Contribution 11). These articles describe the excellent properties of ILs and DESs for the extraction of gold, other metal ions from waste batteries, lanthanoids, and ReO_4^-. Magnetic ionic liquids (MILs) are a unique class of materials that combine the desirable properties of ionic liquids with intrinsic magnetic behavior. This combination enables a range of innovative applications in catalysis, separation, electrochemistry, biomedicine, and environmental remediation. Given their multifunctional nature, MILs have gained significant attention in recent years for developing smart, efficient, and green technologies. In this issue, one article describes MIL is a multifunctional platform for the design of hybrid graphene/carbon nanotube networks as electromagnetic wave-absorbing materials (Contribution 12). Apart from their use in innovative solvents, both ILs and DESs find exponential increases in APIs; antimicrobial, antifungal, and anticancer applications; and even in drug delivery systems

https://doi.org/10.3390/molecules31162852

(DDSs), which are wonderful applications of these materials to the global community. Compared to conventional systems delivering antibiotics without a polymer carrier, the choline-based polymers in DDSs attained satisfactory levels of drug loading content and co-release from the polymer carriers, offering a promising alternative for antibiotic delivery (Contribution 13). Among the many potential applications of ILs and DESs, the most significant one is their use in energy storage systems. The search for clean and sustainable energy has become one of the most important research challenges of this century, and they are considered a class of electrolytes with the most potential for the creation of more advanced and safer energy storage systems, including batteries, supercapacitors, and fuel cells. Non-substituted imidazolium-based electrolytes as potential alternatives to the conventional acidic electrolytes of polyaniline-based (PANI) electrode materials for supercapacitors. These electrolytes could enhance the electrochemical performances of PANI electrodes and could be a good alternative to the conventional electrolytes for supercapacitors (Contribution 14). Green synthesis involves the one-pot synthesis and antimicrobial activity of 1,4-dihydropyridine derivatives in aqueous micellar solution under microwave irradiation (Contribution 15). Another green synthesis is the preparation, characterization, and biological activities of an oil-in-water nanoemulsion from fish by-products and lemon oil by the ultrasonication method (Contribution 16).

Apart from the 16 articles, this Special Issue also includes six excellent reviews written by experts in this important field. They are as follows. Ionic liquids as starch plasticizers: the state of the art (Contribution 17); research progress in ionic liquid-based electrolytes for electrochromic devices (Contribution 18); the role of ionic liquids in textile processes: a comprehensive review (Contribution 19); computational advances in ionic liquid applications for green chemistry: a critical review of lignin processing and machine learning approaches (Contribution 20); new materials for thin-film solid-phase microextraction (TF-SPME) and their use for isolation and preconcentration of selected compounds from aqueous, biological, and food matrices (Contribution 21); and ionic liquid-catalyzed CO_2 conversion for valuable chemicals (Contribution 22).

In conclusion, we believe that this Special Issue, "Advances of Ionic Liquids in Organic, Polymer and Material Chemistry: Key Trends in Green Chemistry", touches on the latest advancements in many aspects related to ILs and DESs, including their use in electrochromic devices, starch composites for biodegradable materials, even computational advances in IL applications for green chemistry, and conversion of CO_2 to valuable products to combat CO_2 emissions. We wish to express our deepest and sincere gratitude to all authors who contributed for having submitted manuscripts of such excellent quality. We also wish to thank the Editorial Office of *Molecules*, especially Ms. Hanna Xiong, for the fast and professional handling of the manuscripts during the whole submission process and for the invaluable help provided to us.

Conflicts of Interest: The authors declare no conflicts of interest.

List of Contributions:

1. Wong, M.J.; Sagar, V.; Lynam, J.G. Reconcentrating the Ionic Liquid EMIM-HSO_4 Using Direct Contact Membrane Distillation. *Molecules* **2025**, *30*, 211.
2. Verevkin, S.P.; Zaitsau, D.H.; Ludwig, R. Molecular Liquids versus Ionic Liquids: The Interplay between Inter-Molecular and Intra-Molecular Hydrogen Bonding as Seen by Vaporisation Thermodynamics. *Molecules* **2023**, *28*, 539.
3. Di Muzio, S.; Fabio Ramondo, F.; Palumbo, O.; Trequattrini, F.; Roy, P.; Brubach, J.-B.; Paolone, A. Conformational Geometry Matters: The Case of the Low-Melting-Point Systems of Tetrabutylammonium Triflate with Fumaric or Maleic Acid. *Molecules* **2024**, *29*, 5093.

https://doi.org/10.3390/molecules31162852

4. Henni, N.; Henni, A.; Ibrahim, H. Selectivities of Carbon Dioxide over Ethane in Three Methylimidazolium-Based Ionic Liquids: Experimental Data and Modeling. *Molecules* **2024**, *29*, 4152.
5. Cysewski, P.; Jeliński, T.; Przybyłek, M. Exploration of the Solubility Hyperspace of Selected Active Pharmaceutical Ingredients in Choline- and Betaine-Based Deep Eutectic Solvents: Machine Learning Modeling and Experimental Validation. *Molecules* **2024**, *29*, 4894.
6. Quaye, E.; Henni, A.; Shirif, E. Carbon Dioxide Solubility in Three Bis Tri (Fluromethylsulfonyl) Imide-Based Ionic Liquids. *Molecules* **2024**, *29*, 2784.
7. Jeliński, T.; Przybyłek, M.; Różalski, R.; Romanek, K.; Wielewski, D.; Cysewski, P. Tuning Ferulic Acid Solubility in Choline-Chloride- and Betaine-Based Deep Eutectic Solvents: Experimental Determination and Machine Learning Modeling. *Molecules* **2024**, *29*, 3841.
8. Atanassova, M.; Todorova, N.; Simova, S. Synergistic Solvent Extraction of Lanthanoids with Traditional Ligands (4-Acylpyrazolone and Bidentate Nitrogen Bases) in a Nontraditional Diluent Confirmed by Slope Analysis and NMR. *Molecules* **2025**, *30*, 786.
9. Domańska, U.; Wiśniewska, A.; Dąbrowski, Z.; Kolasa, D.; Wróbel, K.; Lach, J. Recovery of Metals from the "Black Mass" of Waste Portable Li-Ion Batteries with Choline Chloride-Based Deep Eutectic Solvents and Bi-Functional Ionic Liquids by Solvent Extraction. *Molecules* **2024**, *29*, 3142.
10. Zhou, Q.; Fan, Y.; Zhang, S. Highly Efficient and Selective Extraction of Gold from Thiosulfate Leaching Solution Using Functionalized Dicationic Ionic Liquids. *Molecules* **2024**, *29*, 2659.
11. Atanassova, M.; Petkova, Z.; Kurteva, V. Aliquat 336 in Solvent Extraction Chemistry of Metallic ReO_4^- Anions. *Molecules* **2024**, *29*, 2257.
12. Carelo, J.C.; Soares, B.G.; Schmitz, D.P.; Henriques, R.R.; Silva, A.A.; Barra, G.M.O.; Barthem, V.M.T.S.; Livi, S. Magnetic Ionic Liquid: A Multifunctional Platform for the Design of Hybrid Graphene/Carbon Nanotube Networks as Electromagnetic Wave-Absorbing Materials. *Molecules* **2025**, *30*, 985.
13. Keihankhadiv, S.; Neugebauer, D. Polymerizable Cholinium-Based Antibiotics for Polymer Carriers: Systems with Combined Load of Cloxacillin and Ampicillin. *Molecules* **2024**, *29*, 5973.
14. Al-Zohbi, F.; Ghamouss, F.; Jacquemin, J.; Schmaltz, B.; Tabcheh, M.F.; Abarbri, M.; Cherry, K.; Tran-Van, F. Non-Substituted Imidazolium-Based Electrolytes as Potential Alternatives to the Conventional Acidic Electrolytes of Polyaniline-Based Electrode Materials for Supercapacitors. *Molecules* **2024**, *29*, 2569.
15. Goswami, A.; Kaur, N.; Kaur, M.; Singh, K.; Sohal, H.S.; Han, H.; Bhowmik, P.K. Facile One-Pot Synthesis and Anti-Microbial Activity of Novel 1,4-Dihydropyridine Derivatives in Aqueous Micellar Solution under Microwave Irradiation. *Molecules* **2024**, *29*, 1115.
16. Azmi, N.A.N.; Elgharbawy, A.A.M.; Salle, H.M.; Moniruzzaman, M. Preparation, Characterization and Biological Activities of an Oil-in-Water Nanoemulsion from Fish By-Products and Lemon Oil by Ultrasonication Method. *Molecules* **2022**, *27*, 6725.
17. Romano, S.; De Santis, S.; Frezza, C.; Orsini, M.; Sotgiu, G.; Feroci, M.; Rocco, D. Ionic Liquids as Starch Plasticizers: The State of the Art. *Molecules* **2025**, *30*, 1035.
18. Zhang, H.; Liu, Y.; Wang, X.; Feng, K.; Wang, Q.; Chen, Z.; Jiang, Z. Research Progress in Ionic Liquid-Based Electrolytes for Electrochromic Devices. *Molecules* **2025**, *30*, 973.
19. Anceschi, A.; Riccardi, C.; Patrucco, A. The Role of Ionic Liquids in Textile Processes: A Comprehensive Review. *Molecules* **2025**, *30*, 353.
20. Taylor, B.R.; Kumar, N.; Mishra, D.K.; Simmons, B.A.; Choudhary, H.; Sale, K.L. Computational Advances in Ionic Liquid Applications for Green Chemistry: A Critical Review of Lignin Processing and Machine Learning Approaches. *Molecules* **2024**, *29*, 5073.
21. Krumplewski, W.; Rykowska, I. New Materials for Thin-Film Solid-Phase Microextraction (TF-SPME) and Their Use for Isolation and Preconcentration of Selected Compounds from Aqueous, Biological and Food Matrices. *Molecules* **2024**, *29*, 5025.
22. Wang, P.; Wang, R. Ionic Liquid-Catalyzed CO_2 Conversion for Valuable Chemicals. *Molecules* **2024**, *29*, 3805.

https://doi.org/10.3390/molecules31162852

References

1. King, D.; Han, H.; Bhowmik, P.K. Dicationic Ionic Liquids as Green Functional Materials. *RSC Adv.* **2026**, *16*, 34385–34421. [CrossRef] [PubMed]
2. Zhao, Y.; Zhen, Y. Recent progress of ionic liquids for life science applications: A critical review. *Results Chem.* **2026**, *26*, 103328. [CrossRef]
3. Al-Bodour, A.; Alomari, N.; Perez-Duran, G.; Rozas, S.; Iglesias-Silva, G.; Aparicio, S.; Gutierrez-Vega, A.; Atilhan, M. Ionic Liquids as Multidimensional Materials: A Review from Fundamentals to Applications. *Energy Fuels* **2025**, *39*, 12791–12829. [CrossRef]
4. Zeger, V.R.; Thapa, B.; Shamsaei, D.; DeLair, J.F.; Tristen, L.; Taylor, T.L.; Anderson, J.L. Ionic Liquids in Analytical Chemistry: Fundamentals, Technological Advances, and Future Outlook. *Anal. Chem.* **2025**, *97*, 4793–4818. [CrossRef] [PubMed]
5. Alreshidi, M.A.; Yadav, K.K.; Gunasekaran, S.; Gacem, A.; Sambandam, P.; Subbiah, G.; Bhutto, J.K.; Palanivel, S.; Fallatah, A.M.; El-Khair, M.A.A.; et al. A review on the evolution of ionic liquids: Sustainable synthesis, applications, and future prospects. *Mater. Today Sustain.* **2025**, *31*, 101160. [CrossRef]
6. Matuszek, K.; Piper, S.L.; Brzeczek-Szafran, A.; Roy, B.; Saher, S.; Pringle, J.M.; MacFarlane, D.R. Unexpected Energy Applications of Ionic Liquids. *Adv. Mater.* **2024**, *36*, 2313023. [CrossRef] [PubMed]
7. Dupont, J.; Leal, B.C.; Lozano, P.; Monteiro, A.L.; Migowski, P.; Jackson, D.; Scholten, J.D. Ionic Liquids in Metal, Photo-, Electro-, and (Bio) Catalysis. *Chem. Rev.* **2024**, *124*, 5227–5420. [CrossRef] [PubMed]
8. Hu, Y.; Xing, Y.; Yue, H.; Chen, T.; Diao, Y.; Wei, W.; Zhang, S. Ionic liquids revolutionizing biomedicine: Recent advances and emerging opportunities. *Chem. Soc. Rev.* **2023**, *52*, 7262–7293. [CrossRef] [PubMed]
9. Shamshina, J.L.; Rogers, R.D. Ionic Liquids: New Forms of Active Pharmaceutical Ingredients with Unique, Tunable Properties. *Chem. Rev.* **2023**, *123*, 11894–11953. [CrossRef] [PubMed]
10. Zhou, T.; Gui, C.; Sun, L.; Hu, Y.; Lyu, H.; Wang, Z.; Song, Z.; Yu, G. Energy Applications of Ionic Liquids: Recent Developments and Future Prospects. *Chem. Rev.* **2023**, *123*, 12170–12253. [CrossRef] [PubMed]
11. Di Pietro, M.E.; Mele, A. Deep eutectics and analogues as electrolytes in batteries. *J. Mol. Liq.* **2021**, *338*, 116597. [CrossRef]

Disclaimer/Publisher's Note: The statements, opinions and data contained in all publications are solely those of the individual author(s) and contributor(s) and not of MDPI and/or the editor(s). MDPI and/or the editor(s) disclaim responsibility for any injury to people or property resulting from any ideas, methods, instructions or products referred to in the content.

molecules

MDPI

Article

Magnetic Ionic Liquid: A Multifunctional Platform for the Design of Hybrid Graphene/Carbon Nanotube Networks as Electromagnetic Wave-Absorbing Materials

Jean C. Carelo [1], Bluma G. Soares [1,2,*], Debora P. Schmitz [2], Ruan R. Henriques [2], Adriana A. Silva [3], Guilherme M. O. Barra [4], Vitoria M. T. S. Barthem [5] and Sebastien Livi [6,*]

1 Centro de Tecnologia, COPPE-PEMM, Universidade Federal do Rio de Janeiro, Bl. F, Rio de Janeiro 21941-598, Brazil; jeancarelo@metalmat.ufrj.br
2 Centro de Tecnologia, Instituto de Macromoléculas, Universidade Federal do Rio de Janeiro, Bl. J, Rio de Janeiro 21941-598, Brazil; dehschmitz@gmail.com (D.P.S.); ruanhenriara@gmail.com (R.R.H.)
3 Centro de Tecnologia, Escola de Química, Universidade Federal do Rio de Janeiro, Bl. E, Rio de Janeiro 21941-909, Brazil; anjosadriana@eq.ufrj.br
4 Departamento de Engenharia Mecânica, Universidade Federal de Santa Catarina, Florianópolis 88040-900, Brazil; guiga@emc.ufsc.br
5 Centro de Tecnologia, Instituto de Física, Universidade Federal do Rio de Janeiro, Bl. A, Rio de Janeiro 21941-909, Brazil; vitoria@if.ufrj.br
6 Université de Lyon, CNRS, Université Claude Bernard Lyon 1, INSA Lyon, Université Jean Monnet, UMR 5223, Ingénierie des Matériaux Polymères, CEDEX F-69621 Villeurbanne, France
* Correspondence: bluma@metalmat.ufrj.br (B.G.S.); sebastien.livi@insa-lyon.fr (S.L.)

Abstract

Magnetic ionic liquid (MIL) based on alkyl phosphonium cation was used as a curing agent for developing epoxy nanocomposites (ENCs) modified with a graphene nanoplatelet (GNP)/carbon nanotube (CNT) hybrid filler. The materials were prepared by a solvent-free procedure involving ball-milling technology. ENCs containing as low as 3 phr of filler (GNP/CNT = 2.5:0.5 phr) exhibited electrical conductivity with approximately six orders of magnitude greater than the system loaded with GNP = 2.5 phr. Moreover, the use of MIL (10 phr) resulted in ENCs with higher conductivity compared with the same system cured using conventional aliphatic amine. The filler dispersion within the epoxy matrix was confirmed by scanning electron microscopy (SEM) and transmission electron microscopy (TEM). The electromagnetic interference shielding effectiveness (EMI SE), evaluated in the X- and Ku-band frequency range, revealed a great contribution of the absorption mechanism for the ENC containing the hybrid filler and cured with MIL. Moreover, the best microwave-absorbing response was achieved with the ENC containing GNP/CNT = 2.5/0.5 phr, and cured with ML, which a minimum RL of −23.61 dB and an effective absorption bandwidth of 5.18 GHz were observed for thickness of 1.5 mm. In summary, this system is a promising material for both civilian and military applications due to its simple and scalable nanocomposite preparation method, the lightweight nature of the composites resulting from the low filler content, the commercial availability and cost-effectiveness of GNP, and its high electromagnetic wave attenuation across a broad frequency range.

Keywords: epoxy resin; magnetic ionic liquid; graphene nanoplatelet; hybrid filler; electromagnetic interference shielding effectiveness; microwave-absorbing properties

1. Introduction

Electromagnetic interference (EMI) poses a significant challenge in modern electronic devices and systems, creating a strong demand for advanced materials with enhanced electromagnetic wave-absorbing properties [1–3]. Conductive polymer composites are commonly used in this context due to their low cost, lightweight nature, ease of processing, and versatility in production with different designs. Moreover, the conductivity and dielectric/magnetic properties of these composites can be easily tailored by selecting suitable fillers and polymer matrices, as well as optimizing the dispersion process [1,4–6].

Epoxy matrices are versatile thermosetting materials, widely used in applications such as coatings, adhesives, fiber-based composites, and electronic devices [7]. For electromagnetic wave (EMW) absorption applications, it is necessary to add conductive and dielectric/magnetic fillers that are able to interact with the incident EMW. In this context, carbon-based fillers, such as carbon nanotube (CNT) and graphene-related materials (graphene nanoplatelets (GNPs), expanded graphite (EG), reduced graphene oxide (rGO) and thermally reduced graphene oxide (TRGO)) have been extensively explored for EMI shielding/absorbing applications [8–15]. Among these graphene materials, GNP is a commercially viable product with relatively low cost, making it ideal for large-scale production. The effectiveness of GN-based epoxy systems for EMW shielding/absorption materials has been discussed in several reports and reviews [10,12]. GNPs are available with varying number of layers and surface areas, which significantly influence the electrical, dielectric, and EMI shielding/absorbing properties of the corresponding composites [16,17].

For example, Kargar et al. [18] blended commercially available few-layer graphene with epoxy resin and achieved a total EMI shielding effectiveness (EMI SE) of 45 dB for the composite 1 mm thick, containing 50 wt% filler content. Liang et al. [19] reported an EMI SE of 21 dB for the epoxy/rGO composite with 3 mm thickness and 15 wt% of filler. Ahmad et al. [20] prepared epoxy composites with 5 wt% of rGO and 6 mm thickness, observing EMI SE ranging from 5 to 25 dB as the microwave frequency varied between 8 and 12 GHz. The attenuation of the radiation through the absorption of epoxy/GNP nanocomposites has also been studied using the reflection loss (RL) parameter. For instance, Min et al. [21] prepared epoxy/GNP composites via a solution method and reported an RL value of −38 dB for a composite containing 2 wt% GNP with a thickness of 1.5 mm. Wang et al. [22] observed a minimum RL of −14.5 dB at 18.9 GHz for epoxy/GNP composite with 15 wt% GNP loading. Silva et al. [23] reported an RL value of −11.7 dB at 8.75 GHz with 0.9 vol% of GNP. These varying results can be attributed to differences in the GNP suppliers, which affect factors such as exfoliation degree, surface area, number of layers, and the synthetic procedure for preparing epoxy/GNP composites.

GNP faces significant dispersion challenges due to strong van der Waals forces and π-π stacking interactions. As a result, relatively large amounts of GNP (10–50 wt%) are often required to achieve EMI SE greater than 10 dB, corresponding to 90% of EMW attenuation [12,17,24]. High filler content, however, can lead to poor mechanical performance, processing difficulties, and increased costs. To address these issues, various strategies have been explored. Recent studies have shown that combining GNP with CNT can significantly enhance the electrical conductivity [25], mechanical strength, rheological behavior, and thermal properties of epoxy composites [26–35]. The GNP/CNT hybrid prevents self-aggregation and re-stacking of graphene layers, improving the electrical response due to the formation of a three-dimensional percolated structure, where the flexible CNTs act as bridges between the planar GNP nanoplatelets [29,36]. These hybrid fillers offer an economical solution for developing conducting polymer composites with low filler content [34].

Several studies have reported on the EMI shielding/absorbing properties of epoxy composites containing hybrid fillers, including graphene-related materials (GNP, rGO, etc.)

and CNT. For example, Kang et al. [37] prepared rGO/single-walled carbon nanotube hybrids by chemical-grafting CNT onto GO, followed by reduction. The addition of 15% of this hybrid to an epoxy matrix resulted in an EMI SE of approximately 71 dB at 12 GHz. Han et al. [38] grafted vertical edge-rich graphene onto a CNT sponge and blended it with epoxy resin, achieving an EMI SE of 46.9 dB in the X-band (8–12 GHz) with a thickness of 1 mm. Lee et al. [39] mixed commercial GNP and CNT with epoxy resin in a three-roll mill, reporting an EMI SE of 27 dB at 100 MHz with a 50:50 GNP/CNT hybrid (10 wt% total filler). Huangfu et al. [40] prepared epoxy composites with varying amounts of CNT/thermally annealed graphene aerogel and reported an EMI SE of approximately 35 dB in the 8–12 GHz frequency range. Zhang et al. [41] synthesized reduced graphene/CNT oxides from mixed powders of expanded graphite and CNT, achieving an RL of −61.8 dB with a 1 wt% hybrid in an epoxy network with a thickness of 1.9 mm. An epoxy/GNP/CNT hybrid with foamed structure was also developed by Liu et al. [42], obtaining RL of −20 dB. Yazdi et al. [43] reported an EMI SE value of 14 dB at 8.2 GHz for an epoxy composite containing TRGO/CNT (2.5:2.5 wt%), and 11 dB for epoxy with 8 wt% CNT.

Non-covalent functionalization agents can improve the dispersion of carbon nanomaterials without affecting their electrical conductivity. In this context, ionic liquids (ILs) play a crucial role, as they can interact with the carbon surface via π-cation and van der Waals forces [44,45]. Several studies have used ILs to enhance the dispersion of CNT in epoxy matrices [46–49], although their use in GNP-based systems remains underexplored. Imidazolium-based ILs with chloride as the counteranion were used to modify GNP [50] and GO [51], enhancing the thermal and mechanical properties of epoxy composites. Liu et al. [52] achieved better dispersion of GNP in an epoxy system by pre-treating it with 1-aminopropyl-3-butylimidazolium hexafluorophosphate. The enhancement of EMW absorption properties in epoxy/GNP systems has been reported by using GNP functionalized with 1-butyl-3-methyl-imidazolium bis(trifluormethylsulfonyl) imide [23]. Additionally, the dual role of magnetic phosphonium- and imidazolium-based ILs as curing agents for epoxy resin and additives for enhancing EMW-absorbing properties has been demonstrated [53]. The presence of 10 phr (9.1 wt%) of magnetic phosphonium IL resulted in RL values of around −13 dB (≈96% of EMW attenuation) at 9.5 GHz.

Building on these foundational studies, the present work aimed to investigate the multifunctional effects of phosphonium-based magnetic ionic liquid (MIL) in an epoxy system containing GNP/CNT hybrids. As discussed in several reports and reviews, the combination of magnetic and dielectric materials in a composite can enhance the microwave absorption performance [54–58]. Although the magnetic ionic liquid exhibits relatively low magnetic loss, its combination with carbonaceous fillers can improve electrical conductivity and enhance microwave absorption properties. Thus, the advantages of using MIL as the curing agent were based on its multifunctionality, that is, its ability to disperse the carbonaceous filler, the ability of curing the epoxy resin with relatively low amount of material, when compared with conventional aliphatic amine and anhydride as hardeners, and the introduction of some magnetic characteristics, which improve the microwave absorption properties. By leveraging the properties of magnetic ILs and the synergistic effects of GNP/CNT hybrids, this study seeks to enhance electrical conductivity, mechanical strength, rheological behavior, thermal properties, and EMI shielding/absorption effectiveness, paving the way for advanced materials in EMI applications.

2. Results and Discussion

2.1. AC Conductivity of the Epoxy Composites

The AC conductivity (σ_{AC}) versus frequency curves for ER/GNP and ER/GNP/CNT hybrids cured with magnetic ionic liquid (MIL) are shown in Figure 1a. The composite

containing 2.2 wt% of GNP (ER/GNP.MIL$_B$) exhibits a typical insulating behavior, characterized by the linear relationship between σ_{AC} and frequency. Increasing the amount of GNP to 8.3 wt% resulted in an increase in σ_{AC} by one order of magnitude and the presence of a very small σ_{DC} plateau at low frequency, but the insulating behavior was still observed. This result suggests that the commercial GNP grade used in this work was not well exfoliated, and its dispersion within the epoxy matrix was insufficient to form a conductive pathway, even at 8.3 wt% of GNP. A similar behavior was reported in the literature for epoxy systems modified with 10 wt% GNP [16].

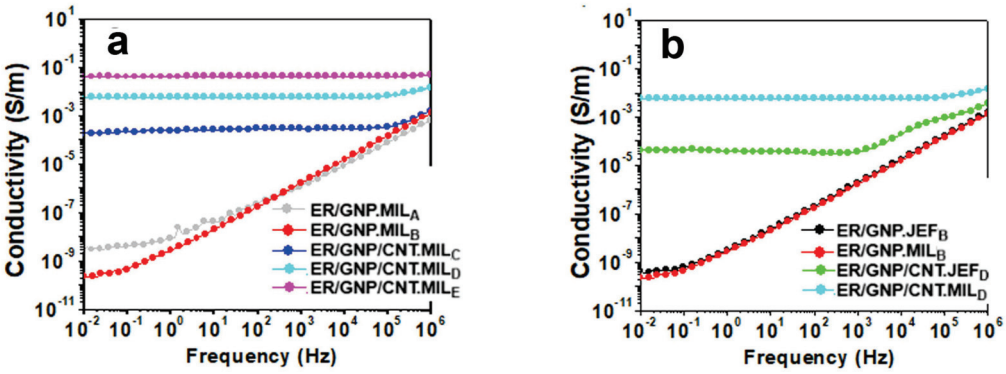

Figure 1. AC conductivity (σ_{AC}) as a function of frequency for ER composites. (**a**) ER/GNP and ER/GNP/CNT cured with MIL; (**b**) comparison between the composites cured with MIL and with Jeffamine D230.

As discussed in the Introduction, the combination of CNT with GNP leads to a synergistic effect in terms of electrical conductivity because the fillers can interact with each other, preventing aggregation and re-stacking of graphene layers [29,31,36]. Therefore, the impact of different CNT amounts on the conductivity of the ER/GNP.MIL systems containing 2.2 wt% of GNP was investigated. As observed in Figure 1a, the addition of just 0.2 wt% of CNT resulted in a significant increase in conductivity, by around six orders of magnitude, reaching a value of 2×10^{-4} S/m at low frequency. Another notable feature is the presence of a σ_{DC} plateau up to a frequency of 10^5 Hz, which characterizes the material as conductive. As stated in various reports, GNP presents a higher tendency of agglomeration and re-stacking than CNT, decreasing the chance in creating the conductive network structure [39,59,60]. On the other hand, CNT, with its one-dimensional structure and higher aspect ratio, can be more easily dispersed in a polymeric matrix. Thus, the addition of a low amount of CNT exerted a positive influence on the electric conductivity of the ER/GNP composites. The CNTs help with the dispersion of GNPs by acting as a bridge between the GNP platelets, facilitating the deagglomeration of GNP and promoting the formation of a three-dimensional percolated structure that enhances the electrical response. This result is interesting because a high conductivity value can be achieved with only 2.4 wt% of filler, which is advantageous for processing the material and reducing cost. Increasing the CNT content further increased the conductivity.

To highlight the dual role of the magnetic ionic liquid (MIL) as both hardener and dispersing agent for the filler, ER/GNP and ER/GNP/CNT were also cured with the conventional aliphatic amine, Jeffamine®D230. For this study, the proportions of GNP/CNT were kept as 2.5/0.5 phr because of the acceptable electrical conductivity and the superior microwave-absorbing properties achieved with this composition. Furthermore, the viscosity was not so high as to affect the processability and dispersion of the fillers. Figure 1b compares the results. The nature of the curing agent did not affect the conductivity of the ER/GNP binary system. Both ER/GNP.MIL$_B$ (2.2 wt% of GNP) and ER/GNP.JEF$_B$ (1.9 wt% of GNP) exhibited similar insulating behavior.

It is important to point out that the ER composites containing the GNP/CNT hybrid filler presented higher conductivity than those loaded with only GNP as the filler, regardless of the nature of the curing system. By comparing the two systems with GNP/CNT hybrid filler, the one cured with MIL presented conductivity value by more than two orders of magnitude higher than the system cured with Jeffamine. The former composite contained a slightly larger amount of GNP (GNP/CNT = 2.2: 0.4 wt%) than that cured with Jeffamine (GNP/CNT—1.8:0.4 wt%), which may be one factor that contributed for its higher conductivity value. However, the difference in the amount of GNP was not excessive. Thus, one can suggest that the MIL interacts with the carbonaceous fillers through cation–π interactions, thus enhancing the dispersion of the fillers, which favors the formation of the three-dimensional networked structure responsible for the increase in electrical conductivity. This characteristic is also suggested from XRD experiments, discussed lately.

2.2. Rheology of Uncured Epoxy Dispersions

Rheological analysis is commonly employed to assess the dispersion behavior of fillers within a polymer matrix. Figure 2a presents the complex viscosity (η*) as a function of frequency, measured at 25 °C, for the epoxy systems before curing. The η* of neat epoxy remained constant across frequencies, characteristic of a Newtonian fluid. A similar trend and η* value were observed for the ER/GNP.MIL$_B$ (2.2 wt% GNP) system. When the GNP content was increased to 8.33 wt%, η* also increased, yet the system maintained its Newtonian behavior. The incorporation of CNT into the ER/GNP.MIL system led to a rise in η* at low frequency, with the effect becoming more pronounced as the CNT content in the hybrid increased. Moreover, the composites with hybrid fillers exhibited shear thinning behavior, which became more prominent with increasing CNT content [61]. This behavior is attributed to the formation of a three-dimensional physical network of fillers within the epoxy matrix, induced by interactions between the fillers, thereby confirming better filler dispersion within the matrix [62]. Figure 2b compares η* versus frequency for the uncured systems containing MIL and Jeffamine. In the case of the ER/GNP system, replacing MIL with Jeffamine resulted in a slight increase in η*, suggesting a plasticizing effect of the ionic liquid. However, for the ER/GNP/CNT system, the η* remained similar. We hypothesize that MIL interacts with CNT, leading to an increase in viscosity, which is counterbalanced by the plasticizing effect of the MIL. Consequently, the interactions between MIL and CNT prevent a decrease in viscosity, resulting in the ER/GNP/CNT/MIL composite exhibiting a viscosity similar to that of the ER/GNP/CNT/Jef composite.

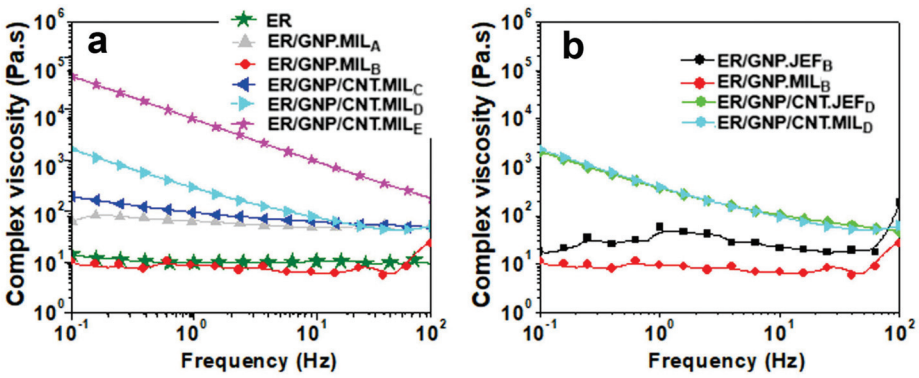

Figure 2. Complex viscosity as a function of frequency for ER composites. (**a**) ER/GNP and ER/GNP/CNT cured with MIL; (**b**) comparison between the composites cured with MIL and with Jeffamine D230.

Figure S1 illustrates the relationship between the elastic and viscous moduli, revealing a marked variation in the viscoelastic behavior of the composites. The straight line in the graph represents the points where the elastic modulus (G′) equals the viscous modulus (G″). Above this line, known as the equimodular line, the elastic component dominates the material's behavior, while below it, viscous mechanisms have a greater influence on the sample's properties [63]. The Han Plot, or modified Cole–Cole plot, shows the correlation between CNT concentration and viscoelastic behavior. Composites with a low CNT concentration lie below the percolation line, indicating a predominance of viscous behavior. On the other hand, at a CNT concentration of 0.4 wt%, rheological percolation occurs, as shown by the alignment of the curves with the equimodular line, suggesting the formation of networks that balance both elastic and viscous properties. Notably, composites with higher CNT content, such as ER/GNP/CNT.MIL$_E$, exhibit a dominance of elastic properties, reflecting greater material rigidity. This underscores the significant impact of CNT concentration on the formation of the physical network.

2.3. XRD and Morphology of Hybrid System

Figure 3 presents the XRD profiles of the composites cured with MIL and Jeffamine. The XRD diffractogram of neat GNP is shown in Figure S2. Neat GNP exhibits an intense diffraction peak at 2θ = 26.43° (d-spacing: 03.37 Å) and a small peak at 2θ = 44.6°, related to the (002) and (100) crystallographic planes of the graphitic structure, respectively. The nanocomposites present a wide diffraction peak from 10° to 28°, attributed to the scattering of the cured epoxy molecules, along with the sharp peak at 2θ = 26.43° related to the graphite planes. This second peak suggests that the GNP layers could not be completely exfoliated. Nevertheless, the intensity of the peak related to the graphite layers varied, indicating some degree of exfoliation. In this context, the ER/GNP.JEF$_B$ displayed the more intense peak, indicating a lower degree of graphite exfoliation. On the other hand, the peak intensity corresponding to the GNP in the composite cured with MIL (ER/GNP.MIL$_B$) significantly decreased, suggesting an increase in the exfoliation degree promoted by the presence of MIL as the curing agent. This result confirms the efficiency of the ionic liquid as a dispersing agent for the GNP filler. The presence of CNT in the composites cured with both Jeffamine and MIL decreased the peak intensity, suggesting an increase in the exfoliation due to the presence of CNT. This behavior confirms the role of MIL as dispersing agent for the carbonaceous filler, and as the curing agent for the epoxy matrix.

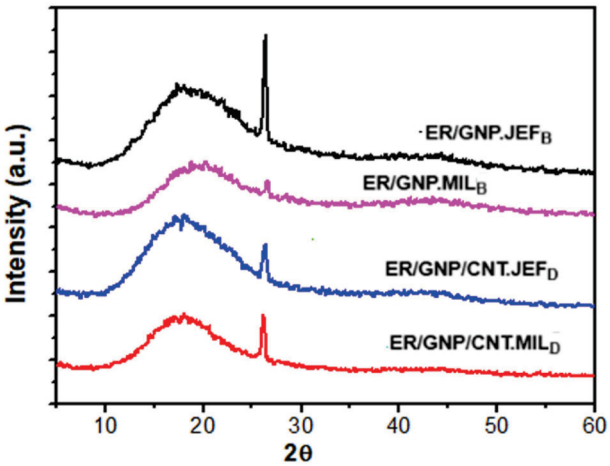

Figure 3. XRD profiles of the ER-based composites.

The effect of MIL on the dispersion of the filler within the epoxy network was evaluated using SEM and TEM microscopy. Figure 4 compares SEM images for ER/GNP and

ER/GNP/CNT nanocomposites cured with MIL and Jeffamine D230. The ER/GNP.MIL$_B$ composite (2.2 wt% GNP) (Figure 4a) displayed more dispersed GNP platelets compared to similar system ER/GNP.JEF$_B$ (Figure 4b). This result indicates that MIL not only serves as the curing agent but also acts as a dispersing agent for the GNP, as was also observed in the XRD analysis. The ER/GNP/CNT.MIL$_D$ system, cured with MIL (Figure 4c), showed even better filler dispersion. In this image, some white spots, attributed to CNT, are observed between the GNP platelets, forming the so-called "bridge" that enhances the conducting pathway. The hybrid system cured with Jeffamine also exhibited some thin layers of GNP (Figure 4d). However, GNP aggregates were also present.

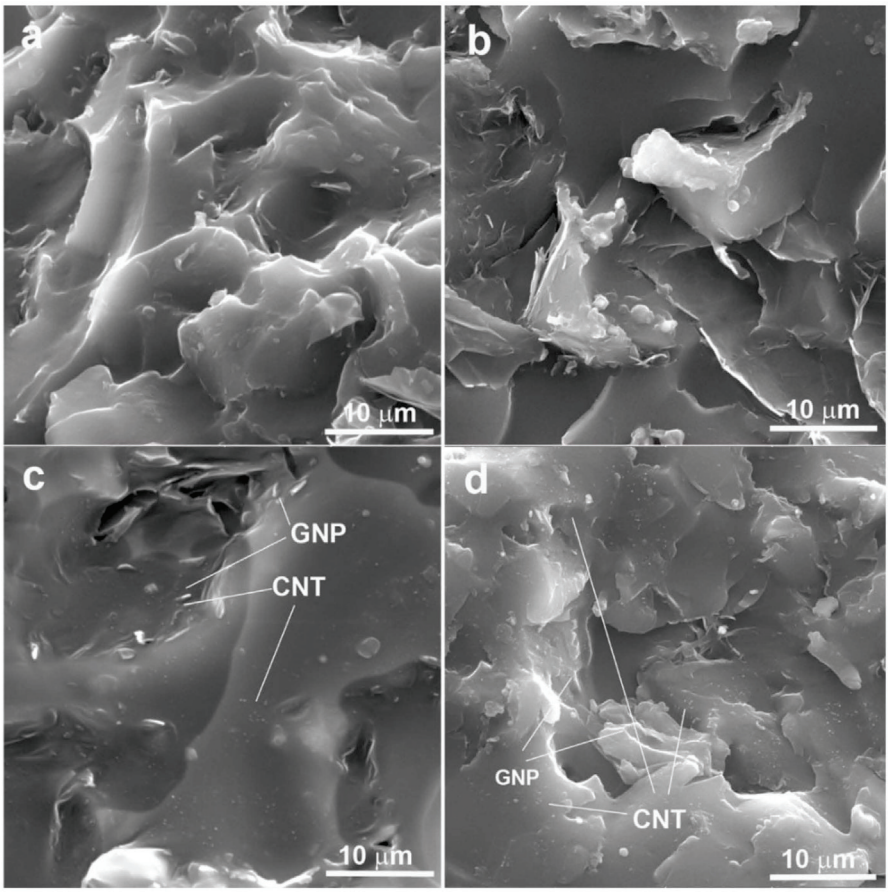

Figure 4. SEM images of (**a**) ER/GNP.MIL$_B$; (**b**) ER/GNP.JEF$_B$; (**c**) ER/GNP/CNT.MIL$_D$, and (**d**) ER/GNP/CNT.JEF$_D$.

The EDS spectra and mapping of the cross-section of ER/GNP.MIL$_B$ and ER/GNP/CNT.MIL$_D$ composites are exhibited in Figure S3 of the Supplementary Materials. The presence of P, Cl, and Fe in the EDS profiles of both systems revealed the presence of the MIL. Moreover, the elemental mapping confirms the homogeneous distribution of the MIL throughout the sample.

The TEM images of ER/GNP/CNT.MIL$_D$ and ER/GNP/CNT.JEF$_D$ are displayed in Figure 5. In both images, it is possible to observe the presence of CNT interacting with the GNP platelets, confirming that CNT acts as a bridge favoring the dispersion of GNP. Furthermore, the CNTs are well dispersed in these systems, which explain the superior conductivity of the hybrid composites.

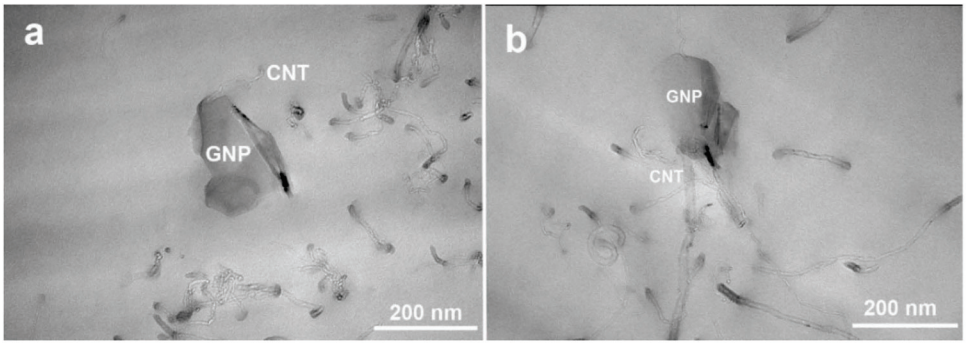

Figure 5. TEM images of (**a**) ER/GNP/CNT.JEF$_D$ and (**b**) ER/GNP/CNT.JEF$_D$ composites.

2.4. Magnetic Properties of Composites Cured with MIL

The magnetic properties of neat MIL (P_{66614}[$FeCl_4$]) and the ER-based composites cured with MIL (ER/GNP.MILB and ER/GNP/CNT.MILD) are illustrated in Figure 6. The magnetization curve for the neat MIL (Figure 6a) presented a linear dependence of the magnetization with the applied magnetic field, indicating paramagnetic behavior [64]. The magnetic susceptibility of (P_{66614}[$FeCl_4$]) was determined from the slope of the fitted line as 6.16×10^{-5} emu/g. Thus, the Curie–Weiss law described in Equation (1) can be applied to determine the main magnetic parameters:

$$\chi^{-1} = \frac{T}{C} - \frac{\theta_P}{C} \tag{1}$$

where χ is the magnetic susceptibility, C is the Curie constant, and θ_P is the paramagnetic Weiss temperature that is proportional to the intensity of the magnetic moment interactions [65].

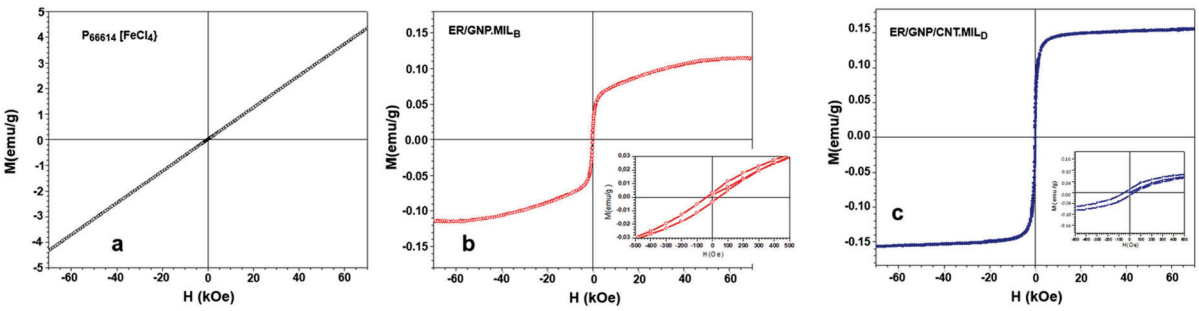

Figure 6. Hysteresis curves at 300 K for the ionic liquid P_{66614}[$FeCl_4$] (MIL) (**a**), and the composites ER/GNP.MIL$_B$ (**b**) and ER/GNP/CNT.MIL$_D$ (**c**), as a function of the applied magnetic field. The inset in (**b**) and (**c**) show the coercivity of about 40 Oe of theses composites.

The thermal variation of the inverse magnetic susceptibility is presented in Figure S4A of the Supplementary Materials. From this Figure, the C and θ_P values corresponding to 0.019 emu K/g OE and -8 K were obtained, which are in agreement with the literature [66]. The negative value of θ_P indicates antiferromagnetic coupling between the magnetic moments. Figure S4B exhibits the thermal variation of magnetization for the neat MIL under a magnetic field of 30,000 Oe. The magnetization increased with the temperature up to 8 K, after which it decreased, following a paramagnetic thermal transition. The reduction in moment for temperatures below 8 K can be associated with the change in moment direction toward an antiparallel alignment. Since θ_P is proportional to the intensity of magnetic interactions, the small magnitude of θ_P (8 K) indicates that these interactions are very weak, as expected for diluted [$FeCl_4$]$^-$ magnetic anions in an ionic liquid matrix.

The hysteresis curves at 300 K for the ER composites are presented in Figure 6b,c, and exhibited the typical S-shape magnetic hysteresis. The magnetization profile of ER/GNP.MILB (Figure 6b) agrees with a mixture of ferromagnetic contribution (evidenced by the saturation) and a slight paramagnetic contribution (indicated by the small linear contribution before saturation). Regarding the composite loaded with the hybrid filler (ER/GNP/CNT.MILD), the curve indicates that the saturation was achieved at low fields, suggesting a "soft" ferromagnetic behavior. The magnetization saturation for the ER/GNP.MIL_B and ER/GNP/CNT.MIL_D corresponded to 0.113 emu/g and 0.155 emu/g, respectively. These values are significantly lower than those usually observed for other magnetic materials, due to the very low amount of $FeCl_4$ in the materials. Liu et al. [67] also reported the magnetization hysteresis of epoxy containing the Fe_3O_4/GNP hybrid. The presence of 0.5% of filler displayed saturation magnetization of 0.63 emu/g. The coercitivity (Hc) of the ER/GNP.MIL_B and ER/GNP/CNT.MIL_D composites is illustrated in the insert of Figures 6b and 6c, respectively. In both composites, a coercitivity of around 40 Oe was observed, which is similar to some other systems in the literature as epoxy nanocomposites loaded with ternary filler involving RGO/polyaniline/Fe_2O_3 [68].

2.5. Dynamic Mechanical Analysis and Thermal Stability

The effect of the curing agent on the main dynamic mechanical properties of ER composites is illustrated in Figure 7 in terms of storage modulus (E′) and tan delta (δ) against temperature. Regarding the ER/GNP systems, the one cured with MIL displayed higher E′ in the glassy region indicating better rigidity. However, the values of glass transition temperature (Tg), determined from the maximum of tan delta peak, for the ER/GNP systems cured with MIL and Jeffamine were slightly lower than the neat epoxy network, which can be attributed to the presence of free volume at the filler–matrix interface causing an increase in the epoxy chain mobility. Moreover, the E′ in the rubbery region was slightly lower than that of neat epoxy, indicating a decrease in the crosslinking density.

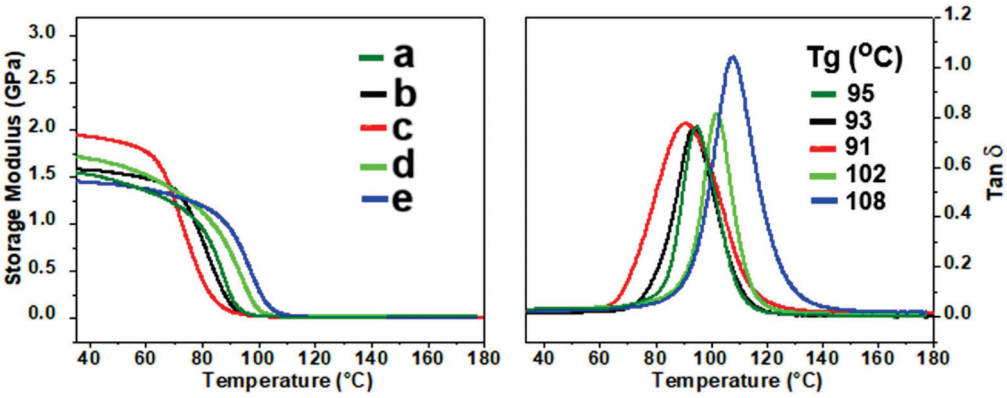

Figure 7. Storage modulus and tan delta against temperature for the ER composites containing GNP/CNT hybrid fillers: a—neat ER network; b—ER/GNP.JEF_B; c—ER/GNP.MIL_B; d—ER/GNP/CNT.JEF_D and e—ER/GNP/CNT.MIL_D.

The hybrid composite cured with MIL displayed slightly lower E′ value, in both glassy and rubbery regions, than that observed for the system cured with Jeffamine, probably due to the plasticizing effect of MIL. However, the Tg of the system cured with MIL (ER/GNP/CNT.MIL_D) displayed the highest Tg value, due to the better distribution of the filler within the epoxy matrix, thus decreasing the free volume at the interface.

The thermo-gravimetric analysis of the ER composites with different curing systems is illustrated in Figure 8. The main decomposition parameters are also summarized in Table S1. All samples were thermally stable until 300 °C. At 5 wt% of mass loss, the

composites cured with MIL presented a lower decomposition temperature due to the decomposition of the ionic liquid moiety. This feature is clearly observed in the DTG curves. However, considering the maximum decomposition temperature, the composites cured with MIL exhibited the shift of the temperature towards higher values, indicating that the systems cured with phosphonium based IL (MIL) presented better thermal stability. The thermal decomposition of the composites resulted in a great amount of residue due to the presence of carbonaceous fillers. In these cases, the amount of residue for the samples cured with MIL presented a greater amount of char due to the presence of iron in the MIL moiety.

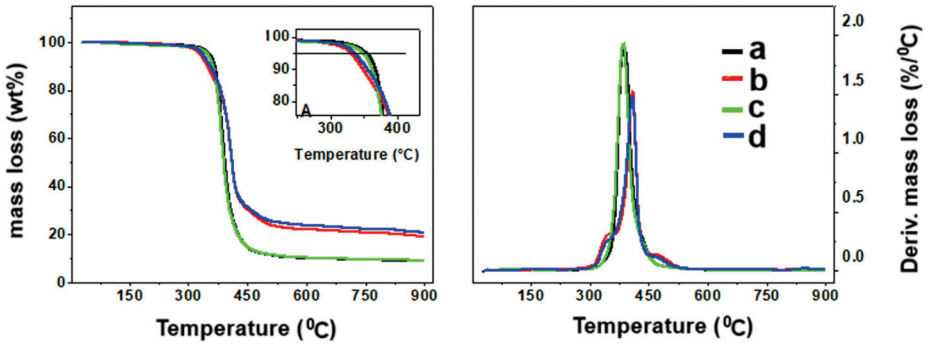

Figure 8. TGA and DTG thermograms of a—ER/GNP.JEF$_B$; b—ER/GNP.MIL$_B$; c—ER/GNP/CNT.JEF$_D$ and d—ER/GNP/CNT.MIL$_D$.

2.6. Electromagnetic Interference Shielding Effectiveness and Absorbing Properties

The electromagnetic interference shielding effectiveness (EMI SE) and the calculated reflection loss (RL) were evaluated in the X-band (8–12 GHz) and Ku-band (12–18 GHz), due to the potential applications in these frequency ranges. The X-band (8–12 GHz) is used in high precision radars (military, earth exploration, and weather) and tactical communication, whereas the Ku-band (12–18 GHz) is useful for military satellite communication, radionavigation/radiolocation, broadcasting, and in-flight Wi-Fi [69]. The effect of the CNT content on the EMI SE of ER/GNP hybrid composites cured with MIL is illustrated in Figure 9a. The composite containing only GNP (2.2 wt%) (ER/GNP.MIL$_B$) displayed relatively low EMI SE (6.8–5.5 dB) in the X-band frequency range due to the small amount of filler in this sample and low conductivity, resulting in little quantities of free charge carrier to interact with the electromagnetic (EM) radiation. Increasing the amount of CNT in the hybrid also increased the EMI SE in both X- and Ku-band, due to the rise in electrical conductivity and interfacial polarization properties [70]. The EMI SE values reached 27.64 dB at around 9 GHz (X-band) and 33.20 dB at 17 GHz (Ku-band) for the composite containing GNP/CNT = 2.2:2.2 wt% (ER/GNP/CNT.MIL$_E$).

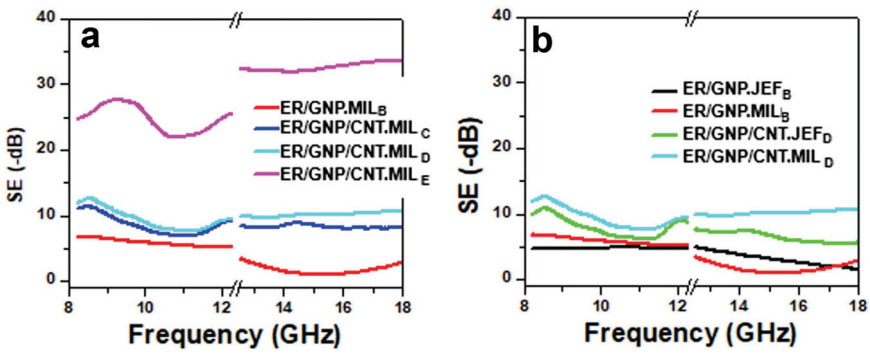

Figure 9. EMI SE in the X- and Ku-bands for ER composites. (**a**) ER/GNP and ER/GNP/CNT composites cured with MIL; (**b**) comparison between the composites cured with MIL and with Jeffamine D230.

The effect of the curing system on this property was also compared in Figure 9b. The characteristics of the curing agent did not exert great influence on the system loaded with 2.2 wt% GNP due to the low conductivity of both materials. However, better EM wave attenuation was observed for the ER/GNP/CNT.MIL$_D$ sample cured with MIL in both X- and Ku-frequency ranges. This behavior is attributed to the higher conductivity and to the presence of the magnetic ionic liquid that can also interact with EM radiation through the magnetic dipoles.

The main mechanisms involved in the EM SE of a material are the reflection of the radiation at the surface of the material and the absorption of the radiation within the material [1–4]. Figure 10 shows the percentage of absorption (A), transmission (T), and reflection (R) for the different systems at frequencies of 10 GHz and 15 GHz, which correspond to the mid-range of the X- and Ku-bands, respectively. The data were determined from the scattering parameters, according to Equations (2)–(4):

$$PR = (S_{11})^2 \tag{2}$$

$$PT = (S_{21})^2 \tag{3}$$

$$PA = 1 - Pr - PT \tag{4}$$

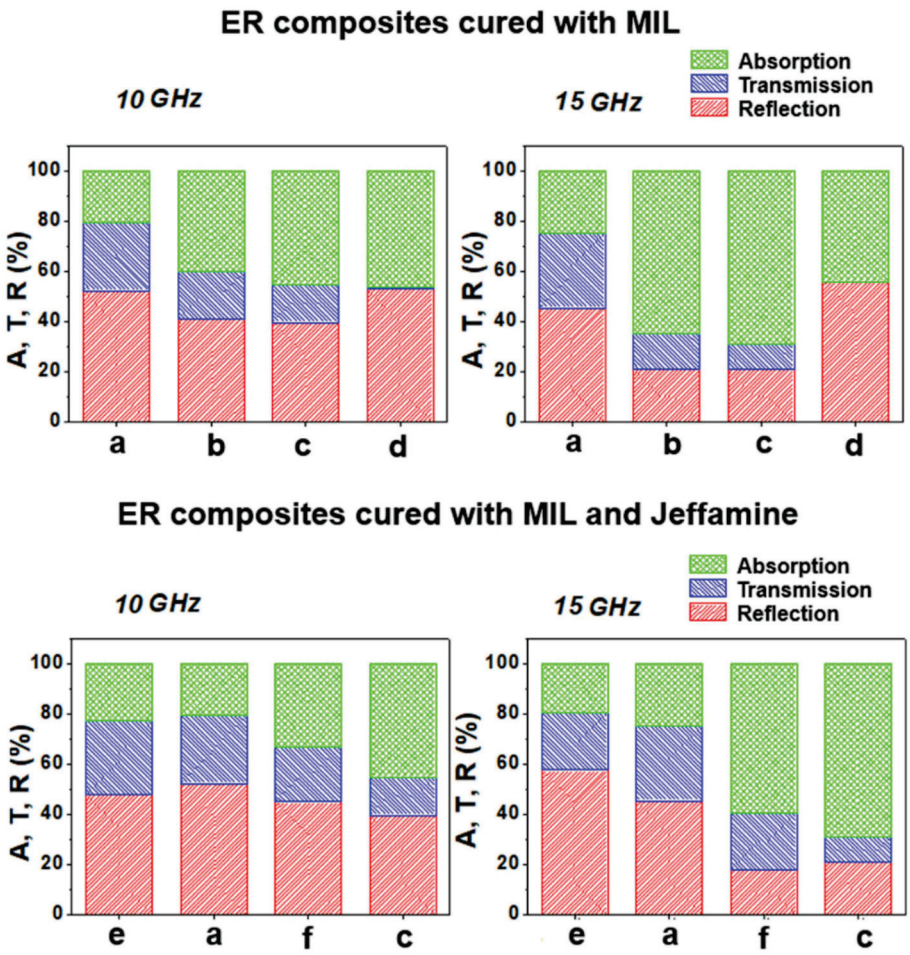

Figure 10. Percentage of absorption, transmission, and reflection of ER hybrid composites a—ER/GNP.MIL$_B$; b—ER/GNP/CNT.MIL$_C$; c—ER/GNP/CNT.MIL$_D$; d—ER/GNP/CNT.MIL$_E$; e—ER/GNP.JEF$_B$; and f—ER/GNP/CNT.JEF$_D$, at frequencies of 10 GHz (X-band) and 15 GHz (Ku-band).

Table S2 of the Supplementary Materials also summarizes these results. The percentage of the EM radiation transmission remained low for most compositions, indicating good EMI

SE of these materials. The percentage of transmitted EMW for the ER/GNP/CNT.MIL_E sample was negligible due to the high conductivity and greater amount of free charge carrier in this sample. This feature also caused an increase in the reflection contribution to the overall EMI SE. The contribution of the absorption to the total SE increased in the hybrids containing GNP/CNT = 2.2:0.2 and 2.2:0.4 wt% and this behavior was more pronounced in the Ku-band.

The EMI SE of materials is influenced by electrical conductivity, as well as dielectric and magnetic properties. The effect of the CNT content on the permittivity (ε) and permeability (μ) of ER/GNP/CNT composites cured with MIL are shown in Figure S5. The real (ε') and imaginary (ε'') parts of the complex permittivity represent the dielectric properties, while the real (μ') and imaginary (μ'') parts of the complex permeability represent the magnetic properties of the material. The complex permittivity (ε' and ε'') values were significantly higher than the permeability (μ' and μ'') values, indicating greater contribution of the dielectric properties to the EMI SE. The real and imaginary parts of permeability present some fluctuation along the frequency range studied due to variation in the interaction of the EMW with the material and the heterogeneous distribution of the magnetic entities. Although the ionic liquid has a magnetic character, the magnetization values of the composites are low, as discussed before, and explain the low values of magnetic permeability. The addition of a small amount of CNT in the system did not exert significant influence on the dielectric properties. However, for the ER/GNP/CNT.MIL_E composite, a great increase in both real and imaginary parts of complex permittivity was observed, due to the higher number of interfaces and space charge polarization [71]. Both real and imaginary parts of permeability were low in all frequency ranges studied. This behavior can be attributed to the low magnetization response of the composites, as observed by the magnetization measurements, due to the low amount of the magnetic ionic liquid. The slight fluctuation of the μ' and μ'' values may be attributed to the magnetic nature of the IL.

An effective shielding material should present the absorption as the dominant mechanism, to minimize the EMW interference caused by the reflection on the neighboring electronic devices. The microwave-absorbing (MWA) performance of a material can be evaluated by a parameter known as reflection loss (*RL*) and the effective absorption bandwidth (EAB), that is, a bandwidth with $RL < -10$ dB, which corresponds to an EMW attenuation of 90%. A good absorbing material should present negative RL values as low as possible (higher attenuation) in a specific frequency and a broad EAB. According to the transmission line theory, *RL* can be calculated from the input impedance (Z_{in}) of the material and the free space impedance (Z_0 = 377 Ω), according to Equation (5), which in turn depends on the relative complex permeability (μ_r), complex permittivity (ε_r), the measured frequency (f), speed of light (c), and the sample thickness (d), according to Equation (6) [72,73]:

$$RL(dB) = -20log\left|\frac{Z_{in} - Z_0}{Z_{in} + Z_0}\right| \tag{5}$$

$$Z_{in} = \sqrt{\frac{\mu_r}{\varepsilon_r}}tanh\left(j\frac{2\pi fd}{c}\sqrt{\varepsilon_r\mu_r}\right) \tag{6}$$

Materials that are effective absorbers have impedance matching values close to one ($Z_{in}/Z_0 \approx 1$) and minimal return loss (*RL*). Under these conditions, electromagnetic radiation can penetrate the material without reflection [74].

Figure 11 shows the 3D plots of calculated reflection loss (*RL*) of ER/GNP/CNT composites, as a function of frequency and thickness. For better detail, the minimum *RL* values, the peak frequency, and the effective absorption bandwidth (EAB) are also summarized in Table 1. The matching thickness corresponds to the thickness that exhibits the highest EMW attenuation (minimum *RL*) and the broader EAB, which is the largest frequency

range with $RL < -10$ dB (EMW attenuation higher than 90%). The composite loaded with 2.2 wt% of GNP presented the minimum *RL* of around −30 dB (99.9% attenuation) with 1.5 mm thickness, regardless of the curing system. The greatest EAB values were achieved with thickness corresponding to 2.5 (EAB = 1.69 GHz) and 3.0 mm (EAB = 1.81 GHz) for the systems cured with MIL and Jeffamine, respectively. Although the *RL* values in these systems correspond to a great EMW attenuation, the EAB values indicate a narrow frequency range for the attenuation.

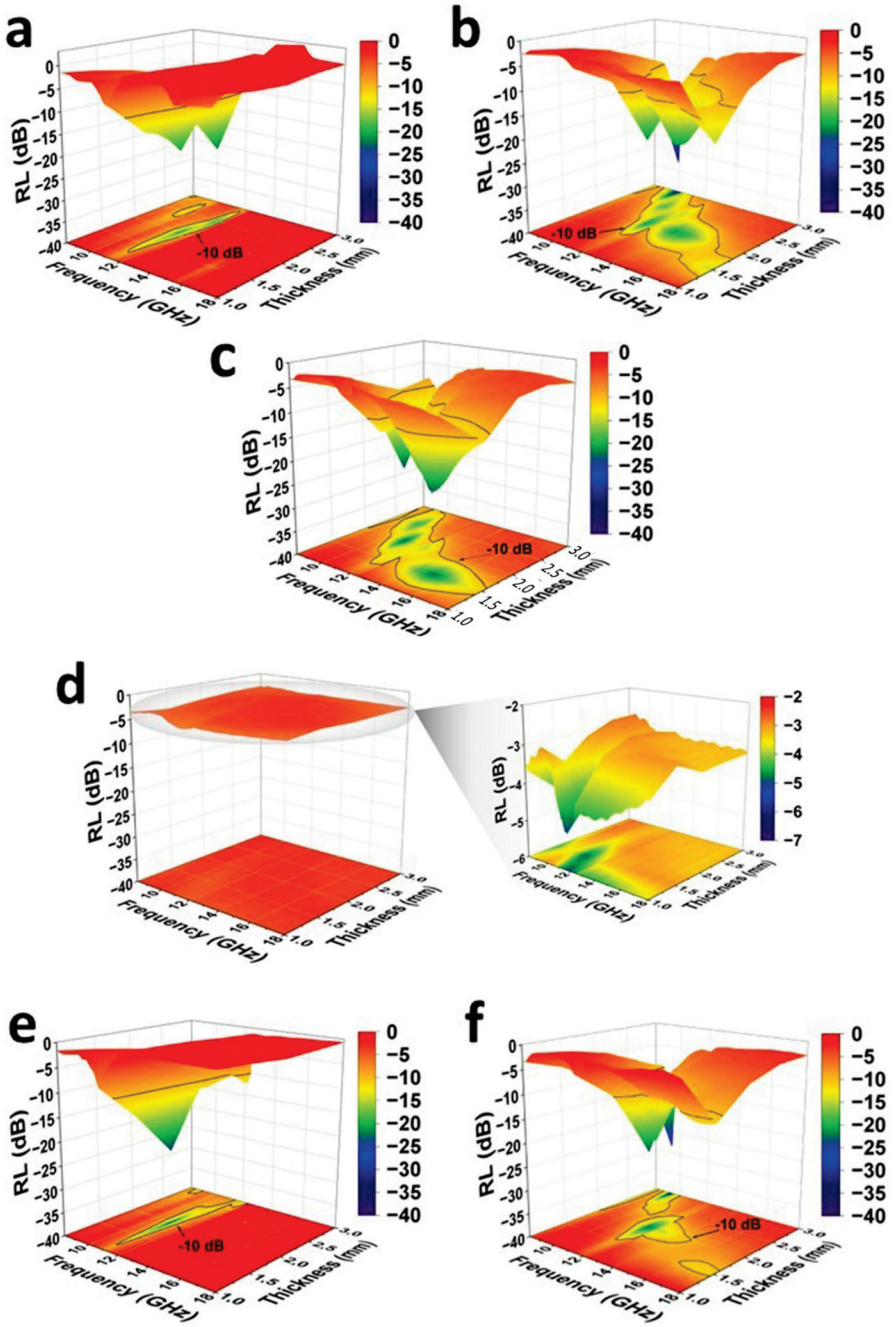

Figure 11. Calculated reflection loss (RL) as function of thickness and frequency for the composites (**a**) ER/GNP.MIL$_B$; (**b**) ER/GNP/CNT.MIL$_C$; (**c**) ER/GNP/CNT.MIL$_D$; (**d**) ER/GNP/CNT.MIL$_E$; (**e**) ER/GNP.JEF$_B$; and (**f**) ER/GNP/CNT.JEF$_D$.

Table 1. Calculated RL and effective absorption bandwidth (EAB) of the composites.

Composites	Thickness (mm)	RL (dB)	Frequency (GHz)	EAB (GHz)
Effect of the CNT content (samples cured with MIL)				
ER/GNP.MIL$_B$	1.0	−8.93	12.97	-
	1.5	−30.41	12.94	1.24
	2.0	−22.71	12.61	1.46
	2.5	−22.26	11.99	1.69
	3.0	−10.68	8.27	0.32
ER/GNP/CNT.MIL$_C$	1.0	−3.58	11.88	-
	1.5	−15.52	18.00	1.96
	2.0	−21.56	11.92	1.16
	2.5	−18.35	10.97	2.33
	3.0	−33.07	9.99	2.14
ER/GNP/CNT.MIL$_D$	1.0	−5.86	18.00	-
	1.5	−23.41	15.03	5.18
	2.0	−23.69	11.10	2.31
	2.5	−20.55	10.01	2.10
	3.0	−10.80	9.21	0.48
ER/GNP/CNT.MIL$_E$	1.0	−5.03	11.75	-
	1.5	−4.91	10.83	-
	2.0	−3.76	10.62	-
	2.5	−3.39	16.99	-
	3.0	−3.35	16.99	-
Effect of the CNT content (samples cured with Jeffamine)				
ER/GNP.JEF$_B$	1.0	−11.49	13.24	0.17
	1.5	−30.74	13.19	1.36
	2.0	−24.17	11.04	1.63
	2.5	−12.09	14.77	1.40
	3.0	−13.51	14.23	1.81
ER/GNP/CNT.JEF$_D$	1.0	−4.06	11.81	-
	1.5	−11.64	17.10	2.07
	2.0	−23.28	11.94	3.65
	2.5	−15.75	8.20	1.64
	3.0	−28.59	9.40	1.53

The addition of 0.2 wt% of CNT in the system (ER/GNP/CNT.MIL$_C$) led to an improvement of the EMW attenuation with 3 mm thickness. At this thickness, RL and EAB values corresponding to −33.07 dB and 2.14 GHz were achieved, respectively. The best compromise between RL and EAB values was observed for the ER/GNP/CNT.MIL$_D$ composite with 1.5 mm thickness, where RL of −23.41 dB (higher than 99% attenuation) and an EAB of 5.18 GHz were observed. The similar composite cured with Jeffamine (ER/GNP/CNT.JEF$_D$) presented the minimum RL (−28.59 dB) with 3 mm thick sample, but the larger EAB (3.65 GHz) was observed for the composite with 2.0 mm thickness. Thus, using hybrid filler and MIL as the curing agent was interesting to develop composites with outstanding EMW attenuation by absorption mechanism with relatively small thickness. This behavior is important for reducing density and cost and improving processability.

Table 2 compares the EMI SE and RL results of some epoxy nanocomposites reported in the literature with the data obtained in this work. The EMI SE value observed in the present work, for the epoxy nanocomposite containing GNP/CNT (2.2:2.2 wt%) of hybrid filler and cured with MIL, was superior to those found in most of the cited systems, with a

lower amount of filler. Moreover, the RL and EAB values were quite favorable if one takes into consideration the simple, scalable, and solvent-free method used in this work.

Table 2. Comparison data of EMI SE and RL of some epoxy nanocomposites reported in the literature.

Filler	Amount	Thickness (mm)	EMI SE (dB)/ Freq (GHz)	RL (dB)/ Freq (GHz)	EAB	Method	Ref.
GNP	30 (wt%)	2.5	20 (11)	−3.5 (10.5)	-	Mechanical mixing	[16]
nanographite	15 (wt%)	7.5	12 (11.6)	−10.5 (12)	1.3	Mechanical mixing	[16]
GNP	17 (wt%)	2	8 (8.4)	-	-	Sonication without solvent	[17]
GNP	30 (wt%)	1	23 (8.2)	-	-	high-shear speed mixer	[18]
RGO	15 (wt%)	3	21 (8–12)			Sonication with solvent	[19]
RGO	5 (wt%)	6	25 (12)	-	-	Mini-mechanical vortex mixer	[20]
GNP	15 (wt%)	3	-	−14 (18.9)	2.0	Sonication with solvent	[22]
GNP	15 (wt%)	2.5	5.85 (2)	-	-	Sonication without solvent	[24]
RGO/CNT	15 (wt%)	1.2	70 (12)	-	-	Chemical grafting of CNT onto GO/reduction	[37]
RGTO	1 (wt%)	1.9	-	−61.8 (13.5)	5.38	Expanded graphite/CNT oxidized together—sonication with solvent	[41]
TRGO/CNT (2.5:2.5)	5 (wt%)	2	12 (10)	-	-	Sonication with solvent	[43]
RGO-imid	1 (wt%)	3	-	−47.2 (12)	6.04	Sonication with solvent—modif. of RGO with imidazole	[75]
MFRGO	40 (wt%)	4	-	−25 (8.6)	1.2	Covalent functionalization of GO by imidazolium IL/reduction	[76]
Exfoliated graphite	44.7 (vol%)	4		−23.8 (11)	5.6	chemical treatment with maceration and microwave-assisted thermal exfoliation	[77]
GNP/CNT	2.6 (wt%)	3	10 (15–18)	-	-	Mixing in a ball-milling and cured with MIL	This work
GNP/CNT	2.6 (wt%)	1.5		−23.4	5.18	Mixing in a ball-milling and cured with MIL	This work
GNP/CNT	4.4 (wt%)	3	33.2 (17)			Mixing in a ball-milling and cured with MIL	This work

3. Experimental

3.1. Materials

Epoxy resin (ER) based on bisphenol A diglycidyl ether (Araldite® GY 260) (epoxide equivalent weight = 182–192 g/mol; viscosity (25 °C) = 12–16 Pa·s) was purchased from Huntsman Advanced Materials (São Paulo, Brazil). Trihexyltetradecylphosphonium chloride (P_{66614}.Cl; ≥95%) (Cyphos® IL101) and poly(propylene glycol) bis(2-aminopropyl ether) (Jeffamine® D-230) were purchased from Sigma-Aldrich (São Paulo, Brazil). A multi-walled carbon nanotube NC7000 (CNT) (average diameter = 9.5 nm; average length = 1.5 μm and carbon purity = 90%) was purchased from Nanocyl S.A (Sambreville, Belgium). Graphene nanoplatelets Grade M (surface area = 150 m^2/g; particle size < 5 μm) (xGnP®) were purchased from Nano Xplore, Inc. (Montreal, QC, Canada). Anhydrous ferric chloride ($FeCl_3$) was purchased from Sigma-Aldrich (São Paulo, Brazil).

3.2. Synthesis of Magnetic Ionic Liquid (MIL)

The synthesis of the magnetic ionic liquid (MIL), trihexyl(tetradecyl)phosphonium tetrachloroferrate ($P_{66614}[FeCl_4]$), was performed according to previous works [53,78]. For the synthesis, P_{66614}.Cl and anhydrous $FeCl_3$ were mixed in equimolar proportions of 0.02 mol and stirred for 24 h at 60 °C under a nitrogen atmosphere. Then, MIL was obtained as a brown viscous oil (yield = 95%; melting point = −6.5 °C). Figure 12 illustrates the structure of the phosphonium ionic liquid.

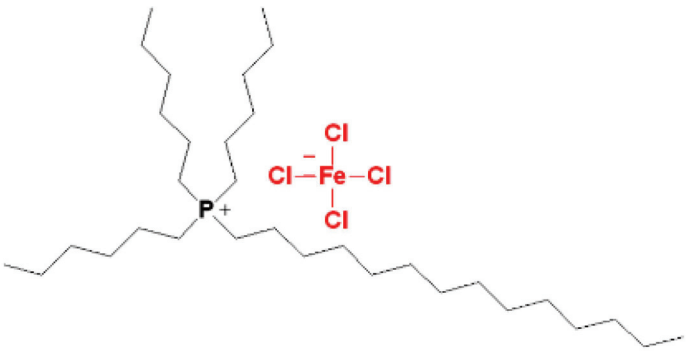

Figure 12. Structure of trihexyl(tetradecyl)-phosphonium tetrachloroferrate ($P_{66614}[FeCl_4]$).

3.3. Preparation of Epoxy Resin (ER) with Hybrid Fillers

For the preparation of ER composites cured with MIL, GNP and CNT fillers were first mixed with MIL and ER in a Cryomill ball mill from Retsch, using the following parameters: 4 cycles of 15 min each at a frequency of 30 Hz, with 3 solid steel balls of 1.0 mm of diameter. After mixing, the system was transferred to a speed mixer operating at 3500 rpm for 5 min to remove possible bubbles and poured into silicone molds, with appropriate dimensions for each characterization. The curing parameters followed protocols described in the literature: 1 h at 130 °C; 3 h at 200 °C; 2 h at 220 °C [53]. The amount of MIL was fixed as 10 phr (part per hundred part of resin), which was enough to achieve good curing level and glass transition temperature, as well as a reasonable response in terms of microwave-absorbing properties, according to previous work [53].

The ER composites cured with Jeffamine were prepared by mixing GNP and CNT with the ER in the Cryomill ball mill, using the same mixing protocol described before. Then, Jeffamine D230 (32 phr, according to the manufacturer) was added and the system was transferred to the speed mixer as previously described. The compositions are summarized in Table 1. Although the amounts of hardener and additives in epoxy formulations are commonly expressed in phr, Table 3 displays the composition of each composite in phr and percentage, to unify the units of measurements with those normally used for conductive polymeric composites. The amount of GNP was fixed as 2.5 phr to emphasize the influence of the presence of low amount of CNT on the electrical properties. However, the amount of filler presents some variation when using percentage as the unit.

Table 3. Compositions in the hybrid composite matrix.

Sample Code	ER		MIL		GNP		CNT		Jef	
	(phr)	(wt%)	(phr)	(wt%)	(phr)	(wt%)	(phr)	(wt%)	(phr)	(wt%)
ER/GNP.MIL$_A$	100	83.4	10.0	8.3	10.0	8.3				
ER/GNP.MIL$_B$	100	88.9	10.0	8.9	2.5	2.2	-			
ER/GNP/CNT.MIL$_C$	100	88.7	10.0	8.9	2.5	2.2	0.25	0.2		
ER/GNP/CNT.MIL$_D$	100	88.5	10.0	8.9	2.5	2.2	0.5	0.4		
ER/GNP/CNT.MIL$_E$	100	87.0	10.0	8.6	2.5	2.2	2.5	2.2		
ER/GNP.JEF$_B$	100	74.3	-		2.5	1.9	-		32	23.8
ER/GNP/CNT.JEF$_D$	100	74.1	-		2.5	1.8	0.5	0.4	32	23.7

ER/GNP.JEF$_B$ Jef = Jeffamine D230.

3.4. Characterization

The rheological characterization of the ER/hybrid systems was carried out in a Discovery DHR 1 rheometer (TA Instruments Inc.—New Castle, DE, USA) at 25 °C, using parallel plate geometry (25 mm) with a gap of 1 mm. The viscoelastic properties were determined through a frequency sweep of 0.1 to 100 Hz with 0.1% of deformation.

Dynamic mechanical analysis (DMA) was performed in a Q800 equipment (TA Instruments Inc.—New Castle, DE, USA), equipped with a single cantilever clamp using sample dimensions of 35.0 D7 12.5 × 3.0 mm. The conditions of the analysis were as follows: frequency = 1 Hz; heating from 25 °C to 180 °C; heating rate = 3 °C/min; deformation = 0.1%.

The electrical conductivity was measured in an Autolab PGSTAT204 impedance analyzer from Metrohm (Herisau, Switzerland) in alternating current (AC) mode. The measurements were conducted at room temperature with discs of 25 mm of diameter and 1 mm thickness, in a frequency range from 10^{-1} Hz to 10^{6} Hz, with a voltage of 0.1 V. The samples were coated with a thin layer of gold to improve electrical contact.

The electromagnetic absorbing properties of the materials were measured in terms of shielding effectiveness (SE) and reflection loss (RL) in the microwave X-band (8.2–12 GHz) and Ku-band (12–18 GHz) ranges, using a VNA Vector Network Analyzer, model E5080B from Keysight Technologies (Chicago, IL, USA) with a rectangular waveguide. Samples with 3.0 mm thickness were used.

Scanning electron microscopy (SEM) was performed on a TESCAN model VEGA II microscope (Brno—Czechia) operating at 20 kV. The fractured surfaces of the epoxy composites were coated with a thin layer of gold before analyzing, using a secondary electron detector and energy dispersive X-ray (EDX) detector from Bruker Nano GmbH (Berlin, Germany), model XFlash 630 M.

The X-ray diffraction (XRD) patterns were obtained on a Rigaku Ultima IV diffractometer (Tokyo, Japan), using a continuous scanning mode in the range of 2θ from 5° to 60°, with a step size of 0.05° s^{-1}, using the Cu-kα radiation at 40 kV and 40 mA.

The magnetic measurements were performed using a Quantum Design MPMS3 magnetometer (San Diego, CA, USA) (applying magnetic fields up to 7 Tesla and temperature ranging from 2 K to 400 K). The available sample holders are designed for solid samples. For the liquid MIL, it was introduced into a quartz tube with a diameter smaller than that of the standard plastic sample holder (~6 mm diameter). To prevent the vacuum in the measurement chamber from aspirating the liquid, the quartz tube was sealed using a flame generated from an acetylene–air mixture.

Transmission electron microscopy images were obtained from a Hitachi model HT 7800 (Tokyo, Japan) operating at 100 kV. The samples were ultramicrotomed in a Leica equipment with a thickness of around 60 nm.

4. Conclusions

Epoxy nanocomposites containing GNP/CNT hybrid filler were prepared in the presence of a magnetic ionic liquid, which served a dual role as both a curing agent for the epoxy matrix and a dispersion agent for the fillers. A significant increase in electrical conductivity was observed when combining 2.2 wt% of GNP with 0.2 wt% of CNT, compared to the ER/GNP binary composites containing 2.2 and 8.3 wt% of GNP. Furthermore, the use of MIL as the curing agent resulted in epoxy nanocomposites (ENCs) with higher conductivity and superior EMI SE compared to conventional aliphatic amine. This indicates that the ionic liquid not only dispersed the fillers efficiently but also facilitated the formation of a conductive pathway.

Additionally, the systems cured with MIL demonstrated greater contribution of the absorption mechanism in their EMI SE measurements, likely due to the presence of magnetic moiety in the ionic liquid. The ENC containing 4.4 wt% of the hybrid filler (GNP/CNT = 2.2:2.2 wt%) exhibited an EMI SE of 33 dB, which surpasses several other epoxy-based systems reported in the literature. Moreover, a significant EMW attenuation response was observed, with a minimum RL of −23.4 dB and a large EAB of 5.18 GHz, for the 1.5 mm thick ENC containing 2.6 wt% of hybrid filler (GNP/CNT = 2.2:0.4 wt%). In sum-

mary, this study presents a cost-effective and scalable approach for developing materials with absorption-dominated EMI shielding properties, since commercial materials such as GNP and CNT were employed in low amounts to decrease cost and maintain a good processability. Furthermore, the ball-milling technique used for mixing the ingredients does not require solvent, making large-scale production easier. Finally, the high microwave-absorbing properties in a large frequency range make this material suitable for civilian and military applications.

Supplementary Materials: The following supporting information can be downloaded at: https://www.mdpi.com/article/10.3390/molecules30050985/s1, Figure S1: Han plots of ER composites. (a) ER/GNP and ER/GNP/CNT cured with MIL (10 phr); (b) comparison between the composites cured with MIL(10 phr) and with Jeffamine D230 (32 phr); Figure S2: XRD profile of neat GNP; Figure S3: EDS data of the composites cured with MIL; Figure S4: Dependence of the (a) inverse magnetic susceptibility and (b) magnetization at 30,000 Oe with temperature of neat ionic liquid $P_{66614}[FeCl_4]$. Figure S5: Permittivity and permeability of ER composites; Table S1: Main thermal decomposition parameters observed from the TGA analysis; Table S2: Percentage of absorption, transmission and reflection related to the EMI SE measurements for ER composites loaded with GNP/CNT hybrid filler.

Author Contributions: Conceptualization, B.G.S.; methodology, J.C.C., D.P.S., R.R.H. and V.M.T.S.B.; validation, G.M.O.B., S.L. and V.M.T.S.B.; formal analysis, J.C.C.; investigation, J.C.C. and A.A.S.; resources, B.G.S.; data curation, B.G.S.; writing—original draft preparation, J.C.C.; writing—review and editing, B.G.S. and S.L.; visualization, G.M.O.B.; supervision, B.G.S.; project administration, B.G.S.; funding acquisition, B.G.S. All authors have read and agreed to the published version of the manuscript.

Funding: Fundação de Amparo à Pesquisa do Estado do Rio de Janeiro—FAPERJ (Grant number E-26/200.848/2021; E-26/010.000982/2019); Conselho Nacional de Desenvolvimento Científico e Tecnológico—CNPq (Grant number 305203/2020-6; 404257/2021-6; 408839/2022-8).

Institutional Review Board Statement: Not applicable.

Informed Consent Statement: Not applicable.

Data Availability Statement: The datasets generated during and/or analyzed during the current study are available from the corresponding author on reasonable request.

Acknowledgments: The authors thank Centro Nacional de Bioimagem—CENABIO/UFRJ for the TEM images.

Conflicts of Interest: The authors declare no conflict of interest.

References

1. Thomassin, J.M.; Jerôme, C.; Pardoen, T.; Bailly, C.; Huynen, I.; Detrembleur, C. Polymer/carbon based composites as electromagnetic interference (EMI) shielding materials. *Mater. Sci. Eng. R Rep.* **2013**, *74*, 211–232. [CrossRef]
2. Li, J.S.; Huang, H.; Zhou, Y.J.; Zhang, C.Y.; Li, Z.T. Research progress of graphene-based microwave absorbing materials in the last decade. *Mater. Res.* **2017**, *32*, 1213–1230. [CrossRef]
3. Wang, C.; Murugadoss, V.; Kong, J.; He, Z.; Mai, X.; Shao, Q.; Chen, Y.; Guo, L.; Liu, C.; Angaiah, S. Overview of carbon nanostructures and nanocomposites for electromagnetic wave shielding. *Carbon* **2018**, *140*, 696–733. [CrossRef]
4. Jayalakshmi, C.G.; Inamdar, A.; Anand, A.; Kandasubramanian, B. Polymer matrix composites as broadband radar absorbing structures for stealth aircrafts. *J. Appl. Polym. Sci.* **2019**, *136*, 47241. [CrossRef]
5. Ganguly, S.; Bhawal, P.; Ravindren, R.; Das, N.C. Polymer nanocomposites for electromagnetic interference shielding: A review. *J. Nanosci. Nanotechnol.* **2018**, *18*, 7641–7669. [CrossRef]
6. Nan, X.; Zhang, Y.; Shen, J.; Liang, R.; Wang, J.; Jia, L.; Yang, X.; Yu, W.; Zhang, Z. A review of the establishment of effective conductive pathways of conductive polymer composites and advances in electromagnetic shielding. *Polymers* **2024**, *16*, 2539. [CrossRef] [PubMed]
7. Jin, F.-L.; Li, X.; Park, S.-J. Synthesis and application of epoxy resins: A review. *J. Ind. Eng. Chem.* **2015**, *29*, 1–11. [CrossRef]

8. Chen, X.; Liu, H.; Hu, D.; Liu, H.; Ma, W. Recent advances in carbon nanotubes-based microwave absorbing composites. *Ceram. Int.* **2021**, *47*, 23749–23761. [CrossRef]
9. Sankaran, S.; Deshmukh, K.; Ahamed, M.B.; Pasha, S.K. Recent advances in electromagnetic interference shielding properties of metal and carbon filler reinforced flexible polymer composites: A review. *Compos. Part A Appl. Sci. Manuf.* **2018**, *114*, 49–71. [CrossRef]
10. Kausar, A. Influence of interfacial aspects on electromagnetic interference shielding performance of graphene reinforced nanocomposites: An overview. *Compos. Interfaces* **2022**, *29*, 1373–1396. [CrossRef]
11. Liang, X.; Liu, W.; Cheng, Y.; Lv, J.; Dai, S.; Tang, D.; Zhang, B.; Ji, G. Recent process in the design of carbon-based nanostructures with optimized electromagnetic properties. *J. Alloys Compd.* **2018**, *749*, 887–899. [CrossRef]
12. Kausar, A.; Ahmad, I.; Zhao, T.; Aldaghri, O.; Ibnaouf, K.H.; Eisa, M.H.; Lam, T.D. Graphene nanocomposites for electromagnetic interference shielding—Trends and advancements. *J. Compos. Sci.* **2023**, *7*, 384. [CrossRef]
13. Cao, M.; Han, C.; Wang, X.; Zhang, M.; Zhang, Y.; Shu, J.; Yang, H.; Fang, X.; Yuan, J. Graphene nanohybrids: Excellent electromagnetic properties for the absorbing and shielding of electromagnetic waves. *J. Mater. Chem. C* **2018**, *6*, 4586–4602. [CrossRef]
14. Schuster, W.R.; Pezzin, S.H.; Lafratta, F.H. Airbrushing of carbon nanotubes on glass fibers for electromagnetic shielding epoxy composites. *Polímeros* **2023**, *33*, e20230001. [CrossRef]
15. Wang, L.; Wei, X.; Bai, Y.A.; Zhou, H.; Wang, X.; Wen, B.; Wang, Y. Designing improved electromagnetic shielding efficacy of poly (3-hydroxybutyrate-co-3hydroxyvalerate) nanocomposites foam using carbon nanotubes and graphene nanoplatelets. *J. Vinyl Addit. Technol.* **2024**, *30*, 72–88. [CrossRef]
16. dos Anjos, E.G.R.; Brazil, T.R.; de Melo Morgado, G.F.; Antonelli, E.; Medeiros, N.C.D.F.L.; Santos, A.P.; Indrusiak, T.; Baldan, M.R.; Rezende, M.C.; Pessan, L.A.; et al. Graphene related materials as effective additives for electrical and electromagnetic performance of epoxy nanocomposites. *FlatChem* **2023**, *41*, 100542. [CrossRef]
17. Abdelal, N.; Dib, N.; Young, D.; Slanker, A. Electromagnetic interference shielding and dielectric properties of graphene nanoplatelets/epoxy composites in the x-band frequency range. *J. Mater. Sci.* **2022**, *57*, 13928–13944. [CrossRef]
18. Kargar, F.; Barani, Z.; Balinskiy, M.; Magana, A.S.; Lewis, J.S.; Balandin, A.A. Dual-functional graphene composites for electromagnetic shielding and thermal management. *Adv. Electron. Mater.* **2019**, *5*, 1800558. [CrossRef]
19. Liang, J.; Wang, Y.; Huang, Y.; Ma, Y.; Liu, Z.; Cai, J.; Zhang, C.; Gao, H.; Chen, Y. Electromagnetic interference shielding of graphene/epoxy composites. *Carbon* **2009**, *47*, 922–925. [CrossRef]
20. Ahmad, A.F.; Ab Aziz, S.; Abbas, Z.; Obaiys, S.J.; Khamis, A.M.; Hussain, I.R.; Zaid, M.H.M. Preparation of a chemically reduced graphene oxide reinforced epoxy resin polymer as a composite for electromagnetic interference shielding and microwave-absorbing applications. *Polymers* **2018**, *10*, 1180. [CrossRef] [PubMed]
21. Min, D.; Zhou, W.; Qing, Y.; Luo, F.; Zhu, D. Single-layer and double-layer microwave absorbers based on graphene nanosheets/epoxy resin composite. *Nano* **2017**, *12*, 1750089. [CrossRef]
22. Wang, Z.; Luo, J.; Zhao, G.L. Dielectric and microwave attenuation properties of graphene nanoplatelet–epoxy composites. *AIP Adv.* **2014**, *4*, 017139. [CrossRef]
23. Silva, A.A.; Stein, R.; Campos, D.; Indrusiak, T.; Soares, B.G.; Barra, G.M. Conducting materials based on epoxy/graphene nanoplatelet composites with microwave absorbing properties: Effect of the processing conditions and ionic liquid. *Front. Mater.* **2019**, *6*, 156. [CrossRef]
24. Collado, I.; Jiménez-Suárez, A.; Vázquez-López, A.; del Rosario, G.; Prolongo, S.G. Ultrasonication Influence on the Morphological Characteristics of Graphene Nanoplatelet Nanocomposites and Their Electrical and Electromagnetic Interference Shielding Behavior. *Polymers* **2024**, *16*, 1068. [CrossRef] [PubMed]
25. de Oliveira, M.M.; Forsberg, S.; Selegård, L.; Carastan, D.J. The influence of sonication processing conditions on electrical and mechanical properties of single and hybrid epoxy nanocomposites filled with carbon nanoparticles. *Polymers* **2021**, *13*, 4128. [CrossRef] [PubMed]
26. Jen, Y.M.; Chang, H.H.; Lu, C.M.; Liang, S.Y. Temperature-dependent synergistic effect of multi-walled carbon nanotubes and graphene nanoplatelets on the tensile quasi-static and fatigue properties of epoxy nanocomposites. *Polymers* **2021**, *13*, 84. [CrossRef]
27. Chatterjee, S.; Nafezarefi, F.; Tai, N.H.; Schlagenhauf, L.; Nüesch, F.A.; Chu, B.T.T. Size and synergy effects of nanofiller hybrids including graphene nanoplatelets and carbon nanotubes in mechanical properties of epoxy composites. *Carbon* **2012**, *50*, 5380–5386. [CrossRef]
28. Safdari, M.; Al-Haik, M.S. Synergistic electrical and thermal transport properties of hybrid polymeric nanocomposites based on carbon nanotubes and graphite nanoplatelets. *Carbon* **2013**, *64*, 111–121. [CrossRef]
29. Yue, L.; Pircheraghi, G.; Monemian, S.A.; Manas-Zloczower, I. Epoxy composites with carbon nanotubes and graphene nanoplatelets–Dispersion and synergy effects. *Carbon* **2014**, *78*, 268–278. [CrossRef]

30. Li, W.; Dichiara, A.; Bai, J. Carbon nanotube–graphene nanoplatelet hybrids as high-performance multifunctional reinforcements in epoxy composites. *Comp. Sci. Technol.* **2013**, *74*, 221–227. [CrossRef]
31. Prolongo, S.G.; Moriche, R.; Ureña, A.; Flórez, S.; Gaztelumendi, I.; Arribas, C.; Prolongo, M.G. Carbon nanotubes and graphene into thermosetting composites: Synergy and combined effect. *J. Appl. Polym. Sci.* **2018**, *135*, 46475. [CrossRef]
32. Ramos-Galicia, L.; Pérez-Ramírez, E.E.; Velasco-Santos, C.; Licea-Jiménez, L.; Martínez-Hernández, A.L.; Pérez-García, S.A.; López-Ortiz, A. Hybrid based on graphene nanoplatelets and carbon nanotubes obtained in a single-step approach and its reinforcement effect in an epoxy matrix. *J. Appl. Polym. Sci.* **2022**, *139*, e53227. [CrossRef]
33. Kopsidas, S.; Olowojoba, G.B. Multifunctional epoxy composites modified with a graphene nanoplatelet/carbon nanotube hybrid. *J. Appl. Polym. Sci.* **2021**, *138*, 50890. [CrossRef]
34. Raimondo, M.; Naddeo, C.; Catauro, M.; Guadagno, L. Viscoelastic Behavior of Structural Epoxy Resins Loaded with Different Carbon Nanostructured Forms. *Macromol. Symp.* **2022**, *405*, 2100209. [CrossRef]
35. Parasuram, S.; Banerjee, P.; Raj, R.; Kumar, S.; Bose, S. Electrophoretically Deposited Multiscale Graphene Oxide/Carbon Nanotube Construct Mediated Interfacial Engineering in Carbon Fiber Epoxy Composites. *ACS Appl. Mater. Interfaces* **2023**, *15*, 28581–28593. [CrossRef] [PubMed]
36. Yu, A.; Ramesh, P.; Sun, X.; Bekyarova, E.; Itkis, M.E.; Haddon, R.C. Enhanced thermal conductivity in a hybrid graphite nanoplatelet–carbon nanotube filler for epoxy composites. *Adv. Mater.* **2008**, *20*, 4740–4744. [CrossRef]
37. Kang, J.S.; Zhang, H.X.; Yoon, K.B. Hybrid rGO–CNT/Epoxy Nanocomposites as Electromagnetic Interference Shielding Materials. *ACS Appl. Nano Mater.* **2014**, *7*, 10770–10778. [CrossRef]
38. Han, L.; Li, K.; Xiao, C.; Yin, X.; Gui, X.; Song, Q.; Ye, F. Carbon nanotube-vertical edge rich graphene hybrid sponge as multifunctional reinforcements for high performance epoxy composites. *Carbon* **2023**, *201*, 871–880. [CrossRef]
39. Lee, Y.S.; Park, Y.H.; Yoon, K.H. Flexural, electrical, thermal and electromagnetic interference shielding properties of xGnP and carbon nanotube filled epoxy hybrid nanocomposites. *Carbon Lett.* **2017**, *24*, 41–46.
40. Huangfu, Y.; Ruan, K.; Qiu, H.; Lu, Y.; Liang, C.; Kong, J.; Gu, J. Fabrication and investigation on the PANI/MWCNT/thermally annealed graphene aerogel/epoxy electromagnetic interference shielding nanocomposites. *Compos. Part A Appl. Sci. Manuf.* **2019**, *121*, 265–272. [CrossRef]
41. Zhang, X.; Wang, X.; Sha, P.; Wang, B.; Ding, Y.; Du, S. High-efficiency electromagnetic wave absorption of epoxy composites filled with ultralow content of reduced graphene/carbon nanotube oxides. *Compos. Sci. Technol.* **2020**, *189*, 108020. [CrossRef]
42. Liu, Y.; He, D.; Dubrunfaut, O.; Zhang, A.; Zhang, H.; Pichon, L.; Bai, J. GO-CNTs hybrids reinforced epoxy composites with porous structure as microwave absorbers. *Compos. Sci. Technol.* **2020**, *200*, 108450. [CrossRef]
43. Yazdi, M.K.; Noorbakhsh, B.; Nazari, B.; Ranjbar, Z. Preparation and EMI shielding performance of epoxy/non-metallic conductive fillers nano-composites. *Prog. Org. Coat.* **2020**, *145*, 105674. [CrossRef]
44. Wang, J.; Chu, H.; Li, Y. Why single-walled carbon nanotubes can be dispersed in imidazolium-based ionic liquids. *ACS Nano* **2008**, *2*, 2540–2546. [CrossRef] [PubMed]
45. Tunckol, M.; Durand, J.; Serp, P. Carbon nanomaterial–ionic liquid hybrids. *Carbon* **2012**, *50*, 4303–4334. [CrossRef]
46. Throckmorton, J.A.; Watters, A.L.; Geng, X.; Palmese, G.R. Room temperature ionic liquids for epoxy nanocomposite synthesis: Direct dispersion and cure. *Compos. Sci. Technol.* **2013**, *86*, 38–44. [CrossRef]
47. Lopes Pereira, E.C.; Soares, B.G. Conducting epoxy networks modified with noncovalently functionalized multi-walled carbon nanotube with imidazolium-based ionic liquid. *J. Appl. Polym. Sci.* **2016**, *133*, 43976–43977. [CrossRef]
48. Sanes, J.; Saurín, N.; Carrión, F.J.; Ojados, G.; Bermúdez, M.D. Synergy between singlewalled carbon nanotubes and ionic liquids in epoxy resin nanocomposites. *Compos. Part B Eng.* **2016**, *105*, 149–159. [CrossRef]
49. Soares, B.G.; Riany, N.; Silva, A.A.; Barra, G.M.O.; Livi, S. Dual-role of phosphonium –based ionic liquid in epoxy/MWCNT systems: Electric, rheological behavior and electromagnetic interference shielding effectiveness. *Eur. Polym. J.* **2016**, *84*, 77–88. [CrossRef]
50. Zhang, Y.; Park, S.J. Imidazolium-optimized conductive interfaces in multilayer graphene nanoplatelet/epoxy composites for thermal management applications and electroactive devices. *Polymer* **2019**, *168*, 53–60. [CrossRef]
51. Dermani, A.K.; Kowsari, E.; Ramezanzadeh, B.; Amini, R. Screening the effect of graphene oxide nanosheets functionalization with ionic liquid on the mechanical properties of an epoxy coating. *Prog. Org. Coat.* **2018**, *122*, 255–262. [CrossRef]
52. Liu, S.; Chevali, V.S.; Xu, Z.; Hui, D.; Wang, H. A review of extending performance of epoxy resins using carbon nanomaterials. *Compos. Part B Eng.* **2018**, *136*, 197–214. [CrossRef]
53. Henriques, R.R.; de Oliveira, C.P.; Stein, R.; Pontes, K.; Silva, A.A.; Soares, B.G. Dual Role of Magnetic Ionic Liquids as Curing Agents of Epoxy Resin and Microwave-Absorbing Additives. *ACS Appl. Polym. Mater.* **2022**, *4*, 1207–1217. [CrossRef]
54. Wu, Z.; Cheng, H.W.; Jin, C.; Yang, B.; Xu, C.; Pei, K.; Zhang, H.; Yang, Z.; Che, R. Dimensional design and core-shell engineering of nanomaterials for electromagnetic wave absorption. *Adv. Mater.* **2022**, *34*, 2107538. [CrossRef]
55. Mamatha, G.M.; Dixit, P.; Krishna, R.H.; Girish Kumar, S. Polymer based composites for electromagnetic interference (EMI) shielding: The role of magnetic fillers in effective attenuation of microwave, a review. *Hybrid Adv.* **2024**, *6*, 100200.

56. Shukla, V. Review of electromagnetic interference shielding materials fabricated by iron ingredients. *Nanoscale* **2019**, *1*, 1640–17671. [CrossRef]
57. Liu, Q.; Cao, Q.; Bi, H.; Liang, C.; Yuan, K.; She, W.; Yang, Y.; Che, R. CoNi@SiO_2@TiO_2 and CoNi@Air@TiO_2 microsphere with strong wideband microwave absorption. *Adv. Mater.* **2016**, *28*, 486–490. [CrossRef] [PubMed]
58. Che, R.; Peng, L.M.; Duan, X.; Chen, Q.; Liang, X. Microwave absorption enhancement and complex permittivity and permeability of Fe encapsulated within carbon nanotubes. *Adv. Mater.* **2004**, *16*, 401–405. [CrossRef]
59. Gabino, A.A.P.; Soares, B.G. Flexible microwave absorbing composites based on polydimethylsiloxane filled with hybrid carbonaceous materials: Statistical analysis of the synergistic effect. *Polym. Comp.* **2023**, *44*, 4623–4640. [CrossRef]
60. Zhao, B.; Zhao, C.; Li, R.; Hamidinejad, M.; Park, C.B. Flexible, ultrathin, and high-efficiency electromagnetic shielding properties of poly(vinylidene fluoride)/carbon composite films. *ACS Appl. Mater. Interfaces* **2017**, *9*, 20873–20884. [CrossRef]
61. Genovese, D.B. Shear rheology of hard-sphere, dispersed, and aggregated suspensions, and filler-matrix composites. *Adv. Colloid Interface Sci.* **2012**, *171*, 1–16. [CrossRef] [PubMed]
62. Gonçalves, F.A.M.M.; Santos, M.; Cernadas, T.; Alves, P.; Ferreira, P. Influence of fillers on epoxy resins properties: A review. *Adv. Colloid Interface Sci.* **2022**, *57*, 15183–15212. [CrossRef]
63. Mohammadi, M.; Yousefi, A.A.; Ehsani, M. Thermorheological analysis of blend of high- and low-density polyethylenes. *J. Polym. Res.* **2012**, *19*, 9798. [CrossRef]
64. Pei, X.; Yan, Y.H.; Yan, L.; Yang, P.; Wang, J.; Xu, R.; Chan-Park, M.B. A magnetically responsive material of single-walled carbon nanotubes functionalized with magnetic ionic liquid. *Carbon* **2010**, *48*, 2501–2505. [CrossRef]
65. Coey, J.M.D. *Magnetism and Magnetic Materials*; Cambridge University Press: Cambridge, UK, 2012.
66. Del Sesto, R.E.; McCleskey, T.M.; Burrell, A.K.; Baker, G.A.; Thompson, J.D.; Scott, B.L.; Wilkes, J.S.; Williams, P. Structure and magnetic behavior of transition metal based ionic liquids. *Chem. Commun.* **2008**, 447–449. [CrossRef]
67. Liu, H.; Liang, C.; Chen, J.; Huang, Y.; Cheng, F.; Wen, F.; Xu, B.; Wang, B. Novel 3D network porous graphene nanoplatelets/Fe_3O_4/epoxy nanocomposites with enhanced electromagnetic interference shielding efficiency. *Comp. Sci. Technol.* **2019**, *169*, 103–109. [CrossRef]
68. Jaiswal, R.; Agarwal, K.; Kumar, R.; Kumar, R.; Mukhopadhyay, K.; Prasad, N.E. EMI and microwave absorbing efficiency of polyaniline-functionalized reduced graphene oxide/γ-Fe_2O_3/epoxy nanocomposites. *Soft Mater* **2020**, *16*, 6643–6653. [CrossRef]
69. Zecchi, S.; Cristoforo, G.; Bartoli, M.; Tagliaferro, A.; Torsello, D.; Rosso, C.; Boccaccio, M.; Acerra, F. A Comprehensive Review of Electromagnetic Interference Shielding Composite Materials. *Micromachines* **2024**, *15*, 187. [CrossRef] [PubMed]
70. Menon, A.V.; Choudhury, B.; Madras, G.; Bose, S. "Trigger-free" self-healable electromagnetic shielding material assisted by co-doped graphene nanostructures. *Chem. Eng. J.* **2020**, *382*, 122816. [CrossRef]
71. Manna, R.; Srivastava, S.K. Reduced graphene oxide/Fe_3O_4/polyaniline ternary composites as a superior microwave absorber in the shielding of electromagnetic pollution. *ACS Omega* **2021**, *6*, 9164–9175. [CrossRef]
72. Li, C.J.; Wang, B.; Wang, J.N. Magnetic and microwave absorbing properties of electrospun $Ba_{(1-x)}La_xFe_{12}O_{19}$ nanofibers. *J. Magn. Magn. Mater* **2012**, *324*, 1305–1311. [CrossRef]
73. Bayrakdar, H. Complex permittivity, complex permeability and microwave absorption properties of ferrite–paraffin polymer composites. *J. Magn. Magn. Mater.* **2011**, *323*, 1882–1885. [CrossRef]
74. Schmitz, D.P.; Soares, B.G.; Barra, G.M.O.; Santana, L. Sandwich structures based on fused filament fabrication 3D-printed polylactic acid honeycomb and poly(vinylidene fluoride) nanocomposites for microwave absorbing applications. *Polym. Compos.* **2023**, *44*, 2250–2261. [CrossRef]
75. Zhang, X.; Wang, X.; Meng, F.; Chen, J.; Du, S. Broadband and strong electromagnetic wave absorption of epoxy composites filled with ultralow content of non-covalently modified reduced graphene oxides. *Carbon* **2019**, *154*, 115–124. [CrossRef]
76. Kowsari, E.; Mohammadi, M. Synthesis of reduced and functional graphene oxide with magnetic ionic liquid and its application as an electromagnetic-absorbing coating. *Compos. Sci. Technol.* **2016**, *126*, 106–114. [CrossRef]
77. Pratap, V.; Soni, A.K.; Siddiqui, A.M.; Abbas, S.M.; Katiyar, R.; Prasad, N.E. Dielectric and radar-absorbing properties of exfoliated graphite dispersed epoxy composites. *J. Electron. Mater.* **2020**, *49*, 3972–3981. [CrossRef]
78. Santos, E.; Albo, J.; Rosatella, A.; Afonso, C.A.M.; Irabien, A. Synthesis and characterization of magnetic ionic liquids (MILs) for CO_2 separation. *J. Chem. Technol. Biotechnol.* **2014**, *89*, 866–871. [CrossRef]

Disclaimer/Publisher's Note: The statements, opinions and data contained in all publications are solely those of the individual author(s) and contributor(s) and not of MDPI and/or the editor(s). MDPI and/or the editor(s) disclaim responsibility for any injury to people or property resulting from any ideas, methods, instructions or products referred to in the content.

molecules

MDPI

Article

Synergistic Solvent Extraction of Lanthanoids with Traditional Ligands (4-Acylpyrazolone and Bidentate Nitrogen Bases) in a Nontraditional Diluent Confirmed by Slope Analysis and NMR

Maria Atanassova [1,*], Nina Todorova [1] and Svetlana Simova [2]

[1] Department of General and Inorganic Chemistry, University of Chemical Technologies and Metallurgy, 8 Kliment Okhridski Blvd., 1756 Sofia, Bulgaria; nina.todorova@uctm.edu
[2] Institute of Organic Chemistry with Centre of Phytochemistry, Bulgarian Academy of Sciences, Acad. G. Bonchev Street, Block 9, 1113 Sofia, Bulgaria; svetlana.simova@orgchm.bas.bg
* Correspondence: ma@uctm.edu

Abstract

The synergistic solvent extraction of La(III), Eu(III) and Lu(III) with a chelating extractant, 4-benzoyl-3-methyl-1-phenyl-2-pyrazolin-5-one (HL), and neutral bidentate heterocyclic amines, such as 1,10-phenanthroline (S1 (phen)) or 2,2′-bipyridine (S2 (bipy)) in an ionic liquid of the imidazolium family $[C_1C_4im^+][Tf_2N^-]$ was investigated. Synergistic effects have been observed to result from the formation of a ternary complex in the organic phase, particularly in cases where the ligand S is a neutral synergistic agent. Examples include $La(L)_2(S2)_2$, $Eu(L)_3(S2)$ and $Lu(L)_x(S2)_2$, as well as $La(L)_3(S1)_2$, $Eu(L)_2(S1)$ and $Lu(L)_3(S1)_x$). The parameters of the solvent extraction process were determined and the influence of the synergistic agent on the extraction process was discussed. Additionally, the synergistic increase and separation factors were determined. The equilibrated organic phases were analyzed using ^{1}H NMR spectroscopy to elucidate the synergism in an extraction mechanism. The role of the ionic diluent in complexation processes and selectivity was investigated with the employment of the two synergistic agents for various metal s-, p-, d- and f-cations in the periodic table, with almost 22 metal ions.

Keywords: lanthanoids; synergistic extraction; 4-benzoyl-3-methyl-1-phenyl-2-pyrazolin-5-one; 1,10-phenanthroline; 2,2′-bipyridine; NMR; separation factors

1. Introduction

The phenomenon observed in the field of solvent extraction chemistry, whereby the combined use of two extractants results in the extraction of a metal ion species with a significantly enhanced efficiency compared to the additive effect observed when they are used separately, is referred to as a synergism [1–4]. The well-known synergistic effect in solvent extraction chemistry, which has been extensively studied over the past six decades in various molecular diluents, involves the enhancement of the extraction of a metal ion with an acidic chelating agent, typically through the addition of a neutral ligand [5]. In comparison with these mixtures, there is a relatively small number of studies dedicated to the solvent extraction of metals using mixtures comprising a neutral bidentate ligand, particularly in an ionic liquid medium [5]. For example, the formation of synergistic adducts containing a β-diketone as the acidic component (acetylacetone, benzoylacetone [6–8], pivaloyltrifluoroacetone [9], thenoyltrifluoroacetone [10–16], LIX 54 [17] and 1-phenyl-3-methyl-4-benzoyl-5-pyrazolone [18]) and bidentate chelating agents,

1,10-phenanthroline or 2,2′-bipyridyl, have been documented for a multitude of metals under a variety of experimental conditions in traditional organic diluents. It is noteworthy that Kassierer and Kertes [10] achieved a remarkably high synergistic effect, up to 10^6, through the combination of two bidentate chelating agents: the β-diketone and a nitrogen base. The two molecules, 1,10-phenanthroline and 2,2′-bipyridine, are among the most well-known base polypyridyl units that exhibit a high complexation affinity toward many metal ions as they represent versatile starting blocks for molecular recognition in supramolecular chemistry [19–21].

One significant area of investigation currently undergoing intensive research is the potential replacement of traditional volatile, toxic and/or flammable organic diluents, which raises safety and environmental issues nowadays with ionic liquid compounds (ILs) [22–25]. In the field of metal solvent extraction, separation and recycling by liquid–liquid processes, hydrophobic ILs of the imidazolium type $[C_nC_mim^+][Tf_2N^-]$ are preferred one, avoiding the problems linked to high viscosity. This type of compounds has already demonstrated their efficacy as organic media for a wide range of metals in the periodic table, including lanthanoids [5]. Cations are denoted as $[C_nC_mim^+]$ for *n*-alkyl-*m*-alkylimidazolium, while the anions $[Tf_2N^-]$ correspond to $(CF_3SO_2)_2N^-$ (bis(trifluoromethylsulfonyl)imide) [26,27].

Indeed, most rare earth elements are employed in a multitude of sectors, both traditional and modern, due to their diverse and advantageous characteristics (such as electronic, luminescent, magnetic and catalytic properties). Nevertheless, given the resemblance in the chemical and physical characteristics, the intra-group separation, especially neighboring elements, is a complex technological challenge that warrants substantial research effort [27]. On the other hand, lanthanoids are applied as critical metals with a strategic role in modern industries, making their effective recovery from various secondary sources through recycling a highly valuable sustainable technology to secure the Earth's green future. Moreover, modern green technology requires non-renewable raw materials sourced from primary geological resources (mines) or secondary supply (reuse or recycling as much as possible) but the research ambition is to achieve a fully circular economy un depending on the type of applied chemical technology [1–3]. In general, liquid–liquid extraction is a well-established hydrometallurgical process for the separation of metals.

This fundamental study concerns the solvent extraction of three trivalent ions, namely La^{3+}, Eu^{3+} and Lu^{3+}, which have been selected as representatives of the beginning, middle and end of the 4f series, respectively. The extraction process was conducted using the water-immiscible imidazolium-type ionic liquid $[C_1C_4im^+][Tf_2N^-]$, which was employed as a diluent for the widely used anionic ligand from the 4-acylpyrazolone family as a chelating extractant, both when used alone and in combination with bidentate nitrogen compounds such as 1,10-phenanthroline or 2,2′-bipyridine. The primary objective is to ascertain the extent of the synergistic enhancement and selectivity produced by the studied mixtures. However, the data interpretation and the slope analysis results assessment may be insufficient from the perspective of solvent extraction mechanism research in an ionic diluent. Nevertheless, they provide sufficient information about the utility of the employed solvent systems in prospective applications. The principal focus is, of course, the capacity to achieve effective selectivity in the intra-group 4f series through the utilization of diverse solvent systems. Finally, organic phases of biphasic solvent systems with the required ligand concentrations, consisting mainly of the $[C_1C_4im^+][Tf_2N^-]$ diluent after contact with the corresponding aqueous phase, were also studied for the first time by ^1H 1D NMR without any dilution.

2. Results and Discussion

2.1. Solvent Extraction of La(III), Eu(III) and Lu(III) Ions with HL Alone and Two Synergistic Mixtures HL–1,10-Phen or HL–2,2′-Bipy

Firstly, the solvent extraction performance of the chelating agent HL alone diluted in an ionic diluent was assessed towards La^{3+}, Eu^{3+} and Lu^{3+} ions as representatives of light, middle and heavy 4f series, *ceteris paribus*. In fact, neutral extractants are readily soluble in imidazolium-based ILs, unfortunately acidic extractants sometimes showed poor solubility and this greatly affects their extraction behavior. The stoichiometric information about the extraction processes, called "slope analysis" method, is based on an examination of the variation in D (the distribution ratio) as a function of the relevant experimental variables [5]. In the IL system, slope analysis of Ln solvent extraction with HL molecule used alone was investigated as a function of ligand concentration in the organic oil phase at a constant pH of the aqueous phase (Figure 1) in order to determine the reaction mechanism, as well as the stoichiometry, of the Ln^{3+}–HL complexes formed in the $[C_1C_4im^+][Tf_2N^-]$ phase. As shown in Figure 1, the obtained plots for HL concentration were linear with a slope very close to three for solvent extraction of La^{3+}, Eu^{3+} and Lu^{3+} ions, suggesting that three ligand molecules were required to extract one Ln^{3+} ion into the IL, in that a 1:3 metal/ligand ratio complex was formed. The formation of 4f metal chelates, LnL_3, with 4-acylpyrazolones in an IL media was also noted previously [28]. The formation of self-adducts $LnL_3{\cdot}HL$ when acylpyrazolones are used as chelating extractant in typical molecular diluent was found in some other studies [29,30], but in refs. [31,32], the extraction of the LnL_3 chelate complex was also reported. However, in an ionic liquid media, the situation is much more complicated as various metallic species have been usually established due to the ionic character of the diluent [5]. In general, the solvent extraction mechanism, when the metal cation forms a chelate complex with available ligands and moves into an organic phase as a single, neutral uncharged species, was represented by the following equation [28]:

$$Ln^{3+}{}_{aq} + 3HL_{org} \rightleftharpoons LnL_{3,org} + 3H^{+}{}_{aq} \quad (1)$$

where subscripts "aq" and "org" denote the aqueous and organic phases, respectively.

The coordination sphere of the trivalent ion is unsaturated in this six-coordinate chelate complex, so the Ln(III) ion can expand it by forming an adduct formation. Depending on the experimental protocol, with participation of water molecules, for example $LnL_3{\cdot}(H_2O)_x$, x = 2 or 3 [5]. Therefore, in an IL solution, the completion of the coordination sphere can be achieved either through binding with the Tf_2N^- anions or by water molecules. The last ones are known to transfer to the IL phase, ca. 12,000 ppm under such chemical conditions [5]. In fact, Tf_2N^- is one of the weakest coordinating anions, so does not compete favorably with H_2O molecules for the Ln(III) coordination sphere [5].

Secondly, the liquid–liquid extraction of La^{3+}, Eu^{3+} and Lu^{3+} ions was carried out by two molecules forming the acidic/neutral couple in order to produce the synergistic enhancement in an IL media, i.e., $[C_1C_4im^+][Tf_2N^-]$. The corresponding plots of $\log D_{I,S}$ vs. pH; $\log D_{I,S}$ vs. log [HL] and $\log D_{I,S}$ vs. log[S] were determined by the investigations of the synergistic extraction of three lanthanoid ions. These plots are shown in Figures 2–5, S1 and S2 (Supplementary Materials). The obtained values of the D ratios of the mixed synergistic systems are greater than those of individual extractants [33,34]. This observation clearly reveals the positive synergistic extraction effects under the applied experimental conditions herein. In other words, the synergistic enhancement in an IL media is realized, but it is difficult to establish the nature of the exact extracting Ln^{3+} complex formed in this oil phase as a different stoichiometry is revealed for the three 4f ions. The arrangement of one unique synergistic complex in the organic phase is probably

an unfavorable extraction mechanism applying one solvent system. Thus, the organic phase synergistic reaction could not be expressed by one equation only. This is due to the intensive ion exchange between the two liquid phases, including the loss of the IL cation or anion to the aqueous phase, in contrast to molecular diluents [5]. Therefore, in the presence of the second extractant, 2,2′-bipyridine molecules (S2), the La^{3+} and Eu^{3+} synergistic extraction process can be expressed by the equations:

$$La^{3+}{}_{(aq)} + 2HL_{IL} + 2S2_{IL} \rightleftharpoons La(L)_2(S2)_{2IL} + 2H^{+}{}_{(aq)}, \quad (2)$$

with the participation at least two chelating ligands and two molecules of the synergistic agent.

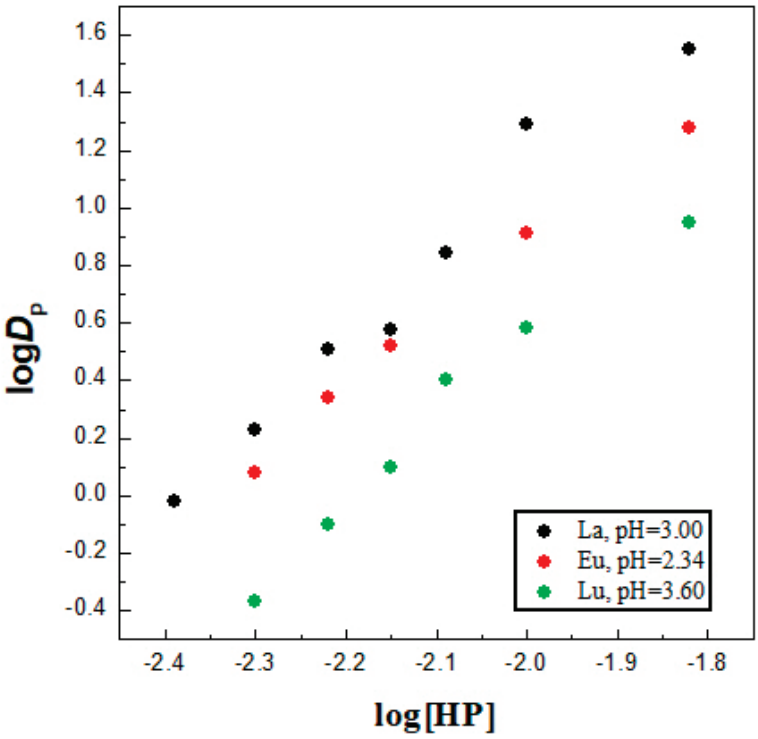

Figure 1. Log D vs. log $[HL]_{IL}$ plots at constant pH for La^{3+} (slope ~2.89), Eu^{3+} (slope ~2.50) and Lu^{3+} (slope ~2.76) in $[C_1C_4im^+][Tf_2N^-]$. The experiment was separately performed under the presence of a single metal ion in each aqueous phase.

The lanthanoid mononuclear β-dicarbonyl complexes generally have very high coordination numbers (C.N.), i.e., varying from 6 to 12, with 8 and 9 being rather common. This phenomenon depends on the ionic radii of the investigated ions (La^{3+}, Gd^{3+} and Lu^{3+}: 103.2, 93.8 and 86.1 pm, respectively), the employed ligand, the reaction medium, the diluent in use and experimental conditions, such as the temperature or ligand to metal ratio [35]. Generally, when ILs are employed, the solvent extraction ability of a neutral ligand is observed to be almost equal to that of the principle acidic compound, even at low concentrations [5].

$$Eu^{3+}{}_{(aq)} + 3HL_{IL} + S2_{IL} \rightleftharpoons Eu(L)_3(S2)_{IL} + 3H^{+}{}_{(aq)}, \quad (3)$$

with the participation of three chelating ligands and one synergistic agent.

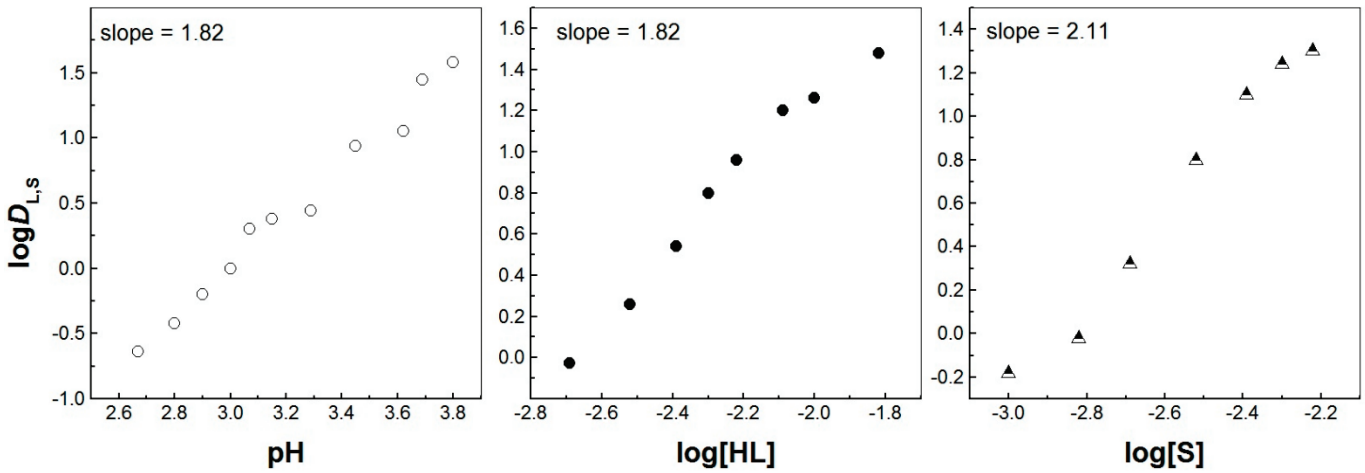

Figure 2. Log $D_{L,S}$ vs. log pH ([HL] = 5 × 10^{-3} mol/dm^3 and [S] = 3 × 10^{-3} mol/dm^3), log $D_{L,S}$ vs. log[HL]$_{IL}$ ([S] = 3 × 10^{-3} mol/dm^3 at pH = 3) and log $D_{L,S}$ vs. log[S] ([HL] = 5 × 10^{-3} mol/dm^3 at pH = 2.78) plots for solvent extraction of La^{3+} with the HL–bipy mixture in [$C_1C_4im^+$][Tf_2N^-].

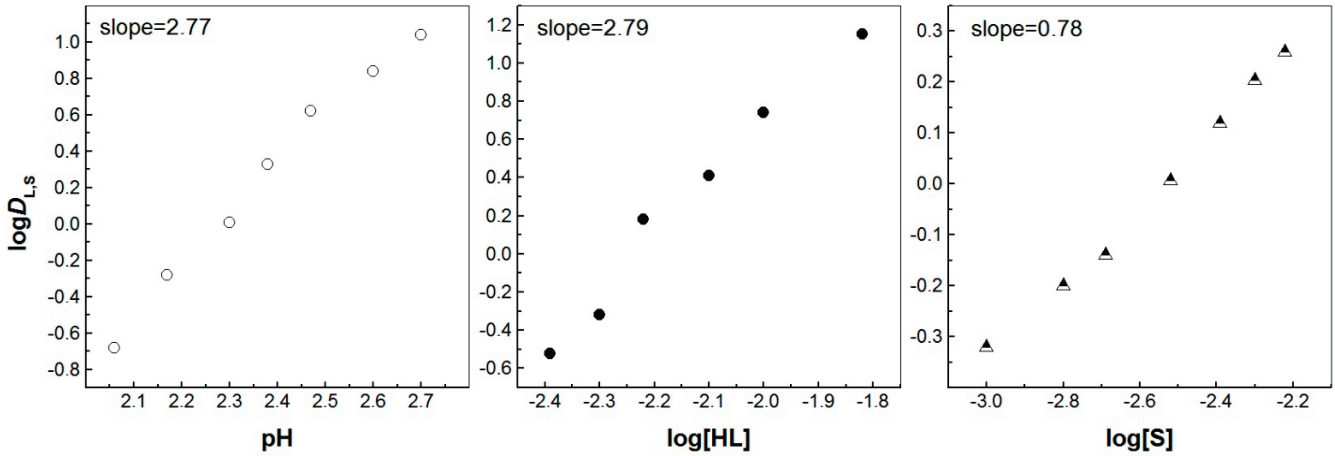

Figure 3. Log $D_{L,S}$ vs. log pH ([HL] = 5 × 10^{-3} mol/dm^3 and [S] = 3 × 10^{-3} mol/dm^3), log $D_{L,S}$ vs. log[HL]$_{IL}$ ([S] = 3 × 10^{-3} mol/dm^3 at pH = 2.30) and log $D_{L,S}$ vs. log[S] ([HL] = 5 × 10^{-3} mol/dm^3 at pH = 2.23) plots for solvent extraction of Eu^{3+} with the HL–bipy mixture in [$C_1C_4im^+$][Tf_2N^-].

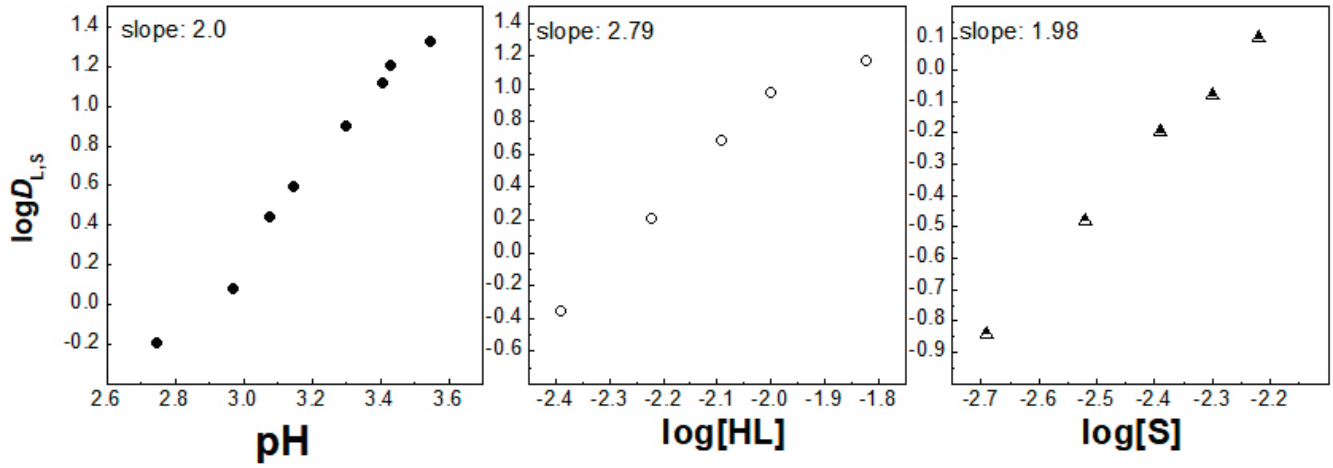

Figure 4. Log $D_{L,S}$ vs. log pH ([HL] = 5 × 10^{-3} mol/dm^3 and [S] = 3 × 10^{-3} mol/dm^3), log $D_{L,S}$ vs. log[HL]$_{IL}$ ([S] = 3 × 10^{-3} mol/dm^3 at pH = 2.55) and log $D_{L,S}$ vs. log[S] ([HL] = 5 × 10^{-3} mol/dm^3 at pH = 2.55) plots for solvent extraction of La^{3+} with the HL–phen mixture in [$C_1C_4im^+$][Tf_2N^-].

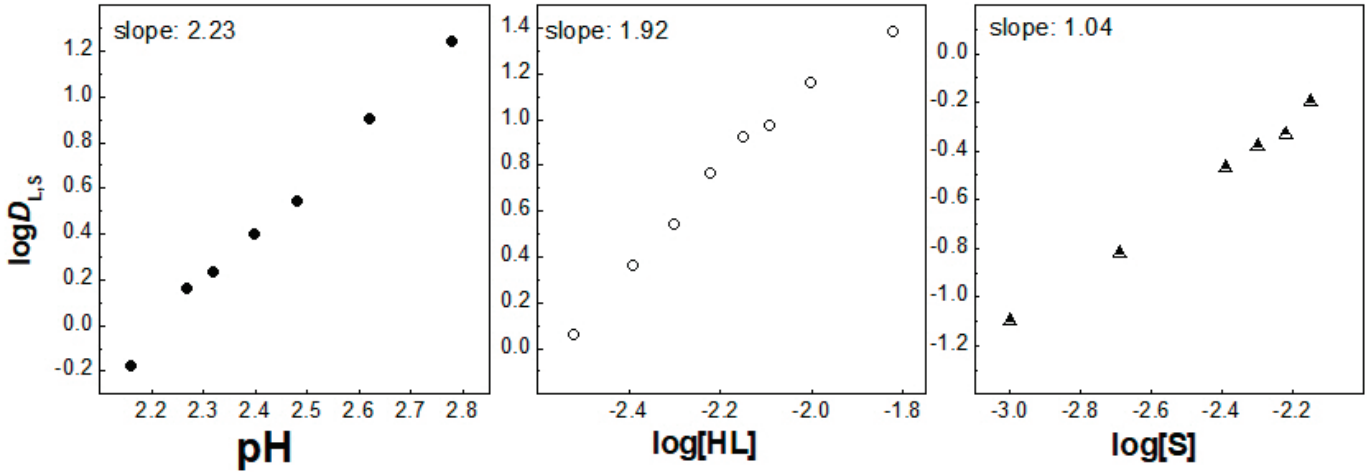

Figure 5. Log $D_{L,S}$ vs. log pH ([HL] = 5 × 10^{-3} mol/dm^3 and [S] = 3 × 10^{-3} mol/dm^3), log $D_{L,S}$ vs. log[HL]$_{IL}$ ([S] = 3 × 10^{-3} mol/dm^3 at pH = 2.25) and log $D_{L,S}$ vs. log[S] ([HL] = 5 × 10^{-3} mol/dm^3 at pH = 2.25) plots for solvent extraction of Eu^{3+} with the HL–phen mixture in [$C_1C_4im^+$][Tf_2N^-].

The proposed complex is, at minimum, eight-coordinated as well, from which it follows that the arrangement of the europium complex in the organic ionic medium follows the generally accepted rules in solvent extraction chemistry. Many years ago, the four conditions for the synergistic extraction of a metal with a mixture including acidic/neutral ligands in molecular diluents were indicated, leading to a considerable effect [36], i.e., formation of a metal chelate complex. The second extractant, i.e., the synergist, can displace any coordinated water from a chelate, rendering it less hydrophobic. On the other hand, the second extracting compound is less coordinated than the first one. Moreover, the maximum coordination number achieved by metal, as well as the obtained architecture of the complex, should be favorable. In synergistic systems, the chelating compound (HL) typically deprotonates to form an anionic ligand L^- that can chelate with the metal ion, M^{n+}. At the same time, the neutral ligand, or in other words, the synergistic agent S, replaces any remaining water molecules from the coordination shell of the neutral complex (chelate), enhancing its solubility in the organic phase. Generally, this process can be expressed as:

$$M^{n+} + nHL + xS \rightleftharpoons ML_n{\cdot}S_x + nH^+ \quad (4)$$

Unfortunately, it is difficult to establish the exact nature of the formed complex for the last cation from 4f series with HL–bipy mixture in [$C_1C_4im^+$][Tf_2N^-] media, as only the number of S2 molecules could be derived approximately from the obtained results (Figure S1): $Lu(L)_x(S2)_2$.

On the other hand, the number of coordinated synergistic molecules was preserved when 1,10-phenantroline was introduced to the solvent system for La^{3+} and Eu^{3+} ions, when again two and one molecules participated in the extracted complexes, respectively (Figures 4 and 5). Despite that, the picture changes with the chelating extractant, probably due to steric hindrances related to the size of the target 4f ion. As a result, in the presence of the second extractant, 1,10-phenatroline (S1), the synergistic extraction of both 4f ions can be expressed by the equations:

$$La^{3+}{}_{(aq)} + 3HL_{IL} + 2S1_{IL} \rightleftharpoons La(L)_3(S1)_{2IL} + 3H^+{}_{(aq)}, \quad (5)$$

$$Eu^{3+}{}_{(aq)} + 2HL_{IL} + S1_{IL} \rightleftharpoons [Eu(L)_2(S1)]^+{}_{IL} + 2H^+{}_{(aq)}, \quad (6)$$

$$Lu^{3+}{}_{(aq)} + 3HL_{IL} + nS1_{IL} \rightleftharpoons Lu(L)_3(S1)_{nIL} + 3H^+{}_{(aq)}, \quad (7)$$

The results show that under the experimental conditions, Lu^{3+} ions are extracted as neutral adduct complexes. However, the stoichiometry of the extracted species in the organic IL phase depends on the pH, Ln^{3+}, HL or S1 concentrations, the solubility of ILs' components in the aqueous phase, etc. In other words, the number of coordinated S1 molecules is unclear for this heavy 4f ion (Figure S2).

In terms of contemporary priorities, the solvent extraction systems must be adjusted in a way to accommodate the green chemistry, both achieving an efficient extraction process and having good selectivity as a target in order to minimize the possible contaminants. For instance, the undesirable IL's component solubility in the aqueous phase, which, in general, has a pronounced impact on metal extraction efficiency, can be successfully reduced when bidentate nitrogen bases are employed in the solvent systems [5]. Thus, an improved understanding of solvation phenomena in both phases, aqueous and organic oil media, of the design of complexing agents that do not create environmental hazards or further waste disposal complications when their utility is accomplished (CHON principle) can be suggested for future research regarding green and sustainable chemistry. Moreover, after forward synergistic solvent extraction, the studied Ln^{3+} ions were easily stripped from the investigated organic phases. The achieving metal removal percentage is ca. 95%, using 0.8 mol/dm^3 HCl acid as a stripping agent for the back extraction process.

The values of the synergistic coefficients calculated in the present study, as well as some previously published data, are given in Table 1. It is seen that lanthanoids are extracted synergistically using both HL–phen and HL–bipy mixtures, (logSC $\geq$ 0). However, the data show that the addition of bidentate nitrogen bases molecules to the chelating ligand causes a rather small synergism, i.e., the values are below one order of magnitude in ionic media. In addition, concerning the synergistic effects in $[C_1C_4im^+][Tf_2N^-]$ media, the two investigated solvent systems display different efficiencies across the 4f series as well. Further, the synergistic solvent extraction of five representatives of 4f series with a chelating extractant 4-benzoyl-3-phenyl-5-isoxazolone (HPBI) or 2-thenoyltrifluoroacetone (HTTA) and the two neutral bidentate heterocyclic amines S1 and S2 in $CHCl_3$ was investigated nearly 14 years ago. Therefore, synergism as a phenomenon was reported to be due to formation of the ternary complex in the molecular organic phase, like $Ln(PBI)_3{\cdot}S$ or $Ln(TTA)_3{\cdot}S$. The synergistic enhancement was established by Atanassova for all five 4f metals and mixtures of extractants (logSC > 0), and it changes approximately from 10^2 to 10^6. So, the two bidentate ligands, the Lewis base phenanthroline or bipyridyl, in combination with an acidic chelating agent, produce a very strong synergistic effect on the solvent extraction of lanthanoids in molecular diluents, like $CHCl_3$ [37]. Those data also show that the SCs obtained for the mixtures including 1,10-phenantroline as a synergistic agent are approximately an order of two and one higher magnitude than that when 2,2′-bipyridyl is used in combination with the two chelating ligands, HTTA or HPBI, respectively. This observation confirms the findings of previous investigations in which the synergistic effect decreases in the order phen > bipy, with differences of up to two orders of magnitude [11]. The larger synergistic effect obtained with the 1,10-phenanthroline compound applied as a synergistic agent is probably due to its stronger donor properties [17]. A similar conclusion could be drawn to some extent for the present study, using an ionic diluent as an organic media. On the other hand, the relatively small synergistic increase observed with ILs in solvent extraction chemistry is, of course, a common finding compared to traditional organic diluents [17]. Further, we must pay attention that the values are logarithmic, i.e., significant synergism was found in addition to the positive effect of ILs in the metal extraction process.

Table 1. Values of the synergistic coefficients ([HPBI = 2.5 × 10^{-3} mol/dm^3, [S] = 5 × 10^{-3} mol/dm^3 phen: pH = 1.70; bipy: pH = 1.90) ([HTTA] = 4 × 10^{-2} mol/dm^3 and [S] = 5 × 10^{-3} mol/dm^3, phen: pH = 2.50; bipy: pH = 3.20) in $CHCl_3$ [37].

Ln^{3+}	logSCs					
	HL–Bipy	**HL–Phen**	**HPBI–Bipy**	**HPBI–Phen**	**HTTA–Bipy**	**HTTA–Phen**
La	0.57	0.09	1.41	3.26	2.91	4.82
Nd			2.48	3.58	4.11	6.04
Eu	−0.4	0.46	2.44	3.31	4.15	5.95
Ho			2.59	3.54	4.51	6.34
Lu			2.55	3.48	4.89	6.49

2.2. Chemical Modeling of Solvent Extraction Processes by NMR Analysis

One goal of this scientific investigation is to propose a plausible solvent extraction model, as simple as possible, that quantitatively captures the reaction process correctly according to the qualitative data obtained. First, a slope analysis was performed to evaluate the stoichiometry due to the synergistic extraction of Ln^{3+} ions in an IL media. To shed new light on the synergistic phenomenon, the phase behavior of the binary system, i.e., the chelating ligand plus the synergistic agent, is studied by a detailed analysis of the ^1H NMR spectra. For the purposes of spectroscopic interpretation, all ionic liquid phases are analyzed after phase separation of organic–aqueous layers using the Eu^{3+} cation (see Table S1 in the Supplementary Materials). To the best of our knowledge, this is the first time that this phenomenon has been detected directly in an IL without the additional application of deuterated diluents and the corresponding dilution of the organic phases used. This approach is novel in the field and extremely labor-intensive, although highly plausible. Such a scenario confirms the hypotheses formulated (as seen in Figures 6, S3 and S4 and Table S1) the involvement of the second synergistic ligand in the chelating metal species during the solvent extraction process. The striking point here is the high value of uncoordinated ligands used, which are usually in excess of the metal concentration in the vicinity of the interface, and the amount of diluent which somehow predominated in the screened NMR samples.

Generally, the enhancement in the synergistic solvent extraction of metallic species may depend on the nature and strength of the possible interaction between the two ligands [38]. It should be noted that a weak but detectable interaction between the two organic extractants (HL and S1 or S2) has been detected in the spectra between them in an IL, mainly reflected in the chemical shift changes in the signals of HL. This trend is like that described for acidic–neutral ligand couples [39]. On the contrary, the metal–synergistic agent interaction with Eu^{3+} ions induces higher shift changes in the neutral bidentate heterocyclic amines (Table S1).

Actually, proton, carbon, fluorine and phosphorus NMR spectra have previously been used to investigate the possible interactions between a series of imidazolium-based ILs and several extractants, acidic chelating or neutral ligands [40]. It was shown by Kurteva et al. that no interactions occur in chloroform-D solution independently of the length of the imidazolium alkyl chain or of the structure of the ligand molecule [40]. In other words, these IL compounds could be considered as pure diluents in the solvent extraction systems.

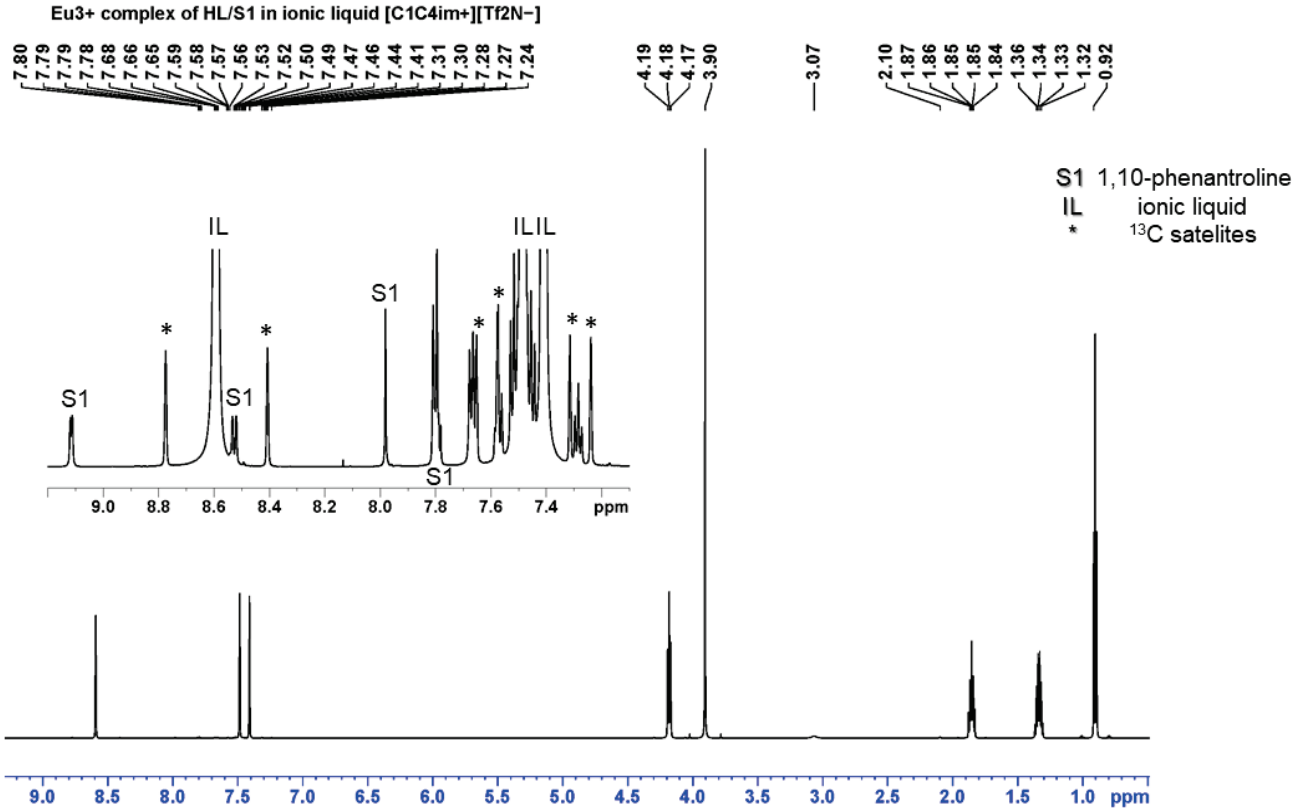

Figure 6. Representative ^{1}H NMR spectrum of HL/S1 in [$C_1C_4im^+$][Tf_2N^-], without dilution of the organic phase with deuterated diluent.

2.3. Solvent Extraction, Synergism and Selectivity Across the Periodic Table

On the whole, green technology likely requires non-renewable raw materials sourced from primary geological resources like mines or a secondary supply via reuse or recycling. Nowadays, the ambition is to create a fully circular economy, in which demand can be satisfied only by recover of almost all metals in the periodic table [39]. Unfortunately, modern society is not yet at that point, even scientifically. The competitive solvent extraction test of almost 22 metal ions by the chelating ligand HL and its mixtures has also been conducted in order to evaluate the role of a second molecule added into the solvent system, Figure 7. Therefore, the studied 22 metal ions could be classified approximately in the following two groups, according to the degree of S1 or S2 extraction performance in an IL media:

(1) Unextractable metal ions, % E < 1: Li^+, Na^+, Tl^+, Ca^{2+}, Mg^{2+}, Ba^{2+}, Sr^{2+}, Al^{3+}, Cr^{3+}. At the same time 4f ions could not be extracted with S2 compound used alone. It can be said that the process is ineffective for K^+ and Pb^{2+} ions.

(2) Overall extraction, % E ≥ 90: Cu^{2+}, Ni^{2+}, Co^{2+}, Bi^{3+}, Ag^+; while Hg^{2+} only with S1. As a matter of fact, both Bi^{3+} and Ag^+ ions could be extracted with pure IL without the need for any complexing agent. The same can be said for iron, based on the data obtained: Fe^{3+}: ≤17%.

Generally, the S1 compound presents a high complexation constant with d-, and to a lesser extent, f-block cations due to their stabilization by favorable enthalpic contributions arising from the formation of strong coordination bonds with the nitrogen atoms [41]. In fact, the implications of the relatively lower affinity of M(III) ions for pyridyl donors in aqueous solution than of M(II) ions is of considerable importance in the design of ligands for selective complexation, particularly in cases where this involves the trivalent Ln(III) and Am(III) ions [42]. Furthermore, in essence, the rigidity of the 1,10-phen molecule and

the permanent juxtaposition of the nitrogen donor atoms somehow provides an entropic advantage relative to its 2,2′-bipyridine analogs, resulting in enhanced kinetics of complex formation, as well as increased surface activity at the oil–water interface due to its hydrogen bonding with water molecules [43]. The following ions, Co^{2+}, Ni^{2+}, Li^{+} and Ln^{3+}, deserve special attention as a part of green sustainable technologies. The results obtained in Figure 7 indicate that Co^{2+} and Ni^{2+} are quantitatively extracted up to 100% applying S1 or S2 ligands, contrary to alkaline and rare earth ions, which is a serious advantage in terms of separation from secondary resources as a diverse range of acceptable sources for the metals via recycling. The predominance of the S1 over the S2 molecule is only observed herein for mercury and of course in the lanthanoid series. In other words, excluding the second series of ions for the first one, we can expect a synergistic effect using the mixed solvent systems for their extraction, especially the lanthanoids. The picture obtained for cobalt and nickel, which are not extracted with the chelating acid ligand HL or an IL, is also of interest. On the other hand, Fe^{3+} is approximately 100% extracted by the HL compound, which means that there is no need for a second ligand addition. Therefore, a synergistic increase could occur for the trivalent lanthanoids and Al^{3+}, given the fact that this phenomenon is not at all characteristic for metals from groups 1 and 2 of the periodic table [5,39]. And if there is insignificant synergism achieved for 4f ions (~5–8% increment), then for aluminum, the liquid–liquid extraction process is more than effective with the participation of 1,10-phenatroline as a synergistic agent.

1	2	3	4	5	6	7	8	9	10	11	12	13	14	15
Li(I) – – – – – –									pH_{eq}= 1.65	IL HP S1 S2 HP–S1 HP–S2				
Na(I) – – – – – –	Mg(II) – – – – – –											Al(III) – 3.2% – – 68.8% 4.5%		
K(I) 6.2% – 8.2% 1.6% – –	Ca(II) – – – – – –	Sc(III)	Ti(IV)	V(V)	Cr(III) – – – – – –	Mn(II)	Fe(III) 15.5% 99.3% 16.9% 16.6% 98.4% 98.2%	Co(II) – – 100% 100% 100% 99.05%	Ni(II) – – 89.3% 99.7% 57.4% 99.7%	Cu(II) 1.9% 87.5% 99.8% 99.8% 100% 100%	Zn(II)	Ga(III)		
Rb(I)	Sr(II) – – – – – –	Y(III)	Zr(IV)	Nb(V)	Mo		Ru(III)	Rh(III)	Pd(II)	Ag(I) 99.7% 99.7% 99.7% 99.7% 100% 100%	Cd(II)	In(III)		
Cs(I)	Ba(II) – – – – – –	Ln(III)	Hf(IV)	Ta(V)	W(VI)	Re(VII)	Os(IV)	Ir(III)	Pt(IV)	Au(III)	Hg(II) 17.2% 11.2% 86.6% 28.9% 70.5% 35.9%	Tl(I) – – – – – –	Pb(II) 21.09% 4.2% 4.0% 3.09% 3.9% 1.5%	Bi(III) 99.8% 99.8% 99.8% 99.8% 100% 100%

Ln(III)													
La(III) – 4.3% 1.05% – 4.07% 6.0%	Ce(III) – 8.3% 1.9% – 7.04% 8.3%	Pr(III)	Nd(III)	Sm(III)	Eu(III) – 39.07% 1.5% – 44.6% 44.3%	Gd(III)	Tb(III)	Dy(III)	Ho(III)	Er(III)	Tm(III)	Yb(III)	Lu(III) – 42.6% 1.9% – 49.7% 48.4%

Figure 7. Solvent extraction performance of pure IL and HL (1×10^{-2} mol/dm^3), S1 and S2 (8×10^{-3} mol/dm^3) ligands diluted in $[C_1C_4im^+][Tf_2N^-]$ as well as the two mixtures (HL–S1 and HL–S2: 1×10^{-2} mol/dm^3 – 5×10^{-3} mol/dm^3) for 22 metal ions (see the explanation under no. 11 cell). The reported extractability values (%) represent the average of three measurements with deviation less than 5%.

Regarding the selectivity, it seems that metals such as Ag, Bi, Pb and Fe can be relatively easily separated from the representatives of the 4f series only with an ionic liquid without the need for additional extracting molecules in the solvent system. On the other hand, the presence of a chelating ligand affects the selectivity of metals like Fe, Cu and the light lanthanoids. For example, the calculated values of SFs of the corresponding pairs are very high: Fe/La = 3288, Fe/Ce = 1547 as well as Cu/La = 165, Cu/Ce = 77.

Unfortunately, as a common rare earth-associated impurity, usually aluminum (Al) in Ln^{3+} solution, not only affects the operation of the purification process, but also greatly reduces the final quality of products. Therefore, it is imperative to somehow develop new methods for the efficient removal of Al from Lns [44]. Hu et al. have recently reported that the SF of the Al/Gd pair could be up to 340 in $[(CH_2)_7COOHpyr^+][Tf_2N^-]/[C_1C_4im^+][Tf_2N^-]$ a solvent system, as the removal rate of Al^{3+} is 97.1% and the recovery rate of Gd^{3+} is 85.6% through the one-time extraction step, which was significantly higher than the results reported in the literature at the time. The resulting separation between the two cations is too high considering that the extraction efficiency of both ions is also quite high. Despite this, the results obtained by Hu and co-workers are far away from those obtained in this study for HL and HL–S2 systems: (Eu/Al) 19.2 and 16.8, as well as (Lu/Al) 22.3 and 19.8, respectively.

Considering the low pH of the experimental conditions, it is normal to obtain a high separation in the 4f series between the light and heavy lanthanoid pairs. The most significant SFs are observed for pairs of light–medium and light–heavy pairs due to the synergistic solvent extraction process with the participation of 1,10-phenantroline, as shown in Table 2. This contrasts with the generally accepted observation that the separation becomes poorer as the extractability increases in the synergistic solvent extraction of metals. However, the investigated mixture, HL–S2 only produces better selectivity for Eu/Ce and Lu/Ce pairs in comparison with HL ligand used alone.

Table 2. Selectivity in 4f series during competitive solvent extraction.

System	Eu/La	Eu/Ce	Eu/Lu	Lu/La	Lu/Ce	Lu/Eu
IL	–	–	–	–	–	–
HL	15	7.1	0.8	17.5	8.2	1.2
S1	1.4	0.7	0.7	1.8	0.9	1.3
S2	–	–	–	–	–	–
HL–S1	19.2	10.6	0.8	23.6	13.1	1.2
HL–S2	12.5	8.9	0.8	14.7	10.5	1.2

In accordance with what is known in molecular diluents, the comparison of selectivity data shows that the SFs are higher for the lighter lanthanoids and the Eu/La pair and extremely low for the heavy Lu/Eu pair, independently of the extracting phase nature, ionic or molecular ($CHCl_3$), as shown in Table 2. However, the impact of the diluent has already been demonstrated on multiple occasions for various solvent systems in the field of extraction chemistry [45]. In other words, in comparison to $CHCl_3$, the ionic liquid offers increased values of distribution ratios *D*, at the expense of a leveling off of the SFs. Despite this, the extracted metal complex would be easier to rearrange in an organic diluent with small carbon chain length in terms of the energetics of the physical distribution of metal solvate. In fact, the SF is a complex function of the chemistry of the metal ions in the two liquid phases, aqueous and organic [46]. Unfortunately, it is also worth mentioning that the ILs prices are generally expensive, and this can result in significant process needing to be justified.

It is interesting to compare the SFs obtained for the solvent extraction of lanthanoids with the same or various chelating extractants (thenoyltrifluoroacetone (HTTA), 4-benzoyl-3-phenyl-5-isoxazolone (HPBI) or 1-phenyldecane-1,3-dione, the active component in the commercial extractant LIX 54) and various synergists, viz. the crown ethers, calix[4]arenes or diphenylsulfoxide. Unfortunately, limited comparisons are possible because data are not available for all lanthanoid metals. The calculated separation factors of two pairs, Eu/La and Lu/Eu, obtained from these systems are listed in Table 3. As can be seen from the data presented in the table, better selectivity is observed with the participation of molecular systems, as compared to Table 1. On the other hand, it clearly reveals the influence of an empty (f^0), half-filled (f^7) and full f-subshell (f^{14}) on lanthanoid's refinement. The results somehow show the influence of Z on the loss of selectivity across the 4f series, which implies an advantage in the distinction of light, middle and heavy ions. Therefore, recycling, and the potential recovery of 4f metals from end-of-life technological objects, for example, could benefit to some extent from the absence of significantly complicated adjacent lanthanoids' intra-group separation at these technological lines by the further application of ILs.

Table 3. Separation factors of the pairs Eu/La and Lu/Eu, applying various molecular synergistic mixtures.

Extractants	Eu/La	Lu/Eu
HTTA–1,10-phen	3.3×10^3	11.74
HTTA–2,2′-bipy	4.2×10^3	18.62
HPBI–2,2′-bipy	263.02	5.62
HPBI–1,10-phen	27.54	6.45
HL/$CHCl_3$	263	3.4
HL–diphenylsulphoxide [47]	75	13
HL–para-*tert*-octylcalix[4]arene with P=O donor groups [48]	213	5.6
HL–para-*tert*-butylcalix[4]arene with P=O donor groups [49]	60.2	12.6
HL–DB18C6–$CHCl_3$ [50]	251.3	54.9
HL–B18C6 [50]	912	87
HL–18C6 [50]	371.5	147.9
HL–DB18C6–$C_2H_4Cl_2$ [51]	72.4	251
HL–DB24C8 [51]	154.8	37.2
LIX54–1,10-phen [17]	2.75×10^3	2.95
LIX54–2,2′-bipy [17]	1.6×10^4	15.84

3. Materials and Methods

3.1. Materials

The commercial product 4-benzoyl-3-methyl-1-phenyl-2-pyrazolin-5-one (HL) with a purity higher than 99% (Fluka, Buchs, Switzerland), 2,2′-bipyridine (Merck (Darmstadt, Germany), p.a.) and 1,10-phenanthroline (Merck, p.a.) were used as supplied (the structural formulas of the extractants are presented in Figure S5). Stock solutions of the lanthanoid ions were prepared from their oxides (Fluka, puriss) by dissolving them in concentrated hydrochloric acid and diluting them with distilled water to the required volume. The diluent was 1-butyl-3-methylimidazolium-bis(trifluoromethanesulfonyl)imides, (purity, 99.5%,

average water content is ca. 200 ppm) purchased from Solvionic (Toulouse, France). The Arsenazo III (Fluka, Switzerland) was of analytical purity, as were the other reagents used.

3.2. Extraction Procedure

The experiments were carried out using aqueous and organic phases in volumes of 2 cm^3 and 1 cm^3, respectively. The extractant solutions were prepared by precisely weighted samples. The samples were shaken mechanically for 2 h at room temperature (22 ± 2) °C, which proved sufficient to achieve equilibrium. The upper layer contained the aqueous phase and the bottom layer included the organic IL phase. After the separation of the phases, the metal concentration in the aqueous phase was determined spectrophotometrically (S-20 Spectrophotometer Boeco (Hamburg, Germany)) using Arsenazo III [52]. The concentration of the metal ion in the organic phase was obtained by the material balance. These concentrations were used to calculate the distribution ratio. The acidity of the aqueous phase was measured by a pH meter with an accuracy of 0.01 pH unit (211 HANNA digital pH meter (Smithfield, RI, USA)). The pH of the aqueous solutions was adjusted by the addition of either HCl or NaOH to a solution of 0.1 mol/dm^3 2-morpholinoethanesulfonic acid (MES) buffer. The initial concentration of the metal ions was 2.5×10^{-4} mol/dm^3 in all experiments.

The distribution ratio (D) at equilibrium was calculated as:

$$D = \frac{[M^{n+}]_{aq,in} - [M^{n+}]_{aq,f}}{[M^{n+}]_{aq,f}} \times \frac{V_{aq}}{V_{IL}} \tag{8}$$

where $[M^{n+}]_{aq,in}$ is the concentration of M^{n+} ion in the aqueous phase before liquid–liquid extraction tests, $[M^{n+}]_{aq,f}$ is the concentration of the same metal ion in the aqueous phase after extraction. In general, V_{aq} and V_{IL} are the volumes of aqueous and organic phases used to perform experiments, herein 2:1 v/v extraction. For instance, duplicate experiments showed that the reproducibility of D measurements was generally within 95%.

The synergistic enhancement upon the addition of a second extractant can be assessed using synergistic coefficients calculated as:

$$\mathrm{SC} = \log\,(D_{1,2}/D_1 + D_2) \tag{9}$$

where $D_{1,2}$, D_1, and D_2 denote the distribution coefficient of a metal ion using mixture of extractants ($D_{1,2}$) and the same extractants when used separately (D_1 and D_2).

For competitive extraction tests, a volume of 2 mL of the prepared aqueous solution containing various M^{n+} metal ions (the corresponding nitrate salts were used, $M^{n+}(NO_3)_n/M^{n+}(NO_3)_n{\cdot}xH_2O$) was equilibrated for 3 h (1500 rpm) with a 2 mL organic phase, which includes the studied ligand molecule(s). After phase separation, the metal ions concentrations in the aqueous solution were determined by ICP-OES ("Prodigy" high-dispersion ICP-OES, Teledyne Leeman Labs, Hudson, NH, USA). The extractability (% E) was evaluated according to the following formula:

$$extractability = \frac{[M^{n+}]_{aq,in} - [M^{n+}]_{aq,f}}{[M^{n+}]_{aq,in}} \times 100 \tag{10}$$

The metal separation between studied elements herein in the periodic table can be estimated using separation factors (SF) determined as a ratio of distribution ratios of two metal ions:

$$\mathrm{SF} = D_1/D_2. \tag{11}$$

3.3. Nuclear Magnetic Resonance (NMR) Analysis

The samples for NMR analysis were prepared in $CDCl_3$ and in the ionic liquid $[C_1C_4im^+][Tf_2N^-]$. The concentration of 4-benzoyl-3-methyl-1-phenyl-2-pyrazolin-5-one (HL) was 1×10^{-2} mol/dm^3, whereas that of the heterocyclic amines S1/S2 was 4×10^{-3} mol/dm^3. The initial concentration of the investigated Eu^{3+} ion was 1×10^{-3} mol/dm^3 (1:1 v/v extraction). All samples were prepared in 5 mm NMR tubes (type 507-PP-7) purchased from Rototec-Spintec GmbH (Bad Wildbad, Germany). The NMR analysis was conducted on a Bruker Avance NEO spectrometer (Bruker BioSpin, Ettlingen, Germany) operating at 600.18 MHz and at a temperature of 298.0 ± 0.1 K. The spectrometer was equipped with a nitrogen-cooled Prodigy probehead, and the chemical shifts were referenced to the diluent signal (7.26 ppm for $CDCl_3$ and 7.41 ppm for H-5 of the ionic liquid). One-dimensional (1D) proton NMR experiments were conducted using the standard zg30 pulse sequence. The diluent signal (7.26 ppm for $CDCl_3$ and 7.41 ppm for H-5 of the ionic liquid) was used as the reference. The NMR spectra of the ionic liquid solutions were acquired without lock. The unambiguous assignment of the majority of signals was achieved through the utilization of two-dimensional homonuclear and heteronuclear NMR experiments. In fact, in order to identify the signals that overlapped with the strong signals of the ionic liquid, a 1D TOCSY (total correlation spectroscopy) experiments were conducted. All data were processed manually using TopSpin 4.4.0 (Bruker BioSpin, Ettlingen, Germany). Zero-filling was employed to augment the number of data points, thereby enhancing the digital resolution. A window function with a 0.3 Hz width was applied prior to Fourier transformation in order to enhance the signal-to-noise ratio (S/N). Fourier transformation was employed to convert the time-domain data to frequency-domain NMR spectra. Zero- and first-order phase correction were meticulously adjusted to eliminate phase errors in the NMR spectra. Baseline correction was applied to ensure a flat baseline for accurate integration and peak analysis. Integration was performed using the Topspin 4.4.0 software integration tools to quantify the areas of the non-overlapping peaks.

4. Conclusions

In this study, the data on the solvent extraction of rare earth elements from aqueous nitrate solutions with synergistic mixtures of chelating ligand HL in combination with 1,10-phenanthroline or 2,2′-bipyridine in an ionic liquid were obtained. As outlined in detail, very slight enhancements of solvent extraction efficiencies were obtained in ionic media when utilizing the basic synergistic ligands, namely 1,10-phenanthroline and 2,2′-bipyridine. An effort was made to explore and understand the equilibrium mechanism, with the main goal of elucidating the nature of the mixed complexes formed in the organic phase. From the experimental results obtained through the slope analysis method and NMR spectroscopy, a model of the synergistic extraction mechanism was proposed. The ^{1}H NMR spectroscopic analyses of the organic ionic liquid phases were performed to confirm the reaction mechanism of the extracted species with the use of synergistic reagents. This was performed to propose a definitive explanation for metal ion transfer into the IL. In addition, very weak interaction between the two extracting molecules (HL–1,10-phen or HL–2,2′-bipy) was also detected in the organic phase. However, this observation should not cause any influence on the synergistic process. It is anticipated that the findings of this investigation will prove beneficial in the design of synergistic solvent extraction systems for environmentally friendly and sustainable processes, thereby extending the applicability of bidentate nitrogen molecules and ILs in this field.

Supplementary Materials: The following supporting information can be downloaded at: https://www.mdpi.com/article/10.3390/molecules30040786/s1, Figure S1: Log $D_{L,S}$ vs. log pH ([HL] = 5×10^{-3} mol/dm^3 and [S] = 3×10^{-3} mol/dm^3), log $D_{L,S}$ vs. log[HL]$_{IL}$ ([S] = 3×10^{-3} mol/dm^3 at pH = 4.80) and log $D_{L,S}$ vs. log[S] ([HL] = 5×10^{-3} mol/dm^3 at pH = 2.85) plots for solvent extraction of Lu^{3+} with HP–bipy mixture in [$C_1C_4im^+$][Tf_2N^-]. Figure S2: Log $D_{L,S}$ vs. log pH ([HL] = 5×10^{-3} mol/dm^3 and [S] = 3×10^{-3} mol/dm^3), log $D_{L,S}$ vs. log[HL]$_{IL}$ ([S] = 3×10^{-3} mol/dm^3 at pH = 3.60) plots for solvent extraction of Lu^{3+} with HP–phen mixture in [$C_1C_4im^+$][Tf_2N^-]. Table S1: Chemical shifts ($\leq \pm 0.01$ ppm) of the compounds measured in $CDCl_3$, in an IL and for the corresponding Eu-complexes in an IL at 298.0 $\pm$ 0.1 K. Figure S3: Representative NMR spectra of compounds 4, 7 and 10, respectively. Figure S4: NMR spectra of compounds 4, 7, and 10 in the region 7.1–9.4 ppm (100-fold amplified). Figure S5: Structural formulas of 4-benzoyl-3-methyl-1-phenyl-2-pyrazolin-5-one (HL), 1,10-phenantroline (S1), 2,2′-bipyridine (S2) and 1-butyl-3-methylimidazolium bis(trifluoromethylsulfonyl)imide [$C_1C_4im^+$][Tf_2N^-].

Author Contributions: Conceptualization, M.A.; methodology, M.A. and S.S.; formal analysis, N.T.; investigation, N.T., M.A. and S.S.; writing—original draft preparation, M.A.; writing—review and editing, M.A. and S.S.; visualization, S.S.; supervision, M.A.; project administration, M.A.; funding acquisition, M.A. All authors have read and agreed to the published version of the manuscript.

Funding: This research was funded by the European Union-NextGenerationEU, through the National Recovery and Resilience Plan of the Republic of Bulgaria, project № BG-RRP-2.004-0002, "BiOrgaMCT" as well as by the Bulgarian Science Fund through the Grant Agreement № KP-06-H69/5(2022), "*Green twist to synergistic solvent extraction and separation of rare earth metals*".

Institutional Review Board Statement: Not applicable.

Informed Consent Statement: Not aplicable.

Data Availability Statement: Data are contained within the article.

Acknowledgments: The authors would like to acknowledge the students Katrin Chavdarova, Ilina Todorova, and Aleyna Chamdere from UCTM for their contribution to some experiments that triggered this study.

Conflicts of Interest: The authors declare no conflicts of interest.

References

1. El-Nadi, Y.A. Lanthanum and neodymium from Egyptian monazite: Synergistic extractive separation using organophosphorus reagents. *Hydrometallurgy* **2012**, *119–120*, 23–29. [CrossRef]
2. Zou, D.; Li, H.; Chen, J.; Li, D. Recovery of scandium from spent sulfuric acid solution in titanium dioxide production using synergistic solvent extraction with D2EHPA and primary amine N1923. *Hydrometallurgy* **2020**, *197*, 105463. [CrossRef]
3. Krea, M.; Khalaf, H. Liquid–liquid extraction of uranium and lanthanides from phosphoric acid using a synergistic DOPPA–TOPO mixture. *Hydrometallurgy* **2000**, *58*, 215–225. [CrossRef]
4. Turanov, A.; Karandashev, V.; Khvostikov, V.; Artyushin, O.; Bondarenko, N. Extraction of rare earth elements(III) with mixtures of some new tridentate carbamoylmethylphosphine oxides and 4-benzoyl-3-methyl-1-phenyl-1H-pyrazol-5(4H)-one from hydrochloric acid solutions. *Russ. J. General Chem.* **2021**, *91*, 383–388. [CrossRef]
5. Petrova, M. *The Crucial Performance of Mutual Solubility Among Water and Ionic Liquids in the Time of Liquid-Liquid Extraction of Metallic Species*; Academic Solutions: Sofia, Bulgaria, 2020.
6. Nakamura, S.; Suzuki, N. Adduct formation constant in the synergic extraction of several rare earth elements with acetylacetone and 1,10-phenanthroline in nonpolar organic solvents. *J. Radional. Nucl. Chem. Artic.* **1986**, *99*, 145–152. [CrossRef]
7. Nakamura, S.; Suzuki, N. Effect of an acidic chelating agent in the synergic extraction systems of rare earths(III)-β-diketones-2,2′-bipyridine. *Inorg. Chim. Acta* **1986**, *114*, 101–107. [CrossRef]
8. Nakamura, S.; Suzuki, N. A new trend in the synergistic extraction of rare-earth(III) complexes with various β-diketones and 1,10-phenanthroline. *Polyhedron* **1986**, *5*, 1805–1813. [CrossRef]
9. Matsubayshi, I.; Hasegawa, Y. Thermodynamic consideration for solvent effects in the synergistic extraction of europium(III) with pivaloyltrifluoroacetone and 1,10-phenanthrolone. *Anal. Sci.* **2001**, *17*, 221–223. [CrossRef]

10. Kassierer, E.; Kertes, A. Synergic extraction of some lanthanides and transition metals by two bidentate chelating agents. *J. Inorg. Nucl. Chem.* **1972**, *34*, 3221–3231. [CrossRef]
11. Kassierer, E.; Kertes, A. Thermodynamics of solvent extraction processes. Synergic adducts of copper and zinc diketonates with bidentate nitrogen bases. *J. Inorg. Nucl. Chem.* **1972**, *34*, 3209–3214. [CrossRef]
12. Bhatti, M.; Desreux, J.; Duyckaerts, G. Behaviour of bidentate amines in the synergic extraction of lanthanides by thenoyltrifluoroacetone. *J. Inorg. Nucl. Chem.* **1980**, *42*, 767–770. [CrossRef]
13. Kikuta, Y.; Watarai, H.; Suzuki, N. Synergic effect of some heterocyclic bidentate amines on the extraction of zinc with 2-thenoyltrifluoroacetone. Correlation between formation constants of amine-complex in organic and aqueous phases. *Polyhedron* **1982**, *4*, 387–392. [CrossRef]
14. Nakamura, S.; Imura, H.; Suzuki, N. Synergic extraction of thulium(III) with thenoyltrifluoroacetone and neutral unidentate and bidentate heterocyclic amines. *Inorg. Chim. Acta* **1985**, *110*, 101–105. [CrossRef]
15. Nakamura, S.; Suzuki, N. Synergic extraction of lanthanide(III) ions with 2-thenoyltrifluoroacetone in the presence of 2,2′-bipyridine or pyridine. *Polyhedron* **1988**, *7*, 155–159. [CrossRef]
16. Ishimori, K.; Imura, H.; Ohashi, K. Effect of 1,10-phenantroline on the extraction and separation of lithium(I), sodium(I) and potassium with thenoyltrifluoroacetone. *Anal. Chim. Acta* **2002**, *454*, 241–247. [CrossRef]
17. Nakamura, S.; Takai, S.; Akiba, K. Synergic extraction of lanthanoids by mixtures of LIX 54 (High molecular weight β-diketone) and bidentate neutral amines. *Anal. Sci.* **2002**, *18*, 319–323. [CrossRef]
18. Roy, A.; Nag, K. Investigation on the lanthanoid chelates of 1-phenyl-3-methyl-4-benzoyl-5-pyrazolone. An examination of the phenomenon of hypersensitivity. *Bull. Chem. Soc. Jpn.* **1978**, *51*, 1525–1529. [CrossRef]
19. Bencini, A.; Lippolis, V. 1,10-Phenanthroline: A versatile building block for the construction of ligands for various purposes. *Coord. Chem. Rev.* **2010**, *254*, 2096–2180. [CrossRef]
20. Tsutsui, N.; Ban, Y.; Suzuki, H.; Nakase, M.; Ito, S.; Inaba, Y.; Matsumura, T.; Takeshita, K. Effects of diluents on the separation of minor actinides from lanthanides with tatradodecyl-1,10-phenanthroline-2,9-diamide from nitric acid medium. *Anal. Sci.* **2020**, *36*, 241–246. [CrossRef]
21. Yamashita, T.; Nishiyama, Y.; Morita, K.; Nagatani, H.; Imura, H. Synergistic ion-pair extraction and separation of trivalent lanthanoid ions with 4-isopropyltropolone and 1,10-phenanthroline into o-dichlorobenzene. *Anal. Sci.* **2020**, *36*, 479–484. [CrossRef]
22. Turanov, A.; Karandashev, V.; Artyushin, O.; Sharova, E. Effect of 1-Alkyl-3-methylimidazolium di-2-ethylhexylsulfosuccinate on the extraction of lanthanides(III) with 1,3-bis[(diphenylphosphorylacetamido)methyl]benzene from nitric acid solutions. *Rus. J. General Chem.* **2023**, *93*, 2805–2812. [CrossRef]
23. Turanov, A.; Karandashev, V.; Artyushin, O.; Brel′, V. Extraction of actinides and lanthanides from nitric acid solutions with diphosphine dioxides in the presence of an ionic liquid. *Radiochemistry* **2023**, *65*, 530–537. [CrossRef]
24. Turanov, A.; Karandashev, V.; Baulin, V. Extraction of lanthanides(III) from aqueous nitric acid solutions with tetra(n-octyl)diglycolamide into methyltrioctylammonium bis(trifluoromethanesulfonul)imide ionic liquid and its mixtures with molecular organic diluents. *Minerals* **2023**, *13*, 736. [CrossRef]
25. Rout, A. Separation of plutonium from other actinides and fission products in ionic liquid medium. *Sep. Purif. Rev.* **2023**, *52*, 98–122. [CrossRef]
26. Guo, Z.; Chu, T. Separation of Mo(VI) from U(VI) and other fission elements in synthetic solutions by di-quinolinol chelating ligand in [C4mim][NTf2] ionic liquid. *Hydrometallurgy* **2023**, *215*, 105968. [CrossRef]
27. Mataev, M.; Sarsenbaeva, Z.; Keskin, B.; Nurbekova, M.; Meldeshov, A.; Tusyn, Z.; Seitbekova, K. Synthesis, structure and electrophysical and electrochemical properties of novel composite $La_{0.9}MnO_3$-$LaFeO_3$. *Molecules* **2025**, *30*, 132. [CrossRef]
28. Atanassova, M.; Kurteva, V.; Lubenov, L.; Billard, I. Compering extraction, synergism and separation of lanthanoids using acidic and neutral compounds in chloroform and one ionic liquid: Is the latter always "better"? *RSC Adv.* **2014**, *4*, 38820–38829. [CrossRef]
29. Mathur, J.; Khopkar, P. Extraction of trivalent actinides with some substituted pyrazolones and their synergistic mixtures with trioctylphosphine oxide in chloroform. *Polyhedron* **1984**, *3*, 1125–1129. [CrossRef]
30. Jia, Q.; Liao, W.; Li, D.; Niu, C. Synergistic extraction of lanthanum(III) from chloride medium by mixture of 1-phenyl-3-methyl-4-benzoyl-pyrazolone-5 and triisobutylphosphine sulphide. *Analytica Chim. Acta* **2003**, *477*, 251–256. [CrossRef]
31. Arichi, J.; Goetz-Grandmont, G.; Brunette, J.P. Solvent extraction of europium(III) from nitrate medium with 4-acyl-isoxazolo-5-ones and 4-acyl-5-hydroxy-pyrazoloes. Effect of salts and diluents. *Hydrometallurgy* **2006**, *82*, 100–109. [CrossRef]
32. Thakur, P.; Dash, K.; Reddy, M.L.P.; Varma, R.; Ramonohan, T.; Damodaran, A. Crown ethers as synergists in the extraction of trivalent lanthanides by 1-phenyl-3-methyl-4-trifluoroacetyl-pyrazolone-5. *Radiochimica Acta* **1996**, *75*, 11–16. [CrossRef]
33. Kumar, P.; Vincent, T.; Khanna, A. Extraction of UO_2^{2+} into ionic liquid using TTA and TBP as extractants. *Sep. Sci. Technol.* **2015**, *50*, 2668–2675. [CrossRef]

34. Rama, R.; Rout, A.; Venkatesan, K.; Antony, M.; Vasudeva Rao, P. Extraction behavior of americium(III) in benzoylpyrazolone dissolved in pyrrolidinium based ionic liquid. *Sep. Sci. Technol.* **2015**, *50*, 2164–2169. [CrossRef]
35. Jensen, M.; Borkowski, M.; Laszak, I.; Beitz, J.; Rickert, P.; Dietz, M. Anion effects in the extraction of lanthanide 2-thenoyltrifluoroacetone complexes into an ionic liquid. *Sep. Sci. Technol.* **2012**, *47*, 233–243. [CrossRef]
36. Marcus, Y.; Kertes, A.S. *Ion Exchange and Solvent Extraction of Metal Complexes*; Willey Interscience: New York, NY, USA, 1969; pp. 815–858.
37. Atanassova, M. Adduct formation constants in the synergistic solvent extraction of several lanthanoids with two chelating extractants: β-diketone and bidentate nitrogen bases. *J. Chem. Eng. Data* **2010**, *55*, 5791–5796.
38. Atanassova, M.; Kurteva, V.; Dukov, I. The interaction of extractants during synergistic solvent extraction of metals. Is it an important reaction? *RSC Adv.* **2016**, *6*, 81250–81265. [CrossRef]
39. Atanassova, M.; Kukeva, R.; Kurteva, V. New sustainable solvent extraction pathways for rare earth metals via oximes molecules. *Molecules* **2023**, *28*, 7467. [CrossRef]
40. Kurteva, V.; Atanassova, M.; Billard, I. NMR study on the possible interactions between imidazolium based ionic liquids and extractants widely applied in solvent extraction and separation of f-ions. *J. Solut. Chem.* **2015**, *44*, 2416–2430. [CrossRef]
41. Anderegg, G. Pyridin derivate als komplexbildner V. die metallkomplexe von 1,10-phenanthrolin und α, α′-dipyridyl. *Helv. Chim. Acta* **1963**, *46*, 2397–2410. [CrossRef]
42. Hancock, R. The pyridyl group in ligand design for selective metal ion complexation and sensing. *Chem. Soc. Rev.* **2013**, *42*, 1500–1524. [CrossRef]
43. Lewis, F.; Harwood, L.; Hudson, M.; Drew, M.; Desreux, J.; Vidick, G.; Bouslimani, N.; Modolo, G.; Wilden, A.; Sypula, M.; et al. Highly efficient separation of actinides from lanthanides by a phenanthroline-derived bis-triazine ligand. *J. Am. Chem. Soc.* **2011**, *133*, 13093–13102. [CrossRef] [PubMed]
44. Hu, K.; Xing, L.; Nie, Y.; Li, X.; Dong, H.; Gao, H. Removal of aluminium to obtain high purity gadolinium with pyridinium-based ionic liquids. *Hydrometallurgy* **2022**, *213*, 105930. [CrossRef]
45. Ying, Z.; Liu, S.; Li, G.; Wei, Q.; Ren, X. The effect of diluent on the extraction: Amide extracting chromium (VI) as an example. *J. Mol. Liq.* **2023**, *384*, 122205. [CrossRef]
46. Nash, K.; Jensen, M.C. 180 Analytical separations of the lanthanides: Basic chemistry and metods. In *Handbook on the Physics and Chemistry of Rare Earths*; Gschneidner, K., Eyring, L., Eds.; Elsevier Science B.V.: Amsterdam, the Netherlands, 2000; Volume 28.
47. Atanassova, M.; Dukov, I. A comparative study of the solvent extraction of the trivalent elements of the lanthanoid series with thenoyltrifluoroacetone and 4-benzoyl-3-methyl-1-phenyl-2-pyrazolin-5-one using diphenylsulphoxide as synergistic agent. *J. Solution Chem.* **2009**, *38*, 289–301. [CrossRef]
48. Atanassova, M.; Vassilev, N.; Tashev, E.; Lachkova, V.; Varbanov, S. Coordination chemistry of a para-tert-octylcalix[4]arene fitted with phosphinoyl pendant arms towards 4f-elements: Extraction, synergism, separation. *Sep. Sci. Technol.* **2016**, *5*, 49–56. [CrossRef]
49. Atanassova, M.; Lachkova, V.; Vassilev, N.; Varbanov, S.; Dukov, I. Effect of p-tert-butylcalix[4]arene fitted with phosphinoyl pendant arms as synergistic agent in the solvent extraction and separation of some trivalent lanthanoids with 4-benzoyl-3-methyl-1-phenyl-5-pyrazolone. *J. Inclus. Phenom. Macrocycl. Chem.* **2007**, *58*, 173–179. [CrossRef]
50. Petrova, M.A.; Dukov, I.L. Effect of crown ethers on the solvent extraction and separation of lanthanoid(III) ions with 4-benzoyl-3-methyl-1-phenyl-2-pyrazolin-5-one. *Chem. Pap.* **2008**, *62*, 207–214. [CrossRef]
51. Atanassova, M.; Dukov, I. Synergistic Solvent extraction of trivalent lanthanoids with mixtures of 1-phenyl-3-methyl-4-benzoyl-5-pyrazolone and crown ethers. *Acta Chim. Slov.* **2006**, *53*, 457–463.
52. Savvin, S.B. *Arsenazo III*; Atomizdat: Moskva, Russia, 1966.

Disclaimer/Publisher's Note: The statements, opinions and data contained in all publications are solely those of the individual author(s) and contributor(s) and not of MDPI and/or the editor(s). MDPI and/or the editor(s) disclaim responsibility for any injury to people or property resulting from any ideas, methods, instructions or products referred to in the content.

molecules

MDPI

Article

Reconcentrating the Ionic Liquid EMIM-HSO_4 Using Direct Contact Membrane Distillation

Mark J. Wong, Viral Sagar and Joan G. Lynam *

Department of Chemical Engineering, Louisiana Tech University, 600 Dan Reneau Drive, P.O. Box 10348, Ruston, LA 71272, USA; mwong4095@gmail.com (M.J.W.)
* Correspondence: lynam@latech.edu; Tel.: +1-318-257-3124

Abstract

Adequate water supplies are crucial for missions to the Moon, since water is essential for astronauts' health. Ionic liquids (ILs) have been investigated for processing metal oxides, the main components of lunar regolith, to separate oxygen and metals. The IL must be diluted in the process. Recycling this diluted IL post-processing is important to reduce the materials required in resupply missions. In addition, water will be needed in lunar greenhouses for growing food and aiding in sustaining a habitable environment. Direct contact membrane distillation (DCMD) is a new technology for water purification that was examined in this study for its feasibility to concentrate IL. Hydrophobic membranes composed of polytetrafluoroethylene (PTFE) and polyvinylidene (PVDF) were found to hold promise in separating solutes from water to concentrate a diluted IL solution and to recover water. A bench-scale DCMD system was employed to test this method at temperatures of 50 °C, 65 °C, and 80 °C. Hence, the benefits and limitations of DCMD with PTFE and PVDF membranes were explored for the aqueous IL 1-ethyl-3 methylimidazolium hydrogen sulfate for DCMD performed at different temperatures.

Keywords: 1-ethyl-3 methylimidazolium hydrogen sulfate; DCMD; polytetrafluoroethylene; polyvinylidene; conductivity; UV-vis

1. Introduction

As humans venture to explore deep space, we must surmount many challenges. Some of the greatest challenges are primary life support systems needed to ensure the long-term survival of astronauts working during extended missions. Functional life support systems must be capable at least of providing oxygen, water, and CO_2 removal [1,2]. Meeting these challenges is a significant hurdle in extraterrestrial exploration. Recycling processes are vital, but no process will have 100% efficiency, so there always will be the necessity to produce new water and oxygen. Using electrolysis, oxygen can be produced from water, similarly to methods used on military naval vessels, but liquid water is rare in our region of space, with most lunar water being concentrated as ice at the Moon's poles [3]. Various technologies have been proposed to deal with this concern in non-polar areas. One potential solution suggested has been separating metal oxides to access the embedded oxygen and then reacting it with hydrogen to create water [4]. This method is thought to be viable due to the discovery that the Moon contains large quantities of various metal oxides, such as iron oxide and titanium oxide [5].

A new approach to meeting oxygen requirements on the Moon is employing ionic liquids (ILs) to process metal oxides common in lunar regolith to create water by using

the oxygen from metal oxides and hydrogen, which can be recycled. One particular IL, 1-ethyl-3 methylimidazolium hydrogen sulfate, has permitted the operating temperature for this process to be reduced to less than 200 °C [6]. Water, however, will be introduced into and dilute the IL. The IL solution must be concentrated to remove the water before it is re-used. The separated water could then be converted with electrolysis to generate oxygen and permit the hydrogen gas to be recycled back into the system. Direct contact membrane distillation (DCMD) was this work's selected method for exploring this process. DCMD has potential for removing water from the diluted IL stream, allowing the IL to be concentrated during the process and lessening the need for system purging.

DCMD is a new method for separating water from aqueous solutions. DCMD has been suggested for processes such as desalination plants and dairy processing. The basis for the system is a temperature difference between hot aqueous solutions being passed on the bottom of a thin and porous hydrophobic membrane, with a cold water stream being passed on the top [7]. During the DCMD process, the temperature gradient creates a vapor pressure difference. The polymer membrane enables water vapor to pass through from the high-temperature stream to condense in the low-temperature water stream. The membrane's hydrophobic nature would be expected to allow only water vapor to pass through the membrane, owing to the IL solution being repulsed by the membrane or the solute molecules being too big to pass through the membrane. DCMD's main advantage is that it does not require the IL solution to be completely vaporized. The complexity of the process is thus reduced significantly, decreasing the construction volume of the module and/or the energy requirements. This is in contrast with the more common method of separation, in which all or most of the liquid is vaporized and then condensed to produce a solute-rich base and a water-rich condensate. Typical distillation permits some contaminants to be entrained in the condensate [8]. Traditional distillation methods work by either providing energy, in the form of heat, to the solution to vaporize it or by reducing the pressure with a vacuum system to cause vaporization at a lower temperature [7]. Nevertheless, these operations have serious drawbacks, since heat-based vaporization is energy-intensive and also requires extra equipment. Vacuum-based methods require a complex system of interconnected pumps that may vary in operation and individual process control systems, which require either a batch-based method or a complex process to allow for continuous processing, increasing possible failure points.

DCMD provides the ability to separate water from aqueous streams in a manner that is energy-efficient and has reduced spatial requirements [9]. DCMD separations do not require full vaporization, so complex, large distillation tower systems are not needed for water reclamation. DCMD also provides the benefits of vacuum distillation without its complexity, because recycled or waste heat sources could be used. For these reasons, the amount of energy that needs to be fed into the system could be reduced, increasing the energy efficiency of the process [7].

A few membrane-based distillation methods have shown adequate results since the 1960s [10]; however, their implementation in the past was considered ineffective due to issues with polymer technology. The underlying basis of the DCMD method relies on hydrophobic polymer-based membranes, with their effectiveness drastically shifting the effectiveness of the process. Advances in membrane and polymer technology have expanded the useful applications of membrane-based systems, but technological issues still remain that must be addressed. Typical concerns include the membranes' costs and quality. Membrane quality difficulties can result in the degradation of the membrane, with rates dependent on the type of aqueous solution being processed and the quantity that is being pumped across the membrane. More research is required to understand mass and energy transfer across membranes with reference to varying molecule sizes in the solution [10].

The present work studied the ability of a DCMD system in separating water from a diluted IL solution, since concentrated IL will be needed for use in acquiring the oxygen in metal oxides from lunar regolith [6]. Little information on using DCMD on diluted IL is available in the literature, so this research is novel [11]. Two of the most commonly used membranes for DCMD are polytetrafluoroethylene (PTFE) and polyvinylidene (PVDF), so these membranes were chosen for the experimental work [12].

2. Results and Discussion

2.1. Conductivity Calibration

The data on the conductivity and concentration of IL displayed a nonlinear relationship. The polynomial relationship between these is shown in Figure 1.

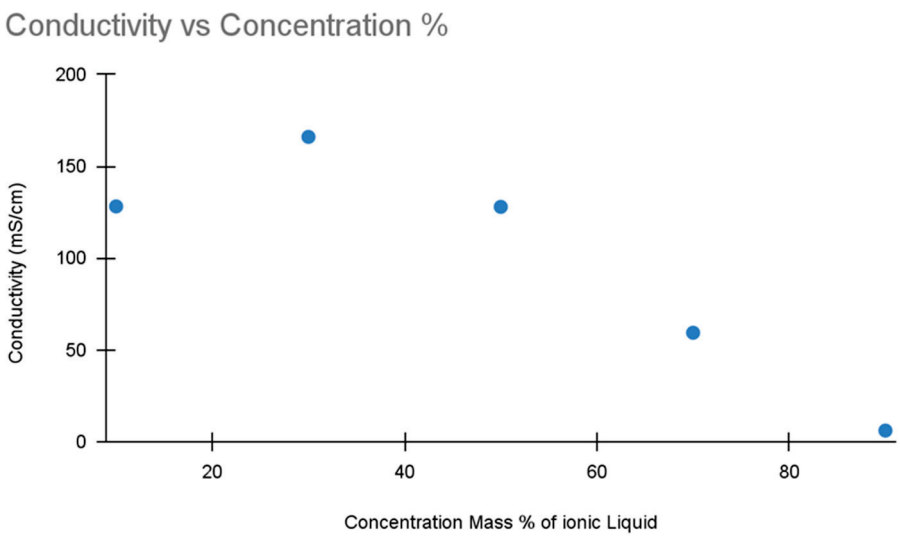

Figure 1. Calibration curve to establish the relationship between the conductivity and mass percentage of ionic liquid (IL).

The conductivity of 1-ethyl-3 methylimidazolium hydrogen sulfate versus concentration was found to be of a parabolic form, as seen in Figure 1. Other researchers have found similar a parabolic form for another IL *n*-(2-hydroxyethyl)piperazinium propionate [13]. Starting at the y-axis with water and then adding IL initially increases the conductivity, possibly due to the ions moving and breaking up hydrogen bonding in the water. As more ions are added, more hydration shells of water molecules form around the ions and the ions may eventually form their own lattice structure [14], causing less mobility and thus lower conductivity. ILs similar to 1-ethyl-3 methylimidazolium hydrogen sulfate have frequently been described as viscous, likely due to intermolecular ionic bonds reducing mobility and thus conductivity [15].

Table 1 shows that at the higher DCMD temperatures, the PTFE membrane permitted an increase in contamination in the water product stream. While these contaminations were low, this finding still represents a consideration for use in long-term water purification methods. This finding also suggests that there is some transfer rate of ions across the membrane that is outpaced by the transfer of water vapor. It is probable that there is an optimum operating temperature differential needed between the two streams to ensure that the rate of water passing through the membrane outstrips the rate of the solute. However, with DCMD using the PVDF membrane, little contamination of the water stream with ions occurred.

Table 1. Change in water conductivity (mS/cm) based on feed temperature and membrane type.

Feed Temp (°C)	ΔConductivity PTFE mS/cm	ΔConductivity PVDF mS/cm
50.0	165.0	14.8
65.0	1162.0	85.8
80.0	1560.9	259.4

UV-Vis spectroscopy was used along with conductivity to provide more reliable data. The conductivity data supplemented the UV-Vis spectroscopy results.

2.2. Absorption Calibration

The typical calibration curve, as shown in Figure 2, for the UV-Vis spectroscopy was as expected for solutions made primarily of two non-water components. Two peaks were seen in the ultraviolet range. The first peak collection was found at ~238 nm and the second presented at ~265 nm. The first peak (238 nm) was neglected since all samples resulted in absorbance peaks greater than 2, conditions that reduce the quality of the data, with the light sensor beginning to become overloaded. Instead, the second peak (265 nm) was used as the primary measuring tool.

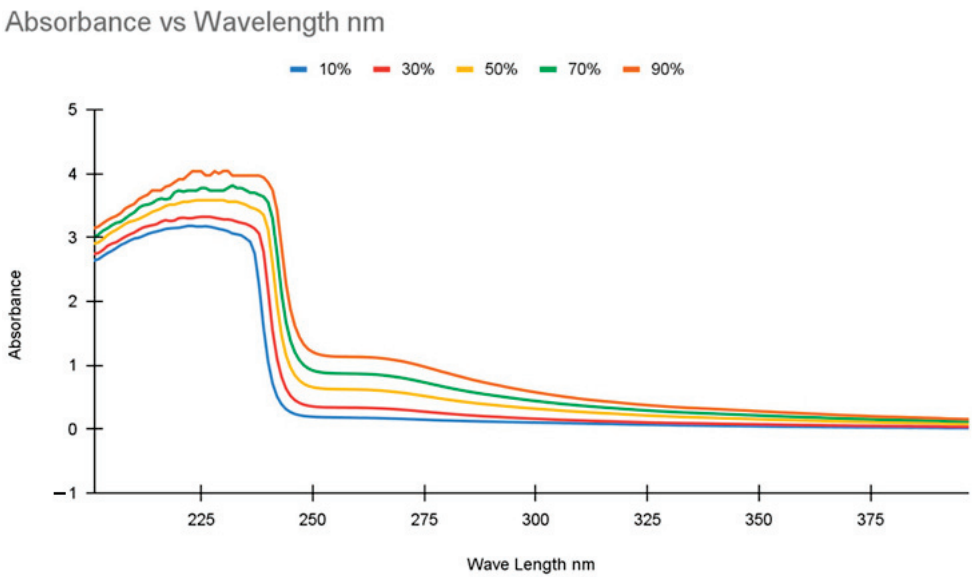

Figure 2. Calibration curve to establish the relationship between mass percentage of IL and light absorption.

A graph was then produced with the absorption of light at 265 nm for both calibration curves and then combined for linear quantification, as shown in Figure 3. UV-Vis spectra were obtained for all samples taken in the experiment's 12 trials.

The concentration of IL and respective absorbance values are seen to be linearly related. These findings allowed all needed calculations to be performed.

Tables 1 and 2 reveal the overall change in the IL solution based on the membrane material and temperature of the run. Tables 2 and 3 show that at 80 °C, the average water flux across the PTFE membrane appears to be almost double that of the PVDF membrane.

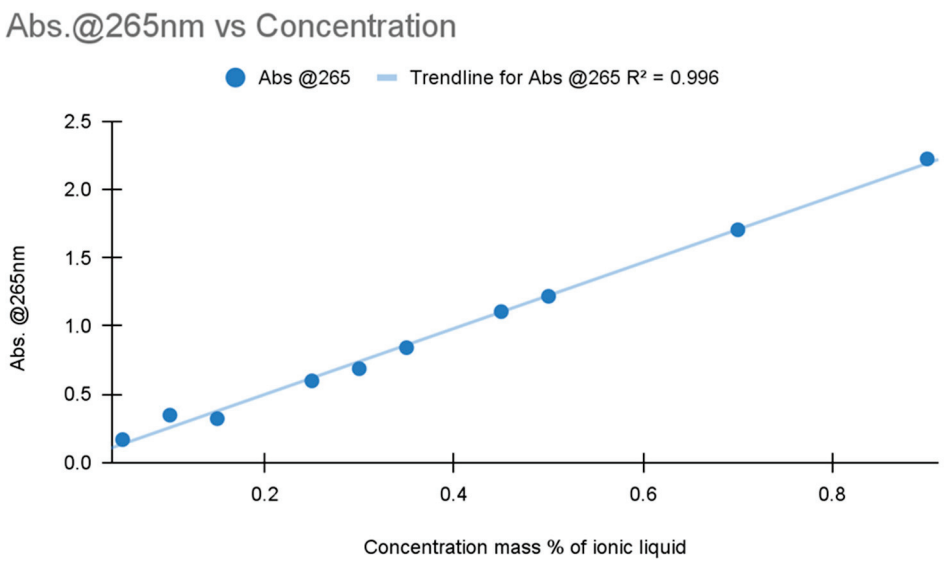

Figure 3. A calibration curve for the absorbance of light at 265 nm for different mass percentages of IL.

Table 2. Total average difference in solution properties with the PTFE membrane at various temperatures.

Temperature °C	Total Water Exchange Grams	Average Flux $g/m^2 \cdot h$	Change in Concentration
50	4.61	0.16	3.71%
65	14.98	534.82	12.52%
80	44.66	1595.00	22.83%

Table 3. Total average change in solution properties with polyvinylidene (PVDF) membrane at various temperatures.

Temperature °C	Total Water Exchange Grams	Average Flux $g/m^2 \cdot h$	Change in Concentration
50	15.58	556.25	1.44%
65	3.83	136.79	2.16%
80	22.47	802.32	17.67%

The change in results is most apparent when the two membranes are compared. The PTFE membrane was much more effective at transferring water from the feed stream. For 80 °C operation, the average water flux across the PTFE membrane was greater than that of the PVDF membrane. Figure 4 shows that both the PVDF and PTFE membranes transfer water through the membrane in a somewhat polynomial fashion. This was expected because the vapor pressure of water has a polynomic form. Nonetheless, the PTFE membrane appears to be much more linear. Also, the concentration of the IL changed more when the PTFE membrane was used compared to the PVDF membrane.

PTFE membranes appear to transfer water at a higher rate at the equivalent temperatures compared to their PVDF counterparts. However, this comes with the drawback of greater permeate contamination. Testing the conductivity of the final water stream confirmed that slight leakage must have occurred (Table 1). A possible explanation for this is the pore size difference between the two membranes. The PTFE membrane had a pore size of 0.45 microns, while the PVDF membrane had a 0.1-micron pore size. The pore size difference could explain the change in distillate contamination rates.

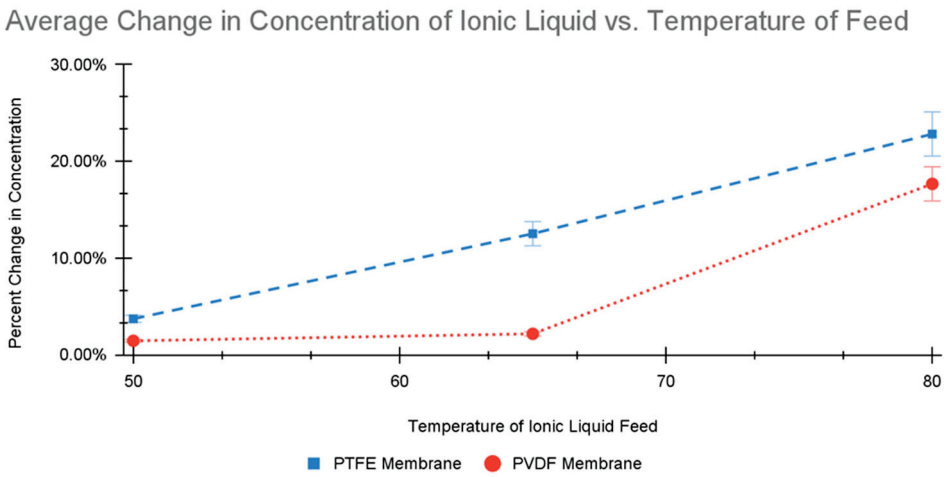

Figure 4. The effect of DCMD temperature on the change in concentration of the IL solution.

3. Materials and Methods

The IL tested was 1-ethyl-3 methylimidazolium hydrogen sulfate with a stock concentration of 95% (Sigma-Aldrich, St. Louis, MO, USA, S/N:49615761, CAS # 412009-61-1). Water content was assumed to be 5%. For the scope of this research project, it was assumed that the processing of metal oxides from lunar regolith had already been conducted and that it had successfully resulted in an aqueous IL solution. The solution's initial desired concentration was chosen to be 20%. This percentage was chosen because it was the concentration used in previous studies [6].

The solutions were processed using DCMD. The setup included a heated IL solution peristaltically pumped underneath the bottom of the polymer membrane and cooled water peristaltically pumped above the top layer of the polymer membrane. The temperatures of the two solutions (cooled and heated) were kept constant using water baths. The temperature of the cooled water was kept constant using a water bath at 5 °C. The heated water bath's temperature was varied to 50 °C, 65 °C, and 80 °C. The reading error for temperature was ±1 °C, while the accuracy of the temperature reading was 0.1 °C. Two runs were performed at each temperature for 2 h with feed rates of 200 mL/min on each side of the membrane. After two tests at each of the three operating temperatures, the membrane used was changed from a PTFE to a PVDF polymer-based membrane (Sterlitech, Kent, WA, USA: 0.45 Micron PTFE Flat Sheet Membrane, with Polypropylene Netting Backer Laminated, Sepa, Lot#: J000014897 11-1; and Novamem 0.1 Micron Flat Sheet Membrane, PVDF100, MF, Sepa, Lot#: 624096PVDF100). The operation was then replicated to test how different membranes would interact with the IL.

During DCMD, 50 mL samples were removed at 30 min intervals from the hot IL solution. Samples were also taken initially before beginning the process and after it had finished. The final water obtained from the cold side was retained to test for the transfer of ions across the membrane. The mass of water from the cold side before and after each experiment was weighed and recorded. This was performed to find the total flux of the water during the experiment. It was observed that for the trials with the PTFE membrane, after 90 min of operation the change in the solution was negligible at the lowest temperature and therefore the DCMD operation was only performed for 90 min. The experimental duration was increased to 2 h when the data recorded indicated that an increase in time was required to reach significant changes with increased feed temperature. An analysis of samples was performed with two methods, conductivity and UV-Visible spectroscopy analysis.

Conductivity tests were performed using 50 mL samples and read from an Ohaus brand conductivity meter (Parsippany, NJ, USA: Model ST20C-B). All samples were created by diluting the stock solution with water prepared with reverse osmosis. An initial calibration curve was created using a 5-point calibration curve ranging from 10% to 90% concentrations at 20% intervals. The DCMD samples were then tested using the same equipment and methodology.

UV-Visible spectroscopy (UV-Vis) functions by sending a stable beam of light through a sample to examine the change in the absorbance of the light beam after it passes through the sample. The light beam used varies within a selected range of wavelengths. The changes in absorbance at different wavelengths depend on the compound being tested. As the concentration of compounds in a sample increases, absorbance increases. Thus, concentrations for samples with compounds that absorb light can be measured quantifiably.

UV-Vis spectroscopy was performed on a Shimadzu spectrometer model no. UV-2401PC (Shimadzu Co., Kyoto, Japan) with a blank water sample as a baseline, and then 3 mL samples were used in quartz cuvettes. Two initial calibration curves were performed. The initial calibration was performed with the same solutions used to calibrate the conductivity meter, five solutions ranging from 10 to 90% concentration spaced out at 20% intervals. The second calibration was performed using five solutions ranging from 5 to 45% concentration spaced at 10% intervals. In the Supplementary Materials, Figures S1–S4 give more detailed UV-Vis data.

4. Conclusions

Overall, the tests performed indicate the potential for DCMD technology to be employed in operating a water recovery system for ILs after use in lunar regolith processing. Both membranes tested offered advantages and drawbacks for use in water recovery depending on the water permeate's end purpose. For purposes where the water quality can be flexible, the PTFE membrane operating at a high temperature would be preferable. These DCDM operating conditions offer a larger change in the concentration of the IL, permitting a faster recovery period before it can be reused in the initial DCMD process. However, this option would have the drawback of contaminating the permeate at a significantly faster rate than for the PVDF counterpart. The disadvantage of water contamination would have to be considered. In situations when high water quality must be maintained, such as for drinking water, the PVDF membrane would be preferred. This membrane gave a decreased water recovery rate but also provided a lower rate of contamination of the permeate. Both membranes did offer viability in the ability to recover water from ILs that have been diluted, resulting in a product stream of increased IL concentration.

Studying the life span viability of a variety of membrane materials will be essential in future work. Sulfuric acid has been reported to increase the pore size of PVDF membranes when exposed to it over a period of weeks [16]. Hydrogen sulfate or bisulfate is considered a weaker form of sulfuric acid. When incorporated in an IL, hydrogen sulfate's activity may be curtailed due to bonds with 1-ethyl-3 methylimidazolium [17]. This study showed the viability of PTFE and PVDF membranes for performing the task of recovering water from IL streams. If put into practice for lunar missions, the resupply of IL and membranes could be reduced. Even so, a significant quantity of membranes would be required. This can only be defined by understanding the effective life spans of the membranes. This study had each membrane operate for approximately 12 h per membrane. In an industrial-level application, these membranes will need to be tested with the IL on the order of weeks of continual operating time

Supplementary Materials: The following supporting information can be downloaded at https://www.mdpi.com/article/10.3390/molecules30020211/s1: Figure S1: Absorption spectra of ionic liquid solution at various operation times for a PVDF with a feed temperature of 50 °C; Figure S2: Absorption of light at 265 nm of ionic liquid solutions at various operation times for a PVDF membrane with a feed temperature of 50 °C; Figure S3: Absorption spectra of ionic liquid solutions at various operation times for a PVDF membrane (LEFT) and PTFE membrane (RIGHT) with a feed temperature of 80 °C; Figure S4: Absorption of light at 265 nm of ionic liquid solution at various operation times for a PVDF membrane (LEFT) and PTFE membrane (RIGHT) with a feed temperature of 80 °C.

Author Contributions: Conceptualization, J.G.L. and M.J.W.; methodology, J.G.L., V.S. and M.J.W.; software, M.J.W.; validation, J.G.L., V.S. and M.J.W.; formal analysis, M.J.W.; investigation, V.S. and M.J.W.; resources, J.G.L.; data curation, V.S. and M.J.W.; writing—original draft preparation, M.J.W.; writing—review and editing, J.G.L. and V.S.; visualization, J.G.L., V.S. and M.J.W.; supervision, J.G.L.; project administration, J.G.L.; funding acquisition, J.G.L. All authors have read and agreed to the published version of the manuscript.

Funding: This research was funded by NASA LaSPACE, grant number LEQSF(2020-24)-LaSPACE.

Institutional Review Board Statement: Not applicable.

Informed Consent Statement: Not applicable.

Data Availability Statement: The original contributions presented in the study are included in the article/Supplementary Materials; further inquiries can be directed to the corresponding author.

Acknowledgments: The authors want to thank Mohammad Tarikuzzaman, Sven Eklund, Lauren M. Mekalip, MeiLan Hardin, and the members of the Biomass Team at Louisiana Tech University for their contributions to this work.

Conflicts of Interest: The authors declare no conflicts of interest. The funders had no role in the design of the study; in the collection, analyses, or interpretation of data; in the writing of the manuscript; or in the decision to publish the results.

References

1. Jackson, S. Life Support Systems. Available online: https://www.nasa.gov/stem-content/life-support-systems (accessed on 17 September 2024).
2. Fu, Y.; Li, L.; Xie, B.; Dong, C.; Wang, M.; Jia, B.; Shao, L.; Dong, Y.; Deng, S.; Liu, H.; et al. How to Establish a Bioregenerative Life Support System for Long-Term Crewed Missions to the Moon or Mars. *Astrobiology* **2016**, *16*, 925–936. [CrossRef] [PubMed]
3. Feldman, W.C.; Maurice, S.; Lawrence, D.J.; Little, R.C.; Lawson, S.L.; Gasnault, O.; Wiens, R.C.; Barraclough, B.L.; Elphic, R.C.; Prettyman, T.H.; et al. Evidence for water ice near the lunar poles. *J. Geophys. Res.* **2001**, *106*, 231. [CrossRef]
4. Schwandt, C.; Hamilton, J.A.; Fray, D.J.; Crawford, I.A. The production of oxygen and metal from lunar regolith. *Planet. Space Sci.* **2012**, *74*, 49–56. [CrossRef]
5. Papike, J.J.; Simon, S.B.; Laul, J.C. The lunar regolith; chemistry, mineralogy, and petrology. *Rev. Geophys. Space Phys.* **1982**, *20*, 761–826. [CrossRef]
6. Barrios, E.A.; Curreri, P. *Oxygen Extraction from Regolith Using Ionic Liquids*; Marshall Space Flight Center: Huntsville, AL, USA, 2011.
7. Tai, Z.S.; Aziz, M.H.A.; Othman, M.H.D.; Ismail, A.F.; Rahman, M.A.; Jaafar, J. *An Overview of Membrane Distillation*; Elsevier: Amsterdam, The Netherlands, 2018; pp. 251–281.
8. Qi, R.B.; Liang, Z.G.; Duan, D.S. Effect of vapor entrainment on distillation tray efficiency under conditions of fully mixed vapor between trays. *Shiyou Daxue Xuebao/J. Univ. Pet. China* **2001**, *25*, 1–4.
9. Barbosa, G.L.; Gadelha, F.D.A.; Kublik, N.; Proctor, A.; Reichelm, L.; Weissinger, E.; Wohlleb, G.M.; Halden, R.U. Comparison of Land, Water, and Energy Requirements of Lettuce Grown Using Hydroponic vs. Conventional Agricultural Methods. *Int. J. Environ. Res. Public Health* **2015**, *12*, 6879–6891. [CrossRef] [PubMed]
10. Kabay, N.; Shirazi, M.M.A.; Güler, E.; Bryjak, M. Grand Challenges in Membrane Modules and Processes. *Front. Membr. Sci. Technol.* **2022**, *1*, 913597. [CrossRef]
11. Wong, M.J. Lunar Applications of Direct Contact Membrane Distillation For Regolith and Hydroponic Water Processing. Master's Theses, Louisiana Tech University, Ruston, LA, USA, 2023.

12. Floros, I.N.; Kouvelos, E.P.; Pilatos, G.I.; Gotzias, A.D.; Favvas, E.P.; Sapalidis, A.A.; Hadjigeorgiou, E.P. Enhancement of flux performance in PTFE membranes for direct contact membrane distillation. *Polymers* **2020**, *12*, 345. [CrossRef] [PubMed]
13. Cao, Q.; Lu, X.; Wu, X.; Guo, Y.; Xu, L.; Fang, W. Density, Viscosity, and Conductivity of Binary Mixtures of the Ionic Liquid N-(2-Hydroxyethyl)piperazinium Propionate with Water, Methanol, or Ethanol. *J. Chem. Eng. Data* **2015**, *60*, 455–463. [CrossRef]
14. Preiss, U.P.; Zaitsau, D.H.; Beichel, W.; Himmel, D.; Higelin, A.; Merz, K.; Caesar, N.; Verevkin, S.P. Estimation of Lattice Enthalpies of Ionic Liquids Supported by Hirshfeld Analysis. *Chemphyschem* **2015**, *16*, 2890–2898. [CrossRef] [PubMed]
15. Ribeiro, M.C.C. High Viscosity of Imidazolium Ionic Liquids with the Hydrogen Sulfate Anion: A Raman Spectroscopy Study. *J. Phys. Chem. B* **2012**, *116*, 7281–7290. [CrossRef] [PubMed]
16. Lasisi, K.H.; Yao, W.; Ajibade, T.F.; Tian, H.; Fang, F.; Zhang, K. Impacts of Sulfuric Acid on the Stability and Separation Performance of Polymeric PVDF-Based Membranes at Mild and High Concentrations: An Experimental Study. *Membranes* **2020**, *10*, 375. [CrossRef]
17. Amarasekara, A.S. Acidic Ionic Liquids. *Chem. Rev.* **2016**, *116*, 6133–6183. [CrossRef] [PubMed]

Disclaimer/Publisher's Note: The statements, opinions and data contained in all publications are solely those of the individual author(s) and contributor(s) and not of MDPI and/or the editor(s). MDPI and/or the editor(s) disclaim responsibility for any injury to people or property resulting from any ideas, methods, instructions or products referred to in the content.

molecules

MDPI

Article

Polymerizable Cholinium-Based Antibiotics for Polymer Carriers: Systems with Combined Load of Cloxacillin and Ampicillin

Shadi Keihankhadiv and Dorota Neugebauer *

Department of Physical Chemistry and Technology of Polymers, Faculty of Chemistry, Silesian University of Technology, 44-100 Gliwice, Poland; shadi.keihankhadiv@polsl.pl
* Correspondence: dneugebauer@polsl.pl

Abstract: Single and dual-drug delivery systems (DDSs) based on linear choline polymers were designed through the controlled polymerization of a pharmaceutically functionalized monomer, i.e., [2-(methacryloyloxy)ethyl]trimethylammonium, with counterions of cloxacillin (TMAMA/CLX), or its copolymerization with [2-(methacryloyloxy)ethyl]trimethylammonium with ampicillin (TMAMA/AMP), providing antibiotic properties. This strategy was effective in attaining well-defined linear copolymers with 38–93 mol. % of TMAMA content, which were regulated by the initial ratio of TMAMA to methyl methacrylate comonomer. The polymer compositions were controlled by the total monomer conversion (40–75%), resulting in a variable degree of polymerization (DP_n = 160–300) and pharmaceutical anion contents (CLX^- 51–80% and AMP^- 78–87%). In aqueous solution, the polymers formed particles with sizes ranging between 274 and 380 nm for CLX^- systems and 288–348 nm for CLX^-/AMP^- systems. In vitro drug release, driven by the exchange of pharmaceutical anions with phosphate ions in phosphate-buffered saline (PBS), imitating a physiological fluid, demonstrated release efficiencies of 58–76% for CLX^- (10.5–13.6 μg/mL) in single systems, and 91–100% for CLX^- (12.9–15.1 μg/mL) and 97–100% for AMP^- (21.1–23.3 μg/mL) in dual systems. Compared to conventional systems delivering antibiotics without a polymer carrier, the choline-based polymer DDS attained satisfactory levels of drug loading content and (co-)release from the polymer carriers, offering a promising alternative for antibiotic delivery.

Keywords: linear polymers; cloxacillin; ampicillin; ionic liquid; choline; drug delivery system

1. Introduction

Choline, identified as 2-hydroxyethyl trimethylammonium chloride, is naturally synthesized in the human liver and is found in phospholipids such as phosphatidylcholine or lecithin. This organic salt is classified as an ionic liquid (IL) [1], known for its chemical stability, ability to enhance solubility, and modifiability through ion exchange to adjust physical and chemical properties [2–4]. Many ILs exhibit nontoxicity and biocompatibility, making them suitable for biomedical applications. Their biological properties include enhancing skin penetration [5], acting as antibacterial agents [6], and functioning as stabilizers [7,8]. They also demonstrate cytotoxicity, local anesthetic effects, anti-fungal and anti-acne activities, and antibiotic properties [3,9,10]. Furthermore, the versatility of ILs extends to their ability to accommodate a wide range of pharmaceutical substances, including antiviral and antimicrobial agents, antioxidants, anticoagulants, nonsteroidal anti-inflammatory drugs, anticancer drugs, ophthalmic drugs, and other drugs [3,11–16]. For instance, betaine- and L-carnitine-based ILs have been reported to be solubilizing and stabilizing agents for bioactive diacerein in eye drops [17]. The widely utilized cholinium cation is particularly notable for its biodegradability, water-solubility, and low cost, making it suitable for various applications [18–20]. Its properties have been studied in combination with various bioactive compounds, including phenytoin [21], ampicillin (AMP) [22], nalidixic acid, niflumic

acid, *p*-aminosalicylic acid, pyrazinoic acid, and picolinic acid [19]. These systems have shown improved solubility of active pharmaceutical ingredients, enhancing their ability to permeate the cell membrane [18].

In recent decades, the synthesis of precisely designed polymers with tailored architectures, compositions, chain homogeneity, and site-specific functionality [23–25], as well as desirable physicochemical and biochemical properties (e.g., mechanical strength, softness, self-healing, processability, tissue adhesiveness, bioactivity, and optional biodegradability) [26–30], has emerged as a powerful tool for developing versatile nanostructures applicable in biology and medicine. Tailored-made polymers synthesized using controlled polymerization methods have significantly advanced drug delivery systems (DDSs), offering both linear and branched polymer carriers with biotherapeutic functions [31–34]. Polymers conjugated with drugs or encapsulating drugs have been intensively studied to address challenges related to drug hydrophilicity [35,36]. Moreover, the co-delivery of multiple bioactive compounds has been explored to enhance primary drugs' efficacy. The combination of conventional pharmacotherapies, including antibiotics, demonstrates improved antibacterial effectiveness and reduced drug resistance, while polymer carriers enhance the controlled pharmacodynamics and pharmacokinetics of DDSs [37–39].

The commercial choline ester derivative, [2-(methacryloyloxy)ethyl]trimethylammonium chloride, commonly referred to as methacroylcholine (TMAMA/Cl), functions as a choline-based IL and serves as the monomer for synthesizing polymerized ionic liquid (PIL) [40]. This PIL has been reported to deliver pharmaceutical anions through anion exchange within the polymer matrix [41,42] or to encapsulate various bioactive compounds [43–47], creating pharmaceutically active polymeric systems. Pharmaceutically active choline-based PILs have also been designed by polymerizing pharmaceutically functionalized choline monomers carrying salicylate [40], *p*-aminosalicylate [48], or fusidate [49] counterions. Additionally, graft copolymers have been synthesized using a combination of choline monomers containing fusidate and cloxacillin (CLX) [49], while other dual-drug systems have been synthesized with both *p*-aminosalicylate- and AMP-functionalized choline comonomers [50].

In this research, we investigated linear polymers based on monomeric choline ionic liquid with a CLX anion (TMAMA/CLX), optionally copolymerized with an AMP-based choline methacrylate monomer (TMAMA/AMP). These well-defined copolymers were designed as either a single DDS carrying CLX^- or a dual DDS with CLX^- and AMP^- (Figure 1), where the drug anion is ionically bonded to the polymer matrix. Both drugs are antibiotics derived from semi-synthetic penicillin, demonstrating antimicrobial efficacy due to the presence of a beta-lactam ring [51,52]. They are effective against both Gram-positive and certain Gram-negative microorganisms [53] and are widely used to treat bacterial infections affecting the ears, nose, throat, bones, and lungs and post-operative wounds [54]. The commercially available combination of AMP and CLX is marketed under various brand names, such as Ampiclox and Cloxam, typically in capsule or oral suspension forms without polymer carriers. This makes both antibiotics suitable for use in either individual treatment or combined therapies. The synthesized polymer systems were characterized to evaluate their effectiveness in drug delivery through the evaluation of drug content and a (co-)release in vitro study in physiological solution via anion exchange with phosphate ions, offering a controlled delivery mechanism. In comparison to previous literature reports for systems delivering AMP and CLX, the advantage of this novel DDS lies in its design, with the controlled radical polymerization of antibiotics incorporated in choline monomers to attain ionic polymers with regulated compositions and drug contents, as well as the option of AMP/CLX co-release by polymer carriers instead of separate delivery by various systems.

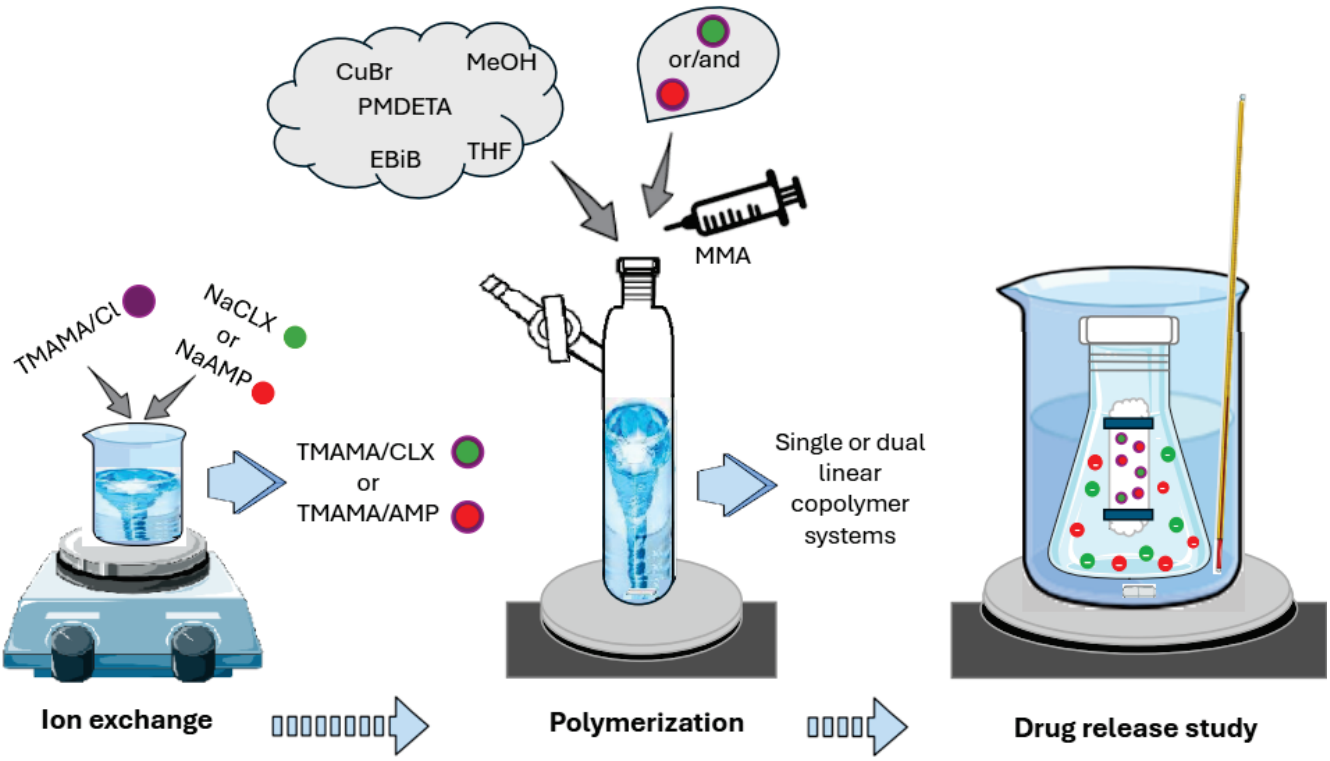

Figure 1. Schematic route from the modification of choline IL by pharmaceutical CLX and AMP anions to linear polymers as single and dual systems, including drug release in PBS at 37 °C.

2. Results and Discussion

2.1. Monomeric Ionic Liquid Functionalized by Pharmaceutical Anions

The proposed strategy for pharmaceutically functionalized copolymers included the modification of water-soluble ionic liquid, that is, [2-(methacryloyloxy)ethyl]trimethylammonium chloride (TMAMA/Cl), which contains a polymerizable methacrylate group and a chloride counterion (Cl^-). The chloride ion was exchanged with pharmaceuticals anions, CLX^- and AMP^-, derived from their sodium salts (NaCLX and NaAMP). This ion exchange reaction resulted in monomers carrying pharmaceutical anions, namely [2-(methacryloyloxy)ethyl]trimethylammonium cloxacillin (TMAMA/CLX) and ampicillin (TMAMA/AMP), as shown in Figure 1. The structures of the resulting monomers were confirmed by ^{1}H-NMR spectroscopy to assess the efficiency of ion exchange by identifying characteristic proton signals of TMAMA. In particular, the trimethylammonium cation in the TMAMA unit was represented by 9 protons (signal F), and the pharmaceutical counterions (Figure 2). In the case of TMAMA/AMP the signal F at 3.16 ppm still existed after the exchange, but a new signal at 3.12 ppm appeared, indicating an exchange efficiency of 47% (Figure 2b). In contrast, for TMAMA/CLX, the signal slightly shifted to 3.14 ppm, proving a 100% anion exchange efficiency (Figure 2c). These results highlight the significant influence of cation–anion interactions, particularly the coordination number, on the efficiency of ion exchange. This reflects the ability of the cation to bind to the anion, as evidenced by the variations in exchange efficiency.

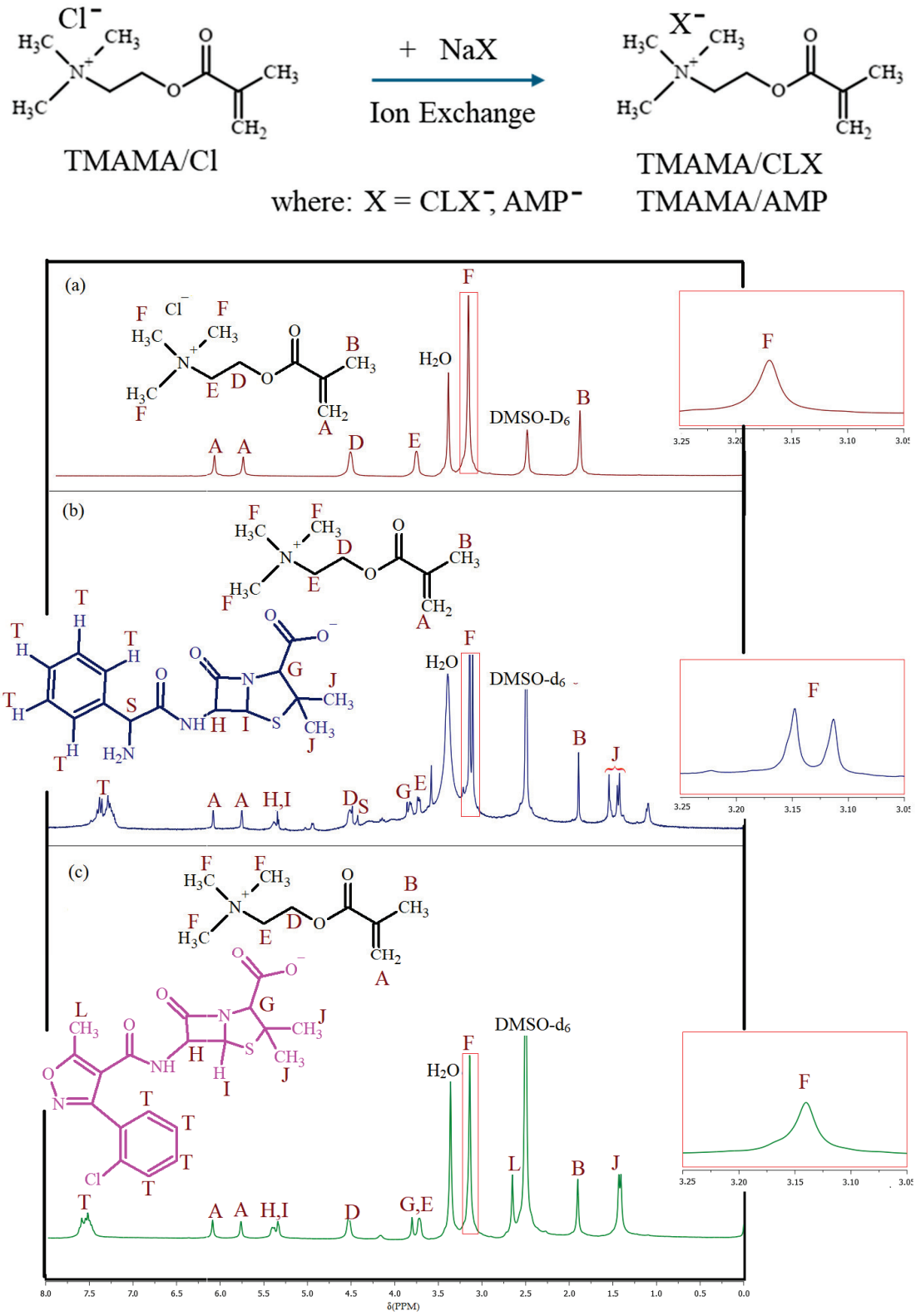

Figure 2. Ionic exchange of TMAMA/Cl with sodium salts of CLX and AMP to produce pharmaceutically functionalized choline monomers and their ^{1}H–NMR spectra before anion exchange (**a**) and after modification to TMAMA/AMP (**b**) and TMAMA/CLX (**c**).

2.2. Linear Polymers Containing CLX⁻ as Single-Drug Delivery Systems

The above-described ionic monomer TMAMA/CLX, with a choline species and a pharmaceutically active counterion, was copolymerized with the non-ionic monomer MMA in molar ratios of 25/75, 50/50, and 75/25 to synthesize well-defined linear copolymers, denoted as P(TMAMA/CLX–*co*–MMA)s (IA–IC), as single-drug systems carrying different ionic contents of TMAMA/CLX. For this purpose, the ATRP reactions were initiated by EBiB as a monofunctional initiator, catalyzed by CuBr/PMDETA complex, dissolved in MeOH/THF solvent mixture, and conducted at 40 °C (Figure 1). The conversion of the monomer to the polymer and resulting polymer structure was confirmed by ^{1}H–NMR spectroscopy (Figure 3). The total conversion of both monomers (X) was calculated using the broad proton signal of the methyl group in the formed polymer backbone (B, 0.54–1.2 ppm) in relation to the signals from a proton in the vinyl groups of unreacted TMAMA and MMA monomers (identified as M1 and M2, in the range of 5.25 to 6.25 ppm). Moreover, the proton signal in the vinyl group of the unreacted monomer M1 at 6.09 ppm and the proton signal associated with the trimethylammonium group present in both the monomer and resulting polymer (referred to F at 3.02–3.30 ppm) were utilized to determine TMAMA conversion (X_{M1}). Further, the conversion values were utilized to calculate additional parameters, including the degree of polymerization (DP), the ionic fraction content in the copolymer (F_{M1}), and the average molecular weight of the copolymer (M_n), as presented in Table 1.

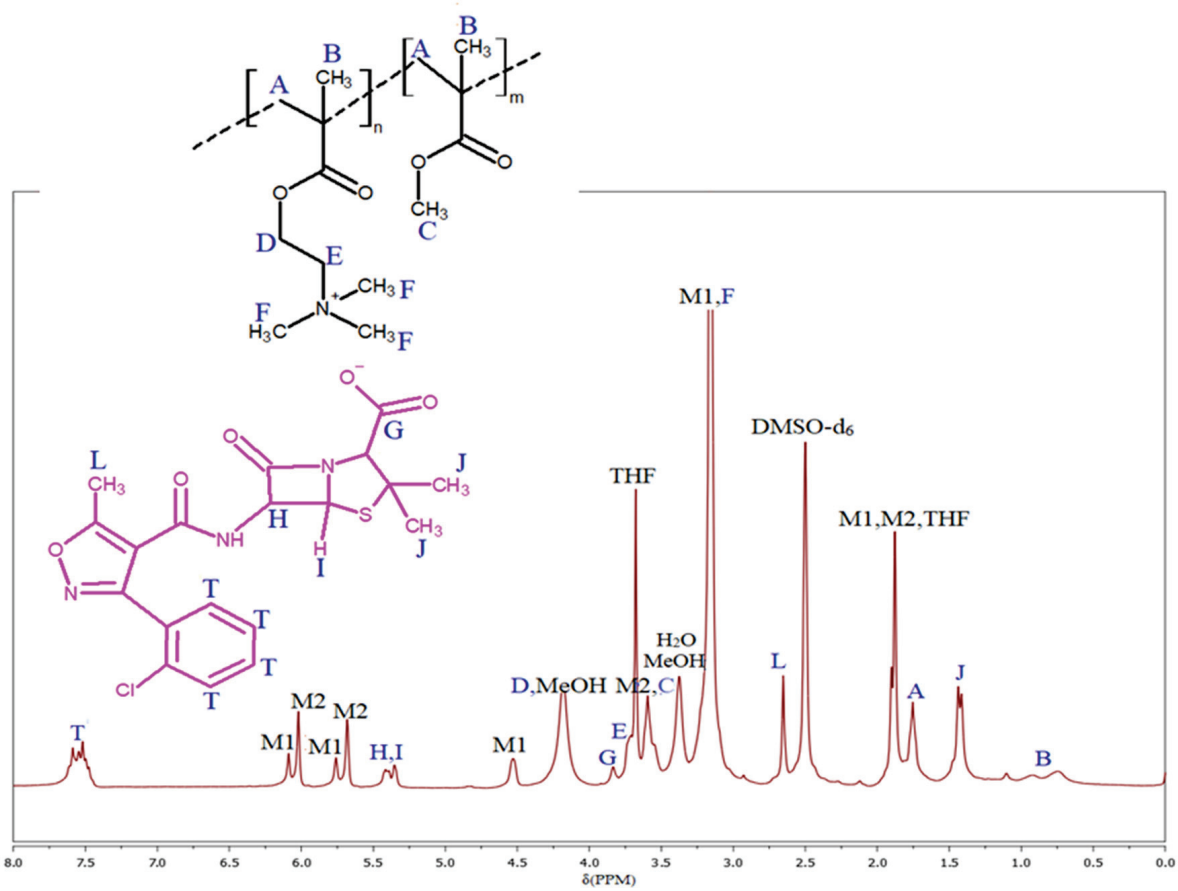

Figure 3. ^{1}H–NMR spectra of the reaction mixture at the end of polymerization in the synthesis of single-drug system IA (P(TMAMA/CLX–*co*–MMA)) (M1 and M2 are related to the signals of TMAMA/CLX and MMA, respectively).

Table 1. Characteristics of linear copolymer P(TMAMA/CLX–*co*–MMA) synthesized by ATRP.

No.	f_{M1}/f_{M2} (mol%)	Time (h)	X_{M1} [a] (%)	X [a] (%)	DP_{M1} [a]	DP_n [a]	F_{M1} [a] (mol)	M_n [a] (g/mol)	M_n [b] (g/mol)	Đ [b]
IA	25/75	2	87	40	87	160	0.54	59,900	10,700	1.24
IB	50/50		90	60	179	241	0.74	115,100	-	-
IC	75/25		92	75	277	299	0.93	170,200	-	-

M1 = TMAMA/CLX, M2 = MMA; conditions: $[TMAMA/CLX + MMA]_0$:$[EBiB]_0$:$[CuBr]_0$:$[PMDETA]_0$ = 400:1:1:1; MeOH:TMAMA/CLX = 1:1 υ/ωt, MeOH:THF = 3:1 υ/υ, 40 °C; f_{M1}, f_{M2}—initial content of monomer in reaction mixture; X_{M1}[a]—TMAMA conversion; X—total monomer conversion; DP_{M1}—polymerization degree of ionic monomers; DP_n—total polymerization degree; F_{M1}—content of ionic fraction in polymer; M_n—average molecular weight; Đ—dispersity index. [a] determined by ^{1}H-NMR (DMSO-d6); [b] determined by SEC (DMF, PEO calibration); - means not determined.

Linear copolymers were synthesized within a short time of 2 h, achieving total monomer conversions ranging from 40 to 75%, while the conversion of the ionic monomer remained similar (87–92%). The observed tendency of the monomer conversion to increase with the initial content of TMAMA monomer shows that the latter factor can be used to regulate the length of the polymer chain (DP_n = 160–299) and the number of ionic units (DP_{M1} = 87–277). The compositions of the resulting copolymers (IA–IC) revealed a higher ionic fraction content than anticipated based on the initial content of the ionic monomer (f_{M1}/F_{M1}: 25/54 (IA); 50/74 (IB); 75/93 (IC)). This phenomenon indicates higher reactivity of the ionic monomer (TMAMA/CLX), which is favored over MMA under polar conditions, probably leading to the formation of copolymers with gradient structures.

2.3. Linear Polymers Containing CLX⁻/AMP⁻ as Dual-Drug Delivery Systems

The dual-drug anions carried by the polymer conjugates were achieved through the terpolymerization of two pharmaceutically functionalized choline monomers, i.e., both TMAMA/CLX and TMAMA/AMP with MMA in ratios equal to 12.5:12.5:75, 25:25:50, and 37.5:37.5:25 via ATRP under conditions similar to those described above for the synthesis of single-drug copolymer conjugates (Figure 1). The resulting terpolymers, P(TMAMA/CLX–*co*–MMA–*co*–TMAMA/AMP) (IIA–IIC, Table 2), were designed to simultaneously transport two drugs. The conversion of monomers into polymers was evaluated using ^{1}H–NMR spectroscopy, as shown in Figure 4, employing analogous signals such as those previously described for the CLX series.

Table 2. Characteristics of linear terpolymers P(TMAMA/CLX–*co*–MMA–*co*–TMAMA/AMP) synthesized by ATRP.

No.	f_{M1}/f_{M2} (mol%)	Time (h)	X_{M1} [a] (%)	X [a] (%)	DP_{M1} [a]	DP_n [a]	F_{M1} [a] (mol)	M_n [a] (g/mol)	M_n [b] (g/mol)	Đ [b]
IIA	25/75	2	91	60	91	239	0.38	55,500	16,200	1.58
IIB	50/50	3.5	90	58	181	231	0.78	85,400	-	-
IIC	75/25	3	92	75	275	300	0.92	124,800	-	-

M1 = TMAMA/CLX + TMAMA/AMP, M2 = MMA; cond.: $[(TMAMA/CLX + TMAMA/AMP) + MMA]_0$: $[EBiB]_0$: $[CuBr]_0$: $[PMDETA]_0$ = 400:1:1:1; MeOH:TMAMA = 1:1 υ/ωt, MeOH:THF = 3:1 υ/υ, 40 °C; f_{M1}, f_{M2}—initial content of comonomers in reaction mixture; X_{M1}[a]—conversion of both TMAMA monomers; X—total conversion; DP_{M1}—polymerization degree of ionic monomers; DP_n—total polymerization degree; F_{M1}—content of ionic fraction in polymer; M_n—average molecular weight of copolymer; Đ—dispersity index. [a] determined by ^{1}H-NMR (DMSO-d6), [b] determined by SEC (DMF, PEO calibration); - means not determined.

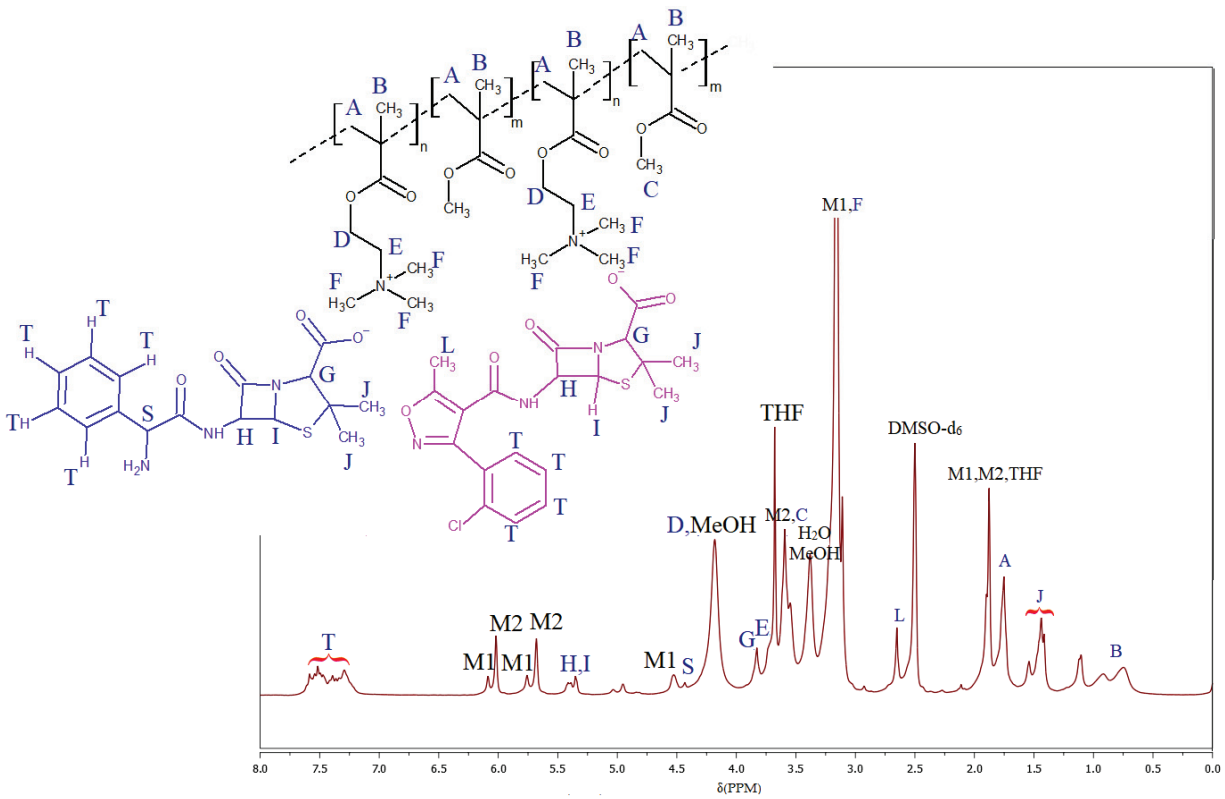

Figure 4. The ^{1}H-NMR spectra of the reaction mixture at the end of the polymerization in the synthesis of dual-drug system IIA (P(TMAMA/CLX–*co*–MMA–*co*–TMAMA/AMP)) (M1 and M2 are related to the signals of TMAMA and MMA, respectively).

The presence of the second drug-based TMAMA in the polymerization with the lowest initial content of ionic monomers affected the formation of significantly higher chain lengths and similar numbers of incorporated ionic units when comparing IIA with IA (DP_n/DP_{M1} = 239/91 vs. 160/87). This observation suggests differences in the relative reactivities of ionic comonomers, where TMAMA with the AMP counterion appears to be more reactive than TMAMA with the CLX counterion. The reduced reactivity of TMAMA/CLX is likely due to its higher steric hindrance, attributed to the Cl-substituted aromatic ring and extra five-membered ring. Furthermore, the structure of CLX renders it less hydrophilic than AMP, making TMAMA/AMP more favorable under the polymerization conditions employed. In relation to MMA, both TMAMAs polymerized faster, as evidenced by the correlation $F_{M1} > f_{M1}$. In the system of three monomer components, MMA was converted at a higher rate than in the two-monomer system, leading to lower ionic content in the polymer IIA compared to IA (38% vs. 54%). However, a higher initial concentration of TMAMAs (f_{M1} = 50 and 75%) provided similar total monomer conversions, as well as DP_n and DP_{M1} values, to analogous systems in series I, but it required a longer duration of polymerization to be convenient for the incorporation of slower TMAMA/CLX. Generally, based on these relationships, the compositions of the resulting polymers IIA–IIC can be estimated from the initial proportions of TMAMA/MMA in the reaction mixture, which is related to the slightly higher content of ionic fraction in the polymer (f_{M1}/F_{M1}: 25/38 (IIA); 50/78 (IIB); 75/92 (IIC)).

The SEC data were obtained for copolymers with an ionic fraction below 60%, which were very soluble in DMF. The molecular weight distribution for the dual-drug polymer IIA was larger compared to the single-drug polymer IA (Đ = 1.58 vs. 1.24), suggesting that the presence of two types of TMAMA counterions with differing natures promoted side reactions. It is worth noting that the SEC data may differ from the NMR-derived

M_n values because the calibration standard used was PEO, a hydrophilic but non-ionic polymer, which differs in nature from the studied ionic copolymers.

The drug content (DC), representing the percentage of pharmaceutical anions incorporated in the polymer chain, was determined by UV-Vis spectroscopy. The DC of CLX^- reached 67–80% in the single-drug systems (IA–IC) and 51–64% in the dual-drug systems (IIA–IIC), where the latter also co-delivered AMP^- with DC values of 78–87% (Figure 5). A simultaneous increase in DCs was observed with increasing total polymerization degree, including the degree of polymerization of TMAMA in the single-drug systems, as shown in Figure 5a ($DC/DP_n/DP_{M1}$: 67/160/87 (IA), 73/241/179 (IB), 80/299/277 (IC)). A similar trend of increasing DC was observed in the dual-drug systems, correlated with the number of TMAMA units, and with additional relationships between the DC of both drugs, that is, $DC_{CLX} < DC_{AMP}$ (IIA: 51% CLX^- vs. 78% AMP^-; IIB: 62% CLX^- vs. 83% AMP^-; IIC: 64% CLX^- vs. 87% AMP^-), as demonstrated in Figure 5b. In summary, the highest values for CLX^- were achieved for IC and IIC, with the longest polymer chain lengths and the highest ionic contents (DP_n ~ 300 and F_{M1} > 92%), which makes them the most advantageous systems.

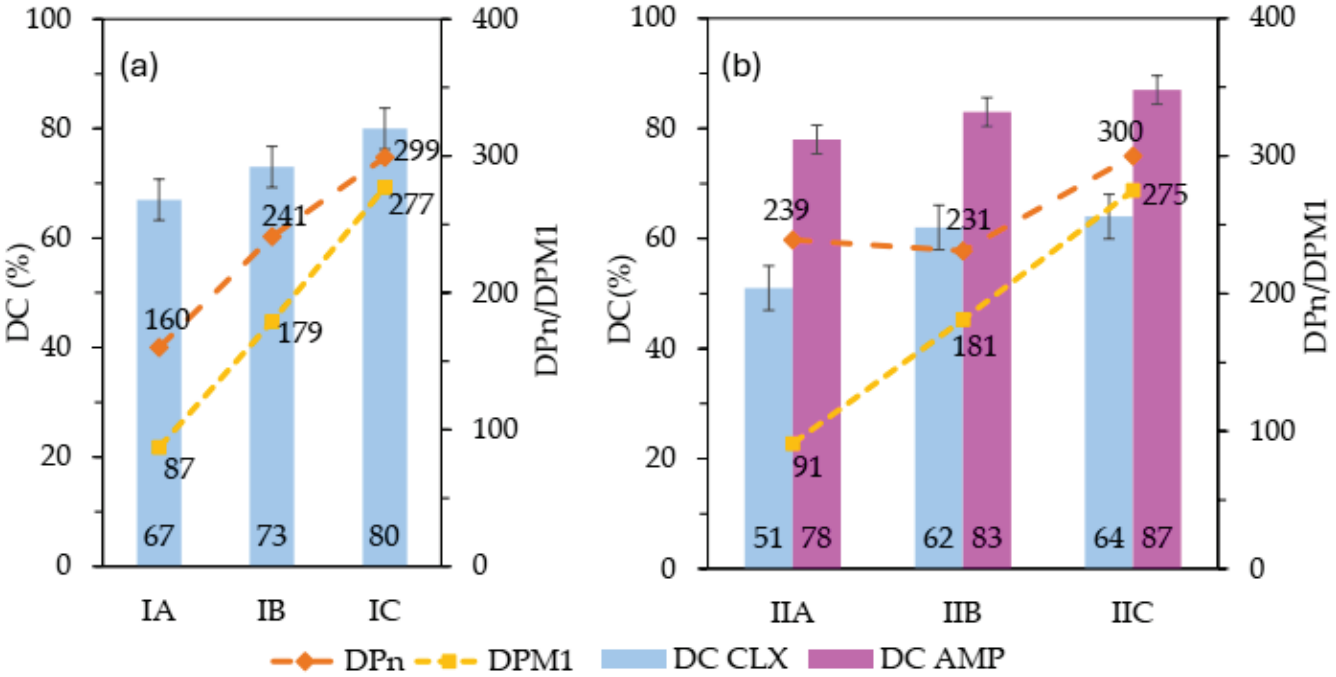

Figure 5. Correlation of drug content (DC) with polymer length chain (DP_n) and number of TMAMA units (DP_{M1}) in single (**a**) and dual (**b**) systems.

2.4. Characteristics of Polymer Particles

Dynamic light scattering (DLS) analysis was conducted to assess the particle size of both types of drug delivery polymer conjugates in an aqueous solution (Table 3). The histograms in Figure 6 depict the particle size distributions, which exhibited a single fraction in all cases. The results for the single-drug polymer systems revealed distinct hydrodynamic diameters (Dh) for IA and IC of Dh $\leq$ 274 nm, whereas IB displayed a larger value of 380 nm. In the dual-drug systems (IIA–IIC), despite the differences in polymer structure, no significant influence was observed on particle sizes, which ranged from 288 nm to 348 nm. Furthermore, the polydispersity index (PDI), which defines the level of heterogeneity of particles as the distribution of their sizes, indicates uniformity of particle sizes (PDI ~0.01). Remarkably, slightly narrower size distributions were exhibited by IB and IIC (PDI: 0.006 and 0.008, respectively), which formed the biggest particles in both series.

Table 3. DLS characteristics of linear polymer particles carrying drug.

Type DDS	Polymer	Dh (nm)	PDI
Single	IA	274	0.01
	IB	380	0.006
	IC	277	0.01
Dual	IIA	288	0.01
	IIB	324	0.01
	IIC	348	0.008

Here, Dh is hydrodynamic diameter and PDI is polydispersity index.

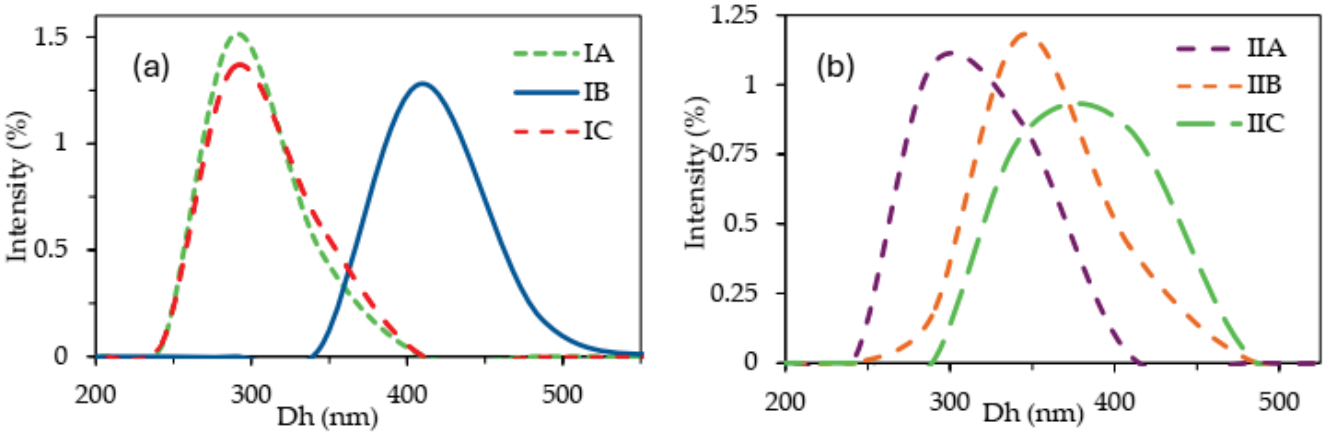

Figure 6. Particle size histograms of single (**a**)- and dual (**b**)-drug polymer systems obtained through DLS analysis. Dh represents hydrodynamic diameters.

The polymer particles of different natures, single- vs. dual-drug systems, were monitored by SEM, showing slight differences in their morphologies depending on the composition and drug type. A brittle form of monolithic and smooth blocks was observed for copolymer IC containing CLX and a higher content of TMAMA (Figure 7a,b) than for copolymer IIA with the presence of accompanying AMP, providing a porous texture, which was crushable (Figure 7c,d).

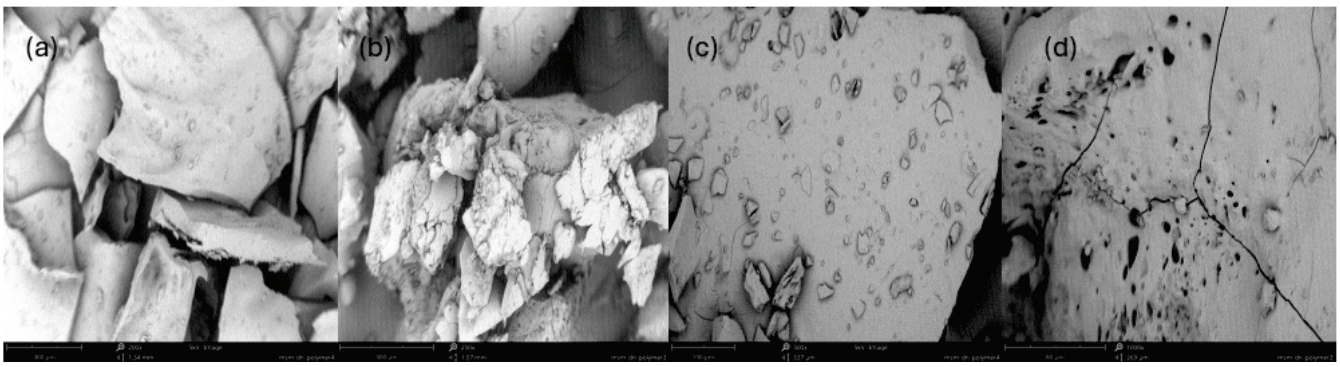

Figure 7. SEM for particles of single IC: 93 mol% of TMAMA (**a**,**c**) and IIA 38 mol% (**b**,**d**) at various magnitudes. (bar 200 nm (**a**,**b**); bar 100 nm (**c**,**d**)).

2.5. Drug Release

In vitro drug release studies were conducted to monitor the exchange of CLX^- or CLX^-/AMP^- anions in the polymer matrix by phosphate anions in the PBS using the dialysis method under physiological conditions in pH 7.4 at 37 °C for 72 h. Drug release

from the polymer samples was detected by UV–Vis spectroscopy at specified time intervals as the percentage amount of released drug (ARD) and the concentration of released drug (CRD) (Figure 8). The kinetic profiles for the single-drug systems illustrated the release of 34–41% of CLX^- within 0.5–1 h, which increased to 58–72% within 4 h. The release stabilized over the next 74 h, with an additional 4–6% of drug release (Figure 8a). However, in the case of sample IC, the release profile differed from the others, exhibiting a more linear pattern. Initially, the release behavior was similar to system IA, but finally achieved the highest ARD value (Figure 8d). The increase in the amount of drug released from the single systems corresponded well with the elevated total polymerization degree and drug content (DP_n/DC/ARD: 160/67/58 (IA), 241/73/66 (IB), 299/80/76 (IC)). Combining the effective content of the drug and its release, polymer IC appeared to be the most promising for achieving an extended therapeutic effect.

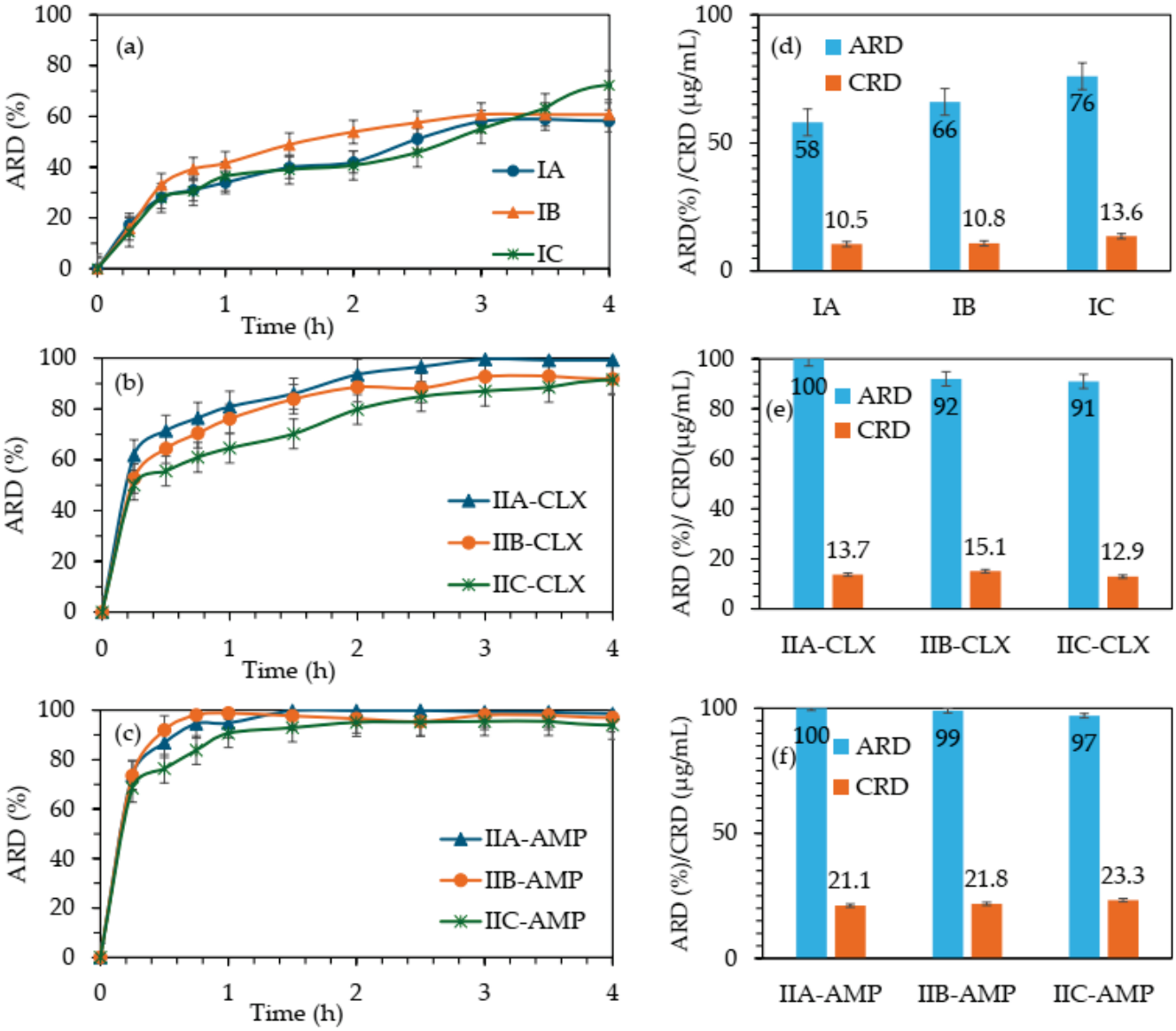

Figure 8. Kinetic release profiles for CLX^- in single-drug systems (**a**) and CLX^- and AMP^- in dual-drug systems (**b**,**c**) up to 4 h, and final ARD and CRD values after 72 h (**d**–**f**). ARD represents the amount of released drug, and CRD is the concentration of released drug.

In the context of the dual co-delivery systems, a significant initial burst release was observed in the first hour for both drugs, yielding 64–80% for CLX^- (Figure 8b) and 90–98% for AMP^- (Figure 8c). Following this, the release rate slowed considerably, with an additional 12–16% of CLX^- released over the next 2 h, ultimately reaching ARD values of 88–100% after 4 h. For systems with incomplete release, the process was extended up to 74 h, but slight progress was detected, maintaining a release plateau. In summary, complete release of both drugs was achieved by system IIA within 4 h, whereas the release from the IIB and IIC systems was slightly slower, reaching >90% of CLX^- and >97% of AMP^-. The results for series II suggested that the interactions between CLX^- and AMP^- improved the co-release of CLX, although its DC was slightly lower than that in series I, but the polymers, especially IIA, were able to completely release both drugs in a relatively short time.

The fitting to kinetic models (Figure S1, Table S1) indicated that CLX release follows the first-order kinetic model as the time depends on the percentage of remaining drug with high correlation coefficients (R^2 = 0.87–0.98 for series I, and 0.91–0.99 for series II). Similar values of R^2 were also obtained for data plotted from the Higuchi equation, which describes the percentage of drug release as a function of the square root of time, indicating the diffusion-controlled release of CLX (R^2 = 0.91–0.97 for series I, and 0.9–0.98 for series II). The diffusion of the ionic CLX was also confirmed by the Korsmeyer–Peppas model, with R^2 = 0.90–0.99, where the release exponent (n) in the equation $M_t/M = kt^n$ allowed us to define the release mechanisms. The systems in series I are on the border between a quasi-Fickian process ($n \leq 0.45$) and a non-Fickian-type release as an anomalous diffusion process ($0.45 < n < 0.89$), while the latter was clearly exhibited by the systems in series II regardless of the drug release type. In the case of AMP release by double systems, the data fittings to all models were lower than for the release of CLX. They were characterized by the lowest R^2 for the Higuchi model (0.65–0.78), whereas values elevated to 0.77–0.89 suggest a good fit, allowing the results to be described by first-order and Korsmeyer–Peppas equations.

3. Materials and Methods

3.1. Materials

Methyl methacrylate (MMA, Alfa Aesar, Warsaw, Poland), tetrahydrofuran (THF, Sigma Aldrich, Poznan, Poland), and methanol (MeOH, Chempur, Piekary Śląskie, Poland) were dried using molecular sieves (type 4A, bulk density 640–670 kg/m^3, Chempur, Piekary Śląskie, Poland) under an argon atmosphere. [2-(Methacryloyloxy)ethyl]trimethylammonium chloride (TMAMA/Cl, 80% aq. solution, Sigma-Aldrich, Poznan, Poland) was concentrated under vacuum conditions to obtain a solid product. Copper (I) bromide (CuBr, Fluka, Steinheim, Germany) was purified by stirring in glacial acetic acid, followed by filtration, washing with ethanol and diethyl ether, and subsequent vacuum drying. Deionized water was prepared using Hydrolab HLP Uv5 equipment (Straszyn, Poland). Other reagents used without prior purification included ethyl 2-bromoisobutyrate (EBiB), *N*,*N*,*N*′,*N*″,*N*″-pentamethyldiethylenetriamine (PMDETA), and ampicillin sodium salt (NaAMP) from Sigma Aldrich (Poznan, Poland) and cloxacillin sodium monohydrate (NaCLX) and deuterated dimethyl sulfoxide (DMSO–d6) from Alfa Aesar, as well as *N*,*N*-dimethylforamide (DMF, POCH, Gliwice, Poland), phosphate-buffered solution (PBS, Sigma Aldrich, Poznan, Poland), and diethyl ether (Chempur, Piekary Śląskie, Poland).

3.2. Preparation of Pharmaceutically Functionalized Choline Ionic Liquids Through Ion Exchange

The vacuum-dried TMAMA/Cl (2.14 mmol, 0.445 g) was dissolved in 2.2 mL of MeOH (forming solution 1). Next, NaCLX (2.14 mmol, 1.02 g) was dissolved in 5.1 mL of MeOH (TMAMA/Cl:MeOH = 1:5 *w*/*v*) and added dropwise to solution 1 with continuous stirring during the drug addition. Then, the mixture was stirred for 3 h constantly in a dark place at room temperature during the ion exchange reaction. After NaCl salt precipitation, the solution was filtered and washed twice with 1 mL MeOH to remove any salt. To accelerate MeOH evaporation, the filtrated solution containing TMAMA/CLX was left on a ventilator at room temperature for 30 min. It was further dried under vacuum conditions until it

solidified into a powder product. Yield: 1.26 g. ^{1}H NMR (DMSO–d$_6$, 300 MHz, δ, ppm): 7.4–7.7 (4H, aromatic ring of CLX), 5.75 and 6.15 (2H, =CH$_2$ in vinyl group), 5.25–5.45 (2H, -CH-N- and -CH-S- in β-lactam ring of CLX), 4.54 (2H, -CH$_2$-O-), 3.82 (1H, -CH-N- in thiazolidine ring of CLX), 3.73 (2H, -CH$_2$-N$^+$-), 3.14 (9H, -N$^+$(CH$_3$)$_3$), 2.65 (3H, -CH$_3$ at isoxazole ring in CLX), 1.92 (3H, -CH$_3$), 1.46 (6H, -C(CH$_3$)$_2$ in thiazolidine ring of CLX). Chloride content: 3.6%.

The synthesis of analogical TMAMA/AMP followed the previously described method, utilizing equimolar ratios of TMAMA/Cl (3.9 mmol, 0.8 g) and NaAMP (3.9 mmol, 1.43 g) in MeOH (4 mL and 7.2 mL, respectively). However, the ion exchange process was completed within 20 h. Yield: 2.04 g. ^{1}H–NMR (DMSO-d$_6$, 300 MHz, δ, ppm): 7.1–7.5 (5H, -CH in aromatic ring in AMP), 5.75 and 6.15 (2H, -CH$_2$ in vinyl group), 5.25–5.5 (2H, -CH-N- and -CH-S- in β-lactam ring of AMP), 4.54 (2H, -CH$_2$-O-), 4.46 (1H, -CH-NH$_2$ in AMP), 3.8–4.0 (1H, -CH-N- in thiazolidine ring of AMP), 3.75 (2H, -CH$_2$-N$^+$-), 3.16 and 3.12 (9H, -N$^+$(CH$_3$)$_3$), 1.92 (3H, -CH$_3$), 1.57 and 1.46 (6H, -C(CH$_3$)$_2$ in thiazolidine ring of AMP). Chloride content: 2.7%.

3.3. Synthesis of Copolymer Conjugates

Ionic linear copolymers containing CLX anion, P(TMAMA/CLX–*co*–MMA) (example for IA): TMAMA/CLX (0.656 mmol, 0.41 g) was dissolved in 0.41 mL of MeOH in a Schlenk flask. Subsequently, MMA (1.968 mmol, 0.21 mL), THF (0.14 mL), and PMDETA (0.007 mmol, 0.001 mL) were added to the flask. The mixture was homogenized and degassed by performing two freeze–pump–thaw cycles. Then, EBiB (0.007 mmol, 0.001 mL) was introduced as the initiator, and an initial sample was taken. Another freeze–pump–thaw cycle was performed. Following this, a CuBr catalyst (0.007 mmol, 0.001 g) was quickly added to the mixture. The reaction flask was immersed in an oil bath at 40 °C. After 2 h, when a noticeable increase in the mixture's viscosity was observed, the reaction was stopped by exposing the mixture to air. The resulting product was dissolved in MeOH (1 mL) and precipitated twice in a chloroform–diethyl ether mixture (1:1) to remove the catalyst from the polymer. The solvents were removed using a syringe, and the remaining solvents were evaporated under a ventilator at room temperature for 15 min. Finally, the polymer was dried under vacuum. Yield: 0.24 g. ^{1}H–NMR (DMSO–d$_6$, 300 MHz, δ, ppm): 7.4–7.7 (4H, aromatic ring of CLX), 5.3–5,5 (2H, -CH-N- and -CH-S- in β-lactam ring of CLX), 4.1–4.3 (2H, -CH$_2$-O-), 3.82 (1H, -CH-N- in thiazolidine ring of CLX), 3.60–3.75 (2H, -CH$_2$-N$^+$-), 3.5–3.6 (3H, -O-CH$_3$), 3.02–3.30 (9H, -N$^+$(CH$_3$)$_3$), 2.65 (3H, -CH$_3$ at isoxazole ring in CLX), 1.75 (2H, -CH$_2$-C-), 1.36–1.46 (6H, -C(CH$_3$)$_2$ in thiazolidine ring of CLX), 0.54–1.2 (3H, -CH$_3$).

Dual bioactive ionic linear copolymers containing CLX$^-$/AMP$^-$, P(TMAMA/CLX–*co*–MMA–*co*–TMAMA/AMP) (example for IIA): TMAMA/CLX (0.557 mmol, 0.35 g) and TMAMA/AMP (0.557 mmol, 0.29 g) were dissolved in 0.64 mL of MeOH in a Schlenk flask. Then, MMA (3.342 mmol, 0.36 mL), THF (0.21 mL), and PMDETA (0.011 mmol, 0.002 mL) were added to the flask. Further steps were carried out, like for the synthesis and purification of P(TMAMA/CLX–*co*–MMA), using proper amounts of EBiB (0.011 mmol, 0.002 mL) and CuBr (0.011 mmol, 0.002 g). Yield: 0.73 g. ^{1}H–NMR (DMSO–d$_6$, 300 MHz, δ, ppm): 7.1–7.7 (9H, -CH in aromatic rings of AMP and CLX), 5.25–5.4 (2H, -CH-NH- and -CH-S- in β-lactam ring of CLX and AMP), 4.43 (1H, -CH-NH$_2$ in AMP), 4.1–4.3 (2H, -CH$_2$-O-), 3.75–3.87 (2H, -CH-N- in thiazolidine ring of CLX and AMP), 3.65–3.75 (2H, -CH$_2$-N$^+$-), 3.4–3.65 (3H, -O-CH$_3$), 3.05–3.25 (9H, -N$^+$(CH$_3$)$_3$), 2.65 (3H, -CH$_3$ at isoxazole ring in CLX), 1.75 (2H, -CH$_2$-C), 1.4–1.7 (12H, -C(CH$_3$)$_2$ in thiazolidine ring of CLX and AMP), 0.6–1.2 (3H, -CH$_3$).

3.4. Release Studies of Copolymer Conjugates Containing CLX$^-$ and AMP$^-$

Copolymer conjugates containing drug anions (1 mg) were dissolved in 1 mL of PBS (pH 7.4) to prepare a 1 mg/mL solution. The solution was then transferred into a dialysis cellulose membrane bag with a molecular weight cutoff (MWCO) of 3.5 kDa. Then, this

membrane bag was placed inside a glass vial filled with 44 mL of PBS and stirred at 37 °C during a 74 h dialysis process. The release progress was monitored by assessing changes in drug concentration in the external PBS solution surrounding the dialysis bag. At different time intervals, 0.5 mL samples of the solution containing the released drug were collected, and 0.5 mL of MeOH was added to the cuvette. These samples were subsequently analyzed using a UV-Vis spectrophotometer to quantify the released drug amount by measuring the absorbance at a wavelength of λ = 206 nm for AMP^- and λ = 203 nm for CLX^-. Each reported result represents the average of three measurements.

3.5. Characterization Methods

Proton nuclear magnetic resonance (^{1}H–NMR) spectra were acquired using a UNITY/NOVA spectrometer (Varian, Mulgrave, Victoria, Australia) operating at a frequency of 300 MHz. Measurements were performed on samples dissolved in DMSO–d_6 with tetramethylsilane used as the internal standard. Size exclusion chromatography (SEC) was conducted using an Ultimate 3000 chromatograph (Thermo Fisher Scientific, Waltham, MA, USA) equipped with a RefractoMax 521 differential refractometer detector. Polymer samples prepared in DMF containing 10 mM LiBr at 40 °C, were passed through a precolumn TSKgel Guardian SuperMP(HZ)-H (4.6 mm × 2 cm, with a particle size of 6 μm), followed by two columns of TSKgel SuperMilipore HZ-H (4.6 mm × 15 cm, with a particle size of 6 μm). The flow rate was maintained at 0.45 mL/min. The average molecular weight (M_n) and dispersity index (Đ) were determined on the basis of poly(ethylene oxide)/poly(ethylene glycol) (PEO) standards with molecular weights ranging from 982 to 969,000 g/mol. The drug content (DC) and the amount of released drug (ARD) were analyzed by ultraviolet–visible spectroscopy (UV-Vis) using an Evolution 300 spectrometer (Thermo Fisher Scientific, Waltham, MA, USA). Polymer samples dissolved in a PBS and MeOH (1:1) at a concentration of 0.05 mg/mL were placed in a quartz cuvette and measured at a maximum wavelength of λ = 206 nm for AMP^- and λ = 203 nm for CLX^-. Calibration curves were prepared for drug concentrations ranging from 0.1 mg/mL to 0.006 mg/mL in a PBS-MeOH mixture (1:1). Dynamic light scattering (DLS) was performed using a Nanotrac Flex with a Mictrac MRB laser particle size analyzer (Microtrac Retsch GmbH, Haan, Germany; Dimensions LS software 1.1.0.), equipped with an external "dip-in" probe with 180° backscattering. Polymer samples were dissolved in deionized water at a concentration of 1.0 mg/mL to determine the hydrodynamic diameters (Dh) and polydispersity index (PDI). Each sample was measured at least three times to ensure reproducibility. The morphology of the polymers was observed by scanning electron microscopy (SEM) using a Phenom ProX electron microscope (PhenomWorld, Eidhoven, The Netherlands) operating at 15 kV. Before measurements, the sample was dusted with a layer of 5 nm gold nanoparticles.

4. Conclusions

The well-defined linear copolymers, including series I with CLX^- (single-drug DDS) and series II containing both CLX^- and AMP^- (dual-drug DDS), were synthesized to demonstrate their potential as nanocarriers (274–380 nm (CLX^-) and 288–348 nm (CLX^-/AMP^-)). In both series, the TMAMA monomers functionalized by pharmaceutical anions with antibiotic activities were incorporated into the polymer chains at different contents (38–93 mol%). The various lengths of the polymer chains (DP_n = 160–300) were adjusted through monomer conversion (40–75%), while the initial proportion of comonomers allowed for the regulation of ionic contents (38–93 mol%) within the polymers.

The drug content within the polymer matrix with 67–80% in the CLX^- systems, and 51–64% of CLX^- and 78–87% of AMP^- in the dual-drug systems, corresponded to the efficient in vitro release of 91–100% of CLX^- (12.9–15.1 μg/mL) and 97–100% of AMP^- (21.1–23.3 μg/mL) from the dual-drug systems, and 67–80% of CLX^- in the single-drug systems, in PBS within 72 h, but AMP release was almost complete after 4 h. The drug content and release were significantly affected by structural factors, such as the polymer

chain length, ionic fraction content in the copolymer, and pharmaceutical anion's nature. Overall, the linear copolymers proved effective in designing both single- and dual-drug systems with tailored release profiles to facilitate efficient drug delivery. The cholinium-based polymer systems combining AMP^- and CLX^- demonstrated significant potential for antibiotic treatment, enabling the simultaneous co-delivery of drugs for optimized therapeutic outcomes.

Supplementary Materials: The following supporting information can be downloaded at: https://www.mdpi.com/article/10.3390/molecules29245973/s1, Figure S1: Fitting of kinetic release profiles for single- and dual-drug systems to first-order (a–c), Higuchi (d–f), and Korsmeyer–Peppas (g–i) models. Table S1: Correlation coefficients (R^2) for kinetic model equations and drug release exponents (n).

Author Contributions: S.K.: investigation, data curation, formal analysis, writing—original draft; D.N.: conceptualization, methodology, writing—review and editing, supervision. All authors have read and agreed to the published version of the manuscript.

Funding: This research was funded by the Grant for Young Scientists, BKM-539/RCH4/2024 (04/040/BKM24/0288).

Institutional Review Board Statement: Not applicable.

Informed Consent Statement: Not applicable.

Data Availability Statement: All data generated or analyzed during this study are included in this published article.

Acknowledgments: The authors express their gratitude to Monika Śmiga-Matuszowicz for conducting the SEM analysis.

Conflicts of Interest: The authors declare that they have no known competing financial interests or personal relationships that could have appeared to influence the work reported in this paper.

References

1. Gouveia, W.; Jorge, T.F.; Martins, S.; Meireles, M.; Carolino, M.; Cruz, C.; Almeida, T.V.; Araújo, M.E.M. Toxicity of Ionic Liquids Prepared from Biomaterials. *Chemosphere* **2014**, *104*, 51–56. [CrossRef]
2. Agatemor, C.; Ibsen, K.N.; Tanner, E.E.L.; Mitragotri, S. Ionic Liquids for Addressing Unmet Needs in Healthcare. *Bioeng. Transl. Med.* **2018**, *3*, 7–25. [CrossRef] [PubMed]
3. Egorova, K.S.; Gordeev, E.G.; Ananikov, V.P. Biological Activity of Ionic Liquids and Their Application in Pharmaceutics and Medicine. *Chem. Rev.* **2017**, *117*, 7132–7189. [CrossRef] [PubMed]
4. Li, X.; Ma, N.; Zhang, L.; Ling, G.; Zhang, P. Applications of Choline-Based Ionic Liquids in Drug Delivery. *Int. J. Pharm.* **2022**, *612*, 121366. [CrossRef]
5. Banerjee, A.; Ibsen, K.; Iwao, Y.; Zakrewsky, M.; Mitragotri, S. Transdermal Protein Delivery Using Choline and Geranate (CAGE) Deep Eutectic Solvent. *Adv. Healthc. Mater.* **2017**, *6*, 1601411. [CrossRef]
6. Messali, M.; Moussa, Z.; Alzahrani, A.Y.; El-Naggar, M.Y.; ElDouhaibi, A.S.; Judeh, Z.M.A.; Hammouti, B. Synthesis, Characterization, and the Antimicrobial Activity of New Eco-Friendly Ionic Liquids. *Chemosphere* **2013**, *91*, 1627–1634. [CrossRef] [PubMed]
7. Vanik, V.; Bednarikova, Z.; Fabriciova, G.; Wang, S.S.S.; Gazova, Z.; Fedunova, D. Modulation of Insulin Amyloid Fibrillization in Imidazolium-Based Ionic Liquids with Hofmeister Series Anions. *Int. J. Mol. Sci.* **2023**, *24*, 9699. [CrossRef]
8. Ishikawa, Y.; Takekiyo, T.; Yoshimura, Y. Recovery and Cryopreservation of Insulin Amyloid Using Ionic Liquids. *J. Mol. Liq.* **2018**, *272*, 1019–1024. [CrossRef]
9. Correia, D.M.; Fernandes, L.C.; Fernandes, M.M.; Hermenegildo, B.; Meira, R.M.; Ribeiro, C.; Ribeiro, S.; Reguera, J.; Lanceros-Méndez, S. Ionic Liquid-Based Materials for Biomedical Applications. *Nanomaterials* **2021**, *11*, 2401. [CrossRef]
10. Shamshina, J.L.; Rogers, R.D. Ionic Liquids: New Forms of Active Pharmaceutical Ingredients with Unique, Tunable Properties. *Chem. Rev.* **2023**, *123*, 11894–11953. [CrossRef]
11. Shamshina, J.L.; Kelley, S.P.; Gurau, G.; Rogers, R.D. Chemistry: Develop Ionic Liquid Drugs. *Nature* **2015**, *528*, 188–189. [CrossRef]
12. Pedro, S.N.; Freire, C.S.R.; Silvestre, A.J.D.; Freire, M.G. Ionic Liquids in Drug Delivery. *Encyclopedia* **2021**, *1*, 324–339. [CrossRef]
13. Jiang, L.; Sun, Y.; Lu, A.; Wang, X.; Shi, Y. Ionic Liquids: Promising Approach for Oral Drug Delivery. *Pharm. Res.* **2022**, *39*, 2353–2365. [CrossRef]
14. Singh, S.K.; Savoy, A.W. Ionic Liquids Synthesis and Applications: An Overview. *J. Mol. Liq.* **2020**, *297*, 112038. [CrossRef]

15. Nasirpour, N.; Mohammadpourfard, M.; Heris, S.Z. Ionic Liquids: Promising Compounds for Sustainable Chemical Processes and Applications. *Chem. Eng. Res. Des.* **2020**, *160*, 264–300. [CrossRef]
16. Ghandi, K. A Review of Ionic Liquids, Their Limits and Applications. *Green Sustain. Chem.* **2014**, *4*, 44–53. [CrossRef]
17. Grassiri, B.; Mezzetta, A.; Maisetta, G.; Migone, C.; Fabiano, A.; Esin, S.; Guazzelli, L.; Zambito, Y.; Batoni, G.; Piras, A.M. Betaine- and L-Carnitine-Based Ionic Liquids as Solubilizing and Stabilizing Agents for the Formulation of Antimicrobial Eye Drops Containing Diacerein. *Int. J. Mol. Sci.* **2023**, *24*, 2714. [CrossRef]
18. Gomes, J.M.; Silva, S.S.; Reis, R.L. Biocompatible Ionic Liquids: Fundamental Behaviours and Applications. *Chem. Soc. Rev.* **2019**, *48*, 4317–4335. [CrossRef]
19. Araújo, J.M.M.; Florindo, C.; Pereiro, A.B.; Vieira, N.S.M.; Matias, A.A.; Duarte, C.M.M.; Rebelo, L.P.N.; Marrucho, I.M. Cholinium-Based Ionic Liquids with Pharmaceutically Active Anions. *RSC Adv.* **2014**, *4*, 28126–28132. [CrossRef]
20. Tao, D.J.; Cheng, Z.; Chen, F.F.; Li, Z.M.; Hu, N.; Chen, X.S. Synthesis and Thermophysical Properties of Biocompatible Cholinium-Based Amino Acid Ionic Liquids. *J. Chem. Eng. Data* **2013**, *58*, 1542–1548. [CrossRef]
21. Dean, P.M.; Turanjanin, J.; Yoshizawa-Fujita, M.; MacFarlane, D.R.; Scott, J.L. Exploring an Anti-Crystal Engineering Approach to the Preparation of Pharmaceutically Active Ionic Liquids. *Cryst. Growth Des.* **2009**, *9*, 1137–1145. [CrossRef]
22. Ferraz, R.; Branco, L.C.; Marrucho, I.M.; Araújo, J.M.M.; Rebelo, L.P.N.; Ponte, M.N.D.; Prudêncio, C.; Noronha, J.P.; Petrovski, Ž. Development of Novel Ionic Liquids Based on Ampicillin. *MedChemComm* **2012**, *3*, 494–497. [CrossRef]
23. Rodrigues, P.R.; Vieira, R.P. Advances in Atom-Transfer Radical Polymerization for Drug Delivery. *Eur. Polym. J.* **2019**, *115*, 45–58. [CrossRef]
24. Yazdi, M.K.; Zarrintaj, P.; Saeb, M.R.; Mozafari, M.; Bencherif, S.A. Progress in ATRP-Derived Materials for Biomedical Applications. *Prog. Mater. Sci.* **2024**, *143*, 101248. [CrossRef]
25. Siegwart, D.J.; Oh, J.K.; Matyjaszewski, K. ATRP in the Design of Functional Materials for Biomedical Applications. *Prog. Polym. Sci.* **2012**, *37*, 18–37. [CrossRef]
26. Dashtimoghadam, E.; Fahimipour, F.; Keith, A.N.; Vashahi, F.; Popryadukhin, P.; Vatankhah-Varnosfaderani, M.; Sheiko, S.S. Injectable Non-Leaching Tissue-Mimetic Bottlebrush Elastomers as an Advanced Platform for Reconstructive Surgery. *Nat. Commun.* **2021**, *12*, 3961. [CrossRef]
27. Dashtimoghadam, E.; Maw, M.; Keith, A.N.; Vashahi, F.; Kempkes, V.; Gordievskaya, Y.D.; Kramarenko, E.Y.; Bersenev, E.A.; Nikitina, E.A.; Ivanov, D.A.; et al. Super-Soft, Firm, and Strong Elastomers Toward Replication of Tissue Viscoelastic Response. *Mater. Horiz.* **2022**, *9*, 3022–3030. [CrossRef]
28. Szewczyk-Łagodzińska, M.; Plichta, A.; Dębowski, M.; Kowalczyk, S.; Iuliano, A.; Florjańczyk, Z. Recent Advances in the Application of ATRP in the Synthesis of Polymers. *Polymers* **2023**, *15*, 1234. [CrossRef] [PubMed]
29. Zaborniak, I.; Chmielarz, P.; Matyjaszewski, K. Synthesis of Riboflavin-Based Macromolecules through Low PPM ATRP in Aqueous Media. *Macromol. Chem. Phys.* **2020**, *221*, 1900496. [CrossRef]
30. Zaborniak, I.; Chmielarz, P.; Wolski, K. Riboflavin-Induced Metal-Free ATRP of (Meth)acrylates. *Eur. Polym. J.* **2020**, *110*, 140. [CrossRef]
31. Bury, K.; Du Prez, F.; Neugebauer, D. Self-Assembling Linear and Star-Shaped Poly(ε-caprolactone)/poly[(meth)acrylic acid] Block Copolymers as Carriers of Indomethacin and Quercetin. *Macromol. Biosci.* **2013**, *13*, 1520–1530. [CrossRef] [PubMed]
32. Geszke-Moritz, M.; Moritz, M. Biodegradable Polymeric Nanoparticle-Based Drug Delivery Systems: Comprehensive Overview, Perspectives, and Challenges. *Polymers* **2024**, *16*, 2536. [CrossRef]
33. Harun-Or-Rashid, M.; Aktar, M.N.; Hossain, M.S.; Sarkar, N.; Islam, M.R.; Arafat, M.E.; Bhowmik, S.; Yusa, S.-I. Recent Advances in Micro- and Nano-Drug Delivery Systems Based on Natural and Synthetic Biomaterials. *Polymers* **2023**, *15*, 4563. [CrossRef]
34. Beach, M.A.; Nayanathara, U.; Gao, Y.; Zhang, C.; Xiong, Y.; Wang, Y.; Such, G.K. Polymeric Nanoparticles for Drug Delivery. *Chem. Rev.* **2024**, *124*, 5505–5616. [CrossRef] [PubMed]
35. Minko, T. Soluble Polymer Conjugates for Drug Delivery. *Drug Discov. Today Technol.* **2005**, *2*, 15–20. [CrossRef]
36. Greenwald, R.B.; Choe, Y.H.; McGuire, J.; Conover, C.D. Effective Drug Delivery by PEGylated Drug Conjugates. *Adv. Drug Deliv. Rev.* **2003**, *55*, 217–250. [CrossRef] [PubMed]
37. Khandare, J.; Minko, T. Polymer–Drug Conjugates: Progress in Polymeric Prodrugs. *Prog. Polym. Sci.* **2006**, *31*, 359–397. [CrossRef]
38. Rohini, N.A.; Joseph, A.; Mukerji, A. Polymeric Prodrugs: Recent Achievements and General Strategies. *J. Antivir. Antiretrovir.* **2013**, *15*, 1–12.
39. Ekladious, I.; Colson, Y.L.; Grinstaff, M.W. Polymer–Drug Conjugate Therapeutics: Advances, Insights, and Prospects. *Nat. Rev. Drug Discov.* **2019**, *18*, 273–294. [CrossRef]
40. Bielas, R.; Mielanczyk, A.; Siewniak, A.; Neugebauer, D. Trimethylammonium-Based Polymethacrylate Ionic Liquids with Tunable Hydrophilicity and Charge Distribution as Carriers of Salicylate Anions. *ACS Sustain. Chem. Eng.* **2016**, *4*, 4181–4191. [CrossRef]
41. Niesyto, K.; Neugebauer, D. Linear Copolymers Based on Choline Ionic Liquid Carrying Anti-Tuberculosis Drugs: Influence of Anion Type on Physicochemical Properties and Drug Release. *Int. J. Mol. Sci.* **2021**, *22*, 284. [CrossRef] [PubMed]
42. Bielas, R.; Siewniak, A.; Skonieczna, M.; Adamiec, M.; Mielańczyk, Ł.; Neugebauer, D. Choline Based Polymethacrylate Matrix with Pharmaceutical Cations as Co-Delivery System for Antibacterial and Anti-Inflammatory Combined Therapy. *J. Mol. Liq.* **2019**, *285*, 114–122. [CrossRef]

43. Ghatak, C.; Rao, V.G.; Mandal, S.; Ghosh, S.; Sarkar, N. An Understanding of the Modulation of Photophysical Properties of Curcumin Inside a Micelle Formed by an Ionic Liquid: A New Possibility of Tunable Drug Delivery System. *J. Phys. Chem. B* **2012**, *116*, 3369–3379. [CrossRef] [PubMed]
44. Lu, B.; Zhou, G.; Xiao, F.; He, Q.; Zhang, J. Stimuli-Responsive Poly(ionic Liquid) Nanoparticles for Controlled Drug Delivery. *J. Mater. Chem. B* **2020**, *8*, 7994–8001. [CrossRef] [PubMed]
45. Niesyto, K.; Keihankhadiv, S.; Mazur, A.; Mielanczyk, A.; Neugebauer, D. Ionic Liquid-Based Polymer Matrices for Single and Dual Drug Delivery: Impact of Structural Topology on Characteristics and In Vitro Delivery Efficiency. *Int. J. Mol. Sci.* **2024**, *25*, 1292. [CrossRef]
46. Niesyto, K.; Mazur, A.; Neugebauer, D. Piperacillin/Tazobactam Co-Delivery by Micellar Ionic Conjugate Systems Carrying Pharmaceutical Anions and Encapsulated Drug. *Pharmaceutics* **2024**, *16*, 198. [CrossRef]
47. Keihankhadiv, S.; Neugebauer, D. Self-Assembling Polymers with p-Aminosalicylate Anions Supported by Encapsulation of p-Aminosalicylate for the Improvement of Drug Content and Release Efficiency. *Pharmaceuticals* **2023**, *16*, 1502. [CrossRef] [PubMed]
48. Keihankhadiv, S.; Neugebauer, D. Synthesis and Characterization of Linear Copolymers Based on Pharmaceutically Functionalized Monomeric Choline Ionic Liquid for Delivery of p-Aminosalicylate. *Pharmaceutics* **2023**, *15*, 860. [CrossRef]
49. Mazur, A.; Niesyto, K.; Neugebauer, D. Pharmaceutical Functionalization of Monomeric Ionic Liquid for the Preparation of Ionic Graft Polymer Conjugates. *Int. J. Mol. Sci.* **2022**, *23*, 14731. [CrossRef] [PubMed]
50. Keihankhadiv, S.; Neugebauer, D. Simple strategy of the use of pharmaceutically functionalized ionic liquids in a new generation of polymer nanocarriers for the combined delivery of ionic p-aminosalicylate and ampicillin. *Int. J. Pharm.* **2024**, *662*, 124483. [CrossRef] [PubMed]
51. Jiamboonsri, P.; Eurtivong, C.; Wanwong, S. Assessing the Potential of Gallic Acid and Methyl Gallate to Enhance the Efficacy of β-Lactam Antibiotics against Methicillin-Resistant *Staphylococcus aureus* by Targeting β-Lactamase: In Silico and In Vitro Studies. *Antibiotics* **2023**, *12*, 1622. [CrossRef] [PubMed]
52. Bornside, G.H. Synergistic Antibacterial Activity of Ampicillin-Cloxacillin Mixtures Against *Proteus morganii*. *Am. Soc. Microbiol.* **1968**, *16*, 1507–1511. [CrossRef]
53. Iheanacho, C.O. An Antibiotic Turned Contraceptive: The Tale of Ampicillin-Cloxacillin. *Health Sci. Rep.* **2022**, *5*, e481. [CrossRef] [PubMed]
54. Faibanks, D.N. Antimicrobial therapy. In *Otolaryngology–Head & Neck Surgery*, 13th ed.; American Academy of Otolaryngology–Head & Neck Surgery: Alexandria, VA, USA, 2007.

Disclaimer/Publisher's Note: The statements, opinions and data contained in all publications are solely those of the individual author(s) and contributor(s) and not of MDPI and/or the editor(s). MDPI and/or the editor(s) disclaim responsibility for any injury to people or property resulting from any ideas, methods, instructions or products referred to in the content.

molecules

MDPI

Article

Conformational Geometry Matters: The Case of the Low-Melting-Point Systems of Tetrabutylammonium Triflate with Fumaric or Maleic Acid

Simone Di Muzio [1,2], Fabio Ramondo [3], Oriele Palumbo [1,*], Francesco Trequattrini [1,4], Pascale Roy [5], Jean-Blaise Brubach [5] and Annalisa Paolone [1]

1 Istituto dei Sistemi Complessi, Consiglio Nazionale delle Ricerche, UOS La Sapienza, Piazzale Aldo Moro 5, 00185 Rome, Italy; simone.dimuzio@ifn.cnr.it (S.D.M.); francesco.trequattrini@uniroma1.it (F.T.); annalisa.paolone@roma1.infn.it (A.P.)
2 Istituto di Fotonica e Nanotecnologie, Consiglio Nazionale delle Ricerche, Piazza Leonardo da Vinci, 32, 20133 Milano, Italy
3 Department of Chemistry, Sapienza Università di Roma, Piazzale Aldo Moro 5, 00185 Rome, Italy; fabio.ramondo@uniroma1.it
4 Department of Physics, Sapienza Università di Roma, Piazzale Aldo Moro 5, 00185 Rome, Italy
5 Synchrotron SOLEIL, L'Orme des Merisiers, Départementale 128, 91190 Saint-Aubin, France; pascale.roy@synchrotron-soleil.fr (P.R.); jean-blaise.brubach@synchrotron-soleil.fr (J.-B.B.)
* Correspondence: oriele.palumbo@infn.roma1.it

Abstract: For this article, the interaction of tetrabutylammonium trifluoromethanesulfonate (TBATFO) with either fumaric (FUM) or maleic (MAL) acid has been investigated. These acids are isomers and can be considered the trans and cis configurations of the same molecular geometry. When TBATFO is mixed with FUM, an eutectic point is obtained for a relative composition of 90-10 (molar ratio), with a melting point of ≈90 °C. If maleic acid is mixed with TBATFO, one obtains an inhomogeneous phase with the retention of a solid portion immersed in a liquid phase, even above 90 °C. DFT calculations helped to model the interaction between the components. It is suggested herein that TBATFO interacts more strongly with FUM than with MAL, due to possible interactions in two different sites for hydrogen bonding (HB) in FUM. In MAL, one of the HB sites is instead retained in the intramolecular interactions; therefore, fewer sites are available for intermolecular interactions. Infrared spectroscopy measurements have confirmed this scenario, in which the hydrogen bonds of the acid molecules are replaced by HB between the acid and the ionic couple: for both kinds of mixtures, the vibration region of the OH bonds is strongly affected by mixing. However, in the case of FUM, the vibrations of the SO_3 group of the TFO anion are displaced, while they remain in practically the same frequency position in the case of MAL.

Keywords: low-melting-point systems; hydrogen bonding; density functional theory; infrared spectroscopy

1. Introduction

The rising demand for solvents that offer both strong solvating capabilities and minimal environmental impact has steered research toward the development of alternative systems, such as deep eutectic solvents (DESs) [1]. These eutectic mixtures are typically formed by combining a hydrogen bond donor (HBD) with a hydrogen bond acceptor (HBA), resulting in a significant reduction in the melting point. DESs can be prepared easily by mixing non-toxic materials in specific molar ratios. Their ease of preparation allows the development of combinations with tunable physicochemical properties that can be tailored to specific applications [2–5]. By varying the HBD and/or HBA, in fact, it is possible to significantly alter the physicochemical properties of the obtained mixtures, such as hydrophobicity or hydrophilicity, density, viscosity, and melting point [6,7]. A comprehensive understanding of the formation mechanisms of these liquids and of the interactions

governing their composing units is essential for accurately predicting and elucidating their different physicochemical properties. In particular, the term "deep" refers to a significant deviation from ideal behavior observed in these mixtures: unlike ideal eutectics, DESs exhibit pronounced non-ideal interactions between the HBD and HBA, which result in a substantial lowering of the melting point compared to the expected values, leading to the formation of a stable liquid phase. In other words, DESs exhibit melting points that are lower than those expected in ideal eutectic mixtures [8–10]. With the growing interest in eutectic systems, in recent years, several systems were proposed wherein the HBA is a tetrabutylammonium (TBA)-based salt, paired either with simple halides, such as bromide, chloride, or iodide [11–14] or with more complex anions, such as acetate [15]. These quaternary ammonium salts have been mixed with various HBDs, such as organic acids [15–18], alcohols [19,20], and imidazole-based molecules [21,22]. Many of the systems proposed thus far were based on TBA bromide or chloride: in these samples, it has been observed that the anions act as an HBA. For the present work, we investigated a more complex anion, specifically, trifluoromethanesulfonate ($CF_3SO_3^-$, TFO). Interest in this ionic pair arises from the fact that TBATFO salt is widely used in various electrochemical applications: TBATFO has been proposed as an additive for Mg-ion batteries, with the aim of increasing the dissolution of magnesium salts and enhancing charge transport efficiency [23]. Furthermore, investigating the role of TFO as a hydrogen bond donor (HBD) is valuable due to its asymmetric structure, which features two potential hydrogen-bond-accepting sites: the SO_3 and CF_3 groups. For this research, TBATFO was mixed with two different dicarboxylic acids, namely, fumaric (FUM) and maleic acid (MAL). The organic acids used (Figure S1) can be considered structural isomers: trans and cis, respectively.

In our previous study [24], we showed that two choline-based ionic liquids, one with the monoanionic form of maleic acid and the other with the monoanionic form of fumaric acid, have significantly different melting points. Specifically, choline-H-maleate melts at 25 °C while choline-H-fumarate melts at 80 °C. The cis conformation of H-maleate allows for the formation of intramolecular H-bonds, which is not possible in the trans conformer.

The presence of intramolecular hydrogen bonds in choline-H-maleate, combined with the distinct structural arrangement of the components in the bulk phases of the two ionic liquids, significantly influenced their physicochemical properties, as indicated by the considerable difference in their melting points. The goal of the present study is to investigate two low-melting-point systems composed of TBATFO in combination with fumaric or maleic acid, with the aim of determining whether the distinct cis (fumaric) or trans (maleic) configurations of the HBD can influence the physicochemical properties of these systems. To achieve these aims, we determined the phase diagram of both systems using differential scanning calorimetry (DSC) measurements. Structural investigation was carried out by means of infrared spectroscopy measurements in the mid-IR and far-IR regions: the latter has been shown in several studies to be particularly useful for examining intermolecular interactions such as hydrogen bonding and dispersion forces [25]. Additionally, the systems were characterized, by means of density functional theory (DFT) calculations, to enhance the interpretation of the experimental results.

2. Results and Discussion

2.1. Determination of Eutectic Compositions by DSC Measurement

The range of compositions that correspond to the formation of the eutectic components was investigated by means of DSC measurements.

Figure 1 reports the DSC measurements of the pure components and of the two series of mixtures between TBATFO and fumaric acid (panel a) or maleic acid (panel b). Pure TBATFO undergoes a melting process around 115 °C. A visual inspection indicated that this sample was certainly solid at around 80 °C. Therefore, the three additional endothermic processes that were present around 13, 50, and 56 °C should be ascribed to solid–solid phase transitions [19]. Fumaric (maleic) acid exhibited a structured endothermic peak between 190 and 215 °C (130 and 190 °C), which was due to the superposition of melting

and the subsequent decomposition (as obtained from the TGA measurements in Figure S2).

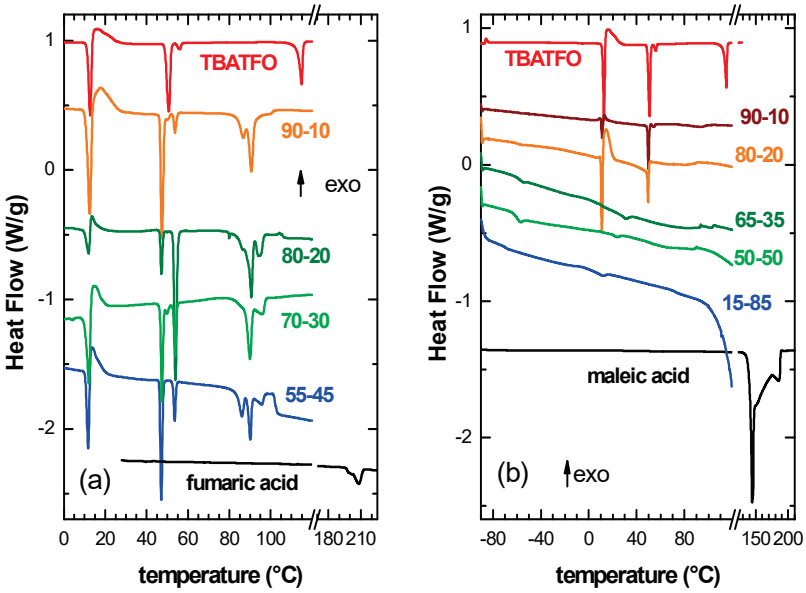

Figure 1. Differential scanning calorimetry measurements collected during heating for TBATFO, fumaric acid (panel (**a**)), maleic acid (panel (**b**)), and their mixtures.

All the mixtures with fumaric acid displayed endothermic peaks below 60 °C, which, in pure TBATFO, can be attributed to solid–solid transition, even though they are displaced by a few degrees to lower temperature values. None of them show the melting process of TBATFO, but rather a multistep melting process between 85 and 100 °C. The eutectic composition is supposed to display a single melting process, and the composition that most resembled this definition was that composed of a molar ratio of 90% TBATFO and 10% fumaric acid (Figure 1a).

Concerning the mixtures with maleic acid (Figure 1b), pure MAL exhibited a broad and complex endothermic peak between 150 and 200 °C, which included the melting process and partial decomposition (TGA measurements, Figure S2). The mixtures with compositions of 90-10 and 80-20 show DSC traces similar to that of pure TBATFO, even though one cannot see the melting process of the ionic salt, but instead show a broad endothermic peak at around 80 °C. The compositions between 65-35 and 15-85 display two broad endothermic processes, one around 40 °C and the other around 80 °C. It must be noted that these samples, when heated to around 90 °C, still present a solid component inside an apparent liquid phase. The lowest temperature at which the high-temperature features are present in the mixtures with maleic acid is around 70 °C for the 50-50 sample. In the following sections, we will indicate this sample as the eutectic of the system TBATFO–maleic acid for simplicity, even though it seems not to be a homogeneous phase. This is clearly different from the mixtures of TBATFO with fumaric acid, which yielded liquid phases when heated to around 90 °C.

In previous papers, the eutectic composition could be analytically determined according to previous knowledge of melting temperatures and the enthalpy of the pure components [19,26]. However, in the present case, the determination of the melting points and enthalpies of both acids is particularly difficult because the melting process is superimposed on the decomposition. Therefore, we only base our present study on a purely experimental approach.

2.2. Interaction Models by Quantum Chemistry

The interactions between the ionic couple and the acids were investigated computationally by means of DFT calculations. Initially, we simulated the pure components, then

we extended the calculations to some of the mixtures. The optimized structure of TBATFO is shown in Figure 2. Based on the previous literature about its crystal structure [27,28], the structural features of fumaric acid (FUM) were studied by considering four centrosymmetric oligomers: the dimer (Figure 3a), tetramer (Figure S3b), hexamer (Figure S3c), and octamer (Figure S3d), all with C_{2h} symmetry, and by considering an open dimeric structure (Figure 3b) where the monomers are connected by a single OH···O hydrogen bond. The self-aggregation of maleic acid (MAL) was considered for the trimer, the hexamer, and the nonamer depicted in Figure 4a–c, respectively: they are fragments of chains where the maleic acid molecules are connected by single hydrogen bonds and each chain is aligned to form planar layers, as reported after previous crystallographic measurements [29,30].

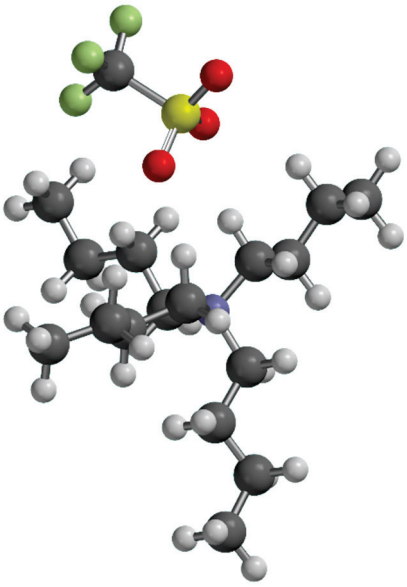

Figure 2. The TBATFO ion pair structure. White spheres are oxygen atoms, grey ones are carbon atoms, the yellow one is sulfur and the green ones are fluorine.

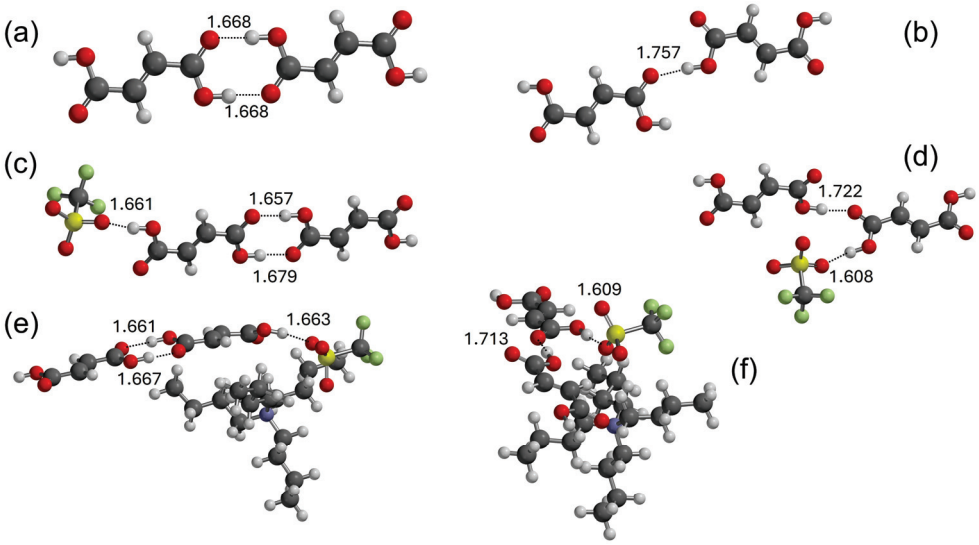

Figure 3. Structures of the closed and open dimers of FUM ((**a**) and (**b**), respectively), along with their complexes with TFO (**c**,**d**) and with TBATFO (**e**,**f**) (distances in Å). The color code is the same used in Figure 2.

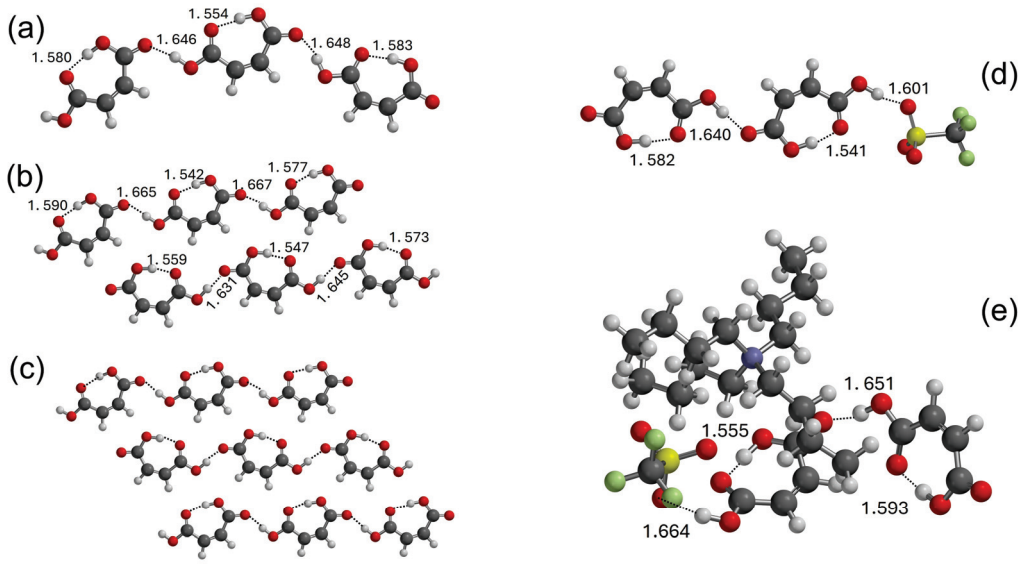

Figure 4. Structures of the oligomers of the MAL trimer (**a**), hexamer (**b**), and nonamer (**c**), and the TFO-MAL (**d**) and TBATFO-MAL (**e**) complexes (distances in Å). The color code is the same used in Figure 2.

Some models have been proposed herein to evaluate the intermolecular interactions between different components in the mixtures. The interactions between TFO and acid have been described as a series of complexes wherein TFO is coupled with a single FUM (Figure S4a) or MAL (Figure S5a) molecule, with a dimer of FUM (Figure 3c,d) or MAL (Figure 4d) and with a trimer of FUM (Figure S4b or Figure S5b). The progressive increase in the number of acid molecules in such complexes allows us to investigate how the interaction of the negative head of the anion TFO with carboxylic acid is affected by the clustering of the acid component. The role of the cation in the aggregation process is then considered by adding a TBA cation to each TFO: the geometry of some TBA-TFO-acid complexes has been optimized and their structures are depicted in Figure 3e,f (TBA-TFO-FUM) and Figure 4e (TBA-TFO-MAL).

The crystal structure of FUM has been the subject of various studies [27,28]: the molecules are linked together by infinite chains of double hydrogen bonds between carboxylic groups, as found in several organic acids, and form planar layers. The structural features of a single layer can be obtained, starting from the centrosymmetric dimer reproduced in Figure 3a, where the equivalent hydrogen bonds show O· · ·H distances of 1.668 Å. The double HB chain observed in the crystal has been simulated here by C_{2h} symmetry oligomers of progressively larger size: the tetramer, the hexamer, and the octamer, as shown in Figure S3. It is interesting to note that the H· · ·O hydrogen bond distances of the central pair of molecules (1.666 Å for the tetramer, 1.666 Å for the hexamer, and 1.667 Å for the octamer) are very close to the value calculated for the dimer. This suggests that the centrosymmetric dimer, although very small, could provide a reasonable description of the structural features of the fumaric acid molecules in the crystal and of its vibrational spectrum. Therefore, notwithstanding the fact that we calculated the vibrational frequencies for all the oligomers proposed here, we employed the infrared spectrum calculated for the dimer to simulate the vibrational features of FUM before mixing. The picture could be more complicated upon the addition of a second component: the interaction with TFO anions could lead to the fragmentation of the double HB chains and to local structures where the acid molecules are still coupled, but by only one hydrogen bond. The second dimer reproduced in Figure 3b has, therefore, been proposed to consider this possible interaction pattern. The hydrogen bond in this open structure dimer is definitely weaker, as suggested by the longer O· · ·H distance (1.757 Å). The AIM analysis of the two dimeric structures is summarized in Table 1: at the bond's critical point (r_c), localized on the O· · ·H distance,

the values of the electron density, $\rho(r_c)$ and its Laplacian, $\nabla^2(r_c)$, confirm that molecules form stronger HBs when they are paired through cyclic structures.

Table 1. Hydrogen bond geometry (Å) and topological analysis (a.u.), obtained at the ωB97XD/6-311++G** level for the different interaction models of FUM.

	FUM Figure 3a		**FUM Figure 3b**	
Hydrogen bond	OH· · ·O=C		OH· · ·O=C	
r ()	1.668		1.757	
$\rho(r_c)$ (a.u.)	0.0470		0.0354	
∇^2 (r_c) (a.u.)	0.1415		0.1273	
	TFO + FUM Figure 3c		**TFO + FUM Figure 3d**	
Hydrogen bond	OH· · ·O=C	OH· · ·O=S	OH· · ·O=C	OH· · ·O=S
r ()	1.657/1.679	1.661	1.722	1.608
$\rho(r_c)$ (a.u.)	0.0483/0.0456	0.0451	0.0391	0.0523
∇^2 (r_c) (a.u.)	0.1427/0.1385	0.1502	0.1337	0.1595
	TBA + TFO + FUM Figure 3e		**TBA + TFO + FUM Figure 3f**	
Hydrogen bond	OH· · ·O=C	OH· · ·O=S	OH· · ·O=C	OH· · ·O=S
r ()	1.661/1.667	1.663	1.713	1.601
$\rho(r_c)$ (a.u.)	0.0477/0.0470	0.0455	0.0401	0.0535
∇^2 (r_c) (a.u.)	0.1419/0.1406	0.1488	0.1361	0.1629

The addition of TBATFO leads to the establishment of interactions of FUM molecules with TFO anions and TBA cations that could give different coupling geometries. Among several interaction structures, we first focused on those involving only the TFO anion by considering the fact that the negative head of the triflate anion, SO_3^-, is a hydrogen bond acceptor that is stronger than the CF_3 group [19]. The Fukui analysis carried out on TFO confirms that the nucleophilicity of oxygen atoms (+0.237 a.u.) is higher than that of fluorine atoms (+0.081 a.u.). Starting from the complex 1:1 (Figure S4a), we considered further models where TFO interacts with a FUM dimer (Figure 3c) and with a FUM trimer (Figure S4b), and we analyzed how the OH· · ·OS hydrogen bond is affected by the model size. It is interesting to observe that the O· · ·. . .OS distance is substantially unchanged in the three models (1.656 Å for the 1:1 complex, 1.661 Å for the 1:2 complex, and 1.660 Å for the 1:3 complex). For the 1:2 complex, we considered two different interaction couplings: the structure reproduced in Figure 3c takes into account a situation in which TFO interacts with FUM molecules that are still part of a double HB chain, whereas the structure in Figure 3d is a complex between the open dimer of FUM and TFO, and describes a local arrangement where anions interact with acid molecules coming from the breaking of the double HB bond chain. The hydrogen bond distances shown in Figure 3 and the AIM analysis reported in Table 1 suggest that the interaction with the TFO anion does not drastically change the geometry and the electronic features of the double HB coupling (Figure 3c), whereas it does produce a small strengthening of the single hydrogen bond (Figure 3d). In addition, the interaction with TFO seems to be stronger when the acid molecules break the double hydrogen bond chain, as suggested by the OH· · ·OS distance (1.661 Å for the structure in Figure 3c and 1.608 Å for the structure in Figure 3d).

The AIM analysis results are consistent with the natural bond orbital (NBO) analysis, which is summarized in Table S1. This was carried out by considering all possible interactions between filled donor and empty acceptor NBOs and estimating their energy importance using second-order perturbation theory. The charge transfer between the lone pair (LP) of oxygen (proton acceptor) and the antibonds of the proton donor (σ*OH) correlates with the strength of the OH· · ·O interaction and can provide a description of the contribution of hydrogen bonding to the total energy of the complex. Our NBO analysis

proves that the oxygen lone pair donation to the anti-bonding orbital of the OH bond (LP(O) → σ*OH) gives strong stabilization (24.6 kcal mol^{-1}) to the centrosymmetric FUM dimer; its interaction with TFO produces appreciable asymmetry on two hydrogen bonds, whereas the LP(O) donation of TFO toward the antibonding of the OH bond of FUM gives lower stabilization (12.6 kcal mol^{-1}). The opening of the ring structure of the FUM dimer lowers the stabilization energy of only one LP(O) → σ*OH donation of the complex (10.5 kcal mol^{-1}), whereas the interaction with TFO strengthens the FUM pairing, as predicted by AIM analysis.

Finally, the role of the cation was evaluated by adding a TBA cation in both the complexes with TFO; the optimized structures are reproduced in Figure 3e,f. The examination of their geometries indicates that the positive nitrogen of TBA is oriented toward the negative head of the triflate anion, SO_3^-, suggesting that coupling between cations and anions is driven, undoubtedly, by electrostatic forces, although this orientation suggests the possibility of aligning some CH groups of TBA to make CH· · ·O and CH· · ·F interactions (the shortest CH···O and CH···F distances are 2.275 Å and 2.578 Å, respectively, for the structure in Figure 3e and 2.233 Å and 2.709 Å, respectively, for the structure in Figure 3f). The main result is that the presence of the TBA cation does not significantly change the strength and geometry of the interaction of acid molecules with themselves and with TFO anions.

If the *trans* configuration of the C=C bond of fumaric acid allows it to form infinite chains of double HBs, the *cis* isomer, i.e., maleic acid, forms infinite chains of single HBs, as one of the protons is involved in an intramolecular hydrogen bond [29,30]. Each molecule shows an intramolecular hydrogen bond (an O· · · O distance equal to 2.50 Å [30]), due to the closing of a six-membered ring, and is linked to the neighboring molecules by longer intermolecular hydrogen bonds (an O· · · O distance equal to 2.64 Å [30]) to form linear chains; each row is interlinked by weaker hydrogen bonds (an O· · · O distance equal to 2.98 Å [29]) to form layers. A simulation of MAL molecules in the crystal environment is suggested by the complexes shown in Figure 4. The trimer of Figure 4a can be considered a fragment of a linear chain in which the molecules are connected by a single intermolecular HB, whereas the hexamer of Figure 4b and the nonamer of Figure 4c are models that show how the molecules can align their chains to form planar layers. The hexamer demonstrates how two linear chains are aligned in the crystal, and the nonamer shows the orientation of three linear chains. The geometries of all the oligomers have been optimized by assuming planar structures. An analysis of the O· · ·O distances calculated for the largest cluster, the nonamer, confirms the presence of an intermolecular hydrogen bond along the linear chains (average value of 2.581 Å) and the O· · ·O and CH· · ·O contacts between chains (2.986 Å and 2.338 Å), along with the intramolecular hydrogen bond for each molecule (an O· · ·O distance equal to 2.581 Å). All the values are in substantial agreement with the experimental values [29,30]. The values of the OH· · ·O hydrogen bond distances calculated for the oligomers herein proposed are shown in Figure 3a,b for the trimer and hexamer, respectively, and in Figure S5 for the nonamer. The nature of the interactions between MAL molecules in the planar layers has been evaluated using the NCI approach, and the RDG isosurface is reproduced in Figure S6. The blue spikes localized in the OH· · ·O region correspond to hydrogen bonding interactions and confirm the presence of intramolecular HBs and intermolecular HBs, which link the molecules in linear chains. The green surface localized in the region between the chains suggests that the association of chains to form layers is largely driven by CH· · ·O interactions. The scatter plot using promolecular density, reproduced in Figure S7a, shows spikes with large negative values (−0.06 a.u.) that indicate the presence of strong hydrogen bonding in the MAL nonamer, along with appreciable van der Waals contributions. A comparison with the RDG scatter plot of the FUM octamer depicted in Figure S7b shows a negative spike at values higher than −0.06 a.u. because FUM does not show the strong intramolecular hydrogen bond of MAL, whereas the green spike is barely pronounced.

As observed with the FUM-based mixtures, the addition of TBATFO to maleic acid can lead to the breaking of the intermolecular HB network and to the formation of SO· · ·HO interactions with the SO_3^- groups. Following the procedure adopted for FUM, we investigated three complexes in which TFO interacts with one MAL molecule (Figure S8a), a MAL dimer (Figure 4d), and a MAL trimer, as shown in Figure S8b. Since the structural features of the complexes are not drastically dependent on the size of the model, we discuss the interaction of TFO with MAL by adopting the complex depicted in Figure 4d, where a maleic acid molecule is paired by an HB with TFO and a second acid molecule. The strength of the intermolecular interactions was once again analyzed using AIM calculations, and the results are reported in Table 2. The electron density features and intermolecular distances indicate that the intramolecular hydrogen bond is stronger than the intermolecular hydrogen bond, both before and after the interaction with TFO. This result is in agreement with the NBO analysis reported in Table S2, where we can observe the largest LP(O) → σ*OH donation from the OH bonds involved in intramolecular hydrogen bonds. Consistently, the RDG scatter plot of the complex of TFO with the MAL dimer (Figure S7c) shows that there are still spikes at low values that are close to those observed for the MAL nonamer, which are caused by the presence of strong intramolecular hydrogen bonding. In addition, the AIM analysis could suggest that MAL forms a hydrogen bond with the TFO anions that is slightly stronger than those formed with the acid molecules; however, the presence of the TBA cation, simulated by the complex depicted in Figure 4e, gives O· · ·O very similar intermolecular distances as TFO-MAL and MAL-MAL. Apart from this small effect, the presence of the TBA cation does not profoundly change the structural features of the complex of TFO with MAL that is considered in Figure 4d, as already observed in the complexes with FUM. Based on these considerations, in the following section, we will discuss the infrared spectra of the mixtures by analyzing the theoretical spectra calculated for those complexes with TFO without including the TBA cation.

Table 2. Hydrogen bond geometry (Å) and topological analysis (a.u.) obtained at the ωB97XD/6-311++G** level for the different interaction models of MAL.

		MAL Figure 4c	
Hydrogen bond	OH· · ·O=C intra	OH· · ·O=C inter	OH· · ·O=S
r (Å)	1.572 [a]	1.648/1.646	
$\rho(r_c)$ (a.u.)	0.0583 [a]	0.0441/0.0446	
$\nabla^2(r_c)$ (a.u.)	0.1600 [a]	0.1400/0.1426	
		TFO + MAL Figure 4d	
r (Å)	1.541/1.582	1.640	1.601
$\rho(r_c)$ (a.u.)	0.0676/0.0608	0.0495	0.0529
$\nabla^2(r_c)$ (a.u.)	0.1658/0.1622	0.14832	0.1604
		TBA + TFO + MAL Figure 4e	
r (Å)	1.555/1.593	1.651	1.664
$\rho(r_c)$ (a.u.)	0.0653/0.0588	0.0475	0.0469
$\nabla^2(r_c)$ (a.u.)	0.1642/0.1616	0.1472	0.144

[a] average value.

2.3. Interaction Between the Components by Computed and Experimental Infrared Spectra

In this section, the spectra measured for the starting materials and the mixtures will be compared and the changes observed upon mixing will be discussed, with the aim of investigating how the different components interact in the mixtures. The main absorptions have been assigned on the basis of the spectra calculated for the molecular models at the ωB97X-D/6-311++G** level, which are described in the previous section.

Starting the discussion with the TBATFO-FUM mixtures, we compare the infrared spectra in Figure 5 that were calculated for the models to simulate the pure components and mixtures. For TBATFO, we assume the ion pair to be a reasonable model for the pure compound, whereas, for FUM, we consider the smallest oligomer between the various clusters proposed (Figure 3a) to be a valid model for simulating the spectrum of pure FUM. The infrared spectra of oligomers are compared in Figure S9, and they show that the absorption bands do not change appreciably along with the size of the oligomer. The spectrum of the mixtures has been simulated by the TFO-FUM complexes, in which a TFO anion interacts with a closed FUM dimer (Figure 3c) or with an open FUM dimer (Figure 3d). The presence of TBA cations has been taken into account for each TFO-FUM complex and the infrared spectra have been calculated for the TBA-TFO-FUM complexes depicted in Figure S10 in the Supplementary Materials. Since the spectral changes are localized mainly on the bands of FUM and TFO components and are only marginally on those of TBA, in Figure 5, we depict the spectra of the TFO-FUM complexes without the TBA cation and we show the assignment of the main bands.

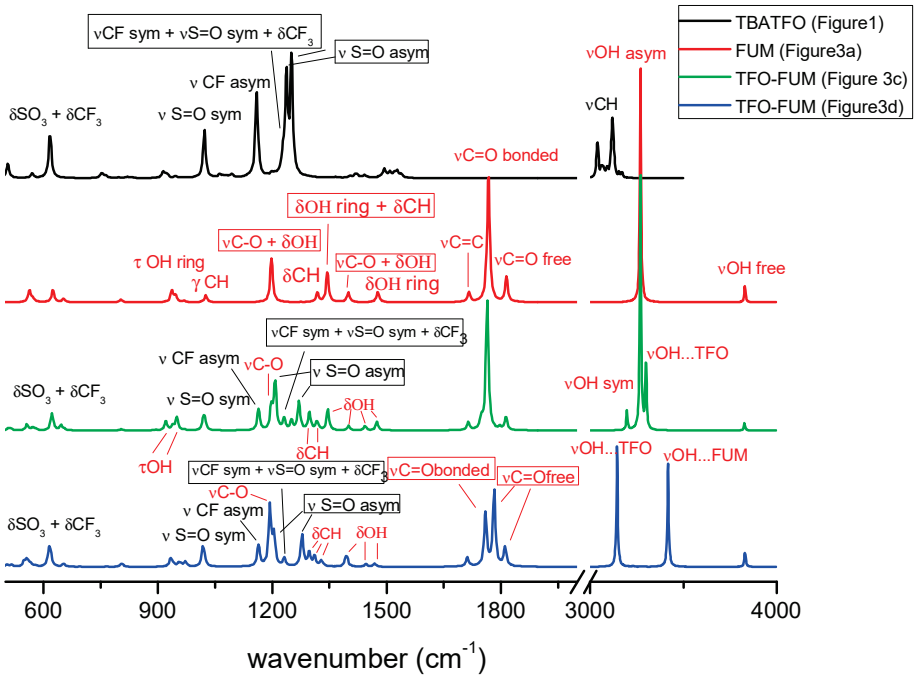

Figure 5. Infrared spectra calculated for the TBATFO ion pair (Figure 1), the FUM dimer (Figure 3a), and the TFO-FUM complexes shown in Figure 3c,d.

In the high-frequency region, we expected the OH stretching vibrations of FUM to be significantly perturbed upon mixing. The centrosymmetric dimer shows a single absorption, i.e., the asymmetric stretching mode of the OH groups involved in the HB cyclic structure; the interaction with TFO causes a lowering of the local symmetry of the dimer, and new bands are observed. In particular, when TFO interacts with a double-hydrogen-bonded fumaric dimer, as occurs in the complex depicted in Figure 3c, we would expect to observe the OH symmetric stretching mode, although at a low intensity, and the stretching of the OH group bonded to TFO. However, the spectrum depicted in Figure 5 indicates that its frequency is not too far from that of the OH asymmetric stretching, which is in agreement with the geometry of the complex where the FUM-FUM and FUM-TFO hydrogen bonds show very close distances. In contrast, when the double HB chain of FUM is broken and FUM can form a single HB with TFO and FUM, as in the complex shown in Figure 3d, the OH stretching vibrations are well separated and we can predict two absorptions: at a lower frequency, we expect the stretching of the OH group bonded to

TFO, while at a higher frequency, we expect that of the OH group bonded to the second FUM molecule.

Figure 6 shows the experimental infrared spectra that were measured for pure components and mixtures at different molar ratios. The line shape of the high-frequency region is very complex and shows a series of absorptions below 3000 cm^{-1}, a large band ranging from ≈3000 cm^{-1} to ≈3400 cm^{-1}, and a fairly sharp peak at 3080 cm^{-1} (Figure 6b). The congestion of the bands in this region reflects the complicated underlying interactions and phenomena involving the OH group [31]. In addition, inhomogeneous broadening can be the result of the presence of different dimeric structures [32]. Although the CH stretching absorptions are predicted to be very weak according to our DFT calculations, in agreement with the spectra measured for FUM isolated in a solid nitrogen matrix [33], the sharp absorption at 3080 cm^{-1} that was measured in the IR spectrum of solid FUM is present, with a very similar line shape that is also in the Raman spectrum [34]; therefore, it can be assigned to the CH stretching mode. The stretching modes of the OH groups of FUM molecules were hydrogen-bonded in a crystal state and are responsible for the remaining and complex series of broad absorptions. The isomerism by proton transfer expected for FUM crystals could explain the presence of OH stretching absorptions below 3000 cm^{-1} [31]. The spectral pattern is deeply changed by adding TBATFO: the complex series of absorptions below 3000 cm^{-1} disappears, and all the mixtures show only quite large absorption at about 3180 cm^{-1}, with an intensity that progressively increases with FUM concentration. This blue shift of OH stretching is consistent with the theoretical spectra of the TFO-FUM complex, where the double HB of the acid molecules is broken and the OH vibration moves at a higher frequency. The CH stretching modes of TBA give a series of strong and sharp absorption values below 3000 cm^{-1}; however, it is very hard to appreciate changes in this region by comparing the spectra of pure TBATFO and its mixtures.

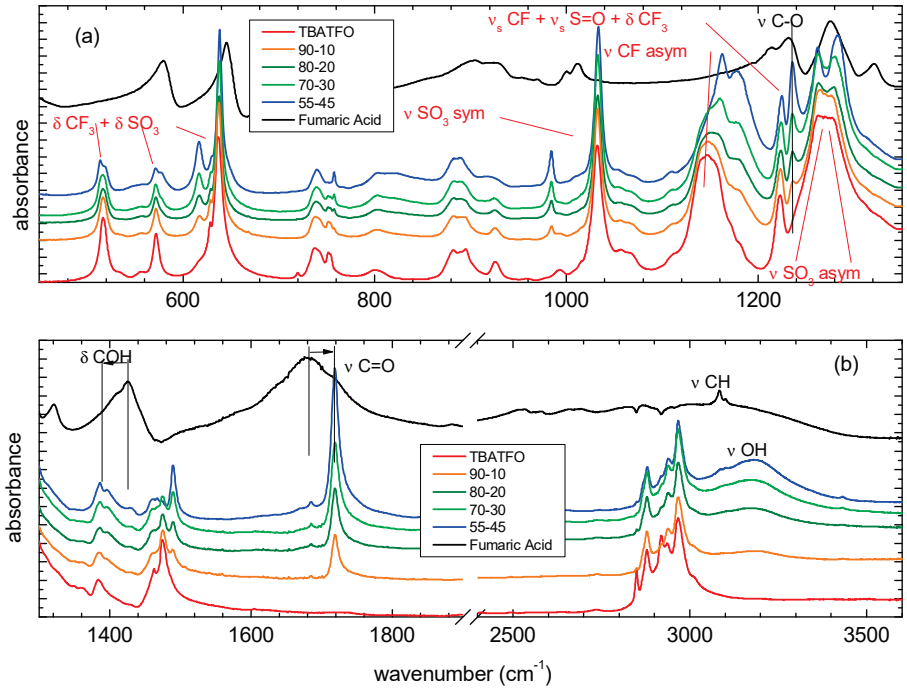

Figure 6. Infrared spectra of TBATFO, fumaric acid, and their mixtures in various compositions in the frequency ranges of 420–1300 cm^{-1} (panel (**a**)) and 1300–3600 cm^{-1} (panel (**b**)).

More interestingly, we observe marked differences in the medium-frequency region, as depicted in Figure 6. The C=O stretching mode of the carboxylic group gives a very strong and large absorption in the spectrum of solid FUM, with maximum absorption at about 1680 cm^{-1} and a very weak shoulder at 1720 cm^{-1} (Figure 6b). The line shape

changes markedly after adding the second component: by comparing the mixtures at different TBATFO:FUM molar ratios, we observe a sharp absorption at 1718 cm^{-1} and a second small peak at 1685 cm^{-1}. Such a weak absorption is found in the Raman spectra as a strong peak at 1687 cm^{-1} [34]; therefore, it can be assigned to the C=C stretching vibration. The changes observed for the C=O stretching bands suggest that the FUM molecules in the mixtures could be involved in interactions with TFO by OH· · ·O=S bonds and simultaneously with FUM by a double HB, as in the complex shown in Figure 3c, or by a single HB, as in the complex shown in Figure 3d. The DFT results indicate that the opening of the ring HB dimeric structure of FUM gives a blue shift to the C=O stretching absorptions, which is in agreement with the spectra measured for the mixtures. Other vibrational modes of the carboxylic group that can be perturbed by the HB are the OH bending (δCOH), the CO stretching (νCO), and the CO torsion (τCO) modes. In the region of the δCOH vibrations, the spectrum of solid FUM shows a strong absorption at 1425 cm^{-1}, with a shoulder at 1407 cm^{-1} and a weaker band at 1320 cm^{-1} (Figure 6). It is interesting to observe that the absorption at 1320 cm^{-1} disappears, whereas that at 1425 cm^{-1} drastically weakens when the second component is added to FUM and a new band appears at about 1400 cm^{-1}. Our interaction models predict a series of vibrational modes involving the OH and CH bending contributions in this region, which are appreciably coupled with each other and give spectral patterns that are different for the various interaction models. The spectral changes observed for these bands are highly indicative of the fact that the interaction of FUM with TFO undoubtedly involves the OH group, forming hydrogen bonding. In addition, the redshifts observed for these absorptions, along with the blueshifts measured for the OH and C=O stretching bands, are consistent with the fact that the dimerization of acid is depressed by adding TBATFO.

In Figure 6a, we compare the spectra in the medium-frequency region where the absorptions of the triflate ion are expected. The stretching modes of the SO_3^- and CF_3 groups give indications as to the nature and strength of the interactions with FUM: the antisymmetric SO stretching (νS=O asym), double-degenerated in the isolated triflate anion, is split into two bands when SO_3^- interacts with TBA or with FUM since the C_{3v} local symmetry of the SO_3 group is lowered; the width of the splitting may be related to the strength of the interaction. As predicted by the DFT calculations, the TBA cation has a low-density charge, and coupling with TFO involves the whole SO_3^- group and causes weak asymmetry. The band that is measured for pure TBATFO is, therefore, quite large, with splitting estimated to be about 10 cm^{-1}. In contrast, when TBA is coupled with high-density charge cations, such as lithium, the splitting is definitely larger (about 100 cm^{-1}) [35]. The band continues to be split (1264 and 1283 cm^{-1}) in the presence of FUM (Figure 6a); the width of the splitting is increased compared to that of pure TBATFO, but it is lower than those predicted from our interaction models, which are significantly more marked (65 cm^{-1} for the complex of Figure 3c, and 74 cm^{-1} for the complex of Figure 3d). This can be explained by considering the fact that the interaction models are static and the intermolecular interaction is described by an extreme localization of the OH· · ·OS hydrogen bond, without any dynamic effect. This suggests that there are interactions between TFO and FUM, but their strength is overestimated by our models. It is interesting to observe that, as for the SO_3^- group, the asymmetric stretching of the CF_3 group (νCF asym) also shows quite a large absorption at 1147 cm^{-1}, suggesting a tendency to split the mode into two components; the splitting is clearly better resolved in those mixtures where two spectral components are measured at 1161 and 1177 cm^{-1}. In addition, we note that this band moves from 1147 cm^{-1} in TBATFO to a higher frequency upon mixing, suggesting that the interactions of TFO with FUM could involve the group of SO_3 through the OH· · ·O(S) hydrogen bond, as well as the group of CF_3 through CF· · ·H interactions. The symmetric S=O stretching (νS=O sym) yields strong and sharp absorption at 1033 cm^{-1} in TBATFO and its mixtures at all FUM concentrations; similarly, the sharp peak at 1225 cm^{-1}, assigned to a complex vibration involving the symmetric stretching of CF_3 and SO_3 and the bending of CF_3, is found to be practically unchanged before and after mixing.

The bending modes of SO_3 and CF_3 are strongly coupled and give sharp absorptions at 637, 572, and 514 cm^{-1}, being substantially unchanged by mixing.

In addition, the spectra of the mixtures show an additional and sharp absorption at 1238 cm^{-1}, also observed before mixing in the FUM solid spectrum. The DFT calculations suggest assignment to some vibration involving νC-O, δCCH, and δCOH contributions. A similar assignment may be proposed for the strong and large absorption observed in the solid FUM spectrum at 1275 cm^{-1}, although it is hard to appreciate the presence of this band in the mixtures since their spectra show strong νS=O asym absorption at the same frequency.

Another interesting part of the infrared spectra is seen below 200 cm^{-1}, where the vibrational modes of the hydrogen bonding and the dispersion forces are present [25,36]. Indeed, the occurrence of such absorption peaks has largely been investigated in ionic liquids, especially the protic ones, where the occurrence of HB is witnessed by the presence of absorption peaks around 50 cm^{-1} for the bending mode of HB and at around 120–150 cm^{-1} for the stretching vibration. In between these two peaks, additional absorption is usually found, centered around 70–80 cm^{-1}, due to the dispersion forces among the tails of the ion chains [25,36,37]. In the case of the mixtures with fumaric acid (see Figure 7), no clear evidence of the bending and stretching bonds of HB is visible. This fact is not intuitive, but it can be explained in the pure acid as being due to the static nature of the interaction. Possibly, in the mixtures, the directionality of the HBs is not sufficient to give strong hydrogen stretching modes.

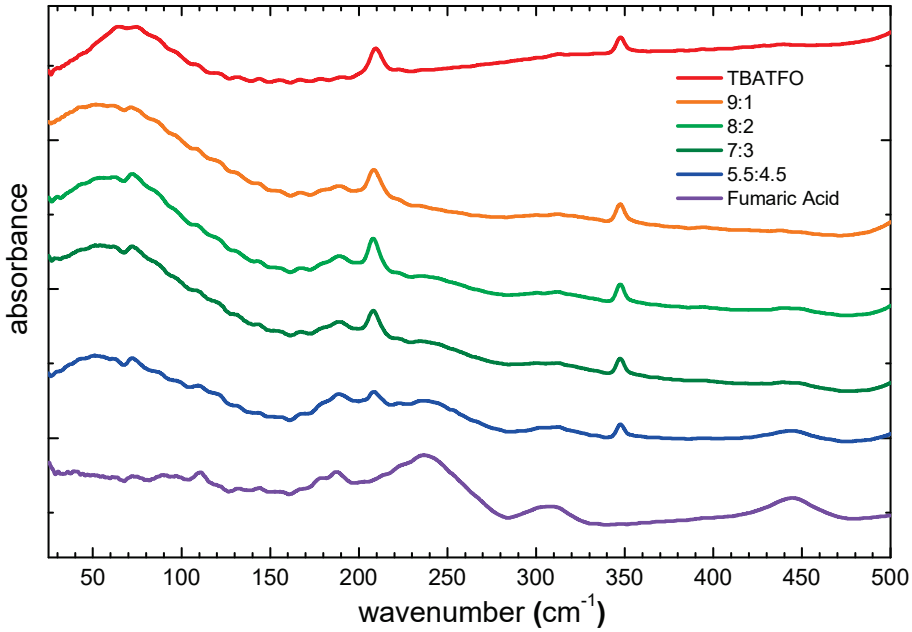

Figure 7. Far-infrared spectra at room temperature of TBATFO, fumaric acid, and their mixtures in various compositions.

In pure TBATFO a well-developed peak around 70 cm^{-1} is observable. Due to the position of its maximum, this can be assigned to the dispersion forces among the alkyl chains of the cation. This peak shifts to a lower frequency (about 60 cm^{-1}) in all mixtures, suggesting a reduction in the interactions among the cations. This can be explained by a possible reduction in the interactions between cations as they become more spatially separated due to the addition of the acid.

2.4. TBATFO-MAL Mixtures

Figure 8 compares the infrared spectra calculated for the TBATFO ion pair (Figure 1), the MAL nonamer (Figure 4c), and the complex between TFO and two MAL molecules (Figure 4, panels d, and shows the assignment of the main bands. Regarding the mixtures

with FUM, we report the spectra of TFO-MAL complexes without the TBA cation: the spectra of the TFO_MAL and TBA-TFO-MAL are compared in Figure S11. In the oligomer that is used to simulate pure maleic acid, the MAL nonamer, the high-frequency region shows an intense CH stretching band and a series of absorptions, due to the vibrations of the OH groups involved in intra- and intermolecular hydrogen bonds. The vibrations at a lower frequency are mainly localized on the OH groups that are intramolecularly hydrogen-bonded, whereas the remaining absorptions are due to the collective stretching vibrations of OH groups that are intramolecularly and intermolecularly hydrogen-bonded.

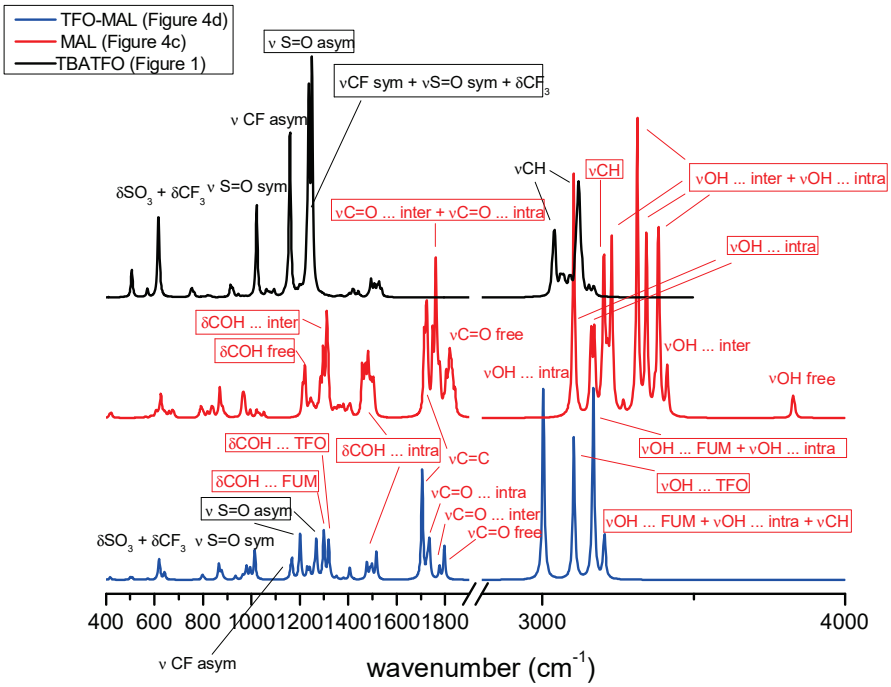

Figure 8. Infrared spectra calculated for the TBATFO ion pair (Figure 1), the MAL nonamer (Figure 4c), and the TFO-MAL complex (Figure 4d).

Figure 9 shows the spectra measured for the pure components and their mixtures. The sharp peak at 3058 cm^{-1} can be assigned to the CH stretching mode, in agreement with the same band that was observed for solid FUM at 3080 cm^{-1}. As for FUM, the OH stretching region of solid MAL also has a complex line shape, with broad absorption between 3100 and 2800 cm^{-1} and a series of bands below 3000 cm^{-1}. The line shape of the OH stretching absorption of the crystalline MAL has been investigated in a previous study using molecular dynamics, considering the proton transfer by intramolecular as well as intermolecular HBs, and absorptions were predicted up to about 2300 cm^{-1} [38]. As for the FUM-based mixtures, the OH stretching absorptions of MAL change upon mixing, although less visibly. While the addition of TBATFO to FUM produces the appearance of a very distinct peak at a higher frequency and the disappearance of absorptions below 3000 cm^{-1}, the mixing of TBATFO and MAL gives only a small shoulder at a higher frequency of the main peak of OH adsorption, which is indicative of the breaking of the HB network present in the crystalline MAL, but this does not markedly change the spectral region below 3000 cm^{-1}, where weak absorptions continue to be observed. This is indicative of the fact that if, in the FUM-based mixtures, the presence of TFO contributes to breaking the strong double HB that pairs the molecules in the FUM crystal to form weaker FUM· · ·TFO interactions, the MAL· · ·TFO interactions formed in the base MAL mixtures may instead have a strength quite similar to that of MAL· · ·MAL HB, as suggested by the structures discussed in the previous sections; therefore, they produce less marked spectral changes. In addition, the MAL nonamer structure reveals that the intermolecular HB network produces

strong coupling between the vibrations of all the OH groups; such a coupling weakens when the HB chains are broken to form interactions with TFO, and the vibrations of OH groups, both intramolecularly and intermolecularly HB-bonded, are better separated. This means that in the mixtures, the acid molecules continue to have intramolecular HBs and to show absorptions below 3000 cm^{-1}.

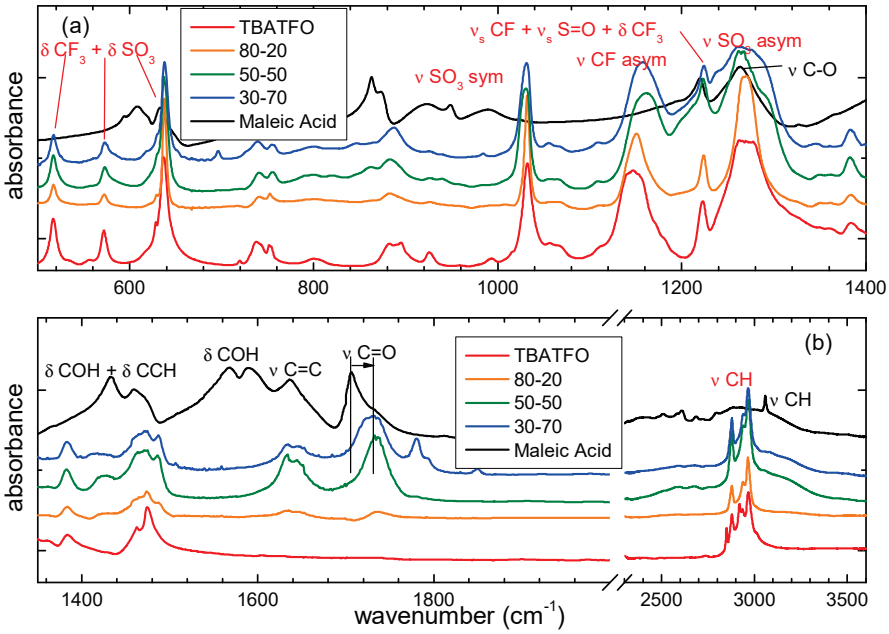

Figure 9. Infrared spectra of TBATFO, maleic acid, and their mixtures at various compositions in the frequency ranges of 500–1400 cm^{-1} (panel (**a**)) and 1350–3600 cm^{-1} (panel (**b**)).

In the medium-frequency region (Figure 9b), we observe some bands of MAL that are substantially unchanged upon mixing, as with the absorption at 1634 cm^{-1}, assigned to the C=C stretching mode, and other bands that move their absorption frequency when TBATFO is added. Two bands are expected for the C=O stretching modes: one is related to the C=O group, intermolecularly HB-bonded, measured at 1706 cm^{-1} in the solid MAL and blue-shifted to 1734 cm^{-1} by adding the second component, as already observed for FUM-based mixtures; the second one, related to the C=O group that is intramolecularly HB-bonded, measured at 1722 cm^{-1} for MAL isolated in a nitrogen matrix [33], could tentatively be assigned to the shoulder at 1734 cm^{-1} that we find again at the same frequency in the mixtures.

At a lower frequency, our interaction models predict a series of vibrational modes involving CCH bending (δCCH), COH bending (δCOH), and CO stretching (νCO): those vibrations with a large contribution of δCOH are more affected by changes in the molecular environment. For example, the bands measured at 1590 and 1586 cm^{-1} in the spectrum of solid MAL can be assigned to vibrations that are mainly localized on the OH group bonded by intramolecular HBs. It is interesting to observe that the spectra of the mixtures do not show any absorption in this region, in agreement with the fact that the strength of intramolecular hydrogen bonding may change from the pure component to its mixtures. Our interaction models suggest that intramolecular HBs are stronger for the complexes MAL-TFO and MAL-TBATFO than for any MAL oligomer; the δCOH vibrations should, therefore, increase their frequencies upon mixing, and the appearance of a new absorption at 1645 cm^{-1} in the mixtures could be interpreted in these terms.

Looking at the absorptions of triflate anion in the mixtures (Figure 9), we find the same spectral pattern being observed for the FUM-based mixtures. The symmetric stretching of the SO_3^- groups (1030 cm^{-1}), the vibrational mode with a mixed contribution of symmetric νCF_3, νSO_3, and δCF_3 (1223 cm^{-1}), and the bending modes of CF_3 and SO_3 (638, 573, and

517 cm^{-1}) are found to be unchanged upon mixing. The antisymmetric νCF_3 and νSO_3 give quite broad absorptions in the MAL spectrum; while these bands are split in the mixtures with FUM, the splitting is not resolved in the mixtures with MAL. These spectral features indicate that the coordination of MAL to TFO causes an asymmetry of the SO_3^- and CF_3 groups that is less marked than that seen due to the coordination of FUM, suggesting that the MAL and TFO components have a spatial distribution driven by weakly directional interactions. Lastly, the spectra of the MAL-based mixtures show additional absorptions at 1293 and 1204 cm^{-1}; they appear as shoulders of the main absorptions and are associated with vibrations involving C-O stretching. In the same spectral region, the spectrum of solid MAL shows two absorptions at 1223 and 1264 cm^{-1}.

The far-infrared spectra of selected mixtures containing maleic acid are depicted in Figure 10 at 160 and 320 K, together with the spectra of the pure components. Maleic acid presents an absorption peak around 170 cm^{-1}, while TBATFO has its peak centered around 70 cm^{-1}, due to the dispersion forces. At low temperatures, it becomes more structured, and a very evident structure around 80 cm^{-1} develops. In the mixtures, contrary to what has been observed in the mixtures with fumaric acid (Figure 7), one can see a broad band similar to that of TBATFO, without any evident frequency shift. This fact suggests a reduced variation of the dispersion forces in the mixtures with maleic acid. Interestingly, in the mixtures close to the eutectic one (30-70, 50-50, and 65-35), it is possible to observe the appearance of broad and poorly intense bands around 120 and 170 cm^{-1}, which, due to their wavenumber, could be ascribed to the stretching mode of hydrogen bonds. This can be explained by the fact that the maleic acid in the mixtures develops HBs with TFO.

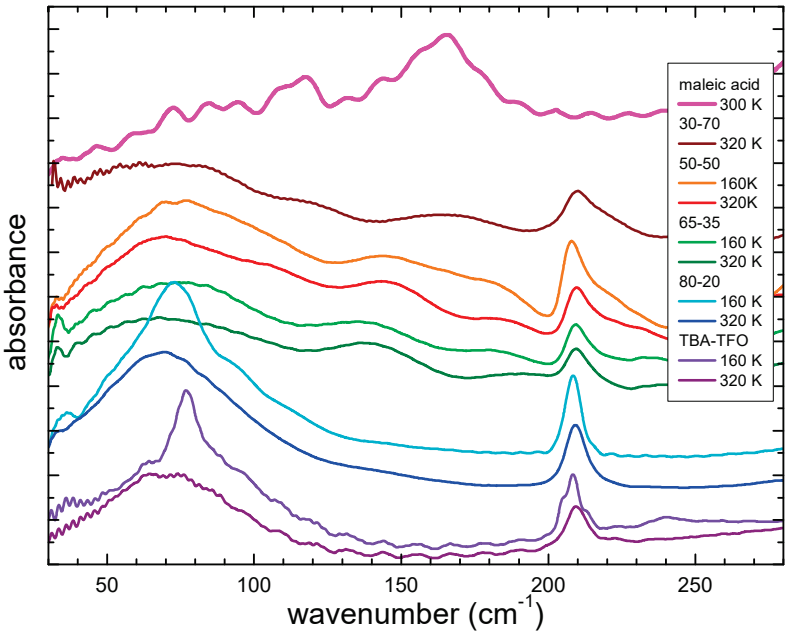

Figure 10. Far-infrared spectra at around room temperature and at 160 K for TBATFO, maleic acid, and their mixtures at various compositions.

To sum up, the mixtures of TBATFO with fumaric acid display more evident marks of the interaction between the ionic couple and the acid than those mixtures with maleic acid: the OH stretching bands are displaced toward the higher frequencies, as well as showing C=O stretching. The νS=O asym is split, due to the interaction with the acid, and the asymmetric stretching of the CF_3 group becomes broader. The vibrational modes of the carboxylic group, in particular δCOH, become shifted toward lower frequencies, due to the instauration of a different HB. In the far-infrared range, one observes a red shift of the peak, due to the dispersion forces between the alkyl chains. All these features are much less pronounced or are even absent in the mixtures with maleic acid.

This phenomenology can be explained by the fact that fumaric acid molecules have two possible sites for the formation of HB while, in maleic acid, one of the sites remains involved in intramolecular HBs, even after mixing. The interactions of fumaric acid with the ionic couple are stronger than those of maleic acid, leading to deeper changes in the mixtures with FUM. This picture is also consistent with the empirical observations of the appearance of the samples when heated to around 90 °C: while mixtures with FUM become liquid at high temperatures, the samples with MAL still retain a small fraction of solid component, as if the interactions among the components are not strong enough to create a homogeneous phase.

3. Materials and Methods

Tetrabutylammonium triflate (TBA-TFO), fumaric (FUM), and maleic acid (MAL), all with a purity of ≥99.0%, were purchased from Merck and were used without further purification. All components were solid at room temperature. The ionic solid and the acids were weighted in a proper molar ratio to obtain well-defined mixtures; typically, for each mixture, 2 g samples were prepared. The solid components were mixed by magnetic stirring at 80 °C for 1 h to obtain liquid phases. All samples were maintained in an inert argon atmosphere to avoid contamination from atmospheric air and water vapor. The compositions of the obtained mixtures will be indicated in the following section by their molar ratio. All mixtures were solid at room temperature.

To define the melting points of the pure components and of the mixtures, DSC measurements were conducted by means of a Star3 Mettler Toledo system, working down to −90 °C thanks to a Huber TC100 Crycooler. All measurements were performed on samples with a typical mass of 15-20 in a protective Ar flux of 40 mL/min, with a scanning rate of 5 °C/min.

Thermogravimetry measures were performed by means of a Setaram Setsys Evolution 1200 instrument with a temperature rate of 10 °C/min and a protective helium flux of 60 mL/min. A mass of about 10–20 mg was used for each sample.

Infrared absorbance spectra were collected in both the far- and mid-infrared range. The measurements in the wavenumber ranging between 30 and 680 cm^{-1} were collected at the AILES beamline of Synchrotron Soleil, by means of a IFS 125 HR spectrometer by Bruker (Billerica, MA, USA), a Si-coated mylar beamsplitter, and a bolometric detector. The temperature of the samples was varied by means of a Cryomec (Syracuse, NY, USA) pulse tube. The spectra in the wavenumber ranging between 450 and 6000 cm^{-1} were collected by means of an Agilent (Santa Clara, CA, USA) Cary 660 spectrometer, a DTGS detector, and a KBr beamsplitter. The temperature of the samples was modified by a Specac (Orpington, UK) Variable Temperature cell. For both types of measurements, the spectral resolution was fixed at 1 cm^{-1}, and 100 scans were mediated for each spectrum. The spectra of the solid starting materials and of the mixtures containing fumaric acid were collected, with the powders dispersed in KBr or polyethylene in a mass ratio of 1:100 for the mid- and far-infrared range, respectively. The mixtures containing maleic acid were heated at 80 °C, where they displayed a partial liquid phase, and were then placed between two optical diamond windows of vacuum-tight cells. In both ranges, the samples were kept in a vacuum during measurement to avoid contamination from atmospheric gases and water vapor.

To allow for the interpretation of the infrared spectra and to evaluate the ionic coupling geometry, the structures of the TBA-TFO ion pairs and fumaric and maleic acids, as well as some combinations of the ion pairs and the acids, were computationally investigated. All calculations were performed using the Gaussian16 computational package [39]. The structure of each molecular species was investigated using density functional theory (DFT) calculations with the hybrid ωB97X-D functional [40], which includes long-range exchange correction (denoted by X), as well as semiclassical London-dispersion correction (indicated by suffix-D), and employing the standard 6-311G++(d,p) basis set. The good reliability of such a functional in describing the structural aspects and electronic properties of several

liquids, considering non-covalent interactions, has been discussed in earlier reports [41]. The liquid environment was simulated by means of the polarized continuum model (PCM), using the parameters of 2-pentanone, which has a dielectric constant of 15 that is slightly higher than that typically found in ionic liquids [42,43]. IR spectra were obtained for each structure at the ωB97X-D/6-311++G** level, and vibrational assignment of the main absorption of each system was carried out on the basis of an analysis of the normal modes. To more deeply investigate the topological and energetic characteristics of the intermolecular interactions in each molecular complex, atoms in molecules (AIM) analysis was performed [44], employing the AIMAll software (Version 19.10.12) [45]. The nature of the interactions between components was investigated by analyzing the reduced-density gradient (RDG) [46] at low density, using the MultiWFN program [47]. Non-covalent interaction (NCI) analysis was carried out for the optimized clusters and the structures were visualized by the VMD program [48]. Fukui analysis [49] was carried out for each component to investigate the nucleophilicity and electrophilicity of the interacting groups.

4. Conclusions

The two isomers, fumaric and maleic acid, display different interactions with the ionic couple TBATFO. While mixtures with FUM give rise to an eutectic, mixtures with MAL retain a solid component, even at high temperatures. DFT computational investigation of the interaction suggests that TFO interacts more strongly with FUM, due to the availability of two sites for the formation of HB, while in MAL, one of the sites continues to be involved in intramolecular HBs. Infrared spectroscopy measurements support the stronger interaction of TBATFO with FUM; in the TBATFO-FUM mixtures, the SO_3 and CF_3 vibrational bands are split and displaced toward higher frequencies by the new HBs that form with the acid; in TBATFO-MAL mixtures, these bands are only slightly altered. In all cases, the OH bands of the acids are altered by HB interactions with the ionic couple. It is interesting to note that in the mixtures with FUM, the dispersion forces of the alkyl chains of the cation become weaker, while in the mixtures with MAL, one can observe weak bands due to the changes from the hydrogen bonds stretching.

Supplementary Materials: The following supporting information can be downloaded at: https://www.mdpi.com/article/10.3390/molecules29215093/s1, Figure S1: Chemical structures of TBA, TFO, fumaric and maleic acids; Figure S2: TGA and DTA curves of maleic (panel a) and fumaric acids (panel b); Figure S3: C_{2h} symmetry structures of dimer (a), tetramer (b), hexamer (c), and octamer (d) of fumaric acid, calculated at the ωB97X-D/6-311++G(d,p) level; Figure S4: Complexes of TFO with fumaric acid (a) and TFO with a trimer of fumaric acid (b) calculated at B97X-D/6-311++G(d,p) level (Distance in Å); Figure S5: Nonamer of maleic acid calculated at B97X-D/6-311++G(d,p) level (Distance in Å); Figure S6: NIC of nonamer of maleic acid (isosurface=0.5); Figure S7: Scatter plot using promolecular density for MAL nonamer (a), FUM octamer (b) and TFO-MAL complexes of Figure 4d (c); Figure S8. Complexes of TFO with maleic acid (a) and TFO with a trimer of maleic acid (b) calculated at B97X-D/6-311++G(d,p) level (Distances in Å); Figure S9: DFT infrared spectra of the C_{2h} symmetry oligomers of FUM; Figure S10: DFT infrared spectra for TFO+FUM dimer and the TBA+TFO+FUM dimer complexes; Figure S11: DFT infrared spectra for TFO+MAL dimer and the TBA+TFO+MAL dimer complexes. Table S1: Second order perturbation theory analysis of Fock matrix of FUM complexes in NBO basis; Table S2: Second order perturbation theory analysis of Fock matrix of MAL complexes in NBO basis; Table S3: wb97xd/6-311++G** energy (Hartree) within the PCM method (Solvent = 2-pentanone).

Author Contributions: Conceptualization, A.P. and F.R.; methodology, A.P. and F.R.; validation, S.D.M., F.T., O.P. and A.P.; investigation, S.D.M., F.T., O.P., A.P., J.-B.B. and P.R.; resources, A.P., J.-B.B. and P.R.; data curation, S.D.M., F.T. and O.P.; writing—original draft preparation, F.R., A.P., S.D.M. and O.P. All authors have read and agreed to the published version of the manuscript.

Funding: This research received no external funding.

Institutional Review Board Statement: Not applicable.

Informed Consent Statement: Not applicable.

Data Availability Statement: Data are contained within the article or the Supplementary Materials.

Acknowledgments: The authors wish to thank Synchrotron Soleil for the provision of synchrotron radiation during beamtimes 20231279 and 20230398. S.D.M and F.R. acknowledge Nico Sanna for free access to DIBAF HPC resources at the University of Tuscia in Viterbo, Italy.

Conflicts of Interest: The authors declare no conflicts of interest.

References

1. Hansen, B.B.; Spittle, S.; Chen, B.; Poe, D.; Zhang, Y.; Klein, J.M.; Horton, A.; Adhikari, L.; Zelovich, T.; Doherty, B.W.; et al. Deep Eutectic Solvents: A Review of Fundamentals and Applications. *Chem. Rev.* **2021**, *121*, 1232–1285. [CrossRef] [PubMed]
2. Huang, C.; Chen, X.; Wei, C.; Wang, H.; Gao, H. Deep Eutectic Solvents as Active Pharmaceutical Ingredient Delivery Systems in the Treatment of Metabolic-Related Diseases. *Front. Pharmacol.* **2021**, *12*, 794939. [CrossRef] [PubMed]
3. Nahar, Y.; Thickett, S.C. Greener, Faster, Stronger: The Benefits of Deep Eutectic Solvents in Polymer and Material Science. *Polymers* **2021**, *13*, 447. [CrossRef]
4. Gurkan, B.; Squire, H.; Pentzer, E. Metal-Free Deep Eutectic Solvents: Preparation, Physical Properties, and Significance. *J. Phys. Chem. Lett.* **2019**, *10*, 7956–7964. [CrossRef]
5. Nejeretti, S.; Antenucci, A.; Pontremoli, C.; Gontrani, L.; Barbero, N.; Carbone, M.; Bonomo, M. Critical assessment of the sustainability of deep eutectic solvents: A case study on six choline chloride-based mixtures. *ACS Omega* **2022**, *7*, 47449–47461. [CrossRef]
6. Ijardar, S.P.; Singh, V.; Gardas, R.L. Revisiting the Physicochemical Properties and Applications of Deep Eutectic Solvents. *Molecules* **2022**, *27*, 1368. [CrossRef]
7. Kianpoor, A.; Sadeghi, R. Novel Acidic Deep Eutectic Solvents: Synthesis, Phase Diagram, Thermal Behavior, Physicochemical Properties and Applications. *J. Iran. Chem. Soc.* **2024**, *21*, 2385–2399. [CrossRef]
8. Pedro, S.N.; Freire, C.S.R.; Silvestre, A.J.D.; Freire, M.G. Deep Eutectic Solvents and Pharmaceuticals. *Encyclopedia* **2021**, *1*, 942–963. [CrossRef]
9. Zhu, Z.; Li, H.; Zhang, M.; Yang, H. Deep Eutectic Solvents as Non-Traditionally Multifunctional Media for the Desulfurization Process of Fuel Oil. *Phys. Chem. Chem. Phys.* **2021**, *23*, 785–805. [CrossRef]
10. Schaffer, N.; Abranches, D.O.; Silva, L.P.; Martins, M.A.R.; Carvalho, P.J.; Russina, O.; Triolo, A.; Paccou, L.; Guinet, Y.; Hedoux, A.; et al. Non-Ideality in Thymol + Menthol Type V Deep Eutectic Solvents. *ACS Sustain. Chem. Eng.* **2021**, *9*, 2203–2211. [CrossRef]
11. Nowosielski, B.; Jamrógiewicz, M.; Cichowska-Kopczyńska, I.; Warmińska, D. Comprehensive Evaluation of Physical Properties and Carbon Dioxide Capacities of New 2-(Butylamino)ethanol-Based Deep Eutectic Solvents. *Pure Appl. Chem.* **2024**, 0228. [CrossRef]
12. Shu, C.; Sun, T. Extractive Desulfurization of Gasoline with Tetrabutyl Ammonium Chloride-Based Deep Eutectic Solvents. *Sep. Sci. Technol.* **2016**, *51*, 1336–1343. [CrossRef]
13. Shokri, S.; Ebrahimi, N.; Sadeghi, R. Combined Experimental and Computational Investigation of the Tetrabutylammonium Bromide-Carboxylic Acid-Based Deep Eutectic Solvents. *J. Mol. Graph. Model.* **2024**, *131*, 108805. [CrossRef]
14. Lu, B.; Chu, F.; Zhao, G.; Zhu, Z.; Su, T.; Yang, K.; Chen, C.; Lu, H. Modulating H-Bond Strength to Enhance Reactivity for Efficient Synthesis of Cyclic Carbonates with Tetrabutylammonium Iodide-Based Deep Eutectic Solvents. *ChemistrySelect* **2024**, *9*, e202400330. [CrossRef]
15. Di Muzio, S.; Palumbo, O.; Trequattrini, F.; Paolone, A. Binary Mixtures of Choline Acetate and Tetrabutylammonium Acetate with Natural Organic Acids by Vibrational Spectroscopy and Molecular Dynamics Simulations. *J. Phys. Chem. B* **2024**, *128*, 857–870. [CrossRef]
16. Wu, H.; Shen, M.; Chen, X.; Yu, G.; Abdeltawab, A.A.; Yakout, S. New Absorbents for Hydrogen Sulfide: Deep Eutectic Solvents of Tetrabutylammonium Bromide/Carboxylic Acids and Choline Chloride/Carboxylic Acids. *Sep. Purif. Technol.* **2019**, *224*, 281–289. [CrossRef]
17. Shishov, A.; Makoś-Chełstowska, P.; Bulatov, A.; Andruch, V. Deep Eutectic Solvents or Eutectic Mixtures? Characterization of Tetrabutylammonium Bromide and Nonanoic Acid Mixtures. *J. Phys. Chem. B* **2022**, *126*, 3889–3896. [CrossRef]
18. Xu, G.; Shi, M.; Zhang, P.; Tu, Z.; Hu, X.; Zhang, X.; Wu, Y. Tuning the Composition of Deep Eutectic Solvents Consisting of Tetrabutylammonium Chloride and n-Decanoic Acid for Adjustable Separation of Ethylene and Ethane. *Sep. Purif. Technol.* **2022**, *298*, 121680. [CrossRef]
19. Di Muzio, S.; Trequattrini, F.; Palumbo, O.; Roy, P.; Brubach, J.-B.; Paolone, A. An Eutectic Mixture in the Tetrabutylammonium Bromide-Octanol System: Macroscopic and Microscopic Points of View. *ChemPhysChem* **2024**, *25*, e202400219. [CrossRef]
20. Abranches, D.O.; Martins, R.O.; Silva, L.P.; Martins, M.A.R.; Pinho, S.P.; Coutinho, J.A.P. Liquefying Compounds by Forming Deep Eutectic Solvents: A Case Study for Organic Acid and Alcohols. *J. Phys. Chem. B* **2020**, *124*, 4174–4184. [CrossRef]
21. Mohan, M.; Naik, P.K.; Banerjee, T.; Goud, V.V.; Paul, S. Solubility of Glucose in Tetrabutylammonium Bromide-Based Deep Eutectic Solvents: Experimental and Molecular Dynamic Simulations. *Fluid Phase Equilib.* **2017**, *448*, 168–177. [CrossRef]
22. Di Muzio, S.; Russina, O.; Mastrippolito, D.; Benassi, P.; Rossi, L.; Paolone, A.; Ramondo, F. Mixtures of Choline Chloride and Tetrabutylammonium Bromide with Imidazole as Examples of Deep Eutectic Solvents: Their Structure by Theoretical and Experimental Investigation. *J. Mol. Liq.* **2022**, *352*, 118427. [CrossRef]

23. Chinnadurai, D.; Li, Y.; Zhang, C.; Yang, G.; Lieu, W.Y.; Kumar, S.; Xing, Z.; Liu, W.; She, Z.W. Chloride-Free Electrolyte Based on Tetrabutylammonium Triflate Additive for Extended Anodic Stability in Magnesium Batteries. *Nano Lett.* **2023**, *23*, 11233–11242. [CrossRef] [PubMed]
24. Di Muzio, S.; Ramondo, F.; Gontrani, L.; Ferella, F.; Nardone, M.; Benassi, P. Choline Hydrogen Dicarboxylate Ionic Liquids by X-Ray Scattering, Vibrational Spectroscopy and Molecular Dynamics: H-Fumarate and H-Maleate and Their Conformations. *Molecules* **2020**, *25*, 4990. [CrossRef] [PubMed]
25. Fumino, K.; Fossog, V.; Stange, P.; Paschek, D.; Hempelmann, R.; Ludwig, R. Controlling the Subtle Energy Balance in Protic Ionic Liquids: Dispersion Forces Compete with Hydrogen Bonds. *Angew. Chem. Int. Ed.* **2015**, *54*, 2792–2795. [CrossRef]
26. Elliott, J.R.; Lira, C.T. *Introductory Chemical Engineering Thermodynamics*, 2nd ed.; Prentice Hall: Upper Saddle River, NJ, USA, 2012.
27. Roldan, L.G.; Rahl, F.J.; Patterson, A.R. Unit Cell and Space Group of Sublimed Fumaric Acid. *Acta Crystallogr.* **1965**, *19*, 1055. [CrossRef]
28. Bednowitz, A.L.; Post, B. Direct Determination of the Crystal Structure of β-Fumaric Acid. *Acta Crystallogr.* **1966**, *21*, 566–571. [CrossRef]
29. Shoat, M. The Crystal and Molecular Structure of Maleic Acid. *Acta Cryst.* **1952**, *5*, 763–768. [CrossRef]
30. James, M.N.G.; Williams, G.J.B. A Refinement of the Crystal Structure of Maleic Acid. *Acta Cryst.* **1974**, *B30*, 1249–1257. [CrossRef]
31. Dopieralski, P.; Panek, J.; Latajka, Z. First-Principles Investigation of Isomerization by Proton Transfer in Fumaric Acid Crystal. *J. Chem. Phys.* **2009**, *130*, 164517. [CrossRef]
32. Emmeluth, C.; Suhm, M.A. A Chemical Approach Towards the Spectroscopy of Carboxylic Acid Dimer Isomerism. *Phys. Chem. Chem. Phys.* **2003**, *5*, 3094–3099. [CrossRef]
33. Nikitin, T.; Lopes, S.; Fausto, R. Matrix Isolation Study of Fumaric and Maleic Acids in Solid Nitrogen. *J. Phys. Chem. A* **2022**, *126*, 4392–4412. [CrossRef] [PubMed]
34. Benítez, A.; Amaro-Gahete, J.; Esquivel, D.; Romero-Salguero, F.J.; Morales, J.; Caballero, A. MIL-88A Metal-Organic Framework as a Stable Sulfur-Host Cathode for Long-Cycle Li-S Batteries. *Nanomaterials* **2020**, *10*, 424. [CrossRef] [PubMed]
35. Frech, R.; Huang, W. Anion-Solvent and Anion-Cation Interactions in Lithium and Tetrabutylammonium Trifluoromethanesulfonate Solutions. *J. Sol. Chem.* **1994**, *23*, 469. [CrossRef]
36. Palumbo, O.; Cimini, A.; Trequattrini, F.; Brubach, J.-B.; Roy, P.; Paolone, A. The Infrared Spectra of Protic Ionic Liquids: Performances of Different Computational Models to Predict Hydrogen Bonds and Conformer Evolution. *Phys. Chem. Chem. Phys.* **2020**, *22*, 7497–7506. [CrossRef]
37. Palumbo, O.; Cimini, A.; Trequattrini, F.; Brubach, J.-B.; Roy, P.; Paolone, A. Evidence of the CH···O Hydrogen Bonding in Imidazolium-Based Ionic Liquids from Far-Infrared Spectroscopy Measurements and DFT Calculations. *Int. J. Mol. Sci.* **2021**, *22*, 6155. [CrossRef]
38. Dopieralski, P.D.; Latajka, Z.; Olovsson, I. Proton Transfer Dynamics in Crystalline Maleic Acid from Molecular Dynamics Calculations. *J. Chem. Theory Comput.* **2010**, *6*, 1455–1461. [CrossRef]
39. Frisch, M.J.; Trucks, G.W.; Schlegel, H.B.; Scuseria, G.E.; Robb, M.A.; Cheeseman, J.R.; Scalmani, G.; Barone, V.; Petersson, G.A.; Nakatsuji, H.; et al. *Gaussian 16, Revision C.01*; Gaussian, Inc.: Wallingford, CT, USA, 2016.
40. Chai, J.D.; Head-Gordon, M. Long-Range Corrected Hybrid Density Functionals with Damped Atom–Atom Dispersion Correction. *Phys. Chem. Chem. Phys.* **2008**, *10*, 6615–6620. [CrossRef]
41. Tsuzuki, S.; Uchimaru, T. Accuracy of Intermolecular Interaction Energies, Particularly Those of Hetero-Atom Containing Molecules Obtained by DFT Calculations with Grimme's D2, D3 and D3BJ Dispersion Corrections. *Phys. Chem. Chem. Phys.* **2020**, *22*, 22508–22519. [CrossRef]
42. Wakai, C.; Oleinikova, A.; Ott, M.; Weingartner, H. How Polar Are Ionic Liquids? Determination of the Static Dielectric Constant of an Imidazolium-Based Ionic Liquid by Microwave Dielectric Spectroscopy. *J. Phys. Chem. B* **2005**, *109*, 17028–17030. [CrossRef]
43. Singh, T.; Kumar, A. Static Dielectric Constant of Room Temperature Ionic Liquids: Internal Pressure and Cohesive Energy Density Approach. *J. Phys. Chem. B* **2008**, *112*, 12968–12972. [CrossRef] [PubMed]
44. Biegler-König, F.W.; Bader, R.F.W.; Tang, T.H. Calculation of the Average Properties of Atoms in Molecules. II. *J. Comput. Chem.* **1982**, *13*, 317–328. [CrossRef]
45. Todd, A.K. *AIMAll (Version 19.10.12)*; TK Gristmill Software: Overland Park, KS, USA, 2010.
46. Johnson, E.R.; Keinan, S.; Mori-Sanchez, P.; Contreras-Garcia, J.; Cohen, A.J.; Yang, W. Revealing Noncovalent Interactions. *J. Am. Chem. Soc.* **2010**, *132*, 6498–6506. [CrossRef] [PubMed]
47. Lu, T.; Chen, F. Multiwfn: A Multifunctional Wavefunction Analyzer. *J. Comput. Chem.* **2012**, *33*, 580–592. [CrossRef]
48. Humphrey, W.; Dalke, A.; Schulten, K. VMD: Visual Molecular Dynamics. *J. Mol. Graph. Model.* **1996**, *14*, 33–38. [CrossRef]
49. Parr, R.G.; Yang, W. Density Functional Approach to the Frontier-Electron Theory of Chemical Reactivity. *J. Am. Chem. Soc.* **1984**, *106*, 4049–4050. [CrossRef]

Disclaimer/Publisher's Note: The statements, opinions and data contained in all publications are solely those of the individual author(s) and contributor(s) and not of MDPI and/or the editor(s). MDPI and/or the editor(s) disclaim responsibility for any injury to people or property resulting from any ideas, methods, instructions or products referred to in the content.

molecules

MDPI

Article

Exploration of the Solubility Hyperspace of Selected Active Pharmaceutical Ingredients in Choline- and Betaine-Based Deep Eutectic Solvents: Machine Learning Modeling and Experimental Validation

Piotr Cysewski *, Tomasz Jeliński and Maciej Przybyłek

Department of Physical Chemistry, Pharmacy Faculty, Collegium Medicum of Bydgoszcz, Nicolaus Copernicus University in Toruń, Kurpińskiego 5, 85-096 Bydgoszcz, Poland; tomasz.jelinski@cm.umk.pl (T.J.); m.przybylek@cm.umk.pl (M.P.)
* Correspondence: piotr.cysewski@cm.umk.pl

Abstract: Deep eutectic solvents (DESs) are popular green media used for various industrial, pharmaceutical, and biomedical applications. However, the possible compositions of eutectic systems are so numerous that it is impossible to study all of them experimentally. To remedy this limitation, the solubility landscape of selected active pharmaceutical ingredients (APIs) in choline chloride- and betaine-based deep eutectic solvents was explored using theoretical models based on machine learning. The available solubility data for the selected APIs, comprising a total of 8014 data points, were collected for the available neat solvents, binary solvent mixtures, and DESs. This set was augmented with new measurements for the popular sulfa drugs in dry DESs. The descriptors used in the machine learning protocol were obtained from the σ-profiles of the considered molecules computed within the COSMO-RS framework. A combination of six sets of descriptors and 36 regressors were tested. Taking into account both accuracy and generalization, it was concluded that the best regressor is nuSVR regressor-based predictive models trained using the relative intermolecular interactions and a twelve-step averaged simplification of the relative σ-profiles.

Keywords: solubility; green solvents; DES; machine learning; COSMO-RS; σ-profiles; sulfonamides

1. Introduction

Active pharmaceutical ingredients (APIs) are the biologically active components of drugs that produce the intended therapeutic effects. They are the key compounds responsible for diagnosing, treating, or preventing diseases in patients [1,2]. The development and optimization of APIs are central to pharmaceutical research, as their chemical properties, such as stability, solubility, and bioavailability, significantly influence a drug's safety, efficacy, and dosage. Solubility is indeed one of the critical parameters in the development and characterization of active pharmaceutical ingredients [3–5], which affects the full lifecycle of a drug, starting with its synthesis and ending with its administration to the patient [6–8]. For an API to exert its pharmacological effect, it must first dissolve in bodily fluids, enabling its absorption into the bloodstream and subsequent distribution to target sites. Poor solubility can limit a drug's absorption, reducing its bioavailability [9,10] and potentially necessitating higher doses, which can lead to adverse effects or therapeutic failure [11–13]. Consequently, optimizing solubility is a fundamental aspect of drug formulation and delivery, ensuring that the APIs achieve the desired clinical outcomes while maintaining safety and efficacy profiles [14–17]. Following this line of thought, many techniques have been proposed to enhance the solubility of poorly dissolvable APIs [18–21]. While experimental measurements are necessary in order to obtain a full understanding of the behavior of a particular API in a selected solvent, the prediction of solubility is also extremely useful, particularly during the development of a drug [22–26]. If the number of potentially

useful solvents can be narrowed down by an initial predictive and screening stage, it is particularly valuable from an environmental perspective since it reduces the chemicals and energy needed for additional experiments. This approach fits perfectly with the concept of "green chemistry" [27,28], and it is no surprise that it was widely adopted [29–31]. The need for accurate, reliable, and relatively fast prediction methods focused the attention of researchers on neural networks and machine learning [32,33]. These techniques have already found numerous applications in the pharmaceutical domain, including solubility predictions [34–37].

The "green chemistry" approach mentioned above establishes not only the reduction of the environmental impact by limiting the number of laboratory operations, but also the introduction of more environmentally friendly solvents, the so-called "green solvents" [38,39]. These solvents, characterized by a lower toxicity and enhanced biodegradability, have quickly found widespread usage and become an alternative to the classical organic solvents [40,41]. Among the different solvents that offer environmentally safety, the deep eutectic solvents (DESs) are one of the most proficient dissolution media [42–45]. These systems can be broadly defined as mixtures of two or more components, usually containing a hydrogen bond acceptor (HBA) and a hydrogen bond donor (HBD), with the melting point of the mixture being lower than the melting points of the individual constituents [46,47]. DESs combine a high solubilizing potential for many APIs with desirable properties, which includes a high potential for tuning [48–52]. The pharmaceutical industry has embraced the beneficial effects of deep eutectic solvents, which have found numerous applications in this field [53–61].

The current study is focused on the development of an effective and reliable predictive model for solubility estimation of active pharmaceutical ingredients in deep eutectic solvents based on choline chloride and betaine. For this purpose, the available solubility data space of 15 selected APIs was explored and supplemented with new experimental data. The COSMO-RS approach was employed to obtain a set of descriptors that characterize the system under consideration and were used in the machine learning protocol. This procedure resulted in the obtainment of the predictive model used for the exploration of the solubility hyperspace of the selected APIs.

2. Results and Discussion

2.1. Experimental Extension of the Solubility Dataset in DESs

The solubility dataset of various active pharmaceutical ingredients in different DES formulations is quite extended. Our research group has contributed to these efforts by measuring the DES solubility of such APIs as ibuprofen and ketoprofen [62], ferulic acid [63], curcumin [64], caffeine [65], theobromine [66], theophylline [67], dapsone [68], edaravone [69], as well as various sulfonamides, including probenecid, sulfamethazine, sulfamethoxazole, sulfasalazine, sulfacetamide, and sulfanilamide [70]. The undisputed advantage of this particular dataset is its consistency, both in terms of the applied measurement protocol and the used eutectic formulations. Nonetheless, there is always room for extending the known solubility space of APIs by conducting new measurements, and such an extension, comprising 128 new data points, is provided here.

New solubility values were obtained for four sulfonamides, namely probenecid (PC), sulfamethazine (SMZ), sulfamethoxazole (SMA), and sulfasalazine (SSZ). Eight distinct eutectic compositions were used by combing two hydrogen bond acceptors (HBAs), i.e., choline chloride (ChCl) and betaine (BI) with four hydrogen bond donors (HBDs), namely 1,2-propanediol (P2D), ethylene glycol (ETG), diethylene glycol (DEG), and triethylene glycol (TEG). The HBA:HBD molar ratio was set to 1:2, and the solubilities were measured at four different temperatures, namely 25 °C, 30 °C, 35 °C, and 40 °C. The obtained solubility values are collected in Figure 1 and in Table S1 in the Supplementary Materials.

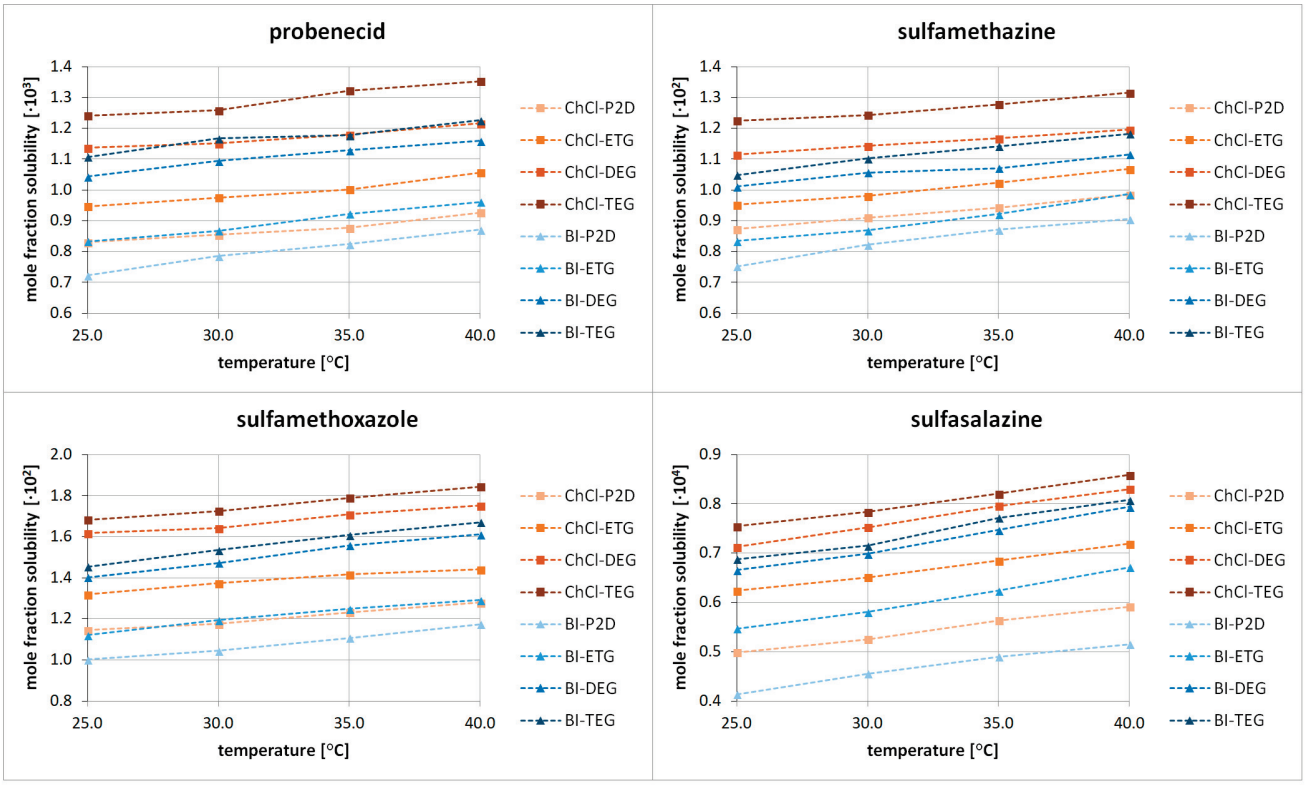

Figure 1. Mole fraction solubilities of four different sulfonamides in DESs composed of choline chloride (ChCl) or betaine (BI) with 1,2-propanediol (P2D), ethylene glycol (ETG), diethylene glycol (DEG), or triethylene glycol (TEG) in a 1:2 molar ratio at various temperatures.

The general picture emerging from the obtained results shows that sulfamethoxazole is characterized by the highest solubility in the studied eutectic formulations, followed closely by sulfamethazine. The solubility of probenecid is about one order of magnitude lower, while the solubility of sulfamethoxazole has been found to be the lowest among the studied sulfonamides. This general observation is in accordance with the solubilities of these compounds in the DES systems studied earlier (see Figure 2). When it comes to the efficiency of the studied eutectic systems, it can be concluded that eutectics utilizing choline chloride have a better overall performance than those with betaine. The influence of the type of HBD is also very important from the perspective of sulfonamide solubility. In all studied cases, triethylene glycol proved to be the most efficient, followed by diethylene glycol, ethylene glycol, and 1,2-propanediol. When considering all the possible systems, a general decreasing trend of solubility can be seen, namely the following: ChCl-TEG > ChCl-DEG > BI-TEG > BI-DEG > ChCl-ETG > ChCl-P2D > BI-ETG > BI-P2D. Also, quite obviously, the temperature increase promotes the solubility of all the sulfonamides. The mole fraction solubilities at 25 °C for the best-performing ChCl-TEG system were the following: x_{SMA} = 0.01681, x_{SMZ} = 0.01225, x_{PC} = 0.00124, and x_{SSZ} = 0.000075. The detailed results can be found in the Supplementary Materials.

The above results should be placed in the context of the solubility values previously obtained for various APIs. Such a comparison is provided in Figure 2, which shows the collection of solubilities of the considered solutes in different DES formulations. For clarity of presentation, only the results obtained for the 1:2 molar proportion of HBA:HBD are shown, and the temperature is restricted to 25 °C.

HBA	HBD	caffeine CAF	theobromine THB	theophylline THP	ferulic acid FA	edaravone EDA	ibuprofen IB	ketoprofen KP	curcumin CUR	dapsone DAP	probenecid PC	sulfacetamide SCM	sulfamethazine SMZ	sulfamethoxazole SMA	sulfanilamide SNM	sulfasalazine SSZ
choline chloride	P2D	-	-	-	−1.4	−1.2	−0.7	−1.4	-	−2.3	−3.1	-	−2.1	−1.9	-	−4.3
	ETG	-	-	-	−1.3	−0.8	−0.5	−1.3	-	−2.0	−3.0	-	−2.0	−1.9	-	−4.2
	DEG	-	-	-	−1.3	−0.7	−0.5	−1.2	-	−1.8	−2.9	-	−2.0	−1.8	-	−4.1
	TEG	-	-	-	−1.3	−0.7	−0.5	−1.2	-	−1.8	−2.9	-	−1.9	−1.8	-	−4.1
	B3D	-	-	-	−1.4	−1.1	−0.7	−1.3	-	−2.2	-	-	-	-	-	-
	GLY	−1.5	−2.9	−1.9	−1.3	−1.0	−0.5	−1.2	-	−2.1	−3.0	−0.8	−2.0	−1.8	−0.7	−4.3
	FRU	−2.0	−3.1	−2.2	-	-	-	-	-	-	−3.1	−0.8	−2.0	−1.9	−0.9	−4.2
	GLU	−1.8	−3.1	−2.2	-	-	-	-	-	-	−3.0	−0.8	−1.9	−1.9	−1.0	−4.2
	SOR	−1.7	−3.2	−2.0	-	-	-	-	-	-	−2.8	−1.0	−1.8	−1.7	−0.9	−4.1
	XYL	−1.7	−3.2	−2.1	-	-	-	-	-	-	−2.9	−1.0	−1.9	−1.8	−1.0	−4.2
	SUC	−2.1	−3.4	−2.4	-	-	-	-	-	-	−3.0	−0.8	−2.2	−1.8	−0.8	−4.1
	MAL	−2.1	−3.5	−2.5	-	-	-	-	-	-	−3.0	−1.0	−2.2	−1.9	−1.0	−4.1
betaine	ETG	-	-	-	−1.4	-	−0.6	−1.3	-	-	−3.1	-	−2.1	−2.0	-	−4.3
	P2D	-	-	-	−1.5	-	−0.7	−1.4	-	-	−3.1	-	−2.1	−2.0	-	−4.4
	DEG	-	-	-	−1.4	-	−0.6	−1.3	-	-	−3.0	-	−2.0	−1.9	-	−4.2
	TEG	-	-	-	−1.4	-	−0.5	−1.2	-	-	−3.0	-	−2.0	−1.8	-	−4.2
	B3D	-	-	-	−1.5	-	−0.7	−1.4	-	-	-	-	-	-	-	-
	GLY	-	-	-	−1.4	-	−0.5	−1.2	-	-	-	-	-	-	-	-

Figure 2. Collection of the API solubility values, expressed as the decadal logarithm of the mole fraction, in choline chloride and betaine deep eutectic solvents in ambient conditions. Newly measured values are marked with black borders. Only the 1:2 proportion of HBA and HBD was included. Colors map the span of solubility values. APIs include the following: caffeine (CAF), theobromine (THB), theophylline (THP), ferulic acid (FA), edaravone (EDA), ibuprofen (IB), ketoprofen (KP), curcumin (CUR), dapsone (DAP), probenecid (PC), sulfacetamide (SCM), sulfamethazine (SMZ), sulfamethoxazole (SMA), sulfanilamide (SNM), and sulfasalazine (SSZ). HBDs: 1,2-propanediol (P2D), ethylene glycol (ETG), diethylene glycol (DEG), triethylene glycol (TEG), 1,3-butanediol (B3D), glycerol (GLY), fructose (FRU), glucose (GLU), sorbitol (SOR), xylitol (XYL), sucrose (SUC), and maltose (MAL).

The coloring scheme allowed a direct comparison of the solubilities at room temperature. For example, SSZ has the lowest solubility among all the studied solids and augmenting the pool of data by adding the results corresponding to the new HBDs does not change this this observation. Similarly, the solubility of SMZ and SMA measured for the purpose of this project also are comparable with the previously published studies. Additionally, Figure 2 documents the significant differences in the absolute solubilities among the included APIs. This shows that DES formulations can often improve the solubility of solutes relative to other solvents, but at the same, they time can be restricted by the generally low solubility of a particular API. Despite this, deep eutectic solvents can be regarded as both universal and effective solvent systems, which has been documented numerous times. For example, in the case of caffeine [65], the optimal DES composition achieved a solubility equal to 165% of the best-performing organic solvent, i.e., DMSO. Similarly, dimethyl sulfoxide, which is the most effective classical solvent for many APIs, was outperformed by theophylline and theobromine [66,67]. In the case of dapsone [68] and edaravone [69], the best organic solvents, i.e., acetone and dichloromethane, respectively, were also inferior to many DES compositions. Of course, the results are not always that impressive, as it was evidenced in the case of COX inhibitors [62]. While for ibuprofen DESs indeed outperformed the best-performing chloroform, for ketoprofen, rather surprisingly, they could not compete with methanol. Of course, one has to keep in mind that many solvents, although offering a high dissolution potential for many solutes, are not pharma-

ceutically acceptable. This emphasizes the advantages of DESs, which can be applied in the pharmaceutical industry, even if they offer a slightly smaller solubilizing efficiency. Also worth mentioning is the often dramatic increase in API solubility when comparing DES to water. The most striking example is curcumin [64], for which the most efficient eutectic was characterized by a 12-thousand-times higher solubility when compared to an aqueous solution. The environmental and health safety impact, although sometimes disputed to some extent [71–74], is also an important factor that favors eutectics. Of course, the difference in performance observed among the deep eutectic solvents is related to their composition. The results obtained for various APIs in different eutectic systems point out some general trends. It seems that such hydrogen bond donors as glycerol, triethylene glycol, and diethylene glycol can be regarded as particularly efficient and worth consideration in future studies. Also, in terms of hydrogen bond acceptors, choline chloride performed generally better than betaine. The above considerations clearly show the importance of DESs as dissolution media, as well as their potential for tuning to specific applications.

2.2. COSMO-RS Derived Solubility

It is commonly accepted [75–77] that the COSMO-RS (Conductor-like Screening Model for Realistic Solvation) is a reliable tool for thermodynamic properties characteristics of bulk systems. Although formally this approach is restricted to fluid systems, it can be extended to treating the solid liquid equilibria (SLE) if the experimental or estimated values of fusion data are provided. This makes the COSMO-RS very attractive for solubility computations. Unfortunately, one encounters problems with this approach, seriously limiting its applicability even for qualitative solubility guesses. There are two major obstacles, originating both from the inaccuracy of the model and also from experimental limitations. A key experimental limitation inherent to all models based on the thermodynamic principles of the dissolution process is the inability to determine the fusion properties for compounds that degrade before reaching their melting point, sublime, or undergo polymorphic or pseudopolymorphic transformations [65,78–82]. Additionally, the COSMO-RS is incapable of predicting the solubility of certain APIs in many cases, for example benzenesulfonamide [83], ferulic acid [63], or caffeine [65]. In such cases, a high concentration of the solutes in the saturated solutions prevents them from using the fast iterative method as it fails to converge, incorrectly predicting the total miscibility. The application of the alternative approach relying on the solution of the full SLE problem is quite time-consuming, and even this type of computation fails occasionally since non-physical immiscible liquid–liquid phases are predicted. Fortunately, this is not a common situation for typical organic solvents although it is encountered for the saturated systems in DESs. Hence an alternative way to determine solubility such as the application of machine learning-based models employing the COSMO-RS descriptors becomes attractive [63,83].

To support the above statements, a graphical representation of the relationships between the computed and measured solubility values is provided in Figure 3. It is evident that the COSMO-RS is unable to predict solubility in many cases as the majority of the computed values suffer from serious inaccuracies especially in the DESs. Among the three studied subsets, the values for the solubility of the binary mixtures were computed with the highest accuracy, which might be attributed to the quite limited range of solvents used for the measurements. This is quite understandable, since a majority of the solvent pair combinations might lead to the immiscibility of the solvents, preventing solubility measurements.

Since the main focus of this paper is on DESs, a closer inspection of this particular subset might be interesting. In Figure 4, the computed and measured solubility data are plotted for pointing out some additional limitations of COSMO-RS applicability as the source of the estimated solubility data. The plots were overlaid with open circles and open triangles as markers of the data corresponding to the new sulfonamides' measurements and the most efficient HBD, respectively. It is quite surprising that the solubility computed for sulfasalazine (SSZ) and probenecid (PC) are very inaccurate. It happened that these

two compounds belong to a class of aromatic carboxylic acids and as such might interact with alcohols and polyalcohols such as DEG, and TEG. Interestingly, ibuprofen, ketoprofen, and ferulic acid also possess a carboxylic group but the deviation between the computed and measured values is significantly less prominent. This seems to be an interesting aspect worth subsequent study for further experimental and theoretical considerations.

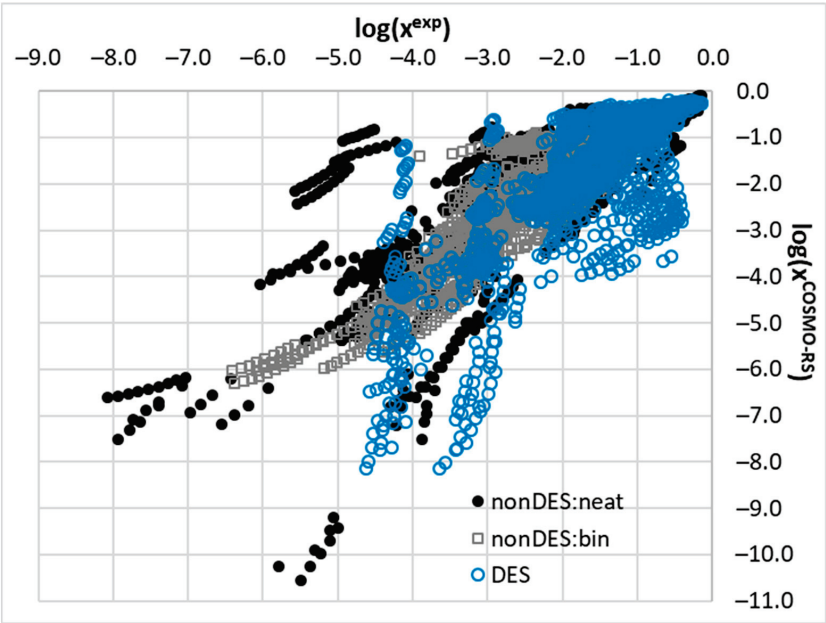

Figure 3. Relationship of experimental solubility and values computed using COSMO-RS for all the included APIs in neat solvents, binary solvent mixtures, and all studied DES systems. The temperature relationships and concentration dependencies of saturated solutions were taken into account.

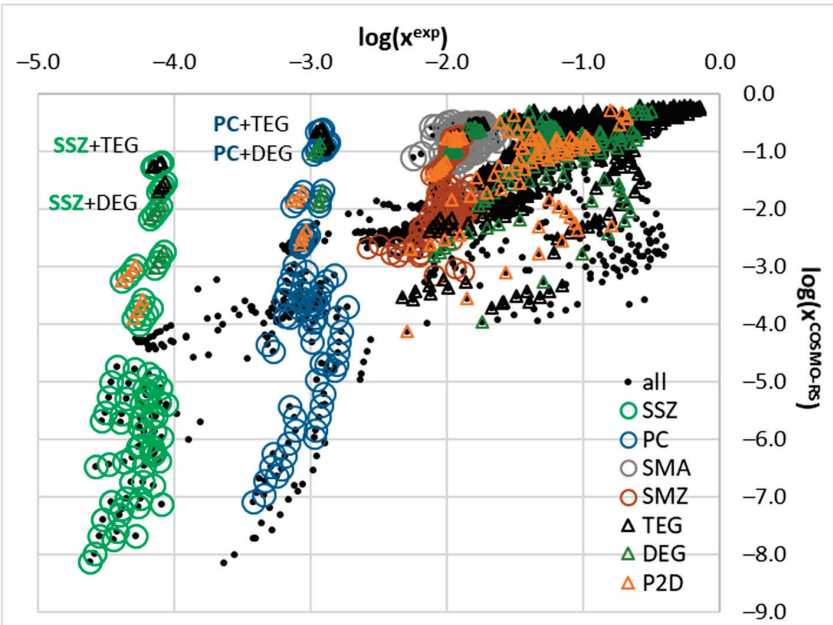

Figure 4. Relationship of experimental solubility and values computed using COSMO-RS for the subset of data presented in Figure 1, characterizing only APIs in DES systems. Open circles mark newly measured sulfonamides, and open triangles point out selected HBD counterparts of the studied DESs. For acronyms and their meanings, refer to Figure 1.

Being aware of the above-mentioned limitations of the COSMO-RS-derived solubility, the authors could not use such values as a direct source of the physical characteristics of the saturated systems as it is incapable of directing a proper selection of new solvents for screening purposes. However, the computed values often can be treated as a reliable source for the physicochemical characteristics of the saturated systems that enables the inclusion of the computed values, such as the valuable descriptor, for machine learning. The significant contribution of such computed solubility values to the model was already documented in our earlier works [62,63].

2.3. Machine Learning Solubility Model

The primary motivation for utilizing machine learning is to develop a robust model that can reliably estimate the solubility for systems not yet studied experimentally. This model is to be used as a guide for further experimental measurements and to reduce investigational efforts. By focusing on the most promising systems with a high likelihood of success, new measurements can be directed efficiently. This approach might include exploring not only different combinations of active pharmaceutical ingredients, hydrogen bond acceptors, and hydrogen bond donors but also varying proportions of deep eutectic solvent constituents and temperature dependencies. Expanding the dataset used for model development is therefore crucial for capturing the relevant factors that influence solute–solvent interactions.

In our previous studies, we examined several combinations of two different HBAs with a variety of HBDs. This led to the optimization of many practically useful solvents that meet the general requirements for pharmaceutical applications as effective dissolution media. However, despite considerable scientific effort, exploring the vast solvent hyperspace remains a challenging task, as only a small fraction of the potential combinations have been investigated. Figure 2 illustrates this limitation, showing that we covered less than 50% of the possible systems while using only a single ratio of HBA:HBD = 1:2. Clearly, exploring other solvent component ratios, even when restricting the investigation to the specified HBAs, HBDs, and water, significantly reduces the known region, leaving much more to be explored if necessary.

Hence, an extensive tuning of 36 regressor hyperparameters was conducted for each of the six descriptor sets to identify the models that not only best fit the experimental solubility data but also exhibited the highest predictive capability. In addition to the standard regularization parameters inherent to many regression models, a custom scoring function was employed. This function assessed the training subset's accuracy using few key metrics: the mean absolute error (MAE), as well as a penalty for the number of outliers and the number of formally not acceptable values as mentioned in the methodology Section 3.6. The final model's accuracy was evaluated using a test subset, consisting of 20% of the solubility data that were not included in the training process.

After an extensive non-linear models search, the process of regressor selection was undertaken for excluding those models that poorly represented the experimental solubility data. This resulted in the elimination of the most regressors, leaving only a few for further evaluation. The second selection criterion was an assessment of their overfitting and generalization capabilities, which was determined by comparing the accuracies of the test subsets. The models that exhibited a low mean absolute error on the training subset, but a high error on the test subset were deemed overfitted and were subsequently excluded. This group included the models generated using for example the MLPRegressor neural network, CatBoost, gradient boosting, and the XGBoost regressors. Following this analysis, the best model, demonstrating both high accuracy and strong predictive performance, was identified as the nu-Support Vector Regressor (nuSVR), a machine learning algorithm often used for regression tasks. This approach is based on the principles of Support Vector Machines (SVMs) and allows for the control of both the number of support vectors and the margin of tolerance through a parameter called "nu", which ranges from zero to one. This flexibility makes the nuSVR effective for modeling complex, non-linear relationships,

as it can balance model complexity and accuracy [84]. Recently, the nuSVR was applied successfully, predicting the solubility of aqueous solutions [85] and organic solvents [86].

Figures 5 and 6 present the final results of the nuSVR model. Instead of the mean absolute error, the mean absolute percentage error was used, as it provides a more intuitive measure of accuracy. A key observation from Figure 5 is that the choice of descriptor set has a significantly greater impact on the overall accuracy than the inclusion of the solubility data computed using the COSMO-RS. This finding is promising as it suggests that the model can be effectively applied to cases where fusion data are unavailable, thereby reducing the preparation time by omitting the solubility calculations. As illustrated in Figures 3 and 4, the computed solubility values for many of the saturated systems in this study exhibit significant inaccuracies, which does not help in model training. While the COSMO-RS has demonstrated satisfactory accuracy in previous studies, including those by our group, this is not generally the case for deep eutectic solvents. Thus, omitting the solubility values from the descriptor set is recommended based on our findings.

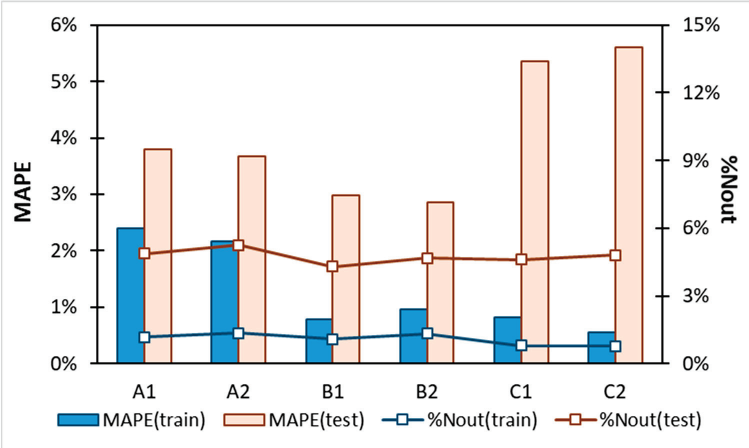

Figure 5. Comparison of nuSVR model's performance, the parameters of which were tuned on all six descriptors sets. Lines represent the percentage of outliers and bars stand for MAPE of train and test subsets.

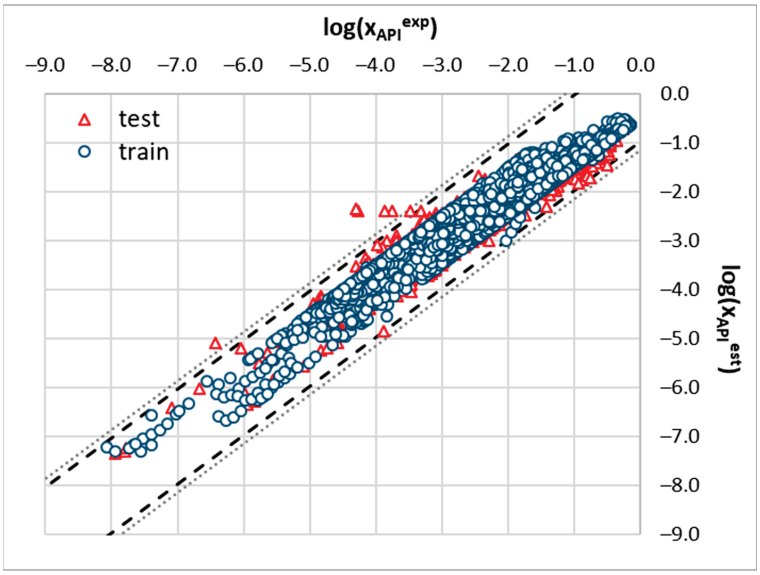

Figure 6. Correlation between experimental solubility values (N = 8014) and those computed using the NuSVR regressor trained on the B2 set of descriptors. Dotted and dashed lines represent values corresponding to three times the standard deviation computed for the whole dataset or test subset, respectively.

Another noteworthy conclusion drawn from Figure 5 is that the full σ-potential representation performed the worst among the tested cases. Conversely, the simplest representation using a six-step function failed to capture the essential information, making it suboptimal. The twelve-step averaging approach, which provides a balanced solute–solvent description while minimizing overfitting, is the most effective. Therefore, the descriptor set denoted as B2 is identified as the most efficient and accurate for the non-linear model training of the APIs' dissolution in DES and non-DES solvents.

3. Materials and Methods

3.1. Materials

Four sulfonamides were used to extend the solubility dataset of the APIs in the DESs. These were as follows: probenecid (PC, CAS: 57-66-9, MW = 285.36 g/mol), sulfamethazine (SMZ, CAS: 57-68-1, MW = 278.33 g/mol), sulfamethoxazole (SMA, CAS: 723-46-6, MW = 253.28 g/mol), and sulfasalazine (SSZ, CAS: 599-79-1, MW = 398.39 g/mol). The deep eutectic solvent formulations involved in this study consisted of a hydrogen bond acceptor (HBA) and a hydrogen bond donor (HBD). Two different HBAs were used, namely choline chloride (ChCl, CAS: 67-48-1) and betaine (BI, CAS: 107-43-7). As for the HBDs, they were represented by four polyols, i.e., ethylene glycol (ETG, CAS: 107-21-1), diethylene glycol (DEG, CAS: 111-46-6), triethylene glycol (TEG, CAS: 112-27-6), and 1,2-propanediol (P2D, CAS: 57-55-6). The above compounds, both the solutes and DES constituents, were supplied by Sigma Aldrich (Saint Louis, MO, USA) and had a purity of ≥99%. Additionally, methanol was used as a supplementary solvent, which was delivered by Avantor Performance Materials (Gliwice, Poland) with a purity of ≥99%. The supplied chemicals were used without any initial procedures, apart from the choline chloride, which was dried before use.

3.2. Solubility Determination

The solubility measurements were preceded by the determination of the calibration curves for the studied sulfonamides. Stock solutions of these compounds were prepared in methanol and subsequently diluted. The obtained series of solutions with decreasing concentrations were then measured spectrophotometrically using an A360 spectrophotometer from AOE Instruments (Shanghai, China) in the wavelength range of 200 nm to 500 nm. Their characteristic wavelengths were determined, and the corresponding absorbance values were plotted against the concentrations of the solutions. Three separate curves were prepared, and the obtained values were averaged. The calibration curves were validated in terms of their linearity, expressed by the determination coefficient R^2, as well as the limits of detection (LOD) and quantification (LOQ). Table 1 shows the details of the calibration curves, and based on the obtained validation values, it can be concluded that all the curves are characterized by a satisfactory linearity, as well as detection and quantification limits below the actual concentrations in the studied samples.

Table 1. Details of the calibration curves prepared for the sulfonamides used in the solubility dataset extension.

Compound	λ_{max} [nm]	Linear Regression Equation	R^2	LOD [mg/mL]	LOQ [mg/mL]
probenecid (PC)	246	A = 27.628 × C + 0.001	0.996	0.00126	0.00378
sulfamethazine (SMZ)	269	A = 80.729 × C + 0.002	0.999	0.00052	0.00157
sulfamethoxazole (SMA)	270	A = 69.820 × C + 0.001	0.998	0.00067	0.00202
sulfasalazine (SSZ)	364	A = 87.917 × C + 0.002	0.998	0.00042	0.00127

For determining the solubility of the studied sulfonamides in different eutectic compositions, a standard shake-flask procedure was applied [66,87–89].

The first step in this procedure involved the preparation of the deep eutectic solvents, which was performed by combining a hydrogen bond donor with a hydrogen bond acceptor. The HBA:HBD molar ratio was set to 1:2. The two HBDs, namely ChCl and BI, together with the four HBAs, namely TEG, DEG, ETG, and P2D, resulted in a total of 8 distinct eutectic compositions for each solute. The eutectics were prepared by weighing appropriate amounts of the two counterparts in glass vessels and heating them until a homogenous solution was obtained.

The samples of sulfonamides in DESs were prepared by adding an excess amount of the solute to the test tube, followed by an addition of the specific eutectic. The saturated solutions obtained in this manner were placed in an Orbital Shaker Incubator ES-20/60 from Biosan (Riga, Latvia) and heated at 25 °C, 30 °C, 35 °C, or 40 °C for 24 h with stirring at 60 rev/min. Before the measurements, the samples were filtered using a 0.22 μm pore-size PTFE syringe filter. The spectra of the filtered solutions were recorded after the dilution with methanol in the 200 nm–500 nm wavelength range with a 1 nm resolution. No solvatochromic effect was observed in the studied samples, and the analytical wavelength did not shift throughout the experiments. The absorbance values found at the characteristic wavelengths were used together with the linear regression equations to calculate the concentration of the considered solutes. Simultaneously, for the computation of the mole fraction solubility, the density of the samples was determined by weighing 1 mL of the sample on a RADWAG (Radom, Poland) AS 110 R2.PLUS analytical balance with 0.1 mg precision. Three separate samples were measured for each system, and the values were averaged.

3.3. Solubility Dataset

The entire solubility dataset used for machine learning, comprising N = 8014 data points, includes the following fifteen active pharmaceutical ingredients: caffeine (CAF), theobromine (THB), theophylline (THP), ferulic acid (FA), edaravone (EDA), ibuprofen (IB), ketoprofen (KP), curcumin (CUR), dapsone (DAP), probenecid (PC), sulfacetamide (SCM), sulfamethazine (SMZ), sulfamethoxazole (SMA), sulfanilamide (SNM), and sulfasalazine (SSZ). The dataset is divided into three subclasses, starting with the deep eutectic solvents (DESs), which include two hydrogen bond acceptors (HBAs): choline chloride (ChCl) (N = 1340) and betaine (BI) (N = 278). Additionally, the newly measured data (N = 128) were included for sulfasalazine (SSZ), sulfamerazine (SMA), sulfamethazine (SMZ), and probenecid (PC). To ensure a high degree of molecular diversity, we also collected data from the literature for each of the included APIs in the neat solvents (N = 2064) and binary solvent mixtures (N = 4332), when available. All data, along with references, are provided in the supporting information (see the MS Excel spreadsheet "SI.xlsx"). We believe this dataset represents the most comprehensive solubility data available for the considered APIs, given the current state of knowledge. Indeed, the dataset covers a wide range of solvent types, including highly polar protic and aprotic solvents, such as water and alcohols on one side and acetone, DMSO, and DMF on the other. The collection also includes representatives of other solvent classes, such as esters and non-polar hydrocarbons. Furthermore, halogenated solvents like dichloromethane, chloroform, and carbon tetrachloride are also present. In total, the solubility data for the 46 different solvents were included for the APIs under consideration. Interestingly, only about 33% of all the possible solute–solvent combinations are available. When accounting for temperature variations, this percentage decreases further. A coverage map, listing the measured and unavailable combinations, is provided in the Supplementary Materials (see Table S2.1). A complete documentation, along with references and solubility values, is included in the supporting materials (see the "Table.S1_neat" spreadsheet in the "SI.xlsx" MS Excel workbook). The subset of data characterizing the binary solvent mixtures is more homogeneous, covering mixtures of water, alcohols, and some other solvents, which are listed in the Supplementary Materials (see Table S2.2). Full documentation, references, and solubility values are also included (see the "Table.S2_bin" spreadsheet in the "SI.xlsx" workbook). Excluding the temperature and

concentration dependencies, only about 15% of the possible binary mixtures were studied for the APIs considered in this study. The third subset of the dataset includes the DESs based on choline chloride and betaine as the HBAs, mixed in various proportions with a range of HBDs. The list is available in the Supplementary Materials (see Table S2.3), and further details are available in the "SI.xlsx" file (see "Table.S3_DES" spreadsheet). These DES systems were optimized to tailor the solubility of specific APIs. It is important to note that the addition of water to DESs is known to enhance solubility at moderate concentrations due to the nanostructuring of the HBA; however, this aspect has not been extensively studied for many API-DES systems. Formally, the coverage of possible API-HBA-HBD combinations in our dataset is about 44%, but the inclusion of varying DES component ratios and the added water significantly reduce the actual coverage. To fill the gaps in the API-DES systems, the solubility of four sulfonamides was measured in four choline chloride and betaine DESs, adding N = 128 new data points to the solubility dataset.

3.4. COSMO-RS Solubility Computations

Solubility is routinely computed using a combination of first principles and statistical thermodynamics termed COSMO-RS (Conductor-like Screening Model for Real Solvents) [90–92]. This two-step approach leverages the macroscopic properties derived from microscopic atomistic modeling, typically employing the density functional theory (DFT) for a detailed structural diversity quantification at the molecular level. The methodology is well established [93–95], so only a brief overview is provided here. The initial step involves the generation of the relevant conformations for both the solutes and solvents. A standard protocol for an extensive conformational analysis was applied using the COSMOconf [96]. In the second step, the COSMOtherm package [97] was utilized to determine the physicochemical properties, including the solubility, intermolecular interaction contributions, and sigma potential distributions. This procedure was applied in our previous studies [62,68,69]. Each molecule was represented by up to ten low-energy conformations identified through independent conformational searches in both the gas and condensed phases. The latter is crucial for accounting for the influence of the surrounding environment within the conductor-like screening model. The outcome of this process is a set of "cosmo" and "energy" files, compatible with the latest parameter set (BP_TZVPD_FINE_24.ctd). This corresponds to a two-step computational procedure: first, optimizing the molecular geometries of the most probable conformations using RI-DFT with the B88-VWN-P86 functional and def-TZVP basis set, followed by single-point energy calculations using def2-TZVPD, as implemented in Turbomole Version 7.8 (compiled 23 October 2023) [98].

The estimated solubility values correspond to the solution of the solid–liquid equilibrium under saturated conditions. This can only be achieved if the fusion data are provided as an additional input, which is essential for characterizing the activity of the pure solute under the conditions corresponding to the solubility measurements. From a general thermodynamic perspective, solubility can be computed based on the melting temperature (T_m), the heat of fusion (ΔH_{fus}), and the heat capacity change upon melting (ΔC_p), using the following equation:

$$\ln(a^s) = -\frac{\Delta G_{fus}}{RT} = \frac{\Delta H_{fus}}{R} \cdot \left(\frac{1}{T_m} - \frac{1}{T}\right) - \frac{1}{RT}\int_{T_m}^{T} \Delta C_p dT + \frac{1}{RT}\int_{T_m}^{T} \Delta C_p dT \quad (1)$$

where R is the gas constant and T is the temperature at which the solubility is measured. For many compounds, including all fifteen APIs considered in this study, the experimental values for the melting point and heat of fusion are available [99,100]. However, the data on ΔC_p are more difficult to measure and are unavailable for the majority of the solutes. To address this, several simplifications have been proposed [83,101–104]. In this study, we assume $\Delta C_p \approx \Delta S_{fus} \approx \Delta H_{fus} \cdot T_m{}^{-1}$. To ensure the reproducibility of the solubility calculations, all ΔG_{fus} values have been included in the supporting materials, completing the experimental dataset (see MS Excel workbook "SI.xlsx"). The solubility values were determined using the COMSOtherm by solving the full SLE problem. While this method is

more computationally intensive than the iterative approaches, it is necessary, particularly for high solubility cases where the iterative procedure fails and inaccurately predicts the total miscibility between the solute and solvent. In contrast, the full SLE approach yields definite solubility values for every case in the dataset.

3.5. Molecular Descriptors

The selection of molecular descriptors is crucial for the quality of the machine learning models. The descriptors must summarize sufficient information to accurately represent the property being predicted. In the case of solubility modeling, three major requirements are essential for developing a successful model. First, the descriptors must be computable independent of the experimental data for any solute and solvent. Second, they must capture structural diversity, including isomers, rotamers, stereoisomers, and other molecular variations. Lastly, temperature dependence must be accounted for, as it plays a significant role in the equilibrium of saturated systems. These criteria exclude many popular sources of molecular descriptors, such as DRAGON [105] and PADEL [106], which rely either on SMILES strings or on 3D structural data limited to a single conformer. Fortunately, the COSMO-RS offers a comprehensive and effective way to meet these requirements. In this study, a straightforward set of descriptors was applied, leveraging the distribution of σ-potentials. This approach was successfully used in our previous projects [62,63], highlighting the predictive potential of this property derived from charge density distributions. For each solute and solvent, the σ-potential profiles were calculated for their pure, single-component state at a given temperature. The molecular descriptors used for machine learning were computed as the difference between the σ-potential of the pure solute and the σ-potential of the solvent at that specific temperature. For multicomponent solvents, the σ-potential was represented as a weighted value based on the solute-free mole fraction and then used to determine the relative σ-potential profile. Typically, the COSMOtherm program generates σ-potential profiles consisting of 61 points for the σ values ranging from -0.03 to $+0.03$ e/Å^2, with a step size of 0.001. Example distributions are provided in Figure 7.

The lines with open circles represent the whole set of 61 points, defining the complete σ-potential of each individual component. In Figure 7, there is also a step function averaging the six subsequent values of the σ potentials provided. It is worth reminding that the entire range of charge densities is often split into three sub-intervals interpreted according to the encoded information. Indeed, the region of $\sigma \in [-0.01, +0.01]$ is typically attributed to hydrophobicity (HYD), the hydrogen bond donicity (HBD) if defined by $\sigma \in [+0.01, +0.03]$, and the hydrogen acceptability (HBA) is addressed to $\sigma \in [-0.03, -0.01]$. This straightforward interpretation allows for the qualitative and quantitative characteristics of the nature of a given compound to be characterized. For example, water, being an amphiprotic agent, has non-zero contributions for the HBD and HBA regions and is insignificant for the non-polar range. Choline chloride has significantly more hydrophobic contributions compared to the other compounds presented in Figure 7, and due to the large negative volume of chloride anion exposed outwardly, it has a significant HBA range. The step function mimics the whole σ potential distribution with a reduced number of values. This defines the two sets of molecular descriptors, either as a 61-point full record or a simplified 12-point representation. The values presented in Figure 1 were used for the determination of the final sets of descriptors used for the machine learning protocol. For this purpose, the relative potential was defined as follows:

$$\Delta\sigma_{pot}(\mathrm{T}) = \mu_{API}(T) - \sum_{i}^{n} x_i^* \cdot \mu_i(T) \tag{2}$$

where i iterates over all n components in the solvent mixture and is equal to 1, 2, 3, or 4 for the neat solvents, binary solvent mixtures, dry DESs, and wet DESs, respectively. Hence, the database of σ potentials for every compound at each temperature was prepared and used for the $\Delta\sigma_{pot}(\mathrm{T})$ computations for every system in the solubility dataset.

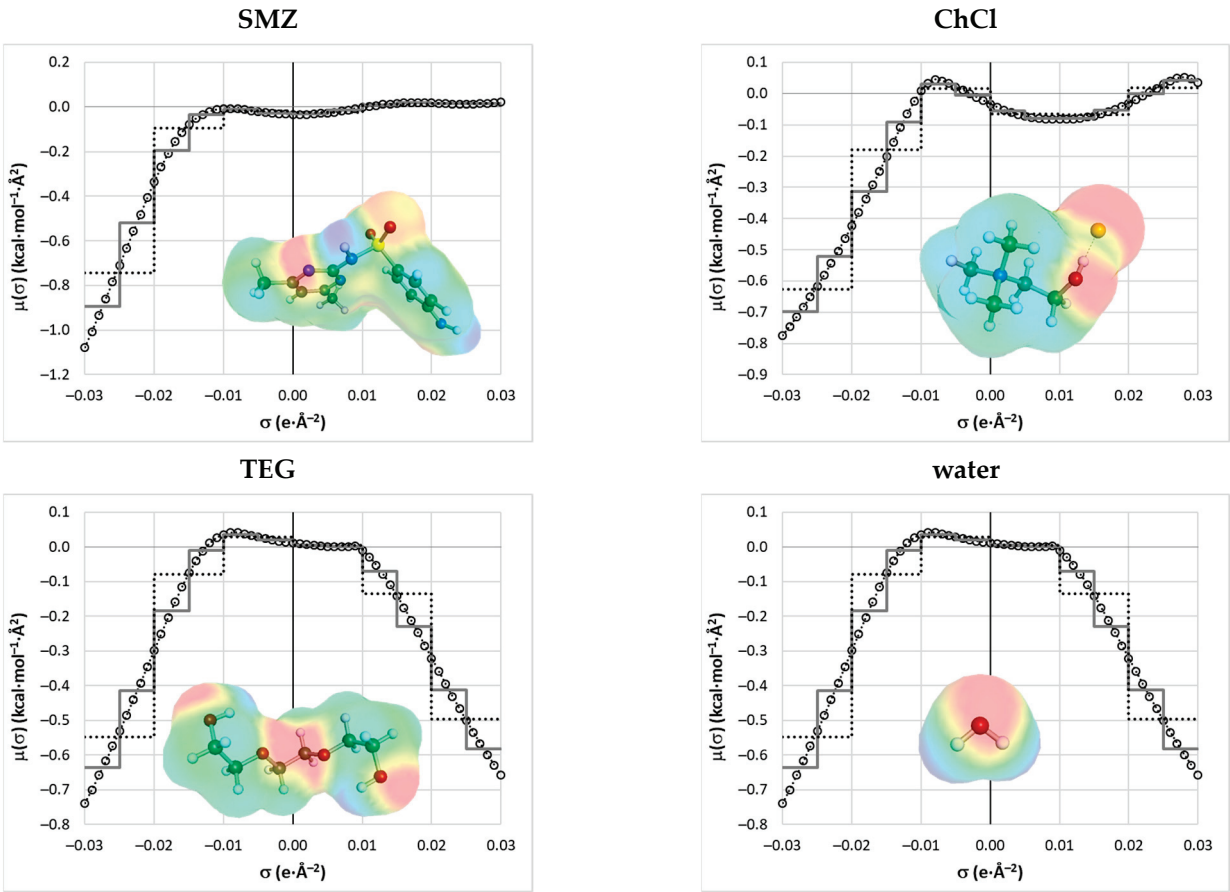

Figure 7. The presentation of the individual σ–potentials enabling the computation of the actual values of $\Delta\sigma_{pot}$ for SMZ + ChCl + TEG + water at T = 25 °C. Three types of resolutions are plotted, illustrating the three sets of molecular descriptors used in the machine learning protocol, namely open circles, which denote a full distribution of 61 points (descriptors set C) and two ways of averaging. The grey solid step line represents every six points (descriptor set B), and the dotted black step line characterizes the average over twelve points (descriptor set A).

Finally, taking advantage of the solubility computations, the energetic contributions of every component were extracted from the output files for characterizing the relative values of $\Delta\mu^{mix}$, ΔE^{tot}, ΔE^{HB}, ΔE^{misfit}, and ΔE^{vDW}. The first quantity represents the chemical potential of the mixture, and the rest characterize the contributions of the energetic components, including the relative values of the total energy, hydrogen bonding, the electrostatic contributions, and the non-polar interactions, respectively. These values were computed analogously to the formula provided in Equation (2). The training of non-linear regressors was performed independently for the four sets of descriptors, as defined in Table 2.

The three sets of descriptors A, B, and C differ significantly by the number of values used for training purposes. The comparison of model performances allows for the learning of how detailed a description of the σ potential should be. In the most extended case, i.e., set C, a very detailed representation is taken into account which might lead to overfitting. On the other hand, the representation of the shape of the σ potential by the step function might be effective since the function is generally quite smooth, and the representation of the three major regions just by the four (set B) or two (set A) averaged values might be sufficiently effective as it provides essentially the same information. It is also important to note that the motivation for excluding the values of the COSMO-RS-derived solubility is the relatively low accuracy of these estimates. This is discussed in more detail in the Section 2.2.

Table 2. Definition of the sets of descriptors used for the hyperparameter tuning of the considered regressors.

Model	Descriptors Set	N_{descr}
A1	Δσ- relative potential profiles simplified by step function (N_{descr} = 6) intermolecular interactions (N_{descr} = 5) COSMO-RS derived solubility(N_{descr} = 1)	12
A2	similar to model A1 but without COSMO-RS derived solubility	11
B1	Δσ- relative potential profiles simplified by step function (N_{descr} = 12) intermolecular interactions (N_{descr} = 5) COSMO-RS derived solubility(N_{descr} = 1)	18
B2	similar to model A1 but without COSMO-RS derived solubility	17
C1	Δσ- relative potential profiles as full profile (N_{descr} = 61) COSMO-RS derived solubility	62
C2	as model B1 is without COSMO-RS derived solubility	61

3.6. Machine Learning Protocol

The machine learning approach employed in this study follows the framework previously established in our earlier research endeavors [62,68,107]. Since the detailed methodology was thoroughly described in earlier publications, only a brief summary is presented here. The solubility prediction model was constructed using the custom Python version 3.10 [108] scripts developed for hyperparameter tuning across 36 distinct regression models. These models span a diverse array of algorithms, including linear regressors, boosting techniques, ensemble methods, nearest neighbors, neural networks, and other types of regressors. Hyperparameter tuning was performed using the Optuna version 3.2 [109], a widely used open-source Python package. The optimization process consisted of 5000 minimization trials, utilizing the tree-structured Parzen estimator (TPE) as the algorithm for sampling the hyperparameter space. To evaluate the performance of each regression model, a custom scoring function was developed, integrating multiple metrics to assess both accuracy and generalizability, as detailed in a previous study [63]. This scoring function incorporates the penalties derived from the learning curve analysis (LCA), performed using the scikit-learn library (version 1.2.2) during the parameter tuning process. It is important to highlight that the custom loss function employed for the solubility prediction models combines several evaluation metrics to ensure both accuracy and robustness, while also addressing the issue of overfitting. A key aspect of the scoring function is the integration of an LCA, which evaluates model performance across different training set sizes. By calculating the mean absolute error (MAE) through a five-fold cross-validation, the function tracks both the training and testing errors at incremental training sizes. Due to the computational demands of an LCA, a limited representation of the learning curve was adopted, using the five points between 50% and 100% of the total dataset. In comparison, our previous work employed only two points (50% and 100%). The extension of an LCA to include more data points aims to provide a more robust early indication of overfitting, albeit at the expense of an increased computational time. The custom loss function also incorporates the mean squared error (MSE) between the predicted and true solubility values, estimated for the training set, along with the penalty terms to further ensure prediction quality. These penalties address the false positive predictions (since the solubility, expressed in a logarithmic form, is expected to be negative) by penalizing any positive predictions based on their frequency. Additionally, the predictions with errors exceeding three standard deviations are classified as outliers and penalized accordingly, encouraging the model to minimize extreme deviations.

From a technical point of view, the whole set of descriptors was split into training (80%) and test (20%) subsets. The evaluation of the models' performance and their selection was performed using the unseen data by computing the root-mean-square deviations

(RMSD) and mean average percentage error (MAPE), which are defined according to the following well-known formula:

$$RMSD = \sqrt{\sum_{i}^{n}\left(\log\left(x_i^{exp}\right) - \log\left(x_i^{exp}\right)\right)^2 / n} \tag{3}$$

$$MAPE = \frac{100\%}{n}\sum_{i}^{n}\left|\frac{\log\left(x_i^{exp}\right) - \log\left(x_i^{exp}\right)}{\log\left(x_i^{exp}\right)}\right| \tag{4}$$

In addition, the percentage of outliers (%N_{out}) representing the percentage of the population with deviations higher than three times the standard deviation was used as the predictive coherence metric.

4. Conclusions

The pharmaceutical industry faces various challenges. One of them is the need for a limitation on the energy used, and waste generated during experiments, according to the "green chemistry" framework. Another one is the constant search for new solubilizing media, which plays a pivotal role in the development of new drugs and improving the formulation of already developed drugs. These requirements can be met using the designed deep eutectic solvents. These solvent systems have found widespread use in the pharmaceutical realm; however, the number of potential DES compositions prohibits the experimental testing of all the combinations. The current study addresses this issue by means of a predictive model based on a machine learning protocol, which can limit the experiments required for selecting the optimal eutectic solvents.

The available solubility data for fifteen active pharmaceutical ingredients, namely caffeine, theobromine, theophylline, ferulic acid, edaravone, ibuprofen, ketoprofen, curcumin, dapsone, probenecid, sulfacetamide, sulfamethazine, sulfamethoxazole, sulfanilamide, and sulfasalazine, were the basis for creating the predictive model. A comprehensive exploration of these data led to as many as 8014 data points for these APIs, which comprise the solubility of neat solvents (N = 2064), binary solvent mixtures (N = 4332), and DESs (N = 1618). In this set, there are 128 new data points for probenecid, sulfamethazine, sulfamethoxazole, and sulfasalazine in the various DESs containing choline chloride or betaine, obtained specifically for this study. The molecular predictors used for the purpose of the machine learning process were computed using the COSMO-RS framework. The solubility computations utilizing this method often lead to unsatisfactory results, especially in the case of eutectics, which prohibit the direct use of such values. However, the COSMO-RS can still provide meaningful and useful values in the form of σ-potentials.

In this study, we demonstrated that machine learning can effectively be used for predicting the solubility of new systems and also for filling the gap of lacking solubility data in partially characterized solvent hyperspace. The developed model can be used for an accurate prediction of solubility in untested systems, thereby guiding experimental efforts and optimizing resource allocation. Our extensive analysis revealed that expanding the dataset and exploring diverse solvent combinations significantly enhances the model's predictive capability. The nu-Support Vector Regressor (nuSVR) has been found to be the most reliable model, achieving high accuracy and generalization, and the most suited for the aim of this paper. Importantly, the choice of descriptor set was found to impact predictive performance more than the inclusion of the COSMO-RS solubility data, suggesting that the models can be streamlined to improve efficiency. It is recommended to use a simplified version of the relative σ-potential in the form of a twelve-step function and omit the solubility values computed in the COSMO-RS. The final robust model is defined by the following parameters of the nuSVR:

- C (6.8251) controls the trade-off between maximizing the margin and minimizing the training error. A higher value of C results in a model that prioritizes fitting the training data closely, potentially at the risk of overfitting.
- Degree (8) is relevant when using polynomial kernels and determines the degree of the polynomial. A degree of eight indicates a highly flexible model capable of capturing the complex relationships in the data.
- Gamma (0.8358) defines the influence of a single training example. A higher gamma value means the model will try to fit the data more closely, as each point has a significant influence on the shape of the decision boundary.
- Max_iter (61,378,442) sets the maximum number of iterations for the algorithm to converge. A high value ensures that the algorithm has sufficient iterations to find an optimal solution, which is especially important for complex models.
- Nu (0.4754) controls the proportion of support vectors and the margin of error, offering a balance between the number of support vectors used and the tolerance for deviations. An optimal value indicates a balanced trade-off, allowing the model to capture the underlying data patterns while controlling the margin of tolerance.

In this configuration, the model is optimized for capturing complex, non-linear relationships in the dataset while maintaining the robustness and generalization capabilities of the extended set of solubility data for DES and non-DES solvents.

Supplementary Materials: The following supporting information can be downloaded at: https://www.mdpi.com/article/10.3390/molecules29204894/s1. The MS Word document contains the following: Table S1: The mole fraction solubility ($\cdot 10^4$) of the sulfonamides in the DESs studied in this work. The HBA:HBD molar ratio is set to 1:2. The standard deviation values are given in parentheses. Table S2.1: the solubility of 15 APIs in the neat solvents. Table S2.2: the solubility of 15 APIs in the binary solvent mixtures. Table S2.3: The solubility of 15 APIs in the DES. The SI.xlsx MS Excel file with the following spreadsheets: Table.S1_neat, Table.S2_bin, and Table.S3_DES. The MS Excel includes the solubility data with references and molecular descriptors used for model development.

Author Contributions: Conceptualization, P.C.; methodology, P.C., T.J. and M.P.; software, P.C.; validation, P.C., T.J. and M.P.; formal analysis, P.C. and T.J.; investigation, P.C., T.J. and M.P.; resources, P.C.; data curation, P.C., M.P. and T.J.; writing—original draft preparation, P.C., T.J. and M.P.; writing—review and editing, P.C., T.J. and M.P.; visualization, P.C. and T.J.; supervision, P.C.; project administration, P.C.; funding acquisition, P.C. All authors have read and agreed to the published version of the manuscript.

Funding: This research received no external funding.

Institutional Review Board Statement: Not applicable.

Informed Consent Statement: Not applicable.

Data Availability Statement: All data supporting the reported results are available on request from the corresponding author.

Conflicts of Interest: The authors declare no conflicts of interest.

References

1. Kumar, V.; Bansal, V.; Madhavan, A.; Kumar, M.; Sindhu, R.; Awasthi, M.K.; Binod, P.; Saran, S. Active pharmaceutical ingredient (API) chemicals: A critical review of current biotechnological approaches. *Bioengineered* **2022**, *13*, 4309–4327. [CrossRef]
2. Kątny, M.; Frankowski, M. Impurities in Drug Products and Active Pharmaceutical Ingredients. *Crit. Rev. Anal. Chem.* **2017**, *47*, 187–193. [CrossRef] [PubMed]
3. Martínez, F.; Jouyban, A.; Acree, W.E. Pharmaceuticals solubility is still nowadays widely studied everywhere. *Pharm. Sci.* **2017**, *23*, 1–2. [CrossRef]
4. Savjani, K.T.; Gajjar, A.K.; Savjani, J.K. Drug Solubility: Importance and Enhancement Techniques. *ISRN Pharm.* **2012**, *2012*, 1–10. [CrossRef]
5. Coltescu, A.R.; Butnariu, M.; Sarac, I. The importance of solubility for new drug molecules. *Biomed. Pharmacol. J.* **2020**, *13*, 577–583. [CrossRef]

6. Yang, Z.; Yang, Y.; Xia, M.; Dai, W.; Zhu, B.; Mei, X. Improving the dissolution behaviors and bioavailability of abiraterone acetate via multicomponent crystal forms. *Int. J. Pharm.* **2022**, *614*, 121460. [CrossRef]
7. Kalam, M.A.; Alshamsan, A.; Alkholief, M.; Alsarra, I.A.; Ali, R.; Haq, N.; Anwer, M.K.; Shakeel, F. Solubility Measurement and Various Solubility Parameters of Glipizide in Different Neat Solvents. *ACS Omega* **2020**, *5*, 1708–1716. [CrossRef]
8. Kim, H.-S.; Kim, C.-M.; Jo, A.-N.; Kim, J.-E. Studies on Preformulation and Formulation of JIN-001 Liquisolid Tablet with Enhanced Solubility. *Pharmaceuticals* **2022**, *15*, 412. [CrossRef]
9. Khadka, P.; Ro, J.; Kim, H.; Kim, I.; Kim, J.T.; Kim, H.; Cho, J.M.; Yun, G.; Lee, J. Pharmaceutical particle technologies: An approach to improve drug solubility, dissolution and bioavailability. *Asian J. Pharm. Sci.* **2014**, *9*, 304–316. [CrossRef]
10. Müller, C.E. Prodrug Approaches for Enhancing the Bioavailability of Drugs with Low Solubility. *Chem. Biodivers.* **2009**, *6*, 2071–2083. [CrossRef]
11. Lipinski, C.A. Drug-like properties and the causes of poor solubility and poor permeability. *J. Pharmacol. Toxicol. Methods* **2000**, *44*, 235–249. [CrossRef] [PubMed]
12. Da Silva, F.L.O.; Marques, M.B.D.F.; Kato, K.C.; Carneiro, G. Nanonization techniques to overcome poor water-solubility with drugs. *Expert Opin. Drug Discov.* **2020**, *15*, 853–864. [CrossRef]
13. Das, B.; Baidya, A.T.K.; Mathew, A.T.; Yadav, A.K.; Kumar, R. Structural modification aimed for improving solubility of lead compounds in early phase drug discovery. *Bioorg. Med. Chem.* **2022**, *56*, 116614. [CrossRef] [PubMed]
14. Black, S.; Dang, L.; Liu, C.; Wei, H. On the measurement of solubility. *Org. Process Res. Dev.* **2013**, *17*, 486–492. [CrossRef]
15. Bergström, C.A.S.; Avdeef, A. Perspectives in solubility measurement and interpretation. *ADMET DMPK* **2019**, *7*, 88–105. [CrossRef] [PubMed]
16. Bhalani, D.V.; Nutan, B.; Kumar, A.; Singh Chandel, A.K. Bioavailability Enhancement Techniques for Poorly Aqueous Soluble Drugs and Therapeutics. *Biomedicines* **2022**, *10*, 2055. [CrossRef]
17. Manallack, D.T.; Yuriev, E.; Chalmers, D.K. The influence and manipulation of acid/base properties in drug discovery. *Drug Discov. Today Technol.* **2018**, *27*, 41–47. [CrossRef]
18. Merisko-Liversidge, E.; Liversidge, G.G. Nanosizing for oral and parenteral drug delivery: A perspective on formulating poorly-water soluble compounds using wet media milling technology. *Adv. Drug Deliv. Rev.* **2011**, *63*, 427–440. [CrossRef]
19. Brewster, M.E.; Loftsson, T. Cyclodextrins as pharmaceutical solubilizers. *Adv. Drug Deliv. Rev.* **2007**, *59*, 645–666. [CrossRef]
20. Korn, C.; Balbach, S. Compound selection for development—Is salt formation the ultimate answer? Experiences with an extended concept of the "100 mg approach". *Eur. J. Pharm. Sci.* **2014**, *57*, 257–263. [CrossRef]
21. Seedher, N.; Kanojia, M. Co-solvent solubilization of some poorly-soluble antidiabetic drugs. *Pharm. Dev. Technol.* **2009**, *14*, 185–192. [CrossRef] [PubMed]
22. Boobier, S.; Hose, D.R.J.; Blacker, A.J.; Nguyen, B.N. Machine learning with physicochemical relationships: Solubility prediction in organic solvents and water. *Nat. Commun.* **2020**, *11*, 5753. [CrossRef] [PubMed]
23. Lovrić, M.; Pavlović, K.; Žuvela, P.; Spataru, A.; Lučić, B.; Kern, R.; Wong, M.W. Machine learning in prediction of intrinsic aqueous solubility of drug-like compounds: Generalization, complexity, or predictive ability? *J. Chemom.* **2021**, *35*, e3349. [CrossRef]
24. Hahnenkamp, I.; Graubner, G.; Gmehling, J. Measurement and prediction of solubilities of active pharmaceutical ingredients. *Int. J. Pharm.* **2010**, *388*, 73–81. [CrossRef] [PubMed]
25. Abraham, M.H.; Smith, R.E.; Luchtefeld, R.; Boorem, A.J.; Lou, R.; Acree, W.E. Prediction of solubility of drugs and other compounds in organic solvents. *J. Pharm. Sci.* **2010**, *99*, 1500–1515. [CrossRef] [PubMed]
26. Hewitt, M.; Cronin, M.T.D.; Enoch, S.J.; Madden, J.C.; Roberts, D.W.; Dearden, J.C. In silico prediction of aqueous solubility: The solubility challenge. *J. Chem. Inf. Model.* **2009**, *49*, 2572–2587. [CrossRef]
27. Lenoir, D.; Schramm, K.W.; Lalah, J.O. Green Chemistry: Some important forerunners and current issues. *Sustain. Chem. Pharm.* **2020**, *18*, 100313. [CrossRef]
28. Kopach, M.; Leahy, D.; Manley, J. The green chemistry approach to pharma manufacturing. *Innov. Pharm. Technol.* **2012**, *43*, 72–75.
29. González-Miquel, M.; Díaz, I. Green solvent screening using modeling and simulation. *Curr. Opin. Green Sustain. Chem.* **2021**, *29*, 100469. [CrossRef]
30. Derbenev, I.N.; Dowden, J.; Twycross, J.; Hirst, J.D. Software tools for green and sustainable chemistry. *Curr. Opin. Green Sustain. Chem.* **2022**, *35*, 100623. [CrossRef]
31. Sánchez-Camargo, A.d.P.; Bueno, M.; Parada-Alfonso, F.; Cifuentes, A.; Ibáñez, E. Hansen solubility parameters for selection of green extraction solvents. *TrAC Trends Anal. Chem.* **2019**, *118*, 227–237. [CrossRef]
32. Wu, Y.c.; Feng, J.w. Development and Application of Artificial Neural Network. *Wirel. Pers. Commun.* **2018**, *102*, 1645–1656. [CrossRef]
33. Sharifani, K.; Amini, M. Machine Learning and Deep Learning: A Review of Methods and Applications. *World Inf. Technol. Eng. J.* **2023**, *10*, 3897–3904.
34. Tosca, E.M.; Bartolucci, R.; Magni, P. Application of artificial neural networks to predict the intrinsic solubility of drug-like molecules. *Pharmaceutics* **2021**, *13*, 1101. [CrossRef] [PubMed]
35. Deng, T.; Jia, G. zhu Prediction of aqueous solubility of compounds based on neural network. *Mol. Phys.* **2020**, *118*, e1600754. [CrossRef]

36. Wesolowski, M.; Suchacz, B. Artificial Neural Networks: Theoretical Background and Pharmaceutical Applications: A Review. *J. AOAC Int.* **2012**, *95*, 652–668. [CrossRef] [PubMed]
37. Agatonovic-Kustrin, S.; Beresford, R. Basic concepts of artificial neural network (ANN) modeling and its application in pharmaceutical research. *J. Pharm. Biomed. Anal.* **2000**, *22*, 717–727. [CrossRef]
38. Becker, J.; Manske, C.; Randl, S. Green chemistry and sustainability metrics in the pharmaceutical manufacturing sector. *Curr. Opin. Green Sustain. Chem.* **2022**, *33*, 100562. [CrossRef]
39. Mishra, M.; Sharma, M.; Dubey, R.; Kumari, P.; Ranjan, V.; Pandey, J. Green synthesis interventions of pharmaceutical industries for sustainable development. *Curr. Res. Green Sustain. Chem.* **2021**, *4*, 100174. [CrossRef]
40. DeSimone, J.M. Practical approaches to green solvents. *Science* **2002**, *297*, 799–803. [CrossRef]
41. Häckl, K.; Kunz, W. Some aspects of green solvents. *Comptes Rendus Chim.* **2018**, *21*, 572–580. [CrossRef]
42. Santana-Mayor, Á.; Rodríguez-Ramos, R.; Herrera-Herrera, A.V.; Socas-Rodríguez, B.; Rodríguez-Delgado, M.Á. Deep eutectic solvents. The new generation of green solvents in analytical chemistry. *TrAC Trends Anal. Chem.* **2021**, *134*, 116108. [CrossRef]
43. Vanda, H.; Dai, Y.; Wilson, E.G.; Verpoorte, R.; Choi, Y.H. Green solvents from ionic liquids and deep eutectic solvents to natural deep eutectic solvents. *Comptes Rendus Chim.* **2018**, *21*, 628–638. [CrossRef]
44. Smith, E.L.; Abbott, A.P.; Ryder, K.S. Deep Eutectic Solvents (DESs) and Their Applications. *Chem. Rev.* **2014**, *114*, 11060–11082. [CrossRef] [PubMed]
45. El Achkar, T.; Greige-Gerges, H.; Fourmentin, S. Basics and properties of deep eutectic solvents: A review. *Environ. Chem. Lett.* **2021**, *19*, 3397–3408. [CrossRef]
46. Omar, K.A.; Sadeghi, R. Physicochemical properties of deep eutectic solvents: A review. *J. Mol. Liq.* **2022**, *360*, 119524. [CrossRef]
47. Paiva, A.; Craveiro, R.; Aroso, I.; Martins, M.; Reis, R.L.; Duarte, A.R.C. Natural Deep Eutectic Solvents—Solvents for the 21st Century. *ACS Sustain. Chem. Eng.* **2014**, *2*, 1063–1071. [CrossRef]
48. Espino, M.; de los Ángeles Fernández, M.; Gomez, F.J.V.; Silva, M.F. Natural designer solvents for greening analytical chemistry. *TrAC Trends Anal. Chem.* **2016**, *76*, 126–136. [CrossRef]
49. Xu, G.; Shi, M.; Zhang, P.; Tu, Z.; Hu, X.; Zhang, X.; Wu, Y. Tuning the composition of deep eutectic solvents consisting of tetrabutylammonium chloride and n-decanoic acid for adjustable separation of ethylene and ethane. *Sep. Purif. Technol.* **2022**, *298*, 121680. [CrossRef]
50. Cao, Y.; Tao, X.; Jiang, S.; Gao, N.; Sun, Z. Tuning thermodynamic properties of deep eutectic solvents for achieving highly efficient photothermal sensor. *J. Mol. Liq.* **2020**, *308*, 113163. [CrossRef]
51. Liu, Y.; Deak, N.; Wang, Z.; Yu, H.; Hameleers, L.; Jurak, E.; Deuss, P.J.; Barta, K. Tunable and functional deep eutectic solvents for lignocellulose valorization. *Nat. Commun.* **2021**, *12*, 5424. [CrossRef] [PubMed]
52. Hansen, B.B.; Spittle, S.; Chen, B.; Poe, D.; Zhang, Y.; Klein, J.M.; Horton, A.; Adhikari, L.; Zelovich, T.; Doherty, B.W.; et al. Deep Eutectic Solvents: A Review of Fundamentals and Applications. *Chem. Rev.* **2021**, *121*, 1232–1285. [CrossRef] [PubMed]
53. Bazzo, G.C.; Pezzini, B.R.; Stulzer, H.K. Eutectic mixtures as an approach to enhance solubility, dissolution rate and oral bioavailability of poorly water-soluble drugs. *Int. J. Pharm.* **2020**, *588*, 119741. [CrossRef]
54. Kapre, S.; Palakurthi, S.S.; Jain, A.; Palakurthi, S. DES-igning the future of drug delivery: A journey from fundamentals to drug delivery applications. *J. Mol. Liq.* **2024**, *400*, 124517. [CrossRef]
55. Jeliński, T.; Przybyłek, M.; Mianowana, M.; Misiak, K.; Cysewski, P. Deep Eutectic Solvents as Agents for Improving the Solubility of Edaravone: Experimental and Theoretical Considerations. *Molecules* **2024**, *29*, 1261. [CrossRef]
56. Duarte, A.R.C.; Ferreira, A.S.D.; Barreiros, S.; Cabrita, E.; Reis, R.L.; Paiva, A. A comparison between pure active pharmaceutical ingredients and therapeutic deep eutectic solvents: Solubility and permeability studies. *Eur. J. Pharm. Biopharm.* **2017**, *114*, 296–304. [CrossRef]
57. Nguyen, C.-H.; Augis, L.; Fourmentin, S.; Barratt, G.; Legrand, F.-X. Deep Eutectic Solvents for Innovative Pharmaceutical Formulations. In *Deep Eutectic Solvents for Innovative Pharmaceutical Formulations*; Springer: Berlin/Heidelberg, Germany, 2021; Volume 56, pp. 41–102.
58. Liu, Y.; Wu, Y.; Liu, J.; Wang, W.; Yang, Q.; Yang, G. Deep eutectic solvents: Recent advances in fabrication approaches and pharmaceutical applications. *Int. J. Pharm.* **2022**, *622*, 121811. [CrossRef]
59. Emami, S.; Shayanfar, A. Deep eutectic solvents for pharmaceutical formulation and drug delivery applications. *Pharm. Dev. Technol.* **2020**, *25*, 779–796. [CrossRef]
60. Pedro, S.N.; Freire, M.G.; Freire, C.S.R.; Silvestre, A.J.D. Deep eutectic solvents comprising active pharmaceutical ingredients in the development of drug delivery systems. *Expert Opin. Drug Deliv.* **2019**, *16*, 497–506. [CrossRef]
61. Mustafa, N.R.; Spelbos, V.S.; Witkamp, G.J.; Verpoorte, R.; Choi, Y.H. Solubility and stability of some pharmaceuticals in natural deep eutectic solvents-based formulations. *Molecules* **2021**, *26*, 2645. [CrossRef]
62. Cysewski, P.; Jeliński, T.; Przybyłek, M.; Mai, A.; Kułak, J. Experimental and Machine-Learning-Assisted Design of Pharmaceutically Acceptable Deep Eutectic Solvents for the Solubility Improvement of Non-Selective COX Inhibitors Ibuprofen and Ketoprofen. *Molecules* **2024**, *29*, 2296. [CrossRef] [PubMed]
63. Jeliński, T.; Przybyłek, M.; Różalski, R.; Romanek, K.; Wielewski, D.; Cysewski, P. Tuning Ferulic Acid Solubility in Choline-Chloride- and Betaine-Based Deep Eutectic Solvents: Experimental Determination and Machine Learning Modeling. *Molecules* **2024**, *29*, 3841. [CrossRef] [PubMed]

64. Jeliński, T.; Przybyłek, M.; Cysewski, P. Natural Deep Eutectic Solvents as Agents for Improving Solubility, Stability and Delivery of Curcumin. *Pharm. Res.* **2019**, *36*, 116. [CrossRef] [PubMed]
65. Jeliński, T.; Cysewski, P. Quantification of Caffeine Interactions in Choline Chloride Natural Deep Eutectic Solvents: Solubility Measurements and COSMO-RS-DARE Interpretation. *Int. J. Mol. Sci.* **2022**, *23*, 7832. [CrossRef] [PubMed]
66. Jeliński, T.; Stasiak, D.; Kosmalski, T.; Cysewski, P. Experimental and theoretical study on theobromine solubility enhancement in binary aqueous solutions and ternary designed solvents. *Pharmaceutics* **2021**, *13*, 1118. [CrossRef]
67. Cysewski, P.; Jeliński, T.; Cymerman, P.; Przybyłek, M. Solvent screening for solubility enhancement of theophylline in neat, binary and ternary NADES solvents: New measurements and ensemble machine learning. *Int. J. Mol. Sci.* **2021**, *22*, 7347. [CrossRef]
68. Cysewski, P.; Jeliński, T.; Przybyłek, M. Experimental and Theoretical Insights into the Intermolecular Interactions in Saturated Systems of Dapsone in Conventional and Deep Eutectic Solvents. *Molecules* **2024**, *29*, 1743. [CrossRef]
69. Cysewski, P.; Jeliński, T.; Przybyłek, M. Intermolecular Interactions of Edaravone in Aqueous Solutions of Ethaline and Glyceline Inferred from Experiments and Quantum Chemistry Computations. *Molecules* **2023**, *28*, 629. [CrossRef]
70. Cysewski, P.; Jeliński, T. Optimization, thermodynamic characteristics and solubility predictions of natural deep eutectic solvents used for sulfonamide dissolution. *Int. J. Pharm.* **2019**, *570*, 118682. [CrossRef]
71. Lomba, L.; Ribate, M.P.; Zaragoza, E.; Concha, J.; Garralaga, M.P.; Errazquin, D.; García, C.B.; Giner, B. Deep Eutectic Solvents: Are They Safe? *Appl. Sci.* **2021**, *11*, 10061. [CrossRef]
72. De Morais, P.; Gonçalves, F.; Coutinho, J.A.P.; Ventura, S.P.M. Ecotoxicity of Cholinium-Based Deep Eutectic Solvents. *ACS Sustain. Chem. Eng.* **2015**, *3*, 3398–3404. [CrossRef]
73. Macário, I.P.E.; Jesus, F.; Pereira, J.L.; Ventura, S.P.M.; Gonçalves, A.M.M.; Coutinho, J.A.P.; Gonçalves, F.J.M. Unraveling the ecotoxicity of deep eutectic solvents using the mixture toxicity theory. *Chemosphere* **2018**, *212*, 890–897. [CrossRef] [PubMed]
74. Nejrotti, S.; Antenucci, A.; Pontremoli, C.; Gontrani, L.; Barbero, N.; Carbone, M.; Bonomo, M. Critical Assessment of the Sustainability of Deep Eutectic Solvents: A Case Study on Six Choline Chloride-Based Mixtures. *ACS Omega* **2022**, *7*, 47449–47461. [CrossRef]
75. Kovács, A.; Neyts, E.C.; Cornet, I.; Wijnants, M.; Billen, P. Modeling the Physicochemical Properties of Natural Deep Eutectic Solvents. *ChemSusChem* **2020**, *13*, 3789–3804. [CrossRef]
76. Deglmann, P.; Hungenberg, K.-D.; Vale, H.M. Dependence of Copolymer Composition in Radical Polymerization on Solution Properties: A Quantitative Thermodynamic Interpretation. *Ind. Eng. Chem. Res.* **2021**, *60*, 10566–10583. [CrossRef]
77. Klamt, A.; Schwöbel, J.; Huniar, U.; Koch, L.; Terzi, S.; Gaudin, T. COSMO plex: Self-consistent simulation of self-organizing inhomogeneous systems based on COSMO-RS. *Phys. Chem. Chem. Phys.* **2019**, *21*, 9225–9238. [CrossRef]
78. Abraham, M.H.; Acree, W.E. Estimation of enthalpies of sublimation of organic, organometallic and inorganic compounds. *Fluid Phase Equilib.* **2020**, *515*, 112575. [CrossRef]
79. Jasim, F.; Talib, T. Some observations on the thermal behaviour of curcumin under air and argon atmospheres. *J. Therm. Anal.* **1992**, *38*, 2549–2552. [CrossRef]
80. Kulkarni, P.P.; Jafvert, C.T. Solubility of C60 in solvent mixtures. *Environ. Sci. Technol.* **2008**, *42*, 845–851. [CrossRef]
81. Manin, A.N.; Drozd, K.V.; Voronin, A.P.; Churakov, A.V.; Perlovich, G.L. A Combined Experimental and Theoretical Study of Nitrofuran Antibiotics: Crystal Structures, DFT Computations, Sublimation and Solution Thermodynamics. *Molecules* **2021**, *26*, 3444. [CrossRef]
82. Wang, Y.; Liu, Y.; Shi, P.; Du, S.; Liu, Y.; Han, D.; Sun, P.; Sun, M.; Xu, S.; Gong, J. Uncover the effect of solvent and temperature on solid-liquid equilibrium behavior of l-norvaline. *J. Mol. Liq.* **2017**, *243*, 273–284. [CrossRef]
83. Cysewski, P.; Jeliński, T.; Przybyłek, M. Finding the Right Solvent: A Novel Screening Protocol for Identifying Environmentally Friendly and Cost-Effective Options for Benzenesulfonamide. *Molecules* **2023**, *28*, 5008. [CrossRef] [PubMed]
84. Awad, M.; Khanna, R. Support Vector Regression. *Effic. Learn. Mach.* **2015**, 67–80. [CrossRef]
85. Ghanavati, M.A.; Ahmadi, S.; Rohani, S. A machine learning approach for the prediction of aqueous solubility of pharmaceuticals: A comparative model and dataset analysis. *Digit. Discov.* **2024**, *3*, 2085–2104. [CrossRef]
86. Vassileiou, A.D.; Robertson, M.N.; Wareham, B.G.; Soundaranathan, M.; Ottoboni, S.; Florence, A.J.; Hartwig, T.; Johnston, B.F. A unified ML framework for solubility prediction across organic solvents. *Digit. Discov.* **2023**, *2*, 356–367. [CrossRef]
87. Przybyłek, M.; Recki, Ł.; Mroczyńska, K.; Jeliński, T.; Cysewski, P. Experimental and theoretical solubility advantage screening of bi-component solid curcumin formulations. *J. Drug Deliv. Sci. Technol.* **2019**, *50*, 125–135. [CrossRef]
88. Jeliński, T.; Przybyłek, M.; Cysewski, P. Solubility advantage of sulfanilamide and sulfacetamide in natural deep eutectic systems: Experimental and theoretical investigations. *Drug Dev. Ind. Pharm.* **2019**, *45*, 1120–1129. [CrossRef]
89. Cysewski, P.; Jeliński, T.; Przybyłek, M. Application of COSMO-RS-DARE as a Tool for Testing Consistency of Solubility Data: Case of Coumarin in Neat Alcohols. *Molecules* **2022**, *27*, 5274. [CrossRef]
90. Klamt, A. Conductor-like screening model for real solvents: A new approach to the quantitative calculation of solvation phenomena. *J. Phys. Chem.* **1995**, *99*, 2224–2235. [CrossRef]
91. Klamt, A. *From Quantum Chemistry to Fluid Phase Thermodynamics and Drug Design*; Elsevier: Amsterdam, The Netherlands, 2005; ISBN 978-0-444-51994-8.
92. Klamt, A.; Eckert, F.; Arlt, W. COSMO-RS: An Alternative to Simulation for Calculating Thermodynamic Properties of Liquid Mixtures. *Annu. Rev. Chem. Biomol. Eng.* **2010**, *1*, 101–122. [CrossRef]

93. Klamt, A. COSMO-RS for aqueous solvation and interfaces. *Fluid Phase Equilib.* **2016**, *407*, 152–158. [CrossRef]
94. Klamt, A. The COSMO and COSMO-RS solvation models. *Wiley Interdiscip. Rev. Comput. Mol. Sci.* **2011**, *1*, 699–709. [CrossRef]
95. Klamt, A.; Eckert, F. COSMO-RS: A novel and efficient method for the a priori prediction of thermophysical data of liquids. *Fluid Phase Equilib.* **2000**, *172*, 43–72. [CrossRef]
96. Dassault Systèmes. *COSMOconf*, version 24.0.0; Dassault Systèmes; Biovia: San Diego, CA, USA, 2022.
97. Dassault Systèmes. *COSMOtherm*, version 24.0.0; Dassault Systèmes; Biovia: San Diego, CA, USA, 2022.
98. TURBOMOLE GmbH. *TURBOMOLE*, version 7.8; TURBOMOLE GmbH: Karlsruhe, Germany, 2023.
99. Acree, W.; Chickos, J.S. Phase Transition Enthalpy Measurements of Organic and Organometallic Compounds. Sublimation, Vaporization and Fusion Enthalpies From 1880 to 2015. Part 1. C 1–C 10. *J. Phys. Chem. Ref. Data* **2016**, *45*, 033101. [CrossRef]
100. Acree, W.; Chickos, J.S. Phase Transition Enthalpy Measurements of Organic and Organometallic Compounds and Ionic Liquids. Sublimation, Vaporization, and Fusion Enthalpies from 1880 to 2015. Part 2. C11–C192. *J. Phys. Chem. Ref. Data* **2017**, *46*, 013104. [CrossRef]
101. Nordström, F.L.; Rasmuson, Å.C. Determination of the activity of a molecular solute in saturated solution. *J. Chem. Thermodyn.* **2008**, *40*, 1684–1692. [CrossRef]
102. Svärd, M.; Valavi, M.; Khamar, D.; Kuhs, M.; Rasmuson, Å.C. Thermodynamic Stability Analysis of Tolbutamide Polymorphs and Solubility in Organic Solvents. *J. Pharm. Sci.* **2016**, *105*, 1901–1906. [CrossRef]
103. Svärd, M.; Hjorth, T.; Bohlin, M.; Rasmuson, Å.C. Calorimetric Properties and Solubility in Five Pure Organic Solvents of N-Methyl- d -Glucamine (Meglumine). *J. Chem. Eng. Data* **2016**, *61*, 1199–1204. [CrossRef]
104. Cysewski, P.; Jeliński, T.; Przybyłek, M.; Nowak, W.; Olczak, M. Solubility Characteristics of Acetaminophen and Phenacetin in Binary Mixtures of Aqueous Organic Solvents: Experimental and Deep Machine Learning Screening of Green Dissolution Media. *Pharmaceutics* **2022**, *14*, 2828. [CrossRef]
105. *Dragon*, version 7.0; Talete srl: Milan, Italy, 2014.
106. Yap, C.W. PaDEL-descriptor: An open source software to calculate molecular descriptors and fingerprints. *J. Comput. Chem.* **2011**, *32*, 1466–1474. [CrossRef]
107. Jeliński, T.; Przybyłek, M.; Różalski, R.; Cysewski, P. Solubility of dapsone in deep eutectic solvents: Experimental analysis, molecular insights and machine learning predictions. *Polym. Med.* **2024**, *54*, 15–25. [CrossRef] [PubMed]
108. Python Software Foundation. *Python Language Reference*, Version 3.10. Python Software Foundation: Wilmington, DE, USA. Available online: http://www.python.org (accessed on 12 October 2024).
109. Akiba, T.; Sano, S.; Yanase, T.; Ohta, T.; Koyama, M. Optuna: A Next-generation Hyperparameter Optimization Framework. In Proceedings of the KDD '19: Proceedings of the 25th ACM SIGKDD International Conference on Knowledge Discovery & Data Mining, Anchorage, AK, USA, 4–8 August 2019; pp. 2623–2631. [CrossRef]

Disclaimer/Publisher's Note: The statements, opinions and data contained in all publications are solely those of the individual author(s) and contributor(s) and not of MDPI and/or the editor(s). MDPI and/or the editor(s) disclaim responsibility for any injury to people or property resulting from any ideas, methods, instructions or products referred to in the content.

molecules

MDPI

Article

Selectivities of Carbon Dioxide over Ethane in Three Methylimidazolium-Based Ionic Liquids: Experimental Data and Modeling

Nadir Henni, Amr Henni * and Hussameldin Ibrahim *

Clean Energy Technologies Research Institute (CETRi), University of Regina, Regina, SK S4S 0A2, Canada; nadir.henni1@gmail.com

* Correspondence: amr.henni@uregina.ca (A.H.); hussameldin.ibrahim@uregina.ca (H.I.)

Abstract: This work focused on the solubility of ethane in three promising ionic liquids {1-Hexyl-3-methylimidazolium bis(trifluormethylsulfonyl) imide [HMIM][Tf2N], 1-Butyl-3-methyl-imidazolium dimethyl-phosphate [BMIM][DMP], and 1-Propyl-3-methylimidazolium bis(trifluoromethyl-sulfonyl)-imide [PMIM][Tf2N]}. The solubilities were measured at 303.15 K to 343.15 K and pressures up to 1.4 MPa using a gravimetric microbalance. The overall ranking of ethane solubility in the ionic liquids from highest to lowest is the following: [HMIM][Tf2N] > [PMIM][Tf2N] > [BMIM][DMP]. The Peng–Robinson equation of state was used to model the experimental data using three different mixing rules: van der Waals one, van der Waals two, and Wong–Sandler mixing rules combined with the Non-Random Two-Liquid model. The average absolute deviations for the three mixing rules for the ionic liquids at the three temperatures were 4.39, 2.45, and 2.45%, respectively. Henry's Law constants for ethane in [BMIM] [DMP] were the highest (lowest solubility) amongst other ionic liquids studied in this work. The solubility ranking for the 3 ILs was confirmed by calculating their overall polarity parameter (N) using COSMO-RS. The selectivity of CO_2 over C_2H_6 was estimated at three temperatures, and the overall ranking of the selectivity was in the following order: [PMIM][Tf2N] > [BMIM][DMP] > [HMIM][Tf2N] > Selexol. Selexol is an efficient and widely used physical solvent in gas sweetening. It has lower selectivity than the three ionic liquids studied. [PMIM][Tf2N], a promising solvent, has the highest selectivity among the three ILs studied and would, therefore, be the best choice if, in addition to carbon dioxide capture, ethane co-absorption was to be avoided. The enthalpy and entropy of solvation at infinite dilution were also estimated.

Keywords: ionic liquid; ethane; carbon dioxide; solubility; selectivity; equation of state

1. Introduction

As reported by the Energy Information Agency (EIA) in 2023, approximately 83% of the total energy produced in the United States came from fossil fuels, i.e., oil, coal, and natural gas [1]. Fossil fuels, when burned, produce large quantities of CO_2 and other gases. These gases will result in greenhouse gas effects, resulting in the absorption of the heat coming from the sun and causing the temperature of the earth's atmosphere to rise. Global warming is consequently considered a detrimental and even catastrophic change in the climate. According to the Scripps Institution of Oceanography and the National Oceanic and Atmospheric Administration (NOAA), the CO_2 May monthly average in 2024 reached 426.7 ppm, an increase of 2.92 ppm over that recorded in 2023 [2]. NOAA also reports that 2023 is the warmest year on record by far [3].

There are multiple ways of slowing down the rate of global warming. One of those methods is through emission reduction with carbon capture. The most up-to-date technology in carbon capture is the process of absorbing CO_2 generated by power generation, steel, and cement plants. This latest technology is similar to the removal of acid gases from natural gas sweetening, except that a mixture of amines is used as a solvent. Capturing

CO_2 using non-aqueous solvents is an advanced, next-generation post-combustion capture technology that seeks to remove CO_2 emitted from power generation and industrial flue gas streams.

Natural gas is one of the types of energy from the diverse portfolio of fossil fuels. It is a naturally occurring hydrocarbon composed mainly of methane. In general, it also contains ethane, propane, butane, and pentane, as well as non-hydrocarbon gases such as nitrogen, carbon dioxide, and hydrogen sulfide. Natural gas is formed from the remains of plants and animals exposed to extreme heat and pressure under the earth's surface hundreds of millions of years ago. It constitutes the major source of energy consumed today; the demand for natural gas has not ceased to increase year after year in the last decade. According to the International Energy Agency, the world's natural gas consumption reached 4138 billion cubic meters (bcm) in 2022 and is expected to reach 4299 bcm in 2050 [4].

To this day, carbon capture is performed by capturing CO_2 from both high-pressure natural gas streams and low-pressure gas streams with amines-based chemical solvents [5]. However, this process is not very economical in the case of flue gases because of the large amount of energy required to regenerate the solvent and the serious solvent degradation that occurs. For natural gas applications, using physical rather than chemical solvents for carbon capture is more economical when the cleaning targets are not at the ppm level. Multiple processes have been used for carbon capture depending on the partial pressure of CO_2 in the feed and the required degree of treatment. Aside from amines and their blends, organic physical solvents are one of these processes. One of the main advantages is the low energy needed for solvent regeneration [5]. Commonly, physical solvents have a low energy of regeneration and relatively low vapor pressure. They are non-corrosive, with high thermal stability. They could be used in treating natural gas as standalone or mixed with aqueous amines in the case of flue gases. Ionic liquids (ILs) represent a category of physical solvents that utilize intermolecular forces for CO_2 capture. ILs are normally defined as compounds composed of ions (a cation and an anion) with a melting point below 100 °C. In this study, three new and promising ionic liquids are studied to analyze their capacities for ethane at three different temperatures (303.15 K, 323.15 K, and 343.15 K). This range of temperatures is of great importance to the industry and the pressures used were up to 1.4 MPa. Using CO_2 solubility data, we recently published, selectivity values are reported for the three solvents at three temperatures. The experiments were conducted using a gravimetric microbalance (IGA-003).

2. Results

2.1. Verification of the C_2H_6 Solubility Measurement

A verification test was performed to ensure the IGA-003 is operating as it should. In this verification test, [BMIM][PF6] was used as the solvent, and the results were compared with Anthony et al. (2005) at 298.15 K [6]. As shown in Figure 1, the results between the measured data and those published by Anthony et al. are in excellent agreement.

2.2. Solubility of C_2H_6 in Ionic Liquids

C_2H_6 solubility data were studied by many researchers who found the ionic liquids to have lower solubility than CO_2. This work used three ionic liquids with different cations and anions to understand the factors affecting the solubility of C_2H_6 in ILs. C_2H_6 solubility in [HMIM][Tf2N], [BMIM][DMP], and [PMIM][Tf2N] were measured at 303.15 K, 323.15 K, and 343.15 K and pressures up to 1.4 MPa. The results were plotted in P-x form in Figures 2–4 for the three solvents. The values of the experimental data can be found in Tables 1–3.

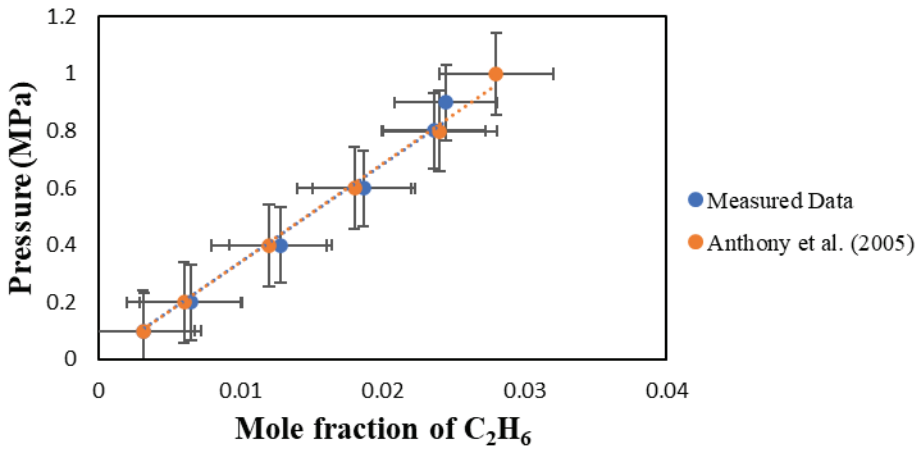

Figure 1. Comparison between the measured data for the solubility of C_2H_6 in [BMIM][PF6] and those reported by Anthony et al. (2005) [6] at 298.15 K.

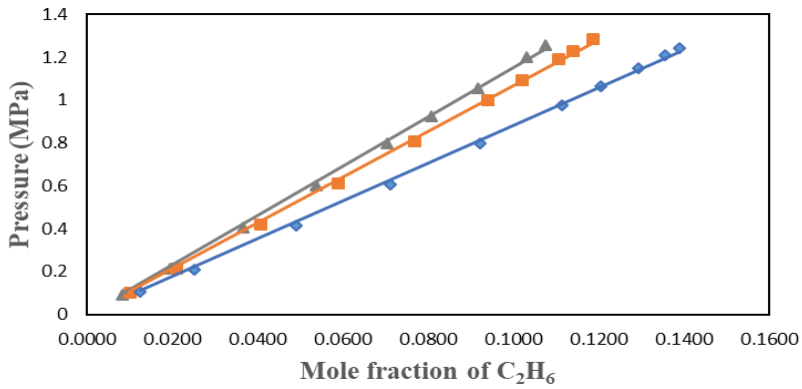

(**a**)

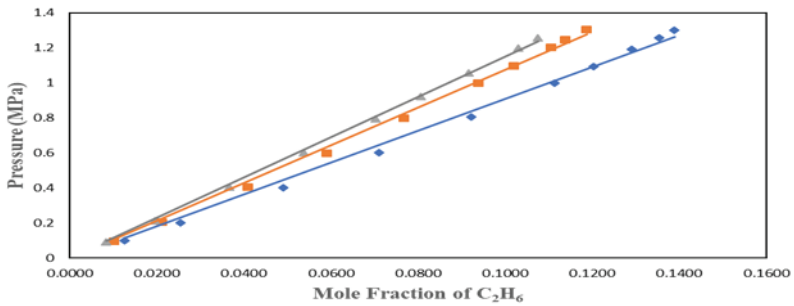

(**b**)

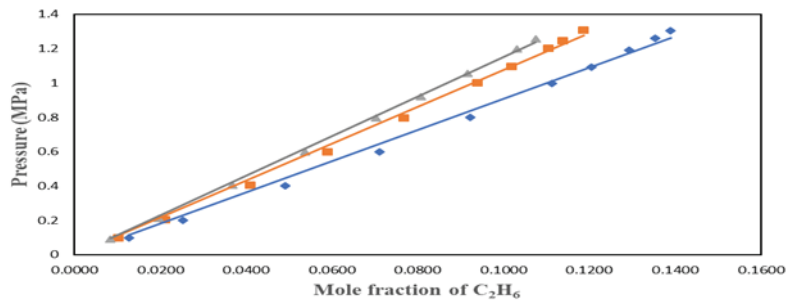

(**c**)

Figure 2. Solubility data for C_2H_6 in [HMIM][Tf2N] at different temperatures and pressures up to 1.4 MPa: ♦ 303.15 K; ■ 323.15 K; ▲: 343.15 K. Experimental VLE data were correlated with (**a**) PR + vdW1, (**b**) PR + vdW2, and (**c**) PR + WS + NRTL.

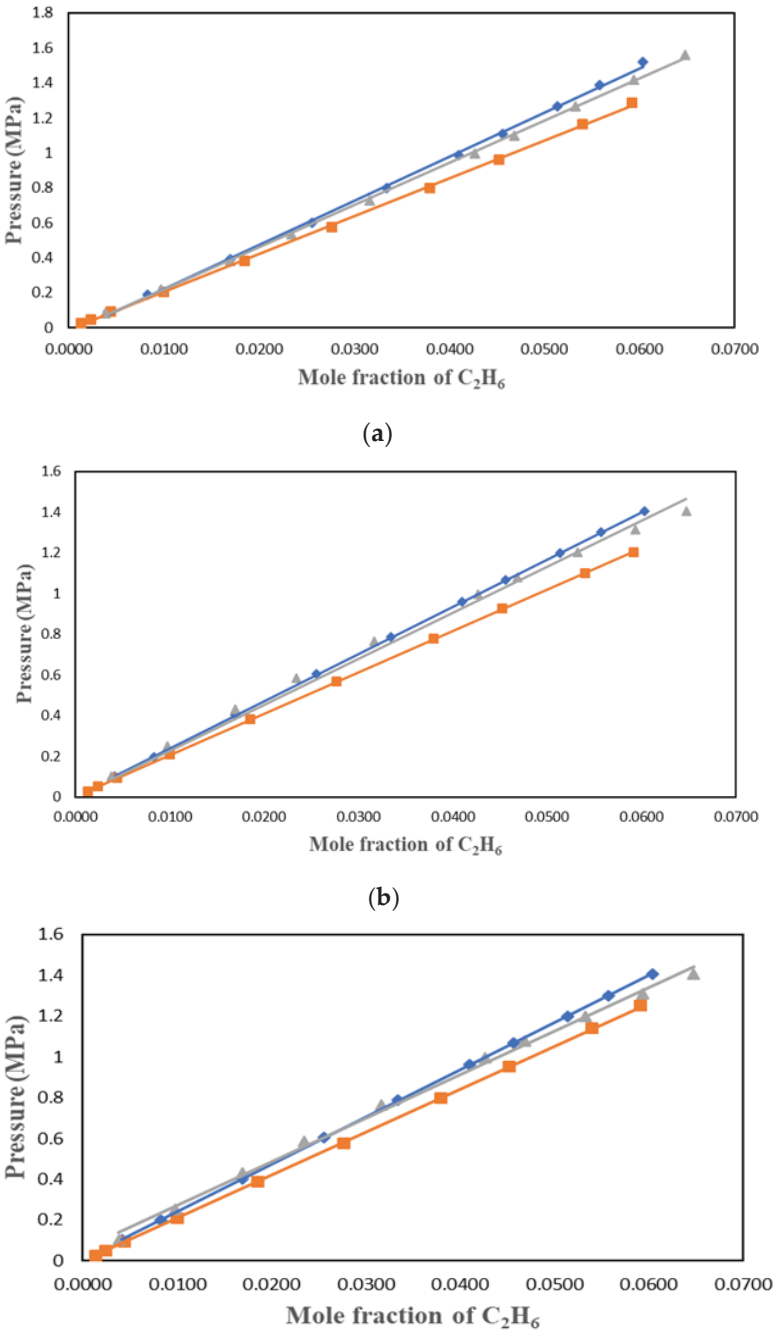

Figure 3. Solubility data of C_2H_6 in [BMIM][DMP] at different temperatures: ♦ 303.15 K; ■ 323.15 K; ▲ 343.15 K. Experimental VLE data were correlated with (**a**) PR + vdW1, (**b**) PR + vdW2, and (**c**) PR + WS + NRTL.

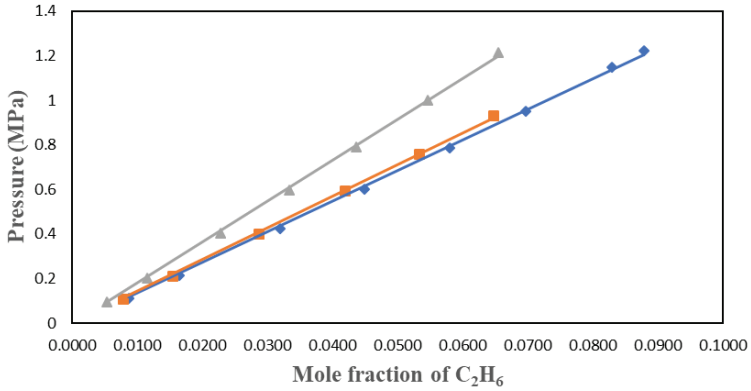

(**a**)

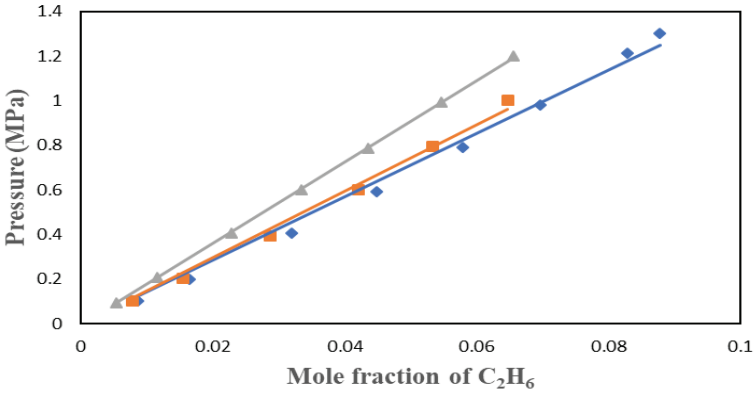

(**b**)

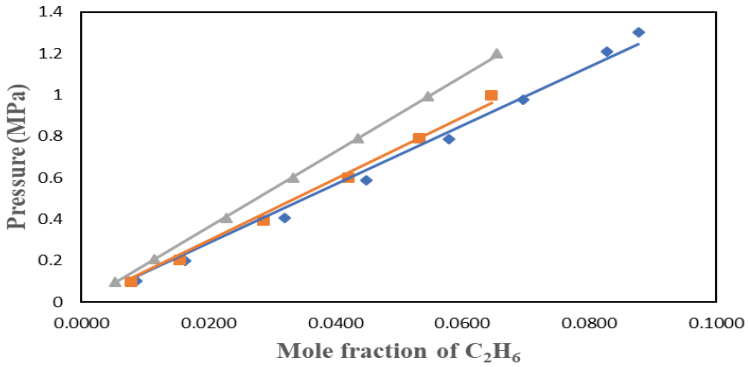

(**c**)

Figure 4. Solubility data of C_2H_6 in [PMIM][Tf2N] at different temperatures: ♦ 303.15 K; ■ 323.15 K; ▲ 343.15 K and model correlation: lines with (**a**) PR + vdW1, (**b**) PR + vdW2, and (**c**) PR + WS + NRTL.

Table 1. Solubility of C_2H_6 in [HMIM][Tf2N] at 303.15 K, 323.15 K, and 343.15 K.

[HMIM][Tf2N]					
303.15 K		**323.15 K**		**343.15 K**	
x_{C2H6}	**Pressure (MPa)**	x_{C2H6}	**Pressure (MPa)**	x_{C2H6}	**Pressure (MPa)**
0.003	0.01991	0.003	0.0199	0.003	0.0199
0.006	0.0499	0.005	0.0499	0.005	0.0499

Table 1. *Cont.*

[HMIM][Tf2N]					
303.15 K		**323.15 K**		**343.15 K**	
x_{C2H6}	**Pressure (MPa)**	x_{C2H6}	**Pressure (MPa)**	x_{C2H6}	**Pressure (MPa)**
0.013	0.09989	0.010	0.1000	0.008	0.0999
0.025	0.20004	0.021	0.1998	0.020	0.2002
0.049	0.3998	0.041	0.3997	0.037	0.3998
0.071	0.59988	0.059	0.5998	0.054	0.5998
0.092	0.7999	0.077	0.7998	0.070	0.7995
0.111	0.9994	0.094	0.9996	0.081	0.9999
0.120	1.0998	0.102	1.0998	0.091	1.1000
0.129	1.1988	0.110	1.2011	0.103	1.1994
0.135	1.2495	0.114	1.2503	0.107	1.2513
0.139	1.3007	0.119	1.3009	-	-

Standard uncertainty u(x) = 0.006; standard uncertainty u(T) = 0.1 K; standard uncertainty u(P) = 0.0008 MPa.

Table 2. Solubility of C_2H_6 in [BMIM][DEP] at 303.15 K, 323.15 K, and 343.15 K.

[BMIM][DMP]					
303.15 K		**323.15 K**		**343.15 K**	
x_{C2H6}	**Pressure (MPa)**	x_{C2H6}	**Pressure (MPa)**	x_{C2H6}	**Pressure (MPa)**
0.001	0.01978	0.001	0.0198	0.002	0.0196
0.002	0.0499	0.002	0.0499	0.002	0.0499
0.004	0.09989	0.004	0.0999	0.004	0.1001
0.008	0.19985	0.010	0.1999	0.010	0.1999
0.017	0.39991	0.018	0.4002	0.017	0.3996
0.026	0.59976	0.028	0.6006	0.023	0.5999
0.034	0.79991	0.038	0.7998	0.032	0.7999
0.0422	0.9998	0.045	0.9998	0.043	1.0006
0.050	1.2003	0.054	1.0997	0.047	1.0998
0.056	1.2996	0.059	1.2005	0.053	1.2012
0.059	1.3486	-	-	0.059	1.3011
0.063	1.4006	-	-	0.065	1.4006

Standard uncertainty u(x) = 0.006; standard uncertainty u(T) = 0.1 K; standard uncertainty u(P) = 0.0008 MPa.

Table 3. Solubility of C_2H_6 in [PMIM][Tf2N] at 303.15K, 323.15K, and 343.15K.

[PMIM][Tf2N]					
303.15 K		**323.15 K**		**343.15 K**	
x_{C2H6}	**Pressure (MPa)**	x_{C2H6}	**Pressure (MPa)**	x_{C2H6}	**Pressure (MPa)**
0.002	0.0198	0.003	0.0199	0.002	0.0198
0.005	0.0499	0.005	0.0499	0.002	0.0500

Table 3. *Cont.*

[PMIM][Tf2N]					
303.15 K		**323.15 K**		**343.15 K**	
x_{C2H6}	**Pressure (MPa)**	x_{C2H6}	**Pressure (MPa)**	x_{C2H6}	**Pressure (MPa)**
0.009	0.0999	0.008	0.0999	0.005	0.0999
0.016	0.1999	0.015	0.1999	0.011	0.1999
0.032	0.4001	0.029	0.3999	0.023	0.4002
0.045	0.5999	0.042	0.5997	0.033	0.6011
0.058	0.7999	0.053	0.7998	0.044	0.8000
0.070	0.9999	0.065	0.9998	0.054	0.9999
0.083	1.1991	-	-	0.065	1.2012
0.088	1.30132	-	-	0.070	1.2998
-	-	-	-	0.079	1.4000

Standard uncertainty u(x) = 0.006; standard uncertainty u(T) = 0.1 K; standard uncertainty u(P) = 0.0008 MPa.

3. Discussion

3.1. Factors That Affect the Solubility of C_2H_6

3.1.1. Pressure and Temperature

Figures 2–4 show that temperature and pressure affect the solubility of C_2H_6 in ionic liquids. As expected, it is observed that as the temperature rises, C_2H_6 solubility in the ionic liquid decreases. As pressure rises, C_2H_6 solubility increases.

As presented in Figure 5, a comparison between the solubility of ethane in the three ionic liquids at 303.15 K shows that the solvent that absorbs ethane the least is [BMIM][DMP].

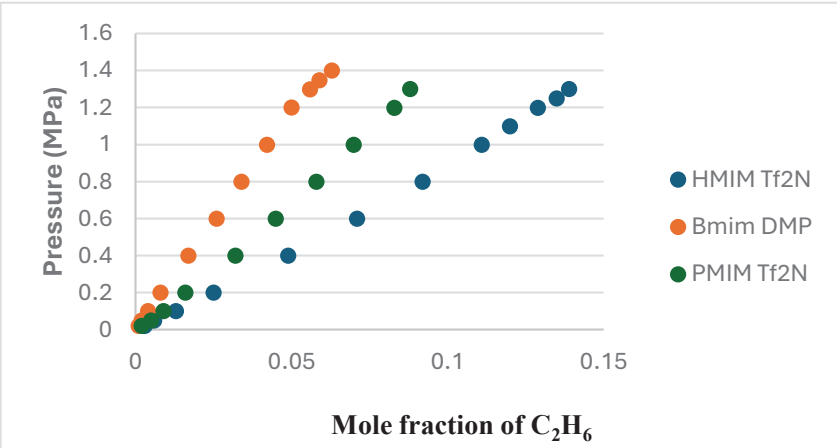

Figure 5. Comparison between the solubility of C_2H_6 in the 3 ILs at 303.15 K.

3.1.2. Anion Effect

A significant amount of research has been performed to understand the mechanism of how different ionic liquids have different solubilities when it comes to capturing gases such as CO_2, CH_4, C_2H_6, and others. Anthony et al. [6] studied the anion effect on CO_2 solubility in [BMIM]-based ionic liquids with three different anions. Experiments were performed between 283.15K and 323.15 K and up to 1.4 MPa for three ionic liquids with three different anions, namely [BMIM][Tf2N], [BMIM][BF4], and [BMIM][PF6]. They reported that ethane, along with other gases, such as ethylene, oxygen, and argon, have the lowest solubilities in ILs compared to other common solvents.

3.1.3. Alkyl Chain Length with [Tf2N]-Anion

As presented in Figure 6, the alkyl chain effect will affect the solubility of C_2H_6 in ionic liquids. [HMIM] and [PMIM] are attached to an imidazolium-based cation with an n-methyl chain. The difference between their molecular structures is due to the hexyl and propyl alkyl chains. In their carbon chains, hexyl has six methyl groups, and propyl has three. The longer the chain, the more gas the ionic liquid will absorb. This observation was made also by Zoubeik (2014) [7] and Tagiuri et al. (2014) [8] based on several studies published in the literature. Note that the polarity parameter (N) for [PMIM] is lower than that of [HMIM], confirming its higher capacity in absorbing ethane. The polarity parameter is discussed further at the end of Section 3.1.4 and also in reference [9].

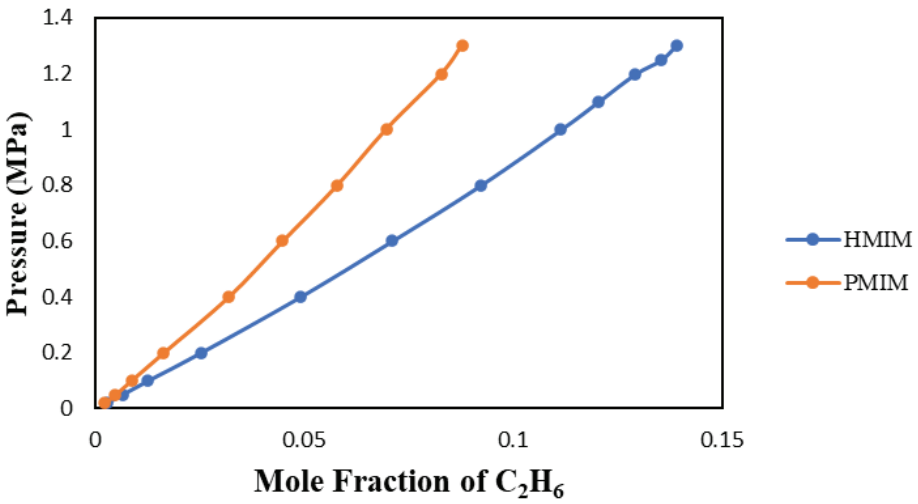

Figure 6. Solubility of C_2H_6 in the two ILs with [Tf2N]-anion at 303.15 K.

3.1.4. Cation with the Same [Tf2N] Anion

The effect of different cations with the same [Tf2N] anion is observed in Figure 6. The [PMIM] cation allowed for less C_2H_6 solubility than the [HMIM] cation. The solubility in ILs with the same anions will depend mostly on the cation. Based on studies published in the literature, methyl imidazolium cation-based ionic liquid tends to usually have a higher C_2H_6 solubility than other cation-based ionic liquids. The solubility of C_2H_6 in [HMIM] is higher than that in [PMIM], most probably because of its longer carbon (alkyl) chain, as discussed earlier in the section entitled "Alkyl Chain Lengths". As reported by Taguiri (2019) [10] and others, this study confirms the fact that the anion of an ionic liquid has more of an impact on gas solubility than its cation.

For detailed information about the mechanism of gas solubility in ionic liquids, please refer to a comprehensive screening study we performed in 2011 [9] using COSMO-RS. In it, molar volumes and polarity of the ionic liquids were used to quantify the solubility of gases in ILs. The study dealt with gases such as CO_2 and the selectivity of methane and nitrogen. A relative overall polarity parameter N was defined and computed for 2701 ionic liquids. N quantifies the degree of chemical affinity of water with ions due to vdW, misfit, and H-bond. The more negative the value of N, the more polar the IL is. N was found to be equal to 6.22 for [Tf2N], −62.04 for [DMP], 37.16 for [HMIM], 32.79 for [BMIM], and 32.70 for a cation similar to [PMIM]. Accordingly, [BMIM][DMP] with the lowest N should have the lowest ethane solubility, followed by [PMIM][Tf2N] and [HMIM][Tf2N]. This predicted trend is confirmed by the experimental data presented in Figure 5. A comprehensive description of the structural variations of the ILs on the solubility can also be found. In addition to the alkyl chain, alkylation of ammonium and phosphonium cation, change in cation family for ring cation and non-ring cation, and presence of hydroxyl and ether groups were discussed in reference [9].

3.2. Optimization of Binary Interaction Parameters

MATLAB was used for the thermodynamic model and was based on a bubble point technique for the three mixing rules [5]. As shown in Equation (1) [10], the binary interaction parameters were optimized by minimizing the objective function (Err). Because experimental data at lower pressures are more likely to be erroneous, the binary interaction parameters were optimized using a pressure range of 0.1 to 1.4 MPa.

$$\mathrm{Err} = \frac{100}{n}\sum_{i=1}^{n}\left[\frac{P_{Exp,i} - P_{Cal,i}}{P_{Exp,i}}\right] \quad (1)$$

The average absolute deviation for the vdW1, vdW2, and WS-NRTL mixing rules when used in the ionic liquids for C_2H_6 were 4.39%, 2.45%, and 2.45%, respectively. The results for C_2H_6 were best when using either the vdW2 or WS-NRTL mixing rule, as shown in Table 4.

Table 4. Optimized binary interaction parameters for different models and calculated AAD%.

Compound	Temperature (K) and Pressure (MPa)	Mixing Rule	k_{12} [a]	l_{12} [b]	τ_{12}	τ_{21}	AAD%
C_2H_6(1) + [HMIM][Tf2N] (**2**)	303.15 and 0.1–1.4	vdW1	0.0797	-	-	-	3.19
		vdW2	0.1566	0.0163	-	-	0.47
		WS + NRTL	1.305	-	0.2151	−0.1848	0.44
	323.15 and 0.1–1.4	vdW1	0.0694	-	-	-	2.11
		vdW2	0.1116	0.0104	-	-	0.83
		WS + NRTL	1.2293	-	0.7031	−0.5823	0.84
	343.15 and 0.1–1.4	vdW1	0.0452	-	-	-	3.37
		vdW2	0.0557	0.0026	-	-	3.30
		WS + NRTL	1.0256		0.0396	0.0123	3.30
C_2H_6 (1) + [BMIM][DMP] (**2**)	303.15 and 0.1–1.4	vdW1	0.1931	-	-	-	4.77
		vdW2	0.052	−0.0377		-	2.35
		WS + NRTL	0.9997	-	1.1024	0.6362	2.34
	323.15 and 0.1–1.4	vdW1	0.1564	-	-	-	7.13
		vdW2	0.0294	−0.0346	-	-	6.65
		WS + NRTL	1.1384	-	0.6327	0.2915	6.66
	343.15 and 0.1–1.4	vdW1	0.1494	-	-	-	7.40
		vdW2	−0.2053	−0.101	-	-	4.44
		WS + NRTL	−0.1133	-	0.4517	1.8268	4.39
C_2H_6 (1) + [PMIM][Tf2N] (**2**)	303.15 and 0.1–1.4	vdW1	0.1240	-	-	-	5.23
		vdW2	0.236	0.0308	-	-	1.47
		WS + NRTL	1.6977	-	−0.0402	−0.0385	1.53
	323.15 and 0.1–1.4	vdW1	0.0987	-	-	-	4.41
		vdW2	0.2757	0.0467	-	-	0.66
		WS + NRTL	1.7468	-	−0.5135	0.1939	0.66
	343.15 and 0.1–1.4	vdW1	0.1028	-	-	-	1.93
		vdW2	0.0678	−0.0093	-	-	1.86
		WS + NRTL	1.1086	-	0.0247	0.3612	1.87

[a] $k_{12} = k_{21}$; [b] $l_{12} = l_{21}$.

3.3. Henry's Law Constants, Enthalpies, and Entropies

Using the solubility data, Henry's Law constants were derived for the three ionic liquids. For each temperature, the fugacities of C_2H_6 were plotted against mole fractions. The limiting slope of the data's second-order polynomial was used to determine Henry's Law constants for each temperature. Henry's Law constants , H_i, of the solute (i) in the solvent (j) is the ratio of the fugacity of the solute (i) to the mole fraction of the solute (i) in solvent (j) at infinite dilution at temperature T and pressure P; f_i^L and f_i^V are the fugacity of solute (i) in the liquid phase and vapor phase, respectively; and x_i and y_i are the mole

fraction of solute (i) in the liquid phase and vapor phase, respectively, at temperature T and pressure P [5]. It is expressed as the following:

$$H_i = \lim_{x_i \to 0} \frac{f_i^L(T, P, x_i)}{x_i} = \lim_{x_i \to 0} \frac{f_i^V(T, P, y_i)}{x_i} \quad (2)$$

Once Henry's Law has been estimated from the solubility data, estimating the enthalpy of solvation (ΔH^∞) at infinite dilution and the entropy of solvation (ΔS^∞) at infinite dilution can also be performed using the following equations:

$$\Delta H^\infty = R\left(\frac{\partial(\ln H)}{\partial(1/T)}\right)_P \quad (3)$$

$$\Delta S^\infty = -R\left(\frac{\partial(\ln H)}{\partial(\ln T)}\right)_P \quad (4)$$

where ΔH^∞ is the enthalpy of solvation at infinite dilution, (ΔS^∞) is the entropy of solvation at infinite dilution, R is the universal gas constant, H is Henry's Law constant, and T is temperature.

The comparison between the three ionic liquids is presented in Figure 7 for the three temperatures studied. Henry's Law constants for C_2H_6 in [HMIM][Tf2N] were published by C. Gomes et al. (2007) [11] and are reported here for comparison. The values are very close, confirming the accuracy of the experimental data. The calculated values are presented in Table 5. Henry's Law constants of the three ionic liquids studied are compared to those found in the literature and presented in Figure 7 for the three temperatures studied.

Overall, the ranking of the Henry's Law constants for C_2H_6 is the following: [BMIM][DMP] > [PMIM][Tf2N] > [HMIM][Tf2N] at all temperatures. As the highest value is the best, and [BMIM][DMP] is therefore the IL that absorbs ethane the least. Compared to other ionic liquids, the three ionic liquids are not the best, but [BMIM][DMP] seems to be the best option.

Table 5. Henry's Law constants, enthalpies, and entropies for the solvation of C_2H_6 in ionic liquids at infinite dilution.

Ionic Liquid	Henry's Law Constant (MPa)			ΔH^∞ (KJ/kmol)	ΔS^∞ (KJ/mol·K)
	T = 303.15 K	T = 323.15 K	T = 343.15 K		
[HMIM][Tf2N]	7.63	9.43	10.69	−1.16	−3.61
[BMIM][DMP]	23.60	22.07	25.93	−0.81	−2.63
[PMIM][Tf2N]	12.85	13.61	17.35	−6.40	−20.02

The decreasing ranking in terms of the heat of absorption is the following: [BMIM][DMP] > [HMIM][Tf2N] > [PMIM][Tf2N]. The solubility of ethane in three ILs {[C3C1pip][FSI], [C3C1pyrr][FSI], and [N1223][FSI]} reported in Figure 7 was published by Nath et al. (2017) [12].

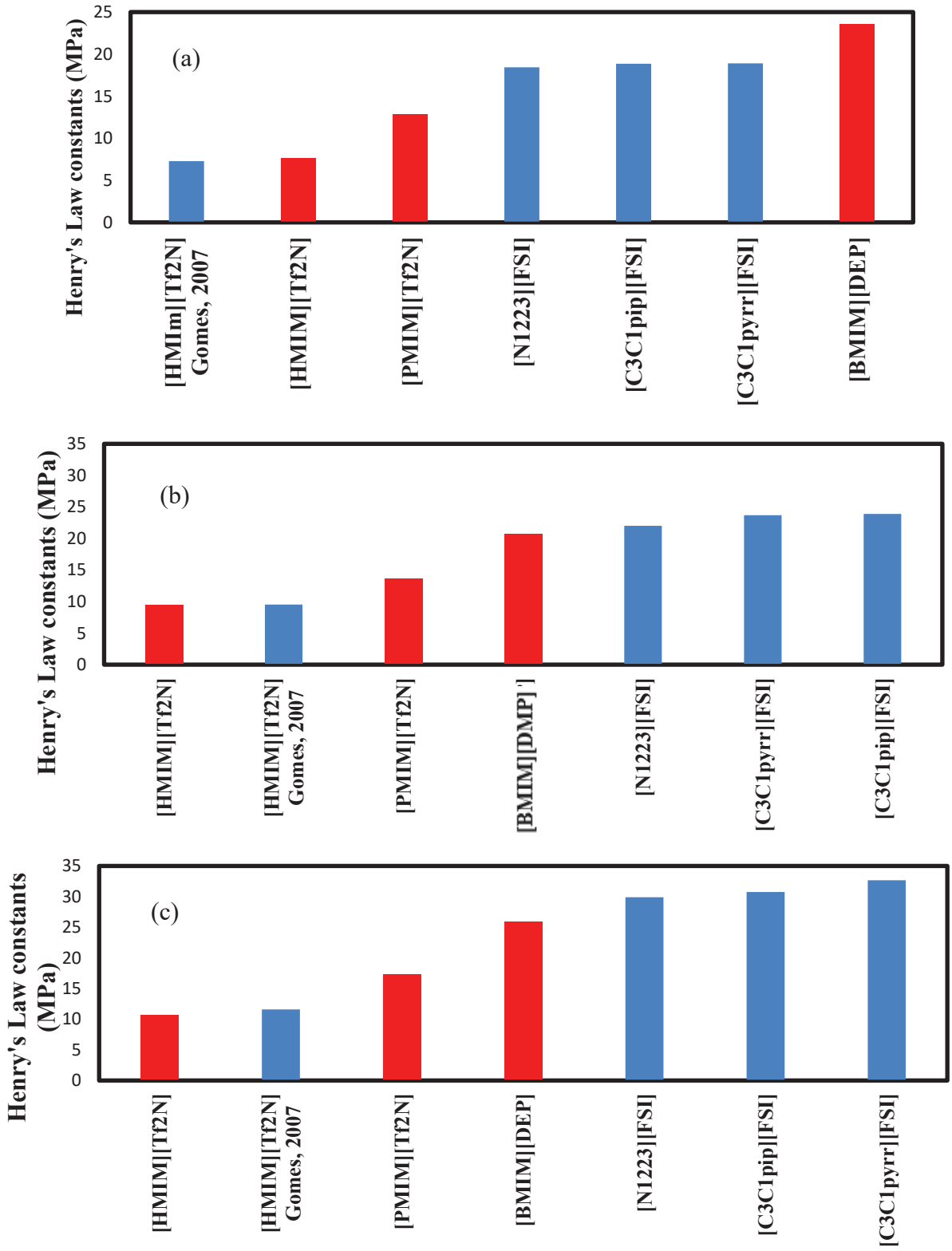

Figure 7. Comparison of Henry's Law constants for C_2H_6 in ILs at (**a**) 303.15 K, (**b**) 323.15 K, and (**c**) 343.15 K; red: ionic liquids used in this work and blue: other ILs obtained from the literature summarized by Nath et al. [12].

3.4. CO_2/C_2H_6 Selectivity in the Three Ionic Liquid Systems

The major criteria for a potential solvent for the use of gas solubility are the following: high removal efficiency, high selectivity toward CO_2, and low energy requirement. Not

much research has been conducted when it comes to the selectivity between gases. When CO_2 is captured, it is not the only gas being absorbed. Other gases are absorbed, such as N_2O, O_2, SO_2, H_2S, CH_4, and many other hydrocarbons. Therefore, with that in mind, it is crucial to study the effect of selectivity on ionic liquids. The selectivity of the ionic liquids used in this work was estimated as the ratio between Henry's Law constant of CO_2 and C_2H_6. The equation used to estimate the selectivity is the following:

$$S_{CO_2/C_2H_6} = \frac{H_{C_2H_6}}{H_{CO_2}} \quad (5)$$

The values of the selectivities are presented in Table 6. CO_2/C_2H_6 selectivity of the ionic liquids is not significantly high; however, they decrease as the temperature rises. The data obtained for the Henry's Law constant of CO_2 was taken from previous research we performed measuring the CO_2 solubility in [HMIM][Tf2N], [BMIM][DMP], and [PMIM][Tf2N] [13]. The study revealed that the three solvents were among the best in capturing CO_2. The three ionic liquids followed this rank in terms of increasing CO_2 solubility: [HMIM] [Tf2N] > [PMIM][Tf2N] >[BMIM][DMP], as reported in reference [13]. The study confirmed that [HMIM][Tf2N] is an excellent solvent for CO_2 capture. [PMIM][Tf2N] was also found to have a high capacity for CO_2 among ILs published in the literature.

The selectivities of the three ionic liquids studied are compared to those found in the literature and presented in Figures 8–10 at the three temperatures studied.

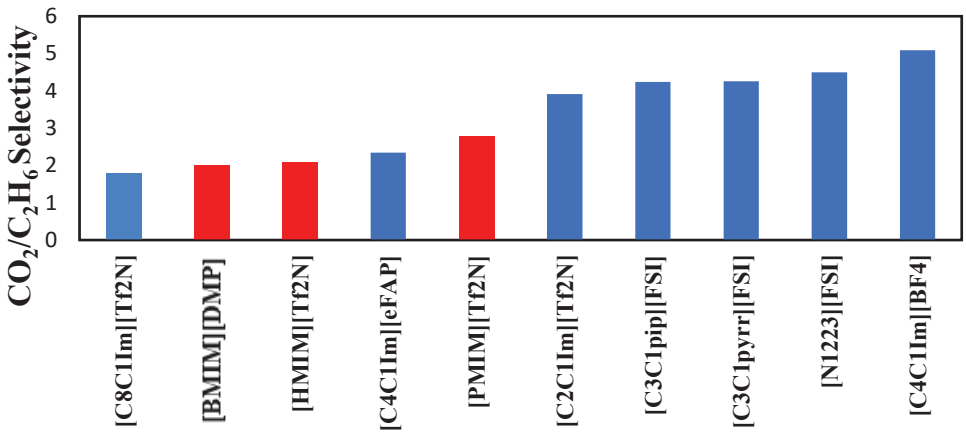

Figure 8. Comparison of CO_2/C_2H_6 selectivity in several ionic liquids reported by Nath et al. [12] at 303.15 K.

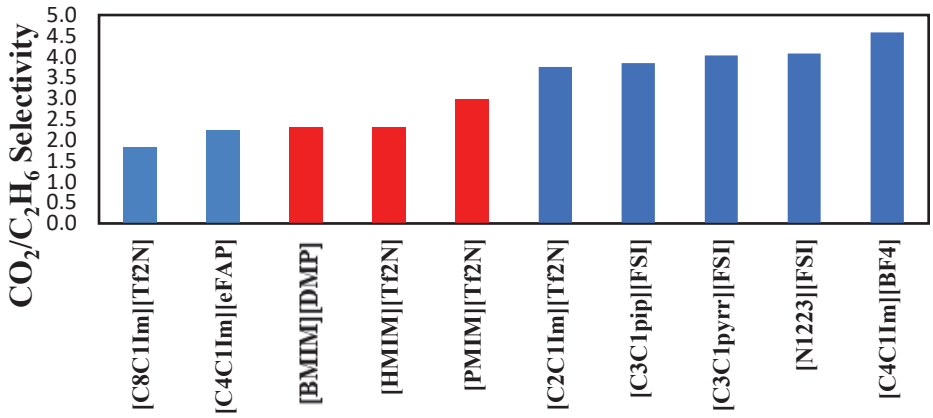

Figure 9. Comparison of CO_2/C_2H_6 selectivity in several ionic liquids reported by Nath et al. [12] at 323.15 K.

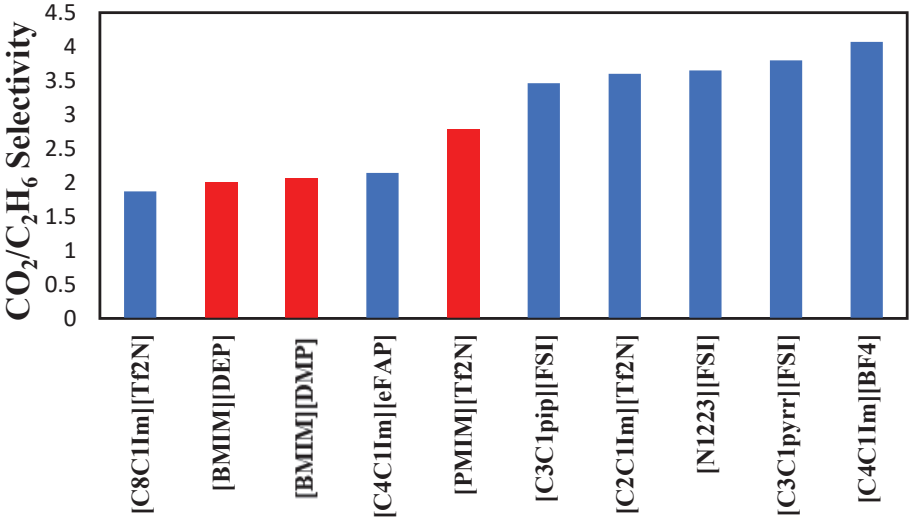

Figure 10. Comparison of CO_2/C_2H_6 selectivity with other ionic liquids reported by Nath et al. [12] at 343.15 K.

Table 6. CO_2/C_2H_6 selectivity of the ionic liquids used in this work.

	Temperature (K)		
	303.15	**323.15**	**343.15**
Solvents			
[HMIM][Tf2N]	2.47	2.32	2.07
[BMIM][DMP]	3.19	2.30	2.01
[PMIM][Tf2N]	3.87	2.98	2.79
Selexol	1.71	1.77	1.88

For a comprehensive comparison, we have added in the table data related to Selexol, a widely used and efficient physical solvent (a mixture of polyethylene glycol dimethyl ethers). Selectivity values were calculated based on values reported by Rayer et al. (2012) [14].

Overall, the ranking of the CO_2/C_2H_6 selectivity is the following: [PMIM][Tf2N] > [BMIM] [DMP] > [HMIM][Tf2N] > Selexol. As the highest selectivity is the one preferred, among the three ionic liquids studied, [PMIM][Tf2N] is considered the best. As shown below, these ILs do not possess the best selectivities among ionic liquids in the literature. Selexol seems to have the lowest selectivity compared to the ILs selected in this study. More details about the solvents in Figures 8–10 can be found in reference [12].

4. Materials and Methods

4.1. Materials

Table 7 lists the structures, acronyms, suppliers, purities, and water content of all of the solvents and solutes used in this study. The manufacturers of the chemicals provided the information related to the purities of the solvents listed in the same table.

Table 7. List of all the solvents and solutes used in this study, structures, acronyms, suppliers, purities, and water content.

Compounds	Structure	Abbreviation	Suppliers and Purities	Water Content
Ethane	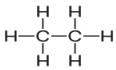	C_2H_6	Linde (Regina, SK, Canada) (99.99%)	-
1-Hexyl-3-methylimidazolium bis(trifluormethylsulfonyl)imide	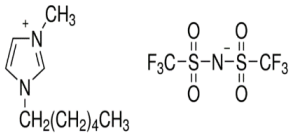	[HMIM][Tf2N]	Sigma-Aldrich (Oakville, ON, Canada) (≥98.0%)	-
1-Butyl-3-methylimidazolium dimethylphosphate	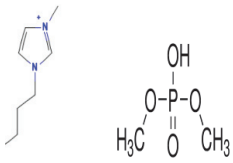	[BMIM][DMP]	IoLiTec (Heilbronn, Germany) (>98.0%)	<2500 ppm
1-Propyl-3-methylimidazolium Bis(trifluoromethylsulfonyl)imide	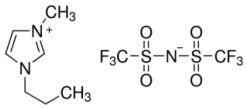	[PMIM][Tf2N]	Sigma-Aldrich (Oakville, ON, Canada) (≥99.0%)	≤0.5 wt%
1-Butyl-3-methylimidazolium hexafluorophosphate	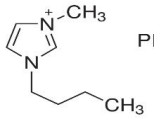	[BMIM][PF6]	Sigma-Aldrich (Oakville, ON, Canada) (≥97.0%)	-

4.2. Solubility Measurement

The gas solubility experiments were performed with the use of an IGA-003 (Intelligent Gravimetric Analyzer, Hidden Isochema Ltd., Warrington, UK). The machine measures the weight change of a liquid sample once a gas/gas mixture has been injected into the system. The IGA-003 can run at a maximum pressure and temperature of up to 2.0 MPa and 773.15 K, respectively.

For each isotherm experiment, around 50 to 90 mg of ionic liquid sample was inserted into the sample container to determine the solubility of the gas in the ionic liquid. A Grant water bath was used to regulate the temperature of the sample. For each experiment, the sample was degassed for around 10 h at high temperatures and under a deep vacuum before beginning the isotherm process to remove any contaminants that may have been in the sample. Throughout the degassing process, the temperature of the sample was kept constant at 349.15 K.

Once the sample weight stabilized after being degassed for over 10 h, the operating temperature was reduced to the isotherm condition using a Grant water bath. The ionic liquid sample was kept under this condition for at least an hour to ensure that the sample weight was at equilibrium. Once the weight of the sample has been stable, the isotherm process can be initiated by choosing a list of pressures at which the gas solubility is to be measured. Once all the necessary parameters have been selected in the IGA computer software (Version 2010), C_2H_6 is injected into the chamber using the mass flow controller (MFC). The system's pressure is kept constant at a pre-set pressure until the system reaches equilibrium. The IGA-003 records all real-time data, such as weight, temperature, and pressure.

Measurement of the density of the solvent is a required input in the experimental procedure. We reported the values of the densities of the 3 solvents in reference [13]. The density values decreased in the following order: [PMIM][Tf2N] > [HMIM][Tf2N] > [BMIM][DMP]. [BMIM][DMP] was reported to have a high viscosity value of 409.88 mPa·s at 303.15 K [13].

Figure 11 shows the setup for the IGA. Each instrument used in this work was numerically labelled. The setup consists of (1) a computer, (2) a microbalance, (3) a gas cylinder, (4) mass flow control, and (5) a water bath.

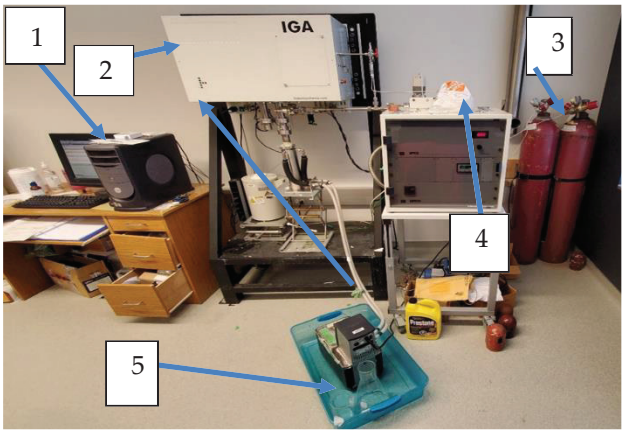

Figure 11. IGA-003 setup.

4.3. Thermodynamic Modeling

The solubility data of C_2H_6 in ILs obtained in this work were correlated using the Peng–Robinson equation of state (PR-EoS), shown in Equation (6) [15], where a_m is the intermolecular attractive force and b_m is the van der Waals co-volume factor. The PR-EoS combined with three different mixing rules was used to build this model. The three mixing rules are the following:

1. Single binary interaction parameter based on van der Waals one (vdW1);
2. Two binary interaction parameters based on van der Waals two (vdW2);
3. Wong–Sandler mixing rules combined with the NRTL model (WS-NRTL).

$$P = \frac{RT}{v - b_m} - \frac{a_m(T)}{v(v + b_m) + b_m(v - b_m)} \tag{6}$$

4.3.1. Van der Waals Mixing Rule

For this case, van der Waals created two different mixing rules to estimate mixture parameters (a_m and b_m): van der Waals one (vdW1) and van der Waals two (vdW2) [15–17]. In the vdW1 mixing rule, only one parameter (lij) is regressed, whereas, for vdW2, two binary interaction parameters are obtained (lij and kij). The parameter a_m for both vdW1 and vdW2 mixing rules was estimated using Equation (7). Using the temperature dependence binary interaction parameters, kij and aij can be estimated with Equation (10). The co-volume factor bm for both vdW1 and vdW2 is estimated with Equation (8) and Equation (9), respectively. Using the interaction parameter (lij), b_{ij} can be estimated with Equation (11).

$$a_m = \sum_i \sum_j x_i x_j a_{ij} \tag{7}$$

$$b_m = \sum_i x_i b_i \tag{8}$$

$$b_m = \sum_i \sum_j x_i x_j b_{ij} \tag{9}$$

where

$$a_{ij} = \sqrt{a_{ii} a_{jj}}\left(1 - k_{ij}\right) \tag{10}$$

$$b_{ij} = \frac{b_i + b_j}{2}\left(1 - l_{ij}\right) \tag{11}$$

where a_{ii} and a_{jj} are the pure component intermolecular attractive force parameter and b_i and b_j are the pure components co-volume factor parameters for the components (i and j).

4.3.2. Wong–Sandler Mixing Rule

The mixture's attractive force parameter, a, and co-volume parameter, b, can be calculated using Equations (12) and (13) [15], respectively, for Wong–Sandler mixing rules. In this paper, the Non-Random Two-Liquid (NRTL) model is utilized to approximate the activity coefficient and Excess Gibbs Energy (Equations (18)–(24)) [16]. The mixture parameters were estimated using three binary interaction parameters (k_{ij}, τ_{ij}, and τ_{ji}), where τ_{ij} and τ_{ji} are the NRTL parameters. The value of α_{ij} in Equations (19) and (20) were set at 0.3 arbitrarily in this work. The energies g_{ij} and g_{jj} are the energies of interaction between molecules 'i' and 'j' [17–19] and are calculated using Equations (21) and (22).

$$a = RT\frac{QD}{1-D} \tag{12}$$

$$b = \frac{Q}{1-D} \tag{13}$$

where

$$Q = \sum_i \sum_j x_i x_j \left(b - \frac{a}{RT}\right)_{ij} \tag{14}$$

$$D = \sum_i x_i \left(\frac{a_i}{b_i RT}\right) + \left(\frac{G^{ex}}{CRT}\right) \tag{15}$$

$$C = -\ln\left(\left(1+\sqrt{2}\right)/\sqrt{2}\right) \tag{16}$$

where $\left(b - \frac{a}{RT}\right)_{ij}$ in Equation (14) calculated using Equation (17):

$$\left(b - \frac{a}{RT}\right)_{ij} = \frac{1}{2}\left[\left(b_i - \frac{a_i}{RT}\right) + \left(b_j - \frac{a_j}{RT}\right)\right](1-k_{ij}) \tag{17}$$

$$\frac{G^{ex}}{RT} = x_i x_j \left(\frac{\tau_{ji}G_{ji}}{x_i + x_j G_{ji}} + \frac{\tau_{ij}G_{ij}}{x_j + x_i G_{ij}}\right) \tag{18}$$

$$G_{ij} = \exp\left(-\alpha_{ij}\tau_{ij}\right) \tag{19}$$

$$G_{ji} = \exp\left(-\alpha_{ij}\tau_{ji}\right) \tag{20}$$

$$\tau_{ij} = \left(g_{ij} - g_{jj}\right)/RT \tag{21}$$

$$\tau_{ji} = \left(g_{ji} - g_{ii}\right)/RT \tag{22}$$

$$\ln\gamma_i = x_j^2\left[\tau_{ji}\left(\frac{G_{ji}}{x_i + x_j G_{ji}}\right)^2 + \frac{\tau_{ij}G_{ij}}{\left(x_j + x_i G_{ij}\right)^2}\right] \tag{23}$$

$$\ln\gamma_j = x_i^2\left[\tau_{ij}\left(\frac{G_{ij}}{x_j + x_i G_{ij}}\right)^2 + \frac{\tau_{ji}G_{ji}}{\left(x_i + x_j G_{ji}\right)^2}\right] \tag{24}$$

4.4. Critical Properties Calculations

The critical parameters of the gas and the solvent examined must be known to be used in the model. The modified Lydersen–Joback–Reid group contribution method was used to determine the critical temperature (Tc), critical pressure (Pc), and the acentric factor (ω) of the ionic liquids in this study using the spreadsheet provided by Valderrama and Rojas [20]. Table 8 lists the critical properties determined for this study's three ionic liquids and C_2H_6.

Table 8. Molecular weights and critical properties of solutes and solvents used in this study.

Components	MW (g/mol)	T_c (K)	P_c (MPa)	ω
[HMIM][Tf2N]	447.4	1292.8	2.39	0.3893
[BMIM][DMP]	264.26	851	2.15	0.961
[PMIM][Tf2N]	405.3	1259.3	3.0	0.2575
C_2H_6	30.07	305.4	48.8	0.099

5. Conclusions

The purpose of this work was to screen three new ionic liquids, measuring their capacity to absorb C_2H_6 at pressures up to 1.4 MPa and at temperatures ranging from 293.15 K to 343.15 K. Thermodynamic properties such as the enthalpies and entropies of absorption are reported and the data used to determine the selectivity values.

The ionic liquids selected were [HMIM][Tf2N], [BMIM][DMP], and [PMIM][Tf2N]. In an earlier publication, we reported that the density values of the solvents decreased in the following order: [PMIM][Tf2N] > [HMIM][Tf2N] > [BMIM][DMP].

As co-absorption of ethane is important in natural gas processing, Henry's Law constants for C_2H_6 were estimated at 303.15 K, 323.15 K, and 343.15 K. As expected, they increased for all ILs as temperature increased. Overall, the ranking of the Henry's Law constants for C_2H_6 is the following: [BMIM][DMP] > [PMIM][Tf2N] > [HMIM][Tf2N] at all temperatures. [BMIM][DMP] is, therefore, found to be the IL that absorbs ethane the least. Compared to other ionic liquids, the three ionic liquids are not the best, but [BMIM][DMP] seems to be the best option. The order in the selectivity can be predicted based on the overall polarity number N and its calculated values obtained from reference [9].

The overall ranking of the CO_2/C_2H_6 selectivity is the following: [PMIM][Tf2N] > [BMIM] [DMP] > [HMIM][Tf2N] > Selexol. The most promising ionic liquid in terms of selectivity is therefore [PMIM][Tf2N]. Note that the three ionic liquids studied had better selectivity than Selexol, a widely used physical solvent in gas sweetening plants.

Solubility data were correlated using the Peng–Robinson equation of state (PR-EoS), and the binary interaction coefficients were reported. The average absolute deviations for the vdW1, vdW2, and WS-NRTL mixing rules when used in the ionic liquids for C_2H_6 were 4.39%, 2.45%, and 2.45%, respectively. The enthalpy and entropies of adsorption were calculated. Negative enthalpies were reported, indicating an exothermic process of absorption.

Author Contributions: Conceptualization, A.H.; methodology, N.H.; software, N.H.; validation, N.H.; formal analysis, N.H.; investigation, N.H.; resources, A.H.; data curation, N.H.; writing—original draft preparation, N.H.; writing—review and editing, A.H. and H.I.; visualization, N.H.; supervision, H.I. and A.H.; project administration, A.H.; funding acquisition, A.H. All authors have read and agreed to the published version of the manuscript.

Funding: This research was funded by the Natural Sciences and Engineering Research Council of Canada (NSERC) under a Discovery Grant number (RGPIN-06805-2018).

Data Availability Statement: All experimental data acquired are reported in the manuscript.

Acknowledgments: The first author would like to thank Devjyoti Nath for training him on the microbalance instrument and for his help in modeling the data.

Conflicts of Interest: The authors declare no conflicts of interest. The funding agency had no role in the design of the study; in the collection, analysis, or interpretation of data; in the writing of the manuscript; or in the decision to publish the results.

Nomenclature

AAD	Average absolute deviation
$[BF_4]$	Tetrafluoroborate
[BMIM][DMP]	1-Butyl-3-methyl-imidazolium dimethyl-phosphate
[N1223][FSI]	N-propyl-n-methyl-n,n-dimethyl-ammonium bis(fluorosulfonyl)imide
[C3C1PIP][FSI]	N-propyl-n-methyl-piperidinium bis(fluorosulfonyl)imide
[C3C1Pyrr][FSI]	1-Methyl-1-propylpyrrolidinium bis(fluorosulfonyl)imide
[C4C1Im] [BF4]	1-Butyl-3-methylimidazolium tetrafluoroborate
CO_2	Carbon dioxide
C_2H_6	Ethane
DCN	Dicyanamide
EoS	Equation of state
[FSI]	Bis(fluorosulfonyl)imide
H	Henry's Law constant
[HMIM][Tf2N]	1-Hexyl-3-methylimidazolium bis(trifluormethylsulfonyl)imide
IGA	Intelligent Gravimetric Analyzer
ILs	Ionic liquids
K	Kelvin
MDEA	Methyldiethanolamine
MEA	Monoethanolamine
P_c	Critical pressure
PF_6	Hexafluoro-phosphate
[PMIM][Tf2N]	1-Propyl-3-methylimidazolium bis(trifluoromethyl-sulfonyl)-imide
PR	Peng–Robinson
RSO4	Alkylsulfate
T_b	Boiling point temperature
T_c	Critical temperature
vdW1	van der Waals one
vdW2	van der Waals two
WS-NRTL	Wong–Sandler mixing rules + Non-Random Two-Liquid model
x	Liquid mole fraction (moles gas/moles gas + moles solVent)
y	Vapor mole fraction
Z_c	Critical compressibility factor

References

1. Energy Information Administration (EIA). U.S. Primary Energy Consumption by Energy Source. 2024. Available online: https://www.eia.gov/energyexplained/us-energy-facts/ (accessed on 22 July 2024).
2. National Oceanic and Atmospheric Administration. During a Year of Extremes, Carbon Dioxide Levels Surge Faster than Ever. 2024. Available online: https://www.noaa.gov/news-release/during-year-of-extremes-carbon-dioxide-levels-surge-faster-than-ever (accessed on 22 July 2024).
3. National Oceanic and Atmospheric Administration. 2023 Was the World's Warmest Year on Record, by Far. 2024. Available online: https://www.ncei.noaa.gov/access/monitoring/monthly-report/global/202313#:~:text=The%20year%202023%20was%20the,decade%20(2014%E2%80%932023) (accessed on 22 July 2024).
4. International Energy Agency (IEA). World Energy Outlook. 2023. Available online: https://iea.blob.core.windows.net/assets/86ede39e-4436-42d7-ba2a-edf61467e070/WorldEnergyOutlook2023.pdf (accessed on 22 July 2024).
5. Nath, D.; Henni, A. Solubility of carbon dioxide (CO_2) in four bis (trifluoromethyl-sulfonyl)imide ([Tf2N]) based ionic liquids. *Fluid Phase Equilibria* **2020**, *524*, 112757. [CrossRef]
6. Anthony, J.L.; Anderson, E.J.; Maginn, E.J.; Brennecke, J.F. Anion effects on gas solubility in ionic liquids. *J. Phys. Chem. B* **2005**, *109*, 6366–6374. [CrossRef] [PubMed]
7. Zoubeik, M.; Henni, A. Experimental and thermodynamic study of CO_2 solubility in promising [Tf2N and DCN] ionic liquids. *Fluid Phase Equilibria* **2014**, *376*, 22–30. [CrossRef]
8. Tagiuri, A.; Sumon, K.Z.; Henni, A. Solubility of carbon dioxide in three [Tf2N] ionic liquids. *Fluid Phase Equilibria* **2014**, *380*, 39–47. [CrossRef]
9. Sumon, Z.K.; Henni, A. Ionic liquids for CO_2 capture using COSMO-RS: Effect of structure, properties and molecular interactions on solubility and selectivity. *Fluid Phase Equilibria* **2011**, *310*, 39–55. [CrossRef]
10. Tagiuri, A. Studies of Solubility of CO_2 in Ionic Liquids, Kinetics, and Heat of Reactions in Promising Cyclic Amines. Ph.D. Thesis, University of Regina, Regina, SK, Canada, 2019.

11. Costa Gomes, M.F. Low-pressure solubility and thermodynamics of solvation of carbon dioxide, ethane, and hydrogen in 1-hexyl-3-methylimidazolium bis(trifluoromethylsulfonyl)amide between temperatures of 283 K and 343 K. *J. Chem. Eng. Data* **2007**, *52*, 472–475. [CrossRef]
12. Nath, D.; Sumon, S.K.; Tagiuri, A.; Henni, A. Effect of cation on the solubility of ethane in three bis(fluorosulfonyl)imide ([FSI]) based low viscosity ionic liquids. *Fluid Phase Equilibria* **2017**, *454*, 78–90. [CrossRef]
13. Henni, N.; Henni, A.; Ibrahim, H. Solubility of carbon dioxide in promising methylimidazolium-based ionic liquids. *Fluid Phase Equilibria* **2023**, *565*, 13619. [CrossRef]
14. Rayer, A.V.; Henni, A.; Tontiwachwuthikul, P. High-Pressure Solubility of Methane (CH4) and Ethane (C2H6) in Mixed Polyethylene Glycol Dimethyl Ethers (Genosorb 1753) and Its Selectivity in Natural Gas Sweetening Operations. *J. Chem. Eng. Data* **2012**, *57*, 764–775. [CrossRef]
15. Peng, D.Y.; Robinson, D.B. A New Two-Constant Equation of State. *Ind. Eng. Chem. Fundam.* **1976**, *15*, 59–64. [CrossRef]
16. Renon, H.; Prausnitz, J.M. Local compositions in thermodynamic excess functions for liquid mixtures. *AIChE J.* **1968**, *14*, 135–144. [CrossRef]
17. Orbey, H.; Sandler, S.I. *Modeling Vapor-Liquid Equilibria: Cubic Equations of State and Their Mixing Rules*; Cambridge University Press: Cambridge, UK, 1998.
18. Eslamimanesh, A.; Mohammadi, A.H.; Salamat, Y.; Shojaei, M.-J.; Eskandari, S.; Richon, D. Phase behavior of mixture of supercritical CO_2+ionic liquid: Thermodynamic consistency test of experimental data. *AIChE J.* **2013**, *59*, 3892–3913. [CrossRef]
19. Lee, M.-T.; Lin, S.-T. Prediction of mixture vapor–liquid equilibrium from the combined use of Peng–Robinson equation of state and COSMO-SAC activity coefficient model through the Wong–Sandler mixing rule. *Fluid Phase Equilibria* **2007**, *254*, 28–34. [CrossRef]
20. Valderrama, J.O.; Rojas, R.E. Critical properties of ionic liquids. Revisited. *Ind. Eng. Chem. Res.* **2009**, *48*, 6890–6900. [CrossRef]

Disclaimer/Publisher's Note: The statements, opinions and data contained in all publications are solely those of the individual author(s) and contributor(s) and not of MDPI and/or the editor(s). MDPI and/or the editor(s) disclaim responsibility for any injury to people or property resulting from any ideas, methods, instructions or products referred to in the content.

molecules

MDPI

Article

Tuning Ferulic Acid Solubility in Choline-Chloride- and Betaine-Based Deep Eutectic Solvents: Experimental Determination and Machine Learning Modeling

Tomasz Jeliński [1], Maciej Przybyłek [1], Rafał Różalski [2], Karolina Romanek [1], Daniel Wielewski [1] and Piotr Cysewski [1,*]

[1] Department of Physical Chemistry, Faculty of Pharmacy, Collegium Medicum in Bydgoszcz, Nicolaus Copernicus University in Toruń, Kurpińskiego 5, 85-096 Bydgoszcz, Poland; tomasz.jelinski@cm.umk.pl (T.J.); m.przybylek@cm.umk.pl (M.P.)

[2] Department of Clinical Biochemistry, Faculty of Pharmacy, Collegium Medicum in Bydgoszcz, Nicolaus Copernicus University in Toruń, Karłowicza 24, 85-950 Bydgoszcz, Poland; rafalr@cm.umk.pl

* Correspondence: piotr.cysewski@cm.umk.pl

Abstract: Deep eutectic solvents (DES) represent a promising class of green solvents, offering particular utility in the extraction and development of new formulations of natural compounds such as ferulic acid (FA). The experimental phase of the study undertook a systematic investigation of the solubility of FA in DES, comprising choline chloride or betaine as hydrogen bond acceptors and six different polyols as hydrogen bond donors. The results demonstrated that solvents based on choline chloride were more effective than those based on betaine. The optimal ratio of hydrogen bond acceptors to donors was found to be 1:2 molar. The addition of water to the DES resulted in a notable enhancement in the solubility of FA. Among the polyols tested, triethylene glycol was the most effective. Hence, DES composed of choline chloride and triethylene glycol (TEG) (1:2) with added water in a 0.3 molar ration is suggested as an efficient alternative to traditional organic solvents like DMSO. In the second part of this report, the affinities of FA in saturated solutions were computed for solute-solute and all solute-solvent pairs. It was found that self-association of FA leads to a cyclic structure of the C_2^8 type, common among carboxylic acids, which is the strongest type of FA affinity. On the other hand, among all hetero-molecular bi-complexes, the most stable is the FA-TEG pair, which is an interesting congruency with the high solubility of FA in TEG containing liquids. Finally, this work combined COSMO-RS modeling with machine learning for the development of a model predicting ferulic acid solubility in a wide range of solvents, including not only DES but also classical neat and binary mixtures. A machine learning protocol developed a highly accurate model for predicting FA solubility, significantly outperforming the COSMO-RS approach. Based on the obtained results, it is recommended to use the support vector regressor (SVR) for screening new dissolution media as it is not only accurate but also has sound generalization to new systems.

Keywords: ferulic acid; solubility; deep eutectic solvents; green solvents; molecular interactions; COSMO-RS; machine learning; support vector regressor

1. Introduction

Ferulic acid, a phenolic compound abundant in various plant tissues [1], has emerged as a captivating subject of scientific inquiry [2,3] and industrial interest [4,5], while as a component of traditional Chinese medicinal herbs, it has been used for centuries [6]. Chemically, it is a 4-hydroxy-3-methoxycinnamic acid, belonging to the wide group of phenolic acids. Its molecular structure is characterized by a phenolic ring with a hydroxyl group and a methoxy group, and can exist in both *cis* and *trans* forms [2]. Ferulic acid exhibits a plethora of biological activities that are the result of this unique structure. First of all, it is well known as an antioxidant agent [7,8]. Specifically, the hydroxyl and methoxy groups on the benzene

ring are capable of donating hydrogen atoms to free radicals, thereby neutralizing their harmful effects and preventing oxidative damage to cells and tissues [9,10]. Additionally, ferulic acid can chelate metal ions involved in oxidative processes, further inhibiting the generation of reactive oxygen species (ROS) [11,12]. Secondly, ferulic acid exhibits anti-inflammatory properties through various mechanisms of action. One significant mechanism involves its ability to inhibit the activity of pro-inflammatory enzymes, such as cyclooxygenase (COX) and lipoxygenase (LOX), which are involved in the production of inflammatory mediators like prostaglandins and leukotrienes [13–15]. Additionally, ferulic acid can suppress the expression of pro-inflammatory genes and cytokines, such as tumor necrosis factor-alpha (TNF-α) and interleukins, which play key roles in promoting inflammation [16,17]. The beneficial actions of this compound do not end here and include the protection of vascular endothelial cells [18,19], anti-fibrosis effect [20,21], anti-apoptotic effect [22,23], anti-platelet effect [24,25], and others [26,27]. In general, ferulic acid from dietary sources and oral administration has low bioavailability due to factors like limited absorption in the gastrointestinal tract and rapid metabolism in the liver [28,29]. However, certain formulations or delivery systems, such as lipid-based formulations or nanostructured carriers, can improve its bioavailability [30,31]. Additionally, co-administration with other compounds, such as piperine or quercetin, may further increase the bioavailability of ferulic acid [32,33]. On the other hand, ferulic acid is well absorbed by the skin through cutaneous administration [34,35], which makes it widely used in the cosmetics industry [36–38].

The importance of solubility in pharmaceutical applications cannot be overstated, as it serves as a critical determinant influencing the efficacy, safety, and overall success of drug development and delivery [39–41]. Solubility profoundly impacts various stages of the pharmaceutical lifecycle, from initial drug formulation to therapeutic administration [42–44]. The ability of a compound to dissolve in a solvent directly influences its bioavailability, governing the rate and extent of absorption into the bloodstream and, consequently, its therapeutic effectiveness [45,46]. Furthermore, solubility plays a pivotal role in the stability of drug formulations, affecting factors such as shelf life and storage conditions [47,48]. Challenges arising from poor solubility necessitate higher doses to achieve therapeutic levels, potentially increasing the risk of adverse effects [49–51]. Therefore, understanding, predicting, and manipulating the solubility of drug molecules are essential endeavors for pharmaceutical scientists [52–57]. Various techniques, including salt formation, co-solvent systems, and nanoparticle delivery systems, are employed to enhance solubility and optimize drug performance [58–61]. However, experimental efforts are not the only means aimed at the development of safer and more efficient medications. Accurate solubility modeling and predictions aid in the selection of promising drug candidates, formulation optimization, and the design of more effective drug delivery systems [39,62–64].

The "green chemistry" approach [65,66], representing a paradigm shift in chemical research and industry and aiming to design and implement processes that minimize environmental impact and maximize sustainability, has been extremely useful also in the realm of pharmaceuticals [67,68]. As stated, solvents play a crucial role in various chemical processes, yet traditional organic solvents often pose significant environmental and health hazards. Therefore, green chemistry emphasizes the development and utilization of alternative solvents with minimal environmental impact [69,70]. An important class of these new solvents, combining environmental safety with high solubilization efficiency, are deep eutectic solvents (DESs) [71,72]. Defined as mixtures of two or more components that form a eutectic mixture with a melting point significantly lower than that of either individual component [73,74], DESs offer several advantages over conventional solvents, including low toxicity, biodegradability, and tunable physicochemical characteristics [75–77]. These properties contribute to the widespread use of eutectic solvent systems, also in the pharmaceutical field [78–85]. It is worth noting that DESs, due to their unique properties, are utilized in the extraction of phenolic compounds, including phenolic acids [86], which suggests they may exhibit significant affinity for ferulic acid. The aim of this work is to expand the knowledge of the solubility of the compound in question in DESs and to interpret the obtained results based on molecular modeling supported by machine learning.

2. Results and Discussion

2.1. Solubility of Ferulic Acid in DESs and DES–Water Mixtures

In the experimental part of the study, deep eutectic solvents were applied to solubilize ferulic acid. While DESs are known for being very effective solubilizers of many compounds, the addition of water to these systems can improve solubility even further [82,87], which was the reason for also including the aqueous mixtures of DESs in the study. The solubility of various compounds in water is usually intensely lower than in the eutectic systems, and the addition of excess amounts of water to the DES systems results in a decrease in the solubility of the considered solute. In this concentration range water can be considered an anti-solvent for DESs. However, small amounts of added water tend to promote the solubility of such a solute. The origins of the observed phenomenon are complex and involve the formation of nanostructures of DES components and water molecules [88,89]. In particular, the stabilization nano-structure around choline chloride or other hydrogen bond acceptor (HBA) components of DESs play an important role [88]. These clusters are remarkably stable, even at modest dilutions. This complex behavior indicates that aqueous–DES mixtures cannot be regarded as typical antisolvent–cosolvent systems, although the favorable effect of the addition of water is still practically valuable and worth in-depth exploration. Here, an extensive search for the optimal water–DES solvent was performed while tuning ferulic acid solubility. In the first phase of experiments, the FA solubility was determined in pure DES systems. These DESs comprised either choline chloride (ChCl) or betaine (BI), both acting as hydrogen bond acceptors (HBA), and one of six polyols, namely ethylene glycol (ETG), diethylene glycol (DEG), triethylene glycol (TEG), 1,3-butanediol (B3D), 1,2-propanediol (P2D), and glycerol (GLY), acting as hydrogen bond donors (HBD). Three molar ratios of HBA to HBD were tested, i.e., 1:1, 1:2, and 1:4. All of the measurements at this screening phase were conducted at 25 °C.

The obtained results show that in general, DESs based on choline chloride are more efficient solubilizers of FA than those comprised of betaine. Nonetheless, the results present a similar overview, regardless of whether ChCl or BI were used as HBAs. When analyzing the molar compositions of the tested systems, it turns out that the 1:2 HBA–HBD molar ratio performs best, followed by the 1:4 ratio, with the 1:1 ratio being the least effective. This general observation is only altered in a few cases in the systems with betaine, where the 1:4 molar ratio outperforms some of the 1:2 systems. The comparison of the effectiveness of individual HBDs reveals differences between systems with choline chloride and betaine. When ChCl is used, the decreasing order of FA solubility is obtained, regardless of the molar ratio of DES constituents: TEG > DEG > GLY > ETG > B3D > P2D. Slightly more complex behavior is observed for systems utilizing betaine. For the optimal 1:2 molar composition, the following trend is obtained: TEG > GLY > DEG > ETG > B3D > P2D. Rather surprisingly, in the 1:4 molar composition, the DES prepared using B3D is the second most effective system, with the one using ETG being the least effective. Overall, it seems that three HBDs stand out as being the most promising, i.e., triethylene glycol, diethylene glycol, and glycerol. The ChCl-TEG eutectic system in a 1:2 molar proportion was the most effective DES among the studied formulations. At 25 °C, the solubility of ferulic acid was found to be x_{FA} = 0.0532. Using the ChCl-DEG system resulted in an FA solubility of x_{FA} = 0.0494, closely followed by the ChCl-GLY eutectic, characterized by x_{FA} = 0.0485. DES formulations with betaine were less efficient in terms of FA solubilization, and the top three systems, namely BI-TEG, BI-DEG, and BI-GLY, were responsible for ferulic acid solubilities of x_{FA} = 0.0432, x_{FA} = 0.0401, and x_{FA} = 0.0392 at 25 °C. Detailed results of FA solubility determination in the studied systems are presented in the Supplementary Materials (please refer to Table S1).

The obtained solubility values of FA in pure DESs served as a starting point for selecting the most promising eutectic systems, which would be used to form aqueous mixtures. Two systems utilizing choline chloride were selected along with two containing betaine, namely ChCl-TEG, ChCl-DEG, BI-TEG, and BI-GLY. The created ternary mixtures were characterized by different amounts of the DES, expressed as its mole fraction in a solute-free

solution. The solubility of FA in such systems was measured at four temperatures in the range of 25 °C to 40 °C.

As it was expected based on previous experiences, small amounts of water added to the eutectic solvent increase the solubility of ferulic acid. As stated, the nature of DES–water systems is complex. However, it is useful to describe their behavior at least as an apparent cosolvency/antisolvency effect. The solubility curves, describing the mole fraction solubility of FA as a function of the composition of ternary aqueous DES mixtures, are presented in Figure 1. The increasing amount of DES in its aqueous mixture leads to the increase of the solubility of ferulic acid, however, after a certain point, which represents the most effective composition, solubility starts to decrease. The composition characterizing the mixture yielding the highest FA solubility corresponds with the molar composition of $x^*_{DES} = 0.7$ in the aqueous mixture. This observation holds for systems using both choline chloride and betaine at all studied temperatures. In the case of the mixture based on the ChCl-TEG eutectic, the solubility of ferulic acid at the optimal composition equaled $x_{FA} = 0.0588$ at 25 °C, which is 112% of the FA solubility in the pure eutectic solvent. For the second-most effective DES, namely ChCl-DEG, the FA solubility was found to be $x_{FA} = 0.0532$ at 25 °C, which corresponds to 108% of the FA solubility in the DES itself. For the aqueous mixtures of eutectics comprising betaine, the BI-TEG and BI-GLY systems were characterized with the solubility of ferulic acid equal $x_{FA} = 0.0494$ and $x_{FA} = 0.0459$, respectively, at 25 °C and at the optimal composition, which stands for about 114% of the water-free DES solubility. Additionally, to no surprise, the elevated temperature of the measurements resulted in increased solubility of ferulic acid. This increase was rather stable, and the difference between the solubility at 25 °C and at 40 °C amounted to around 20% regardless of the eutectic type and aqueous mixture composition. Detailed solubility values are again provided in Supplementary Materials (please refer to Tables S2 and S3).

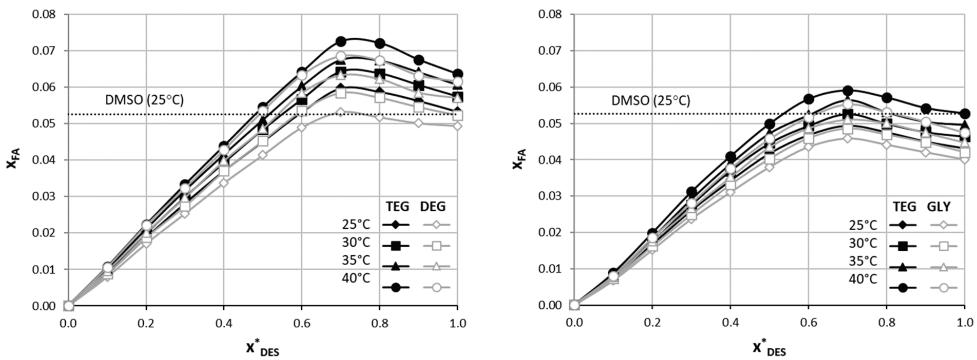

Figure 1. The solubility curves of ferulic acid (FA) in aqueous DES mixtures involving choline chloride (**left panel**) and betaine (**right panel**) and selected polyols at various temperatures, expressed as solvent-composition-related mole fractions. X^*_{DES} stands for mole fractions of solute-free DES in aqueous mixtures. For comparison, the room-temperature solubility of ferulic acid in DMSO is provided.

The obtained results are worth comparing to solubility data available in the literature. The solubility of ferulic acid was studied in several systems, including water [90,91]; ethyl lactate and its mixtures with water [92]; isopropanol and its aqueous mixtures [93]; and a number of organic solvents, such as DMSO, trascutol, methanol, and ethyl acetate [91,94]. When considering these data, the following decreasing order of FA solubility (measured at 25 °C) in various neat solvents can be obtained: DMSO ($x_{FA} = 0.0526$) > transcutol ($x_{FA} = 0.0430$) > methanol ($x_{FA} = 0.0295$) > propylene glycol ($x_{FA} = 0.026$)3 > ethanol ($x_{FA} = 0.0254$) > ethylene glycol ($x_{FA} = 0.0207$) > isopropanol ($x_{FA} = 0.0194$) > 2-propanol ($x_{FA} = 0.0188$) > 2-butanol ($x_{FA} = 0.0168$) > 1-butanol ($x_{FA} = 0.0161$) > ethyl acetate ($x_{FA} = 0.0130$) > water ($x_{FA} = 0.000049$). In the above context, it turns out that among the neat DESs, only the ChCl-TEG 1:2 system offers a slightly better FA solubility than the most efficient classical solvent, namely DMSO, with the ChCl-DEG 1:2, ChCl-GLY 1:2, ChCl-ETG 1:2, and ChCl-TEG 1:4 systems being slightly less effective although outperforming the second classical solvent, which is transcutol. Among the systems with betaine, only the BI-TEG

1:2 system performed better than transcutol. The addition of water to the selected eutectics increased the FA solubility. Thus, the ChCl-TEG 1:2 (x^*_{DES} = 0.7) and ChCl-DEG 1:2 (x^*_{DES} = 0.7) systems gave higher solubility than DMSO, with the BI-TEG 1:2 (x^*_{DES} = 0.7) being close to that.

2.2. Ferulic Acid Intermolecular Interactions in DES

The determination of the structure of ferulic acid in its monomeric form was the starting point of the computational procedure. Within a 5 kcal/mol energy window, three of the most stable and distinct conformers were identified, as schematically presented in Figure 2, where the relative energy values corresponding to the RI-BP97/def2-SVPD//RI-BP/def2-TZVPD-FINE level of theory were included. It is noteworthy that the most stable conformers differ in the orientation of the hydroxyl group connected to the aromatic ring or the hydroxyl group that is part of the carboxylic substituent. The most stable conformer forms an intramolecular hydrogen bond between the hydroxyl and methoxy groups. Through comparison with the second conformer, it can be inferred that this type of interaction contributes approximately 1.9 kcal/mol to intramolecular stabilization. The third conformer is similar to the first one but has an anti-rotated hydroxyl group in the carboxylic moiety, resulting in an energy increase of about 2.0 kcal/mol. The order of conformers remains consistent in both the bulk phase and vacuum.

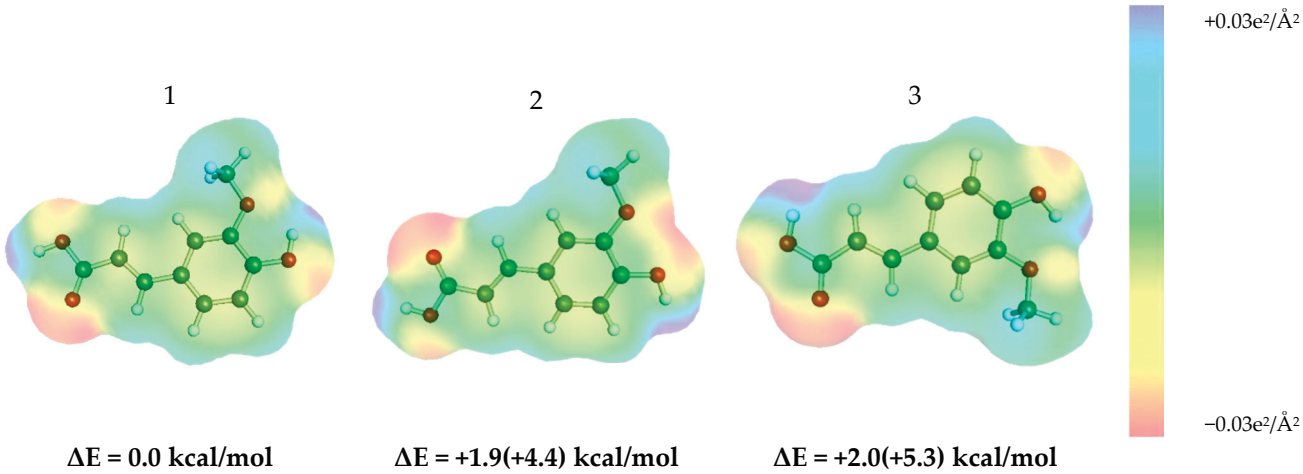

Figure 2. Schematic representation of ferulic acid conformers with electron density distributions and their relative energies in the bulk state, represented by an infinite conductor. Additionally, in parentheses are the relative values of total energies obtained for the gas phase.

The study of intermolecular interactions with DES constituents involved pairing each conformer of ferulic acid and minimizing the supermolecule energy. The most representative results are presented in Figures 3 and 4. The affinities of ferulic acid in the studied DES were expressed using the concentration-independent standard Gibbs free energy values ($\Delta G^o_a = RTln(a^o)$) for the corresponding pair formation reactions at ambient conditions (T = 298.15 K). The subscript "a" indicates the use of mole fraction values corrected with activity coefficients, $a^o_i = x^o_i \cdot f^o_i$. This expression method is convenient, as it characterizes the thermodynamic propensity of interacting components regardless of the solvent environment. It is expected that the self-association behavior of ferulic acid is consistent across all systems, independent of the content and mole fractions of the components. Indeed, ferulic acid shows a strong propensity for self-aggregation, which can be inferred from the dimer structure and standard Gibbs free energy values, indicating the highest affinity among all studied pairs, as shown in Figures 3 and 4. The FA dimer is stabilized by strong bidirectional hydrogen bonds forming a cyclic structure of the C^8_2 type, common for all carboxylic acids. Additionally, the carboxylic group in FA acts as a strong proton donor, directly contributing to the stabilization of both FA-ChCl and FA-BI pairs. Interestingly,

two types of structural motifs were identified. The first type involves the third stable conformer of monomeric FA, where the energy disfavor of this conformer is compensated by non-polar interactions of ChCl or BI with the delocalized electrons of the aromatic ring, making these pairs the most stable. In the case of choline chloride, an alternative structure is stabilized by interactions with the hydrogen carboxylic group. Betaine, having a non-neutralized acetate group, cannot form stable pairs of this type and instead interacts with the hydroxyl group in the para position of FA. Notably, the affinity of FA to BI is significantly stronger compared to ChCl. Interactions between FA and water are much weaker and primarily involve hydrogen bonding with the carboxylic or hydroxyl groups. These observations suggest that the variety of potential contacts between FA and DES constituents might account for the high solvation abilities and consequently high solubility promoted by strong solute–solvent interactions.

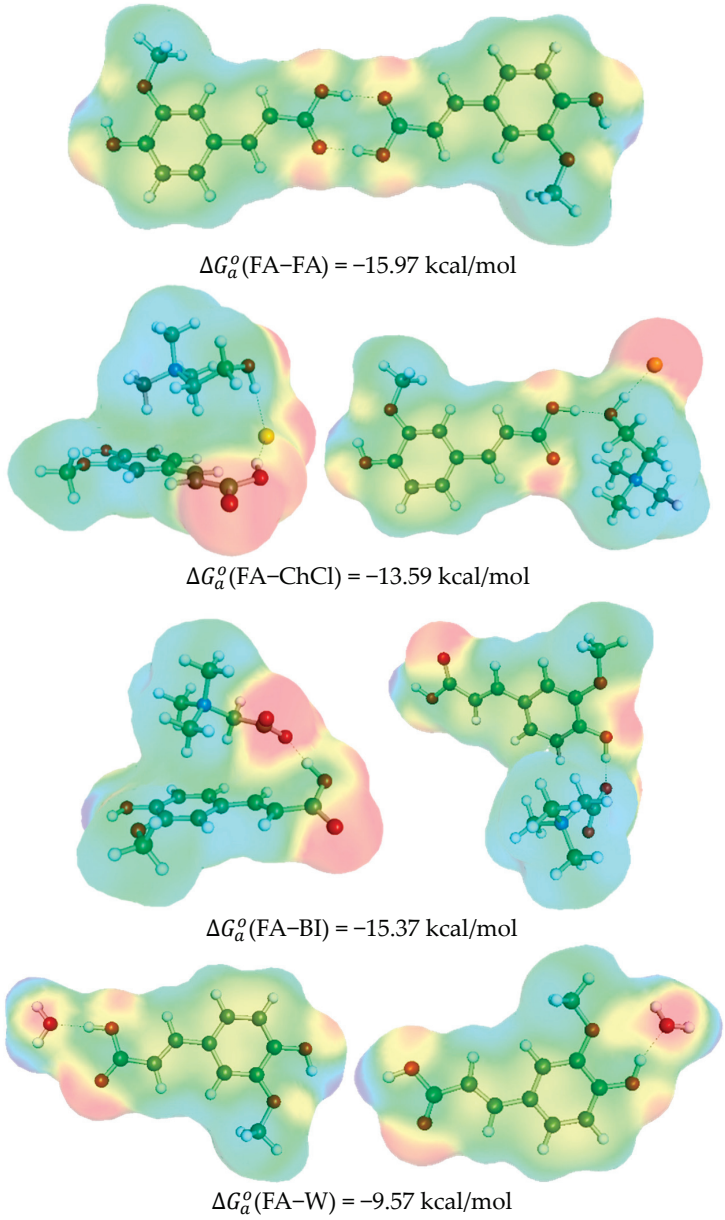

Figure 3. The most representative structures of FA dimers and hetero-molecular pairs formed with choline chloride, betaine, and water.

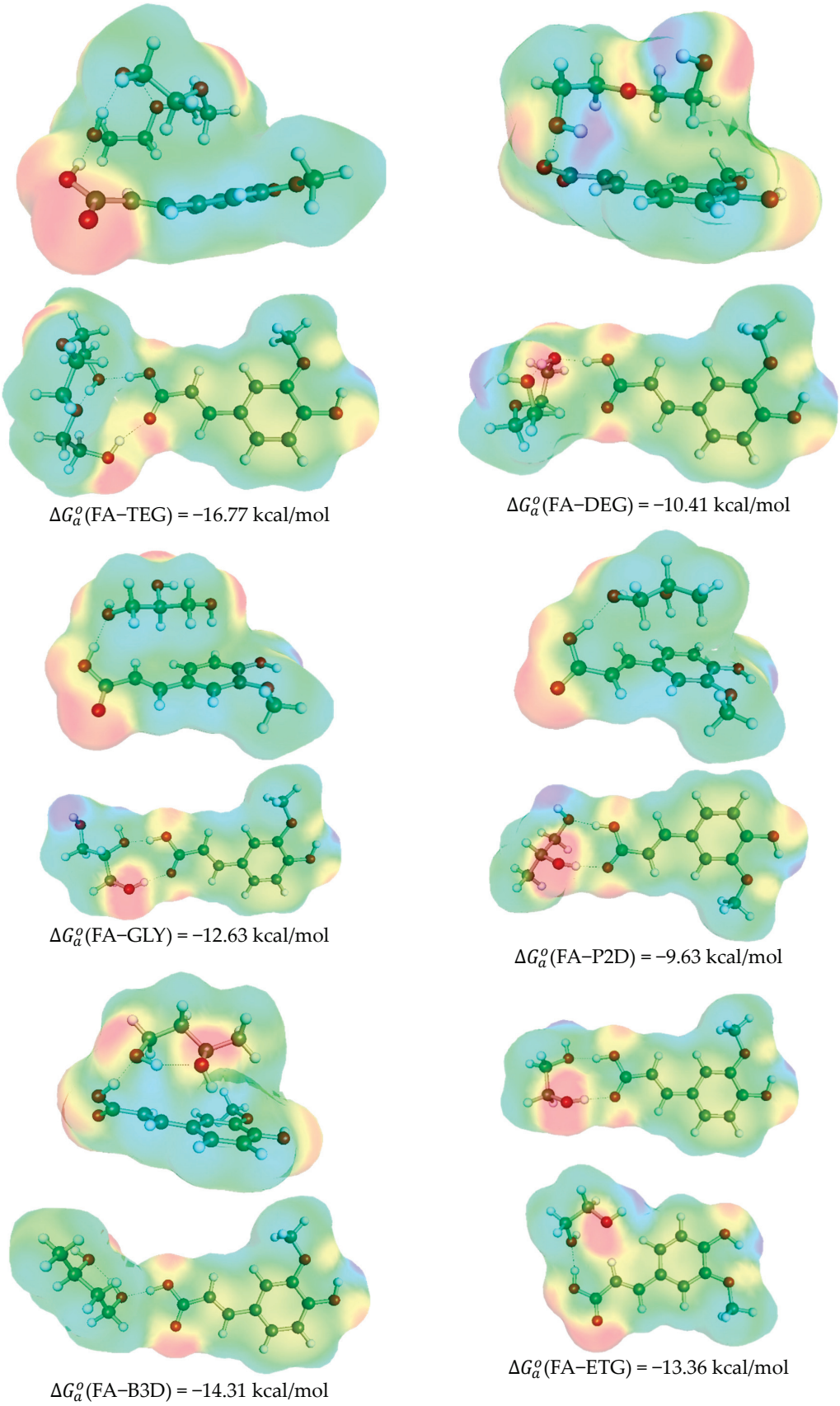

Figure 4. The most representative structures of FA with HBD counterparts of studied DESs.

Ferulic acid can also form stable pairs with all the hydrogen bond donor (HBD) counterparts of the DESs studied here. It is noteworthy that all polyols form two distinct motifs involving direct contact with the carboxylic group. In all cases, similarly to FA-ChCl interactions, the rotation of the hydroxyl group within the carboxylic moiety into the anti-position allows for additional interactions with the delocalized aromatic electron clouds. This behavior is observed for all polyols except ethylene glycol (ETG), which—due to its shortest chain—is unable to adopt a similar position to other proton-donating constituents. This prevents ETG from positioning above the aromatic ring of FA, making a structure stabilized by two hydrogen bonds the most probable configuration.

In all other cases, the non-polar interactions involving the aromatic electron cloud play a crucial role. These interactions not only offset the energy increase caused by the distortion of the carboxylic group but also contribute significantly to the overall stability of the structure. Notably, the highest affinity of FA was found for triethylene glycol (TEG), which correlates well with the highest solubility of FA in DESs containing this polyol regardless of the type of DBA. However, a linear trend between solubility and affinity values is not generally observed, suggesting that other factors contribute to the stabilization of the saturated FA-DES systems.

2.3. Machine Learning Model

Solubility measurements, though simple, are time-consuming experiments with several tricky steps, particularly when using DES as dissolution media. This complexity hinders the exhaustive search for new solvents, given the vast number of potential HBA-HBD combinations, along with concentration and temperature dependencies. Consequently, theoretical exploration of the solvent hyperspace to support experimental screening of the most suitable deep eutectic solvents including therapeutic variants (THEDES) is of significant practical value. In this study, a machine learning approach was employed, conducting an exhaustive search for models with the highest accuracy and predictive potential. A diverse set of non-linear regressors was tested for this purpose.

The training dataset comprised ferulic acid solubility values, including newly measured results for this study and previously published data. This dataset, the largest available at present, offers substantial structural diversity of solvents, which is a promising indicator for the generalization of the obtained model. The dataset (N = 344) includes mole fraction solubility values of FA in neat solvents (11 systems, N = 103), binary mixtures (1 system, N = 45), and DES (all presented in this paper, N = 196). The models were trained on a training subset (two-thirds of the entire set) by tuning the adjustable parameters of each regressor.

It is crucial to note that metrics such as mean absolute error (MAE) or the correlation coefficient (R^2) were not the sole criteria for model accuracy. As mentioned in the methodology section, potential generalization was incorporated into the scoring function as a penalty derived from learning curve analysis (LCA) using scikit-learn. This approach evaluates model performance by increasing the percentage of included data and performing 10-fold cross-validation. This procedure, conducted separately for training and cross-validation subsets, provides comprehensive diagnostics by assessing the risk of overfitting and quantifying the models' sensitivity to the used data. Although computationally expensive, this method ensures a thorough evaluation of the model.

Models characterized by low MAE, high R^2, and failure to meet generalization criteria as revealed by LCA should be approached with caution. Indeed, this was observed in the best-performing model found in this study. As anticipated, utilizing artificial neural networks can lead to models capable of accurately back-computing experimental data. Multi-layer perceptrons (MLPs) were trained, allowing for flexible adjustment of network architecture to excel in capturing non-linear relationships. MLPRegressor, particularly adept at learning complex patterns through interconnected layers of neurons, demonstrated impressive accuracy. Figure 5 presents the accuracy of this regressor model, alongside other computations, including the second-best model, SVR, and solubility predictions based on the COSMO-RS approach. Two important conclusions can be drawn from this

figure. Firstly, the native COSMO-RS results only qualitatively agree with experimental data, predicting general trends but not actual mole fraction solubility. The RMSD (root mean square deviation) and MAPE (mean absolute percentage error) for logarithmic mole fraction values are as high as 0.6 and 54.6%, respectively, which are significantly worse values compared to MLP and SVR, which had values of 0.025 (1.6%) and 0.061 (4.97%), respectively. Secondly, the predictions of both presented models are acceptable, though MLP outperforms SVR. However, the optimal architecture of the MLP network, optimized during the learning process, adopts a highly complex structure consisting of 13 hidden layers. The details of the optimized hyperparameters are provided in Figure 6.

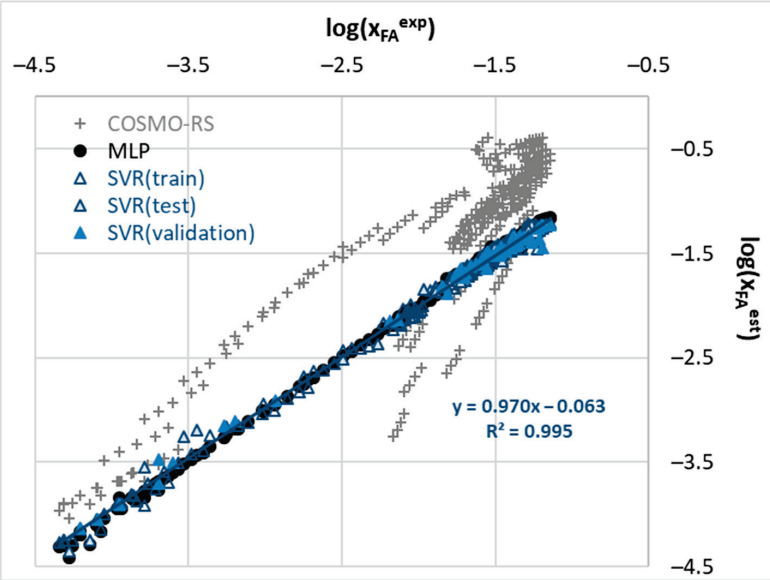

Figure 5. The correlation between experimental and computed solubility of ferulic acid in neat, binary, and deep eutectic solvents. The gray color denotes the results of COSMO-RS computations, blue indicates the SVR model, and in black, the results obtained from the MLP model are marked.

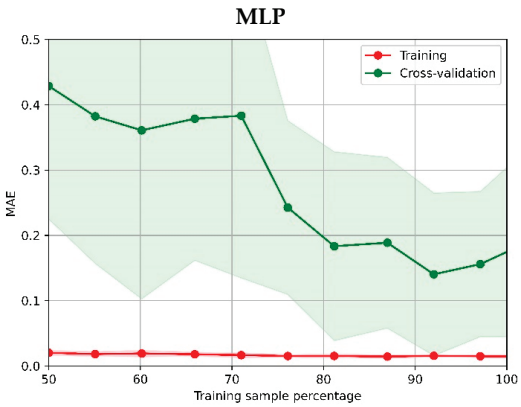

Network architecture: n_layers = 13 with (13, 11, 26, 42, 49, 4, 41, 40, 10, 43, 1, 2, 63) neurons, activation function=hyperbolic tangent (tanh), solver = Limited-memory Broyden-Fletcher-Goldfarb-Shanno (LBFGS), regularization parameter, alpha =0.0016092999926898072, learning rate = constant, random_state seed = 214.

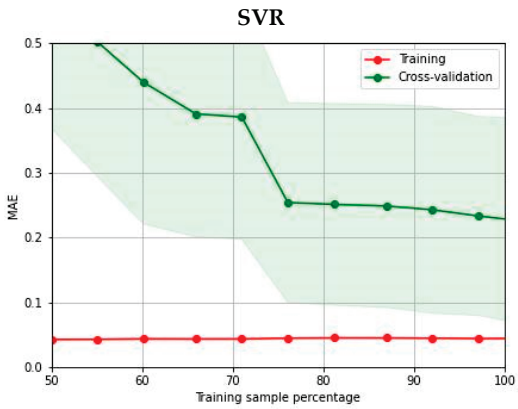

C =9.402354953632003, epsilon: 0.06513857204836664, gamma = float and gamma_val = 0.35179347438435515

Figure 6. *Cont.*

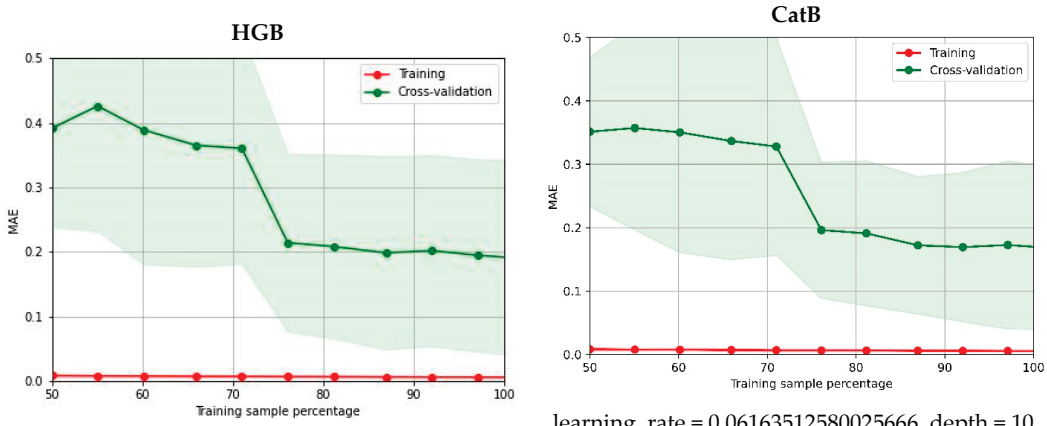

learning_rate = 0.07043986725381524, max_depth =8, max_leaf_nodes = 38, min_samples_leaf =3, max_bins = 245, l2_regularization = 0.12257196822661888, max_iter = 259, random_state = 855

learning_rate = 0.06163512580025666, depth = 10, l2_leaf_reg = 0.7522612693912111, border_count = 126, bagging_temperature = 1.2837120719109396, random_strength = 0.20854808369607702, od_type = 'Iter', od_wait = 43

Figure 6. Characteristics of the best models found by hyper-parameters training for prediction of the ferulic acid solubility. The plots provide the results of the learning curve analysis, which is devoted to testing the consistency of models' performance using both sub-sampling and cross-validation. The optimal values of each model are provided for reproducibility purposes.

It is noteworthy that the MLPRegressor and SVR were not the only non-linear models demonstrating acceptable accuracy in predicting ferulic acid solubility. Other less complex models, such as NuSVR, HistGradientBoosting, and CatBoost regressors, also achieved acceptable accuracy with significantly lower computational costs compared to MLP regressor. The best models can beranked as follows based on their MRSD and MAPE values given in the parenthesis, respectively: MLP (0.026, 1.57%) > SVR (0.062, 4.97%) ≈ NuSVR (0.063, 5.15%) > HGB (0.050, 2.16%) > CatBoost (0.051, 2.03%).

The optimized parameters for these models are summarized in Figure 6, which also includes the results of learning curve analysis for each regressor. It is noteworthy that considering multiple regressor models for experimental data modeling and prediction offers several advantages. Firstly, it can enhance performance by leveraging the strengths of different models, such as their ability to capture linear or non-linear relationships. Secondly, comparing and validating multiple models on the same dataset provides insights into their relative strengths, weaknesses, and overall reliability. Lastly, regressors can be used to formulate ensemble methods with optimized weights, further improving overall performance and generalization by mitigating bias and variance. This approach also promotes better generalization to new data and helps identify uncertainties or inconsistencies in predictions. However, this step was not implemented here, as the accuracy was acceptable even with a single-regressor approach and the available data pool was rather limited. For further examination of model properties, the LCA results are presented in Figure 6. Since NuSVR closely mirrors SVR results in both solubility data back computation and LCA results, it was excluded from further analysis. As previously noted, the MLP model has a complex structure that allows for the most accurate solubility back computations. However, LCA reveals significant limitations when applying this model to new data, as the learning curve shows considerable sensitivity to the data pool used for MLP application. Ideally, lines resulting from LCA should exhibit a smooth decrease in MAE with increasing data sample percentage for both training and cross-validation subsets. In the case of the MLP model, this requirement is met for the training dataset, suggesting excellent fitting to known experimental data, but values not seen in the learning phase are predicted with much less consistency. This suggests that while the complex architecture effectively captures the diversity of known data, it fails with new data, indicating poor generalizability

for theoretical screening of FA solubility in new dissolution media. The second model analyzed in Figure 6 suffers much less from this drawback. Indeed, after the inclusion of at least 75% of the solubility data, a systematic decrease in MAE values is observed. Similar conclusions can be drawn for the other two models included in Figure 6. From a practical point of view, the selection of SVR, NuSVR, or HGB for further application is a fortunate circumstance since these models are relatively fast to optimize and to apply for screening purposes. Because of this, they are recommended for further development and wrapping with a user-friendly application. In general, both support vector regression and its variant, NuSVR, are very effective when dealing with high-dimensional data and can handle non-linear relationships through the use of kernel functions. Support vector regression aims to find a hyperplane that best fits the data while maximizing the margin. It uses a subset of training samples called support vectors to define the regression function. SVR is known for its ability to handle non-linear relationships by applying kernel functions, such as radial basis function (RBF), polynomial, or sigmoid. NuSVR utilizes additional parameters to control the number of support vectors. The HistGradientBoosting regressor belongs to the boosting family of algorithms and is characterized by an ensemble of decision trees. It utilizes a gradient boosting framework, where subsequent trees are built to correct the errors made by previous trees. It incorporates histogram-based gradient boosting, which improves training speed and memory efficiency. The CatBoost regressor, on the other hand, is a gradient boosting algorithm that is particularly effective with categorical features. It requires minimal data preprocessing and is known for its fast training speed and robust handling of various data types.

3. Materials and Methods

3.1. Materials

Trans-ferulic acid (FA, CAS: 537-98-4, MW = 194.18 g/mol) was supplied by Sigma Aldrich (St. Louis, MO, USA) with a purity of ≥99%. Two hydrogen bond acceptors were used in the formation of deep eutectic solvents, namely choline chloride (ChCl, CAS: 67-48-1) and betaine (BI, CAS: 107-43-7). Six different hydrogen bond donors were also used, i.e., ethylene glycol (ETG, CAS: 107-21-1), diethylene glycol (DEG, CAS: 111-46-6), triethylene glycol (TEG, CAS: 112-27-6), glycerol (GLY, CAS: 56-81-5), 1,2-propanediol (P2D, CAS: 57-55-6), and 1,3-butanediol (B3D, CAS: 107-88-0). The constituents of the eutectic systems were all delivered by Sigma Aldrich (St. Louis, MO, USA), and their purity was ≥99%. Methanol (CAS: 67-56-1), which was utilized as a secondary solvent throughout the studies, was obtained from Avantor Performance Materials (Gliwice, Poland) and had a purity of ≥99%. Choline chloride was dried before use, while all the other chemicals were used without any initial procedures.

3.2. Preparation of the Calibration Curve

The spectrophotometric determination of the solubility of ferulic acid in deep eutectic solvents and their aqueous mixtures was preceded by the preparation of a calibration curve. For this purpose, the stock solution of FA was prepared in a 100 mL volumetric flask using methanol as a solvent. This solution was then diluted, which was achieved by transferring fixed amounts of the stock solution into 10 mL volumetric flasks and adding methanol accordingly. Eleven solutions were obtained in this way, with varying concentrations in the range of 0.00618 mg/mL to 0.0206 mg/mL. The absorption spectra of these solutions were then recorded with the help of an A360 spectrophotometer from AOE Instruments (Shanghai, China) in the wavelength range from 200 nm to 500 nm. The absorbance maximum was found to correspond to the 321 nm wavelength and did not change over the course of the measurements. Three separate curves were prepared in this manner, and the final curve was the result of their averaging. The obtained linear regression was found to be $A = 98.226 \times C + 0.002$ (A—absorbance, C—concentration in mg/mL). The validation parameters of the curve included the determination coefficient R^2, the limit of detection (LOD), and the limit of quantification (LOQ). The R^2 coefficient was equal to 0.9989, which ensures satisfactory linearity of the curve. LOD was found to be 0.000494 mg/mL, while

LOQ was 0.001483 mg/mL, which are values far below the concentrations achieved in the studied samples. Overall, the calibration curve can be considered adequate for the determination of the solubility of ferulic acid.

3.3. Preparation of the Samples and Solubility Measurements

The solubility of ferulic acid in the considered eutectic systems was determined using the well-established and reliable shake-flask method [95–98] combined with spectrophotometric measurements.

Deep eutectic solvents were formed by combining a hydrogen bond acceptor with a hydrogen bond donor in various molar ratios, including a unimolar proportion, a 2-fold excess amount of the HBD, and its 4-fold excess amount. One of two substances was used as a HBA, i.e., choline chloride or betaine, while one of six polyols—i.e., TEG, DED, ETG, GLY, P2D, or B3D—was used as an HBD. This resulted in a total of 36 eutectic systems. In order to prepare the eutectic formulation, the two constituents were mixed in glass vessels in a specific molar ratio, placed on a heating plate, and further mixed until the formation of a homogenous solution. DESs prepared in this manner were used in their pure form, and the most promising ones were also selected to form mixtures with water in pre-determined molar compositions.

As the initial step in the solubility determination procedure, saturated solutions of ferulic acid in considered DESs were prepared. This was done by placing an excess amount of FA in a test tube and adding the selected DES or aqueous DES mixture. The Orbital Shaker Incubator ES-20/60 from Biosan (Riga, Latvia) was used to ensure a stable temperature of 25 °C, 30 °C, 35 °C, or 40 °C, depending on the measurement conditions, for 24 h of incubation with simultaneous mixing at 60 rev/min. The samples were then filtered through a 0.22 μm pore-size PTFE syringe filter. All of the test tubes, syringes, pipette tips, and filters were initially heated at the same temperature as the measured sample in order to prevent precipitation. The samples were accordingly diluted with methanol before the measurements. As was the case for the calibration curve, the A360 spectrophotometer was used to record the spectra of the samples in the 200 nm–500 nm wavelength range with a 1 nm resolution and using methanol for calibration. The concentration of ferulic acid was calculated based on the linear equation of the calibration curve and the absorbance values recorded at the characteristic wavelength, i.e., 321 nm. Additionally, the density of the samples was measured, which was necessary for the computation of mole fraction solubility. For this propose, 1 mL of each solution was weighed in a 10 mL volumetric flask using a RADWAG (Radom, Poland) AS 110 R2.PLUS analytical balance with 0.1 mg precision. For each studied system, three samples were prepared and measured, and the obtained values were averaged.

3.4. Conformational Analysis

The most representative structures of either monomeric forms of every DES constituent or their homo- and hetero-molecular pairs were found by employing an extensive conformational analysis using the COSMOconf [99] and COMSOtherm [100] packages. The procedure was already described in our previous papers [101–103], hence only a brief synopsis is provided here. Each molecule, or molecular complex, was represented by a maximum of ten low-energy conformations identified by independent conformational searches for both the gas and condensed phases. The latter is crucial to account for the influence of the surrounding environment within the conductor-like screening model. The outcome of this protocol is a set of "cosmo" and "energy" files compatible with the latest parameter set, which is BP_TZVPD_FINE_24.ctd. This file comprises all the necessary parameters utilized for thermodynamic properties' computation in COMSOtherm [100]. It is worth mentioning that there are available variants of "ctd" files comprising parameter values adjusted for different levels of computation. Here, the RI-BP/def2-TZVPD-FINE level was used as the final step of the conformational analysis and affinity computations. In the manual, there is a recommended two-step procedure starting with geometry optimization on a slightly less demanding level, namely RI-BP/def-TZVP, followed by the final single-

point energy computations and generation of the necessary "cosmo" and "energy" files. This procedure can be followed for many molecules but suffers from serious drawbacks if applied to intermolecular complexes or flexible molecules stabilized by non-bonding type of interactions. It is related to inadequate representation of the dispersive forces by the RI-BP/def-TZVP method, and adding correction to the final energy cannot correct the occasionally obtained improper geometries. This is especially important for complexes with delocalized electrons, the interactions of which are poorly represented using the RI-BP/def-TZVP approach. For example, many stacking complexes are not predicted to be stable. This problem was already stated for edaravone [101] or methylxhanthines [97,104]. Hence, the actual geometry optimization was performed for both monomers and pairs using the RI-BP97/def2-SVPD approach. Apart from the more realistic pair geometries, there is an additional benefit of using this level of computations, namely the straightforward accounting for basis superposition set error (BSSE). This is regarded as an important component of the total interaction energy. However, rigorous computations of the BSSE via counterpoise correction can be time-consuming. Therefore, much less demanding alternatives using the DFT-C approach were proposed [105]. This geometry-based method of BSSE estimation relies on BP97/def2-SVPD geometries and accounts for atom–atom many-body corrections to the total molecular complex energy. Hence, this method was used for the geometry optimization of all structures used in this study. The molecular geometries obtained in such a manner were then used for single energy computations at a level compatible with the parametrization of COSMOtherm mentioned above. Hence, the full acronym describing this approach is as follows: RI-BP97/def2-SVPD//RI-BP/def2-TZVPD-FINE, where the first section before the double slash represents the optimization level and the second part the single energy computations.

The conformational search of the most probable structures or monomers is straightforward and done automatically using COSMOconf. However, identification of the most representative pair conformations posed a more significant computational challenge. Here, the same protocol as previously used for other APIs [101–103] was used. This involved generating conformations for various combinations of ferulic acid dimers and ferulic acid-solvent pairs. To achieve this, the COSMOtherm software employed the "CONTACT = {1 2} ssc_probability ssc_weak ssc_ang = 15.0" command. This command prioritizes the generation of the most probable pairs based on contact probabilities considering both hydrogen bonding and weak interactions. Consequently, this step typically results in a substantial number of initial structures requiring further optimization according to the above procedure with the implementation of data reduction to eliminate redundant and high-energy geometries. Two criteria were used for this selection: root-mean-square deviation (RMSD) and relative energy compared to the most stable conformer. Ultimately, only unique contacts within a 5.0 kcal/mol energy window relative to the most stable structure were retained for each complex, ensuring a representative pool of conformers with diverse structures and energies. The final "cosmo" and "energy" files were generated on the same level of theory and used for affinity computations using COSMOtherm parametrization. The core of all quantum chemistry computations was the Biovia TURBOMOLE [106] interfaced with TmolX. In the final step, the affinity computations were performed to characterize the interaction properties of ferulic acid with every constituent of the studied DESs using the default settings of COSMOtherm.

3.5. Solubility Dataset

The solubility dataset was defined based on both literature studies and augmented with new measurements presented in this paper. The literature review led to finding the data on FA solubility in the following neat solvents, methanol [91,94], ethanol [91,94,107], isopropanol [91,93,94], 1-butanol [91], 2-butanol [91], ethylene glycol [91], propylene glycol [91], transcutol [91], DMSO [91], ethyl acetate [91,92,94], and water [90,91,93,94,107]. Additionally, there are also available data for aqueous mixtures of isopropanol [93]. It happened that the highest solubility was found to be in DMSO.

3.6. Machine Learning Protocol

The machine learning protocol utilized in this study adheres to the methodology previously applied in our earlier projects [79,102,108]. As comprehensive details have been previously reported, only brief remarks are provided here. The solubility prediction model was developed using in-house Python code (version 3.10, https://www.python.org/) designed for hyperparameter tuning across 36 regression models. These models encompass a wide range of algorithms, including linear models, boosting methods, ensembles, nearest neighbors, neural networks, and other regressor types. Hyperparameter optimization was conducted using Optuna (version 3.2, https://optuna.org/), an open-source Python package. The optimization process involved 5000 minimization trials, employing the tree-structured Parzen estimator (TPE) as the search algorithm sampler. To evaluate the performance of each regression model, a custom scoring function was defined, integrating multiple metrics to assess both accuracy and generalizability, as detailed in a previous work [108]. This scoring function includes penalties derived from learning curve analysis (LCA), performed using the scikit-learn library (version 1.2.2) during the parameter tuning process. Due to the computational demands of LCA, initial computations were limited to two points, encompassing 50% and 100% of the total dataset. Subsequent LCA evaluations of the final model involved 20-point calculations within the 50–100% data range. The custom loss function incorporates the mean MAE values obtained from the largest training set size, thereby integrating both accuracy and generalizability aspects and providing insights into the model's performance on unseen data.

3.7. Molecular Descriptors

The set of molecular descriptors was formulated as described in our previous publication [103], based on the σ-potential values. The temperature-dependent σ-potentials were calculated for each compound in its pure, single-component state. The molecular descriptors for complex systems, utilized in machine learning, were represented as the difference between the σ-potential of a pure solute and that of a solvent at a given temperature. For multicomponent solvents, the σ-potential was characterized as the pure state value weighted by the mole fraction of the solute-free mole fraction. Typically, COSMOtherm generates σ-potential profiles consisting of 61 points for σ values between −0.03 and +0.03 e/Å^2 with a 0.001-step increment.

To reduce the number of descriptors, the most promising subset was identified by inspecting the significance of the relationship between experimental solubility and relative σ-potential values. This selection criterion was quantified by restriction to $R^2 > 0.4$ for a given σ value. This is illustrated in Figure 7, which shows two subsets: non-DES solvents (including neat solvents and binary mixtures) and DES systems. Notably, the overall correlation between experimental solubility and σ-potential is modest when considering the entire dataset. However, restricting the analysis to non-DES systems reveals a very high correlation ($R^2 > 0.8$) in the non-polar region, typically attributed to hydrophobicity (HYD). Additionally, the sub-range of hydrogen bond donicity (HBD) shows a high correlation with FA solubility. The points marked with bold black dots in Figure 7 were used for machine learning.

Additionally, solubility was computed by fully solving the solid-liquid equilibrium (SLE) problem using COSMOtherm [100] for two reasons. Firstly, it is interesting how accurate are the predictions based on the COSMO-RS theory [109]. Secondly, the computed solubility can be used as a molecular descriptor for machine learning purposes. It is crucial to note that the COSMO-RS approach is designed for predicting the thermodynamic characteristics of bulk systems, excluding the solid state. Since solubility involves the transition of the crystalline phase into a liquid saturated solution, the contribution of fusion data to the overall thermodynamic characteristics must be added to the input files. The required data include the melting temperature (T_m = 445.83 K), heat of fusion (ΔH_{fus} = 32.49 kJ/mol), and heat capacity change upon melting ($\Delta C_{p,fus} \approx \Delta S_{fus} \approx \Delta H_{fus} T_m$). The values in parentheses correspond to the average data provided in the compilation by Acree et al. [110]. The obtained solubility values were utilized as molecular descriptors in addition to the relative σ-potential values previously defined.

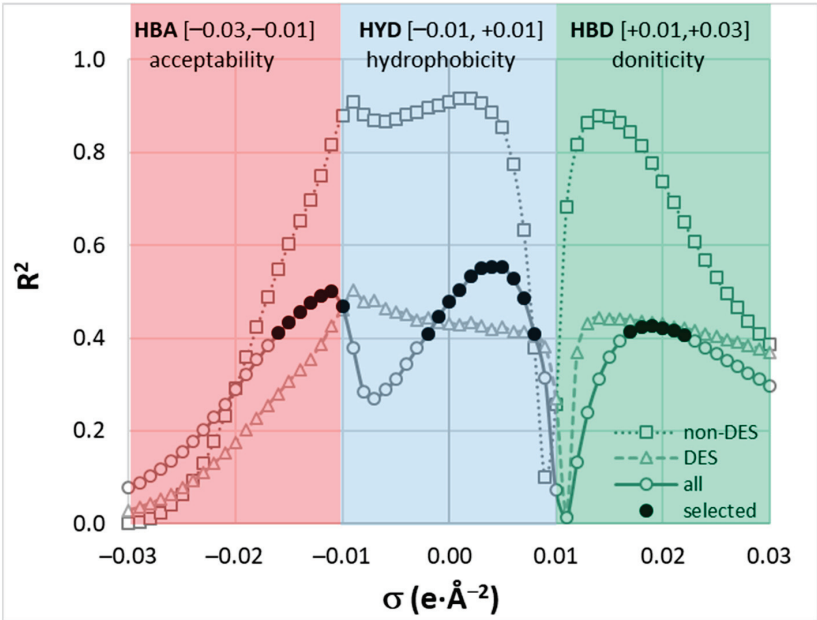

Figure 7. The correlation between relative solute-solvent σ-potentials and experimental solubility expressed as a function of σ values. Two series represent correlations computed for subsets including only non-DES solvents (neat solvents and binary mixtures) or only DES systems. Bold symbols define regions used as a set of molecular descriptors, where $R^2 > 0.4$ for either subset. The split into three distinct subranges is marked with colorful rectangles.

4. Conclusions

Ferulic acid is an important representative of phenolic acids with many practical applications. Since it can be obtained from natural sources, the selection of the most effective and green media for extraction seems to be of immense importance. This is emphasized by efforts to measure the solubility of FA in neat solvents and binary mixtures, as documented by a study of the literature. This paper further extends the knowledge of the dissolution of ferulic acid through a systematic study of two types of deep eutectic solvents involving choline chloride or betaine, acting as hydrogen bond acceptors, with one of six polyols playing the role of hydrogen bond donors. The performed optimization encompassed both the DES composition and its relative concentration in aqueous mixtures. It was found that the eutectics utilizing choline chloride were slightly more effective than those with betaine and that a 1:2 molar ratio of the HBA and HBD counterparts of the eutectic was the optimal one. Furthermore, the addition of small amounts of water to the DES further promotes the solubility of FA compared to the neat eutectic. Among the considered polyols, triethylene glycol proved to be the most effective. The presented results suggest that designed solvents comprising choline chloride and TEG, with an addition of water, can be treated as efficient alternatives to traditional organic solvents, including the first-choice solvent, namely DMSO. In order to gain insight into the saturated systems of FA in liquid media on a molecular level, the intermolecular interactions in the considered systems were studied, which led to the identification of the most stable homo- and hetero-molecular pairs formed between the interacting compounds. For the purpose of solvent screening, aimed at assisting the time-consuming experimental phase, a machine learning protocol was employed for the formulation of a non-linear model being able to predict FA solubility. This phase resulted in obtaining very accurate models that were able to precisely back-compute solubility as a function of solvent type and temperature. It is recommended to utilize the SVR regressor with the provided values of optimized parameters for screening purposes of new dissolution media. It is also worth mentioning that the very popular way of solubility prediction using the COMSO-RS approach is at most qualitatively accurate, and the developed models are much more accurate.

Supplementary Materials: The following supporting information can be downloaded at: https://www.mdpi.com/article/10.3390/molecules29163841/s1, Table S1: Mole fraction solubility of ferulic acid (IP) in neat DES containing either choline chloride or betaine as a HBA and one of six studied polyols as a HBD in various molar proportions at 25 °C. Standard deviation values are given in parentheses; Table S2: Mole fraction solubility of ferulic acid (FA) in aqueous-choline-chloride-based DES mixtures at various temperatures. In the first column, x*DES denotes the mole fraction of DES in solute-free mixtures with water. Standard deviation values are given in parentheses; Table S3: Mole fraction solubility of ferulic acid (FA) in aqueous-betaine-based DES mixtures at various temperatures. In the first column, x*DES denotes the mole fraction of DES in solute-free mixtures with water. Standard deviation values are given in parentheses.

Author Contributions: Conceptualization, P.C.; methodology, P.C., T.J. and M.P.; software, P.C.; validation, P.C., T.J. and M.P.; formal analysis, P.C. and T.J.; investigation, P.C., T.J., M.P., R.R., K.R. and D.W.; resources, P.C.; data curation, P.C., M.P. and T.J.; writing—original draft preparation, P.C., T.J. and M.P.; writing—review and editing, P.C., T.J. and M.P.; visualization, P.C. and T.J.; supervision, P.C.; project administration, P.C.; funding acquisition, P.C. All authors have read and agreed to the published version of the manuscript.

Funding: This research received no external funding.

Institutional Review Board Statement: Not applicable.

Informed Consent Statement: Not applicable.

Data Availability Statement: All data supporting the reported results are available on request from the corresponding author.

Conflicts of Interest: The authors declare no conflicts of interest.

References

1. Ou, S.; Kwok, K.C. Ferulic acid: Pharmaceutical functions, preparation and applications in foods. *J. Sci. Food Agric.* **2004**, *84*, 1261–1269. [CrossRef]
2. Mancuso, C.; Santangelo, R. Ferulic acid: Pharmacological and toxicological aspects. *Food Chem. Toxicol.* **2014**, *65*, 185–195. [CrossRef] [PubMed]
3. Li, D.; Rui, Y.X.; Guo, S.; Luan, F.; Liu, R.; Zeng, N. Ferulic acid: A review of its pharmacology, pharmacokinetics and derivatives. *Life Sci.* **2021**, *284*, 119921. [CrossRef] [PubMed]
4. Babbar, R.; Dhiman, S.; Grover, R.; Kaur, A.; Arora, S. A Comprehensive Review on Therapeutic Applications of Ferulic Acid and its Novel Analogues: A Brief Literature. *Mini-Rev. Med. Chem.* **2021**, *21*, 1578–1593. [CrossRef]
5. Kumar, N.; Pruthi, V. Potential applications of ferulic acid from natural sources. *Biotechnol. Rep.* **2014**, *4*, 86–93. [CrossRef] [PubMed]
6. Sakai, S.; Kawamata, H.; Kogure, T.; Mantani, N.; Terasawa, K.; Umatake, M.; Ochiai, H. Inhibitory Effect of Ferulic Acid and Isoferulic Acid on the Production of Macrophage Inflammatory Protein-2 in Response to Respiratory Syncytial Virus Infection in RAW264.7 Cells. *Mediat. Inflamm.* **1999**, *8*, 173–175. [CrossRef]
7. Graf, E. Antioxidant potential of ferulic acid. *Free Radic. Biol. Med.* **1992**, *13*, 435–448. [CrossRef]
8. Zduńska, K.; Dana, A.; Kolodziejczak, A.; Rotsztejn, H. Antioxidant Properties of Ferulic Acid and Its Possible Application. *Ski. Pharmacol. Physiol.* **2018**, *31*, 332–336. [CrossRef]
9. Kikuzaki, H.; Hisamoto, M.; Hirose, K.; Akiyama, K.; Taniguchi, H. Antioxidant properties of ferulic acid and its related compounds. *J. Agric. Food Chem.* **2002**, *50*, 2161–2168. [CrossRef]
10. Urbaniak, A.; Szelag, M.; Molski, M. Theoretical investigation of stereochemistry and solvent influence on antioxidant activity of ferulic acid. *Comput. Theor. Chem.* **2013**, *1012*, 33–40. [CrossRef]
11. Borges, F.; Lima, J.L.F.C.; Pinto, I.; Reis, S.; Siquet, C. Application of a Potentiometric System with Data-Analysis Computer Programs to the Quantification of Metal-Chelating Activity of Two Natural Antioxidants: Caffeic Acid and Ferulic Acid. *Helv. Chim. Acta* **2003**, *86*, 3081–3087. [CrossRef]
12. Truong, D.H.; Nhung, N.T.A.; Dao, D.Q. Iron ions chelation-based antioxidant potential vs. pro-oxidant risk of ferulic acid: A DFT study in aqueous phase. *Comput. Theor. Chem.* **2020**, *1185*, 112905. [CrossRef]
13. Hosoda, A.; Ozaki, Y.; Kashiwada, A.; Mutoh, M.; Wakabayashi, K.; Mizuno, K.; Nomura, E.; Taniguchi, H. Syntheses of Ferulic Acid Derivatives and Their Suppressive Effects on Cyclooxygenase-2 Promoter Activity. *Bioorg. Med. Chem.* **2002**, *10*, 1189–1196. [CrossRef] [PubMed]
14. Kumar, N.; Pruthi, V. Structural elucidation and molecular docking of ferulic acid from Parthenium hysterophorus possessing COX-2 inhibition activity. *3 Biotech* **2015**, *5*, 541–551. [CrossRef] [PubMed]

15. Amić, A.; Marković, J.M.D.; Marković, Z.; Milenković, D.; Milanović, Ž.; Antonijević, M.; Cagardová, D.M.; Pedregal, J.R.G. Theoretical study of radical inactivation, lox inhibition, and iron chelation: The role of ferulic acid in skin protection against uva induced oxidative stress. *Antioxidants* **2021**, *10*, 1303. [CrossRef]
16. Zhao, J.; Suyama, A.; Tanaka, M.; Matsui, T. Ferulic acid enhances the vasorelaxant effect of epigallocatechin gallate in tumor necrosis factor-alpha-induced inflammatory rat aorta. *J. Nutr. Biochem.* **2014**, *25*, 807–814. [CrossRef] [PubMed]
17. Ganesan, R.; Rasool, M. Ferulic acid inhibits interleukin 17-dependent expression of nodal pathogenic mediators in fibroblast-like synoviocytes of rheumatoid arthritis. *J. Cell. Biochem.* **2019**, *120*, 1878–1893. [CrossRef] [PubMed]
18. Wang, J.; Yuan, Z.; Zhao, H.; Ju, D.; Chen, Y.; Chen, X.; Zhang, J. Ferulic acid promotes endothelial cells proliferation through up-regulating cyclin D1 and VEGF. *J. Ethnopharmacol.* **2011**, *137*, 992–997. [CrossRef] [PubMed]
19. Serreli, G.; Le Sayec, M.; Thou, E.; Lacour, C.; Diotallevi, C.; Dhunna, M.A.; Deiana, M.; Spencer, J.P.E.; Corona, G. Ferulic Acid Derivatives and Avenanthramides Modulate Endothelial Function through Maintenance of Nitric Oxide Balance in HUVEC Cells. *Nutrients* **2021**, *13*, 2026. [CrossRef]
20. Ali, S.A.; Saifi, M.A.; Pulivendala, G.; Godugu, C.; Talla, V. Ferulic acid ameliorates the progression of pulmonary fibrosis via inhibition of TGF-β/smad signalling. *Food Chem. Toxicol.* **2021**, *149*, 111980. [CrossRef]
21. Zhao, X.M.; Zhang, J.; Liang, Y.N.; Niu, Y.C. Astragaloside IV Synergizes with Ferulic Acid to Alleviate Hepatic Fibrosis in Bile Duct-Ligated Cirrhotic Rats. *Dig. Dis. Sci.* **2020**, *65*, 2925–2936. [CrossRef] [PubMed]
22. Gupta, A.; Singh, A.K.; Loka, M.; Pandey, A.K.; Bishayee, A. Ferulic acid-mediated modulation of apoptotic signaling pathways in cancer. *Adv. Protein Chem. Struct. Biol.* **2021**, *125*, 215–257.
23. Nakayama, H.; Nakahara, M.; Matsugi, E.; Soda, M.; Hattori, T.; Hara, K.; Usami, A.; Kusumoto, C.; Higashiyama, S.; Kitaichi, K. Protective Effect of Ferulic Acid against Hydrogen Peroxide Induced Apoptosis in PC12 Cells. *Molecules* **2020**, *26*, 90. [CrossRef] [PubMed]
24. Zhang, K.; Shen, X.; Yang, L.; Chen, Q.; Wang, N.; Li, Y.; Song, P.; Jiang, M.; Bai, G.; Yang, P.; et al. Exploring the Q-markers of *Angelica sinensis* (Oliv.) Diels of anti-platelet aggregation activity based on spectrum–effect relationships. *Biomed. Chromatogr.* **2022**, *36*, e5422. [CrossRef]
25. Nguyen, T.M.H.; Le, H.L.; Ha, T.T.; Bui, B.H.; Le, N.T.; Nguyen, V.H.; Nguyen, T.V.A. Inhibitory effect on human platelet aggregation and coagulation and antioxidant activity of *C. edulis* Ker Gawl rhizome and its secondary metabolites. *J. Ethnopharmacol.* **2020**, *263*, 113136. [CrossRef] [PubMed]
26. Wang, N.Y.; Li, J.N.; Liu, W.L.; Huang, Q.; Li, W.X.; Tan, Y.H.; Liu, F.; Song, Z.H.; Wang, M.Y.; Xie, N.; et al. Ferulic Acid Ameliorates Alzheimer's Disease-like Pathology and Repairs Cognitive Decline by Preventing Capillary Hypofunction in APP/PS1 Mice. *Neurotherapeutics* **2021**, *18*, 1064–1080. [CrossRef] [PubMed]
27. Dong, X.; Huang, R. Ferulic acid: An extraordinarily neuroprotective phenolic acid with anti-depressive properties. *Phytomedicine* **2022**, *105*, 154355. [CrossRef]
28. Bourne, L.C.; Rice-Evans, C. Bioavailability of Ferulic Acid. *Biochem. Biophys. Res. Commun.* **1998**, *253*, 222–227. [CrossRef]
29. Lafay, S.; Gil-Izquierdo, A. Bioavailability of phenolic acids. *Phytochem. Rev.* **2008**, *7*, 301–311. [CrossRef]
30. Zhang, Y.; Li, Z.; Zhang, K.; Yang, G.; Wang, Z.; Zhao, J.; Hu, R.; Feng, N. Ethyl oleate-containing nanostructured lipid carriers improve oral bioavailability of trans-ferulic acid ascompared with conventional solid lipid nanoparticles. *Int. J. Pharm.* **2016**, *511*, 57–64. [CrossRef]
31. Hassanzadeh, P.; Arbabi, E.; Atyabi, F.; Dinarvand, R. Ferulic acid-loaded nanostructured lipid carriers: A promising nanoformulation against the ischemic neural injuries. *Life Sci.* **2018**, *193*, 64–76. [CrossRef] [PubMed]
32. Hithamani, G.; Srinivasan, K. Bioavailability of finger millet (*Eleusine coracana*) phenolic compounds in rat as influenced by co-administered piperine. *Food Biosci.* **2017**, *19*, 101–109. [CrossRef]
33. Scholz, S.; Williamson, G. Interactions Affecting the Bioavailability of Dietary Polyphenols in Vivo. *Int. J. Vitam. Nutr. Res.* **2013**, *77*, 224–235. [CrossRef] [PubMed]
34. Zhang, L.W.; Al-Suwayeh, S.A.; Hsieh, P.W.; Fang, J.Y. A comparison of skin delivery of ferulic acid and its derivatives: Evaluation of their efficacy and safety. *Int. J. Pharm.* **2010**, *399*, 44–51. [CrossRef]
35. Chen, M.; Liu, X.; Fahr, A. Skin delivery of ferulic acid from different vesicular systems. *J. Biomed. Nanotechnol.* **2010**, *6*, 577–585. [CrossRef]
36. Zduńska-Pęciak, K.; Dębowska, R.; Kołodziejczak, A.; Rotsztejn, H. Ferulic acid—A novel topical agent in reducing signs of photoaging. *Dermatol. Ther.* **2022**, *35*, e15543. [CrossRef]
37. Janus, E.; Pinheiro, L.R.; Nowak, A.; Kucharska, E.; Świątek, E.; Podolak, N.; Perużyńska, M.; Piotrowska, K.; Duchnik, W.; Kucharski, Ł.; et al. New Ferulic Acid and Amino Acid Derivatives with Increased Cosmeceutical and Pharmaceutical Potential. *Pharmaceutics* **2023**, *15*, 117. [CrossRef]
38. Cavalcanti, G.R.; Duarte, F.I.C.; Converti, A.; de Lima, Á.A.N. Ferulic Acid Activity in Topical Formulations: Technological and Scientific Prospecting. *Curr. Pharm. Des.* **2020**, *27*, 2289–2298. [CrossRef]
39. Martínez, F.; Jouyban, A.; Acree, W.E. Pharmaceuticals solubility is still nowadays widely studied everywhere. *Pharm. Sci.* **2017**, *23*, 1–2. [CrossRef]
40. Savjani, K.T.; Gajjar, A.K.; Savjani, J.K. Drug Solubility: Importance and Enhancement Techniques. *ISRN Pharm.* **2012**, *2012*, 1–10. [CrossRef]
41. Coltescu, A.R.; Butnariu, M.; Sarac, I. The importance of solubility for new drug molecules. *Biomed. Pharmacol. J.* **2020**, *13*, 577–583. [CrossRef]
42. Yang, Z.; Yang, Y.; Xia, M.; Dai, W.; Zhu, B.; Mei, X. Improving the dissolution behaviors and bioavailability of abiraterone acetate via multicomponent crystal forms. *Int. J. Pharm.* **2022**, *614*, 121460. [CrossRef] [PubMed]

43. Kalam, M.A.; Alshamsan, A.; Alkholief, M.; Alsarra, I.A.; Ali, R.; Haq, N.; Anwer, M.K.; Shakeel, F. Solubility Measurement and Various Solubility Parameters of Glipizide in Different Neat Solvents. *ACS Omega* **2020**, *5*, 1708–1716. [CrossRef]
44. Kim, H.-S.; Kim, C.-M.; Jo, A.-N.; Kim, J.-E. Studies on Preformulation and Formulation of JIN-001 Liquisolid Tablet with Enhanced Solubility. *Pharmaceuticals* **2022**, *15*, 412. [CrossRef]
45. Khadka, P.; Ro, J.; Kim, H.; Kim, I.; Kim, J.T.; Kim, H.; Cho, J.M.; Yun, G.; Lee, J. Pharmaceutical particle technologies: An approach to improve drug solubility, dissolution and bioavailability. *Asian J. Pharm. Sci.* **2014**, *9*, 304–316. [CrossRef]
46. Müller, C.E. Prodrug Approaches for Enhancing the Bioavailability of Drugs with Low Solubility. *Chem. Biodivers.* **2009**, *6*, 2071–2083. [CrossRef]
47. Das, T.; Mehta, C.H.; Nayak, U.Y. Multiple approaches for achieving drug solubility: An in silico perspective. *Drug Discov. Today* **2020**, *25*, 1206–1212. [CrossRef]
48. Tian, Y.; Shi, C.; Sun, Y.; Zhu, C.; Sun, C.C.; Mao, S. Designing micellar Nanocarriers with improved drug loading and stability based on solubility parameter. *Mol. Pharm.* **2015**, *12*, 816–825. [CrossRef] [PubMed]
49. Lipinski, C.A. Drug-like properties and the causes of poor solubility and poor permeability. *J. Pharmacol. Toxicol. Methods* **2000**, *44*, 235–249. [CrossRef]
50. Da Silva, F.L.O.; Marques, M.B.D.F.; Kato, K.C.; Carneiro, G. Nanonization techniques to overcome poor water-solubility with drugs. *Expert Opin. Drug Discov.* **2020**, *15*, 853–864. [CrossRef]
51. Das, B.; Baidya, A.T.K.; Mathew, A.T.; Yadav, A.K.; Kumar, R. Structural modification aimed for improving solubility of lead compounds in early phase drug discovery. *Bioorg. Med. Chem.* **2022**, *56*, 116614. [CrossRef] [PubMed]
52. Bergström, C.A.S.; Avdeef, A. Perspectives in solubility measurement and interpretation. *ADMET DMPK* **2019**, *7*, 88–105. [CrossRef] [PubMed]
53. Black, S.; Dang, L.; Liu, C.; Wei, H. On the measurement of solubility. *Org. Process Res. Dev.* **2013**, *17*, 486–492. [CrossRef]
54. Boobier, S.; Hose, D.R.J.; Blacker, A.J.; Nguyen, B.N. Machine learning with physicochemical relationships: Solubility prediction in organic solvents and water. *Nat. Commun.* **2020**, *11*, 5753. [CrossRef] [PubMed]
55. Lovrić, M.; Pavlović, K.; Žuvela, P.; Spataru, A.; Lučić, B.; Kern, R.; Wong, M.W. Machine learning in prediction of intrinsic aqueous solubility of drug-like compounds: Generalization, complexity, or predictive ability? *J. Chemom.* **2021**, *35*, e3349. [CrossRef]
56. Bhalani, D.V.; Nutan, B.; Kumar, A.; Singh Chandel, A.K. Bioavailability Enhancement Techniques for Poorly Aqueous Soluble Drugs and Therapeutics. *Biomedicines* **2022**, *10*, 2055. [CrossRef] [PubMed]
57. Manallack, D.T.; Yuriev, E.; Chalmers, D.K. The influence and manipulation of acid/base properties in drug discovery. *Drug Discov. Today Technol.* **2018**, *27*, 41–47. [CrossRef]
58. Merisko-Liversidge, E.; Liversidge, G.G. Nanosizing for oral and parenteral drug delivery: A perspective on formulating poorly-water soluble compounds using wet media milling technology. *Adv. Drug Deliv. Rev.* **2011**, *63*, 427–440. [CrossRef] [PubMed]
59. Brewster, M.E.; Loftsson, T. Cyclodextrins as pharmaceutical solubilizers. *Adv. Drug Deliv. Rev.* **2007**, *59*, 645–666. [CrossRef]
60. Korn, C.; Balbach, S. Compound selection for development—Is salt formation the ultimate answer? Experiences with an extended concept of the "100mg approach" . *Eur. J. Pharm. Sci.* **2014**, *57*, 257–263.
61. Seedher, N.; Kanojia, M. Co-solvent solubilization of some poorly-soluble antidiabetic drugs. *Pharm. Dev. Technol.* **2009**, *14*, 185–192. [CrossRef] [PubMed]
62. Hahnenkamp, I.; Graubner, G.; Gmehling, J. Measurement and prediction of solubilities of active pharmaceutical ingredients. *Int. J. Pharm.* **2010**, *388*, 73–81. [CrossRef] [PubMed]
63. Abraham, M.H.; Smith, R.E.; Luchtefeld, R.; Boorem, A.J.; Lou, R.; Acree, W.E. Prediction of solubility of drugs and other compounds in organic solvents. *J. Pharm. Sci.* **2010**, *99*, 1500–1515. [CrossRef] [PubMed]
64. Hewitt, M.; Cronin, M.T.D.; Enoch, S.J.; Madden, J.C.; Roberts, D.W.; Dearden, J.C. In silico prediction of aqueous solubility: The solubility challenge. *J. Chem. Inf. Model.* **2009**, *49*, 2572–2587. [CrossRef] [PubMed]
65. Lenoir, D.; Schramm, K.W.; Lalah, J.O. Green Chemistry: Some important forerunners and current issues. *Sustain. Chem. Pharm.* **2020**, *18*, 100313. [CrossRef]
66. Kopach, M.; Leahy, D.; Manley, J. The green chemistry approach to pharma manufacturing. *Innov. Pharm. Technol.* **2012**, *43*, 72–75.
67. Becker, J.; Manske, C.; Randl, S. Green chemistry and sustainability metrics in the pharmaceutical manufacturing sector. *Curr. Opin. Green Sustain. Chem.* **2022**, *33*, 100562. [CrossRef]
68. Mishra, M.; Sharma, M.; Dubey, R.; Kumari, P.; Ranjan, V.; Pandey, J. Green synthesis interventions of pharmaceutical industries for sustainable development. *Curr. Res. Green Sustain. Chem.* **2021**, *4*, 100174. [CrossRef]
69. DeSimone, J.M. Practical approaches to green solvents. *Science* **2002**, *297*, 799–803. [CrossRef]
70. Häckl, K.; Kunz, W. Some aspects of green solvents. *Comptes Rendus Chim.* **2018**, *21*, 572–580. [CrossRef]
71. Santana-Mayor, Á.; Rodríguez-Ramos, R.; Herrera-Herrera, A.V.; Socas-Rodríguez, B.; Rodríguez-Delgado, M.Á. Deep eutectic solvents. The new generation of green solvents in analytical chemistry. *TrAC Trends Anal. Chem.* **2021**, *134*, 116108. [CrossRef]
72. Vanda, H.; Dai, Y.; Wilson, E.G.; Verpoorte, R.; Choi, Y.H. Green solvents from ionic liquids and deep eutectic solvents to natural deep eutectic solvents. *Comptes Rendus Chim.* **2018**, *21*, 628–638. [CrossRef]
73. Omar, K.A.; Sadeghi, R. Physicochemical properties of deep eutectic solvents: A review. *J. Mol. Liq.* **2022**, *360*, 119524. [CrossRef]
74. Paiva, A.; Craveiro, R.; Aroso, I.; Martins, M.; Reis, R.L.; Duarte, A.R.C. Natural Deep Eutectic Solvents—Solvents for the 21st Century. *ACS Sustain. Chem. Eng.* **2014**, *2*, 1063–1071. [CrossRef]

75. Espino, M.; de los Ángeles Fernández, M.; Gomez, F.J.V.; Silva, M.F. Natural designer solvents for greening analytical chemistry. *TrAC Trends Anal. Chem.* **2016**, *76*, 126–136. [CrossRef]
76. Xu, G.; Shi, M.; Zhang, P.; Tu, Z.; Hu, X.; Zhang, X.; Wu, Y. Tuning the composition of deep eutectic solvents consisting of tetrabutylammonium chloride and n-decanoic acid for adjustable separation of ethylene and ethane. *Sep. Purif. Technol.* **2022**, *298*, 121680. [CrossRef]
77. Cao, Y.; Tao, X.; Jiang, S.; Gao, N.; Sun, Z. Tuning thermodynamic properties of deep eutectic solvents for achieving highly efficient photothermal sensor. *J. Mol. Liq.* **2020**, *308*, 113163. [CrossRef]
78. Pedro, S.N.; Freire, C.S.R.; Silvestre, A.J.D.; Freire, M.G. Deep Eutectic Solvents and Pharmaceuticals. *Encyclopedia* **2021**, *1*, 942–963. [CrossRef]
79. Cysewski, P.; Jeliński, T.; Przybyłek, M. Experimental and Theoretical Insights into the Intermolecular Interactions in Saturated Systems of Dapsone in Conventional and Deep Eutectic Solvents. *Molecules* **2024**, *29*, 1743. [CrossRef]
80. Bazzo, G.C.; Pezzini, B.R.; Stulzer, H.K. Eutectic mixtures as an approach to enhance solubility, dissolution rate and oral bioavailability of poorly water-soluble drugs. *Int. J. Pharm.* **2020**, *588*, 119741. [CrossRef]
81. Kapre, S.; Palakurthi, S.S.; Jain, A.; Palakurthi, S. DES-igning the future of drug delivery: A journey from fundamentals to drug delivery applications. *J. Mol. Liq.* **2024**, *400*, 124517. [CrossRef]
82. Jeliński, T.; Przybyłek, M.; Mianowana, M.; Misiak, K.; Cysewski, P. Deep Eutectic Solvents as Agents for Improving the Solubility of Edaravone: Experimental and Theoretical Considerations. *Molecules* **2024**, *29*, 1261. [CrossRef] [PubMed]
83. Duarte, A.R.C.; Ferreira, A.S.D.; Barreiros, S.; Cabrita, E.; Reis, R.L.; Paiva, A. A comparison between pure active pharmaceutical ingredients and therapeutic deep eutectic solvents: Solubility and permeability studies. *Eur. J. Pharm. Biopharm.* **2017**, *114*, 296–304. [CrossRef] [PubMed]
84. Nguyen, C.-H.; Augis, L.; Fourmentin, S.; Barratt, G.; Legrand, F.-X. *Deep Eutectic Solvents for Innovative Pharmaceutical Formulations*; Springer: Berlin/Heidelberg, Germany, 2021.
85. Liu, Y.; Wu, Y.; Liu, J.; Wang, W.; Yang, Q.; Yang, G. Deep eutectic solvents: Recent advances in fabrication approaches and pharmaceutical applications. *Int. J. Pharm.* **2022**, *622*, 121811. [CrossRef] [PubMed]
86. García-Roldán, A.; Piriou, L.; Jauregi, P. Natural deep eutectic solvents as a green extraction of polyphenols from spent coffee ground with enhanced bioactivities. *Front. Plant Sci.* **2023**, *13*, 1072592. [CrossRef] [PubMed]
87. Cysewski, P.; Przybyłek, M.; Jeliński, T. Predicting sulfanilamide solubility in the binary mixtures using a reference solvent approach. *Polym. Med.* **2024**, *54*, 27–34.
88. Hammond, O.S.; Bowron, D.T.; Edler, K.J.; Hammond, S.; Edler, K.J.; Bowron, D.T. The Effect of Water upon Deep Eutectic Solvent Nanostructure: An Unusual Transition from Ionic Mixture to Aqueous Solution. *Angew. Chem. Int. Ed.* **2017**, *56*, 9782–9785. [CrossRef] [PubMed]
89. Gabriele, F.; Chiarini, M.; Germani, R.; Tiecco, M.; Spreti, N. Effect of water addition on choline chloride/glycol deep eutectic solvents: Characterization of their structural and physicochemical properties. *J. Mol. Liq.* **2019**, *291*, 111301. [CrossRef]
90. Mota, F.L.; Queimada, A.J.; Pinho, S.P.; Macedo, E.A. Aqueous solubility of some natural phenolic compounds. *Ind. Eng. Chem. Res.* **2008**, *47*, 5182–5189. [CrossRef]
91. Shakeel, F.; Salem-Bekhit, M.M.; Haq, N.; Siddiqui, N.A. Solubility and thermodynamics of ferulic acid in different neat solvents: Measurement, correlation and molecular interactions. *J. Mol. Liq.* **2017**, *236*, 144–150. [CrossRef]
92. Manic, M.S.; Villanueva, D.; Fornari, T.; Queimada, A.J.; MacEdo, E.A.; Najdanovic-Visak, V. Solubility of high-value compounds in ethyl lactate: Measurements and modeling. *J. Chem. Thermodyn.* **2012**, *48*, 93–100. [CrossRef]
93. Haq, N.; Siddiqui, N.A.; Shakeel, F. Solubility and molecular interactions of ferulic acid in various (isopropanol + water) mixtures. *J. Pharm. Pharmacol.* **2017**, *69*, 1485–1494. [CrossRef]
94. Vilas-Boas, S.M.; Alves, R.S.; Brandão, P.; Campos, L.M.A.; Coutinho, J.A.P.; Pinho, S.P.; Ferreira, O. Solid-liquid phase equilibrium of trans-cinnamic acid, p-coumaric acid and ferulic acid in water and organic solvents: Experimental and modelling studies. *Fluid Phase Equilib.* **2020**, *521*, 112747. [CrossRef]
95. Przybyłek, M.; Recki, Ł.; Mroczyńska, K.; Jeliński, T.; Cysewski, P. Experimental and theoretical solubility advantage screening of bi-component solid curcumin formulations. *J. Drug Deliv. Sci. Technol.* **2019**, *50*, 125–135. [CrossRef]
96. Jeliński, T.; Przybyłek, M.; Cysewski, P. Solubility advantage of sulfanilamide and sulfacetamide in natural deep eutectic systems: Experimental and theoretical investigations. *Drug Dev. Ind. Pharm.* **2019**, *45*, 1120–1129. [CrossRef]
97. Jeliński, T.; Stasiak, D.; Kosmalski, T.; Cysewski, P. Experimental and theoretical study on theobromine solubility enhancement in binary aqueous solutions and ternary designed solvents. *Pharmaceutics* **2021**, *13*, 1118. [CrossRef]
98. Cysewski, P.; Jeliński, T.; Przybyłek, M. Application of COSMO-RS-DARE as a Tool for Testing Consistency of Solubility Data: Case of Coumarin in Neat Alcohols. *Molecules* **2022**, *27*, 5274. [CrossRef] [PubMed]
99. Dassault Systèmes. *COSMOconf, Version 24.0.0, Dassault Systèmes*; Biovia: San Diego, CA, USA, 2022.
100. *COSMOtherm, Version 24.0.0, Dassault Systèmes*; Biovia: San Diego, CA, USA, 2022.
101. Cysewski, P.; Jeliński, T.; Przybyłek, M. Intermolecular Interactions of Edaravone in Aqueous Solutions of Ethaline and Glyceline Inferred from Experiments and Quantum Chemistry Computations. *Molecules* **2023**, *28*, 629. [CrossRef]
102. Jeliński, T.; Przybyłek, M.; Różalski, R.; Cysewski, P. Solubility of dapsone in deep eutectic solvents: Experimental analysis, molecular insights and machine learning predictions. *Polym. Med.* **2024**, *54*, 15–25. [CrossRef]

103. Cysewski, P.; Jeliński, T.; Przybyłek, M.; Mai, A.; Kułak, J. Experimental and Machine-Learning-Assisted Design of Pharmaceutically Acceptable Deep Eutectic Solvents for the Solubility Improvement of Non-Selective COX Inhibitors Ibuprofen and Ketoprofen. *Molecules* **2024**, *29*, 2296. [CrossRef]
104. Jeliński, T.; Cysewski, P. Quantification of Caffeine Interactions in Choline Chloride Natural Deep Eutectic Solvents: Solubility Measurements and COSMO-RS-DARE Interpretation. *Int. J. Mol. Sci.* **2022**, *23*, 7832. [CrossRef] [PubMed]
105. Witte, J.; Neaton, J.B.; Head-Gordon, M. Effective empirical corrections for basis set superposition error in the def2-SVPD basis: gCP and DFT-C. *J. Chem. Phys.* **2017**, *146*, 234105. [CrossRef] [PubMed]
106. TURBOMOLE GmbH. *TURBOMOLE, Version 7.8*; TURBOMOLE GmbH: Karlsruhe, Germany, 2023.
107. Bitencourt, R.G.; Cabral, F.A.; Meirelles, A.J.A. Ferulic acid solubility in supercritical carbon dioxide, ethanol and water mixtures. *J. Chem. Thermodyn.* **2016**, *103*, 285–291. [CrossRef]
108. Cysewski, P.; Jeliński, T.; Przybyłek, M. Finding the Right Solvent: A Novel Screening Protocol for Identifying Environmentally Friendly and Cost-Effective Options for Benzenesulfonamide. *Molecules* **2023**, *28*, 5008. [CrossRef] [PubMed]
109. Klamt, A.; Schüürmann, G. COSMO: A new approach to dielectric screening in solvents with explicit expressions for the screening energy and its gradient. *J. Chem. Soc. Perkin Trans.* **1993**, *2*, 799. [CrossRef]
110. Acree, W.; Chickos, J.S. Phase Transition Enthalpy Measurements of Organic and Organometallic Compounds and Ionic Liquids. Sublimation, Vaporization, and Fusion Enthalpies from 1880 to 2015. Part 2. C11–C192. *J. Phys. Chem. Ref. Data* **2017**, *46*, 013104.

Disclaimer/Publisher's Note: The statements, opinions and data contained in all publications are solely those of the individual author(s) and contributor(s) and not of MDPI and/or the editor(s). MDPI and/or the editor(s) disclaim responsibility for any injury to people or property resulting from any ideas, methods, instructions or products referred to in the content.

molecules

MDPI

Article

Recovery of Metals from the "Black Mass" of Waste Portable Li-Ion Batteries with Choline Chloride-Based Deep Eutectic Solvents and Bi-Functional Ionic Liquids by Solvent Extraction

Urszula Domańska *, Anna Wiśniewska, Zbigniew Dąbrowski, Dorota Kolasa, Kamil Wróbel and Jakub Lach

Łukasiewicz Research Network—Industrial Chemistry Institute, Rydygiera 8, 01-793 Warsaw, Poland; anna.wisniewska@ichp.lukasiewicz.gov.pl (A.W.); zbigniew.dabrowski@ichp.lukasiewicz.gov.pl (Z.D.); dorota.kolasa@ichp.lukasiewicz.gov.pl (D.K.); kamil.wrobel@ichp.lukasiewicz.gov.pl (K.W.); jakub.lach@ichp.lukasiewicz.gov.pl (J.L.)

* Correspondence: urszula.domanska-zelazna@ichp.lukasiewicz.gov.pl or ula@ch.pw.edu.pl; Tel.: +48-517883150

Abstract: Lithium-ion portable batteries (LiPBs) contain valuable elements such as cobalt (Co), nickel (Ni), copper (Cu), lithium (Li) and manganese (Mn), which can be recovered through solid–liquid extraction using choline chloride-based Deep Eutectic Solvents (DESs) and bi-functional ionic liquids (ILs). This study was carried out to investigate the extraction of metals from solid powder, black mass (BM), obtained from LiPBs, with various solvents used: six choline chloride-based DESs in combination with organic acids: lactic acid (1:2, DES 1), malonic acid (1:1, DES 2), succinic acid (1:1, DES 3), glutaric acid (1:1, DES 4) and citric acid (1:1, DES 5 and 2:1, DES 6). Various additives, such as didecyldimethylammonium chloride (DDACl) surfactant, hydrogen peroxide (H_2O_2), trichloroisocyanuric acid (TCCA), sodium dichloroisocyanurate (NaDCC), pentapotassium bis(peroxymonosulphate) bis(sulphate) (PHM), (glycine + H_2O_2) or (glutaric acid + H_2O_2) were used. The best efficiency of metal extraction was obtained with the mixture of {DES 2 + 15 g of glycine + H_2O_2} in two-stage extraction at pH = 3, T = 333 K, 2 h. In order to obtain better extraction efficiency towards Co, Ni, Li and Mn (100%) and for Cu (75%), the addition of glycine was used. The obtained extraction results using choline chloride-based DESs were compared with those obtained with three bi-functional ILs: didecyldimethylammonium bis(2,4,4-trimethylpentyl) phosphinate, [$N_{10,10,1,1}$][Cyanex272], didecyldimethylammonium bis(2-ethylhexyl) phosphate, [$N_{10,10,1,1}$][D2EHPA], and trihexyltetradecylphosphonium bis(2,4,4-trimethylpentyl) phosphinate, [$P_{6,6,6,14}$][Cyanex272]/toluene. The results of the extraction of all metal ions with these bi-functional ILs were only at the level of 35–50 wt%. The content of metal ions in aqueous and stripped organic solutions was determined by ICP-OES. In this work, we propose an alternative and highly efficient concept for the extraction of valuable metals from BM of LiPBs using DESs and ILs at low temperatures instead of acid leaching at high temperatures.

Keywords: metal extraction from black mass; DESs; bi-functional ionic liquids; extraction efficiency

1. Introduction

In recent years, the number of lithium-ion portable batteries (LiPBs) has increased rapidly because they are widely used as electronic tools due to their superior electrical performance. LiPBs contain metals such as Li, Co, Ni, Mn, Cu, Zn and Al, as well as polymers, ceramics and other substances [1–3]. In a typical Li-ion battery, the positive electrode material is an intercalated lithium compound, e.g., $LiCoO_2$, $LiMn_2O_4$, lithium nickel manganese cobalt oxides $LiNi_xMn_yCo_{1-x-y}O_2$ (abbreviated NMC, Li-NMC, LNMC or NCM) or $LiFePO_4$, while Cu, Al and Zn are present in the electrode current collectors and in the structural elements of the cells [4]. As the amount of LiPBs used increases, waste containing hazardous substances is generated, which is harmful to human life and health and to the environment (Ni and its compounds, together with Cd, Hg, Pb and their compounds, are

included in the group of so-called "priority substances" presenting a significant risk to or via the aquatic environment [5,6]). The regulations on batteries and accumulators in force in the European Union (new Regulation [7], replacing Directive [8] after the transitional period) recommend the development of new, environmentally friendly technologies for the processing and recycling of waste batteries and accumulators [9]. Therefore, the aims are to recover metals from solid powder, black mass (BM), with efficient and green methods using solvents such as Deep Eutectic Solvents (DESs) and ionic liquids (ILs). DESs are environmentally friendly solvents used to replace traditional solvents for a given application [10,11]. DESs are attractive solvents due to their intriguing physicochemical properties, which are a function of the nature of the hydrogen bond acceptor (HBA) and donor (HBD) and their molar ratio [12]. Most DESs are based on choline chloride (ChCl) and organic acids or ethylene glycol, betaine, glycerol and others in different molar ratios [12]. Extraction proceeds from the solid phase to the liquid phase, in which the separation of metals from each other must be realized via successive solvent extractions [13,14]. Given the rapid growth of the market share of lithium-ion batteries (LiBs), now used in electric and hybrid vehicles, laptops, cellphones and energy storage facilities, recycling of Co, Li, Ni, Mn, Al and Cu is very important (these metals are on the list of critical raw materials [15]). The prospect of global production of LiBs will probably amount to 93.1 billion US dollars in 2025. The production of LiBs is expected to gradually increase [16].

A new solvent extraction technology has been proposed by many authors, using different extraction procedures, different extraction solvents with different additives and at different pHs, temperatures and times to recover valuable elements from BM [1–3,17]. Organic acids are widely used instead of inorganic acids and has been described in important reviews [13,14]. The use of DESs and ILs in the metal recycling procedure based on direct solid–liquid leaching decreases the costs of the extraction versus acid leaching (not green); at high temperatures (360–770 K), times of extraction, greenhouse gasses; and with huge amounts of water. However, the primary challenge and opportunity for DESs and ILs is to achieve high selectivity compared to inorganic acids, benchmark extractants and diluents. The extraction of Co, Li and Ni from BM of waste LiBs using ILs, DESs and organophosphorous-based acids has been well described in our previous work [18]. Very promising results were obtained with DES (choline chloride, $[N_{2OH,1,1,1}]$[Cl]: lactic acid, 1:2), giving an extraction efficiency of Co 88.5%, Li 86.7% and Ni 84.5% at pH = 2.5, and DES (choline chloride, $[N_{2OH,1,1,1}]$[Cl]:phenylacetic acid, 1:2), giving a Co extraction efficiency of 98.7% and Li 100% at O:A = 1:1 [18]. Unfortunately, the BM of spent LiPBs versus LiBs contains different amounts of metals, especially much less Co and Li, which is confirmed in this work. The proposed process, which could recover Co, Ni, Li, Cu and Mn simultaneously from the solid to the liquid phase, is believed to be economical and environmentally friendly. Therefore, we grant attention to ILs, where the hydrocarbon chains on the cation are appreciably larger to allow them to be effective surface-active compounds. The most popular ILs are with ammonium or phosphonium cations and carboxylic or thiocyanate anions, especially for extraction from the aqueous phase [19]. The extraction from the solid phase is usually performed using DESs or ILs (tributylmethylammonium chloride $[N_{4,4,4,1}]$[Cl], trihexyl tetradecylphosphonium chloride, $[P_{6,6,6,14}]$[Cl]) with the addition of various oxidizing additives such as hydrogen peroxide, H_2O_2, trichloroisocyanuric acid (TCCA), (glycine + H_2O_2) or (glutaric acid + H_2O_2) [20–22]. A recent study [23] has proposed the extraction of Co(II), Li(I) and Ni(II) from the anodic and cathodic powder of laptops after leaching with 1.5 M H_2SO_4 with the addition of 30% H_2O_2 or/and glutaric acid at the temperature T = 328 K or 363 K at a solid to liquid phase ratio of 1:10 [23].

Our recent studies have shown the extraction of elements using ILs, DESs, bis(2,4,4-trimethylpentyl)phosphinic acid and Cyanex 272 from waste printed circuit boards (WPCBs) after thermal pre-treatment and leaching with various acids [24]. ILs, the Aqueous Biphasic System (ABS) method and DESs were used to extract metals from leachates and from the solid phase to the extent of 20–30 wt% of Ag, Cu and other metals [24].

An excellent overview of metals extraction using ILs and DESs with the addition of various substances, as well as using organophosphorous-based acids, is presented in the works of Liu et al. [25] and Barrueto et al. [26]. Organophosphorous-based acids such as Cyanex 272, bis(2,4,4,-trimethylpentyl)dithiophosphinic acid (Cyanex-301), di-2-ethylhexyl phosphoric acid (D2EHPA) and 2-ethylhexyl phosphonic acid-mono-2-ethylhexyl ester (PC88A) are known as effective extractants for the separation of cobalt and nickel, showing higher selectivity of cobalt over nickel. The separation of Co(II), Ni(II) and Li(I) can be achieved using oxalic acid salts, Mn(II) using D2EHPA, Ni(II) using $C_4H_8N_2O_2$ and Co(II) using $(NH_4)_2C_2O_4$ [27]. The extraction of Co using PC-88A at pH = 6.5 has been proposed [28]. The precipitation of Li(I) from an aqueous solution containing 5 g /dm^3 of Li^+ can be achieved using Na_3PO_4, Na_2CO_3 and K_2HPO_4 [29]. The possibility of extracting 95% Li^+ from LiBs leachate using a new IL (carboxymethyl trimethylammonium bis(trifluoromethylsulfonyl)imide), $[N_{CM,1,1,1}][NTf_2]$ with O/A ratio = 2:1 in time of 20 min, at pH = 3 and also extraction of other metals, such as Ni, Co, Mn, at pH > 3 and temperature T = 298 K, has also been proposed [30]. The extraction of Co (98.23%) from cell phone powdered LiBs using $[N_{8,8,8,1}][Cl]$ (Aliquat 336) at pH = 1 and O/A =1.5 is recommended in [31]. The extraction of Co and Ni from the LIB's cathode material, $LiCoO_2$, was proposed using DESs [32]. High Co extraction efficiency (99.6 wt%) was obtained with DES (choline chloride + citric acid, 1:1 or 2:1) [32]. Efficient extraction of Co from the LIB's cathode material, $LiCoO_2$, was also proposed using 0.5 M glycine (chelating agent) and 0.02 M ascorbic acid (reductant) at T = 353 K for 1 h after the carboxylation process at T = 973 K for 2 h [33]. Literature data on the physicochemical properties of some DESs and their extraction properties are described in [34].

The use of a bi-functional IL synthesized from Aliquat 336 and D2EHPA, cationic and anionic extractants, increased the extraction of Mo and V from the spent petroleum catalysts by more than 30% [35]. Good results in the selective and effective leaching of vanadium and molibdenium from the spent petroleum catalysts were obtained with bi-functional IL composed of Alamine 336 (*N*,*N*-dioctyl-1-octanamine) and ionic liquid Ali-D2 in the presence of oxidizing agent, H_2O_2 [36].

In the solvometallurgy process, a combination of solvent extraction and gradient chemical precipitation is usually used to separate and recover transition metals from the leachate. Since metal ions in solutions, such as Co(II), Ni(II), Cu(II), Li(I) and Mn(II), are similar in nature, a lot of methods and solvents have been proposed in recent years to separate them from each other [37–42]. However, this recycling process requires the use of additional energy and chemical reagents, and it will be the next step in our recycling experiments.

In this paper, the extraction performance of Co, Ni, Li, Cu and Mn from LIPBs' BM has been optimized using different DESs: (1) {choline chloride + lactic acid, 1:2}, (2) {choline chloride + malonic acid, 1:1}, (3) {choline chloride + succinic acid, 1:1}, (4) {choline chloride + glutaric acid, 1:1}, (5,6) {choline chloride + citric acid, 1:1 and 2:1} and bi-functional ILs: didecyldimethylammonium bis(2,4,4-trimethylpentyl) phosphinate, $[N_{10,10,1,1}]$[Cyanex272], didecyldimethylammonium bis(2-ethylhexyl) phosphate, $[N_{10,10,1,1}]$[D2EHPA], trihexyltetradecylphosphonium bis(2,4,4-trimethylpentyl) phosphinate, $[P_{6,6,6,14}]$[Cyanex272]/toluene (an aromatic diluent). Various additives have been used, such as a didecyldimethylammonium chloride (DDACl) surfactant, hydrogen peroxide (H_2O_2), trichloroisocyanuric acid (TCCA), sodium dichloroisocyanurate (NaDCC), pentapotassium bis(peroxymonosulphate) bis(sulphate) (PHM), (glycine + H_2O_2), or (glutaric acid + H_2O_2).

These processes mainly consisted of solid–liquid extraction at different process parameters such as pH, temperature, time and solid to liquid phase ratio. The metal ions concentration in aqueous and stripped organic solutions was determined by the ICP-OES method.

2. Results and Discussion

2.1. Solid BM Composition

The content of valuable elements (Co, Ni, Cu, Mn, Fe, Al, Zn and Li) in spent $LiNi_xMn_yCo_{1-x-y}O_2$ powder is given in Table 1. The material was manually shredded and ground in a mortar into small particles with a diameter of 1.2 mm (see Figure 1). The results of the analysis of the metal content in the starting BM material provided by the microwave digestion method/FAAS and FAES techniques are presented as the EDS spectra concerning only the micro area of the BM surface in Figure 2 and in Figures S1–S3 in the Supplementary Material (SMs).

Table 1. Metal content in the starting LiPBs' BM material.

Co wt%	Ni wt%	Cu wt%	Mn wt%	Fe wt%	Al wt%	Zn wt%	Li wt%
2.95	8.6	4.0	3.4	1.9	1.65	0.067	2.2

Figure 1. Solid LiPBs' BM sample before powdering in a mortar.

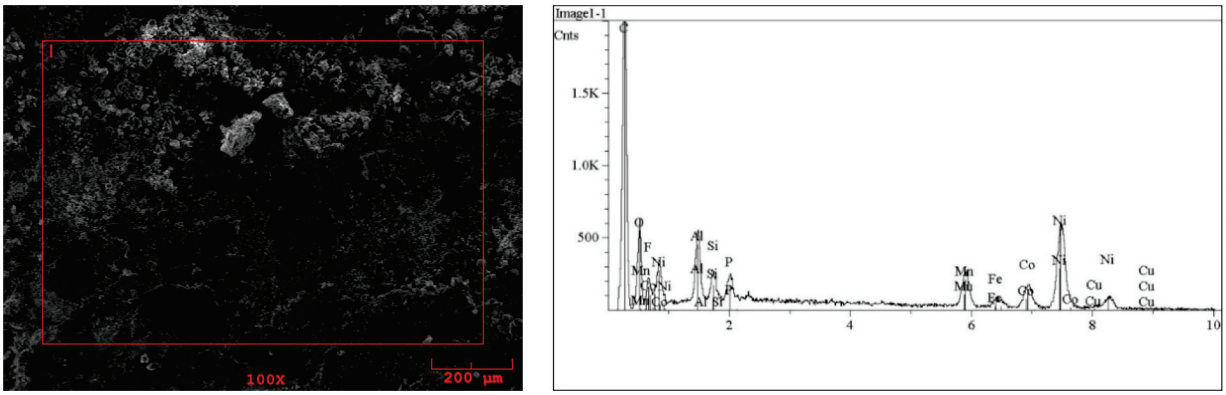

Figure 2. SEM image of the solid LiPBs' BM sample and EDS spectrum of the micro-area marked in the image.

The starting BM contained the following metals: cobalt (Co), nickel (Ni), copper (Cu), manganese (Mn), iron (Fe), aluminum (Al), zinc (Zn) and lithium (Li). The metal content was about 0.1–8.6 wt%. The BM of LiPBs contained significantly less Co (2.95 wt%) and Li

(2.2 wt %) compared to the previously studied BM of LiBs (Co 26.0 wt%, Li 4.0 wt%) [20]. On the other hand, the BM of LiPBs contained more Cu (4.0 wt%) compared to the BM of LiBs (2.8 wt%) [20]. This result provides a proof of concept for the use of modern-green solvents as liquids to enable the recycling of smaller amounts of Co. It also requires better technique and better extraction parameters, especially in the next step of Co-Ni separation.

2.2. Extraction

The metal extraction efficiency (E) was calculated according to the following formula:

$$E\ (\text{wt\%}) = 100 \times (g_{E,A} + g_{E,O})/g_0 \quad (1)$$

where g_0 (g) is the initial metal content in the solid material and g_E (g) is the content of metal ion in the aqueous phase (A) and the organic phase (O) after extraction.

2.2.1. Extraction with DESs

In general, most DESs possess a relatively high viscosity (>100 cP) at room temperature, which significantly limits their application for extraction. Their high viscosity reduces the mass transfer rate between the sample and the extraction phase, owing to the formation of extensive hydrogen bond networks between the hydrogen bond acceptor, HBA (choline chloride), and the hydrogen bond donor, HBD, (organic acid) component. There are two methods to reduce the viscosity: increasing the temperature or adding the diluent. The addition of water to DESs significantly reduces the viscosity of DESs as a result of the gradually weakened hydrogen bonding interaction between the DES components. The interaction between HBA and HBD is weakened or even disappears when the water content is above 50% (v/v). The hydrogen bond interactions between the HBA and HBD are reduced, and, at this stage, the DES loses its unique eutectic properties and exists like a liquid with individual HBA and HBD components [43].

The results of the extraction with DES 1 and DES 2 are summarized in Tables 2 and 3, respectively. The extraction efficiency (E) obtained with these DESs is appreciably much higher than those using other DESs or bi-functional ILs. The extraction efficiency with DES 1 exhibited effective but simultaneous extraction of all metals, including Co, Ni, Li, Cu and Mn at low temperatures, T = 333 K and at a short time of 2 h, at pH = 3. The results depend on oxidizing additives at constant temperature, time and pH. The best results for DES 1 were observed for TCCA, E_{Co} = 48 wt%, E_{Ni} = 57 wt%, E_{Li} = 56 wt% and E_{Mn} = 60 wt%. Similar results were also obtained for (glycine + H_2O_2): E_{Co} = 52 wt%, E_{Ni} = 53 wt%, E_{Li} = 54 wt% and E_{Mn} = 62 wt%. A high extraction efficiency was observed for copper: E_{Cu} = 95 wt% for (DES 1 + H_2O_2), E_{Cu} = 97 wt% for (DES 1 + PHM), E_{Cu} = 70 wt% for (DES 1 + glycine + H_2O_2) and E_{Cu} = 82 wt% for (DES 1 + glutaric acid + H_2O_2). An interesting fact that is worth noting when viewing Table 2 is that the best extraction efficiency of Co is at the level of 48–52 wt% or for Ni at 53–57 wt% when using (DES 1 + TCCA) or (DES 1 + glycine + H_2O_2). However, the results expected by the industry should exceed an extraction efficiency higher than 75%.

The extraction efficiency with DES 2 also showed very good extraction of all metals at the same temperature, time and pH. The best results were observed for (DES 2 + glycine + H_2O_2): E_{Co} = 60 wt%, E_{Ni} = 66 wt%, E_{Li} = 67 wt%, E_{Cu} = 75 wt% and E_{Mn} = 65 wt%. Similar results were also obtained for (DES 2 + TCCA): E_{Co} = 59 wt%, E_{Ni} = 50 wt%, E_{Li} = 65 wt%, E_{Cu} = 86 wt% and E_{Mn} = 69 wt%, and for (DES 2 + NaDCC × $2H_2O$): E_{Co} = 57 wt%, E_{Ni} = 56 wt%, E_{Li} = 66 wt%, E_{Cu} = 37 wt% and E_{Mn} = 62 wt%. The system (DES 2 + H_2O_2) revealed only high extraction of Li, E_{Li} = 76 wt%. The best extraction efficiency for Co is at the level of 60 wt% or for Ni 50–66 wt% using (DES 2 + TCCA) or (DES 2 + NaDCC × $2H_2O$) or (DES 2 + glycine + H_2O_2) (see Table 3).

Table 2. Results of metal extraction with DES 1 at T = 333 K, 2 h, extraction efficiency (E) at pH = 3.

Extrahent	Ion	g_0 * (mg)	g_E * (mg)	E (wt%)
DES 1 + H_2O_2	Co(II)	295	82.44	28
	Ni(II)	860	246.36	29
	Li(I)	220	136.42	62
	Cu(II)	400	381.19	95
	Mn(II)	340	163.00	48
DES 1 + TCCA	Co(II)	295	141.44	48
	Ni(II)	860	492.10	57
	Li(I)	220	123.61	56
	Cu(II)	400	80.83	20
	Mn(II)	340	202.87	60
DES 1 + NaDCC × $2H_2O$	Co(II)	295	88.38	30
	Ni(II)	860	282.45	33
	Li(I)	220	95.39	43
	Cu(II)	400	111.04	28
	Mn(II)	340	100.37	30
DES 1 + PHM	Co(II)	295	108.61	37
	Ni(II)	860	132.32	15
	Li(I)	220	167.00	76
	Cu(II)	400	388.73	97
	Mn(II)	340	231.70	68
DES 1 + (glycine + H_2O_2)	Co(II)	295	153.75	52
	Ni(II)	860	452.75	53
	Li(I)	220	118.02	54
	Cu(II)	400	280.82	70
	Mn(II)	340	212.27	62
DES 1 + (glutaric acid + H_2O_2)	Co(II)	295	113.91	39
	Ni(II)	860	371.38	43
	Li(I)	220	103.76	47
	Cu(II)	400	329.28	82
	Mn(II)	340	165.28	49

* g_0—metal content in the solid phase before extraction, g_E—metal ion content in both aqueous phases after extraction [aqueous phase after extraction of the solid phase and aqueous phase after stripping the organic phase (TCCA only)].

These results confirmed that DES 1 or DES 2 is able to extract metals from the solid phase with an extraction efficiency higher than 75% only for Cu and Li in the presence of H_2O_2, TCCA, PHM and the DDACl surfactant.

The extraction efficiency with DES 3 shows lower metal extraction effects. The best results were observed for (DES 3 + TCCA): E_{Co} = 54 wt%, E_{Ni} = 44 wt%, E_{Li} = 73 wt%, E_{Cu} = 94 wt% and E_{Mn} = 73 wt%. Similar results were also obtained for (DES 2 + TCCA): E_{Co} = 59 wt%, E_{Ni} = 50 wt%, E_{Li} = 65 wt%, E_{Cu} = 86 wt% and E_{Mn} = 69 wt%. Slightly worse results were observed for (DES 3 + NaDCC × $2H_2O$): E_{Li} = 60 wt% and E_{Cu} = 48 wt%, and for the rest of metals, the extraction efficiency was <20 wt%. The system (DES 3 + H_2O_2) revealed considerable extraction only in the case of Li, E_{Li} = 48 wt% and of Mn, E_{Mn} = 42 wt%.

Unfortunately, the extraction efficiency using (DES 3 + glycine + H_2O_2) was not attractive and only lithium extraction was at the level of E_{Li} = 55 wt%. Low extraction efficiency was also observed for (DES 3 + PHM) for all metals except lithium and manganese, E_{Li} = 64 wt% and E_{Mn} = 55 wt%. The best extraction efficiency for Co was 53 wt% using (DES 3 + TCCA) and for Ni 44–49 wt% using (DES 3 + TCCA) or (DES 3 + glycine + H_2O_2) or (DES 3 + glutaric acid + H_2O_2) (see Table 4). As in the case of DESs 1 and 2, extraction efficiencies above 75% were only observed for Cu in the presence of TCCA and the DDACl surfactant.

Table 3. Results of metal extraction with DES 2 at T = 333 K, 2 h, extraction efficiency (E) at pH = 3.

Extrahent	Ion	g_0 * (mg)	g_E * (mg)	E (wt%)
DES 2 + H_2O_2	Co(II)	295	40.65	14
	Ni(II)	860	104.36	12
	Li(I)	220	168.02	76
	Cu(II)	400	164.62	41
	Mn(II)	340	178.52	53
DES 2 + TCCA	Co(II)	295	175.07	59
	Ni(II)	860	429.03	50
	Li(I)	220	143.09	65
	Cu(II)	400	344.28	86
	Mn(II)	340	236.02	69
DES 2 + NaDCC × $2H_2O$	Co(II)	295	166.65	57
	Ni(II)	860	481.23	56
	Li(I)	220	144.06	66
	Cu(II)	400	146.64	37
	Mn(II)	340	210.80	62
DES 2 + PHM	Co(II)	295	58.60	20
	Ni(II)	860	19.55	2
	Li(I)	220	179.27	82
	Cu(II)	400	311.42	78
	Mn(II)	340	208.91	61
DES 2 + (glycine + H_2O_2)	Co(II)	295	177.22	60
	Ni(II)	860	568.86	66
	Li(I)	220	147.06	67
	Cu(II)	400	300.80	75
	Mn(II)	340	221.00	65
DES 2 + (glutaric acid + H_2O_2)	Co(II)	295	53.14	18
	Ni(II)	860	234.61	27
	Li(I)	220	157.42	72
	Cu(II)	400	82.98	21
	Mn(II)	340	152.34	45

* g_0—metal content in the solid phase before extraction, g_E—metal ion content in both aqueous phases after extraction [aqueous phase after extraction of the solid phase and aqueous phase after stripping the organic phase (TCCA only)].

Table 4. Results of metal extraction with DES 3 at T = 333 K, 2 h, extraction efficiency (E) at pH = 3.

Extrahent	Ion	g_0 * (mg)	g_E * (mg)	E (wt%)
DES 3 + H_2O_2	Co(II)	295	103.37	35
	Ni(II)	860	284.53	33
	Li(I)	220	106.13	48
	Cu(II)	400	44.26	12
	Mn(II)	340	144.32	42
DES 3 + TCCA (T = 318 K)	Co(II)	295	157.82	53
	Ni(II)	860	381.36	44
	Li(I)	220	161.45	73
	Cu(II)	400	376.52	94
	Mn(II)	340	249.45	73
DES 3 + NaDCC × $2H_2O$	Co(II)	295	34.92	12
	Ni(II)	860	164.55	19
	Li(I)	220	131.92	60
	Cu(II)	400	191.64	48
	Mn(II)	340	28.21	8
DES 3 + PHM	Co(II)	295	60.03	20
	Ni(II)	860	13.87	2
	Li(I)	220	141.54	64
	Cu(II)	400	87.14	22
	Mn(II)	340	186.00	55
DES 3 + (glycine + H_2O_2)	Co(II)	295	116.19	39
	Ni(II)	860	378.38	44
	Li(I)	220	118.93	54
	Cu(II)	400	147.84	37
	Mn(II)	340	153.19	45
DES 3 + (glutaric acid + H_2O_2)	Co(II)	295	120.76	41
	Ni(II)	860	418.61	49
	Li(I)	220	115.26	52
	Cu(II)	400	109.57	27
	Mn(II)	340	146.68	43

* g_0—metal content in the solid phase before extraction, g_E—metal ion content in both aqueous phases after extraction [aqueous phase after extraction of the solid phase and aqueous phase after stripping the organic phase (TCCA only)].

The DES 4 with the addition of TCCA shows good recovery of Co, Ni, Li, Cu and Mn: E_{Co} = 51 wt%, E_{Ni} = 50 wt%, E_{Li} = 60 wt%, E_{Cu} = 87 wt% and $E_{M\,n}$= 65 wt%. Much smaller extraction effects were observed for DES 4 with the addition of H_2O_2. All extraction efficiencies were lower than 50 wt%. Only affinity for Mn was observed, E_{Mn} = 53 wt%. The extraction of metals was very low using (DES 4 + NaDCC × $2H_2O$), and only the extraction of Li was >50 wt%, E_{Li} = 51 wt%, and for the rest of metals the extraction efficiency was ≤20–30 wt%. The aqueous phase and NaDCC × $2H_2O$ do not interact with the cationic functional group. For the same reasons, not very attractive selectivity was also observed for (DES 4 + PHM): E_{Li} = 65 wt% and E_{Mn} = 61 wt% in one aqueous phase. The extraction efficiency using (DES 4 + glycine + H_2O_2) was not very significant, except E_{Cu}= 76 wt%,

E_{Li} = 49 wt% and E_{Mn} = 48 wt%; for Ni, it was close to 40%. This can be attributed to the physical imprint that does not fit the glycine molecules. The addition of the glutaric acid revealed the extraction efficiency for all metal ions < 50 wt%. The best extraction efficiency for Co was 51 wt% when using (DES 4 + TCCA), and for Ni it was 50 wt% or 43 wt% using (DES 4 + TCCA) or (DES 4 + glutaric acid + H_2O_2) (see Table 5).

Table 5. Results of metal extraction with DES 4 at T = 333 K, 2 h, extraction efficiency (E) at pH = 3.

Extrahent	Ion	g_0 * (mg)	g_E * (mg)	E (wt%)
DES 4 + H_2O_2	Co(II)	295	133.41	45
	Ni(II)	860	360.16	42
	Li(I)	220	108.70	49
	Cu(II)	400	66.99	17
	Mn(II)	340	178.68	53
DES 4 + TCCA (T = 318 K)	Co(II)	295	151.76	51
	Ni(II)	860	426.40	50
	Li(I)	220	131.68	60
	Cu(II)	400	348.66	87
	Mn(II)	340	221.27	65
DES 4 + NaDCC × $2H_2O$	Co(II)	295	36.56	12
	Ni(II)	860	174.50	20
	Li(I)	220	112.19	51
	Cu(II)	400	130.56	33
	Mn(II)	340	36.31	11
DES 4 + PHM	Co(II)	295	55.46	19
	Ni(II)	860	12.67	2
	Li(I)	220	143.40	65
	Cu(II)	400	108.95	27
	Mn(II)	340	206.00	61
DES 4 + (glycine + H_2O_2)	Co(II)	295	109.32	37
	Ni(II)	860	333.66	39
	Li(I)	220	108.69	49
	Cu(II)	400	303.02	76
	Mn(II)	340	164.63	48
DES 4 + (glutaric acid + H_2O_2)	Co(II)	295	122.85	42
	Ni(II)	860	371.96	43
	Li(I)	220	106.67	49
	Cu(II)	400	81.87	20
	Mn(II)	340	167.52	49

* g_0—metal content in the solid phase before extraction, g_E—metal ion content in both aqueous phases after extraction [aqueous phase after extraction of the solid phase and aqueous phase after stripping the organic phase (TCCA only)].

Based on the above extraction behaviours of DES 4 and the earlier discussed DESs 1–3, it appears that the type of additive is an important parameter in the extraction of selected metal species in the DESs leachate. Acceptable extraction efficiency was observed only for DES 4 + TCCA or (glycine + H_2O_2) for Cu.

The DES 5 (1:1) with the addition of H_2O_2 shows good recovery of Co, Ni, Li, and Mn: E_{Co} = 50 wt%, $E_{N\,i}$= 51 wt%, E_{Li} = 62 wt% and E_{Mn} = 61 wt%. Similar results were obtained with the addition of TCCA. The best results were observed for Cu, E_{Cu} = 84 wt% and E_{Cu} = 88 wt% for both extractants, respectively. Metal extraction was very effective

for (DES 5 (1:1) + NaDCC × $2H_2O$) only for Cu, E_{Cu} = 94 wt%. For the rest of the metals, the extraction efficiency was 48–66 wt%. A high extraction efficiency for Li, Cu and Mn was observed for (DES 5 + PHM): E_{Li} = 88 wt%, E_{Cu} = 87 wt% and E_{Mn} = 74 wt%. The extraction efficiency using (DES 5 + glycine + H_2O_2) was not very significant, E_{Cu} = 85 wt% and E_{Li} = 61 wt%, and for the rest of metals was approximately 40–50 wt%. The addition of glutaric acid showed an extraction efficiency for Co, Ni and Mn of <50 wt%, for Li of E_{Li} = 53 wt%, and for Cu of E_{Cu} = 69 wt% (see Table 6). All DESs 1–5 with all oxidizing additives reviled that the extraction efficiency for Co and Ni was not higher than 50%, and only Cu and Li were extracted with a higher extraction efficiency.

Table 6. Results of metal extraction with DES 5 (1:1) at T = 333 K, 2 h, extraction efficiency (E) at pH = 3.

Extrahent	Ion	g_0 * (mg)	g_E * (mg)	E (wt%)
DES 5 + H_2O_2	Co(II)	295	147.47	50
	Ni(II)	860	439.56	51
	Li(I)	220	136.47	62
	Cu(II)	400	335.74	84
	Mn(II)	340	206.09	61
DES 5 + TCCA (T = 318 K)	Co(II)	295	147.12	50
	Ni(II)	860	381.17	44
	Li(I)	220	132.92	60
	Cu(II)	400	350.78	88
	Mn(II)	340	206.69	61
DES 5 + NaDCC × $2H_2O$	Co(II)	295	142.85	48
	Ni(II)	860	442.10	51
	Li(I)	220	145.17	66
	Cu(II)	400	374.00	94
	Mn(II)	340	210.90	62
DES 5 + PHM	Co(II)	295	115,16	39
	Ni(II)	860	208.16	24
	Li(I)	220	193.01	88
	Cu(II)	400	347.42	87
	Mn(II)	340	250.52	74
DES 5 + (glycine + H_2O_2)	Co(II)	295	125.91	43
	Ni(II)	860	388.85	45
	Li(I)	220	134.53	62
	Cu(II)	400	341.59	85
	Mn(II)	340	178.51	53
DES 5 + (glutaric acid + H_2O_2)	Co(II)	295	116.05	39
	Ni(II)	860	367.34	43
	Li(I)	220	116.92	53
	Cu(II)	400	277.37	69
	Mn(II)	340	165.34	49

* g_0—metal content in the solid phase before extraction, g_E—metal ion content in both aqueous phases after extraction [aqueous phase after extraction of the solid phase and aqueous phase after stripping the organic phase (TCCA only)].

The DES 6 (2:1) with the addition of H_2O_2 shows a good recovery of metals: E_{Co} = 52 wt%, E_{Ni} = 59 wt%, E_{Li} = 51 wt%, E_{Cu} = 68 wt% and E_{Mn} = 62 wt%. Similar results were obtained with the addition of TCCA (except Ni), and the best results were observed for Mn,

E_{Mn} = 96 wt%. Metal extraction was very effective for (DES 6 (2:1) + NaDCC × $2H_2O$) only for Cu, E_{Cu} = 65 wt%, and for Mn, E_{Mn} = 68 wt%. For the rest of the metals, the extraction efficiency was 11–42 wt%. Attractive selectivity for Li, Cu and Mn was observed for (DES 6 + PHM): E_{Li} = 62 wt%, E_{Cu} = 66 wt% and E_{Mn} = 83 wt%. The extraction efficiency using (DES 6 + glycine + H_2O_2) was very significant for Cu, E_{Cu}= 71 wt%, and for Mn, E_{Mn}= 84 wt%; for the rest of metals, it was 20–57 wt%. The addition of glutaric acid revealed the extraction efficiency for Co, Ni and Li at the level of approximately 50–57 wt%, for Cu of E_{Cu}= 68 wt% and for Mn of E_{Mn}= 80 wt% (see Table 7). The results presented in Table 7 indicate that only Mn can be extracted at an economical level higher than 75%.

Table 7. Results of metal extraction with DES 6 (2:1) at T = 333 K, 2 h, extraction efficiency (E) at pH = 3.

Extrahent	Ion	g_0 * (mg)	g_E * (mg)	E (wt%)
DES 6 + H_2O_2	Co(II)	295	151.95	52
	Ni(II)	860	510.33	59
	Li(I)	220	111.67	51
	Cu(II)	400	271.66	68
	Mn(II)	340	210.02	62
DES 6 + TCCA (T = 318 K)	Co(II)	295	178.91	61
	Ni(II)	860	173.15	20
	Li(I)	220	132.22	60
	Cu(II)	400	298.25	75
	Mn(II)	340	327.5	96
DES 6 + NaDCC × $2H_2O$	Co(II)	295	103.75	35
	Ni(II)	860	98.36	11
	Li(I)	220	92.80	42
	Cu(II)	400	259.72	65
	Mn(II)	340	229.67	68
DES 6 + PHM	Co(II)	295	94.19	32
	Ni(II)	860	311.5	36
	Li(I)	220	137.06	62
	Cu(II)	400	263.81	66
	Mn(II)	340	281.11	83
DES 6 + (glycine + H_2O_2)	Co(II)	295	168.76	57
	Ni(II)	860	169.91	20
	Li(I)	220	114.94	52
	Cu(II)	400	282.63	71
	Mn(II)	340	286.07	84
DES 6 + (glutaric acid + H_2O_2)	Co(II)	295	147.55	50
	Ni(II)	860	487.22	57
	Li(I)	220	108.68	49
	Cu(II)	400	272.95	68
	Mn(II)	340	271.84	80

* g_0—metal content in the solid phase before extraction, g_E—metal ion content in both aqueous phases after extraction [aqueous phase after extraction of the solid phase and aqueous phase after stripping the organic phase (TCCA only)].

The best extraction efficiency for all metals was obtained with (DES 2 + glycine + H_2O_2), so two-stage extraction was investigated to increase the effect with different amounts of glycine. The results obtained at pH = 3, T = 333 K, 2 h, shown in Table S1 in SMs and in Figures 3 and 4, exhibited an increase in the extraction efficiency of metals with an increase in the glycine content in the extractant. The majority of metals were extracted in 100 wt% in the system with the addition of 15 g of glycine. Only Cu's extraction was 75 wt%.

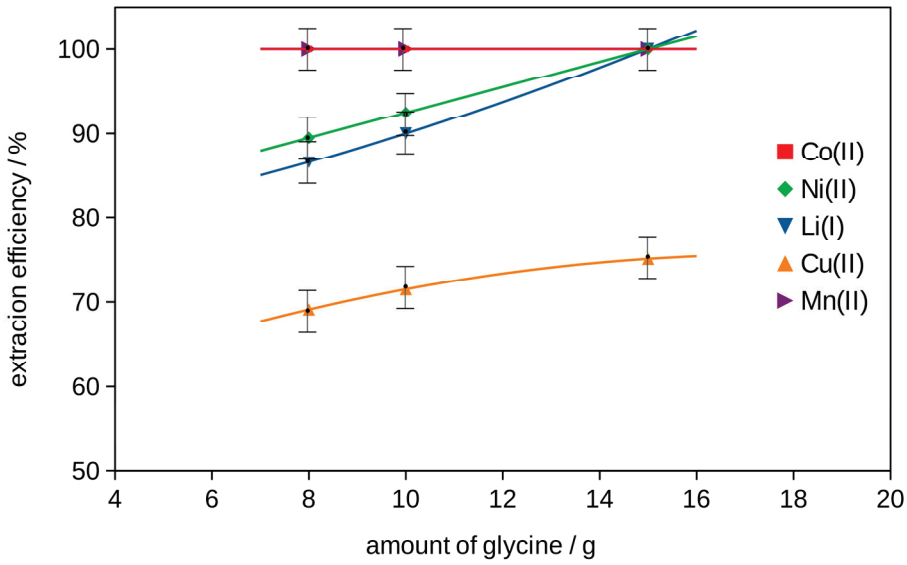

Figure 3. The effect of the amount of glycine on the efficiency of metal ion extraction at temperature T = 333 K, pH = 3, and time 2 h, with two-stage extraction.

Figure 4. Products of extraction at temperature T = 333 K, pH = 3, time 2 h, and two-stage extraction with glycine addition (**left**, 8 g of glycine, **right**, 15 g of glycine).

The effect of the pH of the mixture of (DES 2 + 15 g of glycine + H_2O_2) was not significant (see Table S2 in SMs and Figure 5). Only the extraction efficiency of lithium and copper increases slightly with the increase in pH. The influence of temperature on the extraction for the same mixture (DES 2 + 15 g of glycine + H_2O_2) at pH = 3 is evident. The extraction increases with the increase in temperature from 303 K to 333 K, except for Cu. The best results with an extraction efficiency of 100 wt% were observed for all metals except Cu, 75 wt% (see Table S3 in SMs and Figure 6).

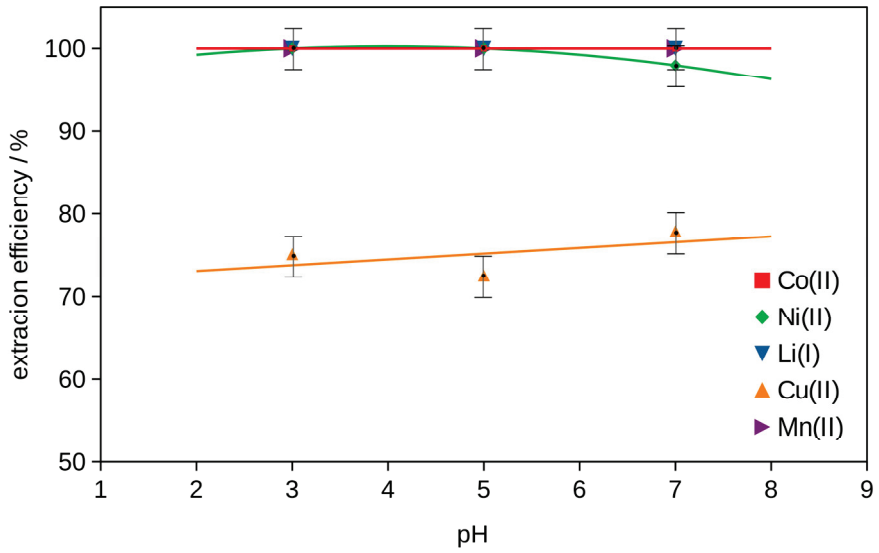

Figure 5. Efficiency of metal ion extraction at T = 333 K, 2 h, with 15 g of glycine and two-stage extraction at different pHs.

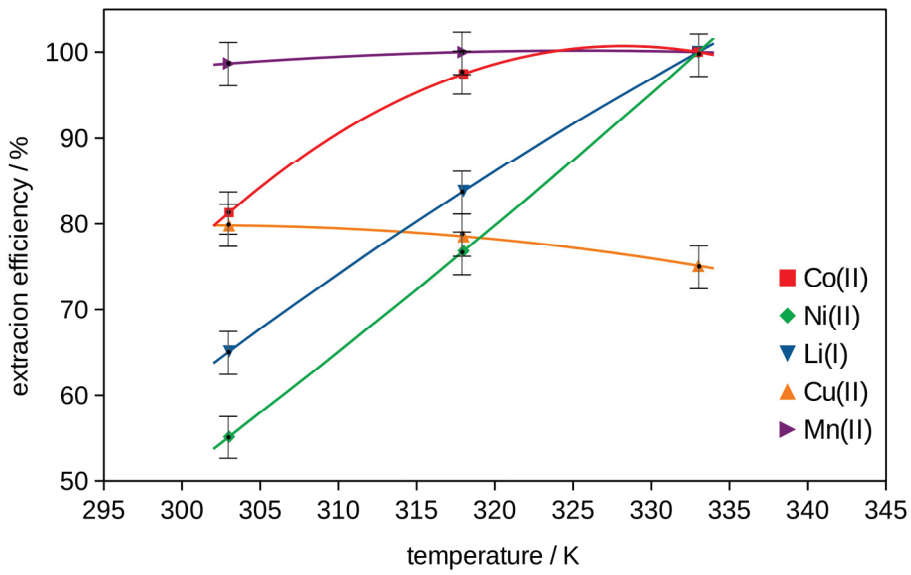

Figure 6. Efficiency of metal ion extraction at pH = 3, 2 h, with 15 g of glycine, and two-stage extraction at different temperatures.

The influence of the time of the two-stage extraction process (t = 0.5 h, 1 h, 1.5 h, 2 h) with 15 g of glycine at pH = 3 on the extraction efficiency using the best selected procedure is shown in Table S4 in SMs and in Figure 7. Again, an increase in the extraction efficiency was observed for all metals (100 wt% for Co and Mn except for Cu 75 wt%.

The mechanism of using a composite of ionic liquid (tetrabutylmethylammonium chloride ($N_{4,4,4,1}Cl$) with TCCA for leaching gold from the ore and spent catalyst was presented earlier [20]. During the leaching process, TCCA acted as a metal oxidant and the oxidized metal ions were then captured by IL, which coordinates well with metal ions. A protic solvent such as water, alcohol or acetone induces the formation of cyanuric acid (the product of TCCA reaction). The possible reaction mechanism presented the metallic gold (Au^0) oxidizing process by TCCA and the resultant [$AuCl_3$] then coordinates with Cl^- in IL (DES and DDACl in our work) to form $[AuCl_4]^-$. Then, a more stable ion pair is formed with $[N_{4441}]^+$ through electrostatic attraction, hydrogen bonding and other forces, and finally diffuses into the bulk phase of IL (DES in our work) [20]. Therefore,

$N_{4441}Cl$:TCCA:Au = 300:30:1 was assumed as the appropriate mass ratio in that work [20]. It can only be assumed that H_2O_2, NaDCC × $2H_2O$ and PHM play a similar role. Additionally, DDACl as an IL provides Cl^- anions and acts as a surfactant thanks to long aliphatic chains (C_{10}).

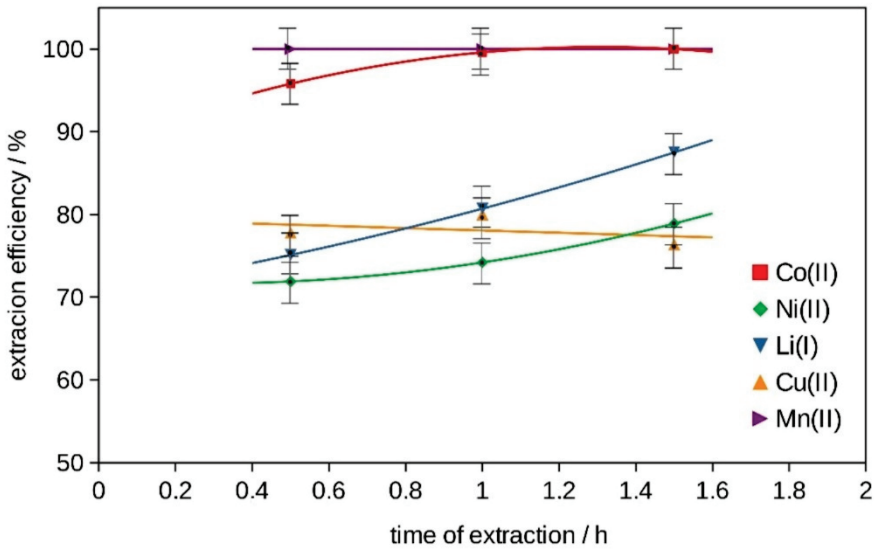

Figure 7. Efficiency of metal ion extraction at T = 333 K, pH = 3, with 15 g of glycine and two-stage extraction at different extraction times.

More than 95% of Co was extracted from spent LIBs using 0.5 M glycine (chelating agent) and 0.02 M ascorbic acid (reductant) at 80 °C for 6 h. UV–vis spectra of the solution confirm the build–up of the Co(III) and Co(II)−glycine complex ($\lambda_{max} \approx 310$ nm) [33]. The work clearly indicates the reduction behaviour of Co(III)–glycine to Co(II)–glycine by ascorbic acid (in our work, it must be malonic acid from DES 2) [33].

The best extraction results were observed for the DES 2 with malonic acid. This result may be interpreted by the different acidity of the HBD—hydrogen bond donor—of the choline chloride–DESs. The acid strength of malonic acid (pK_{a1} = 2.83) is much higher than that of other organic acids used: citric acid, pK_{a1} = 3.13, lactic acid, pK_{a1} = 3.86, succinic acid, pK_{a1} = 4.20 and glutaric acid, pK_{a1} = 4.34 [44].

2.2.2. Extraction with Bi-Functional Ionic Liquids

Further extraction was achieved with three bi-functional ionic liquids. The results obtained with $[N_{10,10,1,1}]$[Cyanex272] are presented in Table 8. The addition of H_2O_2 shows the recovery of metals at the level of 15–34 wt%. Better results were obtained with the addition of TCCA only for Li, E_{Li} = 55 wt%. The results obtained with $[N_{10,10,1,1}]$[D2EHPA] are presented in Table 9. The addition of H_2O_2 shows the recovery of Co, Ni, Li, Cu and Mn at the level of 1–25 wt%. Slightly better results were obtained with the addition of TCCA. The best results were observed for Co, Li and Mn, of E_{Co} = 47 wt%, E_{Li} = 49 wt% and E_{Mn} = 41 wt%. The only high extraction efficiency was observed in the case of PHM for Li, E_{Li} = 47 wt%. The extraction efficiency using (glycine + H_2O_2) was 21–39 wt% for all metals. The results obtained with $[P_{6,6,6,14}]$[Cyanex272] are presented in Table 10. The addition of H_2O_2 at pH = 3 shows metal recovery at the level of 10–36 wt%. Better results were observed with the addition of TCCA, but only for Li, E_{Li} = 51 wt%, and for Mn, E_{Mn} = 46 wt%. Unfortunately, the extraction efficiencies obtained when using the bi-functional ILs with various additives were not as attractive as in the case of the mixture (DES 2 + 15 g of glycine + H_2O_2) after two-stage extraction.

Table 8. Results of metal extraction with $[N_{10,10,1,1}]$[Cyanex272] at T = 303 K, 2 h, extraction efficiency (E) at pH = 3.

Extrahent	Ion	g_0 * (mg)	g_{EAq} * (mg)	g_{EOrg} * (mg)	E (wt%)
$[N_{10,10,1,1}]$[Cyanex272] + H_2O_2	Co(II)	295	14.15	45.99	20
	Ni(II)	860	50.74	75.32	15
	Li(I)	220	33.37	32.63	30
	Cu(II)	400	1.32	133.60	34
	Mn(II)	340	10.79	74.10	25
$[N_{10,10,1,1}]$[Cyanex272] + TCCA	Co(II)	295	12.62	69.93	28
	Ni(II)	860	99.03	141.69	28
	Li(I)	220	46.23	75.38	55
	Cu(II)	400	0.74	134.34	34
	Mn(II)	340	15.49	124.67	41
$[N_{10,10,1,1}]$[Cyanex272] + PHM	Co(II)	295	34.60	18.06	18
	Ni(II)	860	26.07	16.24	5
	Li(I)	220	80.33	20.82	46
	Cu(II)	400	7.25	106.76	29
	Mn(II)	340	26.07	15.75	12
$[N_{10,10,1,1}]$[Cyanex272] + (glycine + H_2O_2)	Co(II)	295	73.06	14.77	30
	Ni(II)	860	171.00	31.56	24
	Li(I)	220	66.57	14.87	37
	Cu(II)	400	114.62	45.77	40
	Mn(II)	340	122.86	131.56	75

* g_0—metal content in the solid phase before extraction, g_E—metal ion content in the aqueous or organic phase after the stripping process.

The synthesis of ILs is presented in SMs. Figure 8 shows, as an example, extraction with bi-functional ILs ($[P_{6,6,6,14}]$[Cyanex272] + TCCA).

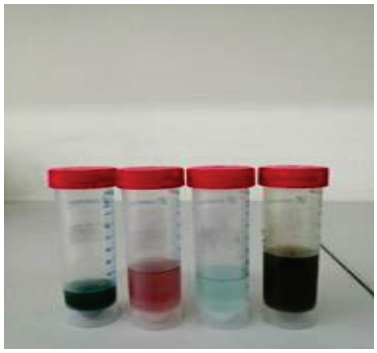

Figure 8. Products of extraction with bi-functional IL ($[P_{6,6,6,14}]$[Cyanex272] + TCCA): from left to right: (1) aqueous phase, dark green; (2) organic phase after the first stripping with 1.2 M H_2SO_4, pink; (3) solution after the second stripping with the 1.2 M H_2SO_4, blue; (4) organic phase (IL) after two stripping processes, brown.

Table 9. Results of metal extraction with $[N_{10,10,1,1}]$[D2EHPA] at T = 303 K, 2 h, extraction efficiency (E) at pH = 3.

Extrahent	Ion	g_0 * (mg)	g_{EAq} * (mg)	g_{EOrg} * (mg)	E (wt%)
$[N_{10,10,1,1}]$[D2EHPA] + H_2O_2	Co(II)	295	1.47	5.79	3
	Ni(II)	860	1.55	10.48	1
	Li(I)	220	21.61	15.37	17
	Cu(II)	400	2.31	97.83	25
	Mn(II)	340	3.02	12.61	5
$[N_{10,10,1,1}]$[D2EHPA] + TCCA	Co(II)	295	20.23	117.74	47
	Ni(II)	860	82.59	112.63	23
	Li(I)	220	57.03	51.27	49
	Cu(II)	400	1.63	119.37	30
	Mn(II)	340	39.82	100.58	41
$[N_{10,10,1,1}]$[D2EHPA] + PHM	Co(II)	295	35.87	6.12	14
	Ni(II)	860	19.22	6.01	3
	Li(I)	220	91.74	11.09	47
	Cu(II)	400	63.62	55.32	30
	Mn(II)	340	100.73	12.92	33
$[N_{10,10,1,1}]$[D2EHPA] + (glycine + H_2O_2)	Co(II)	295	73.97	6.49	27
	Ni(II)	860	168.63	12.63	21
	Li(I)	220	62.74	8.95	33
	Cu(II)	400	126.44	25.58	38
	Mn(II)	340	123.22	9.26	39

* g_0—metal content in the solid phase before extraction, g_E—metal ion content in the aqueous or organic phase after the stripping process.

The synthesis of bi-functional ILs based on commercially available extractants such as Cyanex272, or D2EHPA with ammonium, or phosphonium IL has attracted interest due to the simplicity of synthesis and new properties. These ILs contain cations and anions with the functional groups which can act as both cationic and anionic extractants. In this work, new ILs were synthesized for metal extraction. The combination of these ions would increase the metal extraction. Cyanex 272, or D2EHPA, is widely known as a solvent used for the extraction of Co/Ni and other metal ions from the liquid phase. It is likely that the cations and anions of the synthetized ILs did not produce high selectivity for the extraction of metal ions compared to the $[Cl]^-$ anion from the DES.

The majority of the interpretations of the mechanism of these interactions are explained as "ion exchange" and/or "ion pairing" interactions for metal ions extracted from the aqueous (A) to the organic phase (O) [45]:

$$2\ Me^+_{(A)} + [Cl]^-_{(A)} + [COO]^-_{(O)} = MeCl_{(A)} + Me[COO]_{(O)} \quad (2)$$

This reaction is possible after the extraction process of Me from the "black mass" into the liquid phase in the presence of IL or DES and the additives used in this work.

Table 10. Results of metal extraction with [$P_{6,6,6,14}$][Cyanex272] at T = 303 K, 2 h, extraction efficiency (E) at pH = 3.

Extrahent	Ion	g_0 * (mg)	g_{EAq} * (mg)	g_{EOrg} * (mg)	E (wt%)
[$P_{6,6,6,14}$][Cyanex272] + H_2O_2	Co(II)	295	41.89	34.69	26
	Ni(II)	860	115.04	43.50	18
	Li(I)	220	65.67	14.88	37
	Cu(II)	400	1.81	39.59	10
	Mn(II)	340	36.13	63.85	29
[$P_{6,6,6,14}$][Cyanex272] + TCCA	Co(II)	295	14.96	82.97	33
	Ni(II)	860	221.54	25.84	29
	Li(I)	220	96.37	14.71	50
	Cu(II)	400	0.27	76.36	19
	Mn(II)	340	33.98	120.69	45
[$P_{6,6,6,14}$][Cyanex272] + PHM	Co(II)	295	46.51	1.54	16
	Ni(II)	860	22.31	2.25	3
	Li(I)	220	98.73	1.34	46
	Cu(II)	400	69.86	16.09	22
	Mn(II)	340	109.97	2.66	33
[$P_{6,6,6,14}$][Cyanex272] + (glycine + H_2O_2)	Co(II)	295	106.34	1.79	37
	Ni(II)	860	257.16	3.02	30
	Li(I)	220	90.73	0.85	42
	Cu(II)	400	142.89	4.03	37
	Mn(II)	340	200.30	2.73	60

* g_0—metal content in the solid phase before extraction, g_E—metal ion content in the aqueous or organic phase after the stripping process.

The same additives used with bi-functional ILs did not show high selectivity. The issue of separating metal ions from the obtained liquid phase needs to be solved in the next separation process. It is possible to find many studies and proposals in this field. Unfortunately, there is not usually a whole list of metals discussed in published works, such as Fe, Al, Cu, Mn, Li, Co and Ni. Our leachate solution after using a mixture of DES, water, DDACl, glycine and other additives is assumed to be an aqueous phase; therefore, the next extraction must be carried out with an organic solvent, for example D2EHPA, to separate some metals such as Fe, Cu and Al at different pHs with minimal extraction of Co and Ni. The last problem is the separation of Co and Ni which has been discussed in many papers over the last 20 years [46].

3. Materials and Methods

3.1. Analysis of the Solid LiPBs' BM Material

The BM of LiPBs was provided by MB Recycling Sp. z o. o., a Waste Management Company in Kleszczów, Poland. The BM material (see Figure 1) was crushed and ground in a mortar into a powder of small diameter (approx. 1.2 mm). The qualitative elemental composition of the BM material was analyzed on a solid sample by SEM/EDS using a Jeol (Singapore) JSM-6490 LV scanning electron microscope (SEM) equipped with an energy-dispersive X-ray spectrometer (EDS). In the EDS analysis, the presence of lithium is not visible due to the limitations of the method (possibility to detect elements with an atomic mass equal to or greater than the atomic mass of boron). The presence of lithium was confirmed in quantitative analysis of the BM material. The Milestone (Fremont,

CA, USA) UltraWAVE microwave digestion system was used in combination with the PerkinElmer (Waltham, MA, USA) AAnalyst 800 atomic absorption spectrometer (FAES technique for the determination of lithium and FAAS technique for other metals). Metals were determined after a microwave-assisted digestion of the sample in an UltraWAVE (Plattsburgh, NY, USA) mineralizer (using concentrated nitric acid as the solvent) followed by fusing the acid-insoluble matter with potassium pyrosulfate (and then dissolving the melted sample in dilute hydrochloric acid) to ensure complete sample dissolution prior to a quantitative analysis.

The results of the BM analysis for metal content are presented in Table 1. The EDS spectra, concerning only the micro-area of the BM surface, are shown in Figure 2 and Figures S1–S3 in the SMs.

3.2. Chemicals

Basic information (incl. chemical structure, name, abbreviation, molar mass and mass fraction purity) on the DESs, ILs ingredients and chemicals used in this work are listed in Table 11. The water used was deionized by a Millipore purification system. All other reagents employed in this work were of analytical grade.

Table 11. Basic data on the DESs, the ILs ingredients and the chemicals used: structure, name, name abbreviation, supplier, CAS number, molar mass (M), mass fraction purity.

Chemical Structure	Name, Abbreviation, Supplier, CAS Number	Molar Mass M (g mol^{-1})	Purity * in Mass Percent (%)
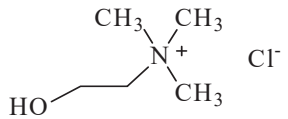	Choline chloride, [$N_{2OH,1,1,1}$][Cl], Sigma-Aldrich, Darmstadt, Germany, CAS: 67-48-1	139.62	>98
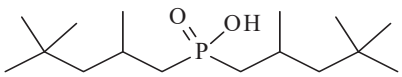	Bis(2,4,4-trimethylpentyl)phosphinic acid, Cyanex 272, Chem Scene LLC (Glenside, (PA)/ USA), CAS: 83411-71-6	290.42	90
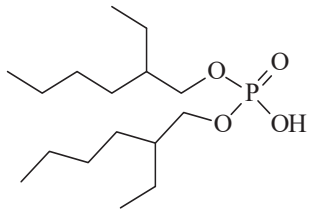	Bis(2-ethylhexyl) phosphate, D2EHPA, Heavy Water, Darmstadt, Germany, CAS: 298-07-7	322.40	>95
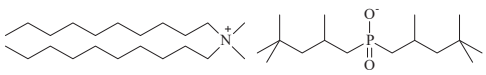	Didecyldimethylammonium bis(2,4,4-trimethylpentyl)phosphinate [$N_{10,10,1,1}$][Cyanex272], Synthesized, Ł-IChP	616.12	>95
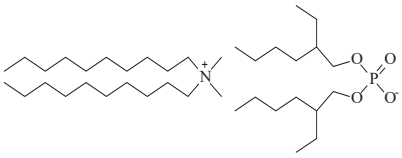	Didecyldimethylammonium bis(2-ethylhexyl)phosphate [$N_{10,10,1,1}$][D2EHPA], $C_{38}H_{82}NO_4P$, Synthesized, Ł-IChP	648.13	>95

Table 11. *Cont.*

Chemical Structure	Name, Abbreviation, Supplier, CAS Number	Molar Mass M (g mol^{-1})	Purity * in Mass Percent (%)
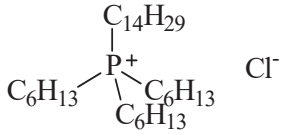	Trihexyltetradecylphosphonium chloride, Cyphos IL 101, [$P_{6,6,6,14}$][Cl], IoLiTec, Heilbronn, Germany, CAS: 258864-54-9	519.42	>95
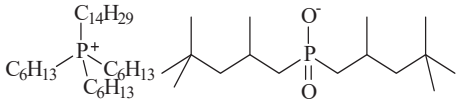	Trihexyltetradecylphosphonium bis(2,4,4-trimethylopentyl)phosphinate [$P_{6,6,6,14}$][Cyanex272], ([$P_{6,6,6,14}$][BTMPP]), IoLiTec, Heilbronn, Germany, CAS: 465527-59-7	773.27	>90
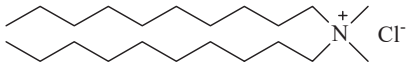	Didecyldimethylammonium chloride, [$N_{10,10,1,1}$][Cl], DDACl, Alpinus Sp. z o.o. (Miszewko, Poland), CAS: 7173-51-5	362.16	50 wt% aq. solution
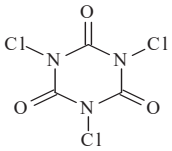	Trichloroizocyjanuric acid, $C_3Cl_3N_3O_3$, TCCA, Sigma-Aldrich, Darmstadt, Germany, CAS: 87-90-1,	232.40	95
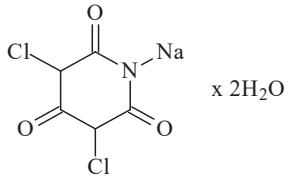	Sodium dichloroizocyjanurian dihydrat, $C_3Cl_2N_3NaO_2 \times 2H_2O$, NaDCC $\times$ $2H_2O$, Sigma-Aldrich, Darmstadt, Germany, CAS: 51580-86-0	239.99	≥98
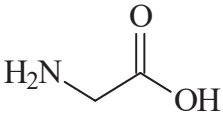	Glycine, $C_2H_5NO_2$, Sigma-Aldrich, Darmstadt, Germany, CAS: 56-40-6	75.07	95
($2KHSO_5 \cdot KHSO_4 \cdot K_2SO_4$)	Pentapotassium bis(peroxymonosulphate) bis(sulphate), PHM, Sigma-Aldrich, Darmstadt, Germany, CAS: 70693-62-8	614.76	98.0
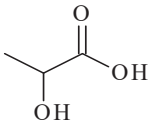	Lactic acid, $C_3H_6O_3$, Sigma-Aldrich, Darmstadt, Germany, CAS: 50-21-5	90.08	98.0
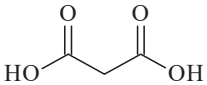	Malonic acid, $C_3H_4O_4$, Reachim, Darmstadt, Germany, CAS: 141-82-2	104.06	99.0
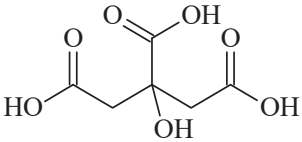	Citric Acid, $C_6H_8O_7$, Riedel-de Haën, Seelze, Germany, CAS: 77-92-2	192.13	99.8

Table 11. *Cont.*

Chemical Structure	Name, Abbreviation, Supplier, CAS Number	Molar Mass M (g mol^{-1})	Purity * in Mass Percent (%)
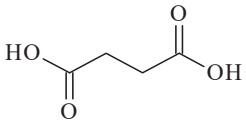	Succinic acid, $C_4H_6O_4$, Avantor (POCh), Gliwice, Poland, CAS: 110-15-6	118.09	>99
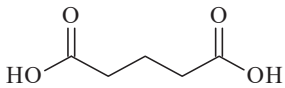	Glutaric acid, $C_5H_8O_4$, Sigma-Aldrich, Darmstadt, Germany, CAS: 110-94-1	132.12	99
Kerosene	Kerosene, Dragon Poland Sp.z.o.o., Skawina, Poland	-	-
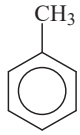	Toluene, $C_6H_5CH_3$, Chempur, Karlsruhe, Germany, CAS: 108-88-3	92.14	98.8
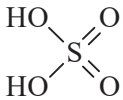	Sulphuric acid, H_2SO_4, Riedel-de Haën, Seelze, Germany, CAS 7664-93-9	98.08	96.0

* As stated by the supplier.

The preparation of DESs, (1) {choline chloride + lactic acid, 1:2} [47], (2) {choline chloride + malonic acid, 1:1} [48], (3) {choline chloride + succinic acid, 1:1}, (4) {choline chloride + glutaric acid, 1:1}, (5,6) {choline chloride + citric acid, 1:1, and 2:1}, is described in the SMs. The choline chloride, [$N_{2OH,1,1,1}$][Cl], used for the synthesis of DESs was dried under reduced pressure (10 hPa) at T = 323 K for 8 h.

The bi-functional IL [$P_{6,6,6,14}$][Cyanex272], CAS: 465527-59-7, was provided by IoLiTec. Two other ILs, [$N_{10,10,1,1}$][Cyanex272] and [$N_{10,10,1,1}$][D2EHPA], were synthesized for this work in our laboratory. The synthesis and NMR spectra recorded on the Bruker (Billerica, MA, USA) 300 MHz spectrometer in the presence of tetramethylsilane (TMS) as an internal standard are presented in the SMs. ILs used in the extraction were dried for 36 h at T = 340 K under reduced pressure, p = 6 kPa, and analyzed by Karl Fischer titration (Metrohm, Herisau, Switzerland, 716 DMS Titrino). The mass fraction of water in the samples was less than 760 $\times$ 10^{-6} g with an uncertainty of u(w.c.) = 10 $\times$ 10^{-6} g. The uncertainty of temperature measurements was $\pm$0.1 K. All weighing was carried out using a Mettler Toledo (Greifensee, Switzerland) AB 204-S balance, with an accuracy of $\pm$1 $\times$ 10^{-4} g. The Litmus bromothymol blue papers were used to measure the pH of the solution after extraction.

3.3. Extraction Procedure

A mixture of 15 g of the DES 1 was dissolved in 10 cm^3 of water at T = 303 K and 10 g of BM, 8 cm^3 of DDACl (50 wt% aqueous solution) was added in small portions, 5 cm^3 of H_2O_2 (30 wt% aqueous solution) was added in small portions at T = 313 K and was stirred with a coated magnetic stirring bar under reflux for 2 h, 3000 rpm at T = 333 K at pH = 3 (regulated with 5 M H_2SO_4). Then, after sedimentation of the residual solid phase under the reduced pressure, the liquid phase was analyzed for the metal ions content. The solid to liquid (S/L) ratio was 10/38 g/cm^3. The liquid phase was (32 cm^3, 35.306 g). The lower, dark blue-greenish colour aqueous phase 30.5 cm^3 + 1.5 cm^3 of the upper organic phase was analyzed. The results are presented in Table 2.

A mixture of 15 g of the DES 2 was dissolved in 10 cm^3 of water at T = 303 K and 10 g of BM, 8 cm^3 of DDACl (50 wt% aqueous solution) was added in small portions, 8 g of TCCA was dissolved in 22 cm^3 of acetone added in small portions at T = 313 K and was stirred with a coated magnetic stirring bar under reflux for 2 h, 3000 rpm at T = 318 K at pH = 3 (regulated with 5M H_2SO_4). Then, after sedimentation of the residual solid phase under the reduced pressure, the liquid phase was analyzed for the metal ions content. The solid to liquid (S/L) ratio was 10/63 g/cm^3. The lower, dark colour aqueous phase (30 cm^3, 32,751 g) and the upper organic phase (12 cm^3, 9841 g) were analyzed. The results are presented in Table 3.

Similarly, mixtures of 10 g of BM and the remaining oxidizing additives were used (see the description of the mixtures in the SMs). The results are presented in Tables 4–7.

The mixture of DES 2 with glycine and H_2O_2 showed the best extraction efficiency results for Co, Ni and Li and was chosen for the two-stage extraction with the same recipe and different amounts of glycine (see Table S1 in the SMs and Figure 3). The effect of pH (pH = 3, 5, 7) on the two-stage extraction in the best system with 15 g of glycine at T = 333 K, for 2 h, is listed in Table S2 in the SMs and in Figure 5. The effect of temperature (T = 303 K, 318 K and 333 K) on the two-stage extraction with 15 g of glycine at pH = 3, for 2 h, using the best selected procedure, is shown in Table S3 and in Figure 6. The influence of the time of the two-stage extraction process (t = 30 min, 1 h, 1.5 h, 2 h) with 15 g of glycine at pH = 3, T = 333 K, on the extraction efficiency using the best selected procedure is shown in Table S4 and in Figure 7. The uncertainty of determining the extraction efficiency, taking into account the uncertainty of the results of determining the metal content in the starting BM material (plus material heterogeneity) and in the liquid phases after the extraction process (triple extraction test), was assumed to be 5%.

The further extraction was proposed with three bi-functional ILs: $[N_{10,10,1,1}]$[Cyanex272], $[N_{10,10,1,1}]$[D2EHPA] and $[P_{6,6,6,14}]$[Cyanex272]/toluene (diluent) with the addition of 8 cm^3 of DDACl (50 wt% aqueous solution) and 5 cm^3 of H_2O_2 (30 wt% aqueous solution), or 8 g of TCCA, 8 g of PHM, or (glycine, 8 g + H_2O_2, 5 cm^3). The mixture was stirred with a coated magnetic stirring bar under reflux for 2 h, 3000 rpm, at T = 333 K at pH = 3 (regulated with 5M H_2SO_4). The aqueous to organic phase was A/O = 1/1. Two phases were obtained after the extraction and the organic phase was stripped with H_2SO_4 as is described in the SMs. The results are presented in Tables 8–10.

4. Conclusions

The article presents six DESs and three bi-functional ionic liquids with various additives used for the extraction of metals from the "black mass" of lithium-ion portable batteries (LiPBs). The aim was to recover Co, Ni, Li, Cu and Mn using different amounts of oxidizing additives or glutaric acid at different pHs and different extraction times. The preparation of six DESs containing choline chloride and acids, lactic acid (1:2, DES 1), malonic acid (1:1, DES 2), succinic acid (1:1, DES 3), glutaric acid (1:1, DES 4) and citric acid (1:1, DES 5), as well as citric acid (2:1, DES 6), is presented in addition to the synthesis of three bi-functional ILs: didecyldimethylammonium bis(2,4,4-trimethylpentyl) phosphinate, $[N_{10,10,1,1}]$[Cyanex272], didecyldimethylammonium bis(2-ethylhexyl) phosphate, $[N_{10,10,1,1}]$[D2EHPA] and trihexyltetradecylphosphonium bis(2,4,4-trimethylpentyl) phosphinate, $[P_{6,6,6,14}]$[Cyanex272]. Various additives, such as didecyldimethylammonium chloride, (DDACl) surfactant, hydrogen peroxide (H_2O_2), trichloroisocyanuric acid (TCCA), sodium dichloroisocyanurate (NaDCC), pentapotassium bis(peroxymonosulphate) bis(sulphate) (PHM) or (glycine + H_2O_2) or (glutaric acid + H_2O_2) were added to the DES or IL solvents for the extraction process at temperature T = 333 K for 2 h at pH = 3. DES 2 was chosen for the two-stage extraction with the addition of different amounts of glycine (8 g, 10 g, 15 g), at different pHs (pH = 3, 5, 7) and at different temperatures (303 K, 318 K, 333 K), as well as using different extraction times (0.5 h, 1 h, 1.5 h, 2 h) in order to search for the best extraction efficiencies. The highest efficiency of metal extraction was obtained with the mixture of {DES 2 + 15 g of glycine + H_2O_2} in the two-stage extraction at

pH = 3, T = 333 K, and for 2 h. The addition of 15 g of glycine showed 100 wt% extraction efficiency for Co, Ni, Li and Mn and 75 wt% extraction efficiency for Cu. The extraction efficiency using bi-functional ILs for all metals was on the level of 35–50 wt%. This was demonstrated in a series of experiments at different pHs and temperatures. However, the issue of separating the metals from the final extraction solution has to be solved quickly, as rapidly increasing consumption of Li-ion batteries has increased the production over the past two years, resulting in a sharp increase in metal prices.

Supplementary Materials: The following supporting information can be downloaded at: https://www.mdpi.com/article/10.3390/molecules29133142/s1, Figure S1: SEM image of the solid LiPBs BM sample and EDS spectrum of the micro-area marked in the image; Figure S2: SEM image of the solid LiPBs BM sample and EDS spectrum of the micro-area marked in the image; Figure S3: SEM image of the solid LiPBs BM sample and EDS spectrum of the micro-area marked in the image; Table S1: Results of metal extraction with DES 2 (1:1) at T = 333 K, 2 h, with different amounts of glycine, extraction efficiency (E) at pH = 3; Table S2: Results of metal extraction with {DES 2 (1:1) + 15 g of glycine + H_2O_2) at different pH at T = 333 K, 2 h, extraction efficiency (E); Table S3: Results of two-stage metal extraction with {DES 2 (1:1) + 15 g of glycine + H_2O_2) at different temperatures at pH = 3, 2 h, extraction efficiency (E); Table S4: Results of two-stage metal extraction with {DES 2 (1:1) + 15 g of glycine + H_2O_2) at different extraction times at pH = 3, T = 333 K, extraction efficiency (E). Refs. [24,47–49] are cited in Supplementary Materials.

Author Contributions: U.D.: Conceptualization, Supervision, Funding acquisition, Methodology, Formal analysis, Validation, Writing—Original draft. A.W.: Data curation, Investigation. Z.D.: Data curation, Investigation. D.K.: Data curation, Investigation. K.W.: Data curation, Investigation. J.L.: Data curation, Investigation, Funding acquisition. All authors have read and agreed to the published version of the manuscript.

Funding: Funding for this research was provided by the ŁUKASIEWICZ Research Network—Industrial Chemistry Research Institute, Rydygiera 8, 01-793 Warsaw, Poland. (Decision No. 841321, 2023).

Institutional Review Board Statement: Not applicable.

Informed Consent Statement: Not applicable.

Data Availability Statement: The data presented in this study are available in the article and Supplementary Materials.

Conflicts of Interest: The authors declare no conflicts of interest.

References

1. Kim, H.-J.; Krishna, T.N.V.; Zeb, K.; Rajangam, V.; Muralee Gopi, C.V.V.; Sambasivam, S.; Raghavendra, K.V.G.; Obaidat, I.M. A Comprehensive Review of Li-Ion Battery Materials and Their Recycling Techniques. *Electronics* **2020**, *9*, 1161. [CrossRef]
2. Botelho, A.B., Jr.; Stopic, S.; Friedrich, B.; Tenório, J.A.S.; Espinosa, D.C.R. Cobalt Recovery from Li-Ion Battery Recycling: A Critical Review. *Metals* **2021**, *11*, 1999. [CrossRef]
3. Ma, L.; Xi, X.; Zhang, Z.; Lyu, Z. Separation and Comprehensive Recovery of Cobalt, Nickel, and Lithium from Spent Power Lithium-Ion Batterie. *Minerals* **2022**, *12*, 425. [CrossRef]
4. Broussely, M.; Pistoia, G. (Eds.) *Industrial Applications of Batteries: From Cars to Aerospace and Energy Storage*; Elsevier: Amsterdam, The Netherlands, 2007.
5. Directive 2000/60/EC of the European Parliament and of the Council of 23 October 2000 Establishing a Framework for Community Action in the Field of Water Policy. *OJ L* **2000**, *327*, 1–73, as Amended. Available online: https://eur-lex.europa.eu/eli/dir/2000/60/oj (accessed on 10 May 2024).
6. Directive 2013/39/EU of the European Parliament and of the Council of 12 August 2013 amending Directives 2000/60/EC and 2008/105/EC as Regards Priority Substances in the Field of Water Policy. *OJ L* **2013**, *226*, 1–17. Available online: https://eur-lex.europa.eu/legal-content/EN/ALL/?uri=celex:32013L0039 (accessed on 10 May 2024).
7. Regulation (EU) 2023/1542 of the European Parliament and of the Council of 12 July 2023 Concerning Batteries and Waste Batteries, Amending Directive 2008/98/EC and Regulation (EU) 2019/1020 and Repealing Directive 2006/66/EC. *OJ L* **2023**, *191*, 1–117. Available online: https://eur-lex.europa.eu/eli/reg/2023/1542/oj (accessed on 10 May 2024).
8. Directive 2006/66/EC of the European Parliament and of the Council of 6 September 2006 on Batteries and Accumulators and Waste Batteries and Accumulators and Repealing Directive 91/157/EEC. *OJ L* **2006**, *266*, 1–14, as Amended. Available online: https://eur-lex.europa.eu/eli/dir/2006/66/oj (accessed on 10 May 2024).

9. Kolasa, D.; Lach, J.; Wróbel, K.; Samsonowska, K.; Kaszuba, A.; Stępkowska, A.; Wróbel, J. Requirements for the Content of Harmful Substances in Market Products of Plastics and Rubber. Part III. Electrical and Electronic Equipment, Batteries and Accumulators. *Polimery* **2023**, *68*, 32–47. [CrossRef]
10. Afonso, J.; Mezzetta, A.; Marrucho, I.M.; Guazzelli, L. History repeats itself again: Will the mistakes of the past for ILs be repeated for DESs? From being considered ionic liquids to becoming their alternative: The unbalanced turn of deep eutectic solvents. *Green Chem.* **2023**, *25*, 59–105. [CrossRef]
11. Hansen, B.B.; Spittle, S.; Chen, B.; Poe, D.; Zhang, Y.; Klein, J.M.; Horton, A.; Adhikari, L.; Zelovich, T.; Doherty, B.W.; et al. Deep Eutectic Solvents: A Review of Fundamentals and Applications. *Chem. Rev.* **2021**, *121*, 1232–1285. [CrossRef]
12. Mero, A.; Koutsoumpos, S.; Giannios, P.; Stavrakas, I.; Moutzouris, K.; Mezzetta, A.; Guazzelli, L. Comparison of physicochemical and thermal properties of choline chloride and betaine-based deep eutectic solvents: The influence of hydrogen bond acceptor and hydrogen bond donor nature and their molar ratios. *J. Mol. Liq.* **2023**, *377*, 121563. [CrossRef]
13. Suffia, S.; Dutta, D. Applications of deep eutectic solvents in metal recovery from E-wastes in a sustainable way. *J. Mol. Liq.* **2024**, *394*, 123738. [CrossRef]
14. Tran, T.T.; Moon, H.S.; Lee, M.S. Separation of Cobalt, Nickel, and Copper from synthetic metallic alloy by selective dissolution with acid solutions containing oxidizing agent. *Miner. Process. Extr. Metall. Rev.* **2022**, *43*, 313–325. [CrossRef]
15. Available online: https://www.consilium.europa.eu/pl/infographics/critical-raw-materials/ (accessed on 10 May 2024).
16. Pillot, C. EU Battery Demand and Supply (2019–2030) in a Global Context, Avicenne Energy, 2020. Available online: https://www.eurobat.org/wp-content/uploads/2021/05/Avicenne_EU_Market_-_summary_110321.pdf (accessed on 10 May 2024).
17. Pagliaro, M.; Meneguzzo, F. Lithium battery reusing and recycling: A circular economy insight. *Heliyon* **2019**, *5*, e01866. [CrossRef]
18. Łukomska, A.; Wiśniewska, A.; Dąbrowski, Z.; Kolasa, D.; Luchcińska, S.; Domańska, U. Separation of cobalt, lithium and nickel from the "black mass" of waste Li-ion batteries by ionic liquids, DESs and organophosphorous-based acids extraction. *J. Mol. Liq.* **2021**, *343*, 117694. [CrossRef]
19. Fischer, L.; Falta, T.; Koellensperger, G.; Stojanovic, A.; Kogelnig, D.; Galanski, M.; Krachler, R.; Keppler, B.K.; Hann, S. Ionic liquids for extraction of metals and metal containing compounds from communal and industrial waste water. *Water Res.* **2011**, *45*, 4601–4614. [CrossRef] [PubMed]
20. Feng, F.; Sun, Y.; Rui, J.; Yu, L.; Liu, J.; Zhang, N.; Zhao, M.; Wei, L.; Lu, C.; Zhao, J.; et al. Study of the "Oxidation-Complexation" Coordination Composite Ionic Liquid System for Dissolving Precious Metals. *Appl. Sci.* **2020**, *10*, 3625. [CrossRef]
21. Łukomska, A.; Wiśniewska, A.; Dąbrowski, Z.; Domańska, U. Liquid-liquid extraction of cobalt(II) and zinc(II) from aqueous solutions using novel ionic liquids as extractants. *J. Mol. Liq.* **2020**, *307*, 112955. [CrossRef]
22. Han, Y.; Yi, X.; Wang, R.; Huang, J.; Chen, M.; Sun, Z.; Sun, S.; Shu, J. Copper extraction from waste printed circuit boards by glycine. *Sep. Pur. Technol.* **2020**, *253*, 117463. [CrossRef]
23. Urbańska, W. Recovery of Co, Li, and Ni from spent Li-Ion batteries by the inorganic and/or organic reducer assisted leaching method. *Minerals* **2020**, *10*, 555. [CrossRef]
24. Łukomska, A.; Wiśniewska, A.; Dąbrowski, Z.; Lach, J.; Wróbel, K.; Kolasa, D.; Domańska, U. Recovery of metals from electronic waste-printed circuit boards by ionic liquids, DESs and organophosphorous-based acid extraction. *Molecules* **2022**, *27*, 4984. [CrossRef] [PubMed]
25. Liu, C.; Lin, J.; Cao, H.; Zhang, H.; Sun, Z. Recovery of spent lithium-ion batteries in view of lithium recovery: A critical review. *J. Clean. Prod.* **2019**, *228*, 801–813. [CrossRef]
26. Barrueto, Y.; Hernández, H.; Jiménez, Y.P.; Morales, J. Properties and application of ionic liquids in leaching base/precious metals from e-waste. A review. *Hydrometallurgy* **2022**, *212*, 105895. [CrossRef]
27. Chen, X.; Chen, Y.; Zhou, T.; Liu, D.; Hu, H.; Fan, S. Hydrometallurgical recovery of metal values from sulfuric acid leaching liquor of spent lithium-ion batteries. *Waste Manag.* **2015**, *38*, 349–356. [CrossRef] [PubMed]
28. Choubey, P.K.; Dinkar, O.S.; Panda, R.; Kumari, A.; Jha, M.K.; Pathak, D.D. Selective extraction and separation of Li, Co and Mn from leach liquor of discarded lithium ion batteries (LIBs). *Waste Manag.* **2021**, *121*, 452–457. [CrossRef] [PubMed]
29. Gerold, E.; Luidold, S.; Antrekowitsch, H. Separation and efficient recovery of lithium from spent lithium-ion batteries. *Metals* **2021**, *11*, 1091. [CrossRef]
30. Zheng, H.; Dong, T.; Sha, Y.; Jiang, D.; Zhang, H.; Zhang, S. Selective extraction of lithium from spent lithium batteries by functional ionic liquid. *ACS Sustain. Chem. Eng.* **2021**, *9*, 7022–7029. [CrossRef]
31. Cheng, J.; Lu, T.; Wu, X.; Zhang, H.; Zhang, C.; Peng, C.-A.; Huang, S. Extraction of cobalt(II) by methyltrioctylammonium chloride in nickel(II)-containing chloride solution from spent lithium ion batteries. *RSC Adv.* **2019**, *9*, 22729–22739. [CrossRef]
32. Peeters, N.; Binnemans, B.; Riaño, S. Solvometallurgical recovery of cobalt from lithium-ion battery cathode materials using deep-eutectic solvents. *Green Chem.* **2020**, *22*, 4210–4221. [CrossRef]
33. Nayaka, G.P.; Pai, K.V.; Santhosh, G.; Manjanna, J. Recovery of cobalt as cobalt oxalate from spent lithium ion batteries by using glycine as leaching agent. *J. Environ. Chem. Eng.* **2016**, *4*, 2378–2383. [CrossRef]
34. Zhang, Q.; De Oliveira Vigier, K.; Royer, S.; Jérôme, F. Deep eutectic solvents: Syntheses, properties and applications. *Chem. Soc. Rev.* **2012**, *41*, 7108–7714. [CrossRef] [PubMed]
35. Tran, T.T.; Lee, M.S. Separation of Mo(VI), V(V), Ni(II), Al(III) from synthetic hydrochloric acidic leaching solution of spent catalysts by solvent extraction with ionic liquids. *Sep. Pur. Technol.* **2020**, *247*, 117005. [CrossRef]

36. Tran, T.T.; Liu, Y.; Lee, M.S. Recovery of pure molybdenum and vanadium compounds from spent petroleum catalysts by treatment with ionic liquid solution in the presence of oxidizing agent. *Sep. Pur. Technol.* **2021**, *255*, 117734. [CrossRef]
37. Yang, Y.; Sun, M.; Yu, W.; Ma, X.; Lei, S.; Sun, W.; Song, S.; Hu, W. Recovering Fe, Mn and Li from $LiMn_{1-x}Fe_xPO_4$ cathode material of spent lithium-ion battery by gradient precipitation. *Sustain. Mater. Technol.* **2023**, *36*, e00625. [CrossRef]
38. Kim, J.P.; Go, C.Y.; Kang, J.; Choi, Y.; Kim, J.Y.; Kim, Y.; Kwon, O.; Kim, K.C.; Kim, D.W. Nanoporous multilayer graphene oxide membrane for forward osmosis metal ion recovery from spent Li-ion batteries. *J. Membr. Sci.* **2023**, *676*, 121590. [CrossRef]
39. Jiang, S.Q.; Nie, C.C.; Li, X.G.; Shi, S.X.; Gao, Q.; Wang, Y.S.; Zhu, X.N.; Wang, Z. Review on comprehensive recycling of spent lithium-ion batteries: A full component utilization process for green and sustainable production. *Sep. Pur. Technol.* **2023**, *315*, 123684. [CrossRef]
40. Tripathy, A.; Bhuyan, A.; Padhy, R.K.; Mangla, S.K.; Roopak, R. Drivers of lithium-ion batteries recycling industry toward circular economy in industry 4.0. *Comp. Ind. Eng.* **2023**, *179*, 109157. [CrossRef]
41. Yan, Z.; Sattar, A.; Li, Z. Priority Lithium recovery from spent Li-ion batteries via carbothermal reduction with water leaching. *Resour. Conserv. Recycl.* **2023**, *192*, 106937. [CrossRef]
42. Mousavinezhad, S.; Kadivar, S.; Vahidi, E. Comparative life cycle analysis of critical materials recovery from spent Li-ion batteries. *J. Environ. Manag.* **2023**, *339*, 117887. [CrossRef]
43. Ling, J.K.U.; Hadinoto, K. Deep Eutectic Solvent as Green Solvent in Extraction of Biological Macromolecules: A Review. *Int. J. Mol. Sci.* **2022**, *23*, 3381. [CrossRef]
44. Pathak, A.; Vinoba, M.; Kothari, R. Emerging role of organic acids in leaching of valuable metals from refinery-spent hydroprocessing catalysts, and potential technoeconomic challenges: A review. *Crit. Rev. Environ. Sci. Technol.* **2021**, *51*, 1–43. [CrossRef]
45. Boudesocque, S.; Mohamadou, A.; Dupont, L.; Martinez, A.; Dechamps, I. Use of dicyanamide ionic liquids for extraction of metal ions. *RSC Adv.* **2016**, *6*, 107894–107904. [CrossRef]
46. Janiszewska, M.; Markiewicz, A.; Regel-Rosocka, M. Hydrometallurgical separation of Co(II) from Ni(II) from model and real solutions. *J. Clean. Prod.* **2019**, *228*, 746–754. [CrossRef]
47. Zhang, W.-H.; Chen, M.-N.; Hao, Y.; Jiang, X.; Zhou, X.-L.; Zhang, Z.-H. Choline chloride and lactic acid: A natural deep eutectic solvent for one-pot rapid construction of spiro[indoline-3,4′-pyrazolo[3,4-*b*]pyridines]. *J. Mol. Liq.* **2019**, *278*, 124–129. [CrossRef]
48. Abbott, A.P.; Boothby, D.; Capper, G.; Davies, D.L.; Rasheed, R.K. Deep Eutectic Solvents Formed between Choline Chloride and Carboxylic Acids: Versatile Alternatives to Ionic Liquids. *J. Am. Chem. Soc.* **2004**, *126*, 9142–9147. [CrossRef]
49. Łukomska, A.; Wiśniewska, A.; Dąbrowski, Z.; Kolasa, D.; Luchcińska, S.; Lach, J.; Wróbel, K.; Domańska, U. Recovery of zinc and manganese from "black mass" of waste Zn-MnO2 alkaline batteries by solvent extraction technique with ionic liquids, DESs and organophosphorous-based acids. *J. Mol. Liq.* **2021**, *338*, 116590. [CrossRef]

Disclaimer/Publisher's Note: The statements, opinions and data contained in all publications are solely those of the individual author(s) and contributor(s) and not of MDPI and/or the editor(s). MDPI and/or the editor(s) disclaim responsibility for any injury to people or property resulting from any ideas, methods, instructions or products referred to in the content.

molecules

MDPI

Article

Carbon Dioxide Solubility in Three Bis Tri (Fluromethylsulfonyl) Imide-Based Ionic Liquids

Eric Quaye [1], Amr Henni [2,*] and Ezeddin Shirif [3]

[1] Industrial Systems Engineering, Faculty of Engineering and Applied Science, University of Regina, Regina, SK S4S 0A2, Canada; enq014@uregina.ca
[2] Process Systems Engineering, Faculty of Engineering and Applied Science, University of Regina, Regina, SK S4S 0A2, Canada
[3] Energy Systems Engineering, Faculty of Engineering and Applied Science, University of Regina, Regina, SK S4S 0A2, Canada; ezeddin.shirif@uregina.ca
* Correspondence: amr.henni@uregina.ca

Abstract: This study delves into the necessity of mitigating carbon dioxide (CO_2) emissions, focusing on effective capture methods to combat global warming by investigating the solubility of CO_2 in three ionic liquids (ILs), 1-Decyl-3-MethylimidazoliumBis (Trifluromethylsulfonyl Imide) [IL1], 1-Hexadecyl-3-Methyl imidazoliumBis (Trifluromethylsulfonyl Imide) [IL2] and Triethytetradecyl Ammonium Bis (Trifluromethylsulfonyl Imide) [IL3]. Solubility experiments were conducted at (30, 50 and 70) °C with pressures up to 1.5 MPa. The research shows [IL2] as the superior candidate for CO_2 capture, with its longer alkyl chain, and is confirmed by its lower Henry's Law constant. Utilizing the Peng Robinson equation of state, the study correlates well with the solubility measurements using three mixing rules. The study reveals promising results for IL1, IL2 and IL3 surpassing all other published ionic liquids including Selexol/Genesorb 1753, except for 1-Methyl-3-octylimidazolium bis(trifluoromethylsulfonyl)imide. Insights into the enthalpy and entropy of absorption underscore the significant impact of IL structure on CO_2 solubility, emphasizing the potential of tailored ILs for advanced carbon capture strategies. In summary, this research highlights [IL2] as the optimal choice for CO_2 capture, offering valuable contributions to the ongoing efforts in combating climate change.

Keywords: ionic liquids; intelligent gravimetric analyzer (IGA); CO_2 capture

1. Introduction

In the past two decades, the escalation of temperatures, largely because of the persistent elevation of atmospheric CO_2 levels, has presented noteworthy concerns for the world in general [1]. This phenomenon has prompted widespread apprehension among researchers, scientists, and environmentalists regarding the broader implications of climate change. Consequently, there is a concerted effort within the research community to develop improved solvents or technologies capable of efficiently capturing CO_2. A significant amount of CO_2 release originates directly from the burning of fossil fuels, particularly hydrocarbons like natural gas, oil and coal. Various technologies, including membrane separation/permeation, adsorption, absorption, and cryogenic distillation, are utilized for carbon dioxide (CO_2) capture from natural gas or flue gases. Among these methods, absorption, noted for its cost-effectiveness and energy efficiency, is widely adopted on a large scale [2].

Over the years, numerous mechanisms and processes have been explored for CO_2 absorption, contingent upon the partial vapor pressures of the gas mixture. According to Zhang (2021) [2], physical solvents and amines have garnered significant attention due to their effectiveness and relatively lower costs. Physical solvents, in particular, offer advantages over amines, notably requiring less energy for solvent regeneration and exhibiting non-corrosive properties that prolong equipment lifespan, thus reducing maintenance

expenses. Ionic liquids can be used for natural gas sweetening and mixed with amines or used in flue gas treatment.

Ionic liquids (ILs) represent a category of physical solvents that utilize intermolecular forces or functional group incorporation for CO_2 capture. Their intrinsic properties, including low volatility, high thermal stability, and chemical resilience, offer distinct advantages. Minimal volatility facilitates nearly solvent-loss-free regeneration processes, thereby reducing operating costs. Additionally, high thermal and chemical stability minimizes degradation and corrosion risks, ensuring prolonged equipment durability. This technology addresses shortcomings observed in chemical solvents like Monoethanolamine (MEA), such as excessive energy consumption and solvent loss [3], potentially serving as a potential MEA substitute [4].

Ionic liquids are typically classified into two types: task-specific ILs (TSILs) and non-functionalized room temperature ILs (RTILs). The key difference lies in RTILs' ability to function as conventional physical absorbents, governed by Henry's Gas constant, whereas TSILs demonstrate both chemical and physical CO_2 solubility. This dual capability enhances TSILs' capacity for CO_2 capture, as elucidated by Vadillo et al. (2022) [5].

The objective of this investigation is to assess the performance of three ionic liquids (ILs), categorized as promising physical solvents, in capturing CO_2 across a range of temperatures (30 °C to 70 °C) and pressures relevant to industrial applications, up to 1.5 MPa utilizing an intelligent gravimetric microbalance (IGA-003).

2. Results and Discussion

2.1. CO_2 Solubility Validation Test

Similar to the density validation, tests were conducted to confirm the repeatability of the IGA-003 and its adherence to the relevant experimental Standard Operating Procedures (SOPs). During this validation phase, the IL, [BMIM][BF4], was employed to evaluate CO_2 absorption. A comparative study was performed, aligning the obtained values with those documented by Shiflett and Yokozeki (2005) [6], who employed the same ionic liquid and referenced density values from a publication (Figure 1).

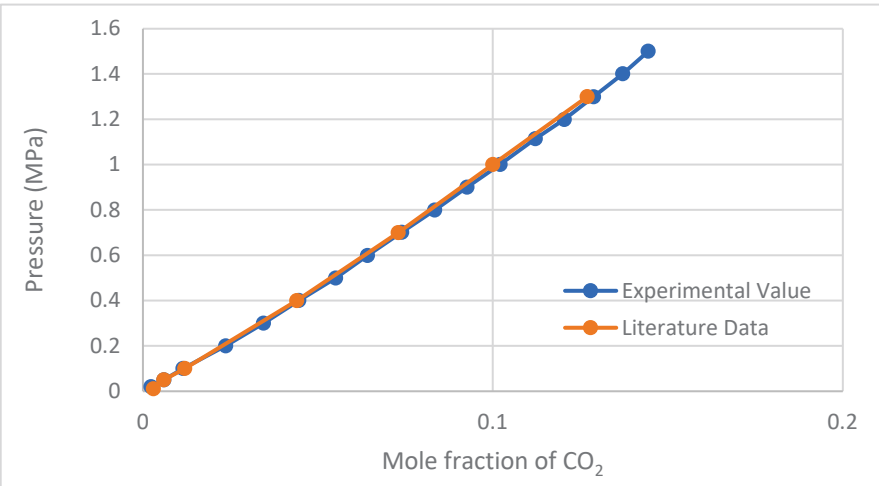

Figure 1. CO_2 solubility validation with 0.0033% deviation from Shiflett and Yokozeki (2005) [6] at 323.15 K.

2.2. ILs CO_2 Solubility

The CO_2 solubility of IL1, IL2 and IL3 was measured at various temperatures and pressures up to 1.5 MPa. The obtained data for the two ILs were plotted in Figure 2 and recorded in Table 1 below.

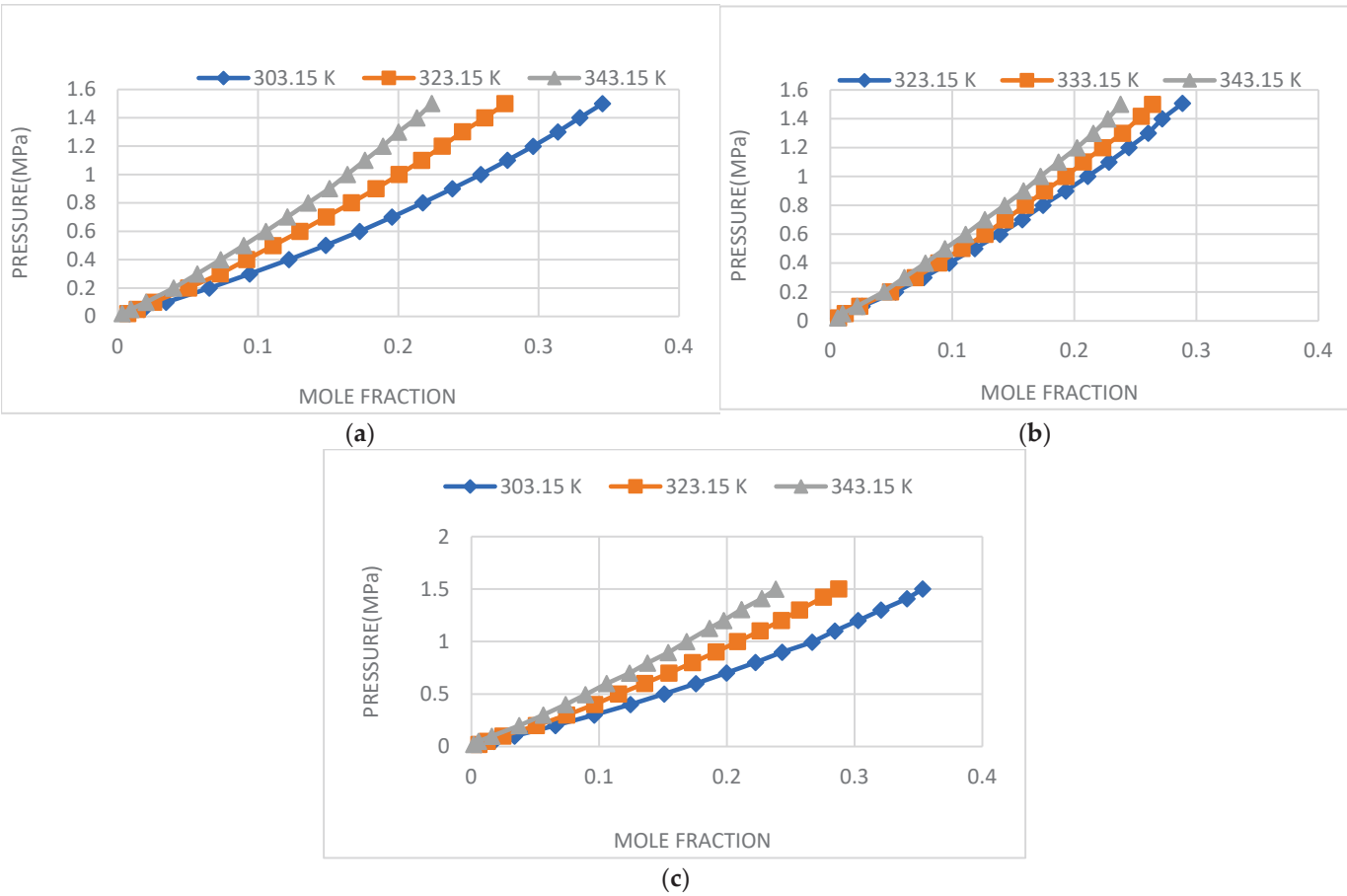

Figure 2. (**a**) CO_2 solubility in IL1; (**b**) CO_2 solubility in IL2; (**c**) CO_2 solubility in IL3.

Table 1. CO_2 solubility data in IL1, Il2 and IL3, respectively.

IL1					
303.15 K		**323.15 K**		**343.15 K**	
x_{CO_2}	**Pressure (MPa)**	x_{CO_2}	**Pressure (MPa)**	x_{CO_2}	**Pressure (MPa)**
0.034	0.0997	0.026	0.1003	0.020	0.0999
0.065	0.1998	0.051	0.2002	0.040	0.1999
0.094	0.2994	0.073	0.2999	0.057	0.2994
0.122	0.4002	0.092	0.4003	0.073	0.3997
0.148	0.5004	0.111	0.4989	0.090	0.4999
0.172	0.5988	0.130	0.5990	0.106	0.5994
0.195	0.7003	0.149	0.7006	0.121	0.7011
0.217	0.8003	0.167	0.8002	0.136	0.7994
0.238	0.9000	0.184	0.8995	0.151	0.9007
0.259	0.9999	0.201	0.9998	0.164	1.0004
0.278	1.1000	0.217	1.0990	0.176	1.1005
0.296	1.1990	0.231	1.1990	0.189	1.1998
0.314	1.3000	0.246	1.3010	0.200	1.2992
0.329	1.4000	0.262	1.3990	0.213	1.3989
0.345	1.4995	0.276	1.4991	0.224	1.5003

Table 1. *Cont.*

IL1					
303.15 K		**323.15 K**		**343.15 K**	
x_{CO_2}	**Pressure (MPa)**	x_{CO_2}	**Pressure (MPa)**	x_{CO_2}	**Pressure (MPa)**
IL2					
323.15 K		333.15 K		343.15 K	
x_{CO_2}	Pressure (MPa)	x_{CO_2}	Pressure (MPa)	x_{CO_2}	Pressure (MPa)
0.026	0.0998	0.024	0.0999	0.022	0.1003
0.053	0.1999	0.049	0.1997	0.044	0.2009
0.077	0.2999	0.070	0.2985	0.061	0.2993
0.098	0.3999	0.089	0.4001	0.078	0.3996
0.118	0.5005	0.108	0.5008	0.094	0.4988
0.139	0.5991	0.127	0.5987	0.111	0.5990
0.157	0.7006	0.143	0.6992	0.127	0.7008
0.174	0.8010	0.160	0.8009	0.143	0.7998
0.193	0.8993	0.176	0.8997	0.158	0.8997
0.211	1.0006	0.193	0.9996	0.172	1.0007
0.228	1.0998	0.207	1.1006	0.187	1.0997
0.245	1.2002	0.223	1.1998	0.202	1.1997
0.261	1.2999	0.240	1.2995	0.216	1.2991
0.272	1.3999	0.255	1.4165	0.227	1.3989
0.289	1.5071	0.264	1.4991	0.238	1.5003
IL3					
303.15 K		323.15 K		343.15 K	
x_{CO_2}	Pressure (MPa)	x_{CO_2}	Pressure (MPa)	x_{CO_2}	Pressure (MPa)
0.034	0.0999	0.025	0.0999	0.016	0.0986
0.066	0.1998	0.051	0.1998	0.037	0.1997
0.096	0.3004	0.075	0.2996	0.056	0.2999
0.124	0.4004	0.097	0.4003	0.074	0.4000
0.151	0.5009	0.115	0.5001	0.089	0.4941
0.176	0.5994	0.136	0.6005	0.106	0.6003
0.200	0.7012	0.155	0.6987	0.124	0.6991
0.222	0.8006	0.173	0.7992	0.138	0.7956
0.243	0.8988	0.192	0.9007	0.154	0.8949
0.267	0.9937	0.208	0.9996	0.169	1.0003
0.284	1.1005	0.226	1.1007	0.186	1.1251
0.303	1.2000	0.243	1.2004	0.198	1.2005
0.321	1.3002	0.257	1.3005	0.211	1.3053
0.341	1.4084	0.276	1.4219	0.227	1.4093
0.353	1.5013	0.288	1.5003	0.238	1.4990

Standard uncertainty u(x) = 0.006, standard uncertainty u(T) = 0.1 K, standard uncertainty u(P) = 0.0008 MPa.

2.3. Simulation Interaction Parameters

The experimental data were correlated using three mixing rules: (a) PR + vdW1, (b) PR + vdW2, and (c) PR + WS + NRTL. Table 2 below provides an overview of the calculated interaction binary parameters and their corresponding average absolute deviations (AADs %) for each mixing rule. The average absolute deviations (AADs %) for the vdW1, vdW2, and WS-NRTL rules applied to CO_2 absorption in these ILs were determined to be 6.52%, 0.67%, and 0.62%, respectively, for IL1, 6.21%, 1.16%, and 1.10% for IL2, and 5.14%, 0.99%, and 0.94% for IL3. Notably, the Wong–Sandler (WS-NRTL) mixing rule exhibited the lowest average absolute deviation in both cases, indicating its superiority as the preferred choice among these options.

Table 2. Optimized binary interaction parameters for vdW1, vdW2 and WS-NRTL with their corresponding average absolute deviation percentages (AAD %).

Ionic Liquids + CO_2	**Temperature (°C)**	**Binary Interaction Parameter (k_{12})**			**% AAD**
IL1	30	−0.0711			7.52
	50	−0.0857			6.37
	70	−0.1090			5.68
IL2	50	−0.1030			6.39
	60	−0.1200			6.57
	70	−0.1310			5.67
IL3	30	−0.0737			6.85
	50	−0.0956			5.43
	70	−0.1160			3.14
Ionic Liquids + CO_2	Temperature (°C)	Binary Interaction Parameter			% AAD
		(k_{12})	(l_{12})		
IL1	30	−0.0029	0.0139		0.38
	50	−0.0081	0.0149		1.01
	70	−0.0107	0.0173		0.63
IL2	50	−0.0372	0.0134		0.96
	60	−0.0455	0.0143		1.04
	70	−0.0493	0.0149		1.49
IL3	30	−0.0166	0.0103		6.85
	50	−0.0347	0.0099		0.87
	70	−0.0717	0.0066		1.48
Ionic Liquids + CO_2	Temperature (°C)	Binary Interaction Parameter			% AAD
		(k_{12})	(τ_{12})	(τ_{21})	
IL1	30	0.8930	−0.4706	0.0017	0.41
	50	0.8619	−0.6007	0.1619	0.87
	70	0.8039	−0.9079	0.6283	0.59
IL2	50	0.7568	−0.4833	−0.1106	0.97
	60	0.7212	−0.4676	−0.1439	1.00
	70	0.7013	−0.5794	0.0076	1.34
IL3	30	0.9156	0.1346	−0.6906	0.43
	50	0.8161	−0.4606	−0.0019	0.85
	70	0.6969	−0.3518	−0.0001	1.53

$k_{12} = k_{21}$. $l_{12} = l_{21}$.

2.4. Henry's Law Constant, Enthalpies and Entropies

The Henry's Law constants (H) were evaluated through a comprehensive analysis involving the plotting of fugacity against mole fraction and the subsequent fitting of a second-order trend line. This analysis enabled the derivation of the slope of the second-order equation, which serves as an essential parameter in determining Henry's Law constant [7]. Similarly, the estimation of entropy involved plotting the natural logarithm of Henry's Law constant against the natural logarithm of temperature (T) for each temperature of the ionic liquid. The resulting negative enthalpy variation signifies an exothermic absorption process. The operation of the absorption of a gas in a liquid results in a decrease in the volume of the molecules from the gas phase to the liquid phase (equivalent to compression), leading to a reduction in the entropy. The negative entropy variation with the increase in temperature, as illustrated in Table 3 below, results from the decrease in the number of absorbed CO_2 moles and a reduction in the solubility.

Table 3. Henry's Law constant, enthalpy and entropy of solvation between CO_2 and ILs.

Ionic Liquid (ILs)	Henry's Law Constant (MPa)			ΔH^{∞} (kJ/mol)	ΔS^{∞} (KJ/Kmol·K)
	T = 30 °C	T = 50 °C	T = 70 °C		
IL1	2.79	3.83	4.90	−12.80	−37.78
IL2	T = 50 °C 3.66	T = 60 °C 4.05	T = 70 °C 4.58	−10.33	−31.04
IL3	T = 30 °C 2.71	T = 50 °C 3.82	T = 70 °C 5.13	−13.79	−42.80

A relatively lower Henry's Law constant (H) implies the IL's capability to absorb a larger quantity of CO_2. In this study, [IL2] demonstrated the highest CO_2 absorption capacity, while [IL1] exhibited the least. When juxtaposing the estimated Henry's Law constants from this research with those of other ILs documented by previous researchers, [OMIM] [TF2N] was the only published IL with the highest solubility among those reported in this study, as seen in Figure 3 below.

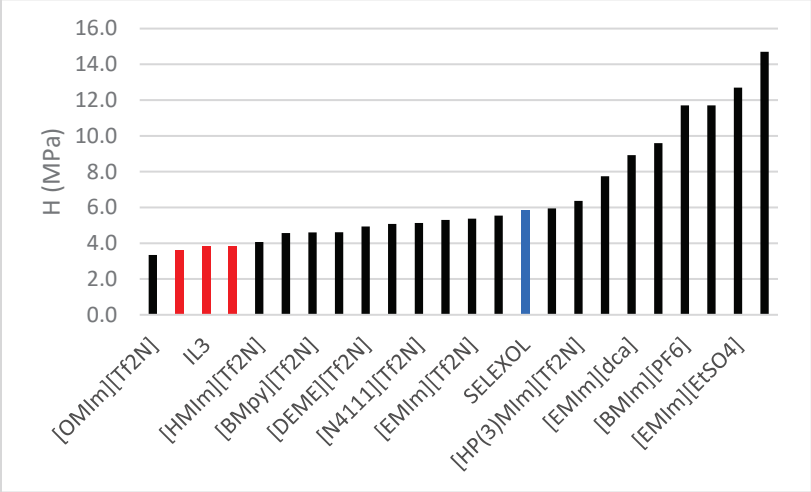

(**a**)

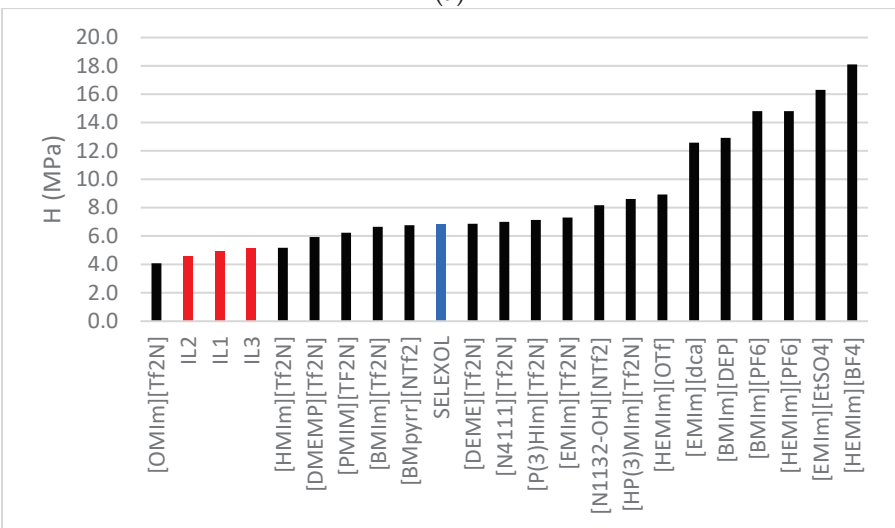

(**b**)

Figure 3. Henry's Law constant comparison for CO_2 solubility between ILs studied in this research against published ILs [7] and Selexol/Genesorb 1753 [8] at (**a**) 323.15 K and (**b**) 343.15 K.

Figure 4 showcases a notable CO_2 absorption capacity exhibited by the studied ionic liquids in comparison to Selexol/Genesorb 1753 [8], a high-performance solvent utilized in gas treatment facilities. Given their superior CO_2 absorption performance, the ILs investigated in this research can be regarded as promising solvents.

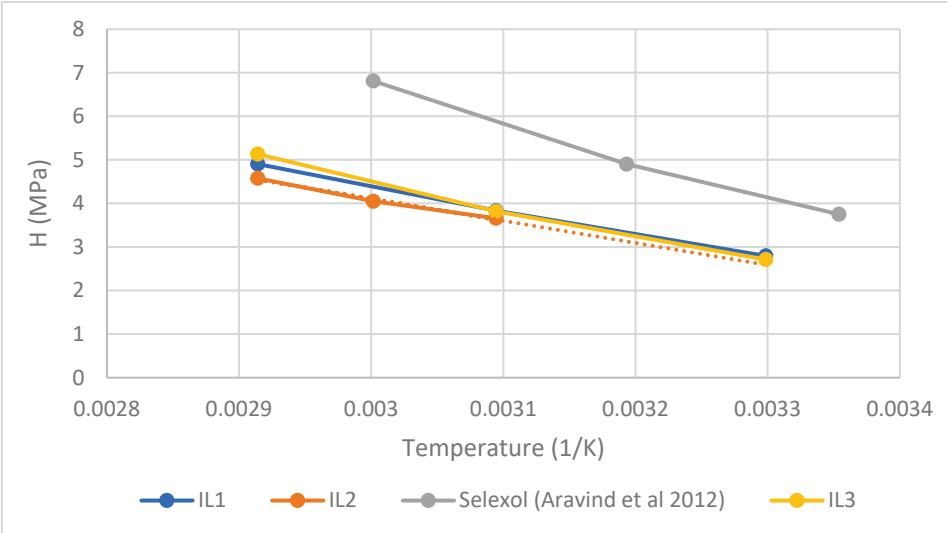

Figure 4. Comparison of Henry's Law constants for CO_2 in ILs obtained in this work and Selexol as reported by Aravind et al. (2012) [8].

3. Materials and Method

3.1. Materials

Table 4 lists the detailed ILs used in this research along with their purity, chemical structures and nomenclature.

Table 4. Detailed list of all ionic liquids.

Ionic Liquid	Nomenclature	Acronym	Structure
1-Decyl-3-MethylimidazoliumBis (Trifluromethylsulfonyl Imide) (≥98.0%, water: 8 ppm) * CAS Number: 433337-23-6	$C_{15}H_{26}F_6N_3O_4S_2$	IL1	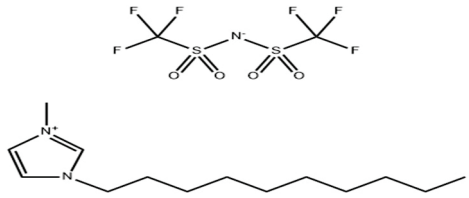
1-Hexadecyl-3-Methyl imidazoliumBis (Trifluromethylsulfonyl Imide) (≥98.0%, water: 146 ppm) * CAS Number: 404001-50-9	$C_{21}H_{40}F_6N_3O_4S_2$	IL2	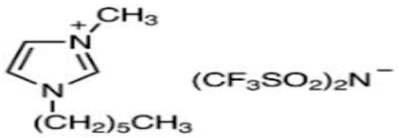
Triethyl tetradecyl Ammonium Bis Bis (Trifluromethylsulfonyl Imide) (≥98.0%, water: 102 ppm) * CAS Number: n/a	$C_{20}H_{44}F_6N_2O_4S_2$	IL3	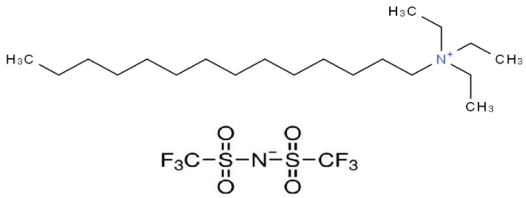

* Provided by manufacturer (IoLiTec, Heilbronn, Germany).

3.2. Density Measurement

Before and after each experiment, at the corresponding temperature, the Anton Paar Density and Speed of Sound instrument (DSA 5000, Anton Paar, Graz, Austria) was tested

with air and double-distilled water at atmospheric pressure to ensure the error was less than 0.00005 g·cm^{-3} when compared to the reference values for water and air stored in the instrument's database. To further ensure the accuracy of the density measurements for the ILs utilized in this study, the density (m/v) of N-methyldiethanolamine (MDEA) with a concentration purity of ≥99% was initially determined using the Anton Paar density meter. These measured data were then compared with those published by Karunarathne et al. (2020) [7] for MDEA with a similar purity level. The comparison revealed an average deviation (AAD) of 0.014%, indicating excellent repeatability/accuracy in the density measurements. Subsequently, the densities of three specific ILs were determined at atmospheric pressure conditions (P = 98.3 kPa) and temperatures ranging from 20 °C to 70 °C using the density meter. The obtained data are provided in Figure 5 and Table 5 below.

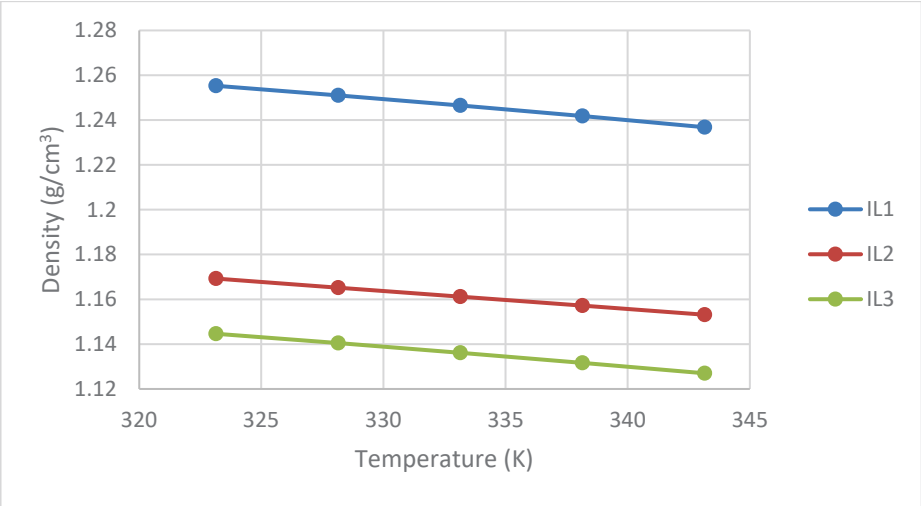

Figure 5. Densities of the ILs used in this work.

Table 5. Density of the ILs used in this work.

Temperature (K)	Density (g/cm^3)		
	IL1	**IL2**	**IL3**
303.15	1.2727	-	1.1608
308.15	1.2684	-	1.1569
313.15	1.2640	-	1.1529
318.15	1.2597	-	1.1488
323.15	1.2553	1.1693	1.1446
328.15	1.2510	1.1652	1.1405
333.15	1.2465	1.1612	1.1362
338.15	1.2418	1.1572	1.1317
343.15	1.2368	1.1532	1.1270

Standard uncertainty u (ρ) = 0.0002 g/cm^3; standard uncertainty u (T) = 0.01 K; standard uncertainty u (P) = 0.8 kPa.

3.3. Solubility Analysis

The IGA-003 analyzer, manufactured by Hiden Isochema Ltd. (Warrington, UK), incorporates cutting-edge components to facilitate gas sorption experiments effectively. A Polyscience water bath, providing precise temperature control within the reactor chamber, up to 343 K in this study, ensures optimal conditions for accurate gas sorption measurements. This system integrates a water jacket around the reactor chamber to provide equal heat/temperature all around. Within the core vessel of the reactor chamber, the IL is placed, creating a controlled environment for the experimental procedure. The experiment gas—carbon dioxide (CO_2)—is introduced into the controlled system to study their sorption characteristics.

Pressure regulation maintains precise pressure conditions for gas injection into the reactor chamber. The Mass Flow Control (MFC) system plays an important role in controlling the rate of experiment gases getting into the reaction chamber, maintaining uniform gas flow for accurate absorption study. The IGA-003 microbalance takes note of the change in ionic liquid mass during gas absorption, providing essential data on ILs' sorption behavior. In addition to the microbalance (IGA-003), a weight counterbalance enclosure compensates the weight of the reaction chamber and other components like the weight of the string, buoyancy, etc., allowing the IGA to measure specific weight changes in the sample material only during gas sorption precisely and accurately. The experimental procedure is automated and overseen by the data acquisition (DAQ) and control system, ideally operated through an onsite computer. This integrated system manages variables such as weight changes, pressure, gas flow, and temperature, maintaining the repeatability, efficiency, and accuracy of experiments performed with the IGA-003.

3.4. Thermodynamic Modelling

We utilized the Peng–Robinson Equation of State (PR EoS), as indicated in Equation (1), a well-established model renowned for its accuracy in describing the phase behavior of fluid mixtures, particularly at elevated pressures and temperatures. Through this model, we were able to estimate the absorption of CO_2 over a range of pressures up to 1.5 MPa and temperatures reaching 70 °C. The selection of the PR EoS was deliberate, as it leverages critical components of both liquids and gases involved in the system, aligning closely with our research objectives.

$$P = \frac{RT}{v - b_m} - \frac{a_m(T)}{v(v + b_m) + b_m(v - b_m)}, \tag{1}$$

The coefficients of this model were predicted using various mixing rules, as stated below [7]:

- van der Waals one single binary interaction parameter;
- van der Waals two binary interaction parameters;
- NRTL model combined with Wong–Sandler mixing rules (WS-NRTL).

3.4.1. van der Waals Mixing Rules

Two distinct mixing rules devised by van der Waals, namely van der Waals two (vdW2) and van der Waals one (vdW1), were employed to estimate the mixture variables represented by a_m and b_m [9]. The vdW1 mixing rule involves estimating a single interaction parameter (lij), whereas vdW2 entails estimating two (2) binary interaction parameters (lij and kij). The parameter a_m for vdW2 and vdW1 mixing rules was determined using Equation (2), while Equation (5) facilitated the estimation of a_{ij} based on the temperature-dependent binary interaction parameter, kij. The co-volume factor bm for both vdW2 and vdW1 was estimated through Equations (3) and (4), respectively. Furthermore, the interaction parameter bij was determined using Equation (6).

$$a_m = \sum_i \sum_j x_i x_j a_{ij} \tag{2}$$

$$b_m = \sum_i x_i b_i \tag{3}$$

$$b_m = \sum_i \sum_j x_i x_j b_{ij} \tag{4}$$

where

$$a_{ij} = \sqrt{a_{ii} a_{jj}} \left(1 - k_{ij}\right) \tag{5}$$

$$b_{ij} = \frac{b_i + b_j}{2} \left(1 - l_{ij}\right) \tag{6}$$

NRTL model combined with Wong–Sandler mixing rule (WS-NRTL).

The modeling approach in this study integrates Wong–Sandler mixing rules, incorporating Equations (7) and (8) to determine the liquid–gas mixture's attractive force parameter 'a' and co-volume parameter 'b'. Utilizing the Non-Random Two Liquid (NRTL) model, the activity coefficient and excess Gibbs energy are computed, as specified in Equations (13)–(19). Binary interaction parameters (τ_ji, τ_ij, τ_ij_kij) are instrumental in estimating the mixture parameters, where τ_ji and τ_ij represent the NRTL parameters, and g_ij and g_jj denote the interaction energies between molecules 'i' and 'j', as elucidated by Nath and Henni (2020) [9]. Additionally, the value of α in Equations (14) and (15) is arbitrarily set at 0.3 in this study.

$$a = RT\left(\frac{QD}{1-D}\right) \tag{7}$$

$$b = \left(\frac{Q}{1-D}\right) \tag{8}$$

$$Q = \sum_i \sum_j x_i x_j b_{ij}\left(b - \frac{a}{RT}\right) \tag{9}$$

$$D = \sum_i x_i\left(\frac{a_i}{b_i RT}\right) + \left(\frac{G^{ex}}{CRT}\right) \tag{10}$$

$$C = -\ln\ln\left(\left(1+\sqrt{2}\right)/\sqrt{2}\right) \tag{11}$$

$$\left(b - \frac{a}{RT}\right)_{ij} = \frac{1}{2}\left[\left(b_i - \frac{a_i}{RT}\right) + \left(b_j - \frac{a_j}{RT}\right)\right](1-k_{ij}) \tag{12}$$

$$\frac{G^{ex}}{RT} = x_i x_j\left(\frac{\tau_{ji}G_{ji}}{x_i + x_j G_{ji}} + \frac{\tau_{ij}G_{ij}}{x_j + x_i G_{ij}}\right) \tag{13}$$

$$G_{ij} = \exp\left(-\alpha_{ij}\tau_{ij}\right) \tag{14}$$

$$G_{ji} = \exp\left(-\alpha_{ij}\tau_{ji}\right) \tag{15}$$

$$\tau_{ij} = \frac{\left(g_{ij} - g_{jj}\right)}{RT} \tag{16}$$

$$\tau_{ji} = \frac{\left(g_{ji} - g_{ii}\right)}{RT} \tag{17}$$

$$\ln\gamma_i = x_j^2\left[\tau_{ji}\left(\frac{G_{ji}}{x_i + x_j G_{ji}}\right)^2 + \frac{\tau_{ij}G_{ij}}{\left(x_j + x_i G_{ij}\right)^2}\right] \tag{18}$$

$$\ln\gamma_j = x_i^2\left[\tau_{ij}\left(\frac{G_{ij}}{x_j + x_i G_{ij}}\right)^2 + \frac{\tau_{ji}G_{ji}}{\left(x_i + x_j G_{ji}\right)^2}\right] \tag{19}$$

3.4.2. Critical Properties Calculations

To utilize the model effectively, it is imperative to possess thermo-critical properties for both the gas and the solvent under investigation. In our study, we employed the modified Lydersen–Joback–Reid group contribution method [9] to ascertain the critical temperature (Tc), the acentric factor (ω) and the critical pressure (Pc) of the ILs. The Lydersen–Joback–Reid method is a chemical group contribution method revisited and updated by Valderrama and Rojas [10] for the prediction of the critical properties and the

acentric factor of the ionic liquids. The full description and an Excel file are reported in reference [10]. The following equations are used:

$$\mathrm{Tb}\ (\mathrm{K}) = 198.2 + \Sigma n \Delta \mathrm{Tb} \tag{20}$$

$$\mathrm{Tc}\ (\mathrm{K}) = \mathrm{Tb} / \left(\left[A + B \Sigma n \Delta \mathrm{Tc} - \Sigma n \Delta \mathrm{Tc}^2 \right] \right) \tag{21}$$

$$\mathrm{Pc}\ (\mathrm{bar}) = M / \left([C + \Sigma n \Delta \mathrm{Pc}]^2 \right) \tag{22}$$

$$\omega = \frac{(T_b - 43)(T_c - 43)}{(T_c - T_b)(0.7T_c - 43)} \log\left[\frac{P_c}{P_b}\right] - \frac{(T_c - 43)}{(T_c - T_b)} \log\left[\frac{P_c}{P_b}\right] + \log\left[\frac{P_c}{P_b}\right] - 1 \tag{23}$$

where A = 0.5703, B = 1.0121, C = 0.2573, D = 6.75 and Pb = 1.01325 bar.

In the equations, M is in g/mol, Tb and Tc are in K and Pc in bar, and n is the number of different groups. A table in reference [9] provides the values of Mi, ΔTc, ΔPc, ΔT_b for a variety of chemical groups for ILs with and without rings. Table 6 shows a summary of the critical properties of the ionic liquids studied.

Table 6. Critical properties.

Component	Tc (K)	Pc (Bar)	ω
IL1	1345.1	18.700	0.5741
IL2	1195.4	18.347	0.9176
IL3	1207.7	14.265	1.1367
CO_2	304.1	73.800	0.2390

3.5. Binary Interaction Parameter Optimization

The thermodynamic models employed in this research were developed by Dr. Nath and Dr. Kazi as reported in reference [9] using the MATLAB R2024a software, utilizing a bubble point algorithm. As illustrated in Equation (24), the optimization of binary interaction parameters was carried out using the Nelder–Mead simplex method, utilizing the 'fminsearch' function integrated within MATLAB to minimize the error in the objective function. Given the likelihood of experimental data inaccuracies at lower pressures, the optimization of binary interaction parameters was conducted within a pressure range of 0.1 to 1.5 MPa.

$$\mathrm{Err} = \frac{100}{n} \sum_{i=1}^{n} \left[\frac{P_{Exp,i} - P_{Cal,i}}{P_{Exp,i}} \right] \tag{24}$$

3.6. Henry's Law Constant, Enthalpy of Absorption and Entropy of Solvation

Henry's Law constant (H) for the two ILs was evaluated by analyzing the slope of the second-order polynomial of a plot with the mole fractions (x) against the fugacity (f) of CO_2 at all temperatures. This constant, denoted as H_i, represents the ratio of the solute (i) fugacity to its mole fraction in the solvent (j) at infinite dilution, occurring at a specific temperature within a specific pressure scope. Within this research, f_i^V and f_i^L signify the solute's fugacity in the vapor and liquid phases, respectively, while y_i and x_i imply the mole fractions of the gas in the vapor and liquid phases, respectively, as outlined by Huseynov (2014) [11]. After the Henry's Law constant (H) is determined from the absorption data points, the subsequent procedure involves evaluating the entropy of solvation (ΔS^∞) at infinite dilution and the enthalpy of absorption (ΔH^∞) at infinite dilution using the provided equations.

$$H_i = \lim_{x_i \to 0} \frac{f_i^L(T, P, x_i)}{x_i} = \lim_{x_i \to 0} \frac{f_i^V(T, P, y_i)}{x_i} \tag{25}$$

$$\Delta H^\infty = R \left(\frac{\partial(\ln H)}{\partial(1/T)} \right)_P \tag{26}$$

$$\Delta S^{\infty} = -R\left(\frac{\partial(\ln H)}{\partial(\ln T)}\right)_P \tag{27}$$

4. Discussion and Conclusions

The observed trends in Henry's Law constants for CO_2 absorption in IL1, IL2 and IL3 reveal a consistent increase with temperature. This thermal dependence suggests the enhanced solubility of CO_2 gas in ionic liquids at lower temperatures, aligning with typical gas solvation behavior.

The alkyl chain lengths and anion fluorination play crucial roles in determining the absorption behavior of CO_2 in the studied ionic liquids (IL1, IL2 and IL3). IL1, composed of 1-decyl-3-methylimidazolium bis(trifluoromethylsulfonyl) imide, possesses a shorter alkyl chain compared to both IL2 and IL3. This difference in alkyl chain length significantly impacts the solvation properties of the ionic liquids, influencing their interaction with CO_2 molecules.

The observed trends in Henry's Law constants reveal interesting insights into the effect of alkyl chain length on gas solubility. Generally, relatively longer alkyl chains, as in IL2, tend to promote stronger interactions with gas molecules, resulting in lower Henry's Law constants compared to shorter alkyl chain counterparts, such as IL1 and IL3. This phenomenon can be attributed to the increased surface area and van der Waals interactions provided by longer alkyl chains, facilitating greater solubility of CO_2 in IL2.

Furthermore, the fluorination of the anion in IL1, IL2 and IL3 introduces additional effects on gas solvation behavior. The presence of fluorine atoms in the anion enhances the polarity and can induce specific interactions with gas molecules, contributing to the overall solvation process. This effect is evident in the observed Henry's Law constants, where IL1, IL2 and IL3 exhibit impressive performance in terms of CO_2 absorption compared to non-fluorinated counterparts reported in the published literature.

Regarding the obtained thermodynamic parameters, the negative enthalpy values (ΔH^{∞}) obtained for CO_2 absorption in IL1, IL2 and IL3 indicate exothermic solvation processes. The enthalpy value calculated was -12.80 kJ/mol in IL1, -10.33 kJ/mol in IL2 and -13.79 kJ/mol in IL3, further confirming the exothermic nature of the absorption processes. Additionally, the negative entropy values imply a decrease in disorderliness within the system upon solvation, reflecting the ordered arrangement of solvent molecules around the solute during absorption.

In conclusion, the alkyl chain lengths and anion fluorination effect significantly influence the absorption behavior of CO_2 in IL1, IL2 and IL3. The observed trends in Henry's Law constants highlight the importance of molecular structure and interactions in gas solvation processes. The exothermic nature of the absorption processes and the decrease in entropy upon solvation further underscore the thermodynamic aspects of gas solvation in ionic liquids.

Comparative analysis with literature data highlights the favorable performance of IL1, IL2 and IL3 in terms of Henry's Law constants for CO_2 absorption. Despite their impressive performance, further investigation into other ionic liquid formulations, such as 1-octyl-3-methyl imidazolium bis(trifluoromethyl) imide, may provide valuable insights into optimizing gas absorption processes.

Overall, the detailed investigation provides valuable insights into the thermodynamics of gas solvation in IL1, IL2 and IL3, offering potential avenues for further research and optimization in gas separation technologies. The observed trends underscore the promise of fluorinated ionic liquids for CO_2 absorption applications, while also suggesting the need for additional studies to elucidate the underlying molecular mechanisms and optimize the performance of these systems.

Author Contributions: Conceptualization, A.H.; Methodology, E.Q.; Validation, E.Q.; Formal analysis, E.Q.; Investigation, E.Q.; Resources, A.H.; Data curation, E.Q.; Writing—original draft, E.Q.; Writing—review & editing, A.H. and E.S.; Supervision, A.H.; Project administration, A.H. and E.S.; Funding acquisition, A.H. and E.S. All authors have read and agreed to the published version of the manuscript.

Funding: Financial support from the Faculty of Graduate Studies and Research at the University of Regina and the Natural Sciences and Engineering Research Council of Canada (NSERC, RGPIN-2024-05070) is greatly appreciated.

Institutional Review Board Statement: Not applicable.

Informed Consent Statement: Not applicable.

Data Availability Statement: All measured experimental data are reported in the manuscript.

Conflicts of Interest: The authors declare no conflict of interest.

References

1. Pachauri, R.; Meyer, L. *Intergovernmental Panel on Climate Change Synthesis Report*; IPCC: Geneva, Switzerland, 2014.
2. Zhang, C. Absorption principle and techno-economic analysis of CO_2 absorption technologies. *IOP Conf. Ser. Earth Environ. Sci.* **2021**, *657*, 012045. [CrossRef]
3. Yethiraj, A.; Phys, J. Structure of room temperature ionic liquids. *J. Phys. Condens. Matter* **2016**, *28*, 414020. [CrossRef] [PubMed]
4. Anthony, J.; Maginn, E.; Brennecke, J. Solubilities and thermodynamic properties of gases. *J. Phys. Chem. B* **2002**, *109*, 7315–7320. [CrossRef]
5. Vadillo, J.; Diaz-Sainz, G.; Gomez-Coma, L.; Garea, A.; Irabien, A. Chemical and Physical Ionic Liquids in CO_2 Capture Systems Using Membrane Vacuum Regeneration. *Membrane* **2022**, *12*, 785. [CrossRef] [PubMed]
6. Shiflett, M.; Yokozeki, A. Solubilities and diffusivities of carbon dioxide in ionic liquids. *Ind. Eng. Chem. Res.* **2005**, *44*, 4453–4464. [CrossRef]
7. Karunarathne, S.; Eimer, D.; Lars, E. Density, Viscosity, and Excess Properties of MDEA + H_2O, DMEA + H_2O, and DEEA + H_2O Mixture. *Appl. Sci.* **2020**, *10*, 3196. [CrossRef]
8. Aravind, V.; Amr, H.; Paitoon, T. High Pressure Physical Solubility of Carbon Dioxide (CO_2) in Mixed Polyethylene Glycol Dimethyl Ethers (Genosorb 1753). *Can. J. Chem. Eng.* **2011**, *90*, 567–583.
9. Nath, D.; Henni, A. Solubility of carbon dioxide (CO_2) in four bis (trifluoromethylsulfonyl)imide ([Tf2N]) based ionic liquids. *Fluid Phase Equilibria* **2020**, *524*, 112757. [CrossRef]
10. Valderrama, J.; Rojas, R. Critical properties of ionic liquids. Revisited. *Ind. Eng. Chem. Res.* **2009**, *48*, 6890–6900. [CrossRef]
11. Huseynov, M. Thermodynamic and Experimental Studies of Ethane Solubility in Promising Ionic Liquids for CO_2 Capture. Master's Thesis, University of Regina, Regina, SK, Canada, 2015.

Disclaimer/Publisher's Note: The statements, opinions and data contained in all publications are solely those of the individual author(s) and contributor(s) and not of MDPI and/or the editor(s). MDPI and/or the editor(s) disclaim responsibility for any injury to people or property resulting from any ideas, methods, instructions or products referred to in the content.

molecules

MDPI

Article

Highly Efficient and Selective Extraction of Gold from Thiosulfate Leaching Solution Using Functionalized Dicationic Ionic Liquids

Qiang Zhou [1], Yunchang Fan [1,*] and Sheli Zhang [2]

[1] College of Chemistry and Chemical Engineering, Henan Polytechnic University, Jiaozuo 454003, China; 212112010027@home.hpu.edu.cn
[2] School of Science and Technology, Jiaozuo Teachers College, Jiaozuo 454000, China; 1295006035@jzsz.edu.cn
* Correspondence: fanyunchang@hpu.edu.cn; Tel.: +86-391-398-6813

Abstract: Thiosulfate leaching has been regarded as a promising alternative to cyanidation, but it still faces the challenge of the recovery of low content of gold from high concentrations of thiosulfate solutions. Liquid–liquid extraction is a method to address this issue but is still limited by the use of volatile and toxic organic solvents. To overcome this limitation, this work synthesized some functionalized dicationic ionic liquids (DILs) to serve as extraction solvents for the recovery of the gold–thiosulfate complex, $[Au(S_2O_3)_2]^{3-}$, from thiosulfate solutions. Experimental results indicated that the DILs showed higher extraction rates toward $[Au(S_2O_3)_2]^{3-}$ compared with their monocationic-based counterparts, likely due to the stronger electrostatic interaction between the dications of the ILs and $[Au(S_2O_3)_2]^{3-}$. The transfer of $[Au(S_2O_3)_2]^{3-}$ from the water phase to the IL phase was identified as an anion exchange and endothermic process. The rate of extraction was limited by the anion exchange process occurring at the IL–water interface. The extraction ability of ILs highly depended on the type of anion; specifically, the ILs with anions that had strong hydrogen-bonding ability exhibited high extraction ability toward $[Au(S_2O_3)_2]^{3-}$. Finally, DILs proved effective in the recovery of $[Au(S_2O_3)_2]^{3-}$ from an actual gold leaching solution and exhibited high selectivity toward coexisting ions, indicating their potential as environmentally friendly solvents for gold recovery.

Keywords: functionalized dicationic ionic liquids (DILs); extraction; thiosulfate leaching; gold recovery

1. Introduction

Cyanidation is the most widely used hydrometallurgical technique worldwide for the recovery of gold from gold ores due to its cost-effectiveness and efficiency [1,2]. However, the high toxicity of cyanides has led to a pressing need for more environmentally friendly alternatives. Thiosulfates have emerged as a promising substitute for cyanides in gold leaching due to their non-toxic and effective properties [1–5]. Despite the environmental benefits of the thiosulfate leaching method, the recovery of a low level of gold from the leaching solution containing a high concentration of thiosulfate [1,2,4] remains a significant challenge. Various methods such as adsorption with anion exchange resin [6], activated carbon [7], and silica gel [8], as well as solvent extraction [9–11], have been employed to recover gold from thiosulfate solutions. Solvent extraction is considered a preferable option for gold recovery due to its continuous operation, high capacity, and ease of scaling up for industrial use [9–11]. Very recently, Li and coworkers reported the extraction of gold–thiosulfate complex, $[Au(S_2O_3)_2]^{3-}$, from a thiosulfate solution with diphenylphosphine (DPP) diluted in benzene, and it was found that DPP demonstrated high selectivity and extraction ability toward $[Au(S_2O_3)_2]^{3-}$, and the extraction mechanism involved the complexation between phosphorus atom in DPP and gold ion via ligand exchange [9]. Furthermore, no research has been carried out to verify the purity of gold after extraction. Despite the high efficiency of the DPP–benzene system in recovering gold, the use of

benzene as a solvent is a concern due to its volatility and toxicity. Therefore, there is an urgent demand to develop more environmentally friendly solvents.

Ionic liquids (ILs), a novel class of versatile solvents, have been introduced as a promising alternative to traditional solvents for the extraction of valuable metals like gold [10,11] silver [12], palladium [13], rhodium [14], copper [12], and platinum [14]. Ammonium, imidazolium, and phosphonium-based ILs have been commonly used in the past two decades due to their high chemical stability, non-flammability, and low toxicity [10–14]. Dicationic ILs (DILs) are a new class of the IL family and composed of one dication formed by two monocations connected via a linkage chain, and two anions [15]. DILs have been used for the extraction of Pb^{2+} and Cd^{2+} and have demonstrated higher metal extraction ability compared with the monocationic ILs, as they have more active interaction sites with metals [15,16]. The extraction mechanisms of metals using ILs as extractants typically rely on the IL solubility in water, with hydrophobic ILs following an ion exchange mechanism and more hydrophilic ILs, leading to an ion-pair mechanism [10–17]. Several reviews have highlighted the various applications of ILs in metal extraction [17–19].

Up to now, the extraction of gold from thiosulfate leaching solutions by ILs has been reported by Mahandra and coworkers. They constructed an extraction system using Cyphos IL 101 (tetradecyl-(trihexyl) phosphonium chloride) or Cyphos IL 102 (tetradecyl-(trihexyl) phosphonium bromide) as extractant and toluene as a diluent to recover gold from thiosulfate leaching solutions [10,11]: The gold–thiosulfate complex $[Au(S_2O_3)_2]^{3-}$ moves into the organic phase via an anion exchange process, and the ionic interaction between the IL cation and $[Au(S_2O_3)_2]^{3-}$ plays an important role during extraction. Finally, the gold extracted into the organic phase could easily be stripped using a NaCl solution or a solution containing 5% thiourea and 1% HCl. While promising outcomes have been achieved using ILs for gold recovery, the use of volatile and toxic toluene as a solvent remains a necessity. Hence, there is a pressing need to develop an IL-based extraction system that eliminates the reliance on such hazardous solvents. Since the ionic interaction between the IL cation and the anion $[Au(S_2O_3)_2]^{3-}$ facilitates the transfer of gold from the water phase into the organic phase, it is suggested that DILs with highly electrophilic cations could exhibit a strong affinity toward $[Au(S_2O_3)_2]^{3-}$.

Inspired by the above discussion, a series of imidazolium-based DILs were designed, and the aims of this work were thus to investigate their extraction ability toward $[Au(S_2O_3)_2]^{3-}$, explore the extraction mechanism, and assess the potential use of DILs for the recovery of gold from thiosulfate leaching solutions in gold ore processing.

2. Results and Discussion

2.1. Screening of the ILs

In this work, twelve monocationic and dicationic ILs were synthesized (Figure 1). Among them, $[C_4(Bim)_2](CF_3SO_3)_2$, $[C_6(Bim)_2](ClO_4)_2$, $[C_6(Bim)_2](CF_3SO_3)_2$, and $[C_8(Bim)_2](ClO_4)_2$ are solid at room temperature with melting points ranging from 54.8 °C to 57.7 °C, 46.4 °C to 48.1 °C, 55.8 °C to 56.4 °C, and 85.7 °C to 87.1 °C, respectively. Operating extraction processes above the melting points of these four solid DILs is not recommended due to the high energy consumption associated with heating. Additionally, the remaining eight ILs also contain ClO_4^-- and $CF_3SO_3^-$-based DILs, and the four solid DILs are not utilized in subsequent extraction procedures.

The extraction ability of the eight different ILs toward $[Au(S_2O_3)_2]^{3-}$ was systematically investigated, and the results illustrated in Figure 2 suggest that the ILs with NTf_2^- anions have low extraction efficiencies for $[Au(S_2O_3)_2]^{3-}$, while those with ClO_4^- and $CF_3SO_3^-$ anions demonstrate high extraction efficiencies. Typically, the extraction of metal ions with hydrophobic ILs involves three main steps: migration of metal ions from the bulk aqueous phase to the water–IL interface, charge neutralization at the IL–water interface through ion exchange or ion-pair mechanisms, and the diffusion of metal ions into the IL phase [20]. Factors such as conductivity and viscosity play a role in the diffusion rates of metal ions, with high conductivity and low viscosity being favorable for

fast diffusion [21,22]. The results depicted in Figure 2a indicate that water phases saturated with ILs have low viscosities similar to the viscosity of water itself (approximately 1 mPa s [23]), yet ILs with ClO_4^- and $CF_3SO_3^-$ anions still exhibit high extraction efficiencies for $[Au(S_2O_3)_2]^{3-}$ despite their high viscosities (Figure 2b). This suggests that viscosity may not be the primary factor influencing the extraction of $[Au(S_2O_3)_2]^{3-}$. Moreover, water phases saturated with $[C_4(Bim)_2](ClO_4)_2$ and $[C_4Bim]ClO_4$, as well as $[C_4(Bim)_2](ClO_4)_2$ and $[C_4Bim]ClO_4$ phases saturated with water, show higher conductivities. These two ILs also show stronger extraction efficiencies toward $[Au(S_2O_3)_2]^{3-}$, indicating the rapid diffusion of $[Au(S_2O_3)_2]^{3-}$ in highly conductive media. Additionally, the conductivity of $[C_8Bim]ClO_4$ is similar to the NTf_2^--based ILs, but its extraction ability for $[Au(S_2O_3)_2]^{3-}$ is significantly higher (Figure 2b). This suggests that conductivity is not the sole determining factor in the extraction of $[Au(S_2O_3)_2]^{3-}$.

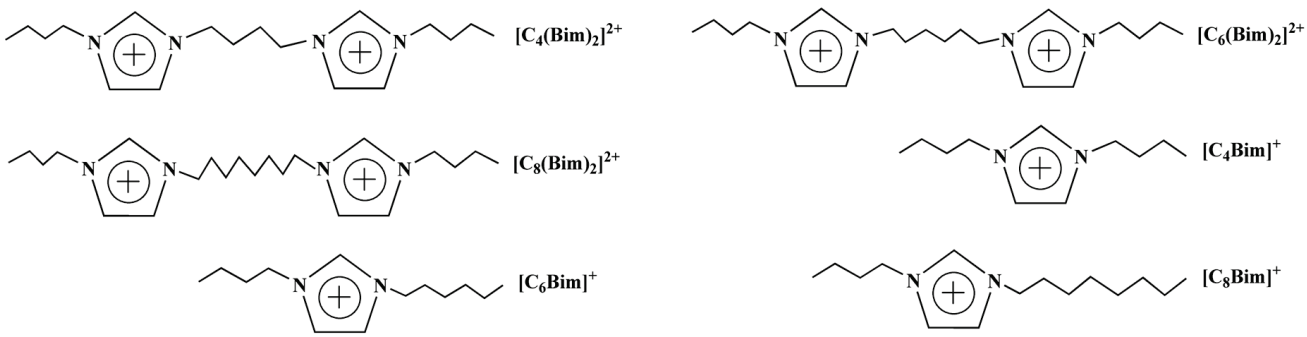

Figure 1. Chemical structures of the IL cations used in this work.

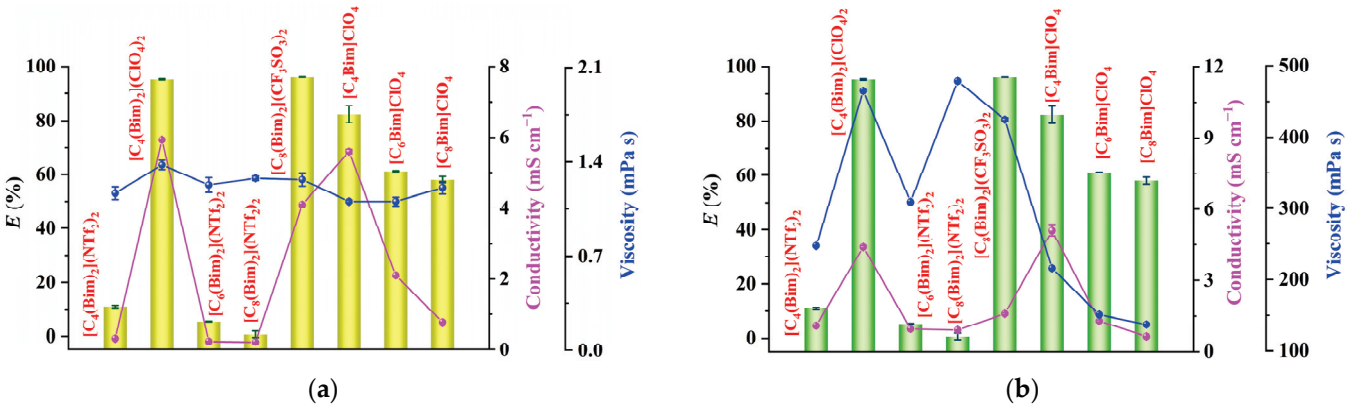

Figure 2. (**a**) Correlation between the extraction ability of ILs and the conductivities of water phases saturated with ILs (purple line) or the viscosities of water phases saturated with ILs (blue line); (**b**) correlation between the extraction ability of ILs and the conductivities of ILs saturated with water (purple line) or the viscosities of ILs saturated with water (blue line). Extraction conditions: 10 mg dm^{-3} of gold, 0.1 mol dm^{-3} of $Na_2S_2O_3$, 1.0 mol dm^{-3} of NH_3, 5 mmol dm^{-3} of $CuSO_4$, 5:1 of volume ratio of water phase to IL phase (V_W:V_{IL}), 25 °C of extraction temperature, and 20 min of extraction time.

Based on the above discussion, it appears that the charge neutralization of $[Au(S_2O_3)_2]^{3-}$ at the water–IL interface is the step that determines the rate of the extraction process. To delve deeper into the extraction kinetics, further experiments were carried out by extending the extraction time to 48 h. The results presented in Figure 3a demonstrate that the extraction efficiencies of the monocationic ILs including $[C_4Bim]ClO_4$, $[C_6Bim]ClO_4$, and $[C_8Bim]ClO_4$ increase remarkably with longer extraction times, from 20 min to 48 h. However, the extraction efficiencies of the DILs remain constant when the extraction time is extended from 20 min to 48 h. This suggests that the charge neutralization of $[Au(S_2O_3)_2]^{3-}$

at the water–DIL interface occurs more rapidly compared with the water–monocationic IL interface, likely due to the higher electrophilicity of the dications, as depicted in Figure 3b. In other words, dicationic structure allows for more active interaction with the $[Au(S_2O_3)_2]^{3-}$ anion, leading to quicker charge neutralization through ion exchange. This ion exchange mechanism will be further elaborated in subsequent discussion (Section 2.3).

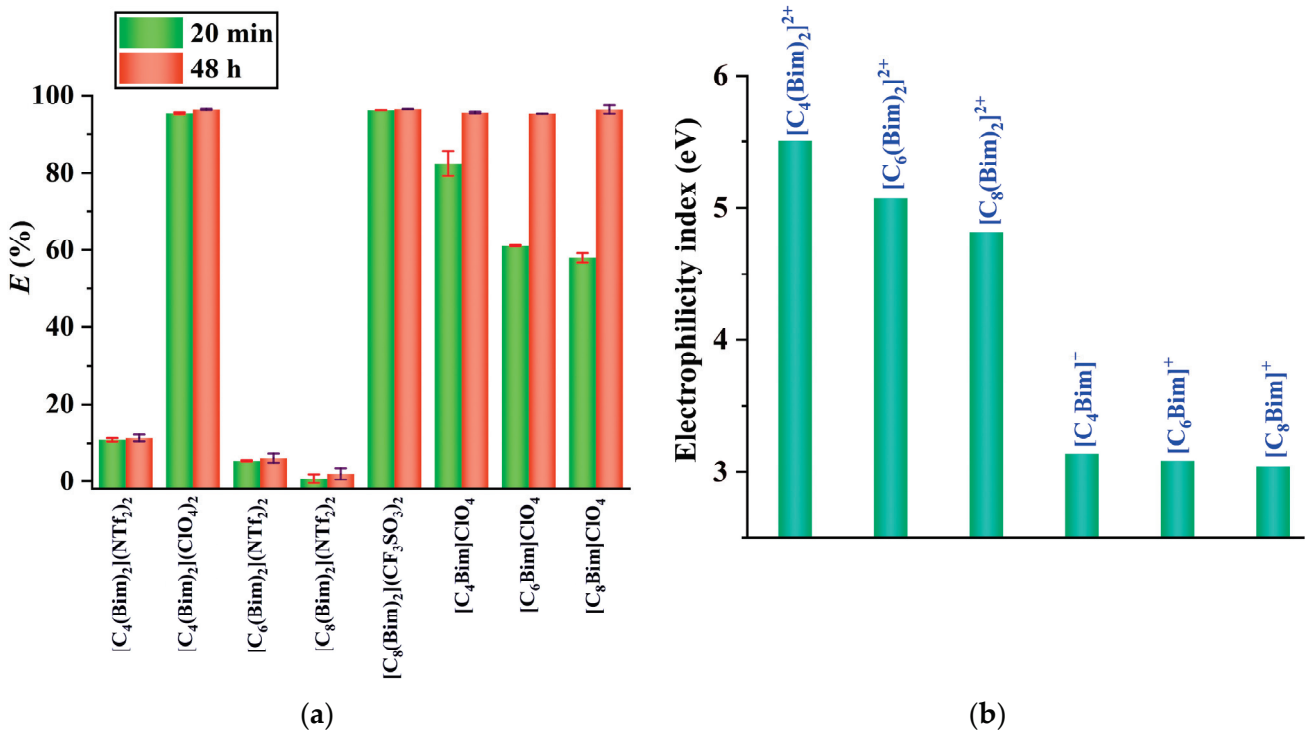

Figure 3. (**a**) The extraction efficiencies of ILs at different extraction times; (**b**) the electrophilicity of ILs.

Figure 3a indicates that ILs with $CF_3SO_3^-$ and ClO_4^- anions have stronger extraction ability compared with those with the NTf_2^- anion. Therefore, it is important to further investigate the driving forces behind this extraction. Previous studies have shown that the product of the hydrogen bond donating ability (α) and the hydrogen bond accepting ability (β) ($\alpha\beta$) can be utilized as a measure to assess the hydrogen-bonding strength of ILs [24]. This approach is also applied in the current study. As shown in Figure 4 (black line), the ILs containing the same anions exhibit similar levels of hydrogen-bonding strength, aligning with existing research [24]. Furthermore, ILs based on $CF_3SO_3^-$- and ClO_4^- exhibit higher extraction ability compared with those with NTf_2^- as the anion. This suggests that ILs with strong hydrogen-bonding strength have higher extraction ability. This could be attributed to the weakening of electrostatic interaction between the IL cation and IL anion, caused by the hydrogen-bonding interaction between the IL and water. This weakening leads to an increase in the water solubilities of ILs (Figure 4, blue line) [25,26] and could potentially improve the electrostatic interaction between the IL cation and $[Au(S_2O_3)_2]^{3-}$, thereby enhancing the extraction ability of ILs.

In terms of $[C_8(Bim)_2](CF_3SO_3)_2$, it exhibits higher hydrogen-bonding strength compared with ClO_4^--based ILs, although its extraction ability is similar to the latter, which may be attributed to its higher water solubility (Figure 4, blue line). The higher water solubility leads to more significant dissolution loss of $[C_8(Bim)_2](CF_3SO_3)_2$ during extraction, ultimately resulting in reduced extraction efficiency.

The above discussion suggests that the DILs $[C_8(Bim)_2](CF_3SO_3)_2$ and $[C_4(Bim)_2](ClO_4)_2$ exhibit quicker extraction rates and greater extraction ability. Additionally, the latter has lower water solubility. Consequently, $[C_4(Bim)_2](ClO_4)_2$ was chosen as the optimal extractant and utilized in subsequent experiments.

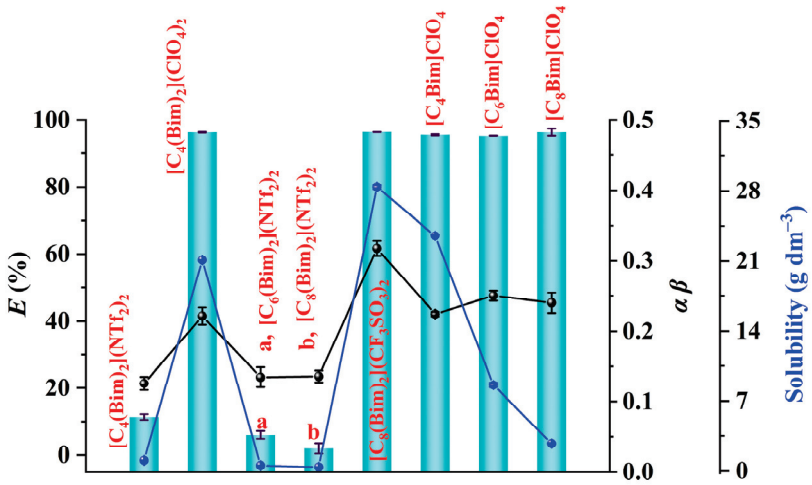

Figure 4. Correlation between the extraction ability of ILs and their hydrogen-bonding ability (black line) or water solubilities (blue line). Extraction conditions: 10 mg dm^{-3} of gold, 0.1 mol dm^{-3} of $Na_2S_2O_3$, 1.0 mol dm^{-3} of NH_3, 5 mmol dm^{-3} of $CuSO_4$, 5:1 of volume ratio of water phase to IL phase (V_W:V_{IL}), 25 °C of extraction temperature, and 48 h of extraction time.

2.2. *Effect of Operating Parameters on the Extraction of $[Au(S_2O_3)_2]^{3-}$*

Generally, the leaching of gold typically involves the use of thiosulfate, $CuSO_4$, and NH_3 [1,2,4], and the effect of the thiosulfate concentration on the extraction of $[Au(S_2O_3)_2]^{3-}$ illustrated in Figure 5a indicates that the extraction efficiency of $[C_4(Bim)_2](ClO_4)_2$ toward $[Au(S_2O_3)_2]^{3-}$ almost remains constant with the thiosulfate concentration ranging from 0.05 mol dm^{-3} to 0.2 mol dm^{-3}, suggesting that the extraction of $[Au(S_2O_3)_2]^{3-}$ by $[C_4(Bim)_2](ClO_4)_2$ can be carried out effectively over a broad spectrum of thiosulfate concentrations.. It has been proven that the presence of trace amounts of copper ions can improve the gold leaching rate, and the addition of NH_3 is necessary to stabilize these copper ions [1,2,4]. The findings presented in Figure 5b show that the extraction efficiency of $[Au(S_2O_3)_2]^{3-}$ remains steady as the $CuSO_4$ concentration varies from 5 mmol dm^{-3} to 25 mmol dm^{-3}. Additionally, the introduction of NH_3 does not affect the extraction efficiency of $[Au(S_2O_3)_2]^{3-}$, as shown in Figure 5c.

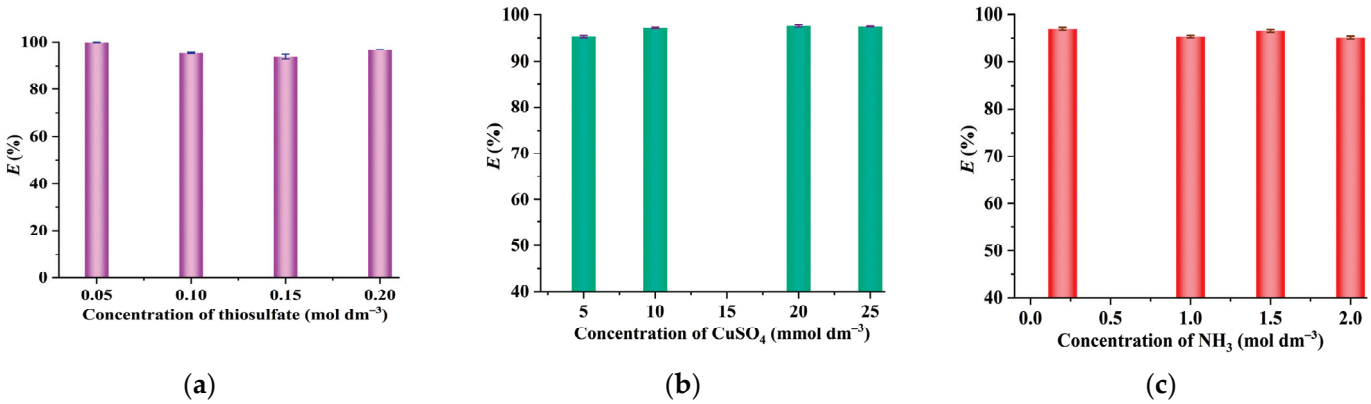

Figure 5. (**a**) The effect of thiosulfate concentration (5 mmol dm^{-3} of $CuSO_4$; 1.0 mol dm^{-3} of NH_3; extraction time, 20 min; extraction temperature, 25 °C; 10 mg dm^{-3} of gold; V_W:V_{IL} = 5:1); (**b**) $CuSO_4$ concentration (0.1 mol dm^{-3} of $Na_2S_2O_3$; 1.0 mol dm^{-3} of NH_3; extraction time, 20 min; extraction temperature, 25 °C; 10 mg dm^{-3} of gold; V_W:V_{IL} = 5:1); and (**c**) NH_3 concentration (0.1 mol Ldm^{-3} of $Na_2S_2O_3$; 5 mmol dm^{-3} of $CuSO_4$; extraction time, 20 min; extraction temperature, 25 °C; 10 mg dm^{-3} of gold; V_W:V_{IL} = 5:1) on the extraction of $[Au(S_2O_3)_2]^{3-}$ by $[C_4(Bim)_2](ClO_4)_2$.

The effect of extraction time on the extraction efficiency of $[Au(S_2O_3)_2]^{3-}$ is depicted in Figure 6a. It is evident that the extraction efficiency rises as the extraction time increases from 5 min to 20 min, after which it stabilizes with further extension of the extraction time. Consequently, 20 min was chosen for subsequent experiments. The results illustrated in Figure 6b suggest that the extraction efficiency of $[Au(S_2O_3)_2]^{3-}$ remains consistent as the gold concentration ranges from 5 mg dm^{-3} to 25 mg dm^{-3}, highlighting the strong extraction ability of $[C_4(Bim)_2](ClO_4)_2$. Figure 6c indicates that the extraction efficiency of $[Au(S_2O_3)_2]^{3-}$ exceeds 95% in the temperature range of 25 °C to 45 °C but drops to 72.0% when the temperature is reduced to 15 °C. This suggests that the extraction of $[Au(S_2O_3)_2]^{3-}$ is sensitive to temperature and is best performed at room temperature or higher.

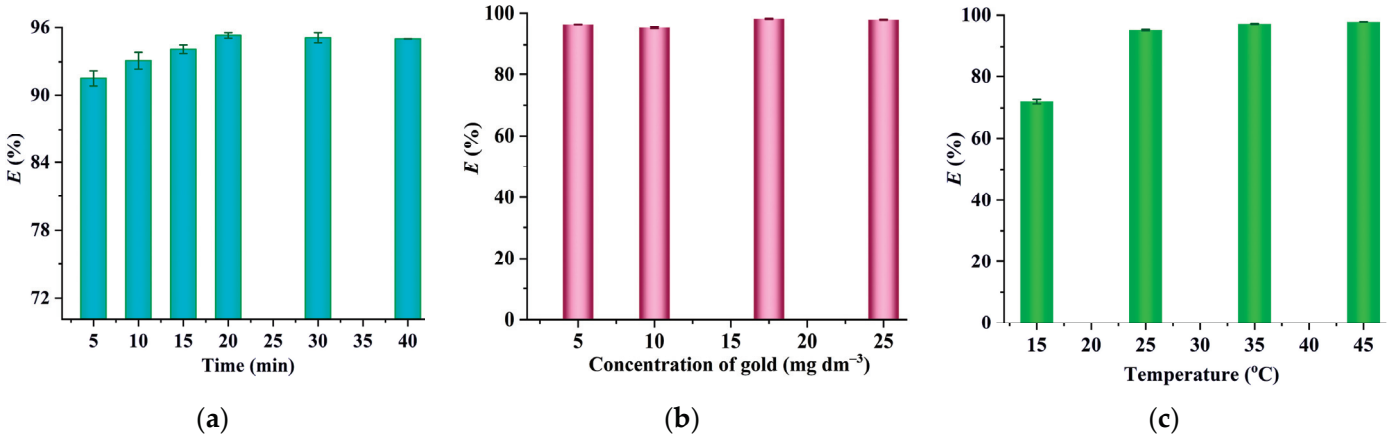

Figure 6. (**a**) The effect of extraction time (0.1 mol dm^{-3} of $Na_2S_2O_3$; 5 mmol dm^{-3} of $CuSO_4$; 1.0 mol dm^{-3} of NH_3; extraction temperature, 25 °C; 10 mg dm^{-3} of gold; V_W:V_{IL} = 5:1); (**b**) gold concentration (0.1 mol dm^{-3} of $Na_2S_2O_3$; 5 mmol dm^{-3} of $CuSO_4$; 1.0 mol dm^{-3} of NH_3; extraction time, 20 min; extraction temperature, 25 °C; V_W:V_{IL} = 5:1); and (**c**) extraction temperature (0.1 mol dm^{-3} of $Na_2S_2O_3$; 5 mmol dm^{-3} of $CuSO_4$; extraction time, 20 min; 1.0 mol dm^{-3} of NH_3; 10 mg dm^{-3} of gold; V_W:V_{IL} = 5:1) on the extraction of $[Au(S_2O_3)_2]^{3-}$ by $[C_4(Bim)_2](ClO_4)_2$.

Additionally, the results illustrated in Figure 7a show that the extraction efficiency of $[Au(S_2O_3)_2]^{3-}$ remains constant within the pH range of 10.8 to 11.8 but significantly decreases as pH levels decrease, which may be ascribed to the fact that copper ions exist in the form of $Cu(NH_3)_4^+$ in the presence of a high concentration of NH_3. When pH values decrease, $Cu(NH_3)_4^+$ converts to $Cu(S_2O_3)_3^{5-}$ due to the reaction between Cu^{2+} and $S_2O_3^{2-}$ ($Cu^{2+} + 4S_2O_3^{2-} = Cu(S_2O_3)_3^{5-} + 0.5S_4O_6^{2-}$) [11,27]. This copper–thiosulphate complex can also be extracted by $[C_4(Bim)_2](ClO_4)_2$, leading to competition with the extraction of $[Au(S_2O_3)_2]^{3-}$ and consequently reducing the extraction efficiency of $[Au(S_2O_3)_2]^{3-}$. To confirm this hypothesis, the extraction efficiencies of Cu^{2+} (5 mmol dm^{-3}) at pH 11, pH 7, and pH 4.5 were measured. It is observed that the extraction efficiency of Cu^{2+} at pH 11 is zero, while at pH 7 and pH 4.5, it increases to 11.7% and 14.6% respectively, supporting the above deduction. Finally, as shown in Figure 7b, the extraction efficiency of $[Au(S_2O_3)_2]^{3-}$ remains above 93% across a wide range of phase volume ratios (V_w:V_{IL}, 3.3 to 25). A phase volume ratio of 10 was chosen for subsequent experiments due to its ability to achieve an extraction efficiency as high as 96.4%.

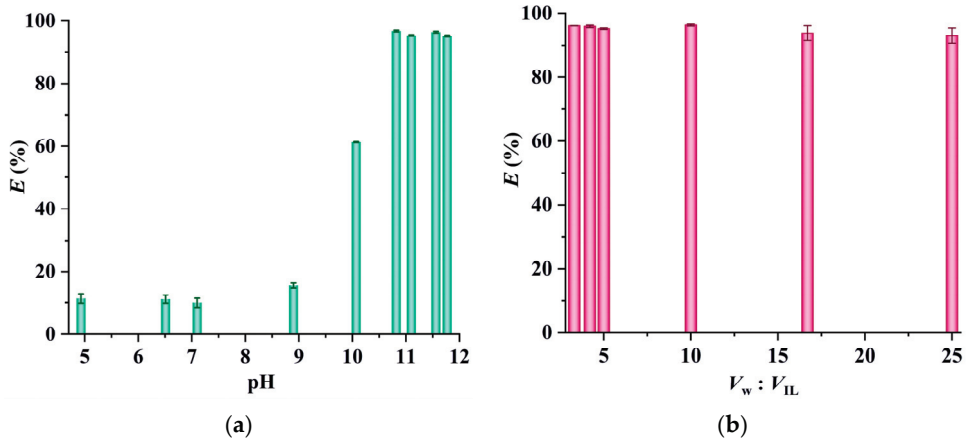

Figure 7. (**a**) The effect of equilibrium pH (0.1 mol dm^{-3} of $Na_2S_2O_3$; 5 mmol dm^{-3} of $CuSO_4$; extraction temperature, 25 °C; 10 mg dm^{-3} of gold; V_W:V_{IL} = 5:1; extraction time, 20 min) and (**b**) phase volume ratio (0.1 mol dm^{-3} of $Na_2S_2O_3$; 5 mmol dm^{-3} of $CuSO_4$; extraction time, 20 min; 1.0 mol dm^{-3} of NH_3; 10 mg dm^{-3} of gold; extraction temperature, 25 °C) on the extraction of $[Au(S_2O_3)_2]^{3-}$ by $[C_4(Bim)_2](ClO_4)_2$.

2.3. Extraction Mechanism

Recently, Mahandra and coworkers have reported that the extraction of $[Au(S_2O_3)_2]^{3-}$ by a phosphonium-based IL–toluene system is an anion exchange process [10,11]. If the extraction of $[Au(S_2O_3)_2]^{3-}$ by $[C_4(Bim)_2](ClO_4)_2$ also operates through an anion exchange mechanism, the extraction process can be described as follows:

$$3\{[C_4(Bim)_2](ClO_4)_2\}_{IL} + 2\{[Au(S_2O_3)_2]^{3-}\}_W \leftrightharpoons \{[C_4(Bim)_2]_3[Au(S_2O_3)_2]_2\}_{IL} + 6(ClO_4^-)_W \quad (1)$$

where the subscripts IL and W refer to the IL and water phases, respectively.

As listed in Equation (1), the anion exchange mechanism means an increase in the concentration of ClO_4^- after extraction. Further experiments were thus carried out to confirm this hypothesis by extracting 7.5 × 10^{-3} mol dm^{-3} of $[Au(S_2O_3)_2]^{3-}$ with $[C_4(Bim)_2](ClO_4)_2$. A high extraction efficiency of 99.1% means that the increment of ClO_4^- concentration in water post-extraction should be 2.23 × 10^{-2} mol dm^{-3}, which closely aligns with the experimental value (2.31 × 10^{-2} mol dm^{-3}) determined through ion chromatography. This result suggests that the extraction of $[Au(S_2O_3)_2]^{3-}$ with $[C_4(Bim)_2](ClO_4)_2$ is an anion exchange process. Additionally, the FT-IR spectra of the IL phases pre- and post-extraction, as demonstrated in Figure 8, reveal the emergence of three new peaks at 1011 cm^{-1}, 655 cm^{-1}, and 579 cm^{-1} in the IR spectrum of the IL phase after extraction. These peaks correspond to the symmetrical stretching of S=O, S-O stretching, and S-S stretching vibrations, respectively [28,29], indicating the transfer of $[Au(S_2O_3)_2]^{3-}$ from the water phase to the IL phase.

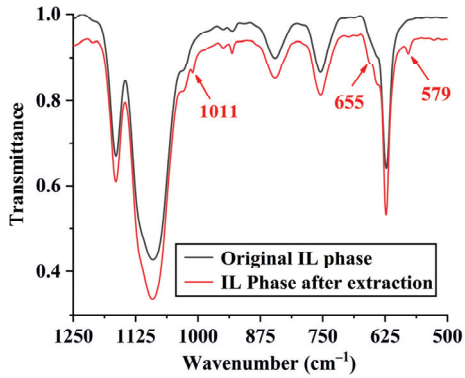

Figure 8. The FT-IR spectra of the IL phases before and after extraction.

2.4. Thermodynamic Analysis

To delve deeper into how extraction works, a thermodynamic analysis was conducted to determine the Gibbs free-energy change (ΔG), enthalpy change (ΔH), and the entropy change (ΔS) of the extraction process. This analysis was based on equations that assume ΔH and ΔS remain consistent across the temperature range investigated [30,31].

$$\Delta G = -\mathrm{R}T\ln D \tag{2}$$

where R and T are the gas constant and the extraction temperature, respectively.

$$\ln D = -\Delta H/\mathrm{R}T + \Delta S/\mathrm{R} \tag{3}$$

The van't Hoff plot for the extraction of $[Au(S_2O_3)_2]^{3-}$ is shown in Figure S1 in the Supplementary Materials, with the resulting thermodynamic parameters detailed in Table 1. Negative ΔG values signify the spontaneity of the $[Au(S_2O_3)_2]^{3-}$ extraction process. A positive ΔH indicates that the extraction is endothermic, while a positive ΔS suggests increased disorder at the liquid–liquid interface during the extraction [30,31].

Table 1. Thermodynamic parameters for the extraction of $[Au(S_2O_3)_2]^{3-}$ by $[C_4(Bim)_2](ClO_4)_2$.

T (K)	ΔG (kJ mol^{-1})	ΔH (kJ mol^{-1})	ΔS (J mol^{-1} K^{-1})
288	−6.4	72.7	278
298	−11.7		
308	−13.4		
318	−14.9		

2.5. Comparison of $[C_4(Bim)_2](ClO_4)_2$ with the Reported Extraction Solvents

Previously, Cyphos IL 101–toluene, Cyphos IL 102–toluene [10,11], and DPP–benzene [9] were applied to the recovery of $[Au(S_2O_3)_2]^{3-}$ from thiosulfate solutions, and the results shown in Figure 9a indicate that the extraction efficiencies of $[C_4(Bim)_2](ClO_4)_2$ toward $[Au(S_2O_3)_2]^{3-}$ are comparable to those of Cyphos IL 101 (102)–toluene and DPP–benzene systems. This suggests that $[C_4(Bim)_2](ClO_4)_2$ has a strong ability to extract $[Au(S_2O_3)_2]^{3-}$ and could be a more environmentally friendly solvent option due to its lack of toxic and volatile components. Additionally, the gold extracted into the IL phase can be recovered through back extraction using an ethylenediaminetetraacetic acid disodium aqueous solution (0.1 mol dm^{-3}) as the extraction solvent, with a high back-extraction efficiency of 94.4%. The recovered IL phase can be reused for subsequent extraction cycles without significantly decreasing its extraction ability (96.9% for recovered IL compared to 97.9% for fresh IL). Furthermore, the structure of the recovered IL was examined by proton nuclear magnetic resonance (^{1}H NMR) spectroscopy, and the results depicted in Figure S2 indicate that the ^{1}H NMR spectrum of the recovered $[C_4(Bim)_2](ClO_4)_2$ is the same as that of the

initial one, indicating that $[C_4(Bim)_2](ClO_4)_2$ maintains its original chemical structure even after being used.

2.6. Selective Recovery of Gold from Real Samples

To assess the potential of using $[C_4(Bim)_2](ClO_4)_2$ to isolate $[Au(S_2O_3)_2]^{3-}$ from the actual thiosulfate leaching solution of a gold ore with a gold concentration of 6.0 mg dm^{-1}, extraction experiments were carried out at a phase volume ratio (V_W:V_{IL}) of 10, and the results illustrated in Figure 9b indicate that the extraction efficiency of $[Au(S_2O_3)_2]^{3-}$ closely resembles that of the simulated thiosulfate leaching solution (Figure 4). This suggests that the presence of other ions may not impede the extraction of $[Au(S_2O_3)_2]^{3-}$, as confirmed by interference tests (Figure 9b, where the extraction efficiencies of the coexisting ions are zero). Therefore, it can be inferred that $[C_4(Bim)_2](ClO_4)_2$ exhibits high selectivity for the extraction of $[Au(S_2O_3)_2]^{3-}$.

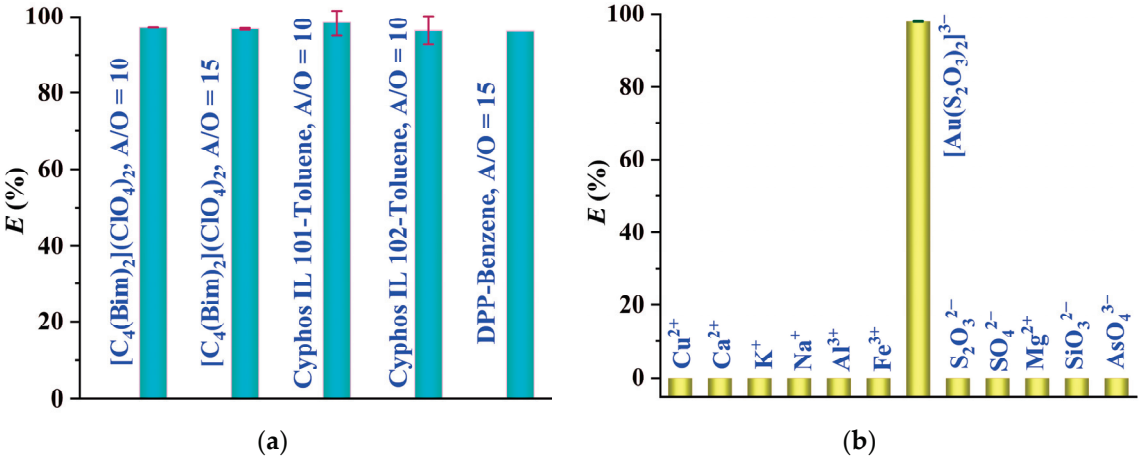

Figure 9. (**a**) Comparison of $[C_4(Bim)_2](ClO_4)_2$ with the reported extraction systems (A/O, the volume ratio of water phase to organic phase; 0.2 mol dm^{-3} of $Na_2S_2O_3$; 10 mg dm^{-3} of gold); (**b**) extraction behavior of $[C_4(Bim)_2](ClO_4)_2$ toward $[Au(S_2O_3)_2]^{3-}$ and coexisting ions.

3. Materials and Methods

3.1. Reagents and Materials

1-(n-Butyl)imidazole (Bim, 98%), 1,4-dibromobutane (98%), 1,6-dibromohexane (97%), 1,8-dibromooctane (98%), n-butylbromide (>99%), barium perchlorate hydrate ($Ba(ClO_4)_2{\cdot}3H_2O$, 99%), potassium trifluoromethanesulfonate (KCF_3SO_3, 98%), bis(trifluoromethane)sulfonimide lithium ($LiNTf_2$, 99.9%), and gold sodium thiosulfate ($Na_3Au(S_2O_3)_2.xH_2O$, 99.9%) were supplied by Macklin Biochemical Technology Co., Ltd. (Shanghai, China). The ILs 1-butyl-3-hexylimidazolium perchlorate ($[C_6Bim]ClO_4$) and 1-butyl-3-octylimidazolium perchlorate ($[C_8Bim]ClO_4$) were prepared as described in our previous work [32]. Reichardt's dye (RD, 90%) and 4-nitroaniline (NA, ≥99%) were obtained from Sigma-Aldrich Co.; *N*,*N*-diethyl-4-nitroaniline (DENA, 97%) was purchased from Fluorochem Ltd., (Hadfield, UK). Unless stated otherwise, all other reagents are analytical grade. Deionized water was used throughout the experiments. Dried gold ore powder (particle size, around 200 mesh; gold content, 60 g t^{-1}) was obtained from a Xinjiang Gold Mine Company (Xinjiang, China), and its main components, measured by an X-ray fluorescence spectrometer (XRF, ARL Perform'X, Thermo Fisher Scientific Inc., Waltham, CA, USA), are 29.8% of Ca, 23.2% of Fe, 22.4% of Si, 7.5% of S, 6.0% of Al, 3.2% of As, 2.2% of Mg, 2.0% of K, 1.3% of Na, and 1.3% of Ti. The leaching of gold from gold ore was performed as follows [33,34]: First, 20 g of gold ore was left to contact with 100 mL of lixiviant composed of 0.1 mol dm^{-3} of $Na_2S_2O_3$, 5.0 mmol dm^{-3} of $CuSO_4$, and 1.0 mol dm^{-3} of NH_3 under stirring at room temperature for 48 h.

3.2. Synthesis of Dicationic Imidazolium-Based ILs

1,4-Bis[*N*-(*N*′-butylimidazolium)]butane perchlorate ($[C_4(Bim)_2](ClO_4)_2$) was prepared as follows: First, 0.06 mol of 1,4-dibromobutane and 0.12 mol of Bim were mixed under stirring at 70 °C for 7 h, and the resultant product was dissolved by 40 mL of water, followed by the addition of 0.12 mol of $BaClO_4$ to generate the IL $[C_4(Bim)_2](ClO_4)_2$. After being washed by water several times until Br-free, as indicated by a $AgNO_3$ test of the water washings [35], the IL phase was dried at 70 °C, and $[C_4(Bim)_2](ClO_4)_2$ was obtained as a light-yellow liquid (yield, 73.0%).

The synthesis of the ILs $[C_4(Bim)_2](NTf_2)_2$ (light-yellow liquid, 97.6% yield) and $[C_4(Bim)_2](CF_3SO_3)_2$ (white solid, melting point: 54.8–57.7 °C; 7.0% yield) followed the same procedure as for $[C_4(Bim)_2](ClO_4)_2$ described above, although $LiNTf_2$ or KCF_3SO_3 was used instead of $Ba(ClO_4)_2$.

1,4-Bis[*N*-(*N*′-butylimidazolium)]hexane-based ($[C_6(Bim)_2](ClO_4)_2$ (white solid, melting point: 46.4–48.1 °C; 79.9% yield), $[C_6(Bim)_2](NTf_2)_2$ (light-yellow liquid, 97.9% yield), and $[C_6(Bim)_2](CF_3SO_3)_2$ (white solid, melting point: 55.8–56.4 °C; 22.8% yield)); 1,4-bis[*N*-(*N*′-butylimidazolium)]octane-based ($[C_8(Bim)_2](ClO_4)_2$ (white solid, melting point: 85.7–87.1 °C; 79.1% yield), $[C_8(Bim)_2](NTf_2)_2$ (light-yellow liquid, 92.3% yield), and $[C_8(Bim)_2](CF_3SO_3)_2$ (light-yellow liquid, 46.3% yield)); and 1-butyl-3-butylimidazolium-based ($[C_4Bim]ClO_4$ (light-yellow liquid, 69.0% yield)) ILs were prepared via the same procedure as for $[C_4(Bim)_2]^{2+}$-based ILs described above. All the synthesized ILs were characterized by ^1H NMR (model Ascend 400, 400 MHz, Bruker Biospin, Rheinstetten, Germany), and the corresponding spectra are demonstrated in Figures S3–S12 in the Supplementary Materials.

3.3. Measurements of the Solubility, Viscosity, and Conductivity

The solubilities of ILs were determined via a previously reported method [36] as follows: The excess amount of a specific IL was mixed with water under stirring for 4 h at 25 °C, and the resultant mixture was left to rest for 12 h to achieve complete phase separation. The IL concentration (solubility) in the water phase was measured by an ultraviolet–visible (UV–Vis) spectrophotometer (Purkinje General Instrument Co., Beijing, China) at 220 nm. The selection of 220 nm as the detection wavelength is based on the characteristics of their ultraviolet absorption spectra, as shown in Figures S13–S16 in the Supplementary Materials [37].

The viscosities of IL phases saturated with water and the water phases saturated with ILs were determined at 25 °C using an NDJ-8S rotary viscometer at a rotation speed of 60 rpm per minute (Changji Geological Instrument Co., Ltd., Shanghai, China). The relative standard deviations of the test viscosity values were in the range of 0.08% to 4.5%.

The conductivities of IL phases saturated with water and the water phases saturated with ILs were determined at 25 °C with a conductivity meter (model SLDS, Sangli Electronic Equipment Factory, Nanjing, China).

3.4. Measurements of Hydrogen Bond Donating Ability and Hydrogen Bond Accepting Ability

The hydrogen-bond donating ability (α) and the hydrogen-bond accepting ability (β) of the ILs used in this work were determined by using the three dyes, RD, DENA, and NA as probes via a previously reported method [38]. Detailed information is listed in the Supplementary Materials.

3.5. Calculation of the Electrophilicity of ILs

The electrophilicity of ILs was quantitatively expressed by the electrophilicity index and calculated using the Multiwfn software (version 3.8) [39].

3.6. Extraction Procedure

For a typical extraction procedure, 1.0 mL of a specific IL was mixed with 5.0 mL of $[Au(S_2O_3)_2]^{3-}$ solution (10 mg dm^{-3} of gold, 0.1 mol dm^{-3} of $Na_2S_2O_3$, 1.0 mol dm^{-3} of NH_3, and 5 mmol dm^{-3} of $CuSO_4$) under stirring at 25 °C for 20 min. After centrifuga-

tion, the gold concentration in the water phase was determined by an atomic absorption spectrophotometer (AAS, TAS-990, Beijing Puxi General Instrument Co., Ltd., Beijing, China) [6–11]. The elemental contents of the actual thiosulfate gold leaching solution were measured by inductively coupled plasma optical emission spectrometry (ICP-OES, model Optima 8000, Perkin Elmer, Waltham, MA, USA) [6–11]. Ammonia solutions ranging from 0.2 mol dm^{-3} to 2 mol dm^{-3} were employed to control the aqueous pH in the range of 10 to 11.8, and 0.1 mol dm^{-3} of ammonium buffer solution was utilized to keep the pH within the range of 8 to 10, while 0.1 mol dm^{-3} of acetic acid solution was used to regulate the aqueous pH under acidic or neutral conditions.

The extraction efficiency (E), the distribution ratio (D), and the relationship between E and D can be calculated using the following equations:

$$E\% = (1 - C_w/C_w{}^\circ) \times 100 \quad (4)$$

$$D = C_w{}^\circ/C_w = E \times (V_w/V_{IL})/(1 - E) \quad (5)$$

where $C_w{}^\circ$ and C_w are the concentrations of gold in the water phase before and after extraction, respectively. The symbols V_w and V_{IL} refer to the volumes of water and IL phases, respectively.

3.7. Ion Chromatographic (IC) Analysis

The IC analysis was conducted on an ion chromatograph (2100 model, Thermo Fisher Scientific Inc., Waltham, CA, USA) equipped with a conductivity detector, and the chromatographic conditions were as follows: separation column, IonPac AS 11-HC (250 mm × 4 mm); guard column, IonPac AG11-HC (50 mm × 4 mm); eluent, 20 mmol dm^{-3} NaOH with a flow rate of 1.0 mL min^{-1}; suppression current, 60 mA; column temperature, 35 °C; injection volume, 15 μL.

The Fourier transform infrared (FT-IR) spectra of the IL phase before and after extraction were measured using a Frontier FT-IR spectrophotometer (PerkinElmer Inc., Waltham, MA, USA).

All the experiments were carried out in triplicate, and the results were expressed as mean ± standard deviation (SD).

4. Conclusions

In this work, a series of DILs were prepared and used to extract gold from a thiosulfate leaching solution. The experimental results suggested that the ILs with strong hydrogen-bonding ability exhibited high extraction ability toward $[Au(S_2O_3)_2]^{3-}$. The extraction efficiency of $[Au(S_2O_3)_2]^{3-}$ by DILs was significantly affected by the aqueous pH, as there was a competitive extraction between $Cu(S_2O_3)_3{}^{5-}$ and $[Au(S_2O_3)_2]^{3-}$ at pH levels ≤ 10, consequently reducing the extraction ability of ILs toward $[Au(S_2O_3)_2]^{3-}$. The extraction of $[Au(S_2O_3)_2]^{3-}$ by DILs followed an anion exchange mechanism, was endothermic, and involved increased entropy. Anion exchange at the IL–water interface was identified as the rate-limiting step in the extraction process. The presence of other ions in the thiosulfate leaching solution did not hinder the extraction of $[Au(S_2O_3)_2]^{3-}$, and gold could be recovered from the IL phase through back extraction. The DILs exhibited superior extraction ability compared with traditional liquid–liquid extraction systems, suggesting their potential as environmentally friendly alternatives to volatile and hazardous solvents for gold recovery from thiosulfate leaching solutions.

Supplementary Materials: The following supporting information can be downloaded at: https://www.mdpi.com/article/10.3390/molecules29112659/s1, Figure S1: The van't Hoff plot for the extraction of $[Au(S_2O_3)_2]^{3-}$; Figure S2: The ^1H NMR spectra of the fresh and the recovered $[C_4Bim]ClO_4$ (400 MHz, DMSO-d_6); Figures S3–S12: the ^1H NMR spectra of $[C_4(Bim)_2](ClO_4)_2$, $[C_4(Bim)_2](CF_3SO_3)_2$, $[C_4(Bim)_2](NTf_2)_2$, $[C_6(Bim)_2](ClO_4)_2$, $[C_6(Bim)_2](CF_3SO_3)_2$, $[C_6(Bim)_2](NTf_2)_2$, $[C_8(Bim)_2](CF_3SO_3)_2$, $[C_8(Bim)_2](NTf_2)_2$, $[C_8(Bim)_2](ClO_4)_2$, $[C_4Bim]ClO_4$; Figures S13–S16: Ultraviolet absorption spec-

tra of $[C_4(Bim)_2](ClO_4)_2$, $[C_6(Bim)_2](ClO_4)_2$, $[C_8(Bim)_2](ClO_4)_2$, $[C_4(Bim)_2](NTf_2)_2$, $[C_6(Bim)_2](NTf_2)_2$, $[C_8(Bim)_2](NTf_2)_2$, $[C_8(Bim)_2](CF_3SO_3)_2$, $[C_4(Bim)_2](ClO_4)_2$; measurements of hydrogen-bond donating ability and hydrogen-bond accepting ability of the ILs.

Author Contributions: Conceptualization, Y.F.; methodology, Y.F.; investigation, Y.F., Q.Z., and S.Z.; resources, Y.F.; data curation, Q.Z.; writing—original draft preparation, Y.F.; writing—review and editing, Y.F. All authors have read and agreed to the published version of the manuscript.

Funding: This research was funded by the National Natural Science Foundation of China, grant number 21307028; the Foundation of the "Double First Class" Creation Project of Safety Discipline of Henan Polytechnic University, grant number AQ20230769; and 2021 High-Level Scientific Research Cultivation Project of Jiaozuo Teachers College, grant number 2021-4.

Institutional Review Board Statement: Not applicable.

Informed Consent Statement: Not applicable.

Data Availability Statement: The data presented in this study are available in article and supplementary materials.

Conflicts of Interest: The authors declare no conflicts of interest.

References

1. Vashist, U.; Sadri, F.; Choi, Y.; Ghahreman, A. Systematic study of critical parameters on magnesium saturated thiosulfate gold leaching process; part A: Effect of ammonia and lime for pH adjustments and concentration of magnesium and copper(II). *Hydrometallurgy* **2022**, *213*, 105943. [CrossRef]
2. Lin, Y.; Hu, X.; Zi, F.; Chen, Y.; Chen, S.; Li, Y.; Zhao, L.; Li, Y. Synergistical thiourea and thiosulfate leaching gold from a gold concentrate calcine with copper-ammonia catalysis. *Sep. Purif. Technol.* **2023**, *327*, 124928. [CrossRef]
3. Tang, J.; Yang, Z.; Zi, F.; Zhang, Y.; Hu, X. New insights into the mechanism of pyrite oxidation in copper(II)–ammonia–thiosulfate gold leaching system: An electrochemical, AFM, Raman spectroscopy and XPS investigation. *Appl. Surf. Sci.* **2024**, *655*, 159665. [CrossRef]
4. Dong, Z.; Jiang, T.; Xu, B.; Zhang, B.; Liu, G.; Li, Q.; Yang, Y. A systematic and comparative study of copper, nickel and cobalt-ammonia catalyzed thiosulfate processes for eco-friendly and efficient gold extraction from an oxide gold concentrate. *Sep. Purif. Technol.* **2021**, *272*, 118929. [CrossRef]
5. Nicol, M.J.; O'Malley, G. Recovering gold from thiosulfate leach pulps via ion exchange. *JOM* **2002**, *54*, 44–46. [CrossRef]
6. Azizitorghabeh, A.; Mahandra, H.; Ramsay, J.; Ghahreman, A. Selective gold recovery from pregnant thiocyanate leach solution using ion exchange resins. *Hydrometallurgy* **2023**, *218*, 106055. [CrossRef]
7. Xie, F.; Chen, J.N.; Zhang, X.Z.; Xu, B.; Wang, W. Adsorption mechanism of copper and gold thiosulfates onto activated carbon. *Trans. Nonferrous Met. Soc. China* **2023**, *33*, 3210–3221. [CrossRef]
8. Chen, S.; Zi, F.; Hu, X.; Chen, Y.; Yang, P.; Wang, Q.; Qin, X.; Cheng, H.; Liu, Y.; He, Y.; et al. Interfacial properties of mercaptopropyl-functionalised silica gel and its adsorption performance in the recovery of gold(I) thiosulfate complex. *Chem. Eng. J.* **2020**, *393*, 124547. [CrossRef]
9. Li, X.; Zhao, L.; Chen, S.; Lin, Y.; Hu, X.; Zi, F. Highly efficient and selective extraction of Au(I) from thiosulfategold-leaching solution using diphenylphosphine. *J. Environ. Chem. Eng.* **2024**, *12*, 111750. [CrossRef]
10. Mahandra, H.; Faraji, F.; Ghahreman, A. Novel extraction process for gold recovery from thiosulfate solution using phosphonium ionic liquids. *ACS Sustain. Chem. Eng.* **2021**, *9*, 8179–8185. [CrossRef]
11. Mahandra, H.; Faraji, F.; Azizitorghabeh, A.; Ghahreman, A. Selective extraction and recovery of gold from complex thiosulfate pregnant leach liquor using Cyphos IL 101. *Ind. Eng. Chem. Res.* **2022**, *61*, 5612–5619. [CrossRef]
12. Masilela, M.; Ndlovu, S. Extraction of Ag and Au from chloride electronic waste leach solutions using ionic liquids. *J. Environ. Chem. Eng.* **2019**, *7*, 102810. [CrossRef]
13. Jin, C.; Chen, M.; Fan, M.; Luo, G.; Shao, M.; Huang, Z.; Xie, X. Hydrophobic phosphonium-based ionic liquids as novel extractants for palladium(II) recovery from alkaline cyanide solutions. *J. Mol. Liq.* **2021**, *336*, 116358. [CrossRef]
14. Nguyen, V.T.; Riaño, S.; Binnemans, K. Separation of precious metals by split-anion extraction using water-saturated ionic liquids. *Green Chem.* **2020**, *22*, 8375–8388. [CrossRef]
15. Kashyap, N.; Paul, S.; Bora, D.B.; Kalita, S.; Borah, R. Dual functional behaviour of dicationic ionic liquid as extractant and hydrophobic biphasic solvent for extraction of Pb(II) in water. *J. Mol. Liq.* **2023**, *392*, 123521. [CrossRef]
16. Lu, T.; Li, D.; Feng, J.; Zhang, W.; Kang, Y. Efficient extraction performance and mechanisms of Cd^{2+} and Pb^{2+} in water by novel dicationic ionic liquids. *J. Environ. Manag.* **2024**, *351*, 119767. [CrossRef] [PubMed]
17. Wongsawa, T.; Traiwongsa, N.; Pancharoen, U.; Nootong, K. A review of the recovery of precious metals using ionic liquid extractants in hydrometallurgical processes. *Hydrometallurgy* **2020**, *198*, 105488. [CrossRef]
18. Lee, J.C.; Kurniawan, K.; Kim, S.; Nguyen, V.T.; Pandey, B.D. Ionic liquids-assisted solvent extraction of precious metals from chloride solutions. *Sep. Purif. Rev.* **2023**, *52*, 242–261. [CrossRef]

19. Inman, G.; Nlebedim, I.C.; Prodius, D. Application of ionic liquids for the recycling and recovery of technologically critical and valuable metals. *Energies* **2022**, *15*, 628. [CrossRef]
20. Chaumont, A.; Wipff, G. Strontium nitrate extraction to ionic liquids by a crown ether: A molecular dynamics study of aqueous interfaces with C_4mim^+- vs. C_8mim^+-based ionic liquids. *J. Phys. Chem. B* **2010**, *114*, 13773–13785. [CrossRef]
21. Yoon, T.J.; Patel, L.A.; Vigil, M.J.; Maerzke, K.A.; Findikoglu, A.T.; Currier, R.P. Electrical conductivity, ion pairing, and ion self-diffusion in aqueous NaCl solutions at elevated temperatures and pressures. *J. Chem. Phys.* **2019**, *151*, 224504. [CrossRef] [PubMed]
22. Asrami, M.R.; Tran, N.N.; Nigam, K.D.P.; Hessel, V. Solvent extraction of metals: Role of ionic liquids and microfluidics. *Sep. Purif. Technol.* **2021**, *262*, 118289. [CrossRef]
23. Goodwin, A.R.H.; Marsh, K.N. An absolute viscometer for liquids: Measurement of the viscosity of water at T = 298.15 K and p = 0.1 MPa. *J. Chem. Eng. Data* **2011**, *56*, 167–170. [CrossRef]
24. Lungwitz, R.; Strehmel, V.; Spange, S. The dipolarity/polarisability of 1-alkyl-3-methylimidazolium ionic liquids as function of anion structure and the alkyl chain length. *New J. Chem.* **2010**, *34*, 1135. [CrossRef]
25. Sheridan, Q.R.; Schneider, W.F.; Maginn, E.J. Anion dependent dynamics and water solubility explained by hydrogen bonding interactions in mixtures of water and aprotic heterocyclic anion ionic liquids. *J. Phys. Chem. B* **2016**, *120*, 12679–12686. [CrossRef] [PubMed]
26. Zhang, Q.G.; Wang, N.N.; Wang, S.L.; Yu, Z.W. Hydrogen bonding behaviors of binary systems containing the ionic liquid 1-butyl-3-methylimidazolium trifluoroacetate and water/methanol. *J. Phys. Chem. B* **2011**, *115*, 11127–11136. [CrossRef] [PubMed]
27. Senanayake, G. Analysis of reaction kinetics, speciation and mechanism of gold leaching and thiosulfate oxidation by ammoniacal copper(II) solutions. *Hydrometallurgy* **2004**, *75*, 55–75. [CrossRef]
28. Liu, C.; Wang, C.; Li, Y.; Rao, Z. Preparation and characterization of sodium thiosulfate pentahydrate/silica microencapsulated phase change material for thermal energy storage. *RSC Adv.* **2017**, *7*, 7238–7249. [CrossRef]
29. Fu, W.W.; Zou, T.; Liang, X.H.; Wang, S.F.; Gao, X.; Zhang, Z.G.; Fang, Y.T. Characterization and thermal performance of microencapsulated sodium thiosulfate pentahydrate as phase change material for thermal energy storage. *Sol. Energy Mater. Sol. Cell.* **2019**, *193*, 149–156. [CrossRef]
30. Khanramaki, F.; Shirani, A.S.; Safdari, J.; Torkaman, R. Investigation of liquid extraction and thermodynamic studies on uranium from sulfate solution by Alamine 336 as an extractant. *Int. J. Environ. Sci. Technol.* **2018**, *15*, 1467–1476. [CrossRef]
31. Liao, Y.; Fan, F.; Zhu, A.; Zhao, J.; Peng, Y. Kinetics characteristics and thermodynamics analysis of soybean podssterols extraction process. *Environ. Chall.* **2021**, *5*, 100357. [CrossRef]
32. Fan, Y.; Li, X.; Song, L.; Li, J.; Zhang, L. Effective extraction of quinine and gramine from water by hydrophobic ionic liquids: The role of anion. *Chem. Eng. Res. Des.* **2017**, *119*, 58–65. [CrossRef]
33. Nie, Y.; Yang, L.; Sun, W.; Gao, Z.; Wang, Q. Research on leaching of carbonaceous gold ore with copper-ammonia-thiosulfate solutions. *Hydrometallurgy* **2020**, *197*, 105473. [CrossRef]
34. Zhao, H.F.; Yang, H.Y.; Tong, L.L.; Zhang, Q.; Kong, Y. Biooxidation-thiosulfate leaching of refractory gold concentrate. *Int. J. Miner. Metall. Mater.* **2020**, *27*, 1075–1082. [CrossRef]
35. Gusain, R.; Gupta, P.; Saran, S.; Khatri, O.P. Halogen-free bis(imidazolium)/bis(ammonium)-di[bis(salicylato)borate] ionic liquids as energy-efficient and environmentally friendly lubricant additives. *ACS Appl. Mater. Interfaces* **2014**, *6*, 15318–15328. [CrossRef] [PubMed]
36. Wong, D.S.H.; Chen, J.P.; Chang, J.M.; Chou, C.H. Phase equilibria of water and ionic liquids [emim][PF_6]and [bmim][PF_6]. *Fluid Phase Equilibr.* **2002**, *194–197*, 1089–1095. [CrossRef]
37. Kolobova, E.; Kartsova, L.; Kravchenko, A.; Bessonova, E. Imidazolium ionic liquids as dynamic and covalent modifiers of electrophoretic systems for determination of catecholamines. *Talanta* **2018**, *188*, 183–191. [CrossRef] [PubMed]
38. Hauru, L.K.J.; Hummel, M.; King, A.; Kilpeläinen, I.; Sixta, H. Role of solvent parameters in the regeneration of cellulose from ionic liquid solutions. *Biomacromolecules* **2012**, *13*, 2896. [CrossRef]
39. Lu, T.; Chen, F. Multiwfn: A multifunctional wavefunction analyzer. *J. Comput. Chem.* **2012**, *33*, 580–592. [CrossRef]

Disclaimer/Publisher's Note: The statements, opinions and data contained in all publications are solely those of the individual author(s) and contributor(s) and not of MDPI and/or the editor(s). MDPI and/or the editor(s) disclaim responsibility for any injury to people or property resulting from any ideas, methods, instructions or products referred to in the content.

molecules

MDPI

Article

Non-Substituted Imidazolium-Based Electrolytes as Potential Alternatives to the Conventional Acidic Electrolytes of Polyaniline-Based Electrode Materials for Supercapacitors

Fatima Al-Zohbi [1,*], Fouad Ghamouss [2], Johan Jacquemin [2], Bruno Schmaltz [3], Mohamad Fadel Tabcheh [1], Mohamed Abarbri [3], Khalil Cherry [4] and François Tran-Van [3,*]

[1] Department of Chemistry, Faculty of science III, Lebanese University, Tripoli 1300, Lebanon; mtabcheh@ul.edu.lb
[2] Materials Science and Nano-Engineering, Mohammed VI Polytechnic University, Lot 660 Hay Moulay Rachid, Ben Guerir 43150, Morocco; fouad.ghamouss@um6p.ma (F.G.); johan.jacquemin@um6p.ma (J.J.)
[3] Laboratoire de Physico-Chimie des Matériaux et des Electrolytes pour l'Energie (EA 6299), Université de Tours, Parc de Grandmont, 37200 Tours, France; bruno.schmaltz@univ-tours.fr (B.S.); mohamed.abarbri@univ-tours.fr (M.A.)
[4] Laboratoire Matériaux, Catalyse, Environnement et Méthodes Analytiques (MCEMA), Campus Universitaire de Hadath, Beirut 1500, Lebanon; khalil.cherry@ul.edu.lb
* Correspondence: alzohbi-fatima@hotmail.com (F.A.-Z.); francois.tran@univ-tours.fr (F.T.-V.)

Abstract: Although disubstituted imidazolium cation is sterically crowded, hundreds of ionic liquids based on this cation have been reported as electrolytes for energy storage devices. In contrast to disubstituted imidazolium, non-substituted imidazolium is uncrowded sterically and has not yet been investigated as an electrolyte, to the best of our knowledge. Hence, imidazolium hydrogen sulfate [Imi][HSO_4], in mixture with water, was studied as an electrolyte for PANI-based electrode materials. For comparison, pyrrolidinium with hydrogen sulfate or *p*-toluene sulfonate ([Pyrr][HSO_4] or [Pyrr][PTS]), in mixture with water, were also investigated as alternatives to the conventional electrolyte (i.e., aqueous H_2SO_4) for PANI electrodes. Walden plots of binary mixture ionic liquid–water weight ratios with the optimal ionic conductivity (i.e., [Imi][HSO_4]/water 48/52 wt% (195.1 mS/cm), [Pyrr][HSO_4]/water 41/59 wt% (186.6 mS/cm), and [Pyrr][PTS]/water 48/52 wt% (43.4 mS/cm) along with the electrochemical performances of PANI in these binary mixtures showed that [Pyrr][HSO_4]$_{aq}$ or [Imi][HSO_4]$_{aq}$ are convenient electrolytes for PANI/PIL, as opposed to [Pyrr][PTS]$_{aq}$. Furthermore, replacing the conventional aqueous electrolyte H_2SO_4 with [Imi][HSO_4] $_{aq}$ increased the specific capacitance of PANI/PIL from 249.8 to 268.5 F/g at 15 mV/s. Moreover, PANI/PIL electrodes displayed a quasi-ideal capacitive behavior in [Imi][HSO_4]$_{aq}$ (the correction factor of CPE_4 was 0.99). This primary study has shown that non-substituted imidazolium as an electrolyte could enhance the electrochemical performances of PANI electrodes and could be a good alternative to the conventional electrolyte.

Keywords: polyaniline; protic ionic liquid-based electrolytes; Walden plot; electrochemical behaviors

1. Introduction

Polyaniline (PANI) is one of the conducting polymers that have been considered as promising electrode materials for supercapacitors, owing to its properties such as thermal and electrochemical stability, high electronic conductivity in its doped state, low cost, and simple synthesis. Furthermore, the theoretical mass specific capacitance of PANI is relatively high: about 750 F/g for a potential range of 0.7 V and a maximum doping rate of 0.5 [1–11]. However, it has been found that the specific capacitance and the other electrochemical performances of PANI are widely dependent on the nature and the structure of the electrolytes [12–15].

The scientific community looks forward to replacing conventional electrolytes with ionic liquids in order to improve the electrochemical properties of energy storage devices such as supercapacitors or batteries [16]. Ionic liquids are promising candidates since they can display intrinsic stability and broad electrochemical windows depending on the nature of the selected ions (−2.5 to +2.5 V versus Ag/Ag^+) [10,16]. Furthermore, they are characterized with negligible vapor pressure and good ionic conductivity [10].

Pairing PANI with ionic liquids seems an effective strategy to provide long-cycle-stable supercapacitors with high capacitance [10,17]. It is possible to categorize these combinations between PANI and ionic liquids into three approaches. The first approach (approach I) consists of focusing on the morphology of PANI alert by replacing the conventional acidic polymerization media with ionic liquids, followed by an electrochemical investigation of the obtained nanostructured PANI in the conventional electrolytes [3,18–22]. The second approach (approach II) concentrates on the electrochemical study of the PANI in the ionic liquid-based electrolytes [23–25]. The third approach (approach III) is established on the synchronization of the previously mentioned two approaches: synthesis of PANI in the ionic liquid and thus, electrochemical investigation of the resulted PANI in the same ionic liquid in which it was prepared [21].

Disubstituted imidazolium-based ionic liquids (i.e., aprotic ionic liquids, AILs) are the most investigated ionic liquids that have been used to evaluate the electrochemical performances of PANI [10]. This type of ionic liquid has also been investigated for other materials-based supercapacitors [16,26]. At the other extreme, non-substituted imidazolium-based ionic liquids, i.e., protic ionic liquids (PILs), to the best of our knowledge, have not yet been investigated as electrolytes for PANI, although they can be easily prepared with a neutralization reaction between imidazole and the corresponding acid. It is thus crucial to study the electrochemical performances of PANI following approach III using non-substituted imidazolium-based ionic liquid as electrolyte.

In our previous work, it was reported that PANI prepared in imidazolium hydrogen sulfate [Imi][HSO_4] (i.e., non-substituted imidazolium salt) exhibited nanostructured morphology, enhanced electrical conductivity, and better electrochemical performance in conventional acidic electrolytes (following approach I) compared with the conventional PANI [18]. In the current work, the electrochemical performances of PANI prepared in [Imi][HSO_4] was investigated in aqueous solution of [Imi][HSO_4]. This study involved not only examination via approach III, but also analysis of the electrochemical performances of PANI in non-substituted imidazolium as electrolyte. For comparison, the electrochemical performances of PANI was also studied in pyrrolidinium with hydrogen sulfate or *p*-toluene sulfonate as electrolyte. Pyrrolidinium hydrogen sulfate was used as it has been reported as a convenient electrolyte for PANI [11].

2. Results and Discussion

This paper is divided into two main parts. In the first part, we present the synthesis and characterization of the investigated PILs. The other part shows the electrochemical performances of PANI/PIL electrodes in the selected PIL-based aqueous electrolytes.

Part I: Synthesis and characterization of the protic ionic liquids

The investigated PILs were imidazolium hydrogen sulfate [Imi][HSO_4], pyrrolidinium hydrogen sulfate [Pyrr][HSO_4], and pyrrolidinium *p*-toluene sulfonate [Pyrr][PTS]. They were prepared through simple acid–base reaction and dried under vacuum. The structures of these ionic liquids were studied using ^{1}H NMR spectroscopy in deuterated dimethyl sulfoxide $(CD_3)_2SO$ at room temperature (i.e., 20 °C); the obtained spectra are shown in Figures S1 and S2 in the Supporting Information. The chemical shifts (ppm) of the identified peaks are summarized in Table 1. It is noticeable that the chemical shift of the peak attributed to labile hydrogen of the H-N^+ group (δ(N-H)) of imidazolium-based ionic liquids (5.5 ppm) was much lower than that of pyrrolidinium-based ionic liquids (8.53–8.55 ppm). Our team found that the δ(N-H) values of some PILs were related to the water content [27]. Herein, the difference between the δ(N-H) of the different PILs cannot

be attributed to the water ratio as the residual water, quantified via Karl Fischer titration, was low and similar for all the selected PILs (i.e., 1.5, 1.8, and 2.7 wt% for neat [Imi][HSO_4], [Pyrr][HSO_4], and [Pyrr][PTS], respectively). On the other hand, Snook et al. [28] reported that δ(N-H) reflects the degree of proton activity (i.e., the concentration of protons) of electrolytes: δ(N-H) of about 7.05 ppm is an indication of highly acidic properties while δ(N-H) of 9.15 ppm designates a highly basic product. pH, estimated using an indicator paper, showed that [Imi][HSO_4] was slightly more acidic than [Pyrr][HSO_4] and [Pyrr][PTS] (all the estimated pH was below 1). As a result, the shift of δ(N-H) was not due to the acidity. Therefore, the difference between the δ(N-H) of imidazolium and pyrrolidinium was due to its electronic environment and its capability to interact with the anions.

Table 1. ^{1}H NMR spectrum characteristics of the PILs.

Structure of the selected PILs	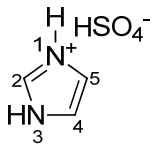 [Imi][HSO_4]	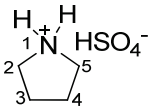 [Pyrr][HSO_4]	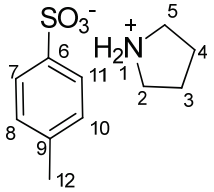 [Pyrr][PTS]
δ(N-H) ppm	5.5 (broad singlet, 1H, H_1)	8.53 (broad singlet, 2H, H_1),	8.55 (broad singlet, 2H, H_1)
δ(C-H) ppm	8.9 (s, 1H, H_2) 7.6 (d, 2H, J = 1.2, H_5, H_4)	3.09–3.07 (m, 4H, H_2, H_5) 1.81–1.77 (m, 4H, H_3, H_4)	7.54–7.44 (m, 2H, H_7 and H_{11}) 7.13 (d, J = 8.0 Hz, 2H, H_8, H_{10}) 2.98–3.18 (m, 4H, H_2, H_5) 2.29 (s, 3H, H_{12}) 1.87–1.76 (m, 4H, H_3, H_4)

As the transport properties (ionic conductivity, viscosity) of the ionic liquids largely affect the electrochemical behaviors of PANI and significantly depend on the ionic liquid–solvent ratio [11,24,29–33], the ionic conductivities of the different investigated PILs were measured as a function of water weight ratio. Note that water was chosen as solvent because it is a green solvent and well adapted for electrochemical storage of PANI. Figure 1 presents the evolution of the ionic conductivity as a function of the PILs' water weight ratio. From Figure 1, as expected based on the literature [27,33], it can be seen that the obtained ionic conductivity values gradually increased with the addition of water until an optimum, then progressively decreased for all the selected PILs. The ionic conductivity was relatively low for the selected PILs mixed with the minimum amount of water required to become liquid (i.e., the ionic conductivity was 8, 6, and 20 mS/cm for [Pyrr][HSO_4] (1.5 wt% of water), [Pyrr][PTS] (10 wt% of water), and [Imi][HSO_4] (20 wt% of water), respectively). The optimal ionic conductivity was obtained at different water weight ratio for each mixture (i.e., 54, 59, and 52% for [Imi][HSO_4], [Pyrr][HSO_4] and [Pyrr][PTS], respectively). This nonmonotonic behavior is rationalized by competition between the dissociation, concentration, and mobility of the charge carriers, and has previously been observed for several imidazolium-based aprotic ionic liquids upon addition of water or ethanol [34]. It was also noticeable that the optimal ionic conductivity of [Imi][HSO_4] (195.1 mS/cm) was higher than that of [Pyrr][HSO_4] (186.6 mS/cm). As for [Pyrr][PTS], its ionic conductivity (43.4 mS/cm) was the lowest. For an explanation of the order of the obtained optimal ionic conductivity of the PILs, the ions–ions interactions of these PILs in water were visualized by predicting the cation–anion Coulombic interactions, calculated using a conductor-like screening model for real solvent (COSMO-RS).

Table 2 presents the predicted surface charge distributions (i.e., an illustration of the surface polarity) and the sigma profiles of all the investigated ions. The polar regions of ions are coded in red and blue colors on the map of surface charge distribution. The red color, for example, reflects the region of positive polarization charge or a negative charge density (the polarization charge density and the charge distribution have opposite

signs). In other words, the red region indicates the ability of the anion to accept protons or preferable interactions with proton donors.

Table 2. 3D molecular surface charge distributions, COSMO volume, surface, and sigma profiles for the ions of the investigated ionic liquids.

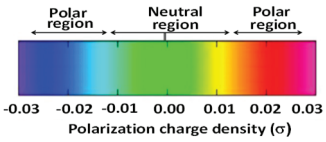	COSMO volume (Å^3)	Surface (Å^2)	Sigma profiles
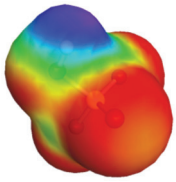 Hydrogen sulfate (HSO_4^-)	81	98	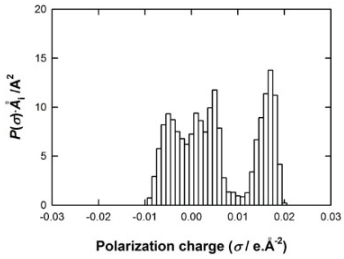
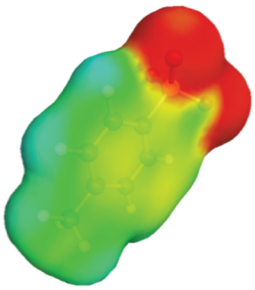 *p*-toluene sulfonate (PTS^-)	187	187	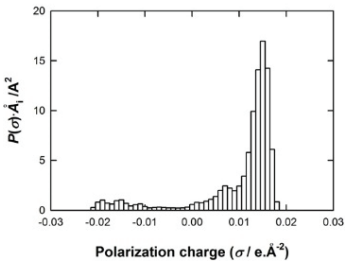
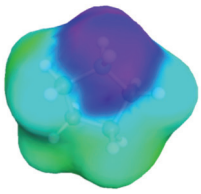 Pyrrolidinium ($Pyrr^+$)	106	117	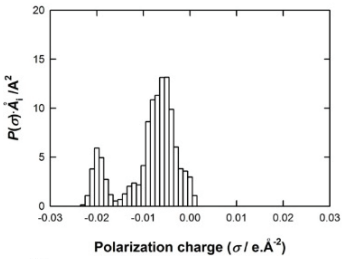
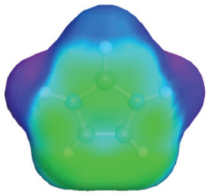 Imidazolium (Imi^+)	88	103	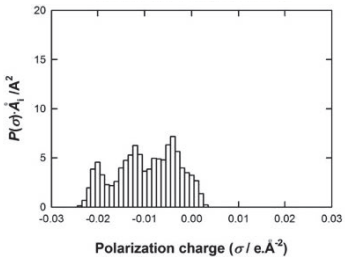

When [Pyrr][HSO_4] was compared with [Pyrr][PTS], it was found that they differed from each other by their anion. For PTS^- (anion of [Pyrr][PTS]), the red color in the 3D molecular surface charge distribution map is located on the sulfonate group SO_3^-. The localization of the charge on SO_3^- is due to the presence of the benzene ring, which is electron-donating via resonance. Regarding the surface of HSO_4^-, the red and dark blue colors over its whole surface indicate that the charge densities were distributed over almost its entire surface. The localization of the charge in the case of PTS^- indicates relatively stronger anion–cation Coulombic interactions for [Pyrr][PTS] compared with [Pyrr][HSO_4],

reflecting that [Pyrr][PTS] tends to form ion pairing more easily in solution. Concerning COSMO volume, this was more than twice the value for PTS^- (187 $Å^3$) compared with HSO_4^- (81 $Å^3$), indicating that the mobility (strongly depended on the molecular weight and ion sizes [35]) of PTS^- would be lower than that of HSO_4^- in solution. Based on the difference of the mobility between these two anions and knowing that the ionic conductivity of ionic liquids is related to the mobility of ions [35], one can predict that the ionic conductivity of [Pyrr][PTS] is lower than that of [Pyrr][HSO_4].

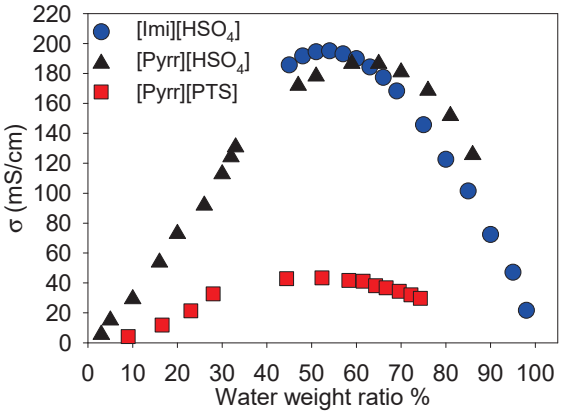

Figure 1. Ionic conductivity (σ) as a function of water mass ratio for [Imi][HSO_4], [Pyrr][HSO_4], and [Pyrr][PTS].

As for [Imi][HSO_4] vs. [Pyrr][HSO_4], the difference between them is their cation. It was observed that the charge was more delocalized at the imidazolium cation (with the dark blue color delocalized between the nitrogen and the acidic proton) compared with the pyrrolidinium cation (with the blue color only on the nitrogen atom). Thus, imidazolium cation could exhibit relatively weaker Coulombic interactions with HSO_4^- relative to pyrrolidinium cation, reflecting better ionic dissociation of [Imi][HSO_4] in solution. Furthermore, the calculated COSMO volume of imidazolium (87 $Å^3$) was much smaller than that calculated for pyrrolidinium (106 $Å^3$), indicating better mobility of imidazolium.

[Imi][HSO_4] was more dissociated in solution than [Pyrr][HSO_4], which was in its turn better dissociated compared with [Pyrr][PTS]. The predicted order of the ionic conductivity was coherent and the obtained optimal ionic conductivity values of the selected PILs were similar (see Figure 1).

[Imi][HSO_4]/water 46/54 wt%, [Pyrr][HSO_4]/water 41/59 wt%, and [Pyrr][PTS]/water 48/52 wt% (i.e., the binary mixtures of PILs/water with the optimum ionic conductivity), were selected to be used as electrolytes for PANI after investigation of their transport properties. Hereinafter, these selected binary mixtures are called [Imi][HSO_4]$_{aq}$, [Pyrr][HSO_4]$_{aq}$, and [Pyrr][PTS]$_{aq}$. The selection of these mixtures is based on our previous work, where we showed that the electrochemical performances of PANI are related to the weight ratio of [Pyrr][HSO_4]/water and the best results were obtained in [Pyrr][HSO_4]/water with the optimal ionic conductivity.

The transport properties (i.e., ionic conductivity, viscosity) as a function of temperature for the selected solutions of the PILs were measured and are presented in Figure S3 of Supporting Information. This data were used to establish the Walden plots, or more accurately, to gain an overview of the ionicity (i.e., the fraction of free ions) [36–38]. Figure 2 presents Walden plots of the selected binary mixtures of PILs/water between 30 and 50 °C. The molar conductivity Λ, presenting the ionic mobility, was calculated through division of ionic conductivity value σ (S/cm) by molar concentration (mol/cm^3). The heavy black line (with a slope of unity) in Figure 2 represents the "ideal" Walden line, which means the absence of any ion–ion interactions. The ideal line is derived from dilute aqueous KCl or LiCl solutions (i.e., fully dissociated ionic solutions). Based on the position of ionic solutions against ideal line, they can be divided into three main classes [39]: subionic or

poor (in the area below the ideal line), ideal (on the ideal line), and superionic solutions (in the area above the ideal line). For the mobility of ions, sometimes the classical Walden rule ($\Lambda\eta$ = constant, i.e., the diffusion of ions is controlled through the macroscopic viscosity of the electrolyte.) is not applicable, and thus, it is replaced by the 'fractional' Walden rule ($\Lambda\eta^{\gamma}$ = constant where $0 < \gamma < 1$; i.e., decoupling of ion motions from viscosity) [37–44].

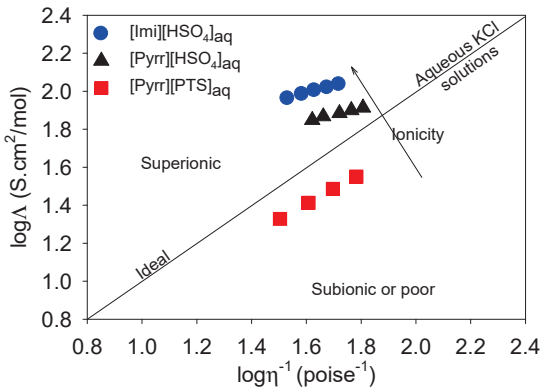

Figure 2. Walden plots for $[Pyrr][PTS]_{aq}$, $[Pyrr][HSO_4]_{aq}$, and $[Imi][HSO_4]_{aq}$ (i.e., [Pyrr][PTS]/water 48/52, $[Pyrr][HSO_4]$/water 41/59 and $[Imi][HSO_4]$/water 48/52).

Like most ionic liquids and other binary mixtures of ionic liquids/water [39–44], the Walden plots of all the investigated electrolytes exhibited a slope (γ) below one, indicating some weak decoupling of ion motions from viscosity in this temperature range. For $[Pyrr][PTS]_{aq}$, the Walden plot points were located below the ideal Walden line (subionic region), confirming the strong ionic pairing of PTS^- with pyrrolidinium. Indeed, Brauer et al. reported that ionic liquid with PTS^- as counter anion exhibited the poorest ionicity relative to [I], $[NO_3]$, [OMs], $[BF_4]$, [OTf] and $[NTf_2]$ accompanied by the strongest cation–anion interactions with triazolium cationic species [45]. When comparing $[Pyrr][HSO_4]_{aq}$ with $[Imi][HSO_4]_{aq}$, it was observed that the points for each were located in the upper part of the Walden diagram, indicating their good ionic behavior. The behavior of $[Imi][HSO_4]_{aq}$ tended more towards the superionic regime in comparison with $[Pyrr][HSO_4]_{aq}$. Imidazolium cation Imi^+ provided ionic liquid with better mobility compared with pyrrolidinium cation $Pyrr^+$, which may be attributed either to the difference between their size (COSMO volume 87 and 106 $Å^3$ for imidazolium and pyrrolidinium, respectively) or, according to the predicted surface polarity, to the better ionic dissociation of $[Imi][HSO_4]$ in solution compared with $[Pyrr][HSO_4]$.

The electrochemical windows of the selected PILs were also studied in order to examine their resistance to the oxidation and reduction. It is well known that the electrochemical window of the electrolytes is a key parameter for electrochemical devices and a large window helps to prevent the side reaction and degradation of doped conjugated polymer [23]. The measurement was recorded via cyclic voltammetry at 20 mV/s in a steel grid (used as courant collector for evaluating the electrochemical behavior of PANI, as described in the next section), while the pseudo-reference electrode was Ag wire. Figure 3 shows the electrochemical stability windows for the investigated electrolytes as well as that of the conventional electrolyte for PANI (H_2SO_4 1 mol/L). In oxidation, the hydrogen sulfate anions (the counter anion of $[Pyrr][HSO_4]_{aq}$, $[Imi][HSO_4]_{aq}$, and H_2SO_4) were oxidized at more positive potential than *p*-toluene sulfonate (the counter anion of $[Pyrr][PTS]_{aq}$). According to Anouti et al. [46], the hydrogen sulfate anion is oxidized giving the persulfate (i.e., $2HSO_4^- \rightarrow H_2S_2O_8 + 2\bar{e}$). A peak was also observed located before that of the oxidation of hydrogen sulfate anions. That peak was attributed to oxidation of water (i.e., $H_2O \rightarrow 1/2O_2 + 2H^+ + 2\bar{e}$). However, in reduction, the pyrrolidinium cation is deprotonated, followed by proton reduction to hydrogen gas (i.e., $Pyrr^+ + \bar{e} \rightarrow Pyrr + H^+$; $H^+ + \bar{e} \rightarrow 1/2H_2$) [46]. It was also noticeable that the electrochemical windows of the PILs were almost equal to that obtained for H_2SO_4. One can conclude that despite the addition of water into the investigated PILs, its

electrochemical window remained suitable for examination of electrochemical behaviors of PANI.

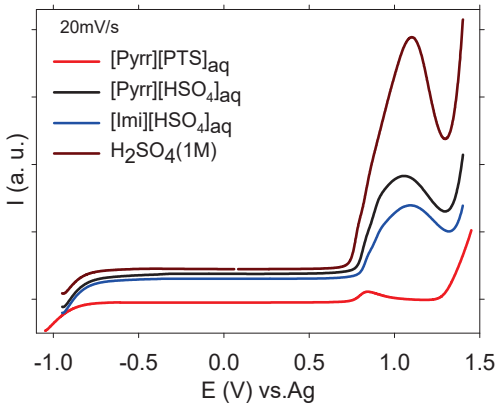

Figure 3. Electrochemical window at 20 mV/s of $[Imi][HSO_4]_{aq}$, $[Pyrr][HSO_4]_{aq}$, $[Pyrr][PTS]_{aq}$, and H_2SO_4 1 mol/L (working electrode and counter electrode: stainless still grid, reference electrode: Ag wire).

Part II: Electrochemical performances of PANI

The electrochemical performances of PANI/PIL were studied in a three-electrode system configuration using the three different kinds of PIL-based aqueous electrolytes: $[Pyrr][PTS]_{aq}$, $[Pyrr][HSO_4]_{aq}$, and $[Imi][HSO_4]_{aq}$, presented in part I. Figure 4a shows the obtained CV curves of PANI/PIL at 5 mV/s in the investigated electrolytes. One can see that the CV curves resulted in $[Imi][HSO_4]_{aq}$ and $[Pyrr][HSO_4]_{aq}$ each presenting a redox couple, whose potential varied with different PILs being used. This redox couple is typically observed for PANI characterized in the conventional aqueous electrolytes [11,19]. It is associated with the reversible transformation between leucoemeraldine base (semiconducting state) and emeraldine salt (conducting state) forms [23,47–50]. The structures of these two oxidation states of PANI are shown in Figure 4b. Briefly, an electron is lost from the dimer aniline rings in the PANI, and thus, counterions diffuse from electrolytes to the PANI surface in order to compensate the created positive charge [23,47]. Regarding the CV curve of PANI/PIL in $[Pyrr][PTS]_{aq}$, it displayed a weak anodic peak but no cathodic peak even at a very low scan rate (see Figure 4a and Figure S4 of the Supporting Information). The absence of a reduction peak could indicate the difficulty of the release of PTS^- out of the polymer, perhaps due to the large size of PTS^- (with a COSMO volume of about 187 $Å^3$) or because $[Pyrr][PTS]_{aq}$, according to Walden plot in Figure 2, is considered as a poor electrolyte (low dissociation). R. Pauliukaite et al. showed that an increase in solution pH caused a larger separation of the redox couple and a decrease in the peak currents, until no peak was observed in the potential region studied at pH 3.2, which was attributed to the loss of PANI conductivity due to deprotonation of the polyaniline at higher solution pH [47].

Figure 5a–c show the CV curves of PANI/PIL measured over 1 V in $[Imi][HSO_4]_{aq}$, $[Pyrr][HSO_4]_{aq}$, or H_2SO_4 1 mol/L at a scan rate of 2, 5, 10, 15, and 20 mV/s. All the CV profiles, obtained at 2, 5, 10, and 15 mV/s, show the redox couple of PANI. However, the reversibility of this couple as well as the peak current depend not only on the electrolyte used but also on the scan rates. It was also noticeable that the cathodic peak disappeared in H_2SO_4 or $[Pyrr][HSO_4]_{aq}$ at 20 mV/s, while this was not the case in $[Imi][HSO_4]_{aq}$. Its disappearance was attributed to the charge transfer and diffusion that mainly occurred not inside the bulk but on the surface of the electrode [47,51].

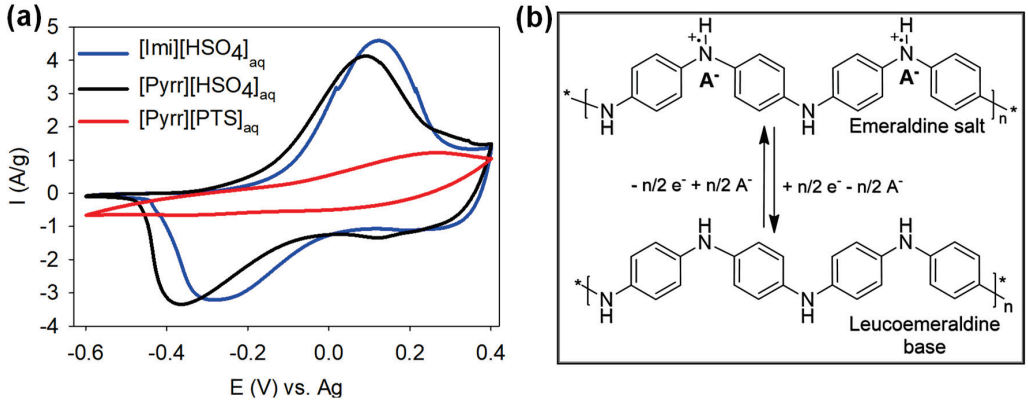

Figure 4. (**a**) CV curves at 5 mV/s for PANI in $[Pyrr][PTS]_{aq}$, $[Pyrr][HSO_4]_{aq}$, and $[Imi][HSO_4]_{aq}$ and (**b**) redox process of PANI where n is the number of aniline units and A^- is the counter anion (A^-: HSO_4^- or PTS^-).

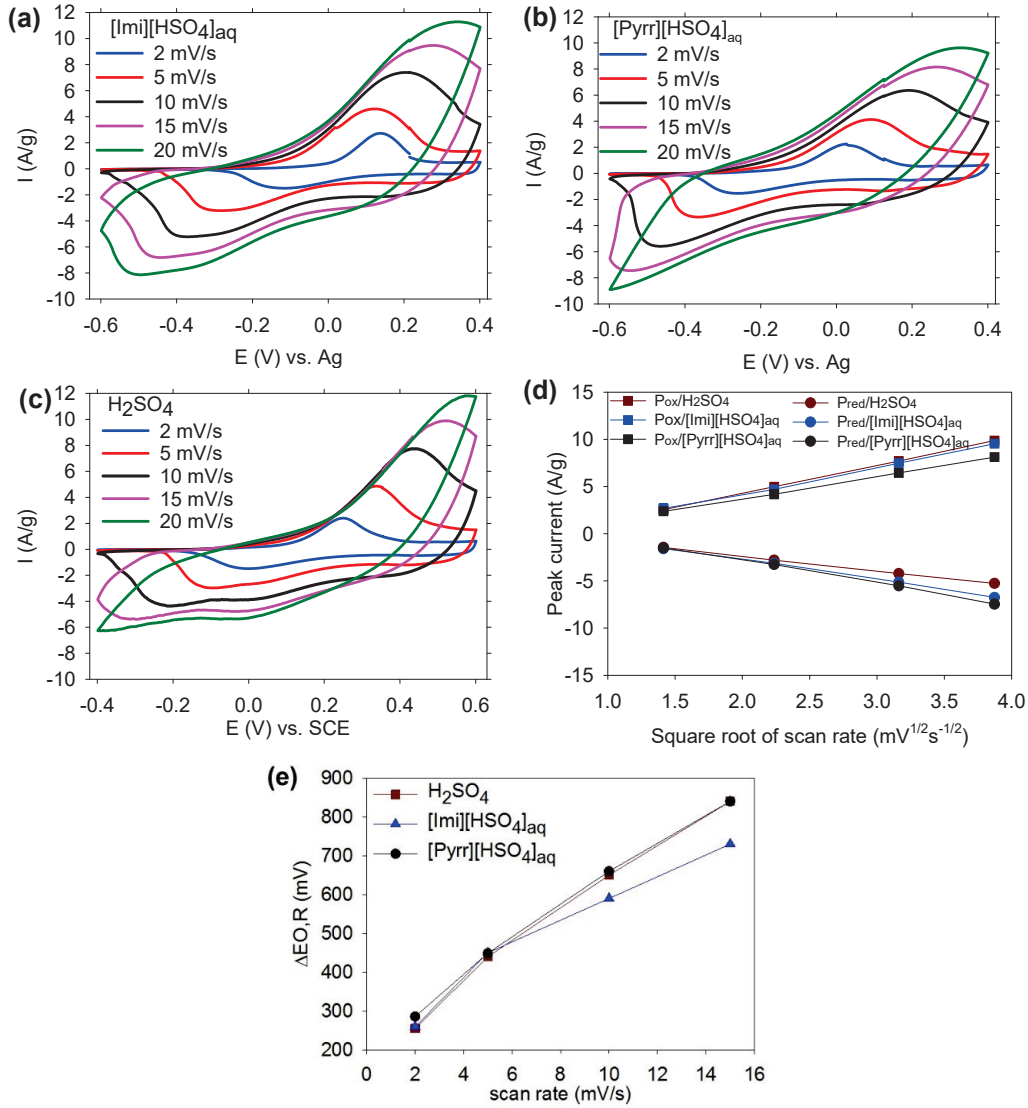

Figure 5. CV curves of PANI/PIL at different scan rates of 2, 5, 10, 15, and 20 mV/s in (**a**) $[Imi][HSO_4]_{aq}$, (**b**) $[Pyrr][HSO_4]_{aq}$, and (**c**) H_2SO_4; (**d**) the dependence of the anodic peak current (Ipox) and cathodic peak current (Ipred) current on the square root of the scan rate for PANI/PIL; and (**e**) plot of $\Delta E_{O,R}$ versus scan rate.

Regarding the peak current of PANI/PIL, this increased along with the increment of scan rate, indicating the good rate capability of the PANI/PIL electrode. Figure 5d shows the currents of the redox peaks as a function of the square root of scan rate in all the electrolytes used, within the range 2–15 mV/s. The peak current value, according to the Randles–Sevcik equation, is related to the square root of the scan rate and the diffusion coefficient of the electroactive material [24,52]. The Randles–Sevcik equation is presented as follows:

$$i_p = 2.69 \times 10^5 n^{\frac{3}{2}} A D_0^{\frac{1}{2}} v^{\frac{1}{2}} c \quad (1)$$

where A is the electrode area (cm^2), D is the diffusion coefficient (cm^2/s) of counter ions, V is the scan rate (V/s), C_b is the concentration of electroactive center (mol/cm^3), and I_p is the peak current (A). Since the peak current is linearly dependent on the root of the scan rate in these electrolytes, one can conclude, based on Equation (1), that the redox reaction of PANI/PIL is controlled by a diffusion process. It was also noticeable that the slope of each obtained line was different. These differences are likely to have been due to the transport properties of the electrolytes, as all the investigated electrolytes shared the same type of counter ion (HSO_4^-) and thus, the same affinity to PANI.

When the scan rate increased from 2 to 20 mV/s, the reduction and oxidation peaks shifted in negative and positive directions, respectively. This shift was due to the resistance of the electrode and some kinetic irreversibility [53,54]. The $\Delta E_{O,R}$ (i.e., the average of the potential of the anodic and the cathodic peaks) of the redox couple was calculated and is illustrated in Figure 5e as a function of the scan rate. At very low scan rates (i.e., 2 or 5 mV/s), $\Delta E_{O,R}$ was almost similar in all the electrolytes investigated. However, at scan rates of 10 or 15 mV/s, the effect of electrolytes on the $\Delta E_{O,R}$ of PANI/PIL was pronounced. The lowest $\Delta E_{O,R}$ was displayed in $[Imi][HSO_4]_{aq}$, indicating more reversibility of the PANI redox couple in $[Imi][HSO_4]_{aq}$, and therefore, faster kinetics of ion diffusion during the redox reaction. It has been shown that more reversibility of the redox couple of PANI may be associated with a higher Walden product ($\Lambda\eta$) of the electrolyte [11]. The Walden product of $[Imi][HSO_4]_{aq}$ (2.7 $S \cdot cm^2 \cdot mol^{-1} \cdot$poise at 30 °C) was higher than that of $[Pyrr][HSO_4]_{aq}$ (1.6 $S \cdot cm^2 \cdot mol^{-1} \cdot$poise at 30 °C), which can explain the greater reversibility of the redox couple of PANI in $[Imi][HSO_4]_{aq}$.

The values of the specific capacitance were calculated from the discharge curves based on the mass of active materials using the following equation (Equation (2)):

$$C = \frac{\int I dt}{m \times \Delta V} \quad (2)$$

where C is the specific capacitance of the active materials of both electrodes (F/g), I is the constant discharge current (mA), dt is the discharge time (s), ΔV is the voltage difference in discharge (V), and m is the total mass of the active material of both electrodes (mg). Obtained capacitance values vs. scan rate are summarized in Table 3. The specific capacitance decreased along with the increment of the scan rate, whichever electrolyte was used. Nevertheless, the decrement rate of the specific capacitance of PANI was related to the nature of the electrolyte. In H_2SO_4, a significant decrease of specific capacitance with the increment of scan rate was observed: the capacitance retention was only 89.1% when the scan rate increased from 5 to 15 mV/s. However, in $[Imi][HSO_4]_{aq}$, the specific capacitance slightly decreased when the scan rate increased from 5 to 15 mV/s, indicating a good retention of capacitance (96.1%). It was noted that the specific capacitance of PANI/PIL in the PIL-based electrolytes was higher than in H_2SO_4 at a scan rate of 15 mV/s.

Electrochemical behaviors of PANI/PIL were also characterized via electrochemical impedance spectroscopy (EIS) in order to evaluate the properties of charge transport in the PANI/PIL electrodes–electrolyte interface. Figure 6 shows the obtained Nyquist plots at open circuit potential for PANI/PIL electrodes in the different aqueous solutions of the PILs as well as in H_2SO_4. All obtained plots displayed a semi-circle followed by a section at 45°, rather than a straight line that is typically observed for PANI electrodes [55–58]. The

semi-circle, located in the high frequency range, was attributed to the charge transfer. In the middle frequency region, the section at 45° was correlated to the Warburg resistance resulting from ion diffusion/transport in the electrolyte to the electrode surface. In the low frequency region, a straight line associated with ion diffusion in the electrode pores was observed. A brief comparison of all the obtained Nyquist plots is given as follows:

- At high frequency region (500 kHz), the intercept of impedance plot with the real axis gives the equivalent series resistance (R_1), which represents the sum of the electrolyte solution resistance, the intrinsic resistance of active material, and the contact resistance at the electrode–electrolyte interface [55]. The R_1 of PANI/PIL was close to 4.61, 6.86, 10.8, and 29.20 Ω in H_2SO_4, $[Imi][HSO_4]_{aq}$, $[Pyrr][HSO_4]_{aq}$, and $[Pyrr][PTS]_{aq}$, which have ionic conductivity values of 237 (this value has been adapted from reference [59]), 195, 186, and 43 mS/cm, respectively. The value of R_1 decreased along with the increasing ionic conductivity of the electrolyte. The dependence of R_1 on the transport properties of the electrolyte is coherent with what has been reported in the literature [24,60].
- The semi-circle is due to a parallel RC element: an interfacial charge–transfer resistance R_2 and double-layer capacitance [61]. R_2 can be estimated from the diameter of the semi-circle. Since the semi-circle obtained for $[Pyrr][PTS]_{aq}$ was much wider that those resulting from in the other investigated electrolytes, the R_2 of PANI/PIL in $[Pyrr][PTS]_{aq}$ was thus significantly higher relative to the others, indicating bad interface properties between the electrode and $[Pyrr][PTS]_{aq}$. This observation is in accord with the CV curves of Figure 4a, where it is shown that $[Pyrr][PTS]_{aq}$ was a poor electrolyte for PANI. As for the two other PIL-based electrolytes ($[Pyrr][HSO_4]_{aq}$ or $[Imi][HSO_4]_{aq}$), the diameter of semi-circle was relatively smaller (associated with lower R_2) than that obtained with H_2SO_4 (see the inset of Figure 6), revealing a good contact between electrode and electrolyte.
- Warburg behavior (i.e., the frequency dependence of the ion diffusion/transport in the electrolyte [62]) was less pronounced in $[Imi][HSO_4]_{aq}$ than the other investigated electrolytes, indicating the capacitive behavior of PANI/PIL in $[Imi][HSO_4]_{aq}$.
- In the low frequency region, PANI/PIL displayed a more vertical line with $[Pyrr][HSO_4]_{aq}$ than H_2SO_4, while the line obtained with $[Imi][HSO_4]_{aq}$ was almost parallel to the imaginary axis. It is known that a line parallel to the imaginary axis reveals a short ion diffusion path and a more ideal capacitor, which means efficient electrolyte accessibility to the electrode surface [63,64].

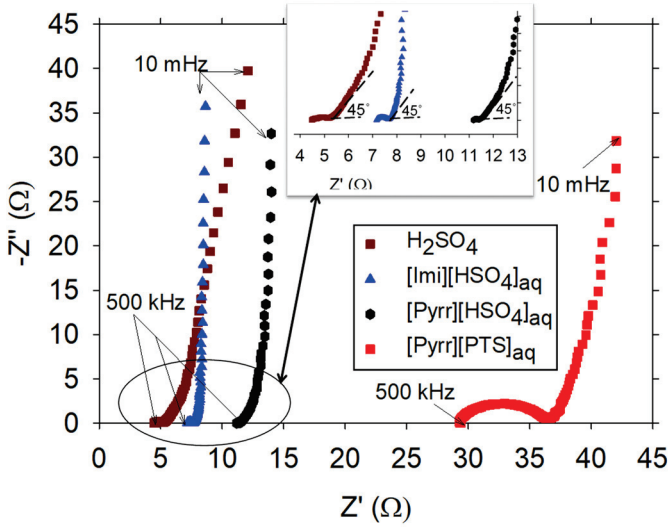

Figure 6. Nyquist plot at open circuit potential with AC amplitude of 10 mV over the frequency range from 500 KHz to 10 mHz.

Table 3. Specific capacitance of PANI/PIL at different scan rates.

Electrolyte	Capacitance (F/g) at Varying Scan Rate (mV/s)			Capacitance Retention (%)
	5	10	15	100 × (C_{15}/C_5)
H_2SO_4	280	272	250	89.1
$[Imi][HSO_4]_{aq}$	279	276	268	96.1
$[Pyrr][HSO_4]_{aq}$	290	285	265	91.4

The EIS data obtained for H_2SO_4 and $[Imi][HSO_4]_{aq}$ were simulated in order to obtain quantitative information. Figure 7 shows the experimental data as well as the fitted model, which was obtained using the equivalent circuit shown in the inset in Figure 7. This model, proposed by Ferloni et al. [58], includes the following elements: the equivalent series resistance (R_1), the electrical double-layer capacitance at the electrolyte–PANI interface (CPE_2), the charge transfer resistance (R_2), the Warburg impedance (W_3), the ionic diffusion resistance of the polymer (R_3), and the pseudocapacitance (CPE_4). Note that CPE is the constant phase element, which is used instead of a pure capacitance due to the non-ideal behavior and related to an empirical constant (α) ranging from 0 to 1 in the following equations (Equations (3) and (4)) [58,65,66]:

$$Z_{CPE} = A_{CPE}(j\omega)^{-n} \tag{3}$$

$$Z_{CPE} = T_{CPE}\ (j\omega)^{-\alpha}_{CPE} \tag{4}$$

where T and α are frequency-independent constants and ω is angular frequency.

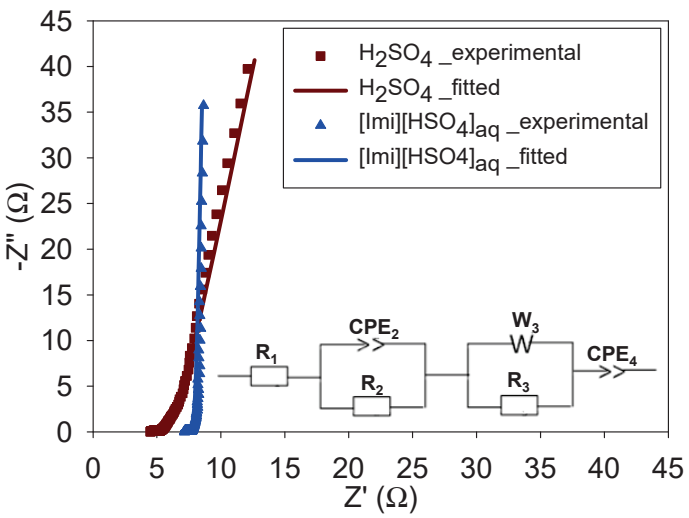

Figure 7. Nyquist plot of PANI/PIL electrodes in H_2SO_4 or $[Imi][HSO_4]_{aq}$; symbols and lines denote experimental and fitted data, respectively. The inset is the equivalent circuit model.

Table 4 lists the obtained EIS fitting values. When H_2SO_4 was replaced with $[Imi][HSO_4]_{aq}$, the R_2 of the PANI/PIL electrode decreased from 0.58 to 0.42 Ω. Similarly, R_3 fell from 1.71 to 0.78 Ω. Note also that the Warburg coefficient for $[Imi][HSO_4]_{aq}$ (0.89 $\Omega \cdot s^{-1/2}$) was smaller than that of H_2SO_4 (1.92 $\Omega \cdot s^{-1/2}$). Regarding the constant phase element, the CPE_4 of PANI/PIL in $[Imi][HSO_4]_{aq}$ showed an improvement compared with that obtained in H_2SO_4, and as a result, its estimated correction factor α_4 (0.99) was close to that of an ideal capacitor ($\alpha = 1$).

Table 4. The resulting fitting values of the Nyquist plot of PANI/PIL electrode in H_2SO_4 or $[Imi][HSO_4]_{aq}$.

Electrolytes	R_1 (Ω)	R_2 (Ω)	CPE_2 ($F \cdot s^{a-1}$)	α_2 (Ω)	R_3 (Ω)	σ_3 ($\Omega \cdot s^{-1/2}$)	CPE_4 ($F \cdot s^{a-1}$)	α_4
$[Imi][HSO_4]_{aq}$	6.86	0.42	1.01×10^{-3}	0.79	0.78	0.89	0.44	0.99
H_2SO_4	4.61	0.58	2.88×10^{-3}	0.67	1.71	1.92	0.3	0.91

3. Materials and Methods

3.1. Materials

Aniline from Acros was distilled under reduced pressure before use. Sulfuric acid (95–98%, Alfa Aesar, Ward Hill, MA, USA), *p*-toluene sulfonic acid (98.5%, Sigma Aldrich, St. Quentin Fallavier, France), ammonium peroxodisulfate (98%, Sigma Aldrich, St. Quentin Fallavier, France), pyrrolidine (≥99%, Fluka, Buchs, Switzerland), imidazole (≥99.5%, Sigma Aldrich, St. Quentin Fallavier, France), activated carbon (Super DLC-50, Norit, Amersfoort, Utrecht, The Netherlands), carbon black (super C65, Timcal, Congleton, UK), and polytetrafluoroethylene (60%wt dispersion in H_2O, Aldrich, St. Quentin Fallavier, France) were used as received.

3.2. Synthesis of the Investigated Ionic Liquids

All the investigated ionic liquids (i.e., pyrrolidinium hydrogen sulfate $[Pyrr][HSO_4]$, pyrrolidinum *p*-toluene sulfonate [Pyrr][PTS], and imidazolium hydrogen sulfate $[Imi][HSO_4]$) were synthesized through equimolar acid–base reactions according to the procedure described in previous articles [11,67]. The synthesis was carried out using a three-necked round-bottomed flask immersed in an ice bath and equipped with a reflux condenser, a dropping funnel, and a thermometer. Pyrrolidine or imidazole was introduced into the three-necked round-bottomed flask while the corresponding acid (sulfuric acid or *p*-toluene sulfonic acid) was added dropwise, through the dropping funnel, to the base under vigorous stirring. The reaction temperature was kept below 20 °C using an ice bath. After finishing the addition of the acid, the reaction mixture was stirred for 30 min at 20 °C and then, the ice bath was removed. The mixture was then stirred overnight at room temperature. The resulting product was then dried for 24 h under primary vacuum. The collected $[Imi][HSO_4]$, $[Pyrr][HSO_4]$, or [Pyrr][PTS] was a dark brown solid, a yellow oily liquid, or a white solid, respectively, at room temperature. The molecular formulas and molecular mass of $[Imi][HSO_4]$, $[Pyrr][HSO_4]$, and [Pyrr][PTS] are $C_3H_5N_2.HSO_4$ (166.2 g/mol), $C_4H_8NH_2.HSO_4$ (169.1 g/mol), and $C_4H_8NH_2.C_7H_7SO_3$ (243.1 g/mol), respectively. Melting points, estimated via Kofler hot bench, are 61 and 67 °C for $[Imi][HSO_4]$, and [Pyrr][PTS], respectively. $[Pyrr][HSO_4]$ is viscous at room temperature.

3.3. Synthesis of the PANI

PANI/PIL was prepared as described in our previous work [18]: 58.9 g of $[Imi][HSO_4]$ was added to anilinium hydrogen sulfate solution (3 g in 18 mL of water) under stirring at 5 °C. Then, the solution of ammonium peroxodisulfate $(NH_4)_2S_2O_8$ (4.56 g in 10 mL of water), cooled to 5 °C, was slowly added to anilinium solution. The oxidant $(NH_4)_2S_2O_8$ to aniline mole ratio was 1.25/1 and the $[Imi][HSO_4]$ to water weight ratio in the final mixture was 70/30. The final obtained mixture was stirred for 24 h at 5 °C with the use of a thermostat. Then, a solid product was isolated via filtration, intensely washed with water to pH neutral, then dried under vacuum at 60 °C for 12 h. Green powder was obtained.

The formation of PANI/PIL was confirmed using attenuated total reflection infrared (ATR-IR) spectroscopy. The collected spectrum, described in our previous work [18], showed peaks at 1544 cm^{-1} (stretching of quinone ring N=Q=N), 1390 cm^{-1} (stretching of benzene rings N-B-N), 1286 cm^{-1} (C-N stretching), 916 cm^{-1} (C–H in-plane deformation), and 728 cm^{-1} (C-H out-of-plane bending vibration). Regarding the morphology of the obtained PANI/PIL, the scanning electron microscopy SEM images presented in our previous work [18] show that PANI/PIL exhibits a fibrillar homogeneous morphology.

3.4. Measurements

The ^{1}H spectrum was recorded using a Varian Unity Inova 300 MHz at room temperature. The data are given as chemical shifts in δ (ppm). $(CH_3)_4Si$ (TMS, 0 ppm) was used as an internal standard.

Residual water content was determined using coulometric Karl Fischer titration (Metrohm, 831 KF coulometer).

Viscosity (η) measurements were conducted using an Anton Paar Lovis 2000 M/ME rolling-ball viscometer. The temperature in the cell was regulated to within ±0.02 °C. The viscosity standard (ASTM Oil Standard S600 of CANNON, 1053 mPa s at 25 °C) and ultra-pure water were used to calibrate the viscometer. In this study, the uncertainty of reported viscosity measurements did not exceed ±1%.

Conductivity measurements were performed using a biologic instrument as a function of temperature from 5 to 70 °C. Temperature control was ensured to within ±0.01 °C by means of a JULABO thermostated bath. The conductometer was first calibrated with standard solutions of known conductivity (i.e., (0.1 and 0.02) mol/dm^3 KCl aqueous solutions). Each conductivity was recorded when its stability was better than 1% within 2 min, and the uncertainty of reported conductivities did not exceed ±2%.

3.5. Electrode Preparation and Electrochemical Measurements

All electrochemistry measurements were carried out on a versatile multichannel potentiostat (Biologic S.A) piloted with the EC Lab V10.32 interface at room temperature (i.e., 20 °C), using a classical three-electrode configuration cell, as illustrated in Figure S5. For the working electrode (WE), a paste was first prepared by mixing 60 wt% of active material (PANI), 32 wt% of carbon black, and 8 wt% of polytetrafluoroethylene (PTFE) in a minimal amount of ethanol using a pestle and mortar to make a homogeneous paste. The obtained paste was then laminated on a glass surface prior to being dried to remove the volatile solvent used. Each WE was then fabricated via pressing the dried paste on stainless steel mesh under 10 tons pressure. The typical mass of paste loading on each WE was close to 1.5 mg/cm^2. Similarly, the counter electrode (CE) was prepared through pressing 7 mg of a paste containing 70 wt% of activated carbon, 20 wt% of carbon black, and 10 wt% of PTFE on a stainless steel grid under 10 tons pressure. The electrolytes used were aqueous H_2SO_4 (1 mol/L) (i.e., the conventional acidic electrolyte for PANI) or aqueous solutions of the investigated protic ionic liquids (i.e., [Imi][HSO_4]/water 46/54 wt%, [Pyrr][HSO_4]/water 41/59 wt%, or [Pyrr][PTS]/water 48/52 wt%).

The cyclic voltammetry was carried out using the previously described three-electrode cell with saturated calomel electrode SCE, with KCl as reference electrode when aqueous H_2SO_4 (1 mol/L) was the electrolyte, while an Ag wire was used as a pseudo reference electrode for an aqueous solution of protic ionic liquid-based electrolyte. No potential correction was needed, as the main goal of this preliminary work was to study the reversibility of the PANI.

For the electrochemical impedance spectroscopy (EIS) measurements, the previously mentioned electrochemical set-up was prepared and the reference electrode was saturated calomel electrode for all the investigated aqueous electrolytes (i.e., H_2SO_4 (1 mol/L), [Imi][HSO_4]/water 46/54 wt%, [Pyrr][HSO_4]/water 41/59 wt%, or [Pyrr][PTS]/water 48/52 wt%).

3.6. Computational Methods

First, the structure of each of the studied ions was optimized in the gas phase with a convergence criterion of 10^{-8} Hartree, through DFT calculations combining the resolution of identity (RI) approximation [68,69] within the Turbomole 7.0 program package [70], using the B3LYP function with the def-TZVP basis set [71–73]. The resulting optimized structures were then used as inputs in the COSMOconfX program (version 4.0, using the DFT/BP-86/def-TZVP COSMO and GAS calculation options available) to generate the conformers of each species, which were then able to be used in the COSMOthermX software (version

C30 17.05, mixture option) to determine the lowest energy contact between two identical clusters. The COSMO volume and the sigma profile of each ion were then generated using the COSMO-RS (conductor-like screening model for real solvent) methodology within the COSMOthermX program (version 2.1, release 01.08).

4. Conclusions

Protic ionic liquids (PILs), namely [Imi][HSO_4], [Pyrr][HSO_4], and [Pyrr][PTS], were investigated as alternatives to the conventional acidic aqueous electrolytes (e.g., H_2O/H_2SO_4) for PANI-based electrodes for supercapacitors. For that purpose, the ionic conductivity of each PIL was optimized by mixing it with water, and thus, the resulted binary mixtures with optimal ionic conductivity were tested as electrolytes using a three-electrode system configuration. The investigated electrolytes were [Imi][HSO_4]/water 48/52 wt%, [Pyrr][HSO_4]/water 41/59 wt%, and [Pyrr][PTS]/water 48/52 wt%, denoted as [Imi][HSO_4]$_{aq}$, [Pyrr][HSO_4]$_{aq}$, and [Pyrr][PTS]$_{aq}$, respectively. This work draws the following conclusions:

- Reversibility of the redox couple of PANI is greatly dependent on the structure of the ionic liquids used as electrolyte. For [Pyrr][PTS]$_{aq}$, no cathodic peak was observed on the CV curve of PANI even at very low scan rates, revealing that the anion of [Pyrr][PTS] was hardly released from the polymer during the reduction process. In [Pyrr][HSO_4]$_{aq}$ and [Imi][HSO_4]$_{aq}$, both the anodic and cathodic peaks of PANI were well defined. However, the redox couple of PANI was more reversible in [Imi][HSO_4]$_{aq}$ relative to [Pyrr][HSO_4]$_{aq}$ (i.e., $\Delta E_{O,R}$ of PANI was about 730 mV at 15 mV/s in [Imi][HSO_4]$_{aq}$, lower than that in [Pyrr][HSO_4]$_{aq}$ (with $\Delta E_{O,R}$ of about 840 mV at 15 mV/s).
- Approach III (presented in the introduction) led to more electrochemically performant PANI electrode materials than approach I. For example, the capacitance retention of the investigated PANI was about 89.1 and 96.1% in H_2SO_4 and [Imi][HSO_4]$_{aq}$, respectively, when the scan rate increased from 5 to 15 mV/s. However, this preliminary conclusion needs to be proven since at this stage it is not possible to deduce whether the enhanced electrochemical performances of PANI in [Imi][HSO_4]$_{aq}$ were due to its better physicochemical properties compared with the other investigated ionic liquids or to the approach followed.
- Non-substituted imidazolium-based ionic liquids or non-substituted pyrrolidinium-based ionic liquids could be good alternatives to the mono- or disubstituted imidazolium salts widely investigated in the literature as electrolytes for storage devices.

Supplementary Materials: The following supporting information can be downloaded at: https://www.mdpi.com/article/10.3390/molecules29112569/s1.

Author Contributions: Conceptualization, F.T.-V. and F.A.-Z.; methodology F.G., B.S. and M.F.T.; software, K.C. and M.A.; validation, F.T.-V. and F.A.-Z.; formal analysis, F.T.-V. and F.A.-Z.; investigation, F.T.-V. and F.A.-Z.; resources, J.J.; data curation, F.T.-V., F.A.-Z., F.G. and M.F.T.; writing—original draft preparation, F.A.-Z.; writing—review and editing, F.T.-V.; visualization, M.A., K.C., M.F.T. and B.S.; supervision, F.T.-V. and M.F.T.; project administration, F.T.-V. and F.A.-Z.; funding acquisition, F.T.-V. and J.J. All authors have read and agreed to the published version of the manuscript.

Funding: This work was supported by French research company RESCOLL and the Lebanese University.

Data Availability Statement: Data are contained within the article and Supplementary Materials.

Acknowledgments: We would like to acknowledge Noha Ghanem and Fadi Masri (professors at the Lebanese University) for their helpful discussion.

Conflicts of Interest: The authors declare no conflicts of interest.

References

1. Bhadra, S.; Khastgir, D.; Singha, N.K.; Lee, J.H. Progress in preparation, processing and applications of polyaniline. *Prog. Polym. Sci.* **2009**, *34*, 783–810. [CrossRef]
2. Veerasubramani, G.K.; Krishnamoorthy, K.; Radhakrishnan, S.; Kim, N.-J.; Kim, S.J. In-situ chemical oxidative polymerization of aniline monomer in the presence of cobalt molybdate for supercapacitor applications. *J. Ind. Eng. Chem.* **2016**, *36*, 163–168. [CrossRef]
3. Li, X.; Liu, Y.; Guo, W.; Chen, J.; He, W.; Peng, F. Synthesis of spherical PANI particles via chemical polymerization in ionic liquid for high-performance supercapacitors. *Electrochim. Acta* **2014**, *135*, 550–557. [CrossRef]
4. Chellachamy Anbalagan, A.; Sawant, S.N. Brine solution-driven synthesis of porous polyaniline for supercapacitor electrode application. *Polymer* **2016**, *87*, 129–137. [CrossRef]
5. Bhandari, S.; Khastgir, D. Template-free solid state synthesis of ultra-long hairy polyaniline nanowire supercapacitor. *Mater. Lett.* **2014**, *135*, 202–205. [CrossRef]
6. Gholivand, M.B.; Heydari, H.; Abdolmaleki, A.; Hosseini, H. Nanostructured CuO/PANI composite as supercapacitor electrode material. *Mater. Sci. Semicond. Process.* **2015**, *30*, 157–161. [CrossRef]
7. Wang, X.; Liu, D.; Deng, J.; Duan, X.; Guo, J.; Liu, P. Improving cyclic stability of polyaniline by thermal crosslinking as electrode material for supercapacitors. *RSC Adv.* **2015**, *5*, 78545–78552. [CrossRef]
8. Khdary, N.H.; Abdesalam, M.E.; El Enany, G. Mesoporous Polyaniline Films for High Performance Supercapacitors. *J. Electrochem. Soc.* **2014**, *161*, G63–G68. [CrossRef]
9. Snook, G.A.; Kao, P.; Best, A.S. Conducting-polymer-based supercapacitor devices and electrodes. *J. Power Sources* **2011**, *196*, 1–12. [CrossRef]
10. Al-Zohbi, F. Research Progress on Polyanilie-ionic liquids for Long Cycle-Stable Supercapacitors with High Capacitance. *Appl. Funct. Mater.* **2022**, *2*, 51–66.
11. Al-Zohbi, F.; Jacquemin, J.; Ghamouss, F.; Schmaltz, B.; Abarbri, M.; Cherry, K.; Tabcheh, M.F.; Tran-Van, F. Impact of the aqueous pyrrolidinium hydrogen sulfate electrolyte formulation on transport properties and electrochemical performances for polyaniline-based supercapacitor. *J. Power Sources* **2019**, *431*, 162–169. [CrossRef]
12. Chaudhari, S.; Sharma, Y.; Archana, P.S.; Jose, R.; Ramakrishna, S.; Mhaisalkar, S.; Srinivasan, M. Electrospun polyaniline nanofibers web electrodes for supercapacitors. *J. Appl. Polym. Sci.* **2013**, *129*, 1660–1668. [CrossRef]
13. Myasoedova, T.N.; Shishlyanikova, E.N.; Moiseeva, T.A.; Brzhezinskaya, M. Preparation and electrochemical characterization of PANI/PVA and PANI/Zr/PVA composites for supercapacitor application. *Adv. Mater. Lett.* **2016**, *7*, 441–444. [CrossRef]
14. Zhu, H.; Peng, S.; Jiang, W. Electrochemical properties of PANI as single electrode of electrochemical capacitors in acid electrolytes. *Sci. World J.* **2013**, *2013*, 940153–940162. [CrossRef]
15. Ko, J.M.; Nam, J.H.; Won, J.H.; Kim, K.M. Supercapacitive properties of electrodeposited polyaniline electrode in acrylic gel polymer electrolytes. *Synth. Met.* **2014**, *189*, 152–156. [CrossRef]
16. Ray, A.; Saruhan, B. Application of Ionic Liquids for Batteries and Supercapacitors. *Materials* **2021**, *14*, 2942. [CrossRef]
17. Al-Zohbi, F. A Review of Tailoring Polyaniline Ionic Liquids for Long Cycle-stable supercapacitors with High Capacitance. *J. Chem. Rev.* **2023**, *5*, 143–158.
18. Al-Zohbi, F.; Ghamouss, F.; Schmaltz, B.; Abarbri, M.; Cherry, K.; Tabcheh, M.F.; Tran-Van, F. Nanostructuration of Polyaniline using Non-substituted Imidazolium-based ionic liquid as a polymerization medium enabling faster supercapacitors operation. *Appl. Funct. Mater.* **2022**, *3*, 1–11.
19. Al-Zohbi, F.; Ghamouss, F.; Schmaltz, B.; Abarbri, M.; Zaghrioui, M.; Tran-Van, F. Enhanced Storage Performance of PANI and PANI/Graphene Composites Synthesized in Protic Ionic Liquids. *Materials* **2021**, *14*, 4275. [CrossRef] [PubMed]
20. Hekmat, F.; Shahrokhian, S.; Mirzaei, Y. Effect of Long-Chain Ionic Liquids on the Capacitive Performance of Carbon NAnotube-Sulfonated Polyaniline Hydrogels for Energy Storage Applications. *J. Phys. Chem. C* **2020**, *124*, 9810–9821. [CrossRef]
21. Li, S.; Yang, C.; Sarwar, S.; Nautiyal, A.; Zhang, P.; Du, H.; Liu, N.; Yin, J.; Deng, K.; Zhang, X. Facile synthesis of nanostructured polyaniline in ionic liquids for high solubility and enhanced electrochemical properties. *Adv. Compos. Hybrid Mater.* **2019**, *2*, 279–288. [CrossRef]
22. Honghong, S.; Jing, Z.; Pengfei, S.; Yubing, X. Maize-like ionic liquid@polyaniline nanocomposites for high performance supercapacitor. *e-Polymers* **2019**, *19*, 313–322. [CrossRef]
23. Wang, K.; Huang, J.; Wei, Z. Conducting Polyaniline Nanowire Arrays for High Performance Supercapacitors. *J. Phys. Chem. C* **2010**, *114*, 8062–8067. [CrossRef]
24. Zhang, J.-L.; Zhang, X.-G.; Xiao, F.; Hu, F.-P. Effect of polar solvent acetonitrile on the electrochemical behavior of polyaniline in ionic liquid electrolytes. *J. Colloid Interface Sci.* **2005**, *287*, 67–71. [CrossRef] [PubMed]
25. Innis, P.C.; Mazurkiewicz, J.; Nguyen, T.; Wallace, G.G.; MacFarlane, D. Enhanced electrochemical stability of polyaniline in ionic liquids. *Curr. Appl. Phys.* **2004**, *4*, 389–393. [CrossRef]
26. Zhang, L.; Tsay, K.; Bock, C.; Zhang, J. Ionic liquids as electrolytes for non-aqueous solutions electrochemical supercapacitors in a temperature range of 20 °C—80 °C. *J. Power Sources* **2016**, *324*, 615–624. [CrossRef]
27. Anouti, M.; Jacquemin, J.; Porion, P. Transport Properties Investigation of Aqueous Protic Ionic Liquid Solutions through Conductivity, Viscosity, and NMR Self-Diffusion Measurements. *J. Phys. Chem. B* **2012**, *116*, 4228–4238. [CrossRef] [PubMed]

28. Snook, G.A.; Greaves, T.L.; Best, A.S. A comparative study of the electrodeposition of polyaniline from a protic ionic liquid, an aprotic ionic liquid and neutral aqueous solution using anilinium nitrate. *J. Mater. Chem.* **2011**, *21*, 7622–7629. [CrossRef]
29. Seddon Kenneth, R.; Stark, A.; Torres, M.-J. Influence of chloride, water, and organic solvents on the physical properties of ionic liquids. *Pure Appl. Chem.* **2000**, *72*, 2275. [CrossRef]
30. D'Angelo, P.; Zitolo, A.; Aquilanti, G.; Migliorati, V. Using a Combined Theoretical and Experimental Approach to Understand the Structure and Dynamics of Imidazolium-Based Ionic Liquids/Water Mixtures. 2. EXAFS Spectroscopy. *J. Phys. Chem. B* **2013**, *117*, 12516–12524. [CrossRef]
31. Maiti, A.; Kumar, A.; Rogers, R.D. Water-clustering in hygroscopic ionic liquids-an implicit solvent analysis. *Phys. Chem. Chem. Phys.* **2012**, *14*, 5139–5146. [CrossRef] [PubMed]
32. Zaitsau, D.H.; Yermalayeu, A.V.; Emel'yanenko, V.N.; Butler, S.; Schubert, T.; Verevkin, S.P. Thermodynamics of Imidazolium-Based Ionic Liquids Containing PF6 Anions. *J. Phys. Chem. B* **2016**, *120*, 7949–7957. [CrossRef]
33. Anouti, M.; Couadou, E.; Timperman, L.; Galiano, H. Protic ionic liquid as electrolyte for high-densities electrochemical double layer capacitors with activated carbon electrode material. *Electrochim. Acta* **2012**, *64*, 110–117. [CrossRef]
34. Rilo, E.; Vila, J.; García-Garabal, S.; Varela, L.M.; Cabeza, O. Electrical Conductivity of Seven Binary Systems Containing 1-Ethyl-3-methyl Imidazolium Alkyl Sulfate Ionic Liquids with Water or Ethanol at Four Temperatures. *J. Phys. Chem. B* **2013**, *117*, 1411–1418. [CrossRef] [PubMed]
35. Greaves, T.L.; Drummond, C.J. Protic Ionic Liquids: Properties and Applications. *Chem. Rev.* **2008**, *108*, 206–237. [CrossRef] [PubMed]
36. Xu, W.; Cooper, E.I.; Angell, C.A. Ionic Liquids: Ion Mobilities, Glass Temperatures, and Fragilities. *J. Phys. Chem. B* **2003**, *107*, 6170–6178. [CrossRef]
37. Fan, F.; Wang, W.; Holt, A.P.; Feng, H.; Uhrig, D.; Lu, X.; Hong, T.; Wang, Y.; Kang, N.-G.; Mays, J.; et al. Effect of Molecular Weight on the Ion Transport Mechanism in Polymerized Ionic Liquids. *Macromolecules* **2016**, *49*, 4557–4570. [CrossRef]
38. Yoshizawa, M.; Xu, W.; Angell, C.A. Ionic liquids by proton transfer: Vapor pressure, conductivity, and the relevance of DeltapKa from aqueous solutions. *J. Am. Chem. Soc.* **2003**, *125*, 15411–15419. [CrossRef] [PubMed]
39. Austen Angell, C.; Ansari, Y.; Zhao, Z. Ionic Liquids: Past, present and future. *Faraday Discuss.* **2012**, *154*, 9–27. [CrossRef]
40. Sanchez, P.B.; Garcia, J.; Salgado, J.; Gonzalez-Romero, E. Studies of Volumetric and Transport Properties of Ionic Liquid-Water Mixtures and Its Viability To Be Used in Absorption Systems. *ACS Sustain. Chem. Eng.* **2016**, *4*, 5068–5077. [CrossRef]
41. Watanabe, M.; Kodama, D.; Makino, T.; Kanakubo, M. Density, Viscosity, and Electrical Conductivity of Protic Amidium Bis(trifluoromethanesulfonyl)amide Ionic Liquids. *J. Chem. Eng. Data* **2016**, *61*, 4215–4221. [CrossRef]
42. Angell, C.A.; Byrne, N.; Belieres, J.-P. Parallel Developments in Aprotic and Protic Ionic Liquids: Physical Chemistry and Applications. *Acc. Chem. Res.* **2007**, *40*, 1228–1236. [CrossRef] [PubMed]
43. Schreiner, C.; Zugmann, S.; Hartl, R.; Gores, H.J. Fractional Walden Rule for Ionic Liquids: Examples from Recent Measurements and a Critique of the So-Called Ideal KCl Line for the Walden Plot. *J. Chem. Eng. Data* **2010**, *55*, 1784–1788. [CrossRef]
44. Thawarkar, S.; Khupse, N.D.; Kumar, A. Comparative Investigation of the Ionicity of Aprotic and Protic Ionic Liquids in Molecular Solvents by using Conductometry and NMR Spectroscopy. *ChemPhysChem* **2016**, *17*, 1006–1017. [CrossRef] [PubMed]
45. Brauer, U.G.; De La Hoz, A.T.; Miller, K.M. The effect of counteranion on the physicochemical and thermal properties of 4-methyl-1-propyl-1,2,4-triazolium ionic liquids. *J. Mol. Liq.* **2015**, *210*, 286–292. [CrossRef]
46. Anouti, M.; Caillon-Caravanier, M.; Dridi, Y.; Galiano, H.; Lemordant, D. Synthesis and Characterization of New Pyrrolidinium Based Protic Ionic Liquids. Good and Superionic Liquids. *J. Phys. Chem. B* **2008**, *112*, 13335–13343. [CrossRef]
47. Pauliukaite, R.; Brett, C.M.A.; Monkman, A.P. Polyaniline fibres as electrodes.: Electrochemical characterisation in acid solutions. *Electrochim. Acta* **2004**, *50*, 159–167. [CrossRef]
48. Aoki, A.; Umehara, R.; Banba, K. Conductive polyaniline/surfactant ion complex Langmuir-Blodgett films. *Langmuir* **2009**, *25*, 1169–1174. [CrossRef]
49. Huang, W.S.; Humphrey, B.D.; MacDiarmid, A.G. Polyaniline, a novel conducting polymer. Morphology and chemistry of its oxidation and reduction in aqueous electrolytes. *J. Chem. Soc. Faraday Trans. 1 Phys. Chem. Condens. Phases* **1986**, *82*, 2385–2400. [CrossRef]
50. Heeger, A.J. Nobel Lecture: Semiconducting and metallic polymers: The fourth generation of polymeric materials. *Rev. Mod. Phys.* **2001**, *73*, 681–700. [CrossRef]
51. Du, F.-P.; Wang, J.-J.; Tang, C.-Y.; Tsui, C.-P.; Xie, X.-L.; Yung, K.-F. Enhanced electrochemical capacitance of polyaniline/graphene hybrid nanosheets with graphene as templates. *Compos. Part B* **2013**, *53*, 376–381. [CrossRef]
52. Li, L.; Liu, L.; Zeng, W.; Guo, H.; Li, Y.; Geng, Q. Investigation into the crystal structure of bis(pyridine)-bis(trichloroacetato) copper(II) and its electrophotochemical properties. *Res. Chem. Intermed.* **2012**, *39*, 1727. [CrossRef]
53. Patil, D.S.; Pawar, S.A.; Patil, S.K.; Salavi, P.P.; Kolekar, S.S.; Devan, R.S.; Ma, Y.R.; Kim, J.H.; Shin, J.C.; Patil, P.S. Electrochemical performance of potentiodynamically deposited polyaniline electrodes in ionic liquid. *J. Alloys Compd.* **2015**, *646*, 1089–1095. [CrossRef]
54. Yan, J.; Wei, T.; Shao, B.; Fan, Z.; Qian, W.; Zhang, M.; Wei, F. Preparation of a graphene nanosheet/polyaniline composite with high specific capacitance. *Carbon* **2010**, *48*, 487–493. [CrossRef]
55. Cong, H.-P.; Ren, X.-C.; Wang, P.; Yu, S.-H. Flexible graphene-polyaniline composite paper for high-performance supercapacitor. *Energy Environ. Sci.* **2013**, *6*, 1185–1191. [CrossRef]

56. Ke, F.; Liu, Y.; Xu, H.; Ma, Y.; Guang, S.; Zhang, F.; Lin, N.; Ye, M.; Lin, Y.; Liu, X. Flower-like polyaniline/graphene hybrids for high-performance supercapacitor. *Comp. Sci. Technol.* **2017**, *142*, 286–293. [CrossRef]
57. Sen, P.; De, A. Electrochemical performances of poly(3,4-ethylenedioxythiophene)-NiFe2O4 nanocomposite as electrode for supercapacitor. *Electrochimica Acta* **2010**, *55*, 4677–4684. [CrossRef]
58. Ferloni, P.; Mastragostino, M.; Meneghello, L. Impedance analysis of electronically conducting polymers. *Electrochim. Acta* **1996**, *41*, 27–33. [CrossRef]
59. Available online: http://myweb.wit.edu/sandinic/Research/conductivity%20v%20concentration.pdf (accessed on 22 May 2024).
60. Jänes, A.; Lust, E. Use of organic esters as co-solvents for electrical double layer capacitors with low temperature performance. *J. Electroanal. Chem.* **2006**, *588*, 285–295. [CrossRef]
61. Komura, T.; Usui, T.; Takahasi, K. Charge Transport at Polypyrrole Film Electrodes: Effect of the Electrolyte Concentration. *Bull. Chem. Soc. Jpn.* **1995**, *68*, 3391–3396. [CrossRef]
62. Hassan, M.; Reddy, K.R.; Haque, E.; Faisal, S.N.; Ghasemi, S.; Minett, A.I.; Gomes, V.G. Hierarchical assembly of graphene/polyaniline nanostructures to synthesize free-standing supercapacitor electrode. *Compos. Sci. Technol.* **2014**, *98*, 1–8. [CrossRef]
63. Gao, Z.; Yang, W.; Wang, J.; Yan, H.; Yao, Y.; Ma, J.; Wang, B.; Zhang, M.; Liu, L. Electrochemical synthesis of layer-by-layer reduced graphene oxide sheets/polyaniline nanofibers composite and its electrochemical performance. *Electrochim. Acta* **2013**, *91*, 185–194. [CrossRef]
64. Li, Z.-F.; Zhang, H.; Liu, Q.; Liu, Y.; Stanciu, L.; Xie, J. Covalently-grafted polyaniline on graphene oxide sheets for high performance electrochemical supercapacitors. *Carbon* **2014**, *71*, 257–267. [CrossRef]
65. Chen, W.-C.; Wen, T.-C.; Teng, H. Polyaniline-deposited porous carbon electrode for supercapacitor. *Electrochim. Acta* **2003**, *48*, 641–649. [CrossRef]
66. Ghosh, D.; Giri, S.; Mandal, A.; Das, C.K. H^+, Fe^{3+} codoped polyaniline/MWCNTs nanocomposite: Superior electrode material for supercapacitor application. *Appl. Surf. Sci.* **2013**, *276*, 120–128. [CrossRef]
67. Anouti, M.; Porion, P.; Brigouleix, C.; Galiano, H.; Lemordant, D. Transport properties in two pyrrolidinium-based protic ionic liquids as determined by conductivity, viscosity and NMR self-diffusion measurements. *Fluid Phase Equilib.* **2010**, *299*, 229–237. [CrossRef]
68. Weigend, F.; Häser, M. RI-MP2: First derivatives and global consistency. *Theor. Chem. Acc.* **1997**, *97*, 331–340. [CrossRef]
69. Weigend, F.; Häser, M.; Patzelt, H.; Ahlrichs, R. RI-MP2: Optimized auxiliary basis sets and demonstration of efficiency. *Chem. Phys. Lett.* **1998**, *294*, 143–152. [CrossRef]
70. Ahlrichs, R.; Bär, M.; Häser, M.; Horn, H.; Kölmel, C. Electronic structure calculations on workstation computers: The program system turbomole. *Chem. Phys. Lett.* **1989**, *162*, 165–169. [CrossRef]
71. Becke, A.D. Density-functional exchange-energy approximation with correct asymptotic behavior. *Phys. Rev. A* **1988**, *38*, 3098–3100. [CrossRef]
72. Lee, C.; Yang, W.; Parr, R.G. Development of the Colle-Salvetti correlation-energy formula into a functional of the electron density. *Phys. Rev. B* **1988**, *37*, 785–789. [CrossRef] [PubMed]
73. Grimme, S. Semiempirical GGA-type density functional constructed with a long-range dispersion correction. *J. Comput. Chem.* **2006**, *27*, 1787–1799. [CrossRef] [PubMed]

Disclaimer/Publisher's Note: The statements, opinions and data contained in all publications are solely those of the individual author(s) and contributor(s) and not of MDPI and/or the editor(s). MDPI and/or the editor(s) disclaim responsibility for any injury to people or property resulting from any ideas, methods, instructions or products referred to in the content.

molecules

MDPI

Article

Aliquat 336 in Solvent Extraction Chemistry of Metallic ReO_4^- Anions

Maria Atanassova [1,*], Zhanina Petkova [2] and Vanya Kurteva [2]

[1] Department of General and Inorganic Chemistry, University of Chemical Technology and Metallurgy, 8 Kliment Okhridski Blvd., 1756 Sofia, Bulgaria
[2] Institute of Organic Chemistry with Centre of Phytochemistry, Bulgarian Academy of Sciences, Acad. G. Bonchev Street, Block 9, 1113 Sofia, Bulgaria; zhanina.petkova@orgchm.bas.bg (Z.P.)
* Correspondence: ma@uctm.edu

Abstract: A study of the liquid–liquid extraction of ReO_4^- anions from hydrochloric acid solutions using the ionic liquid Aliquat 336 (QCl: trialkyl(C_8–C_{10})methylammonium chloride) via the well-known method of slope analysis along with the determination of the process parameters is presented. This study employs CCl_4, $CHCl_3$ and C_6H_{12} as diluents. This study was carried out at room temperature (22 ± 2) °C and an aqueous/organic volumetric ratio of unity. The ligand effect on the complexation properties of ReO_4^- is quantitatively assessed in different organic media. The organic extract in chloroform media is examined through ^1H, ^{13}C and ^{15}N NMR analysis as well as the HRMS technique and UV-Vis spectroscopy in order to view the anion exchange and ligand coordination in the organic phase solution. Final conclusions are given highlighting the role of the molecular diluent in complexation processes and selectivity involving ionic liquid ligands and various metal s-, p-, d- and f-cations. ReO_4^- ions have shown one of the best solvent extraction behaviors compared to other ions. For instance, the Aliquat 336 derivative bearing Cl^- functions shows strongly enhanced extraction as well as pronounced separation abilities towards ReO_4^-.

Keywords: liquid–liquid extraction; Aliquat 336; ReO_4^-; organic diluents; selectivity

1. Introduction

Rhenium is classified as a critical metal of significant industrial importance due to its valuable physicochemical properties including the high melting point (3 182 °C) and a large number of stable valence states, and consequently, it is an integral component in so-called specialist materials such as high-performance alloys, catalysts, nanomaterials, etc. [1]. In the world, its distribution today like all others is evaluated as critical and so valuable metals present an uneven situation. Currently, thirty-four elements of the periodic table have been designated by the European Union as "critical" raw materials of strategic importance to the European economy and of high supply risk. As a matter of fact, the average concentration of rhenium in the Earth's crust is just one part per billion (ppb) and is not included this list [2,3]. On the other hand, the maintenance and development of the European economy and the implementation of a smooth transition to renewable energy sources and waste-free technologies are highly dependent on a number of mineral raw materials. Despite partial successes in recycling, the only source unfortunately remaining is mining and extraction from deposits. Therefore, it is necessary to emphasize and draw attention in the scientific research field to the issue of the separation and extraction of rhenium from its associated minerals or related secondary solutions. In general, rhenium is mostly contained in copper sulfide, molybdenum minerals, rare earth ores or niobium–tantalum-containing ores. At present, the method of recovering this metal mainly includes solvent extraction techniques and separation to obtain over 50% of rhenium produced globally [2,3]. As an example, Muruchi et al. have proposed a sustainable and flexible approach for the extraction and separation of rhenium and molybdate species based on a polymeric aqueous two-phase

system, in which the high metal content in concentrated copper effluents is directly used as the driver of phase demixing [4]. Moreover, it was found that the resulting process achieves very high separation yields and relies exclusively on cheap chemicals with relatively low toxicity. Thus, it could serve as a more sustainable alternative for the extraction of both metals Re and Mo from copper mine effluents.

In fact, metals and metalloids with high oxidation states exist as oxoanions in water [5]. Thus, the design of functional ligands with a suitable size, shape, electronegativity and hydrophobicity which can reorganize these oxoanions, especially toxic ones, is a significant task to attain effective extraction from the viewpoints of environmental monitoring and protection. Rhenium is known to be a non-radioactive congener of Tc and is applicable as its substitute owing to their similar electronic configuration, stereochemistry and thermodynamic properties as well [6,7]. In essence, studying the technology for separating and extracting rhenium is significant for promoting its industrial applications and the safe disposal of spent fuel [8–10]. Therefore, perrhenate anions have adsorption characteristics like those of perchlorate and perthechnate anions (contaminants that cause major environmental concerns), so they can serve as their surrogates. Further, rhenium(VII) is usually present in real technology solutions containing a rather high concentration of sulfuric acid in the form of the perrhenate ion ReO_4^- [11,12]. The equilibria and dynamics of rhenium uptake from innovative materials with anion exchangers have also been studied [13,14]. On the other hand, rhenium(VII) could be recovered from solutions of this kind with anion-exchange extraction agents (aliphatic amines and their salts) or neutral reagents [15,16]. The degree of efficiency of metal ions extracted at the same experimental conditions using amine-based extractants usually follows the order as follows: quaternary > tertiary > secondary > primary. For example, Gerhardt et al. have investigated for the solvent extraction of rhenium various organic extractants, namely tri-*n*-octylamine, bis-isododecylamine, pyridine, Aliquat 336, tributyl phosphate, trioctylphosphine oxide, ethyl xanthate and mesityl oxide [17]. Undoubtedly, among the ionic liquid compounds scientifically investigated the most intensively in the last two decades not only in the field of the liquid–liquid extraction and separation chemistry of metallic species, the one that stands out is Aliquat 336 [18,19]. This colorless viscous liquid compound (0.884 g/cm^3 density) is a water-insoluble quaternary ammonium salt (Q^+Cl^-: Q^+ is the cation) based on the tricaprylmethylammonium cation [$C_{25}H_{54}N^+$] combined with the chloride [Cl^-] anion. Nowadays, focusing on the employment of more benign and sustainable technological processes, this fascinating liquid chemical has already found a large-scale application in the field of solvent extraction chemistry: extracting a compound, additive, modifier or organic phase (2 in 1) [20]. For example, the synergistic extraction of lanthanoids with a chelating ligand like thenoyltrifluoroacetone (HTTA) or 1-phenyl-3-methyl-4-benzoylpyrazol-5-one (HP) in combination with Aliquat 336 in the role of a synergistic agent has been studied in detail by Atanassova and Dukov [21–27]. It has been reported that lanthanoids form anionic complexes of the type $Q^+[Ln(TTA)_4]^-$ in the organic phase. The role of the quaternary ammonium salt anion is important because anionic complex formation depends on the breaking of the bond between the cation and anion of the liquid salt during the extraction process. Taking into account that the bond energy between the cation and anion increases in the order $Cl^- < NO_3^- < ClO_4^-$ [28,29], it is clear why lanthanoid extraction decreases in that order exactly. It has been established that the change in chloride with a perchlorate anion in Aliquat 336 causes a significant decrease in the overall equilibrium constant (3–4 orders). This fact was explained by the authors again with the stronger bond between the cation and the anion in the $QClO_4$ molecule which makes the formation of anionic complexes $Q^+[Ln(PMBP)_4]^-$ more difficult. It was found that the synergistic extraction increases in the sequence $CHCl_3 < C_6H_6 < CCl_4 < C_6H_{12}$. As a whole, the increase in the diluent solvating ability hinders the extraction process. Further, the values of the thermodynamic functions have been determined for the extraction of Pr, Gd and Yb with HTTA and Aliquat chloride in CCl_4, C_6H_6 and $CHCl_3$ in the interval 288–318 K [25]. The values of ΔH, ΔS and ΔG have been established to be negative for the organic phase synergistic reaction. So, the formation

of the anionic complex in the organic phase is favored by the negative enthalpy changes. Perhaps the main disadvantage of this liquid compound, which must be noted, is that it is very viscous; for that reason, it inevitably requires the use of an organic diluent influencing the greenness of the process.

The object of the scientific work undertaken is to present the investigation on the solvent extraction of ReO_4^- ions by the ionic liquid Aliquat 336 diluted in three diluents, $CHCl_3$, CCl_4 and C_6H_{12}, with the goal to elucidate the nature of the extracted complexes into the organic phase as well as to clarify the role of the diluent when its polarity decreases. In addition, the selectivity of Re(VII) and 37 other chemical elements in the periodic table is also studied in detail.

2. Results and Discussion

2.1. Solvent Extraction Study of ReO_4^- Anions Applying Aliquat 336: Effect of pH, Ligand Concentration and Organic Diluent

In fact, one ideal representative of ionic liquid compounds is the quaternary ammonium salt, having an industrial nickname of Aliquat 336 (trialkyl(C_8–C_{10})methylammonium chloride, m.p.: −20 °C; viscosity: 1500 mPa·s). Over and above that, it is an intensively investigated molecule from the broad family of IL compounds in academic fundamental research, with essential application for ion-pair complexation in the mining industry for the role of the extractant [19]. Therefore, it is not a surprise that numerous scientific articles dealing with the evaluation of its coordination ability towards f-elements have also appeared [18,30,31]. However, due to its high viscosity, this IL is mostly used as dissolved in organic molecular diluents, as already mentioned. Additionally, it was found that the solvent extraction mechanism is based on anion exchange and hence strongly depends on the composition of the aqueous phase as well [27,32,33]. The extraction behavior of QCl (Q^+ is the quaternary ammonium salt cation) towards ReO_4^- as a function of the pH in the aqueous phase using the studied three organic diluents is shown in Figure 1. In all three investigated solvent systems, the extractability of ReO_4^- reaches a maximum value in the pH range from 1.2 to 2.3, i.e., 100%. What is good to pay attention to is that a diluent like CCl_4 likely prefers a more acidic extraction (aqueous) medium than the other two diluents. Shimojo et al. have recently found that the tripodal ligand *N*,*N*,*N*′,*N*′, *N*′′,*N*′′-hexa-*n*-octylnitriltriacetamide, composed of three amide groups and a tertiary amine in isooctane medium, quantitatively extracted TcO_4^- and ReO_4^- anions in the pH range from 1.0 to 2.5 [8]. Moreover, it was reported that after five cycles of both forward and back extraction, the ligand retained its high extraction ability for ReO_4^- in the aqueous phase, and the presence of or increase in NO_3^- anions in the aqueous phase unfortunately inhibited the ReO_4^- transfer. The effect of the composition of the organic and aqueous phases on the recovery of rhenium(VII) by triisooctylamine dissolved in 1-octanol or 2-ethyl-1-hexanol was analyzed by Kasilkov and Petrova [34]. Furthermore, the established decrease in D_{Re} on passing from weakly acidic to more concentrated solutions is found to be probably due to a change in the state of the ligand salt in the organic phase under conditions of an increasing concentration of H_2SO_4 from 0.1 to 9 mol/dm^3 in the aqueous phase. The observed effect was accounted for by the competing extraction of the mineral acid by the amine, which hinders the rhenium(VII) solvent extraction. The effect of salt (Na^+) or acid anions was investigated by Zhou and co-researchers that indicated a weaker competition of SO_4^{2-} or Cl^- over ReO_4^- than that of NO_3^- attributed to the largest ΔG_h (standard Gibbs hydration energy) value of NO_3^- among the three anions [9]. Thus, the inhibition of D_{Re} caused by other competitive anions followed the order as follows: $ClO_4^- > NO_3^- > SO_4^- \approx Cl^-$. Accordingly, this shows that exactly the chosen chloride anion investigated herein is an ideal candidate and the most suitable for an ion exchange with metal anion species like ReO_4^-.

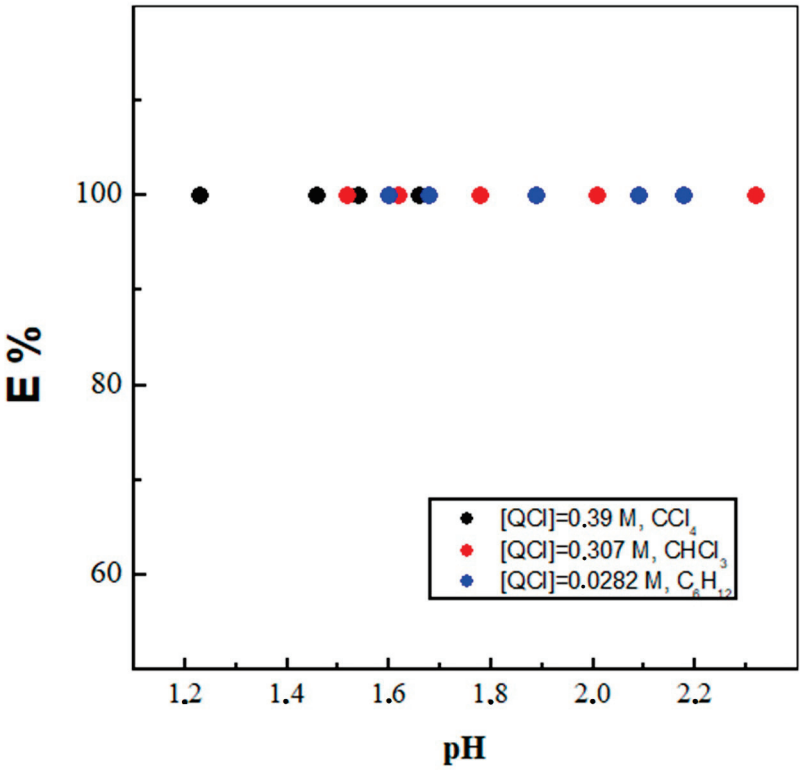

Figure 1. The extraction behavior of ReO_4^- as a function of pH_{eq} in the aqueous phase.

Further, the mechanism of ReO_4^- solvent extraction with QCl was investigated using the known slope analysis method [27]. In this respect, Figure 2 represents logarithmic plots of the distribution ratio (*D*) of ReO_4^- using QCl as a function of the logarithmic extractant concentrations at a constant pH of the aqueous phase in three different organic diluents. It is evident from the obtained results that this liquid compound is quite a strong extractant for metal anions. Therefore, an indisputable advantage is that very small concentrations of the applied extractant QCl completely extract the metal Re(VII) particles from the aqueous to the organic phase. Thus, it is unnecessary for the ligand to be in excess or at a concentration greater than a 1:1 ratio to the metal. Unfortunately, only in a diluent like C_6H_{12} is it possible to report and calculate an approximate slope, i.e., ca. 0.88. Of course, the concentration selected for analysis when using this diluent is also smaller. This result implies that one molecule of QCl ($[R_3CH_3N^+][Cl^-]$) participated in the ReO_4^- extraction and 1:1 QCl: ReO_4^- complexes are formed in the organic phase with possible stoichiometry $Q^+ReO_4^-$. Thus, the reaction mechanism in the organic phase is via ion-exchange mode, and the solvent extraction of metallic anions is much more efficient in solvent systems with chlorine-containing diluents. That is, the whole body of the date obtained, combined with previously published evidence, makes it possible to represent the extraction of Re(VII) with a new formation connected with breaking of the bond between the cation ($[R_3CH_3N^+]$) and the anion ($[Cl^-]$) of the IL salt.

Therefore, the solvent extraction process of the metallic anionic species ReO_4^- can be expressed with equilibrium as follows:

$$[R_3CH_3N^+][Cl^-]_{(o)} + ReO_4^-{}_{(aq)} \rightleftharpoons [R_3CH_3N^+][\,ReO_4^-]_{(o)} + Cl^-{}_{(aq)} \quad (1)$$

where $[R_3CH_3N^+][Cl^-]$ denotes the ligand Aliquat 366, and the subscripts "aq" and "o" denote aqueous and organic phases, respectively.

In general, the solvent extraction mechanism involving the Aliquat 336 molecule alone is based on the anion exchange or ion association reaction mode of behaviors with metal

chloride or sulfate species and somehow strongly depends on the chemical composition and pH of the aqueous phase (formation of different metal species) [18,35].

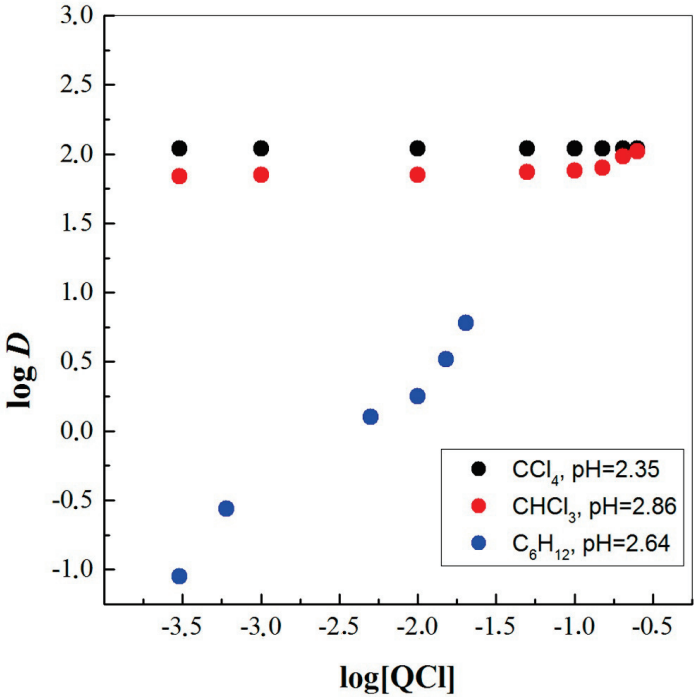

Figure 2. Slope analysis of ReO_4^- extraction by QCl: dependency on extractant concentration.

An additional analysis is undertaken to estimate the degree of anion exchange upon solvent extraction (ligand to metal species concentration ratio 1:1); the latter was performed in deuterated chloroform, and the solutions before and after the extraction of ReO_4^- with the QCl ligand are analyzed by proton, carbon and nitrogen NMR spectra. The signals for methyl and methylene groups neighboring nitrogen are shifted downfield in proton spectra upon anion replacement, 3.211 and 3.342 vs. 3.304 and 3.421, respectively (Figure 3a). The opposite shifting is observed in carbon spectra (Figure 3b), while nitrogen chemical shifts are almost identical (Table 1). Therefore, the fact that these particular chloride signals are not detected in the organic perrhenate spectra indicates that the anion is completely exchanged during the solvent extraction process.

Table 1. Selected signals in ^{1}H and ^{13}C spectra and ^{15}N chemical shifts (extracted from ^{1}H-^{15}N HMBC experiment) of QCl and $QReO_4$ in $CDCl_3$.

Compound	$C\underline{H}_3$-N^+	$\underline{C}H_3$-N^+	$C\underline{H}_2$-N^+	$\underline{C}H_2$-N^+	$^{15}\underline{N}$
$[A336^+][Cl^-]$	3.211	61.65	3.342	62.97	60.2
$[A336^+][ReO_4^-]$	3.304	61.42	3.421	62.83	60.4

In fact, Aliquat 336 is typically specified by the supplier to be a trialkylmethylammonium ion consisting of a mixture of C_8 and C_{10} chains regarding the three alkyl residues with C_8 predominating. As can be seen from the spectrum in Figure 4, the analysis of the supplied Aliquat 336 by positive ion mode HR-MS disclosed its actual composition. Therefore, four groups of signals with different m/z ratios and varying intensities could be clearly distinguished and assigned to trioctylmethylammonium ($A336^+_{C25}$), dioctyldecylmethylammonium ($A336^+_{C27}$), didecyloctylmethylammonium ($A336^+_{C29}$) and tridecylmethylammonium ($A336^+_{C31}$). Note the increasing carbon number in this order from C_{25} to C_{31} as indicated by the subscripts. The observed signal pattern aligns with previously reported ESI-MS data in the literature [36]. The new anion component of the quaternary

ammonium cation after the solvent extraction process is shown in Figure 5. It can be seen that the anion ReO_4^- is present approximately in equimolar amounts to the cation Q^+ (molar ratios close to 1) indicating a quantitative exchange of the chloride counterion of the ligand by the target metallic anion in the course of the solvent extraction process.

In addition, the UV-Vis absorption spectra of the loaded organic phase ($CHCl_3$) after the solvent extraction process and the organic liquid phase before extraction were both measured as well. The representative peak for the ReO_4^- anion at wavelength 246 nm [14] was clearly observed (Figure 6), indicating its quantitative transfer from the aqueous phase through an anion exchange mechanism also confirmed by this analysis.

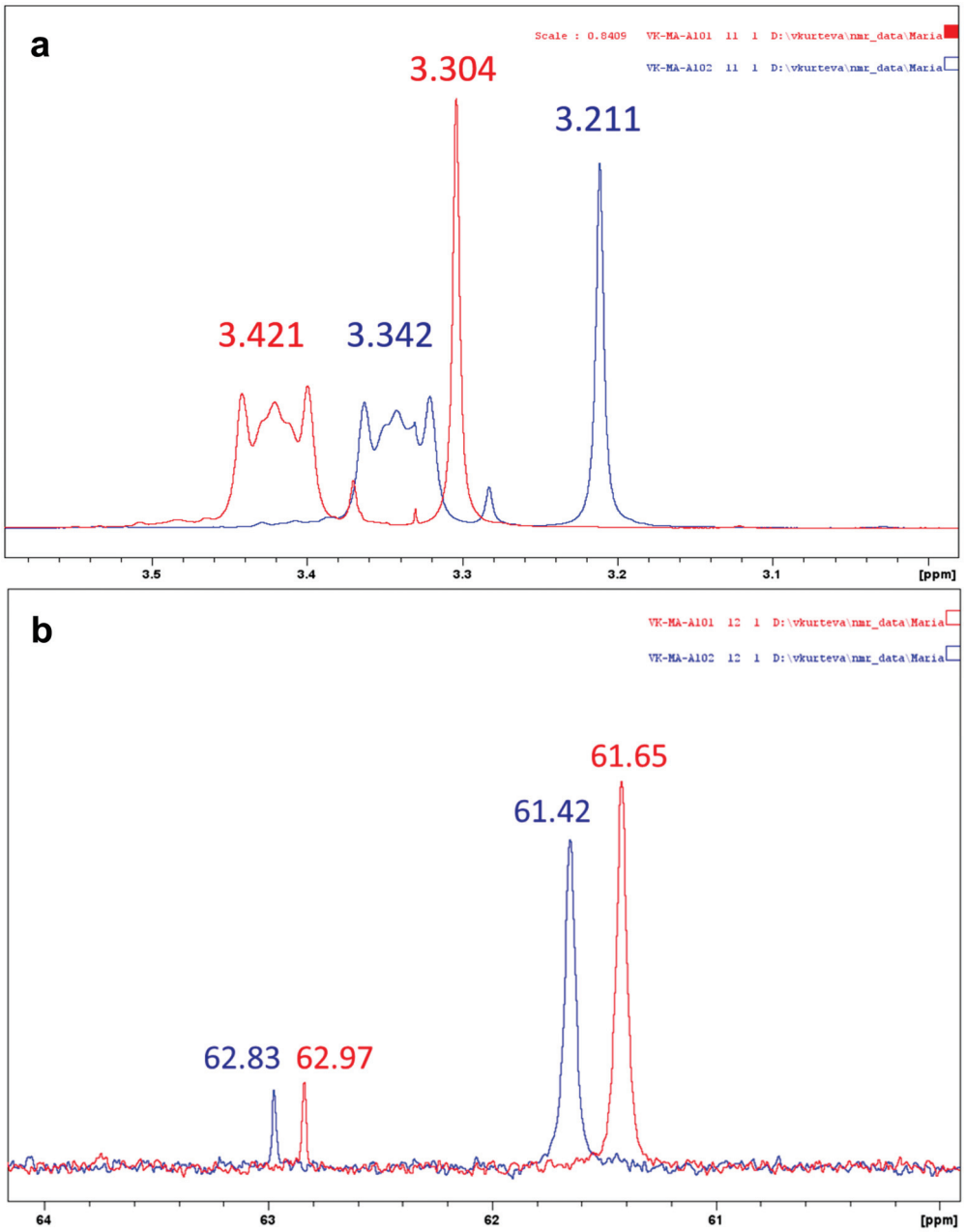

Figure 3. The signals for *N*-methyl and *N*-methylene groups in proton (**a**) and carbon (**b**) spectra of QCl (blue) and $QReO_4$ (red) in $CDCl_3$.

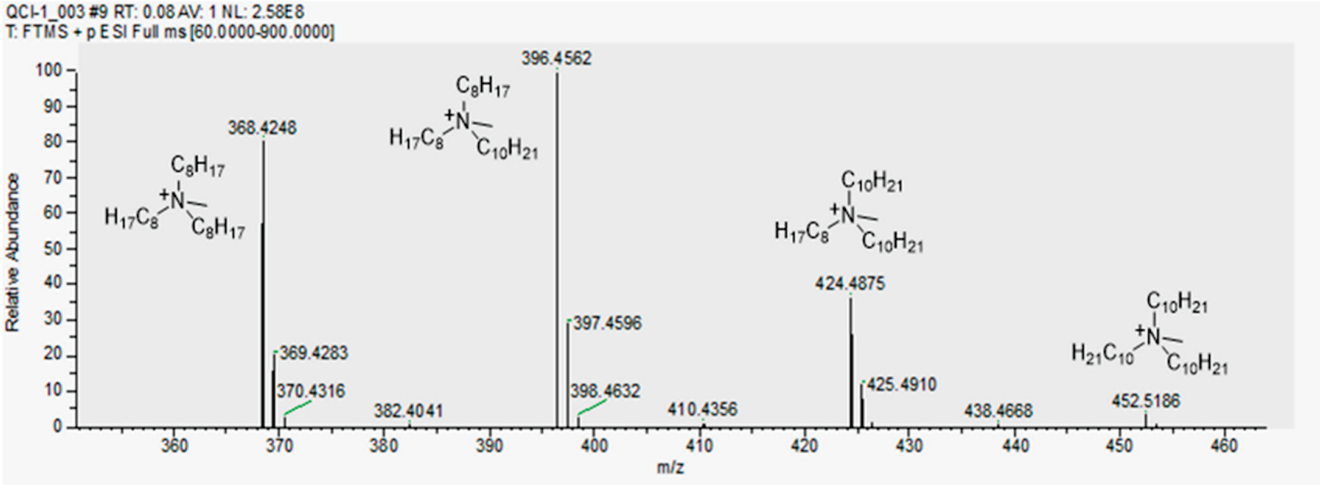

Figure 4. HR–MS (ESI$^+$) m/z calcd. for $C_{25}H_{54}N^+$ $[M]^+$ 368.4251, found 368.4248, $\Delta = -0.3$ mDa; calcd. for $C_{27}H_{58}N^+$ $[M]^+$ 396.4564, found 396.4562, $\Delta = -0.2$ mDa; calcd. for $C_{29}H_{62}N^+$ $[M]^+$ 424.4877, found 424.4875, $\Delta = -0.2$ mDa; calcd. for $C_{31}H_{66}N^+$ $[M]^+$ 452.5190, found 452.5186, $\Delta = -0.4$ mDa.

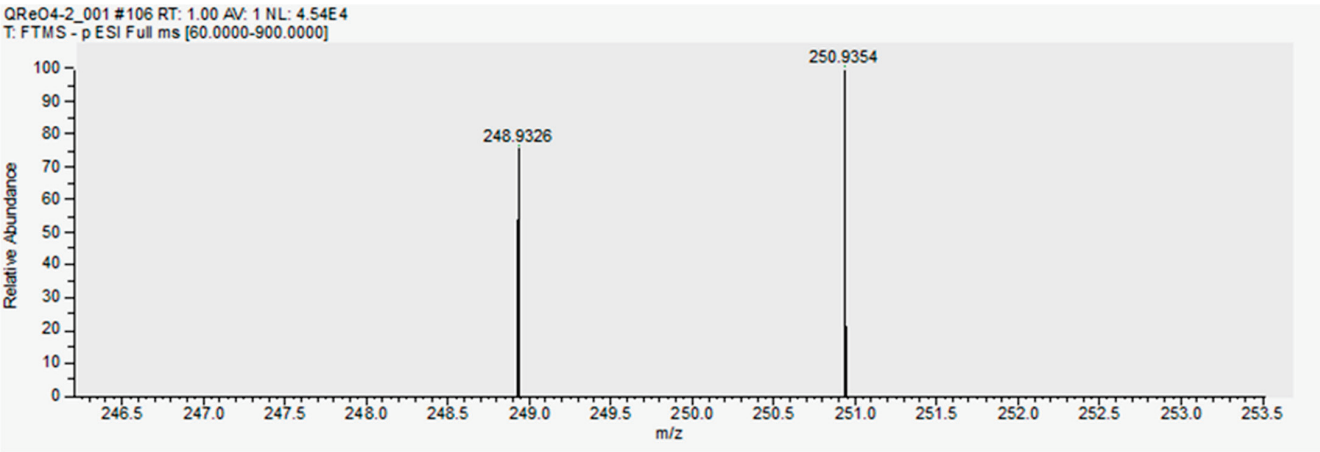

Figure 5. HR–MS (ESI$^-$) m/z calcd. for O_4Re^- $[M]^-$ 250.9349, found 250.9354, $\Delta = 0.5$ mDa.

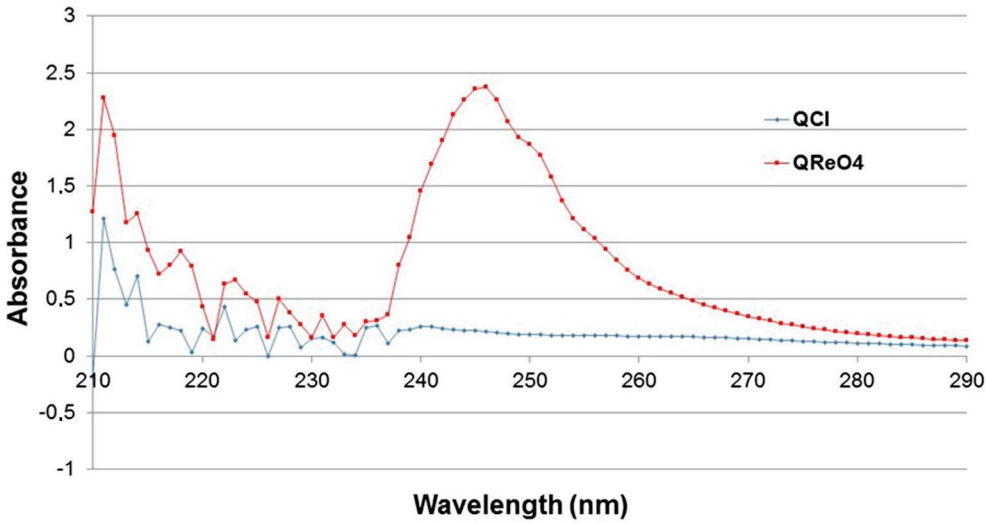

Figure 6. UV–Vis absorption spectra of the formed $Q^+ReO_4^-$ species extracted by Aliquat 336 from the aqueous solution and the ligand.

2.2. Solvent Extraction and Selectivity across the Chemical Elements in the Periodic Table Applying Aliquat 336

Generally, as already mentioned, rhenium is present in very low concentrations in the Earth's crust (0.4 mg·t^{-1}) [37]. Additionally, it is produced primarily as a byproduct of molybdenum and copper solvent extraction regardless of the great environmental costs [38]. It is recovered during the pyrometallurgical processing of molybdenum sulfide and copper sulfide ores. This process traditionally involves removing rhenium (VII) oxide, Re_2O_7, from the sulfurous gas phase generated during hearth roasting (in molybdenum processing) and smelting (in copper processing) [39–41]. The low-grade molybdenite concentrate (20–45%) is also associated with approximately 0.01% Re values, in addition to a number of impurity elements such as Si (7.45%), Fe (1.62%), Ni (0.17%) and Cu (0.35%) [42]. Therefore, it would be interesting to study the behavior of more metals during their simultaneous solvent extraction and to compare the obtained results with the target metal, i.e., rhenium. In general, the extraction efficiency diminishes in competitive extraction tests with respect to the single species extraction, which is probably due to a multi-ion competition, or crowding effect or both of them [43]. From the research study aimed at evaluating the solvent extraction ability of the Aliquat 336 molecule towards various metal cations, it can be seen that it is not a suitable extractant for alkali, alkaline earth metals, Cr, Fe, Al or, of course, lanthanoids [27,44], as shown in Figure 7. The lanthanoid solvent extraction with the quaternary ammonium salt Aliquat 336 in perchlorate form alone is negligible under the experimental conditions applied in the previous study by Atanassova as well [27]. Secondly, regardless of the diluent used, ligand concentration or cation charge, complete quantitative extraction was achieved in all three solvent systems for ions such as Re, Hg, Bi and Ag (Figure 7). Unfortunately, when using Aliquat 336, the increases in metal extraction percentages decreased selectivity regardless of the diluent, since the obtained extraction percentages are very close. This indicates a decrease in the separation factors and, consequently, selectivity between target metals. However, for two of the cations in group 12, viz. Zn^{2+} and Cd^{2+}, changing the diluent leads to a reduction in their extraction process by five times or a lack of it. Moreover, one cannot fail to emphasize the commonly observed better capabilities of the diluent CCl_4 in extraction systems compared to $CHCl_3$ [45,46], as seen for metals such as Co^{2+}, Ni^{2+}, Cu^{2+} and light 4f-ions. Thus, the efficient and selective leaching of specific metals from minerals or wastes is feasible by using the Aliquat 336 compound. In addition, it can be concluded that the proposed solvent extraction system exhibits highly selective extraction for ReO_4^- in the presence of a large number of diverse ions, as shown in Table 2. The corresponding values of separation factors (SFs) for one solvent system are presented only.

Table 2. Separation factors between Re(VII) and various s-, p-, d- and f-ions extracted with QCl = 0.39 mol/dm^3 in CCl_4.

SF	**Li**	**Na**	**Al**	**K**	**Ca**	**Cr**	**Mn**	**Fe**	**Co**	**Ni**	**Cu**	**Zn**	
Re	9×10^3	1×10^4	3×10^3	4×10^4	1×10^5	2×10^4	1×10^5	8×10^3	5×10^3	4×10^3	1×10^3	6.7	
SF	**Sr**	**Ag**	**Cd**	**Ba**	**La**	**Ce**	**Eu**	**Gd**	**Lu**	**Hg**	**Tl**	**Pb**	**Bi**
Re	5×10^5	1.09	0.86	5×10^3	3×10^3	1×10^4	7×10^5	2×10^4	8×10^5	2.4	2×10^3	106	4.5

In summary, the 26 studied metal ions could be classified approximately in the following four groups according to the degree of their separation with Re(VII):

(1) Very difficult to separate, SF < 5: Zn, Ag, Cd, Hg and Bi;
(2) Difficult to separate, SF < 100: Pb;
(3) Overall selectivity $\approx 10^3$: Li, Al, Fe, Co, Ni, Cu, Ba, La and Tl;
(4) Overall selectivity $\approx 10^4 - 10^5$: Na, K, Ca, Cr, Mn, Sr, Ce, Eu, Gd and Lu.

1	2	3	4	5	6	7	8	9	10	11	12	13	14	15
Li(I) – – –										mol/dm^3 CCl_4 0.39 $CHCl_3$ 0.3 C_6H_{12} 0.028	QCl pH_{in}=0.15			
Na(I) – – –	Mg(II)											Al(III) – – –		
K(I) – – –	Ca(II) – – –	Sc(III)	Ti(IV)	V(V)	Cr(III) – – –	Mn(II) – – –	Fe(III) – – –	Co(II) 1.4% – –	Ni(II) 2.2% – –	Cu(II) 5.4% – –	Zn(II) 92.6% 89.6% –	Ga(III)		
Rb(I)	Sr(II) – – –	Y(III)	Zr(IV)	Nb(V)	Mo		Ru(III)	Rh(III)	Pd(II)	Ag(I) 100% 100% 100%	Cd(II) 100% 100% 20.9%	In(III)		
Cs(I)	Ba(II) – – –	Ln(III)	Hf(IV)	Ta(V)	W(VI)	Re(VII) 100% 100% 100%	Os(IV)	Ir(III)	Pt(IV)	Au(III)	Hg(II) 100% 100% 100%	Tl(I) 4.7% 5% 2.5%	Pb(II) 43% 47% –	Bi(III) 100% 100% 100%

La(III)	Ce(III)	Pr(III)	Nd(III)	Sm(III)	Eu(III)	Gd(III)	Tb(III)	Dy(III)	Ho(III)	Er(III)	Tm(III)	Yb(III)	Lu(III)
2.4% – –	1% – –				– – –	– – –							– – –

Figure 7. The extraction performance of the Aliquat 336 ligand towards 26 metal ions. The reported extractability values (%) represent the average of three measurements, with deviations of less than 5%.

From the additional analysis carried out to investigate the selectivity between rhenium and 12 refractory elements, it is seen that only the C_6H_{12} diluent and low extractant concentrations are suitable for this scientific purpose separation except only the Re/Ta pair, as shown in Figure 8. Regarding the environmental pressure today in terms of green chemistry, the C_6H_{12} system may play a role in these efforts so as to create eco-friendly organic solutions, i.e., halogen-free. The solvent system QCl/CCl_4 is obviously quite effective for the competitive extraction of metal ions, like Re, Ta, Mo and Sn, and their pronounced separation from the rest of the ions in the studied mixture, i.e., Si, Ti, Ge, Sb, Te, Zr, Nb, Hf and W. On that account, the obtained extractability followed the following order: Re ≈ Ta > Mo ≈ Sn > Nb > Sb ≈ W > Ti > Hf > (Zr ≈ Ge ≈ Te ≈ Si). It is worthy to mention as well that when changing the diluent CCl_4 with polar one $CHCl_3$, a sensitive difference is noticed as the extraction ability of the ligand molecule remains at 100% only for Re and Ta ions and sharply decreases for the other ions in the series. Therefore, this know-how could be used in order to obtain a certain selectivity among refractory metals. The diluent in use can influence the solvent extraction efficiency through both chemical and entrainment effects. The use of CCl_4 as a diluent increases the solvent extraction of Mo and acts more effectively than $CHCl_3$ or the influence of aromatic diluent components on the selectivity of the extractant, i.e., C_6H_{12}.

Moreover, in hydrometallurgy, the separation between rhenium and molybdenum ions in aqueous solution is a difficult task owing to their relatively adjacent positions in the periodic table and being in possession of similar chemical properties. One example is the recovery of rhenium and molybdenum from a sulfuric acid leaching solution of molybdenite roasting dust performed by tri-octyl-amine dissolved in kerosene. The extraction efficiency of rhenium and molybdenum was obtained and reported by Kang et al. as 99 and 30%, respectively, using 5 vol% TOA at the solution equilibrium pH of 0 and an O/A ratio of 0.4 [47]. So, the published result clearly shows that a pH equal to 0 is somehow a better experimental condition to separate both metals with the highest separation factor. Further, the extraction of some oxonium anions, TcO_4^-, ReO_4^-, $Cr_2O_7^{2-}$, MoO_4^{2-} and WO_4^{2-}, from 1 mol/dm^3 HNO_3 was performed by a new neutral, tridentate ligand, 2,2′-

(methylimino)bis(*N*,*N*-dioctylacetamide) in *n*-dodecane with a reported trend of *D* in the order Tc > Re > W > Mo > Cr [48]. The masking effects of 16 S-, O- and N- donor water-miscible multidentate ligands showing a five- or six-membered ring formation on the solvent extraction of Pd, Ru, Mo and Re from 2 mol/dm^3 HNO_3 were studied using the same ligand as well as NTAamide dissolved in *n*-dodecane. However, no masking agent for Re was found in the cited work, contrary to other metals tested [49].

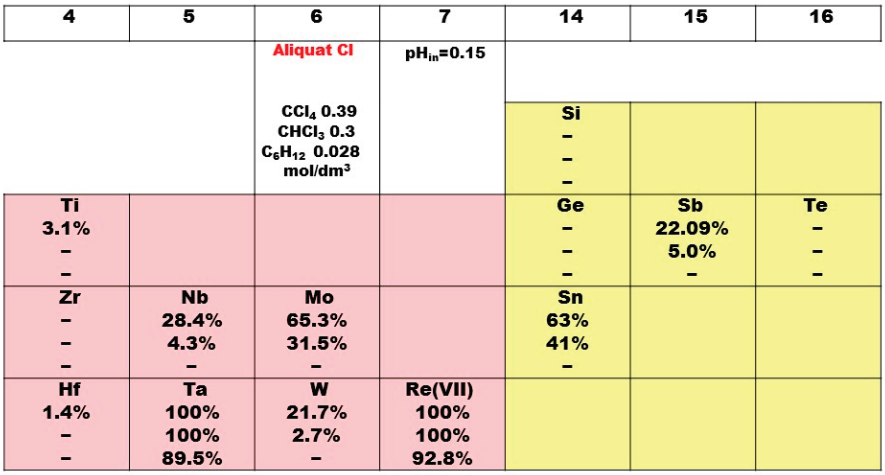

Figure 8. The extraction performance of Aliquat 336 towards 13 metal ions. The reported extractability values (%) represent the average of three measurements, with deviations of less than 5%.

The selectivity of Re(VII) and the twelve refractory ions is studied for the best system, i.e., QCl/CCl_4, and the results are displayed in Table 3. As a whole, the calculated separation factors obtained for all pairs are extremely high with one exception Re/Ta and are not significantly lower for Mo and Sn combinations. In general, the observed strong selective extractant's behavior could be discussed as two possible reaction mechanism effects: an anionic, which, in this case, seems to be the determinant, or cationic extraction process followed by a solvation. In other words, this ionic liquid ligand presents a higher selectivity due to its different extraction force towards s-, p-, d- or f-ions. The quaternary ammonium salt, an economically advantageous class of industrial compounds known for decades, will rest a favorable anion-exchange extraction agent in the field of chemical and environmental engineering.

Table 3. Separation factors between Re(VII) and 12 refractory ions extracted with QCl = 0.39 mol/dm^3 in CCl_4.

SF	Si	Ti	Ge	Sb	Te	Zr	Nb	Mo	Sn	Hf	Ta	W
Re	7.3×10^4	4×10^3	3.3×10^4	464	4.2×10^4	3.8×10^4	332	70	77.4	9.2×10^3	4.6	475

3. Materials and Methods

3.1. Reagents

All reagents were purchased from Aldrich, Merck and Fluka and were used without further purification. The commercial product Aliquat 336 was obtained from Fluka (Bern, Switzerland). The quaternary ammonium salt was purified before use according to the procedure suggested by Goto [29]. The diluents were $CHCl_3$ (Merck, p.a. (Darmstadt, Germany)), C_6H_{12} (Merck, p.a.) and CCl_4 (Merck, p.a.). Re standard for ICP 999 mg/dm^3 $\pm$ 4 mg/dm^3 (Sigma-Aldrich (St. Gallen, Switzerland)) and ICP-MS refractory elements standard—12 components: 10 mg/dm^3 $\pm$ 0.022–0.059 mg/dm^3 each of Ge, Hf, Mo, Nb, Sb, Si, Sn, Ta, Te, Ti, W and Zr (CPAchem Ltd., Bogomilovo, Bulgaria). All other commercially available analytical-grade reagents were used without any further purification.

A stock solution of rhenium ions (2×10^{-3} mol/dm^3) was prepared from $KReO_4$ (Fluka, puriss) by dissolving and diluting with distilled water to the required volume. Hydrochloric acid 37% was used (Merck, p.a.) to adjust the pH of the aqueous solutions added to 0.1 mol/dm^3 2-morpholinoethanesulfonic acid (MES) buffer (Alfa Aesar, 98% (Karlsruhe, Germany)).

3.2. Solvent Extraction Studies

Extraction experiments were carried out at room temperature by mixing the two immiscible liquid phases in a 1:1 v/v ratio (1.5 mL) for 1.5 h (1500 rpm), which was sufficient for attaining equilibrium. After the separation of the liquid phases, the concentration of rhenium in the aqueous phase was determined by using ICP-OES spectroscopy ("Prodigy" High-dispersion ICP-OES, Teledyne Leeman Labs, Hudson, New Hampshire, USA). The concentration of the metal ion in the organic phase was obtained by material balance. The reproducibility of distribution ratio (D) measurements was generally within 95%. The acidity of the aqueous phase at equilibrium was measured by a pH meter (pH 211 HANNA, Hanna, Smithfield, RI, USA) with an accuracy of 0.01 pH unit. The Re(VII) ion initial concentration was 2.6×10^{-4} mol/dm^3 in all experiments.

For competitive extraction tests, a volume of 2 mL of the prepared aqueous solution containing various M^{n+} metal ions (~3×10^{-4} mol/dm^3 including 3×10^{-4} mol/dm^3 Re(VII)) or various refractory elements ((9 mg/dm^3) including 2×10^{-4} mol/dm^3 Re(VII)) was equilibrated for 2 h (1500 rpm) with a 2 mL organic phase, which includes the studied ligand molecule, Aliquat 336. After phase separation, the metal ion concentrations in the aqueous solution were determined by ICP-OES.

The distribution ratio (D) at equilibrium was calculated as follows:

$$D = \frac{[M^{n+}]_{aq,in} - [M^{n+}]_{aq,f}}{[M^{n+}]_{aq,f}} \times \frac{V_{aq}}{V_o} \quad (2)$$

where $[M^{n+}]_{aq,in}$ is the concentration of the M^{n+} ion in the aqueous phase before liquid–liquid extraction tests, and $[M^{n+}]_{aq,f}$ is the concentration of the same metal ion in the aqueous phase after extraction. In general, V_{aq} and V_o are the volumes of the aqueous and organic phase as well as the volumes of two immiscible phases used to perform experiments, herein always a 1:1 v/v extraction. For instance, duplicate experiments showed that the reproducibility of D measurements was generally within 95%.

The extractability (% E) was evaluated as follows:

$$\text{extractability} = \frac{[M^{n+}]_{aq,in} - [M^{n+}]_{aq,f}}{[M^{n+}]_{aq,in}} \times 100 \quad (3)$$

The metal separation between chemical elements in the periodic table can be estimated using separation factors (SFs) determined as a ratio of the distribution ratios of the two studied metal ions:

$$\text{SF} = D_1/D_2. \quad (4)$$

3.3. NMR, UV-Vis and HRMS Measurements

The NMR spectra of the extract solutions at room temperature are recorded directly after Re(VII) solvent extraction (3×10^{-2} mol/dm^3 Re(VII) and QCl, pH_{eq} = 1.4) on Bruker Avance NEO 400 spectrometers (Rheinstetten, Germany) in $CDCl_3$ medium. The chemical shifts are quoted in ppm in δ-values against tetramethylsilane (TMS) as an internal standard. The ^{15}N chemical shifts are extracted from two-dimensional ^1H-^{15}N HMBC experiments. The spectra are processed with the Topspin 3.6.3 program.

The mass spectra are recorded (Aliquat 336 and organic phase after Re(VII) solvent extraction (1×10^{-2} mol/dm^3 Re(VII) and QCl in $CHCl_3$, pH_{eq} = 1.4) using a Q Exactive Plus Hybrid Quadrupole-Orbitrap Mass Spectrometer from Thermo Scientific (HESI HRMS)

in both positive and negative modes. The spectra are processed with the Thermo Scientific FreeStyle program version 1.8 SP1 (Thermo Fisher Scientific Inc., Waltham, MA, USA).

The UV–vis spectra of the extract solution at room temperature is recorded directly after Re(VII) solvent extraction (8×10^{-4} mol/dm^3 Re(VII) and QCl in $CHCl_3$ at pH_{eq} = 1.4) using an Analytic Jena Specord 200 Plus spectrophotometer (Jena, Germany) and 10.0 mm path length quartz cuvettes.

4. Conclusions

The extraction behavior of Re(VII) by an ionic liquid ligand Aliquat 336 indicates a rapid and spontaneous anion exchange reaction at room temperature. The established stoichiometric ratio in the formed extracted compound in the organic phase is 1:1, with the structure $[R_3CH_3N^+][ReO_4{}^-]$. The investigation of the effect of the organic diluent on the extracting properties of the ligand revealed that the efficiency of Aliquat 336 dissolved in CCl_4 was higher than its solutions in $CHCl_3$ or C_6H_{12}. Based on the evaluated SF values, it was concluded that Aliquat 336 demonstrated a higher extraction performance and a better separation characteristic particularly with respect to $ReO_4{}^-$. This study clearly showed the high potential of the investigated affordable ionic liquid compound for the selective separation–recovery of metals such as Re, Ta, Mo, Ag, Hg, Bi, Zn and Cd from multi-component solutions.

Author Contributions: Conceptualization, M.A.; methodology, M.A. and Z.P.; validation, M.A. and V.K.; investigation, M.A., Z.P. and V.K.; writing—original draft preparation, M.A.; writing—review and editing, M.A.; visualization, M.A., Z.P. and V.K.; project administration, M.A. and V.K; funding acquisition, M.A. All authors have read and agreed to the published version of the manuscript.

Funding: The research leading to these results received funding from the European Union-NextGenerationEU, through the National Recovery and Resilience Plan of the Republic of Bulgaria, project No. BG-RRP-2.004-0002, "BiOrgaMCT", and it was supported by the Research and Development Sector at UCTM via project No. 12327 (2023). This work was partly developed within the scope of the project "Green twist to synergistic solvent extraction and separation of rare earth metals" financed by the Bulgarian Science Fund: Grant Agreement No. КП-06-Н69/5(2022).

Institutional Review Board Statement: Not applicable.

Informed Consent Statement: Not applicable.

Data Availability Statement: The original contributions presented in the study are included in the article; further inquiries can be directed to the corresponding author.

Conflicts of Interest: The authors declare no conflicts of interest.

References

1. Shen, Z.; Tesfaye, F.; Li, X.; Lindberg, D.; Taskinen, P. Review of rhenium extraction and recycling technologies from primary and secondary resources. *Miner. Eng.* **2021**, *161*, 106719. [CrossRef]
2. Lou, Z.; Xing, S.; Xiao, X.; Shan, W.; Xiong, Y.; Fan, Y. Selective adsorption of Re(VII) by chitosan modified with imidazolium-based ionic liquid. *Hydrometallurgy* **2018**, *179*, 141–148. [CrossRef]
3. Qi, W.; He, J.; Li, M.; Zhai, M.; Zhao, L. Efficient extraction of rhenium through demulsification of imidazolium ionic liquid based microemulsions from aqueous solution. *Sep. Purif. Tehcnol.* **2022**, *297*, 121574. [CrossRef]
4. Maruchi, L.; Schaeffer, N.; Passos, H.; Mendonça, C.; Coutinho, J.; Jimenez, Y. Sustainable extraction and separation of rhenium and molybdenum from model copper mining effluents using a polymeric aqueous two-phase system. *ACS Sustain. Chem. Eng.* **2019**, *7*, 1778–1785. [CrossRef]
5. Ogata, T.; Takeshita, K.; Tsuda, K.; Mori, A. Solvent extraction of perrhenate ions with podand-type nitrogen donor ligands. *Sep. Purif. Technol.* **2009**, *68*, 288–290. [CrossRef]
6. Xiong, C.; Yao, C.; Wu, X. Adsorption of rhenium(VII) on 4-amino-1,2,4-triazole resin. *Hydrometallurgy* **2008**, *90*, 221–226. [CrossRef]
7. Chen, X.-R.; Zhang, C.-R.; Jiang, W.; Liu, X.; Luo, Q.-X.; Zhang, L.; Liang, R.-P.; Qin, J.-D. 3D Viologen-based covalent organic framework for selective and efficient adsorption of $ReO_4{}^-/TcO_4{}^-$. *Sep. Purif. Technol.* **2023**, *312*, 123409. [CrossRef]
8. Shimojo, K.; Suzuki, H.; Yokoyama, K.; Yaita, T.; Ikeda-Ohno, A. Solvent extraction of technetium (VII) and rhenium (VII) using a hexaoctylnitrilotriacetamide extractant. *Anal. Sci.* **2020**, *36*, 1435–1437. [CrossRef] [PubMed]

9. Zhou, X.; Wu, R.; Kang, J.; Fan, Y.; Huang, C.; Jin, Y.; Xia, C. Study on extraction behavior of Re(VII) with bis-triamide extractants. *Solvent Extr. Ion Exch.* **2022**, *40*, 571–589. [CrossRef]
10. Pan, X.; Zu, J.; Han, G.; Lin, S.; Diao, J.; Xue, Y. Efficient and rapid elimination of $^{99}TcO_4^-/ReO_4^-$ from medium-low level acid-wastewater using anion exchange adsorbent. *Sep. Purif. Technol.* **2023**, *322*, 124123. [CrossRef]
11. Xiong, Y.; Song, Y.; Zhang, P.; Wang, Y.; Lou, Z.; Zhang, F.; Shan, W. Adsorption-controlled preparation of anionic imprinted amino-functionalization chitosan for recognizing rhenium(VII). *Sep. Purif. Technol.* **2017**, *177*, 142–151. [CrossRef]
12. Hori, H.; Otsu, T.; Yasukawa, T.; Morita, R.; Ishii, S.; Asai, T. Recovery of rhenium from aqueous mixed metal solutions by selective precipitation: A photochemical approach. *Hydrometallurgy* **2019**, *183*, 151–158. [CrossRef]
13. Laatikainen, M.; Virolainen, S.; Paatero, E.; Sainio, T. Recovery of ReO_4^- by weakly basic anion exchangers: Modeling of sorption equilibrium and rate. *Sep. Purif. Technol.* **2015**, *153*, 19–28. [CrossRef]
14. Atanassova, M. Ordered mesoporous silicas containing imidazolium substructures for solid-liquid extraction of metallic anions ReO_4^-. *Russ. J. Inorg. Chem.* **2021**, *66*, 696–706. [CrossRef]
15. Travkin, V.; Antonov, A.; Kubasov, V.; Ishchenko, A.; Glubokov, Y. Extraction of rhenium(VII) and molybdenum(VI) with hexabutyltriamide of phosphoric acid from acid media. *Russ. J. Appl. Chem.* **2006**, *79*, 909–913. [CrossRef]
16. Batueva, T.; Radushev, A.; Tuktareva, T.; Degtev, M.; Nasrtdinova, T.; Karmanov, V. Rhenium(VII) extraction with 2-ethylhexanoic acid N,N-dialkylhydrazides from acidic solutions. *Russ. J. Inorg. Chem.* **2010**, *55*, 804–807. [CrossRef]
17. Gerhardt, N.; Palant, A.; Petrova, V.; Tagirov, R. Solvent extraction of molybdenum (VI), tungsten (VI) and rhenium(VII) by diisododecylamine from leach liquors. *Hydrometallurgy* **2001**, *60*, 1–5. [CrossRef]
18. Dukov, I.; Atanassova, M. High molecular weight amines and quaternary ammonium salts as synergistic agents in the solvent extraction of metal ions with chelating extractants. In *Handbook of Inorganic Chemistry Research*; Morrison, D.A., Ed.; Nova Science Publishers, Inc.: New York, NY, USA, 2010; Chapter 7; ISBN 978-1-61668-010-7.
19. Mikkola, J.-P.; Virtanen, P.; Sjöholm, R. Aliquat 336—A versatile and affordable cation source for an entirely new family of hydrophobic ionic liquid. *Green Chem.* **2006**, *8*, 250–255. [CrossRef]
20. Atanassova, M. Solvent extraction chemistry in ionic liquids: An overview of f-ions. *J. Mol. Liq.* **2021**, *343*, 117530. [CrossRef]
21. Genov, L.; Dukov, I.; Kassabov, G. Extraction von europium durch gemische von thenoyltrifluoroaceton and Aliquat 336. *Acta Chim. Acad. Sci. Hung.* **1977**, *95*, 361–365.
22. Dukov, I.; Genov, L. On the mechanism of the synergistic extraction of lanthanides with thenoyltrifluoroacetone and Aliquat-336S. *Acta Chim. Acad. Sci. Hung.* **1980**, *104*, 329–335.
23. Atanassova, M.; Jordanov, V.; Dukov, I. Effect of the quaternary ammonium salt Aliquat 336 on the solvent extraction of lanthanoid (III) ions with thenoyltrifluoroacetone. *Hydrometallurgy* **2002**, *63*, 41–47. [CrossRef]
24. Dukov, I.; Atanassova, M. Effect of the diluents on the synergistic solvent extraction of some lanthanides with thenoyltrifluoroacetone and quaternary ammonium salt. *Hydrometallurgy* **2003**, *68*, 89–96. [CrossRef]
25. Dukov, I.; Genov, L. Temperature effect on the synergistic solvent extaction of lanthanoides. *Solvent Extr. Ion Exch.* **1987**, *5*, 977–987. [CrossRef]
26. Jordanov, V.; Atanassova, M.; Dukov, I. Solvent extraction of lanthanides with 1-phenyl-3-methyl-4-benzoyl-5-pyrazolone. *Sep. Sci. Technol.* **2002**, *37*, 3349–3356. [CrossRef]
27. Atanassova, M. Synergistic solvent extraction and separation of lanthanide(III) ions with 4-benzoyl-3-phenyl-5-isoxazolone and the quaternary ammonium salt. *Solvent Extr. Ion Exch.* **2009**, *27*, 159–171. [CrossRef]
28. Ivanov, N.; Gindin, L.; Tchichagova, G. Izvestiya Sibirskogo otdeleniya Akademii nauk SSSR. *Seriya Khimicheskikh Nauk* **1967**, *3*, 100–104. (In Russian)
29. Goto, T. Extraction of lanthanoids by quaternary ammonium salts. *J. Inorg. Nucl. Chem.* **1969**, *31*, 1111–1119. [CrossRef]
30. Knight, A.; Chiarizia, R.; Soderholm, L. Extraction selectivity of a quaternary alkylammonium salt for trivalent actinides over trivalent lanthanides: Does extractant aggregation play a role? *Solvent Extr. Ion Exch.* **2017**, *35*, 266–279. [CrossRef]
31. Hoogerstraete, T.V.; Souza, E.R.; Onghena, B.; Banerjee, D.; Binnemans, K. Mechanism for solvent extraction of lanthanides from chloride media by basic extractants. *J. Solut. Chem.* **2018**, *47*, 1351–1372. [CrossRef]
32. Paatero, J. *Studies on the System Aliquat 336 in Xylene-Nickel(II) in Aqueous Chloride Solutions*; Part 1. Determination of the composition and average molecular weight of Aliquat 33. Vol. 34, n.1. abo Akademi, Acta Academie Aboensis, ser. B; Abo Academi: Abo, Finland, 1974.
33. Lerum, H.; Andersen, N.; Eriksen, D.; Hansen, E.; Petersen, D.; Wibetoe, G.; Omtvedt, J. Study of cadmium extraction with Aliquat 336 from highly saline solutions. *J. Solut. Chem.* **2018**, *47*, 1395–1417. [CrossRef]
34. Kasilkov, A.; Petrova, A. Recovery of rhenium(VII) with triisoactylamine from sulfuric acid solutions. *Russ. J. Applied Chem.* **2006**, *6*, 914–919. [CrossRef]
35. Stojanovic, A.; Morgenbesser, C.; Kogelnig, D.; Krochler, K.; Keppler, B. Quaternary ammonium amd phosphonium ionic liquids in chemical and environmental engineering. In *Ionic Liquids: Theory, Properties, New Approaches*; Kokorin, A., Ed.; IntechOpen: London, UK, 2011; Chapter 26; pp. 657–680.
36. Stojanovic, A.; Lämmerhofer, M.; Kogelnig, D.; Schiesel, S.; Sturm, M.; Galanski, M.; Krachler, R.; Keppler, B.; Lindner, W. Analysis of quaternary ammonium and phosphonium ionic liquids by reversed-phase high-performance liquid chromatography with charged aerosol detection and unified calibration. *J. Chromatogr. A* **2008**, *1209*, 179–187. [CrossRef]

37. Casas, J.M.; Sepúlveda, E.; Bravo, L.; Cifuentes, L. Crystallization of sodium perrhenate from $NaReO_4-H_2O-C_2H_5OH$ solutions at 298 K. *Hydrometallurgy* **2012**, *113−114*, 192–194. [CrossRef]
38. Vosough, M.; Shahtahmasebi, N.; Behdani, M. Recovery Rhenium from roasted dust through super Para-magnetic Nanoparticles. *Int. J. Refract. Hard Met. Hard Mater.* **2016**, *60*, 125–130. [CrossRef]
39. Nebeker, N.; Hiskey, J.B. Recovery of rhenium from copper leach solution by ion exchange. *Hydrometallurgy* **2012**, *125–126*, 64–68. [CrossRef]
40. Lessard, J.; Gribbin, D.; Shekhter, L. Recovery of rhenium from molybdenum and copper concentrates during the looping sulfide oxidation process. *Int. J. Refract. Hard Met. Hard Mater.* **2014**, *44*, 1–6. [CrossRef]
41. Amer, A. The hydrometallurgical extraction of rhenium from copper industrial wastes. *JOM* **2008**, *60*, 52–54. [CrossRef]
42. Jumeja, J.; Singa, S.; Bose, D. Investigations on the extraction of molybdenum and rhenium values from low grade molybdenite concentrate. *Hydrometallurgy* **1996**, *41*, 201–209. [CrossRef]
43. Safarbali, R.; Reza Yaftian, M.; Zamani, A. Solvent extraction-separation of La(III), Eu(III) and Er(III) ions from aqueous chloride medium using carbamoyl-carboxylic acid extractants. *J. Rare Earths* **2016**, *34*, 91–98. [CrossRef]
44. Li, Z.; Li, X.; Raiguel, S.; Binnemans, K. Separation of transition metals from rare earths by non-aqueous solvent extraction from ethylene glycol solutions using Aliquat 336. *Sep. Purif. Technol.* **2018**, *201*, 318–326. [CrossRef]
45. Atanassova, M.; Kukeva, R.; Kurteva, V. New sustainable solvent extraction pathways for rare earth metals via oximes molecules. *Molecules* **2023**, *28*, 7467. [CrossRef] [PubMed]
46. Ramachandra Reddy, B.; Kumar, J.; Varade Reddy, A. 3-Phenyl-4-acyl-isoxazolones as reagents for liquid-liquid extraction of tetravalent zirconium and hafnium from acidic chloride solutions. *J. Braz. Chem. Soc.* **2006**, *17*, 780–784. [CrossRef]
47. Kang, J.; Kim, Y.-U.; Joo, S.-H.; Yoon, H.-S.; Kumar, J.; Park, K.-H.; Parhi, P.; Shin, S. Behaviour of extraction, stripping and separation possibilities of rhenium and molybdenum from molybdenite roasting dust leaching solution using amine based extractant tri-octyl-amine. *Mater. Trans.* **2013**, *54*, 1209–1212. [CrossRef]
48. Sasaki, Y.; Kitatsuji, Y.; Kimura, T. Highly selective extraction of TcO_4^-, ReO_4^- and MoO_4^- by the new ligand 2,2′-(methylimino)bis(N,N-dioctylacetamide). *Chem. Lett.* **2007**, *36*, 1394–1395. [CrossRef]
49. Sasaki, Y.; Morita, K.; Shimazaki, S.; Tsubata, Y.; Ozawa, M. Masking effects for Mo, Re, Pd and Ru by S and N- donor reagents through MIDOA and NTaamide extraction. *Solvent Extr. Res. Dev. Jpn.* **2016**, *23*, 161–174. [CrossRef]

Disclaimer/Publisher's Note: The statements, opinions and data contained in all publications are solely those of the individual author(s) and contributor(s) and not of MDPI and/or the editor(s). MDPI and/or the editor(s) disclaim responsibility for any injury to people or property resulting from any ideas, methods, instructions or products referred to in the content.

molecules

MDPI

Article

Facile One-Pot Synthesis and Anti-Microbial Activity of Novel 1,4-Dihydropyridine Derivatives in Aqueous Micellar Solution under Microwave Irradiation

Asmita Goswami [1], Navneet Kaur [1], Manvinder Kaur [1], Kishanpal Singh [2], Harvinder Singh Sohal [1,*], Haesook Han [3] and Pradip K. Bhowmik [3]

[1] Medicinal and Natural Product Laboratory, Department of Chemistry, Chandigarh University, Mohali 140413, Punjab, India; asmitagoswami3@gmail.com (A.G.)
[2] Department of Chemistry, Punjabi University, Patiala 147002, Punjab, India; kishanpal.3112@gmail.com
[3] Department of Chemistry and Biochemistry, University of Nevada Las Vegas, 4505 S. Maryland Parkway, Box 454003, Las Vegas, NV 89154, USA; hanh3@unlv.nevada.edu (H.H.)
* Correspondence: drharvinder.cu@gmail.com

Abstract: The current study describes a novel and eco-conscious method to synthesize 1,4-dihydropyridine derivatives utilizing an aqueous micellar solution containing aluminum dodecyl sulfate, $Al(DS)_3$, using readily available starting material. The final products were synthesized with excellent yields within remarkably quick reaction durations, promoting remarkable atom economy and minimizing environmental impacts. The present protocol has several advantages over other methodologies in terms of high yield (up to 97%) with excellent purity. Further, the synthesized 1,4-DHPs exhibit favorable to excellent resistance against examined bacterial and fungal species. Intriguingly, polar groups on the phenyl ring (**5b**, **5c**, **5i** and **5j**) make the 1,4-DHPs equally potent against the microbes as compared to the standard drugs.

Keywords: multi-component reaction; 1,4-dihydropyridines; microwave; heterocyclic compounds; $Al(DS)_3$; green synthesis

1. Introduction

Researchers have long been intrigued by the biological properties of 1,4-dihydropyridines (1,4-DHPs). 1,4-DHPs constitute a significant category within the N-heterocyclic ring, consisting of a biologically vital nucleus that exhibits various important pharmacological properties and is used as an antibacterial, anticancer [1], anticoagulant, antileishmanial, anticonvulsant, antitubercular [2], antioxidant [3], antiulcer, antifertility, neuroprotection properties, antimalarials, HIV-1 protease inhibitor, antihypertensive [4], anti-atherosclerotic, hepato-protective, vasodilator, anti-mutagenic, bronchodilator, geroprotective, anti-tumor [5], and anti-diabetic agent [6]. Moreover, they constitute an essential category of agents that modulate calcium channels and have been widely employed in the treatment of cardiovascular disorders, exhibiting functions such as antihypertensive, antianginal, vasodilator, and cardiac depressant activities [7]. 1,4-DHP attracts more attention, due to its bioactivity and presence in coenzymes, diphosphate pyridine nucleotide (DPNH). In the pharmaceutical field, DHPs are already commercialized as amlodipine, felodipine, isradipine [8], lacidipine [9], nicardipine [10], nitrendipine [11], nifedipine, and nemadipine B [12], among them, nitrendipine and nemadipine B stand out for their potent calcium channel blocking activities.

In general, 1,4-DHPs are synthesized using multicomponent reactions, where a combination of β-keto-ester, aldehyde, as well as ammonia undergoes reaction to produce the required DHPs. Arthur Hantzsch described the first one-pot formation of symmetrically substituted 1,4-DHP in the year 1882 [13]. The Hantzsch reaction proved to be

the most widely used protocol to access 1,4-DHPs and its numerous biologically active derivatives [14]. But due to drawbacks *such as* harsh reaction conditions, long reaction time, and generally low yield of products, new modifications were made to it to obtain the targeted compounds,1,4-DHPs, in good to excellent yields [15]. It has been reported that in multicomponent reactions (MCRs), a wide variety of catalysts has been studied for the production of 1,4-DHP derivatives, encompassing various Lewis or Bronsted acids *such as* $Y(OTf)_3$ [16], free nano-Fe_2O_3 [17], TMU-33 [18], $InCl_3$ [19]; heterogeneous catalyst *such as* $HClO_4$–SiO_2 [20], PdRuNi@GO NPs [7], zeolite [21], IRMOF-3 [22]; organ catalyst, CAN [23], Montmorillonite K10 clay [24], $HClO_4$-SiO_2 [25], tetrabutylammonium hydrogen sulfate, sodium- and Cs-Norit carbons, fermenting Baker's yeast [26], metal triflates with the incorporation of numerous methodologies *such as* stirring [2], conventional heating [27], refluxing [22], microwave [1], visible light [4], and ultrasound irradiations [21]. Researchers are now focusing on the green aspects of this reaction leading to the usage of various green solvents such as glycerol [18], water [19], and ionic liquids [6]. Unless otherwise stated, aqueous surfactant solutions, as well as neat conditions, have also been incorporated to obtain the required products.

Persisting on our work, in the present work, we describe the synthesis of novel 1,4-DHP scaffolds using a one-pot method using an aqueous micellar solution as a greener solvent. The microwave-assisted reaction method stands out as superior due to its rapid reaction times, cost-effectiveness, and straightforward operational procedures compared to other methods. To begin our investigation into a sustainable and effective approach for synthesizing 1,4-DHPs, we commenced by employing a catalytic quantity of $Al(DS)_3$ with a combination of substituted benzaldehyde, diethyl acetylene dicarboxylate, and either ammonium acetate or aniline, along with malononitrile under microwave irradiations at ambient temperature.

2. Result and Discussion

2.1. Characterization of Aluminum Dodecyl Sulfate, $Al(DS)_3$

2.1.1. SEM Characterization

The SEM images depicted in Figure 1a–f, magnified from 500 to 7500 times, provide valuable insights into the morphology of the $Al(DS)_3$ surfactant. This compound was produced as dense aggregates (Figure 1a) which are irregular in shape. At higher magnifications, it becomes evident that randomly organized microplates arranged to compose the micro-objects are in an edge-to-face style (Figure 1a–d).

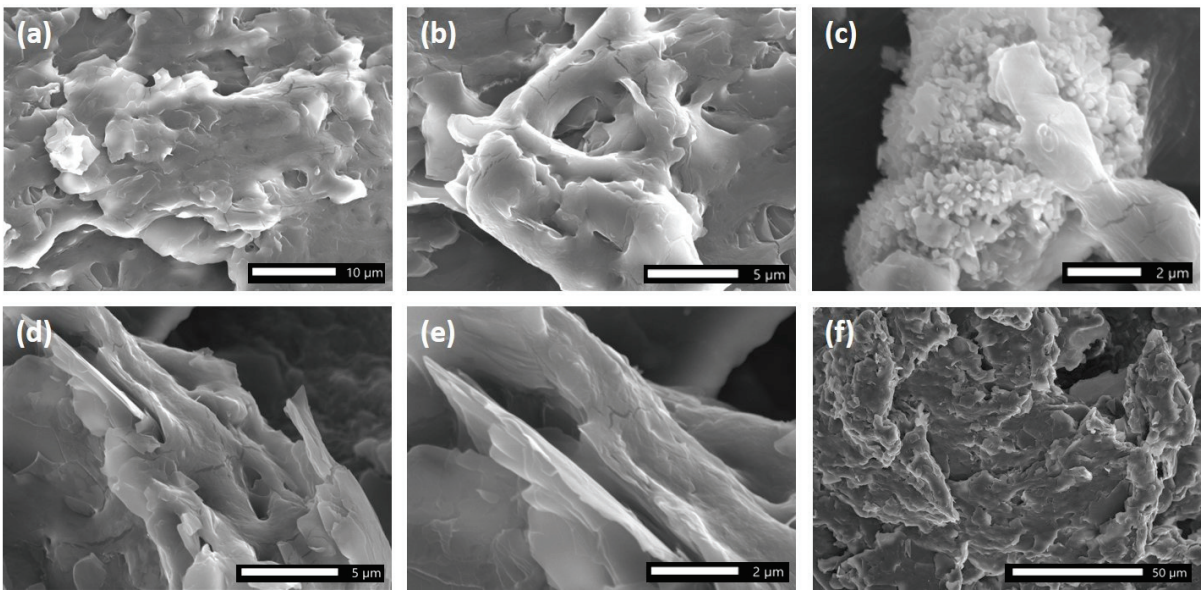

Figure 1. SEM images of $Al(DS)_3$.

Based on the elemental investigation conducted on microscopic sectors of $Al(DS)_3$ using EDS (as shown in Figure S1), the atomic percentages of Al and S were determined to be 22.40% and 77.60%, respectively, which indicates a 1:3 stoichiometry.

2.1.2. XRD Characterization

The XRD patterns in the range of 2θ = 5–25° for the $Al(DS)_3$ sample are shown in Figure 2. The prepared sample of Al(DS)3 gave rise to XRD peaks at 2θ = 6.596, 7.184, 10.965, 13.166, 17.587, 20.387, 20.674, and 21.875, corresponding to (110), (110), (111), (111), (200), (210), (211), (211), and (211) diffraction peaks, respectively. According to the above data, the XRD patterns of $Al(DS)_3$ show a prominent diffraction peak at (110) with preferential orientation around 2θ = 6.596° with 100% relative intensity, which shows a reasonable degree of crystallinity of 65.3%.

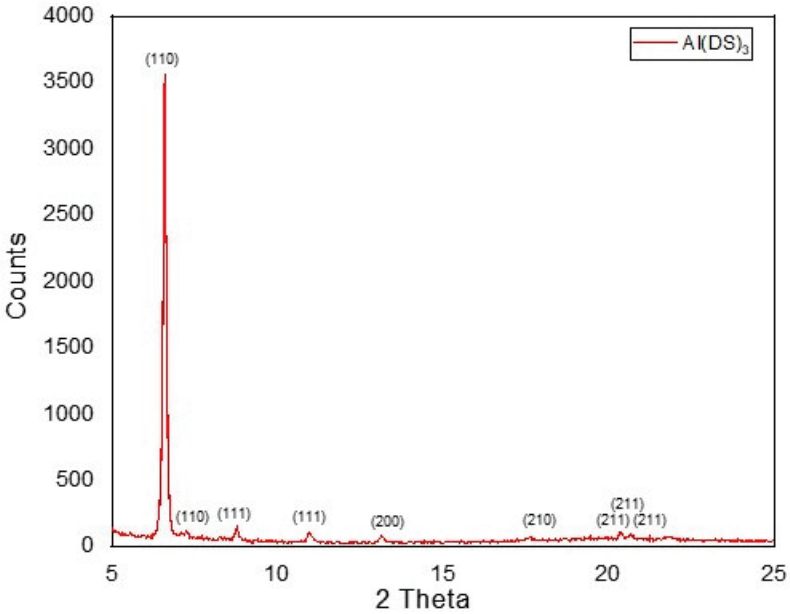

Figure 2. XRD images of $Al(DS)_3$.

*2.2. Preparation of [1,4-DHPs] 10-Amino-3,3,6,6-Tetramethyl-9-Aryl-3,4,6,7,9,10-Hexa-Hydroacridine-1,8(2H,5H)-Dione Derivatives (**5a–n**) Using $Al(DS)_3$*

Various solvents, including water, ethanol, ethanolic solution of *p*-TSA, glycerol, aqueous solution of SDS, and aqueous solution $Al(DS)_3$, were employed for the condensation of benzaldehyde **1**, dialkyl acetylene dicarboxylate **2**, ammonium acetate **3**, and malononitrile **4**. Among these, water as a solvent proved to be the most effective, as indicated in Table 1. The maximum yield was achieved through an $Al(DS)_3$ + water catalyst system.

Table 1. Impact of solvents on production of the **5a–h**.

Solvent	Time (min)	Yield [a] (%)
Ethanol	10	87%
Glycerol	8	91%
p-TSA + Ethanol	8	89%
PEG	9	90%
Water	15	42%
$Al(DS)_3$ + Water	5	97%
SDS + Water	6	92%
CH_3CN	6	95%
Ethylene glycol	8	94%

[a] Reactions supported using various solvents. Reactions occurred at 100 °C in MW irradiation.

Table 2 illustrates the optimal temperature for a reaction carried out in an aqueous micellar solution and it was also observed that increasing the temperature has a significant increase in yield with time. Conversely, further temperature increases, result in a decrease in product yield as the products start decomposing at higher temperatures.

Table 2. Impact of pressure on the percentage yield of **5a**–**h** using $Al(DS)_3$ in water.

Watt	Time (min)	Yield [a] (%)
65	8	93%
70	7	93%
75	6	95%
80	5	97%
85	4	91%
90	3	88%
95	2	85%

[a] Yield refers to the combined yield of all crops.

Similarly, various other aldehydes **3b**–**g** will undergo reactions with diethyl acetylene dicarboxylate, malononitrile, and either ammonium acetate or aniline using the same procedure, with the formation monitored by TLC and melting point analysis. The reactions proceed smoothly even in the company of various electron-donating (-Me and -OMe) as well as electron-withdrawing substituents (-NO_2) on the aldehyde, facilitating efficient reactions. The effectiveness of this method is notable, yielding high percentages (92–97%) for the final products.

*2.3. Characterization of Diethyl 6-Amino-5-Cyano-4-Phenyl-1,4-Dihydropyridine-2,3-Dicarboxylate (**5a**) Using $Al(DS)_3$*

The structural elucidation of the novel scaffold is accomplished by using various spectroscopic methods such as FTIR, ^{1}H NMR, ^{13}C NMR, Mass, and elemental analysis. In the series, the IR spectra of compound **5a** reveal three significant absorptions at 3360.7, 2250.6, and 1740.5 cm^{-1} corresponding to the N-H, C≡N, and C=O groups stretching. In ^{1}H NMR spectra (500 MHz, $CDCl_3$) of compound **5a**, three singulets at δ 11.94, 6.59, and 4.54 were observed for NH, NH_2, and CH, respectively, confirming the formation of 1,4-DHP. The multiplet for 5 protons was at δ 7.13–7.27 for the phenyl ring attached at the C-4 position. One quadruplet and one triplet at δ 4.17–4.13 and 0.90–0.91 were observed for CH_2 and CH_3 protons of ester linkage.

In ^{13}C, NMR spectra of molecule **5a**, most down-shielded peaks at δ 190.26 and 189.73 ppm were observed for the C=O group. Peaks at δ 160.57, 157.91, 154.74, 153.24, and 54.77 ppm were observed for C-2, C-6, C-3, C-5, and C-4 carbon atoms of the main 1,4-DHP skeleton, whereas carbon atoms belonging to the aromatic region were observed at δ 136.15 (C-1′), 135.43 (C-2′ and C-6′), 128.34 (C-3′ and C-5′), and 120.71 (C-4′) ppm. The peaks for C≡N and other sp^3 carbons were observed at the appropriate position. Furthermore, ESI-MS fragmentation Pattern and Elemental analysis also support the formation of final 1,4-DHP derivatives. The spectral data of compound **5a** strongly corroborates the assigned structure.

2.4. Anti-Microbial Activity

The novel synthesized compounds **5a**–**n** underwent testing against two Gram-positive bacteria (*Streptococcus pyogenes* MTCC 442, and *Bacillus subtilis* MTCC 441), three Gram-negative bacteria (*Klebsiella pneumonia* MTCC 3384, *Escherichia coli* MTCC 443, and *Staphylococcus aureus* MTCC 96), as well as three fungal strains (*Aspergillus niger* MTCC 281, *Aspergillus janus* MTCC 2751, and *Aspergillus sclerotiorum* MTCC 1008). Fungal strains were cultivated in malt extract medium prior to inoculation for a duration of 72 h at 28 °C, whereas bacterial samples were grown in nutrient broth for 24 h at 37 °C. Each synthesized chemical underwent triplicate testing after being dissolved in DMSO at concentrations of 2, 4, 8, 16, 32, 64, and 128 g/mL using a serial dilution procedure.

3. Experimental Section

3.1. Materials and Methods

3.1.1. Chemicals

All chemicals used in this study were obtained from Sigma-Aldrich (St. Louis, MO, USA) which were employed without additional distillation, while the solvents were ordered from Loba Chemie (Mumbai, India).

3.1.2. Analytical Instruments

The digital melting point apparatus was employed to measure the melting point of all the resulting products via the open capillary method. IR spectra of the targeted compound were taken using ATR mode on Perkin Elmer (Waltham, MA, USA) Spectrum II. NMR such as ^{1}H and ^{13}C are collected on a Bruker (Billerica, MA, USA) Avance NEO 500 MHz NMR spectrometer using DMSO as solvent. Chemical shifts (δ) are accounted for in ppm relative to that of TMS as an internal standard. The mass spectroscopy was recorded on LC-MS Spectrometer Model Q-ToF Micromass Thermo Scientific (Waltham, MA, USA) (FLASH 2000) CHN Elemental Analyser is used for fundamental analysis. The thin layer chromatographic (TLC) technique was used to observe the reaction time as well as to check the purity of the compound, and then the visualization of TLC was performed with the help of a UV chamber. XRD patterns of the dried (lyophilized) samples were captured at room temperature using a Bruker D8 advance. The compounds were exposed to monochromatic Cu-Kα radiation (λ = 1.5418 Å, 50 kV, 40 mA) across the 2θ range between <1 and >150°, with steps of 0.02°. SEM micrographs were obtained utilizing a JSM IT500 scanning electron microscope. Elemental analysis on microscopic sections of the $Al(DS)_3$ sample was conducted via EDS. SEM images were acquired under high vacuum mode, ranging from 30 nm (30 kV) to 15.0 nm (1.0 kV).

3.2. Synthesis of Aluminum Dodecyl Sulfate

The preparation of aluminum dodecyl sulfate was conducted following the procedure outlined in the literature (Scheme 1) [28]. Anhydrous $AlCl_3$ (0.1 mol) and sodium dodecyl sulfate (SDS) (0.3 mol) were dissolved using the minimum amount of water required. The solutions were gradually diluted with continuous stirring at room temperature, resulting in the precipitation of a colorless solid. This solid was filtered to isolate the solid $Al(DS)_3$.

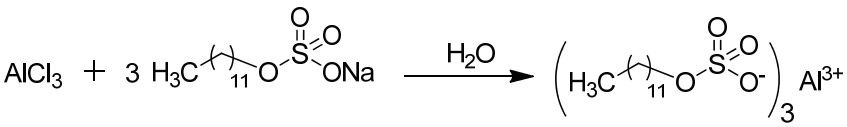

Scheme 1. Preparation of $Al(DS)_3$ in water.

*3.3. Synthesis of 1,4-DHPs Derivatives (**5a–n**)*

Using $Al(DS)_3$ catalyst (5 mole%), a mixture composed of substituted benzaldehyde (5 mmol), diethyl acetylene dicarboxylate (5 mmol), and either ammonium acetate or aniline (5 mmol), along with malononitrile (5 mmol), was subjected to MW irradiation at 80 watts for 5 min in H_2O (Scheme 2). The reaction's progress was monitored using TLC (Merck, Darmstadt, Germany) (EtOAc: Toluene; 8:2). After determining that the reaction had concluded, the mixture was cooled to ambient temperature, filtered, rinsed with water, and subsequently subjected to extraction using ethyl acetate. Subsequently, the resulting solid was recrystallized using ethyl alcohol to yield colorless crystals with an efficiency of 93–97%.

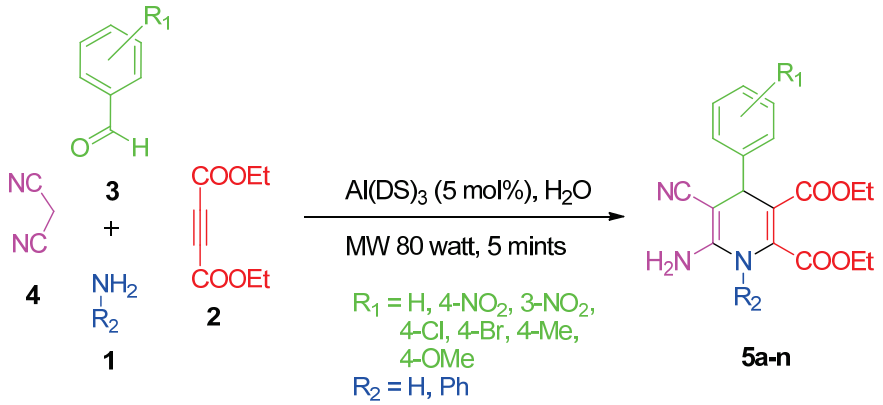

Scheme 2. Synthesis of 1,4-DHPs using $Al(DS)_3$ in water under microwave radiations.

By the optimized reaction conditions, a diversity of 1,4-DHP was prepared using various substituted aldehydes in aqueous micellar solution under MW irradiations at 80 watts for 5 min (Table 3).

Table 3. 1,4-DHP derivatives **5a–n** synthesis using $Al(DS)_3$ + water for 5 mints under MW radiations.

Compound	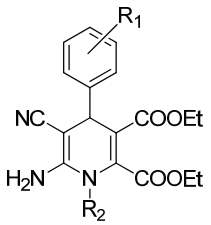		Rf	Yield (%)	Melting Point (°C)	Literature Melting Point (°C)
	R_1	R_2				
5a	H	H	0.65	97	227–228	-
5b	4-NO_2	H	0.77	96	240	-
5c	3-NO_2	H	0.73	94	242	-
5d	4-Cl	H	0.70	94	237–239	-
5e	4-Br	H	0.57	95	267–268	-
5f	4-Me	H	0.61	93	230–231	-
5g	4-OMe	H	0.63	94	238–240	-
5h	H	Ph	0.66	96	173–174	170–172 [29]
5i	4-NO_2	Ph	0.69	94	171–173	172–174 [30]
5j	3-NO_2	Ph	0.71	95	270–272	-
5k	4-Cl	Ph	0.67	96	186–187	188–189 [31]
5l	4-Br	Ph	0.60	96	151–153	152–154 [32]
5m	4-Me	Ph	0.61	93	286–287	-
5n	4-OMe	Ph	0.65	92	253–255	-

diethyl 6-amino-5-cyano-4-phenyl-1,4-dihydropyridine-2,3-dicarboxylate (**5a**): Yield 97%, colorless crystals, mp 227–228 °C. IR spectrum, ν, cm^{-1}: 3360.7 (N-H **stretch**, -NH_2), 2250.6 (C≡N), 1740.5 (C=O stretch). ^1H NMR spectrum, δ, ppm (*J*, Hz): 11.94 (*s*, 1H, NH), 7.13–7.27 (m, 5H, Ar-H), 4.54 (*s*, 1H, CH), 6.59 (*s*, 1H, NH_2), 4.17–4.13 (*q*, 4H, CH_2), 0.90–0.91 (*t*, 6H, CH_3). ^{13}C NMR spectrum, δ, ppm: 190.26, 189.73, 160.57, 157.91, 154.74, 153.24, 136.47, 135.43, 128.34, 120.71, 113.47, 54.77, 57.95, 57.96, 13.72, 13.51. Mass spectrum, m/z (I_{rel}, %): 342.138 (M + 1), Found: 342.136. Anal. calcd. for $C_{18}H_{19}N_3O_4$: C, 63.33; H, 5.61; N, 12.31%.

diethyl 6-amino-5-cyano-4-(4-nitrophenyl)-1,4-dihydropyridine-2,3-dicarboxylate (**5b**): Yield 96%, colorless crystals, mp 240 °C. IR spectrum, ν, cm^{-1}: 3361.1 (N-H stretch, -NH_2), 2251.3 (C≡N), 1740.7 (C=O stretch). ^1H NMR spectrum, δ, ppm (*J*, Hz): 12.23 (*s*, 1H, NH), 7.66–7.97 (m, 4H, Ar-H), 4.46 (*s*, 1H, CH), 6.89 (*s*, 1H, NH_2), 4.16–4.12 (*q*, 4H, CH_2), 1.19–1.20 (*t*, 6H,

CH_3). ^{13}C NMR spectrum, δ, ppm: 190.52, 190.07, 160.85, 158.23, 155.07, 153.57, 136.77, 135.78, 128.63, 121.03, 113.75, 55.03, 58.28, 58.27, 14.03, 13.86. Mass spectrum, m/z (I_{rel}, %): 387.123 (M + 1), Found: 387.122. Anal. calcd. for $C_{18}H_{18}N_4O_6$: C, 55.96; H, 4.70; N, 14.50%.

diethyl 6-amino-5-cyano-4-(3-nitrophenyl)-1,4-dihydropyridine-2,3-dicarboxylate (**5c**): Yield 94%, colorless crystals, mp 242 °C. IR spectrum, ν, cm^{-1}: 3361.3 (N-H stretch, -NH_2), 2251.6 (C≡N), 1741.1 (C=O stretch). ^1H NMR spectrum, δ, ppm (*J*, Hz): 12.10 (*s*, 1H, NH), 7.58–8.12 (m, 4H, Ar-H), 4.81 (*s*, 1H, CH), 6.85 (*s*, 1H, NH_2), 4.49–4.53 (*q*, 4H, CH_2), 1.14–1.15 (*t*, 6H, CH_3). ^{13}C NMR spectrum, δ, ppm: 190.41, 189.99, 160.74, 158.17, 154.93, 153.42, 136.64, 135.63, 128.55, 120.97, 113.61, 58.11, 58.10, 54.92, 13.94, 13.74. Mass spectrum, m/z (I_{rel}, %): 387.123 (M + 1), Found: 387.122. Anal. calcd. for $C_{18}H_{18}N_4O_6$: C, 55.96; H, 4.70; N, 14.50%.

diethyl 6-amino-4-(4-chlorophenyl)-5-cyano-1,4-dihydropyridine-2,3-dicarboxylate (**5d**): Yield 94%, colorless crystals, mp 237–239 °C. IR spectrum, ν, cm^{-1}:3361.6 (N-H stretch, -NH_2), 2251.7 (C≡N), 1741.5 (C=O stretch). ^1H NMR spectrum, δ, ppm (*J*, Hz): 12.31 (*s*, 1H, NH), 7.60–7.87 (m, 4H, Ar-H), 4.76 (*s*, 1H, CH), 6.93 (*s*, 1H, NH_2), 4.09–4.13 (*q*, 4H, CH_2), 1.16–1.17 (*t*, 6H, CH_3). ^{13}C NMR spectrum, δ, ppm: 190.68, 190.18, 160.96, 158.35, 155.09, 153.65, 136.91, 135.95, 128.81, 121.18, 113.97, 58.35, 58.37, 55.14, 14.26, 14.04. Mass spectrum, m/z (I_{rel}, %): 376.099 (M + 1);377.099 (M + 2), Found: 376.098(M + 1); 377.098 (M + 2). Anal. calcd. for $C_{18}H_{18}N_3BrO_4$: C, 57.53; H, 4.83; N, 11.18%.

diethyl 6-amino-4-(4-bromophenyl)-5-cyano-1,4-dihydropyridine-2,3-dicarboxylate (**5e**): Yield 95%, colorless crystals, mp 267–268 °C. IR spectrum, ν, cm^{-1}: 3361.9 (N-H stretch, -NH_2), 2251.9 (C≡N), 1741.6 (C=O stretch). ^1H NMR spectrum, δ, ppm (*J*, Hz): 12.27 (*s*, 1H, NH), 7.52–7.73 (m, 4H, Ar-H), 4.85 (*s*, 1H, CH), 6.90 (*s*, 1H, NH_2), 4.51–4.54 (*q*, 4H, CH_2), 1.13–1.12 (*t*, 6H, CH_3). ^{13}C NMR spectrum, δ, ppm: 190.62, 190.05, 160.91, 158.30, 155.01, 153.61, 136.73, 135.72, 128.58, 121.11, 113.79, 58.31, 58.32, 55.11, 14.20, 13.96. Mass spectrum, m/z (I_{rel}, %): 420.048 (M + 1); 421.048 (M + 2), Found: 420.047; 421.047 (M + 2). Anal. calcd. for $C_{18}H_{18}N_3ClO_4$: C, 51.44; H, 4.32; N, 10.00%.

diethyl 6-amino-5-cyano-4-p-tolyl-1,4-dihydropyridine-2,3-dicarboxylate (**5f**): Yield 93%, colorless crystals, mp 230–231 °C. IR spectrum, ν, cm^{-1}: 3361.0 (N-H stretch, -NH_2), 2250.9 (C≡N), 1740.9 (C=O stretch). ^1H NMR spectrum, δ, ppm (*J*, Hz): 12.15 (*s*, 1H, NH), 7.09–7.41 (m, 4H, Ar-H), 4.87 (*s*, 1H, CH), 6.87 (*s*, 1H, NH_2), 4.50–4.52 (*q*, 4H, CH_2), 2.15 (*s*, 3H, CH_3), 0.89–0.91 (*t*, 6H, CH_3). ^{13}C NMR spectrum, δ, ppm: 190.33, 189.78, 160.79, 158.09, 154.87, 153.48, 136.51, 135.57, 128.42, 120.83, 113.56, 58.01, 58.03, 54.96, 13.95, 13.71. Mass spectrum, m/z (I_{rel}, %): 356.153 (M + 1), Found: 356.151. Anal. calcd. for $C_{19}H_{21}N_3O_4$: C, 64.21; H, 5.96; N, 11.82%.

diethyl 6-amino-5-cyano-4-(4-methoxyphenyl)-1,4-dihydropyridine-2,3-dicarboxylate (**5g**): Yield 94%, colorless crystals, mp 238–240 °C. IR spectrum, ν, cm^{-1}: 3360.9 (N-H stretch, -NH_2), 2250.8 (C≡N), 1741.3 (C=O stretch). ^1H NMR spectrum, δ, ppm (*J*, Hz): 12.01 (*s*, 1H, NH), 7.19–7.49 (m, 4H, Ar-H), 4.79 (*s*, 1H, CH), 6.67 (*s*, 1H, NH_2), 4.07–4.09 (*q*, 4H, CH_2), 3.89 (*s*, 3H, OCH_3), 1.11–1.13 (*t*, 6H, CH_3). ^{13}C NMR spectrum, δ, ppm: 190.09, 189.63, 160.47, 157.83, 154.65, 153.13, 136.38, 135.32, 128.28, 120.64, 113.39, 57.83, 57.81, 54.65, 13.66, 13.50. Mass spectrum, m/z (I_{rel}, %): 372.148 (M + 1) Found: 372.146. Anal. calcd. for $C_{19}H_{21}N_3O_5$: C, 61.45; H, 5.70; N, 11.31%.

diethyl 6-amino-5-cyano-1,4-diphenyl-1,4-dihydropyridine-2,3-dicarboxylate (**5h**): Yield 96%, colorless crystals, mp 170–172 °C. IR spectrum, ν, cm^{-1}: 3362.3 (N-H stretch, -NH_2), 2252.5 (C≡N), 1742.1 (C=O stretch). ^1H NMR spectrum, δ, ppm (*J*, Hz):6.85–8.12 (m, 10H, Ar-H), 4.58 (*s*, 1H, CH), 6.95 (*s*, 1H, NH_2), 4.40–4.47 (*q*, 4H, CH_2),2.13–2.14 (*t*, 6H, CH_3). ^{13}C NMR spectrum, δ, ppm: 190.49, 189.99, 160.93, 158.33, 155.12, 153.65, 137.20, 136.87, 136.24, 135.83, 129.15, 128.74, 121.23,121.13, 113.81, 58.36, 58.35, 54.17, 14.12, 13.92. Mass spectrum, m/z (I_{rel}, %): 417.169 (M + 1) Found: 417.167. Anal. calcd. for $C_{24}H_{23}N_3O_4$: C, 69.05; H, 5.55; N, 10.07%.

diethyl 6-amino-5-cyano-4-(4-nitrophenyl)-1-phenyl-1,4-dihydropyridine-2,3-dicarboxylate (**5i**): Yield 94%, colorless crystals, mp 171–173 °C. IR spectrum, ν, cm^{-1}: 3362.6 (N-H stretch, -NH_2), 2252.8 (C≡N), 1742.5 (C=O stretch). ^{1}H NMR spectrum, δ, ppm (*J*, Hz): 7.33–8.63 (m, 9H, Ar-H), 4.51 (*s*, 1H, CH), 7.31 (*s*, 1H, NH_2), 4.46–4.50 (*q*, 4H, CH_2), 2.15–2.16 (*t*, 6H, CH_3). ^{13}C NMR spectrum, δ, ppm: 190.96, 190.47, 161.24, 158.61, 155.48, 153.94, 137.47, 137.17, 136.51, 136.17, 129.31, 129.03, 121.55,121.45, 114.12, 58.68, 58.67, 55.43, 14.43, 14.27. Mass spectrum, *m*/*z* (I_{rel}, %): 462.154 (M + 1) Found: 462.153. Anal. calcd. for $C_{24}H_{22}N_4O_6$: C, 62.33; H, 4.79; N, 12.12%.

diethyl 6-amino-5-cyano-4-(3-nitrophenyl)-1-phenyl-1,4-dihydropyridine-2,3-dicarboxylate (**5j**): Yield 95%, colorless crystals, mp 270–272 °C. IR spectrum, ν, cm^{-1}: 3362.8 (N-H stretch, -NH_2), 2252.9 (C≡N), 1742.7 (C=O stretch). ^{1}H NMR spectrum, δ, ppm (*J*, Hz): 7.27–8.15 (m, 9H, Ar-H), 4.92 (*s*, 1H, CH), 7.27 (*s*, 1H, NH_2), 4.47–4.51 (*q*, 4H, CH_2), 1.52–1.53 (*t*, 6H, CH_3). ^{13}C NMR spectrum, δ, ppm: 190.81, 190.41, 161.17, 158.54, 155.36, 153.87, 137.45, 137.04, 136.57, 136.12, 129.26, 128.96, 121.49, 121.40, 114.07, 58.52, 58.51, 55.32, 14.31, 14.19. Mass spectrum, *m*/*z* (I_{rel}, %): 463.154 (M + 1) Found: 463.153. Anal. calcd. for $C_{24}H_{22}N_4O_6$: C, 62.33; H, 4.79; N, 12.12%.

diethyl 6-amino-4-(4-chlorophenyl)-5-cyano-1-phenyl-1,4-dihydropyridine-2,3-dicarboxylate (**5k**): Yield 96%, colorless crystals, mp 186–187 °C. IR spectrum, ν, cm^{-1}: 3363.2 (N-H stretch, -NH_2), 2253.1 (C≡N), 1742.9 (C=O stretch). ^{1}H NMR spectrum, δ, ppm (*J*, Hz): 7.30–7.81 (m, 9H, Ar-H), 4.86 (*s*, 1H, CH), 7.34 (*s*, 1H, NH_2), 4.48–4.52 (*q*, 4H, CH_2), 1.78–1.79 (*t*, 6H, CH_3). ^{13}C NMR spectrum, δ, ppm: 191.07, 190.58, 161.33, 158.79, 155.49, 154.16, 137.74, 137.32, 136.89, 136.36, 129.38, 129.27, 121.71, 121.62, 114.35, 58.75, 58.74, 55.54,14.66, 14.41. Mass spectrum, *m*/*z* (I_{rel}, %): 452.130 (M + 1); 453.130 (M + 1) Found: 452.128 (M + 1); 453.128 (M + 2). Anal. calcd. for $C_{24}H_{22}ClN_3O_4$: C, 63.79; H, 4.91; N, 9.30%.

diethyl 6-amino-4-(4-bromophenyl)-5-cyano-1-phenyl-1,4-dihydropyridine-2,3-dicarboxylate (**5l**): Yield 96%, colorless crystals, mp 151–153 °C. IR spectrum, ν, cm^{-1}:3363.5 (N-H stretch, -NH_2), 2253.3 (C≡N), 1743.1 (C=O stretch). ^{1}H NMR spectrum, δ, ppm (*J*, Hz): 7.21–7.69 (m, 9H, Ar-H), 4.95 (*s*, 1H, CH), 7.32 (*s*, 1H, NH_2), 4.48–4.51 (*q*, 4H, CH_2), 1.67–1.68 (*t*, 6H, CH_3). ^{13}C NMR spectrum, δ, ppm: 191.02, 190.45, 161.21, 158.72, 155.41, 154.02, 137.52, 137.15, 136.50, 136.19, 129.24, 128.98, 121.68, 121.56, 114.29, 58.72, 58.71, 55.51, 14.60, 14.31. Mass spectrum, *m*/*z* (I_{rel}, %): 496.079 (M + 1); 497.079 (M + 2) Found: 496.075(M + 1); 497.075 (M + 2). Anal. calcd. for $C_{24}H_{22}BrN_3O_4$: C, 58.07; H, 4.47; N, 8.47%.

diethyl 6-amino-5-cyano-1-phenyl-4-p-tolyl-1,4-dihydropyridine-2,3-dicarboxylate (**5m**): Yield 93%, colorless crystals, mp 286–287 °C. IR spectrum, ν, cm^{-1}:3362.5 (N-H stretch, -NH_2), 2252.1 (C≡N), 1742.6 (C=O stretch). ^{1}H NMR spectrum, δ, ppm (*J*, Hz): 6.97–7.93 (m, 9H, Ar-H), 4.96 (*s*, 1H, CH), 7.29 (*s*, 1H, NH_2), 4.47–4.49 (*q*, 4H, CH_2), 2.10–2.12 (*t*, 6H, CH_3), 2.17 (*s*, 3H, CH_3). ^{13}C NMR spectrum, δ, ppm: 190.73, 190.13, 161.11, 158.44, 155.28, 153.89, 137.33, 136.93, 136.32, 135.95, 129.17, 128.82, 121.37, 121.21, 113.96, 58.43, 58.41, 55.37, 14.35, 14.10. Mass spectrum, *m*/*z* (I_{rel}, %): 432.185 (M + 1) Found: 432.176. Anal. calcd. for $C_{25}H_{25}N_3O_4$: C, 69.59; H, 5.84; N, 9.74%.

diethyl 6-amino-5-cyano-4-(4-methoxyphenyl)-1-phenyl-1,4-dihydropyridine-2,3-dicarboxylate (**5n**): Yield 92%, colorless crystals, mp 253–255 °C. IR spectrum, ν, cm^{-1}: 3362.7 (N-H stretch, -NH_2), 2252.4 (C≡N), 1742.3 (C=O stretch). ^{1}H NMR spectrum, δ, ppm (*J*, Hz): 7.08–7.95 (m, 9H, Ar-H), 4.89 (*s*, 1H, CH), 7.05 (*s*, 1H, NH_2), 4.39–4.45 (*q*, 4H, CH_2),3.95 (*s*, 3H, OCH_3), 1.93–1.94 (*t*, 6H, CH_3). ^{13}C NMR spectrum, δ, ppm: 190.47, 190.04, 160.93, 158.25, 155.07, 153.43, 137.19, 136.79, 136.18, 135.71, 128.99, 128.68, 121.16, 121.09, 113.79, 58.23, 58.21, 55.05, 14.08, 13.87. Mass spectrum, *m*/*z* (I_{rel}, %): 448.179 (M + 1) Found: 448.166. Anal. calcd. for $C_{25}H_{25}N_3O_5$: C, 67.10; H, 5.63; N, 9.39%.

3.4. Plausible Mechanism

As per literature [32], a conceivable mechanism can be reasonably suggested for the production of pyran pyrazole **5a** from the four-component reaction between aniline **1**, di-

ethyl acetylene dicarboxylate **2**, substituted benzaldehyde **3**, and malononitrile **4** (Scheme 3). The hypothesis suggests that the substituted benzaldehyde **3** may undergo activation by water, leading to increased electrophilicity of the carbonyl carbon. It is suggested that this process involves the establishment of hydrogen bonds between the oxygen atom of the carbonyl group and water molecules, while simultaneously, hydrogen bonds form between the acidic hydrogen of malononitrile and the oxygen of water. Following this, Knoevenagel condensation takes place [33], resulting in the generation of an intermediate **7**. Subsequently, aniline **1** reacts with diethyl acetylene dicarboxylate **2**, resulting in the generation of enolate intermediate **6**. Afterward, the Michael reaction takes place between intermediate **6** and intermediate **7**, which leads to the generation of transient intermediate [34] **8** which undergoes intramolecular cyclization, followed by tautomerization, ultimately resulting in the formation of the target compound, the 1,4-dihydropyridine derivative **9**.

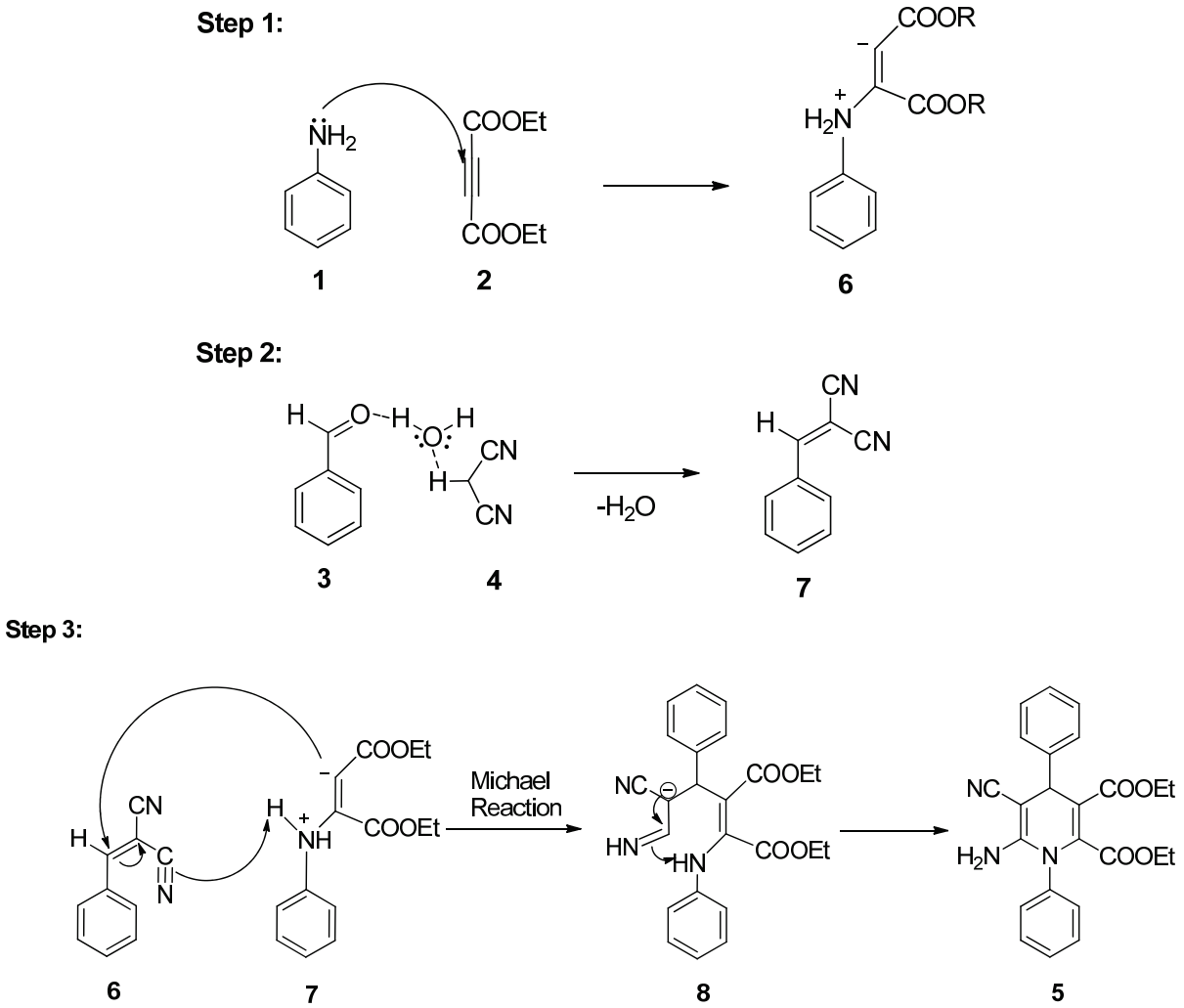

Scheme 3. Plausible mechanism for synthesis of 1,4-DHPs using $Al(DS)_3$ in water under microwave radiations.

3.5. Anti-Microbial Activity

The antimicrobial activities of the synthesized compounds **5a**–**n** were evaluated using the Minimum Inhibitory Concentration (MIC) method. The results were compared to the reference drugs Fluconazole and Amoxicillin, with concentrations of 4 g/mL and 2 g/mL, respectively, in their respective areas of application. Table 4 shows that compound **5a**–**n** exhibits moderate to excellent resistance against the tested strains. 1,4-DHPs with polar electron-withdrawing groups (**5b**, **5c**, **5i**, and **5j**) attached to the phenyl ring at position

4 exhibited effectiveness against all the tested strains, comparable to the standard drugs Amoxicillin (MIC 4 µg/mL) and Fluconazole (MIC 2 µg/mL) this may be due the formation of H-bonds with the different parts of the protein of microbes. However, the resistance efficiency against the tested microbes decreases if the same phenyl ring is substituted with less polar groups such as Me (**5f** and **5m**), OMe (**5g** and **5n**), and Halogens (**5d**, **5e**, **5k**, and **5l**) this is due to their less or no ability of formation of H-Bonds.

Table 4. Anti-microbial activity of synthesized 1,4-DHP derivatives **5a–n**.

Compound	Gram (+ve) Bacteria		Gram (−ve) Bacteria			Fungi		
	B. subtilis	*S. pyogenes*	*E. coli*	*K. pneumonia*	*S. aureus*	*A. janus*	*A. niger*	*A. sclerotiorum*
5a	16	8	8	8	16	8	16	8
5b	4	4	4	8	4	4	4	8
5c	4	8	4	4	8	8	8	32
5d	16	8	16	32	32	16	32	32
5e	16	32	-	64	64	32	16	16
5f	32	8	16	8	16	16	16	8
5g	16	16	8	8	16	8	16	–
5h	64	16	32	16	32	32	32	16
5i	4	4	4	4	4	4	4	4
5j	4	8	8	4	4	8	4	4
5k	8	16	16	-	–	16	16	32
5l	32	64	128	16	32	16	32	16
5m	8	16	64	32	64	16	16	32
5n	16	8	8	16	8	16	32	16
Amoxicillin	4	4	4	4	4	–	–	–
Fluconazole	–	–	–	–	–	2	2	2

4. Conclusions

An environmentally green procedure was performed for the synthesis of a novel 1,4-DHP scaffold via a one-pot, four-component reaction using aqueous micellar solution under microwave irradiation by treatment of a mixture of substituted benzaldehyde, diethyl acetylene dicarboxylate, and either ammonium acetate or aniline, along with malononitrile in an equivalent ratio. In summary, the outlined procedure illustrates remarkable efficacy in generating 1,4-DHP derivatives from easily accessible starting materials in a single step, utilizing a micellar solution of $Al(DS)_3$ in water. The resulting crops are swiftly attained with adaptability and variety, achieving outstanding yields and purity. This approach demonstrates efficiency in terms of labor, cost-effectiveness, and minimal waste generation while operating under mild reaction conditions. Furthermore, all synthesized 1,4-DHPs display potent activity against the evaluated microbial strains. On a note, it finds that the presence of polar groups such as NO_2 on the phenyl ring imparts comparable resistance to standard drugs such as Amoxicillin and Fluconazole.

Supplementary Materials: The following supporting information can be downloaded at: https://www.mdpi.com/article/10.3390/molecules29051115/s1, Scheme S1: Synthesis of 1,4-DHPs using $Al(DS)_3$ in water under microwave radiations; Table S1: Synthesis of 1,4-DHP derivatives 5a-n using Al(DS)3 in water for 5 mints under microwave radiations; Table S2: Indexing of XRD using the Debye Scherrer Method; Figure S1: Energy-Dispersive X-ray Spectroscopy (EDS) data; Figure S2: 1H-NMR of diethyl 6-amino-5-cyano-4-phenyl-1,4-dihydropyridine-2,3-dicarboxylate (**5a**); Figure S3: 1H-NMR of diethyl 6-amino-5-cyano-4-(3-nitrophenyl)-1,4-dihydropyridine-2,3-dicarboxylate (**5c**); Figure S4: 1H-NMR of diethyl 6-amino-5-cyano-1,4-diphenyl-1,4-dihydropyridine-2,3-dicarboxylate (**5h**); Figure S5: 1H-NMR of diethyl 6-amino-5-cyano-4-(3-nitrophenyl)-1-phenyl-1,4-dihydropyridine-2,3-dicarboxylate (**5j**).

Author Contributions: Methodology, P.K.B.; Investigation, H.H.; Writing—original draft, A.G. and H.S.S.; Writing—review & editing, N.K., K.S., H.H. and P.K.B.; Supervision, M.K. and H.S.S. All authors have read and agreed to the published version of the manuscript.

Funding: This research received no external funding.

Institutional Review Board Statement: Not applicable.

Informed Consent Statement: Not applicable.

Data Availability Statement: Data are contained within the article and Supplementary Materials.

Acknowledgments: The authors express sincere gratitude to Chandigarh University, Gharuan, Punjab, India, for providing all the essential facilities to conduct this research. The publication fees for this article were supported by the UNLV University Libraries Open Article Fund.

Conflicts of Interest: The authors declare that they have no conflicts of interest.

References

1. Sirisha, K.; Achaiah, G.; Reddy, V.M. Facile synthesis and antibacterial, antitubercular, and anticancer activities of novel 1,4-dihydropyridines. *Arch. Pharm.* **2010**, *343*, 342–352. [CrossRef] [PubMed]
2. Trivedi, A.; Dodiya, D.; Dholariya, B.; Kataria, V.; Bhuva, V.; Shah, V. Synthesis and biological evaluation of some novel 1,4-dihydropyridines as potential antitubercular agents. *Chem. Biol. Drug Des.* **2011**, *78*, 881–886. [CrossRef]
3. Kumar, A.; Maurya, R.A.; Sharma, S.; Kumar, M.; Bhatia, G. Synthesis and biological evaluation of N-aryl-1,4-dihydropyridines as novel antidyslipidemic and antioxidant agents. *Eur. J. Med. Chem.* **2010**, *45*, 501–509. [CrossRef]
4. De Luca, M.; Ioele, G.; Ragno, G. 1,4-dihydropyridine antihypertensive drugs: Recent advances in photostabilization strategies. *Pharmaceutics* **2019**, *11*, 85. [CrossRef] [PubMed]
5. Mohamed, M.F.; Darweesh, A.F.; Elwahy, A.H.M.; Abdelhamid, I.A. Synthesis, characterization and antitumor activity of novel tetrapodal 1,4-dihydropyridines: P53 induction, cell cycle arrest and low damage effect on normal cells induced by genotoxic factor H_2O_2. *RSC Adv.* **2016**, *6*, 40900–40910. [CrossRef]
6. Tajbakhsh, M.; Alinezhad, H.; Norouzi, M.; Baghery, S.; Akbari, M. Protic pyridinium ionic liquid as a green and highly efficient catalyst for the synthesis of polyhydroquinoline derivatives via Hantzsch condensation in water. *J. Mol. Liq.* **2013**, *177*, 44–48. [CrossRef]
7. Mathur, R.; Negi, K.S.; Shrivastava, R.; Nair, R. Recent developments in the nanomaterial-catalyzed green synthesis of structurally diverse 1,4-dihydropyridines. *RSC Adv.* **2021**, *11*, 1376–1393. [CrossRef] [PubMed]
8. Johnson, B.; A Johnson, B.; Ait-Daoud, N.; Wells, L.T. Effects of isradipine, a dihydropyridine-class calcium channel antagonist, on D-methamphetamine-induced cognitive and physiological changes in humans. *Neuropsychopharmacology* **2000**, *22*, 504–512. [CrossRef]
9. Huai, Y.; Wang, H.; Zhao, L.; Zhao, L.; Pei, J. Lacidipine inhibits endoplasmic reticulum stress and myocardial remodeling induced by pressure overload in rat heart. *Eur. J. Pharmacol.* **2013**, *718*, 441–447. [CrossRef]
10. Amenta, F.; Tomassoni, D.; Traini, E.; Mignini, F.; Veglio, F. Nicardipine: A hypotensive dihydropyridine-type calcium antagonist with a peculiar cerebrovascular profile. *Clin. Exp. Hypertens.* **2008**, *30*, 808–826. [CrossRef]
11. Wu, J.Y.; Zhang, L.; Cai, L.L.; Zhang, Y. Catalyzing synthesis of chiral nitrendipine. *Adv. Mater. Res.* **2012**, *518–523*, 3943–3946. [CrossRef]
12. Affeldt, R.F.; Benvenutti, E.V.; Russowsky, D. A new In-SiO_2 composite catalyst in the solvent-free multicomponent synthesis of Ca^{2+} channel blockers nifedipine and nemadipine B. *New J. Chem.* **2012**, *36*, 1502–1511. [CrossRef]
13. Hantzsch, A. Ueber die Synthese pyridinartiger Verbindungen aus Acetessigäther und Aldehydammoniak. *Justus Liebigs Ann. Chem.* **1882**, *215*, 1–82. [CrossRef]
14. Jassem, A.M.; Almashal, F.A.K.; Mohammed, M.Q.; Jabir, H.A.S. A catalytic and green method for one-pot synthesis of new Hantzsch 1,4-dihydropyridines. *SN Appl. Sci.* **2020**, *2*, 359. [CrossRef]
15. Machado, I.V.; dos Santos, J.R.; Januario, M.A.; Corrêa, A.G. Greener organic synthetic methods: Sonochemistry and heterogeneous catalysis promoted multicomponent reactions. *Ultrason. Sonochem.* **2021**, *78*, 105704. [CrossRef] [PubMed]
16. Davarpanah, J.; Ghahremani, M.; Najafi, O. Synthesis of 1,4-dihydropyridine and polyhydroquinoline derivatives via Hantzsch reaction using nicotinic acid as a green and reusable catalyst. *J. Mol. Struct.* **2019**, *1177*, 525–535. [CrossRef]
17. Koukabi, N.; Kolvari, E.; Khazaei, A.; Zolfigol, M.A.; Shirmardi-Shaghasemi, B.; Khavasi, H.R. Hantzsch reaction on free nano-Fe2O3 catalyst: Excellent reactivity combined with facile catalyst recovery and recyclability. *Chem. Commun.* **2011**, *47*, 9230–9232. [CrossRef]
18. Shaibuna, M.; Sreekumar, K. Dual solvent-catalyst role of deep eutectic solvents in Hantzsch dihydropyridine synthesis. *Synth. Commun.* **2021**, *51*, 1742–1753. [CrossRef]
19. Elumalai, D.; Gnanasekaran, R.; Leelakrishnan, S.; Nachimuthu, G.; Kannan, T.; Paramasivam, T.P.; Jayabal, K. $InCl_3$-Assisted Eco-Friendly Approach for N-Fused 1,4-Dihydropyridine Scaffolds via Ring Opening Michael Addition of Cyclic Nitroketene and Iminocoumarin: Synthesis and DFT Studies. *ChemistrySelect* **2018**, *3*, 2070–2079. [CrossRef]

20. Sharma, V.K.; Singh, S.K. Synthesis, utility and medicinal importance of 1,2- & 1,4-dihydropyridines. *RSC Adv.* **2017**, *7*, 2682–2732. [CrossRef]
21. Sutarni, Y.D.S.Y.D.; Purwono, B.; Kunarti, E.S.K.E.S.; Mardjan, M.I.D. Fe/ZSM-5-Catalyzed-Synthesis of 1,4-Dihydropyridines under Ultrasound Irradiation and Their Antioxidant Activities. *Sains Malays.* **2023**, *52*, 1189–1202. [CrossRef]
22. Rostamnia, S.; Morsali, A. Basic isoreticular nanoporous metal-organic framework for Biginelli and Hantzsch coupling: IRMOF-3 as a green and recoverable heterogeneous catalyst in solvent-free conditions. *RSC Adv.* **2014**, *4*, 10514–10518. [CrossRef]
23. Parthiban, A.; Makam, P. 1,4-Dihydropyridine: Synthetic advances, medicinal and insecticidal properties. *RSC Adv.* **2022**, *12*, 29253–29290. [CrossRef]
24. Zonouz, A.M.; Hosseini, S.B. Montmorillonite K10 clay: An efficient catalyst for Hantzsch synthesis of 1,4-dihydropyridine derivatives. *Synth. Commun.* **2008**, *38*, 290–296. [CrossRef]
25. Sadeghi, B.; Namakkoubi, A.; Hassanabadi, A. BF3.SiO_2 nanoparticles: A solid phase acidic catalyst for efficient one-pot Hantzsch synthesis of 1,4-dihydropyridines. *J. Chem. Res.* **2013**, *37*, 11–13. [CrossRef]
26. Lee, J.H. Synthesis of Hantsch 1,4-dihydropyridines by fermenting bakers' yeast. *Tetrahedron Lett.* **2005**, *46*, 7329–7330. [CrossRef]
27. Sivamurugan, V.; Kumar, R.S.; Palanichamy, M.; Murugesan, V. Synthesis of Hantzsch 1,4-dihydropyridines under solvent-free condition using Zn[(L)proline]2 as Lewis acid catalyst. *J. Heterocycl. Chem.* **2005**, *42*, 969–974. [CrossRef]
28. Yadav, J.S.; Reddy, B.V.S.; Basak, A.K.; Narsaiah, A.V. Three-component coupling reactions in ionic liquids: An improved protocol for the synthesis of 1,4-dihydropyridines. *Green Chem.* **2003**, *5*, 60–63. [CrossRef]
29. Kumar, A.; Sharma, S. A grinding-induced catalyst- and solvent-free synthesis of highly functionalized 1,4-dihydropyridines via a domino multicomponent reaction. *Green Chem.* **2011**, *13*, 2017–2020. [CrossRef]
30. Hesari, Z.; Hadavand, B.S. Deep Eutectic Solvent Based on Choline Chloride/Urea as an Efficient Catalytic System for the One-Pot Synthesis of Highly Functionalized 1,4-Dihydropyridines and Polysubstituted 4H- Chromenes. *J. Appl. Chem. Res.* **2019**, *13*, 97–106.
31. Jeffrey, K.; Elizabeth, R.; Samuel, B.; Shannon, S.; Beata, D.; Bojarski, A.J.; Strekowski, L. Synthesis of 4-Substituted 2-(4-Methylpiperazino)pyrimidines and Quinazoline Analogs as Serotonin 5-HT 2A Receptor Ligands. *J. Heterocycl. Chem.* **2009**, *46*, 1259–1265. [CrossRef]
32. Ramesh, R.; Lalitha, A. Facile and Green Chemistry Access to 5-aryl-1,2,4-Triazolidine-3-thiones in Aqueous Medium. *ChemistrySelect* **2016**, *1*, 2085–2089. [CrossRef]
33. Kerru, N.; Gummidi, L.; Bhaskaruni, S.V.H.S.; Maddila, S.N.; Jonnalagadda, S.B. Green synthesis and characterization of novel 1,2,4,5-tetrasubstituted imidazole derivatives with eco-friendly red brick clay as efficacious catalyst. *Mol. Divers.* **2020**, *24*, 889–901. [CrossRef] [PubMed]
34. Maddila, S.; Nagaraju, K.; Chinnam, S.; Jonnalagadda, S.B. Microwave-Assisted Multicomponent Reaction: A Green and Catalyst-Free Method for the Synthesis of Poly-Functionalized 1,4-Dihydropyridines. *ChemistrySelect* **2019**, *4*, 9451–9454. [CrossRef]

Disclaimer/Publisher's Note: The statements, opinions and data contained in all publications are solely those of the individual author(s) and contributor(s) and not of MDPI and/or the editor(s). MDPI and/or the editor(s) disclaim responsibility for any injury to people or property resulting from any ideas, methods, instructions or products referred to in the content.

molecules

MDPI

Article

Molecular Liquids versus Ionic Liquids: The Interplay between Inter-Molecular and Intra-Molecular Hydrogen Bonding as Seen by Vaporisation Thermodynamics

Sergey P. Verevkin [1,2,3,*], Dzmitry H. Zaitsau [3,4] and Ralf Ludwig [1,3,5]

1 Department of Physical Chemistry, University of Rostock, Albert-Einstein-Str. 27, 18059 Rostock, Germany
2 Department of Physical Chemistry, Kazan Federal University, 420008 Kazan, Russia
3 Department LL&M, University of Rostock, Albert-Einstein-Str. 25, 18059 Rostock, Germany
4 Department of Technical Thermodynamics, University of Rostock, Albert-Einstein Str. 2, 18059 Rostock, Germany
5 Leibniz-Institut für Katalyse an der Universität Rostock e.V., Albert-Einstein-Str. 29a, 18059 Rostock, Germany
* Correspondence: sergey.verevkin@uni-rostock.de

Abstract: In this study, we determined the enthalpies of vaporisation for a suitable set of molecular and ionic liquids using modern techniques for vapour pressure measurements, such as the quartz crystal microbalance, thermogravimetric analysis (TGA), and gas chromatographic methods. This enabled us to measure reasonable vapour pressures, avoiding the problem of the decomposition of the ionic liquids at high temperatures. The enthalpies of vaporisation could be further analysed by applying the well-known "group contribution" methods for molecular liquids and the "centerpiece" method for ionic liquids. This combined approach allowed for the dissection of the enthalpies of vaporisation into different types of molecular interaction, including hydrogen bonding and the dispersion interaction in the liquid phase, without knowing the existing species in both the liquid and gas phases.

Keywords: ionic liquid; hydrogen bonding; enthalpy of vaporisation; structure–property relationship

1. Introduction

At room temperature, methane, ethane, propane, and butane are gases, but pentane and hexane are already very volatile liquids. Admittedly, the weak van der Waals attractions are the obvious reason these non-polar molecules are held together in the liquid phase. At room temperature, the first representative of the homologous series of alkanols, methanol, is already a volatile liquid. The inter-molecular hydrogen bonding is the obvious reason for such behaviour of these polar molecules. The energetics of inter-molecular interactions of molecules in the liquid phase (and thus their volatility) can be quantitatively determined using vaporisation thermodynamics. According to the textbook, a vaporisation enthalpy is the amount of energy required to disrupt the network of inter-molecular interactions in the liquid and to transfer one mole of molecules in the ideal gas, where interactions between molecules are assumed to be absent. Admittedly, the enthalpy of vaporisation is the "bulk" thermodynamic quantity that fails to distinguish between the energetics of van der Waals forces and the energetics of hydrogen bonding coexisting in typical *molecular liquids*. Nevertheless, the vaporisation enthalpies, $\Delta_{\mathrm{l}}^{\mathrm{g}} H_{\mathrm{m}}^{\mathrm{o}}$, are reliably measured by various experimental techniques [1], challenging the task of separating and understanding the energetics of molecular interactions using these thermodynamic data. Indeed, in a number of recent publications, we have developed a few thermodynamically based methods to quantify hydrogen bond strengths (inter- and intra-HB) for molecular [2–4] and ionic liquids [5–15]. In this work, we develop and apply these methods to a series of molecular liquids (MLs) containing a six-membered aliphatic ring (alkyl-piperidines) and a hydroxyl group as a special feature (see Figure 1 left); we also apply these methods to corresponding

ionic liquids (ILs) that also contain a six-membered aromatic ring (alkyl-pyridinium) with the hydroxyl attached to the alkyl chain (see Figure 1 right).

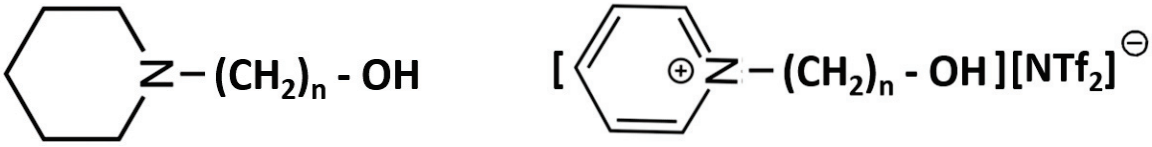

Figure 1. Structures of the hydroxyl-alkyl-piperidines (**left**) and hydroxyl-alkyl-pyridinium bis(trifluoromethylsulfonyl)imides = [N-C_nOH-Py][NTf_2] (**right**). The number of the methylene groups n = 2, 3, and 4.

The association of the hydroxyl-containing molecules (e.g., alcohols, diols, amino alcohols, etc.) in the liquid phase via the OH···O and OH···N hydrogen bond types (see Figure 2) is a well-established phenomenon [2–4,9].

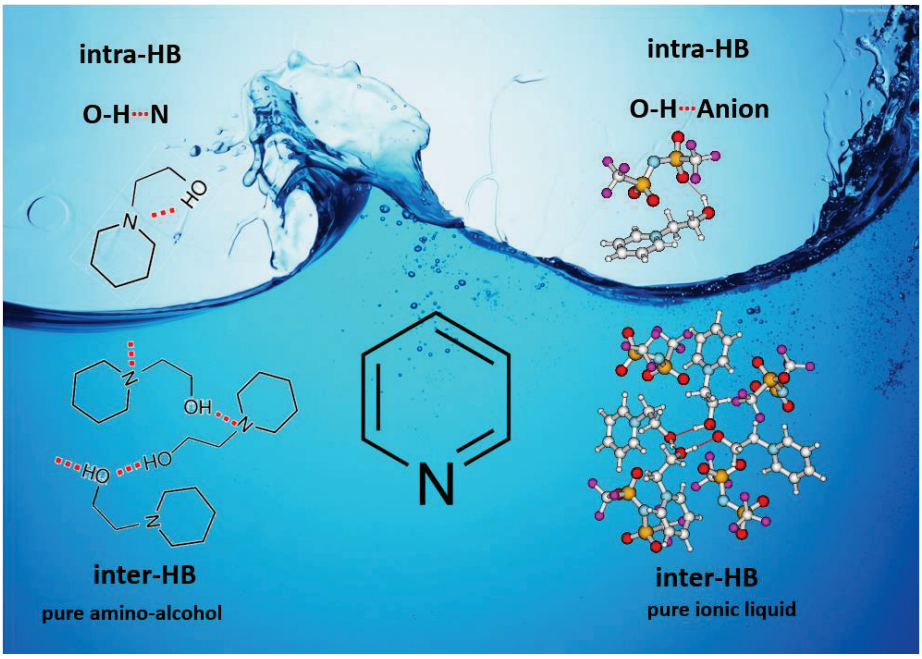

Figure 2. The inter-molecular (HB_{inter}) and intra-molecular (HB_{intra}) hydrogen bonding in MLs and corresponding ILs.

The formation of both the inter- and intra-types of association is theoretically feasible, but in practice, most molecules (even in amino alcohols and diols) in the liquid are connected via the OH···O and OH···N inter-molecular hydrogen bonds, which are more thermodynamically favourable [2–4]. In contrast, the amino alcohol molecule, which has left the liquid phase and freely flies in the gas phase (or in vacuum) without adjacency, has only one option—to build the intra-molecular H-bond, which brings the molecule into the energetic lowest conformations. Depending on the molecular flexibility and temperature, the number of coexisting intra-H-bonded conformations can be significant, making the quantification of the intra-HB strength in the gas phase a difficult task [2–4]. Similar complications apply to the hydroxyl-containing ionic liquids. In the liquid phase, the formation of both inter- and intra- OH···O and OH···N association types is also feasible (see Figure 2), but the presence of the large and charged anion indicates the additional competition for H-bonding modes in ILs. The determination of ratios and relationships between the possible HB modes is a challenging task that could only be partially solved with the help of molecular dynamics simulations [9]. It should be mentioned that the definition of intra-molecular hydrogen bonding in ionic liquids has a certain peculiarity.

When a hydrogen bond occurs within two functional groups of the same molecule, it is called an intra-molecular hydrogen bond; however, in the case of hydroxyl-containing ionic liquids, the formation of the non-covalent bond occurs between the OH group and the anion of the same molecule [9].

Furthermore, in the gas phase, the interpretation of the intra-HB by the free-flying IL molecule is thwarted with complications. Although we have only recently shown that the OH group in the hydroxyl-containing ILs is definitely linked to the anion, the coexistence of numerous intra-molecular H-bonded conformers with comparatively low energy makes it difficult to properly quantify the HB strength.

We hope that the apparent structural similarity of molecules chosen for this work (see Figure 1) could enable the development and understanding of the interplay between inter-molecular (HB_{inter}) and intra-molecular (HB_{intra}) hydrogen bonding in both MLs and the corresponding ILs.

A proven method for determining the strength of the HB_{inter} hydrogen bond in alkanols is to use the method of homomorphs [16]. The idea behind this is to compare the vaporisation enthalpies of alkanols (R–OH) with those of the homomorphic alkanes, which are obtained by replacing the OH group with a CH_3 group (R–CH_3). The vaporisation enthalpies of such homomorphic alkanes essentially model the van der Waals forces contributions to the vaporisation enthalpies of the alkanols (R–OH). The difference in the enthalpy of vaporisation between an alkanol (R–OH) and its corresponding homomorph (R–CH_3)

$$HB_{\text{inter}} = \Delta_{\text{l}}^{\text{g}} H_{\text{m}}^{\text{o}}(\text{R–CH}_3) - \Delta_{\text{l}}^{\text{g}} H_{\text{m}}^{\text{o}}(\text{R–OH}) \quad (1)$$

could be taken as a crude measure of the contribution to the enthalpy of vaporisation due to the inter-molecular hydrogen bonding in alkanols. The numerical values for $\Delta_{\text{l}}^{\text{g}} H_{\text{m}}^{\text{o}}$ of some alkanols and their homomorphs are collected in Table 1.

Table 1. Experimental enthalpies of vaporisation of alkanols and alkanes and the strength of inter- and intra-HB calculated from these values (at 298 K, in kJ·mol^{-1}).

Compound	$\Delta_{\text{l}}^{\text{g}} H_{\text{m}}^{\text{o}}$(exp) [a]	Compound	$\Delta_{\text{l}}^{\text{g}} H_{\text{m}}^{\text{o}}$(exp) [a]	HB_{inter} (Equation (1))	FW [b]	HB_{intra} (Equation (2))
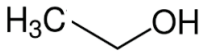 ethanol	42.5	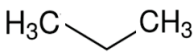 propane	16.3	−26.0	42.5	−0.2
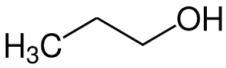 1-propanol	47.5	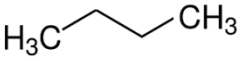 butane	22.4	−25.1	47.5	0.0
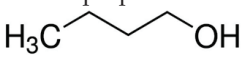 1-butanol	52.4	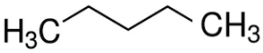 pentane	26.8	−25.6	52.5	−0.1
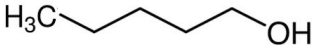 1-pentanol	57.0	hexane	31.7	−25.3	57.5	−0.5

[a] Experimental data from ref. [17] with uncertainties of ±0.2 kJ·mol^{-1}. [b] Enthalpies of vaporisation referred to the frameworks (see text).

The HB_{inter} values calculated according to Equation (1) are shown in column 5. They are practically independent of the chain length and the general level of a hydrogen bond strength of −25 kJ·mol^{-1} agrees with the results of IR and NMR spectroscopic methods [18,19].

2. Molecular Liquids: Strength of the Inter-Molecular Hydrogen Bonding

2.1. Series of Hydroxy-Alkyl-Piperidines

The application of the homomorphic method is straightforward and simple. The vaporisation enthalpies of the hydroxy-alkyl-piperidines required for this analysis were derived from the temperature dependence of their vapour pressures (see details in the

Supplementary Materials), which were measured using the transpiration method (the primary experimental data are given in Tables S1–S5). The final experimental $\Delta_l^g H_m^o$ (298 K) values relevant to the discussion are presented in Table 2, column 2.

Table 2. Experimental enthalpies of vaporisation of hydroxy-alkyl-piperidines and N-alkyl-piperidines and the strength of inter- and intra-HBs calculated from these values (at 298 K, in kJ·mol^{-1}).

Compound	$\Delta_l^g H_m^o$(exp) [a]	Compound	$\Delta_l^g H_m^o$(exp) [b]	HB_{inter} (Equation (1))	FW [c]	HB_{intra} (Equation (2))	HB_{intra} (Equation (3))
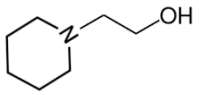 1-piperidine-ethanol	58.1 ± 0.4	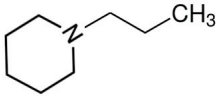 N-propyl-piperidine	44.9 ± 0.4	−13.2	72.0	−13.9	−11.9
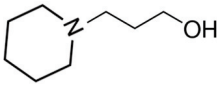 1-piperidine-propanol	62.1 ± 0.4	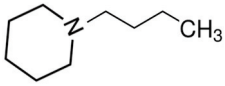 N-butyl-piperidine	48.9 ± 0.2	−13.2	77.0	−14.9	−12.4
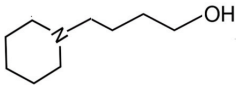 1-piperidine-butanol	70.0 ± 2.6	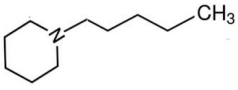 N-pentyl-piperidine	53.7 ± 1.0	−16.3	82.0	−12.0	−9.0
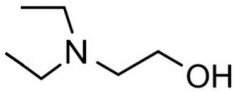 N,N-diEt-2-aminoethanol	52.6 ± 0.2 [20]	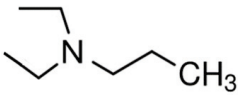 N,N-diEt-propylamine	39.8 ± 0.2 [17]	−12.8	66.2	−13.6	−12.3

[a] Experimental data from Table S4. [b] Experimental data from Table S5. [c] Enthalpies of vaporisation referred to the frameworks (see text).

The vaporisation enthalpies of the corresponding N-alkyl-piperidines required for comparison were taken from our preliminary work [21] and checked for internal consistency (see Table S4); the experimental $\Delta_l^g H_m^o$ (298 K) values essential for the discussion are presented in Table 2, column 4. The HB_{inter} values calculated according to Equation (1) for hydroxy-alkyl-piperidines are listed in column 5. Similar to aliphatic alcohols, they are (within their experimental uncertainties) hardly dependent on chain length, but the general hydrogen bond strength level of −13 kJ·mol^{-1} is two times lower than in alkanols. This level is quite explainable as the general level of −9 kJ·mol^{-1} is specific for the association in pure amines (see Table S9), and consequently, the strength of the inter-molecular hydrogen bonds in amino alcohols decreases to the approximate mean between alcohols and amines. Some peculiarities of the chain-length dependence and influence of alkyl substituents on the HB_{inter} in amino alcohols have been just recently reported [2]. Essential to this discussion is that the six-membered ring specific to the hydroxy-alkyl-piperidines does not impact the HB_{inter} strength in these types of amino alcohols. To show a comparative example, HB_{inter} strength for the open-alkyl-chain N,N-di-ethyl-2-aminoethanol can hardly be distinguished from those in the hydroxy-alkyl-piperidines of interest in this work (see Table 2). Other examples can be found elsewhere [2,20,22].

2.2. Series of Hydroxy-Alkylbenzenes

It is now clear that the aliphatic six-membered ring specific to the hydroxy-alkyl-piperidines plays no role in the association intensity in such MLs. Considering that in the next step we want to perform the comparison with corresponding ILs that also contain a six-membered but aromatic ring, it makes sense to understand if the aromatic ring can influence the association in the hydroxy-alkyl-benzenes, C_6H_5-$(CH_2)_n$-OH, and roughly mimic the intended ILs structures. The vaporisation enthalpies of phenyl-methanol and phenyl-ethanol required for this analysis were taken from our previous work [23,24]. For 3-phenyl-1-propanol and 4-phenyl-1-butanol, we collected vapour pressures at different temperatures that are available in the literature (see Table S2). The vaporisation enthalpies

of homomorphic alkyl-benzenes are well-known from the literature [25]. The experimental $\Delta_l^g H_m^o$(298 K) values that are relevant to the discussion are given in Table 3 under column 2 and column 4.

Table 3. Experimental enthalpies of vaporisation of hydroxy-alkyl-benzene and alkyl-benzenes and the strength of inter- and intra-HB calculated from these values (at 298 K, in kJ·mol^{-1}).

Compound	$\Delta_l^g H_m^o$(exp)	Compound	$\Delta_l^g H_m^o$(exp) [a]	HB_{inter} (Equation (1))	FW [b]	HB_{intra} (Equation (2))	HB_{intra} (Equation (3))
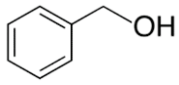 phenyl-methanol	65.8 ± 0.5 [23]	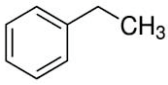 ethylbenzene	42.3	−23.5	68.5	−2.7	−2.7
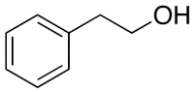 2-phenyl-ethanol	66.7 ± 0.3 [24]	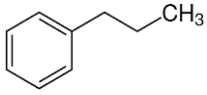 1-propylbenzene	46.2	−20.5	73.5	−6.8	−4.6
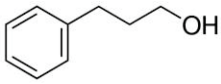 3-phenyl-1-propanol	75.1 ± 2.4 [Table S4]	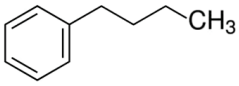 1-butylbenzene	50.8	−24.3	78.5	−3.4	−1.3
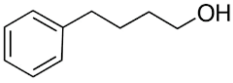 4-phenyl-1-butanol	80.2 ± 3.0 [Table S4]	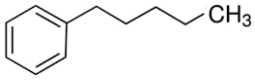 1-pentylbenzene	55.1	−25.1	73.5	−3.3	−0.2

[a] Experimental data from ref. [16] with uncertainties of ±0.2 kJ·mol^{-1}. [b] Enthalpies of vaporisation referred to the frameworks (see text).

The HB_{inter} values calculated according to Equation (1) for hydroxy-alkyl-benzene and given in Table 3, column 5 make it clear that even the aromatic ring cannot significantly affect the inter-molecular hydrogen bonding network in this type of ML. The common level of hydrogen bond strength of −25 kJ·mol^{-1} remains more or less the same as for aliphatic alkanols. A slight decrease in the HB_{inter} in 2-phenylethanol is later explained as a consequence of the interplay of the inter- and intra-HB specific to this molecule, where the OH group is in very close proximity to the phenyl ring.

Thus, after HB_{inter} analysis in aliphatic and aromatic alkanols, as well as in aliphatic amino alcohols bearing the six-membered ring, we could expect the HB_{inter} level in the similarly shaped hydroxyl-alkyl-pyridinium bis(trifluoromethylsulfonyl)imides (Figure 1 right) to be roughly comparable to those found in amino alcohols, provided that the NTf_2 anions do not participate in the association of these ILs. Will our expectation come true?

2.3. Ionic Liquids: Strength of the Inter-Molecular Hydrogen Bonding

Admittedly, the reliable measurement of the vapour pressure of extremely low-volatility ionic liquids is an extremely demanding task [5–15]. The reason for this is that the conventional techniques used for ML studies are not applicable as they are not sensitive enough to detect the vanishingly small ILs vapour pressures. Increasing the temperature enables reaching measurable vapour pressures, but at such high temperatures, the thermal stability of ILs approaches, and the limit and decomposition products aggravate the measurements. To overcome these difficulties, several methods have been developed in our laboratory. A brief description of the quartz crystal microbalance (QCM) [26], thermogravimetric analysis (TGA) [27], and gas chromatographic (GC) [28] methods is given in the Supplementary Materials. The TGA and QCM methods were applied to derive vaporisation enthalpies for the [N-C_nOH-Py][NTf_2] series (see Table 4). Complementary results for ionic liquids containing the [N-C_nOH-Py] cation, but connected to the dicyanoamide [DCA] and tetrafluoroborate [BF_4] anions were derived using the TGA and GC techniques. The details of the experimental conditions and results are compiled in Table 4.

Table 4. Experimental vaporisation enthalpies of pyridinium-based ionic liquids [a].

IL	Method	T_{range}	T_{av}	$\Delta_l^g H_m^o(T_{av})$ [b]	$\Delta C_{p,m}^o$ [c]	$\Delta_l^g H_m^o$ (298 K) [d]
		K	*K*	kJ·mol^{-1}	J·mol^{-1}·K^{-1}	kJ·mol^{-1}
1	2	3	4	5	6	7
[N-C_2OH-Py][NTf_2]	TGA	532–592	562	125.2 ± 1.1	68	143.1 ± 3.8
	QCM	379–428	403.6	134.6 ± 1.0		141.8 ± 1.7
						142.0 ± 1.6 [e]
[N-C_3OH-Py][NTf_2]	QCM	389–436	412.5	136.8 ± 1.0	72	145.0 ± 1.9
	GC		298			143.6 ± 3.0 [f]
						144.6 ± 1.9 [e]
[N-C_4OH-Py][NTf_2]	QCM	359–409	382.6	143.0 ± 0.8	76	149.4 ± 1.5
[N-C_3OH-Py][DCA]	TGA	532–592	563.7	141.6 ± 2.0	81	163.1 ± 4.7
	GC	298				163.9 ± 3.0 [g]
						163.7 ± 2.5 [e]
[N-C_3OH-Py][BF_4]	TGA	532–592	563.7	134.5 ± 2.1	67	152.3 ± 4.1
[N-C_3H_7-Py][NTf_2]	QCM	375.1–422.4	398.2	127.9 ± 0.5	66	134.5 ± 1.4
[N-C_4H_9-Py][NTf_2]	QCM	377.6–422.3	399.5	131.0 ± 0.5	70	138.0 ± 1.5
[N-C_2OH-Py][OMs]	QCM	394.1–444.2	419.1	136.0 ± 1.0	74	145.0 ± 2.1
[N-C_3OH-Py][OMs]	QCM	379.2–451.2	412.7	136.8 ± 1.0	81	146.1 ± 2.1

[a] Uncertainties of vaporisation enthalpy ($\Delta_l^g H_m^o$) are twice the standard uncertainties. Abbreviations for anions: [DCA] = [NC-N-CN] = dicyanoamide; [OMs] = [CH_3SO_3] = methanesiulfonate. [b] Vaporisation enthalpy measured in the specified temperature range and in reference to the average temperature T_{av}. [c] Heat capacities differences were taken from Table S3. [d] Vaporisation enthalpy $\Delta_l^g H_m^o(T_{av})$ were treated using Equations (S2) and (S3) with the help of heat capacity differences from Table S3 to evaluate the enthalpy of vaporisation at 298 K. The final uncertainties of vaporisation enthalpy are expanded, taking into account the uncertainty of the heat capacity difference $\Delta_l^g C_{p,m}^o$, which was assigned to be ±20 J·K^{-1}·mol^{-1}. [e] Weighted mean value (uncertainty was taken as the weighing factor). [f] From Tables S6 and S8. [g] From Tables S7 and S8.

From the analysis of the data compilation given in Table 4, it is interesting to note that in the series [N-C_nPy][NTf_2] with n = 3, 4, an expected increase in vaporisation enthalpies of ≈4 kJ·mol^{-1} per CH_2 group is observed. At the same time, in the series [N-C_nOH-Py][NTf_2] with n = 2, 3, and 4, this trend is less pronounced with increasing chain length, indicating a specific influence of the OH group placed on the alkyl chain in close proximity to the charged cation.

The summary of results relevant for the discussion in the frame of this work is given in Table 5, column 2. The vaporisation enthalpies of the corresponding homomorphic ionic liquids containing the N-alkyl-pyridinium-cation required for comparison are compiled in Table 4, column 4. The HB_{inter} values calculated according to Equation (1) for the [N-C_nOH-Py][NTf_2] ionic liquids are listed in Table 5, column 5.

It was overoptimistic to expect that the anion would not participate in the hydrogen-bonding network in ionic liquids. Indeed, the overall level of the inter-molecular hydrogen bond strength of ≈−7 kJ·mol^{-1} (see Table 5) in the [NTf_2]-containing ILs is two times lower than in the corresponding ML of hydroxy-alkyl-piperidines (see Table 2). The significant decrease in the HB_{inter} values of the ILs compared with the MLs is clear evidence that a considerable part of the OH groups in the ionic liquid structure are excluded from the OH···O inter-molecular hydrogen bonding network and are most likely involved in the formation of the intra-molecular hydrogen bonding with the anion. The quantification of the individual inter- and intra-HB contributions to the vaporisation enthalpies goes beyond the experimental methods used in this work, but it is interesting to point out some general trends that are evident for "bulk" HB_{inter} values in Tables 5 and 6.

Table 5. Experimental enthalpies of vaporisation of hydroxyl-alkyl-pyridinium [NTf_2] and alkyl-pyridinium [NTf_2] and the strength of inter- and intra-HB calculated from these values (at 298 K, in kJ·mol^{-1}).

Cation	$\Delta_l^g H_m^o$(exp) [a]	Cation	$\Delta_l^g H_m^o$(exp) [a]	HB_{inter} (Equation (1))	FW [b]	HB_{intra} (Equation (2))	HB_{intra} (Equation (3))
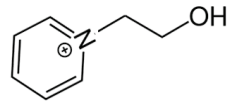 1-(2-hydroxyethyl)pyridinium	142.0 ± 1.6	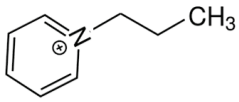 1-propyl-pyridinium	134.5 ± 1.4	−7.5	162.1	−20.1	−17.6
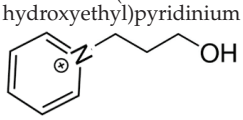 1-(3-hydroxypropyl)pyridinium	144.6 ± 1.9	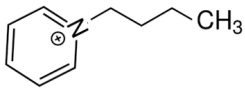 1-butyl-pyridinium	138.0 ± 1.5	−6.6	165.7	−21.1	−19.0
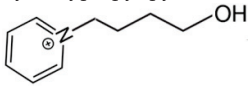 1-(4-hydroxybutyl)pyridinium	149.4 ± 1.5	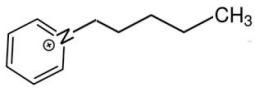 1-pentyl-pyridinium	141.7 ± 1.8 [29]	−7.7	169.3	−19.9	−17.6

[a] Experimental data from Table 4. [b] Enthalpies of vaporisation referred to the frameworks (see text).

Table 6. Experimental enthalpies of vaporisation of hydroxyl-alkyl-pyridinium and alkyl-pyridinium ionic liquids containing [DCA], [BF_4], and [OMs] anions and the strength of inter- and intra-HB calculated from these values (at 298 K, in kJ·mol^{-1}).

IL	$\Delta_l^g H_m^o$(exp) [a]	IL	$\Delta_l^g H_m^o$(exp)	HB_{inter} (Equation (1))	HB_{intra} (Equation (3))
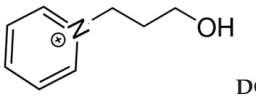 **DCA** 1-(3-hydroxypropyl)pyridinium	163.7 ± 2.5	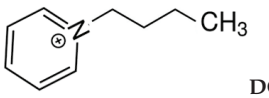 **DCA** 1-propyl-pyridinium	162.1 ± 4.1 [b]	−1.6	−24.0
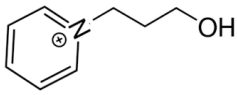 **BF_4** 1-(3-hydroxypropyl)pyridinium	152.3 ± 4.1	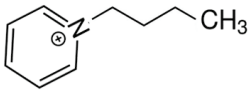 **BF_4** 1-butyl-pyridinium	149.9 ± 2.3 [30]	−2.4	−23.2
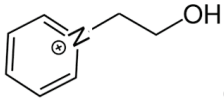 **OMs** 1-(2-hydroxyethyl)pyridinium	145.0 ± 2.1	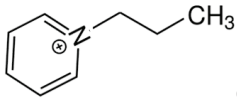 **OMs** 1-propyl-pyridinium	152.6 ± 2.1 [c]	7.6	−32.7
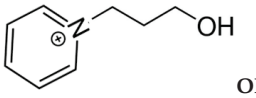 **OMs** 1-(3-hydroxypropyl)pyridinium	146.1 ± 2.1	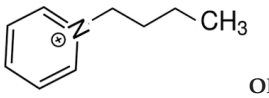 **OMs** 1-butyl-pyridinium	156.0 ± 2.1 [c]	9.9	−35.5

[a] Experimental data from Table 4. [b] Enthalpy of vaporisation of 1-propyl-pyridinium [DCA] is supposed to be equal to those of 3-methyl-1-propyl-pyridinium [DCA] derived in our previous work [31]. [c] Enthalpy of vaporisation was assessed as shown in Figures S3 and S4.

First, the HB_{inter} chain-length dependence within the series [N-C_nOH-Py][NTf_2] is absent, indicating more favourable OH-[NTf_2]-anion interactions. Second, the HB_{inter} strength is slightly anion-dependent. As can be seen in Table 6, for ionic liquids with the [N-C_3OH-Py]-cation with [DCA] and [BF_4], the OH···O interactions are at the level of disappearing (≈−2 kJ·mol^{-1}, see Table 6, column 5). However, in the [OMs]-containing ILs, the OH–anion interactions have already overcome the ML-specific OH···O hydrogen bonding among hydroxyl groups, which is now practically absent in these ILs (≈+9 kJ·mol^{-1}, see Table 6, column 5). Thus, it can finally be concluded that the OH groups connected to the [N-C_nOH-Py]-cations favour the intra-molecular type of hydrogen bonding rather than the inter-molecular type OH···O expected from MLs.

How does one determine the strength of intra-molecular hydrogen bonds in MLs and ILs?

3. Thermodynamic Methods: Strength of the Intra-Molecular Hydrogen Bonding

The strength of inter-molecular hydrogen bonding is easily measurable by mixing two components bearing the specific groups, e.g., alcohol and amine [32]. In the case of intra-molecular hydrogen bonding, the desired interaction takes place within the same molecule, so direct measurements are out of the question. As a rule, the strength of the intra-molecular hydrogen bond (HB_{intra}) is determined by comparing the H-bonded and non-H-bonded frequencies, shifts, conformers, etc. In terms of vaporisation thermodynamics, the main challenge is to find a suitable reference system that mimics the desired molecule without the intra-HB. In our earlier work, we proposed the reference system based on conventional group additivity [2,3]. In this work, we improve this concept of group additivity (GA) and propose an alternative method based on the well-balanced equations (WBE).

3.1. Basics of the Group Additivity Concept ("Centerpiece" Approach)

Group additivity methods have been successfully used to predict vaporisation enthalpies of molecular [33,34] and ionic liquids [29,35]. The idea behind conventional GA methods is to split the experimental vaporisation enthalpies of molecules into relatively small groups in order to obtain well-defined numerical contributions for them. The prediction then proceeds as a construction of a framework of the desired model molecule from the appropriate number and type of these contributions. A comprehensive system of group contributions (or increments) is developed and covers the main classes of molecular organic compounds [33,34]. A general transferability of these increments to ionic liquids has only recently been demonstrated [29]. However, using this conventional GA method for ionic liquids composed of large organic cations and large organic/inorganic anions is impractical due to the very limited amount of available experimental enthalpies of vaporisation required for the parameterisation of specific groups. To overcome this limitation, we developed a general approach for assessing vaporisation enthalpies based on a so-called "centerpiece" molecule [29].

The idea of the "centerpiece" approach is to select a potentially large "centerpiece" molecule that has a reliable vaporisation enthalpy and that can generally mimic the structure of the molecule of interest. Then, the necessary groups are attached to the "centerpiece", resulting in the construction of the desired molecule. For example, we selected N-ethyl-piperidine for the series of hydroxy-alkyl-piperidines and obtained the "centerpiece" -CH_2-(piperidine) (see Figure 3 left) suitable for calculations of the framework by cutting off the CH_3 group. We selected [N-C_3-Py][NTf_2] for the series of hydroxy-alkyl-piperidines and obtained the "centerpiece" -CH_2-(Py-NTf_2) (see Figure 3 right) suitable for calculations of the framework by cutting off the CH_2 and CH_3 groups.

Figure 3. The development of the "centerpieces" for calculating the vaporisation enthalpies of hydroxy-alkyl-piperidines and hydroxy-alkyl-pyridinium [NTf_2] ionic liquids.

Such an approach significantly increases the reliability of the prediction, as the main energetic contribution is already stored in the "centerpiece" and the appended groups taken from the ML compounds are exactly parameterised [33,34]. The development of

the groups and other "centerpieces" used in this work is shown in Figure S5, and their numerical values are given in Table S10.

3.2. Intra-HB Strength from Group-Additivity

Although we developed the "centerpiece" approach, it is worth noting that predicting the enthalpies of vaporisation of hydroxy-alkyl-piperidines and hydroxy-alkyl-pyridinium [NTf_2] ionic liquids was not the aim of this work, as we could measure them for both series (see Table 4). The goal of developing groups and "centerpieces" (see Table S10) was to create a "non-hydrogen-bonded" reference system for estimating the intra-molecular hydrogen-bonding strength in hydroxy-alkyl-piperidines and hydroxy-alkyl-pyridinium [NTf_2] ionic liquids. Indeed, the existence of the intra-molecular hydrogen bonding in the hydroxy-alkyl-piperidines is well-known [36]; however, as shown in Figure 2, the framework of 1-piperidine-propanol collected from "centerpiece", -CH_2-(piperidine) and two additional groups does not contain intra-molecular hydrogen bonding a priori, as it is composed of groups in which intra-molecular hydrogen bonding is originally absent. Therefore, the difference between the experimental vaporisation enthalpy of 1-piperidine-propanol and that of its framework, $\Delta_l^g H_m^o$(framework) (see Figure 4) directly provides a measure of the intra-molecular hydrogen-bonding strength, HB_{GA}, in this molecule:

$$HB_{GA} = \Delta_l^g H_m^o(\text{exp}) - \Delta_l^g H_m^o(\text{framework}) \quad (2)$$

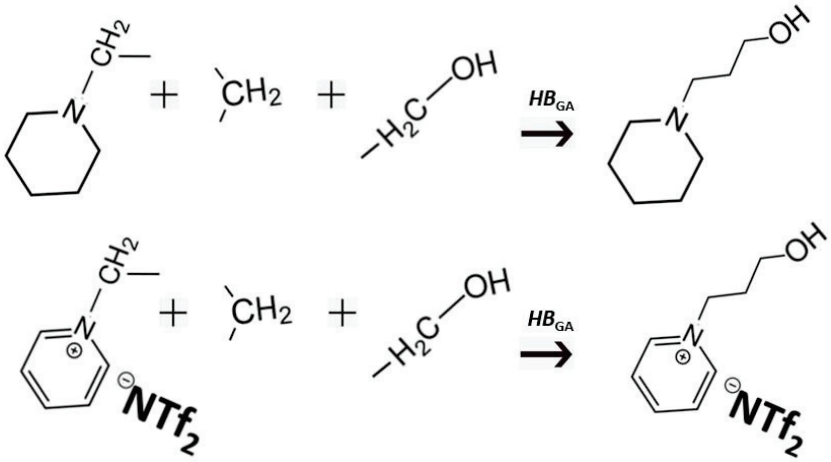

Figure 4. Group additivity: the development of the "non-hydrogen-bonded" frameworks for calculating the intra-molecular hydrogen-bonding strength, HB_{GA}, in hydroxy-alkyl-piperidines and hydroxy-alkyl-pyridinium [NTf_2] ionic liquids.

The development of the "non-hydrogen-bonded" framework for calculating the intra-molecular hydrogen-bonding strength, HB_{GA}, in 1-(3-hydroxypropyl)pyridinium [NTf_2] follows the same pattern as is shown in Figure 4.

The HB_{GA} values calculated for 1-piperidine-propanol and for 1-(2-hydroxyethyl) pyridinium [NTf_2] according to Equation (2), as well as for other MLs and ILs of interest for this work, are given in Tables 1–3 and Tables 5 and 6 for comparison. For the sake of completeness, the $\Delta_l^g H_m^o$(framework) values denoted by *FW* are also given in these tables. The application of the GA method is straightforward and easy and allows for the estimation of intra-molecular hydrogen bond strengths, particularly conveniently in homologous series. However, this method required some preliminary work to develop the system of groups and the selection of the appropriate "centerpiece".

3.3. Intra-HB Strength from Well-Balanced Equations

Another alternative way to create the "non-hydrogen-bonded" reference system is shown in Figure 5 for piperidine-ethanol and 1-(2-hydroxyethyl)pyridinium [NTf_2].

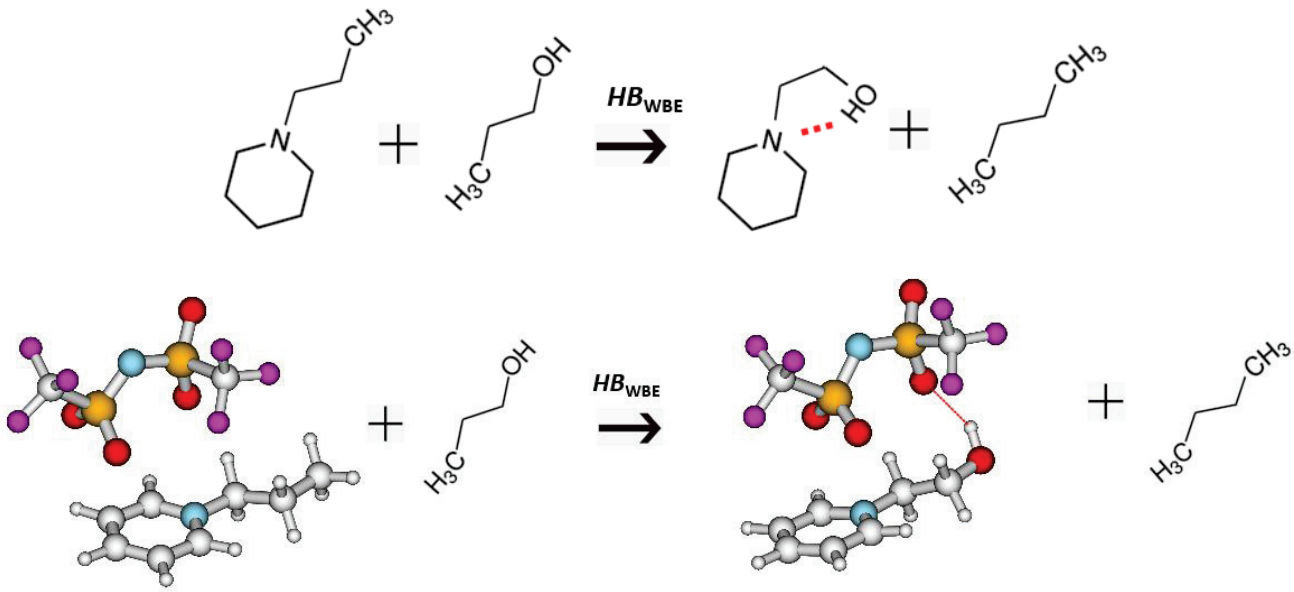

Figure 5. Well-balanced equations: the development of the "non-hydrogen-bonded" reference systems for calculating the intra-molecular hydrogen-bonding strength, HB_{WBE}, in hydroxy-alkyl-piperidines and hydroxy-alkyl-pyridinium [NTf_2] ionic liquids.

The idea comes from the quantum chemical calculations, where the enthalpies of formations are derived using isodesmic, homodesmic, well-balanced reactions, etc. [37]. The main criteria for choosing the reactants is that the structures (or bond types) on the left and right should be as similar as possible and the enthalpy of such a reaction should be as close to zero as possible. To redirect this idea to enthalpies of vaporisation, we should set up a well-balanced equation where the participants at the left and right side are "dressed" with the same functional groups, but the groups are distributed in such a way that there are no other specific interactions on the left and right sides and only one task-specific interaction governs the right side of the equation. This idea is illustrated in Figure 5 using piperidine-ethanol and 1-(2-hydroxyethyl)-pyridinium [NTf_2] as examples. The task-specific interaction in piperidine ethanol is the intra-molecular hydrogen bond. To extract this interaction, we balanced this molecule with n-butane, n-propyl-piperidine, and propanol so that the stoichiometry is retained but the intra-HB is missing from the left part of the equation. Therefore, the difference in enthalpy between the right and left sides can be considered as a measure of the intra-molecular hydrogen bonding strength, HB_{WBE}, in this molecule:

$$HB_{\mathrm{WBE}} = \left[\Delta_{\mathrm{l}}^{\mathrm{g}} H_{\mathrm{m}}^{\mathrm{o}}\,(\mathrm{piperidine-ethanol,\ exp}) + \Delta_{\mathrm{l}}^{\mathrm{g}} H_{\mathrm{m}}^{\mathrm{o}}(\mathrm{n-butane,\ exp})\right] - \left[\Delta_{\mathrm{l}}^{\mathrm{g}} H_{\mathrm{m}}^{\mathrm{o}}\,(1-\mathrm{propyl-piperidine,\ exp}) + \Delta_{\mathrm{l}}^{\mathrm{g}} H_{\mathrm{m}}^{\mathrm{o}}(1-\mathrm{propanol,\ exp})\right] \quad (3)$$

The same logistic was applied for HB_{WBE} values calculations for 1-(2-hydroxyethyl) pyridinium [NTf_2] shown in Figure 5, as well as for other MLs and ILs of interest in this work. These HB_{WBE} values are given in Tables 1–3, 5 and 6 for analysis.

3.4. Intra-HB Strength in ML and IL Series

It is quite obvious that there are no intra-molecular hydrogen bonds in aliphatic alcohols, but just to confirm that Equation (2) correctly worked, we applied this equation to the aliphatic alcohol series with the completely negative result (see Table 1, column 7). It is known that the weak intra-molecular bond is observed for both phenyl-methanol (or benzyl alcohol) and phenyl-ethanol [36]. This observation is now numerically verified (see Table 3), along with the weak strength of the intra-HB for both phenyl-methanol ($\approx$3 kJ$\cdot$ mol^{-1}) and for phenyl-ethanol ($\approx$5 kJ$\cdot$mol^{-1}) from the GA and WBE methods. It is

interesting to note that a very subtle interplay of intra- and inter-HB can be revealed for phenyl-methanol and phenyl-ethanol as calculated by both methods. Taking into account the average inter-HB strength of -25 kJ·mol^{-1} in aliphatic alcohols (see Table 1), it can be seen from Table 3 that the increase in intra-HB strength resulted in a decrease in inter-HB, particularly pronounced in phenyl-ethanol. This observation makes it clear that a non-negligible part of intra-molecularly bound molecules is also incorporated into the mainly inter-molecular hydrogen-bonded network.

For the series of hydroxy-alkyl-piperidines, the chain-length dependence of intra-HB was found to be hardly distinguishable, and the overall level of strength of -13 kJ·mol^{-1} (see Table 2, columns 7 and 8) was estimated using both methods. Interestingly, this level is quite comparable to that of the inter-HB strength in this series (see Table 2, column 5). This observation indicates that qualitatively, a significant amount of the intra-molecularly bound molecules is involved in the association. However, the enthalpy of vaporisation as a thermodynamic tool is unable to quantify the ratio between the inter- and intra-HBs.

For the series of hydroxy-alkyl-pyridinium [NTf_2] ionic liquids, the chain-length dependence of intra-HB is also absent, and the overall level of strength of ≈-20 kJ·mol^{-1} (see Table 5, column 7 and 8) was estimated using both methods. Moreover, the MD simulations performed in our previous work [9] showed that the OH···O hydrogen bond between the OH in the alkyl chain and the oxygen in the anion is definitely present in the gas phase ion pairs (see Figure 6).

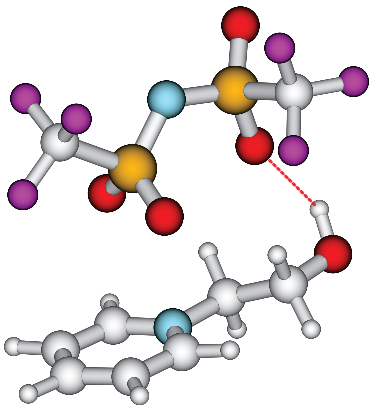

Figure 6. Gas phase ion pair of [C_2OH-Py][NTf_2] from snapshots of MD simulations. The existing hydrogen bond in the [C_2OH-Py][NTf_2] ion pair is shown as a dotted red line [9].

Furthermore, quantum chemical calculations on these ion pairs showed that the favourable OH···O hydrogen bond energies of about ≈-20 kJ·mol^{-1} in the hydroxy-alkyl-pyridinium [NTf_2] ionic liquids [9]. Such a perfect quantitative agreement between the empirical and quantum chemical assessment of the intra-molecular hydrogen bond strength supports the validity of the empirical models used in this work.

This level of intra-HB of ≈-20 kJ·mol^{-1} in the hydroxy-alkyl-pyridinium [NTf_2] ionic liquids is considerably higher compared with that of the inter-HB strength of -7 kJ·mol^{-1} in this series (see Table 5, column 5). However, apparently a certain part of the IL molecules still determines the degree of association of the ionic liquids. This delicate interplay between the intra- and inter-HB is also evident for ILs with an anion other than [NTf_2]: for 1-(3-hydroxypropyl)pyridinium [BF_4] and 1-(3-hydroxypropyl)pyridinium [DCA], the intra-HB strength increased to ≈-24 kJ·mol^{-1} (see Table 6, column 6) and the strength of the inter-HB decreased to ≈-2 kJ·mol^{-1} (see Table 6, column 5). Finally, for the [N-C_nOH-Py][OMs] series, the intra-HB strength increased independently of the chain-length up to ≈-35 kJ·mol^{-1} (see Table 6, column 6), but the level of inter-HB strength was $\approx+9$ kJ·mol^{-1} in this series. Consequently, in the [DCA]-, [BF_4]-, and [OMs]-containing ILs, the molecules are practically not associated via OH groups, and all OH groups are bound to the anions in the liquid phase.

4. Conclusions

For understanding inter- and intra-molecular hydrogen bonding in molecular and ionic liquids, we measured the enthalpies of vaporisation by applying a large variety of thermodynamic methods. Because ionic liquids exhibit vanishingly small vapour pressures at low temperature and start to decompose at the required high temperature, we developed new techniques for measuring the vapour pressures and determining the enthalpies of vaporisation, which included the use of quartz crystal microbalance, thermogravimetric analysis (TGA), and gas chromatographic methods. Applying the well-known "group contribution" methods for molecular liquids and the "centerpiece" method for ionic liquids, we were able to dissect the enthalpies of vaporisation into different types of molecular and ionic interaction, such as hydrogen bonding and dispersion interactions. Considering molecular mimics of the IL cations and thus combining both approaches even allowed for the distinguishing between inter- and intra-molecular hydrogen bonding, which is shown here for the first time.

Supplementary Materials: The following supporting information can be downloaded at: https://www.mdpi.com/article/10.3390/molecules28020539/s1, Figure S1: The scheme of the QCM experimental setup; Figure S2: Regression of solubility parameters $\delta_{298.15}$ of different solutes and Y-module ($Y = (\delta_1)^2/(RT) - \chi_{12}/V_1^*$ is the left part of Equation (S13)) for [N-C_3OH-Py][NTf_2] derived from experimental γ_1^∞-values; Figure S3: Algorithm for estimating the vaporization enthalpies, $\Delta_l^g H_m^o$ (298.15 K), of N-propyl- and N-butyl pyridinium methanesulfonates starting from pyridinium based ILs [C_n-Py][NTf_2]. Development of the [Py][OMs] fragment (left). Attachment of the alkyl chain to the [Py][OMs]; Figure S4: Algorithm for estimating the vaporization enthalpies, $\Delta_l^g H_m^o$ (298.15 K), of N-propyl- and N-butyl pyridinium methanesulfonates starting from imidazolium based ILs [C_n-mim][NTf_2]; Figure S5: The development of groups for calculating the vaporisation enthalpies of hydroxy-alkyl-benzenes, hydroxy-alkyl-piperidines and hydroxy-alkyl-pyridinium [NTf_2] ionic liquids; Table S1: Results of the transpiration method: absolute vapor pressures, p, standard molar vaporisation enthalpies, $\Delta_l^g H_m^o$, and standard molar vaporisation entropies, $\Delta_l^g S_m^o$; Table S2: Vapor pressures, p, at different temperatures compiled standard molar vaporisation enthalpies, $\Delta_l^g H_m^o$, and standard molar vaporisation entropies, $\Delta_l^g S_m^o$; Table S3: Compilation of data on molar heat capacities $C_{p,m}^o$(liq) and heat capacity differences $\Delta_l^g C_{p,m}^o$ at T = 298.15 K (in J·K^{-1}·mol^{-1}); Table S4: Compilation of enthalpies of vaporisation; $\Delta_l^g H_m^o$, derived in this work and from the data available in the literature; Table S5: Correlation of vaporisation enthalpies, $\Delta_l^g H_m^o$ (298.15 K), of alkyl-piperidines with their Kovats indices (J_x); Table S6: Data used for regression with Equation (S13) for [N-C_3OH-Py][NTf_2]: solubility parameters δ_1 (at 298.15 K) of different solutes and the left part of Equation (S13); Table S7: Data used for regression with Equation (S13) for [N-C_3OH-Py][DCA]: solubility parameters δ_1 (at 298.15 K) of different solutes and the left part of Equation (S13); Table S8: Results of regression with Equation (S13) for [N-C_3OH-Py][NTf_2] and [N-C_3OH-Py][DCA]^a; Table S9: Compilation of Data Used for Evaluation of the Inter-Molecular Hydrogen Bonding in linear Amines, and Alkanes (at 298 K, in kJ·mol^{-1}); Table S10: Group-additivity values Γ_i for calculation of enthalpies of vaporization, $\Delta_l^g H_m^o$, at 298.15 K (in kJ·mol^{-1}). References [9,15–17,21,26,28–30,34,38–63] are cited in the Supplementary Materials.

Author Contributions: Conceptualization: S.P.V. and R.L.; Methodology: S.P.V.; Validation: S.P.V.; Formal analysis: S.P.V.; Investigation: D.H.Z.; Writing—original draft: S.P.V.; Writing—review & editing: D.H.Z. and R.L.; Visualization: R.L.; Funding acquisition: S.P.V. All authors have read and agreed to the published version of the manuscript.

Funding: This research was funded by German Science Foundation (DFG) in the frame of the priority program SPP 1807 SPP 1807 "Control of London Dispersion Interactions in Molecular Chemistry" (grant VE 265-9/2 to S.P.V.; grant LU-506/12-2 to R.L.; and grant ZA 872/3-1, 407078203 to D.H.Z.) This paper has been supported by the Kazan Federal University Strategic Academic Leadership Program ("PRIORITY-2030").

Institutional Review Board Statement: Not applicable.

Informed Consent Statement: Not applicable.

Data Availability Statement: All data are available in the text of manuscript and in Supporting Materials to this paper.

Conflicts of Interest: The authors declare no conflict of interest.

Sample Availability: Samples of the compounds are not available from the authors.

References

1. Verevkin, S.P.; Zaitsau, D.H.; Schick, C.; Heym, F. Development of direct and indirect methods for the determination of vaporization enthalpies of extremely low-volatile compounds. In *Handbook of Thermal Analysis and Calorimetry*; Elsevier: Amsterdam, The Netherlands, 2018; Volume 6, ISBN 9780444640628.
2. Siewert, R.; Ludwig, R.; Verevkin, S.P. Non-covalent interactions in molecular systems: Thermodynamic evaluation of the hydrogen bond strength in aminoalcohols. *Phys. Chem. Chem. Phys.* **2021**, *23*, 25226–25238. [CrossRef]
3. Siewert, R.; Zherikova, K.V.; Verevkin, S.P. Non-covalent interactions in molecular systems: Thermodynamic evaluation of the hydrogen-bond strength in amino-ethers and amino-alcohols. *Chem. Eur. J.* **2022**, *28*, e2022000802022. [CrossRef]
4. Emel'yanenko, V.N.; Stange, P.; Feder-Kubis, J.; Verevkin, S.P.; Ludwig, R. Dissecting intermolecular interactions in the condensed phase of ibuprofen and related compounds: The specific role and quantification of hydrogen bonding and dispersion forces. *Phys. Chem. Chem. Phys.* **2020**, *22*, 4896–4904. [CrossRef]
5. Verevkin, S.P.; Kondratev, S.O.; Zaitsau, D.H.; Zherikova, K.V.; Ludwig, R. Quantification and understanding of non-covalent interactions in molecular and ionic systems: Dispersion interactions and hydrogen bonding analysed by thermodynamic methods. *J. Mol. Liq.* **2021**, *343*, 117547. [CrossRef]
6. Hunger, L.; Al-Sheakh, L.; Zaitsau, D.H.; Verevkin, S.P.; Appelhagen, A.; Villinger, A.; Ludwig, R. Dissecting noncovalent interactions in carboxyl-functionalized ionic liquids exhibiting double and single hydrogens bonds between ions of like charge. *Chem. Eur. J.* **2022**, *28*, e2022009492022. [CrossRef]
7. Zaitsau, D.H.; Ludwig, R.; Verevkin, S.P. Determination of the dispersion forces in the gas phase structures of ionic liquids using exclusively thermodynamic methods. *Phys. Chem. Chem. Phys.* **2021**, *23*, 7398–7406. [CrossRef]
8. Shelepova, E.A.; Paschek, D.; Ludwig, R.; Medvedev, N.N. Comparing the void space and long-range structure of an ionic liquid with a neutral mixture of similar sized molecules. *J. Mol. Liq.* **2020**, *299*, 112121. [CrossRef]
9. Zaitsau, D.H.; Neumann, J.; Niemann, T.; Strate, A.; Paschek, D.; Verevkin, S.P.; Ludwig, R. Isolating the role of hydrogen bonding in hydroxyl-functionalized ionic liquids by means of vaporization enthalpies, infrared spectroscopy and molecular dynamics simulations. *Phys. Chem. Chem. Phys.* **2019**, *21*, 20308–20314. [CrossRef]
10. Zaitsau, D.H.; Emel´yanenko, V.N.; Stange, P.; Verevkin, S.P.; Ludwig, R. Dissecting the vaporization enthalpies of ionic liquids by exclusively experimental methods: Coulomb interaction, hydrogen bonding, and dispersion forces. *Angew. Chem. Int. Ed.* **2019**, *58*, 8589–8592. [CrossRef]
11. Bonsa, A.-M.; Paschek, D.; Zaitsau, D.H.; Emel´yanenko, V.N.; Verevkin, S.P.; Ludwig, R. The relation between vaporization enthalpies and viscosities: Eyring's theory applied to selected ionic liquids. *ChemPhysChem* **2017**, *18*, 1242–1246. [CrossRef]
12. Zaitsau, D.H.; Emel´yanenko, V.N.; Stange, P.; Schick, C.; Verevkin, S.P.; Ludwig, R. Dispersion and hydrogen bonding rule: Why the vaporization enthalpies of aprotic ionic liquids are significantly larger than those of protic ionic liquids. *Angew. Chem. Int. Ed.* **2016**, *55*, 11682–11686. [CrossRef] [PubMed]
13. Ludwig, R. The effect of dispersion forces on the interaction energies and far infrared spectra of protic ionic liquids. *Phys. Chem. Chem. Phys.* **2015**, *17*, 13790–13793. [CrossRef]
14. Emel´yanenko, V.N.; Boeck, G.; Verevkin, S.P.; Ludwig, R. Volatile times for the very first ionic liquid: Understanding the vapor pressures and enthalpies of vaporization of ethylammonium nitrate. *Chem. Eur. J.* **2014**, *20*, 11640–11645. [CrossRef] [PubMed]
15. Fumino, K.; Wulf, A.; Verevkin, S.P.; Heintz, A.; Ludwig, R. Estimating enthalpies of vaporization of imidazolium-based ionic liquids from far-infrared measurements. *ChemPhysChem* **2010**, *11*, 1623–1626. [CrossRef] [PubMed]
16. Kulikov, D.; Verevkin, S.P.; Heintz, A. Enthalpies of vaporization of a series of aliphatic alcohols: Experimental results and values predicted by the ERAS-model. *Fluid Phase Equilib.* **2001**, *192*, 187–207. [CrossRef]
17. Majer, V.V.; Svoboda, V.V.; Kehiaian, H.V. *Enthalpies of Vaporization of Organic Compounds: A Critical Review and Data Compilation*; Blackwell Scientific Publications: Oxford, MO, USA, 1985; ISBN 0632015292.
18. Pimentel, G.C.; McClellan, A.L. *Hydrogen Bond*; Freeman: San Francisco, CA, USA, 1960.
19. Jeffrey, G.A.; Saenger, W. *Hydrogen Bonding in Biological Structures*; Springer: Berlin/Heidelberg, Germany, 1991; ISBN 978-3-540-57903-8.
20. Verevkin, S.P.; Konnova, M.E.; Zherikova, K.V.; Pimerzin, A.A. Sustainable hydrogen storage: Thermochemistry of amino-alcohols as seminal liquid organic hydrogen carriers. *J. Chem. Thermodyn.* **2021**, *163*, 106591. [CrossRef]
21. Verevkin, S.P. Thermochemistry of amines: Experimental standard molar enthalpies of formation of N-alkylated piperidines. *Struct. Chem.* **1998**, *9*, 113–119. [CrossRef]
22. Verevkin, S.P.; Andreeva, I.V.; Pimerzin, A.A. Evaluation of vaporization thermodynamics of pure amino-alcohols. *J. Mol. Liq.* **2021**, *335*, 116568. [CrossRef]
23. Verevkin, S.P.; Vasiltsova, T.V. Thermochemistry of Benzyl Alcohol: Reaction Equilibria Involving Benzyl Alcohol and tert-Alkyl Ethers. *J. Chem. Eng. Data* **2004**, *49*, 1717–1723. [CrossRef]

24. Emel´yanenko, V.N.; Dabrowska, A.; Hertel, M.O.; Scheuren, H.; Sommer, K. Vapor Pressures, Enthalpies of Vaporization, and Limiting Activity Coefficients in Water at 100 °C of 2-Furanaldehyde, Benzaldehyde, Phenylethanal, and 2-Phenylethanol. *J. Chem. Eng. Data* **2007**, *52*, 468–471. [CrossRef]
25. Verevkin, S.P. Vapour pressures and enthalpies of vaporization of a series of the linear n-alkyl-benzenes. *J. Chem. Thermodyn.* **2006**, *38*, 1111–1123. [CrossRef]
26. Verevkin, S.P.; Zaitsau, D.H.; Emel´yanenko, V.N.; Heintz, A. A new method for the determination of vaporization enthalpies of ionic liquids at low temperatures. *J. Phys. Chem. B* **2011**, *115*, 12889–12895. [CrossRef]
27. Verevkin, S.P.; Zaitsau, D.H.; Emel´yanenko, V.N.; Ralys, R.V.; Yermalayeu, A.V.; Schick, C. Vaporization enthalpies of imidazolium based ionic liquids. A thermogravimetric study of the alkyl chain length dependence. *J. Chem. Thermodyn.* **2012**, *54*, 433–437. [CrossRef]
28. Verevkin, S.P. Imidazolium based ionic liquids: Unbiased recovering of vaporization enthalpies from infinite-dilution activity coefficients. *Molecules* **2021**, *26*, 5873. [CrossRef]
29. Verevkin, S.P.; Zaitsau, D.H.; Ludwig, R. Aprotic ionic liquids: A framework for predicting vaporization thermodynamics. *Molecules* **2022**, *27*, 2321. [CrossRef]
30. Zaitsau, D.H.; Yermalayeu, A.V.; Emel´yanenko, V.N.; Schulz, A.; Verevkin, S.P. Thermochemistry of pyridinium based ionic liquids with tetrafluoroborate anion. *ZAAC* **2017**, *643*, 87–92. [CrossRef]
31. Emel´yanenko, V.N.; Verevkin, S.P.; Heintz, A. Pyridinium based ionic liquids. N-Butyl-3-methyl-pyridinium dicyanoamide: Thermochemical measurement and first-principles calculations. *Thermochim. Acta* **2011**, *514*, 28–31. [CrossRef]
32. Krueger, P.J.; Mettee, H.D. Spectroscopic studies of alcohols: VI. Intramolecular hydrogen bonds in ethanolamine and its o- and n-methyl derivatives. *Can. J. Chem.* **1965**, *43*, 2970–2977. [CrossRef]
33. Verevkin, S.P.; Emel´yanenko, V.N.; Diky, V.; Muzny, C.D.; Chirico, R.D.; Frenkel, M. New group-contribution approach to thermochemical properties of organic compounds: Hydrocarbons and oxygen-containing compounds. *J. Phys. Chem. Ref. Data* **2013**, *42*, 33102. [CrossRef]
34. Ducros, M.; Gruson, J.F.; Sannier, H.; Velasco, I. Estimation des enthalpies de vaporisation des composes organiques liquides. Partie 2. Applications aux ethersoxydes, thioalcanes, cetones et amines. *Thermochim. Acta* **1981**, *44*, 131–140. [CrossRef]
35. Verevkin, S.P. Predicting enthalpy of vaporization of Ionic Liquids: A simple rule for a complex property. *Angew. Chem. Int. Ed.* **2008**, *47*, 5071–5074. [CrossRef]
36. Flett, M.S.C. Studies of the band near 3 μ in some hydroxy compounds. *Spectrochim. Acta* **1957**, *10*, 21–37. [CrossRef]
37. Wheeler, S.E.; Houk, K.N.; Schleyer, P.v.R.; Allen, W.D. A hierarchy of homodesmotic reactions for thermochemistry. *J. Am. Chem. Soc.* **2009**, *131*, 2547–2560. [CrossRef]
38. Kulikov, D.; Verevkin, S.P.; Heintz, A. Determination of vapor pressures and vaporization enthalpies of the aliphatic branched C5 and C6 alcohols. *J. Chem. Eng. Data* **2001**, *46*, 1593–1600. [CrossRef]
39. Verevkin, S.P.; Emel´yanenko, V.N. Transpiration method: Vapor pressures and enthalpies of vaporization of some low-boiling esters. *Fluid Phase Equilib.* **2008**, *266*, 64–75. [CrossRef]
40. Verevkin, S.P.; Sazonova, A.Y.; Emel´yanenko, V.N.; Zaitsau, D.H.; Varfolomeev, M.A.; Solomonov, B.N.; Zherikova, K.V. Thermochemistry of halogen-substituted methylbenzenes. *J. Chem. Eng. Data* **2015**, *60*, 89–103. [CrossRef]
41. Emel´yanenko, V.N.; Verevkin, S.P. Benchmark thermodynamic properties of 1,3-propanediol: Comprehensive experimental and theoretical study. *J. Chem. Thermodyn.* **2015**, *85*, 111–119. [CrossRef]
42. Chickos, J.S.; Acree, W.E. Enthalpies of vaporization of organic and organometallic compounds, 1880–2002. *J. Phys. Chem. Ref. Data* **2003**, *32*, 519–878. [CrossRef]
43. Chickos, J.S.; Hosseini, S.; Hesse, D.G.; Liebman, J.F. Heat capacity corrections to a standard state: A comparison of new and some literature methods for organic liquids and solids. *Struct. Chem.* **1993**, *4*, 271–278. [CrossRef]
44. Scifinder. Available online: https://scifinder.cas.org/ (accessed on 29 December 2022).
45. Nichols, N.; Wadsö, I. Thermochemistry of solutions of biochemical model compounds 3. Some benzene derivatives in aqueous solution. *J. Chem. Thermodyn.* **1975**, *7*, 329–336. [CrossRef]
46. Zaitsau, D.H.; Yermalayeu, A.V.; Emel'yanenko, V.N.; Verevkin, S.P.; Welz-Biermann, U.; Schubert, T. Structure-property relationships in ILs: A study of the alkyl chain length dependence in vaporisation enthalpies of pyridinium based ionic liquids. *Sci. China Chem.* **2012**, *55*, 1525–1531. [CrossRef]
47. Diedrichs, A.; Gmehling, J. Measurement of heat capacities of ionic liquids by differential scanning calorimetry. *Fluid Phase Equilib.* **2006**, *244*, 68–77. [CrossRef]
48. Ahmadi, A.; Haghbakhsh, R.; Raeissi, S.; Hemmati, V. A simple group contribution correlation for the prediction of ionic liquid heat capacities at different temperatures. *Fluid Phase Equilib.* **2015**, *403*, 95–103. [CrossRef]
49. Ribeiro da Silva, M.A.V.; Cabral, J.I.T.A. Standard molar enthalpies of formation of 1-methyl-2-piperidinemethanol, 1-piperidineethanol, and 2-piperidineethanol. *J. Chem. Thermodyn.* **2006**, *38*, 1461–1466. [CrossRef]
50. Lepori, L.; Matteoli, E.; Gianni, P. Vapor pressure and its temperature dependence of 28 organic compounds: Cyclic amines, cyclic ethers, and cyclic and open chain secondary alcohols. *J. Chem. Eng. Data* **2017**, *62*, 194–203. [CrossRef]
51. Zhuravleva, I.L. Evaluation of the polarity and boiling points of nitrogen-containing heterocyclic compounds by gas chromatography. *Russ. Chem. Bull.* **2000**, *49*, 325–328. [CrossRef]

52. Sauerbrey, G. Verwendung von Schwingquarzen zur Wägung dünner Schichten und zur Mikrowägung. *Zeitschrift Phys.* **1959**, *155*, 206–222. [CrossRef]
53. Zaitsau, D.H.; Yermalayeu, A.V.; Emel´yanenko, V.N.; Butler, S.; Schubert, T.; Verevkin, S.P. Thermodynamics of imidazolium-based ionic liquids containing PF6 anions. *J. Phys. Chem. B* **2016**, *120*, 7949–7957. [CrossRef]
54. Verevkin, S.P.; Ralys, R.V.; Zaitsau, D.H.; Emel´yanenko, V.N.; Schick, C. Express thermo-gravimetric method for the vaporization enthalpies appraisal for very low volatile molecular and ionic compounds. *Thermochim. Acta* **2012**, *538*, 55–62. [CrossRef]
55. Flory, P.J. *Principles of Polymer Chemistry*; Cornell University Press: Ithaca, NY, USA, 1953.
56. Yoo, B.; Afzal, W.; Prausnitz, J.M. Solubility parameters for nine ionic liquids. *Ind. Eng. Chem. Res.* **2012**, *51*, 9913–9917. [CrossRef]
57. Hansen, C.M. 50 Years with solubility parameters—Past and future. *Prog. Org. Coat.* **2004**, *51*, 77–84. [CrossRef]
58. Lide, D.R. *CRC Handbook of Chemistry and Physics: A Ready-Reference Book of Chemical and Physical Data*, 90th ed.; CRC Press: Boca Raton, FL, USA, 2009; ISBN 9781420090840.
59. Marciniak, A. Activity coefficients at infinite dilution and physicochemical properties for organic solutes and water in the ionic liquid 1-(3-hydroxypropyl)pyridinium bis(trifluoromethylsulfonyl)-amide. *J. Chem. Thermodyn.* **2011**, *43*, 1446–1452. [CrossRef]
60. Marciniak, A. The Hildebrand solubility parameters of ionic liquids—Part 2. *Int. J. Mol. Sci.* **2011**, *12*, 3553–3575. [CrossRef]
61. Domańska, U.; Wlazło, M.; Karpińska, M.; Zawadzki, M. Separation of binary mixtures hexane/hex-1-ene, cyclohexane/cyclohexene and ethylbenzene/styrene based on limiting activity coefficients. *J. Chem. Thermodyn.* **2017**, *110*, 227–236. [CrossRef]
62. Verevkin, S.P.; Zaitsau, D.H.; Emel´yanenko, V.; Yermalayeu, A.V.; Schick, C.; Liu, H.; Maginn, E.J.; Bulut, S.; Krossing, I.; Kalb, R.; et al. Making sense of enthalpy of vaporization trends for ionic liquids: New experimental and simulation data show a simple linear relationship and help reconcile previous data. *J. Phys. Chem. B* **2013**, *117*, 6473–6486. [CrossRef]
63. Zaitsau, D.H.; Yermalayeu, A.V.; Pimerzin, A.A.; Verevkin, S.P. Imidazolium based ionic liquids containing methanesulfonate anion: Comprehensive thermodynamic study. *Chem. Eng. Res. Des.* **2018**, *137*, 164–173. [CrossRef]

Disclaimer/Publisher's Note: The statements, opinions and data contained in all publications are solely those of the individual author(s) and contributor(s) and not of MDPI and/or the editor(s). MDPI and/or the editor(s) disclaim responsibility for any injury to people or property resulting from any ideas, methods, instructions or products referred to in the content.

molecules

MDPI

Article

Preparation, Characterization and Biological Activities of an Oil-in-Water Nanoemulsion from Fish By-Products and Lemon Oil by Ultrasonication Method

Nor Azrini Nadiha Azmi [1], Amal A. M. Elgharbawy [1,2,*], Hamzah Mohd Salleh [1] and Muhammad Moniruzzaman [3,4]

[1] International Institute of Halal Research and Training (INHART), International Islamic University Malaysia, Gombak 53100, Malaysia
[2] Bioenvironmental Engineering Research Centre (BERC), Department of Biotechnology Engineering, Faculty of Engineering, International Islamic University Malaysia (IIUM), Kuala Lumpur 53100, Malaysia
[3] Chemical Engineering Department, Universiti Teknologi PETRONAS, Seri Iskandar 32610, Malaysia
[4] Center for Research in Ionic Liquids, Universiti Teknologi PETRONAS, Seri Iskandar 32610, Malaysia
* Correspondence: amal.elgharbawy@gmail.com

Abstract: Fish by-product oil and lemon oil have potential applications as active ingredients in many industries, including cosmetics, pharmaceuticals and food. However, the physicochemical properties, especially the poor stability, compromised the usage. Generally, nanoemulsions were used as an approach to stabilize the oils. This study employed an ultrasonication method to form oil-in-water nanoemulsion of lemon and fish by-product oils (NE-FLO). The formulation is produced at a fixed amount of 2 wt% fish by-product oil, 8 wt% lemon oil, 10 wt% surfactant, 27.7 wt% co-surfactants and 42 min of ultrasonication time. The size, polydispersity index (PDI) and zeta potential obtained were 44.40 nm, 0.077, and −5.02 mV, respectively. The biological properties, including antioxidant, antibacterial, cell cytotoxicity, and anti-inflammatory, showed outstanding performance. The antioxidant activity is comparable without any significant difference with ascorbic acid as standard and is superior to pure lemon oil. NE-FLO successfully inhibits seven Gram-positive and seven Gram-negative bacterial strains. NE-FLO's anti-inflammatory activity is 99.72%, comparable to nordihydroguaiaretic acid (NDGA) as the standard. At a high concentration of 10,000 $\mu g \cdot mL^{-1}$, NE-FLO is non-toxic to normal skin cells. These findings demonstrate that the NE-FLO produced in this study has significant potential for usage in various industries.

Keywords: nanoemulsion; nano-materials; ultrasonication; fish oil; lemon oil; antioxidant; antibacterial; anti-inflammatory; cell cytotoxicity

1. Introduction

The fish industry produces large amounts of fish by-products such as skin, heads, frames, fins, viscera, and trimmings. While always being discarded, the fish by-products have a high content of valuable nutritional compounds, including essential fatty acids. Some of these fatty acids, such as long-chain n-3 polyunsaturated fatty acids (PUFAs), are beneficial to human health [1,2] and could be a potential source of oil for various industries. Fish oil has been widely reported as a developing supplement to improve the severity of skin disorders such as dermatitis, photoaging, allergy, skin cancer, melanogenesis, and cutaneous wounds [3]. Omega-3 polyunsaturated fatty acids (PUFAs), docosahexaenoic acid (DHA), and eicosapentaenoic acid (EPA) are said to be responsible for the relationship of fish oil with skin protection and homeostasis [3]. Owing to their nutrients, fish by-products have been used to produce products for topical administration. However, fish oils are usually associated with problems such as being inherently unstable and highly susceptible to oxidation, which imperils the oil quality [4].

Citrus limonum, often known as lemon oil, is a highly volatile essential oil that can be applied therapeutically due to its anti-oxidative, anti-proliferative, antibacterial, and anti-cancerous merits [5,6]. Lemon essential oil's antioxidant properties benefit human skin as it undergoes environmental and chronological ageing [7]. Other than that, lemon oil could help to restore the skin's natural balance and nourish damaged skin while hydrating the skin. However, the physicochemical properties of lemon oil, such as high volatility, poor stability and rapid degradability upon exposure, lamentably, impede its potency [6]. Thus, to overcome the issue of oil degradation, one of the methods to stabilize the oil is through nanoemulsions formulation. Studies have shown that fish oil characteristics could be improved through this system [8,9].

Nanoemulsion (NE) is a colloidal particulate system in the submicron size range that consists of oil, water, and emulsifiers or surfactants. NE particle size can vary substantially across different studies, with particle sizes as small as 5 nm to 200 nm [10]. These carriers are solid spheres whose surface is amorphous and lipophilic with a negative charge. Their small size results in a greater surface area providing a greater absorption enabling NE to effortlessly find its way into commercial preparations in many industries. Ample studies have been done as NE has numerous advantages over other technologies, such as ease of manufacture, adjustable particle sizes, and excellent kinetic stability [11]. Since NEs consist of oil, water, and interfacial regions, lipophilic, hydrophilic, and amphiphilic components can be easily integrated into the formulation. Hence, they are suitable to be used in various products. Because of their flexibility, a broad range of delivery formulations with various functional qualities and improved sensorial properties can be developed.

Currently, low and high-energy emulsification methods can be utilized to fabricate NEs. The low-energy method transforms a water-in-oil (W/O) emulsion into an oil-in-water emulsion (O/W NE). By changing the experimental parameters, such as the composition or the temperature, phase inversion can be achieved to produce fine oil droplets at the inversion point where there is very little interfacial tension [11]. On the other hand, high-energy procedures use specific mechanical tools, such as high-pressure homogenizers, ultrasonicator, or microfluidizers, to break the droplets into extremely small particles. The ultrasonication method is frequently employed because of its appealing features where the cavitation principles are utilized. In this method, when an asymmetric cavity collapses, strong turbulence is produced by ultrasound, which starts the emulsification process by creating droplets in the acoustic field. The bigger droplets are fragmented into smaller ones, which disperse into the continuous phase as a result [8]. In recent years, research has explored ultrasonication to produce nanoemulsions with various components for various purposes. For example, Nirmal et al. [12] focused on different essential oils to produce nanoemulsions, while Nirmala et al. [13] employed ultrasonication to study the anticancer and antibacterial activities of celery oil-based nanoemulsions.

Considering that the selected oils are composed of chemical components that are sensitive to high temperatures, light, and the presence of oxygen; and that nanoemulsion systems have improved the stability and quality of many essential oils, this research aimed to produce oil-in-water nanoemulsion of lemon and fish by-product oils by ultrasonication technique for topical application. The physicochemical properties of the obtained nanoemulsions were characterized, and their antioxidant, anti-inflammatory and antibacterial activity were also assessed. This nanoemulsion produced is suitable as a topical application for skin treatment and cosmetics. It could be used as nanocarriers to improve skin penetration and provide a controlled release of active compounds for cosmetic products. Although it is not reported in this study, this formulation is currently in development for drug delivery for the rapid metabolism of active pharmaceutical ingredients and improve their bioavailability, especially the hydrophobic drugs.

2. Results and Discussions

An oil-in-water nanoemulsion of lemon and fish by-product oils (NE-FLO) was successfully produced, and the biological activity was tested in this study. This section reported and discussed the results obtained.

2.1. Organoleptic Properties of NE-FLO

Organoleptic properties are the aspects of food or other substances experienced by the senses, including taste, sight, smell, and touch. They are among the most important features to be considered in the formulation of various products as they give an aesthetic attribute to the product, which affects the customers' choices [14]. A careful evaluation of the properties of the finished product should be conducted. This study assessed three organoleptic properties: odor, appearance, and texture. The NE-FLO exhibit a strong citrus smell owing to the incorporation of lemon oil, while its appearance exhibits translucent, yellowish color. For the texture, NE-FLO is non-sticky and has a lightweight texture which are good attributes for a product to possess. A product's quality must be enticing to fill shelf space, capture consumer interest, and encourage repeat purchases. The performance, texture, look, and odor are among the elements that determine its quality and appeal. Figure 1 shows the NE-FLO produced by using the ultrasonication method.

Figure 1. Nanoemulsion produced using ultrasonication method (NE-FLO).

2.2. Measurement of Particle Size, Polydispersity Index (PDI) and Zeta Potential

Photon correlation spectroscopy (PCS), also known as dynamic light scattering (DLS), was used to determine the particle size and PDI of nanoemulsions, which monitors the difference in light scattering caused by the Brownian motion of particles as a function of time. The PCS principle is based on the theory that a smaller particle will travel at a higher speed. The laser beam gets diffracted by submicron particles present in the samples. Due to particle dispersion, rapid fluctuations in laser scattering intensity arise around a mean value at a constant angle. The estimated photoelectron time correlation function generates a histogram of line width distribution that can be attributed to particle size [10,15]. Particle size distribution, mean particle diameter (Z-averages), and polydispersity index (PDI) are critical nanoemulsion quality, homogeneity, and dispersibility measures. The size for the NE-FLO recorded is 44.40 $\pm$ 0.11 nm. For most administration routes, the favorable particle size value for nanoemulsion is accepted as $\leq$500 nm [16]. Thus, the formulation for NE-FLO achieved the desired particle size, which is far less than 500 nm. This was

also supported by a study by Rocha-Filho et al. [17], which attained an almost similar size for vegetable oil-based nanoemulsion using an ultrasonication technique. Additionally, nanoemulsions were also obtained by ultrasonication using capsaicin in the oil phase and Tween 80, glycerol in the aqueous phase where the mean droplet size is below 65 nm [18].

Reduced particle size enhanced the stability of nanoemulsions against coalescence and flocculation. When the particle size reduces, the attractive forces become weaker rapidly than the repulsive forces. Many factors are associated with the small size of nanoemulsions, such as the constitution of the formulation, production techniques, and conditions. The small particle size of NE-FLO might be due to the ultrasonication process's energy. The primary effect of ultrasound is cavitation, which is the rapid production of vapor bubbles in a liquid at ambient temperature under decreased pressure. The resulting bubbles rapidly collapse, generating pressurized shock waves. This results in highly localized turbulence and large shear forces traversing the liquid, creating high-velocity liquid jets and breaking down the emulsion into minuscule droplets [19]. Size, on the other hand, is often not provided as a single value but rather as a representative value of a distribution that can be narrow, moderate, or broad. This means when the size of all droplets is nearly identical, the size distribution is narrow; when the size of most droplets is varied, the size distribution is broad.

The polydispersity index (PDI) in nanoemulsions is the ratio of standard deviation to mean droplet size, which reflects homogeneity in droplet size within the formulation. PDI represents the deviation from the average size. The PDI value ranges from 0 to 1, where 0 (zero) represents a monodisperse system and (1) is for a polydisperse particle dispersion [15]. A PDI lower than 0.2 is desirable as it implies that the nanoemulsion droplets are almost similar in size and free of adhesion and aggregation [19]. The PDI for NE-FLO is 0.077, indicating the homogeneity of the formulation. Ultrasonication employed by Espinosa-Andrews and Paez-Hernandez [20] produced small droplet nanoemulsions with a small polydispersity index, which is better than nanoemulsion produced by microfluidization. This study showed that ultrasonication was an efficient technique to generate nanoemulsions than microfluidization. Other studies also have shown that the ultrasonication method is good for producing nanoemulsions with a narrow polydispersity index [21–23]. The external power of ultrasonication used in the preparation might be the reason for the small PDI compared to the spontaneous emulsification process. Furthermore, the high concentration of surfactant and co-surfactant allows ease of dispersion, reduces aggregation, and thus, decreases PDI value.

Zeta potential is utilized to estimate dispersion stability. The value depends on many factors, such as the physicochemical characterization of the emulsion components, the presence of any electrolytes, and their adsorption ability [24]. The zeta potential's magnitude can be used to evaluate particle stability in suspension. In theory, the molecules will repel any suspension with a highly negative or positive zeta potential value, evading aggregation and increasing the suspension's stability. When the zeta potential obtained has an almost zero value, the surface charge is absent, which can enhance interactions between particles, facilitating aggregation or flocculation processes. Generally, for a suspension to be considered stable, a zeta potential value of greater than $|30|$ mV should be achieved [25].

This study's zeta potential average value for NE-FLO is -5.02 ± 0.22 mV. As a result of the addition of lemon oil and a co-surfactant into the formulation, the pH of the NE-FLO is low, which is 4.27 ± 0.01. Acidic pH can significantly decrease the zeta potential value by increasing the positive charges on the surface of the particles [26]. Conversely, at a lower pH, the electrical charge on the particles is reduced, which decreases electrostatic repulsion between them and leads to aggregation [27]. This might explain the low value of zeta potential. However, even though the zeta potential value is not in the ideal range, the charge in the nanoemulsions is sufficient to make it stable for a long time, which can be seen in the steric and electrostatic stabilization presented by colloidal dispersions [25]. This is evident in this study, where significant instability problems such as flocculation, coalescence, and sedimentation were not detected in NE-FLO at temperatures of 4 and 25 °C. Kaur et al. [6]

also observed a zeta potential value lower than 30 mV, but the nanoemulsion produced had a higher stability percentage compared to the individual oil tested. Cossetin et al. [28] also encountered the same situation when their nanoemulsion zeta potential value was only 11 mV, but the formulation was remarkably stable for more than three months.

2.3. Morphological Analysis by Scanning Electron Microscopy

NE-FLO are subjected to SEM examination to study the structure and morphology at various magnifications, where the three-dimensional image of the surface morphology of the dispersed phase is created. Figure 2 shows that NE-FLO had an irregular shape with a range of 50 nm, proving the particle size recorded by the particle size analyzer. Hatziantoniou et al. [29] also demonstrated irregular shapes of nanoemulsions containing ceramide. Some studies have shown spherical shapes [30,31], which were a product of the results of this study. This might be due to the components and the way the nanoemulsions were prepared.

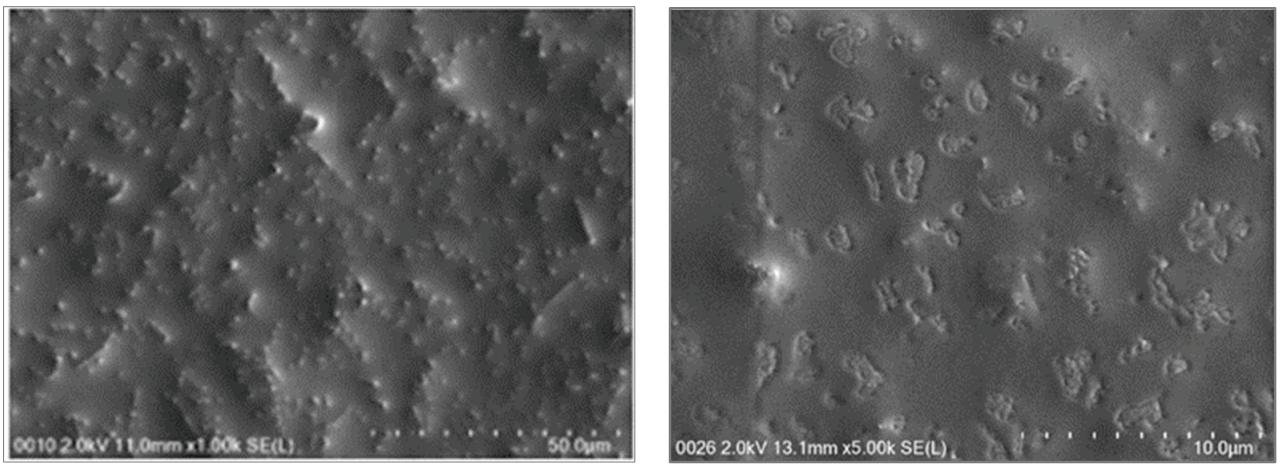

(**a**) (**b**)

Figure 2. SEM images of NE-FLO in different conditions: (**a**) the SEM image taken at 1 kX magnification, (**b**) the SEM images taken at 5 kX magnification. The voltages used for both images are 2.0 kilovolts.

2.4. Stability Assessment

Stability studies are conducted to determine the drug substance's stability under various environmental conditions such as temperature, humidity, and light. The impact of external factors on the quality of a drug substance or a formulated product is evaluated in a stability test, which is used to estimate shelf life, identify optimum storage conditions, and recommend labelling instructions. Stability tests of nanoemulsions can be carried out by differing the storage time or temperatures. In this study, visible observations and also physical analyses of the size and pH changes were carried out over 90 days of storage at 4 and 25 °C, respectively, to evaluate the stability of the nanoemulsions. NE-FLO still exhibits the same organoleptic qualities, such as odor, color, and texture, and there is no phase separation after 90 days. Overall, as shown in Table 1, the size of both nanoemulsions increased significantly with time ($p \leq 0.05$). It is indeed crucial to emphasize that systems containing water, oil, and surfactant have a kinetic barrier preventing the phases from reaching kinetic equilibrium, resulting in larger droplets [28]. However, despite particle size increment, the emulsions were still in the nano range. The NE-FLO was translucent at the end of the storage period. At the end of 90 days, significant instability problems, such as flocculation, coalescence, and sedimentation, were not detected in the samples under both temperatures. It can also be observed that the room temperature conditions at 25 °C increased the particle size compared to the chilled condition. This could be due to the key

mechanism of instability in these systems, the Ostwald maturation, which occurs when smaller droplets molecularly diffuse into larger droplets at higher temperatures [32].

Table 1. Stability study of NE-FLO at different storage temperatures assessed using size analysis at different storage times.

Temperature	Size Day 0 (nm)	Size Day 90 (nm)
25 °C	44.40 ± 0.11 [a]	89.24 ± 0.025 [b]
4 °C	44.40 ± 0.11 [a]	125.15 ± 0.00 [c]

Data are presented as mean ± SD (n = 3). Different letters in the columns indicate statistically significant values compared to day 0 ($p < 0.05$).

Table 2 shows that the pH reduced significantly at room temperature on day 90. The reduction in the observed pH may again be attributed to changes in the nanoemulsion interface, which causes more contact of the oil with the aqueous phase and favours the degradation of some of its compounds and their volatilization, as was seen at elevated temperatures [28]. However, the pH remained constant throughout the 90 days of the study at 4 °C ($p > 0.05$). Maintaining the pH of a product, especially in the cosmetic market, is important. A low pH is favorable because it inhibits the growth of a wide range of bacteria in the product. Some bacteria can be dangerous and impact a product's shelf life and stability. Products with increased pH might impact the condition of healthy skin. For cosmetic-relevant skin conditions, skin disorders and specific consumer groups, maintaining the acidic pH of the skin surface is beneficial for epidermal physiology and cutaneous microflora. Several epidermal barrier functions, like skin barrier regeneration and antimicrobial response, are related to the acidic nature of the skin surface pH. In this context, cleansing and skincare products with a pH of 4.0–5.0 may be helpful [33]. Thus, products with low pH are preferable and more helpful than a product with a higher pH.

Table 2. Stability study of NE-FLO at different storage temperatures assessed using pH measurement at different storage times.

Temperature	pH Day 0	pH Day 90
25 °C	4.27 ± 0.01 [a]	4.22 ± 0.025 [b]
4 °C	4.27 ± 0.005 [a]	4.27 ± 0.00 [a]

Data are presented as mean ± SD (n = 3). Different letters in the columns indicate statistically significant values compared to day 0 ($p < 0.05$).

2.5. Antioxidant Evaluation

The DPPH assay is one of the most utilized antioxidant assays because it is relatively simple with outstanding sensitivity. The impact of antioxidants on DPPH is based on their hydrogen-donating ability. DPPH is reduced to yield DPPH-H when an unpaired electron of DPPH is accepted by hydrogen atoms from antioxidants, causing the absorbance spectrum to change [34]. Okonogi et al. [35] interpreted inhibitory concentration (IC50) as a concentration of sample required for scavenging DPPH radical in the solution by 50%. The lesser the IC50 value, the more powerful the samples' antioxidant activity.

From Table 3, it can be seen that there is no significant difference between the IC50 value of NE and ascorbic acid. However, the IC50 value is significantly lower than pure lemon oil.

Table 3. The IC50 value of lemon oil, NE-FLO, and ascorbic acid used in the DPPH assay.

Samples	IC_{50} Values ($mg \cdot mL^{-1}$)
Lemon oil	0.424 ± 0.0013
Ascorbic acid	0.281± 0.0013
NE-FLO	0.300± 0.0565

The high antioxidant value of NE-FLO might be a contribution from the components used in the formulation, such as lemon and fish oil. The free radical scavenging activity was visible in all samples and the control, ascorbic acid. Increasing the concentration of NE-FLO from 0.039 mg·mL^{-1} to 10 mg·mL^{-1} also increased the scavenging activity.

Lemon oil, as one of the major components, might have the greatest effect on the antioxidant level of the NE-FLO. This activity may contribute to the presence of monoterpene components in lemon oil, such as limonene and terpinene, which may act as radical scavenging agents [5]. Monoterpenes and sesquiterpenes were also reported to be accountable for the neutralization of the DPPH radical [36]. However, it can be seen that NE-FLO exhibits higher antioxidants than pure lemon oil as the IC50 is lower. This observation is also supported by Liu et al. [37], in which the lemon oil nanoemulsions had better antioxidant capacities than the essential oils. It is explained that not only the primary constituents of the lemon oil should be considered, but each and every one of its constituents.

The fish oil might also cause the higher antioxidant activity of the NE-FLO in the dispersions. The fatty acids and other compounds in fish oil, such as polyphenols, have been proven to reduce DPPH radicals [38]. In addition, the NE-FLO has a higher number of hydroxyl groups from other components than the pure lemon oil, which impacts their hydrogen-donating ability, and thus neutralizes the DPPH radical. Figure 3 shows the neutralization of the DPPH radical by the antioxidants.

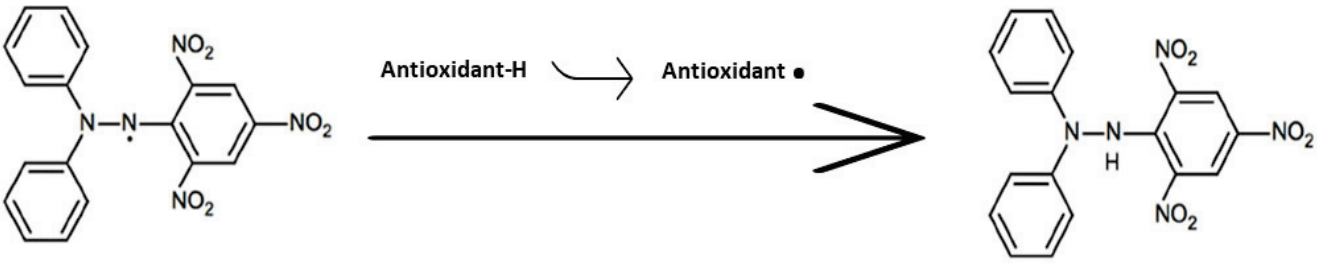

Figure 3. Reaction mechanism of 2,2-diphenyl-1-picrylhydrazyl (DPPH) with antioxidant.

Pure lemon oil was insoluble in the aqueous system, which might decrease its antioxidant activity. On the other hand, the nanoemulsions showed great water solubility, making them ideal for the efficient delivery of active components, and the huge surface area allows for excellent penetration of active chemicals [39]. Therefore, NE-FLO can more effectively scavenge radicals and have stronger reducing power, enhancing the radical scavenging capacity of the DPPH.

2.6. Antibacterial Evaluation

The disc diffusion approach is among the most versatile methods to measure microbes' resistance against antibacterial agents. Generally, the filter paper disc mounted on top of the agar's surface acts as an agent reservoir. After incubation, an inhibition area would form surrounding the filter paper disc if the samples examined were microbiologically active. The diameter of the inhibition zone appropriately defines the antibacterial ability. Nearly all of the published methods consider any inhibition zone around the filter paper disc to indicate antibiotic activity [40].

Fourteen microbial strains were selected to evaluate the ability of NE-FLO to inhibit their growth. DMSO is used as the negative control because this universal aprotic polar solvent can dissolve NE-FLO as a test sample and is a solvent with no antibacterial properties [41]. Tetracycline is commonly employed because of its wide spectrum of antimicrobial activity, including Gram-positive and Gram-negative bacteria, spirochetes, obligate intracellular bacteria, and protozoan parasites [42]. The results in Table 4 show that the NE-FLO possesses antibacterial activity as there are inhibition zones for all plates. The biggest inhibition zone for the antibacterial activity is observed in Gram-positive bacteria, *Corynebacterium diphtheriae*. From most of the results shown, Gram-positive bacteria have

a larger inhibition zone compared to Gram-negative bacteria. This might be caused by the Gram-positive bacteria morphology with a cell wall that readily absorbs the nanoemulsions, making its way easily through the inner membrane, hence interacting with intracellular sites, which is crucial for antibacterial activity [43]. Gram-negative bacteria possess high resistance to nanoemulsions' antibacterial activity because their membrane structure is more complex [44]. Some studies reported that the lipopolysaccharides on the cell wall prohibit the nanoemulsions from penetrating and impacting the cell membrane [5,44,45]. The results presented are consistent with earlier research on citral nanoemulsions that showed significant antimicrobial activities against *Listeria monocytogenes* and *Staphylococcus aureus* [46]. Salvia-Trujillo et al. [47] also showed that the soybean oil-based nanoemulsion demonstrated bactericidal effects against *Vibrio cholerae*, *Neisseria gonorrhoeae*, *Bacillus cereus*, and *B. subtilis*. Figure 4 shows the inhibition zones for NE-FLO, the positive and negative control against *B. cereus*.

Table 4. Antimicrobial activity of NE-FLO and controls against different bacterial strains by disc diffusion method.

Gram-Positive Bacteria	NE-FLO	Positive Control (Tetracycline 10 mg·mL^{-1})	Negative Control (DMSO)
Bacillus cereus	3 ± 0 mm	11 ± 2 mm	
B. subtilis	6 ± 0 mm	18.3 ± 1.15 mm	
Clostridium perfringens	2 ± 0 mm	14.67± 1.15 mm	
Corynebacterium diphtheriae	8.67 ± 0.57 mm	19 ± 0 mm	0 ± 0 mm
Listeria monocytogene	4.33 ± 0.57 mm	19.67± 0.57 mm	
Staphylococcus aureus	3 ± 0 mm	19 ± 0 mm	
Streptococcus pneumoniae	4.33 ± 0.57 mm	6.67 ± 1.15 mm	
Gram-Negative Bacteria	**NE-FLO**	**Positive Control (Tetracycline 10 mg·mL^{-1})**	**Negative Control (DMSO)**
Escherichia coli	4 ± 0 mm	18.67 ± 0.57 mm	
Proteus mirabilis	3.33 ± 0.57 mm	19.33 ± 1.53 mm	
Vibrio vulnificus	4 ± 0 mm	10.33 ± 1.53 mm	
Vibrio parahaemolyticus	4 ± 0 mm	16.33 ± 2.5 mm	0 ± 0 mm
Salmonella enteritidis	4 ± 0 mm	18.67 ± 0.57 mm	
S. typhimurium	3 ± 0 mm	18 ± 0 mm	
Shigella sonnei	3.33 ± 0.57 mm	5 ± 1 mm	

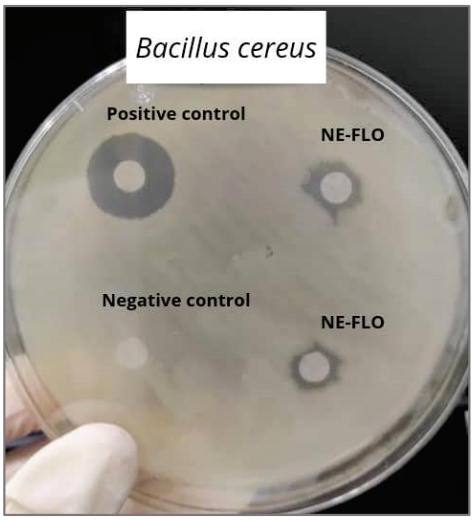

Figure 4. The inhibition zones for NE-FLO, the positive and negative control against *B. cereus* as, an example of the antibacterial activity of the NE-FLO.

The presence of components, such as lemon oil, fish oil, and hydrophobic DES impacted the antimicrobial activity of the NE-FLO. This might be due to the fatty acids found in the fish oil, which could suppress the growth of the tested strains. NE-FLO can destroy bacteria through two means: bactericidal action and, secondly, prevent its growth (bacteriostatic action), which is reversible. In other words, in the presence of the tested samples, the bacterium cannot undergo cell division, although it remains viable [48]. Antimicrobial lipids such as fatty acids and monoglycerides have membrane-lytic capabilities due to their amphipathic qualities, which result in overlapping biophysical processes, such as membrane instability and pore formation. Membrane-destabilizing activity, in particular, induces enhanced cell permeability and lysis, resulting in bacterial cell growth inhibition (bacteriostatic action) or cell death (bactericidal action) [49]. Figure 5 shows the proposed mechanism of the antibacterial activity of NE-FLO.

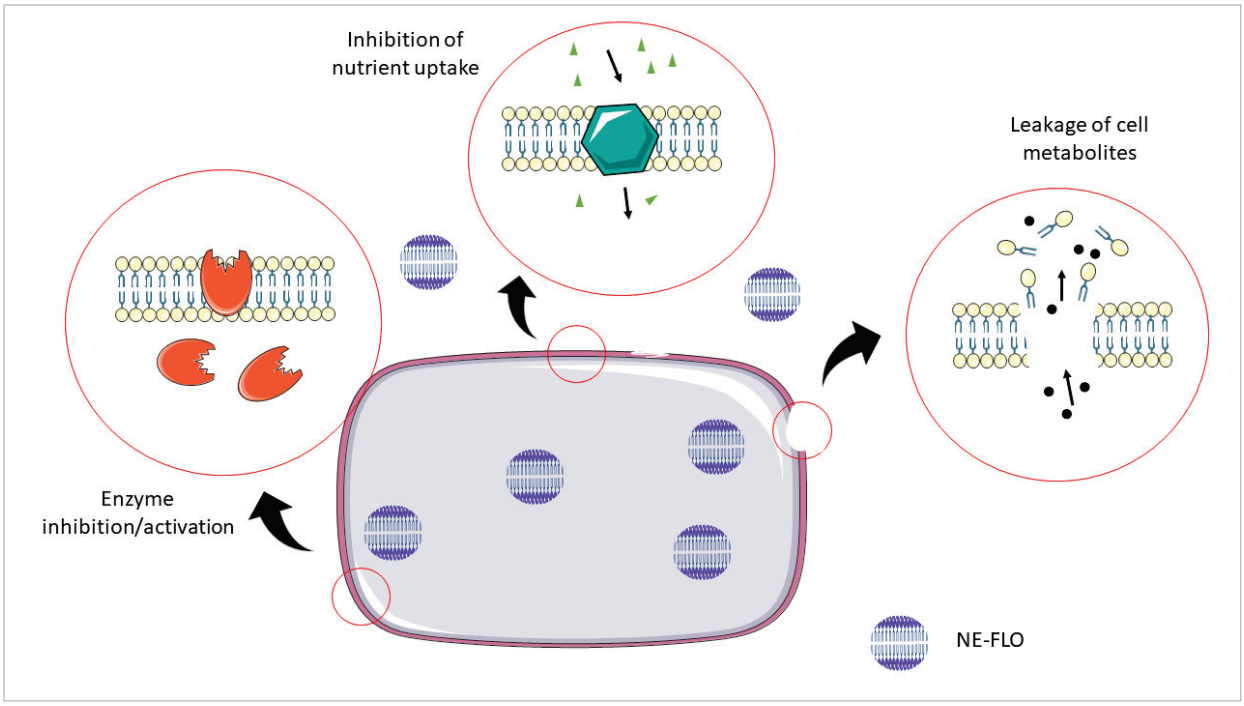

Figure 5. Possible mechanism of antibacterial activity of NE-FLO.

2.7. Minimum Inhibitory Concentration (MIC) and Minimum Bactericidal Concentration (MBC) Determination

DDT only provides a qualitative assessment of the antibacterial activity; hence, the minimum inhibitory concentration (MIC) test was employed in this study to provide insight into the quantitative measurement of antibacterial activity. From Table 5, it can be observed that NE-FLO effectively inhibits the growth and killing of the bacteria. Among the bacteria tested, *Staphylococcus aureus* had the highest sensitivity since a lower concentration of NE-FLO was needed to inhibit the growth. While the highest concentration of NE-FLO (500 mg·mL^{-1}) was required to inhibit the growth of *Proteus mirabilis*. This might be because of the nature of the bacteria. Gram-negative bacteria are harder to destroy because of their complex membrane structure [43]. The results from Lou et al. [39] indicated that the inhibition rate of *Staphylococcus aureus* of the nanoemulsified essential oil was significantly higher at (80.4%) than that of the pure essential oil (40.8%) at similar concentrations. This strongly suggests that incorporating the oil inside the nanoemulsion system improved the oil's antibacterial activity.

Table 5. Evaluation of Minimum Inhibitory Concentration and Minimum Bactericidal Concentration (MBC) of NE-FLO on different bacteria.

Bacteria/Test	MIC (mg·mL^{-1})	MBC (mg·mL^{-1})
Bacillus cereus	250	250
B. subtilis	250	500
Corynebacterium diphtheriae	250	500
Clostridium perfringens	125	125
Listeria monocytogenes	250	250
Staphylococcus aureus	62.5	125
Streptococcus pneumoniae	250	250
Escherichia coli	250	250
Proteus mirabilis	500	500
Salmonella enteritidis	125	250
Shigella sonnei	125	250
Salmonella typhimurium	125	250
Vibrio parahaemolyticus	250	250
V. vulnificus	250	500

Generally, the antibacterial activity of the nanoemulsion is said to be highly dependent on its components, the tested microbial strain, and the emulsion formulation and size. Yazgan et al. [50] also observed this, and reported that lemon essential oil-based nanoemulsion could potentially be a natural antimicrobial agent against foodborne pathogens and spoilage bacteria. It remains unknown how the antibacterial activity of nanoemulsions is exhibited. Still, the primary target is the cell membrane of the bacteria and the different basic processes inside and at the membrane. Cell lysis, destruction of nutrient absorption, production of toxic peroxidation and auto-oxidation products, and inhibition of enzyme activity are among the other mechanisms that might lead to growth inhibition or death of bacteria [44].

2.8. Anti-Inflammatory Evaluation

Lipoxygenase inhibition assay was used to determine the in vitro anti-inflammatory activity of the NE-FLO. NE-FLO has outstanding anti-inflammatory activity as nordihydroguaiaretic acid (NDGA), the positive control ($p > 0.05$), for the inhibition of 5-LOX activity. The results tabulated in Table 6 show that the lipoxygenase inhibition of NE-FLO is 99.72%, indicating more than 99% of the lipoxygenase enzyme are inhibited by NE-FLO. This might be due to arachidonic acid, high fatty acid content from catfish oil, and other chemical components, such as polyphenols, in the NE-FLO reported by Zadeh-Ardabili and Rad [38], who found high anti-inflammatory activity in fish and krill oil. The antioxidant activity of the NE-FLO might also be the factor for high anti-inflammatory activity [51].

Table 6. Anti-inflammatory activity of NE-FLO assessed using lipoxygenase inhibition assay.

Samples	NDGA	NE-FLO
Lipoxygenase inhibition (%)	99.83 ± 0.27 [a]	99.72 ± 0.23 [a]

The control used is the nordihydroguaiaretic acid (NDGA). Data are presented as mean ± SD ($n = 3$). The same letter in the columns indicates the values are not statistically significant compared to NDGA.

The flavonoids and phenolic compounds responsible for the antioxidant effect might also exert an anti-inflammatory effect. Bioactive extracts and their natural constituents have been shown to exert biological characteristics by inhibiting two important signaling pathways, NF-B and mitogen-activated protein kinases (MAPKs), which are involved in the production of numerous proinflammatory mediators [52]. Randy et al. [53], who studied the anti-inflammatory activity of partially purified Bromelain-loaded nanoemulsion, also showed similar results where the bromelain-loaded nanoemulsion has the highest activity compared to commercial bromelain and the standard. The NE-FLO has thus demonstrated

the potent inhibition of LOX activity due to their constituents from lemon and fish oil. Hence, it shows potential for future development into a functional cosmeceutical product for treating and preventing of inflammatory-associated diseases.

2.9. Cell Cytotoxicity Evaluation

The in vitro cytotoxic and anti-proliferative activity of the NE-FLO were evaluated using the MTT assay. This assay is commonly used to assess the in vitro cytotoxic effects of active drugs on cell lines or primary patient cells because the total mitochondrial activity corresponds with the percentage of viable cells in most cell populations [54]. In addition, the nanoemulsion must be biocompatible with mammalian cells for applications in cosmeceutical products. Nanoemulsions that are toxic or could release toxic by-products would destroy the skin cells and eventually worsen the conditions of the targeted area. Therefore, the toxicities of the NE-FLO were examined by indirect MTT assays using human skin fibroblasts (HSF 1184) as the model cells.

Among all the treatments with different concentrations of conditioned media obtained from the NE-FLO, no significant decrease in cell viability was observed compared to control cells. The results in Figure 6 revealed that NE-FLO increased cell growth and is nontoxic toward the HSF1184 normal skin cell lines. Vater et al. [54] found that nanoemulsions containing traditional herbal plants showed higher skin cell viability in MTT tests than the control. Similar findings from Zanela da Silva Marques et al. [55] also showed that a nanoemulsion containing propranolol is nontoxic and maintains the growth of over 80% of the fibroblast cell.

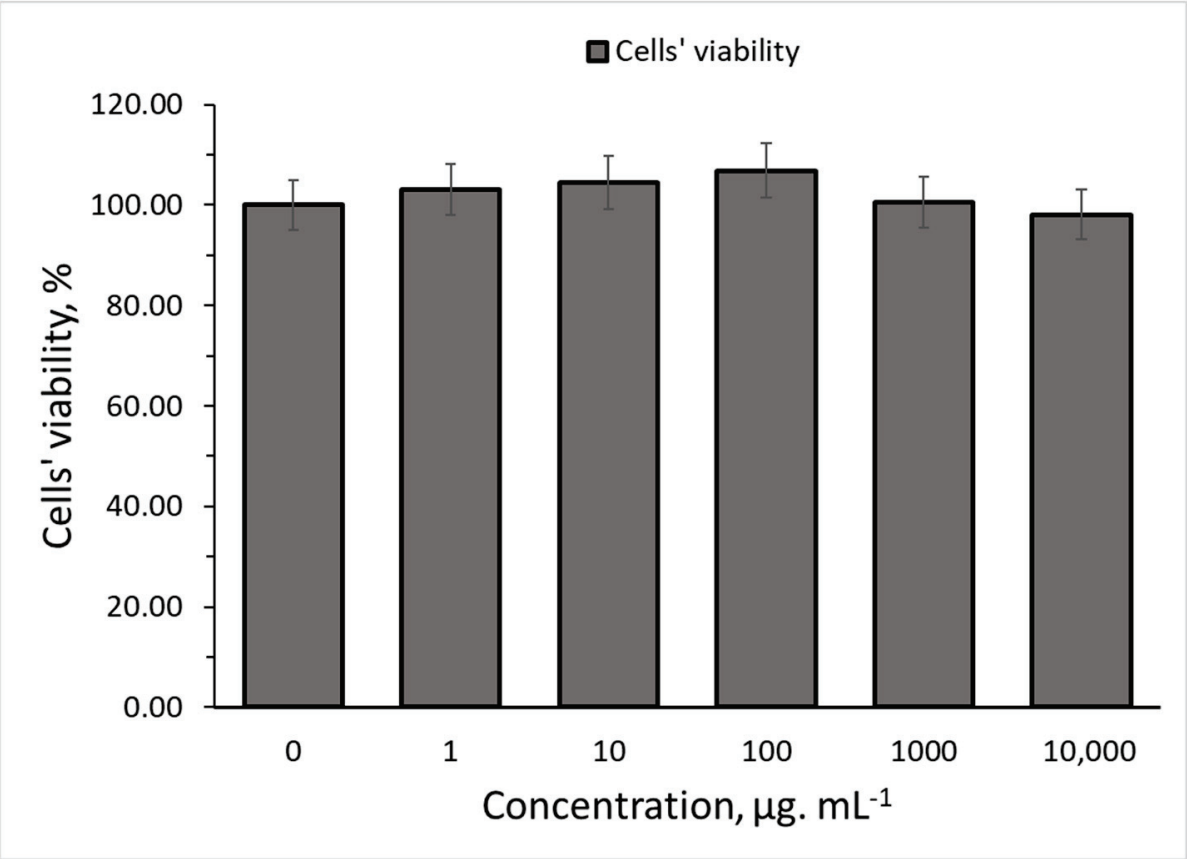

Figure 6. Cell viability of fibroblast cells (HSF 1184) cultured with increasing concentrations of NE-FLO using the MTT assay. Data are presented as mean ± SD (n = 3). Control is the cell treated with DMEM only.

Increasing the concentration of NE-FLO caused the HSF cell viability to increase as well. The highest peak was at a 100 $\mu g \cdot mL^{-1}$ concentration, which reached 106 ± 4% cell viability compared to the control. It can also be seen that even at high concentrations of 10,000 $\mu g \cdot mL^{-1}$, the NE-FLO did not display any toxic effect on the skin.

Fatty acids from fish oil might also be one of the reasons for skin cell proliferation. The fatty acids, such as palmitic acid, aided in keratinocytes and fibroblast proliferation, possibly by additionally fuelling cellular metabolism [56]. A review by Carvalho et al. [57] shows that omega-6 fatty acids have received much attention because they can modulate cell migration and proliferation, phagocytic capacity, and synthesis of inflammatory mediators, which are also found in the fish oil used in the NE-FLO. Moreover, the nano-sized emulsions could penetrate better into the cells and proliferate skin cells due to their small size [58].

3. Materials and Methods

3.1. Materials

2,2-diphenyl-1-picrylhydrazyl (DPPH) reagent and Folin–Ciocalteu reagent were obtained from Merck, Darmstadt, Germany. Sodium linoleate, soybean lipoxygenase enzyme solution and nordihydroguaiaretic acid (NDGA) for anti-inflammatory studies were purchased from Merck. Dulbecco's Modified Eagle's Medium (DMEM), fetal bovine serum and 3-(4,5-dimethylthiazol-2-yl)-2,5-diphenyltetrazolium bromide (MTT) were purchased from Life Technologies Corporation, Carlsbad, CA, USA. Human skin fibroblast cells (HSF 1184) were obtained from Life Technologies Bio Diagnostic, Malaysia. South African lemon oil was obtained from a local supplier (Wellness Original Ingredient, Malaysia). Catfish by-product oil was prepared in the laboratory as previously described by Djaeni and Listyadevi [59]. The anionic co-surfactants used in the study are not stated as it is under a patent application. All other solvents and chemicals used were analytical and/or pharmaceutical grade.

3.2. Preparation of Nanoemulsion of Fish by-Product and Lemon Oils (NE-FLO)

The method for ultrasonication is adopted from Espinosa-Andrews and Paez-Hernandez [60]. A two-step process was used to prepare the oil-in-water nanoemulsion of fish by-products and lemon oils (NE-FLO). Briefly, the continuous phase, known as the aqueous phase, was prepared by adding 10 wt% of Tween 80 and 27.7% cosurfactant to pure distilled water and stirred for 15 min. The oil phase consisted of 2 wt% fish oil and 8% lemon oil. The aqueous and the oil phases were mechanically stirred at 500 rpm until both mixtures were well combined. The oil phase was then added dropwise into the continuous aqueous phase while stirring at the same speed. A T25 digital Ultra-Turrax homogenizer was used to combine the mixture for 3 min at 20,000 rpm to form a coarse oil-in-water emulsion. The coarse emulsion was ultrasonicated at a predetermined amplitude using an ultrasonicator (LABSONIC M, Sartorius, Teltow, Germany) for 42 min to obtain the nano-sized droplet. The ultrasonication time is based on the optimization of this study. The sonication was set at 80% of the maximum output of 100 W.

There is no pulse used; however, to avoid an increase in temperature, the beaker is put inside a water-filled beaker. Thus, even when the samples were sonicated for a long time, there was no increase in temperature detected. Tween 80 was used as a surfactant as it is a hydrophilic non-ionic surfactant that is well-established in the emulsification and dispersion of substances in pharmaceutical and food products. Other than that, Tween 80 was also listed as one of the generally regarded safe agents (GRAS). For the co-surfactant, it was proven that it can form hydrogen bonds with water, lowering the water−oil interfacial tensions and improving the interface's fluidity. The percentage of the surfactant and co-surfactant used were optimized. Figure 7 shows the schematic diagram of NE-FLO preparation using the ultrasonication method.

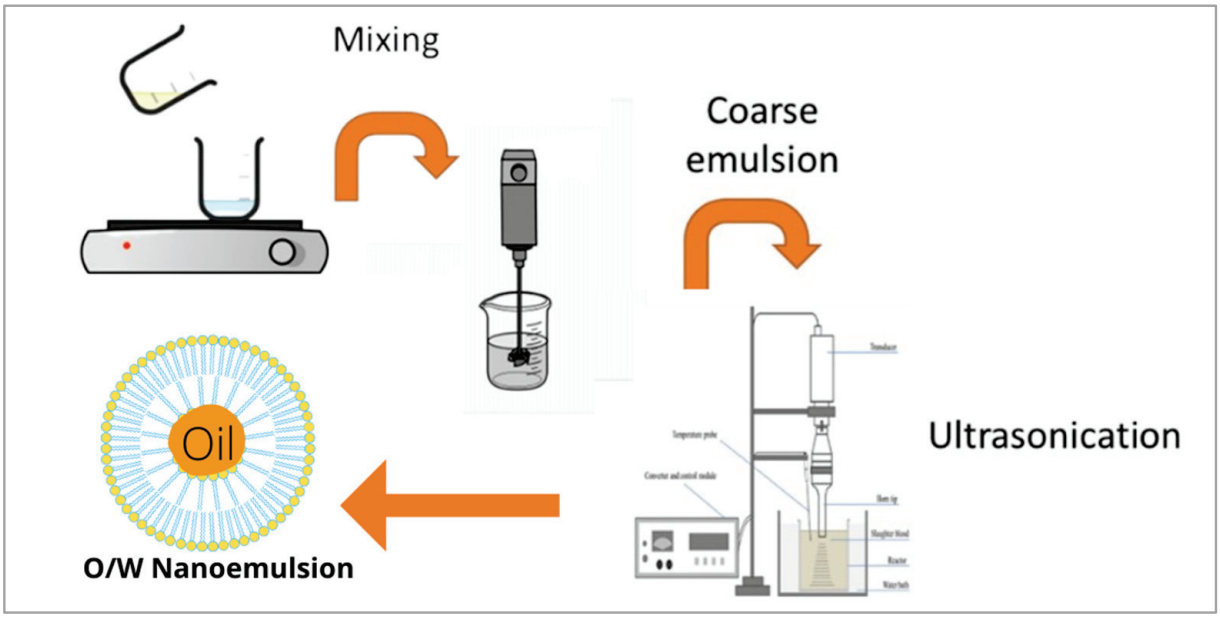

Figure 7. Schematic diagram of the preparation of NE-FLO using the ultrasonication method.

3.3. Measurement of Particle Size, Polydispersity Index (PDI) and Zeta Potential

The determination of particle size, PDI and Zeta potential of NE-FLO were analyzed using a particle size analyzer (Malvern Instruments, Malvern, UK) at 25 °C. Dilution using distilled deionized water at a ratio of 1:9 of all samples was carried out to prevent back-scattering phenomena. The particles and water refractive indices employed were 1.54 and 1.33, respectively. Each measurement was repeated in triplicate.

3.4. Morphological Analysis by Microscopic Techniques

Scanning electron microscopy (Vega3 Tescan, Kohoutovice, Czech Republic) was used to observe the morphology of the NE-FLO following a method by Krithika and Preetha [31]. NE-FLO samples were mounted on the stabs with adhesive tape, and SEM images were captured at a 20 kV accelerating voltage with a magnification of ×100 k. To examine the NE-FLO images, multiple resolutions ranging from magnification ranging from 20× to approximately 30,000× were used accordingly.

3.5. Stability Assessment

The emulsion stability, or an emulsion's ability to withstand changes in its properties over time, was studied by storing the NEs at various temperatures. Measurements were carried out at 0, 7, 14, 21, 28, and 90 days of storage. The visual instability (creaming, phase separation, or flocculation) was observed and recorded (if any). The determination of particle size of NE-FLO at day 0 and day 90 were analyzed using a particle size analyzer (Malvern Instruments, Malvern, UK) at 25 °C. The stability was also evaluated by monitoring changes in pH at different intervals of time using a pH meter (Mettler Toledo, Zurich, Switzerland).

3.6. Antioxidant Evaluation

The in vitro antioxidant activity of the NE-FLO was conducted using the 1,1-diphenyl-2-picrylhydrazyl (DPPH) assay. DPPH solution at an amount of 2.5 mL (60 μmol·L^{-1} in ethanol) was combined with 0.3 mL of the NE-FLO and 0.2 mL of ethanol in a 10 mL test tube with a final volume of 3.0 mL. The absorbance of the solution was measured at 517 nm after allowing the mixture to stand for 30 min at room temperature.

3.7. Antibacterial Evaluation

The disc diffusion test (DDT) and minimum inhibitory concentration (MIC) are the most used tests for antimicrobial properties against Gram-positive and Gram-negative bacteria. In this study, seven strains of Gram-negative bacteria and seven strains of Gram-positive bacteria were used. All the bacterial strains were first precultured by placing a loopful of cells into 10 mL of autoclaved tryptone soy broth (TSB) and incubated at 37 °C for 24 h. Then, the cells were spread evenly on the agar plates using a sterile cotton bud. A sterile filter paper (Whatman No. 1, 6 mm diameter) was immersed in NE-FLO and equilibrated before being placed on the seeded plates before incubation. The plates were then allowed for incubation (24 h, 37 °C). The diameter of the inhibition zones was measured to quantify the antimicrobial activity. The analysis was repeated in triplicate for each of the evaluated bacterial strains. The positive and negative controls used are tetracycline at 5 $mg \cdot mL^{-1}$ and dimethyl sulfoxide (DMSO), respectively [45].

MIC is the minimum concentration of an antibacterial agent that completely inhibits the microorganism's growth in tubes or microdilution wells detected by the unassisted eye, and it was observed through 96-well agar plates. The antibacterial activity of the NEs was assessed with a broth micro-dilution assay, using a serial dilution in sterile 2 mL 96-well microplates [61]. Each of the rows was filled with 0.1 mL sterilized tryptone soy broth. Wells 2–11 were topped up with 0.1 mL of NE-FLO and diluted serially to form a sequence of concentrations from 500 $mg \cdot mL^{-1}$ to 0.488 $mg \cdot mL^{-1}$. The first well served as growth control. Then, 10 μL of the culture medium was placed in each well containing NE-FLO. The microplates were then incubated (37 °C, 24 h). The turbidity assessment was carried out at the time of incubation, tT = 0, and t = 24 by reading the optical density at 600 nm (UV–vis spectrophotometer, Thermo fisher, Massachusetts, USA). The analysis was done in triplicate for each assay. Minimum bactericidal concentration (MBC) is the minimum concentration of an antibacterial agent needed to kill and prevent the growth of a bacterium over a fixed and extended time, such as 18 h or 24 h, under a specific set of conditions. A loophole from each well that is equal and higher than MIC is streaked on Mueller–Hinton agar to validate the MIC value. All plates were incubated at 37 °C for 24 h. The minimum bactericidal concentration (MBC) is expressed as the concentration at which no apparent and visible growth of bacteria occurs. The test was performed in triplicates.

3.8. Anti-Inflammatory Evaluation

The activity of lipoxygenase inhibitors was accurately determined by slightly altering the spectrometric approach described by Azhar-Ul-Haq et al. [62]. In the protocol of the assay, 160 μL of sodium phosphate buffer (100 mM, pH 8.0), 20 μL of soybean lipoxygenase enzyme solution, and 10 μL of the NE-FLO were thoroughly mixed and incubated at 25 °C for 10 min, without shaking. The addition of 10 μL sodium linoleate (0.3 mM) as substrate solution initiated the enzyme reaction, and it was incubated once again in a spectrophotometer at 25 °C for 10 min. Linoleic acid was converted to form (9Z,11E)-(13S)-13-hydroperxyoctadeca-9,11-dienoate (13-HPODE) following the incubation period and measured by spectrophotometer at 234 nm. The initial reaction rate was measured by spectrophotometry, and the inhibitory activity of a sample was measured by the reduction of this initial rate [63]. The test compounds and the positive control were dissolved in DMSO because this universal aprotic polar solvent can dissolve NE-FLO as a test sample. All the reactions were performed in triplicates, and the absorbance was measured at 234 nm. Nordihydroguaiaretic acid (NDGA) was used as the reference standard. The percentage of inhibition was calculated using Equation (1).

$$\% \text{ inhibition} = ((OD_{control} - OD_{sample})/OD_{control}) \times 100 \quad (1)$$

where $OD_{control}$ is the optical density of control, and OD_{sample} is the optical density of the sample.

3.9. Cell Cytotoxicity Study

Cell lines used in this study, human skin fibroblast cells (HSF 1184), were cultivated in Dulbecco's Modified Eagle's Medium (DMEM), with 1% penicillin with streptomycin and 10% fetal bovine serum. The cells were maintained at 37 °C in a humidified atmosphere of 5% CO_2. The reduction of MTT dye by viable cells to yield purple formazan products was used to assess the NE-FLO cytotoxicity to the cell according to the method by Azrini et al. [64]. Firstly, fibroblast cells were seeded at a density of 1 × 104 cells using a 96-well plate, followed by incubation in a culture medium until 100% confluence. Next, the varied concentrations of NE-FLO were used to treat the cells for 24 h. Different concentrations of NE-FLO were used to determine the concentration at which the NE-FLO is toxic to the cells. After 24 h, the media was withdrawn and washed with phosphate-buffered saline. The cell was incubated in the dark with 20 μL of 5 mg·mL^{-1} MTT solution for four hours at 37 °C. Next, 100 μL of DMSO was added to each well. The absorbance was measured at 570 nm using a Tecan M200 Pro Multiplate reader. The percentage of viable cells was determined with the assumption that the cell viability without treatment was 100%.

4. Conclusions

This study successfully produced oil-in-water nanoemulsions of lemon and fish by-product oils with the desired particle size and the polydispersity index (PDI) using the ultrasonication method. The antioxidant activity showed comparable results with ascorbic acid and was superior to lemon oil. The results also showed that NE-FLO possessed antibacterial activity against all of the bacteria strains tested in the study. NE-FLO also showed no signs of toxicity against normal skin cells. The anti-inflammatory activities of the NE-FLO were remarkably high and demonstrated no significant difference compared to the nordihydroguaiaretic acid (NDGA). The findings from the study revealed that NE-FLO could be a potential topical product for skin problems. Further research on the NE-FLO ability in cosmeceutical products should be conducted to support this study.

Author Contributions: Conceptualization, A.A.M.E.; methodology, A.A.M.E. and N.A.N.A.; software, N.A.N.A.; validation, H.M.S., A.A.M.E. and M.M.; formal analysis, N.A.N.A.; investigation, N.A.N.A.; resources, A.A.M.E. and H.M.S.; data curation, N.A.N.A.; writing—original draft preparation, N.A.N.A.; writing—review and editing, A.A.M.E., H.M.S. and M.M.; visualization, N.A.N.A.; supervision, A.A.M.E. and H.M.S.; project administration, A.A.M.E.; funding acquisition, H.M.S. All authors have read and agreed to the published version of the manuscript.

Funding: This research was funded by the Fundamental Research Grant Scheme (FRGS/1/2018/STG01/UIAM/01/1), Ministry of Higher Education, Malaysia.

Institutional Review Board Statement: Not applicable.

Informed Consent Statement: Not applicable.

Data Availability Statement: Data is contained within the article.

Acknowledgments: The authors would like to manifest their appreciation to the International Institute for Halal Research and Training (INHART) Laboratory and Kulliyyah of Pharmacy, IIUM Kuantan, for providing the facilities and support to complete this research.

Conflicts of Interest: The authors declare no conflict of interest.

Sample Availability: Samples of the compounds used in this study are available from the corresponding authors upon request, subjected to availability.

References

1. Kara, K.; Ouanji, F.; Lotfi, E.M.; El Mahi, M.; Kacimi, M.; Ziyad, M. Biodiesel production from waste fish oil with high free fatty acid content from Moroccan fish-processing industries. *Egypt. J. Pet.* **2018**, *27*, 249–255. [CrossRef]
2. Khoddami, A.; Ariffin, A.A.; Bakar, J.; Ghazali, H.M. Fatty Acid Profile of the Oil Extracted from Fish Waste (Head, Intestine and Liver) (Sardinella lemuru). *World Appl. Sci. J.* **2009**, *7*, 127–131.
3. Huang, T.-H.; Wang, P.-W.; Yang, S.-C.; Chou, W.-L.; Fang, J.-Y. Cosmetic and Therapeutic Applications of Fish Oil's Fatty Acids on the Skin. *Mar. Drugs* **2018**, *16*, 256. [CrossRef] [PubMed]
4. Phung, A.S.; Bannenberg, G.; Vigor, C.; Reversat, G.; Oger, C.; Roumain, M.; Galano, J.-M.; Durand, T.; Muccioli, G.G.; Ismail, A.; et al. Chemical Compositional Changes in Over-Oxidized Fish Oils. *Foods* **2020**, *9*, 1501. [CrossRef] [PubMed]
5. Hsouna, A.B.; Halima, N.B.; Smaoui, S.; Hamdi, N. Citrus lemon essential oil: Chemical composition, antioxidant and antimicrobial activities with its preservative effect against Listeria monocytogenes inoculated in minced beef meat. *Lipids Health Dis.* **2017**, *16*, 1–11. [CrossRef] [PubMed]
6. Kaur, H.; Pancham, P.; Kaur, R.; Agarwal, S.; Singh, M. Synthesis and Characterization of *Citrus limonum* Essential Oil Based Nanoemulsion and Its Enhanced Antioxidant Activity with Stability for Transdermal Application. *J. Biomater. Nanobiotechnol.* **2020**, *11*, 215–236. [CrossRef]
7. Bertuzzi, G.; Tirillini, B.; Angelini, P.; Venanzoni, R. Antioxidative Action of Citrus limonum Essential Oil on Skin. *Eur. J. Med. Plants* **2013**, *3*, 1–9. [CrossRef]
8. Li, Y.; Li, M.; Qi, Y.; Zheng, L.; Wu, C.; Wang, Z.; Teng, F. Preparation and digestibility of fish oil nanoemulsions stabilized by soybean protein isolate-phosphatidylcholine. *Food Hydrocoll.* **2020**, *100*, 105310. [CrossRef]
9. Walker, R.M. *Fish Oil Nanoemulsions: Optimization of Physical and Chemical Stability for Food System Applications*; University of Massachusetts: Amherst, MA, USA, 2015; Available online: https://www.semanticscholar.org/paper/Fish-Oil-Nanoemulsions%3A-Optimization-of-Physical-Walker/315fab60feaf5ed6eaf58fbe186363c5b608ed10 (accessed on 30 August 2022).
10. Nastiti, C.M.R.R.; Ponto, T.; Abd, E.; Grice, J.E.; Benson, H.A.E.; Roberts, M.S. Topical Nano and Microemulsions for Skin Delivery. *Pharmaceutics* **2017**, *9*, 37. [CrossRef]
11. Azmi, N.A.N.; Elgharbawy, A.A.M.; Motlagh, S.R.; Samsudin, N.; Salleh, H.M. Nanoemulsions: Factory for food, pharmaceutical and cosmetics. *Processes* **2019**, *7*, 617. [CrossRef]
12. Nirmal, N.; Mereddy, R.; Li, L.; Sultanbawa, Y. Formulation, characterisation and antibacterial activity of lemon myrtle and anise myrtle essential oil in water nanoemulsion. *Food Chem.* **2018**, *254*, 1–7. [CrossRef]
13. Nirmala, M.J.; Durai, L.; Gopakumar, V.; Nagarajan, R. Preparation of Celery Essential Oil-Based Nanoemulsion by Ultrasonication and Evaluation of Its Potential Anticancer and Antibacterial Activity. *Int. J. Nanomed.* **2020**, *15*, 7651–7666. [CrossRef] [PubMed]
14. Patil, A.; Bhide, S.; Bookwala, M.; Soneta, B.; Shankar, V.; Almotairy, A.; Almutairi, M.; Murthy, S.N. Stability of Organoleptic Agents in Pharmaceuticals and Cosmetics. *AAPS PharmSciTech* **2018**, *19*, 36–477. [CrossRef]
15. Changediya, V.V.; Jani, R.; Kakde, P. A Review on Nanoemulsions: A Recent Drug Delivery Tool. *J. Drug Deliv. Ther.* **2019**, *9*, 185–191. [CrossRef]
16. Kohli, A.; Alpar, H. Potential use of nanoparticles for transcutaneous vaccine delivery: Effect of particle size and charge. *Int. J. Pharm.* **2004**, *275*, 13–17. [CrossRef]
17. Filho, P.A.R.; Ferrari, M.; Maruno, M.; Souza, O.; Gumiero, V. In Vitro and In Vivo Evaluation of Nanoemulsion Containing Vegetable Extracts. *Cosmetics* **2017**, *4*, 32. [CrossRef]
18. Akbas, E.; Soyler, B.; Oztop, M.H. Formation of capsaicin loaded nanoemulsions with high pressure homogenization and ultrasonication. *LWT* **2018**, *96*, 266–273. [CrossRef]
19. Marzuki, N.H.C.; Wahab, R.A.; Hamid, M.A. An overview of nanoemulsion: Concepts of development and cosmeceutical applications. *Biotechnol. Biotechnol. Equip.* **2019**, *33*, 779–797. [CrossRef]
20. Páez-Hernández, G.; Mondragón-Cortez, P.; Espinosa-Andrews, H. Developing curcumin nanoemulsions by high-intensity methods: Impact of ultrasonication and microfluidization parameters. *LWT* **2019**, *111*, 291–300. [CrossRef]
21. Farshi, P.; Tabibiazar, M.; Ghorbani, M.; Mohammadifar, M.; Amirkhiz, M.B.; Hamishehkar, H. Whey protein isolate-guar gum stabilized cumin seed oil nanoemulsion. *Food Biosci.* **2019**, *28*, 49–56. [CrossRef]
22. Gundewadi, G.; Sarkar, D.J.; Rudra, S.G.; Singh, D. Preparation of basil oil nanoemulsion using Sapindus mukorossi pericarp extract: Physico-chemical properties and antifungal activity against food spoilage pathogens. *Ind. Crop. Prod.* **2018**, *125*, 95–104. [CrossRef]
23. Rebolleda, S.; Sanz, M.T.; Benito, J.M.; Beltrán, S.; Escudero, I.; San-José, M.L.G. Formulation and characterisation of wheat bran oil-in-water nanoemulsions. *Food Chem.* **2015**, *167*, 16–23. [CrossRef]
24. Gurpret, K.; Singh, S.K. Review of Nanoemulsion Formulation and Characterization Techniques. *Indian J. Pharm. Sci.* **2018**, *80*, 781–789. [CrossRef]
25. Seibert, J.B.; Rodrigues, I.V.; Carneiro, S.P.; Amparo, T.R.; Lanza, J.S.; Frézard, F.J.G.; de Souza, G.H.B.; Santos, O.D.H.D. Seasonality study of essential oil from leaves of Cymbopogon densiflorus and nanoemulsion development with antioxidant activity. *Flavour Fragr. J.* **2019**, *34*, 5–14. [CrossRef]
26. Nurdin, I.; Ridwan; Satriananda. The Effect of pH and Time on The Stability of Superparamagnetic Maghemite Nanoparticle Suspensions. *MATEC Web Conf.* **2016**, *39*, 3–6. [CrossRef]

27. McClements, D.J.; Rao, J. Food-Grade Nanoemulsions: Formulation, Fabrication, Properties, Performance, Biological Fate, and Potential Toxicity. *Crit. Rev. Food Sci. Nutr.* **2011**, *51*, 285–330. [CrossRef]
28. Cossetin, L.F.; Garlet, Q.I.; Velho, M.C.; Gündel, S.; Ourique, A.F.; Heinzmann, B.M.; Monteiro, S.G. Development of nanoemulsions containing Lavandula dentata or Myristica fragrans essential oils: Influence of temperature and storage period on physical-chemical properties and chemical stability. *Ind. Crop. Prod.* **2021**, *160*, 113115. [CrossRef]
29. Hatziantoniou, S.; Deli, G.; Nikas, Y.; Demetzos, C.; Papaioannou, G.T. Scanning electron microscopy study on nanoemulsions and solid lipid nanoparticles containing high amounts of ceramides. *Micron* **2007**, *38*, 819–823. [CrossRef]
30. Dasgupta, N.; Ranjan, S.; Mundra, S.; Ramalingam, C.; Kumar, A. Fabrication of Food Grade Vitamin E Nanoemulsion by Low Energy Approach, Characterization and Its Application. *Int. J. Food Prop.* **2015**, *19*, 700–708. [CrossRef]
31. Krithika, B.; Preetha, R. Formulation of protein based inulin incorporated synbiotic nanoemulsion for enhanced stability of probiotic. *Mater. Res. Express* **2019**, *6*, 114003. [CrossRef]
32. Taylor, P. Ostwald ripening in emulsions. *Adv. Colloid Interface Sci.* **1998**, *75*, 107–163. [CrossRef]
33. Blaak, J.; Staib, P. The Relation of pH and Skin Cleansing. *Curr. Probl. Dermatol.* **2018**, *54*, 132–142. [PubMed]
34. Antolovich, M.; Prenzler, P.D.; Patsalides, E.; McDonald, S.; Robards, K. Methods for testing antioxidant activity. *Analyst* **2002**, *127*, 183–198. [CrossRef]
35. Okonogi, S.; Duangrat, C.; Anuchpreeda, S.; Tachakittirungrod, S.; Chowwanapoonpohn, S. Comparison of antioxidant capacities and cytotoxicities of certain fruit peels. *Food Chem.* **2007**, *103*, 839–846. [CrossRef]
36. Mimica-Dukic, N.; Bozin, B.; Sokovic, M.; Simin, N. Antimicrobial and Antioxidant Activities of *Melissa officinalis* L. (Lamiaceae) Essential Oil. *J. Agric. Food Chem.* **2004**, *52*, 2485–2489. [CrossRef]
37. Liu, T.; Gao, Z.; Zhong, W.; Fu, F.; Li, G.; Guo, J.; Shan, Y. Preparation, Characterization, and Antioxidant Activity of Nanoemulsions Incorporating Lemon Essential Oil. *Antioxidants* **2022**, *11*, 650. [CrossRef] [PubMed]
38. Zadeh-Ardabili, P.M.; Rad, S.K. Anti-pain and anti-inflammation like effects of Neptune krill oil and fish oil against carrageenan induced inflammation in mice models: Current statues and pilot study. *Biotechnol. Rep.* **2019**, *22*, e00341. [CrossRef] [PubMed]
39. Lou, Z.; Chen, J.; Yu, F.; Wang, H.; Kou, X.; Ma, C.; Zhu, S. The antioxidant, antibacterial, antibiofilm activity of essential oil from *Citrus medica* L. var. sarcodactylis and its nanoemulsion. *Food Sci. Technol.* **2017**, *80*, 371–377. [CrossRef]
40. Balouiri, M.; Sadiki, M.; Ibnsouda, S.K. Methods for in vitro evaluating antimicrobial activity: A review. *J. Pharm. Anal.* **2016**, *6*, 71–79. [CrossRef] [PubMed]
41. Prasetya, N.B.A.; Ngadiwiyana; Ismiyarto; Sarjono, P.R. Synthesis and study of antibacterial activity of polyeugenol. *IOP Conf. Series Mater. Sci. Eng.* **2019**, *509*, 012101. [CrossRef]
42. Grossman, T.H. Tetracycline Antibiotics and Resistance. *Cold Spring Harb. Perspect. Med.* **2016**, *6*, a025387. [CrossRef]
43. Piran, P.; Kafil, H.S.; Ghanbarzadeh, S.; Safdari, R.; Hamishehkar, H. Formulation of Menthol-Loaded Nanostructured Lipid Carriers to Enhance Its Antimicrobial Activity for Food Preservation. *Adv. Pharm. Bull.* **2017**, *7*, 261–268. [CrossRef]
44. Desbois, A.P.; Smith, V.J. Antibacterial free fatty acids: Activities, mechanisms of action and biotechnological potential. *Appl. Microbiol. Biotechnol.* **2010**, *85*, 1629–1642. [CrossRef]
45. Silva, J.M.; Silva, E.; Reis, R.L.; Duarte, A.R.C. A closer look in the antimicrobial properties of deep eutectic solvents based on fatty acids. *Sustain. Chem. Pharm.* **2019**, *14*, 100192. [CrossRef]
46. Lu, W.-C.; Huang, D.-W.; Wang, C.-C.; Yeh, C.-H.; Tsai, J.-C.; Huang, Y.-T.; Li, P.-H. Preparation, characterization, and antimicrobial activity of nanoemulsions incorporating citral essential oil. *J. Food Drug Anal.* **2018**, *26*, 82–89. [CrossRef]
47. Salvia-Trujillo, L.; Rojas-Graü, M.A.; Soliva-Fortuny, R.; Martín-Belloso, O. Impact of microfluidization or ultrasound processing on the antimicrobial activity against Escherichia coli of lemongrass oil-loaded nanoemulsions. *Food Control* **2014**, *37*, 292–297. [CrossRef]
48. McGaw, L.; Jäger, A.; van Staden, J. Antibacterial effects of fatty acids and related compounds from plants. *S. Afr. J. Bot.* **2002**, *68*, 417–423. [CrossRef]
49. Yoon, B.K.; Jackman, J.A.; Valle-González, E.R.; Cho, N.-J. Antibacterial Free Fatty Acids and Monoglycerides: Biological Activities, Experimental Testing, and Therapeutic Applications. *Int. J. Mol. Sci.* **2018**, *19*, 1114. [CrossRef]
50. Yazgan, H.; Ozogul, Y.; Kuley, E. Antimicrobial influence of nanoemulsified lemon essential oil and pure lemon essential oil on food-borne pathogens and fish spoilage bacteria. *Int. J. Food Microbiol.* **2019**, *306*, 108266. [CrossRef]
51. Gunathilake, K.D.P.P.; Ranaweera, K.K.D.S.; Rupasinghe, H.P.V. In Vitro Anti-Inflammatory Properties of Selected Green Leafy Vegetables. *Biomedicines* **2018**, *6*, 107. [CrossRef]
52. Arulselvan, P.; Fard, M.T.; Tan, W.S.; Gothai, S.; Fakurazi, S.; Norhaizan, M.E.; Kumar, S.S. Role of Antioxidants and Natural Products in Inflammation. *Oxid. Med. Cell. Longev.* **2016**, *2016*, 5276130. [CrossRef]
53. Randy, F.; Setiasih, S.; Jufri, M.; Handayani, S.; Hudiyono, S. Evaluation of The Stability and In Vitro Anti-inflammatory Activity of Partially Purified Bromelain Nanoemulsion. *IOP Conf. Series Mater. Sci. Eng.* **2020**, *833*, 012038. [CrossRef]
54. Vater, C.; Adamovic, A.; Ruttensteiner, L.; Steiner, K.; Tajpara, P.; Klang, V.; Elbe-Bürger, A.; Wirth, M.; Valenta, C. Cytotoxicity of lecithin-based nanoemulsions on human skin cells and ex vivo skin permeation: Comparison to conventional surfactant types. *Int. J. Pharm.* **2019**, *566*, 383–390. [CrossRef]
55. Zanela da Silva Marques, T.Z.; Santos-Oliveira, R.; de Siqueira, L.B.d.O.; da Silva Cardoso, V.; de Freitas, Z.M.F.; Barros, R.d.C.d.S.A.; Villa, A.L.V.; Monteiro, M.S.d.S.d.B.; dos Santos, E.P.; Ricci, E., Jr. Development and characterization of a nanoemulsion containing propranolol for topical delivery. *Int. J. Nanomedicine.* **2018**, *13*, 2827–2837. [CrossRef]

56. Dudau, M.; Codrici, E.; Tarcomnicu, I.; Mihai, S.; Popescu, I.D.; Albulescu, L.; Constantin, N.; Cucolea, I.; Costache, T.; Rambu, D.; et al. A Fatty Acid Fraction Purified from Sea Buckthorn Seed Oil Has Regenerative Properties on Normal Skin Cells. *Front. Pharmacol.* **2021**, *12*, 1–10. [CrossRef]
57. Carvalho, A.M.; Marques, A.P.; Silva, T.H.; Reis, R.L. Evaluation of the Potential of Collagen from Codfish Skin as a Biomaterial for Biomedical Applications. *Mar. Drugs* **2018**, *16*, 495. [CrossRef]
58. Patra, J.K.; Das, G.; Fraceto, L.F.; Campos, E.V.R.; del Pilar Rodriguez-Torres, M.; Acosta-Torres, L.S.; Diaz-Torres, L.A.; Grillo, R.; Swamy, M.K.; Sharma, S.; et al. Nano based drug delivery systems: Recent developments and future prospects. *J. Nanobiotechnol.* **2018**, *16*, 71. [CrossRef]
59. Djaeni, M.; Listyadevi, Y.L. The Ultrasound-Assisted Extraction of Rice Bran Oil with n-Hexane as a Solvent. *J. Physics Conf. Ser.* **2019**, *1295*, 012027. [CrossRef]
60. Espinosa-Andrews, H.; Paez-Hernandez, G. Development of curcuminoids oil nanoemulsions produced by high-energy methods: Microfluidization vs ultrasonication. *Adv. Mater.* **2018**, *3*, 5–7.
61. Abakar, H.O.M.; Bakhiet, S.E.; Abadi, R.S.M. Antimicrobial activity and minimum inhibitory concentration of Aloe vera sap and leaves using different extracts. *J. Pharmacogn. Phytochem.* **2017**, *6*, 298–303.
62. Azhar-Ul-Haq, A.-U.; Malik, A.; Anis, I.; Khan, S.B.; Ahmed, E.; Ahmed, Z.; Nawaz, S.A.; Choudhary, M.I. Enzymes Inhibiting Lignans from Vitex negundo. *ChemInform* **2005**, *36*, 1269–1272. [CrossRef]
63. Baylac, S.; Racine, P. Inhibition of 5-lipoxygenase by essential oils and other natural fragment extracts. *Int. J. Aromather.* **2003**, *13*, 138–142. [CrossRef]
64. Azrini, N.; Azmi, N.; Hasham, R.; Ariffin, F.D.; Elgharbawy, A.A.M.; Salleh, H.M. Characterization, Stability Assessment, Antioxidant Evaluation and Cell Proliferation Activity of Virgin Coconut Oil-based Nanostructured Lipid Carrier Loaded with Ficus deltoidea Extract. *Cosmetics* **2020**, *7*, 83.

molecules

MDPI

Review

Ionic Liquids as Starch Plasticizers: The State of the Art

Susanna Romano [1], Serena De Santis [1], Chiara Frezza [1], Monica Orsini [1], Giovanni Sotgiu [1], Marta Feroci [2,*] and Daniele Rocco [1,*]

[1] Department of Industrial, Electronic and Mechanical Engineering, Roma Tre University, via Vito Volterra, 62, 00146 Rome, Italy; susanna.romano@uniroma3.it (S.R.); serena.desantis@uniroma3.it (S.D.S.); chiara.frezza@uniroma3.it (C.F.); monica.orsini@uniroma3.it (M.O.); giovanni.sotgiu@uniroma3.it (G.S.)

[2] Department of Fundamental and Applied Sciences for Engineering, Sapienza University of Rome, via Castro Laurenziano, 7, 00161 Rome, Italy

* Correspondence: marta.feroci@uniroma1.it (M.F.); daniele.rocco@uniroma3.it (D.R.)

Abstract

Over the past 15 years, ionic liquids (ILs) have gained increasing attention as potential replacements for traditional organic compounds. Thanks to their remarkable properties, such as non-volatility, chemical stability, low toxicity, solvation power, and the tunability of properties—due to different combinations of cations and anions—ILs are considered ideal in the processing of polymers. Indeed, they have been extensively studied for the dissolution, derivatization, and plasticization of biopolymers to address the growing issue of plastic pollution. The aim of this review is to investigate the recent years' literature using ILs in starch plasticization. In particular, two major classes of ionic liquids were addressed, the imidazole-based ionic liquids and the choline-derived bioILs. Furthermore, this review aims to provide a comprehensive understanding of the mechanisms behind the interactions between ILs and starch and to study their effect on biopolymer properties.

Keywords: ionic liquids; plasticizers; starch; imidazolium; choline-derived bioIL

1. Introduction

Non-volatility, non-flammability, low viscosity, chemical and electrochemical stability, negligible vapor pressure, conductivity, solvating power, and low toxicity are just some of the outstanding properties of ionic liquids (ILs) [1,2]. In view of the simultaneous presence of all these interesting properties, it is not surprising that these salts, consisting of a large organic cation coupled with a non-coordinating organic or inorganic anion, were involved with completely different roles in a large number of application fields. Organocatalysis [3], electrochemistry [4], separation and purification methods [5–7], energy applications [8], and cultural heritage protection [9] are only some of them. In addition, if their ability to form hydrogen bonds simultaneously with the capability of dissolving high molecular weight molecules, such as polysaccharides [10–13], is taken into consideration, the potential of ILs is greatly increased, as is their applications. This is because all the described physico-chemical properties are consistent with those required to be considered as plasticizers in the plasticizing processes of biopolymers [14]. The problem of pollution due to the overuse of fossil-based plastics is certainly one of the challenges of our time. Recycling plastics is surely a valid solution, but the world plan has not yet taken off fully, especially in some parts of the planet, with the unsatisfactory result that only 10% of waste plastics are recycled and more than 60% of global plastics are disposed of directly into landfills [15].

Therefore, the obligation is to find safer alternatives to synthetic plastics, and from this point of view, scientific research is not going to back out. In this respect, the development of bioplastics is a central topic and is currently considered the main way forward. Among them, starch results as one of the most promising candidates, obtainable from plant sources like wheat, tapioca, potatoes, and maize and possessing excellent biodegradability and biocompatibility properties [16]. However, the intermolecular forces and hydrogen bonds existing between polymeric chains determine the semicrystalline granular structure responsible for its poor mechanical properties and low processability with the common production techniques of plastic materials, like extrusion and injection molding [17,18]. As a result, one of the most valuable methods for rendering starch suitable consists of using plasticizers that are able to weaken starch hydrogen bonds and disrupt its 3D structure to obtain a homogeneous amorphous material named thermoplastic starch (TPS) [18]. Therefore, an ideal plasticizer should be able to interact with starch, be safe for humans and the environment, have good chemical and thermal stability in addition to low volatility [19]. From a strictly chemical point of view, the choice falls on species capable of forming hydrogen bonds, replacing those already present between starch chains, with the ultimate goal to decrease the glass transition temperature *Tg* and improve the starch chain mobility [20,21]. Water, polyols (glycerol, glycol, sorbitol, etc.), citric acid, and urea were the first starch plasticizers but all of them possess only some of the above-mentioned features, forcing the researchers in the field to find other solutions. Some of them have decided to focus on ILs. The IL properties described above are fully in line with plasticizer ones, with the peculiarity that in the case of ILs, the latter can be tuned as necessary thanks to the infinite choice of possible ion pairs. It should be highlighted that despite the wide variety of plasticizers employed, much of the current research makes use of the solution casting method, although the process is not scalable. To date, there is limited research on the applicability of ionic liquids in industrial processes. However, the most recent studies are already examining the effects of ionic liquids on starch extrusion, albeit still on a laboratory scale [22].

However, it is worth taking into account that some of their characteristics, such as their high solubility in water, may lead ILs to have a significant impact on living organisms. Indeed, to date, there is a limited number of studies on their potential toxicity. Nevertheless, it is highlighted in the literature that the main structural factor determining cytotoxicity is the alkyl side chains of the cation, while the impact of the anion is lower, especially the chloride [23].

The purpose of this review is therefore to present the research works concerning the use of ILs as starch plasticizers. The reviewed scientific articles have been reported on to shed light on how the authors demonstrated the interaction between starch and plasticizers according to the considered characterization technique. Consequently, the effects of the interaction with ILs on the properties of the crystallinity, thermal stability, electrical conductivity, and Fourier transform infrared spectroscopy (FTIR) response of the starch are shown.

Additionally, to the performances shown by the common imidazolium ILs, a part is devoted to the description of the efficiency as starch plasticizers of bioionic liquids (bioILs) based on a choline cation.

1.1. Starch Plasticized by Imidazolium Ionic Liquids

Figure 1 reports the structures of imidazolium ILs, which have been used as starch plasticizers in the scientific publications considered in this review.

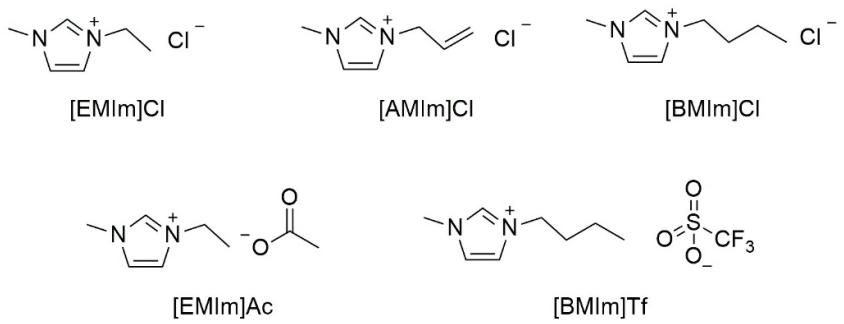

Figure 1. Structures of imidazolium ILs considered in this review.

When imidazolium ILs are considered, the possibility of hydrogen bonding with starch seems to be mainly due to the anionic part of the IL and to a lesser extent to the imidazolium cation [24], as reported in Figure 2.

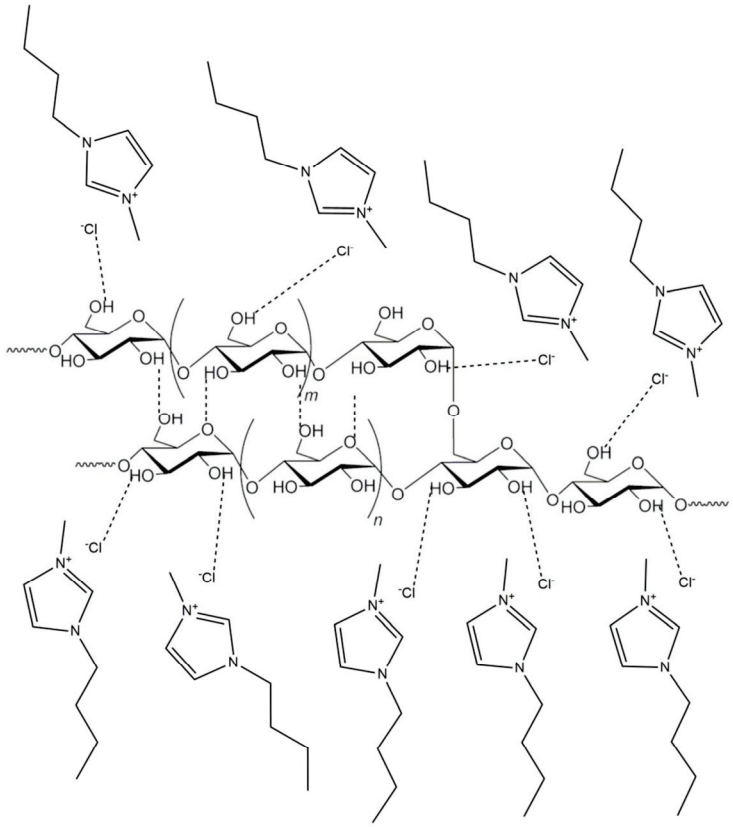

Figure 2. Hydrogen bonding between starch and 1-butyl-3-methylimidazolium chloride. Ref. [24] © 2020 by the authors. Licensee MDPI, Basel, Switzerland. This article is an open access article distributed under the terms and conditions of the Creative Commons Attribution (CC BY) license.

Using the solvent casting method, Ning et al. prepared several conductive corn starch-based films with glycerol and 1-allyl-3-methylimidazolium chloride [AMIm]Cl as plasticizers [25]. For the purpose of conducting a comparative study, the authors formulated some proportional glycerol/[AMIm]Cl mixtures, starting from glycerol and gradually increasing the IL content. In the first instance, atomic force microscopy (AFM) was chosen to evaluate the plasticization of native starch by defining the average diameter of residual starch granules. The AFM images (Figure 3) showed a similar starch particle size (10 nm) incorporated in the thermoplastic starch matrix (TPS) in the cases where glycerol and [AMIm]Cl were alone and therefore more comparable.

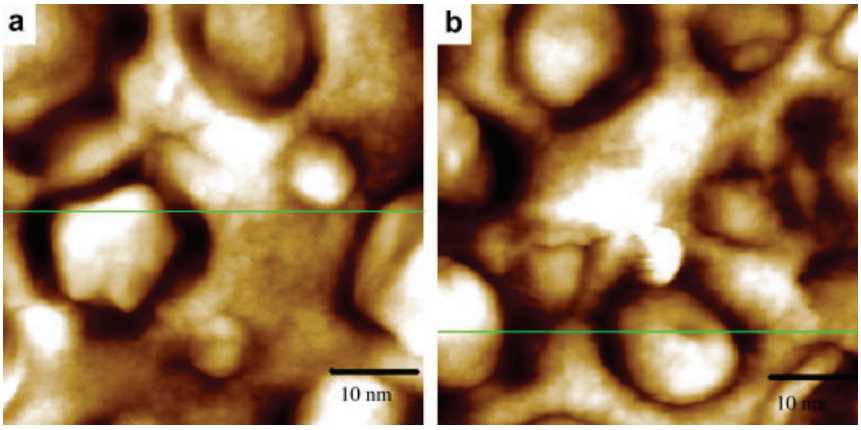

Figure 3. AFM images of (**a**) glycerol/TPS and (**b**) [AMIm]Cl. Reproduced under terms of the CC-BY license [25]. Copyright © 2008 Elsevier Ltd. All rights reserved.

Certainly, the AFM microscopy revealed an interaction between the IL and the starch, showing the presence of homogeneous TPS. Consequently, availing of FT-IR spectroscopy (Figure 4), the type of interaction survey was performed, focusing the attention on the peak frequency of starch C-O group and following the rule for which the frequency decrease coincides with greater interaction between starch and the plasticizer [26,27]. As a result, the shift in the peak positions to higher frequencies, increasing the [AMIm]Cl content, suggested less of a hydrogen bond-forming ability of the IL than glycerol.

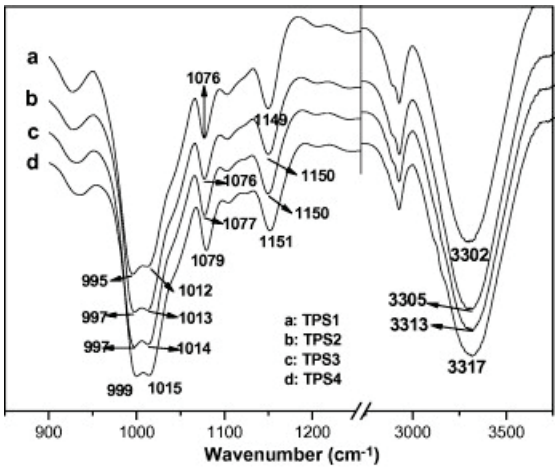

Figure 4. FT-IR spectra of TPS films. TPS1 contains only glycerol. TPS4 contains only [AMIm]Cl Reproduced under terms of the CC-BY license [25]. Copyright © 2008 Elsevier Ltd. All rights reserved.

Nevertheless, [AMIm]Cl-plasticized-TPS films showed interesting conductance values compared to glycerol-plasticized-one, proving to be an excellent compromise between the interaction ability with the starch and the possibility to obtain electroactive polymers. Therefore, for the first time, an IL shall be considered as a plasticizer to produce TPS.

Subsequently, Sankri and co-workers investigated the plasticization of the native starch using 1-butyl-3-methylimidazolium chloride ([BMIm]Cl) as the IL [28]. In this case, the authors compared not only two different plasticizers, an IL and glycerol, but also two different processing scales: a twin-screw extruder to evaluate the practicability of the [BMIm]Cl on the industrial scale and a micro compounder for laboratory scales. An initial macromolecular structure characterization revealed similar molecular weights for both cases of starch/[BMIm]Cl and starch/glycerol extruded samples, with slightly smaller values in the IL plasticizer case. The small difference was attributed to the small derivatizing effect

of [BMIm]Cl. Although the hydrophilic behavior of the IL [29] surprisingly TPS/[BMIm]Cl showed lower hydrophilic properties than the TPS/glycerol sample. The authors explain this incongruity as the presence of a particular interaction between [BMIm]Cl and starch, which would limit the interaction of the latter with water. If confirmed, this hypothesis could be a potential additional tool to study the interaction between ILs and biopolymers in general. Again, FT-IR spectroscopy proved to be a valuable tool to study the possible interaction between starch and plasticizer. Regarding the hydrogen atoms of the O-H groups, Sankri and co-workers decided to follow a different path, not being able to trust the peak positions due to the presence of the high noise. They concluded that the interactions of [BMIm]Cl with O-H groups were demonstrated observing the peaks above 3000 cm^{-1}, which have an amplitude band from 391 cm^{-1} in the presence of glycerol to 447 cm^{-1} in the presence of the IL. As regards the other reference starch functional groups, such as C–O bonds in C–O–C of anhydroglucose rings and C-O-H groups, the authors have always seen an increase in the wavenumber values of the maximum absorption peaks. By invoking past research work [30], they claim that the interaction between the IL and starch takes place through hydrogen bonds involving the ion pair $BMIm^+$ and Cl^- with the oxygen and hydrogen of the same C-O-H group of starch, respectively.

All this leads to an overall loss of the hydrogen bonding intensity to which TPS is submitted with an increase in the vibrational mode wavenumber values of the functional groups involved. Moreover, they suggested a different interaction mechanism in the previous case, where the other authors used [AMIm]Cl. Since Ning et al. observed a decrease in frequency related to O-H stretching at 3300 cm^{-1} increasing the IL content, [AMIm]Cl probably interacts through the Cl^- anion with the hydrogen of O-H groups of starch, while the $[AMIm]^+$ cation weakly binds the oxygen atom of another different group (Figure 5). Consequently, starch is still able to form hydrogen bonds with water or other O-H groups of starch.

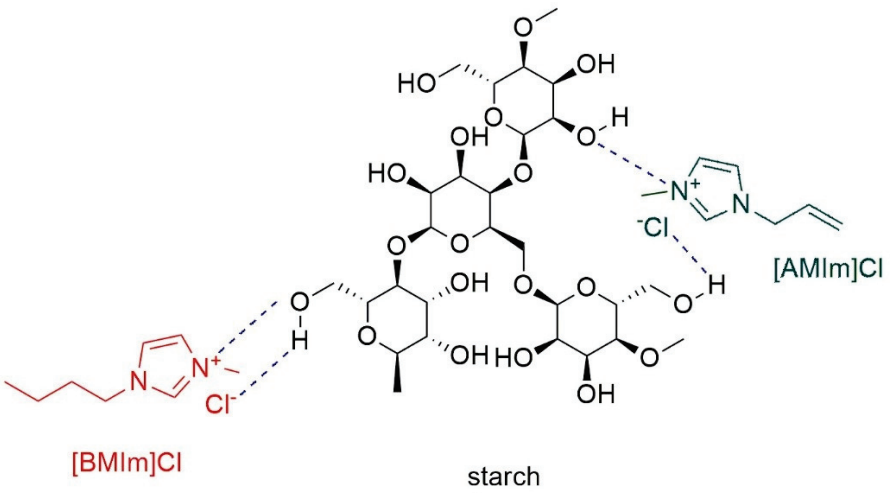

Figure 5. The hypothesis of the interaction mechanism between starch with [BMIm]Cl and [AMIm]Cl [28].

Finally, the authors showed mechanical tensile results, which confirmed a strong plasticization of starch by [BMIm]Cl. The papers described before encouraged other research groups of the field, and the use of imidazolium ILs as starch plasticizers became popular. Zdanowicz et al. investigated the [AMIm]Cl-plasticized-TPS properties performing several characterization techniques, including rheometric analysis, hot compression molding tests, and X-ray diffraction (XRD) [31]. In particular, [AMIm]Cl-plasticized-TPS XRD curves showed the reduction of the signal intensity relating to B-type crystallinity in the range of

18–20° when compared with native starch, showcasing high amorphization degree of the sample. Figure 6 shows most common crystalline arrangements of the starch.

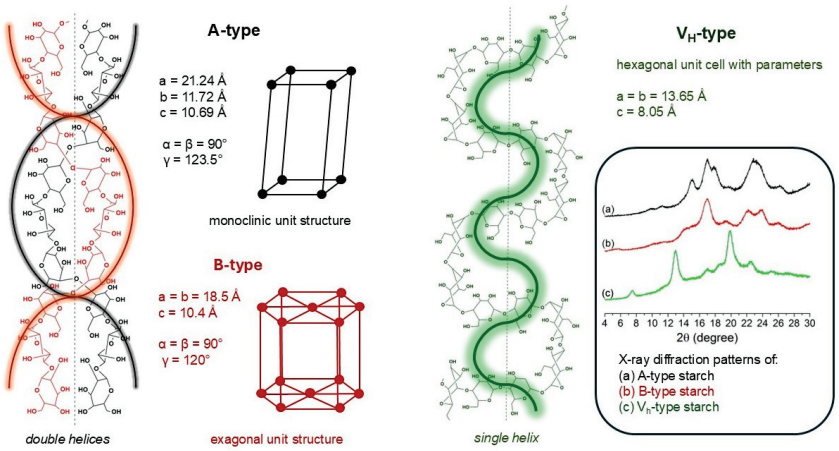

Figure 6. Schematic view of possible crystalline arrangements of the starch [32].

IL-plasticized-TPS intercepted the requirements of multiple research lines and challenges of present day, including ionic liquid-based biopolymer electrolytes [33,34]. Liew et al. decided to stake on starch and its renewable and biodegradable properties as a polymer matrix to develop a new environmentally friendly polymer electrolyte [35]. The plasticizer choice fell on the IL, 1-butyl-3-methylimidazolium trifluoromethanesulfonate [BIMIm]Tf. Differential scanning calorimetry (DSC) showed a strong plasticizing effect of [BIMIm]Tf with a glass transition temperature (T_g) value of [BIMIm]Tf/TPS well below the starch native value of 56 °C (30 wt.% of [BIMIm]Tf, T_g of −22 °C). Moreover, the further increase in the IL content led to a supplementary decrease in the T_g values and simultaneously the improvement of the ionic conducting character of the TPS complex. Therefore, the authors observed an influence of the high plasticization ability of the IL [BIMIm]Tf, demonstrated also by the XRD analysis, on the ionic conductivity of the polymer matrix. In 2013, Bendaoud and Chalamet expanded the list of potential IL plasticizers of starch, introducing 1-ethyl-3-methylimidazolium acetate [EMIm]Ac [36]. An XRD analysis immediately showed the competitiveness of [EMIm]Ac in the thermoplasticization process of the starch not only with glycerol but even with other ILs. Despite the percentage of the residual crystallinity of the [EMIm]Ac/TPS sample being less than the [AMIm]Cl/TPS value, it was still comparable with the [BMIm]Cl/TPS one. In addition, for the formulation of [EMIm]Ac/TPS 30% (w/w), the authors defined the system as amorphous, while they were still able to calculate the crystallinity in the same formulation with glycerol. Moreover, water absorption studies have been performed in order to investigate the interaction of starch/water/starch in different experimental conditions (relative humidity percentage RH and plasticizer content). AMImCl/TPS and BMImCl/TPS showed the lowest trend in terms of water absorption among the IL/TPS samples.

Xie et al. continued the starch plasticization studies with [EMIm]Ac, using the compression molding method to disperse the IL in the native starch and obtain different TPS samples [37]. They performed several characterization techniques, such as SEM, NMR, DMTA analysis, and so on, but the most interesting results seemed to arrive from the XRD analysis. The native starch XRD profile is characterized by the presence of diffraction peaks at 2θ of 17° and by a series of weaker signals, which together describe the B-type crystalline structure (Figure 7) [38,39].

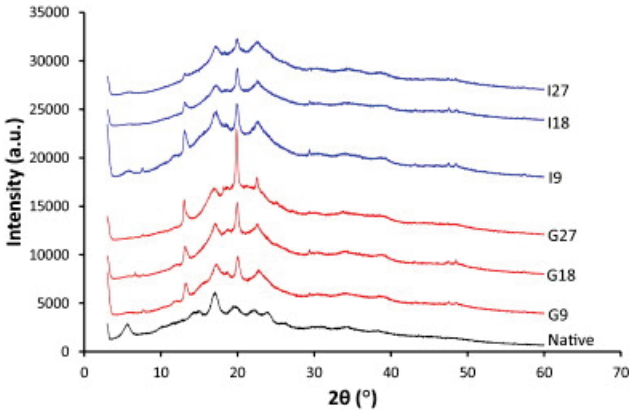

Figure 7. XRD patterns of native starch (Gelose 80) and the different TPS samples. The red color refers to samples with glycerol. The blue color refers to samples with [EMIm]Ac. Reproduced under terms of the CC-BY license [37]. Copyright © 2014 Elsevier Ltd. All rights reserved.

However, after processing, regardless of which plasticizer is used, glycerol or [EMIm]Ac, several other peaks appear related to the V_H-type crystalline structure, a single-helical amylose structure [38,40]. Nevertheless, while the increase in glycerol content resulted in an enhancement of V_H-type crystallinity, in the case of [EMIm]Ac, the increase in IL content led to the simultaneous loss of the V_H-type crystallinity and B-type crystallinity. As a result, not promoting the single-helical structure formation [EMIm]Ac allowed for a major decrease in the total crystallinity if compared with glycerol, which showed an inverse trend regarding B-type crystallinity and the V_H-type one.

The experimental results induced the same authors to investigate more specifically the starch/[EMIm]Ac interaction, preparing several samples using the same preparation technique and two different starch amylose contents [41]. Gelose 80 (G80) and regular maize starch (RMS) were used, with amylose contents of 82.9% and 24.4%, respectively. The first corresponded to the starch used in the previous work, and therefore, it showed the B-type crystallinity as described above. RMS XRD pattern was different, showing a diverse crystalline arrangement belonging to A-type crystalline structure occurring with strong peaks at 15° and 23° and an unresolved doublet at 2θ of 17° and 18° [32,42]. However, XRD results revealed that [EMIm]Ac was able to interact with both crystalline structures because after processing of RMS samples, the two signals at 2θ of 17° and 18° disappeared. Moreover, the final result was a similar crystalline pattern of G80 plasticized samples with newly formed V_H-type and B-type crystalline structures.

In summary, despite the different crystal structure of the starting point, [EMIm]Ac interacted with both native starches and led to a similar final crystal structure. This would explain the similar mechanical properties, glass transition temperature, and thermal stability of G80 and RMS starch films. Consequently, later RMS starch plasticized with [EMIm]Ac was the reference polymer of the research group in the preparation of electroconductive films [43]. This choice was successful because TPS/[EMIm]Ac films displayed excellent electrical conductivity (>10^{-3} S/cm).

IL/starch interaction was now proven and the plasticizing capabilities of some ILs confirmed. Thus, first application studies in the direction of industrial demands took hold, and the possibility of using ILs as an effective solution was beginning to be tested.

For example, Liu and co-workers prepared for the first time PBS/starch blends composed of [BIMIm]Cl plasticized starch [44]. After SEM image acquisition on the studied blends, the authors claimed that the better plasticization ability of the IL than glycerol allowed for the major dispersion of the TPS in PBS. In addition, the increased polymer compatibility due to an effective plasticizing process led to an improvement in the mechan-

ical properties as tensile strength and elongation at the break. Later, Zhao et al. used the same blends and IL to study a possible synergistic effect of [BIMIm]Cl and inorganic salts with different anions to improve these same polymer compatibilization and mechanical properties [45].

Bendaoud and Chalamet focused on other, no-less-important issues as the development of new sustainable processing techniques and green approaches [46]. They decided to combine the supercritical fluid technology ($ScCO_2$) with ILs in the thermoplasticization obtained through the extrusion process of the starch using carbon dioxide as the fluid and [BIMIm]Cl as the IL [47]. The effect of the pressure, temperature, and treatment time have been investigated, comparing the experimental results of several characterization techniques with those obtained on starch plasticized with 20 wt% of glycerol. In particular, focusing on the thermal characterization, the authors observed that the effect of the different processing parameters on the T_g values was more pronounced in the case of [BIMIm]Cl than the glycerol one, leading to more variety of T_g values distributed over a wider range. As a result, TPS with different properties can be obtained depending on the supercritical fluid conditions adopted by exploiting $scCO_2$ with the IL with respect to glycerol. Effectively, the idea of developing new processing techniques or real versatile plasticizers, allowing to tune the properties of TPS according to the demands, became widespread. Ren et al. adopted the approach of the combined plasticizers with different formulations of the glycerol/[BMIM]Cl mixture, trying to tune some essential properties of the TPS [48]. Actually, the experimental observations previously described suggested this option, especially regarding the crystallinity issue and the inverse impact that glycerol and [BMIm]Cl showed against the V_H-type crystallinity formation growing. Moreover, the authors proved that a high content of [BMIm]Cl led to a decrease in the thermal stability of TPS. Consequently, a correct formulation of the two plasticizers allowed them to exploit the greater plasticizing ability of the IL safeguarding the thermal stability of the final starch film.

Ismail et al. made use of DSC to extensively study starch/[EMIm]Ac interaction and how the latter would affect the behavior of the final TPS samples towards water [49]. A DSC analysis was carried out on several TPS samples containing different [EMIM]Ac content with the intention of extrapolating the onset temperature (T_o), the peak temperature (T_p), the melting temperature (T_m), and the melting enthalpy (ΔH). All these parameters turn out to be crucial to derive information regarding the interaction with starch, all of them susceptible to the hydrogen bonding capacity of plasticizers [50]. In all examined cases, the authors observed a single endothermic transition, corresponding to the melting process and gelatinization of the starch, and extrapolated higher T_o and T_p values, increasing the IL content (Figure 8). Therefore, the presence of the IL would actually contribute negatively on the gelatinization process of starch, highlighting, despite the high plasticizing properties of ILs, the importance of the water contribution in the overall process. As before, a correct formulation of the two plasticizers (water and [EMIm]Ac) should be developed.

Subsequently, the same research group compared the thermal behavior of TPS plasticized by two different ILs: [EMIm]Ac and [EMIm]Cl [51]. In this paper, based on the experimental results obtained by TGA and DTG curves and comparing the peak temperature of the TPSs, a higher plasticizing ability of [EMIm]Ac was declared. At the same time, however, the authors found lower thermal stability of the TPS/[EMIm]Ac samples.

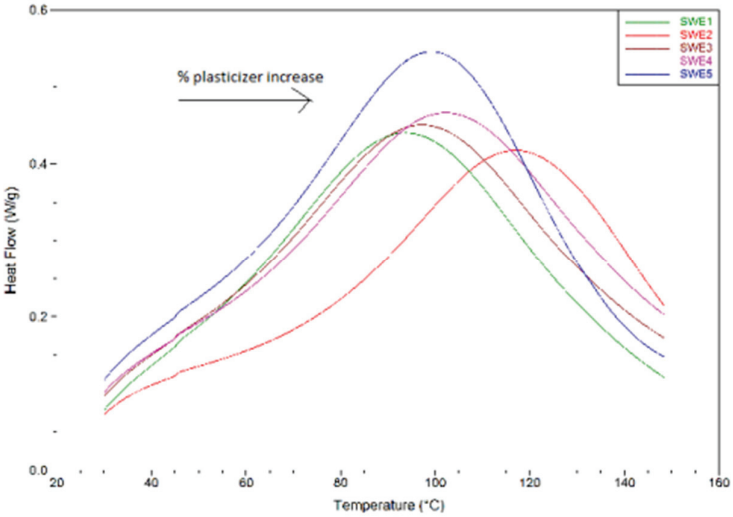

Figure 8. DSC curves of gelatinization for starch/water/[EMIm]Ac system. Reproduced under terms of the Creative Commons CC-BY-NC-ND license and permits [49] © 2016 The Author(s). Published by Elsevier Ltd.

However, in general, [EMIm]Ac began to prevail over other ILs thanks to its favorite skills to interact with starch polymer chains. Following this conclusion, Domene-López and co-workers selected [EMIm]Ac as the IL plasticizer reference to prepare several TPS films starting from starch derived from different botanical origin [52]. The literature reported that generally, tuber starch contains a higher phosphate monoester concentration than cereal starch [53], and indeed, differences in the functional group content should lead to having TPS films with diverse physico-chemical and mechanical properties. In fact, the XRD analysis showed a greater degree of crystallinity of corn and wheat TPS films than those of potato TPS ones, determining higher opacity but better mechanical properties. Certainly, given the promising TPS properties and the large number of application fields that are now investing on the starch, in future perspectives, any effort to find new, different sources is essential. Abera and co-workers tested a less common typology starch obtained from anchote (*Coccinia abyssinica*), and again, [EMIm]Ac was selected as plasticizer to prepare TPS films [54]. [EMIM]Ac proved good ability to interact with Anchote starch and the resulting TPS films showed higher flexibility and better mechanical properties than those obtained from polyols (glycerol, sorbitol, and triethylene glycol). Recently, we reported the preparation of TPS films using 1-ethyl-3-methyl imidazolium-based ionic liquids as plasticizers studying the influence of different anions ($[SO_4Et]^-$, $[N(CN)_2]^-$, $[OAc]^-$, and $[Cl]^-$) on the morphology, crystalline structure, glass transition temperature, thermal stability, and electrical conductivity (Figure 9) [55]. All characterization techniques (DSC, XRD, FT-IR, and mechanical tests) proven the plasticizing effect of all ILs, although [EMIm]Ac turned out to be the best IL to interact with starch. Regarding the crystallinity, [EMIm]Ac and [EMIm]Cl led to the same crystal structure after recrystallization, with weak XRD signals related to V_H-type comparing with B-type ones. Finally, a first attempt of the use of a dicationic imidazolium salt (DIL) as plasticizer of the starch was performed, obtaining promising experimental results. These salts possess a bidentate nature and more different structural combinations compared with their corresponding monocationic ones, also having the variable of the spacer chain [56]. As a result, DILs may open endless possibilities of new plasticizers, not only for starch but for biopolymers in general. DSC traces the gelatinization for the starch/water/[Emim]Ac system.

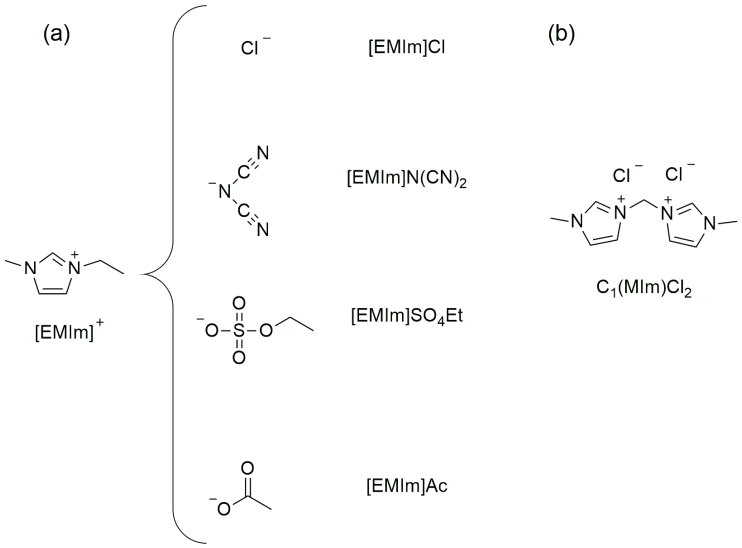

Figure 9. Structures of (**a**) imidazolium ILs and (**b**) dicationic imidazolium salt.

Table 1 summarizes the properties and characteristics of the different types of starch plasticized by imidazolium ionic liquids. Plasticizer concentrations of 30 wt% and 40 wt% were considered as the most common.

Table 1. Properties of plasticized starch, referred to as 30% or 40%, as IL weight percentage with respect to starch (indicated in parentheses).

IL	Starch Crystallinity	T_g (°C) [a]	T_{deg} (°C) [b]	Young Modulus (MPa)	Tensile Strength (MPa)	Elongation at Break (%)	σ (S cm^{-1}) [c]	Conditions [d]	Ref.
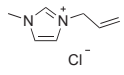	A-type	-	-	-	-	-	$10^{-1.6}$ (30%)	RH = 50% SC	[22]
		−49 (30%) −62 (40%)	-	-	-	-	-	RH = 35% TC	[33]
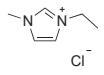	A-type	−28 (30%) −59 (40%)	-	-	-	-	-	RH = 35% TC	[33]
		-	261 (40%)	14 (40%)	1 (40%)	22 (40%)	10^{-5} (40%)	RH = 50% SC	[52]
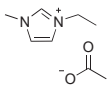	A-type	−28 (30%) −59 (40%)	-	-	-	-	-	RH = 35% TC	[33]
	B-type	-	266 (30%)	50 (30%)	5 (30%)	20 (30%)	-	RH = 52% TC	[34]
	A-type	-	266 (30%)	50 (30%)	5 (30%)	65 (30%)	-	RH = 52% TC	[34]
	A-type	-	265 (30%)	150 (30%)	10 (30%)	80 (30%)	-	RH = 33% TC	[38]
	B-type	-	260 (30%) 260 (40%)	105 (30%) 50 (40%)	6 (30%) 4 (40%)	49 (30%) 43 (40%)	-	RH = 50% SC	[51]
	A-type	-	269 (40%)	53 (40%)	3 (40%)	42 (40%)	10^{-6} (40%)	RH = 50% SC	[52]
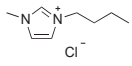	A-type	−13 (30%)	-	0.5 (30%)	0.6 (30%)	392 (30%)	$10^{-4.6}$ (30%)	RH = 50% TC	[25]
		−60 (30%) −87 (40%)	-	-	-	-	-	RH = 35% TC	[33]
		-	-	-	1.5 (30%)	316 (30%)	-	RH = 33% TC	[45]
		-	255 (30%)	-	0.8 (30%)	350 (30%)	-	RH = 52% TC	[45]
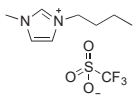	A-type	−22 (30%)	-	-	-	-	10^{-4} (30%)	RH = nr [e] SC	[32]

[a] Glass transition temperature. [b] Degradation temperature. [c] Conductivity. [d] RH: Relative humidity. TC: Thermocompression. SC: Solution casting. [e] nr: not reported.

1.2. Starch Plasticized by Bio Ionic Liquids

In 2016, Colomines et al. synthesized a series of bioionic liquids (bioILs) based on choline cation, with the aim of screening their properties as potential biobased starch plasticizers [57]. By using the solvent casting method as well, they prepared corn starch films plasticized with 30 wt% (dry basis) of choline ionic liquids by varying the anions. Starting with choline chloride ([Chol]Cl), they then employed choline acetate ([Chol]Ac), choline salicylate ([Chol]Sal), choline saccharinate ([Chol]Sac), tricholinium citrate ([Chol]Cit), cholinium furoate ([Chol]Fur), and cholinium lactate ([Chol]Lac) (Figure 10).

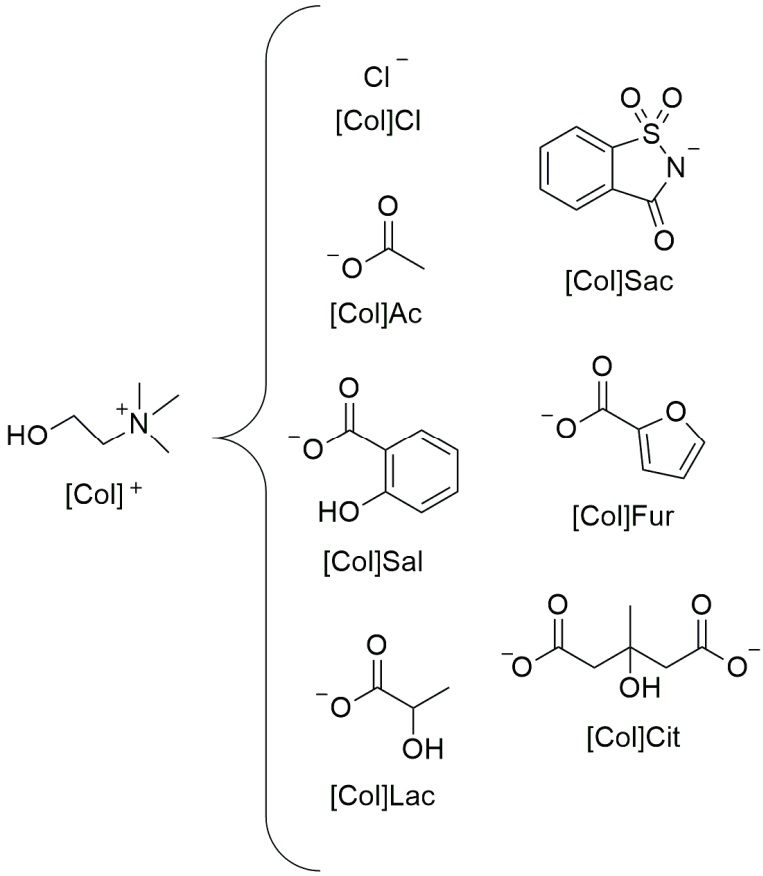

Figure 10. Structures of bio-ionic ILs based on choline cation considered in this review.

First, from a qualitative point of view, Colomines and the coworkers asserted that not all the bioionic liquids used were able to plasticize starch and thus have good film-forming abilities. In fact, only three ionic liquids ([Chol]Ac, [Chol]Cit, and [Chol]Lac) produced films comparable to those prepared using glycerol as a plasticizer. In particular, using [Chol]Sac failed to produce the film, while employing [Chol]Sal and [Chol]Fur resulted in brittle and less homogeneous films. The first characterization of the films concerned their crystal structure and its evolution over time performed through an XRD analysis. After successful solubilization and processing, the authors observed the disappearance of the native A-type crystalline structure characteristic of corn starch. It is important to note, however, that for no sample did they observe the emergence of the V_H-type structure typically associated with films upon preparation. When [Chol]Ac was employed, the film exhibited the characteristic peaks of the B-type crystalline structure after just 2 weeks of storage, a behavior comparable to that of glycerol-plasticized films. In contrast, all other bioILs destroyed the starch crystalline order and promoted a highly amorphous structure, which was preserved over time for up to 8 weeks of storage. Despite the highly amorphous structure of some films, the differential scanning calorimetry analysis (DSC)

revealed that the efficiency of these bioILs to lower the T_g of starch appeared to be similar to conventional plasticizers, such as glycerol. Comparing these results with those of their previous work [28] on [BMIm]Cl, the authors, however, showed that the T_g and water uptake values were more influenced by the type of cation, whereas the anion slightly modulated this property.

Moreover, investigating the evolution of thermo(hydro)mechanical behavior, Colomines and co-workers found that, again, the cation had a greater effect. Indeed, despite the very different T_g and water content values, the mechanical behavior of the films plasticized by the choline bioILs was very similar to each other and in contrast to that containing [BMIm]Cl.

Subsequently, Decaen et al. continued the study on choline ionic liquids, selecting choline chloride ([Chol]Cl), choline acetate ([Chol]Ac), and choline lactate ([Chol]Lac) as starch plasticizers and glycerol as a reference [58].

The authors' aim was to investigate the influence of such ionic plasticizers in starch processing methods, in particular through simple compression molding and through extrusion. In this study, the authors again investigated the effect of these ionic plasticizers on the crystal structure of starch and then performed High-Performance Size-Exclusion Chromatography coupled with Multi-Angle Laser Light Scattering and Differential Refractive Index Detection (HPSEC-MALLS-DRI), DSC, and DMTA analyses.

Again, the presence of the ionic liquids resulted in the loss of the A-type crystal structure, highlighting this efficiency for both processing techniques. However, it is interesting to note that when using compression molding or extrusion as opposed to film casting, the choline ionic liquids induced the formation of a minimal percentage of V_H-type structure, except for [Chol]Ac. Furthermore, the authors observed that during storage for one year at 25 °C/50% RH, processing via the extrusion of these samples resulted in a progressive re-crystallization of starch with the formation of B-type crystallinity. In particular, the values obtained in the presence of [Chol]Lac and [Chol]Cl were similar, while in the presence of [Chol]Ac, the B-type re-crystallization was significantly stronger, confirming the behavior of this ionic liquid highlighted in their previous work.

The study continued with the evaluation of the macromolecular characteristics of starch samples processed through compression molding and extrusion using HPSEC-MALLS-DRI.

The chromatograms and molecular weight distributions of corn starches obtained after compression molding showed similar patterns to those of native starch, however, with higher mean molecular weight (Mw) values for starches with all ionic plasticizers. Considering the extrusion process, the chromatogram of extruded corn starches mainly showed a peak and lower molecular weight due to the degradation of amylopectin, as already observed for extruded starches (Figure 11) [59,60] and also for starches treated with ionic liquids.

Decaen and co-workers pointed out that considering the effect of plasticizers on extruded starches, choline salts induced a greater degradation of amylopectin than glycerol during the processing process, thus explaining the higher efficiency of ionic plasticizers for starch destruction/thermoplasticization. More specifically, the authors observed that the degradation of chains was lower using [Chol]Cl than [Chol]Ac and [Chol]Lac, in contrast to what had been evidenced by Sciarini et al. [61] and thus highlighting that the use of [Chol]Cl allowed for a better compromise between efficient degradation at low specific mechanical energies and limited starch chains' scission during extrusion. The results of the thermal characterization by DSC were in line with their previous work, obtaining similar T_g values for all extruded starch samples plasticized with choline ionic liquids. The results of the thermal characterizations by DSC were in line with previous work, obtaining similar T_g values for all extruded starch samples plasticized with choline ionic liquids. Finally, the

results of the thermomechanical characterization showed that the nature of the cation had a greater influence on the behavior of the plasticized starch.

Decaen and collaborators have furthered and deepened the investigation into the influence of ionic plasticizers on starch processing methods, comparing the use of a micro-compounder for extrusion with Rheoplast processing [62]. In particular, they made a comparison between the use of choline-based ionic liquids ([Chol]Cl and [Chol]Ac) and those based on imidazoles ([EMIm]Cl and [EMIm]Ac). The work focuses more on a study of the processing technique, confirming the results of the previous research. However, the authors observed that imidazole-based ionic liquids were able to reduce the starch viscosity. Specifically, it was demonstrated that among various plasticizers, [EMIm]Ac emerged as the most promising ionic liquid for starch processing, as it achieved the lowest shear viscosity values while minimizing macromolecular degradation.

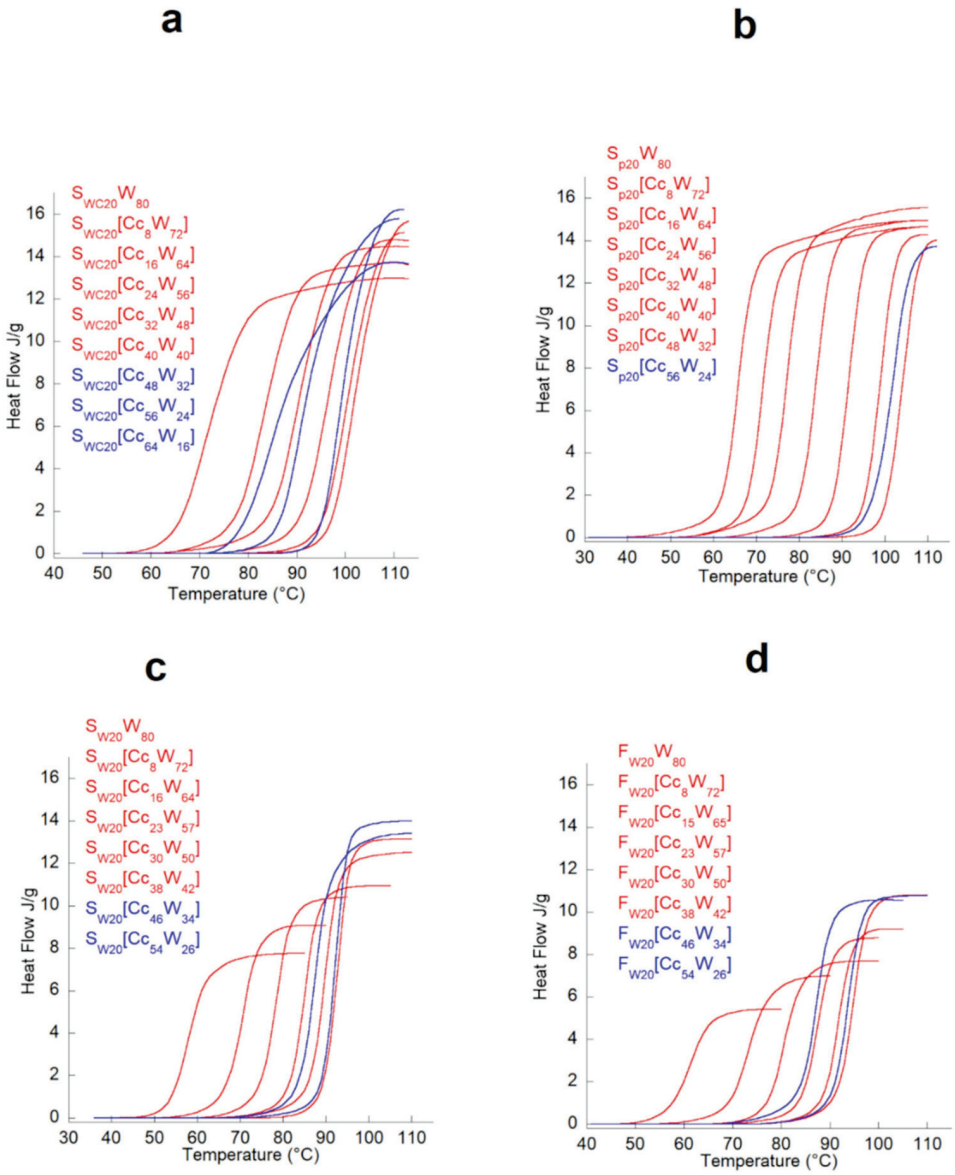

Figure 11. A thermal analysis of gelatinization for all the plasticizer contents studied. (**a**) Waxy-corn starch, (**b**) potato starch, (**c**) wheat starch, (**d**) wheat flour [63] © 2021 by the authors. Licensee MDPI, Basel, Switzerland. This article is an open access article distributed under the terms and conditions of the Creative Commons Attribution (CC BY) license.

Finally, in 2021, Crucean et al., based on the research previously conducted by Decaen and coworkers, studied more thoroughly the influence of choline chloride on the gelatinization process of starch [63]. Evaluating the effect of [Chol]Cl on three different types of starch, the authors investigated the mechanism of gelatinization and ionic liquid penetration into starch granules through DSC and XRD techniques. The results of the thermal analysis showed that at low concentrations of [Chol]Cl, the starch underwent typical gelatinization, represented by an endothermic transition (Figure 11). Later, when the concentration of [Chol]Cl increased, the gelatinization peak shifted to higher temperatures but then decreased for all three starches. Indeed, the authors assert that the shift in gelatinization temperature toward higher values as well as the increase in total gelatinization enthalpy in the presence of [Chol]Cl could be due to the reduction in water activity in the starch/plasticizer solution, which causes an increase in the energy required for chemical and physical reactions involving water. In addition, the study of cumulative enthalpy curves showed how the type of starch, and thus of granules and their polymorphic structures, affects ionic liquid penetration. In fact, the increase in the total enthalpy of gelatinization of wheat starch at high concentrations of [Chol]Cl suggested a better organization of the ordered regions of this type of starch in the presence of the ionic plasticizer.

Finally, to understand the phenomena underlying the observed exothermic transitions, the authors performed XRD measurements in a heating cell on systems with [Chol]Cl and without. The results confirmed that the addition of the ionic plasticizer resulted in a loss of crystalline order for all types of starch at room temperature. However, when [Chol]Cl was added to the systems, the collapse of the remaining starch crystal structures was observed at much higher temperatures than in systems without a plasticizer. This result confirmed that the addition of the ionic liquid caused a reorganization of the internal structure of the starch grains.

2. Conclusions

Ionic liquids are ideal for starch processing, in particular offering an interesting alternative to conventional plasticizers of this polysaccharide. Over the past few years, research is increasingly investigating the interaction mechanisms between starch and ILs, expanding the potential of this biopolymer in numerous fields of application. Indeed, thanks to the properties of ILs, starch-based materials are gaining more and more interesting characteristics, competing with conventionally plasticized films from glycerol. Therefore, it has become important to understand how ionic plasticizers interact with the starch matrix. All the scientific contributions investigated in this review showed that FT-IR spectroscopy, X-ray diffraction analysis (XRD), differential scanning calorimetry (DSC), and mechanical tests are techniques capable of obtaining information on starch/IL interactions. First, studies evaluated the effect of imidazolium ILs and their plasticizer ability, starting with 1-allyl-3-methylimidazolium chloride ([AMIm]Cl) and varying the cation with 1-butyl-3-methylimidazolium ([BMIm]Cl). The results showed that these ILs were able to decrease the ability of starch to form hydrogen bonds compared to glycerol, and furthermore, different cations correspond to different interaction mechanisms with starch. Indeed, the ability of [BMIm]Cl to interact with the oxygen and hydrogen of the same C-O-H groups was revealed, thus preventing starch chains from forming interchain hydrogen bonds. Finally, the good plasticizing abilities of [BMIm]Cl led to the exploration of the possibility of blending thermoplastic starch with other polymers and to the exploration of new sustainable processing technologies and green approaches.

Subsequently, expanding the research to different anions, [EMIm]Ac was found to be one of the ideal ILs for starch plasticization. Indeed, it interacts well with all starch structures, regardless of amylose and amylopectin content and processing technique.

Finally, the investigation also highlighted the importance of the water contribution in starch plasticization processes through ILs, prompting research on finding a proper formulation that balances the contribution of ILs with that of water.

On the other hand, the search for more environmentally friendly alternatives has led to the exploration of biobased plasticizers, with particular interest in choline-based ionic liquids. Not all ionic liquids derived from choline have been found to have good plasticizer properties. In fact, in three cases, namely [Chol]Cl, [Chol]Ac, and [Chol]Lac, TPS films were prepared following an industrial perspective by selecting extrusion and thermocompression as processing techniques [64,65]. Assured of the familiarity of glycerol with these techniques [66], a truthful comparative study of the physico-chemical properties of the latter with those based on the reference plasticizer glycerol was possible. Moreover, the comparative survey between bioILs and imidazolium ILs was conducted. It is interesting to note that research has shown a greater influence of the cation on starch/bioIL interactions than imidazolium IL ones, especially if T_g and water uptake were taken as reference parameters. In both cases, however, the good plasticizer properties of the acetate anion have been observed.

Ongoing research and development efforts are moving towards the exploration of new ILs, with the new family of dicationic ionic liquids also being explored. Furthermore, as environmental concerns drive society to replace current plasticizers with more environmentally friendly alternatives, the adoption of natural-based plasticizers is expected to grow.

Funding: This study received no external funding.

Institutional Review Board Statement: Not applicable.

Informed Consent Statement: Not applicable.

Data Availability Statement: No new data were created or analyzed in this study. Data sharing is not applicable.

Conflicts of Interest: The authors declare no conflicts of interest.

References

1. Mezzetta, A.; Guglielmero, L.; Mero, A.; Tofani, G.; D'Andrea, F.; Pomelli, C.S.; Guazzelli, L. Expanding the Chemical Space of Benzimidazole Dicationic Ionic Liquids. *Molecules* **2021**, *26*, 4211. [CrossRef] [PubMed]
2. Billeci, F.; D'Anna, F.; Feroci, M.; Cancemi, P.; Feo, S.; Forlino, A.; Tonnelli, F.; Seddon, K.R.; Gunaratne, H.N.; Plechkova, N.V. When functionalization becomes useful: Ionic liquids with a "sweet" appended moiety demonstrate drastically reduced toxicological effects. *ACS Sustain. Chem. Eng.* **2019**, *8*, 926–938. [CrossRef]
3. Pandolfi, F.; Bortolami, M.; Feroci, M.; Fornari, A.; Scarano, V.; Rocco, D. Recent advances in imidazolium-based dicationic ionic liquids as organocatalysts: A mini-review. *Materials* **2022**, *15*, 866. [CrossRef] [PubMed]
4. Rocco, D.; Folgueiras-Amador, A.A.; Brown, R.C.; Feroci, M. First example of organocatalysis by cathodic N-heterocyclic carbene generation and accumulation using a divided electrochemical flow cell. *Beil. J. Org. Chem.* **2022**, *18*, 979–990. [CrossRef]
5. Zhao, H.; Xia, S.; Ma, P. Use of ionic liquids as "green" solvents for extractions. *J. Chem. Technol. Biotechnol.* **2005**, *80*, 1089–1096. [CrossRef]
6. Dietz, M.L. Ionic liquids as extraction solvents: Where do we stand? *Sep. Sci. Technol.* **2006**, *41*, 2047–2063. [CrossRef]
7. Flieger, J.; Grushka, E.B.; Czajkowska-Zelazko, A. Ionic liquids as solvents in separation processes. *Austin J. Anal. Pharm. Chem.* **2014**, *1*, 1–8.
8. MacFarlane, D.R.; Tachikawa, N.; Forsyth, M.; Pringle, J.M.; Howlett, P.C.; Elliott, G.D.; Davis, J.H., Jr.; Watanabe, M.; Simon, P.; Angell, C.A. Energy applications of ionic liquids. *Energy Environ. Sci.* **2014**, *7*, 232–250. [CrossRef]
9. Lo Schiavo, S.; De Leo, F.; Urzì, C. Present and future perspectives for biocides and antifouling products for stone-built cultural heritage: Ionic liquids as a challenging alternative. *Appl. Sci.* **2020**, *10*, 6568. [CrossRef]

10. Biswas, A.; Shogren, R.L.; Stevenson, D.G.; Willett, J.L.; Bhowmik, P.K. Ionic Liquids as Solvents for Biopolymers: Acylation of Starch and Zein Protein. *Carbohydr. Polym.* **2006**, *66*, 546–550. [CrossRef]
11. El Seoud, O.A.; Koschella, A.; Fidale, L.C.; Dorn, S.; Heinze, T. Applications of Ionic Liquids in Carbohydrate Chemistry: A Window of Opportunities. *Biomacromol.* **2007**, *8*, 2629–2647. [CrossRef] [PubMed]
12. Wilpiszewska, K.; Spychaj, T. Ionic Liquids: Media for Starch Dissolution, Plasticization and Modification. *Carbohydr. Polym.* **2011**, *86*, 424–428. [CrossRef]
13. Zakrzewska, M.E.; Bogel-Łukasik, E.; Bogel-Łukasik, R. Solubility of Carbohydrates in Ionic Liquids. *Energy Fuels* **2010**, *24*, 737–745. [CrossRef]
14. Xie, F.; Pollet, E.; Halley, P.J.; Avérous, L. Starch-based nano-biocomposites. *Prog. Polym. Sci.* **2013**, *38*, 1590–1628. [CrossRef]
15. Wang, Q.; Xu, Y.; Xu, P.; Yang, W.; Chen, M.; Dong, W.; Ma, P. Crystallization of microbial polyhydroxyalkanoates: A review. *Int. J. Biol. Macromol.* **2022**, *209*, 330–343. [CrossRef]
16. Baranwal, J.; Barse, B.; Fais, A.; Delogu, G.L.; Kumar, A. Biopolymer: A sustainable material for food and medical applications. *Polymers* **2022**, *14*, 983. [CrossRef]
17. Khan, B.; Bilal Khan Niazi, M.; Samin, G.; Jahan, Z. Thermoplastic starch: A possible biodegradable food packaging material—A review. *J. Food Proc. Eng.* **2017**, *40*, e12447. [CrossRef]
18. Mohammadi Nafchi, A.; Moradpour, M.; Saeidi, M.; Alias, A.K. Thermoplastic starches: Properties, challenges, and prospects. *Starch* **2013**, *65*, 61–72. [CrossRef]
19. Liu, H.; Xie, F.; Yu, L.; Chen, L.; Li, L. Thermal processing of starch-based polymers. *Prog. Polym. Sci.* **2009**, *34*, 1348–1368. [CrossRef]
20. Laohakunjit, N.; Noomhorm, A. Effect of plasticizers on mechanical and barrier properties of rice starch film. *Starch–Stärke* **2004**, *56*, 348–356. [CrossRef]
21. Pushpadass, H.A.; Marx, D.B.; Hanna, M.A. Effects of extrusion temperature and plasticizers on the physical and functional properties of starch films. *Starch–Stärke* **2008**, *60*, 527–538. [CrossRef]
22. Montilla-Buitrago, C.E.; Gómez-López, R.A.; Solanilla-Duque, J.F.; Serna-Cock, L.; Villada-Castillo, H.S. Effect of Plasticizers on Properties, Retrogradation, and Processing of Extrusion-Obtained Thermoplastic Starch: A Review. *Starch/Staerke* **2021**, *73*, 2100060. [CrossRef]
23. Arakelyan, L.A.; Arkhipova, D.M.; Seitkalieva, M.M.; Vavina, A.V.; Sahharova, L.T.; Kurbanalieva, S.K.; Posvyatenko, A.V.; Egorova, K.S.; Ananikov, V.P. A Comprehensive Dataset on Cytotoxicity of Ionic Liquids. *Sci. Data* **2024**, *11*, 1379. [CrossRef] [PubMed]
24. Ptak, S.; Zarski, A.; Kapusniak, J. The importance of ionic liquids in the modification of starch and processing of starch-based materials. *Materials* **2020**, *13*, 4479. [CrossRef] [PubMed]
25. Ning, W.; Xingxiang, Z.; Haihui, L.; Benqiao, H. 1-Allyl-3-methylimidazolium chloride plasticized-corn starch as solid biopolymer electrolytes. *Carbohydr. Polym.* **2009**, *76*, 482–484. [CrossRef]
26. Ma, X.F.; Yu, J.G.; He, K. Thermoplastic starch plasticized by glycerol as solid polymer electrolytes. *Macromol. Mat. Eng.* **2006**, *291*, 1407–1413. [CrossRef]
27. Yang, J.H.; Yu, J.G.; Ma, X.F. Preparation of a novel thermoplastic starch (TPS). Material using ethylenebisformamide as the plasticizer. *Starch* **2006**, *58*, 330–337. [CrossRef]
28. Sankri, A.; Arhaliass, A.; Dez, I.; Gaumont, A.C.; Grohens, Y.; Lourdin, D.; Pillin, I.; Rolland-Sabaté, A.; Leroy, E. Thermoplastic starch plasticized by an ionic liquid. *Carbohydr. Polym.* **2010**, *82*, 256–263. [CrossRef]
29. Heng, H.; Deng, Q.; Yang, Y.; Wang, F. Recent research progress of ionic liquid dissolving silks for biomedicine and tissue engineering applications. *Int. J. Mol. Sci.* **2022**, *23*, 8706. [CrossRef]
30. Hanke, C.G.; Atamas, N.A.; Lynden-Bell, R.M. Solvation of small molecules in imidazolium ionic liquids: A simulation study. *Green Chem.* **2002**, *4*, 107–111. [CrossRef]
31. Zdanowicz, M.; Spychaj, T. Ionic liquids as starch plasticizers or solvents. *Polimery* **2011**, *56*, 861–864. [CrossRef]
32. Kong, L.; Lee, C.; Kim, S.H.; Ziegler, G.R. Characterization of Starch Polymorphic Structures Using Vibrational Sum Frequency Generation Spectroscopy. *J. Phys. Chem. B* **2014**, *118*, 1775–1783. [CrossRef] [PubMed]
33. Shamshina, J.L.; Berton, P. Renewable Biopolymers Combined with Ionic Liquids for the Next Generation of Supercapacitor Materials. *Int. J. Mol. Sci.* **2023**, *24*, 7866. [CrossRef] [PubMed]
34. Ning, W.; Xingxiang, Z.; Haihui, L.; Na, H. Ionically Conducting Polymers Based on Ionic Liquid-Plasticized Starch Containing Lithium Chloride. *Polym. Polym. Compos.* **2010**, *18*, 53–58. [CrossRef]
35. Liew, C.W.; Ramesh, S.; Ramesh, K.; Arof, A.K. Preparation and characterization of lithium ion conducting ionic liquid-based biodegradable corn starch polymer electrolytes. *J. Solid State Electrochem.* **2012**, *16*, 1869–1875. [CrossRef]
36. Bendaoud, A.; Chalamet, Y. Effects of relative humidity and ionic liquids on the water content and glass transition of plasticized starch. *Carbohydr. Polym.* **2013**, *97*, 665–675. [CrossRef]

37. Xie, F.; Flanagan, B.M.; Li, M.; Sangwan, P.; Truss, R.W.; Halley, P.J.; Strounina, E.V.; Whittaker, A.K.; Gidley, M.J.; Dean, K.M.; et al. Characteristics of starch-based films plasticised by glycerol and by the ionic liquid 1-ethyl-3-methylimidazolium acetate: A comparative study. *Carbohydr. Polym.* **2014**, *111*, 841–848. [CrossRef]
38. Cheetham, N.W.H.; Tao, L. Variation in crystalline type with amylose content in maize starch granules: An X-ray powder diffraction study. *Carbohydr. Polym.* **1998**, *36*, 277–284. [CrossRef]
39. Tan, I.; Flanagan, B.M.; Halley, P.J.; Whittaker, A.K.; Gidley, M.J. A methodfor estimating the nature and relative proportions of amorphous, single, and double-helical components in starch granules by13C CP/MAS NMR. *Biomacromolecules* **2007**, *8*, 885–891. [CrossRef]
40. Pérez, S.; Bertoft, E. The Molecular Structures of Starch Components and Their Contribution to the Architecture of Starch Granules: A Comprehensive Review. *Starch* **2010**, *62*, 389–420. [CrossRef]
41. Xie, F.; Flanagan, B.M.; Li, M.; Truss, R.W.; Halley, P.J.; Gidley, M.J.; McNally, T.; Shamshina, J.L.; Rogers, R.D. Characteristics of starch-based films with different amylose contents plasticised by 1-ethyl-3-methylimidazolium acetate. *Carbohydr. Polym.* **2015**, *122*, 160–168. [CrossRef] [PubMed]
42. Zhang, Y.; Rempel, C. Retrogradation and Antiplasticization of Thermoplastic Starch. In *Thermoplastic Elastomers*; InTech: London, UK, 2012.
43. Zhang, B.; Xie, F.; Shamshina, J.L.; Rogers, R.D.; McNally, T.; Wang, D.K.; Halley, P.J.; Truss, R.W.; Zhao, S.; Chen, L. Facile preparation of starch-based electroconductive films with ionic liquid. *ACS Sus. Chem. Eng.* **2017**, *5*, 5457–5467. [CrossRef]
44. Liu, D.; Qi, Z.; Zhang, Y.; Xu, J.; Guo, B. Poly (butylene succinate)(PBS)/ionic liquid plasticized starch blends: Preparation, characterization, and properties. *Starch* **2015**, *67*, 802–809. [CrossRef]
45. Zhao, Z.; Lei, B.; Du, W.; Zhang, X. The effects of inorganic salts with different anions on the structure and properties of starch/poly (butylene succinate) blends plasticized with ionic liquid. *Polymers* **2019**, *11*, 2004. [CrossRef]
46. Bendaoud, A.; Chalamet, Y. Effect of a supercritical fluid on starch-based polymer processed with ionic liquid. *Eur. Polym. J.* **2015**, *63*, 237–246. [CrossRef]
47. Ayoub, A.; Rizvi, S.S. Reactive supercritical fluid extrusion for development of moisture resistant starch-based foams. *J. Appl. Polym. Sci.* **2011**, *120*, 2242–2250. [CrossRef]
48. Ren, J.; Zhang, W.; Lou, F.; Wang, Y.; Guo, W. Characteristics of starch-based films produced using glycerol and 1-butyl-3-methylimidazolium chloride as combined plasticizers. *Starch* **2017**, *69*, 1600161. [CrossRef]
49. Ismail, S.; Mansor, N.; Majeed, Z.; Man, Z. Effect of water and [Emim][OAc] as plasticizer on gelatinization of starch. *Procedia Eng.* **2016**, *148*, 524–529. [CrossRef]
50. Edhirej, A.; Sapuan, S.M.; Jawaid, M.; Zahari, N.I. Effect of various plasticizers and concentration on the physical, thermal, mechanical, and structural properties of cassava-starch-based films. *Starch* **2017**, *69*, 1500366. [CrossRef]
51. Ismail, S.; Mansor, N.; Man, Z. A Study on Thermal Behaviour of Thermoplastic Starch Plasticized by [Emim] Ac and by [Emim] Cl. *Procedia Eng.* **2017**, *184*, 567–572. [CrossRef]
52. Domene-López, D.; Delgado-Marín, J.J.; Martin-Gullon, I.; García-Quesada, J.C.; Montalbán, M.G. Comparative study on properties of starch films obtained from potato, corn and wheat using 1-ethyl-3-methylimidazolium acetate as plasticizer. *Int. J. Biol. Macromol.* **2019**, *135*, 845–854. [CrossRef] [PubMed]
53. Zhang, B.; Zhao, Y.; Li, X.; Zhang, P.; Li, L.; Xie, F.; Chen, L. Effects of amylose and phosphate monoester on aggregation structures of heat-moisture treated potato starches. *Carbohydr. Polym.* **2014**, *103*, 228–233. [CrossRef] [PubMed]
54. Abera, G.; Woldeyes, B.; Demash, H.D.; Miyake, G. The effect of plasticizers on thermoplastic starch films developed from the indigenous Ethiopian tuber crop Anchote (*Coccinia abyssinica*) starch. *Int. J. Biol. Macromol.* **2020**, *155*, 581–587. [CrossRef] [PubMed]
55. Romano, S.; De Santis, S.; Martinelli, A.; Rocchi, L.A.; Rocco, D.; Sotgiu, G.; Orsini, M. Starch films plasticized by imidazolium-based ionic liquids: Effect of mono-and dicationic structures and different anions. *ACS Appl. Polym. Mat.* **2023**, *5*, 8859–8868. [CrossRef]
56. Rocco, D.; Chiarotto, I.; D'Anna, F.; Mattiello, L.; Pandolfi, F.; Rizzo, C.; Feroci, M. Cathodic behaviour of dicationic imidazolium bromides: The role of the spacer. *ChemElectroChem* **2019**, *6*, 4275–4283. [CrossRef]
57. Colomines, G.; Decaen, P.; Lourdin, D.; Leroy, E. Biofriendly Ionic Liquids for Starch Plasticization: A Screening Approach. *RSC Adv.* **2016**, *6*, 90331–90337. [CrossRef]
58. Decaen, P.; Rolland-Sabaté, A.; Guilois, S.; Jury, V.; Allanic, N.; Colomines, G.; Lourdin, D.; Leroy, E. Choline Chloride vs Choline Ionic Liquids for Starch Thermoplasticization. *Carbohydr. Polym.* **2017**, *177*, 424–432. [CrossRef]
59. Myllymaki, O.; Eerikainen, T.; Suortti, T.; Forssell, P.; Linko, P.; Poutanen, K. Depolymerization of barley starch during extrusion in water glycerol mixtures. *Food Sci. Technol.* **1997**, *30*, 351–358. [CrossRef]
60. van den Einde, R.M.; Akkermans, C.; van der Goot, A.J.; Boom, R.M. Molecular breakdown of corn starch by thermal and mechanical effects. *Carbohydr. Polym.* **2004**, *56*, 415–422. [CrossRef]

61. Sciarini, L.S.; Rolland-Sabate, A.; Guilois, S.; Decaen, P.; Leroy, E.; Le Bail, P. Understanding the destructuration of starch in water-ionic liquid mixtures. *Green Chem.* **2015**, *17*, 291–299. [CrossRef]
62. Decaen, P.; Rolland-Sabaté, A.; Colomines, G.; Guilois, S.; Lourdin, D.; Della Valle, G.; Leroy, E. Influence of Ionic Plasticizers on the Processing and Viscosity of Starch Melts. *Carbohydr. Polym.* **2020**, *230*, 115591. [CrossRef] [PubMed]
63. Crucean, D.; Pontoire, B.; Debucquet, G.; Le-Bail, A.; Le-Bail, P. Influence of the Presence of Choline Chloride on the Classical Mechanism of "Gelatinization" of Starch. *Polymers* **2021**, *13*, 1509. [CrossRef] [PubMed]
64. Luchese, C.L.; Uranga, J.; Spada, J.C.; Tessaro, I.C.; de la Caba, K. Valorisation of blueberry waste and use of compression to manufacture sustainable starch films with enhanced properties. *Int. J. Biol. Macromol.* **2018**, *115*, 955–960. [CrossRef] [PubMed]
65. Verbeek, C.J.; Van Den Berg, L.E. Extrusion processing and properties of protein-based thermoplastics. *Macromol. Mater. Eng.* **2010**, *295*, 10–21. [CrossRef]
66. Pushpadass, H.A.; Marx, D.B.; Wehling, R.L.; Hanna, M.A. Extrusion and characterization of starch films. *Cereal Chem.* **2009**, *86*, 44–51. [CrossRef]

Disclaimer/Publisher's Note: The statements, opinions and data contained in all publications are solely those of the individual author(s) and contributor(s) and not of MDPI and/or the editor(s). MDPI and/or the editor(s) disclaim responsibility for any injury to people or property resulting from any ideas, methods, instructions or products referred to in the content.

molecules

MDPI

Review

Research Progress in Ionic Liquid-Based Electrolytes for Electrochromic Devices

Hao Zhang, Yixuan Liu, Xuehan Wang, Keying Feng, Qilin Wang, Zheng Chen * and Zhenhua Jiang *

Key Laboratory of High-Performance Plastics, Ministry of Education, National and Local Joint Engineering Laboratory for Synthesis Technology of High-Performance Polymers, College of Chemistry, Jilin University, Changchun 130012, China; haozhang23@mails.jlu.edu.cn (H.Z.)
* Correspondence: chenzheng2013@jlu.edu.cn (Z.C.); jiangzhenhua@jlu.edu.cn (Z.J.)

Abstract

Electrochromic (EC) technology has become one of the smart technologies with the most potential for development and application at this stage. Based on electrochromic devices (ECDs), this technology has shown extraordinary potential in the fields of smart windows, display devices, and sensing systems. With the optimization and iteration of various core components in ECDs, the electrolyte layer, a key component, evolved from its initial liquid state to a quasi-solid state and solid state. As driven by increasing application demands, the development trend indicates that all-solid-state, transparent electrolytes will likely become the future form of the electrolyte layer. Recently, the application of ionic liquid (IL)-based electrolytes in the field of electrochromism attracted a lot of attention due to their ability to bring outstanding EC cycling stability, thermal stability, and a wider operating voltage range to ECDs, and they are regarded as the new generation of electrolyte materials with the most potential for application. Although compared with conventional electrolytes, IL-based electrolytes have the characteristics of high price, high viscosity, and low conductivity, they are still considered the most promising electrolyte materials for applications. However, so far, there has been a lack of comprehensive analysis reports on "Research progress in ionic liquid-based electrolytes for electrochromic devices" within the EC field. In this article, the research progress of IL-based electrolytes in ECDs will be summarized from three perspectives: liquid, quasi-solid, and solid state. The future development directions of IL-based electrolytes for ECDs are discussed.

Keywords: ionic liquid-based electrolytes; polymeric ionic liquid-based electrolytes; electrochromic devices

1. Introduction

Electrochromism refers to the phenomenon of reversible changes in transmittance, reflectance, and color of electrochromic materials under an applied voltage [1]. Electrochromism aroused the research interest of many researchers due to the fact that it only requires a low driving voltage to complete the modulation of color and transparency. Since the first appearance of electrochromic devices (ECDs) in 1969 [2], after years of development, ECDs have been used in smart windows, aircraft portholes, automotive anti-glare mirrors, smart displays, military camouflage, flexible devices, energy storage, and so on [3–8]. Electrochromic technology has become one of the smart technologies with the most development and application potential at this stage.

High-performance ECDs are the basis for the rapid development and wide application of EC technology. In this paper, only the EC technology based on the electrochemical

redox mechanism is discussed. The EC technology based on a polymer-dispersed liquid crystal mechanism has been commercially available, but it has not been widely studied due to the high driving voltage, complex production process, and other limitations [9]. At present, many types of ECDs have been developed, but they are derived from the classic sandwich structure. A typical electrochromic device is usually composed of the following five structures [10,11] (as shown in Figure 1, in order from bottom to top): (a) transparent conductive electrode (e.g., ITO-Glass, ITO-PET, etc.), (b) ion storage layer, (c) ionic conductive layer (electrolyte layer), (d) EC active layer, and (e) another transparent conductive electrode [12]. All of them are crucial for the construction of high-performance ECDs, Therefore, research on each layer is a central focus in this field. However, researchers generally agree that in ECDs, with the exception of the EC active layer, which determines the color change characteristics, the ion conduction layer has a wider choice and scope for development compared with other structural layers, both in terms of material selection and construction method. As in the case of EC active materials, there have been many reported research works on ionic conductive layers. The literature review on various electrolytes is also very rich and comprehensive.

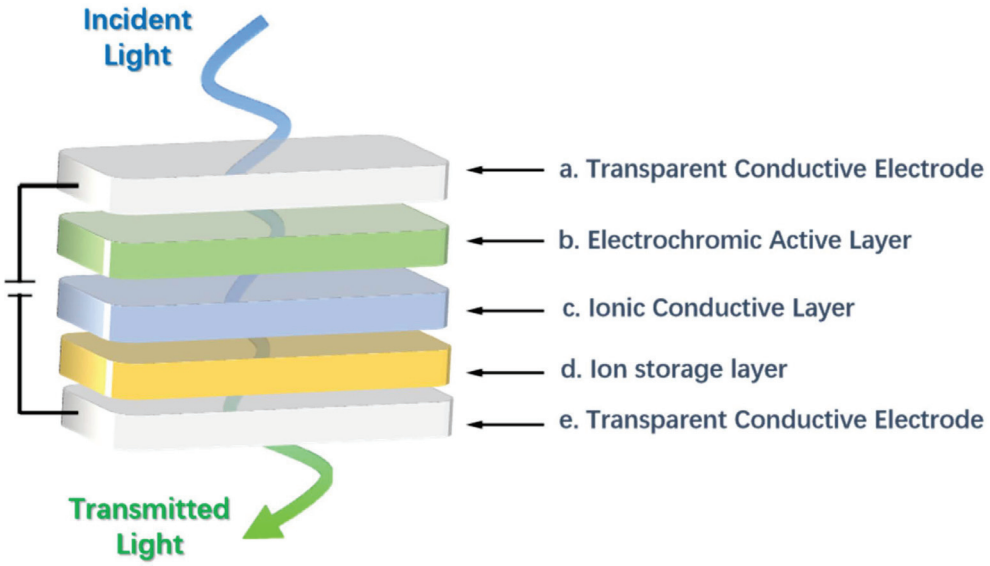

Figure 1. The structure of a typical electrochromic device.

In ECD, the ion transport layer, also called the electrolyte layer, which is usually located between the EC active layer and the ion storage layer, mainly plays the role of transporting ions and isolating electrodes. On the one hand, it allows the charged ions to move in a directional manner under the effect of an electric field to ensure that the EC active layer can achieve a controllable color (absorption spectrum) conversion through the doping detonation (redox) process of the ions. On the other hand, the electrolyte layer can also effectively isolate the EC active layer and the ion storage layer, preventing them from directly contacting and short-circuiting, ensuring the safe and stable operation of ECDs. It is found that the ion conduction layer has an important influence on the coloring efficiency, optical contrast, transmittance, response time, and cycle stability of ECDs [13].

During the development of electrochromic devices, three forms of electrolyte layers have been developed and applied one after another: liquid electrolyte, gel electrolyte, and solid electrolyte. To more intuitively illustrate the differences among these three types of electrolytes, we have provided examples of several reported electrolytes in Table 1. Liquid electrolytes: Liquid electrolytes used in ECDs are usually composed of solvents (e.g., water, propylene carbonate, vinyl carbonate, dimethyl carbonate, diethyl carbonate, etc.) and electrolyte salts (e.g., tetrabutylammonium perchlorate TBAP, as well as lithium salts, such

as $LiClO_4$, $LiPF_6$, $LiBF_4$, and $LiCF_3SO_3$, etc.), which have high ionic conductivity and a good wettability to electrodes. However, during the use of ECDs, the liquid electrolyte suffers from leakage and volatilization, which seriously affects the safety and service life of the ECDs, limiting their wide application in more fields.

Gel electrolyte: The gel electrolyte used in ECD is mainly a gel polymer electrolyte, which consists of a polymer matrix, electrolyte salts, and a solvent. On the one hand, the solvent plays the role of dissolving and dispersing the electrolyte salts; on the other hand, it plasticizes the polymer matrix. The solvent, together with the electrolyte salt, is filled into the internal spatial network of the polymer, which triggers the swelling phenomenon of the polymer, thus obtaining a semi-solid gel polymer electrolyte with a three-dimensional reticular structure. Both the polymer and the plasticizer are continuous phases. Although this electrolyte system is composed of liquid electrolyte components, the polymer network restricts the mobility and volatility of the solution electrolyte components; thus, the problem of leakage and volatilization of the liquid electrolyte is solved to a certain extent.

Solid-state electrolytes: Inorganic solid-state electrolytes [14–19], as well as polymer solid-state electrolytes [20–27], have begun to be investigated and employed in ECDs. Researchers are looking to replace conventional liquid electrolytes with such materials that have ionic conductivity in the solid state. Compared with traditional liquid electrolytes, in ECDs, solid-state electrolytes, due to the absence of liquid components, solved the solvent leakage problem of the device and the application safety problem at high temperatures on the one hand, and on the other hand, will also greatly simplify the assembly and production process of ECDs, which will contribute to the promotion of the development and application of electrochromic technology.

Table 1. Conductivity comparison of several liquid electrolytes, gel electrolytes, and solid-state electrolytes.

State	Content	Ionic Conductivity (S/cm)	Ref.
liquid	$LiClO_4$/PC	/	[28]
	LiTFSI/PC	/	[28]
	[BMIM][BF_4]	1.81×10^{-3}	[29]
Gel state	PEGDA/PMMA/LiTFSI/PC	2.6×10^{-4}	[30]
	PAM/KCl/H_2O	6.4×10^{-2}	[31]
	PVDF/$LiClO_4$/PC	4.6×10^{-4}	[32]
	PMMA/$LiClO_4$/[Emim]BF_4	2.9×10^{-3}	[33]
Solid state	PMMA/KTFSI	5.7×10^{-3}	[23]
	P(MEEMIm TFSI)	1.0×10^{-5}	[34]
	LiPON	2.6×10^{-6}	[35]
	$Li_{2.5}TaO_x$	1.0×10^{-8}	[36]

Each of these three electrolytes mentioned above has its own advantages and disadvantages for use in ECDs. Although the specific values applied to ECD liquid electrolytes are not listed in the above table, there are literature reports that liquid electrolytes have the highest ion conductivity (10^{-3}~10^{-2} S/cm) [37] and are the most extensively studied. However, due to the influence of solvent evaporation and leakage, the devices face great challenges in terms of safety and lifetime. Solid-state electrolytes offer higher safety and stability, and their use can avoid the leakage problems of liquid electrolytes. However, the research work on the use of solid-state electrolytes as ionic conductive layers is still in the exploratory stage due to their low ionic conductivity (10^{-8}~10^{-3} S/cm) [13], which limits their wide use in practical applications. Gel electrolytes combine the advantages of liquid electrolytes and solid electrolytes, possessing high ionic conductivity (10^{-4}~10^{-2} S/cm) [31] and good mechanical properties. However, most of the commonly used gel elec-

trolytes currently use organic solvents, such as propylene carbonate, as the main component of the electrolyte. However, these solvents are highly volatile. Consequently, their evaporation at both ambient and elevated temperatures can cause irreversible damage to the electrolyte. This severely affects the thermal stability of the electrolyte and, moreover, the volatility of the organic solvents also impacts the long-term stability of the electrochromic devices. Therefore, it is very important to adopt electrolyte materials with better thermal stability and low volatility to improve the performance and reliability of ECDs.

In contrast, ionic liquid (IL) is an ideal substitute material for organic solvents in electrolytes [38] due to its high thermal stability (200~500 °C) [39,40], electrochemical stability (electrochemical window 4~6 V) [40], and negligible vapor pressure [41] (Figure 2). At present, the application of IL-based electrolytes in ECDs attracted high attention from researchers and a large amount of research work has been carried out. Current research results indicate that the use of ionic liquid electrolytes can improve the cycle life and environmental weather resistance of ECDs [42–45]. Moreover, IL can serve as not only an electrolyte in ECDs, but also as an electrochromic active material. Introducing units with color-changing activity into ILs through covalent bonds constructs electrochromic ILs. Thus, this approach endows ionic liquids with electrochromic properties. Therefore, IL-based electrolytes are one of the most promising types of electrolytes in the field of electrochromic technology.

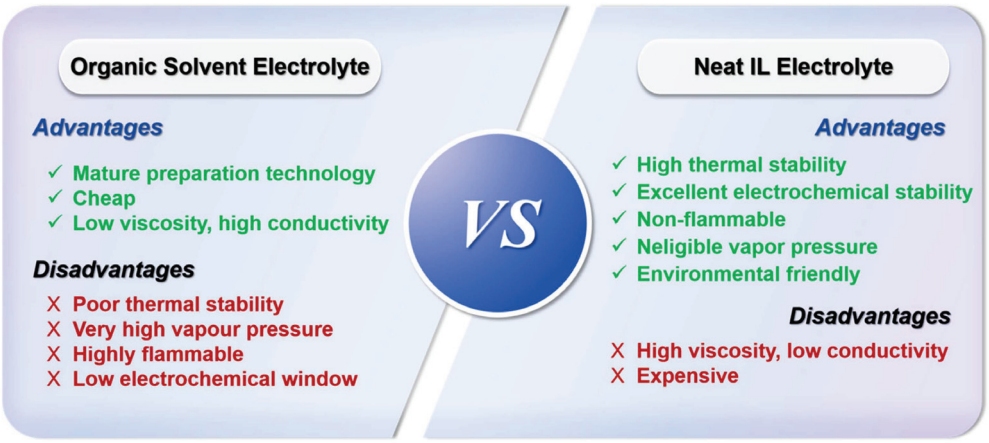

Figure 2. Comparison between organic solvent electrolytes and neat IL electrolytes.

However, up to now, there has been a lack of comprehensive introductions and analysis reports regarding the research progress of IL-based electrolytes in ECDs. This review aims to summarize the cutting-edge progress of ionic liquid electrolytes in the field of electrochromism, to sort out the advantages and characteristics of different types of IL-based electrolytes, and to discuss the challenges and future development trends in their applications in electrochromic devices. This will facilitate researchers in this field or those engaged in related research to gain a comprehensive understanding and quickly grasp the development status and future trends in this direction, thereby aiding further technological breakthroughs in this area.

2. Ionic Liquid Electrolyte

Ionic liquid (IL) [46] is a kind of ionic compound consisting entirely of anions and cations. Generally, ILs are salts formed by the combination of organic cations and organic anions (or inorganic anions). At relatively low temperatures (generally below 100 °C), IL is in a liquid state. There are four common cations: N,N′-dialkyl-substituted imidazolium ions, alkyl quaternary ions, alkyl quaternary ammonium ions, and N-alkyl-substituted pyrrolium ions. Common anions include trifluoromethanesulfonic acid ion,

bis(trifluoromethanesulfonyl)imide ion, tetrafluoroborate ion, hexafluorophosphate ion, etc. (Figure 3) [47]. Although there are many types of ionic liquids, they should also be weighed and selected according to actual needs in the application process. For example, when selecting ionic liquids for use in ECDs, trade-offs should be made between IL viscosity, conductivity, transparency, cost, and compatibility with electrochromic materials.

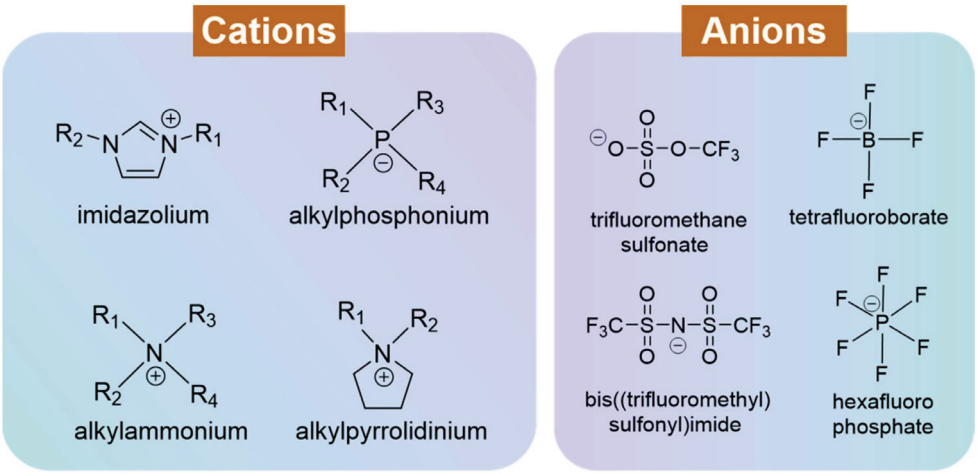

Figure 3. Common anions and cations in ionic liquids.

Compared with conventional organic solvents, IL has excellent physical and chemical properties [48]: ionic liquids generally have low volatility, which allows them to remain stable at high temperatures or under vacuum conditions. Ionic liquids have a wide electrochemical window. Meanwhile, they can be used in a wide voltage range without electrochemical reaction, which gives them a wide range of applications in the field of electrochemistry. In addition, ionic liquids can be used to dissolve many organic and inorganic substances, which makes them an excellent reaction medium and solvent. The solubility of ionic liquids can be adjusted by choosing different combinations of cations and anions. Furthermore, most ionic liquids have high thermal stability and can be kept in a liquid state under high-temperature conditions, which makes them have application potential in the field of high temperature reaction and thermal catalysis.

Owing to their unique physicochemical properties, ionic liquids have been widely used in electrochemistry, chemical synthesis, separation technology, catalysts, drug delivery, environmental protection, wearable electronics, and so on [44,49–56]. Its development prospect is promising. Especially in the field of electrochemistry, as an electrolyte that is widely used in lithium-ion batteries [57–59], supercapacitors [60–62], fuel cells [63–65], and other energy storage and conversion equipment. In recent years, as people's research on the application of IL-based electrolytes in the field of electrochromism deepened, its advantages in ECDs are also becoming more and more prominent. For example, ECDs that use IL-based electrolytes can achieve higher cycling stability, better optical contrast, higher thermal stability, and the ability to operate at low temperatures. All these features give IL-based electrolytes in electrochromic technology great prospects for development.

Similar to traditional electrolytes, IL-based electrolytes used in the field of electrochromism can be categorized into the following three types based on their composition and state: IL-based liquid electrolytes, IL-based gel polymer electrolytes (IL-GPE), and IL-based solid polymer electrolytes (IL-SPE). These three electrolytes also have their own advantages in practical applications (as shown in Figure 4). In this paper, the characteristics and applications of each type of electrolyte will be discussed in this order of classification.

	IL based Liquid Electrolyte	IL based Gel Polymer Electrolyte	IL based Solid Polymer Electrolyte
Conductivity (S/cm)	√ (10^{-1}~10^{-3})	○ (10^{-3}~10^{-4})	× (10^{-4}~10^{-5})
Risk of leakage	× (Yes)	○ (Low risk)	√ (No)
Packaging difficulty	× (Difficult)	√ (Easy)	√ (Easy)
Mechanical strength	× (Poor)	○ (Medium)	√ (Good)
Interfacial contact	√ (Good)	○ (Medium)	× (Poor)

Figure 4. Characteristics of different types of IL-based electrolytes.

2.1. IL-Based Liquid Electrolyte

Due to the large size and structural asymmetry of the anions and cations contained in ionic liquids, the anions and cations cannot be tightly stacked at the microscopic level, and the weak interactions between the anions and cations lead to the relatively low melting point of these materials, which are liquid at room temperature. In addition, this weak inter-ionic interaction also leads to the fact that the anions and cations in the ionic liquids can dissociate without the participation of other solvents, exhibiting excellent ionic conductivity (10^{-5}~10^{-2} S/cm) [66]. Therefore, ionic liquids can be directly applied as electrolytes in the ion conduction layer of electrochromic devices without any solvent addition.

In the field of ECDs, IL-based electrolytes were first applied in the form of liquid electrolytes. In order to solve the problem of poor EC cycling stability of π-conjugated polymer EC smart windows (compared with inorganic ECDs), Mattes' team carried out research work in 2002 from the perspective of an ionic conductive layer [42]. For the first time, IL-based electrolytes [BMIM][BF_4] were used instead of aqueous electrolytes and conventional organic solvent electrolytes to construct an ECD with PEDOT-POT (poly(3,4-ethylene dioxythiophene)-poly(3-octylthiophene)) and polyaniline PANI as the EC active layers (transparent yellow to dark-blue interconverted, Figure 5). The ECDs exhibited excellent EC cycle stability (up to 10^6 cycles) and extremely fast color change switching speed (1 ms). The EC cycle stability of the conductive polymer-based electrochromic device broke the highest record (3×10^5 cycles) at that time. The research work in these ECDs was subsequently reported in more detail in a separate article [67]. The results of the team's research show that the use of IL electrolytes as the ion conduction layer can play a crucial role in improving and enhancing EC cycling stability.

In 2017, Kim's team constructed an ECD based on poly(3,4-ethylenedioxythiophene)/poly(styrenesulfonate) (PEDOT: PSS) using the ionic liquid electrolyte [EMIM][TFSI] [68]. With the same device structure (FTO glass/PEDOT: PSS/Electrolyte/ATO/FTO glass), the ECDs using [EMIM][TFSI] electrolyte exhibited a higher optical contrast (17–23%) compared with those using $LiClO_4$ gel polymer electrolyte (optical contrast: 12%). The researchers believe that the key reason for the enhanced optical contrast of the ECDs was the higher conductivity of the [EMIM][TFSI] electrolyte (6.37×10^{-4} S/cm), which is approximately 3.5 times that of the $LiClO_4$ polymer electrolyte (1.82×10^{-4} S/cm).

Due to the negligible vapor pressure and high thermal stability of IL electrolytes [38], they can address the issue of device failure caused by the volatility of traditional electrolytes in high-temperature environments, which is a common problem with conventional organic or aqueous electrolytes [29,43]. In 2019, Sanjoy Mondal's team used the ionic

liquid 1-butyl-1-methylpyrrolidinium bis(trifluoromethanesulfonyl)imide (BMPyr(NTf)$_2$) as the electrolyte for ECDs and fabricated the ECD (Figure 6a) based on a Fe(II)-based metallosupramolecular polymer (poly Fe), with Prussian blue (PB) serving as the ion storage layer [43]. It was found that the ECD with IL electrolytes could not only achieve a color change from blue-violet to colorless at room temperature (at an operating voltage of +3.0/−1.5 V) (Figure 6b), but could also continue to complete 100 reversible EC cycles at room temperature after 80 cycles at a high temperature of 100 °C (chronoamperometry method). Although the optical contrast of the device reduced from 51% (first cycle) to 33% (last cycle), it still had a reversible EC change that could be seen with the naked eye. In contrast, $LiClO_4^-$ based gel electrolyte ECDs (after heat treatment at 100 °C) no longer have EC capability.

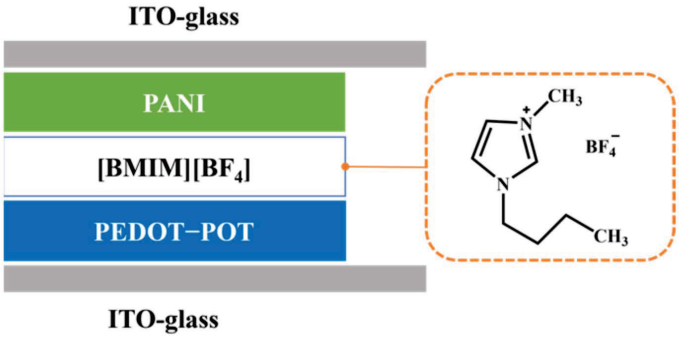

Figure 5. Electrochromic device (ECD) structure based on PANI-PEDOT-POT.

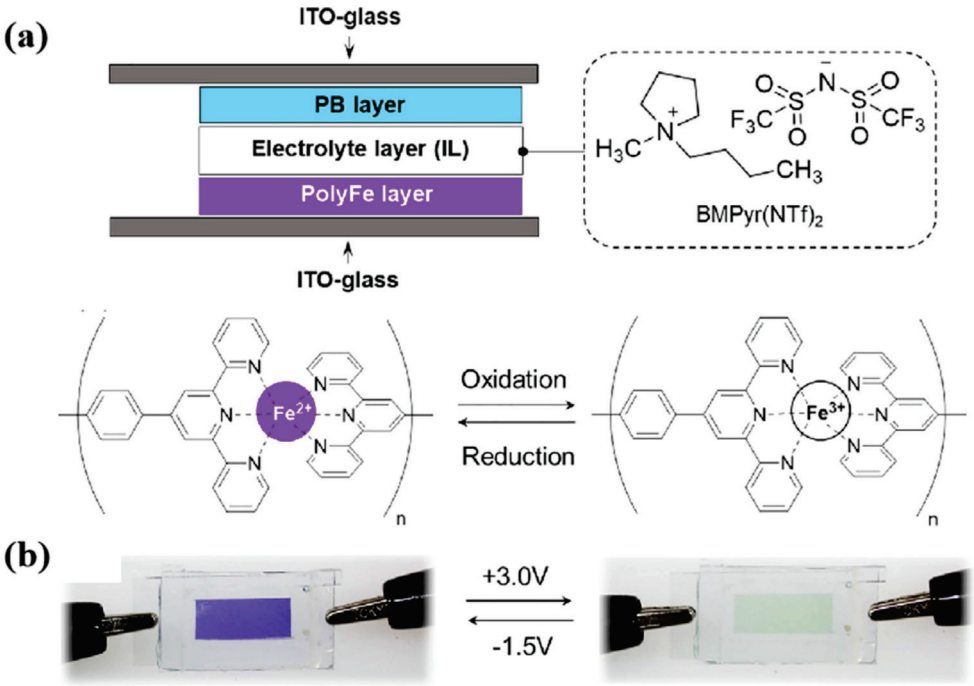

Figure 6. (**a**) Schematic presentation of the fabricated electrochromic (EC) device. (**b**) Color change in device redox by applying voltage +3.0/−1.5 V [43].

With the increasing number of studies employing IL as the electrolyte for ECDs, researchers found that selecting the best-matched ionic liquid electrolyte from the perspective of the ionic radius will result in better-performing ECDs. In 2022, Wang's group developed a novel MOF electrochromic material, Mg-PDI (Figure 7a), with an intrinsic pore structure [29]. In order to obtain the ideal EC cycling stability, such ECDs used IL as the electrolyte. This study was also the first report of combining ILs with MOF for electrochromic

applications. Unlike other works, the authors successively used four imidazolium-based ILs with similar structures but different sizes ($C_1[BF_4]$, $C_3[BF_4]$, $C_3[BF_4]$, and $C_4[BF_4]$, shown in Figure 7b), and determined that $C_4[BF_4]$ (4.57 Å) was the most compatible ionic liquid electrolyte for Mg-PDI via a three-electrode test (1000 cycles, ΔT retention > 99%, Figure 7c). In addition, to investigate the reasons for the differences in EC characteristics between different IL electrolytes, the authors tested the diffusion coefficients of five ILs (Figure 7b) in Mg-PDI electrochromic films with COF structure using cyclic voltammetry (CV) and electrochemical impedance spectroscopy (EIS). After comparing the data shown in Figure 7c, they found that $C_4[BF_4]$ exhibited the highest diffusion constant in Mg-PDI. Therefore, the authors believe that $C_4[BF_4]$ is more suitable as an electrolyte for ECDs in this system. Based on these results, the authors further prepared the corresponding ECDs C_4/Mg-PDI, which exhibited excellent EC cycling stability (500 cycles, ΔT retention rate > 95%), and the test results show that the C_4/Mg-PDI devices could achieve reversible switching from red to purplish-red and purple in the temperature range of −40 °C to 150 °C, highlighting the excellent performance of IL electrolyte-based ECDs under extreme temperature conditions. The authors observed that the intrinsic pore structure (35 Å) of Mg-PDI provided channels for ion transport of ionic liquids and showed well-matched properties. As IL tends to have a large ionic radius, compared with the MOF materials with pore structure, it is difficult for IL to enter EC materials (e.g., inorganic materials and conjugated polymers) with small crystal spacing and small molecular gaps. Although by increasing the voltage, ions could enter the EC active layer and achieve electrochromism, many times embedding and disembedding of large cations will cause irreversible damage to the EC materials, which will reduce the cycling life of the ECDs. Therefore, the authors also prepared WO_3 and P3HT-based ECDs (C_4/WO_3 and C_4/P3HT), which were tested and characterized under the same test method. The test results show that after only 30 cycles, the electrochromic cycling stability of the C_4/WO_3 and C_4/P3HT devices undergoes significant degradation, and reversible EC cycling cannot be achieved.

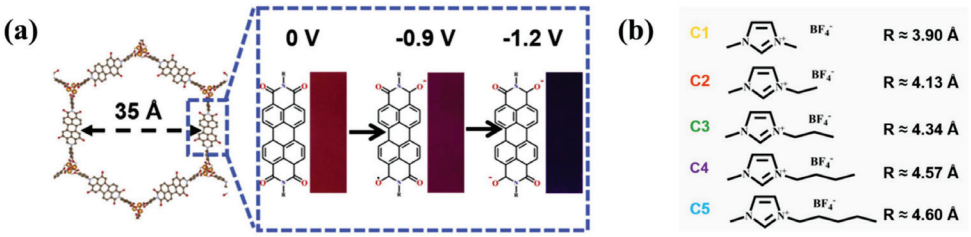

(c)

Ionic liquid	ΔT (%)	ΔT after 1000 cycles/initial ΔT(%)	D_{CV}(cm^2 s^{-1})	D_{EIS} (cm^2 s^{-1})
[C_1mim]BF_4	27.7	79.31	1.28×10^{-12}	1.37×10^{-17}
[C_2mim]BF_4	36.8	95.35	3.02×10^{-12}	3.18×10^{-17}
[C_3mim]BF_4	40.5	96.43	4.77×10^{-12}	4.65×10^{-17}
[C_4mim]BF_4	42.0	>99	5.45×10^{-12}	5.16×10^{-17}
[C_5mim]BF_4	31.3	91.39	2.54×10^{-12}	3.19×10^{-17}

Figure 7. (**a**) Structure of Mg-PDI and its color changes under different voltages, transitioning from red to purplish-red and then to purple. (**b**) Chemical structural formula of ionic liquids of C1, C2, C3, C4, and C5. (**c**) The electrochromic properties and the ion diffusion coefficient of Mg-PDI thin films in different RTILs [29].

In addition to serving as electrolytes in electrochromic devices, researchers also hope that ionic liquids can be endowed with more functional properties, such as redox ionic

liquids (RILs) electrolytes. Introducing units with redox activity into ionic liquids through covalent bonds will construct multifunctional redox-active ionic liquids [69,70], thereby endowing ionic liquids with electrochemical activity. These RILs, not only can play the role of ionic conduction in ECDs, but also have the function of electrochromism or balancing charge (reaction generated). The emergence of these RIL electrolytes demonstrates their huge potential for development and application in terms of simplifying the structure of ECDs and reducing production costs [71,72].

Since Branco et al. [73,74] reported the EC behavior of a series of ionic liquids with cobalt ethylenediaminetetraacetic acid complex as an anion and vanadium oxide as an anion in 2011, the possibility of IL acting as both an electrochromic material and electrolyte in ECDs was confirmed, which provides a new way to realize ECDs with simpler compositions. Specifically, ECDs could be achieved by simply encapsulating electrochromic ILs between two ITO glasses, without the need for additional electrolytes or EC materials, which greatly simplifies the structure and preparation process compared with the classic five-layer-structure ECD (Figure 8a). However, the above electrochromic ionic liquids have slow response times (t_c = 300~700 min, t_b = 270~483 min). Therefore, in 2014, Branco et al. prepared a series of non-symmetric disubstituted oxo-Bipyridinium ionic liquids by employing viologen, a more commonly used EC material in the field of electrochromism, as the redox unit of the ILs [75]. $[C_1C_5O_2bpy][NTf_2]_2$ (Figure 8b) was used to assemble liquid ECDs due to its liquid state at room temperature and lower redox potential. With the authors reporting that this electrochromic IL-based ECD could achieve a reversible change from pale yellow to blue color in a short period of time (compared with their former work [73,74]), the voltages ranged from −2 to 0 V (cyclic voltammetry) (Figure 8c).

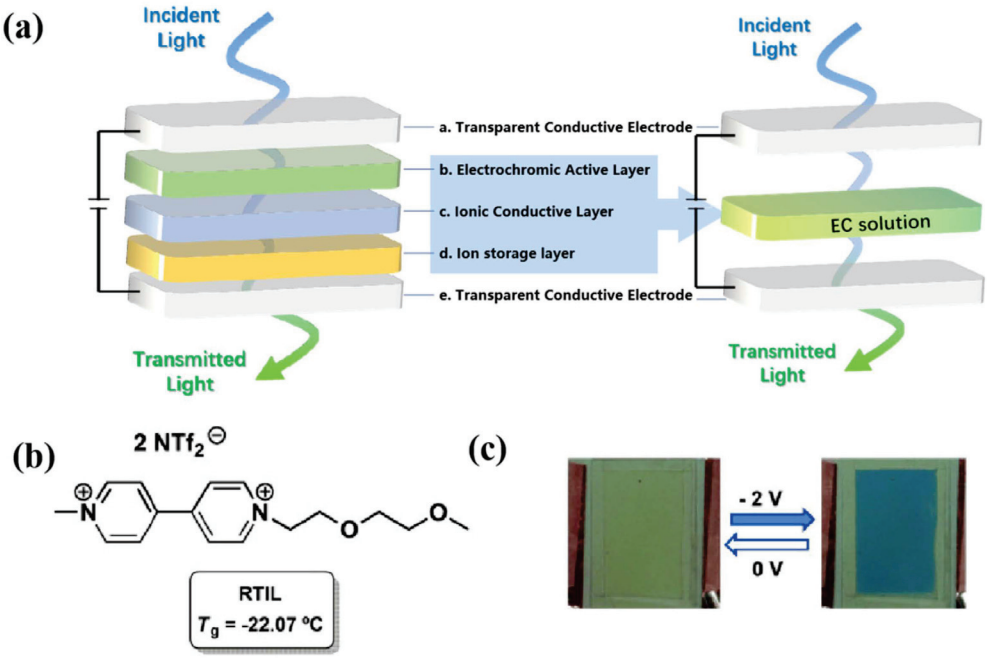

Figure 8. (**a**) Schematic diagram of the structure of five-layer and three-layer electrochromic devices. (**b**) the structure of $[C_1C_5O_2bpy][NTf_2]_2$. (**c**) Reversible electrochromic device containing the electrochromic RTIL $[C_1C_5O_2bpy][NTf_2]_2$ dissolved in the adequate electrolyte (50 mg mL^{-1}) between two PET-ITO layers [75].

Previous studies have shown that the response time and driving voltage of viologen could be reduced by introducing ferrocene as a redox mediator in viologen-based ECDs [76,77]. However, ferrocene's neutral nature makes it difficult to dissolve in ILs, thereby limiting its application as a redox mediator in ECDs with ILs as electrolytes. To

enhance the solubility of ferrocene in ILs, Bruno's team developed a series of new ferrocene-based redox ionic liquids in 2017 (Figure 9) [78]. According to the Stokes–Einstein equation, the diffusion coefficient is inversely proportional to viscosity and solvation radius. In contrast, BMIm FcNTf exhibited the highest diffusion rate (1.65×10^{-7} cm^2/s) in ionic liquid $[BMIm][NTf]_2$ due to its lower viscosity (51.6 cP) and smaller solvation radius (3.2 Å). Therefore, it was used for the assembly of the all-in-one ECDs (FcNTf/EV/IL-ECD). In FcNTf/EV/IL-ECD, $[BMIm][NTf]_2$ serves as the redox mediator, ethyl viologen $[EV][(NTf)_2]_2$ as the electrochromic active material, and $[BMIm][NTf]_2$ as the electrolyte. The FcNTf/EV/IL-ECD demonstrates short response time (t_c = 9.5 s, t_b = 5.5 s), good coloration efficiency (CE = 113.7 cm^2/C), fairly optical contrast (ΔT = 38.8%), and excellent EC cycling stability (after 1000 cycles, ΔT retention rate is 94.8%).

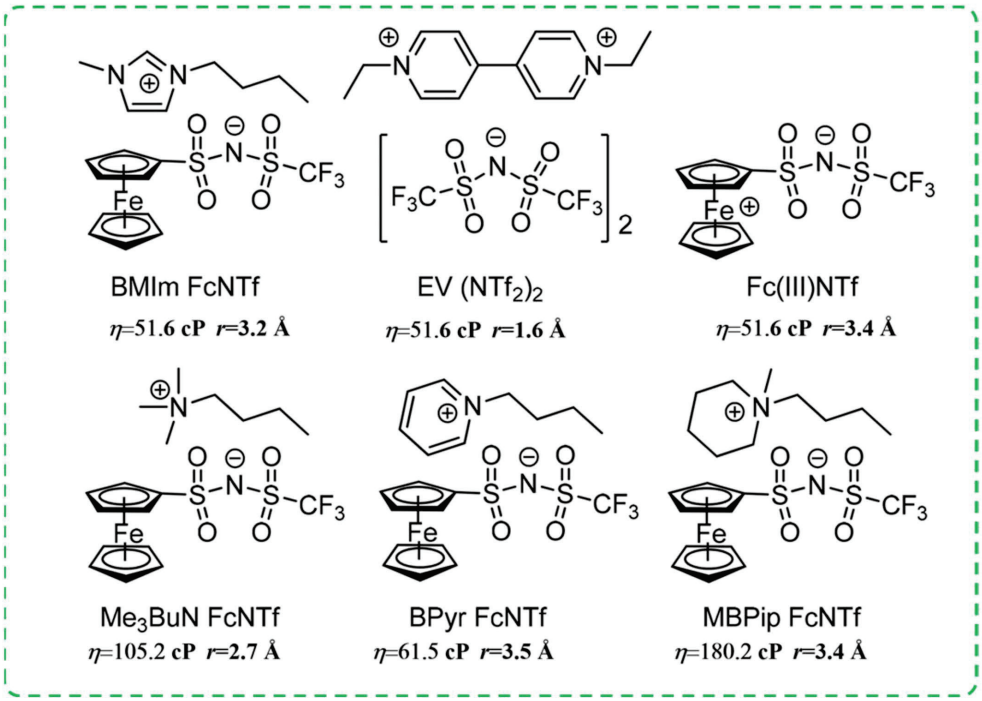

Figure 9. Chemical structure, viscosity, and solvated radius of redox ionic liquids based on ferrocenyl sulfonyl (trifluoromethyl sulfonyl) imide [FcNTf] with different counter cations: 1-butyl-3-methylimidazolium [BMIm], trimethyl butylammonium [Me_3BuN], butyl pyridinium [BPyr], and 1-butyl-1-methylpiperidinium [MBPip]. Ferrocenium sulfonyl(trifluoromethyl sulfonyl)imide [Fc(III)NTf] and ethyl viologen di[bis(trifluoromethyl sulfonyl)imide] ($[EV][(NTf_2)_2]$) are also shown [78].

In 2017, Hironobu's team developed a new electrochromic ionic liquid $[FcC_{11}VC_1][TFSI]_2$ (as shown in Figure 10a). Because the cationic part of this new ionic liquid contains both a viologen unit and a ferrocene unit, it could serve the triple functions of electrolyte, EC active material, and redox mediator. Therefore, $[FcC_{11}VC_1][TFSI]_2$ was used to produce the ECDs without any additional components (such as other electrolyte salts or organic solvents, shown in Figure 10b) [71]. The ECD based on $[FcC_{11}VC_1][TFSI]_2$ could change from light brown to dark purple at a voltage of 1 V and showed good coloration efficiency (91.4 cm^2/C at 540 nm). Additionally, after 10,000 cycles (chronoamperometry), the current response of the device shows no significant change, demonstrating the excellent electrochromic stability of the ECD. The author argues that although $[FcC_{11}VC_1][TFSI]_2$ greatly reduces the complexity of the liquid EC material, its high viscosity results in a slow coloring rate, and further optimization research on this kind of material is needed.

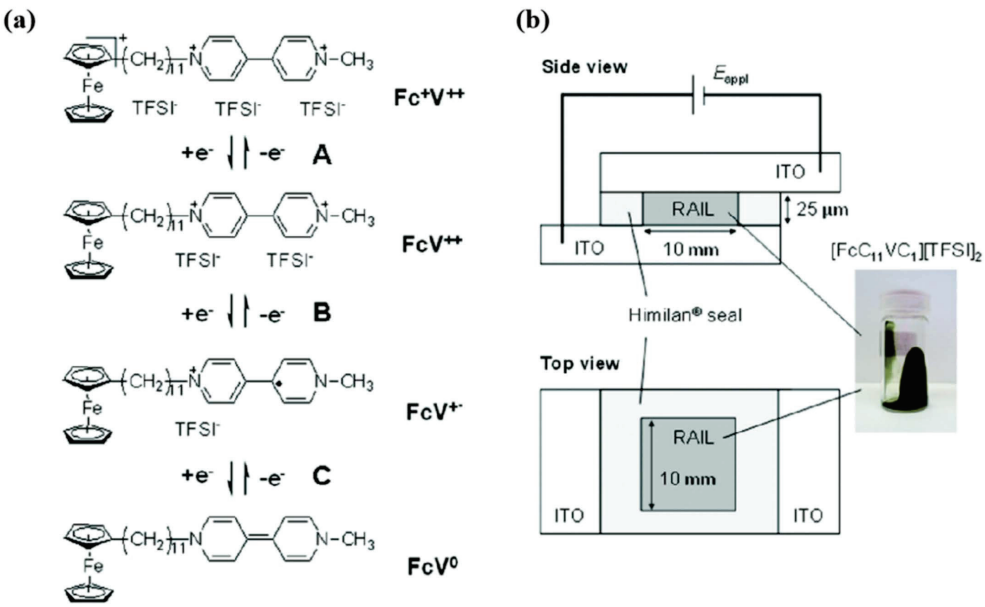

Figure 10. (**a**) Redox behavior of $[FcC_{11}VC_1][TFSI]_2$. X^- stands for the TFSI anion. (**b**) Structure of the ITO two-electrode electrochromic cell [71].

Subsequently, in 2018, Hironobu's team prepared a composite ionic liquid [79] composed of ionic liquids $[C_4VC_7][TFSI]_2$ and $[FcC_6ImC_1][TFSI]$ in an equal molar ratio (Figure 11). Compared with the previous work, the viscosity of the composite ionic liquid decreased significantly when the molar ratio of viologen to ferrocene was kept constant. The corresponding ECD test results show that under a 1 V voltage, the ECD could achieve a reversible color change, and the coloring efficiency is improved to 91.4 cm^2/C.

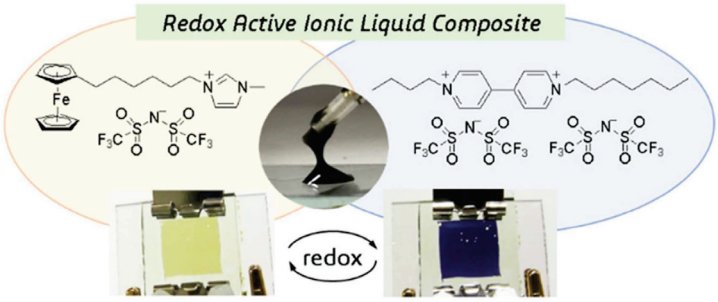

Figure 11. Chemical structure and physical photos of $[C_4VC_7][TFSI]_2$ and $[FcC_{11}VC_1][TFSI]_2$ [79].

In 2021, Xiong's team prepared a new EC ionic liquid composite material (as shown in Figure 12) using chalcogenoviologen-based ionic liquid ($[C_6EVC_6][TFSI]_2$, E = S, Se, Te) and ferrocene ionic liquid ($[FcC_{11}ImC_1][TFSI]$) [80]. Several electrochromic composite ILs were dissolved in 0.05 M $[nBu_4N][PF_6]$/acetonitrile to prepare ECDs. The ECD based on $[C_6EVC_6][TFSI]_2$, (E = S) exhibited the best electrochromic properties. At −1.1 V and 0 V, the coloring and bleaching times were, respectively, 15.0 s and 23.4 s, with an optical contrast of 63.2%. After 3000 cycles, the ΔT retention rate of the device reached 98.2%, demonstrating excellent electrochromic stability. The authors consider that the introduction of chalcogenide elements could increase the rigidity and conjugation degree of the molecular structure. The larger atomic mass and higher polarization ability could promote the ion migration rate of compounds, thereby improving their electrochemical and electrochromic properties, significantly reducing the driving voltage of $[C_6EVC_6][TFSI]_2$, and shortening the coloring time. It also shows that PET-based flexible ECDs made of $[C_6EVC_6][TFSI]_2$ and $[FcC_{11}ImC_1][TFSI]$ could be colored and discolored when applied with ±1.3 V voltage at the bending state.

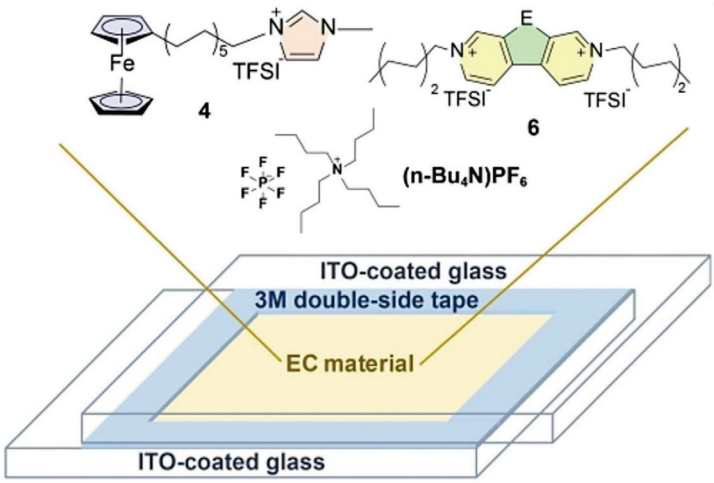

Figure 12. Schematic diagram of electrochromic devices based on $[C_6EVC_6][TFSI]_2$, (E = S, Se, and Te) and $[FcC_{11}ImC_1][TFSI]$ [80].

Although many viologen-based ILs meet the strict definition of ionic liquids (melting point < 100 °C), a melting point higher than room temperature does not favor the application of viologen ILs in ECDs. In 2024, Xu et al. prepared two new room-temperature ionic liquids (RTILs) [72], viologen-based RTIL containing polyethylene glycol (vio-IL) and ferrocenyl RTIL (Fc-IL) (as shown in Figure 13). The introduction of long-chain polyethylene glycol makes vio-IL difficult to crystallize, and the large volume of [TFSI] in vio-IL helps to reduce the interaction between ions, thus making vio-IL liquid at room temperature. The ferrocenylmethyl dimethyl propylammonium bromide previously synthesized by the research group could also change from a solid state to a liquid state after [TFSI] ion exchange. The team prepared an ECD using $[EMIm][NTf_2]$ as the electrolyte, and vio-IL and Fc-IL as the electrochromic materials and redox mediator, respectively. The ECD exhibited a large optical contrast (ΔT = 79.4%) and excellent electrochromic cycle stability (1000 cycles, ΔT retention rate of 96.2%), with a coloring time of 23.6 s and a fading time of 9.5 s. Additionally, the team reported an ultra-thin (10 μm) ECD based on these two ionic liquids. The shorter ion transport path shortens the response time of the ECD. The ultra-thin ECD had a coloring time of 13.3 s and a fading time of 3.7 s, and it also showed good cycle stability (ΔT retention rate was 95.6% after 1000 cycles).

In addition to the application of ionic liquids based on viologen and ferrocene derivatives in ECDs, the TEMPO (2,2,6,6-tetramethylpiperidinyl-1-oxide) structure has also been introduced into ILs for applications in the field of electrochromism. TEMPO's N-O• has the advantage of rapid electron transfer in electrochemical reactions due to its high intrinsic heterogeneous rate constant (about 10^{-1} cm/s), and nitroxyl free radicals (N-O•) are protected by their spatial structure, showing good chemical stability in organic solvents. Consequently, this structure has been incorporated into ionic liquids for applications in electrochromic devices.

Additionally, in 2017, Fan et al. [81] combined TEMPO with ionic liquids through chemical modification to prepare a novel ionic liquid 1-butyl-3-(2-oxo-2-((2,2,6,6-tetramethylpiperidin-1-oxyl-4-yl)amino)ethyl)-1H-imidazol-3-ium tetrafluoroborate ($TILBF_4$). Poly (3,3-diethyl-3,4-dihydro-2H-thieno-[3,4-b] dioxepine) ($PProDOT\text{-}Et_2$) were used as the EC materials. A PC solution of 0.01 M $TILBF_4$ and 0.1 M $LiClO_4$ was used as the electrolyte to prepare $PProDOT\text{-}Et_2/TILBF_4$ ECD (as shown in Figure 14). The prepared electrochromic device exhibited a high optical contrast (ΔT = 62.2%), good electrochromic cycling stability (ΔT retention ratio is 96.8%, after 1000 cycles), and a fast switching speed with a coloration time (t_c) of 3.6 s and a bleaching time (t_b) of 4 s (reaching 95% of the saturated ΔT), as well as superior coloring efficiency (983.0 cm^2/C at 590 nm).

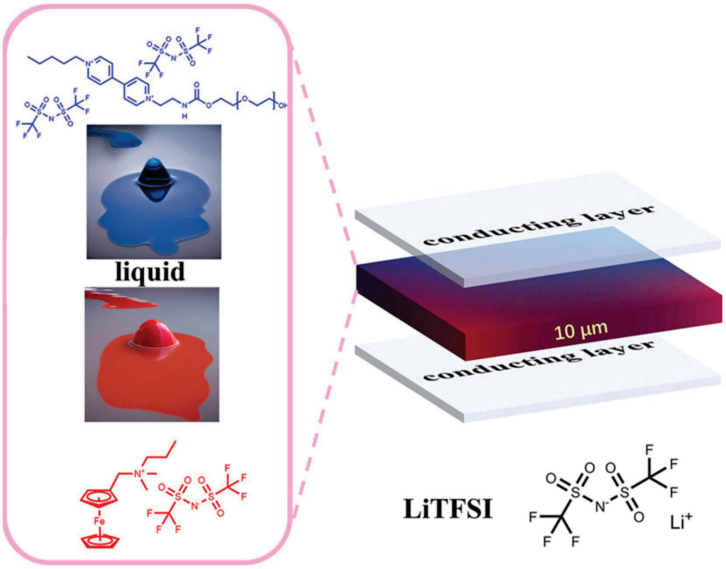

Figure 13. The structure of RTIL (Vio-IL and Fc-IL) and the ultra-thin (10 μm) ECD based on Vio-IL and Fc-IL [72].

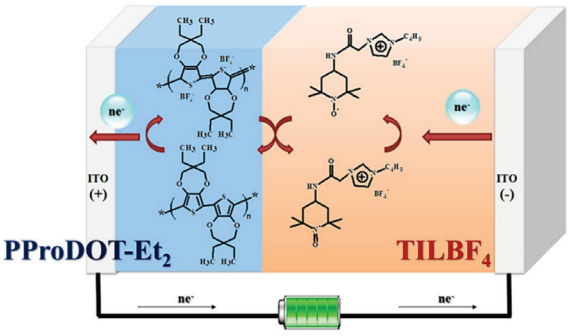

Figure 14. Schematic diagram of the proposed hybrid type ECD based on PProDOT-Et_2 and $TILBF_4$ [81].

In 2022, Kim et.al. [82] synthesized three novel redox ionic liquids RILs (RIL1, RIL2, and RIL3) by connecting TEMPO units with imidazole cations through methylene or pyrimidine structures (as shown in Figure 15a). Due to their redox activity, these RILs could provide not only ion storage, but also redox mediators for the regeneration of dyes in the photoenergy harvesting process, and they could be ideal electrolytes for smart windows with energy storage and self-recharging functions in a single cell. The author used three types of RILs to manufacture three self-powered electrochromic capacitor windows (PECWs) (as shown in Figure 15b). Among them, the PECW based on RIL2 showed the best characteristics in terms of electrochromic performance and energy harvesting performance, with a photochromic efficiency of 65 $cm^2/W/min$, an optical contrast of 90.8%, and excellent electrochromic cycle stability (basically no decay in ΔT after 4000 cycles).

The application of ionic liquids as electrolytes in ECDs can not only enhance the thermal stability, electrochromic cycling stability, and optical contrast of electrochromic devices, but also enables them to serve as both ion conduction layers and, through modification, electrochromic layers and ion storage layers. These studies clearly demonstrate the significant advantages of liquid IL-based electrolytes in electrochromic applications and also offer technical insights into the exploration of more structurally simplified ECD designs. For clarity, Table 2 presents a comprehensive summary of the key performance characteristics of IL liquid electrolytes and their corresponding ECDs. However, ECDs employing IL-based

electrolytes as ion transport layers still encounter challenges related to device packaging and electrolyte leakage, which are attributed to their liquid nature at ambient temperature.

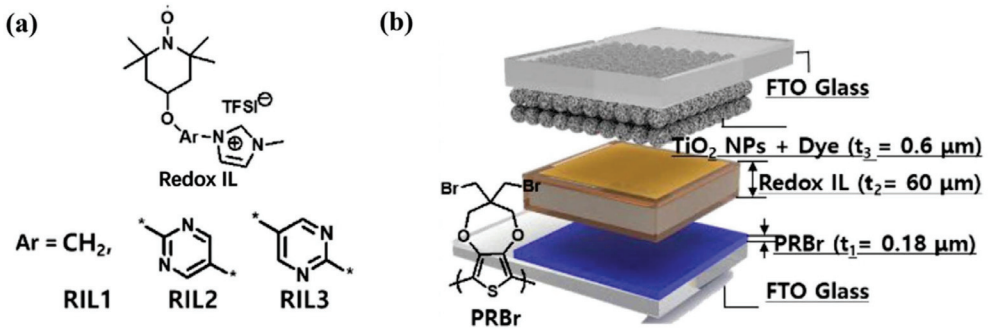

Figure 15. (**a**) The structure of RIL1, RIL2, and RIL3 (asterisks indicate the positions of the substituents). (**b**) Schematic diagram of the PECWs and chemical structure of the electrochromic polymer [82].

Table 2. The performance of IL liquid electrolytes and electrochromic devices (ECDs).

Electrolytes	Conductivity (S/cm)	ECM	Color Changes	t_c/t_b (s)	ΔT(%)	CE (cm^2/C)	Cycle	Ref.
$[BMIM][BF_4]$	/	PANI	transparent yellow to dark blue	1 ms	63	/	10^6	[42]
[EMIM][TFSI]	6.37×10^{-4}	PEDOT: PSS	Light blue to dark blue	12.0/4.0	36	/	/	[68]
BMPyr $(NTf)_2$	7.8×10^{-4}	polyFe	transparent to blueish-violet	12.0/20.5	51	254.5	More than 300 cycles	[43]
$[BMIM][BF_4]$	1.81×10^{-3}	Mg-PDI	red to purple	9.2/0.6	42	305	200 cycles ΔT retention rate 95.8%	[29]
$[C_1C_5O_2bpy][NTf_2]_2$	/	/	yellow to blue	/	/	/	/	[75]
$[EV][(NTf)_2]_2$ [BIMI][FcNTf]	/	$[EV][(NTf)_2]_2$	to blue	9.5/5.5	38.8	113.7	10^3 cycles ΔT retention rate 94.8%	[78]
$[FcC_{11}VC_1][TFSI]_2$	/	$[FcC_{11}VC_1][TFSI]_2$	light brown to dark purple	/	/	70	10^4 cycles	[71]
$[C_4VC_7][TFSI]_2$ $[FcC_6ImC_1][TFSI]$	/	$[C_4VC_7][TFSI]_2$	/	/	/	91.4	10^4 cycles	[79]
$[C_6SVC_6][TFSI]_2$ $[FcC_{11}ImC_1][TFSI]$	/	$[C_6SVC_6][TFSI]_2$	blue to yellow	15.0/23.4	63.2	80.3	3000 cycles ΔT retention rate 98.2%	[80]
Vio-IL Fc-IL	1.4×10^{-5} Vio-IL 5.6×10^{-5} Fc-IL	Vio-IL	transparent to blue-violet	13.3/3.7	79.4	/	10^6	[72]
$TILBF_4$	1.9×10^{-2}	$PProDOT\text{-}Et_2$	light blue to deep blue	3.6/4.0	62.2	983.0	/	[81]
RIL2 (in [BMIM][TFSI])	2.0×10^{-3}	PRBR	transparent to deep blue–purple	/	>85	/	More than 300 cycles	[82]

2.2. IL-Based Gel Polymer Electrolyte (IL-GPE)

Although IL-based liquid electrolytes have many application advantages in the field of ECDs, any liquid electrolyte with fluidity, whether in rigid or flexible devices, faces challenges related to device packaging and electrolyte leakage. At present, there are two approaches to solving this problem: one is to develop gel polymer electrolytes, and the other is to develop solid-state electrolytes. Compared with the latter, gel electrolytes, due to their higher ionic conductivity, have seen faster development and wider application. Gel polymer electrolytes can limit the fluidity of the liquid electrolyte, thus improving device safety [37]. Furthermore, gel polymer electrolytes offer lightweight and excellent viscoelastic properties, which provide significant advantages for the development of lightweight, thin, flexible, wearable, and large-area ECDs.

In IL-based gel polymer electrolytes (IL-GPEs), ILs exist in two forms: One is in a free state within the electrolyte, not covalently fixed in polymer networks, serving as a

plasticizer and electrolyte salt; common polymer matrices, such as PEO, PMMA, PVDF, PU, PVC, etc., [33,83–91] are used to limit the mobility of the electrolyte. The other form involves the covalent attachment of ILs to a polymer backbone to form a polymeric ionic liquid (PIL), which serves as a polymer matrix to limit the mobility of the electrolyte and exhibits a specific level of ionic conductivity [92]. These two forms of ILs in IL-GPEs contribute differently to the overall performance of the electrolytes, influencing factors such as conductivity and mechanical stability. To provide clarity, in this section, we will analyze and introduce the development of polymer matrix materials in gel polymer electrolytes according to their types. In this section, we will analyze and discuss the development of IL-GPEs according to the types of polymer matrix materials. This classification helps to understand the unique contributions of each polymer matrix to the overall performance of gel polymer electrolytes. It can be divided into electrolytes based on polyvinylidene fluoride, poly (ethylene oxide), polyacrylate, PILs, and other polymer matrices.

2.2.1. PIL-Based IL-GPEs

One way to develop ionic liquid gel polymer electrolytes (IL-GPEs) is to incorporate ionic liquids into polymers, forming PILs. These PILs not only retain their high ionic conductivity, chemical stability, and thermal stability, but also retain the processability of polymers, thereby overcoming challenges related to phase separation due to poor compatibility between ionic liquids and certain polymer matrices. These combined properties enable the PILs to effectively address issues of phase separation, making them suitable for a variety of ECDs. This type of PIL-based electrolyte also finds extensive application in electrochromic devices, as will be discussed below. In an effort to elucidate the key performance characteristics of PIL-based IL-GPEs and their associated ECDs, we have systematically collated the pertinent data, which are detailed in Table 3 (located at the end of Section 2.2.1).

In 2006, Marcilla synthesized a series of polyelectrolyte liquid electrolytes, including poly[ViEtIm][Tf_2N], poly[ViEtIm][BF_4], and poly[ViEtIm][Br] [93] (Figure 16a), through thermally initiated polymerization. These PIL electrolytes were synthesized. Subsequently, ionic liquids with analogous structures, such as [bmim][Tf_2N], [bmim][BF_4], and [bmim][Br], were used to prepare gel polymer electrolytes employed as the plasticizer. Considering the excellent electrochromic cycling stability exhibited by liquid ECDs based on [BMIM][Br] (symmetric devices with PEDOT as the EC layer), poly [ViEtIm][Br]-based ECD (symmetric devices with PEDOT as the EC layer) (Figure 16b) were selected from among these gel electrolytes for further assembly and performance evaluation. The test results indicate that, compared with the PEO/lithium salt-based gel electrolyte as the ion conduction layer (where ΔOD (optical density change) was reduced by 80% after 3000 cycles), the electrochromic cycling stability of this ECD was significantly enhanced, with ΔOD exhibiting a marked decrease after 3×10^4 cycles (Figure 16c). This work represents the first application of a gel-based ionic liquid polymer electrolyte in the electrochromic field.

In 2008, Pozo Gonzalo et al. reported a PIL-based gel polymer electrolyte with a similar composition, focusing primarily on the application of symmetric PEDOT-based ECDs in near-infrared light modulation [94]. The ECD prepared using an electrolyte of poly (1-vinyl-3-ethylimidazolium tetrafluoroborate) and 1-butyl-3-ethylimidazolium tetrafluoroborate exhibited superior electrochromic performance, with a visible ΔT of 50.5% and an infrared ΔT of 44%, outperforming ECDs prepared using PEO-ClO_4^- (which had a visible region ΔT of 39.9% and an infrared region ΔT of 3.3%). This ECD also demonstrated a coloring time of 2.7 s and a fading time of 3.8 s. As reported by the team, this work achieved the highest ΔT value in the infrared region for plastic-based ECDs utilizing conductive polymers at that time.

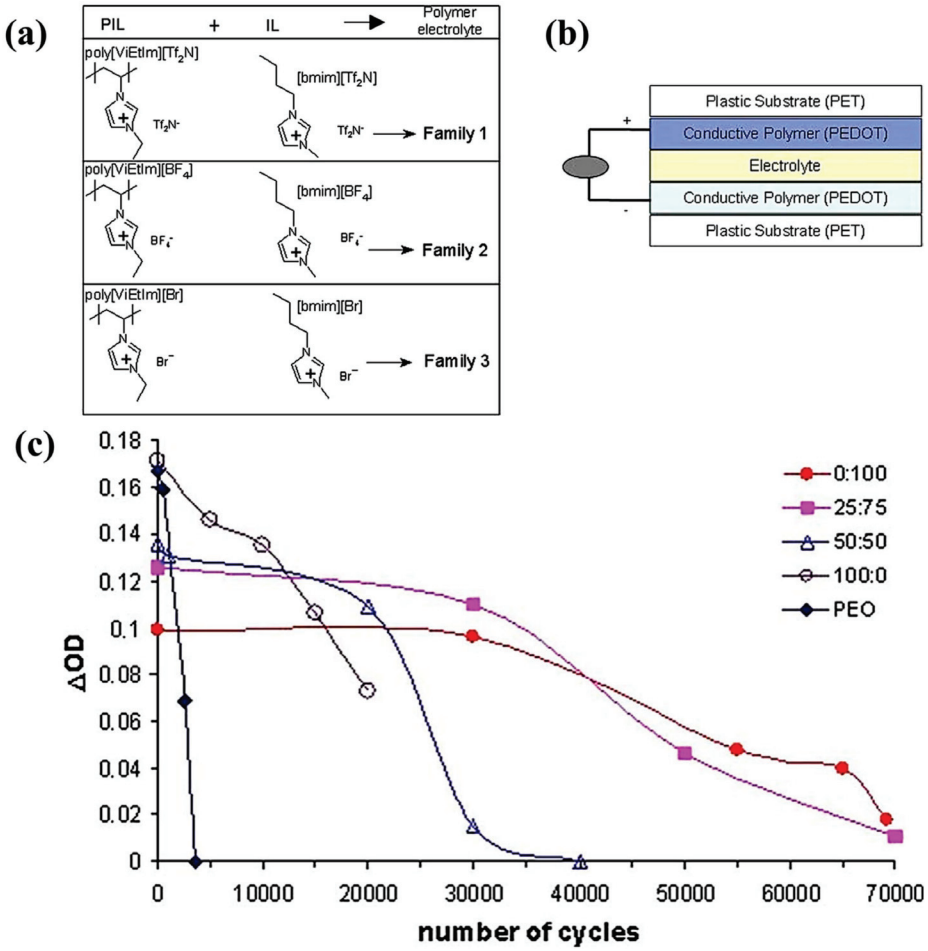

Figure 16. (**a**) Composition of the polymer electrolyte families. (**b**) Schematic diagram of electrochromic device structure based on PEDOT. (**c**) Variation in ΔOD as a function of the number of cycles for ECDs using polymer electrolytes with different ratios [emim][Br]:poly[ViEtIm][Br] and using the PEO/lithium triflate electrolyte [93].

As the broad application of in situ polymerization technology in the field of gel electrolytes, researchers prepared gel polymer electrolytes based on a PIL matrix, achieving promising results. In 2022, Lee's team prepared two gel electrolytes, PIL-A and PIL-B [95], based on PILs using an in situ photocuring process (Figure 17a,b). For PIL-A, the ethylene-functionalized ionic liquid VBIMTFSI and the acrylic end-capping crosslinking agent PEGDA700 undergo in situ polymerization under UV light irradiation at 395 nm, forming a three-dimensional PIL network structure. The ionic liquid EMIMTFSI (1,3-ethylmethylimidazolium bis(trifluoromethanesulfonyl)imide) serves as both an electrolyte salt and a plasticizer. PIL-B is derived from the formula of PIL-A, with the addition of PC as a plasticizer and vinyl-functionalized lithium salt (LiMA), incorporating the lithium salt structure into the three-dimensional network of the PIL through in situ polymerization. Respectively, PIL-A and PIL-B are suitable for ECDs with iron-centered coordination polymer (Fe-CP) and P-WO_3 as the EC materials. Notably, the P-WO_3-ECD using PIL-B as the ion conduction layer exhibited high electrochromic cycling stability, maintaining over 90% of its initial ΔT after 5000 cycles (Figure 17c,d). Based on these findings, the researchers developed a pair of curved eye protectors (Figure 17e) based on WO_3 and a flexible digital display (Figure 17f), highlighting the significant advantages of PIL-based electrolytes in the fabrication of flexible ECDs.

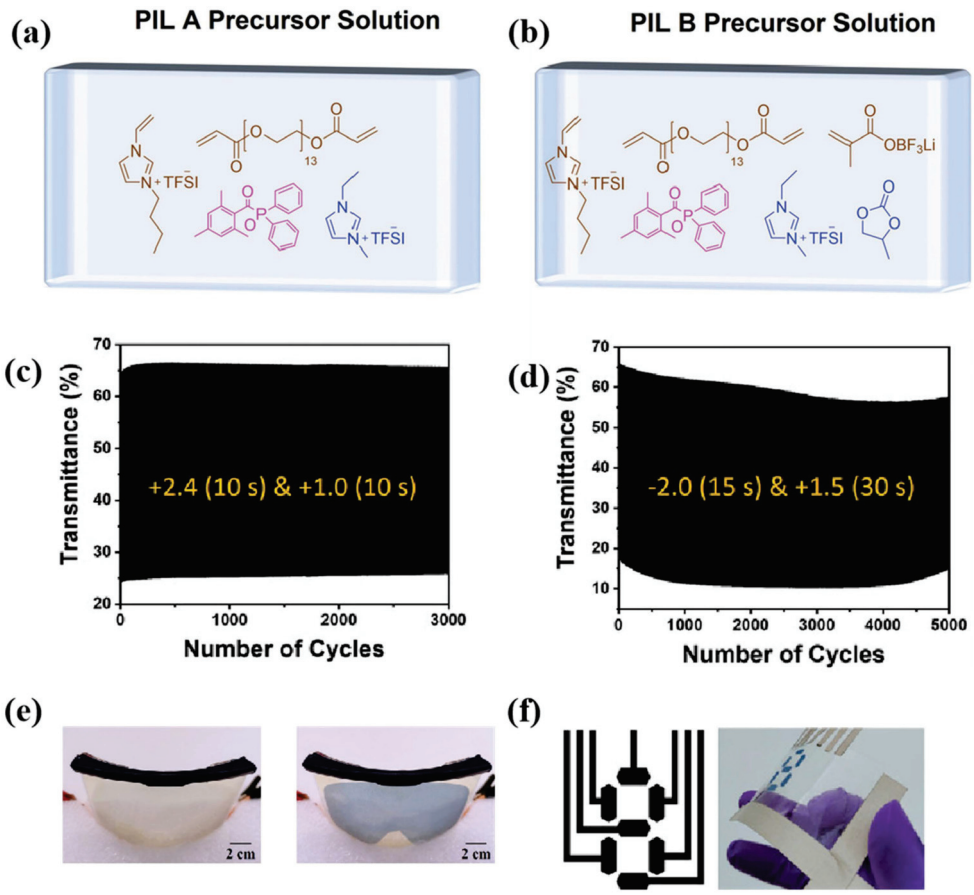

Figure 17. Composition of PIL A (**a**) and PIL B (**b**) precursor solutions (brown: stationary phase; blue: mobile phase; and pink: photoinitiator) (**c**). Changes in transmittance of the FeCP device at 572 nm recorded over 3000 cycles. (**d**). Changes in transmittance of the P-WO_3 device at 660 nm recorded over 5000 cycles. (**e**) Top view a flexible electrochromic eye protector device captured in a photography lightbox to stimulate outdoor bright sunlight conditions. (**f**) Patterned digital arrays produced by wet etching approach to realize displays of various number patterns [95].

PIL-based IL-GPE can also be used for the preparation of integrated ECDs and demonstrates its unique advantages in integrated ECDs. In 2016, the Ho team developed a series of PIL-GPE featuring an interpenetrating network structure (Figure 18a) composed of polymer ETPTA and varying mass percentages of poly[AMIM][TFSI] (5-PIL, 20-PIL, 40-PIL, 60-PIL, 80-PIL) [44]. In addition, the researchers introduced the electrochromic material $NV(BF_4)_2$ and the redox mediator Fc into the gel electrolyte. This allows for a simple assembly of an "all in one" ECD by clamping the gel electrolyte between transparent electrodes. The test results show that the ECD based on the 20-PIL gel electrolyte exhibited the best electrochromic cycling stability, with a ΔT retention rate of 97.5% after 10,000 cycles, outperforming other PIL-GPE compositions (e.g., 80-PIL:4000 cycles, ΔT retention rate 77.7%) and liquid organic solvent electrolytes (4000 cycles, ΔT retention rate 80.1%) (Figure 18b,c). In addition, the researchers found that the electrochromic cycling stability of this type of ECD initially increased and then decreased with increasing polyelectrolyte content. They suggest that the higher cycling stability observed with 5-PIL and 20-PIL ECDs may be attributed to a reduced diffusion rate, which has been previously proved to positively affect the stability of viologen-based ECDs. However, as the PIL content increases further, despite the continued decrease in diffusion rate, the electrochromic cycling stability also significantly decreases. They speculate that one possible reason for this decline is the excessive polymer matrix capturing $NV(BF_4)_2$.

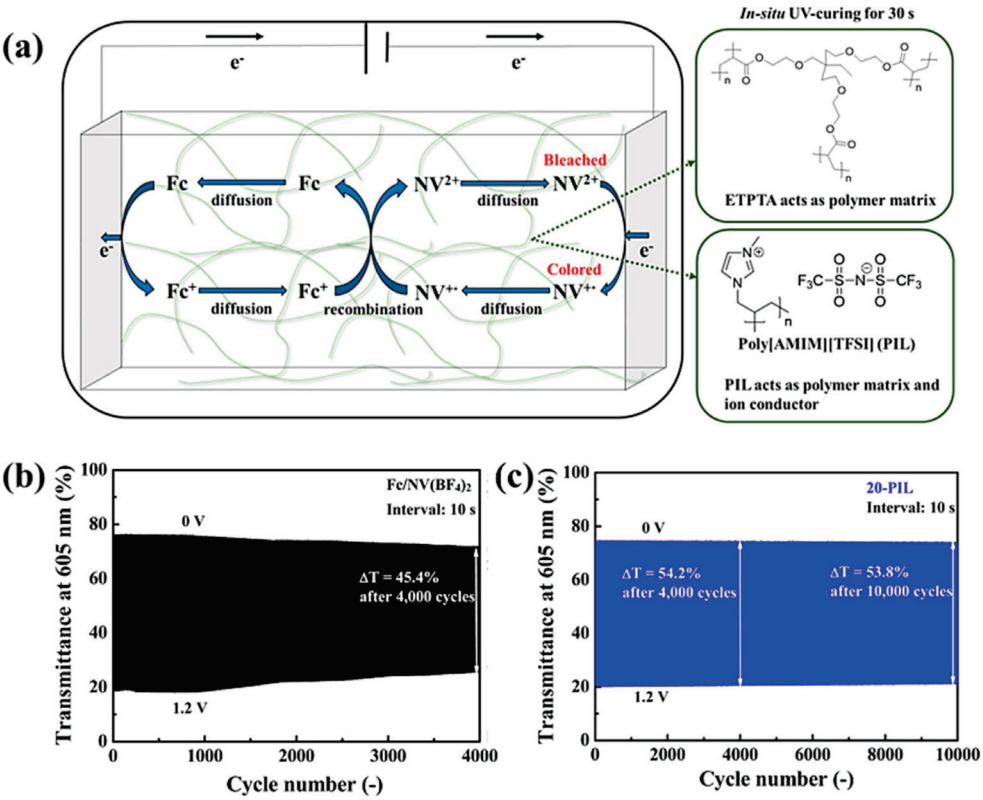

Figure 18. (**a**) Design concept and the working principle of the proposed PIL ECD. Long-term stability data for (**b**) the Fc/NV$(BF_4)_2$ ECD and (**c**) the 20-PIL ECD under continuous cycling between 1.2 and 0 V [44].

In 2017, Chen et al. first reported a novel polyelectrolyte material P(NIPAMx-BVImy-DACVz) [96] that combines thermochromic and electrochromic functions (as shown in Figure 19a). It is a cross-linked polymer prepared by ternary copolymerization of N-isopropylacrylamide (NIPAM), 3-butyl-1-vinyl-imidazolium bromide [BVIm][Br], and diallyl viologen (DAV). In this polymer, the P(NIPAM)x segment exhibits thermochromic properties, the P(BVIm)y segment has ion conductivity, and the P(DACV)z segment has electrochromic properties and is responsible for constructing cross-linking structures between polymer chains. The IL-GPE, prepared with this PIL and water as a plasticizer, was sandwiched between ITO glass to fabricate thermochromic electrochromic devices (TEDs). These TEDs could achieve over 20 reversible transparency switching cycles between 20 °C and 33 °C and also exhibit reversible electrochromic (EC) changes from colorless and transparent to blue-purple under an applied voltage of 2 V (Figure 19b). The coloring and fading times are approximately 3 s and 5 s, respectively, and after 100 cycles, the current response shows minimal variation, suggesting high electrochemical cycling stability.

In 2021, Kim's team also conducted similar research and prepared a new type of PIL material, Smart PIL [97], that combines thermochromic and electrochromic functions. In the structure of this cross-linked polymer, PEGDA segments are responsible for ion transport and constructing cross-linked networks; the P(NIPAM) segment exhibits thermochromic properties; and polymer segments containing viologen units display electrochromic properties (Figure 20). With water as a plasticizer, Smart PIL was formulated as an IL-GPE, which was then sandwiched between ITOs to fabricate a thermoelectric double-responsive smart window (Figure 20). TEDs could complete more than 20 reversible transparent switches between 16 °C and 25 °C. In terms of electrochromic performance, TEDs could also realize the reversible cycle from colorless transparent to blue under the application of voltage (4 V). These reversible switches and color changes demonstrated the device's robust

electrochromic capabilities. The optical contrast change in the prepared electrochromic device is 66.92%. Although the coloring time of 55 s is not ideal, it is worth noting that the device had an ultra-long memory effect. Under the voltage-off state, it takes the device 13 days to completely bleach.

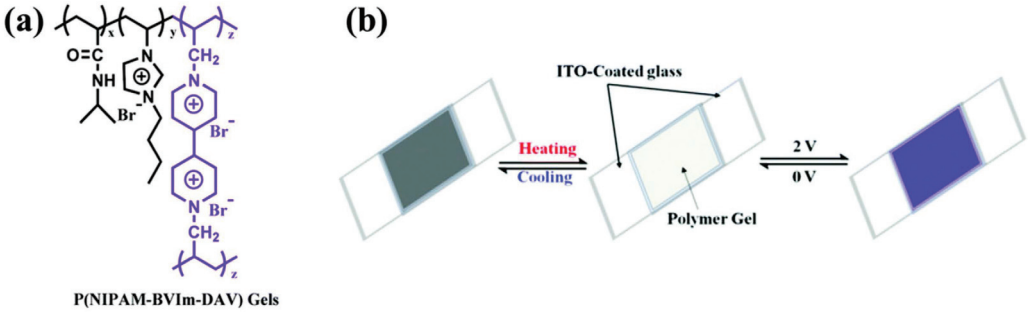

Figure 19. (**a**) Polymer structure of P(NIPAM–BVIm–DAV). (**b**) Schematic mechanism of thermochromic and electrochromic devices (TEDs) based on the prepared polymer gels [96].

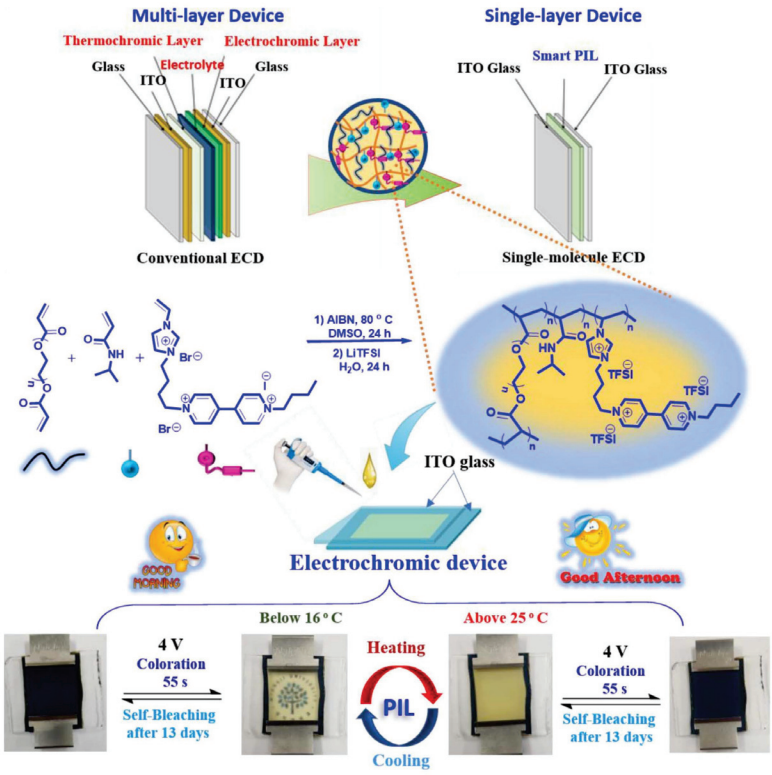

Figure 20. Schematic of the integrated thermochromic and electrochromic device using one single-molecule Smart PIL [97].

In 2022, the He team designed and synthesized a novel polymer called poly (vinylidene fluo-ride-co-difluoroethyleneaminooxyethyl-1-butylimidazolium-co-vinylaminooxyethyl-1-butylimidazolium tetrafluoroborate) (PFI-BF_4) (Figure 21a). After electrospinning PFI-BF_4 into a film, it was immersed into a PC solution containing 0.05 M phenyl viologen (PV) and 0.05 M Fc to obtain gel electrolyte [45]. This kind of gel was sandwiched between ITO glass to form an ECD. Compared with the ECD using PVDF-HFP (ΔT = 68.9%, t_b/t_c = 5.6/1.6 s) as the polymer matrix, the ECD based on PFI-BF_4 showed more excellent optical contrast and switching time (ΔT = 72–74.6%, t_b/t_c = 3.5–4.3/2.6–3.3 s). This is because the PFI-BF_4^- based electrolyte had more excellent conductivity (8.61–9.28 $\times$ 10^{-3} S/cm) than the PVDF-HFP-based electrolyte (5.94 $\times$ 10^{-3} S/cm). The ECD based on PFI-BF^- 1.5 showed excellent electrochromic stability (maintaining 95.9% of its initial ΔT value after

10,000 cycles and 88.3% of its initial ΔT value after 50,000 cycles), while the ECD based on PVDF-HFP exhibited rapid decay within 10,000 cycles. They believe that this is due to the balanced repulsive and attractive interactions provided by PFI-BF_4^- 1.5 for the migration of PV^+ ions so that PV^+ ions will not be captured by fluorine nor undergo dimerization and quenching (Figure 21b–d).

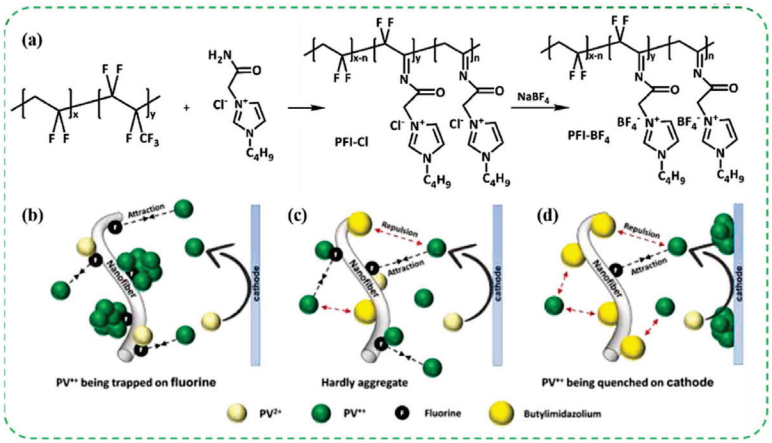

Figure 21. (**a**) The synthesized processes of PFI-BF_4. (**b**–**d**) The sketches of the molecular interaction between the viologen ions and the PFI-BF_4^- based membranes. (**b**) The raw PVDF-HFP membrane possessed a large number of lone-pair electrons of fluorine atoms, which provided strong attractive interaction for the $PV^{\bullet+}$ ions being trapped and aggregated on the membrane. (**c**) The PFI-BF_4_1.5 membrane exhibited the optimal molar ratio of imidazoliums to fluorines; the former supplied repulsive interaction, and the latter offered attractive interaction towards the $PV^{\bullet+}$ ions. The equilibrium electrostatic interactions established among imidazoliums, fluorines, and $PV^{\bullet+}$ ions could render the ECD with fewer viologen aggregation. (**d**) The PFI-BF_4_2 membrane had excess imidazoliums, which provided overwhelming repulsive interaction that caused the $PV^{\bullet+}$ to be quenched on the cathode [45].

To meet the application requirements of ECD in the field of flexible wearables, in addition to improving the flexibility of the device, it is also desirable that the core components of the device have a self-healing ability under certain conditions, especially the polymer electrolyte layer. In 2024, Kim's team designed and developed a stretchable, self-adhesive, and self-healing PIL material (UPy-PEGM-VBMI-TFSI) [98]. The self-complementary quadruple hydrogen bonds (QHB) formed by UPyMA endow the polyelectrolyte electrolyte with self-healing properties and excellent mechanical properties, while VBMI endows the polymer network with ion conductivity. The mobile ions of PEGMA are transported through the soft phase of the PEGMA chain. Subsequently, based on the aforementioned PIL material, the research group used PC and EMIMTFSI as plasticizers, DHHV as EC material, Fc as redox mediator, LiTFSI as an electrolyte salt, and A PIL-based IL-GPE membrane (the ion gel film shown in Figure 22a) integrating EC and ion transport was prepared. The gel electrolyte was sandwiched between two layers of ITO-PET, and the all-in-one flexible ECD showed excellent EC performance. In addition, the flexible ECD also exhibits self-healing properties. Through self-healing and self-adhesive functions, interconnected modular large-area ECDs (38×40 cm^2) have been achieved, providing insights into constructing devices with expandable areas (Figure 22b). More importantly, the PIL-based IL-GPE membrane could also be applied to the stretchable ECD (Figure 22c). Even under 53% strain, the ECD could still show 42.7% optical contrast, fast switching time (8.4 s for coloring, 13.5 s for fading), and ΔT = 41.6% after 600 cycles, exhibiting excellent electrochromic stability. After 100 cycles of tensile/recovery testing (between 0 and 40% strain), the device still maintains excellent electrochromic cycling stability, with a ΔT of 30%.

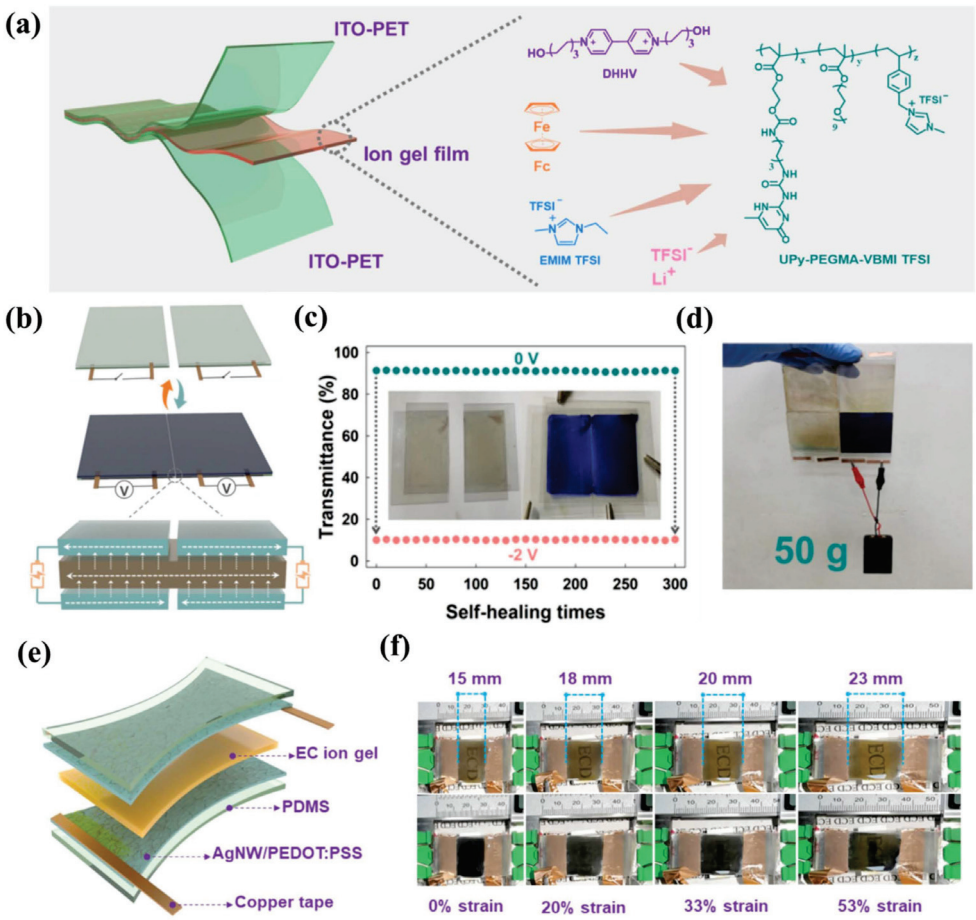

Figure 22. (**a**) Chemical structures of the constituents of electrochromic ion gels and a demonstration diagram of the single-layered flexible ECDs containing the ion gel. (**b**) Schematic diagrams illustrate the self-healing and coloring processes of modular flexible ECDs. (**c**) Transmittance changes in neutral and colored states of modular flexible ECDs after 0 to 300 cycles of separation and self-healing processes. (**d**) A photo image featuring four modular flexible ECDs (6 × 5 cm^2) supporting a weight of 50 g after re-joining and coloring. (**e**) The demonstration diagram of the stretchable electrochromic devices containing the ion gel. (**f**) Photos of the stretchable ECDs (2 × 1.5 cm^2, 0 and −2.5 V) at 0%, 20%, 33%, and 53% strain states [98].

Table 3. The performance of PIL-based IL-GPEs and ECDs.

Electrolyte Membrane			Performance of ECD						
Electrolyte	**Conductivity (S/cm)**	**Thickness (μm)**	**ECM**	**Color Changes**	**t_c/t_b (s)**	**ΔT (%)**	**CE (cm^2/C)**	**Cycles**	**Ref.**
poly[ViEtIm][Br] /[BMIM][Br]	10^{-5}~10^{-2}	/	PEDOT	/	/	/	/	7×10^5	[93]
poly[ViEtIm][BF_4] /[BMIM][BF_4]	/	/	PEDOT	/	3.6/2.7	44(IR)	/	/	[49]
PILA	/	1000	FECP	transparent to purplish-blue	1.5/1.9	45.2	/	3000	[95]
PILB	/	1000	P-WO_3	colorless to dark blue	6.4/1.7	56.4	/	3000	[95]
Poly[AMIM][TFSI]	/	/	NV(BF_4)$_2$	colorless to dark blue	2.1/2.13	55.2	273.5	10^4	[44]
P(NIPAMx-BVImy-DACVz)	/	/	P(NIPAMx-BVImy-DACVz	colorless to transparent purple	5/3	/	/	100	[96]
PIL-6	/	60	PIL-6	transparent to blue	t_c 55 s	/	73.1	/	[97]
PFI-BF_4_1.5	/	/	PFI-BF_4_1.5	transparent to green	3.9/1.7	73	460	5×10^4	[45]
UPy-PEGM-VBMI TFSI	3.84×10^{-3}	/	DHHV	colorless to dark blue	5.1/5.3	42.7	443.83	300	[98]

2.2.2. Polyoxyethylene-Based IL-GPEs

Polyethylene oxide polymer is one of the most important polymer matrices in polymer electrolytes. It mainly includes two types of polymers: polyethylene oxide (PEO) and polyethylene glycol (PEG). Polymers with a molecular weight below 20,000 g/mol are referred to as PEG, while those with a molecular weight above 20,000 g/mol are referred to as PEO [99]. Polyethylene oxide polymers are widely used in the preparation of electrolytes for electrochemical devices due to their simple synthesis, low cost, and good processability [100]. These advantages make polyethylene oxide polymers ideal candidates for various electrochemical applications. At the same time, the soft backbone of these polymers endows them with good flexibility, making them promising in providing mechanical stability for flexible electrochromic devices. Some researchers combined IL with polyoxyethylene to carry out related work on ionic conductive layers [83,101–108]. In the next section, we will introduce polyoxyethylene gel polymer electrolytes containing ionic liquids. In an effort to elucidate the key performance characteristics of polyoxyethylene-based IL-GPEs and their associated ECDs, we have systematically collated the pertinent data, which are detailed in Table 4 (located at the conclusion of Section 2.2.2).

1. PEO-based IL-GPEs.

In 2007, Brazier's team developed a PEO-based gel polymer electrolyte, $P(EO)_{10}$LiTFSI + 0.96 PYR_{14}TFSI [101]. Unlike conventional PEO gel electrolytes, it used the ionic liquid PYR14TFSI as a substitute for propylene carbonate (PC). This innovative substitution enhances the performance of the electrolyte, as evidenced by the following ECD application. Based on the P(EO)10LiTFSI + 0.96 PYR_{14}TFSI, the team developed an ECD using WO_3 as the electrochromic material and V_2O_5 as the counter electrode. This ECD had an optical contrast of 40–50% and still exhibits electrochromic ability after 1000 cycles, achieving an optical contrast of 28%. In addition, it is worth noting that this work represents the first application of electrolytes combining lithium salts with ionic liquids in the field of electrochromism. This pioneering work provides important insights and assistance for the preparation and development of ionic liquid-based electrolytes used in the field of ECDs.

In 2010, Desai's team also reported an ionic liquid gel electrolyte (PEO)10LiTFSI: 25% P14TFSI [103] with a similar composition. It was used to assemble complementary electrochromic devices (PEDOT/PPY ECD) based on PEDOT/PPY. The test results show that the PEDOT/PPY ECDs prepared with (PEO)10LiTFSI: 25% P14TFSI (ΔT = 43%) exhibit lower optical contrast than the gel electrolyte (ΔT = 45%) using EC/PC as plasticizers. They believe that this is due to the higher ionic conductivity (1.00×10^{-4} S/cm) of 75% (PEO)8LiTFSI: 25% PC/EC (2.74×10^{-4} S/cm) compared with (PEO)10LiTFSI: 25% P14TFSI. However, the ECD prepared using IL-based electrolytes had excellent cycling stability (after 10^4 cycles ΔT is still 43%). In contrast, PEDOT/PPY ECD based on 75% (PEO)8LiTFSI: 25% PC/EC showed a significant decrease after 10,000 cycles, with ΔT = 37%. This demonstrated the unique advantage of IL as an electrolyte in ECD.

In 2024, Bai et al. reported an ionic gel (VGE) [83] based on divalent viologen cation. In VGE, PEO serves as the polymer matrix, PC as the plasticizer, TiO_2 provides a nearly white background for ECDs, $EtV(TFSI)_2$ serves as the electrolyte salt, and Fc serves as the redox mediator (Figure 23a). Additionally, a V-ECD based on PProDOT-Me_2 as an electrochromic material was prepared using VGE. Compared with LGE using monovalent Li^+ as the transport ion (ΔR = 13.3%), V-ECD prepared based on VGE exhibits higher optical contrast (ΔR = 39.4%). They believe that this is due to the presence of divalent viologen cations (Vio_2^+), which facilitates the insertion and extraction of a greater number of TFSI anions in PProDOT-Me_2 compared with Li^+. In addition, as Vio_2^+ is an electrochromic cation, while PProDOT-Me_2 is bleached, Vio_2^+ could be reduced on the opposite side of the ECD (opposite side of the PProDOT-Me_2 layer), thereby achieving color change on the opposite

side of the ECD (as shown in Figure 23b). In their follow-up, the team prepared a series of EC gels capable of red, blue, and green changes by introducing viologen derivatives capable of different color changes into similar systems [108]. Based on this EC gel, all-in-one ECDs were assembled, which showed good electrochromic performance. These EC gels, with their versatile color-changing capabilities, enable the fabrication of simple displays and laid a foundation for the development of electrochromic e-paper.

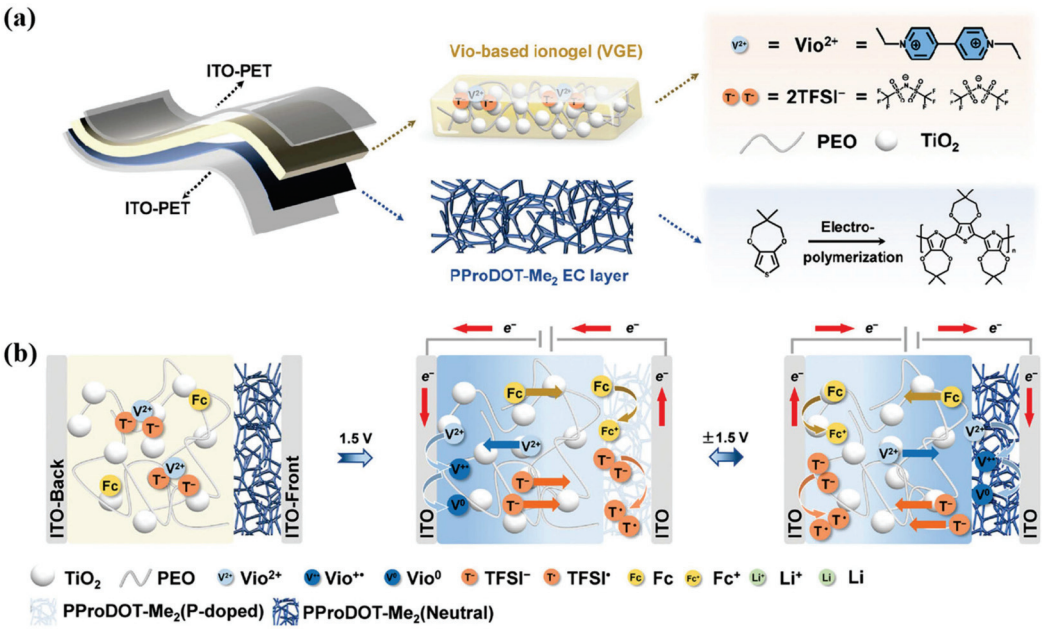

Figure 23. (**a**) Device structure of the VGE-based ECD. (**b**) Schematic diagrams of EC mechanism of the V-ECD at the initial, bleached, and colored states [83].

2. PEG-based IL-GPE.

In 2008, by in situ photocuring, Sun et al. prepared a series of new ionic liquid gel electrolytes based on PEGDA [102]. In addition to the PEGDA monomer and photoinitiator, the formula also contains different amounts of ionic liquid [BMIM][BF_4] or [BMIM][PF_6]. These gel electrolytes were used to produce PEDOT-based, poly [3,6-bis(2-(3,4-vinyldioxy)thiophenyl)-N-methylcarbazole] (PBEDOT-NMCz) complementary ECDs. The researchers found that with the increase in ionic liquid content, ECDs exhibit faster switching times, and the coloring and fading times of all ECDs are around 1 s. This is an early attempt to use PEGDA as a polymer matrix.

Kim et al. prepared three kinds of EC gels through UV curing technology. In these EC gels, PEGDA crosslinked after UV curing was used as the polymer matrix, [EMIM][TFSI] was used as the plasticizer and conductive ion, and dmFc was used as the redox mediator. MHV, DHV, and DHV-DPV composites were used as electrochromic materials to realize magenta, blue, and green EC gels (Figure 24a) [105]. These three EC gels could be directly sandwiched between two ITO-PET films to form an all-in-one flexible ECD. All three ECDs exhibit high transmittance (>90%) and electrochromic stability, showing stable performance over 3600 s of repeated operation. In addition, the researchers prepared multi-color flexible pixelated ECDs using the mask method, which exhibits excellent mechanical stability even after 1000 bending tests at a curvature radius of 10 mm and outstanding electrochemical stability (after 1000 cycles the current response is almost unchanged) (Figure 24b–d). It should be highlighted that this work represents the first report to achieve multi-color changes and image display through direct patterning of EC materials.

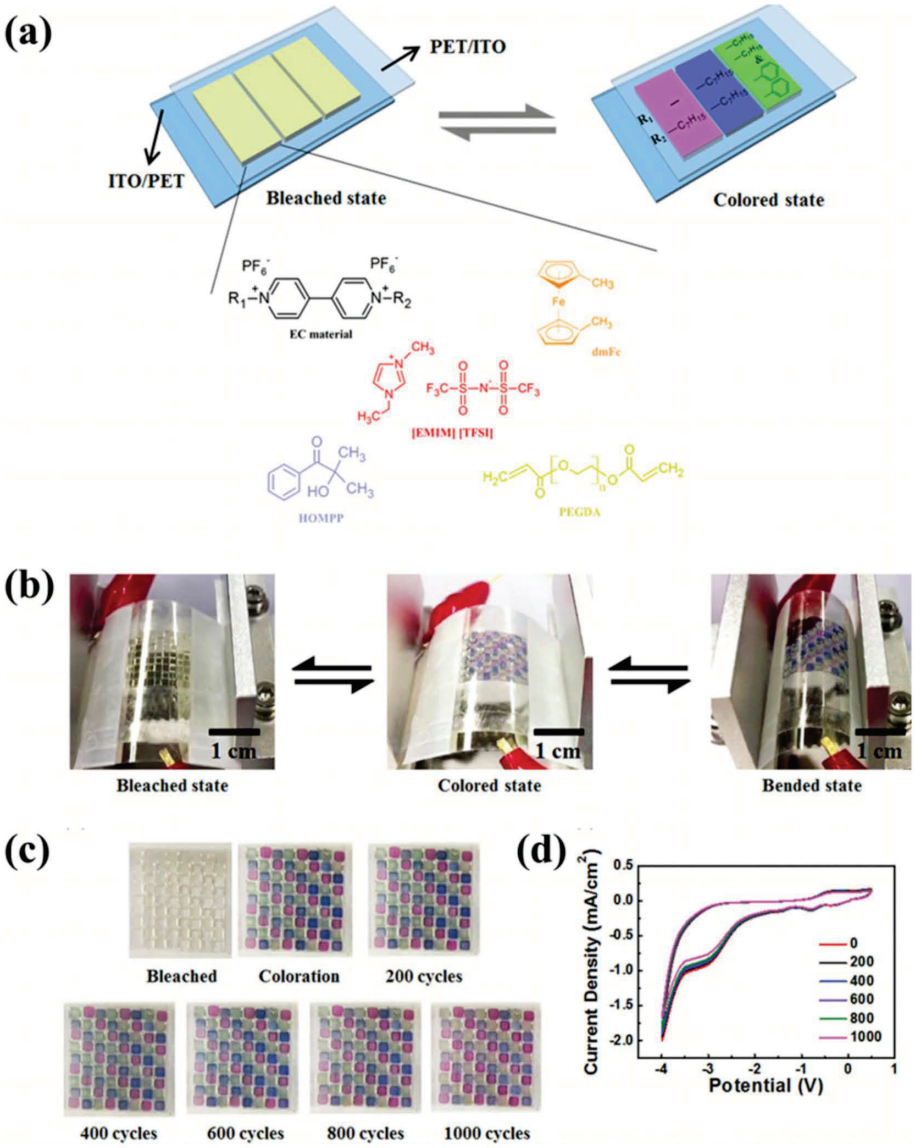

Figure 24. (**a**) Illustration of the chemical structures of the materials forming the EC gels and the basic schematic of an ion gel-based ECD. (**b**) Characteristics of flexible ECDs during dynamic bending tests. (**c**) Camera images and (**d**) CVs of ECDs during the dynamic bending cycles. Camera images in the colored state were captured at −2.5 V [105].

Table 4. The performance of polyoxyethylene-based IL gel polymer electrolytes and ECDs.

Electrolyte Membrane				Performance of ECD						
Electrolyte	Conductivity (S/cm)	Transmittance (%)	Thickness (μm)	ECM	Color Changes	t_b/t_c (s)	ΔT (%)	CE (cm^2/C)	Cycle	Ref.
$P(EO)_{10}LiTFSI$ + 0.96 $PYR_{14}TFSI$	1.1×10^{-4}	/	/	WO_3	/	/	40–50	/	10^3	[101]
$(PEO)_{10}LiTFSI$: 25% $P_{14}TFSI$	1.0×10^{-4}	90%	80	PEDOT PPY	/	1.1/4.0	43	/	10^4	[103]
VGE	4.27×10^{-3}	/	200	PProDOT-Me	light blue to dark blue	3.3/2.9	ΔR = 39.4%	76.2	2000	[83]
PEDGA(40%)/ [BMIM][BF_4] (60%)	$3.78\sim9.49 \times 10^{-3}$	/	/	PEDOT PBEDOT-NMCz	deep blue to yellow transparent	0.4/0.5	/	/	/	[102]
PEGDA/ [EMIM][TFSI]	/	/	60	MHV DHV DHV-DPV	Transparent to magenta, to blue, and to green	31/19 (magenta), 34/20 (blue), 21/39 (green)	/	80.7 (magenta), 81.3 (blue), 54.6 (green)	/	[105]

2.2.3. Polyvinylidene Fluoride-Based IL-GPEs

Polyvinylidene fluoride (PVDF) is a common polymer matrix for gel polymer electrolytes. It is easy to process and possesses good mechanical properties, a high dielectric constant, hydrophobicity, and thermal and chemical stability, making it suitable for the processing and manufacturing of electrolytes [84]. However, due to the high crystallinity of pure PVDF, copolymers with lower crystallinity, such as poly(vinylidene fluoride-co-hexafluoropropylene) (PVDF-HFP) and poly(vinylidene fluoride-trifluoroethylene) (PVDF-TrFE), have been applied in the preparation of electrochemical devices [32,109]. The amorphous regions are beneficial for retaining liquid electrolytes, and the crystalline regions help to maintain mechanical properties and improve the overall performance of polymer electrolytes. Currently, polyvinylidene fluoride-based ionic liquid gel polymer electrolytes have been widely used in the field of electrochromism, and their applications will be discussed below. To elucidate the key performance characteristics of polyvinylidene fluoride-based IL-GPEs and their associated ECDs, we have systematically collated the pertinent data, which are detailed in Tables 5 and 6 (located at the conclusion of Section 2.2.3).

Electrospinning technology is simple to operate and easy to prepare, and it can effectively combine with different components. This technology can efficiently synthesize composite nanofibers that are thin, highly porous, and flexible. It is a universal and powerful method for preparing one-dimensional nanofibers [110]. The high porosity and thinness of these nanofibers are beneficial for the polymer matrix to absorb electrolytes and transport ions. Therefore, this technology had been widely applied in the preparation of electrolytes.

In 2011, Lu et al. first reported a gel polymer electrolyte using a PVDF-HFP electrospun membrane as the polymer matrix and ionic liquid [BMIM][TFSI] as the plasticizer and electrolyte salt [111]. The thickness of the electrospun film was 33 μm. The ionic conductivity of this gel electrolyte, based on the electrospun membrane, remained essentially unchanged after two days of heat treatment at 60 °C (1.13×10^{-3} S/cm after annealing), and the transmittance was greater than 80%. This demonstrated the excellent thermal stability of the gel polymer electrolyte based on the PVDF-HFP electrospun membrane and ionic liquid. The structure of the complementary electrochromic device prepared by the team using PANI and poly(3,4-ethylenedioxythiophene)-poly(4-styrenesulfonic acid) (PEDOT: PSS) (as shown in Figure 25). Under a constant applied potential of ±1.4 V, the device could switch well between the reduced state (yellow-green) and the oxidized state (blue), with a maximum absorbance change of $\Delta A = 0.242$ (at 695 nm). Later, the team carried out extensive related work on the preparation of ionic liquid gel polymer electrolytes based on PVDF-HFP electrospinning membranes. By adjusting the thickness of the electrolyte membrane [112], introducing inorganic fillers [113,114], and incorporating proton conduction [115], the ionic conductivity of the electrolyte was improved, thereby enhancing the performance of ECDs based on PANI-TiO_2 (as shown in Table 5: properties of IL-GPE and ECD based on polyvinylidene fluoride electrospinning membrane).

In addition, ionic liquid gel electrolyte based on PVDF can also be made into EC gel to realize an all-in-one electrochromic device. In 2016, Moon et al. prepared three kinds of EC gels based on PVDF-HFP [116]. In these EC gels, PVDF-HFP was used as the polymer matrix, [EMI][TFSI] was used as the electrolyte salt and plasticizer, and HV$[TFSI]_2$, CN-PV$[TFSI]_2$, and CF_3-PV$[TFSI]_2$ were used as EC materials to realize blue, green, and red, respectively (as shown in Figure 26a). The three EC gels are, respectively, made into three all-in-one ECDs. All three types of ECDs exhibited excellent optical contrast ($\Delta T = 95\%$), high coloring efficiency (blue 78 cm^2/C, green 155 cm^2/C, and red 81 cm^2/C), and fast coloring time (blue 11 s, green 18 s, and red 40 s). Furthermore, it is important to note that compared with other ultra-low power displays, such as cholesterol LCD displays with 1 mW/cm^2,

this ECD had extremely low energy consumption (90 μW/cm^2 for blue, 4 μW/cm^2 for green, and 32 μW/cm^2 for red). Finally, the researchers also demonstrated the patterned multi-color flexible ECD prepared with EC gels, which could be electrochromic in the bending state (as shown in Figure 26b). In their follow-up, the team achieved voltage adjustable flexible multi-color ECDs by mixing MHV^+ and DHV_2^+ on this basis [117].

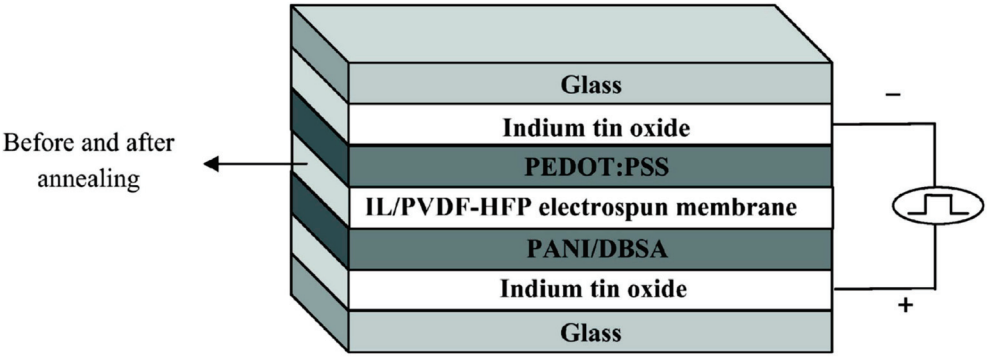

Figure 25. Configuration of the complementary electrochromic devices using the IL/PVDF-HFP electrospun membrane as the electrolyte layer [111].

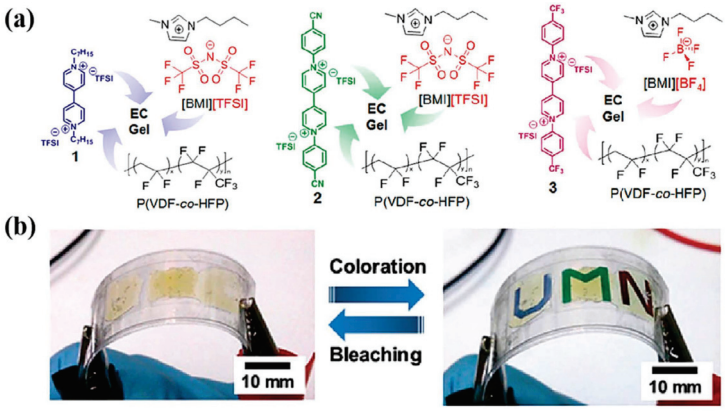

Figure 26. (**a**) Composition diagram of blue, green, and red electrochromic gels (dmFc is not shown). (**b**) Photographs of bleached (at 0.00 V) and colored (at −0.70 V) flexible ECDs with bending [116].

In order to obtain PVDF-based gel electrolytes with stronger mechanical strength, in 2022, Zhang's team prepared a series of high-strength ionic liquid polymer composite electrolytes by introducing glass fibers (GFs) and epoxy resin into PVDF-HFP [118]. In this composite electrolyte, PVDF-HFP was used as the polymer matrix, 1 M LiTFSI/[BMIM][TFSI] solution was used as the electrolyte solution, modified glass fiber KH550-GFs enhance the mechanical properties of the polymer electrolyte, and epoxy resin E-51 was used to improve the interfacial compatibility between GFs and PVDF-HFP (as shown in Figure 27). They studied the transmission spectra, ionic conductivity, and tensile stress–strain of polymer electrolytes made from PVDF-HFP, GFs, and E-51 resins at different ratios. Finally, considering the comprehensive performance of the above aspects, a polymer electrolyte with a PVDF-HFP/E-51 resin mass ratio of 3:1 was used for subsequent assembly and testing. The ECD was assembled with PPRODOT as the working electrode and PPRODOT-BisEDOT as the counter electrode and exhibits a very quick switching speed (t_b = 0.5 s, t_c = 1.2 s), high coloring efficiency (453 cm^2/C), and ultra-high electro-chromic stability (with almost no change in optical contrast after 18,000 cycles). In addition, the team also developed a substrate-free ECD based on PPRODOT. This substrate-free ECD exhibits significant color changes, and even after 10,000 compression bending cycles, T_{rec}/T_{neu} only undergoes a slight change of about 3% (T_{rec} represents the transmittance of ECD in the recolored state,

and Tneu represents the transmittance of ECD in the initial neutral state at a wavelength of 638 nm).

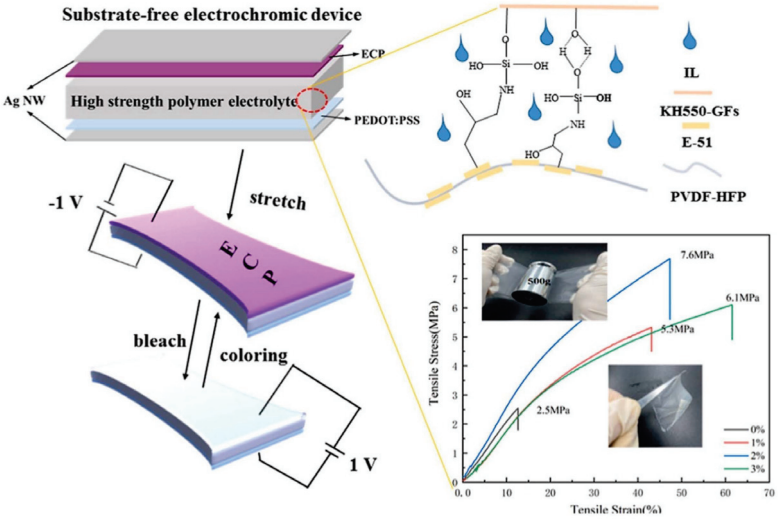

Figure 27. Schematic diagram of ECD using high strength ionic liquid polymer composite electrolyte [118].

Table 5. Properties of IL-GPE and ECD based on polyvinylidene fluoride electrospinning membrane.

Name of Electrospinning Membrane	Thickness (μm)	EC Materials	Conductivity (S/cm)	Tensile Strength (MPa)	Optical Contrast	t_c/t_b (s)	Ref.
PVDF-HFP $SCCO_2$	33	PANI/DBSA	1.1×10^{-3}	6.5 ± 0.4	$\Delta A = 0.23$	/	[111]
P(VDF-HFP)/DAP	2	PANI/DBSA	2.6×10^{-3}	11.4 ± 0.5	$\Delta A = 0.53$	/	[112]
PVDF-co-HFP/POSS-OH	/	PANI-TiO_2	5.2×10^{-3}	/	$\Delta T = 71.9\%$	2.0/2.3	[70]
SiO_2-on-P(VDF–HFP)	/	PANI-TiO_2	8.6×10^{-3}	/	$\Delta T = 72\%$	/	[71]
sulfonic acid-grafted P(VDF-HFP)	/	PANI-TiO_2	6.7×10^{-3}	/	$\Delta T = 56\%$	2.0/2.5	[115]

Table 6. Properties of IL-GPE and ECD based on polyvinylidene fluoride.

Electrolyte Membrane				Performance of ECD						
Electrolyte	Conductivity (S/cm)	Transmittance (%)	Thickness (μm)	ECM	Color Changes	t_b/t_c (s)	ΔT(%)	CE (cm^2/C)	Cycles	Ref.
PVDF/EC-gel	10^{-4}~10^{-3}	/	60	HV[TFSI]$_2$ CN-PV[TFSI]$_2$ CF_3-PV[TFSI]$_2$	yellow to blue, green, and red	11/280 (blue) 18/300 (green) 40/180 (red)	>95%	78 (blue) 155 (green) 81 (red)	10^3	[116]
PVDF-HFP/GFs/E-51	1.75×10^{-5}	80	40	PPRODOT	blue to puple	1.2/0.5	40	451	18,000	[118]

2.2.4. Polyacrylate-Based IL-GPEs

Polyacrylate-based polymers attracted the attention of many researchers in the field of electrochromism due to their transparency and excellent adhesion. In addition, electrolyte systems based on polyacrylate can be polymerized in situ using corresponding acrylic monomers, which can greatly improve the interface contact between EC electrodes and electrolytes. Such promising properties of polyacrylate-based systems led to significant advancements in electrochromic application. At present, some researchers combined IL with polyacrylic esters to carry out related work on electrolytes [33,119–127]. In the following section, the application of gel polymer electrolytes, which contain ionic liquids and are based on polyacrylate polymers, in the field of electrochromism will be discussed. To explain the key performance characteristics of polyacrylate-based IL-GPEs and their associated ECDs, we have summarized the relevant data, which are detailed in Table 7 (located at the conclusion of Section 2.2.4).

In 2017, Wang's team prepared a new poly(methyl methacrylate)(PMMA)-based ionic liquid gel electrolyte (PMMA–[Emim] BF_4) [33] by mixing ionic liquid [EMIM][BF_4] with a system of PMMA and Li+. PMMA serves as the polymer matrix, with PC acting as the plasticizer and $LiClO_4$ along with [EMIM][BF_4] serving as electrolyte salts in the overall system. PMMA–[Emim] BF_4 was applied in ECD using WO_3 as the electrochromic material. Compared with the ECD using PMMA gel electrolyte without ionic liquid (ΔT = 61%, t_b = 61.4 s, CE = 33.5 cm^2/C, and bleaching voltage 2 V), ECD based on PMMA–[Emim] BF_4 composite electrolyte shows higher optical contrast (ΔT = 71%) (as shown in Figure 28a,b), shorter bleaching time (t_b = 41.2 s), lower bleaching voltage (1.5 V), and higher coloring efficiency (55.3 cm^2/C). The author believes that this improvement is attributed to the higher conductivity (2.9×10^{-3} S/cm) of the PMMA–[Emim] BF_4 composite electrolyte compared with the PMMA gel electrolyte (1.7×10^{-3} S/cm).

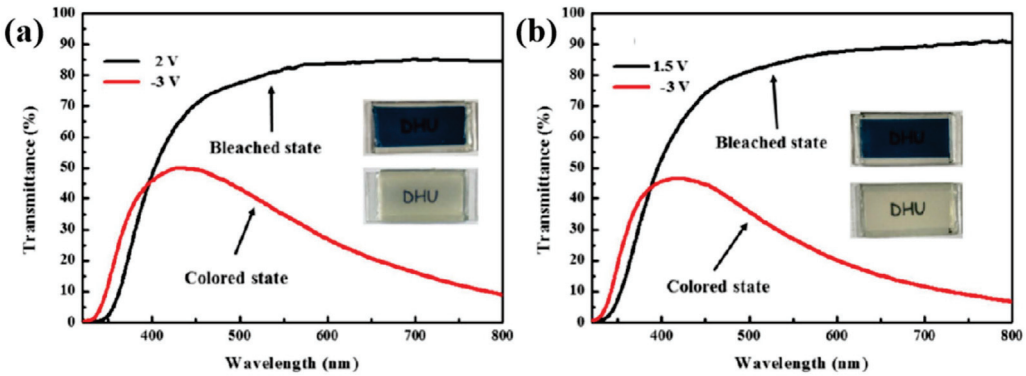

Figure 28. UV–vis transmittance spectra of ECDs with (**a**) PMMA-based electrolyte and (**b**) PMMA–[Emim]BF_4 composite electrolyte measured at −3 V/2 V and −3 V/1.5 V, respectively. Insets show digital photographs of ECDs [33].

The biggest advantage of polyacrylate-based gel electrolytes is that they can be synthesized by photo or thermal initiation in situ polymerization, which can not only reduce the preparation difficulty of gel electrolytes, but also makes good contact between the electrode and electrolyte interface. There have been previous studies [119,120] on the preparation of electrochromic gels containing ionic liquids through photoinduced in situ polymerization. However, no study had been conducted on the effect of in situ polymerization of gel polymer electrolytes containing ILs on the performance of ECDs. Given the potential benefits of in situ polymerization for electrochromic applications, further exploration was essential, as demonstrated by the following study. In 2012, Deepa et al. [128] prepared polyacrylate-based ionic liquid gels with polymer electrolytes in two ways. One is to inject the MMA monomer containing ionic liquid into ECDs for thermal initiation in situ polymerization (Figure 29a), and the other is to directly inject the prepared PMMA ionic liquid gel electrolyte into ECDs (Figure 29b). The author used PEDOT and WO_3 as EC materials, with PB as the counter electrode, to prepare four ECDs using the two methods mentioned above: WO_3-PB (MMA) and PEDOT-PB (MMA) were prepared by injecting the MMA monomer containing ionic liquid into ECD for thermal initiation in situ polymerization, while WO_3-PB (PMMA) and PEDOT-PB (PMMA) were prepared by directly injecting the prepared PMMA ionic liquid gel electrolyte into ECD. The test results show that WO_3-PB (MMA), prepared using in situ polymerized polyelectrolyte (Δ Amax = 0.79 a.u., CE = 119 cm^2/C), shows about four times the absorbance change and twice the coloration efficiency compared with WO_3-PB (PMMA) directly injected into gel electrolyte (ΔAmax = 0.2 a.u., CE = 54 cm^2/C). Researchers also found that when PEDOT-PB (MMA) and PEDOT-PB (PMMA) (at −1.5 V) have similar coloring efficiencies, PEDOT-PB (MMA) requires a smaller driving voltage (−0.7 V). In addition, the author also reported the charge transfer resistance of PEDOT-PB ECDs, with

the test results showing that the charge transfer resistance of PEDOT-PB (MMA) was 11.5 Ω, while that of PEDOT-PB (PMMA) was 32 Ω. It is believed that the electrolyte polymerized in situ has lower viscosity before polymerization, allowing it to better penetrate into the EC electrode, form better interface contact, and thus reduce charge transfer resistance.

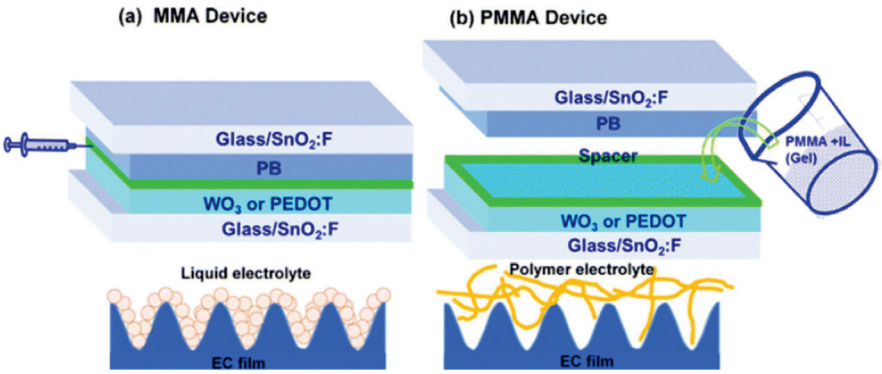

Figure 29. Schematics of the protocols used for device fabrication in (**a**) MMA and (**b**) PMMA-based devices and the corresponding electrode–electrolyte interface in each case [128].

In 2020, Hong's team used different proportions of styrene (Sty) and butyl acrylate (BA) to copolymerize a series of poly(styrene-ran-butyl acrylate) copolymers (PS-r-PBAs) [121] through RAFT polymerization. A series of ionic gels was prepared with [BMI][TFSI] as a plasticizer and electrolyte salt (Figure 30a). For the comprehensive consideration of transparency, mechanical properties, and conductivity, the ionic gel containing 60 wt% [BMI][TFSI] and 40 wt% of a specific copolymer (53-PS-r-PBA-H) was applied to the preparation of EC gel (shown as Figure 30b,c). In addition to the above ionic gel components, ethyl viologen (EV^{2+}) and dimethyl ferrocene (dmFc) were added to EC gel as electrochromic materials and redox mediators, respectively. The resulting EC gel was then utilized to fabricate a flexible integrated ECD, which demonstrated remarkable performance characteristics. The flexible integrated ECD based on EC gel exhibits high optical contrast (ΔT = 90.1%), switching time (t_c = 50 s, t_b = 87 s), and high coloring efficiency of 120.8 cm^2/C. After 1500 cycles, the ΔT retention rate of the flexible ECD was 71.7%, indicating that the EC gel had electrochromic cycle stability. Finally, the author also made a smart window with dot-like EC gel lattice patterns. Because the appearance and disappearance of the dot patterns could be adjusted as needed, this ECD smart window could also be used for bird anti-collision, as the author suggests (Figure 30d).

In 2021, Hong's team prepared a series of ternary gel electrolytes [124] (TGE-0, TGE-20, and TGE-45) composed of copolymer PS-r-PBAs, [EMI][TFSI], and PC (Figure 31a). Among them, TGE-45, which contains 45% PC and [EMI][TFSI] by mass, exhibited the best ion conductivity (5.84×10^{-3} S/cm), while TGE-0 (serves as the control group) without PC showed the lowest ion conductivity (2.40×10^{-3} S/cm). Therefore, both TGE-0 and TGE-45 were used for further research on all-in-one ECDs. In these ECDs, ethyl viologen (EtV^{2+}) and dmFc were used as electrochromic materials and redox mediators, respectively, while [EMI][TFSI] played an ion conducting role. The research results indicate that compared with the ECD based on TGE-0 (t_b = 106 s, t_c = 65 s), the ECD based on TGE-45 exhibits shorter switching times (t_b = 24 s, t_c = 8.4 s) (Figure 31b). It is believed that this is because the ternary mixture reduces the overall viscosity of the electrolyte, which is more conducive to the diffusion of EtV2+ ($D_{EtV2+} = 1.5 \times 10^{-11}$ cm^2/s in TGE-0, $D_{EtV2+} = 1.38 \times 10^{-10}$ cm^2/s in TGE-45). In addition, the ECD based on TGE-45 demonstrated high cycling stability, with a ΔT retention ratio of 84% after 2000 cycles.

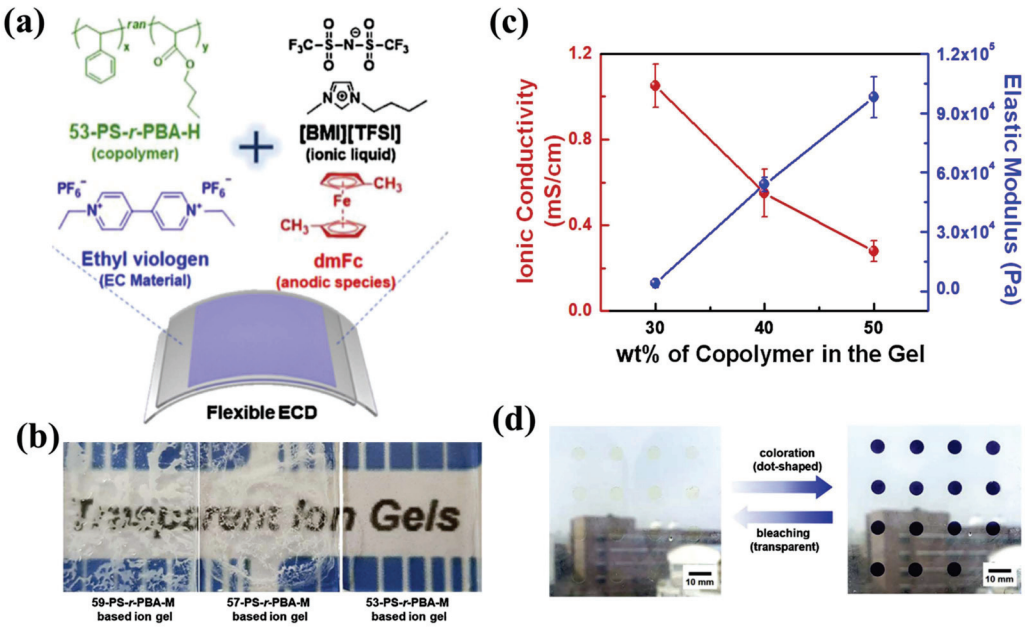

Figure 30. (**a**) Molecular structures of EC gel components. (**b**) Photographs of ion gels based on three PS-r-PBAs having similar molecular weights: 59-PS-r-PBA-M, 57-PS-r-PBA-M, and 53-PS-r-PBA-M, in which 60 wt% of [BMI][TFSI] was included in the gels. (**c**) Plots of ionic conductivity and elastic modulus as a function of wt% of copolymer gelators. All experiments were conducted at 25 °C. (**d**) photographs of coloration/bleaching states of EC smart windows involving dot-shaped EC gel arrays [121].

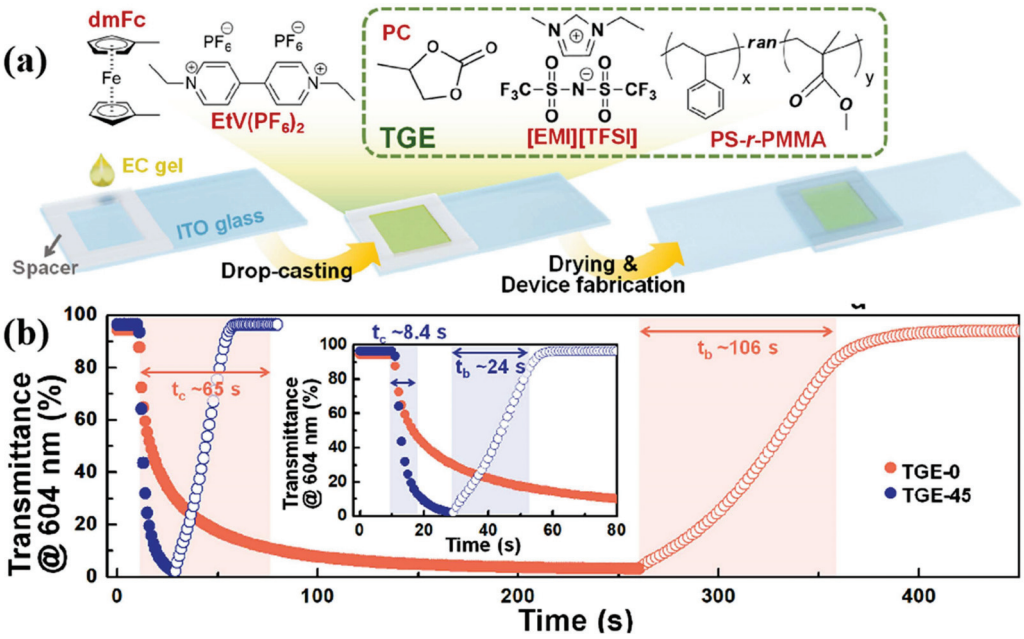

Figure 31. (**a**) Schematic of the fabrication process of ternary gel electrolyte (TGE)-based electrochromic supercapacitors (ECSs) and molecular structures included in the gel. (**b**) Transient transmittance profiles of TGE-0 and TGE-45 ECSs during coloration at +0.9 V and bleaching under a short-circuit condition (i.e., at 0.0 V) [124].

Additionally, the development of polyacrylate-based electrolytes is also trending towards functionalization. In 2021, Chen et al. prepared a self-healing ionic liquid gel polymer electrolyte (GPE-IL) [123] based on polyacrylate through in situ thermal initiation polymerization (Figure 32a). In this electrolyte, the ion crosslinked polymer network is formed by copolymerization of methyl methacrylate (MMA), acrylic acid (AA), and 2-diethylaminoethyl methacrylate (DEA), with ionic liquid [Emim][TFSI] serving as plasti-

cizer and LiTFSI as electrolyte salt. Due to the presence of the ionic liquid, the gel electrolyte exhibits a high ionic conductivity of 3.29×10^{-3} S/cm. A WO_3-based ECD was prepared using the IL-GPE, which exhibited an optical contrast of 49.9%, a coloring efficiency of 96.2 cm^2/C, and a fast switching speed with t_b = 4 s and t_c = 7 s. These outstanding properties of the IL-GPE electrolyte not only enhance the performance of the ECD, but also contribute to its unique self-healing capability, as detailed below. Within the cross-linked polymer networks, due to the electrostatic interaction between $-COO^-$ and $-N^+(CH_3CH_2)_2$, when GPE-IL is cut and the pieces are placed together again, the network could reconnect to form ionic bonds through electrostatic attraction, thereby exhibiting a self-healing capability (Figure 32b). After self-healing, it could retain 80% of its original tensile strength.

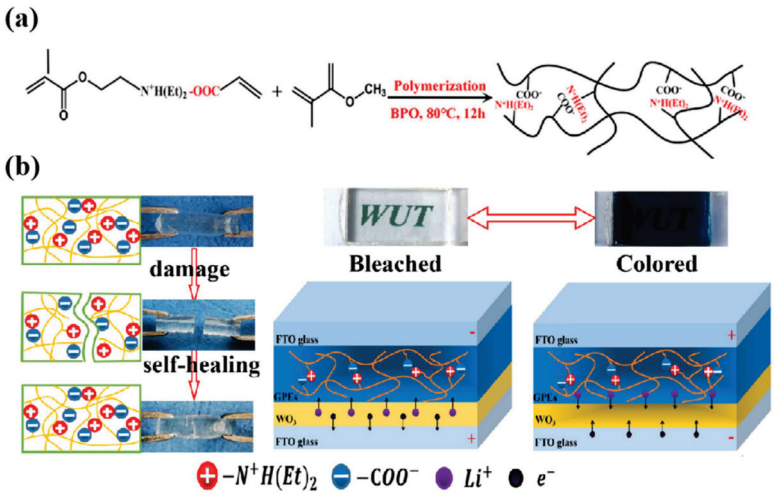

Figure 32. (**a**) Synthesis process of an ionic liquid-based ionically cross-linked gel polymer electrolyte (GPE-ILs). (**b**) Self-healing mechanism of GPE-ILS and schematic diagram of electrochromic device [123].

In 2023, He et al. prepared a series of double-network IL-GPE based on polyacrylate ethyl ester for sensing applications [126]. The double-network polymer matrix in the ionic gel was prepared through a two-step process involving photoinitiated polymerization. First, the single network film was prepared using EA monomer and ethylene glycol dimethacrylate (EGDMA) as a crosslinker (Figure 33a). Subsequently, the second network was formed by swelling the initial film and then conducting photoinitiated polymerization. In addition to the polymer matrix, the ionic gel also contains the ionic liquid [EMIM][TFSI] as both a conductive medium and a plasticizer, as well as viologen derivatives for electrochromism and electrofluorescence. In this work, three kinds of ionic gels made of three viologen derivatives, [MV][TFSI], [MTV][TFSI], and [ImTV][TFSI], were prepared. Compared with the other two ionic gels, the ionic gel based on [ImTV][TFSI] shows the best adhesion to the substrate and the shortest coloring time, making it suitable for subsequent tests (Figure 33b,c). The ECD based on [ImTV][TFSI] demonstrated excellent long-term cycling performance, with a ΔT retention rate of 93% after 500 cycles (Figure 33d). Moreover, owing to the nonvolatile nature of the ionic liquid, the ionic gel exhibits robust environmental stability. After two years of storage in air, it maintains stable operation, with a ΔT retention rate of 88% for 500 cycles (Figure 33e). Additionally, the authors further developed a stretchable ECD. With the increase in ionic gel strain levels, the conductivity of the ionic gel shows a downward trend, which weakens the EC and EFC performance of the ECD. At strain levels exceeding 300%, the ionic gel cannot accommodate the EC/EFC phenomenon, thereby reducing the device's EFC and EC effects (Figure 33f,g). This advanced ionic gel, with its exceptional sensitivity and stability, is highly promising for integration into

visible light strain sensors, offering potential benefits in fields such as smart textiles and health monitoring.

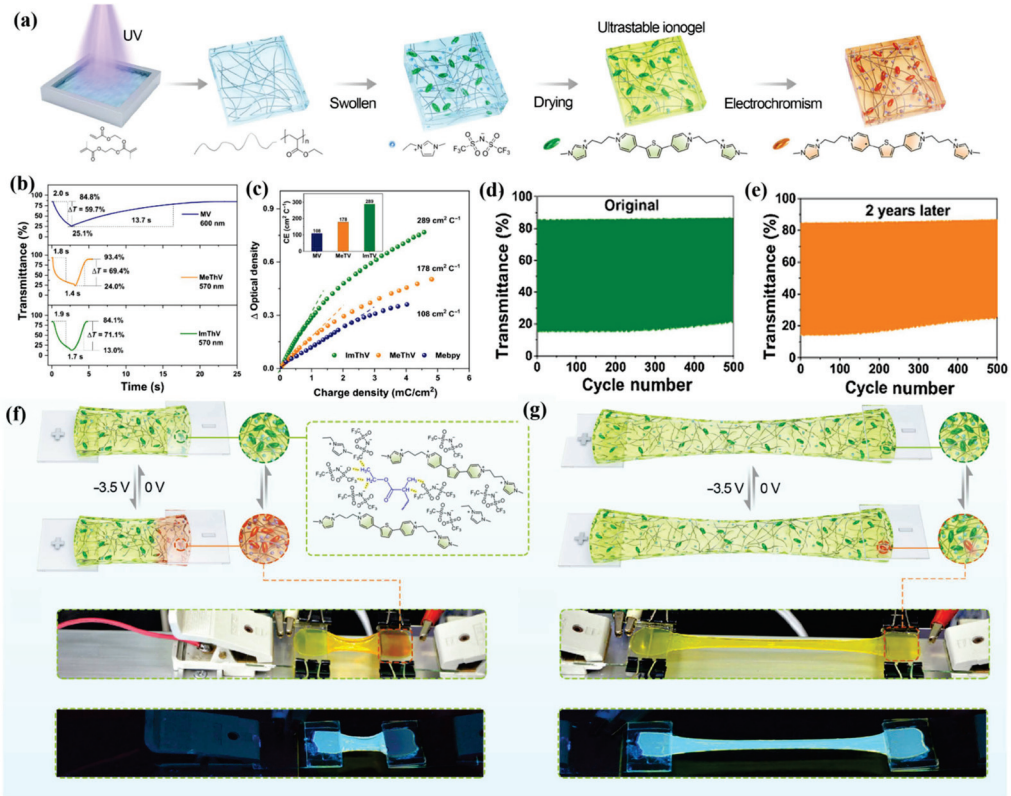

Figure 33. (**a**) Schematic illustration of the fabrication procedure of the ionogel. (**b**) Coloration and bleaching time of [MV][TFSI], [MTV][TFSI], and [ImTV][TFSI]-containing ionogels-based ECDs. (**c**) Plots of the optical density versus charge density and the slope as coloration efficiency (η) for ECDs with EC gel under −3.5 V. (**d**) Freshly made ionogels and (**e**) ionogels stored in ambient atmosphere for 2 years. Illustration and digital pictures of EC properties of stretchable ionogel-based ECD at relaxed (**f**) and stretched state (**g**) [126].

In 2024, Zhang's team developed a lower critical solution temperature (LCST) ionic gel based on butyl polyacrylate(PBA) [3]. The PBA ionic gel was prepared by in situ UV polymerization of butyl acrylate (BA) and N,N′-methylenebisacrylamide (MBAA) in ionic liquid [EMIM][TFSI] (Figure 34b). An 'all-in-one' smart window was prepared using PEDOT as an electrochromic material and the PBA ionic gel as an electrolyte. In this system, the PBA gel serves the functions of thermochromism and self-powering. The ionic liquid could convert heat energy into electric energy due to its Soret effect [129], thus endowing the 'all-in-one' smart window with self-power generation capability. These properties of the PBA ionic gel enable the realization of multiple functionalities in the smart window (Figure 34a). The thermal response temperature range of this smart window is 28–35 °C, and it exhibits significant optical modulation capability, with the visible light transmittance (T_{vis}) dropping to 7.5% at 35 °C, effectively blocking visible light (Figure 34c). In terms of electrochromic performance, the smart window achieves an optical contrast of 21%, featuring a coloring time of 7 s and a fading time of 6.8 s. After 100 CV cycles, the smart window demonstrated stable electrochemical performance, with no significant changes in current. This work provides valuable insights and an effective approach for designing multifunctional, intelligent electrochromic smart windows, which hold great promise for reducing building energy consumption and enhancing occupant comfort.

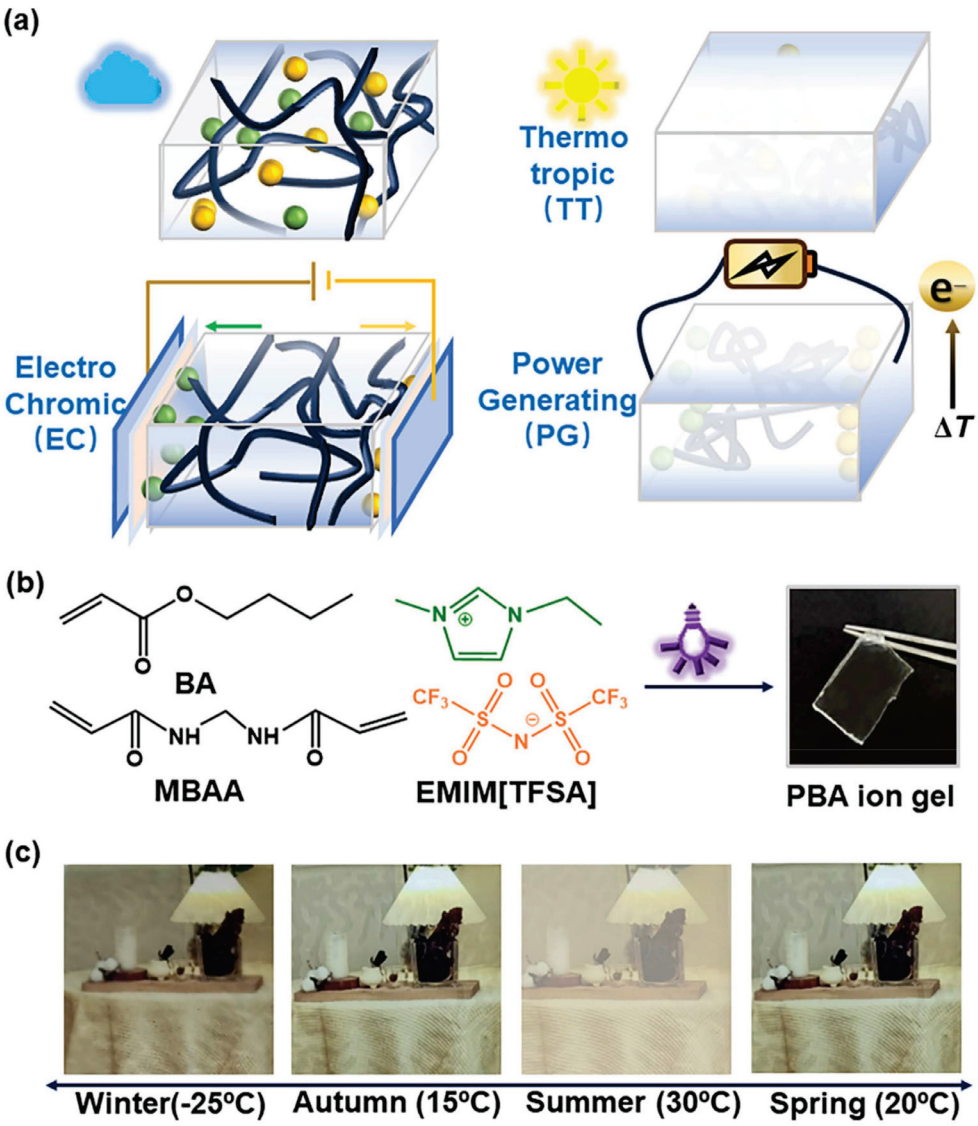

Figure 34. (**a**) An illustration of "all-in-one" smart windows with TT, EC, and PG functions; (**b**) chemical structures of each component to prepare the transparent PBA ion gel via in situ UV polymerization; and (**c**) light transmittance changes in the PBA ion gel-based smart windows at typical temperatures in each season [3].

Table 7. Performance of polyacrylate-based IL-GPEs and ECDs.

Electrolyte Membrane			Performance of ECD						
Electrolyte	Conductivity (S/cm)	Thickness (μm)	ECM	Color Changes	t_b/t_c (s)	ΔT (%)	CE (cm^2/C)	Cycling Stability	Ref.
PMMA/ $LiClO_4$/ $[Emim]BF_4$	2.9×10^{-3}	50	WO_3	/	41.2/61.4	61	55.3	1500 cycles ΔT retention ratio is 71.7%	[33]
MMA (IL-GPE)	1.6×10^{-4}	/	WO_3	/	1.7/2.1	0.79 a.u.	119 (at 550 nm)	/	[128]
PS-r-PBAs/ [BMI][TFSI]	5.5×10^{-4}	88	EV	Yellow to purple	50/87	90.1	120.8	1500 cycles ΔT retention ratio is 71.7%	[121]
TGE-45	5.84×10^{-3}	88	$EtV[PF_6]_2$	Colorless to dark blue	24 s and 8.4 s	94	116.1	2000 cycles ΔT retention ratio is 84%	[124]
P(MMA-AA-DEA)-IL	3.29×10^{-3}	/	WO_3	Colorless to blue	4 s and 7 s	49.9	96.2	200 cycles ΔT retention ratio is 70%	[123]
PEA-Ionogel	9×10^{-4}	1000	[ImTV][TFSI]	light yellow to maroon	1.7 s and 1.7 s	71.7	289	500 cycles ΔT retention ratio is 93%	[126]
LCST-Ionogel	2×10^{-4} to 3×10^{-4}	/	PEDOT	pale blue to dark blue	6.8/7	21.6	/	100 cycles ΔT retention ratio is unknown	[3]

2.2.5. Natural Polymer-Based IL-GPEs

In the research on IL-GPE, in addition to the above common polymer matrix materials, some natural polymer matrix materials have also been used in electrolytes for environmental protection, cost, and other considerations [87–91]. Driven by these considerations, researchers also explored various natural polymer-based IL-GPE for ECDs, pushing forward green and sustainable development in the field.

In 2022, Alves et al. used the natural polymer gellan gum as the matrix material to develop a new type of IL-GPE (Figure 35) [89]. The chain structure of gellan gum contains a large number of -COOH and -OH groups that easily form complexes with the selected electrolyte salt, thereby facilitating the dissociation of the electrolyte salt and enhancing ion conductivity. In this gel electrolyte, the ionic liquid 1-ethyl-3-methylimidazolium thiocyanate ([Emim][SCN]) and glycerol act as plasticizers, thereby reducing the crystallinity of gellan gum and enhancing conductivity. At 30 °C, the ion conductivity of this environmentally friendly IL-GPE reaches 6.0×10^{-3} S/cm. The optical contrast of the ECD prepared by PEDOT: PSS as the working electrode is 30.1% ± 0.1%. Subsequently, the research group reported on agar [90] and carrageenan [91] as polymer matrices to prepare IL-GPE. These works offer promising new avenues for the preparation of high-performance and environmentally friendly ECDs.

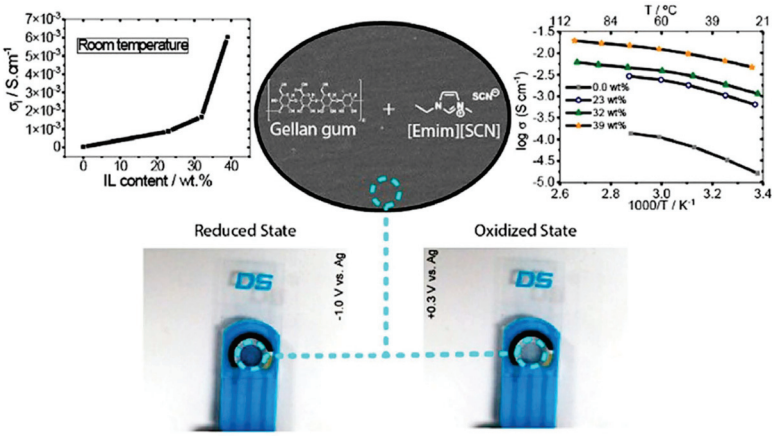

Figure 35. Conductivity of gelled polymer electrolyte containing ionic liquid based on gellan gel and its application in electrochromic devices (The blue circles at the bottom of the figure indicate the location of the electrolyte in the electrochromic device) [89].

2.2.6. Other Polymer-Based IL-GPEs

In addition to the above-mentioned types of polymer electrolytes that have been widely reported, there are also other polymer matrices that have been made into IL-GPE for application in the field of electrochromic technology, such as PU, PVC, PAM, etc., [85,86,130–133] demonstrating excellent performance. The applications of these materials in ECDs will be elucidated in the following discussion. To clarify the key performance characteristics of these IL-GPEs and their associated ECDs, we have sorted the pertinent data, which are detailed in Table 8 (located at the conclusion of Section 2.2.6).

Gao et al. prepared a series of hydrogel polymer electrolytes containing ionic liquids, denoted as BMII-$ZnSO_4$-PAM [85], and based on PAM with varying BMI contents (0.1 M, 0.3 M, and 0.5 M, respectively). The gel electrolyte was used as an ion conduction layer in a new type of electrochromic battery, namely a zinc polyaniline/iodide electrochromic battery (ZPIECB). In the gel polymer electrolyte, cross-linked polyacrylamide serves as the polymer matrix, $ZnSO_4$ functions as the inorganic electrolytic salt, ionic liquid BMII acts as the organic electrolyte salt, and water serves both as the solvent for the electrolyte salts and as a plasticizer for the gel electrolyte. Considering both the conductivity (3.32×10^{-2} S/cm)

and transparency of the electrolyte, the gel electrolyte 0.3 M BMII-1.5 M $ZnSO_4^-$-PAM, with a BMII content of 0.3 M, was selected for the preparation and testing of ZPIECBs (Figure 36a). The test results show that, in terms of electrochromic performance, ZPIECBs could achieve multi-color changes from light blue (transparent) to green (transparent) to brown (opaque) over a voltage range of 0.3 V to 1.45 V, with a transmittance change (ΔT) of approximately 67.54% at 500 nm. In addition, regarding battery performance, the ZPIECB based on BMII-$ZnSO_4$-PAM electrolyte demonstrated superior energy density and coulomb efficiency (1020 μWh/cm^2, 98.9%) compared with those prepared using the KI-$ZnSO_4$-PAM polymer gel electrolyte (182 μWh/cm^2, 73.2%), which does not contain BMI. This is attributed to the fact that the BMI^+ ions in BMII could effectively combine with I_3^+ to form liquid $BMII_3^+$ (Figure 36b), which not only suppresses the diffusion of I^{3-}, but also converts the solid–solid interface between the electrodes into a solid–liquid interface, thereby effectively facilitating interfacial charge transfer and consequently enhancing the electrochemical performance of the battery, resulting in high Coulombic efficiency and rapid reaction kinetics.

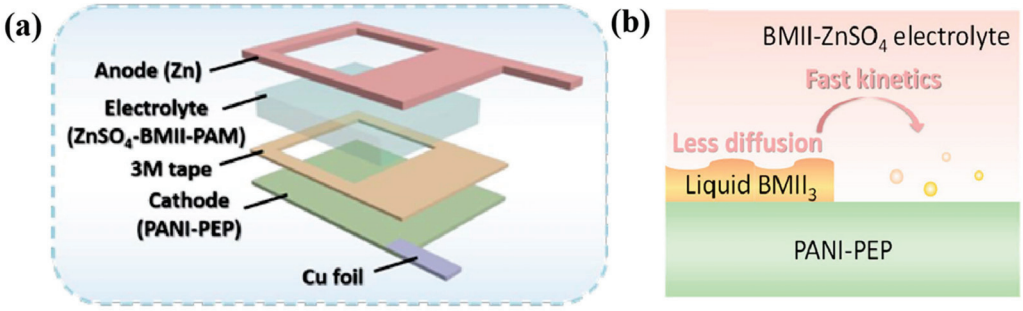

Figure 36. (**a**) Structure diagram of ZPIECBs. (**b**) Schematic of the redox reaction in systems of PANI–PEP/BMII–$ZnSO_4$ [85].

Kim et al. prepared a series of IL-GPEs based on TPU (5i TPU, 10i TPU, 20i TPU, 40i TPU, and 60i TPU) [132]. Ionic liquid [EMIM][TFSI] was used as a plasticizer and electrolyte salt, while TPU was used as a polymer matrix to bind the ionic liquid and provide mechanical properties. Considering the transmittance (93.4%), ionic conductivity (5.4×10^{-5} S/cm), and mechanical properties (Young's modulus 13.4 MPa), 20i TPU was chosen for the manufacture of dynamic multi-color electrochromic skin (DMECS). The team assembled flexible ECDs using three types of EC polymers (P3HT, MEH-PPV, and P4a (green)) that could achieve different color changes (Figure 37a). P3HT-ECD exhibited a fast switching speed (t_b = 1.75 s, t_c = 1.5 s) and maintained good electrochromic cycling stability even after continuous operation for 35,000 s within the ±3 V potential range (as shown in Figure 37b). Meanwhile, ECDs prepared using MEH-PPV and P4a also exhibit stable long-term cycling behavior. In addition, the team reported on the performance of stretchable ECDs utilizing P3HT. The test results show that the P3HT-DMECS exhibited excellent electrochromic (EC) stability at both 50% and 100% strain, enduring 600 cycles with minimal change in ΔT (as shown in Figure 37c). Finally, the team demonstrated the application of this multi-color ECD for camouflage purposes (as shown in Figure 37d).

Li's team synthesized a room-temperature self-healing polyurethane, SHPU [86], which contains an acylamino urea structure (Figure 38a). The IL-GPEs containing different [EMIM][TFSI] mass percentages (SHPU-50% IL, SHPU-60% IL, SHPU-70% IL, SHPU-80% IL, and SHPU-90% IL) were prepared with SHPU as the polymer matrix. Although SHPU-90% IL showed the highest ionic conductivity (5.28×10^{-3} S/cm), a balance between conductivity and mechanical properties was sought, leading to the selection of SHPU-80% IL for further development into an electrochromic application (Figure 38b,c).

SHPU-80% IL was formulated into an EC gel (SHPU-80% IL-EV), containing ethyl viologen bis(hexafluorophosphate) (EV(PF6)2) and hydroxymethyl ferrocene (hmFc), for the assembly and evaluation of ECDs. SHPU-80% IL-EV is sandwiched between two ITO glasses, forming HI-ECD. HI-ECD exhibited a high optical contrast of 94.7% and demonstrated relatively stable electrochromic cycling stability, with a ΔT retention ratio of 93%. Furthermore, it should be highlighted that after cutting the HI-ECD with a glass cutter, the separated parts could be reconnected, and following 18 h of self-repair at room temperature, the cut HI-ECD could achieve a robust connection. This is attributed to the formation of a large number of hydrogen bonds by the acyl amino urea structure in SHPU (Figure 38d), which ensures the excellent self-healing ability of the SHPU-IL at room temperature.

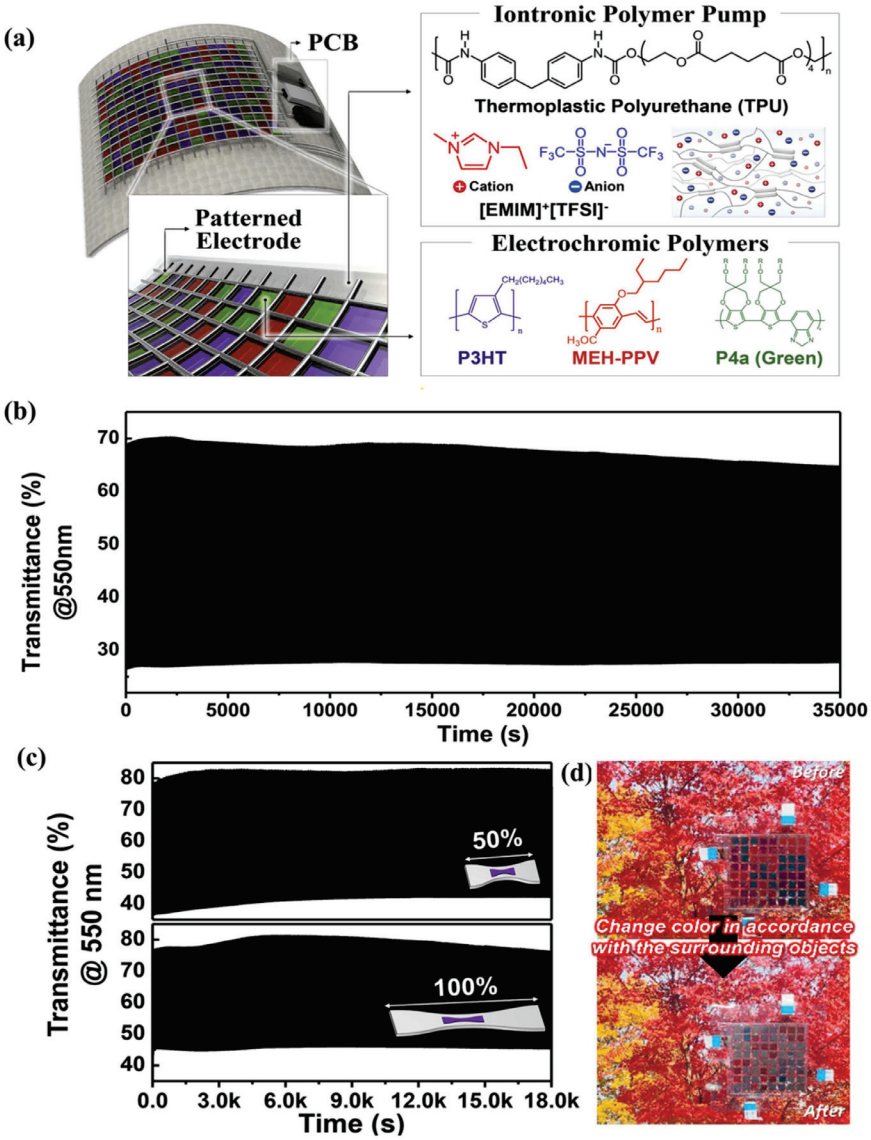

Figure 37. (**a**) Schematic of our DMECS and the chemical structures of its associated components. P3HT, MEH-PPV, and P4a ECPs were used to create purple, orange, and green colors, respectively, while i-TPU ([EMIM]$^{+}$[TFSI]$^{-}$ loaded in TPU polymer chains) was used as a highly flexible solid-state electrolyte. The DMECS was fabricated by sandwiching a multicolor pattern-ECP-incorporated i-TPU film between two flexible electrodes. (**b**) Transient transmittance profile at 550 nm during continuous coloration/bleaching switching cycles of the P3HT ECD. (**c**) Transient transmittance profile of P3HT-incorporated i-TPU active layer in 50% and 100% stretched states. Inset right shows the photographs of P3HT-incorporated i-TPU film in normal and stretched states. (**d**) Real-time photographs of DMECS over various backgrounds showing active camouflage for adaptive camouflage applications [132].

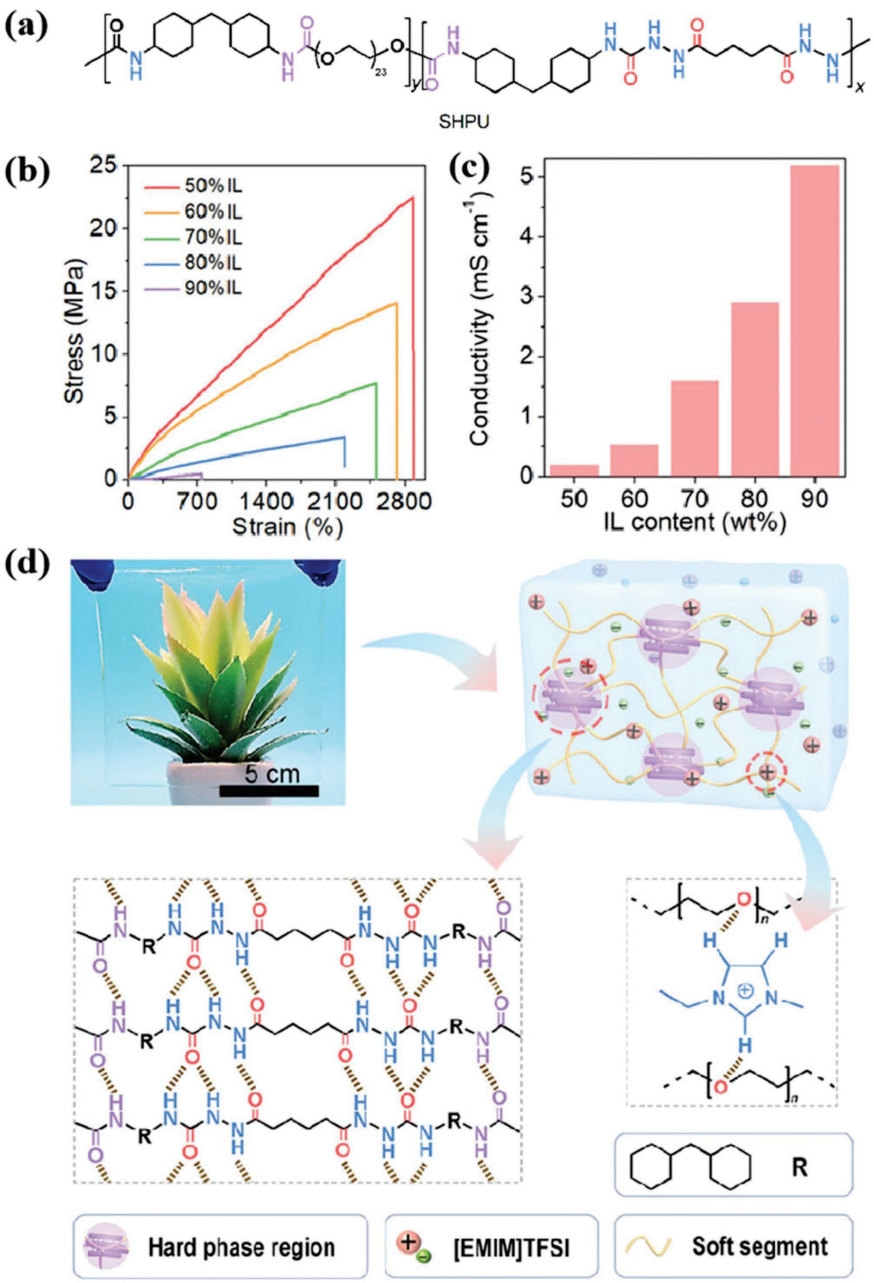

Figure 38. (**a**) Chemical structure of SHPU. (**b**) Stress–strain curves of the SHPU-zIL ionogels. (**c**) Ionic conductivity of the SHPU-zIL ionogels. (**d**) Photograph of the SHPU-60%IL ionogel and schematic illustration of the internal structure of the SHPU-zIL ionogels [86].

Bae et al. used polyvinyl chloride (PVC) as the matrix polymer to prepare a series of IL-GPEs, denoted as pECIonogels (-I0.4-M, -I0.8-M, -I1.0-M, -I1.2-M, and -I1.4-M) [133]. Its detailed ingredients (Figure 39a) include dibutyl hexanoic acid (DBA, as a plasticizer), 1-ethyl-3-methylimidazolium bis(trifluoromethanesulfonyl)imide (EMIM TFSI, as an electrolyte salt), DHV[TFSI]$_2$ (EC material), and dmFc (redox mediator). These pECIonogels were designed to combine high ionic conductivity with desirable mechanical properties for applications in flexible electronics, and among the pECIonogel series, pECIonogel-I1.2-M exhibited high ionic conductivity (2.8×10^{-4} S/cm) and excellent mechanical softening behavior (maximum tensile strain could reach 1664.1%, tensile strength 97.3 kPa, Young's modulus 8.4 MPa), and was thus used for assembly and testing of subsequent ECDs (Figure 39b). Consequently, flexible ECDs were prepared based on pECIonogel-I1.2-M. The

test results show that the flexible ECD prepared based on pECIonogel-I1.2-M demonstrated a high optical contrast of 80.30% and excellent electrochromic cycling stability, with a ΔT retention ratio of 95% after 800 cycles. Furthermore, the team prepared a stretchable ECD based on pECIonogel-I1.2-M. At 0% and 50% tensile strain, the stretchable ECD exhibited optical contrast of 44.24% and 36%, respectively, indicating its responsiveness to mechanical deformation. After 100 cycles of stretching/releasing, the CV curve of the stretchable ECD showed no significant change, thereby demonstrating the electrochemical stability of the stretchable electrochromic device based on pECIonogel-I1.2-M.

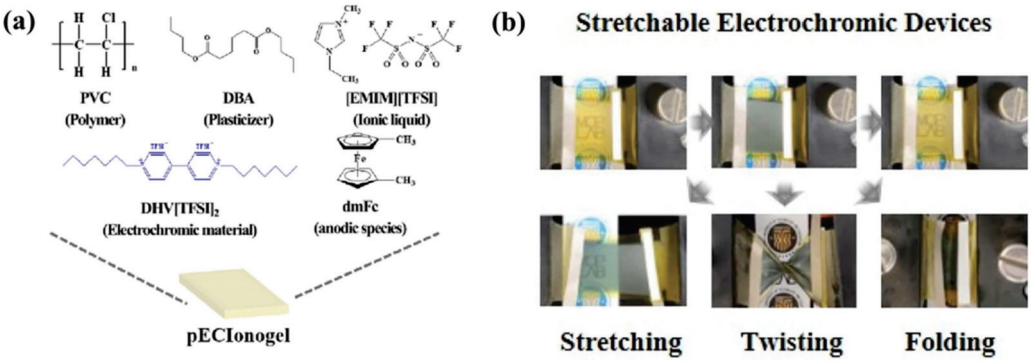

Figure 39. (**a**) Molecular structures of the pECIonogel components: PVC, DBA, EMIMTFSI, DHV[TFSI]$_2$, and dmFc. (**b**) Schematic diagram of stretching, twisting, and bending of stretchable electrochromic devices [133].

Table 8. The performance of natural polymer-based IL-GPEs and other polymer-based IL-GPEs in ECDs.

Electrolytes	Conductivity (S/cm)	Transmittance (%)	Thickness (μm)	ECM	Color Changes	t_c/t_b (s)	ΔT (%)	CE (cm^2/C)	Cycles	Ref.
Gellan Gum-[Emim][SCN]	6.0×10^{-3}	70–74	120	PEDOT:PSS	/	/	30	/	/	[89]
0.3 M BMII-1.5 M $ZnSO_4$-PAM	3.3×10^{-2}	/	/	PANI-FEP	light blue (transparent)–green (transparent)–brown (opaque) to purple	50/9	67.54	/	/	[85]
20i-TPU	/	93.4	150	P3HT		1.5/1.75	/	/	/	[132]
SHPU-80%IL	/	/	300	$EV(PF_6)_2$	/	63/255	97.4	106.24	220 cycles ΔT retention ratio93%	[86]
pECIonogel-I1.2-M	2.8×10^{-4}	90	500	pECIonogel-I1.2-M	yellow to blue	222/178	36	226.67	/	[133]

2.3. IL-Based Solid Polymer Electrolyte (IL-SPE)

So far, research on using all solid-state electrolytes (without any liquid components) as EC ionic conductive layers is still in the exploratory stage due to factors such as ion conductivity and transmittance. At present, all solid-state electrolytes reported in the field of electrochromic could be divided into two types: inorganic solid-state electrolytes and solid polymer electrolytes. For example, inorganic solid electrolytes such as Ta_2O_5, $LiNbO_3$, CaF_2, etc., Refs [15–17,19,134–140] have been applied in the field of electrochromic. Solid polymer electrolytes based on PVB, PEO, PVA, PVP, etc., [20,22,23,37,141–148] have also been applied in ECDs. In addition to the polymer matrix mentioned above, PIL has also been applied in solid-state polymer electrolytes [24–27,34,149]. However, to date, there have been limited studies on the application of IL-based solid polymer electrolytes (IL-SPEs) in ECDs. This article briefly analyzes and introduces the relevant reported literature.

In 2011, Fu et al. reported on an IL-SPE for application in ECDs. A novel IL (MMEIm TFSI) was first synthesized, followed by the preparation of a PIL, PMMEIm-TFSI [149], via free radical polymerization (Figure 40). After completely dissolving P(MMA-co-VAc), PMMEIm-TFSI, and LiTFSI in THF at various ratios, a series of IL-SPE membranes based

on PMMEIm-TFSI could be obtained by casting them into films. The conductivity tests show that the PIL-GPE membrane with 25 wt% P(MMA-co-VAc), 75 wt% PMMEIm-TFSI, and 30 wt% LiTFSI had the highest ion conductivity of 1.78×10^{-4} S/cm. Furthermore, the electrolyte membrane exhibited a transparency of 92.1% in the visible light region. Consequently, the membrane was used to fabricate and evaluate ECD, with viologen derivatives serving as the electrochromic layers. The results indicate that this ECD could withstand up to 10^7 cycles with a response time of about 100 ms.

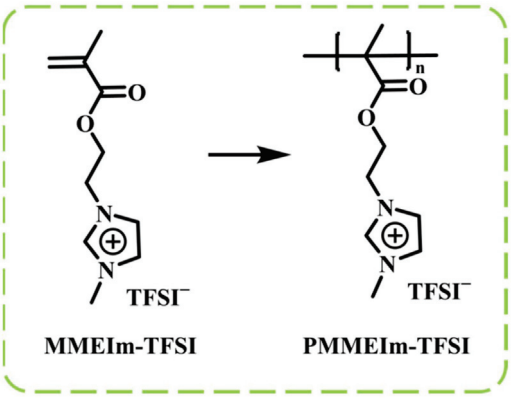

Figure 40. The preparation process of PMMEIm-TFSI.

In 2014, Alexander's team developed a solid polymer electrolyte P (MEEMIm TFSI) [34] based on a novel ionic liquid 1-[2-(2-(Methcryloyloxy) ethoxy) ethoxy]-3-methylimidazolium bis (trifluoromethylsul fonyl) imide (MEEMIm TFSI). After casting P (MEEMIm TFSI) into an IL-SPE film, its conductivity was measured to reach 1.0×10^{-5} S/cm, indicating that the IL-SPE film had the potential to be used as an electrolyte for ECDs alone. The team applied P (MEEMIm TFSI) as an electrolyte to an all-solid-state ECD using PEDOT as the electrochromic material (Figure 41). The ECD exhibited an optical contrast of 22% at 620 nm, and after 1000 cycles at 0.5–2.5 V, the optical contrast remained unchanged (ΔT remained between 21% and 22%), demonstrating excellent EC cycling stability. Furthermore, it is worth noting that this all-solid-state ECD had a short switching time (3 s for 90% ΔT), which is comparable to the switching times of ECDs using gel or liquid electrolytes (1–8 s) [150,151], and faster than those using other solid polymer electrolytes (4–60 s) [152–154].

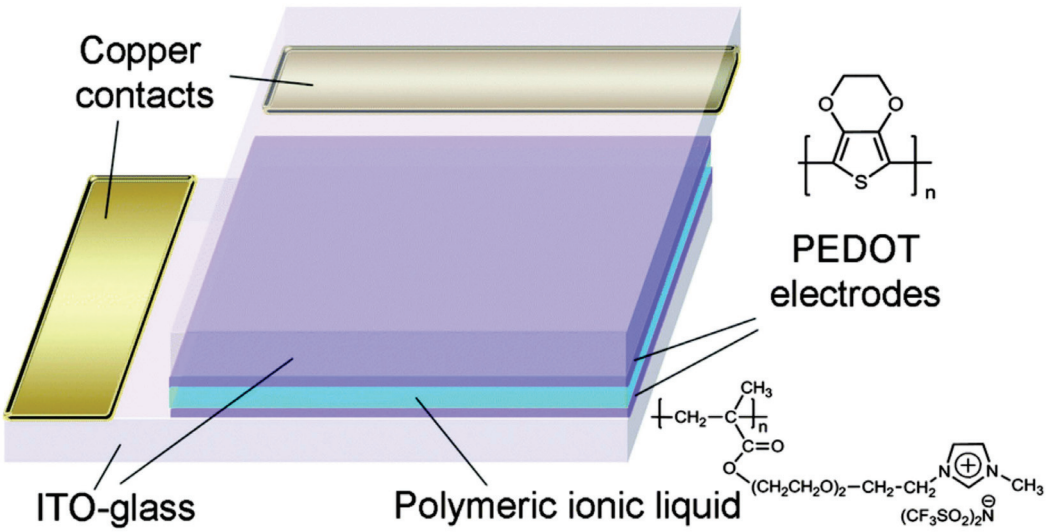

Figure 41. Schematic representation of a symmetrical PEDOT/PIL/PEDOT electrochromic device [34].

In 2018, Puguan et al. synthesized a series of linear structured polyionic liquids PIL6, PIL7, PIL8, PIL9, and PIL10 containing 1, 2, and 3-triazole units (Figure 42) [26,27]. The ionic conductivity test results show that the all-solid poly(ionic liquid) film prepared by PIL10 had the best conductivity, which could reach 1.20 × 10^{-4} S/cm. The PIL10 is therefore used for the construction and testing of all-solid-state ECD. A symmetric all-solid ECD was prepared by combining the all-solid poly(ionic liquid) film (as electrolyte) with PEDOT: PSS(EC active layer). It also shows the characteristics of fast response (t_c = 2.5 s, t_b= 3.2 s) and good EC cycle stability (after 2000 cycles, CR (contrast ratio) decreased from 2.1 to 1.78, only 15%). In addition, although the optical contrast of the device is low (ΔT= 22%), it is higher than ECD (ΔT = 15%) prepared with PEO + $Li(CF_3SO_3)$ all-solid electrolyte in devices with the same EC active layer [97].

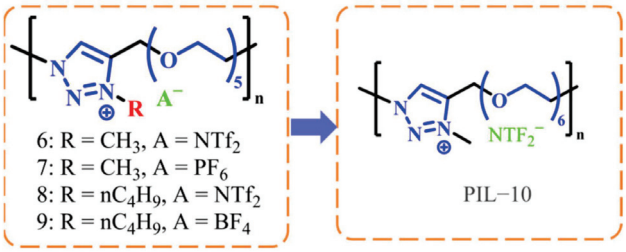

Figure 42. Chemical structure of polymeric ionic liquids (PIL-6, PIL-7, PIL-8, PIL-9, and PIL-10).

In 2019, Puguan et al. introduced a viologen structural unit with electrochromic ability onto the PIL side chain containing triazole groups and prepared a series of novel multifunctional Poly (ionic liquid) TEG-[C_4C_3bpy]TFSI, TEG-[C_6C_3bpy]TFSI, and HEG-[C_6C_3bpy]TFSI that combine electrochromic and ion conductivity (Figure 43) [25]. The authors dissolved the three types of PIL mentioned above in acetonitrile and deposited them onto ITO glass to form all-solid electrolyte films. These Poly (ionic liquid) were then utilized to fabricate all-solid ECDs, aiming to evaluate their electrochromic performance. They combined the films with another piece of ITO glass to construct three types of all-solid integrated ECDs. All three ECDs could achieve color changes from yellow-orange to purple, but in comparison, the ECD based on TEG-[C_6C_3bpy] TFSI exhibited the highest transmittance change (ΔT = 21.6%), the highest electrochromic cycle stability with a ΔT retention ratio of 97.22% after 1000 cycles, and exhibited the shortest response time of 14 s.

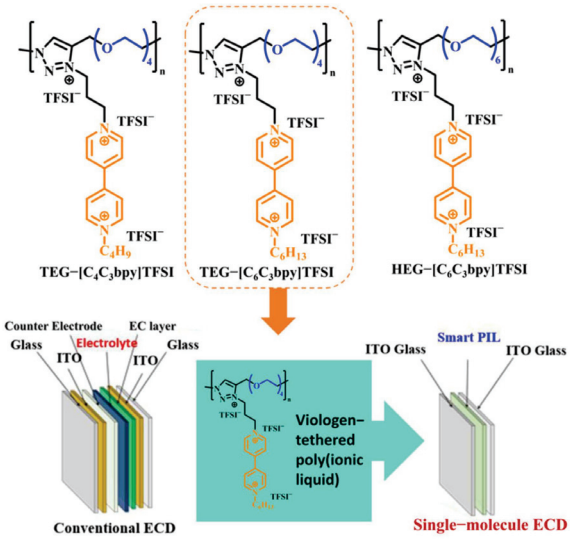

Figure 43. Chemical structures of three types of EC PIL and structural display of single-molecule ECD [25].

In 2023, Li's team synthesized a series of novel solid-state PIL electrolytes, P(IL-MEA) [24] (Figure 44a), through in situ photopolymerization. The precursor solution of P(IL-MEA) consists of different mass ratios of 1-butyl-3-vinylimidazolium bis(trifluoromethanesulfonyl)imide VBIm [TFSI] and 2-methoxyethyl acrylate (MEA), as well as succinonitrile (SN) that appears as a solid at room temperature. MEA and VBIm [TFSI] copolymerize to form a polymer matrix that can conduct ions, and SN exists as a plasticizer. P(IL-MEA)-60 had the highest ion conductivity (as shown in Figure 44c), so it was used to construct ECDs with PEDOT: PSS as the electrochromic (EC) layer for subsequent characterization tests. In rigid ECDs, compared with PVDF-based gel electrolytes (after 5000 cycles, ΔT retention rate = 44.6%) and PMMA-based gel electrolytes (after 5000 cycles, ΔT retention rate = 44.6%), ECD based on P(IL-MEA) shows more excellent electrochromic cycle stability (after 5000 cycles, with a ΔT retention rate of 92.5%) (Figure 44d). In addition, in flexible ECDs, after 5000 bending cycles, compared with the PVDF-based gel electrolyte (interfacial separation) and PMMA-based gel electrolyte (electrolyte leakage), P(IL-MEA)-based ECDs exhibit higher mechanical stability (with a ΔT retention rate of 96.3% after 5000 bending cycles). More importantly, based on P(IL-MEA)-60, the research group demonstrated a convenient single-layer EC 'window tint film' that simplifies the assembly and maintenance processes for window glass with a conductive layer (Figure 44b). By simply covering the ITO-PET substrate (pre-coated with EC material) with a P(IL-MEA) precursor solution, a smart window can be assembled without the need for packaging. Additionally, if the window tint film is damaged or reaches the end of its service life, it could be quickly repaired or replaced with a new EC film. This research work not only proves that the use of PIL solid polymer electrolyte could improve the electrochromic (EC) cycle life of ECDs, but also provides robust technical support for the convenient assembly, installation, and maintenance of electrochromic smart windows. This work demonstrated the enormous development and application potential of all-solid-state PIL electrolytes in the field of electrochromic smart windows.

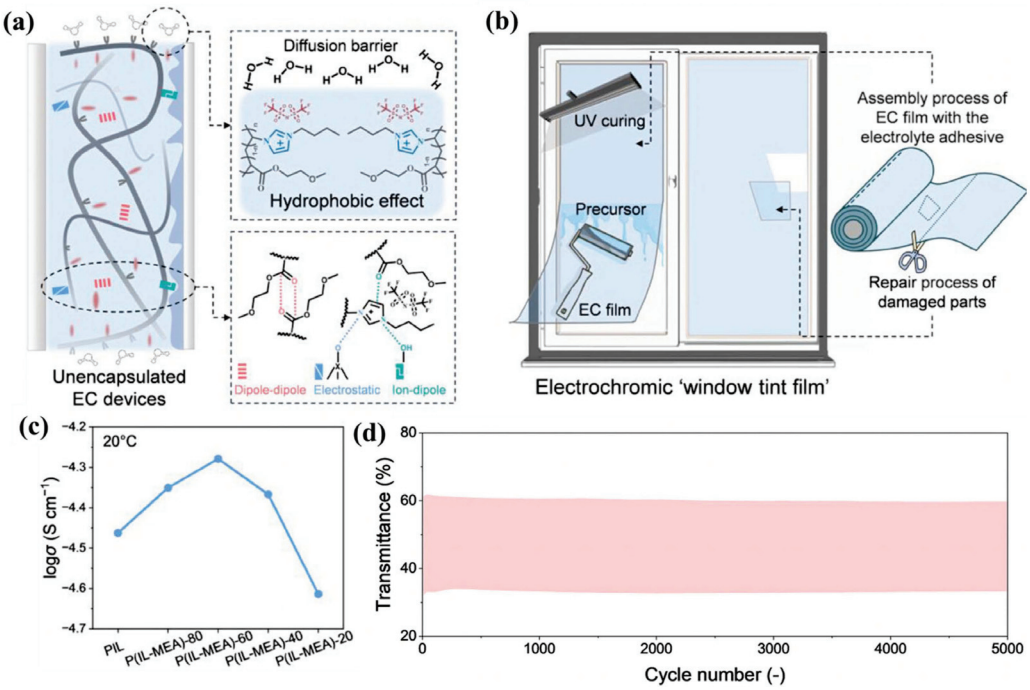

Figure 44. (**a**) Schematic illustration of structural properties for unencapsulated EC devices based on the P(IL-MEA) electrolyte. (**b**) The assembly, installation, and repair process of unencapsulated, removable electrochromic "window tint film". (**c**) Ionic conductivity of PIL and P(IL-MEA) electrolytes at 20 °C. (**d**) (g) Long-term cyclic test for the EC devices based on P(IL-MEA)$^{-}$ 60 electrolyte [24].

Although the application of all-solid-state electrolytes in the field of electrochromism is still in the exploratory phase, it is not difficult to see from the existing research results that the use of solid-state electrolytes especially IL-SPE offers significant advantages in simplifying the device fabrication process, improving the packaging quality, enhancing environmental tolerance, and extending the service life of electrochromic devices (ECDs). To clarify the performance characteristics of IL-SPEs and their corresponding ECDs, we have assembled the relevant data, which are presented in Table 9 (located at the end of Section 2.3).

Table 9. The performance of partial solid polymer electrolytes and ECDs.

Electrolytes	Conductivity (S/cm)	Transmittance (%)	Thickness (μm)	ECM	Color Changes	t_b/t_c (s)	ΔT (%)	CE (cm^2/C)	Cycle	Ref.
PVB + $LiClO_4$	1.78×10^{-4}	>90	400	WO_3	/	14.47/17.30	70	/	20,000	[143]
PVA + $LiCH_3COO$	1.593×10^{-11}	90	/	WO_3	/	0.12/0.1	/	/	150	[146]
PVP-$LiClO_4$	/	/	300	WO_3	Transparent to dark blue	3.36/3.88	/	/	100	[148]
p(TMC)/ PEO/$LiClO_4$	1.33×10^{-6}	/	150	PEDOT	light blue to dark blue	Long cycle times (>600 s)	22	/	/	[20]
P(MMA-Vac)/ PMMEIm-TFSI/LiTFSI	1.78×10^{-4}	92.1	/	viologen derivative	/	0.1	/	/	10^7	[149]
P(MEEMIm TFSI)	1.0×10^{-5}	/	0.5	PEDOT	light blue to dark blue	3/3	22	390	10^3	[34]
PIL-6	1.16×10^{-4}	/	206	PEDOT: PSS	Transparent to blue	11.8/4.7	18	356	/	[23]
PIL-10	1.20×10^{-4}	/	24	PEDOT: PSS	pale blue to dark blue	3.2/2.5 s	22	/	2000	[24]
TEG-[C_6C_3bpy]TFSI	/	/	/	TEG-[C_6C_3bpy]TFSI	yellow-orange to purple	14 s	21.6	76.8	10^3	[25]
P(IL-MEA)	/	92%	200	PEDOT: PSS	/	6.5/1.5 s	/	1021	5000	[24]

3. Summarization and Prospect

The application of IL-based electrolytes in ECDs demonstrated significant advantages. However, there is currently a lack of comprehensive introduction and analysis reports on the research progress of the application of ionic liquid electrolytes in electrochromic devices in the EC field. Therefore, this article reviews the cutting-edge progress of IL-based electrolytes in the field of electrochromism, summarizes the advantages and characteristics of different types of IL-based electrolytes, and explores the challenges and future development trends they face in the application of ECDs. Based on the summary and induction of existing literature, we found that the use of IL not only effectively improves the electrochromic (EC) cycling stability of ECDs at both room temperature and high temperature, but also broadens the working voltage range of ECDs.

However, low conductivity (high viscosity) and high cost are urgent problems to be solved in the application of IL-based electrolytes in the field of electrochromism (as shown in Table 10). The viscosity of $LiClO_4$/organic solvent electrolytes is lower than 3 cP [155], while the viscosity of ionic liquids is much higher than this value. The high viscosity of electrolytes is unfavorable for ion transport, thereby reducing the conductivity of IL-based electrolytes. In addition, the current price of ILs used as electrolytes is relatively high. We researched the prices of several commonly used ionic liquids, which range from USD 500/100 g to USD 3000/100 g. The high cost is a major limitation that restricts the commercial application of ionic liquid electrolytes in ECDs.

We believe that the future development of electrolyte materials based on ILs in the field of EC technology will have the following trends and characteristics:

Towards high-performance electrolytes.

Although the current ionic conductivity of IL-based electrolytes can basically meet the application requirements of ECDs, a higher ionic conductivity will definitely provide a significant boost in achieving ECDs with higher electrochromic performance. How to further improve the ionic conductivity of IL-based electrolytes will be one of the main

research directions in this field in the future. In addition, for gel-state and all-solid-state IL-based electrolytes, both the mechanical strength of the electrolyte and its adhesion to the EC electrode should also be considered. Electrolytes with good adhesion and excellent mechanical strength can help to achieve ECDs (especially flexible ECDs) with high electrochromic cycle stability and mechanical stability.

Table 10. The prices, conductivity, and viscosity of several common ionic liquids.

Brand	Product Name	η (cP)	Window (V)	Conductivity (S/cm)	Price (USD/100 g)
Sigma-Aldrich (St. Louis, MO, USA)	[EMIm][TFSI]	37 [156]	4.3 [157]	8.6×10^{-4} [157]	530
	[EMIm][BF_4]	41 [156]	4.3 [157]	1.38×10^{-3} [157]	1337
	[BMIm][TFSI]	52 [157]	4.76 [157]	4×10^{-3} [158]	530
	[BMIm][BF_4]	112 [156]	6.1 [157]	4×10^{-4} [159]	1200
	[BMIm][PF_6]	216 [156]	5 [157]	1.59×10^{-4} [159]	2765

Towards all-solid-state electrolytes.

All solid-state ECDs must be the inevitable trend of future development. Due to their solvent-free nature, the application of all-solid-state electrolytes can significantly enhance both the safety and weather resistance of ECDs. Moreover, all-solid-state ECDs may meet the process requirement of "less packaging or no packaging", thereby reducing the production cost of ECDs and facilitating their popularization and application. At present, the PIL electrolyte has shown its convenient processing characteristics and great application potential in this aspect and is one of the strong candidates for realizing high-performance all-solid-state ECDs in the future.

Towards low cost.

At present, IL-based electrolytes still face the issue of relatively high cost, which may be one of the current obstacles restricting their further commercial production and application. Currently, as the huge application potential of IL in various fields has been recognized, it can be predicted that with the development of new ionic liquid materials and the maturity of large-scale production technology for ionic liquid materials, cost will no longer be a barrier to its application in the future.

Towards functionalization and intelligence.

With the increasing research on the application of ECDs in military camouflage, biosensors, smart windows, and other fields, IL-based electrolytes are expected to become more functional and intelligent in the future. Currently, some researchers already carried out related work focusing on functionality and intelligence, such as strain response, temperature response, and self-powering. As research in this field continues to deepen, more innovative applications of ECDs based on IL-based electrolytes will undoubtedly emerge in the future.

Towards green and sustainable development.

Green and sustainable development has been the concern of many countries around the world. Therefore, ECD electrolytes should also develop in this direction in the future. Due to its extremely low vapor pressure, IL will not volatilize into the atmosphere and has been considered as a green solvent. Currently, there have been some reports on natural polymer-based IL-gel polymer electrolytes (IL-GPEs), but the number of such reports is limited. In the future, more natural polymer-based IL-gel polymer electrolytes (IL-GPEs) will be widely studied and applied in ECDs.

Author Contributions: Conceptualization, Z.C. and Z.J.; investigation, H.Z. and K.F.; software, H.Z.; writing—original draft preparation, H.Z.; writing—review and editing, H.Z. and Z.C.; supervision, X.W. and Y.L.; resources, X.W.; project administration, K.F. and Q.W.; visualization, Y.L. and Q.W.; funding acquisition, Z.C. and Z.J. All authors have read and agreed to the published version of the manuscript.

Funding: This work was supported by the Jilin Province Industry Key Core Technology Research Project (No. 20240302101GX).

Institutional Review Board Statement: Not applicable.

Informed Consent Statement: Not applicable.

Data Availability Statement: Data are available in the source publications listed in the bibliography.

Conflicts of Interest: The authors declare no conflicts of interest.

Abbreviations

The following abbreviations are used in this manuscript:

EC	Electrochromism
ECD	Electrochromic device
CE	Coloration Efficiency
IL	Ionic liquid
PIL	Polymeric ionic liquid
IL-GPE	Ionic liquid-based gel polymer electrolyte
IL-SPE	Ionic liquid-based solid polymer electrolyte
ITO	Indium Tin Oxide
FTO	Fluorine-doped Tin Oxide
ATO	Antimony-doped Tin Oxide
PET	Polyethylene Terephthalate
PB	Prussian Blue
Fc	Ferrocene
dmFc	Dimethyl Ferrocene
PANI	Polyaniline
PEDOT	Poly(3,4-ethylenedioxythiophene)
PEDOT:PSS	Poly(3,4-ethylenedioxythiophene):Polystyrene Sulfonate
TEMPO	2,2,6,6-Tetramethylpiperidine 1-oxyl
[AMIM][TFSI]	1-Aminomethyl-3-methylimidazolium bis(trifluoromethylsulfonyl)imide
[BMIM][BF_4]	1-Butyl-3-methylimidazolium tetrafluoroborate
[BMIM][Br]	1-Butyl-3-methylimidazolium bromide
[BMIM][PF_6]	1-Butyl-3-methylimidazolium hexafluorophosphate
[BMIm][$NTf]_2$	1-Butyl-3-methylimidazolium bis(trifluoromethylsulfonyl)imide
[BVIm][Br]	1-Butyl-2-vinylimidazolium bromide
[EMIM][BF_4]	1-Ethyl-3-methylimidazolium tetrafluoroborate
[EMIM][Br]	1-Ethyl-3-methylimidazolium bromide
[EMIM][SCN]	1-Ethyl-3-methylimidazolium thiocyanate
[EMIM][TFSI]	1-Ethyl-3-methylimidazolium bis(trifluoromethylsulfonyl)imide
[emim][Br]	1-Ethyl-3-methylimidazolium bromide
[ViEtIm][Br]	1-Vinyl-2-ethylimidazolium bromide
[ViEtIm][Tf_2N]	1-Vinyl-2-ethylimidazolium bis(trifluoromethylsulfonyl)imide
VBIMTFSI	Vinyl-1-butyl-3-methylimidazolium bis(trifluoromethylsulfonyl)imide

References

1. Mortimer, R.J. Electrochromic materials. *Chem. Soc. Rev.* **1997**, *26*, 147–156. [CrossRef]
2. Deb, S.K. A novel electrophotographic system. *Appl. Opt.* **1969**, *8*, 192–195. [CrossRef] [PubMed]
3. Ma, Y.; Wang, Y.; Zhou, J.; Lan, Y.; Jiang, S.; Ge, Y.; Tan, S.; Zhang, S.; Wang, C.; Wu, Y. LCST ion gels fabricating "all-in-one" smart windows: Thermotropic, electrochromic and power-generating. *Mater. Horiz.* **2024**, *11*, 3825–3834. [CrossRef]
4. Shao, Z.; Huang, A.; Cao, C.; Ji, X.; Hu, W.; Luo, H.; Bell, J.; Jin, P.; Yang, R.; Cao, X. Tri-band electrochromic smart window for energy savings in buildings. *Nat. Sustain.* **2024**, *7*, 796–803. [CrossRef]
5. Riganti, M.; Li Castri, G.; Serra, V.; Manca, M.; Favoino, F. Energy saving potential of advanced dual-band electrochromic smart windows for office integration. *Energy Build.* **2025**, *327*, 115084. [CrossRef]
6. Cai, G.; Wang, J.; Lee, P.S. Next-Generation Multifunctional Electrochromic Devices. *Acc. Chem. Res.* **2016**, *49*, 1469–1476. [CrossRef]

7. Li, W.; Bai, T.; Fu, G.; Zhang, Q.; Liu, J.; Wang, H.; Sun, Y.; Yan, H. Progress and challenges in flexible electrochromic devices. *Sol. Energy Mater. Sol. Cells* **2022**, *240*, 111709. [CrossRef]
8. Fu, H.; Zhang, L.; Dong, Y.; Zhang, C.; Li, W. Recent advances in electrochromic materials and devices for camouflage applications. *Mater. Chem. Front.* **2023**, *7*, 2337–2358. [CrossRef]
9. Shen, W.; Li, G. Recent Progress in Liquid Crystal-Based Smart Windows: Materials, Structures, and Design. *Laser Photonics Rev.* **2023**, *17*, 2200207. [CrossRef]
10. Meng, H. Introduction. In *Organic Electronics for Electrochromic Materials and Devices*; Wiley: Hoboken, NJ, USA, 2021; pp. 1–16. [CrossRef]
11. Wu, W.; Guo, S.; Bian, J.; He, X.; Li, H.; Li, J. Viologen-based flexible electrochromic devices. *J. Energy Chem.* **2024**, *93*, 453–470. [CrossRef]
12. Gu, C.; Jia, A.-B.; Zhang, Y.-M.; Zhang, S.X.-A. Emerging Electrochromic Materials and Devices for Future Displays. *Chem. Rev.* **2022**, *122*, 14679–14721. [CrossRef]
13. Thakur, V.K.; Ding, G.; Ma, J.; Lee, P.S.; Lu, X. Hybrid Materials and Polymer Electrolytes for Electrochromic Device Applications. *Adv. Mater.* **2012**, *24*, 4071–4096. [CrossRef] [PubMed]
14. Patel, K.J.; Bhatt, G.G.; Ray, J.R.; Suryavanshi, P.; Panchal, C.J. All-inorganic solid-state electrochromic devices: A review. *J. Solid State Electrochem.* **2017**, *21*, 337–347. [CrossRef]
15. Zhao, Y.; Zhang, X.; Chen, X.; Li, W.; Li, Z.; Chen, M.; Sun, W.; Zhao, J.; Li, Y. All-solid-state electrochromic devices based on the LiAlSiO4 electrolyte. *Mater. Lett.* **2021**, *292*, 129592. [CrossRef]
16. Chen, X.; Zhang, H.; Li, W.; Xiao, Y.; Zhang, X.; Li, Y. CaF2: A novel electrolyte for all solid-state electrochromic devices. *Environ. Sci. Ecotechnol.* **2022**, *10*, 100164. [CrossRef] [PubMed]
17. Chen, X.; Zhang, H.; Li, W.; Xiao, Y.; Ge, Z.; Li, Y.; Zhang, X. Electro-optical performance of all solid state electrochromic devices with NaF electrolytes. *Mater. Lett.* **2022**, *324*, 132692. [CrossRef]
18. Liu, R.; Ren, Y.; Hou, C.; Wang, J.; Wang, Y.; Tang, K.; Zhao, G. Preparation of all-solid-state electrochromic devices based on li+-contained phosphate electrolyte. *Ceram. Int.* **2024**, *50*, 38632–38640. [CrossRef]
19. Wang, J.; Wang, X.; Zhang, C.; Lin, S.; Dai, M.; Wang, H.; Xie, S.; Shi, Q. Influence of N-doped aluminosilicate as an electrolyte on the properties of all-solid-state electrochromic devices. *Sol. Energy Mater. Sol. Cells* **2023**, *257*, 112352. [CrossRef]
20. Barbosa, P.C.; Rodrigues, L.C.; Silva, M.M.; Smith, M.J.; Parola, A.J.; Pina, F.; Pinheiro, C. Solid-state electrochromic devices using pTMC/PEO blends as polymer electrolytes. *Electrochim. Acta* **2010**, *55*, 1495–1502. [CrossRef]
21. Lim, B.H.; Kim, J.M.; Nguyen, V.-T.; Kim, H.; Park, C.W.; Lee, J.K.; Lee, C.-H.; Yoo, J.; Min, B.K.; Kim, S.K. Functionalized methyl cellulose/LiClO4 composite as an environmentally friendly quasi-solid polymer electrolyte for solid-state electrochromic devices and cellulose-based supercapacitors. *Mater. Today Energy* **2023**, *33*, 101263. [CrossRef]
22. Kiristi, M.; Bozduman, F.; Gulec, A.; Teke, E.; Oksuz, L.; Oksuz, A.U.; Deligöz, H. Complementary all solid state electrochromic devices using carboxymethyl cellulose based electrolytes. *J. Macromol. Sci. Part A* **2014**, *51*, 481–487. [CrossRef]
23. Yang Jeong, C.; Kubota, T.; Chotsuwan, C.; Wungpornpaiboon, V.; Tajima, K. All-solid-state electrochromic device using polymer electrolytes with a wet-coated electrochromic layer. *J. Electroanal. Chem.* **2021**, *897*, 115614. [CrossRef]
24. Wu, X.; Bai, Z.; Bao, B.; Zhang, Q.; Jiang, W.; Li, Y.; Hou, C.; Li, K.; Wang, H. A Lithium-Salt-Free, Hydrophobic, Solid-State Poly(Ionic Liquid) Electrolyte Enables Rapid Assembly of Unencapsulated, Removable Electrochromic "Window Tint Film". *Adv. Funct. Mater.* **2023**, *34*, 2312358. [CrossRef]
25. Puguan, J.M.C.; Kim, H. A switchable single-molecule electrochromic device derived from a viologen-tethered triazolium-based poly(ionic liquid). *J. Mater. Chem. A* **2019**, *7*, 21668–21673. [CrossRef]
26. Puguan, J.M.C.; Jadhav, A.R.; Boton, L.B.; Kim, H. Fast-switching all-solid state electrochromic device having main-chain 1,2,3-triazolium-based polyelectrolyte with extended oxyethylene spacer obtained via click chemistry. *Sol. Energy Mater. Sol. Cells* **2018**, *179*, 409–416. [CrossRef]
27. Puguan, J.M.C.; Boton, L.B.; Kim, H. Triazole-based ionene exhibiting tunable structure and ionic conductivity obtained via cycloaddition reaction: A new polyelectrolyte for electrochromic devices. *Sol. Energy Mater. Sol. Cells* **2018**, *188*, 210–218. [CrossRef]
28. Wei, Y.; Chen, M.; Liu, W.; Li, L.; Yan, Y. Electrochemical investigation of electrochromic devices based on NiO and WO3 films using different lithium salts electrolytes. *Electrochim. Acta* **2017**, *247*, 107–115. [CrossRef]
29. Lu, Z.; Li, R.; Ping, L.; Bai, Z.; Li, K.; Zhang, Q.; Hou, C.; Li, Y.; Jin, W.; Ling, X.; et al. Ultra-stable ionic-liquid-based electrochromism enabled by metal-organic frameworks. *Cell Rep. Phys. Sci.* **2022**, *3*, 100866. [CrossRef]
30. Tan, C.; Hu, Z.; Guo, Z.; Cui, Z.; Bai, L.; Wu, X.; Huang, C.; Su, W. In-situ-selective-UV crosslinking fabrication of solid liquid host guest electrolyte: A facile one-step method realizing highly flexible electrochromic device. *Nano Res.* **2024**, *17*, 9712–9720. [CrossRef]
31. Cai, H.; Chen, Z.; Guo, S.; Ma, D.; Wang, J. Polyacrylamide gel electrolyte for high-performance quasi-solid-state electrochromic devices. *Sol. Energy Mater. Sol. Cells* **2023**, *256*, 112310. [CrossRef]

32. Li, W.; Bai, T.; Zhang, Q.; Liu, J.; Zhou, K.; Wang, H. A highly transparent ion conducting film enabling a visual electrochromic battery. *J. Mater. Chem. C* **2023**, *11*, 7740–7749. [CrossRef]
33. Tang, Q.; Li, H.; Yue, Y.; Zhang, Q.; Wang, H.; Li, Y.; Chen, P. 1-Ethyl-3-methylimidazolium tetrafluoroborate-doped high ionic conductivity gel electrolytes with reduced anodic reaction potentials for electrochromic devices. *Mater. Des.* **2017**, *118*, 279–285. [CrossRef]
34. Shaplov, A.S.; Ponkratov, D.O.; Aubert, P.-H.; Lozinskaya, E.I.; Plesse, C.; Vidal, F.; Vygodskii, Y.S. A first truly all-solid state organic electrochromic device based on polymeric ionic liquids. *Chem. Commun.* **2014**, *50*, 3191–3193. [CrossRef] [PubMed]
35. Oukassi, S.; Giroud-Garampon, C.; Dubarry, C.; Ducros, C.; Salot, R. All inorganic thin film electrochromic device using LiPON as the ion conductor. *Sol. Energy Mater. Sol. Cells* **2016**, *145*, 2–7. [CrossRef]
36. Zhu, Y.; Xie, L.; Chang, T.; Bell, J.; Huang, A.; Jin, P.; Bao, S. High performance all-solid-state electrochromic device based on LixNiOy layer with gradient Li distribution. *Electrochim. Acta* **2019**, *317*, 10–16. [CrossRef]
37. Wang, W.; Guo, S.; Feng, F.; Li, Q.; Cai, H.; Rougier, A.; Ma, D.; Wang, J. Research Progress in Polymer Electrolytes for Electrochromic Devices. *Polym. Rev.* **2024**, *65*, 302–328. [CrossRef]
38. Saha, M.; Kumar, A.; Kanaoujiya, R.; Behera, K.; Trivedi, S. A Comprehensive Review of Novel Emerging Electrolytes for Supercapacitors: Aqueous and Organic Electrolytes Versus Ionic Liquid-Based Electrolytes. *Energy Fuels* **2024**, *38*, 8528–8552. [CrossRef]
39. Hu, X.; Wang, Y.; Feng, X.; Wang, L.; Ouyang, M.; Zhang, Q. Thermal stability of ionic liquids for lithium-ion batteries: A review. *Renew. Sustain. Energy Rev.* **2025**, *207*, 114949. [CrossRef]
40. Xue, Z.; Qin, L.; Jiang, J.; Mu, T.; Gao, G. Thermal, electrochemical and radiolytic stabilities of ionic liquids. *Phys. Chem. Chem. Phys.* **2018**, *20*, 8382–8402. [CrossRef] [PubMed]
41. Wang, T.; Luo, H.; Bai, Y.; Li, J.; Belharouak, I.; Dai, S. Direct Recycling of Spent NCM Cathodes through Ionothermal Lithiation. *Adv. Energy Mater.* **2020**, *10*, 2001204. [CrossRef]
42. Lu, W.; Fadeev, A.G.; Qi, B.; Smela, E.; Mattes, B.R.; Ding, J.; Spinks, G.M.; Mazurkiewicz, J.; Zhou, D.; Wallace, G.G.; et al. Use of Ionic Liquids for π-Conjugated Polymer Electrochemical Devices. *Science* **2002**, *297*, 983–987. [CrossRef] [PubMed]
43. Mondal, S.; Yoshida, T.; Higuchi, M. Electrochromic devices using Fe(II)-based metallo-supramolecular polymer: Introduction of ionic liquid as electrolyte to enhance the thermal stability. *J. Soc. Inf. Disp.* **2019**, *27*, 661–666. [CrossRef]
44. Lu, H.-C.; Kao, S.-Y.; Yu, H.-F.; Chang, T.-H.; Kung, C.-W.; Ho, K.-C. Achieving Low-Energy Driven Viologens-Based Electrochromic Devices Utilizing Polymeric Ionic Liquids. *ACS Appl. Mater. Interfaces* **2016**, *8*, 30351–30361. [CrossRef] [PubMed]
45. Yu, H.-F.; Li, C.-T.; Ho, K.-C. Stable viologen-based electrochromic devices: Control of Coulombic interaction using multifunctional polymeric ionic liquid membranes. *Sol. Energy Mater. Sol. Cells* **2022**, *250*, 112072. [CrossRef]
46. Wang, Y.-L.; Li, B.; Laaksonen, A. Coarse-grained simulations of ionic liquid materials: From monomeric ionic liquids to ionic liquid crystals and polymeric ionic liquids. *Phys. Chem. Chem. Phys.* **2021**, *23*, 19435–19456. [CrossRef] [PubMed]
47. Oke, E.A.; Oluyinka, O.A.; Afolabi, S.D.; Ibe, K.K.; Raheem, S.A. Latest insights on technologies for halides and halogenated compounds extraction/abatement from water and wastewater: Challenges and future perspectives. *J. Water Process Eng.* **2023**, *53*, 103724. [CrossRef]
48. Zaidi, S.S.H.; Li, X. Li–O2/Air Batteries Using Ionic Liquids—A Comprehensive Review. *Adv. Energy Mater.* **2023**, *13*, 2300985. [CrossRef]
49. Khan, A.S.; Ibrahim, T.H.; Jabbar, N.A.; Khamis, M.I.; Nancarrow, P.; Mjalli, F.S. Ionic liquids and deep eutectic solvents for the recovery of phenolic compounds: Effect of ionic liquids structure and process parameters. *RSC Adv.* **2021**, *11*, 12398–12422. [CrossRef] [PubMed]
50. Oke, E.A.; Ijardar, S.P. Insights into the separation of metals, dyes and pesticides using ionic liquid based aqueous biphasic systems. *J. Mol. Liq.* **2021**, *334*, 116027. [CrossRef]
51. Qian, W.; Texter, J.; Yan, F. Frontiers in poly(ionic liquid)s: Syntheses and applications. *Chem. Soc. Rev.* **2017**, *46*, 1124–1159. [CrossRef]
52. Md Moshikur, R.; Goto, M. Pharmaceutical Applications of Ionic Liquids: A Personal Account. *Chem. Rec.* **2023**, *23*, e202300026. [CrossRef] [PubMed]
53. Wang, X.; Hu, X.; Zhang, D.; Zhang, Y.; Xu, H.; Sun, Y.; Gu, X.; Luo, J.; Gao, B. Environmental applications and toxicity of ionic liquids. *J. Environ. Chem. Eng.* **2024**, *12*, 114638. [CrossRef]
54. Liu, S.; Wu, Y.; Jiang, L.; Xie, W.; Davis, B.; Wang, M.; Zhang, L.; Liu, Y.; Xing, S.; Dickey, M.D.; et al. Highly Stretchable, Tissue-like Ag Nanowire-Enhanced Ionogel Nanocomposites as an Ionogel-Based Wearable Sensor for Body Motion Monitoring. *ACS Appl. Mater. Interfaces* **2024**, *16*, 46538–46547. [CrossRef] [PubMed]
55. Wang, Z.; Si, Y.; Zhao, C.; Yu, D.; Wang, W.; Sun, G. Flexible and Washable Poly(Ionic Liquid) Nanofibrous Membrane with Moisture Proof Pressure Sensing for Real-Life Wearable Electronics. *ACS Appl. Mater. Interfaces* **2019**, *11*, 27200–27209. [CrossRef] [PubMed]

56. Chen, C.; Ying, W.B.; Li, J.; Kong, Z.; Li, F.; Hu, H.; Tian, Y.; Kim, D.H.; Zhang, R.; Zhu, J. A Self-Healing and Ionic Liquid Affiliative Polyurethane toward a Piezo 2 Protein Inspired Ionic Skin. *Adv. Funct. Mater.* **2022**, *32*, 2106341. [CrossRef]
57. Cai, Y.; Hou, Y.; Lu, Y.; Zhang, Q.; Yan, Z.; Chen, J. Ionic Liquid Electrolyte with Weak Solvating Molecule Regulation for Stable Li Deposition in High-Performance Li-O_2 Batteries. *Angew. Chem. Int. Ed.* **2023**, *62*, e202218014. [CrossRef] [PubMed]
58. Liu, K.; Wang, Z.; Shi, L.; Jungsuttiwong, S.; Yuan, S. Ionic liquids for high performance lithium metal batteries. *J. Energy Chem.* **2021**, *59*, 320–333. [CrossRef]
59. Francis, C.F.J.; Kyratzis, I.L.; Best, A.S. Lithium-Ion Battery Separators for Ionic-Liquid Electrolytes: A Review. *Adv. Mater.* **2020**, *32*, 1904205. [CrossRef] [PubMed]
60. Wang, Y.; Xue, K.; Zhang, X.; Zhang, X.; Ma, P.; Yang, B.; Xu, S.; Lang, J. High-voltage electrochemical double layer capacitors enabled by polymeric ionic liquid. *Electrochim. Acta* **2023**, *441*, 141829. [CrossRef]
61. Eftekhari, A. Supercapacitors utilising ionic liquids. *Energy Storage Mater.* **2017**, *9*, 47–69. [CrossRef]
62. Feng, J.; Wang, Y.; Xu, Y.; Sun, Y.; Tang, Y.; Yan, X. Ion regulation of ionic liquid electrolytes for supercapacitors. *Energy Environ. Sci.* **2021**, *14*, 2859–2882. [CrossRef]
63. Nakamoto, H.; Noda, A.; Hayamizu, K.; Hayashi, S.; Hamaguchi, H.-o.; Watanabe, M. Proton-Conducting Properties of a Brønsted Acid—Base Ionic Liquid and Ionic Melts Consisting of Bis(trifluoromethanesulfonyl)imide and Benzimidazole for Fuel Cell Electrolytes. *J. Phys. Chem. C* **2007**, *111*, 1541–1548. [CrossRef]
64. Elwan, H.A.; Thimmappa, R.; Mamlouk, M.; Scott, K. Applications of poly ionic liquids in proton exchange membrane fuel cells: A review. *J. Power Sources* **2021**, *510*, 230371. [CrossRef]
65. Hou, H.; Schütz, H.M.; Giffin, J.; Wippermann, K.; Gao, X.; Mariani, A.; Passerini, S.; Korte, C. Acidic Ionic Liquids Enabling Intermediate Temperature Operation Fuel Cells. *ACS Appl. Mater. Interfaces* **2021**, *13*, 8370–8382. [CrossRef] [PubMed]
66. Nancarrow, P.; Al-Othman, A.; Mital, D.K.; Döpking, S. Comprehensive analysis and correlation of ionic liquid conductivity data for energy applications. *Energy* **2021**, *220*, 119761. [CrossRef]
67. Lu, W.; Fadeev, A.G.; Qi, B.; Mattes, B.R. Fabricating Conducting Polymer Electrochromic Devices Using Ionic Liquids. *J. Electrochem. Soc.* **2004**, *151*, H33. [CrossRef]
68. Kim, H.; Kim, K.; Choi, D.; Lee, C.S. Evaluation of a reliable electrochromic device based on PEDOT:PSS-TiO 2 heterostructure fabricated at low temperature. *Ionics* **2017**, *23*, 2465–2474. [CrossRef]
69. Rochefort, D. Enabling new electrochemical methods with redox-active ionic liquids. *Curr. Opin. Electrochem.* **2019**, *15*, 125–132. [CrossRef]
70. Sun, L.; Zhuo, K.; Chen, Y.; Du, Q.; Zhang, S.; Wang, J. Ionic Liquid-Based Redox Active Electrolytes for Supercapacitors. *Adv. Funct. Mater.* **2022**, *32*, 2203611. [CrossRef]
71. Tahara, H.; Baba, R.; Iwanaga, K.; Sagara, T.; Murakami, H. Electrochromism of a Bipolar Reversible Redox-Active Ferrocene-Viologen Linked Ionic Liquid. *Chem. Commun.* **2017**, *53*, 2455–2458. [CrossRef]
72. Zhao, J.; Chen, Q.; Wang, Z.; Zheng, J.; Xu, C. All-ionic liquid electrochromic devices based on viologen-type and ferrocene-type room-temperature ionic liquids with temperature adaptability and environmental friendliness. *Sol. Energy Mater. Sol. Cells* **2024**, *271*, 112862. [CrossRef]
73. Branco, A.; Branco, L.C.; Pina, F. Electrochromic and magnetic ionic liquids. *Chem. Commun.* **2011**, *47*, 2300–2302. [CrossRef]
74. Branco, A.; Belchior, J.; Branco, L.C.; Pina, F. Intrinsically electrochromic ionic liquids based on vanadium oxides: Illustrating liquid electrochromic cells. *RSC Adv.* **2013**, *3*, 25627–25630. [CrossRef]
75. Jordão, N.; Cruz, H.; Branco, A.; Pina, F.; Branco, L.C. Electrochromic Devices Based on Disubstituted Oxo-Bipyridinium Ionic Liquids. *ChemPlusChem* **2015**, *80*, 202–208. [CrossRef]
76. Hwang, E.; Seo, S.; Bak, S.; Lee, H.; Min, M.; Lee, H. An Electrolyte-Free Flexible Electrochromic Device Using Electrostatically Strong Graphene Quantum Dot–Viologen Nanocomposites. *Adv. Mater.* **2014**, *26*, 5129–5136. [CrossRef] [PubMed]
77. Lu, H.-C.; Kao, S.-Y.; Chang, T.-H.; Kung, C.-W.; Ho, K.-C. An electrochromic device based on Prussian blue, self-immobilized vinyl benzyl viologen, and ferrocene. *Sol. Energy Mater. Sol. Cells* **2016**, *147*, 75–84. [CrossRef]
78. Gélinas, B.; Das, D.; Rochefort, D. Air-Stable, Self-Bleaching Electrochromic Device Based on Viologen- and Ferrocene-Containing Triflimide Redox Ionic Liquids. *ACS Appl. Mater. Interfaces* **2017**, *9*, 28726–28736. [CrossRef] [PubMed]
79. Tahara, H.; Uranaka, K.; Hirano, M.; Ikeda, T.; Sagara, T.; Murakami, H. Electrochromism of Ferrocene- and Viologen-Based Redox-Active Ionic Liquids Composite. *ACS Appl. Mater. Interfaces* **2018**, *11*, 1–6. [CrossRef] [PubMed]
80. Song, R.; Li, G.; Zhang, Y.; Rao, B.; Xiong, S.; He, G. Novel electrochromic materials based on chalcogenoviologens for smart windows, E-price tag and flexible display with improved reversibility and stability. *Chem. Eng. J.* **2021**, *422*, 130057. [CrossRef]
81. Fan, M.-S.; Lee, C.-P.; Vittal, R.; Ho, K.-C. A novel ionic liquid with stable radical as the electrolyte for hybrid type electrochromic devices. *Sol. Energy Mater. Sol. Cells* **2017**, *166*, 61–68. [CrossRef]
82. Kim, J.; Kim, D.; Jang, H.; Auh, Y.; Kim, B.; Kim, E. Transparent photo-electrochromic capacitive windows with a Bi-dopant redox ionic liquids. *Chem. Eng. J.* **2022**, *450*, 138081. [CrossRef]

83. Bai, Z.; Wu, X.; Fang, R.; Lu, Z.; Hou, C.; Zhang, Q.; Li, Y.; Li, K.; Wang, H. Divalent Viologen Cation-Based Ionogels Facilitate Reversible Intercalation of Anions in PProDOT-Me_2 for Flexible Electrochromic Displays. *Adv. Funct. Mater.* **2024**, *34*, 2312587. [CrossRef]
84. Wu, Y.; Li, Y.; Wang, Y.; Liu, Q.; Chen, Q.; Chen, M. Advances and prospects of PVDF based polymer electrolytes. *J. Energy Chem.* **2022**, *64*, 62–84. [CrossRef]
85. Gao, K.; Ju, S.; Li, S.; Zhang, S.; Liu, J.; Yang, T.; Lv, J.; Yu, W.; Zhang, Z. Decoupling Electrochromism and Energy Storage for Flexible Quasi-Solid-State Aqueous Electrochromic Batteries with High Energy Density. *ACS Nano* **2023**, *17*, 18359–18371. [CrossRef] [PubMed]
86. Xu, F.; Li, H.; Li, Y. Sea Cucumber-Inspired Polyurethane Demonstrating Record-Breaking Mechanical Properties in Room-Temperature Self-Healing Ionogels. *Adv. Mater.* **2024**, *36*, 2412317. [CrossRef]
87. Leones, R.; Sabadini, R.C.; Sentanin, F.C.; Esperança, J.M.S.S.; Pawlicka, A.; Silva, M.M. Polymer electrolytes for electrochromic devices through solvent casting and sol-gel routes. *Sol. Energy Mater. Sol. Cells* **2017**, *169*, 98–106. [CrossRef]
88. Danine, A.; Manceriu, L.; Fargues, A.; Rougier, A. Eco-friendly redox mediator gelatin-electrolyte for simplified TiO2-viologen based electrochromic devices. *Electrochim. Acta* **2017**, *258*, 200–207. [CrossRef]
89. Alves, R.; Fidalgo-Marijuan, A.; Campos-Arias, L.; Gonçalves, R.; Silva, M.M.; Del Campo, F.J.; Costa, C.M.; Lanceros-Mendez, S. Solid Polymer Electrolytes Based on Gellan Gum and Ionic Liquid for Sustainable Electrochromic Devices. *ACS Appl. Mater. Interfaces* **2022**, *14*, 15494–15503. [CrossRef]
90. Alves, R.; Fidalgo-Marijuan, A.; Salado, M.; Gonçalves, R.; Silva, M.M.; Bazán, B.; del Campo, F.J.; Costa, C.M.; Lanceros-Mendez, S. Agar-Based Solid Polymer Electrolyte-Containing Ionic Liquid for Sustainable Electrochromic Devices. *ACS Sustain. Chem. Eng.* **2023**, *11*, 16575–16584. [CrossRef]
91. Serra, J.P.; Salado, M.; Correia, D.M.; Gonçalves, R.; Del Campo, F.J.; Lanceros-Mendez, S.; Costa, C.M. High-Performance Sustainable Electrochromic Devices Based on Carrageenan Solid Polymer Electrolytes with Ionic Liquid. *ACS Appl. Eng. Mater.* **2023**, *1*, 1416–1425. [CrossRef]
92. Zhang, H.; Shi, W.; Cheng, H.; Chen, S.; Wang, L. Effect of ionic liquid on crystallization kinetics and crystal form transition of poly(vinylidene fluoride) blends. *J. Therm. Anal. Calorim.* **2018**, *132*, 1153–1165. [CrossRef]
93. Marcilla, R.; Alcaide, F.; Sardon, H.; Pomposo, J.A.; Pozo-Gonzalo, C.; Mecerreyes, D. Tailor-made polymer electrolytes based upon ionic liquids and their application in all-plastic electrochromic devices. *Electrochem. Commun.* **2006**, *8*, 482–488. [CrossRef]
94. Pozo-Gonzalo, C.; Mecerreyes, D.; Pomposo, J.A.; Salsamendi, M.; Marcilla, R.; Grande, H.; Vergaz, R.; Barrios, D.; Sánchez-Pena, J.M. All-plastic electrochromic devices based on PEDOT as switchable optical attenuator in the near IR. *Sol. Energy Mater. Sol. Cells* **2008**, *92*, 101–106. [CrossRef]
95. Poh, W.C.; Eh, A.L.-S.; Wu, W.; Guo, X.; Lee, P.S. Rapidly Photocurable Solid-State Poly(ionic liquid) Ionogels For Thermally Robust and Flexible Electrochromic Devices. *Adv. Mater.* **2022**, *34*, 2206952. [CrossRef] [PubMed]
96. Chen, F.; Ren, Y.; Guo, J.; Yan, F. Thermo- and electro-dual responsive poly(ionic liquid) electrolyte based smart windows. *Chem. Commun.* **2017**, *53*, 1595–1598. [CrossRef]
97. Rathod, P.V.; Puguan, J.M.C.; Kim, H. Self-bleaching dual responsive poly(ionic liquid) with optical bistability toward climate-adaptable solar modulation. *Chem. Eng. J.* **2021**, *422*, 130065. [CrossRef]
98. Sun, F.; Sik Kim, K.; Yeon Eom, S.; Won Choi, J.; Kim, E.J.; Abdul Raheem, A.; Jeon, S.-P.; Gi Seong, D.; Ahn, S.-K.; Kyu Park, S.; et al. Stretchable interconnected modular electrochromic devices enabled by self-healing, self-adhesive, and ion-conducting polymer electrolyte. *Chem. Eng. J.* **2024**, *494*, 153107. [CrossRef]
99. Su, X.; Xu, X.-P.; Ji, Z.-Q.; Wu, J.; Ma, F.; Fan, L.-Z. Polyethylene Oxide-Based Composite Solid Electrolytes for Lithium Batteries: Current Progress, Low-Temperature and High-Voltage Limitations, and Prospects. *Electrochem. Energy Rev.* **2024**, *7*, 2. [CrossRef]
100. Ding, P.; Lin, Z.; Guo, X.; Wu, L.; Wang, Y.; Guo, H.; Li, L.; Yu, H. Polymer electrolytes and interfaces in solid-state lithium metal batteries. *Mater. Today* **2021**, *51*, 449–474. [CrossRef]
101. Brazier, A.; Appetecchi, G.B.; Passerini, S.; Surca Vuk, A.; Orel, B.; Donsanti, F.; Decker, F. Ionic liquids in electrochromic devices. *Electrochim. Acta* **2007**, *52*, 4792–4797. [CrossRef]
102. Bircan, H.; Seshadri, V.; Padilla, J.; Invernale, M.; Otero, T.F.; Sotzing, G.A. Use of polymer/ionic liquid plasticizers as gel electrolytes in electrochromic devices. *J. Phys. Conf. Ser.* **2008**, *127*, 012011. [CrossRef]
103. Desai, S.; Shepherd, R.L.; Innis, P.C.; Murphy, P.; Hall, C.; Fabretto, R.; Wallace, G.G. Gel electrolytes with ionic liquid plasticiser for electrochromic devices. *Electrochim. Acta* **2010**, *56*, 4408–4413. [CrossRef]
104. Zanarini, S.; Garino, N.; Nair, J.R.; Francia, C.; Wojcik, P.J.; Pereira, L.; Fortunato, E.; Martins, R.; Bodoardo, S.; Penazzi, N. Contrast Enhancement in Polymeric Electrochromic Devices Encompassing Room Temperature Ionic Liquids. *Int. J. Electrochem. Sci.* **2014**, *9*, 1650–1662. [CrossRef]
105. Kim, J.W.; Myoung, J.M. Flexible and Transparent Electrochromic Displays with Simultaneously Implementable Subpixelated Ion Gel-Based Viologens by Multiple Patterning. *Adv. Funct. Mater.* **2019**, *29*, 1808911. [CrossRef]

106. Chaudhary, A.; Poddar, M.; Pathak, D.K.; Misra, R.; Kumar, R. Electron Donor Ferrocenyl Phenothiazine: Counter Ion for Improving All-Organic Electrochromism. *ACS Appl. Electron. Mater.* **2020**, *2*, 2994–3000. [CrossRef]
107. Pathak, D.K.; Chaudhary, A.; Tanwar, M.; Goutam, U.K.; Kumar, R. Nano-cobalt oxide/viologen hybrid solid state device: Electrochromism beyond chemical cell. *Appl. Phys. Lett.* **2020**, *116*, 141901. [CrossRef]
108. Fang, R.; Bai, Z.; Wu, X.; Fan, Q.; Bao, B.; Hou, C.; Zhang, Q.; Li, Y.; Li, K.; Wang, H. Electro-Induced Self-Reduction TiO_2 in Viologen-Based Ionogels for Multi-Color Electrochromic Displays. *Adv. Opt. Mater.* **2024**, *12*, 2400498. [CrossRef]
109. Gong, H.; Li, A.; Fu, G.; Zhang, M.; Zheng, Z.; Zhang, Q.; Zhou, K.; Liu, J.; Wang, H. Ultrathin flexible electrochromic devices enabled by highly transparent ion-conducting films. *J. Mater. Chem. A* **2023**, *11*, 8939–8949. [CrossRef]
110. Yang, G.; Li, X.; He, Y.; Ma, J.; Ni, G.; Zhou, S. From nano to micro to macro: Electrospun hierarchically structured polymeric fibers for biomedical applications. *Prog. Polym. Sci.* **2018**, *81*, 80–113. [CrossRef]
111. Jia, P.; Yee, W.A.; Xu, J.; Toh, C.L.; Ma, J.; Lu, X. Thermal stability of ionic liquid-loaded electrospun poly(vinylidene fluoride) membranes and its influences on performance of electrochromic devices. *J. Membr. Sci.* **2011**, *376*, 283–289. [CrossRef]
112. Zhou, R.; Liu, W.; Kong, J.; Zhou, D.; Ding, G.; Leong, Y.W.; Pallathadka, P.K.; Lu, X. Chemically cross-linked ultrathin electrospun poly(vinylidene fluoride-co-hexafluoropropylene) nanofibrous mats as ionic liquid host in electrochromic devices. *Polymer* **2014**, *55*, 1520–1526. [CrossRef]
113. Zhou, R.; Pramoda, K.P.; Liu, W.; Zhou, D.; Ding, G.; He, C.; Leong, Y.W.; Lu, X. Electrospun poly(vinylidene fluoride) copolymer/octahydroxy-polyhedral oligomeric silsesquioxane nanofibrous mats as ionic liquid host: Enhanced salt dissociation and its function in electrochromic device. *Electrochim. Acta* **2014**, *146*, 224–230. [CrossRef]
114. Zhou, R.; Liu, W.; Yao, X.; Leong, Y.W.; Lu, X. Poly(vinylidene fluoride) nanofibrous mats with covalently attached SiO_2 nanoparticles as an ionic liquid host: Enhanced ion transport for electrochromic devices and lithium-ion batteries†. *J. Mater. Chem. A* **2015**, *3*, 16040–16049. [CrossRef]
115. Zhou, R.; Liu, W.; Leong, Y.W.; Xu, J.; Lu, X. Sulfonic Acid- and Lithium Sulfonate-Grafted Poly(Vinylidene Fluoride) Electrospun Mats As Ionic Liquid Host for Electrochromic Device and Lithium-Ion Battery. *ACS Appl. Mater. Interfaces* **2015**, *7*, 16548–16557. [CrossRef]
116. Moon, H.C.; Kim, C.-H.; Lodge, T.P.; Frisbie, C.D. Multicolored, Low-Power, Flexible Electrochromic Devices Based on Ion Gels. *ACS Appl. Mater. Interfaces* **2016**, *8*, 6252–6260. [CrossRef] [PubMed]
117. Oh, H.; Seo, D.G.; Yun, T.Y.; Kim, C.Y.; Moon, H.C. Voltage-Tunable Multicolor, Sub-1.5 V, Flexible Electrochromic Devices Based on Ion Gels. *ACS Appl. Mater. Interfaces* **2017**, *9*, 7658–7665. [CrossRef]
118. Xing, G.; Kuang, G.; Tao, Y.; Wang, Y.; Kang, Y.; Guo, Y.; Zhang, S. Ultra-strong ionic liquid-based polymer composite electrolyte for high performance electrochromic devices. *Sol. Energy Mater. Sol. Cells* **2022**, *248*, 111968. [CrossRef]
119. Kavanagh, A.; Copperwhite, R.; Oubaha, M.; Owens, J.; McDonagh, C.; Diamond, D.; Byrne, R. Photo-patternable hybrid ionogels for electrochromic applications. *J. Mater. Chem.* **2011**, *21*, 8687–8693. [CrossRef]
120. Kavanagh, A.; Fraser, K.J.; Byrne, R.; Diamond, D. An Electrochromic Ionic Liquid: Design, Characterization, and Performance in a Solid-State Platform. *ACS Appl. Mater. Interfaces* **2012**, *5*, 55–62. [CrossRef] [PubMed]
121. Kim, Y.M.; Lee, W.Y.; Choi, W.Y.; Moon, H.C. Impact of Chain Flexibility of Copolymer Gelators on Performance of Ion Gel Electrolytes for Functional Electrochemical Devices. *J. Ind. Eng. Chem.* **2020**, *90*, 341–350. [CrossRef]
122. Pande, G.K.; Choi, J.H.; Lee, J.-E.; Kim, Y.E.; Choi, J.H.; Choi, H.W.; Chae, H.G.; Park, J.S. Octa-Viologen Substituted Polyhedral Oligomeric Silsesquioxane Exhibiting Outstanding Electrochromic Performances. *Chem. Eng. J.* **2020**, *393*, 124690. [CrossRef]
123. Chen, W.; Liu, S.; Guo, L.; Zhang, G.; Zhang, H.; Cao, M.; Wu, L.; Xiang, T.; Peng, Y. A Self-Healing Ionic Liquid-Based Ionically Cross-Linked Gel Polymer Electrolyte for Electrochromic Devices. *Polymers* **2021**, *13*, 742. [CrossRef] [PubMed]
124. Jang, Y.J.; Kim, S.Y.; Kim, Y.M.; Lee, J.K.; Moon, H.C. Unveiling the diffusion-controlled operation mechanism of all-in-one type electrochromic supercapacitors: Overcoming slow dynamic response with ternary gel electrolytes. *Energy Storage Mater.* **2021**, *43*, 20–29. [CrossRef]
125. Xing, G.; Wu, L.; Kuang, G.; Ma, T.; Chen, Z.; Tao, Y.; Kang, Y.; Zhang, S. Integration of high surface-energy electrochromic polymer with in-situ polymerized quasi-solid electrolyte for efficient electrochromism. *Electrochim. Acta* **2022**, *432*, 141216. [CrossRef]
126. Zhang, Y.; Guo, M.; Li, G.; Chen, X.; Liu, Z.; Shao, J.; Huang, Y.; He, G. Ultrastable Viologen Ionic Liquids-Based Ionogels for Visible Strain Sensor Integrated with Electrochromism, Electrofluorochromism, and Strain Sensing. *CCS Chem.* **2022**, *5*, 1917–1930. [CrossRef]
127. Zhou, X.; Zhou, K.; Tang, L.; Chen, Z.; Hu, Q.; Gao, J.; Zhang, Y.; Zhang, J.; Zhang, S. A Strong and Highly Transparent Ionogel Electrolyte Enabled by In Situ Polymerization-Induced Microphase Separation for High-Performance Electrochromic Devices. *Macromol. Rapid Commun.* **2024**, *45*, 2300736. [CrossRef]
128. Sydam, R.; Deepa, M.; Srivastava, A.K. Electrochromic device response controlled by an in situ polymerized ionic liquid based gel electrolyte. *RSC Adv.* **2012**, *2*, 9011–9021. [CrossRef]

129. He, X.; Cheng, H.; Yue, S.; Ouyang, J. Quasi-solid state nanoparticle/(ionic liquid) gels with significantly high ionic thermoelectric properties. *J. Mater. Chem. A* **2020**, *8*, 10813–10821. [CrossRef]
130. Zhang, F.; Dong, G.; Liu, J.; Ye, S.; Diao, X. Polyvinyl butyral-based gel polymer electrolyte films for solid-state laminated electrochromic devices. *Ionics* **2017**, *23*, 1879–1888. [CrossRef]
131. Okutan, M.; Evecan, D.; Yıldırım, S.; Özkan Zayim, E.; Deligöz, H. Investigating the effect of electrolyte types with various ionic liquids on the electrochromic performance of PEDOT:PSS based LbL multilayers. *Microelectron. Eng.* **2020**, *234*, 111454. [CrossRef]
132. Koo, J.; Amoli, V.; Kim, S.Y.; Lee, C.; Kim, J.; Park, S.-M.; Kim, J.; Ahn, J.M.; Jung, K.J.; Kim, D.H. Low-power, deformable, dynamic multicolor electrochromic skin. *Nano Energy* **2020**, *78*, 105199. [CrossRef]
133. Oh, S.-J.; Bae, J.W. All-in-One plasticized Ionogel-based stretchable electrochromic devices. *Chem. Eng. J.* **2023**, *467*, 143367. [CrossRef]
134. Li, J.; Liu, W.; Wei, Y.; Yan, Y. SiO2: A Novel Electrolyte for High-Performance All-Solid-State Electrochromic Devices. *ACS Sustain. Chem. Eng.* **2023**, *11*, 824–830. [CrossRef]
135. Wang, H.; Wang, J.; Shi, Q.; Su, Y.; Tang, P.; Huang, S.; Lin, S.; Dai, M. Influence of LiPON thickness on the electro-optical performance of inorganic all-solid-state electrochromic devices. *Sol. Energy Mater. Sol. Cells* **2023**, *251*, 112140. [CrossRef]
136. Song, Y.; Cheng, B.; Cheng, H.; Meng, Z.; Liu, D. All-Solid-State Infrared Electrochromic Devices Based on Thin Metal Films. *ACS Appl. Mater. Interfaces* **2024**, *16*, 35372–35380. [CrossRef]
137. Jia Hanxiang, S.Z.H.A.J.I.N.P.C.A.O.X. Sandwich Structured Electrolyte of High Sputtering Efficiency for All-solid-state Electrochromic Devices by Optical Design. *J. Inorg. Mater.* **2021**, *36*, 479–484. [CrossRef]
138. Lin, C.-C.; Chen, P.-H.; Chen, M.-C.; Wang, M.-C.; Yang, C.-C.; Huang, H.-C.; Wu, C.-W.; Chou, S.-Y.; Tsai, T.-M.; Chang, T.-C. Improved diffusion and storage of lithium ions via recrystallization induced conducting pathways in a li:Ta2O5-based electrolyte for all-solid-state electrochromic devices with enhanced performance. *Nanotechnology* **2022**, *33*, 275711. [CrossRef]
139. Chen, H.-C.; Chen, Y.-R.; Liu, T.-F. Photoelectrochemical performance of a UV-cured all-solid-state complementary ITO/WO_3/Ta_2O_5/electrolyte/NiO/ITO electrochromic device deposited by ion-beam assisted electron-beam evaporation. *Electrochim. Acta* **2021**, *382*, 138355. [CrossRef]
140. Zhang, T.; Mu, X.; Li, Y.; Cong, S.; Zheng, S.; Huang, R.; Geng, F.; Zhao, Z. Optical-Cavity-Incorporated Colorful All-Solid-State Electrochromic Devices for Dual Anti-Counterfeiting. *Adv. Mater.* **2024**, *36*, 2402670. [CrossRef]
141. Zhang, J.; Tu, J.P.; Xia, X.H.; Qiao, Y.; Lu, Y. An all-solid-state electrochromic device based on NiO/WO_3 complementary structure and solid hybrid polyelectrolyte. *Sol. Energy Mater. Sol. Cells* **2009**, *93*, 1840–1845. [CrossRef]
142. Li, N.; Bao, S.; Zhang, Q.; Xie, L.; Jin, P. Wide-Band Reflection-Type, All-Solid-State Switchable Mirror Composed of WO_3–Mg_4Ni Thin Films and Proton-Conductive Polymer Electrolytes. *ChemistrySelect* **2018**, *3*, 7507–7512. [CrossRef]
143. Rong, D.; Wu, Y.; Wang, W.; Shang, X.; Wang, S.; Wang, S. Polyvinyl Butyral Solid Electrolyte Film and Its Electrochromic Laminated Safety Glass. *ACS Appl. Mater. Interfaces* **2024**, *16*, 65394–65401. [CrossRef] [PubMed]
144. Lin, C.-L.; Chen, A. Electrochromic devices composed of polyaniline and tungsten trioxide thin films with succinonitrile/polyethylene glycol solid-state composite electrolyte. *Surf. Coat. Technol.* **2022**, *434*, 128124. [CrossRef]
145. Liu, H.; Wang, M.; Wang, X.; Pawlicka, A.; Diao, X. In situ synthesis and structural morphology analysis of 3D porous hierarchical V_2O_5 films for transmissive-to-black all-solid-state electrochromic devices. *Chem. Eng. J.* **2024**, *500*, 156657. [CrossRef]
146. Vijayaraghavan, S.; Raj, N.; Kumar, M.M.; Mohan, P.A.; Ak, N.K. Ionic conductivity and dielectric characteristics of a Li incorporated PVA electrolyte membrane and a study of a fully solid-state electrochromic device based on it. *Electrochim. Acta* **2024**, *504*, 144948. [CrossRef]
147. Ganesh, G.P.T.; Deb, B. Designing an All-Solid-State Tungsten Oxide Based Electrochromic Switch with a Superior Cycling Efficiency. *Adv. Mater. Interfaces* **2017**, *4*, 1700124. [CrossRef]
148. Wu, X.; Wang, Q.; Zhang, W.; Wang, Y.; Chen, W. Preparation of all-solid-state supercapacitor integrated with energy level indicating functionality. *Synth. Met.* **2016**, *220*, 494–501. [CrossRef]
149. Du, Q.; Fu, X.; Liu, S.; Niu, L. The effect of ionic liquid fragment on the performance of polymer electrolytes. *Polym. Int.* **2012**, *61*, 222–227. [CrossRef]
150. Aubert, P.-H.; Argun, A.A.; Cirpan, A.; Tanner, D.B.; Reynolds, J.R. Microporous Patterned Electrodes for Color-Matched Electrochromic Polymer Displays. *Chem. Mater.* **2004**, *16*, 2386–2393. [CrossRef]
151. Rauh, R.D.; Wang, F.; Reynolds, J.R.; Meeker, D.L. High coloration efficiency electrochromics and their application to multi-color devices. *Electrochim. Acta* **2001**, *46*, 2023–2029. [CrossRef]
152. Mecerreyes, D.; Marcilla, R.; Ochoteco, E.; Grande, H.; Pomposo, J.A.; Vergaz, R.; Sánchez Pena, J.M. A simplified all-polymer flexible electrochromic device. *Electrochim. Acta* **2004**, *49*, 3555–3559. [CrossRef]
153. Tran-Van, F.; Beouch, L.; Vidal, F.; Yammine, P.; Teyssié, D.; Chevrot, C. Self-supported semi-interpenetrating polymer networks for new design of electrochromic devices. *Electrochim. Acta* **2008**, *53*, 4336–4343. [CrossRef]
154. De Paoli, M.A.; Casalbore-Miceli, G.; Girotto, E.M.; Gazotti, W.A. All polymeric solid state electrochromic devices. *Electrochim. Acta* **1999**, *44*, 2983–2991. [CrossRef]

155. Wang, J.; Zhao, Y.; Zhuo, K.; Lin, R. Viscosity Properties of Electrolytes in Propylene Carbonate Based Lithium Battery Electrolyte Solutions. *Z. Phys. Chem.* **2003**, *217*, 637–652. [CrossRef]
156. Yu, G.; Zhao, D.; Wen, L.; Yang, S.; Chen, X. Viscosity of ionic liquids: Database, observation, and quantitative structure-property relationship analysis. *AlChE J.* **2012**, *58*, 2885–2899. [CrossRef]
157. Eftekhari, A.; Liu, Y.; Chen, P. Different roles of ionic liquids in lithium batteries. *J. Power Sources* **2016**, *334*, 221–239. [CrossRef]
158. Simonis, E.D.; Blanchard, G.J. Evaluating the contributions to conductivity in room temperature ionic liquids. *Phys. Chem. Chem. Phys.* **2024**, *26*, 17048–17056. [CrossRef] [PubMed]
159. Wu, K.-J.; Luo, H.; Yang, L. Structure-based model for prediction of electrical conductivity of pure ionic liquids. *AlChE J.* **2016**, *62*, 3751–3762. [CrossRef]

Disclaimer/Publisher's Note: The statements, opinions and data contained in all publications are solely those of the individual author(s) and contributor(s) and not of MDPI and/or the editor(s). MDPI and/or the editor(s) disclaim responsibility for any injury to people or property resulting from any ideas, methods, instructions or products referred to in the content.

molecules

MDPI

Review

The Role of Ionic Liquids in Textile Processes: A Comprehensive Review

Anastasia Anceschi [1], Claudia Riccardi [2] and Alessia Patrucco [1,*]

[1] CNR-STIIMA, Italian National Research Council, Institute of Intelligent Industrial Technologies and Systems for Advanced Manufacturing, 13900 Biella, Italy; anastasia.anceschi@stiima.cnr.it
[2] Dipartimento di Fisica, Università di Milano-Bicocca, Piazza della Scienza 3, 20126 Milano, Italy; claudia.riccardi@unimib.it
* Correspondence: alessia.patrucco@stiima.cnr.it

Abstract

Thanks to their unique physicochemical properties, ionic liquids (ILs) have moved from niche academic interest to critical components in various industrial applications. The textile industry, facing significant environmental and economic pressures, has begun to explore ILs as sustainable alternatives to traditional solvents and chemicals. This review summarizes research on the use of ILs in various textile processes, including dyeing, finishing, and fiber recycling, where their high thermal stability, tunable solubility, and low volatility are exploited to reduce resource consumption and environmental impact. The discussion also extends to the integration of ILs in textile waste recycling, highlighting innovative approaches to fiber dissolution and regeneration aimed at circular economy goals. Despite these advances, challenges such as high production costs and scalability remain barriers to the widespread adoption of ILs in the textile sector. Addressing these barriers through continued research and development is essential to fully realize the potential of ILs for sustainable transformation in textiles.

Keywords: textile; ionic liquids; sustainability

1. Introduction

Twenty years ago, research into ionic liquids was a small area of academic interest, with only a limited number of scientists investigating salts with melting points close to room temperature. Today, there are over 125,000 scientific publications and 17,000 patent applications in the field of ionic liquids [1]. The first ionic liquids were reported in 1877 and were called "red oil". They were obtained as a separate phase in Friedel–Crafts reactions [2,3]. The substance was subsequently identified as a chloroaluminate with an alkylated aromatic cyclic cation [4]. Other early ionic liquids were identified at the turn of the century, including alkylpicolinium halides and quaternary anilinium salts [5,6]. These substances were also referred to as "intractable oils", indicating that a new phenomenon was emerging. From these early compounds, the history of these innovative compounds continued until 1943, when the scientist Barrer coined the first name to define them: ionic liquids [7]. The history of ionic liquids can be described in terms of "generations" [8]. Three distinct generations of ionic liquids can be distinguished, as summarized in Figure 1.

- First generation

The first known ionic liquid, ethylammonium nitrate, was identified by Walden [9]. However, the scientific community has identified a divergence in the attribution of the

initial synthesis of ionic liquids (ILs). Some experts ascribe the pioneering achievement of IL synthesis, specifically to Gabriel and Weiner, citing the 1888 synthesis of ethanolammonium nitrate [10]. This discrepancy stems from the reported melting point of the substance. While Walden's compound was found to have a melting point of 13–14 °C, Gabriel and Weiner's formulation possessed a melting point of over room temperature (around 50 °C). These findings signify the inception of the initial generation of ILs [8].

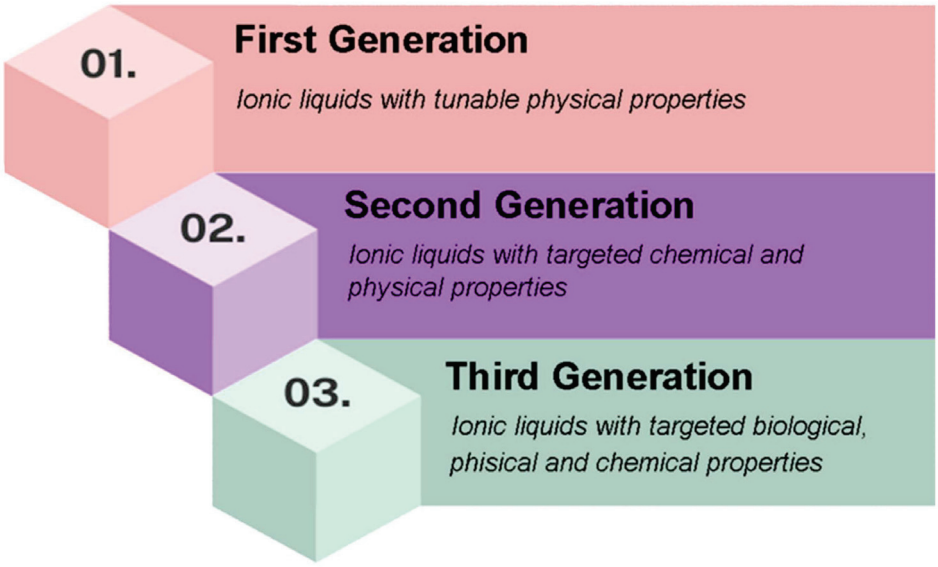

Figure 1. Ionic liquid generations.

Subsequently, a number of other ionic liquids were synthesized using a variety of anions and cations. In particular, the cations, including alkylpyridinium, alkylimidazolium, and dialkylimidazolium, have been the most extensively studied. For anions, chloroaluminate and metal halides have been the most widely used. This first generation of ionic liquids showed high reactivity with water and air, which required the use of inert conditions, making them unsuitable for use in open conditions [2].

- Second generation

To overcome the problem of high reactivity with water exhibited by the first generation of ionic liquids, the traditional anions were replaced by chloroaluminate anions, including Cl^-, Br^-, I^-, PF_6^-, BF_4^-, and $C_6H_5COO^-$, while the cations were replaced by ammonium and phosphonium-based cations, in addition to alkylpyridinium, alkylimidazolium, and dialkylimidazolium [11]. This second generation of ionic liquids has remarkable properties such as low melting point, low viscosity, and high solubility. This new class of ionic liquids has been rapidly adopted in the field of biocatalysis, leading to a significant increase in research activity in this area [12]. Despite the promising potential of the second generation of ionic liquids, they were found to have toxic properties and were associated with a significant financial burden in terms of production costs [13].

- Third generation

In order to improve environmental sustainability and reduce the financial burden associated with the synthesis of ionic liquids, the cations have predominantly been replaced by choline. However, for cations, a variety of alternative species were investigated, including amino acids, alkylphosphates, alkylsulfates, bis(trifluoromethanesulfonyl)amide (TFSI) [$(CF_3\ SO_2)_2\ N^-$], and sugars [14]. This third generation of ionic liquids exhibits remarkable properties that can be tailored based on the anions or cations used. In addition, this third generation of ionic liquids comprises a novel class of solvent system called deep eutectic

solvents (DES) [15]. These substances are essentially mixtures of salts, including choline chloride, alcohols, amides, carboxylic acids, amines, and urea.

The third generation of ionic liquids has excellent properties that make them suitable for exploitation for commercial use [14]. The potential use of ionic liquids has been explored in various fields, such as hydrogenation, oxidation, Diels-Alder reaction, electrochemical reactions, biocatalysis, nanomaterial synthesis, hydrogen storage, liquid mirror production, and separation processes [16–24]. Despite the potential benefits, the use of ionic liquids in some sectors, such as the textile industry, remains relatively limited and restricted to a narrow range of applications [25].

The textile industry is an important sector with a significant economic and environmental impact. Conventional textile production processes often involve the extensive use of water, energy, and chemicals, ultimately leading to environmental pollution and depletion of natural resources [26]. Ionic liquids, with distinctive properties such as low vapor pressure, high thermal stability, and tunable solubility, offer a compelling prospect as replacements for a range of textile applications. Accordingly, this review aims to assess the current state of research into the use of ionic liquids in the textile industry, with particular emphasis on their applications, benefits, challenges, and future developments.

2. Overview of Ionic Liquids

2.1. Structure of Ionic Liquids

The exact definition of ionic liquids remains controversial. The definition of ionic liquids has evolved over time. Historically, the term "room temperature ionic liquids" (RTILs) was used to refer to ionic liquids that are liquid at 0.1 MPa and at or below 100 °C, the boiling point of water. However, this definition has become less common as the field has expanded to include ionic liquids with a broader range of melting points and applications. In any case, ionic liquids are typically composed of asymmetric and univalent ions, which prevent tight crystal packing and consequently lower the melting point [27]. Therefore, the choice of cation and anion is an important consideration in the design of an ionic liquid. There are currently nearly 1000 ionic liquids documented in the literature, and the main cations and anions are shown in Figure 2.

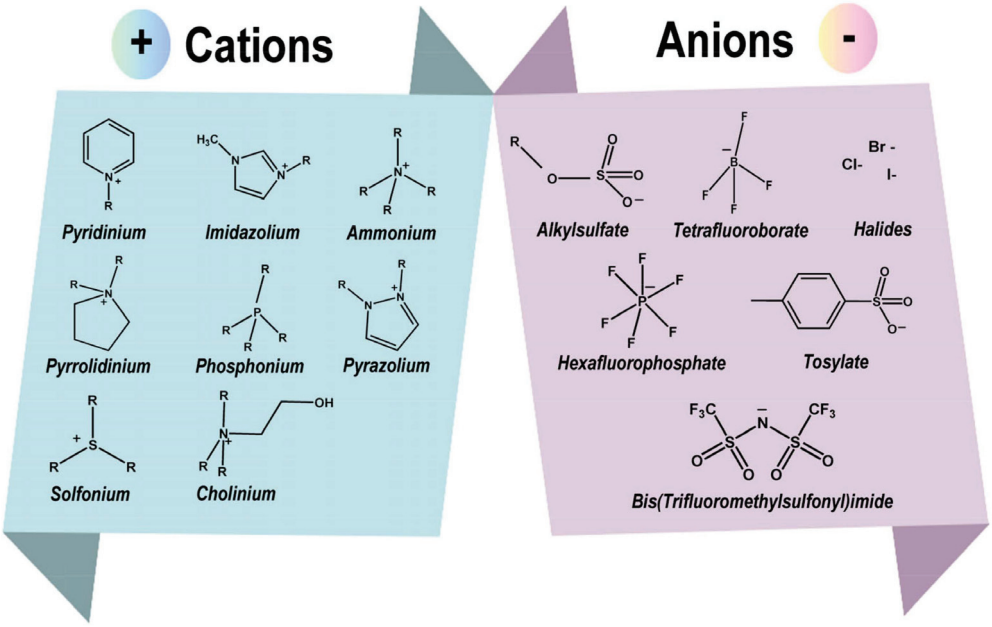

Figure 2. Common cations and anions that are present in ionic liquids.

The choice of cations appears to be limited in many organic chemistry groups, but they can be divided into two categories. The first category includes phosphonium, sulphonium, chloronium, and ammonium ions, which are classified as acyclic. The second class is classified as the cyclic group and includes molecules such as pyridinium, imidazolium, pyrazolium, and pyrrolidium ions [28]. For anions, the range of possibilities is wider, and the most commonly used anions are halides such as chloride and bromide, alkyl sulphate derivatives, thiocyanate, triflate, tosylate, and fluorophosphate [24]. The possible combinations of cations and anions are limitless, resulting in a wide range of ionic liquids that can be used in a variety of applications.

2.2. Properties of Ionic Liquids

Due to their unique properties, ionic liquids are attracting increasing interest as potential replacements for existing organic solvents. Among the most important properties of ionic liquids are the following. A brief illustration of the properties of ionic liquids is shown in Figure 3.

Figure 3. Common properties of ionic liquids.

- Low Volatility

The main advantage of ionic liquids is that they have negligible vapor pressure. This is a significant advantage over conventional organic solvents. This allows products to be removed by distillation without the risk of further contamination, reducing the risk of air pollution and occupational hazards [27].

- High Thermal Stability

Ionic liquids can withstand high temperatures, a significant advantage over traditional solvents. Ionic liquids have remarkable stability even at elevated temperatures and nonflammable properties, making them a viable alternative to traditional solvents in applications involving high temperatures and the possibility of explosions [29]. This includes the textile industry, where ionic liquids offer a safer alternative for use in various processes [30].

- Tunable Solubility

It is possible to alter the solvating properties of ionic liquids through appropriate modifications. Specifically, the physical, chemical, or biological properties of ionic liquids can be adjusted or modified by changing the ratio of cations to anions or by incorporating specific functionalities into the cations or anions. Finally, the combination of two or more ionic liquids can be used to achieve desired properties. As a result, ionic liquids offer a distinct advantage over conventional solvents in their ability to dissolve a wide range of organic and inorganic compounds [24].

- Recyclability

Due to their chemical stability, ionic liquids can be recycled and reused as solvents with excellent recovery rates. In addition, the use of ionic liquids as reaction media can facilitate the recycling and recovery of catalysts in chemical processes. Therefore, the use of ionic liquids can effectively reduce the generation of waste [31].

Summarizing, the excellent properties of ionic liquids are intrinsically linked to their unique structure–property relationships. Ionic liquids are composed entirely of ions, typically a bulky, asymmetrical cation paired with a smaller anion. This ionic composition disrupts lattice packing, leading to lower melting points and high fluidity at room temperature. Furthermore, the electrostatic interactions between ions confer high thermal stability, while their negligible vapor pressure stems from the strong Coulombic forces that prevent evaporation under normal conditions [32]. The tunable solubility of ILs is a particularly noteworthy property. By altering the cation or anion structure—such as incorporating functional groups (e.g., hydroxyl, alkyl, or aromatic groups)—researchers can modulate solvation properties, polarity, and hydrophilicity/hydrophobicity. For example, imidazolium-based ILs with longer alkyl chains exhibit enhanced solubility for nonpolar solutes, while ILs with functionalized anions can improve compatibility with polar compounds [33]. This structure–property relationship enables the customization of ionic liquids for specific applications, such as dye solubilization, fiber modification, or environmental remediation, making them versatile tools for the textile industry and beyond [34].

3. Applications of Ionic Liquids in Textile Processes

After a brief overview of ionic liquids and their properties, this section will examine the applications of ionic liquids in the textile industry. The textile industry is a major contributor to global pollution, with extensive use of water, energy, and chemicals. Conventional solvents used in textile processing are often toxic and nonbiodegradable, posing serious environmental risks. In light of these considerations, there has been a recent shift toward research into more sustainable alternatives. In this context, it is interesting to examine the applications of ionic liquids, which are increasingly being studied and used in the textile sector [35]. A summary of the textile sectors where the use of ionic liquids is beginning to attract attention is shown in Figure 4.

Figure 4. Sectors of the textile industry where ionic liquids are used.

3.1. Dyeing Processes

Dyeing is a key step in the textile manufacturing process. However, traditional dyeing techniques rely on extensive water and energy consumption, resulting in significant waste. Ionic liquids can offer an alternative solution, as they have been shown to provide several benefits when used in dyeing processes [35]. For example, they facilitate dye solubility as they are able to dissolve a wide range of dyes, including those that are poorly soluble in water. They also improve the durability of the dye, reducing the likelihood of fading over time and facilitating the dyeing process, reducing the time and energy required for production. From an economic and environmental perspective, ionic liquids can be a viable alternative to water as a solvent, significantly reducing water consumption and wastewater generation [6,35,36]. Their potential applications in the textile dyeing process are outlined in Table 1.

Table 1. Various applications of ionic liquids in textile dyeing processes.

Dye Type	Type of Material	Ionic Liquids	Dyeing Process	Process Condition	Role of Ionic Liquid	Reference
Acid dyes	Wool	Methylimidazolium-based ionic liquids Diethylethanolamine-based ionic liquids	Exhaustion	60 °C, 60 min	Pretreatment	[37]
	Polyamide 6.6	Methylimidazolium-based ionic liquids Diethylethanolamine-based ionic liquids	Exhaustion	80 °C, 45 min	Dyeing medium	[38]
	Silk	Methylimidazolium-based ionic liquids	Exhaustion	60 °C, 30 min	Pretreatment	[39]
	Cotton	Diethylethanolamine-based ionic liquids	/	/	Dyeing medium	[40]
	Polyester	Diethylethanolamine-based ionic liquids	/	/	Dyeing medium	[40]
	Polyacrylonitrile	Diethylethanolamine-based ionic liquids Imidazole-based ionic liquids	/	/	Dyeing medium	[40]

Table 1. *Cont.*

Dye Type	Type of Material	Ionic Liquids	Dyeing Process	Process Condition	Role of Ionic Liquid	Reference
Reactive dyes	m-aramid	Methylimidazolium-based ionic liquids	Exhaustion	180 °C, 60 min	Dyeing medium	[41]
	Wool	Methylimidazolium-based ionic liquids	Exhaustion	80 °C, 60 min	Pretreatment	[39]
	Silk	Methylimidazolium-based ionic liquids	Exhaustion	80 °C, 60 min	Pretreatment	[39]
	Cotton	Quaternary ammonium salt ionic liquids	Pad-dry-cure	60 °C, 10–20 min	Auxiliary	[36]
	Flax	Methylimidazolium-based ionic liquids	/	40–80 °C, 150 min	Auxiliary	[42]
Basic dyes	Polyacrylonitrile	Methylimidazolium-based ionic liquids	Exhaustion	85 °C, 50 min	Retardant	[43]
Disperse dyes	Polyester	Methylimidazolium-based ionic liquids	Open-vessel	95 °C	Additives	[35,44]
	Wool	Methylimidazolium-based ionic liquids	Open-vessel	95 °C	Additives	[35]
	Cotton	Methylimidazolium-based ionic liquids	Open-vessel	95 °C	Additives	[35]
Direct dyes	Cotton	Methylimidazolium-based ionic liquids	Impregnation	50 °C, 30 min	Dyeing medium	[44]

The underlying mechanisms by which ionic liquids (ILs) enhance textile dyeing processes are multifaceted. In particular, ionic liquids are used for:

- Dye Solubility: Ionic liquids exhibit remarkable solvation properties attributable to their ionic composition and tunable polarity. Imidazolium-based ionic liquids, for instance, effectively dissolve a wide range of dyes, including those sparingly soluble in water, by disrupting dye aggregates and enhancing molecular dispersion [45]. This results in higher dye solubility, which is critical for achieving uniform and vibrant coloration.
- Fiber Modification: Ionic liquids can chemically modify fiber surfaces to enhance dye absorption. For example, when used on polyamide fibers, ionic liquids can generate positive charges on the fiber surface, strengthening electrostatic interactions with anionic dyes [38]. Similarly, for natural fibers like wool and silk, ionic liquids partially disrupt the keratin or cellulose network, allowing deeper penetration of dye molecules [39].
- Temperature and Energy Efficiency: Ionic liquids facilitate dyeing at reduced temperatures, minimizing thermal degradation of both dye and fiber. This property not only conserves energy but also supports the preservation of fabric integrity, particularly for heat-sensitive textiles [35].

An interesting methodology that explores the use of ionic liquids in the textile dyeing process comprises two phases. In the initial phase, the textile fibers are subjected to a pretreatment process involving the use of ionic liquids. This is followed by a second phase, in which the fibers are dyed using a conventional methodology. This procedure was initially proposed by Yuan and colleagues, who investigated the potential of 1-butyl-3-methylimidazolium chloride in the dyeing of wool fibers [37]. It was established that these ionic liquids are capable of effectively damaging the external cuticles of wool fibers, facilitating a greater penetration of dyes. These notable outcomes were additionally corroborated by Kantouch et al. [39]. In their study, the impact of ionic liquids on the dyeability of wool and silk was investigated. Notably, the employment of ionic liquids appears to facilitate the dyeing of wool and silk fabrics with acid and reactive dyes at relatively low temperatures. Other noteworthy results were reported by Dong et al. [38]. The objective of the study was to investigate the impact of four distinct 1-alkyl-3-methylimidazolium

bromine ionic liquids on the adsorption capacity of nylon 6.6 fibers. It was observed that the amount of dye adsorbed was directly proportional to the concentration and the length of the alkyl groups of the ionic liquids when the pH was maintained at 5 and 7. This phenomenon can be attributed to the ability of ionic liquids to generate positive charges on the surface of nylon 6.6 fibers, thereby enhancing the ability of nylon 6.6 fibers to absorb the dye.

Recently, a new class of ionic liquids has attracted considerable interest in the field of fiber dyeing: Gemini ionic liquids. They typically consist of two ionic groups linked by a spacer [46]. A generic representation is reported in Figure 5.

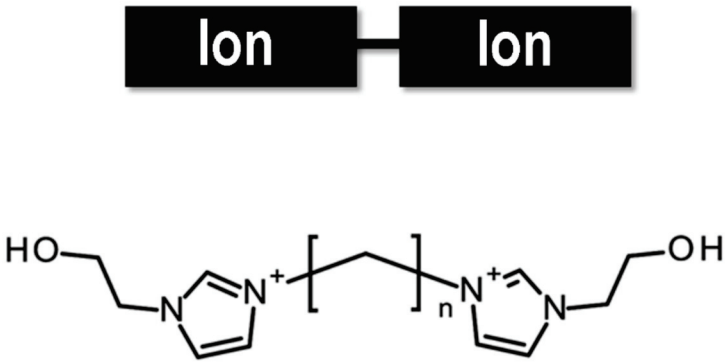

Figure 5. Schematic representation and example of gemini ionic liquids.

Nevertheless, the potential for their application in dyeing has been investigated by Zhuang and colleagues [47]. In particular, a gemini dicationic imidazolium ionic liquid has been synthesized for the pretreatment of ramie fibers to increase their dye uptake capacity. This study examined the impact of treatment conditions, specifically temperature and duration time, on the color strength of ramie fibers. The ramie fibers were subjected to a dyeing process using CI Reactive Yellow 4, with a concentration of 0.1%, at a bath ratio of 1:30. The study revealed a significant correlation between the treatment temperature and the K/S value of the fibers. It was observed that as the temperature increased from 20 °C to 80 °C, the K/S value exhibited a marked increase, reaching a maximum of 16.7 at 100 °C. Conversely, the effect of treating time on K/S value was studied by varying reacting times from 10 min to 60 min. In this case, the K/S value increased to 15.6 as the reaction time was extended. However, after 30 min, the K/S value stabilized.

Another notable application of ionic liquids is as auxiliaries in dyeing baths [36]. The experimental results show that the use of these ionic liquids results in comparable dye uptake and fixation rates to those achieved with conventional inorganic salts, thereby establishing their viability as an alternative to the dominant textile auxiliaries. Similarly, Cheng and colleagues observed comparable results [48]. In this case, ionic liquids were used to replace sodium chloride in a Reactive Red B dye bath. The results showed that this ionic liquid acts as an accelerator in silk dyeing, facilitating the rate of dye uptake. In particular, the results obtained from this study indicated that the rate of dye uptake was approximately 85.4%, and the K/S value was 11.2. In fact, the proposed ionic liquids are capable of interacting with acidic groups on the silk surface, thereby enhancing the electrostatic interaction between the dyes and the silk.

Another interesting research study has shown that ionic liquids can act as efficient dye retardants. In particular, imidazole-based ionic liquids were found to be effective in dyeing acrylic fibers [43]. Furthermore, Bianchini et al. have demonstrated the feasibility of wool, polyester, and cotton dyeing in an open vessel using dispersed dyes and appropriate ionic liquids [35]. In particular, the use of 1-(2-hydroxyethyl)-3-methylimidazolium chloride resulted in excellent dyeing of wool and polyester with good colorfastness. In other studies,

the potential of ionic liquids as solvents in the dyeing of cellulosic fibers, proteins, and fiber blends was investigated [40,42].

Another methodology for the use of ionic liquids in textile dyeing involves their employment as auxiliaries within the dyeing bath. A Chinese patent details the synthesis of quaternary ammonium salt ionic liquids and their application in the dyeing of cotton with triazine reactive dyes. In this case, the ionic liquid was used with a concentration of 10–20 g/L to replace traditional inorganic salts, resulting in a dye uptake and fixation rate that was comparable to that of traditional dyeing methods. The dyeing process was conducted at a temperature of 60 °C, with the pH of the dyeing bath being maintained within the range of 8–11 [49].

Furthermore, Barros and colleagues investigated the potential application of ionic liquids as dye auxiliaries in aqueous dyeing procedures [36]. In their study, they examined various types of fabrics in conjunction with a polyfunctional reactive dye and protic ionic liquids. The researchers examined a diverse array of fibers, encompassing diacetate, cotton, polyester, polyamide, acrylic, and wool. The K/S value exhibited a range consistent with the utilized ionic liquids. The reported K/S values were found to be approximately 1.5 for diacetate, 0.60 for cotton, 0.5 for polyamide, 0.50 for polyester, and 0.8 and 0.5 for acrylic and wool, respectively.

Recently, the dyeing of m-aramid fibers using ionic liquids has also been investigated. Indeed, the established dyeing process for aramid fibers fails to meet the contemporary benchmarks for occupational safety and environmental protection. Consequently, novel methodologies must be developed to address these shortcomings. In this approach, Opwis et al. discovered an effective method for dyeing m-aramid fibers utilizing 1-ethyl-3-methylimidazolium ethyl sulfate with acid dyestuffs. Specifically, they developed a process for dyeing m-aramide fibers without the use of hazardous carriers, achieving excellent coloration and outstanding wash, rub, and light fastness [41].

Compared to conventional water-based dyeing methods, ionic liquids offer several distinctive advantages. Traditional methods often require large amounts of water as a solvent, which leads to high water consumption and significant effluent generation containing unbound dyes and auxiliaries [41,50]. Ionic liquids, on the other hand, minimize water usage by serving as the primary medium for dye solubility. Furthermore, the enhanced dye uptake facilitated by ionic liquids reduces dye wastage and effluent toxicity. Their ability to operate effectively at lower temperatures also contrasts with conventional high-temperature dye baths, resulting in notable energy savings [51,52].

Other notable research into ionic liquids involves their use in textile printing. In this case, ionic liquids have been used as a component in the formulation of aqueous ink compositions for inkjet printing, with the aim of replacing hazardous solvents, preventing dye precipitation and providing good heat stability [53]. In a more recent study, methylimidazolium-based ionic liquids were investigated for their potential use in the burn-out printing of polyester/viscose blend fabrics [54]. Although the method investigated appears to be efficient and promising, it has not yet been demonstrated that it can completely replace the conventional technique.

3.2. Fiber Preparation and Textile Finishing

Textile finishing is a process used in the manufacture of fibers, fabrics, or garments to impart new and desired functional properties. Typically, the finishing process includes treatments designed to improve the softness, durability, wrinkle resistance, water repellency, or flame retardancy of the material. The finishing process plays a key role in the textile manufacturing process, determining the final properties and quality of the fabric and

ensuring the suitability of the finished product for its intended use. Ionic liquids have shown promise as textile finishing agents, as summarized in Figure 6.

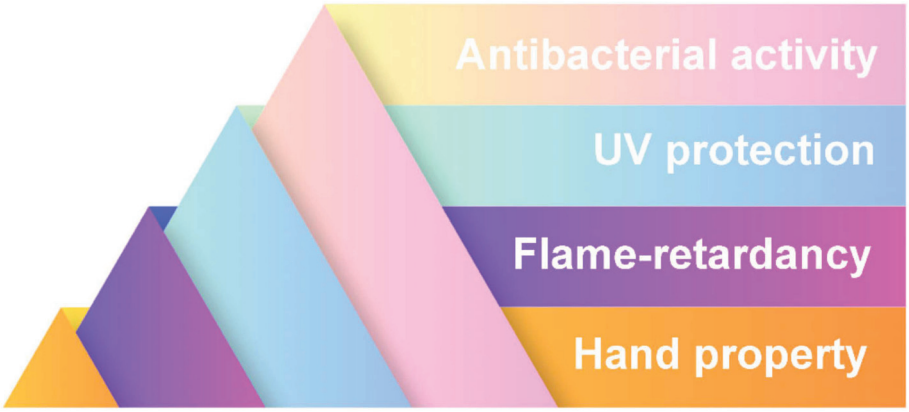

Figure 6. Example of applications of ionic liquids in textile finishing.

The application of ionic liquids in textile finishing extends beyond physical modification to include chemical interactions that impart functional properties. For example:

- Antibacterial properties: Imidazolium-based ionic liquids chemically bond with keratin in wool, forming stable complexes that exhibit durable antibacterial effects against both Gram-positive and Gram-negative bacteria, even after repeated washing [55].
- UV resistance and flame retardancy: Ionic liquids facilitate the incorporation of agents such as nano-zinc oxide or phosphonium cations [56,57]. This results in textiles with enhanced UV protection and improved flame-retardant properties without requiring additional chemical agents.
- Surface modification: Ionic liquids enable surface-level transformations of synthetic fibers, such as imparting a cotton-like texture to polyester through deposition of cellulosic material [58]. These interactions are facilitated by the unique solvating and catalytic properties of ionic liquids, making them versatile tools for advanced textile finishing.

The use of ionic liquids in textile finishing processes is typically associated with the imparting of antibacterial and antimicrobial properties. The various applications are summarized in Table 2:

Table 2. Summary of ionic liquid applications in textile finishing.

Application	Material	Ionic Liquids	Process	Outcome	Reference
Antimicrobial properties	Wool	Imidazolium-based ionic liquids	Pretreatment with ionic liquids to bind keratin.	Longlasting effect against *E. coli*.	[59]
	Viscose	Imidazolium-based ionic liquids	Treated with anionic agents followed by ionic liquids.	Antibacterial resistance against Gram-positive and Gram-negative bacteria.	[60]
Flame retardancy	Cotton	Methylimidazolium and pyridinium-based ionic liquids	Coating applied via sol-gel method.	Improved LOI (limiting oxygen index) and flame retardancy.	[61]
	Cotton	Various (e.g., PF_6^-)	Ionic liquid applied in finishing bath.	Enhanced flame retardant and water repellency properties.	[62]

Table 2. *Cont.*

Application	Material	Ionic Liquids	Process	Outcome	Reference
UV protection	Cotton	1-Butyl-3-methylimidazolium chloride + nano-ZnO	Nano-zinc oxide applied to cotton fabric using ionic liquids.	Excellent UV protection and bacteriostatic activity.	[63]
Surface Tactility	Polyester	Cetyltrimethylammonium bromide and 1-butyl-3-methylimidazolium chloride	Deposition of cellulosic materials on polyester fibers.	Imparts a cotton-like feel to synthetic fibers.	[58]

For example, Kantouch and colleagues investigated the effect of treating wool fabric with two imidazolium-based ionic liquids in order to impart long-lasting antimicrobial properties [59]. It was found that pretreatment of wool was necessary to induce structural changes that facilitated the binding of ionic liquids to the keratin structure. This process resulted in a stable antibacterial effect against *Escherichia coli*. However, the antimicrobial activity of wool fabric treated with ionic liquid at different temperatures is a subject of considerable variation. Wool fabric treated with ionic liquid at 30 °C, for instance, is not durable for washing and is reduced by about 50% after 10 washing cycles and entirely eliminated after 20 washing cycles. Conversely, wool fabric treated with ionic liquid at 80 °C exhibited persistent antibacterial properties, maintaining its efficacy even after 20 washing cycles. In a similar study, the potential antibacterial effect of ionic liquids on viscose was investigated [60]. In this case, the viscose fabric was first treated with anionic agents and then with ionic liquids. The treated viscose exhibits remarkable antibacterial resistance to both Gram-positive and Gram-negative bacteria, even after 10 wash cycles. In addition to antibacterial properties, ionic liquids can be used to impart other desirable properties, such as UV resistance and flame retardancy. For example, Arputharaj et al. applied nano-zinc oxide to cotton fabric using 1-butyl-3-methyl imidazolium chloride [63]. The treated cotton fabric exhibited remarkable bacteriostatic activity against both Gram-positive and Gram-negative bacteria, as well as excellent UV protection and a certain durability.

In addition, the presence of ammonium, phosphonium, and sulphonium cations in a number of ionic liquids prompted research into their potential as flame-retardant coatings for textile materials. As numerous studies have shown, this new class of flame retardants based on ionic liquids offers several advantages [57,62]. These include the absence of hazardous compounds, minimal volatility, and thermal stability. For example, Bentis and colleagues developed a cotton fabric treatment using methylimidazolium and pyridinium cations combined with anions including Cl^-, PF_6^-, $(CF_3SO_2)_2N^-$, BF_4^-, and $CH_3CO_2^-$ in a sol-gel process. The LOI test showed a superior LOI value of 25% for the treated cotton fabrics compared to the untreated fabrics (LOI = 20%), suggesting that the ionic liquid-based treatment has improved the protective capacity of the fabric against degradation [61]. Finally, Opwis et al. presented an intriguing application of ionic liquids [56], their paper describes the development of a novel finishing process for polyester fibers. Specifically, the process involves the deposition of cellulosic materials onto polyester fibers using ionic liquids, which creates a cotton surface on the synthetic fibers, imparting the tactile quality associated with the natural fiber.

The initial investigation into the potential applications of ionic liquids was conducted on the use of 1-ethyl-3-methylimidazolium acetate and 1-butyl-3-methylimidazolium chloride on the felting resistance of wool [55]. This study considers a number of factors, including temperature and time, the yellowing index, tenacity, and elongation at the break of the treated wool fibers. In a similar study, Yuan et al. demonstrated that treating wool with 1-butyl-3-methylimidazolium chloride significantly alters its surface state [64]. In another interesting study, the use of two ionic liquids for the degumming of silk was explored.

In this case, the 1-butyl-3-methylimidazolium chloride and 1-butyl-3-methylimidazolium hydrogen sulfate were successfully applied as a green solvent for the silk degumming process, resulting in better weight loss and absorbency than the conventional hydrogen peroxide process [65]. An additional intriguing approach is the alkaline hydrolysis of polyester, which has the potential to impart hydrophilicity, a smooth surface, and brightness [58]. In this study, polyester was treated with methanolic solutions of sodium hydroxide in the presence of a quaternary ammonium compound, cetyltrimethylammonium bromide, and 1-butyl-3-methylimidazolium chloride. The process yielded promising results in comparison to the conventional hydrolysis process with sodium hydroxide, indicating its potential as an alternative method.

In general, in comparison to conventional finishing techniques, which often rely on a combination of water-based processes and chemical agents, ionic liquids stand out due to their versatility and efficiency. For instance, conventional flame retardants or antibacterial finishes frequently involve the use of volatile or toxic chemicals that can have adverse environmental impacts. Ionic liquids, by contrast, achieve similar functionalization with minimal emissions and better recyclability [66]. Additionally, their low volatility and chemical stability make them safer alternatives for certain high-temperature processes, such as flame-retardant treatments, compared to conventional solvent-based systems.

3.3. Recycling of Textile Waste

Textile waste is a major environmental challenge, with millions of tons of discarded fabrics ending up in landfill every year [67]. The rapid growth of the fast-moving fashion industry has accelerated this problem, as clothing is often produced cheaply, worn for a short time, and discarded quickly. This waste is not only the result of consumer behavior but also includes significant amounts of preconsumer waste generated during manufacturing, such as fabric scraps, offcuts and unsold stock [68,69]. In addition, most textiles are made of synthetic fibers such as polyester, which are difficult to treat. The high volume of textile waste contributes to the depletion of natural resources, increased greenhouse gas emissions, and severe contamination of water and soil, so there is an urgent need to develop sustainable alternatives for the production, consumption, and disposal of textiles. In this context, ionic liquids offer a promising solution to enable more sustainable processing and recycling methods within the textile industry. Due to their intrinsic properties, ionic liquids can effectively dissolve and separate different components of textile materials. As shown in Table 3, there have been some developments in this area of research.

Table 3. Ionic liquids used in textile recycling.

Material Recycled	Type of Ionic Liquids	Reference
Cotton	1-allyl-3-methylimidazolium chloride	[70]
	1,5-diazabicyclo[4.3.0]non-5-enium acetate	[57]
	1-butyl-3-methylimidazolium acetate and DMSO as a cosolvent.	[71]
Cotton/PET	Superbase-based ionic liquid	[72]
	1-allyl-3-Methylimidazolium chloride	[73]
	1-ethyl-3-methylimidazolium diethyl phosphate DMSO system	[74]
	1-allyl-3-methylimidazole chloride in conjunction with DMSO	[74]
	1-allyl-3-methylimidazolium dicyanamide	[75]
Wool	1-allyl-3-methylimidazolium dicyanamide	[75]
Wool/Polyester	1,3-dimethylimidazolium dimethyl phosphate	[76]
Hemp	1,5-diazabicyclo[4.3.0]non-5-enium acetate	[77]

In 2002, Swatloski et al. carried out the first study on the dissolution of cellulose in ionic liquids. These solvents show considerable potential for cellulose processing and the production of regenerated cellulose fibers such as rayon [78]. A mechanism for dissolving cellulose in ionic liquids was then proposed, involving a direct chemical reaction that disrupts the hydrogen bonding network of cotton fibers [79]. Nevertheless, Bentivoglio and coworkers are investigating the use of a number of ionic liquids, including 1-butyl-3-methylimidazolium chloride and 1-allyl-3-methylimidazolium chloride, as potential replacements for N-methylmorpholine N-oxide in the commercial production of Lyocell fibers [70]. In addition, Assadi et al. present a novel chemical recycling process for cotton waste, which enables the production of high-quality virgin textile fibers of significantly higher quality than those produced by the mechanical recycling processes currently in use [57]. In this case, postconsumer cotton waste was completely dissolved in 1,5-diazabicyclo[4.3.0]non-5-enium acetate to produce continuous filaments with high tenacity and good modulus, exceeding the mechanical properties of virgin cotton fibers [57]. More recently, the potential use of ionic liquids for the separation and recovery of textile blends has been investigated. For example, Haslinger et al. investigated the potential of a superbase-based ionic liquid for the separation of cotton and polyester [72]. The selective dissolution of the cotton allowed the removal of the polyester, and the solution could then be used to dry-jet, wet-spin, textile-grade cellulose fibers with good tenacity and elongation comparable to those of commercial lyocell fibers. Another interesting approach explored was the use of 1-allyl-3-methylimidazolium chloride to separate and recover cotton from cotton/polyester blends [73]. In their work, cotton waste was directly dissolved and coagulated in water, demonstrating the potential for this process to be developed into a highly promising technology with significant industrialization potential. Another interesting study investigated the potential of 1-allyl-3-methylimidazole chloride in combination with DMSO to dissolve cotton from poly/cotton waste [74]. In their work, the dissolution temperature, time, and performance were subjected to comprehensive investigation. The combination of 1-allyl-3-methylimidazole chloride and DMSO yielded favorable results, but the 1-ethyl-3-methylimidazolium diethyl phosphate DMSO system demonstrated superior performance in terms of separation. This ionic liquid exhibited a viscosity of 0.1 Pa·s, which was advantageous for the separation of polyester from the cellulose solution. Additionally, Sun et al. investigated the potential for the separation and regeneration of cotton/polyester and wool/polyester blended fabrics from used garments using ionic liquids [76]. After dissolution, the synthetic polymer could be collected and then recycled, while the extracted cellulose and keratin could be regenerated by wet spinning. It was also found that the ionic liquids could be recovered and reused repeatedly by distillation, creating a complete closed-loop system for textile recycling.

Similarly, the use of ionic liquids to recycle hemp fabrics has yielded intriguing results [77]. In this approach, the hemp fabrics were subjected to a pretreatment with a sulfuric acid solution, with the objective of adjusting the viscosity, and then dissolved in 1,5-diazabicyclo[4.3.0]non-5-enium acetate. The resulting pulp was regenerated by dry-jet wet spinning, and the regenerated fibers were spun into yarn and knitted into a fabric. In particular, the mechanical analysis showed that the fabrics made with regenerated fibers had a good modulus of elasticity and improved abrasion resistance compared to the original hemp fabric. In the same way, Ma and colleagues investigated the dissolution of cotton from denim waste [71]. In this case, the process involved the use of an ionic liquid and DMSO as a cosolvent. The addition of the cosolvent facilitated the rapid dissolution of the cotton, thereby improving the spinnability of the resulting pulp. The mechanical test showed that the mechanical properties were adequate and comparable to those observed for traditional viscose fibers.

Following the recovery of cellulose from textile waste using ionic liquids, a recent study explored a promising new method for regenerating short wool fibers [75]. These fibers, which cannot normally be spun, have been dissolved using 1-allyl-3-methylimidazolium dicyanamide at 130 °C in the presence of a suitable reducing agent such as mercaptoethanol. In particular, the dissolution of wool results in the formation of a soluble fraction containing low molecular weight polypeptide chains and an insoluble fraction that can be further processed. Another interesting study involves the separation of natural fibers such as wool and cotton from polyester [76]. In this study, Sun and colleagues attempted to recycle fast fashion products by separating the cotton/polyester and wool/polyester blends using 1-butyl-3-methylimidazolium chloride and 1,3-dimethylimidazolium dimethyl phosphate. As in the previous case, the undissolved solid polyester was easily removed, while the extracted cellulose and wool keratin could be regenerated by wet spinning. A schematic representation of the process for cotton is given in Figure 7.

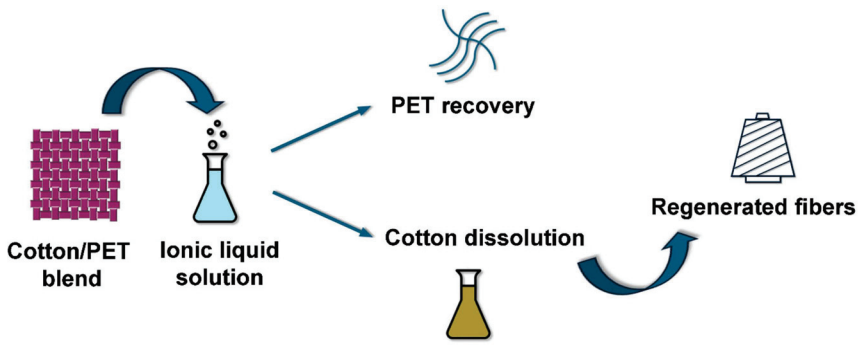

Figure 7. Schematic representation of cotton/PET separation and recovery.

In contrast, other studies have looked at the potential use of ionic liquids in open-loop systems to convert textile waste into high-value-added products. For example, Arshi et al. investigated the importance of pretreating cotton waste for the production of bioethanol [80]. Specifically, the cotton waste was treated with ionic liquids instead of the conventional acid pretreatment with phosphoric acid. It appears that the application of an ionic liquid at 175 °C facilitates the conversion of cotton waste to bioethanol via a process of simultaneous saccharification and fermentation. This represents a promising strategy for utilizing cotton waste textiles as a source of biomass for the future production of renewable biofuels. Similarly, Hong et al. investigated the potential of cotton-based waste textiles as an alternative feedstock for bacterial cellulose production [81]. In this case, the cellulosic fabrics were subjected to pretreatment with 1-allyl-3-methylimidazolium chloride and subsequently processed through enzymatic saccharification. The pretreated fabrics demonstrated a five- to sevenfold increase in the rate of enzymatic hydrolysis and produced a sevenfold greater yield of fermentable sugars in comparison to the unprocessed fabrics. Furthermore, the resulting bacterial cellulose exhibited a yield of 10.8 g/L, representing an 83% enhancement in productivity when compared to that of the culture grown in a glucose-based medium.

3.4. Dyed Textiles and Wastewater Treatment

Textile wastewater is a major environmental concern, as the industry generates large volumes of polluted water containing toxic chemicals, dyes, and heavy metals [82]. This wastewater is often difficult to treat and, when discharged into natural water bodies, can damage aquatic ecosystems, contaminate drinking water sources, and affect human health [83]. It is, therefore, imperative to develop effective methods for the treatment of dye effluent in order to prevent the adverse ecological impacts associated with its direct release into the environment. In recent years, a number of studies have demonstrated the

efficacy of ionic liquids in the removal of textile dyes from aqueous solutions and textile products, as summarized in Figure 8.

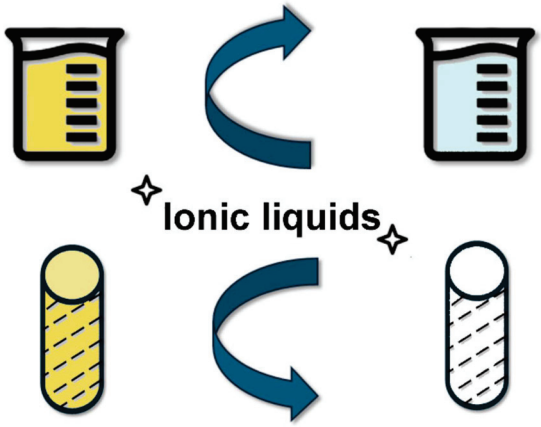

Figure 8. Schematic representation of the use of ionic liquids in dyed textile and wastewater treatment. In particular, the figure illustrates the dual role of ionic liquids as effective extraction agents for dye removal from wastewater and textiles. Key mechanisms include dye adsorption, solubilization, and ionic exchange. Applications depicted range from the removal of acid dyes and reactive dyes from aqueous solutions to the recovery of colorants and reuse of treated textiles. The process highlights the potential of ILs for sustainable wastewater treatment and recycling in the textile industry.

For example, Vijayaraghavan et al. successfully removed CI Acid Blue 113 and CI Acid Red 115 from water with an extraction efficiency of 98% using 1-butyl-1-methylpyrrolidinium bis(trifluoromethylsulfonyl)imide [84]. Concurrently, Li et al. explored the extraction of CI Acid Yellow 25 and CI Acid Red 14 from aqueous solutions using 1-butyl-3-methylimidazolium hexafluorophosphate, achieving extraction yields of 60–99% for these dyes [85,86]. A similar study showed that the use of imidazolium-based ionic liquids is an effective method for the removal of acid dyes, especially when the pH is carefully regulated. Under optimized pH conditions, the extraction efficiency ranged from 52% to 100%, depending on the type of acid dye [87]. As an additional consideration, Fan et al. have demonstrated that the efficacy of dye removal by ionic liquids is closely correlated with the length of the alkyl chain on the cations [88].

Another approach is based on the synthesis or modification of some known absorbents using ionic liquids to improve their performance. For example, Fat'hi et al. stabilized 1-butyl-3-methylimidazolium hexafluorophosphate on alumina to increase the absorbent's capacity to remove indigo carmine [89]. It has been reported that, under optimized conditions, removal efficiencies of more than 95% can be achieved. In other studies, 1-methyl-3-(triethoxysilylpropyl)imidazolium and 1-propyl-3-methylimidazolium chloride were grafted onto nanoporous silica [90,91]. In both cases, the silica properties were improved in acid dye removal. Later, Lawal et al. reported the adsorption of C.I. Acid Red 1 on kaolin modified with 1-hexyl-3-decahexylimidazolium bromide. They showed that this modified kaolin offers a high adsorption capacity [92]. Moreover, amino ionic liquid modified super paramagnetic mesoporous core/shell nanocomposite and its application as adsorbent to remove two azo acid dyes has been explored [93]. In a recent study, Thasneema et al. investigated the potential of phosphonium-based room-temperature ionic liquids for the extraction of toxic compounds, including textile dyes such as Rhodamine B, Methylene Blue, Methyl Orange, Malachite Green, Alizarin Red S, and Congo Red dyes, from their aqueous solution [24]. The results showed that this class of ionic liquids exhibited remarkable removal capabilities by adjusting concentration, pH, and contact time.

However, the potential for the functionalization of ionic liquids was also investigated. For example, functionalized ionic liquids were synthesized through a cross-linking reaction between 1-aminoethyl-3-vinylimidazolium chloride and divinylbenzene. The functionalized ionic liquids were shown to selectively remove acid dyes selectively [94]. In a similar approach, Kamran et al. investigated the modification of Fe_3O_4 using 1-octyl-3-methylimidazolium bromide and its potential to remove several reactive dyes [95]. As evidenced by their experimental results, the modified Fe_3O_4 nanoparticles showed remarkable efficacy in the removal of reactive dyes, with a removal efficiency of over 98% observed.

Ionic liquids have also been shown to be effective in removing dyes from textiles. Chen et al. investigated the potential use of nonfluorine quaternary ammonium-based ionic liquids for the removal of acid dyes. Among the ionic liquids investigated, tricaprylmethylammonium thiocyanate showed the optimal ability to extract acid dyes, with an extraction efficiency of 89% [96]. In a recent study, Mu and colleagues demonstrated that precise control of fiber density could be achieved by using a combination of water, glycerol, dimethylsulfoxide (DMSO), tetramethylurea, ethylene carbonate, isopropyl alcohol and 1,4-butanediol to remove dyes from fabrics effectively. The results showed that the process was able to remove 100% of dispersed dyes, acid, and direct dyes from PET, nylon 6,6, and cotton effectively. In addition, the molecular weight of the polymers remaining after dye removal was found to be almost identical [97]. Another interesting approach is the use of no-ionic surfactants, such as Triton X in the removal of CI Basic Blue 9 with 1-butyl-3-methylimidazolium hexafluorophosphate [98]. The inclusion of the nonionic surfactant was found to increase the extraction efficiency to 97.8%.

4. Benefits of Ionic Liquids in Textile Applications

As shown in the previous paragraphs, ionic liquids are increasingly being used in the textile industry. Their success is due not only to their intrinsic properties but also to a number of additional benefits. For example, the use of ionic liquids is considered to have a minimal impact on the environment, as they facilitate sustainability throughout the various stages of textile production, including fiber dissolution, dyeing, and recycling [24]. Firstly, unlike traditional solvents, the negligible volatility of ionic liquids significantly reduces the emission of volatile organic compounds (VOCs), which are known to contribute to air pollution and associated health risks [99]. In textile processing and recycling, ionic liquids enable the efficient dissolution and regeneration of some fibers, such as cellulose, facilitating recycling processes that use less energy and water than conventional mechanical or chemical methods [71,75,80]. Some of the advantages of ionic liquids are summarized in Figure 9.

Furthermore, one of the critical advantages of ionic liquids is their potential for recovery and reuse, which is particularly important in ensuring the environmental and economic sustainability of textile applications. Due to their negligible vapor pressure and high thermal stability, ionic liquids can often be recovered through distillation, liquid-liquid extraction, or adsorption techniques [100]. During textile applications such as dyeing and finishing, spent ionic liquids can be separated from wastewater using processes like phase separation or membrane filtration, as used for other applications [101]. For instance, the ionic liquid can be precipitated by altering the solution's pH or by adding a secondary solvent that induces phase separation. This allows for efficient recovery with minimal loss of material. Recycled ionic liquids typically retain their functional properties, enabling multiple cycles of reuse in processes like modification [76]. However, challenges such as contamination with impurities or partial degradation may arise. The integration of closed-loop systems utilizing ionic liquids has the potential to significantly reduce waste

generation and environmental impact, aligning with circular economy principles in the textile industry [76].

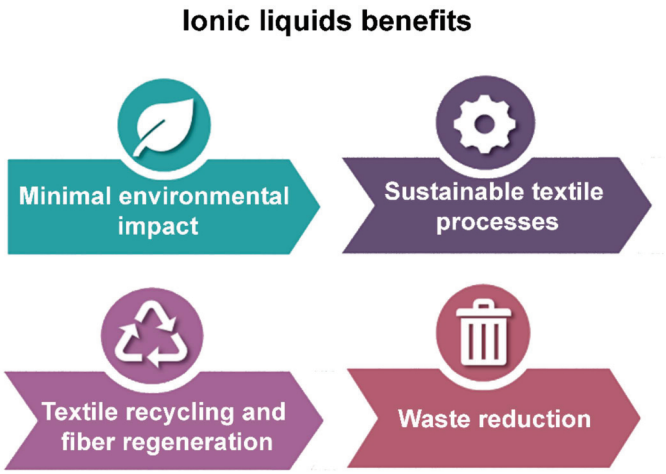

Figure 9. Benefits associated with the use of ionic liquids in the textile sector.

In addition, ionic liquids offer significant advantages in textile dyeing, a process typically associated with large volumes of water and chemical waste [24]. Their tunable solubility and ability to act as selective solvents allow dyes to be incorporated into fibers, reducing the need for auxiliary chemicals. This not only minimizes the volume of wastewater generated but also reduces the concentration of residual dyes in the effluent, thereby reducing the environmental impact of textile dyeing operations [102]. The biodegradability and recyclability of many ionic liquids further enhance their environmental profile. Unlike traditional solvents, which can persist in the environment, most ionic liquids can be recovered and reused, minimizing waste generation [100]. However, some research has also shown that ionic liquids can support innovative textile treatments, such as antimicrobial or flame retardant properties, without relying on hazardous substances, thereby promoting safer and more sustainable product development [103]. Taken together, these benefits highlight the potential of ionic liquids not only to reduce the environmental impact of the textile industry but also to drive the transition to a circular economy by enabling closed-loop processes and more efficient resource use.

5. Ecological Concerns of Ionic Liquids

While ionic liquids have gained significant attention for their unique properties, their environmental impact raises some concerns. Their persistence, toxicity, and limited biodegradability pose ecological risks that must be carefully evaluated [104]. For example, it has been demonstrated that the ecological effects of ionic liquids are influenced by their chemical structure [105]. The cation type, side-chain length, and hydrophobicity play major roles in toxicity, while the anion typically contributes to a lesser extent. Furthermore, ionic liquids are often poorly biodegradable, making them persistent pollutants in the environment. For instance, they exhibit resistance to microbial degradation, and even when degradation occurs, intermediates may still exhibit toxicity. This underscores the need for further research into degradation pathways [11,104]. In the end, there is a possibility that ionic liquids can be discharged into aquatic or terrestrial ecosystems. ILs have the potential to persist for extended periods, accumulating in soil and water bodies. Their environmental degradation pathways are not well understood, and studies suggest that their biodegradability depends heavily on the specific cation–anion combination [104,106,107].

6. Future Research Directions

Ionic liquids have attracted considerable attention in the textile industry due to their unique properties, which make them ideal for various applications such as dyeing, textile finishing and fiber recycling. For example, their low vapor pressure reduces the emission of harmful volatile organic compounds (VOCs) during processing, making them a more environmentally friendly alternative to conventional solvents. In addition, their ability to dissolve both organic and inorganic compounds, including natural fibers such as cellulose, opens up opportunities for more sustainable textile production methods. Despite these advantages, the textile industry has not yet fully embraced ionic liquids for widespread use.

Although research into the use of ionic liquids to recycle natural fibers such as cotton or wool has shown positive results, further research is needed to make these methods more efficient and commercially viable on a larger scale. However, while there has been considerable progress in the use of ionic liquids for natural fibers, synthetic fibers such as polyester present a greater challenge. Preliminary studies on PET recycling have used both deep eutectic solvents based on choline chloride and imidazole-based ionic liquids, but further research is essential to fully develop efficient recycling methods for synthetic fibers [108]. In addition, further efforts are being made to ensure that ionic liquids are fully exploited in the textile sector. While many ionic liquids are currently synthesized from traditional chemical compounds, there is growing interest in creating biobased ionic liquids. These would be derived from renewable resources and designed to be nontoxic and biodegradable, reducing the environmental impact of their use in textiles. Further research is needed to develop these biobased variants, optimize their performance in textile processes and ensure that they are safe for both humans and the environment [109]. Finally, a significant barrier to the widespread use of ionic liquids in textiles is their cost. Ionic liquids are generally more expensive to produce than conventional solvents, which limits their appeal for large-scale industrial applications [110]. Future research must focus on cost reduction strategies, such as finding cheaper raw materials for ionic liquid production, developing more efficient synthesis processes and improving their recyclability. In addition, the integration of ionic liquids into existing textile processing systems is crucial, as industries are reluctant to overhaul their infrastructure for new technologies unless the benefits (cost savings, environmental, etc.) are clear and significant. All these barriers are summarized in Figure 10.

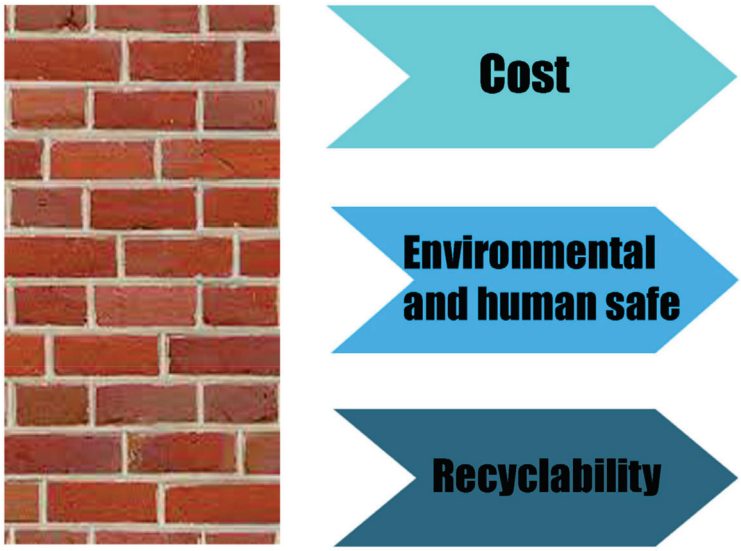

Figure 10. Potential obstacles to the use of ionic liquids in the textile industry.

This breakdown shows that while ionic liquids hold great promise for the textile industry, particularly in recycling, dyeing and sustainable fiber production, significant research is still needed to optimize their performance, reduce costs and expand their commercial application. The future of ionic liquids in textiles will depend on overcoming these scientific and economic hurdles.

7. Conclusions

Ionic liquids have emerged as a promising alternative to conventional solvents in the textile industry, offering a number of advantages, including low volatility, high thermal stability, tunable solubility, and recyclability. Although the use of ionic liquids is still at the laboratory scale, this review highlights their potential applications in dyeing processes, textile finishing, fiber preparation, and textile waste recycling. Despite these considerable advantages, the full potential of ionic liquids has yet to be realized due to a number of challenges, including high production costs, limited scalability, and the need for further integration into existing textile infrastructures. Overcoming these barriers will not only stimulate innovation within the textile industry but will also make a significant contribution to the transition to a circular economy, where waste is minimized and resources are efficiently reused. The future of ionic liquids in textiles is promising, but it depends on continued research efforts to realize their potential fully.

Author Contributions: Conceptualization: A.A. and A.P.; Writing—original draft: A.A. and A.P.; Writing—review & editing, A.P., A.A. and C.R. All authors have read and agreed to the published version of the manuscript.

Funding: This research received no external funding.

Conflicts of Interest: The authors declare no conflicts of interest.

References

1. Kalb, R.S. *Toward Industrialization of Ionic Liquids*; Springer: Berlin/Heidelberg, Germany, 2020; ISBN 9783030352448.
2. Pernak, J.; Rzemieniecki, T.; Materna, K. Ionic liquids "in a nutshell" (history, properties and development). *ChemiK* **2016**, *70*, 476–480.
3. Freemantle, M.; Welton, T.; Rogers, R. *An Introduction to Ionic Liquids*; RSC Publishing: Cambridge, UK, 2019; ISBN 978-1-84755-161-0.
4. Nambu, N.; Hiraoka, N.; Shigemura, K.; Hamanaka, S.; Ogawa, M. A Study of the 1,3,5-Trialkylbenzenes with Aluminum Chloride-Hydrogen Chloride Systems. *Bull. Chem. Soc. Jpn.* **1976**, *49*, 3637–3640. [CrossRef]
5. Ramsay, W. XXXIV. On picoline and its derivatives. *Lond. Edinb. Dublin Philos. Mag. J. Sci.* **1876**, *2*, 269–281. [CrossRef]
6. Laus, G.; Bentivoglio, G.; Schottenberger, H.; Kahlenberg, V.; Kopacka, H.; Roeder, T.; Sixta, H. Ionic Liquids: Current Dev Elopments, Potential and Drawbacks for Industr Ial Applications. *Lenzing. Ber.* **2005**, *84*, 71–85.
7. Barrer, R.M. The viscosity of pure liquids. II. Polymerised ionic melts. *Trans. Faraday Soc.* **1943**, *39*, 59–67. [CrossRef]
8. Silva, W.; Zanatta, M.; Ferreira, A.; Corvo, M.; Cabrita, E. Revisiting Ionic Liquid Structure-Property Relationship: A Critical Analysis. *Int. J. Mol. Sci.* **2020**, *21*, 7745. [CrossRef]
9. Walden, P.T. Molecular weights and electrical conductivity of several fused salts. *Bull. Acad. Imper. Sci.* **1914**, *1800*.
10. Gabriel, S.; Weiner, J. Ueber einige abkömmlinge des propylamins. *Berichte Der Dtsch. Chem. Ges.* **1888**, *21*, 2669–2679. [CrossRef]
11. Zhang, S.; Wang, J. *Structures and Interactions of Ionic Liquids*; Springer: Berlin/Heidelberg, Germany, 2014; ISBN 9783642386183.
12. Vekariya, R.L. A review of ionic liquids: Applications towards catalytic organic transformations. *J. Mol. Liq.* **2017**, *227*, 44–60. [CrossRef]
13. Welton, T. Ionic liquids: A brief history. *Biophys. Rev.* **2018**, *10*, 691–706. [CrossRef]
14. Hough, W.L.; Smiglak, M.; Rodríguez, H.; Swatloski, R.P.; Spear, S.K.; Daly, D.T.; Pernak, J.; Grisel, J.E.; Carliss, R.D.; Soutullo, M.D.; et al. The third evolution of ionic liquids: Active pharmaceutical ingredients. *New J. Chem.* **2007**, *31*, 1429–1436. [CrossRef]
15. Turguła, A.; Stęsik, K.; Materna, K.; Klejdysz, T.; Praczyk, T.; Pernak, J. Third-generation ionic liquids with N-alkylated 1{,}4-diazabicyclo[2.2.2]octane cations and pelargonate anions. *RSC Adv.* **2020**, *10*, 8653–8663. [CrossRef] [PubMed]

16. Kim, T.Y.; Kim, W.J.; Hong, S.H.; Kim, J.E.; Suh, K.S. Ionic-Liquid-Assisted Formation of Silver Nanowires. *Angew. Chem. Int. Ed.* **2009**, *48*, 3806–3809. [CrossRef] [PubMed]
17. Gordon, C.M. New developments in catalysis using ionic liquids. *Appl. Catal. A Gen.* **2001**, *222*, 101–117. [CrossRef]
18. Fischer, T.; Sethi, A.; Welton, T.; Woolf, J. Diels-Alder reactions in room-temperature ionic liquids. *Tetrahedron Lett.* **1999**, *40*, 793–796. [CrossRef]
19. Tzschucke, C.C.; Markert, C.; Bannwarth, W.; Roller, S.; Hebel, A.; Haag, R. Modern Separation Techniques for the Efficient Workup in Organic Synthesis. *Angew. Chem. Int. Ed.* **2002**, *41*, 3964–4000. [CrossRef]
20. Dupont, J.; de Souza, R.F.; Suarez, P.A.Z. Ionic Liquid (Molten Salt) Phase Organometallic Catalysis. *Chem. Rev.* **2002**, *102*, 3667–3692. [CrossRef]
21. Borra, E.F.; Seddiki, O.; Angel, R.; Eisenstein, D.; Hickson, P.; Seddon, K.R.; Worden, S.P. Deposition of metal films on an ionic liquid as a basis for a lunar telescope. *Nature* **2007**, *447*, 979–981. [CrossRef]
22. Doroodian, A.; Dengler, J.E.; Genest, A.; Rösch, N.; Rieger, B. Methylguanidinium borohydride: An ionic-liquid-based hydrogen-storage material. *Angew. Chem. Int. Ed.* **2010**, *49*, 1871–1873. [CrossRef]
23. Sheldon, R.A.; Lau, R.M.; Sorgedrager, M.J.; van Rantwijk, F.; Seddon, K.R. Biocatalysis in ionic liquids. *Green Chem.* **2002**, *4*, 147–151. [CrossRef]
24. Meksi, N.; Moussa, A. A review of progress in the ecological application of ionic liquids in textile processes. *J. Clean. Prod.* **2017**, *161*, 105–126. [CrossRef]
25. Salas, R.; Villa, R.; Velasco, F.; Cirujano, F.G.; Nieto, S.; Martin, N.; Garcia-Verdugo, E.; Dupont, J.; Lozano, P. Ionic liquids in polymer technology. *Green Chem.* **2024**. [CrossRef]
26. Christis, M.; Vercalsteren, A.; Arnold, M.; Nicolau, M.; Lafond, E.; Mortensen, L.; Coscieme, L.; Manshoven, S. *Textiles and the Environment in a Circular Economy*; ETC/WMGE: Copenhagen, Denmark, 2019.
27. Keskin, S.; Kayrak-Talay, D.; Akman, U.; Hortaçsu, Ö. A review of ionic liquids towards supercritical fluid applications. *J. Supercrit. Fluids* **2007**, *43*, 150–180. [CrossRef]
28. Cruz, C.; Ciach, A. Phase Transitions and Electrochemical Properties of Ionic Liquids and Ionic Liquid—Solvent Mixtures. *Molecules* **2021**, *26*, 3668. [CrossRef]
29. Al Hassan, M.K.; Alfarsi, A.; Nasser, M.S.; Hussein, I.A.; Khan, I. Ionic liquids and NADES for removal of organic pollutants and heavy metals in wastewater: A comprehensive review. *J. Mol. Liq.* **2023**, *391*, 123163. [CrossRef]
30. Atashnezhad, A.; Akhtarmanesh, S.; Al Dushaishi, M.F. Rheology characterization of ionic liquids under high pressure and high temperature. *J. Ion. Liq.* **2024**, *4*, 100105. [CrossRef]
31. Yu, L.; Li, Z.; Huang, W.; Ali, A.; Chen, Y.; Zhao, G.; Yao, S. Recovery and post-treatment processes for ionic liquids and deep eutectic solvents. *J. Mol. Liq.* **2024**, *402*, 124767. [CrossRef]
32. Hayes, R.; Warr, G.G.; Atkin, R. Structure and Nanostructure in Ionic Liquids. *Chem. Rev.* **2015**, *115*, 6357–6426.
33. Johnson, K. What's an Ionic Liquid? *Electrochem. Soc. Interface* **2007**, *16*, 38. [CrossRef]
34. Thakur, A.; Kumar, A. Exploring the potential of ionic liquid-based electrochemical biosensors for real-time biomolecule monitoring in pharmaceutical applications: From lab to life. *Results Eng.* **2023**, *20*, 101533. [CrossRef]
35. Bianchini, R.; Cevasco, G.; Chiappe, C.; Pomelli, C.S.; Rodríguez Douton, M.J. Ionic Liquids Can Significantly Improve Textile Dyeing: An Innovative Application Assuring Economic and Environmental Benefits. *ACS Sustain. Chem. Eng.* **2015**, *3*, 2303–2308. [CrossRef]
36. Barros, S.M.; Andrade, R.S.; Torres, D.; Chiari-Andrèo, B.G.; Veloso, G.B.R.; Gonzalez, C.; Iglesias, M. Eco-Friendly Technology for Reactive Dyeing of Cationized Fabrics: Protic Ionic Liquids as Innovative Media. *Cellul. Chem. Technol.* **2022**, *56*, 403–425. [CrossRef]
37. Yuan, J.; Wang, Q.; Fan, X.; Wang, P. Enhancing Dye Adsorption of Wool Fibers with 1-butyl-3-methylimidazolium Chloride Ionic Liquid Processing. *Text. Res. J.* **2010**, *80*, 1898–1904. [CrossRef]
38. Dong, Z.Q. Influence of ionic liquids on the sorption of acid dyes by nylon fibers. *Adv. Mater. Res.* **2011**, *175*, 602–607. [CrossRef]
39. Kantouch, A.; Khalil, E.M.; Mowafi, S.; Allam, O.G.; El-Sayed, H. Utilization of ionic liquids in improving dyeability of proteinic fabrics with acid and reactive dyes. *Egypt. J. Chem.* **2011**, *54*, 189–203.
40. Ribeiro, F.R.G.; Cabral, V.F.; Silva, C.; Andreaus, J.; Cardozo-Filho, L.; Croscato, G.S.; Silva, A.B.; Moraes, M.R. Alternative sustainable dyeing of textiles with ionic liquid. Integrating Cleaner Production into Sustainability Strategies. In Proceedings of the 4th International Workshop Advances in Cleaner Production, São Paulo, Brazil, 22–24 May 2013; p. 27.
41. Opwis, K.; Celik, B.; Benken, R.; Knittel, D.; Gutmann, J.S. Dyeing of m-Aramid Fibers in Ionic Liquids. *Polymers* **2020**, *12*, 1824. [CrossRef]
42. Earle, M.J.; Seddon, K.R. Dyeing Process in Ionic Liquid Solvents. WO Patent 2009024766A2, 26 February 2009.
43. Dong, Z.; Tang, R.; Chen, G. The retarding action of imidazole ionic liquid in acrylic dyeing. *China Dye. Finish.* **2011**, *37*, 1–5.
44. Farbeverfahren, D.T.N.-W.E. V Für Synthese-Und Naturfasermaterial Mit Hilfe Ionischer Flüssigkeiten. DE Patent 102006040075A1, 15 August 2008.

45. Buettner, C.S.; Cognigni, A.; Schröder, C.; Bica-Schröder, K. Surface-active ionic liquids: A review. *J. Mol. Liq.* **2022**, *347*, 118160. [CrossRef]
46. Kawai, R.; Niki, M.; Yada, S.; Yoshimura, T. Physicochemical and solution properties of quaternary-ammonium-salt-type amphiphilic gemini ionic liquids with spacers containing oxygen or nitrogen. *Colloids Surf. A Physicochem. Eng. Asp.* **2020**, *603*, 125218. [CrossRef]
47. Zhuang, L.; Zheng, C.; Sun, J.; Yuan, A.; Wang, G. Performances of ramie fiber pretreated with dicationic imidazolium ionic liquid. *Fibers Polym.* **2014**, *15*, 226–233. [CrossRef]
48. Cheng, D. Application of ionic liquid in silk dyeing. *Adv. Mater. Res.* **2011**, *331*, 253–256. [CrossRef]
49. Dyeing Method of Reactive Dye Containing Ionic Liquid. Patent CN102493222A, 8 November 2011.
50. Khatri, A.; Peerzada, M.; Mohsin, M.; White, M. A review on developments in dyeing cotton fabrics with reactive dyes for reducing effluent pollution. *J. Clean. Prod.* **2015**, *87*, 50–57. [CrossRef]
51. Lindström, F. Chemical and Physical Changes in PET Fibres Due to Exhaust Dyeing. Master's Thesis, University of Borås, Borås, Sweden, 2018.
52. El-Sayed, H. Chapter 6—Wool Dyeing. In *The Wool Handbook*; The Textile Institute Book Series; Jose, S., Thomas, S., Basu, G., Eds.; Woodhead Publishing: Sawston, UK, 2024; pp. 139–158, ISBN 978-0-323-99598-6.
53. Schwarz, W.M. Ink Compositions Containing Ionic Liquid Solvents. US Patent 6,048,388, 11 April 2000.
54. Hibbert, R. 19–What Textile Fibres are Applicable for the Layering System for the Active Ageing? In *Woodhead Publishing Series in Textiles, Proceedings of the MRS Spring Meeting & Exhibition San Francisco, CA, USA, 1–5 April 2013*; Woodhead Publishing: Sawston, UK, 2015; pp. 329–359, ISBN 978-0-85709-538-1.
55. Kantouch, A.; Khalil, E.M.; El-Sayed, H.; Mowafi, S. A novel application of ionic liquid in improvement of the felting resistance of wool. *Egypt. J. Chem.* **2011**, *54*, 481–493.
56. Opwis, K.; Textor, T.; Gutmann, J. *Use of Ionic Liquids in Textile Finishing*; ResearchGate: Berlin, Germany, 2013.
57. Asaadi, S.; Hummel, M.; Hellsten, S.; Härkäsalmi, T.; Ma, Y.; Michud, A.; Sixta, H. Renewable High-Performance Fibers from the Chemical Recycling of Cotton Waste Utilizing an Ionic Liquid. *ChemSusChem* **2016**, *9*, 3250–3258. [CrossRef]
58. Musale, R.M.; Shukla, S.R. Weight reduction of polyester fabric using sodium hydroxide solutions with additives cetyltrimethylammonium bromide and [BMIM]Cl. *J. Text. Inst.* **2017**, *108*, 467–471. [CrossRef]
59. Kantouch, A.; Khalil, E.M.; Mowafi, S.; El-Sayed, H. Antimicrobial finishing of wool fabric using ionic liquids. *J. Text. Inst.* **2013**, *104*, 363–369. [CrossRef]
60. El-Sayed, A.; Kantouch, A.; El-Sayed, H. An approach to impart bactericidal effect to viscose fabric using ionic liquids. *Egypt. J. Chem.* **2011**, *54*, 495–507.
61. Bentis, A.; Boukhriss, A.; Grancaric, A.M.; El Bouchti, M.; El Achaby, M.; Gmouh, S. Flammability and combustion behavior of cotton fabrics treated by the sol gel method using ionic liquids combined with different anions. *Cellulose* **2019**, *26*, 2139–2153. [CrossRef]
62. Boukhriss, A.; Gmouh, S.; Hannach, H.; Roblin, J.-P.; Cherkaoui, O.; Boyer, D. Treatment of cotton fabrics by ionic liquid with PF6− anion for enhancing their flame retardancy and water repellency. *Cellulose* **2016**, *23*, 3355–3364. [CrossRef]
63. Arputharaj, A.; Prasad, V.; Saxena, S.; Nadanathangam, V.; Shukla, S.R. Ionic liquid mediated application of nano zinc oxide on cotton fabric for multi-functional properties. *J. Text. Inst.* **2017**, *108*, 1189–1197. [CrossRef]
64. Jiugang, Y.; Qiang, W.; Ping, W.; Li, C.; Xuerong, F. Promotional effect of 1-butyl-3-methylimidazolium chloride ionic liquid on the enzymatic finishing of wool. *Eng. Life Sci.* **2012**, *12*, 209–215. [CrossRef]
65. Vyas, S.K.; Shukla, S.R. Degumming of eri silk using ionic liquids and optimization through response surface methodology. *J. Text. Inst.* **2016**, *107*, 1096–1111. [CrossRef]
66. De Barros, A.G.; Tomber, D.D. Quantitative analysis of passenger and baggage security screening at airports. *J. Adv. Transp.* **2007**, *41*, 171–193. [CrossRef]
67. Moazzem, S.; Wang, L.; Daver, F.; Crossin, E. Environmental impact of discarded apparel landfilling and recycling. *Resour. Conserv. Recycl.* **2021**, *166*, 105338. [CrossRef]
68. Hoti, G.; Caldera, F.; Trotta, F.; Zoccola, M.; Patrucco, A.; Anceschi, A. A Novel Approach for Nanosponge: Wool Waste as a Building Block for the Synthesis of Keratin-Based Nanosponge and Perspective Application in Wastewater Treatment. *ACS Omega* **2024**, *9*, 43319–43330. [CrossRef] [PubMed]
69. Anceschi, A.; Trotta, F.; Zoccola, M.; Caldera, F.; Magnacca, G.; Patrucco, A. From Waste to Worth: Innovative Pyrolysis of Textile Waste into Microporous Carbons for Enhanced Environmental Sustainability. Available online: https://papers.ssrn.com/sol3/papers.cfm?abstract_id=4960149 (accessed on 9 January 2025).
70. Bentivoglio, G.; Röder, T.; Fasching, M.; Buchberger, M.; Schottenberger, H.; Sixta, H. Cellulose processing with chloride-based ionic liquids. *Lenzing. Ber.* **2006**, *86*, 154–161.
71. Ma, Y.; Zeng, B.; Wang, X.; Byrne, N. Circular Textiles: Closed Loop Fiber to Fiber Wet Spun Process for Recycling Cotton from Denim. *ACS Sustain. Chem. Eng.* **2019**, *7*, 11937–11943. [CrossRef]

72. Haslinger, S.; Hummel, M.; Anghelescu-Hakala, A.; Määttänen, M.; Sixta, H. Upcycling of cotton polyester blended textile waste to new man-made cellulose fibers. *Waste Manag.* **2019**, *97*, 88–96. [CrossRef]
73. Villalta, E.; Riba-Moliner, M.; Lis, M. Recovery of cellulose from polyester/cotton fabrics making use of ionic liquids. *Polym. Sci. Peer Rev. J.* **2022**, *4*, 000590.
74. Wu, H.; Wang, B.; Li, T.; Wu, Y.; Yang, R.; Gao, H.; Nie, Y. Efficient recycle of waste poly-cotton and preparation of cellulose and polyester fibers using the system of ionic liquid and dimethyl sulfoxide. *J. Mol. Liq.* **2023**, *388*, 122757. [CrossRef]
75. Idris, A.; Vijayaraghavan, R.; Rana, U.A.; Patti, A.F.; MacFarlane, D.R. Dissolution and regeneration of wool keratin in ionic liquids. *Green Chem.* **2014**, *16*, 2857–2864. [CrossRef]
76. Sun, X.; Wang, X.; Sun, F.; Tian, M.; Qu, L.; Perry, P.; Owens, H.; Liu, X. Textile Waste Fiber Regeneration via a Green Chemistry Approach: A Molecular Strategy for Sustainable Fashion. *Adv. Mater.* **2021**, *33*, 2105174. [CrossRef] [PubMed]
77. Rissanen, M.; Schlapp-Hackl, I.; Sawada, D.; Raiskio, S.; Ojha, K.; Smith, E.; Sixta, H. Chemical recycling of hemp waste textiles via the ionic liquid based dry-jet-wet spinning technology. *Text. Res. J.* **2022**, *93*, 2545–2557. [CrossRef]
78. Swatloski, R.; Spear, S.; Hobrey, J.D.; Rogers, R. Dissolution of cellulose with ionic liquids. *J. Am. Chem. Soc.* **2002**, *124*, 4947–4975. [CrossRef]
79. Acharya, S.; Liyanage, S.; Parajuli, P.; Rumi, S.S.; Shamshina, J.L.; Abidi, N. Utilization of Cellulose to Its Full Potential: A Review on Cellulose Dissolution, Regeneration, and Applications. *Polymers* **2021**, *13*, 4344. [CrossRef]
80. Arshi, S.; Zhao, Y.; Seyen, T.; Vreckem, E.; Buelens, L. A comparative study between ionic liquid and acidic pretreatment of waste cotton textiles with simultaneous saccharification and fermentation. *Bangladesh J. Sci. Ind. Res.* **2022**, *57*, 41–48. [CrossRef]
81. Hong, F.; Guo, X.; Zhang, S.; Han, S.; Yang, G.; Jönsson, L.J. Bacterial cellulose production from cotton-based waste textiles: Enzymatic saccharification enhanced by ionic liquid pretreatment. *Bioresour. Technol.* **2012**, *104*, 503–508. [CrossRef]
82. Azanaw, A.; Birlie, B.; Teshome, B.; Jemberie, M. Textile effluent treatment methods and eco-friendly resolution of textile wastewater. *Case Stud. Chem. Environ. Eng.* **2022**, *6*, 100230. [CrossRef]
83. Singh, B.J.; Chakraborty, A.; Sehgal, R. A systematic review of industrial wastewater management: Evaluating challenges and enablers. *J. Environ. Manag.* **2023**, *348*, 119230. [CrossRef]
84. Vijayaraghavan, R.; Vedaraman, N.; Surianarayanan, M.; MacFarlane, D.R. Extraction and recovery of azo dyes into an ionic liquid. *Talanta* **2006**, *69*, 1059–1062. [CrossRef]
85. Li, C.; Xin, B. Extraction and Mechanisms of Acid Dyes into a Room Temperature Ionic Liquid. In Proceedings of the 2008 2nd International Conference on Bioinformatics and Biomedical Engineering, Shanghai, China, 16–18 May 2008; pp. 3519–3522.
86. Li, C.; Xin, B.; Xu, W.; Zhang, Q. Study on the extraction of dyes into a room-temperature ionic liquid and their mechanisms. *J. Chem. Technol. Biotechnol.* **2007**, *82*, 196–204. [CrossRef]
87. Pei, Y.C.; Wang, J.J.; Xuan, X.P.; Fan, J.; Fan, M. Factors Affecting Ionic Liquids Based Removal of Anionic Dyes from Water. *Environ. Sci. Technol.* **2007**, *41*, 5090–5095. [CrossRef] [PubMed]
88. Fan, J.; Fan, Y.; Zhang, S.; Wang, J. Extraction of Azo Dyes from Aqueous Solutions with Room Temperature Ionic Liquids. *Sep. Sci. Technol.* **2011**, *46*, 1172–1177. [CrossRef]
89. Fat'hi, M.R.; Parham, H.; Pourreza, N.; Golmohammadi, H. Removal of indigo carmine from water samples using ionic liquid immobilized on alumina as a new adsorbent. *Fresenius Environ. Bull.* **2012**, *21*, 1873–1878.
90. Zarezadeh-Mehrizi, M.; Badiei, A.; Mehrabadi, A.R. Ionic liquid functionalized nanoporous silica for removal of anionic dye. *J. Mol. Liq.* **2013**, *180*, 95–100. [CrossRef]
91. Tkachenko, O.; Panteleimonov, A.; Padalko, I.; Korobov, A.; Gushikem, Y.; Kholin, Y. Silica functionalized with 1-propyl-3-methylimidazolium chloride as an efficient adsorbent for the removal of Eosin Yellow and Reactive Blue 4. *Chem. Eng. J.* **2014**, *254*, 324–332. [CrossRef]
92. Lawal, I.A.; Moodley, B. Synthesis, characterisation and application of imidazolium based ionic liquid modified montmorillonite sorbents for the removal of amaranth dye. *RSC Adv.* **2015**, *5*, 61913–61924. [CrossRef]
93. Cheng, J.; Shi, L.; Lu, J. Amino ionic liquids-modified magnetic core/shell nanocomposite as an efficient adsorbent for dye removal. *J. Ind. Eng. Chem.* **2016**, *36*, 206–214. [CrossRef]
94. Gao, H.; Kan, T.; Zhao, S.; Qian, Y.; Cheng, X.; Wu, W.; Wang, X.; Zheng, L. Removal of anionic azo dyes from aqueous solution by functional ionic liquid cross-linked polymer. *J. Hazard. Mater.* **2013**, *261*, 83–90. [CrossRef]
95. Kamran, S.; Tavallali, H.; Azad, A. Fast Removal of Reactive Red 141 and Reactive Yellow 81 From Aqueous Solution by Fe_3O_4 Magnetic Nanoparticles Modified With Ionic Liquid 1-Octyl-3-methylimidazolium Bromide. *Iran. J. Anal. Chem.* **2014**, *1*, 78–86.
96. Chen, X.; Li, F.; Asumana, C.; Yu, G. Extraction of soluble dyes from aqueous solutions with quaternary ammonium-based ionic liquids. *Sep. Purif. Technol.* **2013**, *106*, 105–109. [CrossRef]
97. Mu, B.; Yang, Y. Complete separation of colorants from polymeric materials for cost-effective recycling of waste textiles. *Chem. Eng. J.* **2022**, *427*, 131570. [CrossRef]

98. Talbi, Z.; Haddou, B.; Ghouas, H.; Kameche, M.; Derriche, Z.; Gourdon, C. Cationic Dye Removal From Aqueous Solutions Using Ionic Liquids AND nonionic Surfactant-Ionic Liquids Systems: A Comparative Study Based Upon Experimental Design. *Chem. Eng. Commun.* **2014**, *201*, 41–52. [CrossRef]
99. Inman, G.; Nlebedim, I.C.; Prodius, D. Application of Ionic Liquids for the Recycling and Recovery of Technologically Critical and Valuable Metals. *Energies* **2022**, *15*, 628. [CrossRef]
100. Khoo, Y.S.; Tjong, T.C.; Chew, J.W.; Hu, X. Techniques for recovery and recycling of ionic liquids: A review. *Sci. Total Environ.* **2024**, *922*, 171238. [CrossRef]
101. Zhou, J.; Sui, H.; Jia, Z.; Yang, Z.; He, L.; Li, X. Recovery and purification of ionic liquids from solutions: A review. *RSC Adv.* **2018**, *8*, 32832–32864. [CrossRef]
102. Bento, R.M.F.; Almeida, M.R.; Bharmoria, P.; Freire, M.G.; Tavares, A.P.M. Improvements in the enzymatic degradation of textile dyes using ionic-liquid-based surfactants. *Sep. Purif. Technol.* **2020**, *235*, 116191. [CrossRef]
103. Latifi, S.; Saoiabi, S.; Boukhriss, A.; Gmouh, S.; Saoiabi, A. Ionic Liquids as an Ecological Flame-retardant Agent for Textile Fabrics. *NanoWorld J.* **2023**, *9*, S157–S162.
104. Gonçalves, A.R.P.; Paredes, X.; Cristino, A.F.; Santos, F.J.V.; Queirós, C.S.G.P. Ionic liquids—A review of their toxicity to living organisms. *Int. J. Mol. Sci.* **2021**, *22*, 5612. [CrossRef]
105. Wang, X.; Hu, X.; Zhang, D.; Zhang, Y.; Xu, H.; Sun, Y.; Gu, X.; Luo, J.; Gao, B. Environmental applications and toxicity of ionic liquids. *J. Environ. Chem. Eng.* **2024**, *12*, 114638. [CrossRef]
106. Docherty, K.M.; Aiello, S.W.; Buehler, B.K.; Jones, S.E.; Szymczyna, B.R.; Walker, K.A. Ionic liquid biodegradability depends on specific wastewater microbial consortia. *Chemosphere* **2015**, *136*, 160–166. [CrossRef] [PubMed]
107. Wei, P.; Pan, X.; Chen, C.-Y.; Li, H.-Y.; Yan, X.; Li, C.; Chu, Y.-H.; Yan, B. Emerging impacts of ionic liquids on eco-environmental safety and human health. *Chem. Soc. Rev.* **2021**, *50*, 13609–13627. [CrossRef] [PubMed]
108. Paparella, A.N.; Perrone, S.; Salomone, A.; Messa, F.; Cicco, L.; Capriati, V.; Perna, F.M.; Vitale, P. Use of Deep Eutectic Solvents in Plastic Depolymerization. *Catalysts* **2023**, *13*, 1035. [CrossRef]
109. Ali, S.S.; Abdelkarim, E.A.; Elsamahy, T.; Al-Tohamy, R.; Li, F.; Kornaros, M.; Zuorro, A.; Zhu, D.; Sun, J. Bioplastic production in terms of life cycle assessment: A state-of-the-art review. *Environ. Sci. Ecotechnol.* **2023**, *15*, 100254. [CrossRef]
110. Baaqel, H.; Tulus, V.; Chachuat, B.; Guillén-Gosálbez, G.; Hallett, J. Uncovering the True Cost of Ionic Liquids using Monetization. In *Computer Aided Chemical Engineering*; Elsevier: Amsterdam, The Netherlands, 2020; Volume 48, pp. 1825–1830, ISBN 9780128233771.

Disclaimer/Publisher's Note: The statements, opinions and data contained in all publications are solely those of the individual author(s) and contributor(s) and not of MDPI and/or the editor(s). MDPI and/or the editor(s) disclaim responsibility for any injury to people or property resulting from any ideas, methods, instructions or products referred to in the content.

molecules

MDPI

Review

Computational Advances in Ionic Liquid Applications for Green Chemistry: A Critical Review of Lignin Processing and Machine Learning Approaches

Brian R. Taylor [1,2,†], Nikhil Kumar [1,2,†], Dhirendra Kumar Mishra [1,3,†], Blake A. Simmons [1,4], Hemant Choudhary [1,3,*] and Kenneth L. Sale [1,2,*]

1 Joint BioEnergy Institute, Emeryville, CA 94608, USA
2 Department of Biosecurity and Bioassurance, Sandia National Laboratories, Livermore, CA 94551, USA
3 Department of Bioresource and Environmental Security, Sandia National Laboratories, Livermore, CA 94550, USA
4 Biological Systems and Engineering Division, Lawrence Berkeley National Laboratory, Berkeley, CA 94720, USA
* Correspondence: hchoudhary@lbl.gov or hchoudh@sandia.gov (H.C.); klsale@lbl.gov or klsale@sandia.gov (K.L.S.)
† These authors contributed equally to this work.

Abstract: The valorization and dissolution of lignin using ionic liquids (ILs) is critical for developing sustainable biorefineries and a circular bioeconomy. This review aims to critically assess the current state of computational and machine learning methods for understanding and optimizing IL-based lignin dissolution and valorization processes reported since 2022. The paper examines various computational approaches, from quantum chemistry to machine learning, highlighting their strengths, limitations, and recent advances in predicting and optimizing lignin-IL interactions. Key themes include the challenges in accurately modeling lignin's complex structure, the development of efficient screening methodologies for ionic liquids to enhance lignin dissolution and valorization processes, and the integration of machine learning with quantum calculations. These computational advances will drive progress in IL-based lignin valorization by providing deeper molecular-level insights and facilitating the rapid screening of novel IL-lignin systems.

Keywords: Density Functional Theory (DFT); biomass processing; lignocellulosic biorefineries; lignin depolymerization; reactive force fields (ReaxFF); solvent screening; quantum chemistry; multi-scale modeling

1. Introduction

The need for sustainable alternatives to fossil-based resources has driven significant interest in lignocellulosic biomass as a renewable feedstock for biofuels and chemicals. Lignin, which constitutes 15–35% [1] of this feedstock, offers significant potential as a source for high-value products such as biofuels [2], materials [3], and pharmaceuticals [4]. Unlocking this potential is critical to the economic viability of the biobased economy [5].

The valorization of lignin presents several unique challenges. It resists solubilization and depolymerization and is chemically complex [2]. Furthermore, the structure and composition of lignin vary significantly depending on its biomass source and extraction method, resulting in different types of technical lignins (e.g., Kraft, lignosulfonate, Organosolv, Soda) with distinct properties. These different types of technical lignins often have different associated purities, molecular weights, and functional groups [6–9]. This variability complicates efforts to develop universally applicable conversion technologies. Most current biorefineries often combust the lignin rather than turn it into high-value products [10–13].

Ionic liquids (ILs) are promising solvents for lignin dissolution and processing, offering a potential solution to the challenges associated with lignin depolymerization. ILs are effective biomass solvents because of their thermostability, ability to dissolve a wide range of substances, tunable nature, and low vapor pressure [14–16]. Their tunability is due to the large number of possible cation–anion combinations. However, it is costly, labor-intensive, and time-consuming to conduct experimental screenings of ILs due to the wide range of cation and anion combinations. Computational screening, on the other hand, has proven to be a viable option for multi-scale screening of "notable" solvents in biomass processing [17–20]

The vast improvement in computational resources provides an opportunity for computational studies to play a large role in identifying amenable ILs. However, significant challenges remain in applying computational methods to IL-based lignin valorization. These include accurately representing lignin's structural heterogeneity, balancing computational cost with predictive accuracy, and translating molecular-scale insights to process-level optimization. Additionally, the scarcity of standardized, high-quality experimental data for training and validating computational models poses a barrier to developing robust predictive tools.

This review aims to critically assess the current state of computational methods for understanding and optimizing the IL-based lignin dissolution and valorization processes reported since 2022. We examine the strengths and limitations of various approaches, from quantum chemistry to machine learning. The scope of this review excludes experimental methods, industrial-scale applications, and non-IL-based solvent systems. By highlighting recent advances and identifying key knowledge gaps, we seek to provide a roadmap for future research that will support the design of IL-based systems that allow for lignin dissolution and valorization, ultimately contributing to the development of sustainable biorefinery processes and a circular bioeconomy.

2. Screening of Ionic Liquids (ILs) Based on Modeling

Conducting experimental tests on all the potential cation–anion combinations in ILs is difficult due to their multitude. To effectively handle this level of complexity in ILs, computational screening methods are required. Because lignin is heterogeneous and has different bonding patterns, it is difficult to say how it will solvate. When simplified lignin models are used in simulations, they might not accurately represent how real lignin made from biomass behaves, which lowers the accuracy of the screening data. Despite advances in IL screening for lignin solvation, there are no general rules to predict which ILs are most effective in deconstructing biomass. The absence of such guidelines leads to trial-and-error approaches and slows down the discovery of optimal solvents. Accurately predicting the critical thermodynamic properties (such as activity coefficients, excess enthalpy, and solubility parameters) for IL-lignin systems is challenging, as these depend on specific interactions that vary widely among ILs and model lignin structures. Robust theoretical techniques are required for efficient screening of the extensive range of ILs for lignin dissolution. Recent improvements have facilitated the implementation of several predictive methodologies for simulating the thermodynamic parameters of IL-containing systems. Earlier prominent techniques encompass the Perturbed Chain Statistical Associating Fluid Theory (PC-SAFT) [21], which was used to calculate the thermodynamic properties of different homologous series of ILs based on the bis(trifluormethylsulfonyl)imide anion ($[NTf_2]^-$); group contribution approaches [22] were explored for estimating critical properties, normal boiling temperatures, and acentric factors for IL; Quantitative Structure–Property Relationships (QSPRs) [23] were used to estimate the infinite dilution activity coefficients for organic solutes in IL; Monte Carlo (MC) molecular simulations [24] explored the understanding the gas solubility in IL; Molecular Dynamics (MD) simulations [25] were performed to understand the pure and mixed gas absorption in the ionic liquids; and the Conductor-like Screening Model for Real Solvents (COSMO-RS) [26,27] model was applied for screening of solvents for multiple applications such as asphaltene dispersion, gas absorption, and

extraction of biologically active compounds [28–30]. It follows that the COSMO-RS model is one of the most effective predictive approaches for screening ILs for various applications due to its ability to quickly process vast IL datasets. Experimental investigations might be conducted with much less time, money, and effort if ILs could be screened using predictive techniques that only needed a small number of input parameters.

While emerging methods like COSMO-RS and machine learning (ML) have shown promise, scaling these models to screen thousands of ILs with diverse lignin models requires significant computational resources and optimization to ensure practical, cost-effective screening [31,32]. Translating predictions into real-world applications is often hindered by the complexity of IL synthesis, cost, and the need for reliable experimental data to find the best solvents. COSMO-RS has previously been successfully used to predict thermodynamic properties such as solubility in IL systems, activity coefficients (γ), and excess enthalpy (HE). Several research articles emphasize the ability of these parameters to screen ILs for lignin solvation [17,33,34]. The basic schematic diagram for in silico screening of ILs for lignin solvation is shown in Figure 1. Various researchers used basic lignin model compounds, such as p-coumaryl alcohol, sinapyl alcohol, and coniferyl alcohol, to represent the lignin structure. The main links between the structural units of lignin are β-O-4 (β-aryl ether), β-β (resinol), and β-5 (phenylcoumaran) [35]. As a result, researchers developed various lignin models, which consist of three basic units (H, G, and S) with some basic linkages, to investigate the impact of lignin structure on dissolving behavior. However, the current understanding of ILs and lignin models remains relatively basic, posing a challenge in formulating comprehensive guidelines for identifying the best solvents for lignin.

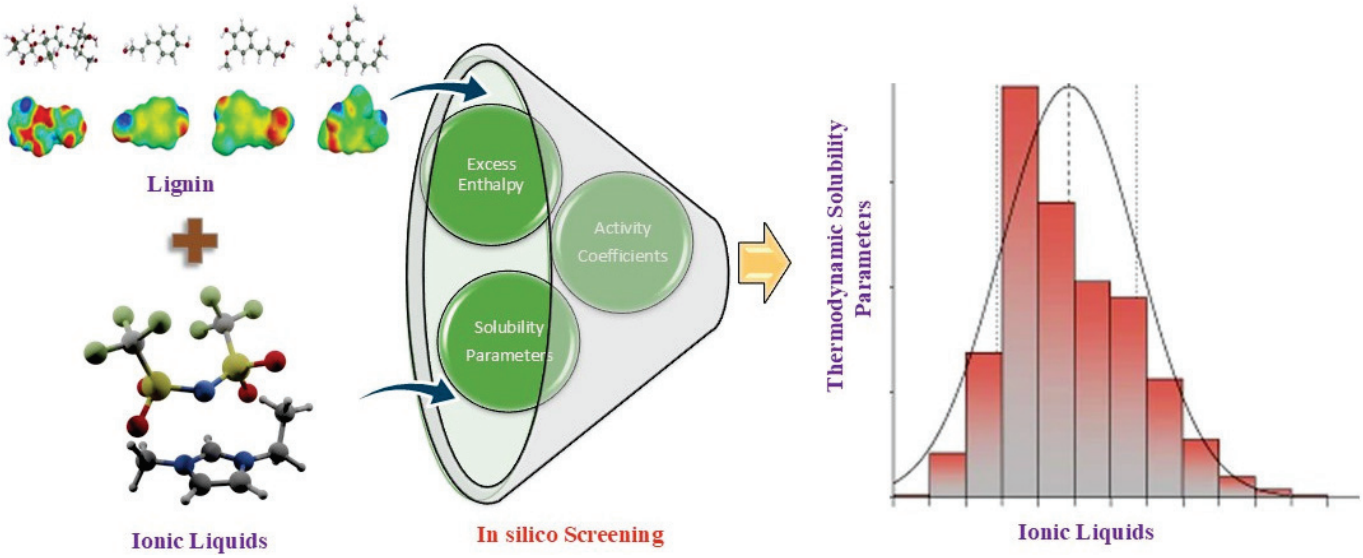

Figure 1. The schematic diagram for screening of solvents for lignin dissolution.

Mohan et al. conducted an extensive screening of 5670 ILs, generated from 63 cations and 90 anions, to assess their effectiveness in lignin dissolution [17]. The lignin structure was built by joining all the major lignin linkages (β-O-4, β-β, 4-O-5, α-O-4, and β-5) present in the native lignin, and the screening results were validated using the experimental data. They identified that anions like acetate, methyl carbonate, glycinate, alaninate, and lysinate were particularly efficient in breaking down lignin, especially when paired with cations such as tetraalkylammonium ($[TAA]^+$), tetraalkylphosphonium ($[TAP]^+$), and pyridinium. Specifically, ILs containing $[TAA]^+$ and $[TAP]^+$ showed great promise as solvents due to their low viscosity, favorable Hansen solubility parameter alignment, and enhanced hydrogen-bonding basicity. Yu et al. further studied 3886 ILs using COSMO-RS. They used the 19 model structures of lignin (monomers, dimers, and trimers) for predictions and validated them through experimental solubility tests [30]. The monomeric, dimeric, and trimer structures of lignin fail to correctly represent the lignin molecule due to the absence

of several different linkages found in lignin. Additionally, Kamlet–Taft parameters were used to clarify the mechanisms involved in lignin dissolution, highlighting the importance of IL screening in optimizing lignin processing. In a further extension of this work, Mohan and coworkers explored the molecular mechanisms behind the effectiveness of cholinium lysinate ([Ch][Lys]) IL in lignin processing [36]. Using MD simulations alongside COSMO-RS, they determined that [Ch][Lys] serves as a promising solvent for lignin dissolution. This preference is attributed to multiple factors, including increased molecular interactions, extensive hydrogen bonding, a higher dissociation constant, and reduced viscosity. These characteristics collectively enhance the efficiency of [Ch][Lys] in the dissolution of lignin.

2.1. Limitations of Solvent Screening for Lignin

2.1.1. Complexity of Lignin Structure

Most computational screening models simplify lignin's structure to make simulations feasible, but this can lead to inaccurate predictions. It is challenging to make a plausible model of how lignin interacts with ILs because it is a very heterogeneous polymer with many different functional groups and bonding patterns. Simplifying lignin into small model compounds (such as guaiacol or syringol) does not capture the full complexity of the polymer [31]. Lignin is a complex and diverse biopolymer that poses substantial obstacles for characterization, depolymerization, and applications. Elaborating on the discourse regarding the "complex parameters" of lignin necessitates examining the following elements that enhance its intricacy:

Structural Heterogeneity

The structural elucidation of lignin has revealed that 50% of lignin's constituents contain aromatic rings. Lignin consists of three principal monolignol units: p-coumaryl alcohol, coniferyl alcohol, and sinapyl alcohol. These units constitute a stochastic network of ether (C-O) and carbon–carbon (C-C) bonds. The irregular polymerization results in significant structural diversity, complicating the prediction of lignin's reactivity in processes or its solubility in solvents. The composition of these monomers differs throughout plant species and even within various tissues of the same plant, contributing to its complexity [37].

Branching and Cross-Linking

Lignin, in contrast to linear polymers, exhibits extensive branching characterized by several inter-unit connections, including β-O-4 (alkyl aryl ether), β-5 (phenylcoumaran), 5-5 (biphenyl), and β-β (pinoresinol), among others. Likewise, the most abundant linkage in both softwood and hardwood lignin is the β-O-4 linkage. These linkages provide a three-dimensional matrix that inhibits depolymerization, leaving lignin more recalcitrant than other biopolymers such as cellulose and hemicellulose.

Bond Variability

Lignin comprises robust C-C bonds and more reactive C-O bonds, necessitating targeted cleavage strategies. The existence of many functional groups (hydroxyl, methoxy, carbonyl, etc.) hinders selective bond cleavage. The reaction of various bonds is contingent upon variables such as the solvent, catalyst, and temperature, complicating the regulation of the breakdown of lignin and resulting in erratic product distributions.

Polydispersity

Lignin has a strong polydisperse molecular weight distribution, indicating a broad spectrum of molecular weights and structural changes within any specific sample. The polydispersity influences both the physical qualities and chemical reactivity, as varying molecular weights react differently to processing conditions [38].

Functional Group Diversity

Lignin possesses an abundance of functional groups (hydroxyl, methoxy, phenolic, and carbonyl), with their distribution exhibiting variability. This variation affects lignin's reactivity, solubility, and interactions with other substances (e.g., catalysts, solvents). Furthermore, phenolic hydroxyl groups are crucial for antioxidant action, yet they can complicate depolymerization due to their resistance to certain chemical transformations.

Lignin–Cell Wall Interactions

Lignin is not found in isolation; it is closely associated with other cell wall constituents, especially cellulose and hemicellulose. These interactions create a rigid framework that hinders the extraction and separation of lignin. The matrix inherently resists enzymatic and chemical destruction, necessitating extreme conditions or innovative solvents for effective fractionation of lignocellulosic biomass [39].

Source Variability

The composition and structure of lignin vary considerably based on the plant source (e.g., hardwood, softwood, grasses). Softwood lignin is predominantly composed of guaiacyl (G) units, whereas hardwood lignin comprises both guaiacyl (G) and syringyl (S) units. These variations modify lignin's reactivity and require distinct methodologies for its conversion or valorization.

Future research should focus on improving computational power or algorithms to allow simulations of larger, more complex lignin structures without compromising accuracy.

2.1.2. Solubility vs. Selectivity

While some ILs are excellent at dissolving lignin, their selectivity toward different lignin fractions and derivatives remains a challenge. Current screening methods often prioritize solubility over selectivity, potentially resulting in inefficient lignin fractionation or subpar product quality. Future research should focus on ILs that are both highly soluble and selective for specific lignin components [40].

2.1.3. Computational Screening and Predictive Models

While computational tools such as COSMO-RS and MD simulations can predict IL-lignin interactions, their accuracy remains limited. There is a need for improved algorithms and more comprehensive datasets that account for the variability in lignin structure and IL chemistry. Future efforts should aim at integrating machine learning models with quantum calculation data from first-principle calculation to enhance screening efficiency. Fixing these issues will significantly advance future research in creating ILs for lignin valorization. This will result in biorefinery processes that work better and last longer. In the context of IL screening for lignin, computational screening and predictive models are becoming vital tools. However, to improve their accuracy and efficiency, we must address several challenges. One of the primary challenges in developing accurate predictive models for IL-lignin interactions is the scarcity of high-quality "standardized" experimental data. Most computational models, including machine learning (ML) approaches, require extensive datasets to predict IL performance. Because there are not any standardized experimental data for how lignin dissolves or depolymerizes in different ILs, it is challenging to make reliable models. Future work should focus on generating large, consistent datasets that capture both the structural variability of lignin and the wide range of IL chemistry.

2.1.4. Accuracy of Force Fields and Interaction Parameters

MD simulations and other computer methods utilize pre-established force fields to illustrate the interactions between lignin and ILs. The complexity of IL chemistry and lignin variability often limits the accuracy of these force fields, which is critical. Current force fields might not capture subtle interactions such as hydrogen bonding or π-π stacking

accurately. We need better machine-learned force fields that are made for ILs interacting with biopolymers like lignin in order to make MD simulations more accurate.

2.1.5. Computational Cost

High-level computational methods, like ab initio MD (AIMD) or quantum mechanical (QM) calculations, can give us a lot of information about how IL and lignin interact, but they are time- and computer-intensive. Large-scale screening, which involves evaluating hundreds or thousands of ILs, makes these methods impractical. To enhance the overall efficiency of the screening process, it could be beneficial to strike a balance between the costs associated with each step's calculations and how accurate they are. We could achieve this by developing hybrid methods that blend faster or less detailed models with occasional high-precision calculations.

2.1.6. Uncertainty in Thermodynamic Predictions

We often use tools like COSMO-RS to guess the thermodynamic features of IL-lignin systems, like their activity coefficients, how well they dissolve, and their Gibbs free energy. However, these methods often have limitations for complex mixtures or systems with strong intermolecular interactions and averaging predictions might not accurately capture the specific behavior of the system [41]. Furthermore, predicting the impact of solvent impurities can be challenging. Temperature variations and the impact of IL recycling on lignin solubility continue to pose challenges. These uncertainties can lead to suboptimal IL selection during screening. Future efforts should focus on refining these thermodynamic models and incorporating uncertainty quantification to improve their predictive capabilities.

In light of the aforementioned limitations, a conclusion table elaborating on the constraints of the solvent screening for lignin is presented in Table 1.

Table 1. Conclusion table elaborating on the constraints of the solvent screening for lignin.

Factor	Limitation	Impact on Lignin Screening
Lignin Structural Variability	High structural diversity of lignin not fully represented	Inconsistent solvent performance across different lignin structural types
Lack of Universal Solvent	No single solvent effectively dissolves all lignin types due to their structural diversity	Screening results vary depending on the source of lignin
Process Optimization Complexity	Optimizing conditions like temperature and pressure is resource-intensive and may not yield consistent results	Makes difficult for the benchmarking of results with available data
Computational Expense	High computational cost for large-scale solvent screening with real lignin	Constrains the number of solvents and conditions evaluated
Cosolvents System	Neglect co-solvent system or presence of water	Incomplete or limited understanding of lignin dissolution in real-world scenarios
Predictive Models	Over reliance on specific models without experimental validation	Potential inaccuracies in predicting lignin solubility

3. Ionic Liquids for Lignin Valorization

The process of breaking down lignin through the use of ILs is a developing area of study aimed at transforming this intricate biopolymer, which is plentiful in plant biomass, into useful low-molecular-weight substances [42]. The application of ILs in lignin depolymerization has become increasingly popular because of their distinctive characteristics, such as adjustable acidity and basicity, excellent thermal stability, and re-usability to some extent, which makes them perfect for promoting chemical reactions [43].

A lot of research using Density Functional Theory (DFT) and MD simulations has provided crucial insights into the reaction mechanisms, energy barriers, and dynamics of

interactions for complex reactions [44–48]. Recent investigations have explored the use of ILs as solvents and catalysts for the depolymerization of lignin and model compounds, utilizing DFT and MD simulations to reveal the mechanisms by which these substances dissolve and decompose lignin into valuable compounds. This theoretical framework allows for the optimization of conditions to enhance the yield and selectivity of targeted phenolic monomers throughout the depolymerization process. Disputes in the discipline frequently center on the effectiveness and ecological consequences of employing ILs in contrast to conventional techniques like reductive and oxidative depolymerization. Although some researchers advocate for the selectivity and reaction control benefits of ILs, others express apprehensions about their overall sustainability for their use in large-scale applications [49].

Furthermore, as discussed in the previous section, the complex nature of lignin's composition and structure requires continuous research to thoroughly understand how various ILs affect the depolymerization results and to enhance computational models for precise predictions. With the ongoing evolution of computational techniques, the combination of DFT and MD simulations is anticipated to significantly improve the comprehension and optimization of lignin depolymerization, leading to more sustainable methods for biomass valorization [50].

The comprehension of lignin depolymerization in the presence of ILs has consistently been a captivating area of research; however, insights into the process via QM methods have been limited when compared with experimental investigations. Nevertheless, there have been limited theoretical investigations aimed at enhancing comprehension of the process. This builds on several earlier investigations aimed at elucidating the cleavage mechanism of traditional C-O bonds in lignin when exposed to different combinations of ILs [45,46,51]. The earlier research focused on elucidating the catalytic mechanism for the depolymerization of lignin model compounds in the presence of ILs. This was achieved by examining the thermodynamics of the process, investigating the activation energy barriers, and analyzing the bonding parameters within the lignin-IL complex system. Building on a similar methodology, a recent investigation conducted by Liu et al. examined the electrocatalytic depolymerization of lignin into valuable chemicals, presenting a promising avenue for sustainable biorefineries [52]. The study utilizes dispersion-corrected DFT calculations to elucidate the electrocatalytic reduction mechanism associated with the depolymerization of lignin model dimers and oxidized lignin. The computational study was completely focused on understanding the depolymerization of β-O-4-based model compounds. The calculations clarify the role of the trimetallic ILs-PdNiBi catalytic system in promoting the generation of a crucial radical intermediate and the release of products. The anticipated energies of the reaction pathways validated the function of ILs with metals in achieving total substrate conversion and elevated yields of phenols and acetophenones by reducing the activation energy barriers, thereby aiding in C-O bond cleavage. The development of C-O bond cleavage can enhance lignin valorization and utilization by facilitating the selective breakdown of lignin into valuable chemicals while preserving the functional groups necessary for material applications. For example, demethylation, a specific form of C-O bond cleavage, involves breaking the bond between the methyl group and oxygen in methoxy ($-OCH_3$) substituents on aromatic rings. The process results in increased phenolic content and the reactivity of lignin fragments serving as valuable precursors for materials, phenolic resins, polyurethanes, etc. [53].

With recent advancements in the conversion of lignin into materials, DFT calculations have been critical in elucidating the electron transport process and material's electronic structure. Chen et al. recently published a study in which they used lignosulfonate as a carbon source from biomass to make ultrahigh-energy density supercapacitor electrodes. Calculations were performed to gain a deeper insight into the process of electron transport. Simulations grounded in DFT also contributed to a deeper understanding of the electronic and ionic characteristics, as well as the adsorption energies of the fabricated supercapacitor electrodes. This kind of research concerning material synthesis involving lignin and ILs is experimentally accessible, yet it remains limited from a theoretical standpoint, owing to the

challenges posed by lignin's complicated structure that requires resolution [54]. DFT-based optimization of lignin modifications and studying structure–property relationships can be achieved and would be of great help in the future. By revealing lignin's complex molecular behavior, these multidisciplinary approaches help speed the development of lignin-based materials and sustainable technologies.

The integration of QM calculations with ML techniques has proven to be a significant advantage in this domain, accelerating the prediction and validation of reaction mechanisms while minimizing computational effort and associated expenses. A recent investigation by Ding et al. effectively utilized machine learning alongside QM calculations to predict the bond cleavage efficiency of a set of approximately 10^3 possible ILs on the β-O-4 bond of guaiacyl glycerol-β-guaiacyl ether (GGE), achieving a strong correlation between the predicted bond dissociation energy and the experimental yield of guaiacol, emphasizing the reliability of the ML model [55]. The study pinpointed imidazolium-based cations paired with tyrosine anions as ideal candidates for future applications in the precise cleavage of lignin. This approach showcases an innovative method that bypasses the necessity for intricate activation barrier energy calculations while greatly minimizing the time required for evaluating potential ILs. DFT calculations have been helpful to generate a lot of useful molecular descriptors that can be used by the ML models. In another study performed, DFT-generated datasets were used as the input parameters for training ML models to understand the photocatalytic cleavage of C-C bonds in lignin-derived structures [56]. The extent of datasets for training ML models is restricted by the high computational cost of DFT. The generalization of ML models to a variety of systems may be impeded by the scarcity of data. Furthermore, while ML can expedite predictions, it frequently compromises accuracy in comparison to DFT. Nevertheless, these studies were limited to model monomeric/dimeric molecules and there is an urgent need to expand these calculations to various model polymeric lignin structures to gain further insights. The primary challenge in combining these methods is the delicate balance between the reliability of results and computational efficiency, especially when dealing with a combination of ILs and lignin systems.

On the contrary, methods such as MD simulations have emerged as a key tool in deciphering the intricate process of lignin depolymerization. These simulations offer a deeper understanding of the structural dynamics and interactions with solvents. In a study by Hackenstrass et al., the authors conducted classical MD simulations to uncover intricate details about the structural dynamics of lignin dimers, illustrating how different linkages influence lignin conformation and its interaction with water [44]. The structures used for predictions were based on dimers composed of common linkages found in lignin, including 4-O-5, 5-5, α-O-4, β-1, β-5, β-β, and β-O-4. This information is essential for predicting the solubility and reactivity of lignin in polar solvents. The study reveals that the β-O-4 linkage exhibits unique characteristics regarding its conformational flexibility and water interaction, which are essential for its solubility and depolymerization processes. Similar predictions can be noted in the presence of ionic solvents. In a recent study, the behavior of lignin with multiple chains was investigated within the 1-ethyl-3-methylimidazolium acetate and water system. The analysis of simulation trajectories revealed that lignin formed an aggregated complex in pure water, preserving its hydrophobic regions. Lignin chains were observed to disentangle and extend their conformation at varying concentrations of ILs in the system. The authors investigated the interaction patterns of multiple lignin chains with guaiacyl decamer in the presence of ILs, which can offer insights into the dissolution phenomenon of lignin at the atomic level [18]. Additionally, reactive force field (ReaxFF) simulations have emerged as an essential asset to the community. The ability to realistically replicate the dynamics, reactivity, and effects of solvents on the solute is a further advantage of using ReaxFF-based simulations [57]. As a result of the ease of simulating small chemical structures, ReaxFF-based simulations have been conducted on lignin-derived structures. Since it is difficult to replicate the complex and heterogeneous nature of lignin, model compounds are frequently used by researchers. A model compound

of lignin serves as a simplified representation of a particular structural unit, allowing for a focused investigation of the specific bonds or functional groups present in natural lignin. Nonetheless, a few studies have investigated the use of this method for the thermo-oxidation of lignin or lignin-based products. ReaxFF simulations were employed in a study to investigate thermal decomposition in an oxygen environment for models that represented the most prevalent linkages found in softwood. This revealed the reaction pathways of dominant reaction products [58]. A ReaxFF-based simulations were used to investigate the oxidative stabilization of softwood lignin for carbon fiber production. It focuses on lignin fragments derived from coniferyl alcohol units, revealing that the 5-5 linkage exhibits the highest reactivity towards cyclization and dehydrogenation, which is crucial for forming the rigid connections necessary for stabilization [59]. The structures used in this study consist of five to six coniferyl alcohol units connected through different linkages (namely 4-O-5, 5-5, α-O-4, β-1, β-5, β-β, and β-O-4). Two structures were preferred, including 9 lignin fragments containing 5 monolignols, 9 lignin fragments containing 6 monolignols, and 396 oxygen molecules. The cost-effectiveness associated with ReaxFF in comparison to conventional MD simulations facilitated the utilization of large structures. In a recent study, Ahmad et al. presented a technique for identifying products and their pathways in thermo-oxidation reactions through ReaxFF simulations, aiming to elucidate the dynamics and reactivity of the thermo-oxidation of two model structures of modified lignin [60]. Nonetheless, employing ReaxFF simulations to comprehend the utilization and valorization of lignin with ILs requires significant advancement, particularly in the development of accurate force fields for extensive lignin structures and ILs.

Recently, a new theoretical strategy named "Advanced real-time molecular sensing strategy" was introduced, which is claimed to be capable of capturing the dynamic nature of lignin reactions, including delignification and de/repolymerization. The work integrated the combination of DFT, AIMD, and kinetic Monte Carlo (kMC) simulations, constituting a comprehensive framework for assessing various lignin properties. This approach was capable of providing real-time molecular level information about dissolved lignin chains during delignification, including molecular weight distributions and the S/G ratio under diverse reaction conditions. However, this study was not conducted with ILs, but it can surely be a usable synergistic integration of theoretical approaches with experimental data for the understanding of the lignin systems in presence of ILs and their potential for sustainable biorefineries in the future [61]. A comprehensive grasp of this subject can aid in the formulation of a cost-effective process for lignin dissolution using ILs and even depolymerization, ultimately facilitating an improved biorefinery operation.

3.1. Challenges

Despite the advances made using DFT and MD simulations, several challenges remain. One significant challenge is the computational cost associated with simulating large lignin structures. While DFT is excellent for small systems, its computational expense becomes prohibitive for larger systems, necessitating the use of simplified lignin models, which may not fully capture the complexity of real lignin.

One significant challenge lies in the accuracy of the models used to represent lignin's complex structure. Different approaches, such as using repeating building blocks or a stochastic approach to vary linkages and monomers, aim to create representative lignin models. However, these models often come with inherent uncertainties, especially regarding the linkage distributions, which can have a margin of error of up to 5% [62]. Such discrepancies can lead to variations in the predicted behavior of lignin during depolymerization processes. Furthermore, the MD simulations are influenced by the time step chosen, with common practices employing smaller time steps. However, lower Metropolis temperatures or increased Monte Carlo (MC) events might improve simulated statistics but also increase computational complexity.

Additionally, accurately modeling ILs is challenging due to the wide range of interactions, such as hydrogen bonding, van der Waals forces, and electrostatic interactions,

present in these systems. High-level quantum chemical methods are often required to model these interactions accurately, making simulations computationally intensive. Moreover, the dynamic behavior of ILs, especially when mimicking the real experimental conditions, adds another layer of complexity to the simulations. Reactive simulation techniques can be useful to understand the dynamic structures of lignin and ILs, as well as being capable of tracking the reaction in the presence of solvents and catalysts. Polarizable force fields were introduced in conjunction with reactive force field simulations to address the simulation concerns related to ILs, and they may be more accurate in capturing local electronic effects than non-polarizable force fields. Their limited DFT use to date is certainly due to increasing computing cost or difficulty in implementation, despite their capacity to mimic more delicate electronic characteristics [63,64]. The major advantage of the method of ReaxFF is its ability to show how chemical reactions occur with no preassigned connectivity, which is useful for a number of dynamic studies in the chemistry and materials science fields. However, the method has limitations, especially when applied on larger structures. These are the advanced processes of parameterization, lower precision in relation to QM calculations, and difficulties in interpreting the simulation results of complex systems. Also, it should be noted that while ReaxFF allows carrying out simulations that are many times larger than QM calculations allow, there are also limitations in practical terms for the size of the model and for the duration that can be simulated [57]. Table 2 presents a comprehensive overview of the simulation parameters discussed in this section of the paper, which covers the types of lignin structures, ILs, and simulation methodologies that are pertinent to the valorization of lignin.

Table 2. Details about the lignin structure, ILs, and simulation methods discussed related to the valorization of lignin using ILs or solvents.

Types of Lignin or Lignin-Derived Structures	Ionic Liquids	Simulation Methods	Reference
Phenyl p-hydroxycinnamate	[Bmim][$FeCl_4$]	DFT calculations	[45]
Guaiacyl glycerol-β-guaiacyl ether	[C_3SO_3Hmim][HSO_4]	DFT calculations MD Simulations	[51]
Phenethoxybenzene 2-Phenoxyacetophenone	[Pyr_{13}][NTf_2] [Pyr_{14}][OTf] [N_{1113}][NTf_2]	Periodic DFT calculations	[52]
Guaiacyl glycerol-β-guaiacyl ether	Combination of 29 cations and 33 anions, around 1000 possible ILs	DFT calculations; ML Technique	[55]

3.2. Future Perspectives

Numerous prospective avenues may aid in addressing these challenges and enhancing the theoretical comprehension of lignin depolymerization through the use of ILs.

3.2.1. Integration of ML

By training models on existing data from DFT and MD simulations, researchers could forecast the properties of new ILs and the structural properties of lignin without relying on resource-intensive quantum chemical calculations. This method has the potential to greatly accelerate the identification of novel ILs for the depolymerization of lignin.

3.2.2. Advanced Multi-Scale Modeling

The combination of DFT and MD within a unified multi-scale framework would enable researchers to effectively capture both the electronic and dynamic behaviors involved in the depolymerization of lignin in ILs. This method may offer a comprehensive perspective on the depolymerization process and contribute to the formation of more effective ILs. The development of accurate reactive force fields for lignin and ILs can also be a solution to this field, as they can capture the reactive dynamics of the system at a lower computational cost in comparison to classical MD simulations. Another method to be worked on intensively is

DFT-based transition state calculations for complex molecules such as lignin, which are time-intensive, challenging, and susceptible to convergence issues. In order to resolve this matter, the implementation of multi-level hybrid methods that integrate semi-empirical approaches with DFT has the potential to expedite these calculations, thereby enhancing accuracy and efficiency.

3.2.3. Selective Catalysis

Formulating tailored ILs that focus on particular lignin linkages (e.g., C-O, and C-C) while reducing unwanted side reactions will be essential for enhancing lignin depolymerization. The computational data analyzed through DFT and MD simulations are quite limited and have primarily been applied to a specific group of ILs, which restricts the overall understanding and should be expanded.

4. ML Methods for Lignin Processes

ML techniques are increasingly being applied to optimize and predict the outcomes in lignin valorization processes using ILs, as also highlighted in the previous sections. This emerging approach offers significant potential to accelerate research and development by reducing the need for time-consuming and costly experimental work across various scales—from molecular interactions to process development.

The synthetic flexibility of ILs lends itself to large datasets. As a result, they provide ample opportunity for ML methods. As a result, a growing amount of research has been published on the use of ML for ILs [65]. The use of ML for ILs in general has been comprehensively reviewed before [66]. Furthermore, the use of ILs with ML for applications such as CO_2 capture [67] and thermo-chemical properties [68] has also been reviewed. But in this section of the review, we focus specifically on ML applications for lignin extraction and valorization.

At the molecular level, ML is proving valuable for predicting the fundamental properties crucial for IL-based lignin processing. More sophisticated approaches using graph-based genetic algorithms and graph neural networks have been developed for solvent design in lignin-first biorefineries. This framework designed numerous solvents with high potential for lignin solubilization, demonstrating solubilities between 20 and 60 wt% across different lignin types, including Kraft lignin from softwood, organosolv lignin from hardwood, and herbaceous lignin from corn cob by mild acidolysis [19]. Complementing this, other researchers have developed predictive toolsets that combine Hansen solubility parameters, COSMO-RS predictions, and ML models to identify effective lignocellulosic pretreatment solvents. These approaches not only predict solvent effectiveness but also provide insights into the dissolution mechanism through quantum chemical calculations [32]. Furthermore, recent work has utilized explainable ML models based on Kamlet–Taft and polarity parameters to predict and optimize lignocellulose pretreatment efficiency, offering both high predictive accuracy and the interpretability of solvent properties crucial for lignin processing [69].

Moving to catalyst design, ML is also being applied to optimize both chemical and biological catalysts for lignin processing. While not specifically focused on ILs, work on using ML to engineer cytochrome P450 enzymes for the optimal bioconversion of lignin fragments demonstrates the potential of this approach [70]. Similar techniques could be adapted to design catalytic ILs or to optimize IL-enzyme systems for lignin valorization. In the realm of chemical catalysis, ML models have been developed to predict the catalytic activity of ILs for cleaving the β-O-4 bond in lignin. The best model achieved an R2 value over 0.93, allowing rapid screening of potential IL catalysts [55]. This work highlights how ML can accelerate the discovery and optimization of IL-based catalytic systems for lignin depolymerization.

Considering larger scales, ML is being applied to optimize reaction conditions and predict process outcomes. Random forest regression has been used to predict bio-oil yield and char yield from IL-catalyzed lignin depolymerization, achieving R2 scores of

0.91 and 0.94, respectively [71]. These types of predictive models can help researchers identify promising reaction conditions without extensive experimental trials. The power of ML in uncovering non-obvious relationships in lignin processing has been further demonstrated. Using algorithms like XGBoost to model lignin hydrogenolysis revealed that parameters such as the lignin-to-solvent ratio and catalyst pore size had large impacts on outcomes [72]. This type of insight can guide more targeted experimental design and process optimization. At the process development level, Bayesian optimization has been applied to simultaneously optimize multiple lignin properties in an IL-based biorefinery process. This allowed efficient navigation of the multi-dimensional process parameter space and identification of optimal conditions, significantly accelerating the development and scale-up of IL-based lignin valorization processes [73].

An important consideration in applying ML to lignin valorization is the selection and engineering of appropriate descriptors or input features. While many studies use readily available parameters like IL cation/anion identities and reaction conditions, more sophisticated approaches are emerging. Various molecular representation techniques for ILs have been reviewed, highlighting the potential of natural language processing methods that can learn directly from SMILES strings or other text-based molecular notations [66]. Building on this, Transformer Convolutional Neural Networks operating on SMILES inputs have been found to outperform traditional descriptor-based models for predicting IL melting points [74]. This suggests that advanced text-based ML models could offer improved predictive power for IL properties relevant to lignin processing. The use of explainable ML models is particularly noteworthy. Models have been developed to predict lignocellulose pretreatment efficiency based on Kamlet–Taft and polarity parameters [69]. Such approaches not only achieve high predictive accuracy but also provide insights into the relative importance of different solvent properties. This type of interpretable ML model is crucial for gaining scientific insights and building trust in ML predictions for lignin valorization processes.

Beyond reaction optimization, ML is also being applied to analytical techniques relevant to lignin research. ML models have been used to predict the lignin content in poplar wood using Raman spectroscopy data [75]. This showcases how ML can enhance rapid characterization methods, potentially enabling real-time monitoring and control of lignin processing for downstream processing.

Despite these advances, challenges remain in applying ML to IL-based lignin valorization. The available datasets are often small and fragmented, and the complex, heterogeneous nature of lignin poses difficulties for developing universally applicable models. Proper validation is crucial, as the random splitting of limited IL datasets can lead to overly optimistic performance estimates [74].

Looking forward, integrating ML with high-throughput experimentation could enable rapid closed-loop optimization of IL-lignin systems. Incorporating mechanistic knowledge into ML architectures may improve accuracy and interpretability. There is also significant potential in applying ML to analyze spectroscopic and analytical data from IL-lignin reactions, potentially yielding new chemical insights. ML methods have already demonstrated clear value in accelerating research on IL-based lignin valorization across multiple scales, from molecular design to process optimization (Table 3). As datasets grow and algorithms improve, ML is likely to play an increasingly central role in this field.

Table 3. ML applications in IL-based lignin valorization.

Key Findings/Outcomes	ML Methods	Reference
Predicted solvent properties	XGBoost, RF, GPR, SVR, KNR	[69]
Predicted IL catalytic activity	ANN, SVR, LR, RF, GBDT	[55]
Predicted bio-oil yield and char yield from IL-catalyzed depolymerization	RF	[71]

Table 3. *Cont.*

Key Findings/Outcomes	ML Methods	Reference
Optimized hydrogenolysis outcomes using lignin-to-solvent ratio and catalyst pore size	LightGBM, XGBoost, and CatBoost	[72]
Optimized multiple lignin properties in IL-based biorefinery process	Bayesian optimization	[73]
Predicted IL melting points using SMILES inputs	Transformer Convolutional Neural Networks	[74]
Predicted lignin content in poplar wood	SVR, RF, LightGBM, CatBoost, XGBoost	[75]

Abbreviations: Extreme gradient boosting (XGBoost), Random forest (RF), Gaussian process regression (GPR), Support vector regression (SVR), Linear regression (LR), K-neighbor regression (KNR), Artificial neural network (ANN), Gradient boosting decision tree (GBDT).

5. Conclusions

Given the need to valorize lignin for a sustainable biorefinery, this review highlights the expanding influence of computational methods and machine learning approaches in lignin processing using ILs. The substantial progress in computational resources, including the integration of ML techniques, has significantly reduced the timeline of optimizing deconstruction through data-driven methods to gaining atomic- and molecular-level insights into complex lignin-IL interactions. This review additionally identifies the major research gaps and potential future directions to tackle unknown challenges in lignin valorization using ILs. For instance, the need for the (a) extensive experimental validation of simulated/predicted data, (b) introduction of complexity in lignin structure, (c) standardization of simulated data and open access data-sharing, and (d) integration of ML with high-throughput experimentation. Ongoing advancement and expansion of computational methods to enhance lignin dissolution and valorization, particularly through next-generation predictive paradigms, are crucial for establishing the fundamental science needed to develop and optimize effective lignin conversion processes. In summary, realizing the full potential of lignin as a renewable feedstock will require continued collaboration between data scientists, chemists, and chemical engineers to develop ML tools tailored for the unique challenges of IL-lignin systems.

Author Contributions: Conceptualization, B.R.T., N.K., D.K.M., B.A.S., H.C. and K.L.S.; writing—original draft, B.R.T., N.K. and D.K.M.; writing—review and editing, B.R.T., N.K., D.K.M., B.A.S., H.C. and K.L.S.; visualization, B.R.T., N.K. and D.K.M.; supervision, B.A.S., H.C. and K.L.S.; project administration, H.C. and K.L.S.; funding acquisition, B.A.S. All authors have read and agreed to the published version of the manuscript.

Funding: This research was funded by the U.S. Department of Energy, Office of Science, Biological and Environmental Research Program under Award Number DE-AC02-05CH11231.

Acknowledgments: This material is based upon work supported by the Joint BioEnergy Institute, U.S. Department of Energy, Office of Science, Biological and Environmental Research Program under Award Number DE-AC02-05CH11231 with Lawrence Berkeley National Laboratory. The U.S. Government retains, and the publisher, by accepting the article for publication, acknowledges that the U.S. Government retains a nonexclusive, paid-up, irrevocable, worldwide license to publish or reproduce the published form of this manuscript or allow others to do so, for the U.S. Government purpose. Sandia National Laboratories is a multi-mission laboratory managed and operated by National Technology and Engineering Solutions of Sandia, LLC, a wholly owned subsidiary of Honeywell International Inc., for the U.S. DOE's National Nuclear Security Administration under contract DE-NA0003525. This paper describes objective technical results and analysis. Any subjective views or opinions that might be expressed in the paper do not necessarily represent the views of the U.S. DOE or the U.S. Government.

Conflicts of Interest: B.A.S. has a financial interest in Illium Technologies, Caribou Biofuels, and Erg Bio. All other authors declare the absence of any commercial or financial relationships that could be construed as a potential conflict of interest.

References

1. Ralph, J.; Lapierre, C.; Boerjan, W. Lignin structure and its engineering. *Curr. Opin. Biotechnol.* **2019**, *56*, 240–249. [CrossRef] [PubMed]
2. Schutyser, W.; Renders, T.; Van den Bosch, S.; Koelewijn, S.F.; Beckham, G.T.; Sels, B.F. Chemicals from lignin: An interplay of lignocellulose fractionation, depolymerisation, and upgrading. *Chem. Soc. Rev.* **2018**, *47*, 852–908. [CrossRef] [PubMed]
3. Yu, O.; Kim, K.H. Lignin to materials: A focused review on recent novel lignin applications. *Appl. Sci.* **2020**, *10*, 4626. [CrossRef]
4. Domínguez-Robles, J.; Cárcamo-Martínez, Á.; Stewart, S.A.; Donnelly, R.F.; Larrañeta, E.; Borrega, M. Lignin for pharmaceutical and biomedical applications—Could this become a reality? *Sustain. Chem. Pharm.* **2020**, *18*, 100320. [CrossRef]
5. Shrestha, S.; Goswami, S.; Banerjee, D.; Garcia, V.; Zhou, E.; Olmsted, C.N.; Majumder, E.L.-W.; Kumar, D.; Awasthi, D.; Mukhopadhyay, A.; et al. Perspective on lignin conversion strategies that enable next generation biorefineries. *ChemSusChem* **2024**, *17*, e202301460. [CrossRef]
6. Ekielski, A.; Mishra, P.K. Lignin for bioeconomy: The present and future role of technical lignin. *Int. J. Mol. Sci.* **2020**, *22*, 63. [CrossRef]
7. José Borges Gomes, F.; de Souza, R.E.; Brito, E.O.; Costa Lelis, R.C. A review on lignin sources and uses. *JABB* **2020**, *7*, 100–105. [CrossRef]
8. Eraghi Kazzaz, A.; Fatehi, P. Technical lignin and its potential modification routes: A mini-review. *Ind. Crops Prod.* **2020**, *154*, 112732. [CrossRef]
9. Sadeghifar, H.; Ragauskas, A. Perspective on technical lignin fractionation. *ACS Sustain. Chem. Eng.* **2020**, *8*, 8086–8101. [CrossRef]
10. Sethupathy, S.; Murillo Morales, G.; Gao, L.; Wang, H.; Yang, B.; Jiang, J.; Sun, J.; Zhu, D. Lignin valorization: Status, challenges and opportunities. *Bioresour. Technol.* **2022**, *347*, 126696. [CrossRef]
11. Jassal, V.; Dou, C.; Sun, N.; Singh, S.; Simmons, B.A.; Choudhary, H. Finding values in lignin: A promising yet under-utilized component of the lignocellulosic biomass. *Front. Chem. Eng.* **2022**, *4*, 1059305. [CrossRef]
12. Luo, H.; Abu-Omar, M.M. Chemicals from Lignin. In *Encyclopedia of Sustainable Technologies*; Elsevier: Amsterdam, The Netherlands, 2017; pp. 573–585, ISBN 9780128047927.
13. Abu-Omar, M.M.; Ford, P.C. The lignin challenge in catalytic conversion of biomass solids to chemicals and fuels. *RSC. Sustain.* **2023**, *1*, 1686–1703. [CrossRef]
14. Lei, Z.; Dai, C.; Hallett, J.; Shiflett, M. Introduction: Ionic liquids for diverse applications. *Chem. Rev.* **2024**, *124*, 7533–7535. [CrossRef] [PubMed]
15. Zhang, Z.; Song, J.; Han, B. Catalytic Transformation of Lignocellulose into Chemicals and Fuel Products in Ionic Liquids. *Chem. Rev.* **2017**, *117*, 6834–6880. [CrossRef] [PubMed]
16. Wang, B.; Qin, L.; Mu, T.; Xue, Z.; Gao, G. Are ionic liquids chemically stable? *Chem. Rev.* **2017**, *117*, 7113–7131. [CrossRef]
17. Mohan, M.; Simmons, B.A.; Sale, K.L.; Singh, S. Multiscale molecular simulations for the solvation of lignin in ionic liquids. *Sci. Rep.* **2023**, *13*, 271. [CrossRef]
18. Radhakrishnan, R.; Manna, B.; Ghosh, A. Molecular insights into dissolution of lignin bunch in ionic liquid-water mixture for enhanced biomass conversion. *Renew. Energy* **2023**, *206*, 47–59. [CrossRef]
19. König-Mattern, L.; Komarova, A.O.; Ghosh, A.; Linke, S.; Rihko-Struckmann, L.K.; Luterbacher, J.; Sundmacher, K. High-throughput computational solvent screening for lignocellulosic biomass processing. *Chem. Eng. J.* **2023**, *452*, 139476. [CrossRef]
20. Pham, L.T.M.; Choudhary, H.; Gauttam, R.; Singer, S.W.; Gladden, J.M.; Simmons, B.A.; Singh, S.; Sale, K.L. Revisiting Theoretical Tools and Approaches for the Valorization of Recalcitrant Lignocellulosic Biomass to Value-Added Chemicals. *Front. Energy Res.* **2022**, *10*, 863153. [CrossRef]
21. Paduszyński, K.; Domańska, U. Thermodynamic modeling of ionic liquid systems: Development and detailed overview of novel methodology based on the PC-SAFT. *J. Phys. Chem. B* **2012**, *116*, 5002–5018. [CrossRef]
22. Valderrama, J.O.; Robles, P.A. Critical properties, normal boiling temperatures, and acentric factors of fifty ionic liquids. *Ind. Eng. Chem. Res.* **2007**, *46*, 1338–1344. [CrossRef]
23. Eike, D.M.; Brennecke, J.F.; Maginn, E.J. Predicting Infinite-Dilution Activity Coefficients of Organic Solutes in Ionic Liquids. *Ind. Eng. Chem. Res.* **2004**, *43*, 1039–1048. [CrossRef]
24. Shah, J.K.; Maginn, E.J. Monte Carlo simulations of gas solubility in the ionic liquid 1-n-butyl-3-methylimidazolium hexafluorophosphate. *J. Phys. Chem. B* **2005**, *109*, 10395–10405. [CrossRef]
25. Shi, W.; Maginn, E.J. Molecular simulation and regular solution theory modeling of pure and mixed gas absorption in the ionic liquid 1-n-hexyl-3-methylimidazolium bis(trifluoromethylsulfonyl)amide ([hmim][Tf2N]). *J. Phys. Chem. B* **2008**, *112*, 16710–16720. [CrossRef] [PubMed]
26. Klamt, A. Conductor-like Screening Model for Real Solvents: A New Approach to the Quantitative Calculation of Solvation Phenomena. *J. Phys. Chem.* **1995**, *99*, 2224–2235. [CrossRef]
27. Klamt, A.; Eckert, F. COSMO-RS: A novel and efficient method for the a priori prediction of thermophysical data of liquids. *Fluid Phase Equilib.* **2000**, *172*, 43–72. [CrossRef]
28. Kumar, N.; Mohan, M.; Smith, J.C.; Simmons, B.A.; Singh, S.; Banerjee, T. Inhibition of asphaltene aggregation using deep eutectic solvents: COSMO-RS calculations and experimental validation. *J. Mol. Liq.* **2024**, *400*, 124471. [CrossRef]

29. Hadj-Kali, M.K.; Althuluth, M.; Mokraoui, S.; Wazeer, I.; Ali, E.; Richon, D. Screening of ionic liquids for gas separation using COSMO-RS and comparison between performances of ionic liquids and aqueous alkanolamine solutions. *Chem. Eng. Commun.* **2020**, *207*, 1264–1277. [CrossRef]
30. Khan, H.W.; Reddy, A.V.B.; Nasef, M.M.E.; Bustam, M.A.; Goto, M.; Moniruzzaman, M. Screening of ionic liquids for the extraction of biologically active compounds using emulsion liquid membrane: COSMO-RS prediction and experiments. *J. Mol. Liq.* **2020**, *309*, 113122. [CrossRef]
31. Yu, K.; Ding, W.-L.; Lu, Y.; Wang, Y.; Liu, Y.; Liu, G.; Huo, F.; He, H. Ionic liquids screening for lignin dissolution: COSMO-RS simulations and experimental characterization. *J. Mol. Liq.* **2022**, *348*, 118007. [CrossRef]
32. Achinivu, E.C.; Mohan, M.; Choudhary, H.; Das, L.; Huang, K.; Magurudeniya, H.D.; Pidatala, V.R.; George, A.; Simmons, B.A.; Gladden, J.M. A predictive toolset for the identification of effective lignocellulosic pretreatment solvents: A case study of solvents tailored for lignin extraction. *Green Chem.* **2021**, *23*, 7269–7289. [CrossRef]
33. Zhao, J.; Zhou, G.; Fang, T.; Ying, S.; Liu, X. Screening ionic liquids for dissolving hemicellulose by COSMO-RS based on the selective model. *RSC Adv.* **2022**, *12*, 16517–16529. [CrossRef] [PubMed]
34. Zhou, L.; Liu, Y.; Zhang, J.; Li, Q.; Yuan, M.; Kang, Z. Ionic liquid screening for lignocellulosic biomass fractionation: COSMO–RS prediction and experimental verification. *J. Mol. Liq.* **2024**, *407*, 125214. [CrossRef]
35. Ralph, J.; Lundquist, K.; Brunow, G.; Lu, F.; Kim, H.; Schatz, P.F.; Marita, J.M.; Hatfield, R.D.; Ralph, S.A.; Christensen, J.H.; et al. Lignins: Natural polymers from oxidative coupling of 4-hydroxyphenyl- propanoids. *Phytochem. Rev.* **2004**, *3*, 29–60. [CrossRef]
36. Mohan, M.; Huang, K.; Pidatala, V.; Simmons, B.; Singh, S.; Sale, K.L.; Gladden, J. Prediction of Solubility Parameters of Lignin and Ionic Liquids Using Multi-resolution Simulation Approaches. *Green Chem.* **2022**, *24*, 1165–1176. [CrossRef]
37. Liu, R.; Willför, S.; Xu, C. New insights into the effects of structural and constituent heterogeneities in lignin on the formation of nanoparticles. *Ind. Crops Prod.* **2024**, *220*, 119149. [CrossRef]
38. Lu, Y.; Joosten, L.; Donkers, J.; Andriulo, F.; Slaghek, T.M.; Phillips-Jones, M.K.; Gosselink, R.J.A.; Harding, S.E. Characterisation of mass distributions of solvent-fractionated lignins using analytical ultracentrifugation and size exclusion chromatography methods. *Sci. Rep.* **2021**, *11*, 13937. [CrossRef]
39. Terrett, O.M.; Dupree, P. Covalent interactions between lignin and hemicelluloses in plant secondary cell walls. *Curr. Opin. Biotechnol.* **2019**, *56*, 97–104. [CrossRef]
40. Rashid, T.; Sher, F.; Rasheed, T.; Zafar, F.; Zhang, S.; Murugesan, T. Evaluation of current and future solvents for selective lignin dissolution–A review. *J. Mol. Liq.* **2021**, *321*, 114577. [CrossRef]
41. Yao, A.; Choudhary, H.; Mohan, M.; Rodriguez, A.; Magurudeniya, H.; Pelton, J.G.; George, A.; Simmons, B.A.; Gladden, J.M. Can multiple ions in an ionic liquid improve the biomass pretreatment efficacy? *ACS Sustain. Chem. Eng.* **2021**, *12*, 4371–4376. [CrossRef]
42. Bourmaud, C.L.; Bertella, S.; Bosch Rico, A.; Karlen, S.D.; Ralph, J.; Luterbacher, J.S. Quantification of Native Lignin Structural Features with Gel-Phase 2D-HSQC0 Reveals Lignin Structural Changes During Extraction. *Angew. Chem. Int. Ed.* **2024**, *63*, e202404442. [CrossRef] [PubMed]
43. Nanayakkara, S.; Patti, A.F.; Saito, K. Lignin Depolymerization with Phenol via Redistribution Mechanism in Ionic Liquids. *ACS Sustain. Chem. Eng.* **2014**, *2*, 2159–2164. [CrossRef]
44. Hackenstrass, K.; Hasani, M.; Wohlert, M. Structure, flexibility and hydration properties of lignin dimers studied with Molecular Dynamics simulations. *Holzforschung* **2024**, *78*, 98–108. [CrossRef]
45. Zhang, T.; Zhang, Y.; Wang, Y.; Huo, F.; Li, Z.; Zeng, Q.; He, H.; Li, X. Theoretical Insights into the Depolymerization Mechanism of Lignin to Methyl p-hydroxycinnamate by [Bmim][FeCl4] Ionic Liquid. *Front. Chem.* **2019**, *7*, 446. [CrossRef] [PubMed]
46. Tian, X.-Y.; Zheng, Y.-Z.; Zhang, Y.-C. Molecular design of efficient SO3H-functionalized ionic liquid to catalyse chitin into levulinic acid: NMR and DFT study. *J. Mol. Liq.* **2022**, *368*, 120735. [CrossRef]
47. Mishra, D.K.; Banerjee, B.; Pugazhenthi, G.; Banerjee, T. Metal-Free, Ionic Liquid-Mediated Hydrogen Release from Amine Borane Complexes: An Experimental and Density Functional Theory Investigation. *Ind. Eng. Chem. Res.* **2021**, *60*, 9764–9776. [CrossRef]
48. Mishra, D.K.; Hussain, R.; Pugazhenthi, G.; Banerjee, T. Catalytic Effect of Ionic Liquid Induced H_2 -Release from Morpholine Borane Complex: An Efficient Hydrogen Storage Carrier. *ACS Sustain. Chem. Eng.* **2022**, *10*, 6157–6164. [CrossRef]
49. Mukesh, C.; Huang, G.; Qin, H.; Liu, Y.; Ji, X. Insight into lignin oxidative depolymerization in ionic liquids and deep eutectic solvents. *Biomass Bioenergy* **2024**, *188*, 107305. [CrossRef]
50. Singh, S.K. Ionic liquids and lignin interaction: An overview. *Bioresour. Technol. Rep.* **2022**, *17*, 100958. [CrossRef]
51. Zhang, Y.; Huo, F.; Wang, Y.; Xia, Y.; Tan, X.; Zhang, S.; He, H. Theoretical Elucidation of β-O-4 Bond Cleavage of Lignin Model Compound Promoted by Sulfonic Acid-Functionalized Ionic Liquid. *Front. Chem.* **2019**, *7*, 78. [CrossRef]
52. Liu, G.; Lu, Y.; Lu, J.; Wang, Y.; Liang, S.; He, H.; Jiang, L. Ionic liquid-trimetallic electrocatalytic system for C-O bond cleavage in lignin model compounds and lignin under ambient conditions. *Nano Res.* **2024**, *17*, 2420–2428. [CrossRef]
53. Luo, Q.; Li, C.; Zhao, W.; Ding, W.; Liu, Y.; Xiao, W.; Liu, H.; Pang, X.; Sun, J. Lignin Demethylated by Protic Ionic Liquid as a Novel and Sustainable Chrome-Free Tanning Agent for Eco-Leather Production. *ACS Sustain. Chem. Eng.* **2024**, *12*, 9682–9694. [CrossRef]
54. Chen, R.; Tang, H.; He, P.; Zhang, W.; Dai, Y.; Zong, W.; Guo, F.; He, G.; Wang, X. Interface Engineering of Biomass-Derived Carbon used as Ultrahigh-Energy-Density and Practical Mass-Loading Supercapacitor Electrodes. *Adv. Funct. Mater.* **2023**, *33*, 2212078. [CrossRef]

55. Ding, W.-L.; Zhang, T.; Wang, Y.; Xin, J.; Yuan, X.; Ji, L.; He, H. Machine Learning Screening of Efficient Ionic Liquids for Targeted Cleavage of the β-O-4 Bond of Lignin. *J. Phys. Chem. B* **2022**, *126*, 3693–3704. [CrossRef] [PubMed]
56. Zhang, T.; Wu, C.; Xing, Z.; Zhang, J.; Wang, S.; Feng, X.; Zhu, J.; Lu, X.; Mu, L. Machine learning prediction of photocatalytic lignin cleavage of C–C bonds based on density functional theory. *Mater. Today Sustain.* **2022**, *20*, 100256. [CrossRef]
57. Senftle, T.P.; Hong, S.; Islam, M.M.; Kylasa, S.B.; Zheng, Y.; Shin, Y.K.; Junkermeier, C.; Engel-Herbert, R.; Janik, M.J.; Aktulga, H.M.; et al. The ReaxFF reactive force-field: Development, applications and future directions. *NPJ Comput. Mater.* **2016**, *2*, 15011. [CrossRef]
58. Beste, A. ReaxFF study of the oxidation of lignin model compounds for the most common linkages in softwood in view of carbon fiber production. *J. Phys. Chem. A* **2014**, *118*, 803–814. [CrossRef]
59. Beste, A. Reaxff study of the oxidation of softwood lignin in view of carbon fiber production. *Energy Fuels* **2014**, *28*, 7007–7013. [CrossRef]
60. Ahmed, S.; Eder, S.J.; Dörr, N.; Martini, A. Tracking Thermo-Oxidation Reaction Products and Pathways of Modified Lignin Structures from Reactive Molecular Dynamics Simulations. *J. Phys. Chem. A* **2024**, *128*, 5398–5407. [CrossRef]
61. Lee, C.H.; Kim, J.; Ryu, J.; Won, W.; Yoo, C.G.; Kwon, J.S.-I. Lignin structure dynamics: Advanced real-time molecular sensing strategies. *Chem. Eng. J.* **2024**, *487*, 150680. [CrossRef]
62. Wang, Y.; Kalscheur, J.; Ebikade, E.; Li, Q.; Vlachos, D.G. LigninGraphs: Lignin structure determination with multiscale graph modeling. *J. Cheminform.* **2022**, *14*, 43. [CrossRef] [PubMed]
63. Bodo, E. Perspectives in the computational modeling of new generation, biocompatible ionic liquids. *J. Phys. Chem. B* **2022**, *126*, 3–13. [CrossRef] [PubMed]
64. Borodin, O. Polarizable force field development and molecular dynamics simulations of ionic liquids. *J. Phys. Chem. B* **2009**, *113*, 11463–11478. [CrossRef] [PubMed]
65. Wei, Z.; Chen, F.; Liu, H.; Huang, R.; Pan, K.; Ji, W.; Wang, J. Mapping the application research on machine learning in the field of ionic liquids: A bibliometric analysis. *Fluid Phase Equilib.* **2024**, *583*, 114117. [CrossRef]
66. Koutsoukos, S.; Philippi, F.; Malaret, F.; Welton, T. A review on machine learning algorithms for the ionic liquid chemical space. *Chem. Sci.* **2021**, *12*, 6820–6843. [CrossRef]
67. Sun, J.; Sato, Y.; Sakai, Y.; Kansha, Y. A review of ionic liquids and deep eutectic solvents design for CO2 capture with machine learning. *J. Clean. Prod.* **2023**, *414*, 137695. [CrossRef]
68. Yusuf, F.; Olayiwola, T.; Afagwu, C. Application of Artificial Intelligence-based predictive methods in Ionic liquid studies: A review. *Fluid Phase Equilib.* **2021**, *531*, 112898. [CrossRef]
69. Ge, H.; Bai, Y.; Zhou, R.; Liu, Y.; Wei, J.; Wang, S.; Li, B.; Xu, H. Explicable Machine Learning for Predicting High-Efficiency Lignocellulose Pretreatment Solvents Based on Kamlet–Taft and Polarity Parameters. *ACS Sustain. Chem. Eng.* **2024**, *12*, 7578–7590. [CrossRef]
70. Dias, A.H.S.; Cao, Y.; Skaf, M.S.; de Visser, S.P. Machine learning-aided engineering of a cytochrome P450 for optimal bioconversion of lignin fragments. *Phys. Chem. Chem. Phys.* **2024**, *26*, 17577–17587. [CrossRef]
71. Castro Garcia, A.; Shuo, C.; Cross, J.S. Machine learning based analysis of reaction phenomena in catalytic lignin depolymerization. *Bioresour. Technol.* **2022**, *345*, 126503. [CrossRef]
72. Liu, Y.; Cheng, S.; Cross, J.S. Machine learning assisted chemical process parameter mapping on lignin hydrogenolysis. *Energies* **2022**, *16*, 256. [CrossRef]
73. Löfgren, J.; Tarasov, D.; Koitto, T.; Rinke, P.; Balakshin, M.; Todorović, M. Machine learning optimization of lignin properties in green biorefineries. *ACS Sustain. Chem. Eng.* **2022**, *10*, 9469–9479. [CrossRef]
74. Makarov, D.M.; Fadeeva, Y.A.; Shmukler, L.E.; Tetko, I.V. Beware of proper validation of models for ionic Liquids! *J. Mol. Liq.* **2021**, *344*, 117722. [CrossRef]
75. Gao, W.; Zhou, L.; Liu, S.; Guan, Y.; Gao, H.; Hui, B. Machine learning prediction of lignin content in poplar with Raman spectroscopy. *Bioresour. Technol.* **2022**, *348*, 126812. [CrossRef]

Disclaimer/Publisher's Note: The statements, opinions and data contained in all publications are solely those of the individual author(s) and contributor(s) and not of MDPI and/or the editor(s). MDPI and/or the editor(s) disclaim responsibility for any injury to people or property resulting from any ideas, methods, instructions or products referred to in the content.

molecules

MDPI

Review

New Materials for Thin-Film Solid-Phase Microextraction (TF-SPME) and Their Use for Isolation and Preconcentration of Selected Compounds from Aqueous, Biological and Food Matrices

Witold Krumplewski and Iwona Rykowska *

Department of Chemistry, Adam Mickiewicz University, Ul. Uniwersytetu Poznańskiego 8, 61-614 Poznań, Poland; witkru@st.amu.edu.pl
* Correspondence: obstiwo@amu.edu.pl

Abstract: Determination of a broad spectrum of analytes, carried out with analytical instruments in samples with complex matrices, including environmental, biological, and food samples, involves the development of new and selective sorption phases used in microextraction techniques that allow their isolation from the matrix. SPME solid-phase microextraction is compatible with green analytical chemistry among the sample preparation techniques, as it reduces the use of toxic organic solvents to the minimum necessary. Over the past two decades, it has undergone impressive progress, resulting in the development of the thin-film solid-phase microextraction technique, TF-SPME (the thin-film solid-phase microextraction), which is characterized by a much larger surface area of the sorption phase compared to that of the SPME fiber. TF-SPME devices, in the form of a mostly rectangular metal or polymer substrate onto which a thin film of sorption phase is applied, are characterized, among others, by a higher sorption capacity. In comparison with microextraction carried out on SPME fiber, they enable faster microextraction of analytes. The active phase on which analyte sorption occurs can be applied to the substrate through techniques such as dip coating, spin coating, electrospinning, rod coating, and spray coating. The dynamic development of materials chemistry makes it possible to use increasingly advanced materials as selective sorption phases in the TF-SPME technique: polymers, conducting polymers, molecularly imprinted polymers, organometallic frameworks, carbon nanomaterials, aptamers, polymeric ionic liquids, and deep eutectic solvents. Therefore, TF-SPME has been successfully used to prepare analytical samples to determine a broad spectrum of analytes in sample matrices: environmental, biological, and food. The work will be a review of the above-mentioned issues.

Keywords: microextraction; thin-film solid-phase microextraction; thin-film microextraction; extraction coatings; sorption phase

1. Introduction

Modern instrumental methods of analytical chemistry, including gas chromatography GC and high-performance liquid chromatography HPLC methods, allow the determination of trace amounts of analytes in tiny sample volumes. In analytical procedures for determining micro-trace amounts of analytes, the sample preparation stage plays a crucial role because it involves the separation of analytes from the matrix and their preconcentration to such values that allow analysts to conduct detection or determination. The stage of analytical procedures mentioned above should be consistent with the tenets of sustainable eco-development and the principles of green chemistry, which include the need to reduce the use of toxic organic solvents as much as possible. Compatible with green analytical chemistry, sample preparation techniques include solid-phase microextraction techniques, which are increasingly used in analytical laboratories. Solid-phase microextraction (SPME),

developed in the 1990s by J. Pawliszyn, enables rapid, accurate, reproducible, and selective isolation of compounds from a liquid or gas matrix. Over the past two decades, there has been significant development of SPME, which has resulted, among other things, in the development of the thin-film solid-phase microextraction technique, TF-SPME (thin-film solid-phase microextraction). The SPME technique involves the sorption of analytes from a matrix into a solid phase placed on the surface of a thin glass fiber or metal rod. In the TF-SPME technique, the sorption phase is applied to a flat substrate or is a self-supporting membrane. Microextraction sorbents used in the TF-SPME technique are characterized by a larger surface area of the sorption phase than the SPME fiber. Consequently, they have a higher sorption capacity, enabling faster microextraction of analytes than microextraction conducted on the SPME fiber. The dynamic development of materials chemistry makes it possible to use increasingly advanced materials as sorption phases in TF-SPME techniques and to perform selective microextractions from very complex matrices with analytes in trace amounts.

Over the last few years, a large number of reviews, dedicated to solid-phase microextraction, have been published. They present various aspects of the application of solid-phase microextraction techniques in the determination of analytes isolated from complex aqueous [1], biological, and food matrices [2–6]. However, there are few publications of the review type devoted exclusively to the TF-SPME technique. According to the knowledge of the authors of this publication, only three review-type papers are related to the TF-SPME technique. Fatemeh, Pawliszyn, and co-workers discuss the fundamental principle of TFME and its benefits versus the rod fiber geometry of SPME and demonstrate the agreements of the experimental data for the available TFME systems with the theoretical concept [7]. Olcer and co-workers show, in their review, coating techniques for applying sorption layers to solid substrates [8]. In addition to the techniques used in the preparation of TF-SPME devices, Emmons and co-workers describe pivotal steps in the development of the TF-SPME technique with thermal desorption [9]. The main aim of our review is to present the development of the TF-SPME technique over the period 2010–2024. It contains an overview of the most commonly used techniques of applying active phases in the preparation of TF-SPME instruments, the characteristics of materials used as sorption phases, and the characteristics of analytes isolated from water, food, and biological matrices, using the TF-SPME technique.

2. Microextraction Techniques

Microextraction techniques (METs) are based on sorption processes in which the volume of the extraction phase is very small compared to the volume of the sample. METs can be divided into techniques based on extraction to the solid-phase SPME (solid-phase microextraction) and to the liquid-phase LPME (liquid-phase microextraction). In LPME liquid-phase microextraction techniques, the extraction system consists of microliters of an immiscible solvent and an aqueous phase containing analytes.

Solid-phase microextraction methods can be broadly divided into static and dynamic. In the former methods, microextraction is conducted in a closed vessel with a stirrer, and mass transfer of the analyte, from the matrix to the extraction phase, is assisted by stirring (sample stir microextraction). In the latter case, the sample flows through a capillary or a needle with an inside deposited sorptive phase (sample flow microextraction) (Figure 1) [10].

In sample stirred systems, the sorption surface is applied to the following:

1. Thin glass fiber or metal rod (fiber SPME);
2. Rotating magnetic dipole (SBSE);
3. Solid substrate in the form of a thin film (TF-SPME).

In the TF-SPME technique, the polymeric sorption phase can also be a self-supporting membrane.

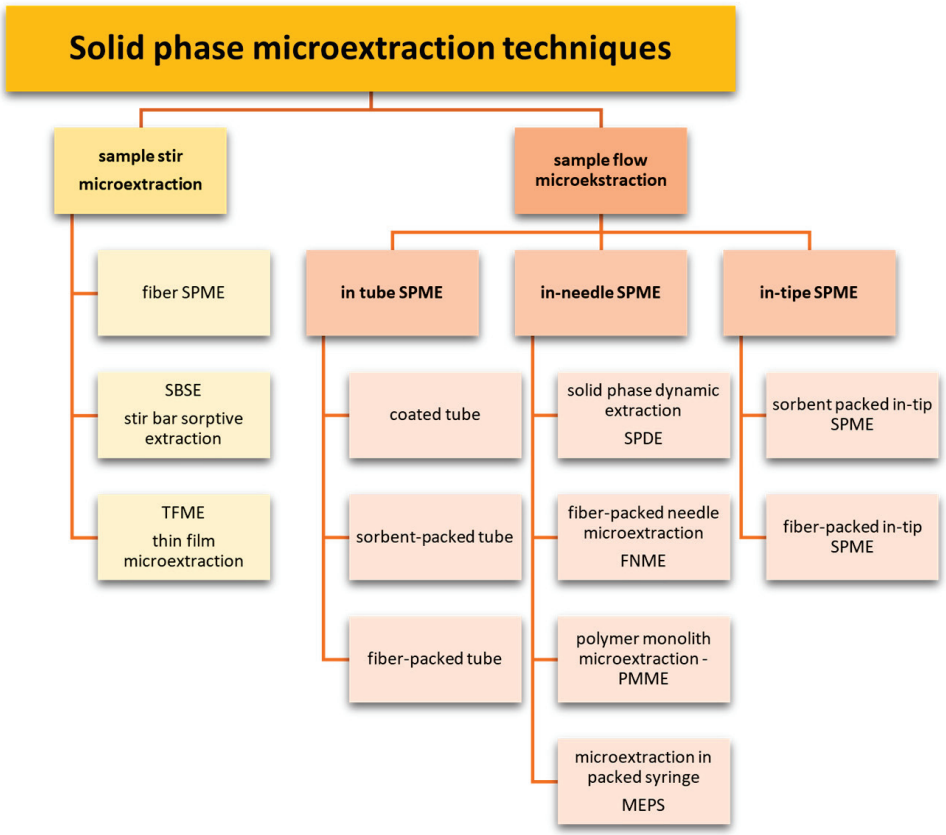

Figure 1. Division of microextraction techniques to the solid phase (SPME).

In sample flow systems, the sorption phase is placed on the surface of a capillary (in-tube SPME), inside a needle (in-needle SPME), or in a micropipette tip (in-tip SPME). Illustrative diagrams of solid-phase microextraction techniques are shown in Figures 2 and 3.

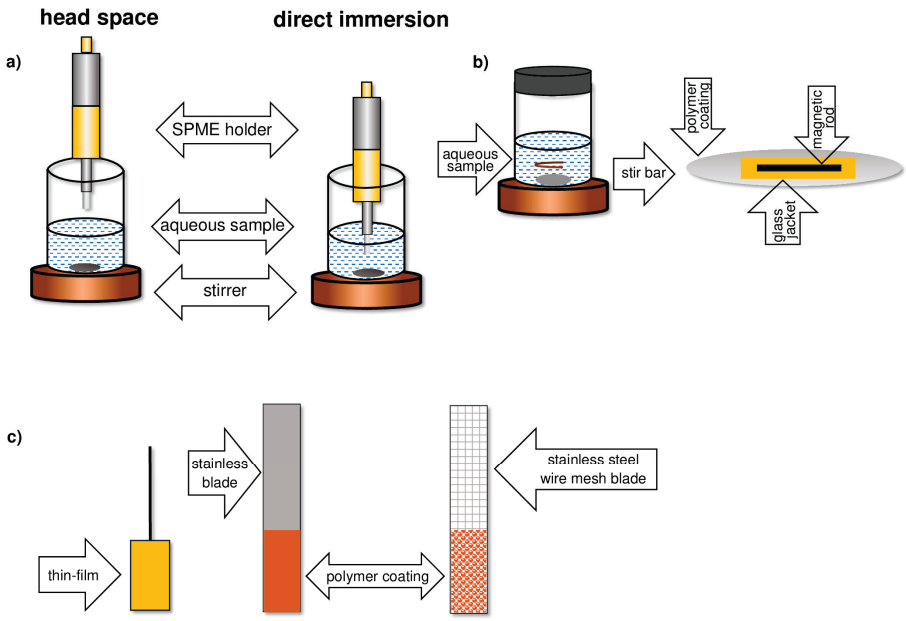

Figure 2. Solid-phase microextraction with sample stirring: (**a**) fiber SPME, (**b**) stir bar sorptive extraction—SBSE, (**c**) thin-film microextraction—TFME.

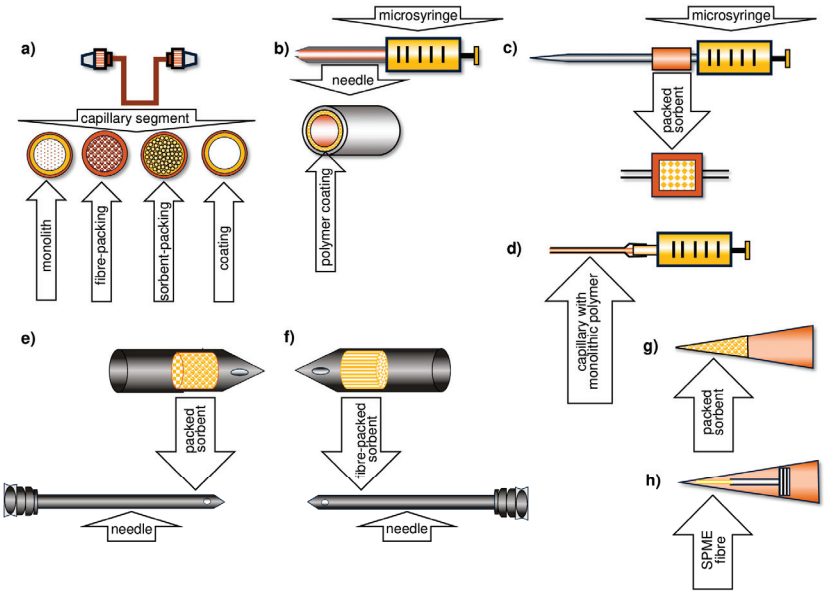

Figure 3. Solid-phase microextraction with sample flow: (**a**) in tube SPME, (**b**) solid-phase dynamic extraction—SPDE, (**c**) microextraction in packed syringe—MEPS, (**d**) polymer monolith microextraction—PMME, (**e**) fiber-packed needle microextraction—FNME, (**f**) microextraction "in needle", (**g**) sorbent-packed in-tip SPME, (**h**) fiber-packed in-tip SPME.

3. Solid-Phase Microextraction SPME

SPME microextraction is one of the static methods for isolating and concentrating analytes from solid, liquid, and gaseous samples. It involves the sorption of an analyte in a very thin layer of stationary phase deposited on the surface of a glass or quartz fiber. It was first applied in an analytical procedure in 1990 by J. Pawliszyn [11]. It is now widely used in analytical laboratories in the preparation and testing of environmental [11], food, clinical, and pharmaceutical samples [12] primarily considering:

1. Complete elimination of organic solvents from the analytical workflow;
2. Short time of the analyte extraction step;
3. Simplicity and speed of performing the analysis;
4. The possibility of sampling in situ and in vivo systems [13];
5. High sensitivity of substance determination at the ppt level;
6. An ability to automate the analytical procedure [14];
7. The possibility of desorption of analytes directly in the dispenser of the measuring device.

Since 1993, commercial devices have been produced that allow microextraction to be carried out using the SPME technique. They contain a quartz fiber coated either with a polymer film or a polymer layer with a solid sorbent. The fiber is placed in a thin steel tube fixed to a micro-syringe-like holder. When the piston is pressed, the fiber slides out of the steel needle (Figure 4).

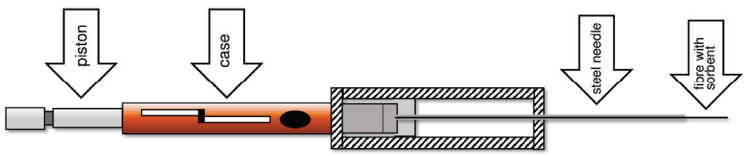

Figure 4. Commercial SPME apparatus construction diagram.

The adsorption process takes place on the surface of a fiber that is placed in a vial with the test sample. After the adsorption has been completed, the fiber is retracted into the steel needle of the micro syringe. The adsorbed analytes are thermally desorbed in the dispenser chamber of a gas chromatograph, from which they, together with the carrier gas,

are transferred to the crucial chromatography column. Here, the analytes are separated, which is a key step in the process, and, in the chromatograph detector, they are detected.

Depending on how the sorptive phase is placed about the sample, the SPME technique can be carried out as follows:

1. In a direct immersion (DI) manner;
2. As adsorption from a headspace (HS) phase;
3. As adsorption with a protective membrane (Figure 5) [15].

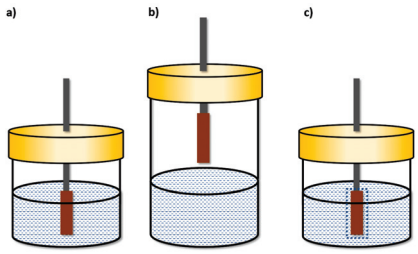

Figure 5. Types of SPME extraction: (**a**) direct extraction, (**b**) superficial extraction, (**c**) protective membrane extraction.

In direct DI-SPME microextraction (Figure 5a), the fiber is immersed in the analyzed solution. As a result, analytes are transferred directly from the sample matrix to the sorptive phase of the fiber. In HS-SPME microextraction, relatively volatile analytes that have passed from the liquid phase to the gas phase above the solution surface are adsorbed. During extraction from the headspace (Figure 5b), the fiber is not in direct contact with the solution and, as a result, is not exposed to damage that can be caused by non-volatile impurities present in the sample matrix. However, microextraction with a protective membrane is used for the microextraction of non-volatile compounds from solutions containing interferents with high molecular weights, such as humic acids or proteins (Figure 5c) [16].

The type of organic compound requires selecting an appropriate fiber-coating material to be sorbed since the microextraction efficiency is determined by the affinity of the analytes to the stationary phase. A commonly used group of polymers as extraction phases are silicones, characterized by high thermal and chemical stability and ease of chemical modification. Therefore, these materials enable the selectivity of the sorptive phase to be changed. Extraction fibers coated with polydimethylsiloxane (PDMS), divinylbenzene (DVB), polyacrylate, carboxene (CAR), and polyethylene glycol (PEG/CW) [17] are commercially available.

4. Thin-Film Microextraction—TFME

It arises from the theory of microextraction that the total amount of analyte, extracted into a solid phase in a solution in which equilibrium has been established, is directly proportional to the volume of the sorption phase according to the Equation:

$$n = \frac{C_o V_p V_s K}{V_p + V_s K} \tag{1}$$

in which C_o is the concentration of the analyte in the original sample, V_p—the volume of the sample, V_s—the volume of the sorption phase (extractant), and K—the equilibrium constant. Thus, with an increase in the thickness of the solid sorption phase, the sorption efficiency increases; at the same time, the sensitivity of the analytical method in which microextraction is used also increases.

Simultaneously, in accordance with the Equation (2) [16]:

$$t_{95\%} = B \cdot \frac{\delta K d}{D_f} \tag{2}$$

where the time in which a state of equilibrium is established in the sorption system is prolonged with the increase in the thickness of the extraction phase. In Equation (2), B—denotes the coefficient related to the geometry of the sorption surface, δ—the thickness of the boundary layer, d—the thickness of the sorption surface, K—the equilibrium constant (the partition coefficient of the analyte between the sorption phase and the sample), and D_f—the diffusion coefficient of the analyte in the sample.

The rate of solid-phase microextraction is determined by the Equation (3) [18]:

$$\frac{dn}{dt} = \left(\frac{D_f A}{\delta}\right) C_o \tag{3}$$

is directly proportional to the surface area of the extraction phase. In Equation (3), D_f—denotes the diffusion coefficient of the analyte in the sample, A—the sorption area, δ—the thickness of the boundary layer, and C_o—the initial concentration of the analyte in the sample. As a result, the geometry of the extraction phase, in the form of a thin film, for which the surface-to-volume ratio is large, causes an increase in the following:

1. The rate at which the system reaches equilibrium;
2. The sorption capacity of the solid phase.

Hence, the use of a microextraction device with a developed sorption surface increases the speed of sample execution, and it is also a suitable solution for trace analysis [9].

5. Development of the TF-SPME Technique

In 2001, Wilcockson and collaborators conceived the first microextraction system, which possessed a solid extraction phase with a higher surface-to-volume ratio than a traditional SPME device. It consisted of a thin film of ethylene-vinyl acetate as the extraction phase, which was applied to glass disks with a diameter of 22 mm [19].

In comparison to 100 μm SPME fiber, the disk had the following:

1. More than 1000 times larger surface-area-to-volume ratio of the sorption phase;
2. A smaller volume of the extraction phase.

As a result, Wilcockson's microextraction solution significantly reduced the time the system reached equilibrium but did not increase the sensitivity of the analytical method [9].

In 2003, Bruheim and colleagues developed a microextraction device that contained a 25.4 μm thick membrane of prefabricated PDMS as the extraction phase attached to a stainless-steel rod [18]. The sorption process occurred on an unrolled PDMS sheet, which, together with a metal support, resembled a flag (Figure 6).

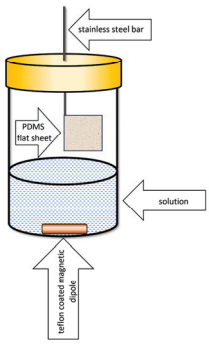

Figure 6. Bruheim TF-SPME system during sorption [18].

After the sorption was completed, the PDMS membrane was rolled up and placed in the thermal desorption unit of the gas chromatograph. In comparison to SPME microextraction performed with a fiber-coated glass with a 100 μm PDMS, a 20-fold higher extraction efficiency of polycyclic aromatic hydrocarbons, extracted from an aqueous matrix, was obtained for a 1 cm × 1 cm PDMS membrane [18].

In 2006, Bragg and co-workers used a 127 μm thick PDMS sheet in microextraction in a 2 cm × 2 cm rectangular shape with an attached 1 cm high triangle hooked to a stainless-steel wire [20] (Figure 7).

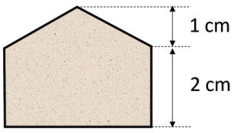

Figure 7. Bragg's membrane TF-SPME [20].

The applied modification of the shape of the extraction phase determined the increase in its surface area and its volume compared to the rectangular shape used by Bruheim; so, the sensitivity of the determination of analytes increased. At the same time, the "house shape" of the PDMS sheet allowed it to be rolled around a metal carrier and conveniently placed in the thermal desorption unit of a gas chromatograph.

In the same year, Rodil and his co-workers used for the first time a composite obtained from a combination of polyacrylate and glass wool [21] for the construction of a TF-SPME device. To obtain the microextraction device, they placed the fabric on polyethylene film, which was then saturated with polyacrylate solution and covered with the second sheet of film. After removing the foil layers, they cut the obtained material into strips with dimensions of 6 cm × 0.3 cm, adapted to the dimensions of the thermal desorption unit of the chromatograph. The obtained polyacrylate strips were characterized by significantly higher mechanical stability compared to membranes made of pure PDMS. However, after repeated use, they underwent thermal decomposition resulting in reduced mechanical strength and chromatograph defilement [9].

Six years later, Riazi and colleagues developed a TF-SPME device with an extraction phase composed of two components: polydimethylsiloxane and divinylbenzene (PDMS/DVB) or carboxene and divinylbenzene (Car/PDMS) [22]. Adsorbent particles (carboxene or DVB) were dispersed in PDMS solution, then applied to a thin sheet of glass wool mesh and spread by spin coating. The resulting material was cut into a "house shape"—the rectangle measuring 2 cm per 2 cm—and attached to a 1 cm high triangle, which was then linked to a metal pin. Ultimately, the material was placed in an extraction vessel. After sorption was completed, the active surface was rolled, and thermal desorption was carried out (Figure 8).

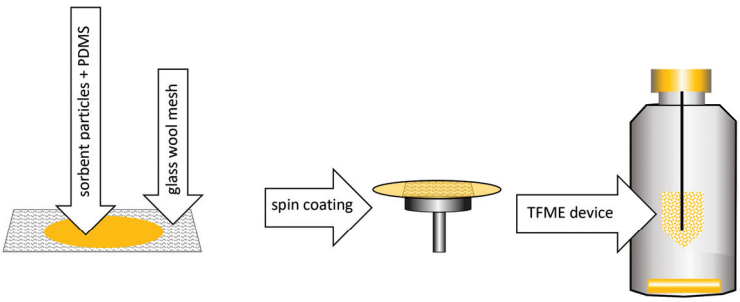

Figure 8. Diagram of the sorption process using the Riazi TF-SPME device [22].

During the desorption process, the developed sorption material showed significantly higher mechanical and thermal stability compared to Rodil's strips [22].

In 2013, Jiang and J. Pawliszyn made a PDMS membrane with applied divinylbenzene with a rod-coating method, which was used for the adsorption and determination of benzene in air [23]. PDMS was added to divinylbenzene dispersed in hexane, and then, after sufficiently long sonification, a drop of the resulting mixture was taken with a pipette and applied to aluminum foil. After being mechanically formed, the membrane was vacuum-dried at 120 °C. It was determined that the use of a twenty-percent weight addition of

divinylbenzene to PDMS was the optimal ratio to obtain a membrane with good mechanical strength. Compared to the use of SPME fiber or a single-phase PDMS membrane, the use of the DVB/PDMS membrane, obtained by rod coating, determined the increase in the sensitivity of benzene determination in the gas matrix.

In 2016, Grandy and co-workers used a carbon mesh to develop a TF-SPME device, onto which the extraction phase was applied in the form of dispersed DVB in PDMS [24]. The polymer-coated carbon support was cut into rectangular strips with a width determined by the dimensions of the TD unit of the gas chromatograph. The obtained micro-extraction device allowed extraction with high efficiency and had higher mechanical strength compared to previous technical solutions in the TF-SPME method. The carbon mesh strip, coated with a polymer layer as an extraction phase, became part of the first commercial microextraction kit offered by GERSTEL Inc. (Gerstel GmbH, Mulheim, Germany).

The technique of microextraction on a developed surface has not just remained a theoretical concept. It has been successfully applied to a high-throughput automated analytical procedure using robotic autosamplers. In 2009, J. Pawliszyn's team presented a solution for simultaneous microextraction of 96 samples. The developed TF-SPME device, with the extraction phase as C18 silica applied to stainless steel plates, has proven its practicality. The silica-coated plates were combined into twelve-element batteries and then into an array containing ninety-six elements, which were, among others, used in the analysis of benzodiazepines in urine [25]. This practical application underscores the real-world relevance of our research and its potential to revolutionize analytical procedures.

In recent years, the development of the TF-SPME method has manifested itself in the use of a variety of advanced materials as increasingly selective sorption phases that enable microextraction to be carried out with high efficiency.

6. Methods for Obtaining Active Coatings in TFME

The choice of the type of extraction phase and the method of its application to the substrate in the process of constructing a TF-SPME device is determined by the chemical properties of the analyte, the type of matrix from which it is sorbed, and the type of desorption method [9]. Thermal desorption requires resistance to high temperatures, while desorption in solvent demands adequate mechanical strength. Consequently, materials with different mechanical and thermal properties are used as extraction-phase supports (Figure 9).

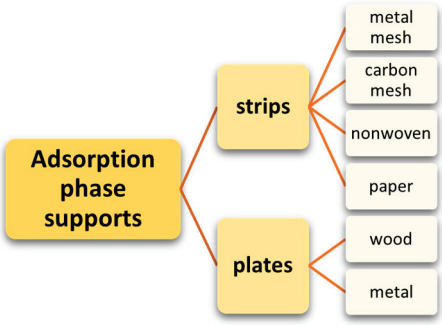

Figure 9. Types of sorptive phase supports in TF-SPME devices.

The following techniques for applying thin-film coatings to solid substrates are used: dip coating, spin coating, electrospinning, rod coating, and spray coating.

According to the dip-coating method, a suspension of the extraction phase in a suitable solvent or adhesive is prepared. The polymer or metal substrate is then immersed in it. The thickness of the coating of the active phase is controlled by the rate at which the substrate is removed from the solution and the number of repetitions of the above-mentioned operation (Figure 10).

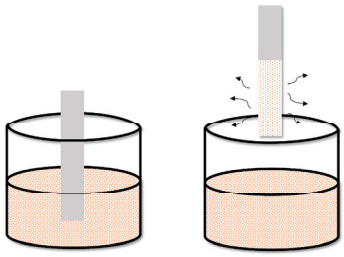

Figure 10. Schematic diagram of the dip-coating method [8].

The dip-coating method is one of the technically more straightforward methods of applying an extraction layer to a solid substrate and, at the same time, the most convenient method for obtaining a homogeneous, very thin active layer with a thickness of a few micrometers. This method is used, among others, in the construction of TF-SPME devices dedicated to detecting analytes by mass spectrometry, in which a short desorption time is crucial because it depends on the thickness of the sorption layer [8].

Spin coating is a mechanical method of applying a sorption layer to a solid substrate, making it possible to obtain a self-supporting TF-SPME membrane. The extraction phase in liquid form is placed on a disk, which is then set in rotary motion at high angular speed (Figure 11).

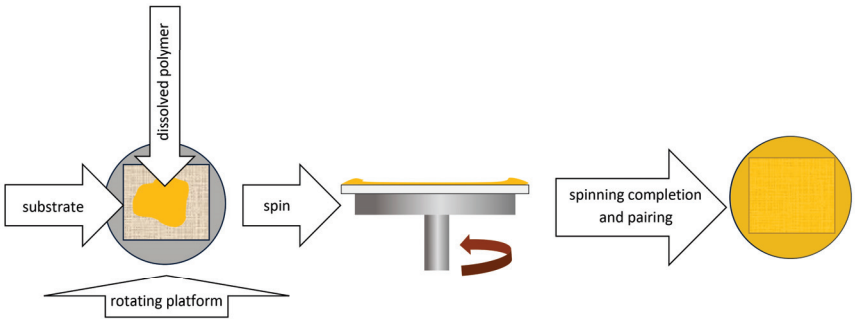

Figure 11. Schematic diagram of the spin-coating method [8].

As a result of centrifugal force, the suspension particles move toward the edge of the substrate, forming a thin polymer layer on its surface. Its thickness is controlled by the rotational speed of the disk [9]. Using the spin-coating method, it is possible to apply several layers that differ in chemical composition. One of the main limitations of the vortex-coating method is the difficulty in obtaining a sorption surface of uniform thickness in both its central and outer parts [8].

The first thermally stable polydimethylsiloxane membranes, thermally desorbed and used in TF-SPME, were made using spin-coating and rod-coating methods. Both of the above-mentioned methods make it possible to prepare a TFME device on a support or as a self-supporting membrane. In the rod-coating method, the extraction phase in liquid form is placed on a substrate, such as a film, and then spread using a rod-shaped cylinder to obtain a thin and uniform coating (Figure 12).

The thickness of the extraction layer is controlled by the size of the clearance between the substrate and the mechanical liquid-polymer-spreading element, and by the force of its pressure on the substrate [8].

The electrospinning-coating method uses an electric field to pull electrically charged polymer threads from a polymer solution or polymer melt. The aim of the procedure is to produce mechanically stable membranes with nanofibrous structures [8]. The apparatus, enabling electrospinning, contains a high-voltage generator, a pump, a syringe ending in a capillary, and a conductive collector. The collector can have a flat or oval shape (Figure 13).

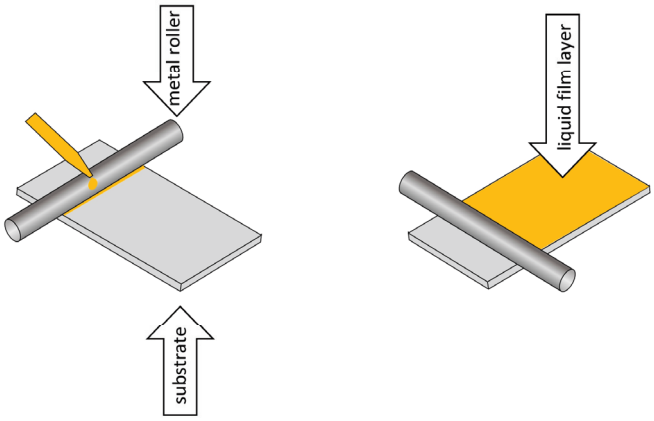

Figure 12. Schematic diagram of the bar-coating method [26].

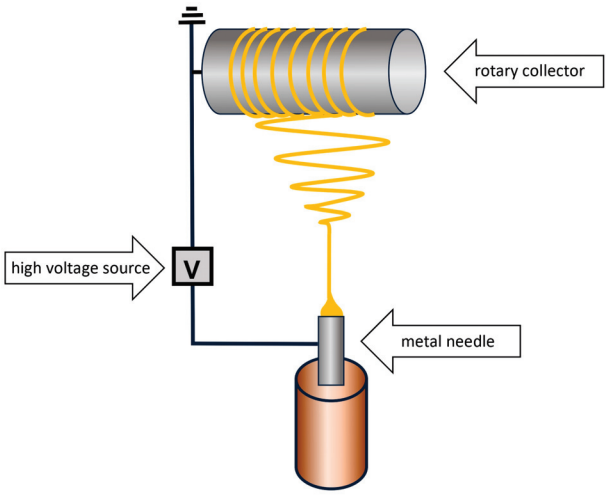

Figure 13. Schematic diagram of the electrospinning-coating method [27].

Free electric charges appear in a polymer solution placed in a syringe. They flow through an electrode that is immersed in the polymer solution and connected to a high-voltage generator. They move in the generated electric field toward the electrode of opposite polarity. The movement of ionized polymer particles causes a conical deformation in the droplet. When the electric potential, applied to the system, reaches the value required to overcome the surface tension of the liquid polymer, a thin stream of liquid is emitted from the conical end of the droplet. As the liquid polymer jet travels through the electric field, created between the syringe needle and the collector, solvent evaporation occurs. Consequently, a dry polymer fiber is placed on the collector [28]. The thickness of the polymer membrane, formed on the surface of the collector, is under your complete control, determined by the duration of the process.

Spray coating, along with dip coating, is one of the simplest methods of preparing TF-SPME devices. The extraction phase, dissolved or dispersed in a suitable solvent, is placed in the tank of the spray instrument and then pressurized with an inert gas. In the next step, the suspension is sprayed onto a solid support in the form of microscopic droplets (Figure 14).

The method's disadvantage is the difficulty in obtaining a coating of uniform thickness. This problem can be partially solved by spraying several layers. However, this solution is not perfect. It often causes a coating with a significant thickness, calculated in millimeters, to appear instead of a desirable uniformly thick layer [8].

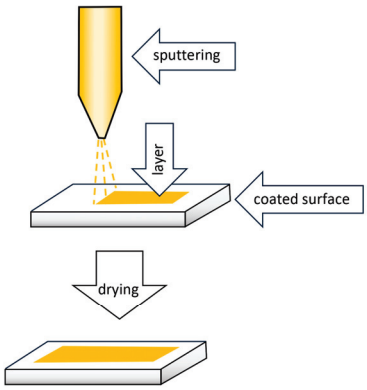

Figure 14. Schematic diagram of the spray-coating method [29].

The advantages and disadvantages of the TF-SPME device preparation methods, outlined above, are shown in Table 1.

Table 1. Techniques used for preparation of TF-SPME devices.

Technique	Film Thickness Achieved	Advantages	Disadvantages
Dip coating	Low µm range	• High homogeneity and mechanical stability of a layer • Simple process and setup • Low cost	• Difficult to coat flexible substrates • Large amount of solution wastage.
Spin coating	Hundreds of µm	• High mechanical stability of a layer • A simple and effective process that requires minimal training to master • Cost-effective • No requirement for any high-energy processes • Possibility to produce TF-SPME extractive phase with or without a supportive core	• Variation in the thickness between the central part and outer part of the prepared extractive phase • High level of solution waste
Electrospinning coating	nm–µm range	• High homogeneity and mechanical stability of a layer • Possibility to produce TF-SPME extractive phase without a supportive core	• Sensitivity to the manufacturing environment (temperature and humidity) • Slow process rate
Bar coating	Hundreds of µm	• Possibility to produce TF-SPME extractive phase with or without a supportive core • Possibility to prepare uniform films on rigid or flexible substrates • High homogeneity and mechanical stability of a layer • Simplicity to change the coating thickness • Simple and quick process • Low cost	• Thickness of layer depends on rod structure and solution properties • Difficult to obtain repeatable coatings
Spray coating	µm–mm range	• Simple process • High mechanical stability of a layer • Low cost	• Poor homogeneity of the layer

7. Sorbents Used in the TFME Technique

The variety of physicochemical properties of analytes in samples with complex matrices such as food, biological, and environmental samples requires the use of extraction phases in the TF-SPME technique, which are characterized by sufficient high sensitivity, selectivity, sorption capacity, and mechanical, thermal, and chemical resistance [15]. The K_{eq} partition constant of the sorption surface and the analyte extracted from a given matrix directly impact its microextraction process's selectivity, efficiency, and speed. The value

of the partition constant is determined mainly by the chemical and physical structure of the extraction medium used in the TF-SPME device. The selection of the material constituting the extraction phase is, therefore, a key factor affecting the method's sensitivity for determining the analyte [30]. Polar sorbents have an affinity to hydrophilic compounds whose molecules contain polar functional groups such as hydroxyl, amine, and carboxyl. A principal feature of non-polar sorbents is a high affinity to hydrophobic organic compounds whose molecules are mainly composed of non-polar hydrocarbon chains or rings.

The achievements of recent years in the field of materials chemistry have contributed to the use of the most diverse classes of materials in microextraction techniques. The materials show features such as high specific surface area, good wettability and ease of their chemical modification, and the presence of suitable functional groups that enhance interactions with the analyte [31]. Once they have been used as sorption media in microextraction devices, the characteristics of modern materials permit microextraction with high selectivity and sensitivity to be carried out. In the TF-SPME technique, advanced polymeric materials, carbon nanomaterials, aptamers, and poly (ionic liquids) are used as extraction media (Figure 15).

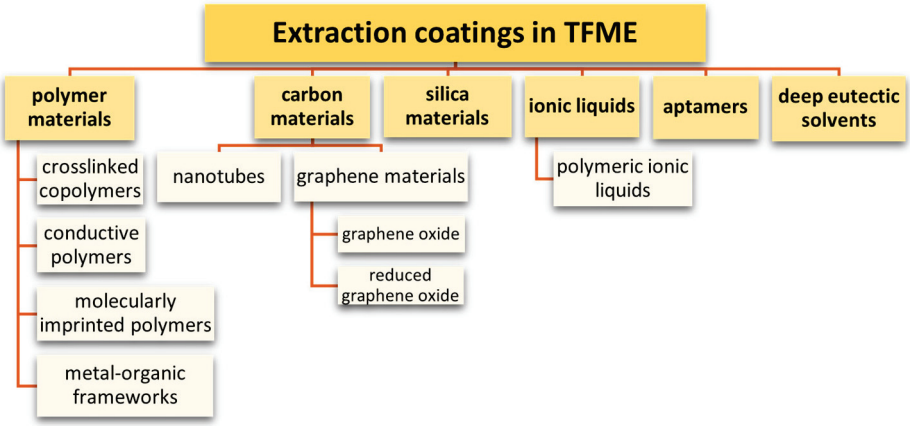

Figure 15. Types of materials used as extraction phases in the TFME technique.

7.1. Polymeric Adsorbents

In TF-SPME, polymers are used as sorptive phases in the form of self-supporting TFME membranes and as sorptive phase dispersion media or as a glue that attaches the solid sorptive phase to the support.

A developed internal surface and the presence of various types of functional groups characterize polymeric adsorbents, which are often cross-linked copolymers. Non-specific dispersive interactions mainly occur between the macromolecules of the polymer and analyte molecules. Various types of specific interactions can also occur, which are related to the presence of functional groups in the polymer macromolecule. Specific interactions allow the formation of hydrogen or ionic bonds between analyte particles and polymer macromolecules. Polymers frequently used in the TF-SPME technique include PDMS, polyacrylonitrile (PAN), polystyrene (PS), and the natural polymer cellulose (Figure 16).

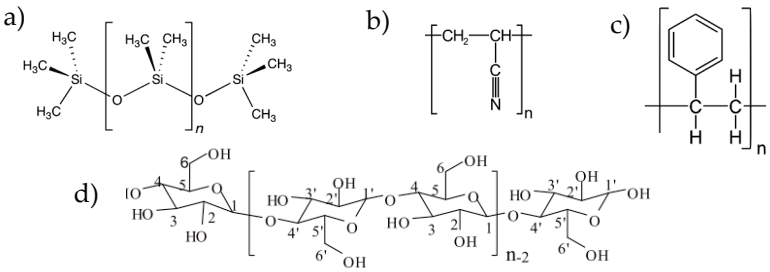

Figure 16. Structural formulas: (**a**) polydimethylsiloxane, (**b**) polyacrylonitrile, (**c**) polystyrene, (**d**) cellulose.

PDMS belongs to the group of first polymers used in the TFME technique. Polydimethylsiloxane is a polymer classified as siloxane. Its macromolecule contains Si-O-Si silicon bridges in its structure, in which each silicon atom is connected to methyl groups (Figure 16a).

PDMS is commonly used as a sorbent in solid-phase microextraction techniques because of its properties, which include the following:

1. High thermal resistance;
2. The ease with which it undergoes desorption;
3. Chemical and physiological inertness;
4. Flexibility and mechanical strength;
5. Low chemical reactivity.

In addition, PDMS is resistant to matrix effects. Its sorption properties do not change even in highly complex matrices such as plasma, animal adipose tissues, or digestive juices [30].

Despite its many positive features, PDMS, as an extraction phase, also has its limitations. It shows low selectivity toward apolar compounds; thus, analyzing samples with complex matrices becomes difficult when used as an extraction phase. As an apolar material, it shows a low affinity to polar analytes. In order to increase the microextraction efficiency of polar analytes, combinations of polydimethylsiloxane with other sorbents, including divinylbenzene (PDMS/DVB) and carboxene (PDMS/CAR), are currently applied in TF-SPME techniques. TFME membranes, made of PDMS-coated carbon mesh and DVB/PDMS or CAR/PDMS, are also found in commercially produced TFME microextraction kits by Markes International, among others.

Polyacrylonitrile (PAN) is a synthetic resin formed by the polymerization of acrylonitrile (Figure 16b). It belongs to the hard and rigid thermoplastic materials. Due to the presence of highly polar nitrile (-CN) groups in the macromolecule, it does not dissolve in typical organic solvents. In the TF-SPME technique, it mainly performs the function either of a dispersion medium, or of a linker of the sorption phase to the substrate.

Polystyrene (PS) is a polymer of the thermoplastic group (with limited elasticity) obtained by polymerization of styrene (Figure 16c). It is soluble in aromatic and chlorinated hydrocarbons and in ketones. It does not dissolve in aliphatic hydrocarbons, alcohols, and water. In microextraction to the solid phase, it is used as both a sorption phase and a dispersant.

Cellulose is a natural polymer commonly found in nature. It is a component of plant cell walls. It belongs to natural raw materials extracted mainly for industrial purposes from wood and cotton. Cellulose products are environmentally safe as they decompose through a natural carbon cycle [32]. The polymer chain of cellulose has a simple, unbranched structure consisting of glucose rings linked by β-1,4-glycosidic bonds (Figure 16d). In view of the absence of hydrocarbon side chains, the cellulose chains form ordered and fibrous semi-crystalline structures. The -OH groups, bonded to carbon atoms, determine the chemical and physical properties of cellulose. Hydrogen bonds are formed between the oxygen and hydrogen atoms of the various hydroxyl groups belonging to other polymer chains. The network of hydrogen bonds makes cellulose insoluble in water and most organic solvents [33]. The fibrous structure of cellulose, which contributes to enlarging the specific surface area, good mechanical stability, ease of chemical modification, and environmental safety, makes it a sorption material with great potential for applications in microextraction techniques. In TF-SPME, cellulose paper is used as a support for the actual sorbent and a component of the sorption phase. It is often subjected to modification with polymeric ionic liquids or other polymers, e.g., polyaniline, polyamide, polydopamine, and zinc oxide or silver nanoparticles.

Examples of the use of the above-described polymers as extraction phases in the TF-SPME technique, used in the analysis of environmental, biological, and food samples and reported in scientific publications, are summarized in Tables 2 and 3.

Table 2. Examples of the use of polymer sorption phases in TF-SPME.

Sorption Phase	Analyte	Matrix	Detection	Reference
PDMS	PAHs	water	GC-MS	[34]
	polychlorinated biphenyls	fish tissue	LC-MS	[35]
	pesticides	water	DCBI-MS	[36]
	volatile organic compounds	skin	GC-MS	[37]
	insect pheromones	air	GC-MS	[38]
	drugs and explosive substances	standards in different solvents	IMS	[39]

Table 3. Examples of the use of polymer sorption phases in TF-SPME.

Sorption Phase	Preparation	Analyte	Matrix	Detection	Reference
DVB/PDMS	bar coating	VOCs/SVOCs	water	GC-TMS	[40]
DVB/PDMS	spin coating	N-nitrosamines	water	GC-MS	[22]
DVB/PDMS	bar coating	VOCs	water	GC-MS	[24]
DVB/PAN	ready for use	anti-inflammatory antibacterial drugs	drinking water	LC-ESI-MS/MS	[41]
DVB/PDMS	bar coating	pesticides	water	GC-MS	[42]
DVB/PDMS	bar coating	pesticides	water	GC-MS	[43]
C18/PAN	dip coating spray coating	benzodiazepines	blood plasma	LC-MS/MS	[44]
C18/PAN	spray coating	doping agents	urine, blood plasma	LC-MS	[45,46]
C18/PAN	spray coating	estrogens	water	LC-UV	[47]

7.2. Conductive Polymers

Conductive polymers (CPs) are among the polymeric materials that exhibit electrical conductivity along their long molecular chains because they contain conjugated π-electron backbones in the macromolecule. With regard to their electrical, mechanical, thermal, and optical properties, CPs find applications in many fields of science and technology. They are often used as electromagnetic screens, corrosion inhibitors, and electroluminescent displays [48]. The large specific surface area and excellent chemical, mechanical, and thermal stability also make CP materials suitable sorbents often applied in microextraction techniques, including TF-SPME [49].

Polymers showing conductivity are, for example:

1. Polyacetylene (PA) and polyphenylacetylene (PPA), containing double bonds;
2. Polyfluorene (PF) and polyparaphenylene (PPP), polyaniline (PANI), and polyphenylenevinylene (PPV), containing aromatic rings in the polymer chain;
3. Heterocyclic polymers with a nitrogen atom: polypyrrole (PPy) and polypyridine (PPY);
4. Heterocyclic polymers with a sulfur atom: polythiophene (PTh) and polyethylene dioxythiophene (PEDOT), polyfuran (PFu), as well as polycyanamide (PCN) and polyvinylferrocene (pVFc).

Examples of structural formulas of conductive polymers are shown in Figure 17.

Conductive polymers, used as a sorption phase in the microextraction process, can interact with analytes through hydrophobic interactions, acid–base interactions, polar functional group interactions, ion exchange, hydrogen bonding, and π–π interactions. Because of their acid–base properties, CPs exhibit diverse extraction selectivity in relation to acidic and basic compounds. They also allow direct extraction of charged particles without derivatization or the application of complexing agents [50].

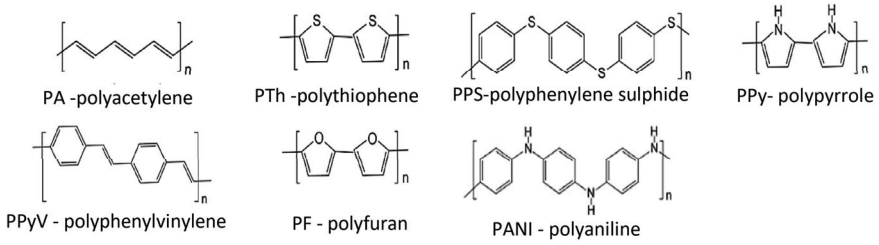

Figure 17. Structural formulas of conductive polymers.

Examples of the use of conductive polymers in the TF-SPME technique, reported in scientific publications, are summarized in Table 4.

Table 4. Examples of the use of conductive polymers in TF-SPME.

Sorption Phase	Preparation	Analyte	Matrix	Detection	Reference
PmPDA/CNT	electrospinning coating	copper	water, food	FAAS	[51]
PPy/PA	electrospinning coating	pesticides	water	GC-MS	[52]
PANI	gluing	hormones	urine	HPLC-FLD	[53]
PANI-N6	electrospinning coating	chlorobenzenes	water	GC-MS	[54]

7.3. Molecularly Imprinted Polymers

Molecularly imprinted polymers (MIPs) are an essential group of the most selective sorption phases used in TF-SPME. MIP materials acquire their ability to selectively recognize an analyte during their synthesis, which proceeds with the participation of template molecules, functional monomers, a crosslinking reagent, an initiator, and a solvent. MIP synthesis occurs at high temperatures or by UV-light irradiation. During its course, template molecules combine with functional monomers to form complexes via covalent bonds or hydrogen bonds, π–π interactions, ionic interactions, and van der Waals forces. As a result of the polymerization reaction taking place around these complexes with the participation of a crosslinking agent, the complexes are immobilized in the polymer network. After synthesis, the template is removed, and the complex is degraded. Consequently, molecular cavities are formed with affinities for chemical structures identical or similar to those of the removed template. A scheme of the MIP synthesis is shown in Figure 18.

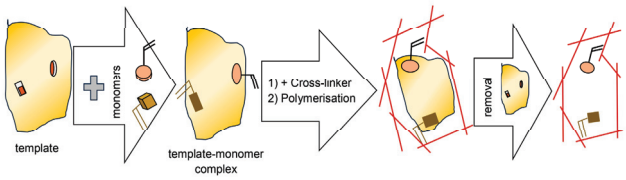

Figure 18. Synthesis diagram of MIPs [55].

The template molecules used for the synthesis of MIP should exhibit chemical stability during the polymerization reaction and have functional groups that do not block the actual polymerization reaction and retain their capacity to interact with the functional monomer. A desirable feature of template molecules is also low molecular weight. Low-molecular-weight molecules are rigid and ensure the formation of permanent molecular cavities in the three-dimensional polymer network. Suitable functional monomers are selected for the template molecules, enabling the formation of chemical interactions leading to the formation of monomer–template transition complexes. Functional monomers also determine the formation of active sites in the MIP polymer that interact with analyte molecules.

The cross-linking reagent (cross-linker) forms bonds during MIP synthesis. The formed bounds stabilize the polymer structure, and thanks to them, the cross-linked structure remains stable after the removal of the template molecule. An important factor affecting the

quality of the polymer product is the amount of cross-linking reagent used in the synthesis. Too little of it results in the polymer's mechanical stability being lacking. At the same time, too much of it blocks functional groups and thus influences a reduction in the number of molecular cavities that are selective to the analyte [56].

In the synthesis of molecularly imprinted polymers, solvents of low polarity that generate the formation of large pores are used to provide the polymer material with the largest possible specific surface area. Solvent molecules of low polarity do not interfere with the interactions formed between the polymer and the template molecules, and simultaneously, they make it possible to obtain a material with high selectivity [57].

The MIP-TFME device is obtained by applying several microliters of the prepolymer solution to a silanized microscope slide or stainless substrate, then covering it with a coverslip and exposing it to UV light to initiate polymerization. The obtained polymer thin films are then washed with a suitable solvent to remove the template molecules from the polymer network. An alternative way of obtaining a MIP-TFME device involves immersing a porous membrane in a MIP prepolymer solution, placing the already-soaked membrane between two glass plates, and exposing it to UV light [58]. A diagram of the procedures described above is shown in Figure 19.

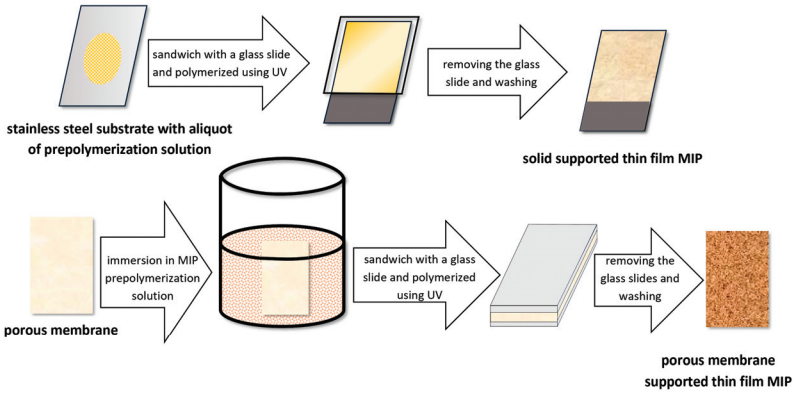

Figure 19. MIP-TFME preparation [58].

Examples of the application of MIPs in the TF-SPME technique, which have been reported in selected scientific publications, are summarized in Table 5.

Table 5. Examples of the use of MIPs in TF-SPME.

Template	Functional Monomer	Crosslinking Reagent	Analyte	Matrix	Detection	Ref.
2-thiophenocarboxyaldehyde	1-vinylimidazole	bisphenol dimethacrylate	PASHs	seawater	GC–MS	[59]
2-{[diethoxy(sulfanylidene)-λ-phosphanyl]amino}acetic acid	methacrylic acid	ethylene glycol dimethacrylate	OPPs	water	LC-MS/MS	[60]
catechol	4-vinyl benzoic acid	ethylene glycol dimethacrylate	phenols	water	UHPLC-PDA	[61]
(3-(10,11-dihydro-5H-dibenzo[b,f]azepin-5-yl)propyl)(methyl) carbamate	methacrylic acid	ethylene glycol dimethacrylate	TCAs	plasma	LC-MS/MS	[62]
phenol	itaconic acid, 4-vinylpyridine, styrene	ethylene glycol, dimethacrylate, triethylene glycol dimethacrylate, pentaerythritol triacrylate	phenols	water	LC-MS	[63]
mycophenolate mofetil	4-vinylpyridine	ethylene glycol dimethacrylate	MPA	plasma	UPLC	[64]

7.4. Metal-Organic Frameworks

The term metal–organic frameworks (MOFs) is used to describe solid polymeric materials containing metal cations or secondary building units (SBUs) in their structure.

SBUs are metallic clusters in which coordination bonds link the metal ion to multifunctional organic groups (linkers) such as carboxylates [65]. The most common transition metal ions used in MOF syntheses are, for example: Cr^{3+}, Fe^{3+}, Co^{2+}, Zn^{2+}, and Cu^{2+} acting as electron pair acceptors, which are provided by ligands containing atoms with free electron pairs, oxygen, nitrogen, or sulfur atoms. The function of ligands in MOF structures can be performed, inter alia, by polycarboxylic acids, for example, terephthalic, 1,3,5-benzenetricarboxylic [66].

MOFs are porous materials with the largest specific surface areas. MOF-5 is the first synthesized metal–organic skeleton-type structure, reported in "*Nature*" in 1999. Its skeleton is formed by zinc $[Zn_4O]^{6+}$ clusters and tetraphthalic acid anions. It has a specific surface area (Langmuir) of 2900 m^2/g [67].

Considering vast specific surface areas, MOFs are characterized by good thermal and mechanical stability, homogeneous nanoscale cavity structure, uniform pore topology, ultra-low density, and high affinity to adsorption of various analytes [68]. The characteristics of MOF-type polymeric materials make them suitable for a variety of applications in science and technology (including catalysis, gas adsorption, and storage). Extraction techniques also apply to them as drug carriers and sorbents [69].

The adsorption of analytes on the surface of the MOF, used as a sorption phase, occurs through various types of interactions. Ligands in the crystal structure interact hydrophobically with analytes, while aromatic rings are present in linkers through π–π interactions. Ligands, containing oxygen and nitrogen polar functional groups, bind analytes through hydrogen bonds, ionic interactions, and dipole–dipole interactions. Metals at nodes of the crystal lattice, which have free coordination sites, enable acid–base Lewis interactions with molecules of the corresponding analyte [31].

Examples of the application of MOFs in the TF-SPME technique, described in scientific publications, are summarized in Table 6.

Table 6. Examples of the use of MOFs in TF-SPME.

Sorption Phase	Preparation	Analyte	Matrix	Detection	Reference
DUT-52/PVDF	bar coating	PCPs	cosmetics	UHPLC-UV/VIS	[70]
Co-MOF-74/polyfam	electrospinning coating	anti-cancer drugs	water sewage, plasma	HPLC-UV	[71]
MIL-53(Al)/PVDF MIL-53(Fe)/PVDF MIL-100(Fe)/PVDF MIL-101(Cr)/PVDF UiO-66(Zr)/PVDF	bar coating	estrogens	urine	HPLC-FLD	[72]
ZIF-8/LDH/GO/PVDF	bar coating	caffeine	urine	HPLC-UV	[73]
amino-Zr-MOF/PAN	electrospinning coating	pesticides	water	CD-IMS	[74]
MIL-100(Fe)/PS/cellulose	dip coating	PCPs	pool water, cosmetics	HPLC-PDA	[75]
MOF-199/PS	electrospinning coating	aldehydes	urine	HPLC-VWD	[76]

7.5. Carbon Nanomaterials

Carbon nanomaterials (CNMs) span a group of various allotropic carbon structures, which include, for example, fullerenes, carbon tubes, and graphene. CNMs are characterized by unique physical properties. They have a very high specific surface area, very high tensile, and high-temperature mechanical strength, as well as unique electrical and thermal conductivity. They also exhibit high affinity to many organic compounds. The properties enable extensive applications of carbon nanostructures in many fields of science and technology, including as adsorption materials [77].

7.5.1. Graphene Materials

Graphene is an allotropic variety of carbon containing one or more layers of atoms in the sp^2 hybridized state connected to each other on a single plane by strong σ bonds in a manner resembling a honeycomb structure.

The non-hybridized π atomic orbitals, perpendicular to the plane on which the carbon atoms make the graphene layer, overlap to form a delocalized, all-encompassing atomic plane π electron arrangement responsible for the specific optical, thermal, mechanical, and electrical properties of graphene [78]. The atomic structure of graphene can be considered basic to other allotropic carbon varieties such as graphite, carbon nanotubes, and fullerenes. Stacked graphene layers form the graphite structure. The rolled-up graphite layer constitutes a carbon nanotube, while curled up in a sphere constitutes fullerene [78].

Graphene and its derivatives, such as reduced graphene oxide (rGO) and graphene oxide (GO) are classified as graphene-based materials (GBMs). Graphene nanolayers allow the adsorption of molecules on both sides of the plane formed by carbon atoms. In contrast, in the case of nanotubes or fullerenes, adsorption of analyte molecules is not possible on the inner side of nanostructures due to steric crowding. Consequently, the specific surface areas of GBMs are very large (theoretical value for graphene: 2630 m^2 g^{-1}) and much larger than the specific surface areas of carbon nanotubes and fullerenes [79].

In regard to their high specific surface area, which is greater than that of SWCNTs and MWCNTs, rGO, and GO are used in extraction and microextraction techniques. Graphene-based materials adsorb various types of analytes via van der Waals-type interactions, electrostatic interactions, hydrogen bonds, π–π, dispersion forces, coordination bonds, and hydrophobic effect [80]. Due to π electron systems, rGO adsorbs aromatic rings of organic compounds via strong π–π interactions. The functional groups in graphene oxide play a key role in forming hydrogen bonds or electrostatic interactions with organic compounds containing functional groups with oxygen and nitrogen atoms in the molecules [81].

Table 7 summarizes examples of the application of graphene materials in the TFSPME technique presented in scientific publications.

Table 7. Examples of the use of graphene materials in TF-SPME.

Sorption Phase	Preparation	Analyte	Matrix	Detection	Ref.
CY-GO-LDH	dip coating	non-steroidal anti-inflammatory drugs	plasma, urine	HPLC-UV	[82]
graphene membrane	drop casting	metal ions	water	TXRF	[83]
LDH/GO/PVDF	application to a Petri dish	diclofenac	urine	HPLC-UV	[84]
GO	ESD	metal ions	water	LIBS	[85]
PS/G	electrospinning coating	aldehydes	exhaled air condensate	HPLC	[86]
GO/PEG	dip coating	β-blockers	saliva	LC-MS/MS	[87]
ZIF-8@GO	dip coating	macrolides, lincosamides	honey	UPLC-MS/MS	[88]
PAMAM@GO-PVDF	application to a Petri dish	OPPs	water	HPLC-UV	[89]

7.5.2. Carbon Nanotubes

Carbon nanotubes (CNTs) are an allotropic variety of carbon with cylindrical nanostructures that are made up of coiled monolayer sheets of sp^2 carbon atoms linked together via covalent bonds. Depending on the number of layers of carbon atoms that make up the tube, CNTs are divided into single-wall carbon nanotubes (SWCNTs) and multi-wall carbon nanotubes (MWCNTs) consisting of several concentric graphene layers connected via van der Waals forces [90]. SWCNTs are nanostructures with diameters ranging from 1 nm to 10 nm, whereas MWCNT diameters are much larger, ranging from 5 nm to several hundred nanometers [91].

Carbon nanotubes are characterized by high thermal, mechanical, and chemical stability, a specific surface area of between 150 and 1500 m^2 g^{-1}, as well as high sorption capacity. The large sorption capacity of CNTs is a consequence of their large length-to-width ratio. Unlike activated carbons, carbon nanotubes are not porous materials. Adsorption in porous materials is related to the diffusion of analyte particles deep into the pores of the sorbent, whereas sorption-active sites are located on the surface of CNTs and in the spaces between the rolled graphene layers that form MWCNTs.

Nanotubes are easily accessible to analyte particles during adsorption. Compared to desorption occurring in the pores of a porous sorbent, the nanotubes enable faster thermal desorption of analytes and solvents. Due to the mechanism of adsorption and desorption, which is not controlled by diffusion, carbon nanotubes are used to concentrate a wide range of analytes [92].

The hexagonal carbon backbone of graphene layers is responsible for the low affinity of CNTs to polar molecules; as a result, pure carbon nanotubes are used as a sorption material in the microextraction of hydrophobic analytes. Carbon nanotubes, functionalized by oxidation reaction, are used in the microextraction of polar analytes. The redox reaction allows the connection between carbon atoms and -OH, -COOH, and -NH_2 groups, among others.

Sorption of analytes on pure and functionalized CNTs can occur via hydrogen bonds, π–π interactions, electrostatic forces, and hydrophobic interactions. π–π interactions between graphene layers of CNTs and molecules of analytes containing benzene rings in their structure, enable extraction using carbon nanotubes as a sorption phase of polycyclic aromatic hydrocarbons (PAHs), pharmaceuticals, phthalates, pesticides, and parabens. The extraction of metal ions, positively charged particles, and polar molecules occurs via hydrogen bonds, and electrostatic interactions between them and the functional groups present on the CNT surface [31].

Table 8 summarizes examples of the application of carbon nanotubes in the TF-SPME technique, which are used to analyze environmental and food samples and have been described in scientific publications.

Table 8. Examples of the use of carbon nanotubes in TF-SPME.

Sorption Phase	Preparation	Analyte	Matrix	Detection	Ref.
SDS-MWCNTs/PP	application on PP substrate	glucocorticoids	water	UHPLC-MS	[93]
MWCNT/Agr-Ch	application to a Petri dish	non-steroidal anti-inflammatory drugs	water	HPLC-UV	[94]
MWCNTs/Agr	application to a Petri dish	PAHs	green tea drink	HPLC-UV	[95]
MWCNTs/CTA	application to a Petri dish	fungicides personal care products PCPs	water	GC-MS	[96]
MWCNTs-COOH/PDMS	dip coating	phenolic compounds	water	HPLC-UV	[97]
Agr-Ch-MWCNTs	application to a Petri dish	TCAs	water	HPLC-UV-Vis	[98]
MWCNTs-COOH-Ch/PP	dip coating	PCBs	water	GC-MS	[99]
MWCNTs/CTA	application to a Petri dish	PAHs	water	HPLC-UV	[100]

7.6. Silica Materials

Silica gel SiO_2 (silica) and chemically modified silica are materials commonly used in analytical chemistry, both in extraction techniques, filtration, and as a stationary phase in chromatography. Hydrated silicon oxide with the general formula SiO_2-nH_2O (hydrated silica) is an amorphous and porous substance whose spatial network is formed by tetrahedral SiO_4. On the surface of its microparticles, there are silanol (≡Si-OH) or siloxane (≡Si-O-Si≡) groups (Figure 20).

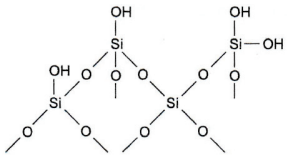

Figure 20. Chemical surface structure of silica gel.

The active groups of silica can react with organic compounds to form so-called bound phases. The bonded phases can contain bonds of the following types:

1. Ester, formed in the reaction of a silanol group with an alcohol:

$$\equiv\text{Si-OH} + \text{R-OH} \rightarrow \equiv\text{Si-O-R} + H_2O$$

2. Carbon, formed in the reaction of a silanol group with thionyl chloride and then with an organometallic compound:

$$\equiv\text{Si-OH} + SOCl_2 \rightarrow \equiv\text{Si-Cl} + SO_2 + \text{HCl}$$

$$\equiv\text{Si-Cl} + \text{R-Li} \rightarrow \equiv\text{Si-R} + SO_2 + \text{LiCl}$$

3. Siloxane, formed by the reaction of the silanol group with organ chlorosilanes:

$$\equiv\text{Si-OH} + \text{Cl-SiR}_3 \rightarrow \equiv\text{Si-O-SiR}_3 + \text{HCl}.$$

The phases, formed by the reaction of silanol groups of silica with organ chlorosilanes, are characterized by the non-polar (hydrophobic) nature of the surface, as there are alkyl chains bound to silicon atoms. The polarity of the surface of silica, modified with siloxane bonds, depends on the number of bound alkyl chains and their length, as well as the number of unbound -OH groups. It decreases with an increase in the length of the carbon chains and with a decrease in the number of free hydroxyl groups. Of most significant practical importance are the bonded phases in which alkyl groups, with two (C2), eight (C8), or eighteen (C18) carbon atoms, are attached to the surface of the silica gel. A non-polar octadecyl phase with eighteen carbons in the chain (C18) is the most commonly used in extraction and microextraction techniques. It is applied in the microextraction of non-polar analytes, such as polycyclic aromatic hydrocarbons.

Table 9 summarizes examples of the application of C18 silica in the TF-SPME technique used to analyze environmental, biological, and food samples, which have been described in scientific publications.

Table 9. Examples of the use of C18 silica in TF-SPME.

Sorption Phase	Preparation	Analyte	Matrix	Detection	Reference
C18-TEOS	dip coating	benzodiazepines	plasma	LC–MS/MS	[101]
C18/PAN	spray coating	pharmaceuticals	fish tissue	LC/MS–MS	[102]
C18/PAN	spray coating	steroid hormones	fish plasma	LC–MS/MS	[103]
C18/SCX	commercial strips	carbamazepine triclosan	water	DESI-MS	[104]
C18/glue	dip coating	benzodiazepines	urine	HPLC-MS	[25]

7.7. Aptamers

Aptamers are single-stranded oligonucleotides of ribonucleic acid (RNA) or deoxyribonucleic acid (DNA), most often between 20 and 80 nucleotides in length. They form three-dimensional undulating conformations and, like antibodies, have the ability to bind to a variety of biological and molecular targets. The main characteristics of aptamers are their high specificity and affinity to binding well-defined biomolecules of different sizes such as nucleotides, amino acids, biopolymers, polysaccharides, peptides, or proteins.

Aptamers can combine with molecules of varying chemical structure, for example, metal ions, enzymes, regulatory proteins, growth factors, antibodies (both mono- and poly-

clonal), lectins, vitamins, antibiotics, amino acids, peptides, nucleotides, or organic dyes. Their characteristics enable them to be used as highly selective sorbents in microextraction to the solid phase. Used as selective microextraction sportive phase, aptamers must be bound to solid supports. The aptamer-binding substrate should be characterized by chemical and biochemical inertness and good mechanical stability. The aptamer immobilization procedure must preserve its affinity to the target analyte [105].

Table 10 summarizes examples of the use of aptamers in the TF-SPME technique, which are used to analyze environmental, biological, and food samples and have been described in scientific publications.

Table 10. Examples of the use of aptamers in TF-SPME.

Sorption Phase	Preparation	Analyte	Matrix	Detection	Reference
aptamer/cellulose	dip coating	codeine acetamiprid	urine, vegetable juice water	ESI-IMS	[106]
aptamer/CDs/cellulose	dip coating	methamphetamine	urine, plasma saliva	ESI-IMS	[107]
aptamer/cellulose	dip coating	codeine	urine	ESI-IMS	[108]

7.8. Ionic Liquids and Poly(Ionic Liquids)

Ionic liquids (ILs) are salts containing organic cations and organic, or inorganic anions with a melting point equal to or below 100 °C. The cation of an ionic liquid is usually a branched organic structure with low symmetry. The cations forming ionic liquids include imidazolium (IM), pyrrolidine (Pyrr), pyridine, tetraalkylammonium, or tetralkylphosphonium. The anions included in the ionic liquids are the halide anions Cl^-, Br^- I^-, but also triflate ([TfO^-]), bis(trifluoromethylsulfonyl) imide ([$TFSI^-$]), tetrafluoroborate ([BF_4^-]), or hexafluorophosphate ([PF_6^-]) [109]. Figure 21 show the molecular structures and nomenclature of various cations and anions commonly found in synthesizing second- and third-generation ionic liquids [110].

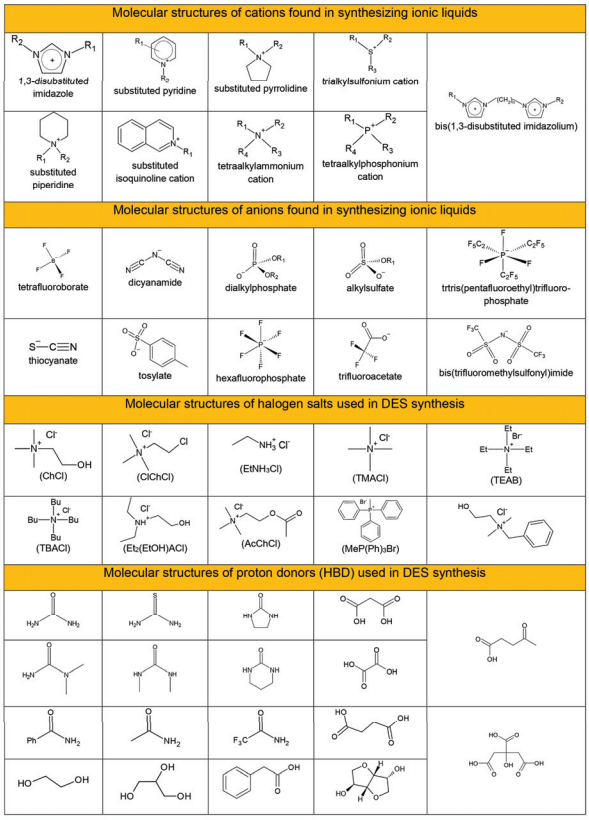

Figure 21. Molecular structures of substrates found in synthesizing ILs and DES [110,111].

Ionic liquids are among chemical compounds with unique physicochemical properties, such as high thermal stability, near-zero vapor pressure, high viscosity, non-flammability, and the ability to dissolve a wide range of organic and inorganic chemicals. Physical properties such as miscibility and thermal stability depend primarily on the anion. In contrast, other properties, such as viscosity and surface tension, are controlled by the length of the alkyl chain on the cation and the shape and symmetry of the cation [110]. The negligible vapor pressure of ionic liquids, their good thermal stability, and controllable viscosity, as well as their miscibility with water and organic solvents, are the main properties that make ionic liquids applicable in microextraction to the solid phase. The high viscosity of ILs facilitates their application to the substrate and positively influences the homogeneity of the sorption film. Simultaneously, their liquid state makes it easier to conduct the extraction process due to the higher diffusion rates of analytes compared to solid phases. The ability to design ILs by matching the type of cation and anion to the target analyte is a factor that determines high selectivity and sensitivity to determinations carried out using solid-phase microextraction [112]. Ionic liquids (ILs) are used in SPME microextraction, while poly(ionic liquids) PILs—in TF-SPME techniques. Poly(ionic liquids) are a subgroup of polyelectrolytes that can be obtained by polymerizing ionic liquid monomers or post-polymerization processes [109]. The polymer chains of PILs repeat ionic units: cationic, anionic, or zwitterionic. In the cationic structure, groupings endowed with a positive electrical charge are covalently attached to the polymer backbone. Typical cationic PILs are based on imidazole, pyridine, pyrrolidine, and quaternary ammonium cations. Groupings with a negative electrical charge, such as sulfonates, carboxylates, and phosphates, covalently link to the polymer chain in anionic PILs. In the case of zwitterionic PILs, both cations and anions are covalently attached to the polymer chains [113].

The physicochemical characteristics of polymeric ionic liquids, such as high thermal, chemical, and mechanical stability and excellent plasticity, make them applicable in various fields of science and technology, including microextraction techniques. ILs, used as sorption phases in microextraction, provide high extraction efficiencies for a wide range of compounds due to their porous structure and the presence of functional groups in the polymer chain that enable a variety of interactions with the analyte molecules [113].

Table 11 summarizes examples of the use of polymeric ionic liquids in the TF-SPME technique, which are used to analyze environmental, biological, and food samples and have been described in scientific publications.

Table 11. Examples of the use of polymeric ionic liquids in TF-SPME.

Sorption Phase	Preparation	Analyte	Matrix	Detection	Reference
HVImBr/MMA	application to the Petri dish	sulfathiazole	milk, honey	SF	[114]
p-PIL-AcO	dip coating	nonsteroidal anti-inflammatory drugs	urine	LC-MS/MS.	[115]
p-Poly-(MMA-IL)	dip coating	sulfonamides	water	HPLC-DAD	[116]
poly-(MMA-BVImBr)	application to the Petri dish	aniline	water	LC-MS/MS	[117]

7.9. Deep Eutectic Solvents

Deep eutectic solvents (DES) are systems formed from a mixture of various types of cationic and anionic Lewis or Brønsted acids and bases [118]. The ions in the mixture, as a result of hydrogen bonding, form a eutectic mixture. A eutectic mixture is characterized by a much lower melting point than the melting point of each of its components [111]. They are mainly obtained by mixing the quaternary ammonium salt with metal salts or a hydrogen bond proton donor (HBD). A hydrogen bond proton donor (HBD) has the ability to form a complex with the halide anion as a hydrogen bond acceptor (HBA) from the quaternary ammonium salt. Figure 21 shows quaternary ammonium salts and hydrogen bond proton donors (HBD) widely used in DES formation [111].

DES have similar properties to ionic liquids, but unlike them, they are less toxic, non-flammable, and biodegradable [119]. The physicochemical properties of deeply eutectic solvents depend both on the properties of each component of the eutectic mixture, and on the interaction between them. The values of the physical quantities, such as freezing point, viscosity, electrical conductivity, and pH value, can be modified by an appropriate combination of different quaternary ammonium salts (e.g., ChCl) and hydrogen bond donors (HBD) [111]. The density of deeply eutectic solvents ranges from 1.041 to 1.63 $g \cdot cm^{-3}$. Its value is influenced by temperature (with an increase in temperature, the density of DES decreases linearly) and the molar ratio of the components of the eutectic mixture [120]. Most deep eutectic solvents have higher viscosity and surface tension at room temperature than conventional solvents. The extensive interconnection of DES-forming particles via hydrogen bonds, van der Waals forces, and electrostatic interactions are responsible for the high viscosity and surface tension values [120].

DES are increasingly used in analytical chemistry, mainly as mobile phase modifiers in chromatography and extractants in various microextraction techniques to the liquid phase, and in recent years, also in microextractions to the solid phase [121]. A significant number of DES between room temperature and 70 °C occur in the liquid state [111]. However, there are solid eutectic systems at room temperature that can be used as sorption phases in microextraction to the solid phase.

Table 12 summarizes examples of the use of DES in the TF-SPME technique, which has been described in scientific publications, to perform surface water analysis.

Table 12. Examples of the Use of DES in TF-SPME.

Sorption Phase	Preparation	Analyte	Matrix	Detection	Ref.
DES	dip coating	parabens	water	HPLC-UV	[119]
	dip coating	formaldehyde	water	HPLC-UV-Vis	[122]
PDMS/DES	dip coating	parabens	water	HPLC-UV	[121]

8. TF-SPME with Thermal and Solvent Desorption

Desorption of analytes from the TF-SPME device can be carried out at high temperatures or in an organic solvent. Thermal desorption requires the sorptive phase and its support to be highly thermally stable. Due to the larger size of the TF-SPME device than the SPME fiber, performing thermal desorption of analytes from the TF-SPME sorbent involves the use of a gas chromatograph column dispenser adapter. The adapter, a thermal desorption unit (TDU), is an accessory for the GC gas chromatograph. During thermal desorption, the sorptive phase is heated with hot gas to release all volatile analytes adsorbed on it. The increase in temperature of the sorption phase increases the partition coefficient of the analytes and consequently promotes their release from the sorbent solid phase into the gas phase. Thermal desorption in the TDU of the gas chromatograph allows direct introduction of all analytes, except non-volatile substances, into the chromatographic column. The non-volatile substances remain on the TF-SPME device [9].

Liquid desorption is commonly used in conjunction with liquid chromatography. It uses a small amount of organic solvent (or a mixture of water and multiple organic solvents) to re-extract all compounds from the solid phase of the TF-SPME device to the liquid phase. After desorption, the analytically enriched organic solvent is injected into the liquid chromatograph. Desorption in the solvent is most commonly used while analyzing non-volatile, thermally labile compounds and biomolecules. Diffusion of analytes in the liquid occurs more slowly than in the gas phase, and consequently, desorption in organic solvents is a longer process than thermal desorption [8].

9. Application of the TFME Technique in the Analysis of Organic Compounds

The TF-SPME technique has been used to concentrate and analyze a wide range of organic compounds in aqueous, biological, and food matrices for over twenty years. In

addition to the possibility of preparing samples in the laboratory, the TF-SPME technique allows sampling onsite [43] and in vivo [37,123,124]. The TF-SPME technique has been successfully used to extract in vivo prohibited substances and oral cancer markers from human saliva [125] and analytes from human skin [37].

The different types of matrices containing analytes, whose determination by TF-SPME have been described in scientific publications, are shown in Figure 22.

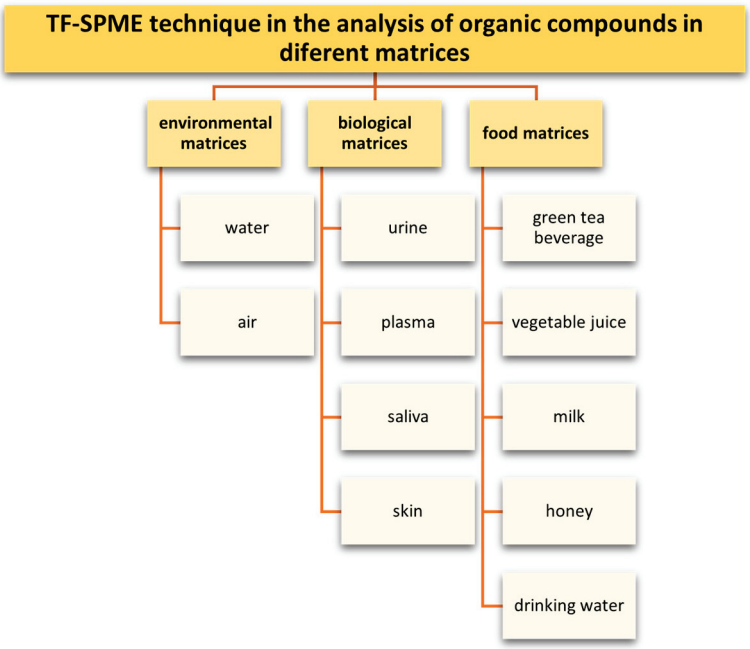

Figure 22. Matrix types containing analytes determined using the TF-SPME technique.

Organic analytes whose determination procedures were developed using TF-SPME mainly belong to the following:

1. Compounds that are environmental contaminants in aqueous and food matrices (polycyclic aromatic hydrocarbons, polycyclic aromatic sulfur heterocycles (PASHs), plant protection products, phenols, chlorophenols, alkylphenols, bisphenol A);
2. Preservatives determined in aqueous matrices (parabens and personal care products PCPs);
3. Biologically active compounds determined in aqueous and biologic matrices (drugs from various therapeutic groups including nonsteroidal anti-inflammatory drugs, antibiotics, antidepressants, tranquilizers, opioids, anti-cancer drugs, sex hormones, doping agents, narcotics).

Polycyclic aromatic hydrocarbons (PAHs) and polycyclic aromatic sulfur heterocycles PASHs, along with polychlorinated biphenyls (PCBs), organochlorine, and organophosphate pesticides are among the hazardous pollutants of surface water and food. Due to the toxicity of PAHs, environmental pollution by polycyclic aromatic hydrocarbons is a factor that has a very negative impact on the human and animal bodies. They negatively affect endocrine, reproductive, and developmental processes [126]. For many compounds, among several hundreds of known PAHs, the initiation of tumor transformations has been proven. Similarly to PAHs, polycyclic aromatic sulfur heterocycles PASHs, such as dibenzothiophene (DBT), are components of petroleum products with mutagenic and carcinogenic effects.

Analytical procedures have been developed for the determination of PAHs in aqueous matrices, using TF-SPME with sorption phases: PDMS [34] and MWCNTs/CTA [100], while in food matrices, using MWCNTs/Agr [95]. In the determination of PASHs in water samples, MIP [59] was used as the sorption phase (Tables 13 and 14).

The need to maintain global food production at a level sufficient to feed the earth's growing population necessitates the use of crop protection products. These products, while increasing yields in agricultural production, also contribute to the pollution of the environment with hazardous organic compounds. This underscores the critical need to monitor even trace amounts of pesticides and fungicides in treated water for drinking and food products [127].

Analytical procedures have been developed for the determination of pesticides and fungicides in aqueous matrices using TF-SPME with sorptive phases in the form of PDMS/DVB [42], polypropylene/polyamide nanofibers [52], MOFs [74], MWCNTs/CTA [96], (MOF)/(PU) [128], MIP [54], and DES/CTA [127]. For the determination of plant protection agents in food samples, sorption phases were used in TF-SPME devices such as HLB/PTFE AF [129], POM@UIO-66-NH2/GO [130], POM@UIO-66-NH2/GO [131], UiO-66/PS [132], and PU/PMMA [133] (Tables 13 and 14).

Phenol and its derivatives, chlorophenols, alkylphenols, and bisphenol A, are another group of organic compounds, along with PAHs and pesticides, that pollute surface waters and pose a threat to aquatic organisms and human health. They come from a variety of sources, such as oil extraction and processing, wood and coal pyrolysis, industrial organic synthesis, and plastic production [134]. Chlorophenols are persistent toxic substances that cause histopathological changes and mutations in aquatic organisms, and some are probable human carcinogens, such as pentachlorophenol (PCP). Alkylphenols are endocrine disruptors and have widespread effects on the health and function of a range of aquatic organisms, as well as humans [135]. Bisphenol A, as a polymer additive, is used to manufacture polycarbonate plastic bottles used to store beverages and infant milk. BPA is released from the polycarbonate bottle into the liquid it contains. As a result, an infant's consumption of liquids from polycarbonate bottles contributes to an increase in the concentration of BPA in urine. BPA exhibits xenobiotic activity, estrogenic activity, and endocrine-disrupting properties. In addition, bisphenol A has been linked to decreased fertility and cancer. The adverse effects of bisphenol A on human health imply the need for its determination in drinking water and food matrices [136].

The authors of the referenced TF-SPME studies used sorptive phases to determine phenolic compounds in aqueous matrices: MIP [61,63], MWCNTs-COOH/PDMS [97], MWCNTs-COOH-Ch/PP [99], PVA/PVP/PES [136], and polyamide-coated paper [137]. In the determination of chlorophenols in the food matrix, AC/GO [138] was used as the sorption phase (Tables 13 and 14).

Parabens are a family of synthetic p-hydroxybenzoic acid esters that includes methylparaben (MP), ethylparaben (EP), propylparaben (PP), butylparaben (BP), isobutylparaben (IBP), isopropylparaben (IPP), benzylparaben (BeP), and heptylparaben (HP) and their respective sodium salts. They are used as preservatives in everyday products such as cosmetics, food, toiletries, etc. [139]. European Union legislation has restricted the use of parabens in cosmetics because they can cause allergic reactions and disrupt human hormonal metabolism [140]. However, limits have yet to be set for the concentrations of parabens in environmental samples [121].

The researchers used TF-SPME to determine parabens in aqueous matrices using the following sorption phases: DES [119], PDMS/DES [121], and CA-MIL-101(Cr)@CNFs [141] (Table 13).

Non-steroidal anti-inflammatory drugs (NSAIDs) are among the most widely used pharmaceuticals, often applied to suppress inflammation, treat allergies, and reduce pain. Due to their hydrophilicity and stability in water, NSAIDs can persist in the aqueous phase for long periods and thus adversely affect aquatic organisms and human health [142]. Side effects of non-steroidal anti-inflammatory drugs include cardiovascular disorders, gastrointestinal disorders, increased blood pressure, and kidney damage. Thus, monitoring the level of a non-steroidal anti-inflammatory drug in a patient's body can significantly contribute to better diagnosis and treatment of effects caused by, among other things, its overdose [143].

In the determination of non-steroidal anti-inflammatory drugs in aqueous matrices, the authors of the publications used TF-SPME, in which the following sorption phases were applied: MWCNT/Agr-Ch [94], while in biological matrices: CY-GO-LDH [82], p-PIL-AcO [115], MOF-5 [143], and LDH/GO/PVDF [84] (Tables 13 and 15).

Glucocorticoids are among the drugs used to treat allergies, asthma, and estrogen and autoimmune disorders [144]. They enter the aquatic environment as a result of wastewater discharges directly into the environment or as an effect of incomplete removal from contaminated water in wastewater treatment plants [145]. The presence of glucocorticoids in concentrations at ng L^{-1} levels is a factor that adversely affects aquatic organisms [146]. In the determination of glucocorticoids in aqueous matrices, the authors of the publications used TF-SPME, in which they used SDS-MWCNTs/PP [93] as a sorption phase (Table 13).

Antibiotics are widely used in both human and veterinary medicine. Global consumption of antibiotics in industrial animal husbandry is increasing year by year. Through animal manure, which is used as fertilizer in agricultural production, antibiotics enter the soil in small amounts and then into post-surface water. Ineffective degradation of pharmaceuticals during wastewater treatment can lead to contamination of surface water, groundwater, and, consequently, drinking water. Residues of antibiotics in water can enter the food chain and adversely affect human health, including causing allergic reactions. As a consequence, there is a need to determine the level of antibiotic concentrations in environmental waters [147]. In the determination of antibiotics in aqueous matrices, the researchers used TF-SPME, in which they used sorption phases: p-Poly-(MMA-IL)FP [147] and PVA-SA-βCD [148] (Table 13).

Steroid hormones are a group of hormones that have a steroid skeleton in their chemical structure. Natural steroid hormones are usually synthesized from cholesterol in the adrenal cortex. Steroid hormones regulate such physiological processes as, for example, carbohydrate, protein, and fat metabolism (glucocorticoids) and water and mineral balance (mineralocorticoids). Estrogens, including estradiol, are involved in the development of primary and secondary female sexual characteristics, while progestins (e.g., progesterone) are involved in the maintenance of pregnancy. Androgens (e.g., testosterone) control the development and maintenance of reproductive function and are responsible for secondary sexual characteristics in men [149]. Estrogens play an important role at different stages of human development. In the case of post-menopausal women, estrogen levels are low, and abnormal levels of estrogen concentrations may be associated with the development of breast cancer [150]. In the microextraction of hormones by the TF-SPME technique from biological matrices, researchers have used sorption phases: PANI [53,151], C18/PAN, PS/DVB [149], MIL-53(Al)/PVDF, MIL-53(Fe)/PVDF, MIL-100(Fe)/PVDF, MIL-101(Cr)/PVDF, and UiO-66(Zr)/PVDF [72] (Table 15). From the aqueous matrix, estrogens were extracted into the C18/PAN sorption phase [47] (Table 13).

One of the most prevalent mental illnesses today is depression. Antidepressants impede serotonin reuptake in presynaptic neurotransmission. Monitoring drug concentrations in the patient's blood or urine is essential to determine the optimum therapeutic dose for the patient, to increase the efficacy of therapy, and to reduce the risk of laccase intoxication [62]. Recent publications have presented analytical procedures for the determination of sedative and antidepressant drugs in biological matrices using TF-SPME with sorption phases: C18/glue [25], C18-TEOS [101], C18/PAN [44], GO/CS [152], Ni-Co MOFs-PAN [153], MIP [62], and poly(vinyl alcohol) (PVA)/citric acid(CA)/β-cyclodextrin/Bi2S3@g-C3N4 [154] (Table 15).

Opioids include all substances that act on opioid receptors: natural opiates, semi-synthetic poppy alkaloids, their synthetic derivatives, and endogenous peptides. The main use of opioids is to manage severe pain (post-operative, post-traumatic, cancer), often chronic. Using them for purposes other than therapeutic can be dangerous and addictive [155]. Procedures for the labeling of opioids, for example, codeine, tramadol, and fentanyl in biological matrices, have been developed using TF-SPME microulceration with

sorption phases in the form of aptamer/cellulose [106,108], Ni(DMG)2-NiO-Cell [156], and octyl-cyanopropyl/PAN [157] (Table 15)

Beta-blockers are essential clinical drugs that are used to treat cardiovascular diseases such as hypertension, irregular heart rhythms, strokes, and angina. Additionally, β-blockers improve cardiac function by relaxing muscles and reducing heart rate, which is often abused by athletes competing in professional sports [87]. Procedures for the determination of beta-blockers in biological matrices have been developed using TF-SPME with sorption phases such as GO/PEG [87] and g-C3N4/N6 NC [158] (Table 15).

Tables 13–15 provide details of the quantification of analytes in aqueous, food, and biological matrices using TF-SPME reported by researchers in the last few years.

Table 13. Applicability of TF-SPME technique for quantitative analysis of different analytes in water matrix.

Analyte	Sorption Phase	Detection	LOD	Recovery [%]	RSD [%]	Ref.
PAHs	PDMS	GC-MS	-	-	6–11	[34]
	MWCNTs/CTA	HPLC-UV	0.02–0.09 ng/mL	99–101	1–8	[100]
Polycyclic aromatic sulfur heterocycles	MIP	GC-MS	0.029–0.166 μg L^{-1}	-	≤6.0	[59]
Pesticides/fungicides	DVB/PDMS	GC-MS	0.01–0.25 μg L^{-1}	90–130	2–20	[42]
		GC-MS	1.0–4.0 ng L^{-1}	71–124	3–20	[43]
Pesticides/fungicides	PPy/PA	GC-MS	50 ng L^{-1}	96–98	4	[52]
	amino-Zr-MOF/PAN	CD-IMS	0.6 μg L^{-1}	-	11	[74]
	MWCNTs/CTA	GC-MS	1 μg L^{-1}	-	≤20	[96]
	MIP	LC-MS/MS	0.002–0.02 μg L^{-1}	90–110	<15	[60]
	PAMAM@GO-PVDF	HPLC-UV	0.12–0.20 μg L^{-1}	98–99	-	[89]
	MOF/PU	GC-MS	0.005–0.1 μg L^{-1}	72–110	4–5	[128]
	DES/CTA	GC-MS	0.4–1.3 μg L^{-1}	69–103	3–14	[127]
	PVA/CA/C)/AV	HPLC-UV	-	86–97	6–7	[159]
	DES	HPLC-UV	-	72–94	3–11	[160]
	DVB/PDMS	GC-TMS	-	-	-	[40]
VOCs/SVOCs		GC-MS	-	-	-	[24]
N-nitrosamines	DVB/PDMS	GC-MS	3 ng L^{-1}	-	8	[22]
Chlorobenzenes	PANI-N6	GC-MS	19–33 ng L^{-1}	93–103	5–14	[54]
Phenols	MIP	UHPLC-PDA	0.1–2 μg L^{-1}	85–100	1–14	[61]
		LC-MS	-	-	-	[63]
	MWCNTs-COOH/PDMS	HPLC-UV	1–2 μg L^{-1}	64–90	-	[97]
Polychlorinated biphenyls	MWCNTs-COOH-Ch/PP	GC-MS	<0.60 ng L^{-1}	86–104	0.17–5.01	[99]
Bisphenol A	PVA/PVP/PES	FS	0.3 ng mL^{-1}	84–96	5–10	[136]
Phthalates, alkylphenols, bisphenols	Polyamide-coated paper	HPLC-DAD	1.5–7.6 μg L^{-1}	-	≤24%	[137]
Sulfonamides	p-Poly-(MMA-IL)	HPLC-DAD	0.14–0.52 μg L^{-1}	90–110	10	[116]
Aniline	poly-(MMA-BVImBr)	LC-MS/MS	0.5 μg L^{-1}	91–96	8.3	[117]
Parabens	DES	HPLC-UV	0.018–0.055 ng L^{-1}	68–94	4–7	[119]
Parabens	PDMS/DES	HPLC-UV	0.023–0.062 ng mL^{-1}	79–88	3–6	[121]
	CA-MIL-101(Cr)@CNFs	HPLC-DAD	11 ng L^{-1}	92–100	<5	[141]
Formaldehyde	DES	HPLC-UV-Vis	0.15 ng mL^{-1}	78–99	3–5	[122]
Personal care products	MIL-100(Fe)/PS/cellulose	HPLC-PDA	7.5 μg·L^{-1}	78–128	11	[75]

Table 13. *Cont.*

Analyte	Sorption Phase	Detection	LOD	Recovery [%]	RSD [%]	Ref.
Flame retardants:	ZIF-8@N-rGO	HPLC	0.03–0.14 ng L^{-1}	89–106	-	[161]
Nonsteroidal anti-inflammatory drugs	MWCNT/Agr-Ch	HPLC-UV	0.89–8.05 ng mL^{-1}	-	<5	[94]
Estrogens	C18/PAN	LC-UV	1.2–1.6 ng mL^{-1}	87–109	3–6	[47]
Glucocorticoids	SDS-MWCNTs/PP	UHPLC-MS	0.019–0.098 ng mL^{-1}	-	2–4	[93]
Carbamazepine	C18/SCX	DESI-MS	<ng L^{-1}	-	-	[104]
Triclosan	C18/SCX	DESI-MS	<ng L^{-1}	-	-	[104]
Antibiotics: sulfonamides, tetracyclines, fluoroquinolones, penicillin, macrolides	p-Poly-(MMA-IL)FP	LC-MS/MS	0.05–4.52 μgL^{-1}	79–127	1–12	[147]
Antibiotics: Amoxicillin, enrofloxacin, tetracycline, doxycycline	PVA-SA-βCD	HPLC-UV	0.02–0.03 μgL^{-1}	70–100	1–2	[148]
Illicit drugs: methamphetamine ketamine methaqualone	DVB/PDMS	GC-MS	For methamphetamine: 5.5 ng L^{-1} For ketamine: 2.0 ng L^{-1} For methaqualone: 1.1 ng L^{-1}	95–111	<6	[162]
Chlorpyrifos, triclosan, tonalide	CTA with plasticizers	GC-MS	0.05–0.42 μgL^{-1}	>80	<10	[163]
Haloacetic acids	PDMS HLB/PDMS Carboxen/PDMS	GC-ECD	-	51–92	7–19	[164]
Sexual hormones: 17β-estradiol, 17α-ethinylestradiol, estrone, progesterone, medroxyprogesterone acetate, hydroxyprogesterone	CTA/NPOE CTA/DBS	HPLC–MS/MS	0.1–5.7 ng L^{-1}	>60	<12	[165]
Organic pollutants: benzene, 2-hexanone, hexanal, α-pinene, limonene, eucalyptol, 2-nona- none, 2-nonanol, 2-undecanone, ethyl nonanoate, 1-undecanol, ethyl undecanoate	GO/PS-DVB s	GC-MS	0.4–8.1 ng L^{-1}	78–111	2–6	[166]

Table 14. Applicability of TF-SPME technique for quantitative analysis of different analytes in food matrices.

Matrix	Analyte	Sorption Phase	Detection	LOD	Recovery [%]	RSD [%]	Ref.
Green tea beverage	PAHs	MWCNTs/Agr	HPLC-UV	0.1–50 ng L^{-1}	91–107	-	[95]
Vegetable juice	Codeine, acetamiprid	Aptamer/cellulose	ESI-IMS	1.8–3.7 ng mL^{-1}	-	2–6	[106]
Honey, pork, chicken, milk	Sulfonamides: sulfathiazole, sulfamerazine, sulfadimidine, sulfamethoxazole, sulfisoxazole	MIL-101(Cr)/CC	HPLC-PDA	2.5–4.5 μg mL^{-1}	82–114	<9	[167]

Table 14. *Cont.*

Matrix	Analyte	Sorption Phase	Detection	LOD	Recovery [%]	RSD [%]	Ref.
Milk	Sulfathiazole	HVImBr/MMA	SF	0.07–0.23	84–107		[114]
	Phthalates	C18-FMSNs/PAN	HPLC	0.096–0.26 ng mL^{-1}	86–110	<7	[168]
Honey	Macrolides, lincosamides	ZIF-8@GO	UPLC-MS/MS	0.1–04 μg kg^{-1}	68–107		[88]
Honey, tea	Chlorophenols	ACGO	HPLC-UV	0.03–0.13 μg mL^{-1}	-	3–6	[138]
Drinking water	Anti-inflammatory antibacterial drugs	DVB/PAN	LC-ESI-MS/MS	ng L^{-1}	-		[41]
Cod liver oil	Polychlorinated n-alkanes	HLB/PDMS	GC-MS	0.07–0.22 μg/g	-	2–12	[169]
Apple, tomato	Benzoylurea insecticides	PAN/ZIF8@E coli	HPLC-UV	0.12–0.15 μgL^{-1}	93–110	≤8	[170]
Fruit juice, black tea	Flavonoids: morin, quercetin	Co_3O_4@GO-Nylon-6	HPLC-UV	For morin: 1.3 μgL^{-1} For quercetin: 1.6 μgL^{-1}	For morin: 73 For quercetin: 64	<5	[171]
Fruit and tea beverages	Pesticides	polyurethane	GC-ECD	0.001–0.015 μgL^{-1}	77–106	-	[172]
Apple juice		HLB/PTFE AF	GC-MS	1.0–5.0 ng mL^{-1}	-	≤20	[129]
Cereal		PVA/MCS/HC-POF	HPLC-UV	≤4.0 ng mL^{-1}	63–79	≤7	[130]
Vegetables and fruits		POM@UIO-66-NH_2/GO	HPLC-UV	0.31–0.34 μgL^{-1}	89–102	2–4	[131]
Vegetables and fruits		UiO-66/PS	GC	1.5–3 μg kg^{-1}	88–96	5–7	[132]
Carrot juice, apple juice, strawberry juice		phosphotungstic acid/polyvinylidene fluoride membrane.	HPLC-UV-Vis	0.29–0.31 μgL^{-1}	96–105	4–6	[173]
Fruit juice, tea	Neonicotinoid insecticides	PU/PMMA	UPLC-MS/MS	0.001–0.1 μgL^{-1}	81–108	-	[133]
Fruit juice	Thiram fungicide	Silver nano network/silicon wafer	SERS	0.01 μgL^{-1}	-	7	[174]
Milk, honey, fruits, vegetables	Conazole fungicides	MIL-88A@CNTs	CD-IMS	For penconazole: 0.30 ng mL^{-1} For propiconazole: 0.50 ng mL^{-1}	86–97	5–7	[175]
Dry chili, chili powder, dry Sichuan pepper, Sichuan pepper powder	Rhodamine B	COF-117-PTFE	HPLC-FLD	0.007 μgL^{-1}	68–71	7	[176]

Table 15. Applicability of TF-SPME technique for quantitative analysis of different analytes in biological matrices.

Matrix	Analyte	Sorption Phase	Detection	LOD	Recovery [%]	RSD [%]	Ref.
Urine	Doping agents	C18/PAN	LC-MS	0.25–10 ng mL^{-1} LOQ	85–130	<20	[45,46]
	Hormones	PANI	HPLC-FLD	0.30–3.03 μg L^{-1}	71–115	≤12	[53]
	Steroidal hormones	C18/PAN PS/DVB	UHPLC-ESI-QTOF/MS	-	74–99	-	[149]

Table 15. *Cont.*

Matrix	Analyte	Sorption Phase	Detection	LOD	Recovery [%]	RSD [%]	Ref.
Urine	Estrogens	MIL-53(Al)/PVDF MIL-53(Fe) /PVDF MIL-100(Fe) /PVDF MIL-101(Cr) /PVDF UiO-66(Zr) /PVDF	HPLC-FLD	0.005–1 ng mL^{-1}	80–103	≤11.4	[72]
	Urinary androgens	-	HPLC-QqQ/MS	0.04–0.09 ng mL^{-1}	-	-	[177]
	Caffeine	ZIF-8/LDH/GO/PVDF	HPLC-UV		-	-	[73]
	Aldehydes	MOF-199/PS	HPLC- VWD	4.2–17.3 nmol L^{-1}	82–112	2–13	[76]
	Non-steroidal anti-inflammatory drugs	CY-GO-LDH	HPLC-UV	0.25 μg L^{-1}	-	6	[82]
Urine	Diclofenac	LDH/GO/PVDF	HPLC-UV	0.14 μg L^{-1} in water 0.23 μg L^{-1} in urine 0.57 μg L^{-1} plasma samples	89–93	7 7 7	[84]
	Benzodiazepines	C18/glue	HPLC-MS	0.05−0.15 ng mL^{-1}	-	5−7	[25]
	Codeine acetamiprid	Aptamer/cellulose	ESI-IMS	3.7 ng mL^{-1}	87–91	2–6	[106]
	Methamphetamine	Aptamer/CDs/cellulose	ESI-IMS	0.45 ng·mL^{-1}	87–108	<8	[107]
	Codeine	Aptamer/cellulose	ESI-IMS	3.4 ng·mL^{-1}	90	7	[108]
	Nonsteroidal anti-inflammatory drugs	p-PIL-AcO	LC-MS/MS.	3.8 μg L^{-1} for indomethacin 7.2 μg L^{-1} for diclofenac 6.8 μg L^{-1} for tolmetin 9.4 μg L^{-1} for ketoprofen 15.7 μg L^{-1} for naproxen 5.1 μg L^{-1} for ibuprofen	72–95	1–13	[115]
	Nonsteroidal anti-inflammatory drugs: naproxen, aspirin, tolmetin, celecoxib	MOF-5	HPLC-UV	0.57–0.77 μg L^{-1}	94–108	4–6	[143]
	Endocrine-disrupting compounds	DES	LC-MS/MS	0.01–1.15 ng mL^{-1}	-	3–10	[178]
	Tramadol	Ni(DMG)2-NiO-Cell	HPLC-UV	0.1–1.0 ng mL^{-1}	86	6–8	[156]
	Carvedilol blocker	g-C3N4/N6 NC	FS	1.0 ng mL^{-1}	83	4	[158]
	Fentanyl, methadone, zolpidem	Octyl-cyanopropyl/PAN	HPLC-MS/MS	4.0–17.4 ng mL^{-1}	43–76	<15	[157]
Urine	Fluoxetine	GO/CS	HPLC-UV-Vis	1.0 ng mL^{-1}	82	≤9	[152]
	Tricyclic antidepressants	Ni-Co MOFs-PAN	HPLC-UV	0.06–0.3 μg L^{-1}	91–100	<5	[153]
	Biogenic monoamines	HLB/PAN	UPLC-MS/MS		36–75	<9	[179]

Table 15. *Cont.*

Matrix	Analyte	Sorption Phase	Detection	LOD	Recovery [%]	RSD [%]	Ref.
Plasma	Tricyclic antidepressants	MIP	LC-MS/MS	1.0–5.0 ng mL^{-1}	90–110	15	[62]
	Antidepressant drugs: Clomipramine, Clozapine, Trimipramine	PVA/CA/β-cyclodextrin/Bi_2S_3@g-C_3N_4	GC-FID	0.03–0.15 ng mL^{-1}	78–95	5–7	[154]
	Mycophenolic acid	MIP	UPLC	0.3 ng mL^{-1}	-	4	[64]
	Benzodiazepines	C18-TEOS	LC-MS/MS	0.4–0.7 ng mL^{-1}	11–83	4–8	[101]
		C18/PAN	LC-MS/MS	0.08–0.2 ng mL^{-1}	83–98	<9	[44]
	Anti-cancer drugs	Co-MOF-74/polyfam	HPLC-UV	0.03–0.20 μg L^{-1}	-	3–9	[71]
		polylactic acid PLA	HPLC	0.03 μg L^{-1}	-	8	[180]
	Tramadol	$Ni(DMG)_2$-NiO-Cell	HPLC-UV	0.1–1.0 ng mL^{-1}	92	6–8	[156]
Plasma	Carvedilol	g-C_3N_4/N_6 NC	FS	1.0 ng mL^{-1}	87	3.6	[158]
	Fentanyl, methadone, zolpidem	Octyl-cyanopropyl/PAN	HPLC-MS/MS	4.3–8.3 ng mL^{-1}	34–62	<15	[157]
	Fluoxetine	GO/CS	HPLC-UV-Vis	1.6 ng mL^{-1}	87	≤9	[152]
Oral fluid	Fentanyl, methadone, zolpidem	Octyl-cyanopropyl/PAN	HPLC-MS/MS	4.8–9.6 ng mL^{-1}	27–38	<15	[157]
Saliva	β-blockers	GO/PEG	LC-MS/MS	1.25–8.00 nmol L^{-1}	80–109	4–13	[87]
	Methamphetamine	aptamer/CDs/cellulose	ESI-IMS	0.6 ng·mL^{-1}	87–108	6	[107]
Exhaled air condensate	Aldehydes	PS/G	HPLC	3.8 nmol L^{-1}	80–106	16	[86]
Skin	Volatile organic compounds	PDMS	GC-MS	-	-	<9	[37]
Fish tissue	Polychlorinated biphenyls	PDMS	LC-MS	-	-	-	[35]
	Pharmaceuticals	C18/PAN	LC/MS-MS	0.08–0.21 ng g^{-1}	-	9–18	[102]
Fish plasma	Steroid hormones		LC-MS/MS	0.006–0.150 ng mL^{-1}	-	≤6 ≤15	[103]

10. Summary

Solid-phase microextraction SPME is one of the sample preparation techniques compatible with green analytical chemistry because it reduces toxic organic solvents to the minimum necessary. TF-SPME devices, in the form of a rectangular metal or polymer substrate onto which a thin layer of sorption phase or self-supporting membranes is applied, are characterized by a higher sorption capacity. They enable faster microextraction of analytes compared to microextraction carried out on SPME fiber and can be applied in the solution of analytical problems in environmental, food, and bioanalysis. TF-SPME strips can also be used as in vivo collection devices for organic compounds emitted from human skin. In recent years, developments in drone technology have enabled the TF-SPME instrument to be used as an extraction probe to collect environmental samples in locations that are difficult to access or where their contamination levels may pose a risk to the analyst.

The active phase on which analyte sorption occurs can be applied to the substrate through techniques such as dip coating, spin coating, electrospinning, rod coating, and spray coating. The dynamic development of material chemistry enables the use of highly advanced materials as selective sorption phases in TF-SPME, such as polymers, conductive polymers, molecularly imprinted polymers, organometallic frameworks, carbon nanomaterials, aptamers, polymeric ionic liquids, and deeply eutectic solvents. The above-mentioned materials differ in their affinity to different analyte groups and consequently in their selec-

tivity in adsorption of analytes from complex matrices. In terms of selectivity, materials such as organometallic frameworks, aptamers, molecularly imprinted polymers take the spotlight. Tables 13–15, containing detection limits and analyte recoveries in microextractions, show that the above-described materials, used as sorption phases, provide selective microextractions and sensitive determinations with detection limits at the nanograms per liter level. As a result, TF-SPME is successfully used to prepare analytical samples to determine a vast spectrum of analytes in sample environmental, biological, and food matrices.

For several years, commercial TF-SPME kits with sorption phases that enable the microextraction of polar as well as non-polar analytes have also been available and offered, among others, by GERSTEL and Markes International. The commercialization of TF-SPME devices could increase their use in analytical procedures carried out in both research and industrial laboratories in the coming years.

It can be conjectured that in the near future, the interest of researchers in developing selective and low-cost sorbents dedicated to the TF-SPME technique, as well as other solid-phase microextraction techniques, will be directed toward biopolymers and recycled materials. Even if the sorption properties of biopolymers and recycled materials are not satisfactory, a suitable research direction will be the modification of their surfaces by introducing new or additional functional groups, as well as the preparation of composite materials based on MIPs, MOFs, or CNMs.

Funding: This research received no external funding.

Conflicts of Interest: The authors declare no conflicts of interest.

Abbreviations

AAS	Atomic absorption spectroscopy
ACGO	Graphene oxide-coated agarose/chitosan
AES	Atomic emission spectroscopy
Agr	Agarose
AV	Aloe vera gel
BVImBr	1-butyl-3-vinylimidazolium bromide
CA	Citric acid
CA	Citric acid
CC	Carbon cloth
CD-IMS	Corona discharge ion mobility spectrometry
CDs	Carbon dots
Ch	Chitosan
CNMs	Carbon nanomaterials
CNT	Carbon nanotube
CPs	Conductive polymers
CS	Chitosan
CTA	Cellulose triacetate
CVD	Chemical vapor deposition
CY	Cotton yarn
CY-GO-LDH	Cotton yarn–graphene oxide-layered double hydroxide composite
DAD	Diode array detector
DBS	Dibutyl sebacate
DCBI-MS	Desorption corona beam ionization mass spectrometry
DES	Deep eutectic solvents
DESI-MS	Desorption electrospray ionization mass spectrometry
DI-SDME	Direct immersion single-drop microextraction
DLLME	Dispersive liquid–liquid microextraction
DNA	Deoxyribonucleic acid
ESD	Electrospray deposition technique
ESI-IMS	Electrospray ionization ion mobility spectrometer
FAAS	Flame atomic absorption spectroscopy

FID	Flame ionization detector
FMSNs	Fibrous mesoporous silica nanospheres
FS	Fluorescence spectrometry
G	Graphene
GBMs	Graphene-based materials
GC	Gas chromatography
GC-MS	Gas chromatography–mass spectrometry
GC-TMS	Gas chromatography–toroidal ion trap mass spectrometry
GO	Graphene oxide
HBD	Hydrogen bond donor
HF-LPME	Hollow-fiber liquid phase microextraction
HLB	Hydrophilic–lipophilic balance
HPLC	High-performance liquid chromatography
HPLC-VWD	High-performance liquid chromatography system with a variable wavelength ultraviolet detector
HPLC-DAD	High-performance liquid chromatography system with a diode array detector
HPLC-FLD	High-performance liquid chromatography with fluorescence detection
HPLC-MS	High-performance liquid chromatography with mass spectrometry
HPLC-PDA	High-performance liquid chromatography with photodiode array detector;
HPLC-UV	High-performance liquid chromatography with ultraviolet spectrophotometry
HPLC-UV-Vis	High-performance liquid chromatography with ultraviolet–visible spectrophotometry
HS-GC-SCD	Headspace gas chromatography sulfur chemiluminescence detection
HS-SDME	Headspace single-drop microextraction
HVImBr	1-hexyl-3-vinylimidazolium bromide
ILs	Ionic liquids
IMS	Ion mobility spectrometry
LC/MS–MS	Liquid chromatography–tandem mass spectrometry
LC-ESI-MS/MS	Liquid chromatography/electrospray ionization–tandem mass spectrometry
LC-MS	Liquid chromatography and mass spectrometry
LC-UV	Liquid chromatography with ultraviolet spectrophotometry
LIBS	Laser-induced breakdown spectroscopy
LLE	Liquid–liquid extraction
LOD	Limit of detection
LOQ	Limit of quantification
LPME	Liquid-phase microextraction
MALDI-TOF MS	Matrix-assisted laser desorption/ionization time-of-flight mass spectrometry
MEPS	Microextraction in packed syringe
METs	Microextraction techniques
MIPs	Molecularly imprinted polymers
MMA	Methylmethacrylate
MOFs	Metal–organic frameworks
MPA	Mycophenolic acid
MWCNT	Multi-wall carbon nanotubes
NPOE	Nitrophenyl octyl ether
OCTNs	Oxidized carbon nanotubes
OPPs	Organophosphorus pesticides
PA	Polyacetylene
PAMAM	Poly(amidoamine)
PAN	Polyacrylonitrile
PANI	Polyaniline
PASHs	Polycyclic aromatic sulfur heterocycles
PCBs	Polychlorinated biphenyls

PCN	Polycyanamide
PCPs	Personal care products
PDMS	Polydimethylsiloxane
PEDOT	Polyethylenedioxytiofene
PEG	Polyethylene glycol
PES	Polyether sulfone
PF	Polyfluorene
PFu	Polyfuran
PILs	Poly(ionic liquids)
PLOT	Porous layer open tubular
PMMA	Polymethyl methacrylate
PMME	Polymer monolith microextraction
PP	Polypropylene
PPA	Polyphenylacetylene
p-PIL-AcO	Pil-coated paper with acetate
p-Poly-(MMA-IL)FP	Paper-based polymeric ionic liquid
PPP	Polyparaphenylene
PPV	Polyphenylenevinylene
PPy	Polypyrrole
PPY	Polypyridine
PS	Polystyrene
PTFE AF	Polytetrafluoroethylene amorphous fluoropolymer
PTh	Polythiophene
PU	Polyurethane
PVA	Polyvinyl alcohol
PVA/MCS/HC-POF	Polyvinyl alcohol/modified chitosan/hydroxy-containing porous organic framework
PVA-SA-βCD	Polyvinyl alcohol doped with beta cyclodextrin and alginate
PVDF	Poly(vinylidene fluoride)
pVFc	Polyvinylferrocene
PVP	Polyvinyl pyrrolidone
rGO	Reduced graphene oxide
RNA	Ribonucleic acid
SBSE	Stir bar sorptive extraction
SBU	Secondary building units
SCOT	Support-coated open tubular
SDME	Single-drop microextraction
SDS	Sodium dodecyl sulfate
SELEX	Systematic evolution of ligands by exponential enrichment
SEM	Scanning electron microscope
SERS	Surface-enhanced Raman scattering
SF	Spectrofluorometry
SPDE	Solid-phase dynamic extraction
SPE	Solid-phase extraction
SPME	Solid-phase microextraction
SVOCs	Semi-volatile organic compounds
SWCNT	Single-wall carbon nanotubes
TCAs	Tricyclic antidepressant drugs
TEM	Transmission electron microscope
TEOS	Tetraethoxysilane
TFME	Thin-film microextraction
TXRF	Total reflection X-ray fluorescence spectrometry
UHPLC-MS	Ultra-high-performance liquid chromatography with mass spectrometry
UHPLC-PDA	Ultra-high-performance liquid chromatography with photodiode array detector
UHPLC-UV/VIS	Ultra-high-performance liquid chromatography with ultraviolet–visible spectrophotometry

UPLC	Ultra-performance liquid chromatography
UPLC–MS/MS	Ultra-performance liquid chromatography with tandem mass spectrometry
VOCs	Volatile organic compounds
WA	Aliphatic hydrocarbons
WCOT	Wall-coated open tubular
WWA	Polycyclic aromatic hydrocarbons
ZIFs	Zeolitic imidazolate frameworks

References

1. Piri-Moghadam, H.; Ahmadi, F.; Pawliszyn, J. A Critical Review of Solid Phase Microextraction for Analysis of Water Samples. *TrAC—Trends Anal. Chem.* **2016**, *85*, 133–143. [CrossRef]
2. Marín-San Román, S.; Rubio-Bretón, P.; Pérez-Álvarez, E.P.; Garde-Cerdán, T. Advancement in Analytical Techniques for the Extraction of Grape and Wine Volatile Compounds. *Food Res. Int.* **2020**, *137*, 109712. [CrossRef] [PubMed]
3. Drabińska, N.; Marcinkowska, M.A.; Wieczorek, M.N.; Jeleń, H.H. Application of Sorbent-Based Extraction Techniques in Food Analysis. *Molecules* **2023**, *28*, 7985. [CrossRef]
4. Leszczyńska, D.; Hallmann, A.; Treder, N.; Bączek, T.; Roszkowska, A. Recent Advances in the Use of SPME for Drug Analysis in Clinical, Toxicological, and Forensic Medicine Studies. *Talanta* **2024**, *270*, 125613. [CrossRef]
5. Hou, X.; Wang, L.; Guo, Y. Recent Developments in Solid-Phase Microextraction Coatings for Environmental and Biological Analysis. *Chem. Lett.* **2017**, *46*, 1444–1455. [CrossRef]
6. Llompart, M.; Celeiro, M.; García-Jares, C.; Dagnac, T. Environmental Applications of Solid-Phase Microextraction. *TrAC—Trends Anal. Chem.* **2019**, *112*, 1–12. [CrossRef]
7. Mirnaghi, F.S.; Hein, D.; Pawliszyn, J. Thin-Film Microextraction Coupled with Mass Spectrometry and Liquid Chromatography-Mass Spectrometry. *Chromatographia* **2013**, *76*, 1215–1223. [CrossRef]
8. Olcer, Y.A.; Tascon, M.; Eroglu, A.E.; Boyacı, E. Thin Film Microextraction: Towards Faster and More Sensitive Microextraction. *TrAC—Trends Anal. Chem.* **2019**, *113*, 93–101. [CrossRef]
9. Emmons, R.V.; Tajali, R.; Gionfriddo, E. Development, Optimization and Applications of Thin Film Solid Phase Microextraction (TF-SPME) Devices for Thermal Desorption: A Comprehensive Review. *Separations* **2019**, *6*, 39. [CrossRef]
10. Kataoka, H.; Ishizaki, A.; Saito, K. Recent Progress in Solid-Phase Microextraction and Its Pharmaceutical and Biomedical Applications. *Anal. Methods* **2016**, *8*, 5773–5788. [CrossRef]
11. Arthur, C.L.; Pawliszyn, J. Solid Phase Microextraction with Thermal Desorption Using Fused Silica Optical Fibers. *Anal. Chem.* **1990**, *62*, 2145–2148. [CrossRef]
12. Yu, X.; Yuan, H.; Gorecki, T.; Pawliszyn, J. Determination of Lead in Blood and Urine by SPME/GC. *Anal. Chem.* **1999**, *71*, 2998–3002. [CrossRef]
13. Zhang, X.; Oakes, K.D.; Wang, S.; Servos, M.R.; Cui, S.; Pawliszyn, J.; Metcalfe, C.D. In Vivo Sampling of Environmental Organic Contaminants in Fish by Solid-Phase Microextraction. *TrAC—Trends Anal. Chem.* **2012**, *32*, 31–39. [CrossRef]
14. Eisert, R.; Pawliszyn, J. Design of Automated Solid-Phase Microextraction for Trace Analysis of Organic Compounds in Aqueous Samples. *J. Chromatogr. A* **1997**, *776*, 293–303. [CrossRef]
15. Ouyang, G.; Jiang, R. *Solid Phase Microextraction: Recent Developments and Applications*; Springer: Berlin/Heidelberg, Germany, 2016. [CrossRef]
16. Pawliszyn, J. *Handbook of Solid Phase Microextraction*; Elsevier: London, UK, 2012; ISBN 9780124160170.
17. Fontanals, N.; Marcé, R.M.; Borrull, F. New Materials in Sorptive Extraction Techniques for Polar Compounds. *J. Chromatogr. A* **2007**, *1152*, 14–31. [CrossRef]
18. Bruheim, I.; Liu, X.; Pawliszyn, J. Thin-Film Microextraction. *Anal. Chem.* **2003**, *75*, 1002–1010. [CrossRef]
19. Wilcockson, J.B.; Gobas, F.A.P.C. Thin-Film Solid-Phase Extraction to Measure Fugacities of Organic Chemicals with Low Volatility in Biological Samples. *Environ. Sci. Technol.* **2001**, *35*, 1425–1431. [CrossRef]
20. Bragg, L.; Qin, Z.; Alaee, M.; Pawliszyn, J. Field Sampling with a Polydimethylsiloxane Thin-Film. *J. Chromatogr. Sci.* **2006**, *44*, 317–323. [CrossRef]
21. Rodil, R.; von Sonntag, J.; Montero, L.; Popp, P.; Buchmeiser, M.R. Glass-Fiber Reinforced Poly(Acrylate)-Based Sorptive Materials for the Enrichment of Organic Micropollutants from Aqueous Samples. *J. Chromatogr. A* **2007**, *1138*, 1–9. [CrossRef]
22. Riazi Kermani, F.; Pawliszyn, J. Sorbent Coated Glass Wool Fabric as a Thin Film Microextraction Device. *Anal. Chem.* **2012**, *84*, 8990–8995. [CrossRef]
23. Jiang, R.; Pawliszyn, J. Preparation of a Particle-Loaded Membrane for Trace Gas Sampling. *Anal. Chem.* **2014**, *86*, 403–410. [CrossRef] [PubMed]
24. Grandy, J.J.; Singh, V.; Lashgari, M.; Gauthier, M.; Pawliszyn, J. Development of a Hydrophilic Lipophilic Balanced Thin Film Solid Phase Microextraction Device for Balanced Determination of Volatile Organic Compounds. *Anal. Chem.* **2018**, *90*, 14072–14080. [CrossRef] [PubMed]
25. Cudjoe, E.; Vuckovic, D.; Hein, D.; Pawliszyn, J. Investigation of the Effect of the Extraction Phase Geometry on the Performance of Automated Solid-Phase Microextraction. *Anal. Chem.* **2009**, *81*, 4226–4232. [CrossRef]

26. Murata, M.; Oizumi, T.; Gi, M.; Tsuji, R.; Arita, M.; Fujii, A.; Ozaki, M. Highly (100)-Oriented CH3NH3PbI3 Thin Film Fabricated by Bar-Coating Method and Its Additive Effect of Ammonium Chloride. *Sol. Energy Mater. Sol. Cells* **2020**, *208*, 110409. [CrossRef]
27. Electrospinning Services | NEI Corporation. Available online: https://www.neicorporation.com/services/electrospinning/ (accessed on 23 November 2023).
28. Subbiah, T.; Bhat, G.S.; Tock, R.W.; Parameswaran, S.; Ramkumar, S.S. Electrospinning of Nanofibers. *J. Appl. Polym. Sci.* **2005**, *96*, 557–569. [CrossRef]
29. Frederichi, D.; Scaliante, M.H.N.O.; Bergamasco, R. Structured Photocatalytic Systems: Photocatalytic Coatings on Low-Cost Structures for Treatment of Water Contaminated with Micropollutants—A Short Review. *Environ. Sci. Pollut. Res.* **2021**, *28*, 23610–23633. [CrossRef]
30. Lashgari, M.; Yamini, Y. An Overview of the Most Common Lab-Made Coating Materials in Solid Phase Microextraction. *Talanta* **2019**, *191*, 283–306. [CrossRef]
31. Reyes-Garcés, N.; Gionfriddo, E.; Gómez-Ríos, G.A.; Alam, M.N.; Boyacl, E.; Bojko, B.; Singh, V.; Grandy, J.; Pawliszyn, J. Advances in Solid Phase Microextraction and Perspective on Future Directions. *Anal. Chem.* **2018**, *90*, 302–360. [CrossRef]
32. Suhas; Gupta, V.K.; Carrott, P.J.M.; Singh, R.; Chaudhary, M.; Kushwaha, S. Cellulose: A Review as Natural, Modified and Activated Carbon Adsorbent. *Bioresour. Technol.* **2016**, *216*, 1066–1076. [CrossRef]
33. Hokkanen, S.; Bhatnagar, A.; Sillanpää, M. A Review on Modification Methods to Cellulose-Based Adsorbents to Improve Adsorption Capacity. *Water Res.* **2016**, *91*, 156–173. [CrossRef]
34. Qin, Z.; Bragg, L.; Ouyang, G.; Niri, V.H.; Pawliszyn, J. Solid-Phase Microextraction under Controlled Agitation Conditions for Rapid on-Site Sampling of Organic Pollutants in Water. *J. Chromatogr. A* **2009**, *1216*, 6979–6985. [CrossRef] [PubMed]
35. Jahnke, A.; Mayer, P.; Broman, D.; McLachlan, M.S. Possibilities and Limitations of Equilibrium Sampling Using Polydimethylsiloxane in Fish Tissue. *Chemosphere* **2009**, *77*, 764–770. [CrossRef] [PubMed]
36. Rönkkö, T. Recent Developments in Solid Phase Microextraction Techniques. Master's Thesis, University of Helsinki, Helsinki, Finland, 2015.
37. Jiang, R.; Cudjoe, E.; Bojko, B.; Abaffy, T.; Pawliszyn, J. A Non-Invasive Method for in Vivo Skin Volatile Compounds Sampling. *Anal. Chim. Acta* **2013**, *804*, 111–119. [CrossRef]
38. Eom, I.Y.; Risticevic, S.; Pawliszyn, J. Simultaneous Sampling and Analysis of Indoor Air Infested with *Cimex lectularius* L. (Hemiptera: Cimicidae) by Solid Phase Microextraction, Thin Film Microextraction and Needle Trap Device. *Anal. Chim. Acta* **2012**, *716*, 2–10. [CrossRef]
39. Guerra-Diaz, P.; Gura, S.; Almirall, J.R. Dynamic Planar Solid Phase Microextraction-Ion Mobility Spectrometry for Rapid Field Air Sampling and Analysis of Illicit Drugs and Explosives. *Anal. Chem.* **2010**, *82*, 2826–2835. [CrossRef]
40. Grandy, J.J.; Boyaci, E.; Pawliszyn, J. Development of a Carbon Mesh Supported Thin Film Microextraction Membrane As a Means to Lower the Detection Limits of Benchtop and Portable GC/MS Instrumentation. *Anal. Chem.* **2016**, *88*, 1760–1767. [CrossRef]
41. Di Carro, M.; Lluveras-Tenorio, A.; Benedetti, B.; Magi, E. An Innovative Sampling Approach Combined with Liquid Chromatography–Tandem Mass Spectrometry for the Analysis of Emerging Pollutants in Drinking Water. *J. Mass Spectrom.* **2020**, *55*, e4608. [CrossRef]
42. Piri-Moghadam, H.; Gionfriddo, E.; Rodriguez-Lafuente, A.; Grandy, J.J.; Lord, H.L.; Obal, T.; Pawliszyn, J. Inter-Laboratory Validation of a Thin Film Microextraction Technique for Determination of Pesticides in Surface Water Samples. *Anal. Chim. Acta* **2017**, *964*, 74–84. [CrossRef]
43. Piri-Moghadam, H.; Gionfriddo, E.; Grandy, J.J.; Alam, M.N.; Pawliszyn, J. Development and Validation of Eco-Friendly Strategies Based on Thin Film Microextraction for Water Analysis. *J. Chromatogr. A* **2018**, *1579*, 20–30. [CrossRef]
44. Moradi, E.; Ebrahimzadeh, H.; Mehrani, Z. Electrospun Acrylonitrile Butadiene Styrene Nanofiber Film as an Efficient Nanosorbent for Head Space Thin Film Microextraction of Polycyclic Aromatic Hydrocarbons from Water and Urine Samples. *Talanta* **2019**, *205*, 120080. [CrossRef]
45. Boyaci, E.; Gorynski, K.; Rodriguez-Lafuente, A.; Bojko, B.; Pawliszyn, J. Introduction of Solid-Phase Microextraction as a High-Throughput Sample Preparation Tool in Laboratory Analysis of Prohibited Substances. *Anal. Chim. Acta* **2014**, *809*, 69–81. [CrossRef] [PubMed]
46. Reyes-Garcés, N.; Bojko, B.; Pawliszyn, J. High Throughput Quantification of Prohibited Substances in Plasma Using Thin Film Solid Phase Microextraction. *J. Chromatogr. A* **2014**, *1374*, 40–49. [CrossRef] [PubMed]
47. Cai, P.S.; Li, D.; Chen, J.; Xiong, C.M.; Ruan, J.L. Comparison of Two Thin-Film Microextractions for the Analysis of Estrogens in Aqueous Tea Extract and Environmental Water Samples by High Performance Liquid Chromatography-Ultraviolet Detection. *Food Chem.* **2015**, *173*, 1158–1166. [CrossRef]
48. Bahrani, S.; Hashemi, S.A.; Mousavi, S.M.; Arjmand, M.; Ghalamfarsa, F.; Ghaedi, M. Conductive Polymers in Green Analytical Chemistry. *ACS Symp. Ser.* **2022**, *1405*, 1–37. [CrossRef]
49. Li, X.; Wang, Y.; Yang, X.; Chen, J.; Fu, H.; Cheng, T.; Wang, Y. Conducting Polymers in Environmental Analysis. *TrAC—Trends Anal. Chem.* **2012**, *39*, 163–179. [CrossRef]
50. Bagheri, H.; Ayazi, Z.; Naderi, M. Conductive Polymer-Based Microextraction Methods: A Review. *Anal. Chim. Acta* **2013**, *767*, 1–13. [CrossRef]

51. Mehrani, Z.; Ebrahimzadeh, H.; Asgharinezhad, A.A.; Moradi, E. Determination of Copper in Food and Water Sources Using Poly M-Phenylenediamine/CNT Electrospun Nanofiber. *Microchem. J.* **2019**, *149*, 103975. [CrossRef]
52. Bagheri, H.; Aghakhani, A.; Akbari, M.; Ayazi, Z. Electrospun Composite of Polypyrrole-Polyamide as a Micro-Solid Phase Extraction Sorbent. *Anal. Bioanal. Chem.* **2011**, *400*, 3607–3613. [CrossRef]
53. Turazzi, F.C.; Morés, L.; Carasek, E.; Barra, G.M. de O. Polyaniline-Silica Doped with Oxalic Acid as a Novel Extractor Phase in Thin Film Solid-Phase Microextraction for Determination of Hormones in Urine. *J. Sep. Sci.* **2023**, *46*, 2300280. [CrossRef]
54. Bagheri, H.; Aghakhani, A. Polyaniline-Nylon-6 Electrospun Nanofibers for Headspace Adsorptive Microextraction. *Anal. Chim. Acta* **2012**, *713*, 63–69. [CrossRef]
55. Turiel, E.; Martín-Esteban, A. Molecularly Imprinted Polymers-Based Microextraction Techniques. *TrAC—Trends Anal. Chem.* **2019**, *118*, 574–586. [CrossRef]
56. Yan, H.; Kyung, H.R. Characteristic and Synthetic Approach of Molecularly Imprinted Polymer. *Int. J. Mol. Sci.* **2006**, *7*, 155–178. [CrossRef]
57. Chen, L.; Wang, X.; Lu, W.; Wu, X.; Li, J. Molecular Imprinting: Perspectives and Applications. *Chem. Soc. Rev.* **2016**, *45*, 2137–2211. [CrossRef]
58. Díaz-Álvarez, M.; Turiel, E.; Martín-Esteban, A. Recent Advances and Future Trends in Molecularly Imprinted Polymers-Based Sample Preparation. *J. Sep. Sci.* **2023**, *46*, 2300157. [CrossRef]
59. Hijazi, H.Y.; Bottaro, C.S. Molecularly Imprinted Polymer Thin-Film as a Micro-Extraction Adsorbent for Selective Determination of Trace Concentrations of Polycyclic Aromatic Sulfur Heterocycles in Seawater. *J. Chromatogr. A* **2020**, *1617*, 460824. [CrossRef]
60. Azizi, A.; Shahhoseini, F.; Langille, E.A.; Akhoondi, R.; Bottaro, C.S. Micro-Gel Thin Film Molecularly Imprinted Polymer Coating for Extraction of Organophosphorus Pesticides from Water and Beverage Samples. *Anal. Chim. Acta* **2021**, *1187*, 339135. [CrossRef]
61. Abu-Alsoud, G.F.; Bottaro, C.S. Porous Thin-Film Molecularly Imprinted Polymer Device for Simultaneous Determination of Phenol, Alkylphenol and Chlorophenol Compounds in Water. *Talanta* **2021**, *223*, 121727. [CrossRef]
62. Shahhoseini, F.; Langille, E.A.; Azizi, A.; Bottaro, C.S. Thin Film Molecularly Imprinted Polymer (TF-MIP), a Selective and Single-Use Extraction Device for High-Throughput Analysis of Biological Samples. *Analyst* **2021**, *146*, 3157–3168. [CrossRef]
63. Gryshchenko, A.O.; Bottaro, C.S. Development of Molecularly Imprinted Polymer in Porous Film Format for Binding of Phenol and Alkylphenols from Water. *Int. J. Mol. Sci.* **2014**, *15*, 1338–1357. [CrossRef]
64. Langille, E.; Bottaro, C.S. Development and Application of a Thin-Film Molecularly Imprinted Polymer for the Measurement of Mycophenolic Acid in Human Plasma. *J. Clin. Lab. Anal.* **2023**, *37*, e24864. [CrossRef]
65. Eddaoudi, M.; Moler, D.B.; Li, H.; Chen, B.; Reineke, T.M.; Michael, O.; Omar, M.Y. Modular Chemistry: Secondary Building Units as a Basis ForBuilding Units as a Basis for Robust Metal-Organic Carboxylate Frameworks. *Acc. Chem. Res* **2001**, *34*, 319–330. [CrossRef] [PubMed]
66. Cheetham, A.K.; Rao, C.N.R.; Feller, R.K. Structural Diversity and Chemical Trends in Hybrid Inorganic-Organic Framework Materials. *Chem. Commun.* **2006**, *46*, 4780–4795. [CrossRef]
67. Li, H.; Eddaoudi, M.; O'Keeffe, M.; Yaghi, O.M. Design and Synthesis of an Exceptionally Stable and Highly. *Nature* **1999**, *402*, 276–279. [CrossRef]
68. Rocío-Bautista, P.; Pacheco-Fernández, I.; Pasán, J.; Pino, V. Are Metal-Organic Frameworks Able to Provide a New Generation of Solid-Phase Microextraction Coatings?—A Review. *Anal. Chim. Acta* **2016**, *939*, 26–41. [CrossRef]
69. Zhou, H.C.; Long, J.R.; Yaghi, O.M. Introduction to Metal−Organic Frameworks. *Chem. Rev.* **2012**, *112*, 673–674. [CrossRef]
70. Gutiérrez-Serpa, A.; Pasán, J.; Jiménez-Abizanda, A.I.; Kaskel, S.; Senkovska, I.; Pino, V. Thin-Film Microextraction Using the Metal-Organic Framework DUT-52 for Determining Endocrine Disrupting Chemicals in Cosmetics. *Microchem. J.* **2022**, *181*, 107685. [CrossRef]
71. Khodayari, P.; Jalilian, N.; Ebrahimzadeh, H.; Amini, S. Trace-Level Monitoring of Anti-Cancer Drug Residues in Wastewater and Biological Samples by Thin-Film Solid-Phase Micro-Extraction Using Electrospun Polyfam/Co-MOF-74 Composite Nanofibers Prior to Liquid Chromatography Analysis. *J. Chromatogr. A* **2021**, *1655*, 462484. [CrossRef]
72. Gao, G.; Li, S.; Li, S.; Zhao, L.; Wang, T.; Hou, X. Development and Application of Vortex-Assisted Membrane Extraction Based on Metal–Organic Framework Mixed-Matrix Membrane for the Analysis of Estrogens in Human Urine. *Anal. Chim. Acta* **2018**, *1023*, 35–43. [CrossRef]
73. Jafari, Z.; Hadjmohammadi, M.R. In Situ Growth of Zeolitic Imidazolate Framework-8 on a GO-PVDF Membrane as a Sorbent for Thin-Film Microextraction of Caffeine Followed by Quantitation through High-Performance Liquid Chromatography. *Anal. Methods* **2020**, *12*, 1736–1743. [CrossRef]
74. Bahrami, H.; Rezaei, B.; Jafari, M.T. Coupling of a Novel Electrospun Polyacrylonitrile/Amino-Zr-MOF Nanofiber as a Thin Film for Microextraction-Corona Discharge-Ion Mobility Spectrometry for the Analysis of Chlorpyrifos in Water Samples. *Anal. Methods* **2019**, *11*, 1073–1079. [CrossRef]
75. Guerra-Martín, I.; Gutiérrez-Serpa, A.; Jiménez-Abizanda, A.I.; Pasán, J.; Pino, V. Thin Films Using the Greenly Prepared Metal-Organic Framework MIL-100(Fe) and Recycled Polystyrene Supported onto Cellulose for the Microextraction of Personal Care Products from Waters and Cosmetics. *Microchem. J.* **2023**, *195*, 109502. [CrossRef]
76. Liu, F.; Xu, H. Development of a Novel Polystyrene/Metal-Organic Framework-199 Electrospun Nanofiber Adsorbent for Thin Film Microextraction of Aldehydes in Human Urine. *Talanta* **2017**, *162*, 261–267. [CrossRef]

77. Valenzuela, E.F.; de Paula, F.G.F.; Teixeira, A.P.C.; Menezes, H.C.; Cardeal, Z.L. A New Carbon Nanomaterial Solid-Phase Microextraction to Pre-Concentrate and Extract Pesticides in Environmental Water. *Talanta* **2020**, *217*, 121011. [CrossRef] [PubMed]
78. Maciel, E.V.S.; Mejía-Carmona, K.; Jordan-Sinisterra, M.; da Silva, L.F.; Vargas Medina, D.A.; Lanças, F.M. The Current Role of Graphene-Based Nanomaterials in the Sample Preparation Arena. *Front. Chem.* **2020**, *8*, 664. [CrossRef] [PubMed]
79. Liu, Q.; Shi, J.; Jiang, G. Application of Graphene in Analytical Sample Preparation. *TrAC—Trends Anal. Chem.* **2012**, *37*, 1–11. [CrossRef]
80. Valcárcel, M.; Cárdenas, S.; Simonet, B.M.; Moliner-Martínez, Y.; Lucena, R. Carbon Nanostructures as Sorbent Materials in Analytical Processes. *TrAC—Trends Anal. Chem.* **2008**, *27*, 34–43. [CrossRef]
81. Wang, X.; Liu, B.; Lu, Q.; Qu, Q. Graphene-Based Materials: Fabrication and Application for Adsorption in Analytical Chemistry. *J. Chromatogr. A* **2014**, *1362*, 1–15. [CrossRef] [PubMed]
82. Ghani, M.; Haghdoostnejad, K. Woven Cotton Yarn-Graphene Oxide-Layered Double Hydroxide Composite as a Sorbent for Thin Film Microextraction of Nonsteroidal Anti-Inflammatory Drugs Followed by Quantitation through High Performance Liquid Chromatography. *Anal. Chim. Acta* **2020**, *1097*, 94–102. [CrossRef]
83. de la Calle, I.; Ruibal, T.; Lavilla, I.; Bendicho, C. Direct Immersion Thin-Film Microextraction Method Based on the Sorption of Pyrrolidine Dithiocarbamate Metal Chelates onto Graphene Membranes Followed by Total Reflection X-Ray Fluorescence Analysis. *Spectrochim. Acta-Part B At. Spectrosc.* **2019**, *152*, 14–24. [CrossRef]
84. Ghani, M.; Ghoreishi, S.M.; Azamati, M. Magnesium-Aluminum-Layered Double Hydroxide-Graphene Oxide Composite Mixed-Matrix Membrane for the Thin-Film Microextraction of Diclofenac in Biological Fluids. *J. Chromatogr. A* **2018**, *1575*, 11–17. [CrossRef]
85. Ripoll, L.; Legnaioli, S.; Palleschi, V.; Hidalgo, M. Evaluation of Electrosprayed Graphene Oxide Coatings for Elemental Analysis by Thin Film Microextraction Followed by LIBS Detection (TFME-LIBS). *Spectrochim. Acta-Part B At. Spectrosc.* **2021**, *183*, 106267. [CrossRef]
86. Huang, J.; Deng, H.; Song, D.; Xu, H. Electrospun Polystyrene/Graphene Nanofiber Film as a Novel Adsorbent of Thin Film Microextraction for Extraction of Aldehydes in Human Exhaled Breath Condensates. *Anal. Chim. Acta* **2015**, *878*, 102–108. [CrossRef] [PubMed]
87. Karimiyan, H.; Hadjmohammadi, M.R.; Kunjali, K.L.; Moein, M.M.; Dutta, J.; Abdel-Rehim, M. Graphene Oxide/Polyethylene Glycol-Stick for Thin Film Microextraction of β-Blockers from Human Oral Fluid by Liquid Chromatography-Tandem Mass Spectrometry. *Molecules* **2019**, *24*, 3664. [CrossRef] [PubMed]
88. Zhang, X.; Li, Z.; Wu, H.; Wang, J.; Zhao, H.; Ji, X.; Xu, Y.; Li, R.; Zhang, H.; Yang, H.; et al. High-Throughput Method Based on a Novel Thin-Film Microextraction Coating for Determining Macrolides and Lincosamides in Honey. *Food Chem.* **2021**, *346*, 128920. [CrossRef]
89. Jafari, Z.; Hadjmohammadi, M.R. Polyvinylidene Difluoride Film with Embedded Poly(Amidoamine) Modified Graphene Oxide for Extraction of Chlorpyrifos and Diazinon. *Microchim. Acta* **2021**, *188*, 37. [CrossRef]
90. Song, X.Y.; Chen, J.; Shi, Y.P. Different Configurations of Carbon Nanotubes Reinforced Solid-Phase Microextraction Techniques and Their Applications in the Environmental Analysis. *TrAC—Trends Anal. Chem.* **2017**, *86*, 263–275. [CrossRef]
91. Wepasnick, K.A.; Smith, B.A.; Bitter, J.L.; Fairbrother, D.H. Chemical and Structural Characterization of Carbon Nanotube Surfaces. *Anal. Bioanal. Chem.* **2011**, *396*, 1003–1014. [CrossRef]
92. Hussain, C.M.; Mitra, S. Micropreconcentration Units Based on Carbon Nanotubes (CNT). *Anal. Bioanal. Chem.* **2011**, *399*, 75–89. [CrossRef]
93. Goh, S.X.L.; Goh, E.X.Y.; Lee, H.K. Sodium Dodecyl Sulfate-Multi-Walled Carbon Nanotubes-Coated-Membrane Solid Phase Extraction of Glucocorticoids in Aqueous Matrices. *Talanta* **2021**, *221*, 121624. [CrossRef]
94. Wan Ibrahim, W.N.; Sanagi, M.M.; Mohamad Hanapi, N.S.; Kamaruzaman, S.; Yahaya, N.; Wan Ibrahim, W.A. Solid-Phase Microextraction Based on an Agarose-Chitosan-Multiwalled Carbon Nanotube Composite Film Combined with HPLC–UV for the Determination of Nonsteroidal Anti-Inflammatory Drugs in Aqueous Samples. *J. Sep. Sci.* **2018**, *41*, 2942–2951. [CrossRef]
95. Loh, S.H.; Sanagi, M.M.; Wan Ibrahim, W.A.; Hasan, M.N. Multi-Walled Carbon Nanotube-Impregnated Agarose Film Microextraction of Polycyclic Aromatic Hydrocarbons in Green Tea Beverage. *Talanta* **2013**, *106*, 200–205. [CrossRef] [PubMed]
96. Quintanilla, I.; Perelló, C.; Merlo, F.; Profumo, A.; Fontàs, C.; Anticó, E. Multiwalled Carbon Nanotubes Embedded in a Polymeric Matrix as a New Material for Thin Film Microextraction (TFME) in Organic Pollutant Monitoring. *Polymers* **2023**, *15*, 314. [CrossRef] [PubMed]
97. Kueseng, P.; Pawliszyn, J. Carboxylated Multiwalled Carbon Nanotubes/Polydimethylsiloxane, a New Coating for 96-Blade Solid-Phase Microextraction for Determination of Phenolic Compounds in Water. *J. Chromatogr. A* **2013**, *1317*, 199–202. [CrossRef] [PubMed]
98. Ibrahim, W.N.W.; Sanagi, M.M.; Hanapi, N.S.M.; Hadzir, N.M.; Yahaya, N.; Kamaruzaman, S. Agarose-Chitosan-Intergrated Multiwalled Carbon Nanotubes Film Solid Phase Microextraction Combined with High Performance Liquid Chromatography for the Determination of Tricyclic Antidepressant Drugs in Aqueous Samples. *Malaysian J. Anal. Sci.* **2020**, *24*, 33–41.
99. Ge, D.; Lee, H.K. Polypropylene Membrane Coated with Carbon Nanotubesfunctionalized with Chitosan: Application in the Microextraction Ofpolychlorinated Biphenyls and Polybrominated Diphenyl Ethers from Environmental Water Samples. *J. Chromatogr. A* **2015**, *1408*, 56–62. [CrossRef]

100. Mukhtar, N.H.; See, H.H. Carbonaceous Nanomaterials Immobilised Mixed Matrix Membrane Microextraction for the Determination of Polycyclic Aromatic Hydrocarbons in Sewage Pond Water Samples. *Anal. Chim. Acta* **2016**, *931*, 57–63. [CrossRef]
101. Mirnaghi, F.S.; Monton, M.R.N.; Pawliszyn, J. Thin-Film Octadecyl-Silica Glass Coating for Automated 96-Blade Solid-Phase Microextraction Coupled with Liquid Chromatography-Tandem Mass Spectrometry for Analysis of Benzodiazepines. *J. Chromatogr. A* **2012**, *1246*, 2–8. [CrossRef]
102. Togunde, O.P.; Oakes, K.D.; Servos, M.R.; Pawliszyn, J. Optimization of Solid Phase Microextraction for Non-Lethal in Vivo Determination of Selected Pharmaceuticals in Fish Muscle Using Liquid Chromatography-Mass Spectrometry. *J. Chromatogr. A* **2012**, *1261*, 99–106. [CrossRef]
103. Maciążek-Jurczyk, M.; Bessonneau, V.; Ings, J.; Bragg, L.; McMaster, M.; Servos, M.R.; Bojko, B.; Pawliszyn, J. Development of a Thin-Film Solid-Phase Microextraction (TF-SPME) Method Coupled to Liquid Chromatography and Tandem Mass Spectrometry for High-Throughput Determination of Steroid Hormones in White Sucker Fish Plasma. *Anal. Bioanal. Chem.* **2020**, *412*, 4183–4194. [CrossRef]
104. Strittmatter, N.; Düring, R.A.; Takáts, Z. Analysis of Wastewater Samples by Direct Combination of Thin-Film Microextraction and Desorption Electrospray Ionization Mass Spectrometry. *Analyst* **2012**, *137*, 4037–4044. [CrossRef]
105. Pichon, V. *Aptamer-Based and Immunosorbents*; Elsevier Inc.: Amsterdam, The Netherlands, 2019; ISBN 9780128169063.
106. Zargar, T.; Khayamian, T.; Jafari, M.T. Immobilized Aptamer Paper Spray Ionization Source for Ion Mobility Spectrometry. *J. Pharm. Biomed. Anal.* **2017**, *132*, 232–237. [CrossRef] [PubMed]
107. Zargar, T.; Khayamian, T.; Jafari, M.T. Aptamer-Modified Carbon Nanomaterial Based Sorption Coupled to Paper Spray Ion Mobility Spectrometry for Highly Sensitive and Selective Determination of Methamphetamine. *Microchim. Acta* **2018**, *185*, 103. [CrossRef] [PubMed]
108. Hashemian, Z.; Khayamian, T.; Saraji, M. Anticodeine Aptamer Immobilized on a Whatman Cellulose Paper for Thin-Film Microextraction of Codeine from Urine Followed by Electrospray Ionization Ion Mobility Spectrometry. *Anal. Bioanal. Chem.* **2014**, *407*, 1615–1623. [CrossRef]
109. Patinha, D.J.S.; Silvestre, A.J.D.; Marrucho, I.M. Poly(Ionic Liquids) in Solid Phase Microextraction: Recent Advances and Perspectives. *Prog. Polym. Sci.* **2019**, *98*, 101148. [CrossRef]
110. Acree, W.E.; Grubbs, L.M. Analytical Applications of Ionic Liquids. In *Encyclopedia of Analytical Chemistry: Applications, Theory and Instrumentation*; Wiley: Hoboken, NJ, USA, 2012; ISBN 9780470027318.
111. Zhang, Q.; De Oliveira Vigier, K.; Royer, S.; Jérôme, F. Deep Eutectic Solvents: Syntheses, Properties and Applications. *Chem. Soc. Rev.* **2012**, *41*, 7108–7146. [CrossRef]
112. Aguilera-Herrador, E.; Lucena, R.; Cárdenas, S.; Valcárcel, M. The Roles of Ionic Liquids in Sorptive Microextraction Techniques. *TrAC—Trends Anal. Chem.* **2010**, *29*, 602–616. [CrossRef]
113. Mei, M.; Huang, X.; Chen, L. Recent Development and Applications of Poly (Ionic Liquid)s in Microextraction Techniques. *TrAC—Trends Anal. Chem.* **2019**, *112*, 123–134. [CrossRef]
114. Sadeghi, S.; Oliaei, S. Microextraction of Sulfathiazole from Milk and Honey Samples Using a Polymeric Ionic Liquid Membrane Followed by Fluorometric Determination. *J. Food Compos. Anal.* **2021**, *97*, 103774. [CrossRef]
115. Ríos-Gómez, J.; García-Valverde, M.T.; López-Lorente, Á.I.; Toledo-Neira, C.; Lucena, R.; Cárdenas, S. Polymeric Ionic Liquid Immobilized onto Paper as Sorptive Phase in Microextraction. *Anal. Chim. Acta* **2020**, *1094*, 47–56. [CrossRef]
116. Shahriman, M.S.; Mohamad, S.; Mohamad Zain, N.N.; Alias, Y.; Chandrasekaram, K.; Raoov, M. Paper-Based Polymeric Ionic Liquid for Thin Film Micro Extraction of Sulfonamides in Environmental Water Samples Prior to HPLC-DAD Analysis. *Microchem. J.* **2021**, *171*, 106798. [CrossRef]
117. Cai, M.Q.; Wei, X.Q.; Du, C.H.; Ma, X.M.; Jin, M.C. Novel Amphiphilic Polymeric Ionic Liquid-Solid Phase Micro-Extraction Membrane for the Preconcentration of Aniline as Degradation Product of Azo Dye Orange G under Sonication by Liquid Chromatography-Tandem Mass Spectrometry. *J. Chromatogr. A* **2014**, *1349*, 24–29. [CrossRef] [PubMed]
118. Smith, E.L.; Abbott, A.P.; Ryder, K.S. Deep Eutectic Solvents (DESs) and Their Applications. *Chem. Rev.* **2014**, *114*, 11060–11082. [CrossRef]
119. Werner, J.; Zgoła-Grześkowiak, A.; Grześkowiak, T. Development of Novel Thin-Film Solid-Phase Microextraction Materials Based on Deep Eutectic Solvents for Preconcentration of Trace Amounts of Parabens in Surface Waters. *J. Sep. Sci.* **2022**, *45*, 1374–1384. [CrossRef]
120. Nakhle, L.; Kfoury, M.; Mallard, I.; Landy, D.; Greige-Gerges, H. Microextraction of Bioactive Compounds Using Deep Eutectic Solvents: A Review. *Environ. Chem. Lett.* **2021**, *19*, 3747–3759. [CrossRef]
121. Werner, J.; Grześkowiak, T.; Zgoła-Grześkowiak, A. A Polydimethylsiloxane/Deep Eutectic Solvent Sol-Gel Thin Film Sorbent and Its Application to Solid-Phase Microextraction of Parabens. *Anal. Chim. Acta* **2022**, *1202*, 339666. [CrossRef]
122. Werner, J.; Zgoła-Grześkowiak, A.; Grześkowiak, T. Deep Eutectic Solvent-Based Coating Sorbent for Preconcentration of Formaldehyde by Thin-Film Solid-Phase Microextraction Technique. *Processes* **2022**, *10*, 828. [CrossRef]
123. Riazanskaia, S.; Blackburn, G.; Harker, M.; Taylor, D.; Thomas, C.L.P. The Analytical Utility of Thermally Desorbed Polydimethylsilicone Membranes for In-Vivo Sampling of Volatile Organic Compounds in and on Human Skin. *Analyst* **2008**, *133*, 1020–1027. [CrossRef]
124. Yu, M.; Roszkowska, A.; Pawliszyn, J. In Vivo Solid-Phase Microextraction and Applications in Environmental Sciences. *ACS Environ. Au* **2022**, *2*, 30–41. [CrossRef]

125. Bessonneau, V.; Boyaci, E.; Maciazek-Jurczyk, M.; Pawliszyn, J. In Vivo Solid Phase Microextraction Sampling of Human Saliva for Non-Invasive and on-Site Monitoring. *Anal. Chim. Acta* **2015**, *856*, 35–45. [CrossRef]
126. Choi, H.; Jedrychowski, W.; Spengler, J.; Camann, D.E.; Whyatt, R.M.; Rauh, V.; Tsai, W.Y.; Perera, F.P. International Studies of Prenatal Exposure to Polycyclic Aromatic Hydrocarbons and Fetal Growth. *Environ. Health Perspect.* **2006**, *114*, 1744–1750. [CrossRef]
127. Quintanilla, I.; Fontàs, C.; Anticó, E. Deep Eutectic Solvents Incorporated in a Polymeric Film for Organophosphorus Pesticide Microextraction from Water Samples. *Anal. Chim. Acta* **2024**, *1318*, 342940. [CrossRef] [PubMed]
128. Afsordeh, A.; Arbabsadeghi, A.; Javanmardi, H.; Bagheri, H. Incorporation of Cu-TATAB Metal-Organic Framework within Polyurethane Nanocomposite for Enhanced Thin Film Microextraction of Some Chlorinated Pesticides. *J. Chromatogr. A* **2024**, *1730*, 465061. [CrossRef] [PubMed]
129. Kahremanoğlu, K.; Akpınar, Y.; Boyaci, E. Development of Thin Film Microextraction Method for the Multi-Residue Analysis of Selected Pesticides. *Adv. Sample Prep.* **2023**, *6*, 100061. [CrossRef]
130. Majd, M.; Gholami, M.; Fathi, A.; Sedghi, R.; Nojavan, S. Thin-Film Solid-Phase Microextraction of Pesticides from Cereal Samples Using Electrospun Polyvinyl Alcohol/Modified Chitosan/Porous Organic Framework Nanofibers. *Food Chem.* **2024**, *444*, 138647. [CrossRef] [PubMed]
131. Hosseinian, S.B.; Ghani, M.; Raoof, J.B. UIO-66-NH2 Encapsulated Polyoxometalate Loaded on Graphene Oxide Accommodated on Mixed Cellulose Esters (MCE) Paper for Thin Film Microextraction of Pesticides besides Their Quantification via High-Performance Liquid Chromatography-Ultraviolet Detection. *Microchem. J.* **2024**, *199*, 110031. [CrossRef]
132. Ayazi, Z.; Ekhteraei, M.; Pashayi, S.; Seyed Ahmadian, S.M. Zr-Based Metal–Organic Framework Incorporated Polystyrene Nanocomposite as a Novel Sorbent for Ultrasound Assisted-Thin Film Microextraction of Organophosphorus Pesticides from Complex Samples. *Food Chem.* **2022**, *393*, 133343. [CrossRef]
133. Liu, Z.; Li, W.; Zhu, X.; Hua, R.; Wu, X.; Xue, J. Combination of Polyurethane and Polymethyl Methacrylate Thin Films as a Microextraction Sorbent for Rapid Adsorption and Sensitive Determination of Neonicotinoid Insecticides in Fruit Juice and Tea by Ultra High Performance Liquid Chromatography with Tand. *J. Chromatogr. A* **2021**, *1659*, 462646. [CrossRef]
134. Michałowicz, J.; Duda, W. Phenols-Sources and Toxicity. *Polish J. Environ. Stud.* **2007**, *16*, 347–362.
135. Thomas, K.V.; Balaam, J.; Hurst, M.R.; Thain, J.E. Identification of in Vitro Estrogen and Androgen Receptor Agonists in North Sea Offshore Produced Water Discharges. *Environ. Toxicol. Chem.* **2004**, *23*, 1156–1163. [CrossRef]
136. Ayazi, Z.; Safarpour, M.; Ahmadi, F. Monolithic Polyethersulfone Membrane Modified with PVA and PVP as a Novel Extracting Media for Thin Film Microextraction of Bisphenol A from Aquatic Samples. *Microchem. J.* **2022**, *175*, 107143. [CrossRef]
137. Scur, R.; Dagnoni Huelsmann, R.; Carasek, E. Polyamide-Coated Paper-Based Sorptive Phase Applied in High-Throughput Thin Film Microextraction Designed by 3D Printing. *Microchem. J.* **2023**, *189*, 108515. [CrossRef]
138. Ghani, M.; Jafari, Z.; Raoof, J.B. Porous Agarose/Chitosan/Graphene Oxide Composite Coupled with Deep Eutectic Solvent for Thin Film Microextraction of Chlorophenols. *J. Chromatogr. A* **2023**, *1694*, 463899. [CrossRef] [PubMed]
139. Ocaña-González, J.A.; Villar-Navarro, M.; Ramos-Payán, M.; Fernández-Torres, R.; Bello-López, M.A. New Developments in the Extraction and Determination of Parabens in Cosmetics and Environmental Samples. A Review. *Anal. Chim. Acta* **2015**, *858*, 1–15. [CrossRef] [PubMed]
140. Błedzka, D.; Gromadzińska, J.; Wasowicz, W. Parabens. From Environmental Studies to Human Health. *Environ. Int.* **2014**, *67*, 27–42. [CrossRef]
141. Jakavula, S.; Nqombolo, A.; Mpupa, A.; Ren, J.; Nomngongo, P.N. Hybrid Porous Material Supported in a Cellulose Acetate Polymeric Membrane for the Direct Immersion Thin-Film Microextraction of Parabens in Water. *J. Chromatogr. A* **2023**, *1705*, 464187. [CrossRef]
142. Lin, A.Y.C.; Yu, T.H.; Lateef, S.K. Removal of Pharmaceuticals in Secondary Wastewater Treatment Processes in Taiwan. *J. Hazard. Mater.* **2009**, *167*, 1163–1169. [CrossRef]
143. Nahandast, M.; Darvishnejad, F.; Raoof, J.B.; Ghani, M. Modification of Cellulose Substrate by in Situ Synthesis of Metal-Organic Framework-5 for Thin Film Microextraction of Some Non-Steroidal Anti-Inflammatory Drugs and Their Measurement by High-Performance Liquid Chromatography-Ultraviolet Detector. *J. Chromatogr. A* **2024**, *1724*, 464924. [CrossRef]
144. Isobe, T.; Sato, K.; Joon-Woo, K.; Tanabe, S.; Suzuki, G.; Nakayama, K. Determination of Natural and Synthetic Glucocorticoids in Effluent of Sewage Treatment Plants Using Ultrahigh Performance Liquid Chromatography-Tandem Mass Spectrometry. *Environ. Sci. Pollut. Res.* **2015**, *22*, 14127–14135. [CrossRef]
145. Chen, Q.; Jia, A.; Snyder, S.A.; Gong, Z.; Lam, S.H. Glucocorticoid Activity Detected by in Vivo Zebrafish Assay and in Vitro Glucocorticoid Receptor Bioassay at Environmental Relevant Concentrations. *Chemosphere* **2016**, *144*, 1162–1169. [CrossRef]
146. Lalone, C.A.; Villeneuve, D.L.; Olmstead, A.W.; Medlock, E.K.; Kahl, M.D.; Jensen, K.M.; Durhan, E.J.; Makynen, E.A.; Blanksma, C.A.; Cavallin, J.E.; et al. Effects of a Glucocorticoid Receptor Agonist, Dexamethasone, on Fathead Minnow Reproduction, Growth, and Development. *Environ. Toxicol. Chem.* **2012**, *31*, 611–622. [CrossRef]
147. Shahriman, M.S.; Mohamad, S.; Mohamad Zain, N.N.; Raoov, M. Poly-(MMA-IL) Filter Paper: A New Class of Paper-Based Analytical Device for Thin-Film Microextraction of Multi-Class Antibiotics in Environmental Water Samples Using LC-MS/MS Analysis. *Talanta* **2023**, *254*, 124188. [CrossRef] [PubMed]
148. Sereshti, H.; Mousavi Rad, N. Bacterial Cellulose-Supported Dual-Layered Nanofibrous Adsorbent for Thin-Film Micro-Solid-Phase Extraction of Antibiotics in Municipal Wastewaters. *Talanta* **2024**, *276*, 126198. [CrossRef] [PubMed]

149. Struck-Lewicka, W.; Karpińska, B.; Rodzaj, W.; Nasal, A.; Wielgomas, B.; Markuszewski, M.J.; Siluk, D. Development of the Thin Film Solid Phase Microextraction (TF-SPME) Method for Metabolomics Profiling of Steroidal Hormones from Urine Samples Using LC-QTOF/MS. *Front. Mol. Biosci.* **2023**, *10*, 1074263. [CrossRef] [PubMed]
150. Xiao, X.Y.; McCalley, D. Quantitative Analysis of Estrogens in Human Urine Using Gas Chromatography/Nagative Chemical Ionisation Mass Spectrometry. *Rapid Commun. Mass Spectrom.* **2000**, *14*, 1991–2001. [CrossRef]
151. Morés, L.; Dias, A.N.; Carasek, E. Development of a High-Throughput Method Based on Thin-Film Microextraction using a 96-Well Plate System with a Cork Coating for the Extraction of Emerging Contaminants in River Water Samples. *J. Sep. Sci.* **2018**, *41*, 697–703. [CrossRef]
152. Ayazi, Z.; Farshineh Saei, S.; Pashayi Sarnaghi, S. A Novel Self-Supportive Thin Film Based on Graphene Oxide Reinforced Chitosan Nano-Biocomposite for Thin Film Microextraction of Fluoxetine in Biological and Environmental Samples. *J. Pharm. Biomed. Anal.* **2023**, *236*, 115678. [CrossRef]
153. Moosavi, N.S.; Yamini, Y. Growth of Bimetallic Ni-Co MOFs on a Skeleton of Electrospun PAN Nanofibers and Coating on a Thin Film for SPME of Amitriptyline and Nortriptyline in Urine and Plasma Samples. *J. Pharm. Biomed. Anal.* **2023**, *236*, 115755. [CrossRef]
154. Hosseini, F.S.; Kharazmi, F.; Davarani, S.S.H.; Ebrahimzadeh, H. Development of Electrospun Nanofibers Based on Poly (Vinyl Alcohol) for Thin Film Solid-Phase Microextraction of Antidepressant Drugs in Biological Samples. *J. Chromatogr. A* **2023**, *1697*, 463984. [CrossRef]
155. Silberstein, S.D.; Mccrory, D.C. *Health Policy*; USA Gov.: New York, NY, USA, 2000; pp. 854–864.
156. Ayazi, Z.; Hobbivand, S.; Sarnaghi, S.P. Nickel Oxide Nanoparticles Modified with Dimethylglyoxime Grafted on Cellulose Surface as an Efficient Adsorbent for Thin Film Microextraction of Tramadol in Biological Fluids Followed by Its Determination Using HPLC. *Anal. Methods* **2024**, *16*, 5710–5722. [CrossRef]
157. Goryński, K.; Sobczak, Ł.; Kołodziej, D. Developing and Evaluating the Greenness of a Reliable, All-in-One Thin-Film Microextraction Protocol for Determining Fentanyl, Methadone, and Zolpidem in Plasma, Urine, and Oral Fluid. *Molecules* **2024**, *29*, 335. [CrossRef]
158. Ayazi, Z.; Pourtaghi, E.; Pashayi Sarnaghi, S. Graphitic Carbon Nitride Reinforced Nylon 6 Nanocomposite-Based Monolithic Thin Film for Microextraction of Carvedilol from Biological Samples. *Chem. Pap.* **2024**, *78*, 3747–3760. [CrossRef]
159. Hejabri Kandeh, S.; Amini, S.; Ebrahimzadeh, H. Development of Poly(Vinyl Alcohol)/Chitosan/Aloe Vera Gel Electrospun Composite Nanofibers as a Novel Sorbent for Thin-Film Micro-Extraction of Pesticides in Water and Food Samples Followed by HPLC-UV Analysis. *New J. Chem.* **2022**, *46*, 2431–2440. [CrossRef]
160. Werner, J.; Świtek, J.; Frankowski, R.; Zgoła-Grześkowiak, A. Development of a Green Deep Eutectic Solvent-Based Thin Film Solid Phase Microextraction Technique for the Preconcentration of Chlorophenoxy Acid Herbicides in Drainage Ditches and River Waters Using a Central Composite Design. *Microchem. J.* **2022**, *183*, 108101. [CrossRef]
161. Zeng, L.; Cheng, D.; Mao, Z.; Zhou, Y.; Jing, T. ZIF-8/Nitrogen-Doped Reduced Graphene Oxide as Thin Film Microextraction Adsorbents for Simultaneous Determination of Novel Halogenated Flame Retardants in Crayfish-Aquaculture Water Systems. *Chemosphere* **2022**, *287*, 132408. [CrossRef]
162. Chen, X.; Liu, S.; Jiang, R.; Luan, T.; Ouyang, G. Rapid Detection and Speciation of Illicit Drugs via a Thin-Film Microextraction Approach for Wastewater-Based Epidemiology Study. *Sci. Total Environ.* **2022**, *842*, 156888. [CrossRef]
163. Merlo, F.; Profumo, A.; Fontàs, C.; Anticó, E. Preparation of New Polymeric Phases for Thin-Film Liquid Phase Microextraction (TF-LPME) of Selected Organic Pollutants. *Microchem. J.* **2022**, *175*, 107120. [CrossRef]
164. van der Merwe, P.; Forbes, P. Comparison of Three Sorbents for Thin Film Solid Phase Microextraction of Haloacetic Acids from Water. *Anal. Methods* **2024**, *16*, 5154–5165. [CrossRef]
165. Merlo, F.; Quarta, V.; Speltini, A.; Profumo, A.; Fontàs, C.; Anticó, E. Sexual Hormones Monitoring in Surface Waters and Wastewaters from Northern Italy by Thin Film Microextraction Coupled with HPLC–MS/MS. *Environ. Sci. Pollut. Res.* **2024**. [CrossRef]
166. Murtada, K.; Pawliszyn, J. Evaluation of Thin Film Microextraction Based on Graphene Oxide/ Polymer Composite: Experimental and Theoretical Insights. *Talanta* **2024**, *274*, 126032. [CrossRef]
167. Sun, J.-C.; Pang, Y.-H.; Yang, C.; Shen, X.-F. Metal-Organic Framework Modified Carbon Cloth for Electric Field Enhanced Thin Film Microextraction of Sulfonamides in Animal-Derived Food. *J. Chromatogr. A* **2022**, *1674*, 463120. [CrossRef]
168. Yan, K.; Liu, X.; Liu, J.; He, C.; Li, J.; Bai, Q. Octadecyl-Fibrous Mesoporous Silica Nanospheres Coated 96-Blade Thin-Film Microextraction for High-Throughput Analysis of Phthalic Acid Esters in Food and Migration from Food Packages. *J. Chromatogr. A* **2024**, *1716*, 464636. [CrossRef] [PubMed]
169. Gruszecka, D.; Grandy, J.; Gionfriddo, E.; Singh, V.; Pawliszyn, J. Direct Immersion Thin Film Solid Phase Microextraction of Polychlorinated N-Alkanes in Cod Liver Oil. *Food Chem.* **2021**, *353*, 129244. [CrossRef]
170. Ghasemi, S.; Raoof, J.B.; Ghani, M.; Ojani, R. Bacteria-Templated ZIF-8 Embedded in Polyacrylonitrile Nanofibers as a Novel Sorbent for Thin Film Microextraction of Benzoylurea Insecticides. *Talanta* **2024**, *269*, 125403. [CrossRef]
171. Darvishnejad, F.; Bakhsh Raoof, J.; Ghani, M. Thin Film Microextraction Based on Co3O4@GO-Nylon-6 Polymeric Membrane to Extract Morin and Quercetin and Determining Them through High Performance Liquid Chromatography-Ultraviolet Detection. *Microchem. J.* **2021**, *170*, 106684. [CrossRef]

172. Li, W.; Gu, Y.; Liu, Z.; Hua, R.; Wu, X.; Xue, J. Development of a Polyurethane-Coated Thin Film Solid Phase Microextraction Device for Multi-Residue Monitoring of Pesticides in Fruit and Tea Beverages. *J. Sep. Sci.* **2023**, *46*, 2200661. [CrossRef]
173. Darvishnejad, F.; Raoof, J.B.; Ghani, M.; Ojani, R. Keggin-Type Polyoxometalate Embedded Polyvinylidene Fluoride for Thin Film Microextraction of Organophosphorus Pesticides. *Food Chem. X* **2023**, *19*, 100857. [CrossRef]
174. Zhang, H.; Zeng, P.; Guan, Q.; Yan, X.; Yu, L.; Wu, G.; Hong, Y.; Wang, C. Combining Thin-Film Microextraction and Surface Enhanced Raman Spectroscopy to Sensitively Detect Thiram Based on 3D Silver Nanonetworks. *Spectrochim. Acta Part A Mol. Biomol. Spectrosc.* **2023**, *287*, 122073. [CrossRef]
175. Giyahban, F.; Amini, S.; Kandeh, S.H.; Ebrahimzadeh, H. Development of Poly(Vinyl Alcohol)/Citric Acid/MIL-88A@CNTs Electrospun Nanofibers for Thin-Film Micro-Extraction of Conazole Fungicides Followed by CD-IMS Analysis. *Chem. Pap.* **2022**, *76*, 4705–4718. [CrossRef]
176. Cao, H.-L.; Yang, C.; Qian, H.-L.; Yan, X.-P. Urea-Linked Covalent Organic Framework Functionalized Polytetrafluoroethylene Film for Selective and Rapid Thin Film Microextraction of Rhodamine B. *J. Chromatogr. A* **2022**, *1673*, 463133. [CrossRef]
177. Rajska, A.; Raczak-Gutknecht, J.; Struck-Lewicka, W.; Buszewska-Forajta, M.; Wityk, P.; Verding, P.; Kowalewska, A.; Siluk, D.; Rachoń, D.; Jan Markuszewski, M. Determination of Urinary Androgens in Women with Polycystic Ovary Syndrome Using LC-QqQ/MS and the Application of Thin Film Solid-Phase Microextraction (TF-SPME). *J. Chromatogr. A* **2024**, *1718*, 464735. [CrossRef]
178. Chabowska, A.; Werner, J.; Zgoła-Grześkowiak, A.; Płatkiewicz, J.; Frankowski, R.; Płotka-Wasylka, J. Development of Thin Film SPME Sorbents Based on Deep Eutectic Solvents and Their Application for Isolation and Preconcentration of Endocrine-Disrupting Compounds Leaching from Diapers to Urine. *Microchem. J.* **2024**, *199*, 110023. [CrossRef]
179. Chen, L.; Singh, V.; Rickert, D.; Khaled, A.; Pawliszyn, J. High Throughput Determination of Free Biogenic Monoamines and Their Metabolites in Urine Using Thin-Film Solid Phase Microextraction. *Talanta* **2021**, *232*, 122438. [CrossRef] [PubMed]
180. Rezaei, H.; Matin, A.A.; Mohammadnejad, M. Cold Atmospheric Plasma Treated 3D Printed Polylactic Acid Film; Application in Thin Film Solid Phase Microextraction of Anticancer Drugs. *Talanta* **2024**, *266*, 125064. [CrossRef]

Disclaimer/Publisher's Note: The statements, opinions and data contained in all publications are solely those of the individual author(s) and contributor(s) and not of MDPI and/or the editor(s). MDPI and/or the editor(s) disclaim responsibility for any injury to people or property resulting from any ideas, methods, instructions or products referred to in the content.

molecules

MDPI

Review

Ionic Liquid-Catalyzed CO_2 Conversion for Valuable Chemicals

Peng Wang and Rui Wang *

School of Environmental Science and Engineering, Shandong University, No. 72 Seaside Road, Qingdao 266237, China
* Correspondence: wangrui@sdu.edu.cn

Abstract: CO_2 is not only the main gas that causes the greenhouse effect but also a resource with abundant reserves, low price, and low toxicity. It is expected to become an important "carbon source" to replace oil and natural gas in the future. The efficient and clean resource utilization of CO_2 has shown important scientific and economic value. Making full use of abundant CO_2 resources is in line with the development direction of green chemistry and has attracted the attention of scientists. Environmentally friendly ionic liquids show unique advantages in the capture and conversion of CO_2 due to their non-volatilization, designable structure, and good solubility, and show broad application prospects. The purpose of this paper is to discuss the research on the use of an ionic liquid as a catalyst to promote the synthesis of various value-added chemicals in CO_2, hoping to make full use of CO_2 resources while avoiding the defects of the traditional synthesis route, such as the use of highly toxic raw materials, complicated operation, or harsh reaction conditions. The purpose of this paper is to provide reference for the application and development of ionic liquids in CO_2 capture and conversion.

Keywords: CO_2; valuable chemicals; ionic liquids; catalysis

1. Introduction

Since the Industrial Revolution, the widespread use of fossil fuels has dramatically increased CO_2 emissions. The concentration of CO_2 in the atmosphere has increased from 280 μL/L before the Industrial Revolution to 415 μL/L in 2021 [1]. With the increasing CO_2 content in the atmosphere, a series of ecological and environmental problems have been caused, including the greenhouse effect, glacier melting, and climate warming [2]. In addition, the excessive consumption of fossil energy has also led to the emergence of the "carbon source crisis". The utilization of chemical resources has shown more and more important scientific and economic value and has attracted wide attention. The use of ionic liquids to convert CO_2 into high-value-added chemical products is of great significance to alleviate the greenhouse effect and the energy crisis. However, CO_2 is also an abundant, low-cost, non-toxic, and renewable C1 resource. Through the development of efficient catalytic technology, CO_2 can be converted into a series of high-value-added chemical and energy products, such as dimethyl carbonate [3], propylene carbonate [4], α-alkylene cyclic carbonate, and cyclic carbonate [5,6]. CO_2 conversion typically involves the following steps: (1) diffusion of CO_2, (2) uptake of CO_2 in the presence of a catalyst, (3) conversion of CO_2 on a heterogeneous or homogeneous catalyst surface, (4) desorption of the product from the catalyst, and (5) diffusion of the product into the solution/volume phase or into the separation [7,8]. Efficient catalytic techniques can fully utilize CO_2 as a class of carbon-based energy molecules. So far, the industrialization process of producing organic chemicals from CO_2 has been relatively slow. According to statistics, industrial CO_2 consumption accounts for only 0.36% of the total global emissions, indicating that there is still a huge space for development in the utilization of CO_2 resources [9]. Due to the thermodynamic stability and kinetic inertia of CO_2, the high efficiency and high selectivity of CO_2 conversion require rather harsh reaction conditions. Therefore, it is

particularly important to develop new technologies for CO_2 catalytic conversion and find new ways of CO_2 resource utilization in order to achieve high-value utilization of CO_2 under mild conditions.

Ionic liquids (ILs) are a large family of organic salts composed of organic cations (such as imidazole, pyridine, ammonium, phosphorus, guanidine, etc.) and anions (such as Cl^-, Br^-, I^-, BF_4^-, PF_6^-, etc.) [10]. ILs have the characteristics of low volatility, non-flammability, good thermal stability, and physicochemical stability, and they are considered to be excellent CO_2 liquid absorbers [11]. Most ILs absorb CO_2 through physical or chemical action. The physical absorption is mainly affected by the van der Waals force, and the desorption process is relatively simple. Just reduce the pressure or increase the temperature. Chemical absorption is achieved through the establishment of covalent bonds between ILs, which makes the process of CO_2 recovery and solvent regeneration more complicated. There are two main ways in which ILs interact with carbon dioxide. First, for conventional ILs, when carbon dioxide is passed into the reaction system containing the ILs, CO_2 can form the complex EMIm-CO_2 with the C2-(H) of the imidazole ring, as shown in Figure 1a [12]. In this complex, CO_2 is partially negatively charged, and its linear structure is destroyed, thus reducing the activation energy of the reaction and making CO_2 more easily reduced by electrons. Second, the interaction between the amino-functionalized ILs and CO_2 mainly improves the solubility of the CO_2 in the reaction system through -NH_2 and generates -$NHCOO^-$ intermediates, as shown in Figure 1b [13]. When the ILs containing -NH_2 participate in the photocatalytic CO_2 reduction reaction, the -NH_2 at the end of the alkyl chain is more likely to interact with CO_2 to generate -$NHCOO^-$, which promotes the reaction. Dong et al. found through a molecular dynamics simulation that the complex hydrogen bond structure in ILs was the main reason for improving its CO_2 adsorption performance [14]. Conventional and functional ILs are commonly used for CO_2 absorption and gas separation. In conventional ILs, fluorinated anions show good absorption performance, but the absorption of CO_2 is relatively weak. However, functional ILs contain amino, hydroxyl, and other basic functional groups, which are widely used. Functional ILs can absorb CO_2 through chemical action and enhance the absorption effect, which is the most promising type of ILs to realize industrialization at present. As early as 2002, Bates et al. proposed an amine-functionalized task-specific IL that binds CO_2 to a novel amino-functionalized IL through physical and chemical absorption, with an absorption ratio of 1:2, significantly increasing the solubility of CO_2 and meeting theoretical values based on chemical-absorption mechanisms [15].

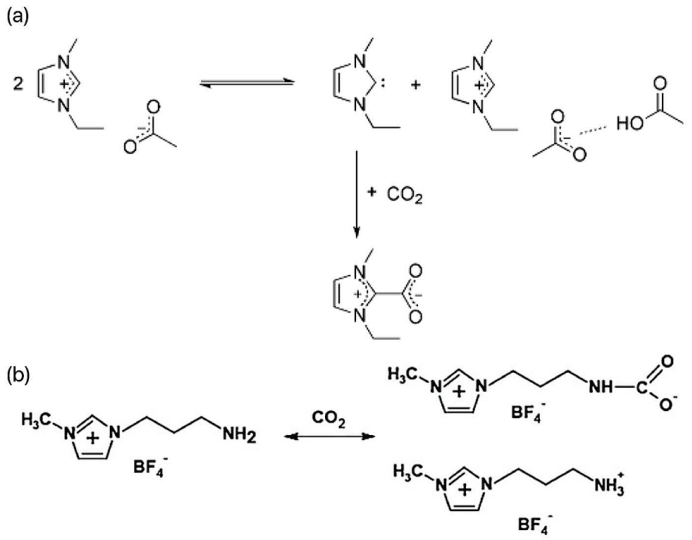

Figure 1. (**a**) Reaction process of CO_2 and [EMIm]Oac [12]. (**b**) Mechanism of CO_2 capture by NH_2-RTIL [13].

2. Ionic Liquids

2.1. Imidazole Ionic Liquids

Cyclic carbonate is a class of important chemical products widely used in chemical and chemical fields, with excellent physical and chemical properties and good biodegradability. It can be used as solvents, additives, electrolytes, pharmaceutical intermediates, and polymer monomers, and is widely used in many fields [16]. At present, the preparation of cyclic carbonates by a cycloaddition reaction between CO_2 and small molecule epoxides has become one of the research hotspots, as shown in Figure 2a. This reaction route is in line with the atom economy, and the use of CO_2 as the carbonylation reagent replaces the use of phosgene in the traditional process, which meets the development needs of green chemistry.

At present, the reaction is catalyzed by a homogeneous KI system in industry. The reaction is efficient because there is a hydrogen bond between the oxygen in PO and the hydroxyl group in cellulose. However, the production scale of the system is small and the reaction conditions of the catalytic process are harsh (180~200 °C, 5~8 MPa) [17]. In order to reduce the energy consumption of the reaction and realize the efficient activation and conversion of CO_2 under milder conditions, researchers developed different types of IL catalysts and investigated their catalytic performance and mechanism in the preparation of cyclic carbonate by coupling CO_2 with epoxide. Among all the ILs, imidazolium ILs are a class of ILs containing imidazole rings in the cations because of their large number and application in many fields. Due to the unique advantages of better solubility, better electrochemical stability, wider electrochemical window, and environmental friendliness, imidazolium ILs have been used in many fields of chemistry. In recent years, the wide application of imidazolium-based ILs in CO_2 cycloaddition reactions has attracted much attention. For example, Du et al.'s research team developed a series of directed vinyl-functionalized imidazole ILs and used these ILs for polymerization and copolymerization with 1,4-divinylbenzene (DVB) [18]. The team successfully synthesized a catalyst named PIL-DVBIV, which showed significant activity and selectivity in the CO_2 cycloaddition reaction. Under the optimized reaction conditions (110 °C, 2.0 MPa, and 6 h), the yield of the IL-DVB-IV catalyst for propylene carbonate reached 93%, and the selectivity reached 99%. In addition, the catalyst also showed good recyclability and versatility for various epoxides, which is of great significance for industrial production. Figure 2b shows the mechanism of the CO_2 cycloaddition reaction on the PIL-DVBIV catalyst, which is designed to efficiently convert CO_2 to organic carbonate products. Li et al. synthesized 1,8-diazabicyclo[5.4.0]nonene (DBU), 1,5-diazabicyclo[4.3.0]-5-nonene (DBN), and imidazole (MIM)-derivatized brominated ILs, which were used to catalyze the cycloaddition reactions of CO_2 with several epoxides to produce cyclic borates [19]. The possible synthetic mechanism of propylene carbonate is shown in Figure 2c. First, the epoxides are activated by hydrogen bond interactions, which makes the opening of the ring easier. Subsequently, the ring of the epoxide opens up on the smaller carbon atoms through a nucleophilic attack. Finally, cyclic carbonates are then formed by intramolecular cyclization nucleophilic attack. The DBU-derived bromide IL systems were found to have the best catalytic activity. The team investigated the effect of reaction conditions (temperature, pressure, and reaction time) on the reaction of CO_2 to generate propylene oxide (PO). The results showed that the conversion of PO, and the selectivity of propylene carbonate (PC) were able to reach 99% and 99% at 120 °C, 1 MPa, and 2.5 h with 2 mol % DBU-derived bromine ILs as the catalyst. The IL system could be reused at least five times without decreasing the selectivity and conversion under optimal reaction conditions. The loop test results are shown in Figure 2d. The results of this study provide useful information for the use of imidazolium-based brominated ILs to catalyze the cycloaddition reaction of CO_2 with epoxides and also demonstrate the feasibility and sustainability of such systems in practice.

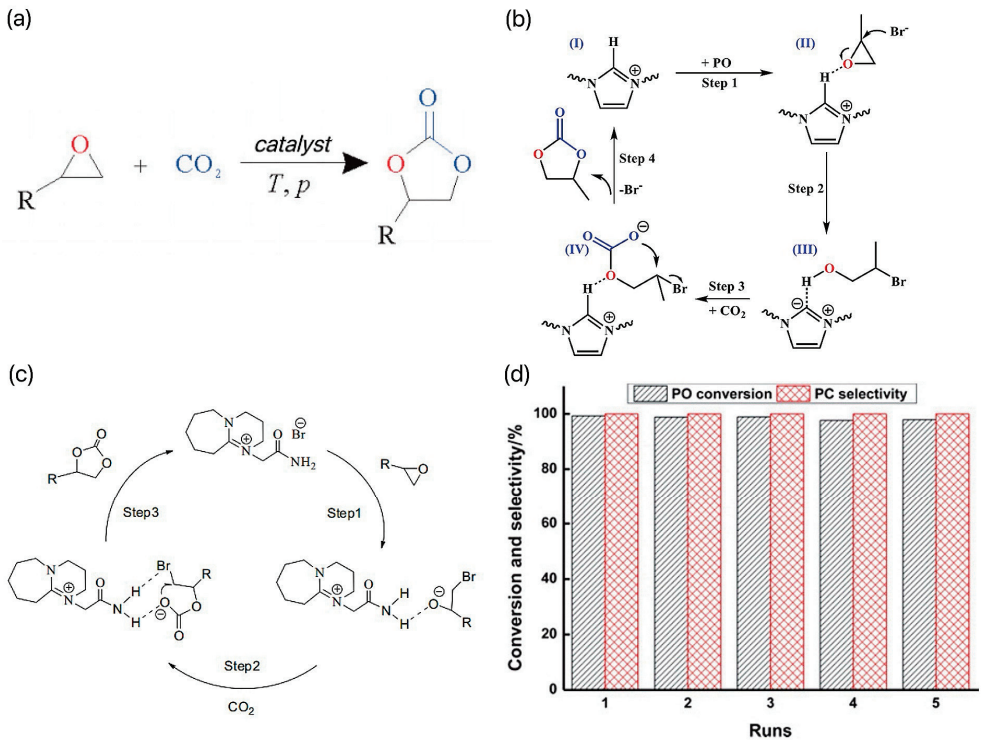

Figure 2. (**a**) Preparation of cyclic carbonates by the cyclization reaction of CO_2 with small-molecule epoxides [16]. (**b**) Mechanism of CO_2 cycloaddition over the PIL-DVBIV catalyst [18]. (**c**) Possible synthetic mechanism of propylene carbonate [19]. (**d**) The loop test results [19].

2.2. Pyridine Ionic Liquids

In contrast, pyridine ILs are less reported. Wang et al. synthesized a series of traditional pyridine ILs, introduced -OH, -COOH, -NH_2, and -SO_3H groups into the structure of 1-butylpyridine bromide ([BPy]Br), respectively, and designed four new hydrogen bond donor functionalized ILs as shown in Figure 3a. The effects of cationic properties, alkyl chain lengths, and anionic species on the catalytic activities were systematically studied by using theoretical calculation methods [20]. The results showed that the insertion reaction energy barrier of CO_2 was almost negligible and did not participate in the decisive step of the reaction; the epoxide ring-opening reaction had a higher energy barrier relative to the ring-closing reaction, which showed a decisive step. Increasing the alkyl chain length can improve the catalytic activity, but the catalytic activity decreases when the alkyl chain length is increased to C4, which is attributed to the large spatial resistance of the cation that prevents the reaction from proceeding. In addition, the catalytic performances of four synthesized functionalized pyridine ILs were comparatively investigated, and the results showed that the ILs containing the carboxyl group had the highest catalytic activity for the cycloaddition reaction. The theoretical study is instructive for the further design and synthesis of functionalized pyridine ILs. Zhang et al. developed an efficient and recoverable catalyst, 4-(dimethylamino)hydrobromopyridine ([DMAPH]Br), for the generation of cyclic carbonates from atmospheric CO_2 and epoxides, and the catalytic conversion mechanism is shown in Figure 3b [21]. In the presence of 1 mol % of [DMAPH]Br in solvent-free conditions, excellent conversion and selectivity were achieved for a variety of terminal epoxides. In addition, the catalyst could be recycled more than five times without a significant loss of catalytic activity, and the cycling performance was tested as in Figure 3c. The excellent catalytic performance of [DMAPH]Br was attributed to the synergistic effect of acidic protons and bromide ions on the epoxides and CO_2 enhanced by the cationic positively charged off-domains. In the same period, Liu et al. developed pyridine anion-based ILs (e.g., [P_{4444}][2-OP]) that could achieve efficient conversion of CO_2 to synthesize a series of epoxides of carbonates at 30 °C and 1 MPa [22]. The high activity

was attributed to the synergistic interaction of the two interaction sites in the PA-ILS anion to activate CO_2 and the cation to activate the epoxide through coordination with the central P+ unit, which led to the high activity of the workhorse catalysts.

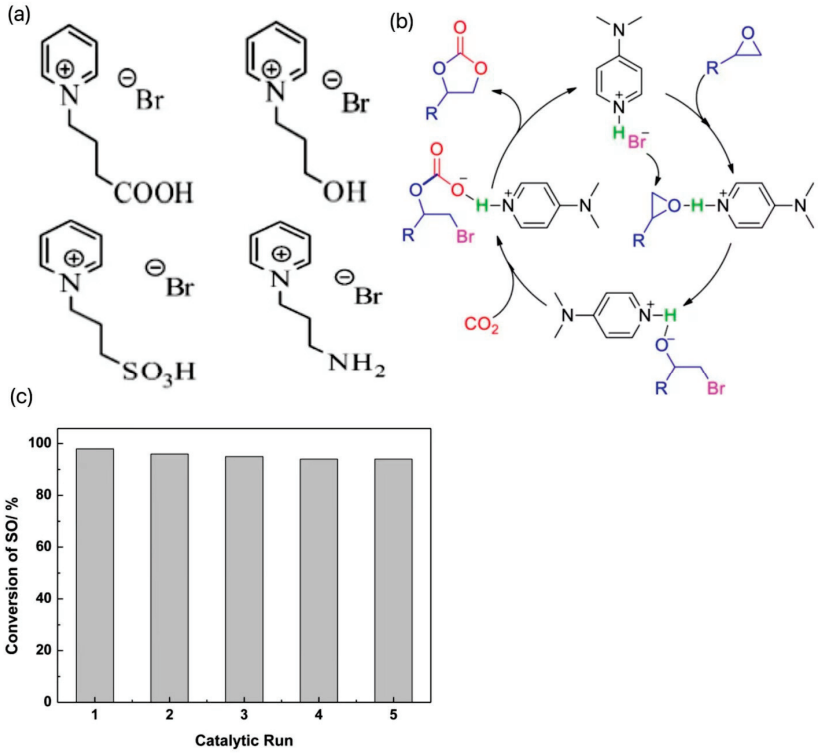

Figure 3. (**a**) Four new hydrogen bond donor-functionalized ILs designed after the introduction of -OH, -COOH, -NH_2, and -SO_3H groups, respectively, into the structure of 1-butylpyridinium bromide ([BPy]Br) [20]. (**b**) The catalytic conversion mechanism [21]. (**c**) The cycling performance test results [21].

2.3. Quaternary Ammonium/Quaternary Phosphonium Salts Ionic Liquids

Inspired by functionalized imidazole and pyridine ions, quaternary ammonium/quaternary phosphonium ILs have attracted attention in recent years. Zhang et al. used the DFT method to theoretically investigate the mechanism of catalytic CO_2 fixation by 2-hydroxy-ethyl-triethylammonium bromide (HETEAB), the structure of which is shown in Figure 4a [23]. The similarities and differences between the two catalysts, HETEAB and 2-hydroxy-ethyl-tributylammonium bromide (HETBAB), were further discussed. The results showed that the presence of -OH functional groups and active H atoms in ILs is an important factor in improving the performance of the catalysts. In order to better understand the reaction mechanism, LAUNAY et al. used the same hydroxyl-substituted quaternary ammonium catalysts to catalyze the coupling reaction between CO_2 and epoxide by combining experimental and density functional theory calculations [24]. The effects of alkyl chain length and anion species on the catalytic activity were systematically investigated. Specific structural and energetic information on each step of the catalytic reaction was obtained, and the following conclusions were obtained. (1) The ring-opening process of epoxide has the highest energy barrier, which is manifested as a decisive step. (2) For the same ammonium salt cation, Br has a higher catalytic activity than C1. (3) For the same cation, the nucleophilicity of the anion is not the only factor affecting catalytic activity. It is also affected by the ion removal and is also influenced by the ion removal. It is also affected by the ion-leaving ability and spatial site resistance. Li et al. systematically designed and synthesized a series of polymer-loaded quaternary phosphorus IL catalysts with a high grafting amount, as shown in Figure 4b [25]. Based on experimental and simulation results, it was also found that the high catalytic activity of the catalyst is attributed to the weak

interaction energy between anions and cations. Among them, PS TPP Cl performed well, with a low interaction energy of 72.2 kJ/mol, which led to a conversion of PO of up to 99.2% and a selectivity of PC of up to more than 99%. Even after five recoveries, its conversion of propylene oxide remained above 95% with almost no loss. Meanwhile, PS TPP Cl also shows good versatility and recyclability.

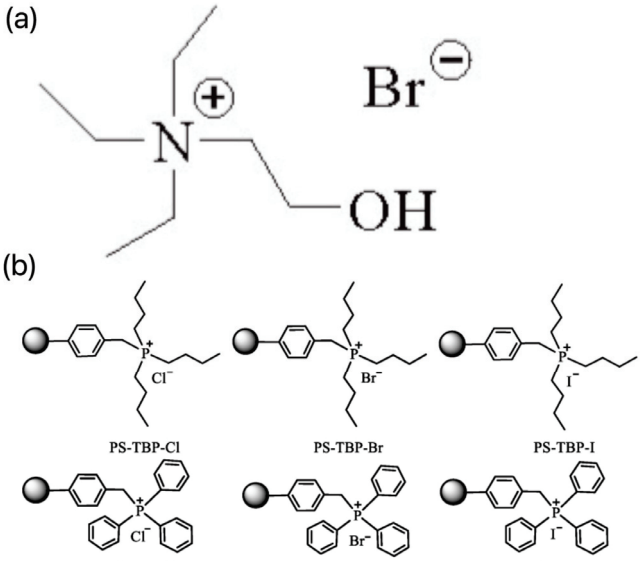

Figure 4. (**a**) Structure of HETEAB [23]. (**b**) A series of polymer-loaded quaternary phosphorus ILs catalysts with high grafting amount [25].

2.4. Loaded Ionic Liquids

Although the above-mentioned homogeneous IL catalysts have high catalytic performance, most of the ILs are difficult to recycle, so loaded ILs have been designed, i.e., the homogeneous ILs are loaded onto the carriers (e.g., carboxymethylcellulose, molecular sieve MCM-22, metal-organic framework composites, silica, etc.) [26].

SILs are catalysts that convert carbon dioxide into various useful compounds [27]. Cyclotronic carbonates have excellent applications in different fields. Cyclotronic carbonates can be used as non-protonic solvents (polar [28–30], as electrolytes in lithium-ion batteries [31,32], as intermediates in reactions [33], and as monomers in polymer preparation and have practical applications in pharmaceutical sciences [34–36]. In this context, the researchers introduced reusable SIL Im-ILs (silica-immobilized imidazolium ILs, ILs content 1.86 mmol/g) for catalyzing the cycloaddition reaction, as shown in Figure 5a [37]. The solvent-free reaction of allyl glycerol ether (AGE) by the addition of CO_2 at 1.76 MPa was successful in generating cyclic carbonates with the highest conversion (98.7%) (penta). Similar reactions were catalyzed by IMIS (silica-loaded various imidazolium ILs) with different halide anions and different alkyl chain lengths as in Figure 5b [37]. The silica-loaded 1-butyl-3-(3-triethoxysilylpropyl) imidazolium iodide showed higher AGE conversion (77.8%) and turnover (TON) (48.2%) than the other synthesized SILs under solvent-free conditions at 110 psi CO_2 pressure. In addition, the researchers probed the effect of zinc halide doping of the SILs on the conversion and selectivity. Thus, the prepared IMIS-zn containing chloride anion was more active than the corresponding IMIS (without zinc) [38]. Silica-modified magnetic nanoparticles (MNPs) loaded with imidazolium ILs were also used for the cycloaddition of CO_2 into styrene oxides at 1 MPa pressure [39].

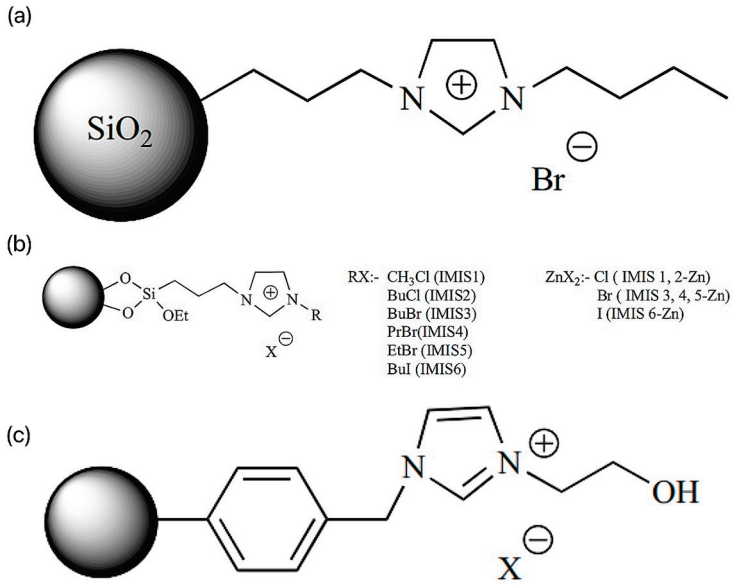

Figure 5. (**a**) Im-IL structure. (**b**) Structure of IMIS and IMIS-Zn. (**c**) PS-HEIMX, X = Br, Cl, I [37].

Researchers prepared porous polymer-carrier PVIm loaded with alkyl chains of different alkyl chain lengths and halide anions for catalyzing the cycloaddition reaction of CO_2 with AGE. Among the synthesized SILs, PVIm2-BuI(poly(n-vinylimidazole-codiinylbenzene) loaded with 1-iodobutane, the carrier with a pore size of 75.5 Å and a surface area of 952 m^2 g^{-1}, performed well and catalyzed the coupling reaction at a pressure of 1.34 MPa CO_2, with high conversion of 92% and a TON of 77% [40]. The researchers carried out a 2.5 MPa CO_2 pressure; chloromethylated polystyrene (CPS)-loaded hydroxyl-functionalized SILs (PS-HEIMX, X = I, Br, Cl) were prepared by the coupling reaction of CO_2 with propylene oxide (PO), as shown in Figure 5c [37]. The easy-to-separate PS-HEIMBr was easier to separate compared to the other SILs synthesized by halide anion [41]. Due to the synergistic effect, the catalytic conversion and selectivity were highly improved [42].

2.5. Plasmonic Ionic Liquids

He et al. prepared a series of protonated ILs by a simple "one-step" neutralization reaction between a strong base and a weak protonated acid and investigated their applications as solvents and catalysts in the carboxylation reaction of CO_2 with o-aminobenzonitrile [43]. Among them, the ILs [HTMG][Im] constructed by the neutralization reaction between TMG and imidazole had the best catalytic activity, and its structure is shown in Figure 6a. The coupling reaction of CO_2 and o-aminobenzonitrile was catalyzed at room temperature and pressure without additional solvent by extending the reaction time appropriately, and the product yield could be up to 90%. A possible catalytic reaction mechanism was proposed, as shown in Figure 6b. On this basis, Liu et al. designed and synthesized several multifunctional succinimide-based ILs, the structures of which are shown in Figure 6c [44]. The ILs have the dual roles of solvent and catalyst, among which [HTMG][Suc] can reach 98% yield at 60 °C and 6 h. However, the molar amount of catalyst required is three times that of the substrate, and even if the reaction is carried out for 24 h at ambient temperature, 88% yield can be achieved. The synergistic activation of CO_2 and 2-aminobenzonitrile by [HTMG][Suc] provides a reference for the reaction mechanism. In recent years, Luo et al. investigated a series of easy-to-prepare plasmonic ILs to synthesize high-value-added GCs (gas-chromatography standards) and the byproducts, benzene Z-ene glycol (SG) and styrene carbonate (SC), in a one-pot synthesis using CO_2, Gly, and styrene oxide (SO) as the feedstock. The synthesis process is shown in Figure 6d [45]. SO was chosen as the substrate, and the GC yield could reach 94% at 45 °C under atmospheric pressure with 1,8-diazabicyclo[5.4.0]undec-7-iodoene (HDBUI) as the catalyst. The experimental results

and density-functional theory (DFT) calculations indicated that the high catalytic activity of HDBUI was due to the strong nucleophilicity and substrate activation resulting from the synergistic interaction of the protonated $HDBU^+$ cation and I^- anion.

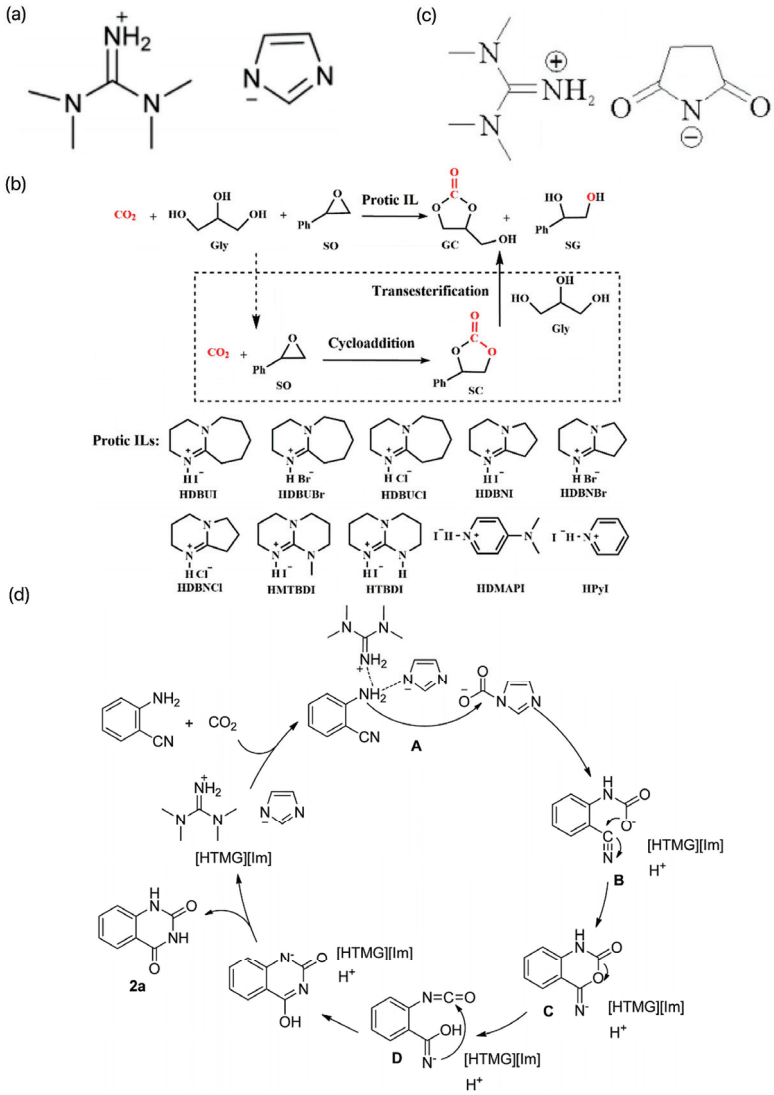

Figure 6. (**a**) Structure of [HTMG][Im] [43]. (**b**) Possible coupling reaction mechanism of CO_2 with o-aminobenzonitrile [43]. (**c**) Structure of several multifunctional succinimide-based ILs [44]. (**d**) One-pot synthesis of high value-added GC and its byproducts Z-benzene glycol (SG) and styrene carbonate (SC) [45].

2.6. Non-Protonic Ionic Liquids

Wang et al. reported a series of catalysts based on imidazole anions, among which [Ch][Im] showed the best catalytic effect [46]. This catalyst promoted the cycloaddition reaction of 2-aminobenzonitrile with CO_2 at atmospheric pressure and 80 °C. In the literature, flue gas was used for the first time to synthesize quinazoline-2,4(1H,3H)-dione, which was reacted at 50 °C and 0.15 bar CO_2 pressure for 36 h, and still yielded a 93% isolated yield of the product, showing excellent catalytic activity. In addition, Wang et al. reported in 2019 a choline-based ILs catalyst that can catalyze the cyclization reaction of 2-aminobenzonitrile with CO_2 at 40 °C under atmospheric pressure and obtained a 99% reaction yield [47]. Compared with the previously reported quaternary ammonium salt catalysts, the reaction conditions were milder. Meanwhile, the quaternary ILs have lower viscosity and higher decomposition temperature compared to the quaternary ILs catalyst. The quaternary salt [Bu,P]-2-MIm based on 2-methylimidazole anion reported by Liu et al.

also gave excellent product yields with a reduced catalyst dosage and further improved catalytic efficiency at 80 °C and 1 bar CO_2 pressure [48]. In this work, it was found that the synthesized ILs can activate atmospheric CO_2 to form carbamates, which in turn, react with 2-aminobenzonitrile to synthesize quinazoline-2,4(1H,3H)-diones.

3. Application of Ionic Liquids in Catalytic CO_2 Conversion

ILs have shown unique advantages in catalyzing and promoting CO_2 conversion. In the process of CO_2 conversion, ILs can be used as solvents, electrolytes, CO_2 adsorbents, activators, catalysts, and co-catalysts to realize the chemical conversion of CO_2 under mild and metal-free conditions and can be coupled with metal catalysts to realize their directed conversion and obtain high-value-added chemicals [49]. Table 1 shows the high catalytic activity and selectivity of ILs to the products. In the IL catalytic system, multiple roles coexist to synergistically realize the activation and conversion of CO_2 [50]. The following discussion is based on the promotion of ILs in four aspects, namely photocatalytic conversion, electrocatalytic conversion, photoelectrocatalytic conversion, and photothermal catalytic conversion of CO_2.

Table 1. High selectivity of ionic liquids to products.

ILs	Catalytic Mode	Catalytic Condition	Catalyst	Sel%	Ref.
$[P_{4444}]_3$[p-2,6-O-4-COO]	Photocatalytic conversion	visible light > 420 nm	CH_4	96.2%	[51]
$[Ru(bpy)_3]Cl_2$	Photocatalytic conversion	1 atm, visible light > 420 nm	CO	96.3%	[52]
ApmimBr	Electrocatalytic conversion	20 °C, voltage 3.5 V,	$C_3H_6O_3$	94.5%	[53]
[APMIm]DCA	Electrocatalytic conversion	50 °C	4-(hydroxymethyl)-1,3-dioxolan-2-one	96.8%	[54]
$[Emim]BF_4$	Photoelectrocatalytic conversion	visible light, −0.9 vs. NHE	CH_3CH_2OH	82.7%	[55]
$[EmimOH]/[NTF_2]$/DBU/SmOCl	Thermocatalytic conversion	140 °C	$C_3H_6O_3$	99.1%	[56]
BzMDH	Thermocatalytic conversion	140 °C	$C_3H_6O_3$	99.7%	[57]

3.1. Photocatalytic Conversion of CO_2 by Ionic Liquids

Most ILs exhibit good photostability under sunlight and utilize stable radicals or anions to activate CO_2 [58]. Theoretical studies have shown that ILs may form excess charge localization or cavities under electrochemical or radiation effects, which makes them attractive materials for CO_2 photoreduction [59,60]. In particular, imidazolium-based ILs are highly solar stable, and their mechanism for promoting CO_2 activation is through the in situ formation of imidazolium CO_2^- adducts, which are considered to be a key intermediate that can dissociate into $BMIm^+$ and CO_2^- radicals. Photocatalytic technology has attracted much attention due to its advantages of easy operation, low energy consumption, and no secondary pollution, but it still faces the challenges of easy compounding of electrons and holes, limited absorption of light by photocatalysts, and high activation energy of the reaction in practical applications. To overcome these problems, in addition to novel photocatalytic technologies that incorporate external fields, the photocatalytic conversion efficiency of CO_2 can be improved by compounding photocatalysts with other compounds, such as ILs [61–63].

For example, imidazolium-based ILs can be used as photocatalysts to realize the reduction of CO_2 in water without the need for semiconductors or scavengers. As an example, the amphoteric IL 1-n-butyl-3-methylimidazole-2-carboxylate (BMIm-CO_2) has an apparent quantum yield of CO as high as 250 μmol/L and an apparent quantum yield of 3.9%. The reaction mechanism involves the generation of BMIm radical cations ($[BMIm]^+$) and CO_2 radical anions (CO_2^-) via the homolytic cleavage of CO_2, a process that is validated both experimentally and theoretically [49]. The reaction mechanism is shown in Figure 7a. Peng et al. studied the relationship between the CO_2 photoreduction efficiency, UV/Vis adsorption capacity, and Kamlet–Taft (K-T) β-parameter value of BMIm·

Oac ILs in water and isopropyl alcohol [64]. We believe that the activation of CO_2 is related to the properties of anions, which drive the formation of CO_2^- reaction intermediates. It was also observed that the pH value of ILs significantly promoted CO_2 photoreduction. For example, BMIm·OC_6F_5 ILs at pH 7.18 strongly induce CO_2 reduction by increasing CO_2 solubility, producing large amounts of HCO_3^-, which is subsequently reduced to CO and CH_4. Wang's group found that, under mild conditions (1 atm CO_2 and visible light), ILs can promote the photoconversion of CO_2 to CO using $[Ru(bpy)_3]Cl_2$ as a photocatalyst [52]. The relevant test results are shown in Figure 7b. The high promotive properties of ILs are due to the task specificity of ILs and the functional groups at the ILs site.

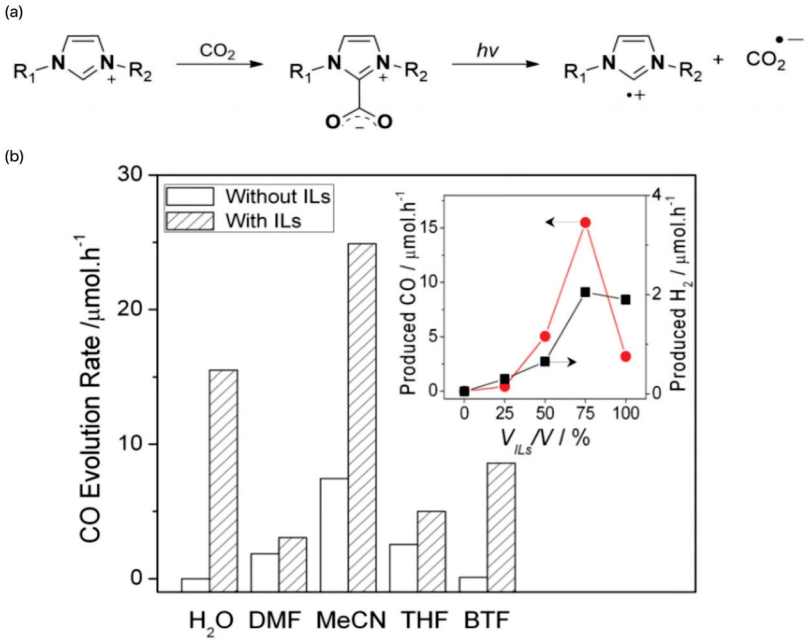

Figure 7. (**a**) Formation of imidazoliumCO_2-adduct and its radical intermediates generated under irradiation [49]. (**b**) Promotion of CO_2 photocatalysis by different ILs. The production of CO and H_2 increases with the increase of the $[EMIM][BF_4]/H_2O$ ratio. However, when H_2O was removed, the activity of CO and H_2 formation slowed down significantly [52].

On the other hand, Chen et al. demonstrated a CO_2 uptake capacity of up to 3.26 mol CO_2/mol ILs at room temperature by designing novel ILs such as tetra-coordinated ILs obtained by the neutralization reaction of citric acid with tetrabutylphosphine hydroxide [51]. These ILs complexed with CO_2 (IL-CO_2) exhibited visible-light absorption properties and promoted the photocatalytic reduction of CO_2 to CH_4 by anatase-type TiO_2 under light conditions, with yields up to 3.52 μmol/g per hour and selectivities up to 96%. Mechanistic studies showed that IL-CO_2 complexes acted as photosensitizers to promote the photocatalytic reduction of the CO_2 reaction under visible-light irradiation.

These studies show the potential and advantages of ILs in a variety of photocatalytic conversion reactions and provide new ideas and possibilities for the development of efficient and environmentally friendly CO_2 conversion technologies.

3.2. Electrocatalytic Conversion of CO_2 by Ionic Liquids

In recent years, the application of ILs as a reaction medium in the electrochemical reduction of CO_2 has shown remarkable catalytic activity and unique advantages. Its main mechanism of action can be summarized as follows. First, compared with the traditional aqueous solution system, CO_2 has a higher solubility in ILs, which is conducive to improving the mass transfer rate in the electrochemical reduction process of CO_2, thus enhancing the driving force of the CO_2 reaction and the conversion rate of products. Second, ILs can effectively inhibit the hydrogen evolution reaction in water, thus improving the

selectivity of the product. In addition, ILs provide a superior microenvironment at room temperature, which can activate CO_2 molecules more effectively and promote the reduction reaction of CO_2 [65–67]. Therefore, the highly efficient activation and catalysis of ILs in the field of CO_2 electrochemical reduction has gradually become the forefront of research.

Researchers have made remarkable progress in the electrochemical reduction reaction of CO_2, especially when using ILs as the reaction medium. These studies mainly focus on improving the efficiency and selectivity of the reaction. For example, Rosen et al. have made significant progress in the conversion of CO_2 to CO through the method of direct electrocatalytic reduction [65]. By introducing ILs, the overpotential of CO_2 reduction is successfully reduced, resulting in highly selective CO generation. The researchers further found that, by adding water to [EMIM]BF_4 and using Ag as the catalytic electrode, not only can the CO_2 reduction overpotential be reduced but also the CO_2 conversion frequency can be increased. Cai et al. used Pt as the working electrode to prepare dimethyl carbonate by the electrocatalytic reduction of CO_2 in 1-butyl-3-methylimidazole bromide (BMIMBr)-potassium methanol-methanol medium using potassium methanol as a cocatalyst [68]. The reaction mechanism is shown in Figure 8. Although this method can simplify the separation process of the product, the yield of the system is only 3.9%. When substituting propylene oxide for potassium methanol, the yield can be increased to more than 75.5%. In addition to the electrochemical conversion of CO_2 to CO and HCOOH, another highly anticipated application is the conversion of CO_2 to methanol, which has been extensively studied in ILs. Han and his team converted CO_2 to methanol by electrochemical activation [69]. The team used a variety of bimetallic catalysts, such as Mo-Bi, Mo-Ag, and Mo-Cu, in the [BmIm][BF_4]/acetonitrile solution. In 0.5 M IL-acetonitrile solution, Mo and Bi metals work together as bimetallic catalysts to achieve 71.2% Faraday efficiency for the electrochemical activation of CO_2. In bimetallic MO-Bi catalysts, Mo promotes the conversion of CO_2 to CO, while Bi contributes to H_2 generation and in situ adsorption of CO, thus increasing the possibility of CO_2 being hydrogenated to CH_3OH.

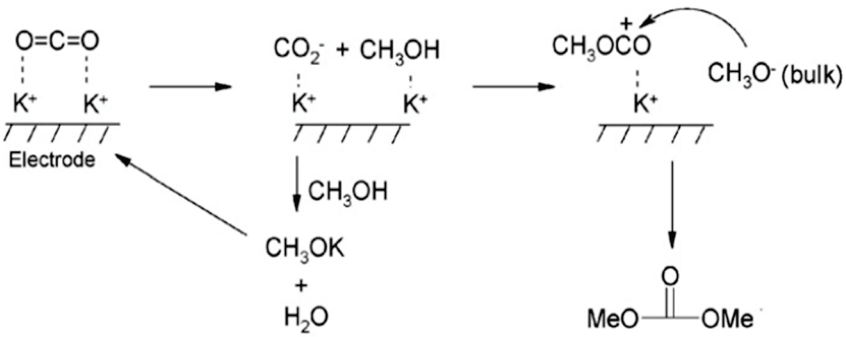

Figure 8. Possible mechanisms for the preparation of dimethyl carbonate [68].

3.3. Photoelectrocatalytic Conversion of CO_2 by Ionic Liquids

Photoelectrocatalysis uses solar and electrical energy to catalyze the conversion of CO_2 into organic matter. Compared with photocatalysis, appropriately applied bias can cause energy-band bending, which contributes to the orderly transfer of photogenerated electrons and thus reduces the recombination of photogenerated electron–hole pairs [70]. In addition, even if the energy-band position of the photocatalyst is unfavorable for CO_2 reduction or H_2O oxidation, it can still be used for the photoelectrocatalytic reduction of CO_2 under appropriate applied bias conditions [71].

Lu et al. introduced an IL (1-aminopropyl-3-methylimidazolium bromide salt) to enhance the reaction system for the photoelectrocatalytic reduction of CO_2 in order to increase the solubility of CO_2 in water and facilitate its catalytic conversion [72]. The solution acted as both absorber and electrolyte at ambient temperature and pressure. Under an applied voltage of 1.7 V, the Faraday efficiency of formic acid was up to 94.1%, which was significantly higher than the photoelectrocatalytic systems without the introduction of ILs (37.2%) and with the introduction of ILs without an amino group (62.4%). In this photoelec-

trocatalytic reduction system, the amino-containing ILs critically facilitated the conversion of CO_2 to formic acid and inhibited the generation of H_2. Cronin's team performed a CO_2 to CO photoelectric conversion study in a non-aqueous [EMIM][BF_4]/CH_3CN solution, obtaining a Faraday efficiency of 99% at an underpotential of +0.78 V [73]. The photocatalytic conversion of CO_2 to CO was investigated by Cronin's team in a non-aqueous [EMIM][BF_4]/CH_3CN solution. It was shown that the photocatalytic yield increased with the increase in the number of TiO_2 layers, which is believed to be due to the increase in the catalytically active sites and thus the rate of electron–hole pair complexation. In addition, the formation of complexes between $[EMIM]^+$ ions and CO_2 lowered the energy barrier of the reaction, which further contributed to the efficiency of the photoelectric conversion.

Gao et al. prepared Cu_2O/TiO_2 nanoarray electrode materials using anodic oxidation and electrodeposition methods and applied them to the photocatalytic reduction of CO_2 [55]. The mechanism of photoelectrocatalytic CO_2 reduction over a Cu_2O/TiO_2 catalyst in the presence of [Emim]BF_4 is shown in Figure 9. In the system without [Emim]BF_4, CO_2 molecules approach and bind to the active site on the catalyst surface to form the intermediate CO_2^-. This process requires overcoming a large activation energy. This intermediate is then protonated to produce HOCO, which is then converted into the key intermediate *CO through a series of electron acquisition, proton acquisition, and dehydration reactions. *CO intermediates can exist in two forms: C≡O and C=O. The former is important for the formation of C1 products, while the latter is important for the formation of C–C coupling to produce multi-carbon products. Without the addition of [Emim]BF_4, the intermediate product *C≡O can be eventually converted into products such as methanol through a series of proton and electron transfer processes [74–76]. However, once [Emim]BF_4 is added, the reaction path of the system changes significantly. [Emim]BF_4 has a strong ability to capture CO_2 and enrich CO_2 on the catalyst surface, thus creating a high-concentration CO_2 microenvironment on the electrolyte and catalyst surface. In addition, imidazole cation [Emim]+ forms [EMIM-CO_2] complexes with CO_2 in the catalyst–electrolyte interface region, further affecting the kinetics and reaction path of the reaction. This complex will improve the CO_2 adsorption and conversion efficiency of the catalyst surface, thereby improving the selectivity and reaction rate of the final product [77]. It was found that the addition of [Emim]BF_4 significantly improved the yield of the alcohol product, resulting in 82.7% selectivity for ethanol. The researchers delved into the promotion mechanism of [Emim]BF_4 and concluded that the enrichment of [Emim]BF_4 in the cathode region enhanced the capture of CO_2. In addition, [Emim]BF_4 formed a strong interaction with the electrode surface, which effectively improved the separation efficiency and migration rate of photogenerated charges.

3.4. Photothermal Catalytic Conversion of CO_2 by Ionic Liquids

The photothermal synergistic catalytic technology combining solar and thermal energy utilizes the integrated photothermal effect to enhance the performance of the catalyst. Meanwhile, the thermal effect had a significant impact on the CO_2 absorption by ILs [78].

Bai et al. tested the thermal stability of four 1-alkyl-3-methylimidazolium bis(trifluoromethylsulfonyl)imides ([C_nMIm][Tf_2N]) for CO_2 absorption at 393.15 K [79]. The results showed that [C_nMIm][Tf_2N] was the most effective catalyst for CO_2 absorption. The results showed that [C_nMIm][Tf_2N] exhibited long-term thermal stability at 393.15 K. The results showed that [C_nMIm][Tf_2N] was a good choice for the thermal stability of CO_2 uptake. The solubility of CO_2 in [C_nMIm][Tf_2N] increased significantly with increasing pressure in the range of 353.15 K to 393.15 K and decreased slightly with increasing temperature. In addition, the solubility of CO_2 in the ILs increased with the increase of alkyl chain length on the cation.

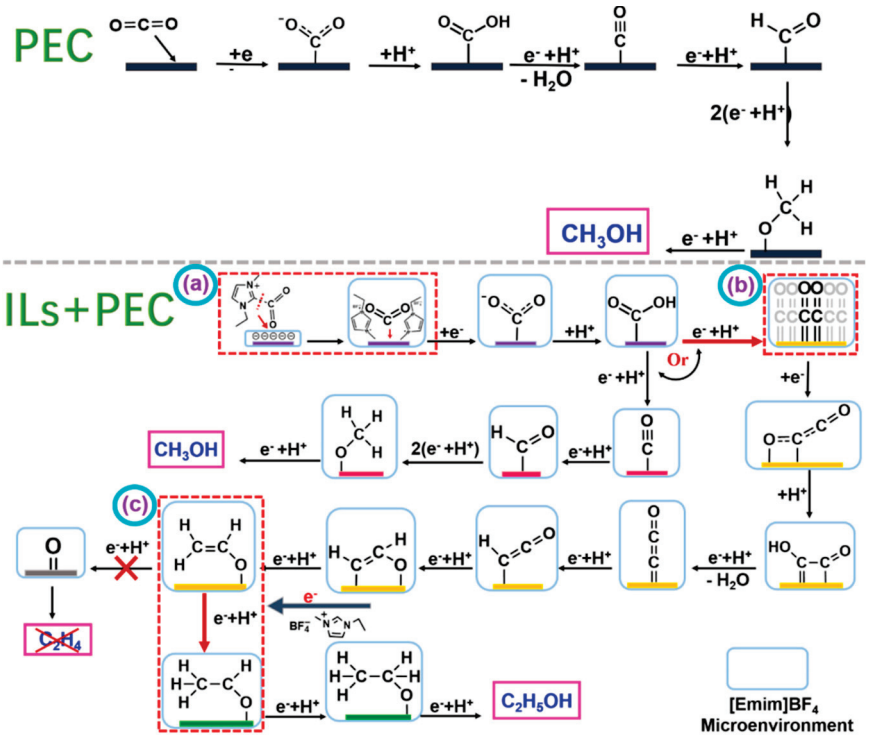

Figure 9. The mechanism of photoelectrocatalytic CO_2 reduction over Cu_2O/TiO_2 catalyst in the presence of [Emim]BF_4. (Step a) CO_2 is complexed with [Emim*] to form [Emim*−CO_2] complex. (Step b) Two adjacent *C=O intermediates form *$C_2O_2^-$ through electron transport−mediated facilitation, which in turn produces C2. However, a small percentage of *C≡O intermediates are converted to CH_3OH. The coupled intermediate *$C_2O_2^-$ is converted to the intermediate CH_2CHO* by a series of proton and electron transfer processes. This reaction produces either ethylene or ethanol. (Step c) The resulting CH_3CHO* intermediate undergoes electron and proton transfer to produce CH_3CH_2OH [55].

Li et al. synthesized $Cu_2O/g\text{-}C_3N_4$ heterojunctions by a simple hydrothermal method to photothermally catalyze the conversion of CO_2 to CH_3CH_2OH in an aqueous solution with the addition of the bromine salt of 1-aminopropyl-3-methylimidazole [80]. The photothermal catalytic conversion of CO_2 to CH_3CH_2OH is shown in Figure 10a. Figure 10b shows the possible reaction pathways of $Cu_2O/g\text{-}C_3N_4$ in an [APMIm][Br] aqueous solution. First, Cu_2O and $g\text{-}C_3N_4$ are excited by light to generate e^- and h^+ ions. The transfer of e— from the CB in Cu_2O to the CB in $g\text{-}C_3N_4$ promotes rapid separation of the carrier. Second, the CO_2 adsorbed by Cu_2O continuously complexes with [AMPIm][Br] to form APMIm-CO_2, which can reduce the overpotential and react with $g\text{-}C_3N_4$ to form *CO. It has been reported that ILs provide a low-energy pathway by forming C_2MIm-CO_2 complexes, which can easily convert CO_2 into *CO and promote continuous coupling of C–C under visible-light irradiation, which is an important reason for improving the ethanol yield [81–83]. In addition, continuous proton and electron transfer completed the conversion from *CO to $^{\bullet}CH_3$. In addition, the thermal field can accelerate the motion and collision between $^{\bullet}OH$ and $^{\bullet}CH_3$, further promoting C–C coupling to generate ethanol. Finally, a series of free-radical reactions and proton–electron transfer processes are completed to achieve the conversion of CO_2 to ethanol. Specifically, the consumption of *CO can reduce the coverage of *CO on the surface of $Cu_2O/g\text{-}C_3N_4$, promote the reduction of CO_2 to CH_3CH_2OH, and weaken the toxic effects of *CO. The yield of CH_3CH_2OH reached 0.71 $mmol{\cdot}g^{-1}{\cdot}h^{-1}$, which is higher than that of the pure aqueous reaction system (0.56 $mmol{\cdot}g^{-1}{\cdot}h^{-1}$), which was 1.27 times higher than that of the pure water reaction system (0.56 $mmol{\cdot}g^{-1}{\cdot}h^{-1}$). Due to the presence of amino groups in the ILs, the solubility of CO_2 in the reaction system was effectively increased. In addition, the current density of

the ILs electrolyte solution was 21.3 mA·cm^{-2}, which was higher than that of the $KHCO_3$ electrolyte solution of 12.8 mA·cm^{-2}, and lowered the overpotential of 0.34 V, which promoted the reduction of CO_2 by reducing the polarization. The ILs played a key role in inhibiting H_2 generation.

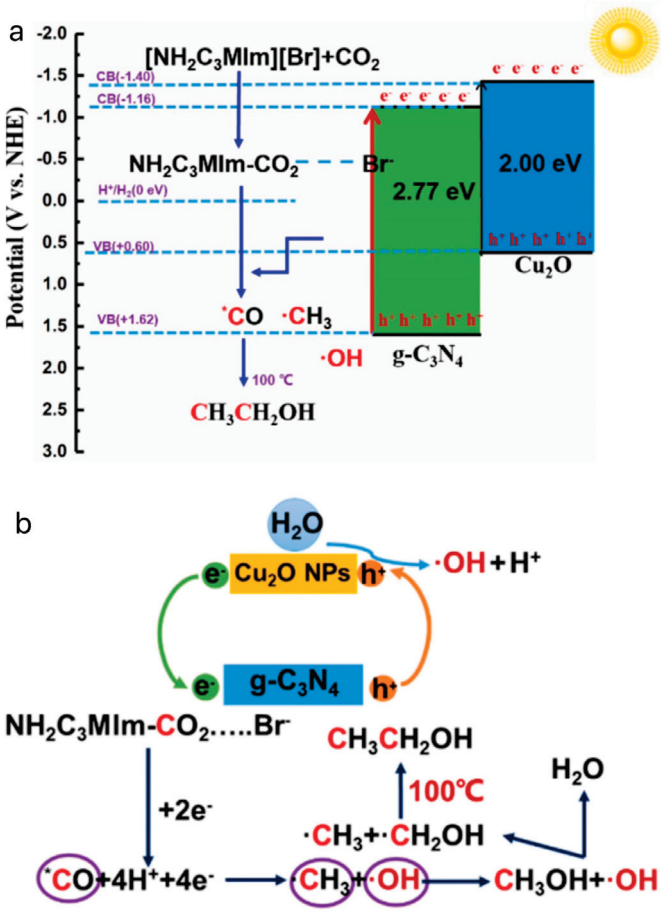

Figure 10. (**a**) Principle of photothermal catalyzed conversion of CO_2 to CH_3CH_2OH [80]. (**b**) The possible reaction pathways of Cu_2O/g-C_3N_4 in [APMIm][Br] aqueous solution [80].

4. Valuable Chemicals

4.1. CO_2 Hydrogenation

The hydrogenation of CO_2 to produce chemical products and fuels is a high-efficiency and energy-saving method that is of wide interest to the chemical industry. By changing the valence of the carbon atoms, CO_2 can be reduced to different products, in the order of HCOOH, CH_2O, CH_3OH, and CH_4. In particular, long-chain hydrocarbons, such as C2–C4, will be the focus of future research [84].

Han et al. developed a reaction–separation system to synthesize formic acid from CO_2 (4–18 MPa) and H_2 (1–9 MPa) under the catalysis of amino ILs using ruthenium immobilized on silica as a heterogeneous catalyst at 60 °C [85]. Subsequent product recovery and catalyst regeneration can be easily achieved through filtration and evaporation. The key was to design ILs with a specific function, with a tertiary amine group on the cation, capable of forming a salt with formic acid. Although some progress has been made by designing diamine-functionalized ILs, the reaction conditions remain challenging. The reaction temperature was raised to 150 °C while maintaining corresponding pressure conditions (hydrogen gas 4–6 MPa, total H_2/CO_2 8 MPa) [86]. Under these conditions, the optimum CH_4 yield is 69%. Further increasing the reaction temperature or increasing the amount of catalyst can improve the methane yield and TON. In addition, the study showed that the increase rate of TON was more significant in the temperature range from 140 °C to 150 °C, while the product formation was not observed below 120 °C.

4.2. C–O Bond

Typical reactions to build C–O bonds typically require highly active reagents, such as organolithium reagents or Grignard reagents. The substrates of these reactions may include alkenes, dienes, alkynes, halogenated aromatic compounds, epoxides, and aromatic compounds containing hydrocarbon groups. However, the use conditions of organolife and Grignard reagents are very strict, which limits their widespread use in practical applications. ILs, as a green and sustainable solvent, offer new opportunities in the process of building C–O bonds, especially in reactions with carbon dioxide and other substances. However, to date, ILs-mediated C–O bond formation reaction products have been largely limited to the form of carbonates, including cyclic and linear carbonates.

Wang's research group conducted an interesting study using epoxides instead of propargyl alcohol for the cycloaddition reaction of CO_2 [87]. At a CO_2 pressure of 1 bar and a temperature of 60 °C, α-alkylene cyclocarbonate, using 200 mol% ILs with a yield of up to 89% and without the use of other solvents, was successfully synthesized. This study shows that ILs can be used not only as solvents or reactants but also as effective catalysts or reaction templates under mild conditions [88]. In some systems, eutectic ILs show excellent selectivity and efficiency in the cycloaddition reaction of CO_2 and epoxide, which provides a new way and possibility for green chemical synthesis [89]. The study by Zhao et al. demonstrates a new method for the efficient synthesis of linear dimethyl carbonate using bicarbonate ILs as a recyclable catalyst and dehydrating agent [90]. The team took advantage of the high tunability of IL bicarbonate and the high polarity, high solubility, and easy activation of CO_2. In this study, the reaction conditions were relatively mild, using 1 MPa of CO_2 and methanol, and carried out at near room temperature. This method not only avoids the toxic substances used in traditional synthesis methods but also utilizes the properties of ILs to achieve a highly efficient synthesis process. This innovative approach provides an important advance for the sustainable preparation of carbonate compounds and promotes the development of green chemical synthesis.

4.3. C–N Bond

The formation of a carbon–nitrogen bond is important for the synthesis of organic substances and intermediates. In recent years, the use of ILs to construct C–N bonds from CO_2 has become a promising approach. ILs can be used as a CO_2 adsorbent, activator, reaction catalyst, substrate solvent, and product separator. In addition, its high adjustability, high stability, and low volatility make it a recyclable solvent and catalyst, conducive to the concept of green chemistry and sustainable development.

Choi et al. demonstrated a method of catalyzing the formation of carbamate from amines, CO_2, and silicate esters using superbasic protonated ILs [DBU][Ac] at 5 MPa CO_2 and 150 °C acetonitrile [91]. The team observed that the activity of aromatic amines was lower than that of fatty amines due to their lower pKa values, which is related to hydrogen bond interactions between basic acetic acid anions in ILs. Despite the success of this study, the disadvantages include the use of a cosolvent (acetonitrile) and the relatively strict reaction conditions (5 MPa CO_2 and 150 °C). In order to improve this method, future studies can try to design new types of metal-ion-free liquids to achieve a more moderate temperature and lower CO_2 pressure that still can efficiently catalyze the synthesis of CO_2 carbamate. This improvement is expected to improve the sustainability and practicality of the reaction and promote the further development of the application of ILs in CO_2 conversion chemistry. He et al. designed a series of Lewis bases and cationic ILs to catalyze the synthesis of chemically and regionally selective 5-aryl-2-oxazolidinones from azacil and CO_2 without the need for any organic solvents or additives [92,93]. Unfortunately, these conditions are relatively stringent, requiring, for example, a CO_2 pressure of 3–9 mpa. 2-oxazolidinone using copper-substituted polyoxometalate-based ILs at one atmosphere of CO_2 and 25 °C was successfully synthesized by improving the carboxylated cyclization of various propylamines through the dual activation of propylamine and CO_2. However, the disadvantages of using metals such as copper provide room for improvement in the

synthesis of oxazolidinone. Han et al. synthesized 3,4, 5-trisubstituent oxazolone using propylamine and CO_2 at 100 °C and one atmosphere of CO_2 [94]. Relevant researchers also improved the conditions and catalyzed the proton-type ILs reaction of propylamine to 2-oxazolidinone at 1 atmosphere CO_2 and 60 °C [95].

4.4. C–S Bond

Liu et al. reported for the first time the efficient synthesis of C–S bonds in benzothiazole using CO_2, 2-aminothiophene, and hydrosilane catalyzed by a metal-ion-free liquid at 40 °C and 5 MPa CO_2 [96]. The team found that [BMIM][Ac] exhibited the best catalytic activity and was able to activate CO_2, hydrosilane, and 2-aminothiophene through hydrogen bonding. The reaction mechanism is as follows: (1) formation of intermediates: first, intermediate A and hydrosilane/A complex B are formed; (2) attack: subsequently, methoxysilane C attacks 2-aminothiophene, forming the intermediate D; (3) release: hydrosilane and water are released through other intermediates E and F, resulting in the final product G. The main contribution of this study is to summarize the mechanism of C–N bond and C–S bond construction by CO_2 in ILs media. To date, this is the only study that uses ILs as a catalyst to construct C–S bonds from CO_2. Under the conditions of low CO_2 pressure and no hydrosilane, ILs as a catalyst and a solvent can maintain high selectivity and high efficiency, which provides valuable consideration for future research.

4.5. C1 Products

Brennecke et al. found that the use of [EMIM][Tf_2N] as the electrolyte promoted the formation of CO on the Pb electrode, but not the formation of oxalate anion [83]. With the increase of [EMIM][Tf_2N] concentration, the tendency of CO formation also increased, and carboxylate was formed.

Han et al. used supercritical CO_2 as a carbon source for CO_2 reduction on the Cu cathode and found that the main product was CO in the ionic liquid medium [BMIM][PF_6] [97]. The team has successfully demonstrated that both the product and the ILs can be effectively recycled without cross-contamination problems. In addition, Rosenzweig's group also explored modifying the product selectivity of CO_2 reduction reactions by changing ILs [98]. Under the same bismuth cathode conditions, the reduction of CO_2 to $HCOO^-$ or CO products can be controlled by choosing different ILs. Han's research group further developed a metal-free catalyst (graphene oxide–multi-walled carbon nanotube composite) that exhibited higher electrical activity than conventional Au and Ag electrodes in ILs/CH_3CN media, particularly in the reaction of reducing CO_2 to CO [99]. These studies show that ILs have great potential for application in the process of CO_2 electroreduction, and more efficient CO_2 conversion can be achieved by adjusting the properties of ILs and selecting suitable catalysts.

The study by Han et al. has pioneered a new pathway for the efficient and highly selective electrochemical conversion of CO_2 to CH_4 by combining a metal–organic framework (MOF) cathode and a pure ILs electrolyte [100]. Their study shows that this approach utilizes intermediates between CO_2 and CO for a more efficient CO_2 reduction process. Regarding the choice of ILs, it was shown that fluorine-containing imidazolium-based ILs (e.g., [BMIM][PF_6] > [BMIM][BF_4] > [BMIM][TFO]) were more efficient than non-fluorine-containing ILs (e.g., [BMIM][ClO_4]) for the CO_2 electroreduction reaction. This is due to the stronger interaction between fluorinated ILs and CO_2, which enhances the solubility and activation of CO_2 and, thus, promotes efficient electrochemical conversion. In addition, Jovanovic's group used [BMIM][BF_4] as a medium in their experiments based on a microscale electrochemical reactor to develop a mathematical model of the CO_2 reduction reaction. This model not only describes the processes involving CO_2 and H_2O as reactants but also predicts the generation of products including CH_4, CH_3OH, H_2, HCOOH, and HCHO [101]. This mathematical model helps to understand and optimize the conditions of the CO_2 electroreduction reaction to achieve higher product selectivity and efficiency. In summary, the work of Han et al. provides a new direction for the development of sustain-

able energy and chemical production by utilizing a combination of MOFs and fluorinated ILs to achieve efficient conversion of CO_2, which is important for mitigating climate change and enhancing energy efficiency.

4.6. C–C Bond

To our knowledge, there have been no reports about the C–C bond construction of CO_2 using thermal energy in ILs. However, with the help of electrochemical action, the construction of C–C bonds by CO_2 in ILs can be achieved with relative ease. Atobe and his team found that CO_2 solubility in [DEME][TFSI] increased significantly under supercritical CO_2 conditions. An ILs/supercritical CO_2 system facilitates the carboxylation of various organic halides on Pt, Cu, GC, and Ag electrodes.

In addition, by increasing the pressure of CO_2 and using the precious metal Pt [102], Dai et al. devised an innovative, direct, and efficient method for reacting CO_2 at atmospheric pressure with benzyl bromide to produce ethyl phenylacetate in [BMIM][BF_4], which is the main product. A Cu-Ni electrode is considered to be the key reason for the efficient reaction because of its high porosity and good adsorption capacity of CO_2 and substrate [103]. Huang et al. used a [BMIM][BF_4] electrolyte to construct a C–C bond between CO_2 and aromatic ketone and synthesized α-hydroxy-carboxylic acid methyl ester [104]. In addition, the results show that temperature, current density, total charge, electrode, and reactant concentration have significant effects on the yield of methyl α-hydroxy-carboxylate. Hiejima's team found that, by increasing the pressure and temperature of CO_2 on the platinum electrode, they could significantly improve the electrochemical carboxylation efficiency of alpha-chloro-ethylbenzene and successfully construct the C–C bond [105]. Huang's team avoided the use of volatile/toxic solvents, catalysts, or other auxiliary electrolytes, and successfully carboxylated 2-amino-5-bromopyridine with CO_2 using only ILs as the medium, with a yield of 75% and a selectivity of 100% for the product 6-aminoniacin [106].

4.7. C–N Bond

The Inesi team first obtained the electrically generated $O_2^{\bullet-}$ substance by electroactivating O_2/CO_2 in ILs. Then, using these electrically generated $O_2^{\bullet-}$ substances and amines and CO_2, the team successfully constructed C–N bonds to synthesize carbamates, of which 2-imidazolone is a byproduct. This process requires a lower negative potential than the direct CO_2 electroreduction method and avoids the use of other volatile and toxic organic solvents, auxiliary electrolytes, and catalysts [107]. Studies have also shown that Ni cathodes exhibit the best electrocatalytic activity at various types of electrodes, such as C, Cu, Pt, Pb, and Cu. In addition, in a [BMIM][BF_4] solution containing amines, CO_2, and the alkylating agent EtI, organic carbamates were successfully synthesized using amines and CO_2. In this process, without the use of other solvents and catalysts, the C–N bond is formed at 1.0 atm CO_2 and 55 °C. The study also shows that Pt electrodes exhibit the most effective cathode properties in Ni, Cu, and Pt [108].

5. Conclusions

ILs, with their unique structure and properties, are widely used in many fields, including as CO_2 adsorbents, activation promoters, electrolytes/solvents, catalysts, or cocatalysts. We discussed different types of ionic liquid catalysts and their catalytic mechanisms. ILs play an important role in the photocatalytic conversion, electrocatalytic conversion, photocatalytic conversion, and photothermal catalytic conversion of CO_2. The type of catalyst, operating temperature, pressure, and other factors (such as solvents or cocatalysts) all have an impact on the efficiency and selectivity of CO_2 conversion. By optimizing the solubility of CO_2 in the reaction system, reducing the overpotential of the electrocatalytic reaction, and reducing the activation energy of the reaction, the efficient catalytic conversion of CO_2 was realized. ILs, as controllable "green solvents", show their importance in various appli-

cations. Although remarkable progress has been made in the field of catalytic conversion of CO_2 into high-value-added products, several challenges remain.

(1) Although functional ILs have multiple functions in CO_2 conversion, problems such as high price, poor stability, and high viscosity still need to be solved. Because ILs are highly designable, they can be modified to meet a variety of requirements for industrial applications, such as reducing cost, improving stability, reducing viscosity, enhancing efficiency, increasing selectivity, and facilitating separation;
(2) Combining metal-free photocatalysts with task-specific ILs to capture CO_2 from the air and simulate artificial photosynthesis to produce high value-added products is a potential research direction in the future;
(3) Consider the use of low-cost metal-free catalysts for thermal conversion of CO_2 at room temperature and pressure to improve economy and practicality;
(4) ILs should be stable during thermal, electrical, and photocatalytic processes. Many ILs may break down or react with other chemicals after prolonged exposure to the environment. In particular, the problem to be solved is how to improve the stability of functionalized task-specific ILs.

Author Contributions: Writing—original draft preparation, P.W.; writing—review and editing, P.W., R.W.; supervision, R.W.; project administration, R.W.; funding acquisition, R.W. All authors have read and agreed to the published version of the manuscript.

Funding: This research was funded by the PetroChina Scientific and Technical Innovation Project (2013D-5006-0507).

Institutional Review Board Statement: Not applicable.

Informed Consent Statement: Not applicable.

Data Availability Statement: Not applicable.

Conflicts of Interest: The authors declare no conflicts of interest.

References

1. Xu, B.-H.; Wang, J.-Q.; Sun, J.; Huang, Y.; Zhang, J.-P.; Zhang, X.-P.; Zhang, S.-J. Fixation of CO_2 into cyclic carbonates catalyzed by ionic liquids: A multi-scale approach. *Green Chem.* **2015**, *17*, 108–122. [CrossRef]
2. Gao, W.; Liang, S.; Wang, R.; Jiang, Q.; Zhang, Y.; Zheng, Q.; Xie, B.; Toe, C.Y.; Zhu, X.; Wang, J.; et al. Industrial carbon dioxide capture and utilization: State of the art and future challenges. *Chem. Soc. Rev.* **2020**, *49*, 8584–8686. [CrossRef] [PubMed]
3. Zhang, M.; Xu, Y.; Williams, B.L.; Xiao, M.; Wang, S.; Han, D.; Sun, L.; Meng, Y. Catalytic materials for direct synthesis of dimethyl carbonate (DMC) from CO_2. *J. Clean. Prod.* **2021**, *279*, 123344. [CrossRef]
4. Guo, L.; Deng, L.; Hu, W.; Jin, X.; Yin, L. Ionic liquids as catalysts for conversion of CO_2 to propylene carbonate. *Chem. Ind. Eng. Prog.* **2017**, *36*, 3323–3328.
5. Cervantes-Reyes, A.; Farshadfar, K.; Rudolph, M.; Rominger, F.; Schaub, T.; Ariafard, A.; Hashmi, A.S.K. Copper-catalysed synthesis of α-alkylidene cyclic carbonates from propargylic alcohols and CO. *Green Chem.* **2021**, *23*, 889–897. [CrossRef]
6. Dong, T.; Zheng, Y.-J.; Yang, G.-W.; Zhang, Y.-Y.; Li, B.; Wu, G.-P. Crosslinked Resin-Supported Bifunctional Organocatalyst for Conversion of CO_2 into Cyclic Carbonates. *Chemsuschem* **2020**, *13*, 4121–4127. [CrossRef]
7. He, M.; Sun, Y.; Han, B. Green Carbon Science: Scientific Basis for Integrating Carbon Resource Processing, Utilization, and Recycling. *Angew. Chem. Int. Ed.* **2013**, *52*, 9620–9633. [CrossRef] [PubMed]
8. Zeng, S.; Zhang, X.; Bai, L.; Zhang, X.; Wang, H.; Wang, J.; Bao, D.; Li, M.; Liu, X.; Zhang, S. Ionic-Liquid-Based CO_2 Capture Systems: Structure, Interaction and Process. *Chem. Rev.* **2017**, *117*, 9625–9673. [CrossRef] [PubMed]
9. Dimitriou, I.; Garcia-Gutierrez, P.; Elder, R.H.; Cuellar-Franca, R.M.; Azapagic, A.; Allen, R.W.K. Carbon dioxide utilisation for production of transport fuels: Process and economic analysis. *Energy Environ. Sci.* **2015**, *8*, 1775–1789. [CrossRef]
10. Zhang, W.; Chen, Y.; Gao, Z.; Jin, F.; Zhang, J.; Li, C. Progress of functionalized ionic liquids for CO_2 absorption. *Mod. Chem. Ind.* **2017**, *37*, 41–45,47.
11. Torralba-Calleja, E.; Skinner, J.; Gutierrez-Tauste, D. CO_2 Capture in Ionic Liquids: A Review of Solubilities and Experimental Methods. *J. Chem.* **2013**, *2013*, 473584. [CrossRef]
12. Gurau, G.; Rodriguez, H.; Kelley, S.P.; Janiczek, P.; Kalb, R.S.; Rogers, R.D. Demonstration of Chemisorption of Carbon Dioxide in 1,3-Dialkylimidazolium Acetate Ionic Liquids. *Angew. Chem.—Int. Ed.* **2011**, *50*, 12024–12026. [CrossRef] [PubMed]
13. Sanchez, L.M.G.; Meindersma, G.W.; de Haan, A.B. Kinetics of absorption of CO_2 in amino-functionalized ionic liquids. *Chem. Eng. J.* **2011**, *166*, 1104–1115. [CrossRef]

14. Dong, K.; Zhang, S.; Wang, D.; Yao, X. Hydrogen bonds in imidazolium ionic liquids. *J. Phys. Chem. A* **2006**, *110*, 9775–9782. [CrossRef] [PubMed]
15. Bates, E.D.; Mayton, R.D.; Ntai, I.; Davis, J.H. CO_2 capture by a task-specific ionic liquid. *J. Am. Chem. Soc.* **2002**, *124*, 926–927. [CrossRef] [PubMed]
16. Zhang, Z.; Pan, S.-Y.; Li, H.; Cai, J.; Olabi, A.G.; Anthony, E.J.; Manovic, V. Recent advances in carbon dioxide utilization. *Renew. Sustain. Energy Rev.* **2020**, *125*, 109799. [CrossRef]
17. Liu, Q.; Wu, L.; Jackstell, R.; Beller, M. Using carbon dioxide as a building block in organic synthesis. *Nat. Commun.* **2015**, *6*, 5933. [CrossRef] [PubMed]
18. Du, H.; Ye, Y.; Xu, P.; Sun, J. Experimental and theoretical study on dicationic imidazolium derived poly(ionic liquid)s for catalytic cycloaddition of CO_2-epoxide. *J. CO_2 Util.* **2023**, *67*, 102325. [CrossRef]
19. Li, W.; Cheng, W.; Yang, X.; Su, Q.; Dong, L.; Zhang, P.; Yi, Y.; Li, B.; Zhang, S. Synthesis of Cyclic Carbonate Catalyzed by DBU Derived Basic Ionic Liquids. *Chin. J. Chem.* **2018**, *36*, 293–298. [CrossRef]
20. Li, Y.; Wang, L.; Huang, T.; Zhang, J.; He, H. Catalytic Activity of a Series of Synthesized and Newly Designed Pyridinium-Based Ionic Liquids on the Fixation of Carbon Dioxide: A DFT Investigation. *Ind. Eng. Chem. Res.* **2015**, *54*, 8093–8099. [CrossRef]
21. Zhang, Z.; Fan, F.; Xing, H.; Yang, Q.; Bao, Z.; Ren, Q. Efficient Synthesis of Cyclic Carbonates from Atmospheric CO_2 Using a Positive Charge Delocalized Ionic Liquid Catalyst. *ACS Sustain. Chem. Eng.* **2017**, *5*, 2841–2846. [CrossRef]
22. Yuan, G.; Zhao, Y.; Wu, Y.; Li, R.; Chen, Y.; Xu, D.; Liu, Z. Cooperative effect from cation and anion of pyridine-containing anion-based ionic liquids for catalysing CO_2 transformation at ambient conditions. *Sci. China-Chem.* **2017**, *60*, 958–963. [CrossRef]
23. Wang, L.; Li, P.; Jin, X.; Zhang, J.; He, H.; Zhang, S. Mechanism of fixation of CO_2 in the presence of hydroxyl-functionalized quaternary ammonium salts. *J. CO_2 Util.* **2015**, *10*, 113–119. [CrossRef]
24. Liu, S.; Suematsu, N.; Maruoka, K.; Shirakawa, S. Design of bifunctional quaternary phosphonium salt catalysts for CO_2 fixation reaction with epoxides under mild conditions. *Green Chem.* **2016**, *18*, 4611–4615. [CrossRef]
25. Li, Y.; Yao, X.; Liu, Y.; Li, M.; Su, Q.; Liu, Y.; Li, Y.; Yang, Z. Polymer-supported Quaternary Phosphonium Ionic Liquid Catalysts for Efficient Fixation of CO_2 into Cyclic Carbonates. *ChemistrySelect* **2023**, *8*, e202301449. [CrossRef]
26. Sun, J.; Li, X.; Yu, K.; Yin, J. A novel supported ionic liquid membrane reactor for catalytic CO_2 conversion. *J. CO_2 Util.* **2022**, *65*, 102216. [CrossRef]
27. Lee, M.-K.; Shim, H.-L.; Dharman, M.M.; Kim, K.-H.; Park, S.-W.; Park, D.-W. Synthesis of cyclic carbonate from allyl glycidyl ether and CO_2 over silica-supported ionic liquid catalysts prepared by sol-gel method. *Korean J. Chem. Eng.* **2008**, *25*, 1004–1007. [CrossRef]
28. Schaeffner, B.; Schaeffner, F.; Verevkin, S.P.; Boerner, A. Organic Carbonates as Solvents in Synthesis and Catalysis. *Chem. Rev.* **2010**, *110*, 4554–4581. [CrossRef]
29. Parker, H.L.; Sherwood, J.; Hunt, A.J.; Clark, J.H. Cyclic Carbonates as Green Alternative Solvents for the Heck Reaction. *ACS Sustain. Chem. Eng.* **2014**, *2*, 1739–1742. [CrossRef]
30. Beattie, C.; North, M.; Villuendas, P. Proline-Catalysed Amination Reactions in Cyclic Carbonate Solvents. *Molecules* **2011**, *16*, 3420–3432. [CrossRef]
31. Eshetu, G.G.; Bertrand, J.-P.; Lecocq, A.; Grugeon, S.; Laruelle, S.; Armand, M.; Marlair, G. Fire behavior of carbonates-based electrolytes used in Li-ion rechargeable batteries with a focus on the role of the LiPF6 and LiFSI salts. *J. Power Sources* **2014**, *269*, 804–811. [CrossRef]
32. Seo, D.M.; Reininger, S.; Kutcher, M.; Redmond, K.; Euler, W.B.; Lucht, B.L. Role of Mixed Solvation and Ion Pairing in the Solution Structure of Lithium Ion Battery Electrolytes. *J. Phys. Chem. C* **2015**, *119*, 14038–14046. [CrossRef]
33. Guo, W.; Laserna, V.; Martin, E.; Escudero-Adán, E.C.; Kleij, A.W. Stereodivergent Carbamate Synthesis by Selective in Situ Trapping of Organic Carbonate Intermediates. *Chemistry* **2015**, *22*, 1722–1727. [CrossRef] [PubMed]
34. Helou, M.; Miserque, O.; Brusson, J.M.; Carpentier, J.F.; Guillaume, S.M. Organocatalysts for the Controlled "Immortal" Ring-Opening Polymerization of Six-Membered-Ring Cyclic Carbonates: A Metal-Free, Green Process. *Chemistry* **2010**, *16*, 13805–13813. [CrossRef] [PubMed]
35. Besse, V.; Camara, F.; Voirin, C.; Auvergne, R.; Caillol, S.; Boutevin, B. Synthesis and applications of unsaturated cyclocarbonates. *Polym. Chem.* **2013**, *4*, 4545–4561. [CrossRef]
36. Suriano, F.; Pratt, R.; Tan, J.P.K.; Wiradharma, N.; Nelson, A.; Yang, Y.-Y.; Dubois, P.; Hedrick, J.L. Synthesis of a family of amphiphilic glycopolymers via controlled ring-opening polymerization of functionalized cyclic carbonates and their application in drug delivery. *Biomaterials* **2010**, *31*, 2637–2645. [CrossRef]
37. Kaur, P.; Chopra, H.K. Recent Advances in Applications of Supported Ionic Liquids. *Curr. Org. Chem.* **2019**, *23*, 2881–2915. [CrossRef]
38. Han, L.; Park, S.-W.; Park, D.-W. Silica grafted imidazolium-based ionic liquids: Efficient heterogeneous catalysts for chemical fixation of CO_2 to a cyclic carbonate. *Energy Environ. Sci.* **2009**, *2*, 1286–1292. [CrossRef]
39. Zheng, X.; Luo, S.; Zhang, L.; Cheng, J.-P. Magnetic nanoparticle supported ionic liquid catalysts for CO_2 cycloaddition reactions. *Green Chem.* **2009**, *11*, 455–458. [CrossRef]
40. Han, L.; Choi, H.-J.; Kim, D.-K.; Park, S.-W.; Liu, B.; Park, D.-W. Porous polymer bead-supported ionic liquids for the synthesis of cyclic carbonate from CO_2 and epoxide. *J. Mol. Catal. A Chem.* **2011**, *338*, 58–64. [CrossRef]

41. Sun, J.; Cheng, W.; Fan, W.; Wang, Y.; Meng, Z.; Zhang, S. Reusable and efficient polymer-supported task-specific ionic liquid catalyst for cycloaddition of epoxide with CO_2. *Catal. Today* **2009**, *148*, 361–367. [CrossRef]
42. Dai, W.-L.; Chen, L.; Yin, S.-F.; Li, W.-H.; Zhang, Y.-Y.; Luo, S.-L.; Au, C.-T. High-Efficiency Synthesis of Cyclic Carbonates from Epoxides and CO_2 over Hydroxyl Ionic Liquid Catalyst Grafted onto Cross-Linked Polymer. *Catal. Lett.* **2010**, *137*, 74–80. [CrossRef]
43. Lang, X.-D.; Yu, Y.-C.; Li, Z.-M.; He, L.-N. Protic ionic liquids-promoted efficient synthesis of quinazolines from 2-aminobenzonitriles and CO_2 at ambient conditions. *J. CO_2 Util.* **2016**, *15*, 115–122. [CrossRef]
44. Liu, F.; Ping, R.; Zhao, P.; Gu, Y.; Gao, J.; Liu, M. Succinimide-Based Ionic Liquids: An Efficient and Versatile Platform for Transformation of CO_2 into Quinazoline-2,4(1H,3H)-diones under Mild and Solvent-Free Conditions. *ACS Sustain. Chem. Eng.* **2019**, *7*, 13517–13522. [CrossRef]
45. Luo, C.; Wang, J.; Lu, H.; Wu, K.; Liu, Y.; Zhu, Y.; Wang, B.; Liang, B. Atmospheric-pressure synthesis of glycerol carbonate from CO_2 and glycerol catalyzed by protic ionic liquids. *Green Chem.* **2022**, *24*, 8292–8301. [CrossRef]
46. Shi, G.; Chen, K.; Wang, Y.; Li, H.; Wang, C. Highly Efficient Synthesis of Quinazoline-2,4(1H,3H)-diones from CO_2 by Hydroxyl Functionalized Aprotic Ionic Liquids. *ACS Sustain. Chem. Eng.* **2018**, *6*, 5760–5765. [CrossRef]
47. Zhu, A.; Tang, M.; Lv, Q.; Li, L.; Bai, S.; Li, Q.; Feng, W.; Li, Q.; Wang, J. Fixation of CO_2 in structurally diverse quinazoline-2,4(1H,3H)-diones under ambient conditions. *J. CO_2 Util.* **2019**, *34*, 500–506. [CrossRef]
48. Zhao, Y.; Wu, Y.; Yuan, G.; Hao, L.; Gao, X.; Yang, Z.; Yu, B.; Zhang, H.; Liu, Z. Azole-Anion-Based Aprotic Ionic Liquids: Functional Solvents for Atmospheric CO_2 Transformation into Various Heterocyclic Compounds. *Chem.—Asian J.* **2016**, *11*, 2735–2740. [CrossRef]
49. Qadir, M.I.; Dupont, J. Thermo- and Photocatalytic Activation of CO_2 in Ionic Liquids Nanodomains. *Angew. Chem. Int. Ed.* **2023**, *62*, e202301497. [CrossRef]
50. Wang, H.; Wu, Y.; Zhao, Y.; Liu, Z. Recent Progress on Ionic Liquid-Mediated CO_2 Conversion. *Acta Phys. Chim. Sin.* **2020**, *37*, 2010022. [CrossRef]
51. Chen, Y.; Zhao, Y.; Yu, B.; Wu, Y.; Yu, X.; Guo, S.; Han, B.; Liu, Z. Visible Light-Driven Photoreduction of CO_2 to CH4 over TiO2 Using a Multiple-Site Ionic Liquid as an Absorbent and Photosensitizer. *ACS Sustain. Chem. Eng.* **2020**, *8*, 9088–9094. [CrossRef]
52. Lin, J.; Ding, Z.; Hou, Y.; Wang, X. Ionic Liquid Co-catalyzed Artificial Photosynthesis of CO. *Sci. Rep.* **2013**, *3*, 1056. [CrossRef]
53. Lu, B.; Wang, X.; Li, Y.; Sun, J.; Zhao, J.; Cai, Q. Electrochemical conversion of CO_2 into dimethyl carbonate in a functionalized ionic liquid. *J. CO_2 Util.* **2013**, *3–4*, 98–101. [CrossRef]
54. Hu, Y.L.; Liu, X.B.; Rong, Q. Novel and highly efficient electro-catalytic cycloaddition of CO_2 and epoxides to cyclic carbonates over reusable ionic liquid-based cooperative catalytic system. *Green Chem. Lett. Rev.* **2023**, *16*, 2163192. [CrossRef]
55. Gao, Y.; Wang, X.; Guo, H.; Liu, L.; Wang, H.; Cui, W. Ionic liquids enhanced highly efficient photoelectrochemical reduction of CO_2 to ethanol over Cu_2O/TiO_2 nanoarrays. *Mol. Catal.* **2023**, *543*, 113161. [CrossRef]
56. Chaugule, A.A.; Bandhal, H.A.; Tamboli, A.H.; Chung, W.-J.; Kim, H. Highly efficient synthesis of dimethyl carbonate from methanol and carbon dioxide using IL/DBU/SmOCl as a novel ternary catalytic system. *Catal. Commun.* **2016**, *75*, 87–91. [CrossRef]
57. Zhao, H.; Lu, B.; Li, X.; Zhang, W.; Zhao, J.; Cai, Q. Hydroxyl-functionalized ionic liquid for activation and conversion of CO_2 and methanol into dimethyl carbonate. *J. CO_2 Util.* **2015**, *12*, 49–53. [CrossRef]
58. Strehmel, V. Radicals in Ionic Liquids. *ChemPhysChem* **2012**, *13*, 1649–1663. [CrossRef]
59. Wang, S.; Wang, X. Imidazolium Ionic Liquids, Imidazolylidene Heterocyclic Carbenes, and Zeolitic Imidazolate Frameworks for CO_2 Capture and Photochemical Reduction. *Angew. Chem.—Int. Ed.* **2016**, *55*, 2308–2320. [CrossRef]
60. Wu, F.; Xu, C.; Margulis, C.J. Dynamics of an excess hole in the 1-methyl-1-butyl-pyrrolidinium dicyanamide ionic-liquid. *J. Chem. Phys.* **2018**, *148*, 193831. [CrossRef]
61. Yilmaz, P.; Lacerda, A.M.; Larrosa, I.; Dunn, S. Photoelectrocatalysis of Rhodamine B and Solar Hydrogen Production by TiO_2 and Pd/TiO_2 Catalyst Systems. *Electrochim. Acta* **2017**, *231*, 641–649. [CrossRef]
62. Wei, Z.; Liang, F.; Liu, Y.; Luo, W.; Wang, J.; Yao, W.; Zhu, Y. Photoelectrocatalytic degradation of phenol-containing wastewater by $TiO_2/g\text{-}C_3N_4$ hybrid heterostructure thin film. *Appl. Catal. B-Environ.* **2017**, *201*, 600–606. [CrossRef]
63. Wang, Z.; Yang, C.; Lin, T.; Yin, H.; Chen, P.; Wan, D.; Xu, F.; Huang, F.; Lin, J.; Xie, X.; et al. Visible-light photocatalytic, solar thermal and photoelectrochemical properties of aluminium-reduced black titania. *Energy Environ. Sci.* **2013**, *6*, 3007–3014. [CrossRef]
64. Peng, Y.; Szeto, K.C.; Santini, C.C.; Daniele, S. Ionic Liquids as homogeneous photocatalyst for CO_2 reduction in protic solvents. *Chem. Eng. J. Adv.* **2022**, *12*, 100379. [CrossRef]
65. Rosen, B.A.; Salehi-Khojin, A.; Thorson, M.R.; Zhu, W.; Whipple, D.T.; Kenis, P.J.A.; Masel, R.I. Ionic Liquid-Mediated Selective Conversion of CO_2 to CO at Low Overpotentials. *Science* **2011**, *334*, 643–644. [CrossRef] [PubMed]
66. Oh, Y.; Hu, X. Ionic liquids enhance the electrochemical CO_2 reduction catalyzed by MoO2. *Chem. Commun.* **2015**, *51*, 13698–13701. [CrossRef] [PubMed]
67. Yang, D.; Li, L.; Wang, Q.; Wang, X.; Li, Q.; Shi, J. Catalytic Mechanism of Ionic Liquid for CO_2 Electrochemical Reduction. *Chem. J. Chin. Univ.—Chin.* **2016**, *37*, 94–99.
68. Yuan, D.; Yan, C.; Lu, B.; Wang, H.; Zhong, C.; Cai, Q. Electrochemical activation of carbon dioxide for synthesis of dimethyl carbonate in an ionic liquid. *Electrochim. Acta* **2009**, *54*, 2912–2915. [CrossRef]

69. Sun, X.; Zhu, Q.; Kang, X.; Liu, H.; Qian, Q.; Zhang, Z.; Han, B. Molybdenum–Bismuth Bimetallic Chalcogenide Nanosheets for Highly Efficient Electrocatalytic Reduction of Carbon Dioxide to Methanol. *Angew. Chem. Int. Ed.* **2016**, *55*, 6771–6775. [CrossRef] [PubMed]
70. Wang, P.; Wang, S.; Wang, H.; Wu, Z.; Wang, L. Recent Progress on Photo-Electrocatalytic Reduction of Carbon Dioxide. *Part. Part. Syst. Charact.* **2018**, *35*, 1700371.
71. Kondratenko, E.V.; Mul, G.; Baltrusaitis, J.; Larrazabal, G.O.; Perez-Ramirez, J. Status and perspectives of CO_2 conversion into fuels and chemicals by catalytic, photocatalytic and electrocatalytic processes. *Energy Environ. Sci.* **2013**, *6*, 3112–3135. [CrossRef]
72. Lu, W.; Jia, B.; Cui, B.; Zhang, Y.; Yao, K.; Zhao, Y.; Wang, J. Efficient Photoelectrochemical Reduction of Carbon Dioxide to Formic Acid: A Functionalized Ionic Liquid as an Absorbent and Electrolyte. *Angew. Chem. Int. Ed.* **2017**, *56*, 11851–11854. [CrossRef]
73. Zeng, G.; Qiu, J.; Hou, B.; Shi, H.; Lin, Y.; Hettick, M.; Javey, A.; Cronin, S.B. Enhanced Photocatalytic Reduction of CO_2 to CO through TiO_2 Passivation of InP in Ionic Liquids. *Chemistry* **2015**, *21*, 13502–13507. [CrossRef]
74. Wang, Y.; Liu, J.; Zheng, G. Designing Copper-Based Catalysts for Efficient Carbon Dioxide Electroreduction. *Adv. Mater.* **2021**, *33*, 2005798. [CrossRef]
75. Zheng, Y.; Vasileff, A.; Zhou, X.; Jiao, Y.; Jaroniec, M.; Qiao, S.-Z. Understanding the Roadmap for Electrochemical Reduction of CO_2 to Multi-Carbon Oxygenates and Hydrocarbons on Copper-Based Catalysts. *J. Am. Chem. Soc.* **2019**, *141*, 7646–7659. [CrossRef] [PubMed]
76. Jin, H.; Guo, C.; Liu, X.; Liu, J.; Vasileff, A.; Jiao, Y.; Zheng, Y.; Qiao, S.-Z. Emerging Two-Dimensional Nanomaterials for Electrocatalysis. *Chem. Rev.* **2018**, *118*, 6337–6408. [PubMed]
77. Feng, J.; Zeng, S.; Liu, H.; Feng, J.; Gao, H.; Bai, L.; Dong, H.; Zhang, S.; Zhang, X. Insights into Carbon Dioxide Electroreduction in Ionic Liquids: Carbon Dioxide Activation and Selectivity Tailored by Ionic Microhabitat. *Chemsuschem* **2018**, *11*, 3191–3197. [CrossRef]
78. Guo, Y.; Chen, W.; Feng, L.; Fan, Y.; Liang, J.; Wang, X.; Zhang, X. Greenery-inspired nanoengineering of bamboo-like hierarchical porous nanotubes with spatially organized bifunctionalities for synergistic photothermal catalytic CO_2 fixation. *J. Mater. Chem. A* **2022**, *10*, 12418–12428. [CrossRef]
79. Bai, L.; Shang, D.; Li, M.; Dai, Z.; Deng, L.; Zhang, X. CO_2 absorption with ionic liquids at elevated temperatures. *J. Energy Chem.* **2017**, *26*, 1001–1006. [CrossRef]
80. Li, P.; Liu, L.; An, W.; Wang, H.; Cui, W. Efficient photothermal catalytic CO_2 reduction to CH3CH2OH over $Cu_2O/g\text{-}C_3N_4$ assisted by ionic liquids. *Appl. Surf. Sci.* **2021**, *565*, 150448. [CrossRef]
81. Asadi, M.; Kim, K.; Liu, C.; Addepalli, A.V.; Abbasi, P.; Yasaei, P.; Phillips, P.; Behranginia, A.; Cerrato, J.M.; Haasch, R.; et al. Nanostructured transition metal dichalcogenide electrocatalysts for CO_2 reduction in ionic liquid. *Science* **2016**, *353*, 467–470. [CrossRef]
82. Rosen, B.A.; Haan, J.L.; Mukherjee, P.; Braunschweig, B.; Zhu, W.; Salehi-Khojin, A.; Dlott, D.D.; Masel, R.I. In Situ Spectroscopic Examination of a Low Overpotential Pathway for Carbon Dioxide Conversion to Carbon Monoxide. *J. Phys. Chem. C* **2012**, *116*, 15307–15312. [CrossRef]
83. Sun, L.; Ramesha, G.K.; Kamat, P.V.; Brennecke, J.F. Switching the Reaction Course of Electrochemical CO_2 Reduction with Ionic Liquids. *Langmuir* **2014**, *30*, 6302–6308. [CrossRef]
84. Qadir, M.I.; Weilhard, A.; Fernandes, J.A.; de Pedro, I.; Vieira, B.J.C.; Waerenborgh, J.C.; Dupont, J. Selective Carbon Dioxide Hydrogenation Driven by Ferromagnetic RuFe Nanoparticles in Ionic Liquids. *ACS Catal.* **2018**, *8*, 1621–1627. [CrossRef]
85. Zhang, Z.; Xie, E.; Li, W.; Hu, S.; Song, J.; Jiang, T.; Han, B. Hydrogenation of carbon dioxide is promoted by a task-specific ionic liquid. *Angew. Chem.—Int. Ed.* **2008**, *47*, 1127–1129. [CrossRef] [PubMed]
86. Melo, C.I.; Szczepanska, A.; Bogel-Lukasik, E.; da Ponte, M.N.; Branco, L.C. Hydrogenation of Carbon Dioxide to Methane by Ruthenium Nanoparticles in Ionic Liquid. *Chemsuschem* **2016**, *9*, 1081–1084. [CrossRef] [PubMed]
87. Qiu, J.; Zhao, Y.; Li, Z.; Wang, H.; Fan, M.; Wang, J. Efficient Ionic-Liquid-Promoted Chemical Fixation of CO_2 into α-Alkylidene Cyclic Carbonates. *Chemsuschem* **2017**, *10*, 1120–1127. [CrossRef] [PubMed]
88. Tak, R.K.; Patel, P.; Subramanian, S.; Kureshy, R.I.; Khan, N.-u.H. Cycloaddition Reaction of Spiro-Epoxy Oxindole with CO_2 at Atmospheric Pressure Using Deep Eutectic Solvent. *ACS Sustain. Chem. Eng.* **2018**, *6*, 11200–11205. [CrossRef]
89. Chen, Y.; Luo, R.; Xu, Q.; Jiang, J.; Zhou, X.; Ji, H. Metalloporphyrin Polymers with Intercalated Ionic Liquids for Synergistic CO_2 Fixation via Cyclic Carbonate Production. *ACS Sustain. Chem. Eng.* **2018**, *6*, 1074–1082. [CrossRef]
90. Zhao, T.; Hu, X.; Wu, D.; Li, R.; Yang, G.; Wu, Y. Direct Synthesis of Dimethyl Carbonate from Carbon Dioxide and Methanol at Room Temperature Using Imidazolium Hydrogen Carbonate Ionic Liquid as a Recyclable Catalyst and Dehydrant. *Chemsuschem* **2017**, *10*, 2046–2052. [CrossRef]
91. Zhang, Q.; Yuan, H.-Y.; Fukaya, N.; Yasuda, H.; Choi, J.-C. Direct synthesis of carbamate from CO_2 using a task-specific ionic liquid catalyst. *Green Chem.* **2017**, *19*, 5614–5624. [CrossRef]
92. Yang, Z.-Z.; He, L.-N.; Peng, S.-Y.; Liu, A.-H. Lewis basic ionic liquids-catalyzed synthesis of 5-aryl-2-oxazolidinones from aziridines and CO_2 under solvent-free conditions. *Green Chem.* **2010**, *12*, 1850–1854. [CrossRef]
93. Yang, Z.-Z.; Li, Y.-N.; Wei, Y.-Y.; He, L.-N. Protic onium salts-catalyzed synthesis of 5-aryl-2-oxazolidinones from aziridines and CO_2 under mild conditions. *Green Chem.* **2011**, *13*, 2351–2353. [CrossRef]
94. Hu, J.; Ma, J.; Zhang, Z.; Zhu, Q.; Zhou, H.; Lu, W.; Han, B. A route to convert CO_2: Synthesis of 3,4,5-trisubstituted oxazolones. *Green Chem.* **2015**, *17*, 1219–1225. [CrossRef]

95. Hu, J.; Ma, J.; Zhu, Q.; Zhang, Z.; Wu, C.; Han, B. Transformation of Atmospheric CO_2 Catalyzed by Protic Ionic Liquids: Efficient Synthesis of 2-Oxazolidinones. *Angew. Chem.—Int. Ed.* **2015**, *54*, 5399–5403. [CrossRef] [PubMed]
96. Gao, X.; Yu, B.; Yang, Z.; Zhao, Y.; Zhang, H.; Hao, L.; Han, B.; Liu, Z. Ionic Liquid-Catalyzed C–S Bond Construction using CO_2 as a C1 Building Block under Mild Conditions: A Metal-Free Route to Synthesis of Benzothiazoles. *ACS Catal.* **2015**, *5*, 6648–6652. [CrossRef]
97. Zhao, G.Y.; Jiang, T.; Han, B.X.; Li, Z.H.; Zhang, J.M.; Liu, Z.M.; He, J.; Wu, W.Z. Electrochemical reduction of supercritical carbon dioxide in ionic liquid 1-n-butyl-3-methylimidazolium hexafluorophosphate. *J. Supercrit. Fluids* **2004**, *32*, 287–291. [CrossRef]
98. Atifi, A.; Boyce, D.W.; DiMeglio, J.L.; Rosenthal, J. Directing the Outcome of CO_2 Reduction at Bismuth Cathodes Using Varied Ionic Liquid Promoters. *ACS Catal.* **2018**, *8*, 2857–2863. [CrossRef] [PubMed]
99. Zhu, Q.; Ma, J.; Kang, X.; Sun, X.; Hu, J.; Yang, G.; Han, B. Electrochemical reduction of CO_2 to CO using graphene oxide/carbon nanotube electrode in ionic liquid/acetonitrile system. *Sci. China-Chem.* **2016**, *59*, 551–556. [CrossRef]
100. Kang, X.; Zhu, Q.; Sun, X.; Hu, J.; Zhang, J.; Liu, Z.; Han, B. Highly efficient electrochemical reduction of CO_2 to CH4 in an ionic liquid using a metal-organic framework cathode. *Chem. Sci.* **2016**, *7*, 266–273. [CrossRef]
101. Miao, Y.; Siri-Nguan, N.; Sornchamni, T.; Jovanovic, G.N.; Yokochi, A.F. CO_2 reduction in wet ionic liquid solution in microscale-based electrochemical reactor. *Chem. Eng. J.* **2018**, *333*, 300–309. [CrossRef]
102. Tateno, H.; Nakabayashi, K.; Kashiwagi, T.; Senboku, H.; Atobe, M. Electrochemical fixation of CO_2 to organohalides in room-temperature ionic liquids under supercritical CO_2. *Electrochim. Acta* **2015**, *161*, 212–218. [CrossRef]
103. Dai, Y.; Niu, L.; Liu, H.; Zou, J.; Yu, L.; Feng, Q. Cu-Ni Alloy Catalyzed Electrochemical Carboxylation of Benzyl Bromide with Carbon Dioxide in Ionic Liquid 1-Butyl-3-methylimidazolium tetrafluoroborate. *Int. J. Electrochem. Sci.* **2018**, *13*, 1084–1095.
104. Feng, Q.; Huang, K.; Liu, S.; Yu, J.; Liu, F. Electrocatalytic carboxylation of aromatic ketones with carbon dioxide in ionic liquid 1-butyl-3-methylimidazoliumtetrafluoborate to α-hydroxy-carboxylic acid methyl ester. *Electrochim. Acta* **2011**, *56*, 5137–5141. [CrossRef]
105. Hiejima, Y.; Hayashi, M.; Uda, A.; Oya, S.; Kondo, H.; Senboku, H.; Takahashi, K. Electrochemical carboxylation of α-chloroethylbenzene in ionic liquids compressed with carbon dioxide. *Phys. Chem. Chem. Phys.* **2010**, *12*, 1953–1957. [CrossRef] [PubMed]
106. Feng, Q.; Huang, K.; Liu, S.; Wang, X. Electrocatalytic carboxylation of 2-amino-5-bromopyridine with CO_2 in ionic liquid 1-butyl-3-methyllimidazoliumtetrafluoborate to 6-aminonicotinic acid. *Electrochim. Acta* **2010**, *55*, 5741–5745. [CrossRef]
107. Feroci, M.; Chiarotto, I.; Orsini, M.; Sotgiu, G.; Inesi, A. Carbon dioxide as carbon source: Activation via electrogenerated $O_2^{\ -}$ in ionic liquids. *Electrochim. Acta* **2011**, *56*, 5823–5827. [CrossRef]
108. Feroci, M.; Orsini, M.; Rossi, L.; Sotgiu, G.; Inesi, A. Electrochemically promoted C–N bond formation from amines and CO_2 in ionic liquid BMIm-BF4: Synthesis of carbamates. *J. Org. Chem.* **2007**, *72*, 200–203. [CrossRef]

Disclaimer/Publisher's Note: The statements, opinions and data contained in all publications are solely those of the individual author(s) and contributor(s) and not of MDPI and/or the editor(s). MDPI and/or the editor(s) disclaim responsibility for any injury to people or property resulting from any ideas, methods, instructions or products referred to in the content.

MDPI AG
Grosspeteranlage 5
4052 Basel
Switzerland
Tel.: +41 61 683 77 34

Molecules Editorial Office
E-mail: molecules@mdpi.com
www.mdpi.com/journal/molecules

Disclaimer/Publisher's Note: The title and front matter of this reprint are at the discretion of the Guest Editors. The publisher is not responsible for their content or any associated concerns. The statements, opinions and data contained in all individual articles are solely those of the individual Editors and contributors and not of MDPI. MDPI disclaims responsibility for any injury to people or property resulting from any ideas, methods, instructions or products referred to in the content.

Academic Open
Access Publishing

mdpi.com

ISBN 978-3-7258-9204-4